Vasken Dilsizian
Jagat Narula
Editors

Atlas of Nuclear Cardiology

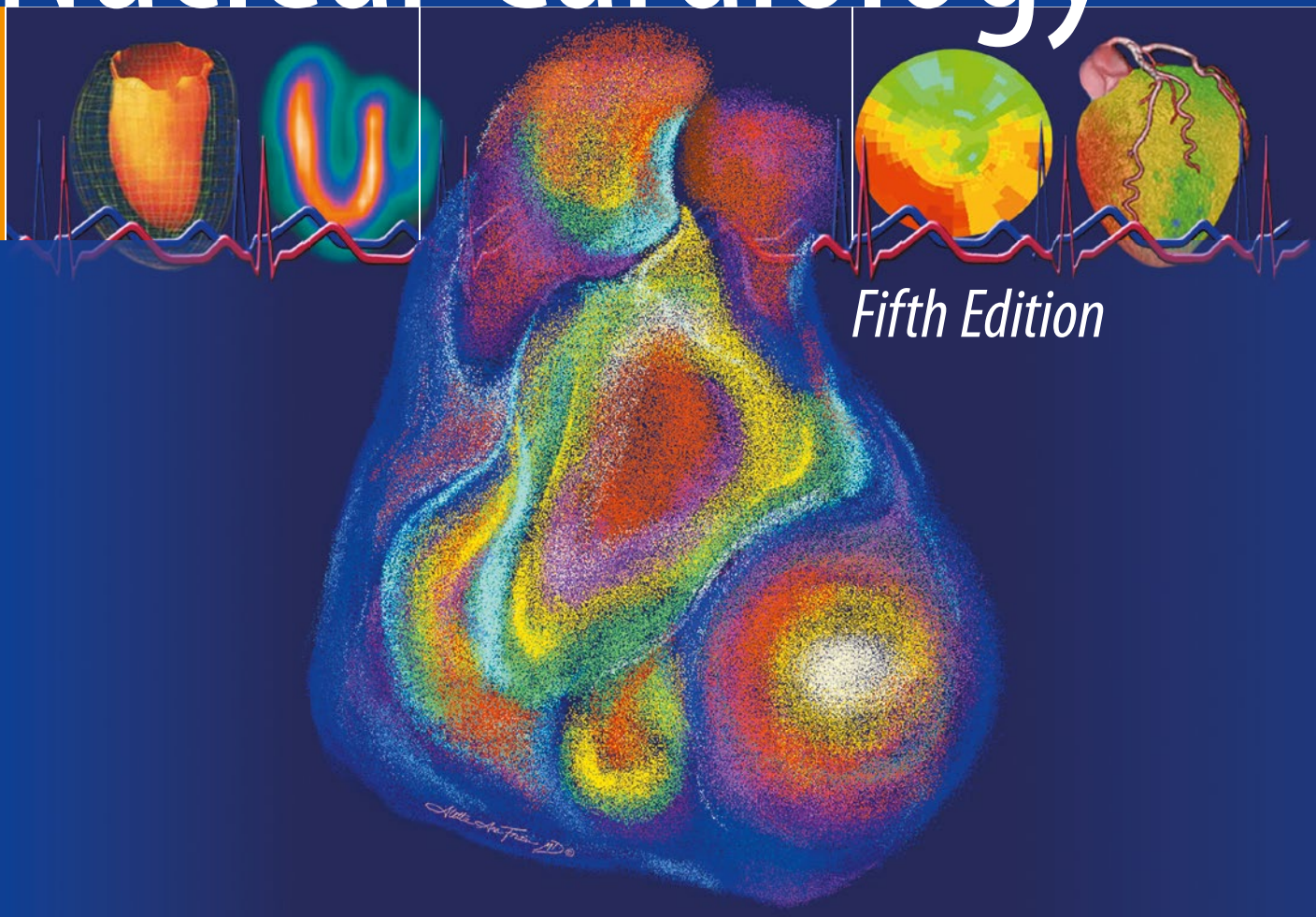

Fifth Edition

Springer

Atlas of Nuclear Cardiology

Vasken Dilsizian • Jagat Narula
Editors

Atlas of Nuclear Cardiology

Fifth Edition

Springer

Editors
Vasken Dilsizian
University of Maryland School of Medicine
Baltimore, MD
USA

Jagat Narula
Icahn School of Medicine at Mount Sinai
New York, NY
USA

The cover illustration is original artwork by Dr. Aletta Ann Frazier, and she retains the copyright to this image (anniefrazier@icloud.com)

ISBN 978-3-030-49884-9 ISBN 978-3-030-49885-6 (eBook)
https://doi.org/10.1007/978-3-030-49885-6

This Springer imprint is published by the registered company Springer Nature Switzerland AG
The registered company address is: Gewerbestrasse 11, 6330 Cham, Switzerland

Preface

Over the past four decades, nuclear cardiology has evolved from a research tool into a well-established clinical discipline. Approximately nine million nuclear cardiology procedures are performed annually in the USA. The field has excelled in the noninvasive evaluation and quantification of myocardial perfusion, function, metabolism, and innervation. Unlike anatomically oriented approaches to diagnostic medicine, the strengths of nuclear techniques are based on physiologic, biochemical, and molecular properties. The ability to define myocardial perfusion, viability, and ventricular function from a single study has become a powerful diagnostic and prognostic tool. As a result of its important contribution to the management and care of cardiac patients, nuclear cardiology is now recognized as a distinct clinical entity.

Nuclear cardiology first originated as a discipline in the early 1970s. A major breakthrough in the field came with the development of myocardial perfusion radiotracers, such as ^{201}TI, which permitted noninvasive detection and physiologic characterization of anatomic coronary artery lesions. First-pass and equilibrium radionuclide angiography allowed for the noninvasive assessment of regional and global left ventricular function. The field blossomed further with incorporation of the concepts of exercise physiology, demand-supply mismatch, coronary vasodilator reserve, and systolic and diastolic left ventricular dysfunction in nuclear testing. Pharmacologic vasodilators, such as dipyridamole, adenosine, and the selective A_{2A} receptor agonist regadenoson, widened the application of myocardial perfusion studies to patients who were unable to exercise, had uncomplicated acute coronary syndromes, or were undergoing intermediate- to high-risk noncardiac surgical procedures. Subsequently, the field advanced from detection of coronary artery disease to risk stratification and prognosis. As such, nuclear cardiology procedures have become the cornerstone of the decision-making process to appropriately select patients for medical or interventional therapy, as well as monitoring the effectiveness of that therapy.

Parallel advances in both radiopharmaceuticals and instrumentation have further fostered the growth of nuclear cardiology. The introduction of ^{99m}Tc-labeled perfusion tracers in the 1990s improved the count rate and image quality of myocardial perfusion studies, which allowed for electrocardiogram-gated acquisition and simultaneous assessment of regional myocardial perfusion and function with a single radiotracer. Because ^{99m}Tc-labeled perfusion tracers demonstrate minimal redistribution over time after injection, they have been used in the emergency room and in the early hours of an infarct to estimate the extent of myocardium in jeopardy. A follow-up study, performed several days later, provides information on final infarct size and myocardial salvage. PET has broadened the scope of the cardiac examination from perfusion and function alone to assessment of metabolic substrate utilization, cardiac receptor occupancy, and adrenergic neuronal function. By allowing the quantification of myocardial blood flow in absolute terms, PET has led to a better understanding of the physiologic mechanisms underlying cardiovascular diseases beyond discrete epicardial coronary artery disease, such as coronary vasomotor function in the early stages of coronary atherosclerosis development, hypertrophic cardiomyopathy, and dilated nonischemic cardiomyopathy. The ability to image the shift in the primary source of myocardial energy production from fatty acids toward glucose utilization in the setting of reduced blood flow has helped explain the pathophysiology of hibernation and myocardial viability, as well as management of patients with chronic

ischemic left ventricular dysfunction and heart failure for the assessment of myocardial viability. Targeted molecular imaging and image-guided therapy will further improve the management of heart disease by identifying patients for whom the response to medical therapy would be optimal or perhaps not beneficial at all, as we move closer to personalized medicine.

The aim of the fifth edition of the *Atlas of Nuclear Cardiology* is to elucidate the role of cardiovascular nuclear procedures in the clinical practice of cardiology. Diagnostic algorithms and schematic diagrams integrated with nuclear cardiology procedures are generously interspersed with color illustrations to emphasize key concepts in cardiovascular physiology, pathology, metabolism, and innervation. The first chapter provides history of nuclear cardiology while the second and third chapters review the principles of nuclear cardiology imaging, an introduction to instrumentation, image acquisition, radionuclide handling techniques, and radiation safety. The next two chapters (Chaps. 4 and 5) detail properties of SPECT and PET myocardial perfusion tracers, mechanisms of uptake, image display, and interpretation along with physiologic and pharmacologic stressors for the detection of coronary artery disease. In Chap. 6, clinical coronary physiology and the potential benefits of quantitative approaches that measure myocardial blood flow with PET and its changes in response to interventions are presented in absolute and relative terms. In Chap. 7, the techniques of first-pass and equilibrium radionuclide angiography and gated myocardial perfusion SPECT are reviewed for assessment of cardiac function. Chapter 8 details current evidence for the use of myocardial perfusion imaging for risk stratification in patients with chronic coronary artery disease, in special populations such as women, diabetics, the elderly, and patients of diverse ethnicity, and for identifying survival benefits with revascularization versus medical therapy. The next three chapters (Chaps. 9, 10, and 11) focus on the role of imaging cardiac metabolism in identifying ischemic and viable myocardium as well as the importance of the myocardial autonomic nervous system and sympathetic neuronal imaging targets for prevention of heart failure and left ventricular remodeling. Chapter 12 addresses the role of cardiac imaging in the diagnosis and risk stratification of patients suffering from acute coronary syndromes. Chapter 13 describes new emerging imaging techniques for the diagnosis of cardiac sarcoidosis, amyloidosis, and cardiovascular prosthetic device infections. The last chapter (Chapter 14) examines the latest molecular approaches of radionuclide techniques for imaging inflammation and calcification in atherosclerosis and its clinical and prognostic relevance.

In the next century, innovative imaging strategies in nuclear cardiology will propel the field into molecular imaging and personalized medicine while it continues to build on its already well-defined strengths of myocardial perfusion, function, metabolism, and innervation. Realization of these ideas and progress in the diagnosis, treatment, and prevention of cardiovascular disease will depend not only on new discoveries but also on meaningful interaction between clinicians and investigators. It is our hope that the fifth edition of the *Atlas of Nuclear Cardiology* will serve as a foundation for clinicians and a reference guide for scientists within and outside the field.

Baltimore, MD, USA — Vasken Dilsizian
New York, NY, USA — Jagat Narula

Contents

Contributors

Jack P. Andrews, MD University of Edinburgh, Edinburgh, UK

Stephen L. Bacharach Department of Radiology, Center for Molecular and Functional Imaging, University of California San Francisco School of Medicine, San Francisco, CA, USA

Frank M. Bengel, MD Department of Nuclear Medicine, Hannover Medical School, Hannover, Germany

Daniel S. Berman, MD S. Mark Taper Foundation Imaging Center, Cedars-Sinai Medical Center, Los Angeles, CA, USA

Elias H. Botvinick University of California San Francisco School of Medicine, San Francisco, CA, USA

Ji Chen, PhD Department of Radiology and Imaging Sciences, Emory University School of Medicine, Atlanta, GA, USA

Nick G. Costouros, MD Department of Radiology, University of California San Francisco School of Medicine, San Francisco, CA, USA

Carlos D. Davila, MD Division of Cardiology, Tufts University Medical Center, Boston, MA, USA

Vasken Dilsizian, MD, MASNC, FACC, FAHA University of Maryland School of Medicine, Baltimore, MD, USA

Sharmila Dorbala, MD, MPH, FACC, FASNC Division of Nuclear Medicine, Cardiovascular Imaging Section, Department of Radiology and Medicine, Brigham and Women's Hospital, Boston, MA, USA

Marc R. Dweck, MD, PhD, FACC Center for Cardiovascular Science, University of Edinburgh, Edinburgh, UK

Rodney H. Falk, MD Department of Medicine, Cardiovascular Medicine, Brigham and Women's Hospital, Boston, MA, USA

James R. Galt, PhD Department of Radiology and Imaging Sciences, Emory University School of Medicine, Atlanta, GA, USA

Ernest V. Garcia, PhD Department of Radiology and Imaging Sciences, Emory University School of Medicine, Atlanta, GA, USA

Guido Germano, MD David Geffen School of Medicine, University of California Los Angeles, Los Angeles, CA, USA

K. Lance Gould, MD Weatherhead PET Center for Preventing and Reversing Atherosclerosis, University of Texas Medical School at Houston, Houston, TX, USA

Rory Hachamovitch, MD Department of Cardiovascular Medicine, Section of Cardiovascular Imaging, Heart and Vascular Institute, Cleveland Clinic, Cleveland, OH, USA

Arnold F. Jacobson, MD, PhD Diagram Consulting, Kihei, HI, USA

Nils P. Johnson, MD, MS Division of Cardiology, University of Texas Medical School at Houston, Houston, TX, USA

Richard Kirkeeide, PhD Department of Internal Medicine, McGovern Medical School, University of Texas Health Sciences Center at Houston, Houston, TX, USA

Jennifer H. Mieres, MD, FACC, MASNC, FAHA Center for Equity of Care, Northwell Health, Zucker School of Medicine at Hofstra/Northwell, New Hyde Park, NY, USA

D. Douglas Miller, MD, CM, MBA Department of Cardiology, Augusta University Medical Center, Augusta, GA, USA

Robert J. H. Miller, MD Departments of Imaging and Medicine, Cedars-Sinai Medical Center, Los Angeles, CA, USA

Jagat Narula, MD, PhD, MACC, MASNC Icahn School of Medicine at Mount Sinai, New York, NY, USA

Tung T. Nguyen, MD Division of Cardiology, University of Texas Medical School at Houston, Houston, TX, USA

J. William O'Connell, MS University of California San Francisco School of Medicine, San Francisco, CA, USA

Lawrence M. Phillips, MD, FACP, FASNC, FACC Department of Nuclear Cardiology, Leon H. Charney Division of Cardiology, New York University Langone Health, New York, NY, USA

Marina Piccinelli, PhD Department of Radiology and Imaging Sciences, Emory University School of Medicine, Atlanta, GA, USA

Azar Radfar, MD, PhD Cardiology Division, Massachusetts General Hospital and Harvard Medical School, Boston, MA, USA

Antti Saraste, MD, PhD, FESC Turku PET Centre, Turku University Hospital and University of Turku, Turko, Finland

Markus Schwaiger, MD Department of Nuclear Medicine, Technical University of Munich, Munich, Germany

Leslee J. Shaw, PhD, MASNC, FACC, FAHA, MSCCT Dalio Institute of Cardiovascular Imaging, New York-Presbyterian Hospital and Weill Cornell Medicine, New York, NY, USA

H. William Strauss, MD Molecular Imaging and Therapy Service, Memorial Sloan Kettering Cancer Center, New York, NY, USA

Heinrich Taegtmeyer, MD, PhD The University of Texas Health Science Center at Houston, McGovern Medical School, Houston, TX, USA

Ahmed Tawakol, MD Cardiology Division, Massachusetts General Hospital and Harvard Medical School, Boston, MA, USA

James E. Udelson, MD Department of Medicine, CardioVascular Center, Tufts University Medical Center, Boston, MA, USA

Pat Zanzonico, PhD, DABR Department of Medical Physics, Memorial Sloan Kettering Cancer Center, New York, NY, USA

History of Nuclear Cardiology

1

H. William Strauss

The field of Nuclear Cardiology utilizes the unique properties of radiopharmaceuticals to characterize the pathophysiology of cardiovascular diseases. The images can be used to calculate global and regional function, perfusion, innervation, and apoptosis, among other characteristics. The ability to perform these measurements is the aggregate result of thousands of investigations and publications by dedicated investigators. This chapter describes some of the key contributions made by a few of these investigators and the role of their contributions in the development of this vibrant field.

Discovery of Natural Radioactivity: Antoine Henri Becquerel

Nuclear Cardiology began in 1896 with the discovery of natural radioactivity by Antoine Henri Becquerel (Fig. 1.1). Less than 1 year after the description of x-rays by Roentgen in November 1895, Becquerel hypothesized that substances demonstrating phosphorescence in the form of *visible* light would also emit *invisible* light in the form of x-rays. (According to Merriam-Webster, a substance is *phosphorescent* if it absorbs radiation at one wavelength followed by reradiation at a different wavelength.) One of the phosphorescent materials tested was potassium uranyl sulfate (^{238}U emits energetic alpha particles, and < 1% gammas.)

Fig. 1.1 Henri Becquerel [2]

Becquerel tested his hypothesis by exciting these materials with sunlight. After "exciting" the specimen, he put the specimen in front of a photographic plate wrapped in black paper (to prevent exposure from ambient light). He also wrapped pieces of metal to absorb some of the invisible rays, to create a pattern on the photographic plate. When he developed the plate he saw the pattern of the attenuator on the photographic plate. Becquerel was surprised to see that the photographic plate was exposed even on a cloudy day, suggesting that factors other than exposure to sunlight caused the exposure. In 1896, Becquerel reported that these invisible rays are similar to the rays studied by Röntgen, but were due to something in the uranium itself. These rays were the result of 'radioactivity', a name given by Marie Curie [1].

The importance of the observation of "natural" radioactivity by Becquerel and his colleagues, Pierre and Marie Curie, was recognized by awarding these investigators the Nobel Prize in 1903 [2].

H. W. Strauss (✉)
Molecular Imaging and Therapy Service, Memorial Sloan Kettering Cancer Center, New York, NY, USA

V. Dilsizian, J. Narula (eds.), *Atlas of Nuclear Cardiology*, https://doi.org/10.1007/978-3-030-49885-6_1

Understanding the Nature of Radiation

In 1899, Ernest Rutherford, working in the laboratory of his mentor J.J Thompson (discoverer of the electron), discovered that there were at least two different forms of radiation: a positively charged particle, which Rutherford called *alpha*, and the other one, more penetrating and negatively charged, which he called *beta*. In 1900, Paul Villard, a French physicist, discovered rays that were much more penetrating than alpha or beta particles and were not affected by electrical or magnetic fields. Rutherford named these *gamma* rays.

Other curious minds enhanced our understanding of the atom and radioactivity. Many of these contributions were recognized with the Nobel prize. Table 1.1 is an incomplete list of Nobel Laureates who contributed to our understanding of the heart and the physics and chemistry of radioactivity.

Laureate	Major contribution	Year
Antoine Becquerel, Pierre Curie, Marie Curie	Discovery of spontaneous radioactivity	1903
Ernest Rutherford	Disintegration of the elements, and the chemistry of radioactive substances	1908
Albert Einstein	Described the photoelectric effect (and the relationship of mass to energy)	1921
Niels Bohr	Investigation into the structure of atoms	1922
Willem Einthoven	Electrocardiogram	1924
Arthur Holly Compton	Discovery of the Compton effect	1927
Otto Warburg	Mode of action of the respiratory enzyme	1931
Paul Dirac	Postulated the existence of the antimatter, including the positron, based on an analysis of the quantum theory and Einstein's theory of relativity	1933
Carl Anderson	Discovered the positron by analyzing vapor trails in a cloud chamber in a magnetic field	1936
Enrico Fermi	Neutron irradiation (nuclear reactor)	1938
Ernest Lawrence	Invention of the cyclotron	1939
George de Hevesy	Use of isotopes as tracers	1943
Glenn Seaborg	Chemistry of transuranium elements; co-discoverer of technetium-99m (with Emilio Segre and Carlo Perrier)	1951
Hans Adolf Krebs	Citric acid cycle	1953
Andre Cournand, Werner Forssmann, Dickinson Richards	Heart catheterization	1956
William Shockley, John Bardeen, Walter Brattan	Inventors of the semiconductor	1956
Pavel Cherenkov	Cherenkov effect	1958
Robert Hofstader	Scintillation detector	1961
Rosalyn Yalow	Radioimmunoassay	1977
Henry Taube	Technetium chemistry	1983
Georges Kohler, Cesar Milstein	Monoclonal antibodies	1984
Michael Brown, Joseph Goldstein	Cholesterol metabolism	1985
Robert Furchgott, Louis Ignarro, Ferid Murad	Nitric oxide cardiovascular signaling	1998

Table 1.1 Incomplete List of Nobel Laureates with Discoveries Contributing to the Advancement of Nuclear Cardiology

First Tracer Study in Humans: Herrmann Blumgart

Thirty years after Becquerel described radioactivity, Herrmann Ludwig Blumgart (Fig. 1.2), a 30-year-old physician, working with a medical student, Otto C. Yens, performed the first radiotracer examination in a human subject, to measure the velocity of blood flow [3]. The seminal manuscript described the criteria for a clinically useful radiotracer and the importance of matching the instrument to the clinical measurement.

Fig. 1.2 Herrmann Blumgart, 1924

Blumgart developed his interest in physiology as a medical student, working under the famed physiologist Walter Cannon [4]. As indicated in the 1927 publication in the *Journal of Clinical Investigation* [3], other investigators had measured the circulation time with other methods, such as injection of methylene blue and observing changes in transillumination of blood in the carotid artery, injection of hypertonic saline while observing changes in conductivity of blood between nonpolarizable electrodes in another vein, or injecting fluorescein in one antecubital vein and taking blood samples every 5 seconds from the contralateral cubital vein. The authors point out the weaknesses in each of these techniques, including difficulty cannulating a vessel, resulting in frequent clotting. There was also a requirement for continuous sampling, which was difficult to control. They noted that "the velocity measurements which depend on the insertion of a mechanical device into the blood stream defeats its ends…and cannot be considered for clinical application. The most feasible method appears to be the injection of some substance at one point in the body, and the measurement of the time of its arrival at another point."

The authors specified the requirements for the tracer material:

- The substance must not be toxic in the amounts utilized.
- The substance should not be present previously in the body.
- The substance must not in any way disturb the very phenomena under investigation.
- It is desirable that the substance disappear from the body with sufficient rapidity to allow repeated measurements.
- The substance must be readily detectable in minute amounts.

After considering many alternatives, they settled on the use of a saline solution containing dissolved radon gas. They tested it on themselves, with Blumgart as the first subject, and concluded that the radiotracer was safe.

Selection of an appropriate detector presented additional challenges. The initial choice was an electroscope, but there were problems with shielding, and difficulty judging the onset of response. An early version of the Geiger counter was also tested, but the "relatively high number of spontaneous discharges discouraged the choice of this mode of detection." The Shimizu modification of the Wilson cloud chamber, a device capable of making measurements 1 to 5 times per second with a rapid response to the arrival of ionizing radiation, was selected. In normal subjects, the time required for the tracer to travel from a vein in one arm to an artery in the other was found to be "from 15 to 21 seconds." In contrast, the velocities in three patients with cardiac decompensation were 53, 65, and 50 seconds.

The Radiocardiogram: Myron Prinzmetal

Fig. 1.3 Myron Prinzmetal

Two decades later, Myron Prinzmetal (Fig. 1.3) and colleagues (yes, the same Myron Prinzmetal of Prinzmetal's variant angina [5]) used a collimated Geiger tube placed over the precordium and ^{24}Na as the tracer in a 1948 publication [6] describing the curves recorded during the passage of the tracer through the heart and lungs. The biphasic curve was analyzed to determine cardiac output, right and left ventricular chamber volume, stroke volume, and pulmonary blood volume [7].

Radionuclide Imaging

In addition to analyzing curves, instruments were being developed to allow images of the distribution of radiotracers. The rectilinear scanner, developed to image the thyroid by Ben Cassen in 1951, was used to image the cardiac blood pool in 1958. The rectilinear scanner consisted of a collimated radiation detector connected to an apparatus that placed dots on a piece of paper each time a certain number of events were detected. The radiation detector moved along a line; when it reached the end of the line it stepped down to the next line, and moved back to reach the end of the line again and repeat the process. The result was a map of the distribution of radioactivity in the field of view

Rejali [8] used ^{131}I-human serum albumin as the blood pool tracer to detect pericardial effusion. He compared the blood pool image to the size of the cardiac silhouette on a chest radiograph (Fig. 1.4). A blood pool that was smaller than the cardiac silhouette (or had a "halo" around it) was evidence of a pericardial effusion [9].

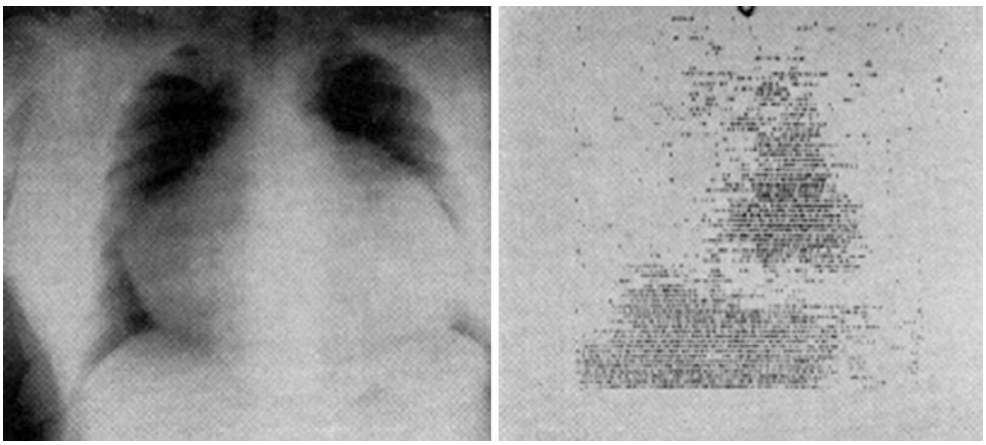

Fig. 1.4 Scan demonstrating marked discrepancy in transverse diameters between the cardiac blood pool and cardiac silhouette seen on the roentgenogram [9]

Scintillation Camera: Hal Anger

In parallel with the development of blood pool imaging, a "Quiet Genius," Hal Anger (Fig. 1.5), was developing a series of nuclear medicine instruments, including the gamma well counter and several imaging devices [10]. Anger recognized the need to record the distribution of all the tracer in a field of view simultaneously, like a photographic camera, rather than point by point, as recorded with a rectilinear scanner. From 1952 to 1960, Anger evolved his "camera." He enlarged the field of view from about 4 inches to 11 inches, and increased the sensitivity by changing from multiple pinhole collimators to parallel-hole collimation. To determine the location of each scintillation in the sodium iodide crystal, Anger used a hexagonal array of 19 photomultiplier tubes (PMTs). The scintillation was localized by comparing the relative amount of light "seen" by each PMT. Each scintillation was displayed as a flash of light on a cathode ray tube in the same relative position as they occurred in the crystal. A record of the distribution of the flashes was recorded on Polaroid film. By 1962, Anger had improved the scintillation camera to a clinically usable and commercially viable instrument. A visionary businessman, John Kuranz, the founder of the Nuclear Chicago Company, produced the first commercial instrument, an early version of which is on display in the Smithsonian Institute [11]. Anger not only developed a single photon gamma camera, but also a positron version [12]. The positron version used a small second detector placed beneath the patient to identify coincidence events.

Fig. 1.5 Hal O. Anger. (From Tapscott [10], with permission from The Society of Nuclear Medicine and Molecular Imaging)

In 1962, Alex Gottschalk, a young clinical radiologist from Paul Harper's laboratory in Chicago, arrived at the Donner Laboratory to work with Anger on clinical applications of the new imaging device. Gottschalk recognized the substantial advantages of the gamma camera over the rectilinear scanner, particularly the clinical value of simultaneous imaging of tracers in large regions of the body, including the brain and heart [13].

Initially, the positron-emitter gallium-68 (as ^{68}Ga-EDTA) was imaged with Anger's positron camera to detect brain tumors (based on loss of integrity of the blood-brain barrier) [14]. Although the instrument worked, the dose of ^{68}Ga was limited to 750 microcuries to avoid paralysis of the coincidence detector. Even with that limitation, the imaging results were impressive (Fig. 1.6).

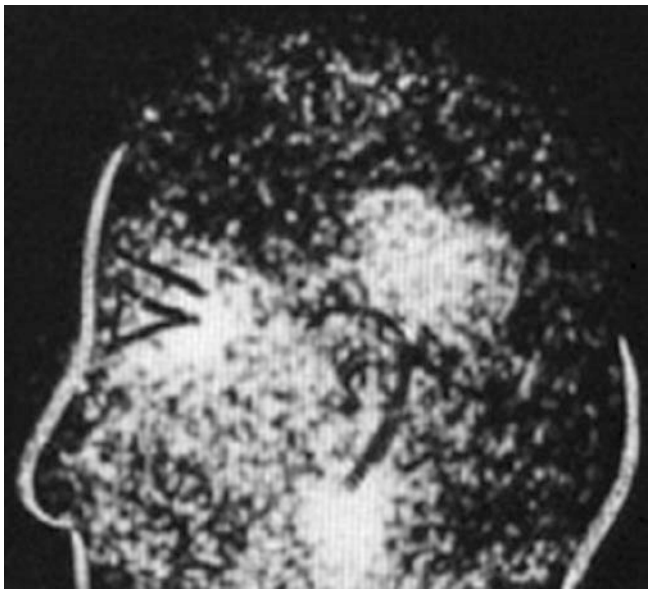

Fig. 1.6 A ^{68}Ga-EDTA brain scan acquired with the Anger positron camera circa 1962, showing the tomographic capability. (From Gottschalk [14], with permission from The Society of Nuclear Medicine and Molecular Imaging)

In 1964, Anger and Gottschalk started working with ^{99m}Tc generators. The combination of a thin scintillation crystal in the camera, the 140 keV gamma emissions from metastable Tc-99 m, and the 6-hour physical half-life made this radionuclide the preferred agent for labeling radiopharmaceuticals for clinical use. Gottschalk and Anger recorded cerebral angiograms and first-pass cardiac studies.

Cardiac Studies

Left Ventricular Ejection Fraction

In 1975, Schelbert and colleagues used the gamma camera to record a first-pass radionuclide angiogram. Instead of recording the data on Polaroid film, the investigators used a video camera. In addition to the images, Schelbert recorded the patient's electrocardiogram on the sound track of the videotape. The EKG served as an indicator of the phase of the cardiac cycle, allowing the images recorded at end-diastole (the P-R interval) and end-systole (the downslope of the T wave) to be summed, to compute the end diastolic, end systolic, and stroke volume counts to calculate the ejection fraction (correlated with cineangiocardiography – r = 0.94) [15] (Fig. 1.7). Although this technique worked well in patients with well-maintained cardiac function, the method did not work well in patients with impaired ventricular function.

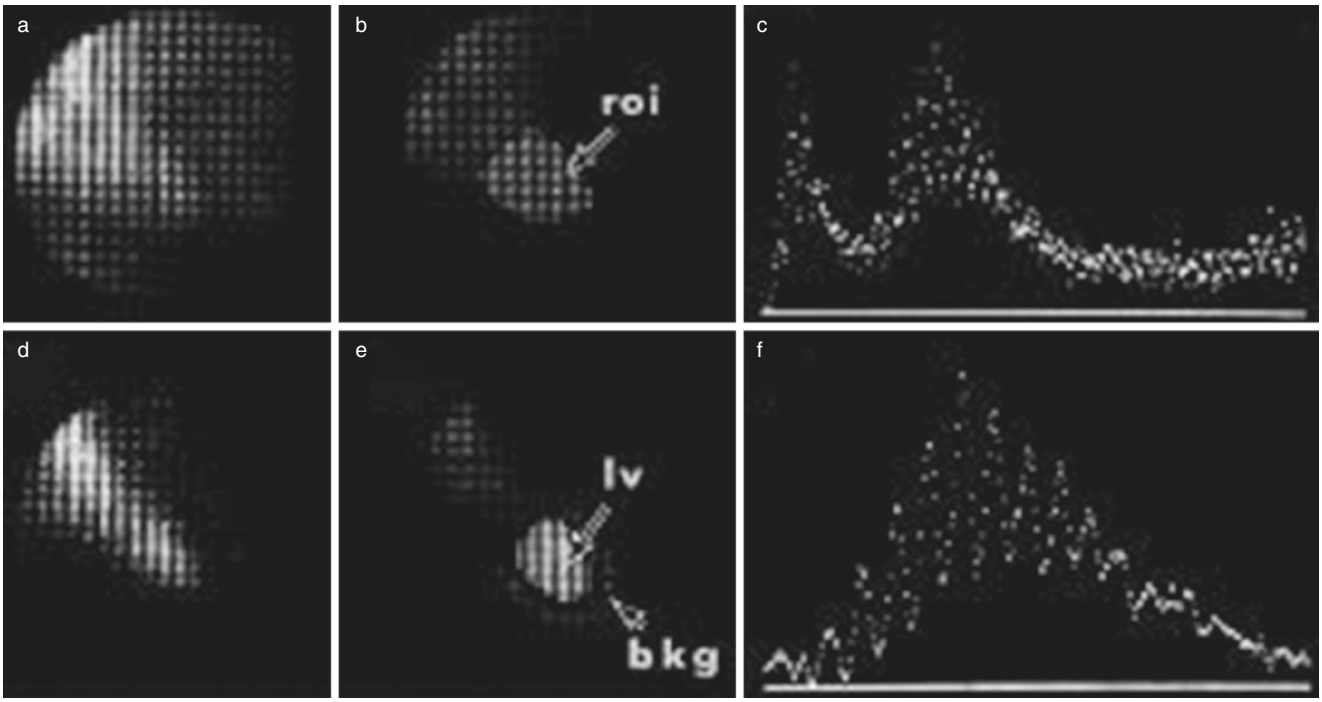

Fig. 1.7 Selected images from videotape replay of a first pass radionuclide angiogram. (**a**) Summed image of right and left heart phases; (**b**) Region of interest (ROI) placed over the RV and LV; (**c**) Graph of time (x axis) and counts (y axis) as tracer traverses the right and left ventricles; (**d**) Summed image of the left ventricular phase of the first pass; (**e**) ROI over LV and background (bkg) during LV phase; (**f**) Time activity curve of background corrected activity

Measuring ventricular function in patients with impaired function required high count density images, which were difficult to record with a first-pass technique. In 1971, Strauss and Zaret introduced the concept of equilibrium blood pool imaging. ^{99m}Tc-labeled albumin had been developed to replace radioiodinated albumin for the detection of pericardial effusions. Equilibrium blood pool imaging, with EKG gating to record data only at end-systole or end-diastole, or throughout the cardiac cycle (when sufficient computer memory was available), allowed high-resolution images of both global and regional ventricular function [16, 17] (Fig. 1.8). The outline of the left ventricle at end-diastole or end-systole was traced, and the outline measured with a planimeter. The relative size of the left ventricle was determined at diastole and systole. The difference represented the stroke volume. Ejection fraction was calculated as the stroke volume area divided by the end diastolic area. Regional wall motion was determined by comparing the outlines traced at end systole and end diastole. Areas of akinesis and dyskinesis were readily identified. Subsequently, Secker-Walker et al. [18] developed a count-based approach to calculate left ventricular ejection fraction.

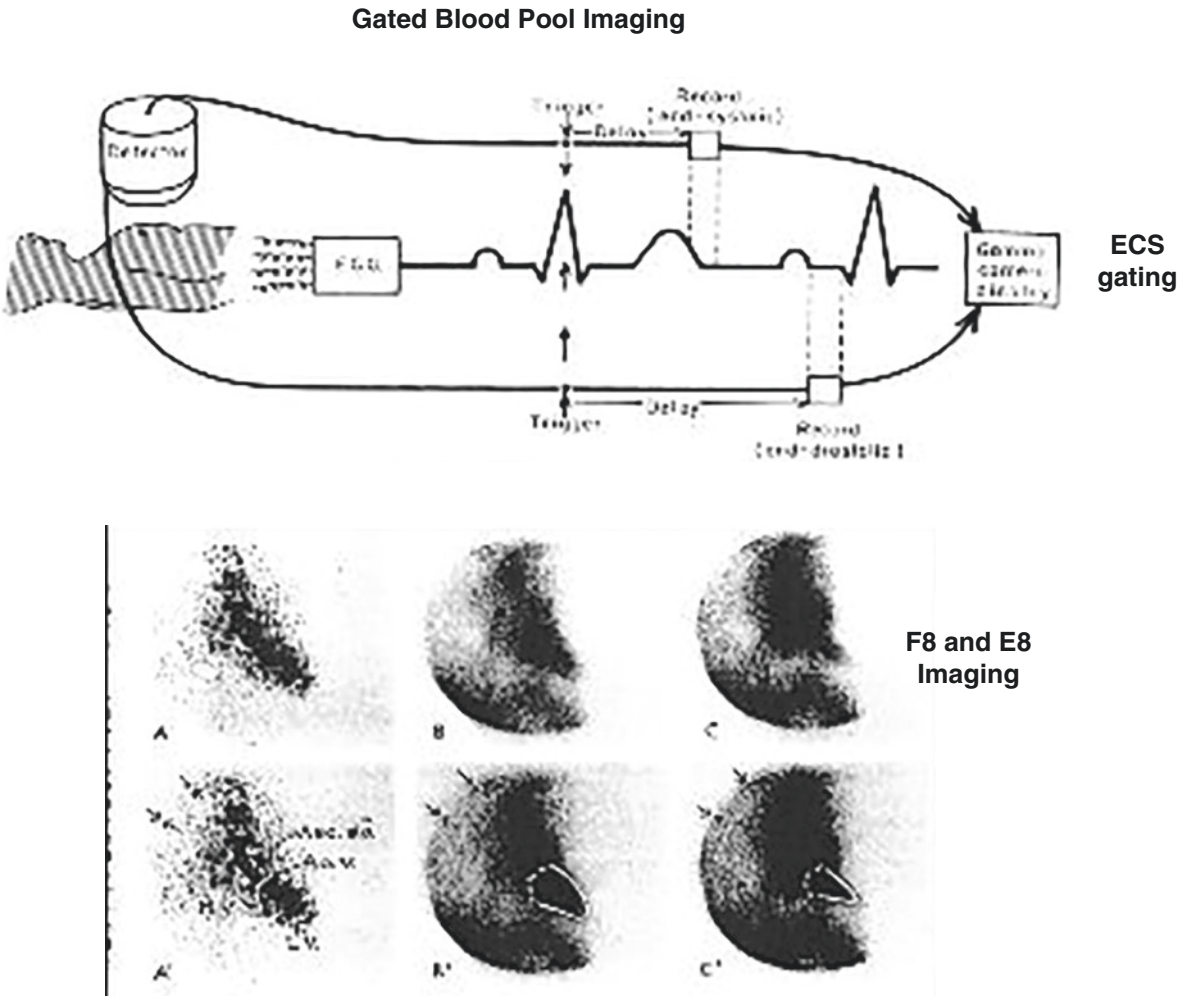

Fig. 1.8 Gated blood pool imaging. (From Strauss et al. [16], with permission from Elsevier)

Myocardial Perfusion

Several approaches were tested to measure myocardial perfusion. The first used the inert gas clearance method, with intracoronary administration of ^{133}xenon recorded with a single detector. This approach did not work well, because the clearance is dominated by normal tissue, making it very difficult to identify regions of decreased perfusion. To measure regional perfusion in all regions of the myocardium required multiple detectors. The multicrystal camera, designed by Bender and Blau [19], allowed the simultaneous independent measurement of tracer clearance from multiple myocardial locations, allowing identification of regions of normal and reduced perfusion. Figure 1.9 shows the relationship of coronary stenoses to the slightly reduced regional perfusion at rest [20]. The requirement for intracoronary injection of the tracer limited this technique to research studies.

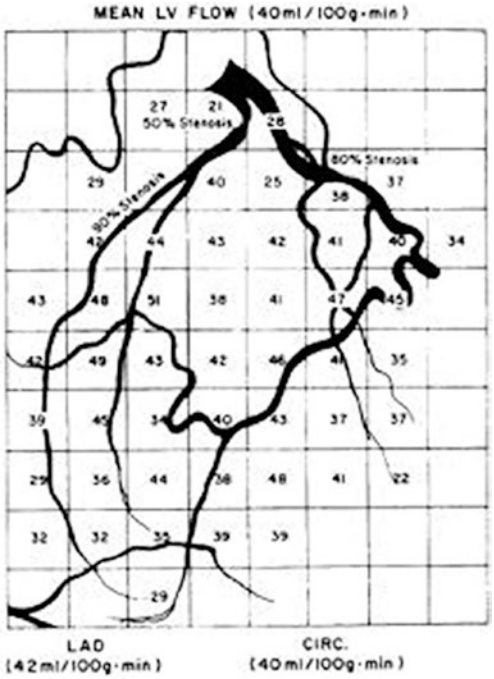

Fig. 1.9 Myocardial perfusion pattern in a patient with coronary stenoses [20]

In the early 1960s, Edward Carr, a nuclear physician working at the University of Michigan with William (Bill) Beierwaltes (the co-inventor of MIBG), was interested in myocardial imaging to detect acute myocardial infarction. Carr explored two techniques: One used myocardial perfusion imaging to detect areas of infarction as a "cold" spot (using the perfusion tracer ^{86}Rb) [21]; the other detected the area of infarction as a hot spot, using the agent employed to detect brain tumors, ^{203}Hg-chlormeridrin [22]. The selection of an isotope of rubidium as the cold spot tracer was based on the observations of the famous cardiologist from Tulane University, George Burch. Burch studied the kinetics of several potassium analogues in human subjects, including isotopes of rubidium [23]. Burch observed rapid clearance of ^{86}Rb from the blood and rapid uptake in multiple tissues (including the myocardium), suggesting that the tracer distribution would reflect myocardial perfusion. Carr selected the beta- and gamma-emitting tracer ^{86}Rb (gamma 1.076 MeV), with an 18.6-day half-life, to image experimental infarcts in dogs as "cold spots" in the myocardium. Areas of infarction appeared as regions of decreased tracer uptake on the scans. These pioneering studies by Carr led Ken Poggenburg, a radiochemist at the Oak Ridge National Laboratory, to synthesize potassium-43 in the Oak Ridge reactor using the ^{43}Ca(n,p)^{43}K reaction. The half-life of 22 hours and major gamma energy of 373 keV was better suited than the rubidium isotopes for imaging with the rectilinear scanner. First-in-man studies with ^{43}K by Hurley et al. in control subjects and patients with acute infarction demonstrated a "cold" area in the myocardial images of each of the five patients with acute infarction [24].

Zaret [25] and Strauss [26] extended the utility of myocardial perfusion imaging to detect ischemia by recording two myocardial perfusion scans: one with the tracer injected with the patient at rest (to distinguish regions of normal perfusion from areas of scar) and a second tracer injection during exercise stress followed by immediate scanning (to distinguish regions capable of increasing perfusion at stress from areas with decreased perfusion reserve (typically supplied by vessels with significant stenoses) (Fig. 1.10).

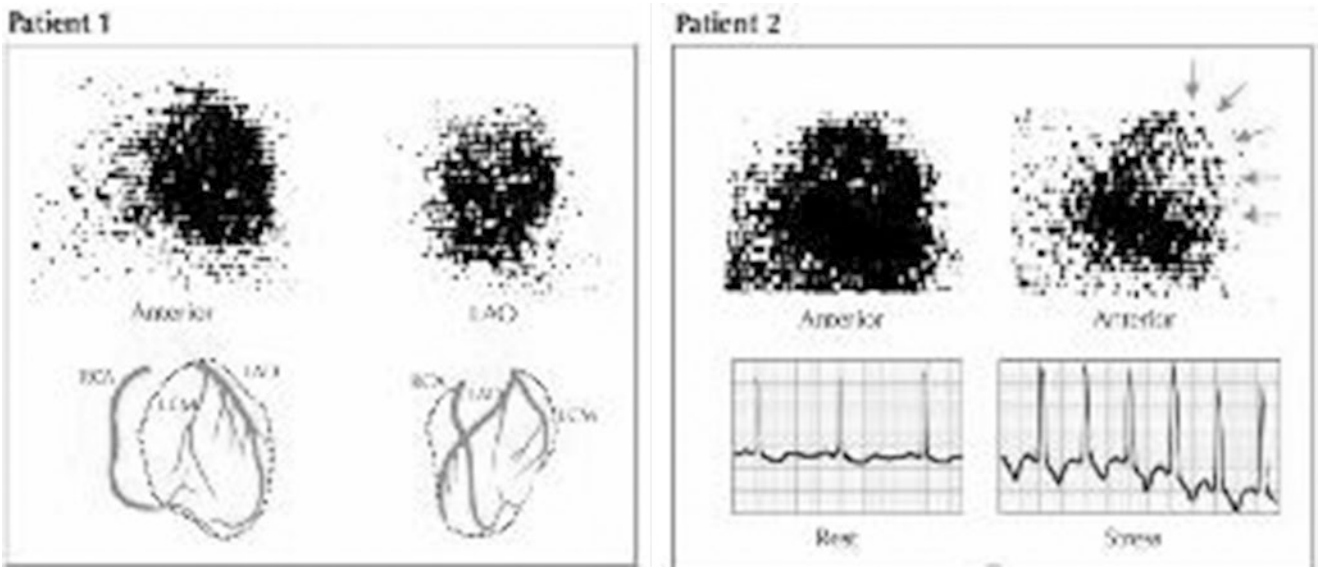

Fig. 1.10 Studies of myocardial perfusion. (From Zaret et al. [25], with permission of the Massachusetts Medical Society)

The development of thallium-201 as a myocardial perfusion agent, with its low-energy photons, facilitated the utilization of the gamma camera to record the rest and stress images [27]. Studies by Pohost and colleagues [28] revealed the dynamic nature of myocardial tracer retention. Patients were injected during exercise stress, and images recorded after exercise demonstrated myocardial regions of decreased tracer uptake. When the images were repeated several hours later, the areas of decreased tracer uptake on initial images, appeared to fill in (redistribute). This phenomenon occurred because of more rapid tracer clearance from regions of normally perfused myocardium than in regions of ischemia [29]. Based on these observations, stress and redistribution imaging, rather than stress and rest-injected images, became the preferred approach to detect ischemia.

In 1984, the synthesis of ^{99m}Tc-sestamibi as a myocardial perfusion tracer allowed administration of much larger doses [30] (20–30 mCi) compared to the typical 4 mCi dose of thallium-201). The high-count-density images recorded with ^{99m}Tc sestamibi enhanced image quality, allowing the measurement of both regional perfusion and ventricular function by gating the acquisition of myocardial perfusion data. Instrumentation improved with the development of the rotating gamma camera [31] to record myocardial perfusion single photon emission computed tomography (SPECT) images. Standardization of image presentation and improvements in the quantitation of perfusion and ventricular function at rest and stress [32–34] enhanced the acceptance of myocardial perfusion imaging by the medical community.

Dr. K. Lance Gould (Fig. 1.11) and colleagues performed a series of laboratory studies that defined the quantitative relationship between the percentage of stenosis on coronary arteriography and myocardial perfusion at rest and at maximum vasodilator stress [35]. The studies demonstrate that a stenosis of about 75% of the luminal diameter is required to decrease resting coronary blood flow. Using hyperemia as a stimulus (induced by intracoronary injection of contrast material or intravenous administration of dipyridamole), coronary narrowing's of only 47% of luminal diameter could be detected. These studies led to the validation of pharmacologic vasodilators (eg, dipyridamole), as an alternative to exercise to induce maximal coronary blood flow in patients who cannot perform maximal exercise [36]. The pathophysiologic rationale for the use of these agents is probably inadequate vasodilatation in coronary vessels with inflamed atheroma. Vessels without inflammatory lesions in the subintima dilate in response to the drug, delivering additional blood flow (and tracer) to the distal myocardium.

Fig. 1.11 K. Lance Gould

In parallel with advances in single photon imaging, numerous investigators were working on advanced instrumentation to image the annihilation radiation resulting from the mass-to-energy conversion of positron-emitting tracers. Pioneers included investigators at the Massachusetts General Hospital [37], at the Mallinckrodt Institute of Radiology at Washington University in St. Louis [38] and at the Crump Institute at the University of California Los Angeles [37, 38] among many others. The results of their investigations resulted in the ring detector, allowing high-count-density images and quantitation of absolute myocardial blood flow and perfusion reserve [39], as well as increased certainty of diagnosis through the high-resolution images. In addition to higher-quality images of myocardial perfusion and ventricular function, direct detection of myocardial viability in patients with myocardial infarction was reported by the UCLA group in 1983 [40]. Ischemia was depicted as an area of decreased perfusion which maintained metabolic activity. Perfusion was usually imaged with ^{13}N-ammonia and myocardial glucose metabolism was imaged with ^{18}F-FDG. Patients demonstrating this disparity had an improved prognosis when treated with revascularization [41].

Fig. 1.12 Dr. David W. Townsend

The remarkable development of hybrid PET/CT instrumentation in the laboratory of David Townsend [42] (Fig. 1.12) resulted in high-quality CT based attenuation correction and enhanced registration of anatomic and radionuclide data. These advances allow more precise characterization of the degree of inflammation in the coronary arterial wall with FDG [43], and more precise determination of the degree of ongoing necrosis in atheroma with fluoride imaging [44, 45].

Investigators and practitioners of Nuclear Cardiology have much to be proud of, and much to look forward to. For example, the development of genetic markers will identify imageable markers to characterize specific abnormalities of contractile proteins in patients with heart failure and inflammatory lesions in atheroma.

The field has a scintillating future.

References

1. Berkeley Lab. The discovery of radioactivity. https://www2.lbl.gov/abc/wallchart/chapters/03/4.html.
2. The Nobel Prize in Physics. 1903. http://www.nobelprize.org/nobel_prizes/physics/laureates/1903.
3. Blumgart HL, Yens OC. Studies on the velocity of blood flow: I. The method utilized. J Clin Invest. 1927;4:1–13.
4. Patton DD. The birth of nuclear medicine instrumentation: Blumgart and Yens, 1925. J Nucl Med. 2003;44:1362–5.
5. Roguin A. Myron Prinzmetal 1908-1987: the man behind the variant angina. Int J Cardiol. 2008;123:129–30.
6. Prinzmetal M, Corday E, Bergman HC, Schwartz L, Spritzler RJ. Radiocardiography: a new method for studying blood flow through the chambers of the heart in human beings. Science. 1948;108:340–1.
7. Donato L, Holmes RA, Wagner HN. The circulation. In: Wagner HN, editor. Principles of nuclear medicine. Philadelphia: WB Saunders; 1968. p. 531–83.
8. Rejali AM, MacIntyre WJ, Friedell HL. A radioisotope method of visualization of blood pools. Am J Roentgenol Radium Therapy Nucl Med. 1958;79:129–37.
9. Rosenthall L. Detection of pericardial effusion by radioisotope heart scanning. Can Med Assoc J. 1964;90:447–51.
10. Tapscott E. Nuclear medicine pioneer, Hal O. Anger, 1920-2005. J Nucl Med Technol. 2005;33:250–3.
11. Anger HO. Scintillation camera with multichannel collimators. J Nucl Med. 1964;5:515–31.
12. Gottschalk A, McCormack KR, Adams JE, Anger HO. A comparison of results of brain scanning using 68Ga EDTA and the positron scintillation camera, with 203Hg neohydrin and the conventional focused collimator scanner. Radiology. 1965;84:502–6.
13. Gottschalk A. The early years with Hal Anger. Semin Nucl Med. 1996;26:171–9.
14. Gottschalk A. Hal Anger, nuclear medicine's quiet genius. J Nucl Med. 2004;45:13N–26N.
15. Schelbert HR, Verba JW, Johnson AD, Brock GW, Alazraki NP, Rose FJ, Ashburn WL. Nontraumatic determination of left ventricular ejection fraction by radionuclide angiocardiography. Circulation. 1975;51:902–9.
16. Strauss HW, Zaret BL, Hurley PJ, Natarajan TK, Pitt B. A scintiphotographic method for measuring left ventricular ejection fraction in man without cardiac catheterization. Am J Cardiol. 1971;28:575–80.
17. Zaret BL, Strauss HW, Hurley PJ, Natarajan TK, Pitt B. A noninvasive scintiphotographic method for detecting regional ventricular dysfunction in man. N Engl J Med. 1971;284:1165–70.
18. Secker-Walker RH, Resnick L, Kunz H, Parker JA, Hill RL, Potchen EJ. Measurement of left ventricular ejection fraction. J Nucl Med. 1973;14:798–802.
19. Harris CC. Hevesy nuclear medicine pioneer lecture (Monte Blau, Merrill A. Bender). J Nucl Med. 1980;21:609–11.
20. Cannon PJ, Schmidt DH, Weiss MB, Fowler DL, Sciacca RR, Ellis K, Casarella WJ. The relationship between regional myocardial perfusion at rest and arteriographic lesions in patients with coronary atherosclerosis. J Clin Invest. 1975;56:1442–54.
21. Carr EA Jr, Beierwaltes WH, Wegst AV, Bartlett JD Jr. Myocardial scanning with rubidium-86. J Nucl Med. 1962;3:76–82.
22. Carr EA Jr, Beierwaltes WH, Patno ME, Bartlett JD Jr, Wegst AV. The detection of experimental myocardial infarcts by photoscanning. A preliminary report. Am Heart J. 1962;64:650–60.
23. Burch G, Threefoot S, Ray C. The rate of disappearance of Rb86 from the plasma, the biologic decay rates of Rb86, and the applicability of Rb86 as a tracer of potassium in man with and without chronic congestive heart failure. J Lab Clin Med. 1955;45:371–94.
24. Hurley PJ, Cooper M, Reba RC, Poggenburg KJ, Wagner HN Jr. ^{43}KCl: a new radiopharmaceutical for imaging the heart. J Nucl Med. 1971;12:516–9.
25. Zaret BL, Strauss HW, Martin ND, Wells HP Jr, Flamm MD. Noninvasive regional myocardial perfusion with radioactive potassium. Study of patients at rest, with exercise and during angina pectoris. N Engl J Med. 1973;288:809–12.
26. Strauss HW, Zaret BL, Martin ND, Wells HP Jr, Flamm MD. Noninvasive evaluation of regional myocardial perfusion with potassium 43. Technique in patients with exercise-induced transient myocardial ischemia. Radiology. 1973;108:85–90.
27. Lebowitz E, Greene MW, Fairchild R, Bradley-Moore PR, Atkins HL, Ansari AN, et al. Thallium-201 for medical use. I J Nucl Med. 1975;16:151–5.
28. Pohost GM, Zir LM, Moore RH, McKusick KA, Guiney TE, Beller GA. Differentiation of transiently ischemic from infarcted myocardium by serial imaging after a single dose of thallium-201. Circulation. 1977;55:294–302.
29. Pohost GM, Okada RD, O'Keefe DD, Gewirtz H, Beller G, Strauss HW, et al. Thallium redistribution in dogs with severe coronary artery stenosis of fixed caliber. Circ Res. 1981;48:439–46.
30. Holman BL, Jones AG, Lister-James J, Davison A, Abrams MJ, Kirshenbaum JM, et al. A new Tc-99m-labeled myocardial imaging agent, hexakis(t-butylisonitrile)-technetium(I) [Tc-99m TBI]: initial experience in the human. J Nucl Med. 1984;25:1350–5.
31. Keyes JW Jr, Orlandea N, Heetderks WJ, Leonard PF, Rogers WL. The humongotron–a scintillation-camera transaxial tomograph. J Nucl Med. 1977;18:381–7.
32. Prigent FM, Maddahi J, Garcia E, Friedman J, Van Train K, Bietendorf J, et al. Thallium-201 stress-redistribution myocardial rotational tomography: development of criteria for visual interpretation. Am Heart J. 1985;109:274–81.
33. Germano G, Kavanagh PB, Berman DS. An automatic approach to the analysis, quantitation and review of perfusion and function from myocardial perfusion SPECT images. Int J Card Imaging. 1997;13:337–46.
34. Verberne HJ, Acampa W, Anagnostopoulos C, Ballinger J, Bengel F, De Bondt P, et al. European Association of Nuclear Medicine (EANM). EANM procedural guidelines for radionuclide myocardial perfusion imaging with SPECT and SPECT/CT: 2015 revision. Eur J Nucl Med Mol Imaging. 2015;42:1929–40.
35. Gould KL. Coronary artery stenosis. New York: Elsevier; 1991.
36. Albro PC, Gould KL, Westcott RI, Hamilton GW, Ritchie JL, Williams DL. Noninvasive assessment of coronary stenoses by myocardial imaging during pharmacologic coronary vasodilation III. Clinical trial. Am J Cardiol. 1978;42:751–60.
37. Hoop B Jr, Smith TW, Burnham CA, Correll JE, Brownell GL, Sanders CA. Myocardial imaging with 13 NH 4+ and a multicrystal positron camera. J Nucl Med. 1973;14:181–3.
38. Ter-Pogossian MM, Phelps ME, Hoffman EJ, Mullani NA. A positron-emission transaxial tomograph for nuclear imaging (PETT). Radiology. 1975;114:89–98.
39. Dorbala S, Di Carli MF. Cardiac PET perfusion: prognosis, risk stratification, and clinical management. Semin Nucl Med. 2014;44:344–57.
40. Marshall RC, Tillisch JH, Phelps ME, Huang SC, Carson R, Henze E, Schelbert HR. Identification and differentiation of resting myocardial ischemia and infarction in man with positron computed tomography, 18F-labeled fluorodeoxyglucose and N-13 ammonia. Circulation. 1983;67:766–78.
41. Bax JJ, Visser FC, Poldermans D, Elhendy A, Cornel JH, Boersma E, et al. Relationship between preoperative viability and postoperative improvement in LVEF and heart failure symptoms. J Nucl Med. 2001;42:79–86.
42. Townsend DW, Cherry SR. Combining anatomy and function: the path to true image fusion. Eur Radiol. 2001;11:1968–74.

43. Vallabhajosula S, Fuster V. Atherosclerosis: imaging techniques and the evolving role of nuclear medicine. J Nucl Med. 1997;38:1788–96.
44. Derlin T, Richter U, Bannas P, Begemann P, Buchert R, Mester J, Klutmann S. Feasibility of 18F-sodium fluoride PET/CT for imaging of atherosclerotic plaque. J Nucl Med. 2010;51:862–5.
45. Nakahara T, Dweck MR, Narula N, Pisapia D, Narula J, Strauss HW. Coronary artery calcification: from mechanism to molecular imaging. JACC Cardiovasc Imaging. 2017;10:582–93.

Principles of Nuclear Cardiology Imaging

2

Ernest V. Garcia, James R. Galt, Marina Piccinelli, and Ji Chen

Introduction

Nuclear cardiology imaging is solidly based on many branches of science and engineering, including nuclear, optical, and mathematical physics; electrical and mechanical engineering; chemistry; and biology. This chapter uses principles from these scientific fields to provide an understanding of both the signals used and the imaging system that captures these signals. These principles have been simplified to fit the scope of this atlas.

Nuclear cardiology's signal is a radioactive tracer, and its imaging systems are either single-photon emission CT (SPECT) or positron emission tomography (PET) cameras. This combination has met with remarkable success in clinical cardiology. This success is the result of the combination of sophisticated electronic nuclear instruments and a highly specific signal. The signal is as important as or more important than the imaging system, which can be explained with the following analogy: When we look at the heavens on a clear night, our naked eye can see stars, objects that are millions of miles away, yet when we look into our patients just a few feet away, even with sophisticated systems, we can sometimes miss a signal associated with cardiac disease. The reason is that a star generates an incredibly powerful signal surrounded by a dark background, a signal much more powerful than the signals we currently use. This analogy provides several lessons. First, it illustrates the need to continue to improve our signals. Second, it provides a motivation: By improving our signal, we have the capacity to detect anything. Finally, it explains the success of nuclear cardiology imaging over cardiovascular MRI, echocardiography, or CT for detecting perfusion abnormalities.

There is a misconception that MRI, echocardiogram, and CT are superior to nuclear cardiology imaging because of their superior spatial resolution. Yet, for detecting perfusion defects, what is really necessary is superior contrast resolution. It is this superior contrast resolution that allows us to differentiate between normal and hypoperfused myocardium, facilitating the visual analysis of nuclear cardiology perfusion images. Because these objects are bright compared with the background, we have been able to develop computer algorithms to totally, automatically, and objectively process and quantify our images, a feat yet to be successfully performed by other modalities.

This chapter explains the many important scientific principles necessary to understand this analogy, as well as nuclear cardiology imaging in general, starting from how radiation is emitted from a nucleus to how these sophisticated imaging systems detect this radiation. These principles are explained at a simple but highly applied level, so the nuclear cardiologist can understand them and apply them in routine clinical practice. The better one's understanding of how images are formed and what can go wrong in their formation, the higher one's accuracy in interpreting studies and the more successful one's practice should be.

E. V. Garcia (✉) · J. R. Galt · M. Piccinelli · J. Chen
Department of Radiology and Imaging Sciences, Emory University School of Medicine, Atlanta, GA, USA
e-mail: ernest.garcia@emory.edu

V. Dilsizian, J. Narula (eds.), *Atlas of Nuclear Cardiology*, https://doi.org/10.1007/978-3-030-49885-6_2

Fundamentals

Figures 2.1, 2.2, 2.3, 2.4, 2.5, and 2.6 introduce some of the fundamentals of radioactivity and radionuclides.

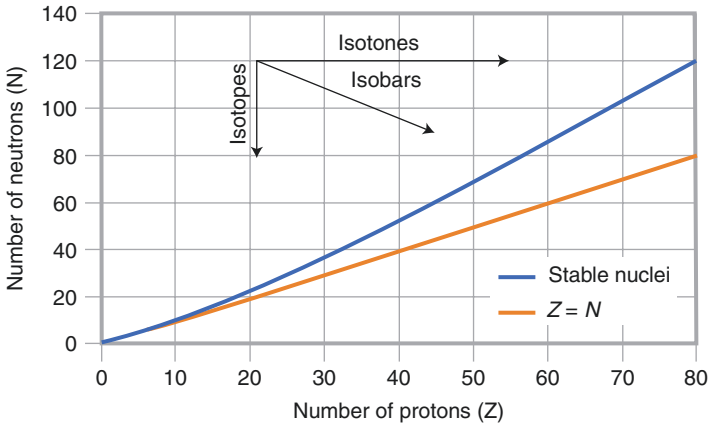

Fig. 2.1 Stability of the nucleus. This graph plots as a *blue line*, the number of neutrons versus the number of protons for stable nuclei. The *yellow line* indicates a neutron–proton ratio of 1. Only nuclides with low proton numbers fall on this line. For the *blue line*, note that as the number of protons increases, more neutrons are required to keep the nucleus stable. Nuclides with neutron–proton ratios that are not on the *blue line* of stable nuclei are unstable and, thus, radioactive. These radioactive nuclides are known as *radionuclides*. The type of radioactivity emitted depends on which side of the line the radionuclide is found. Isotopes are a family of nuclides that all have the same number of protons, or atomic number (Z), and are not necessarily radioactive. Isotones are nuclides with the same number of neutrons (N), and isobars have the same mass number (A) or number of mass particles in the nucleus ($A = Z + N$)

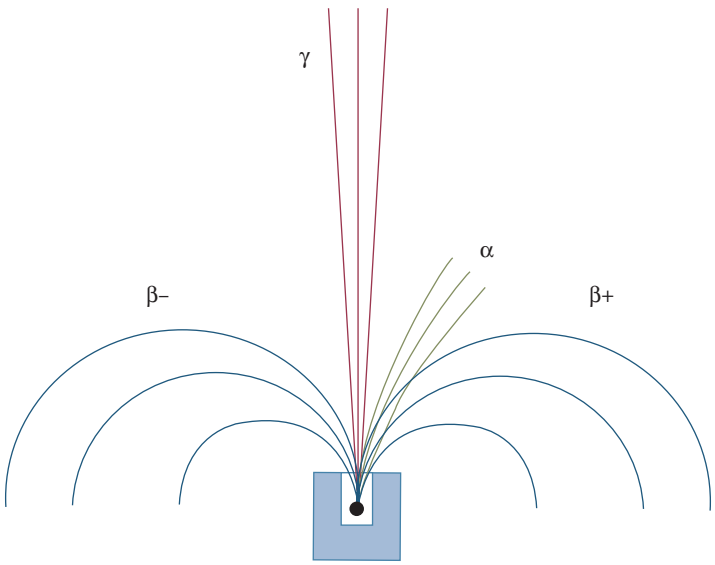

Fig. 2.2 Types of radiation. This diagram represents the path deviation of different types of radiation from nuclei by a magnetic field perpendicular to the page. The direction of the deflection depends on the charge of the radioactive particle. The least penetrating radiation is deflected to the right and corresponds to the heaviest radiation, called an alpha particle (α). An α particle is actually the nucleus of a helium atom (two protons plus two neutrons) with a positive charge. The moderately penetrating radiation deflected in the direction opposite to an α particle consists of negative particles called beta particles (β). Because these particles are more strongly bent, they are lighter than the α particles. The β particles are actually electrons emitted from the nucleus. Showing the same degree of penetration but bending in the direction opposite to the β particles are positron particles, or positive electrons (β+). These particles are made of antimatter and emitted by positron tracers. The radioactive particles that go straight and are not deflected do not consist of charged particles. They are called gamma (γ) rays and have been shown to be identical to particles emitted from an x-ray tube [1]. Both x-rays and γ-rays are called *photons* and are used in nuclear cardiology imaging

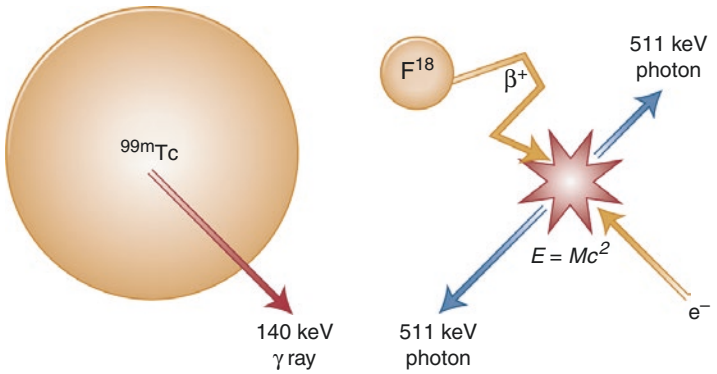

Fig. 2.3 Single-photon emission CT (SPECT) versus positron emission tomography (PET) radionuclides. This figure shows two very different types of radionuclides, technetium-99m (^{99m}Tc) and fluorine-18 (^{18}F). ^{99m}Tc is a large radionuclide that emits a single photon or γ-ray per radioactive decay that is used in SPECT to create images. The energy of the emitted photon is 140 keV (kiloelectron volts). The *m* in ^{99m}Tc means that the nucleus is metastable (almost stable but really unstable). ^{18}F is a much smaller radionuclide that emits a positron (β+) antiparticle. This ionized antiparticle travels through a medium interacting with it, losing energy and slowing down until it interacts with an electron, usually from some atom. Because the electron and the positron are antiparticles of each other (i.e., same mass but opposite charge), they undergo a phenomenon called *pair annihilation*. In pair annihilation, the mass of both particles disintegrates and is converted into energy as explained by Einstein's famous equation, $E = mc^2$, where E is the emitted energy, m is the mass of the two particles, and c is the speed of light in a vacuum. Because of the nature of the interaction, the energy is usually emitted in the form of two photons traveling in exactly opposite directions from each other and each having the same energy, 511 keV, which is the energy equivalent to the rest mass of an electron. These two photons are used to create images in PET

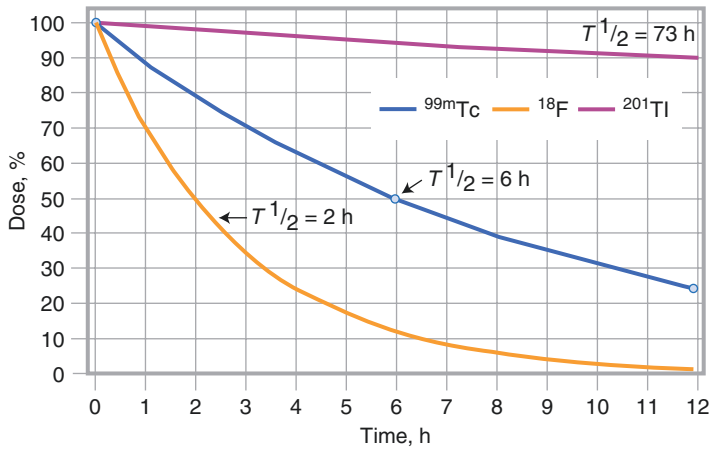

Fig. 2.4 Radioactive decay law: concept of half-life. This diagram shows decay curves for three different radionuclides: technetium-99m (^{99m}Tc), fluorine-18 (^{18}F), and thallium-201 (^{201}Tl). The decay curves express the amount of radioactive nuclides that have not decayed as a function of time. The shorter the interval between emissions for a specific radionuclide, the faster the radioactivity is depleted. It is practical to express the rate of radioactive transformations (disintegrations) by specifying the period during which half of all the atoms initially present will disintegrate. This period of time is known as the *half-life*, or T½. Note from the graph that the ^{18}F curve is disintegrating the fastest of the three radionuclides; it reaches a level of 50% of original at 2 hours; therefore, the half-life of ^{18}F is 2 hours. Compare this with the half-life of ^{201}Tl, which is 73 hours, and the half-life of ^{99m}Tc, which is 6 hours. The amount of radioactive nuclide is specified in terms of its disintegration rate or its activity. This relationship is provided by the radioactive decay law:

$$A(t) = A_0 e^{-(0.693t)} / T\frac{1}{2}.$$

In this equation, $A(t)$ is the radioactivity remaining at time t, A_0 is the activity at time 0, and $T½$ is the half-life of the radionuclide

A common unit of radioactivity is the curie (Ci), which is 3.7×10^{10} disintegrations per second. Another common unit of radioactivity used is the becquerel (Bq), which is one disintegration per second. One thousandth of a curie is a millicurie (mCi), which corresponds to 3.7×10^7 disintegrations per second. Note from the graph that if a 40-mCi dose of a ^{99m}Tc radiopharmaceutical (radioactive pharmaceutical) is delivered to an imaging clinic at 6 a.m., 6 hours later, at noon, only half—or 20 mCi—remains, and at 6 p.m., only half of that—or 10 mCi—remains

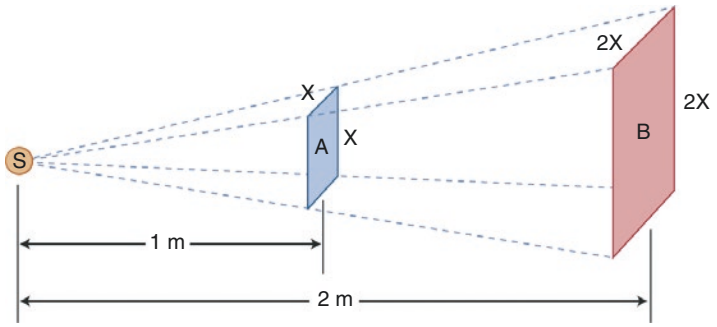

Fig. 2.5 Inverse square law. This diagram illustrates the concept of the inverse square law for radioactivity. The intensity of a radioactive point source at a distance from the source obeys the same law as for visible light. If the amount of radioactivity at the point source (*S*) remains constant, then the intensity of the radioactivity (number of photons) passing through a flat surface is inversely proportional to the square of the distance from the source. At a distance of 1 m, the diverging radioactive beam covers an area (*A*, *small square*) with each side of dimension *x*, or an area of x^2. At 2 m, the diverging beam covers an area (*B*, *large square*) in which each side is now twice as long as *A* (*2x*) and the area is $4x^2$, which is four times the area at 1 m. Because the amount of radioactivity remains constant, the number of photons falling on *square A* must spread out over four times as large an area by the time it reaches *square B*. Thus, the activity per unit area at *B*, which is twice as far as *A* from the source, is one fourth of the activity passing through *A* [2]. The value of this principle to radiation workers is that they can significantly reduce their radiation burden just by increasing their distance between themselves and a radioactive source, such as a patient already injected with a radioactive dose

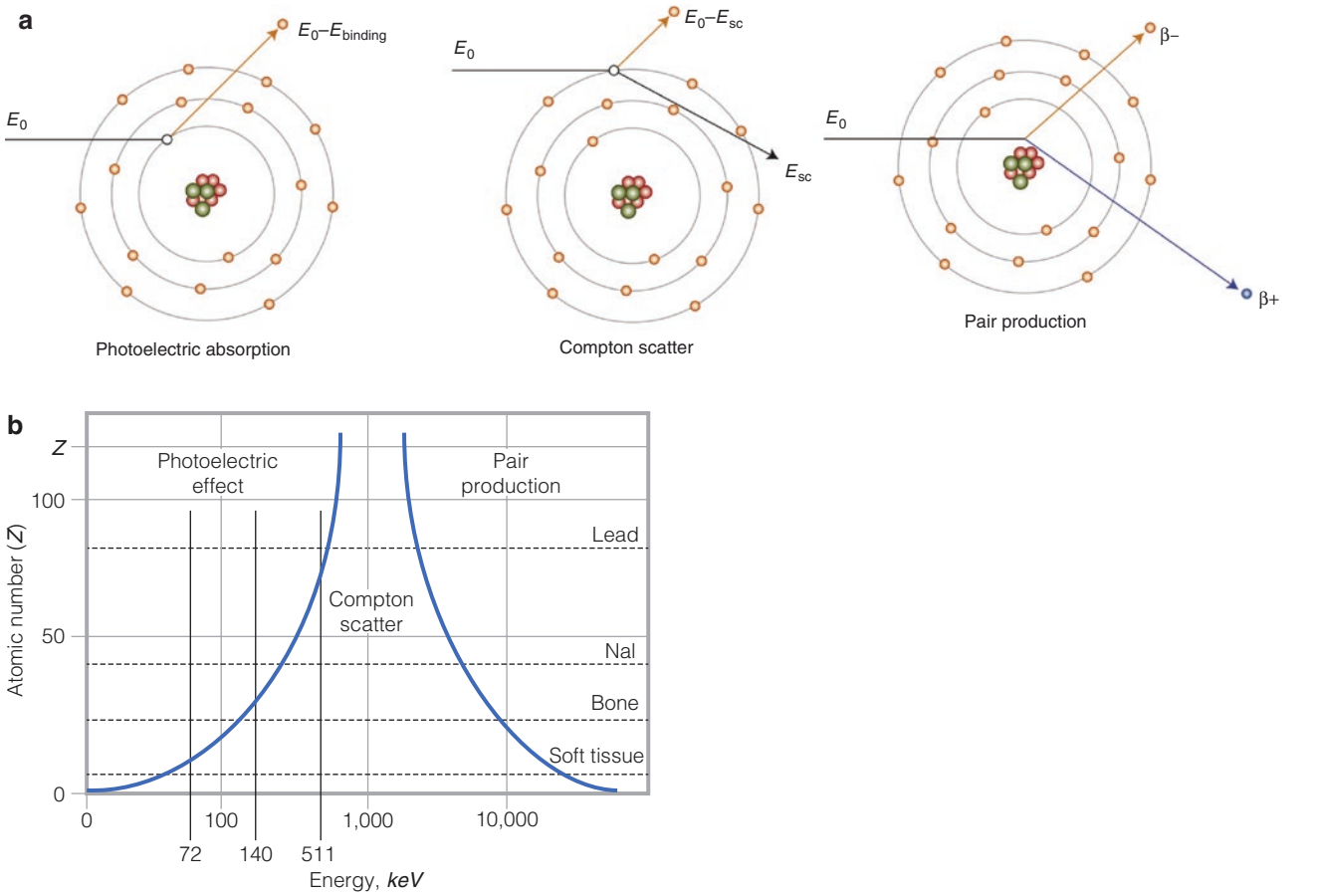

Fig. 2.6 Interaction of radiation with matter: photons. High-energy photons, such as γ-rays and x-rays, interact with matter in three ways that are relevant to nuclear medicine: through the photoelectric effect, Compton scattering, and pair production [3]. Each of these processes results in the emission of charged particles (electrons or positrons) that produce much more ionization than the original event. Thus, high-energy photons are classified as secondary ionizing radiation

(**a**) The photoelectric effect (or photoelectric absorption) occurs when a photon (γ- or x-ray) is completely absorbed as it interacts with an inner-shell electron. All the energy is lost to the electron, now called a *photoelectron*, which is emitted from the atom with an energy equivalent to the photon energy (E_0) less the binding energy of the electron ($E_{Binding}$). After photoelectric absorption, the atom has a vacancy in an inner electron shell that will be filled by an outer-shell electron, resulting in the emission of characteristic x-rays and possibly Auger electrons

Compton scattering occurs when a photon interacts with an outer-shell electron, changing its direction and losing some energy. The amount of energy of the photon after scattering depends on the angle of scatter (θ) according to the following formula:

$E_{sc} = E_0/1 + (E_0/551\ \text{keV}) \times (1 - \cos(\theta))$.

In this formula, E_0 is the energy of the photon before scattering, E_{sc} is the energy of the photon after scattering, and θ is the angle between the photon's original path and its new one. The larger the angle, the more energy is lost. Maximum energy is lost when the photon reverses course ($\theta = 180°$) and backscatters. All the energy lost to the γ-ray ($E_0 - E_{sc}$) is transferred to the electron, which on ejection from the atom is called a *recoil electron* (the binding energy of the outer-shell electron is negligible). Energies of Compton-scattered photons as a function of angle are given in Table 2.1

Pair production occurs when a photon passes near a charged particle (usually the nucleus of an atom). The photon is destroyed and a positron–electron pair (β+, β–) is created. According to the formula $E = mc^2$, the mass of the electron is equivalent to 511 keV; thus, the photon must have at least 1022 keV for pair production to occur. Energy in excess of 1022 keV is shared by the positron and the electron as kinetic energy. Because of the high energy required for the process, it is of little importance in clinical nuclear medicine laboratories

(**b**) The most probable interactions between high-energy photons and matter depend on the energy of the photons and the density of the material. Compton scattering is by far the most common interaction within the patient from the photons produced by clinical radiopharmaceuticals. The photoelectric effect is more likely to take place in the lead shielding of the collimator

Table 2.1 shows the relationship between the photopeak energy of common radionuclides used in nuclear cardiology, the scattering angle of the Compton-scattered photon, and the resulting energy of that photon. Note that in many instances, the original emitted photon may undergo a large scatter angle and still be counted by a 20% energy window in a camera's pulse height analyzer.

		Scattering angle			
Radionuclide	E_0, keV	30°	60°	90°	180°
Thallium-201	72	71	67	63	56
Technetium-99m	140	135	123	110	90
Positron annihilation	511	451	341	256	170

keV kiloelectron volts

Table 2.1 Energies of compton-scattered photons (E_0)

Figure 2.7 illustrates photon attenuation.

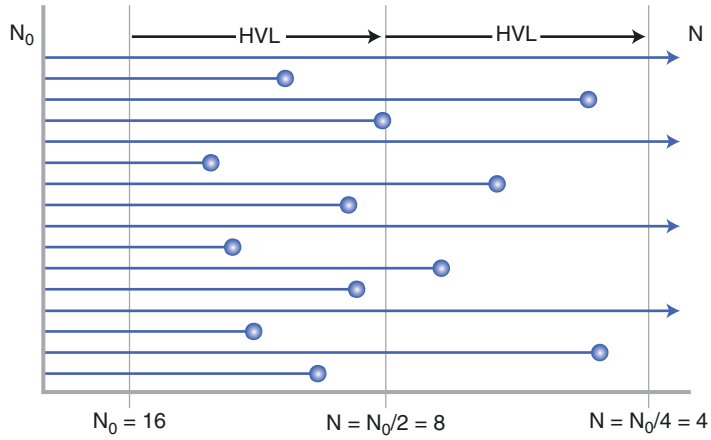

Fig. 2.7 Photon attenuation. As photons are absorbed through the photoelectric effect or scattered away from the detector through Compton scattering, their loss is called *attenuation*. The percentage of photons lost depends on the energy of the photons, the density of the material, and the material's thickness. The dependence on thickness is straightforward: the thicker the material, the more photons will be absorbed. The thickness at which half of the photons are absorbed is called the *half-value layer* (HVL). In the example, N_0 photons pass through a material. After 1 HVL, one half of photons has been lost; after 2 HVLs, only one fourth of the photons is left. In practice, the attenuation of a beam of photons is usually calculated using the linear attenuation coefficient ($\mu = \ln 2/\text{HVL}$) in the following equation:

$I = I_0 e - \mu^x$.

In this equation, I_0 is the initial beam intensity and I is the intensity after traveling through thickness x. The values of linear attenuation coefficients depend on the energy of the photon and the composition of the material. The denser the material and the higher the energy of the photon, the less attenuation and the lower the value of μ. Linear attenuation coefficients and HVLs for radionuclides and materials of interest to nuclear cardiology are given in Table 2.2

Table 2.2 shows the relationship between the photopeak energy of common radionuclides used in nuclear cardiology and their corresponding linear attenuation coefficient (μ) and HVL in soft tissue, bone, and lead. Note that the denser the material, the smaller the HVL has to be in order to reduce the photon beam by 50%. Figure 2.8 shows interaction of radiation (charged particles) with matter.

		Soft tissue (1.0 g/cm³)		Bone (1.9 g/cm³)		Lead (11.3 g/cm³)	
Radionuclide	Energy, *keV*	μ, *1/cm*	HVL, *cm*	μ, *1/cm*	HVL, *cm*	μ, *1/cm*	HVL, *cm*
Thallium-201	72	0.191	3.62	0.493	1.40	39.1	0.018
Technetium-99m	140	0.153	4.52	0.295	2.35	30.7	0.023

The values in the table were calculated from data obtained from Hubble and Seltzer [4]

Table 2.2 Linear attenuation coefficients (μ) and half-value layers (HVLs)

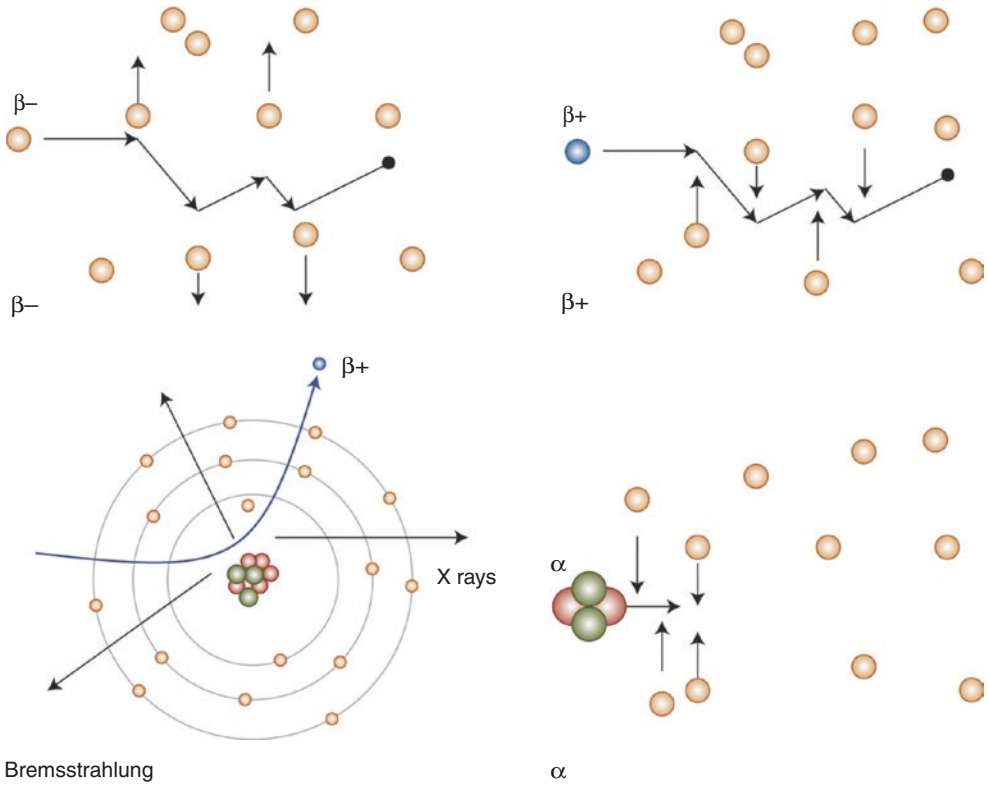

Fig. 2.8 Interaction of radiation with matter: charged particles. High-energy charged particles such as alpha particles (α), beta particles (β), and the photoelectrons and recoil electrons discussed earlier slow down and lose energy as they pass through matter. This loss is a result of the forces their charges exert on the electrons (and, to a lesser extent, on the nuclei) of the material. These interactions are called *collisions*. The loss of energy is termed *collisional losses* (even though it does not actually involve a collision between the two particles) or *radiation losses*, depending on the nature of the encounter

The β particles have the same mass as electrons, and as they pass through material, the electrical forces of the electrons (attractive for β+ and repulsive for β−) cause them to change course with each interaction. These collisions transfer some of the β particles' energy to the orbital electrons, causing them to escape their orbit (the ejected electron is called a delta ray [Δ]) or to be raised to a higher energy state (excitation). Due to their tortuous path, the depth at which β particles will penetrate a material (range) varies between different β particles of the same energy, a process called *straggling*. Two measures of the depth of penetration of beta particles are the extrapolated range (an estimation of the maximum positron penetration) and the average range (the mean penetration). A short positron range is desirable for positron emission tomography (PET) imaging because PET determines the origin of the electron–positron annihilation event, not the actual site of the positron emission. Table 2.3 presents extrapolated and average ranges for several PET radionuclides

The α particles are much more massive than electrons. As collisions occur between α particles and electrons, the electrons are excited or swept from orbit, but the encounter has little effect on the direction of the α particle. As a result, α particles of the same energy all have the same range, with very little straggling. The range is also very small, so that α particles present very little danger as an external radiation source given that they are stopped by a few centimeters of air or a few micrometers of tissue

Table 2.3 shows the relationship between the maximum energy of the emitted positron and the distance range that these particles travel in air and water. Note that the lower the energy and the denser the medium, the less it travels and, thus, the higher the resulting spatial resolution.

		Extrapolated range, *cm*		Average range, *cm*
Radionuclide	Maximum energy, *MeV*	Air	Water	Water
Carbon-11	0.961	302	0.39	0.103
Nitrogen-13	1.19	395	0.51	0.132
Oxygen-15	1.723	617	0.80	0.201
Fluoride-18	0.635	176	0.23	0.064
Rubidium-82	3.35	1280	1.65	0.429

Data from Cherry et al. [5], with permission from Elsevier

Table 2.3 Positron particle range

Formation of Radionuclides

Figures 2.9 and 2.10 illustrate the formation of radionuclides by nuclear reactors and cyclotrons.

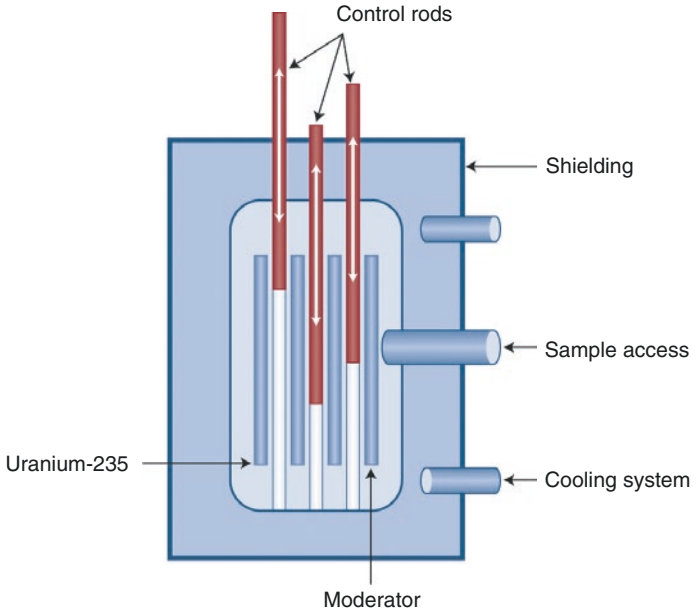

Fig. 2.9 Formation of radionuclides: nuclear reactors. The radionuclides used in nuclear cardiology do not occur naturally and must be manufactured. This may be done by extracting them from the spent fuel of a nuclear reactor, bombarding a target nuclide with high-energy neutrons to make a nuclide that is neutron-rich (too many neutrons to be stable), or bombarding a target with high-energy, positively charged particles, such as protons, using a cyclotron or other particle accelerator to make proton-rich nuclides. Generators are devices that allow the separation of a daughter radionuclide from the parent in a shielded container that may be transported long distances from the manufacturing site (reactor or accelerator)

Nuclear reactors are an important source of radionuclides for nuclear medicine, including iodine-131 and xenon-133. Most importantly, molybdenum-99 (^{99}Mo), the parent of technetium-99m, is produced in a nuclear reactor. The heart of a nuclear reactor is a core of fissionable material (usually uranium-235 [^{235}U] and ^{238}U). Fission splits the uranium nucleus into two lighter nuclei and produces two or three fission neutrons. Some of these neutrons strike other uranium nuclei, converting them to ^{236}U; this quickly undergoes fission and produces many more fission neutrons, which stimulate even more fission events. The uranium in the core is surrounded by a moderator ("heavy water" and graphite) that slows down the fission neutrons to an energy that is more likely to produce further reactions. The ensuing nuclear chain reaction is regulated by control rods made of boron or cadmium, which absorb neutrons. Fission products usually have an excess of neutrons and decay further with emission. More than 100 nuclides are created in the fission process. These fragments can be extracted by chemical means from material removed from the core. Another way to use a nuclear reactor to produce radionuclides, neutron activation, is to place a target into the high-neutron flux of the core while keeping it isolated from the core itself. ^{99}Mo can be produced by either process, but most is extracted as a fission fragment

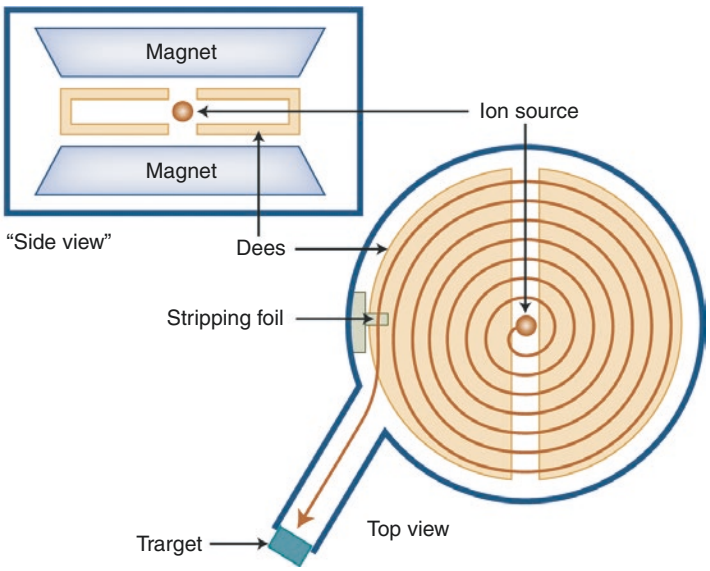

Fig. 2.10 Formation of radionuclides: cyclotrons. Cyclotrons are charged particle accelerators that are used to produce radionuclides by bombarding a target with particles or ions that have been accelerated to high rates of speed. The two basic components of a cyclotron are a large electromagnet and semicircular, hollow electrodes called "dees" because of their shape. Ions are injected into the center of the device between the dees. An alternating current applied to the dees causes the ions to be attracted to one side. Once inside the dee, the ion will travel in a curve because any charged particle moving in a magnetic field (supplied by the electromagnet) moves in a circular path. Although there is no electric field inside the dee, the current is carefully timed so that the polarization of the dees changes as the particles emerge from one side. This accelerates the ions, and their arc of travel becomes larger as they move faster and faster, picking up speed each time they cross the gap between the dees. At the maximum radius, the ions are deflected out of the cyclotron and strike a target, creating new nuclides. An example of this is the use of a cyclotron to bombard an oxygen-18 target with protons, resulting in conversion of the nucleus to fluorine-18 (after the emission of a neutron). Several cyclotron-produced radionuclides used in nuclear cardiology are listed in Table 2.4

Positive-ion cyclotrons accelerate α particles or protons and use an electrostatic deflector to direct the ion beam to the target. Negative-ion cyclotrons, as shown in this figure, accelerate negative hydrogen (H^-) ions, a proton with two electrons. A stripping foil, made of carbon, strips off the two electrons from the ion, leaving a proton. The positive charge of the proton causes it to arch in the opposite direction, which in turn causes the beam to exit the cyclotron and strike the target. Most hospital-based and community-based cyclotrons are negative-ion cyclotrons because they require less shielding and are more compact than positive-ion cyclotrons

Table 2.4 compares the energy of the radiation, half-lives, and modes of production of SPECT radionuclides versus PET radionuclides commonly used in nuclear cardiology procedures. Note that because of the short half-life of most cyclotron-produced PET tracers, a cyclotron must be located nearby. Only fluorine-18 is routinely distributed commercially [6].

Common SPECT radionuclides				
Radionuclide	*Production*	*Decay*	*Emission, keV*	*Half-life*
Iodine-123	Cyclotron	Electron capture	159 (γ-ray)	13.21 hr
Thallium-201	Cyclotron	Electron capture	68–80 x-ray 167 (10%; γ-ray)	73 hr
Technetium-99m	Generator	Internal transition	140 (γ-ray)	6 hr
Common PET radionuclides				
Radionuclide	*Production*		*Positron energy, keV*	*Half-life*
Oxygen-15	Cyclotron		735	122 sec
Nitrogen-13	Cyclotron		491	9.96 min
Carbon-11	Cyclotron		385	20.3 min
Fluoride-18	Cyclotron		248	110 min
Rubidium-82	Generator		1523	1.3 min

Table 2.4 Common radionuclides for use in nuclear cardiology

Figure 2.11 illustrates some types of generators important in preparing radionuclides for use in nuclear medicine.

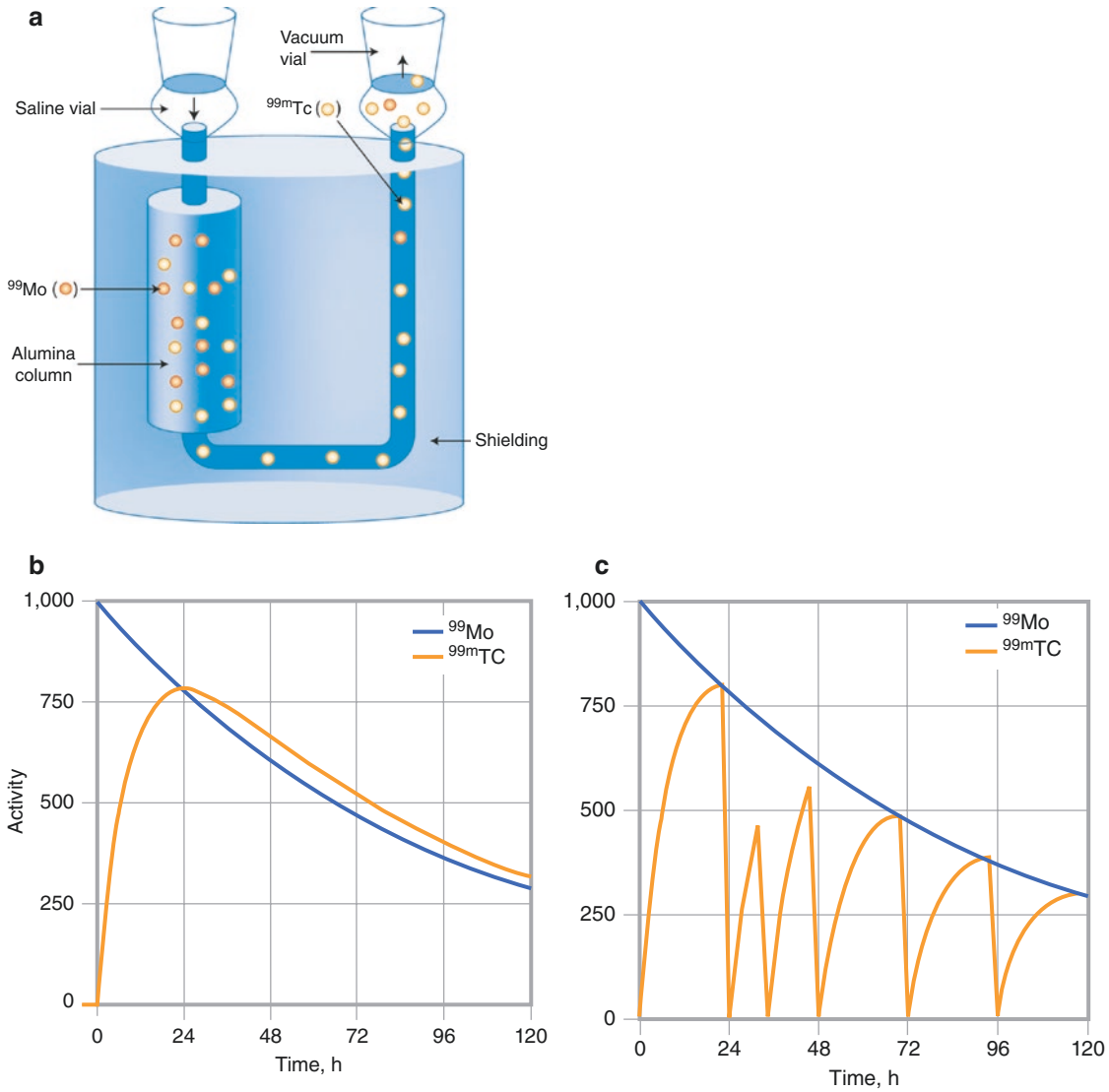

Fig. 2.11 Formation of radionuclides: molybdenum-99–technetium-99m (^{99}Mo–^{99m}Tc) generator. Generators are devices that allow the separation of a radionuclide from a relatively long-lived parent, allowing the production of short-lived radionuclides at a location remote from a reactor or cyclotron (such as a hospital, clinic, or local radiopharmacy). The daughter is continuously replenished by the parent inside the generator, which shields both radionuclides while allowing the daughter to be extracted repeatedly [7]

(**a**) The most common generator used in nuclear medicine is the ^{99}Mo-^{99m}Tc generator, which produces ^{99m}Tc (half-life [t½], 6 h) from the β decay of ^{99}Mo (t½, 66 h). The ^{99}Mo is produced in a nuclear reactor. The heart of the generator is a porous column of alumina impregnated with ^{99}Mo. A vacuum vial is used to pull saline out of a second vial through the porous column. Technetium (both ^{99m}Tc and ^{99}Tc) is washed out of the column by the saline and is collected in a vacuum vial, leaving the ^{99}Mo behind. The generator must be well shielded because ^{99}Mo emits both β particles and 740–780-keV γ-rays. The process of extracting ^{99m}Tc from the generator is called *milking* or *elution*, and the extracted ^{99}Tc-saline solution is called *eluate*. After milking, the ^{99m}Tc solution must be tested for ^{99}Mo and aluminum. ^{99}Mo is detected by using a dose calibrator and a shield that blocks the low-energy photon from ^{99m}Tc. The maximum amount of ^{99}Mo allowed under Nuclear Regulatory Commission regulations is 0.15 Bq ^{99}Mo per kilobecquerel (kBq) ^{99m}Tc (0.15 Ci ^{99}Mo per millicurie ^{99m}Tc). Aluminum is detected chemically, with a maximum permissible level of 10 μg/mL of eluate

(**b**) The ^{99m}Tc is produced by the β decay of ^{99}Mo in the alumina column if the generator is undisturbed. This process is an example of transient equilibrium, in which the parent's half-life is somewhat longer than the daughter's half-life. After a few hours, the daughter activity is almost equal (actually slightly higher) to the parent activity

(**c**) Activity in the generator with repeated milkings is shown. Fortunately, the optimal frequency for milking the generator is at intervals slightly less than 24 h. The dip at 32 h shows that if the generator is milked, the process of ^{99m}Tc buildup begins again (and, in this case, results in only slightly less activity at the next regular milking). ^{99}Mo-^{99m}Tc generators are designed to last at least 2 weeks in the nuclear pharmacy

Another generator of importance to nuclear cardiology is the strontium-82 (^{82}Sr)–rubidium-82 (^{82}Rb) generator. ^{82}Rb (t½ = 1.3 min) is produced by a β decay of ^{82}Sr (t½ = 25 day, manufactured using an accelerator). The daughter activity equals the parent activity very soon after elution and allows elution every hour. This is an example of secular equilibrium in which the parent's half-life is a great deal longer than the daughter's half-life. The short half-life of ^{82}Rb makes it impractical to transport the dose to the patient. The generator is designed to deliver the dose directly into an intravenous line. ^{82}Rb generators are designed to last about 1 month in the clinic. ^{82}Sr and ^{85}Sr may be low-level contaminants and are found in routine quality control by assaying the eluent after complete decay of the ^{82}Rb

Imaging Devices and Principles

Devices and principles of nuclear cardiology imaging are shown in Figs. 2.12, 2.12, 2.13, 2.14, 2.15, 2.16, 2.17, 2.18, 2.19, 2.20, 2.21, 2.22, 2.23, 2.24, 2.25, 2.26, 2.27, 2.28, 2.29, 2.30, 2.31, 2.32, 2.33, 2.34, 2.35, 2.36, 2.37, 2.38, and 2.39.

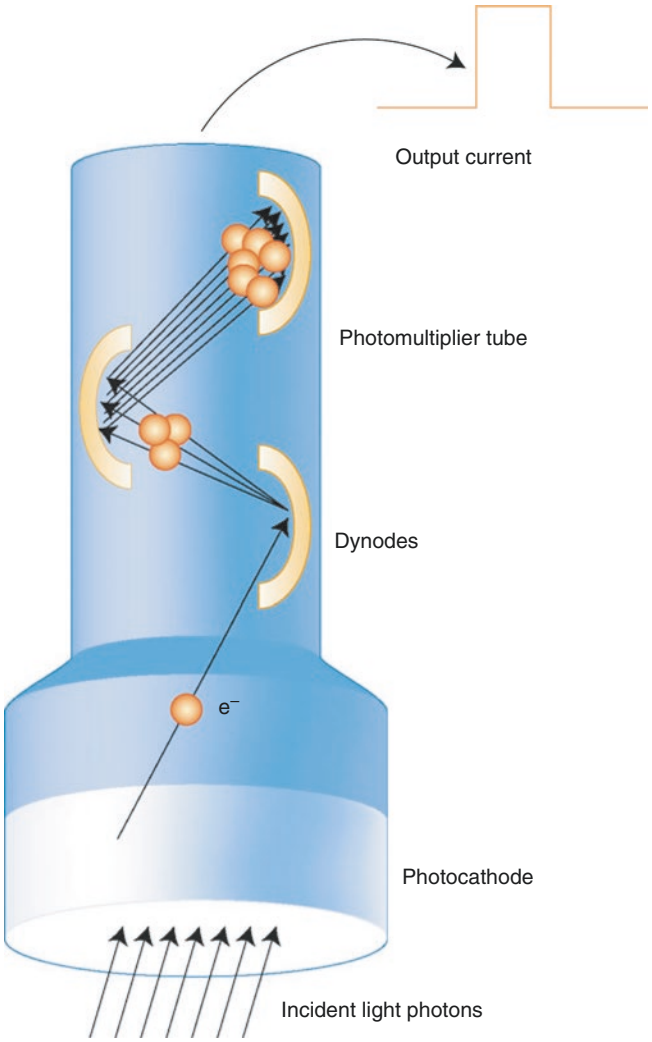

Fig. 2.12 Operation of photomultiplier tubes (*PMTs*). PMTs convert energy from visible light into an electric signal. Light interacting with the material in the photocathode causes it to release electrons, which are accelerated along the tube by a high-voltage differential. As the electrons travel through the tube, they strike metal electrodes called *dynodes*, at which point even more electrons are ejected. This cascade of multiplication continues until the electrons are output as a current at the other end. The voltage (height) of the pulse generated by the PMT is directly proportional to the amount of visible light that strikes the photocathode

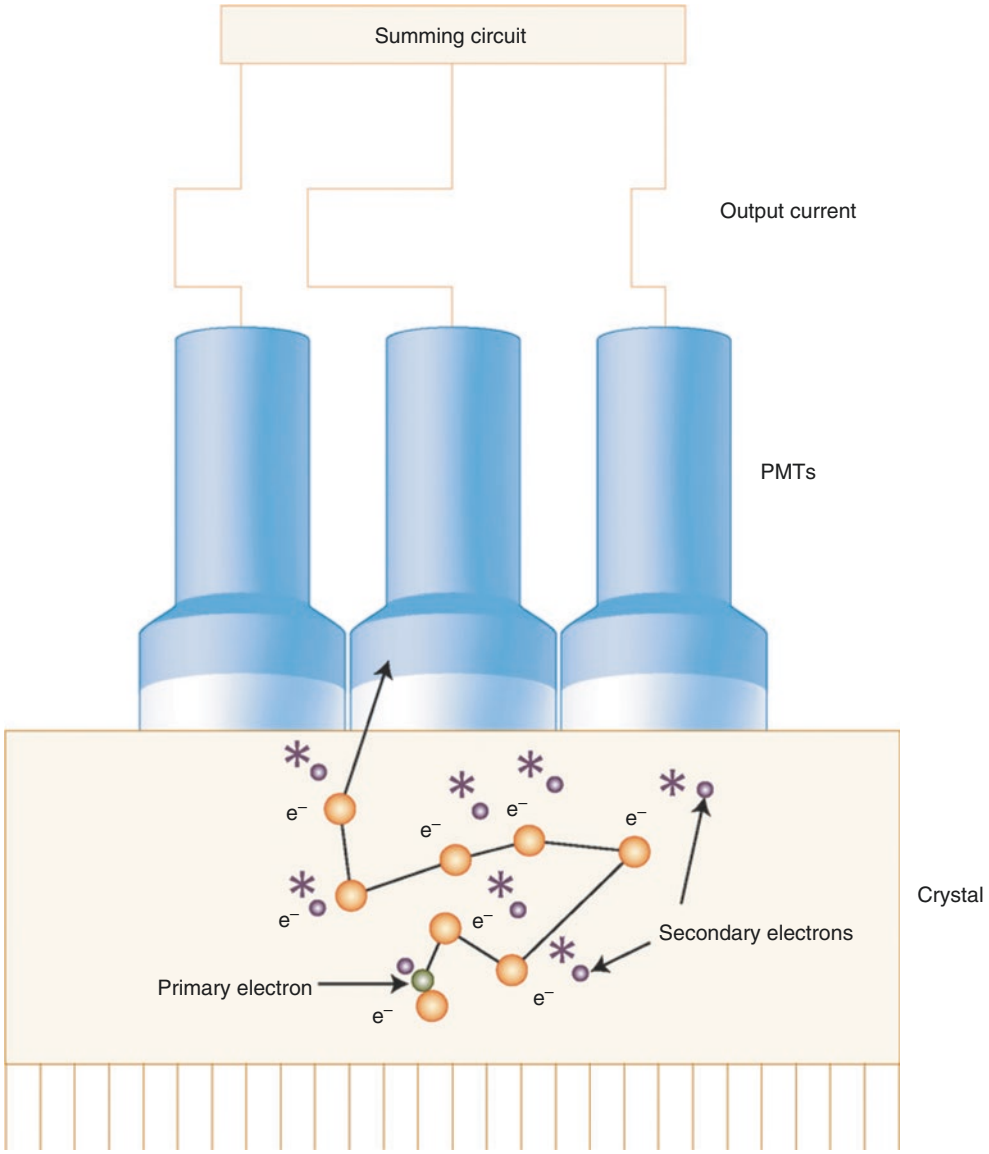

Fig. 2.13 Operation of the crystal. The crystal is used to convert γ-rays into visible light. A γ-ray travels through the collimator and interacts with one of the atoms in the crystal, ejecting an electron (called the primary electron) through the photoelectric effect. This ejected electron continues traveling through the crystal and excites a large number of secondary electrons, which lose their excitation energy by emitting visible light. The glow of the scintillation is converted into electrical signals by the PMTs. The location of the scintillation event is determined by the positioning circuitry based on the relative signals from the different PMTs. The brightness of the scintillation is proportional to the energy of the photon, measured by the pulse height analyzer

Note that the γ-ray travels some distance through the crystal before it interacts with a crystal atom. If the crystal is very thin, a γ-ray may travel through the entire width of the crystal with no interaction. Therefore, a thicker crystal results in a higher sensitivity for the detection of γ-rays. Conversely, note that the primary electron travels in an irregular path and may excite atoms far away from its point of origin. The thicker the crystal is, the farther the electron may travel before it exits the crystal. Thus, a thick crystal implies that the scintillation may be more spread out, which essentially reduces the resolution of the detector. So, just as with collimators (*see* Fig. 2.16), there is a trade-off between sensitivity and resolution with the size and shape of the crystal

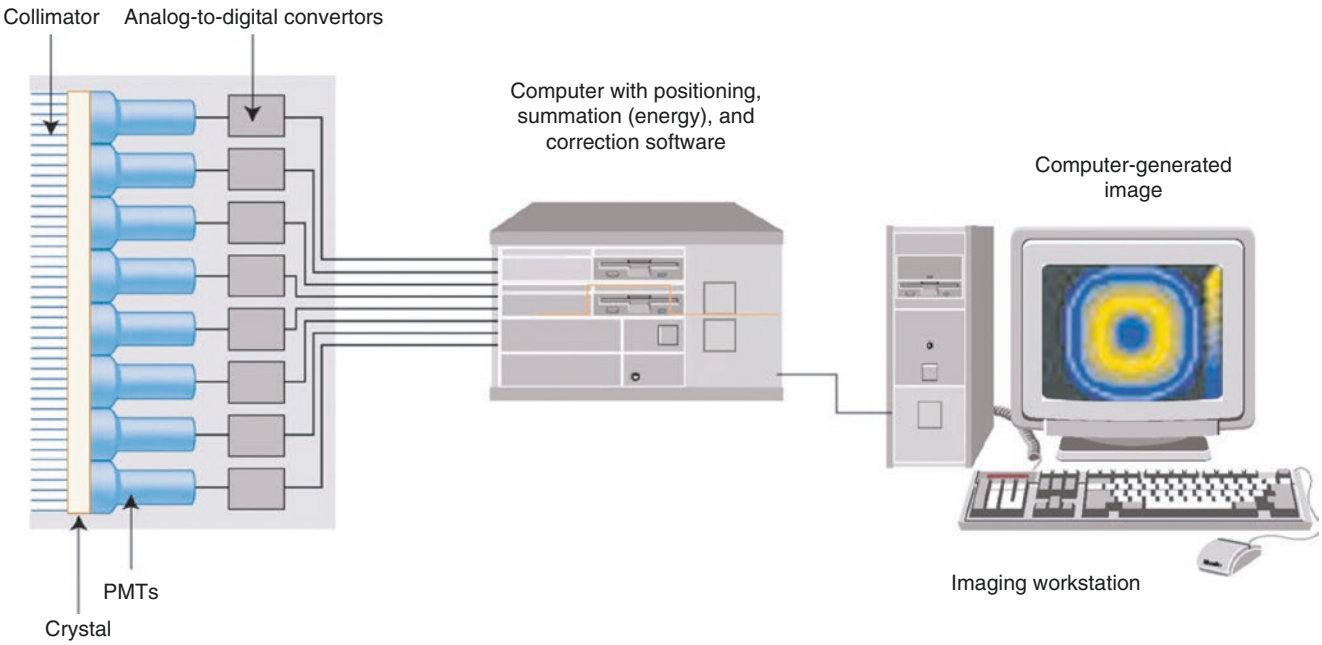

Fig. 2.14 Digital scintillation camera. The main components of SPECT systems are the scintillation camera, the gantry (the frame that supports and moves the heads), and the computer systems (hardware and software). These components work together to acquire and reconstruct the tomographic images

The basic components of a scintillation camera are a collimator, a sodium iodide crystal, PMTs, and an analog or digital computer designed to determine the location and energy of a photon striking the crystal. γ-Rays (photons) pass through the collimator and cause a scintillation event (a short burst of visible light) to occur in the crystal. The glow of the scintillation is converted into electrical signals by the PMTs. The location of the scintillation event is determined based on the relative signals from the different PMTs. The brightness of the scintillation is proportional to the energy of the photon. Scintillation cameras were developed in the late 1950s and early 1960s. These cameras used pulse height analyzers and spatial positioning circuitry invented by Hal Anger of the University of California at Berkeley to determine the location and energy of the incident photon [8]. Early cameras were completely analog devices in which the output was sent to an oscilloscope, creating a flash on the screen. A lens focused the screen on a piece of radiographic film that was exposed, one flash at a time. This allowed for planar imaging, but for SPECT the images must be made available to the computer digitally

Today, camera systems convert the position and pulse height signals generated from analog circuitry in the camera to digital signals using analog-to-digital converters. The signals may then be further corrected for energy and position through digital processing. Camera designs that convert the output of each PMT to a digital signal, as shown here, have become common. The computer may then perform all of the positioning and pulse height analyses without the need for complicated analog circuitry. This results in greater processing flexibility, greater spatial resolution, and higher count rates

Another step in the digitization of scintillation cameras is the replacement of PMTs with solid-state detectors called *photodiodes*. One camera with this design uses individual cesium iodide (CsI) scintillation crystals, each backed with a silicon photodiode. Each CsI crystal is 3 mm^2, giving a resolution similar to that of a conventional camera without the need for positioning circuitry. Eliminating the PMTs greatly reduces the size and weight of the scintillation camera, with some trade-offs in cost and energy resolution. These types of cameras are usually known as solid-state cameras

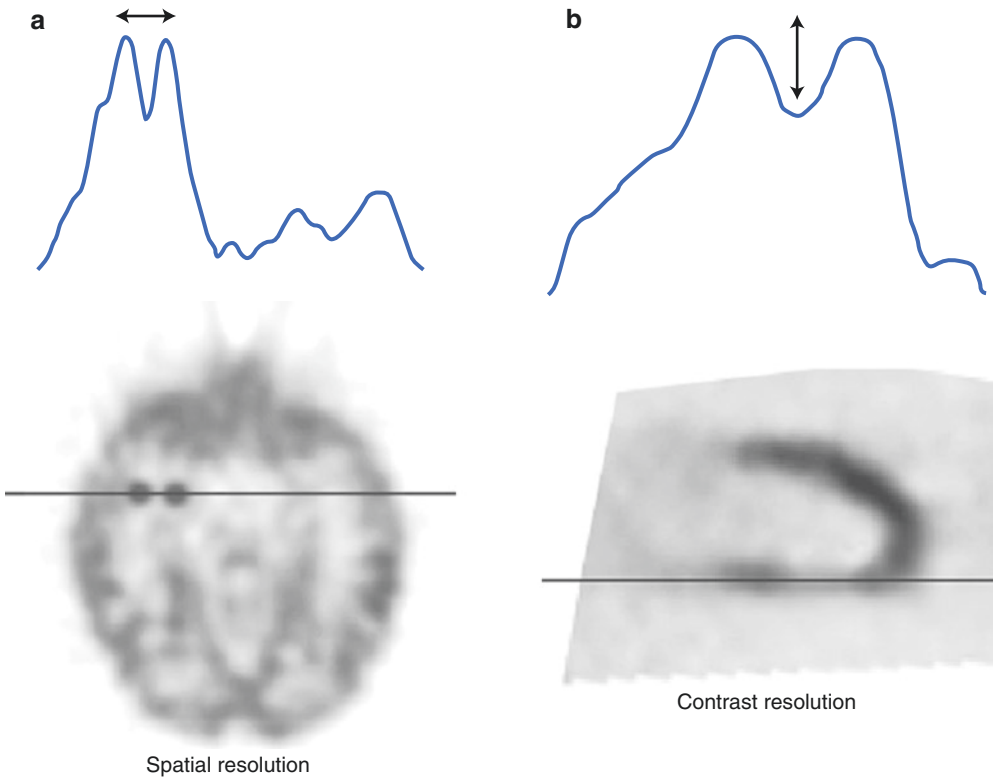

Fig. 2.15 Principle of spatial and contrast resolution. The most common measurements of image quality are spatial resolution and contrast resolution. *Spatial resolution* refers to how well objects can be separated in space (as opposed to blurring them together), and *contrast* refers to how well different levels of brightness (representing radionuclide concentration in a scintigram) can be discriminated

Spatial resolution is the measure of how close two point sources of activity can come together and still be distinguished as separate. Because no medical imaging modality is perfect, a point source never appears as a single bright pixel but instead as a blurred distribution. Two blurry points eventually smear together into a single spot when they are moved close enough to each other. Resolution is measured by taking a profile (a graph of counts encountered along a line drawn through a region of interest in the image) through a point source and analyzing the resulting curve. A profile through a perfect point source would look like a sharp single spike rising above the flat background. A profile through a real point source appears as a Gaussian-shaped curve; this curve is called the *point spread function*. (**a**) When the two Gaussian curves of two point sources get close enough together, they cannot be distinguished as separate. This distance is a measure of image resolution. Two brain tumors are imaged and a profile is taken through the resulting reconstruction. As the tumors move closer together, the discrete peaks of the profile start to merge into a single peak

Contrast resolution in nuclear cardiology images can be defined as the measure of counts (or intensity) in the target (the object we are trying to image) compared with the intensity in a background region. High counts in the target increase contrast; high counts in the background region (e.g., lung uptake) decrease contrast. Low contrast can make the target fade into the background. (**b**) Contrast is also easily measured using a profile. This figure shows a count profile taken through a decreased area of a myocardial perfusion image. In this case, the "target" counts are those in the perfusion abnormality, and the "background" counts are those in the normal myocardium. The depth of the valley in the profile, compared with the overall height of the rest of the curve, is a measure of contrast

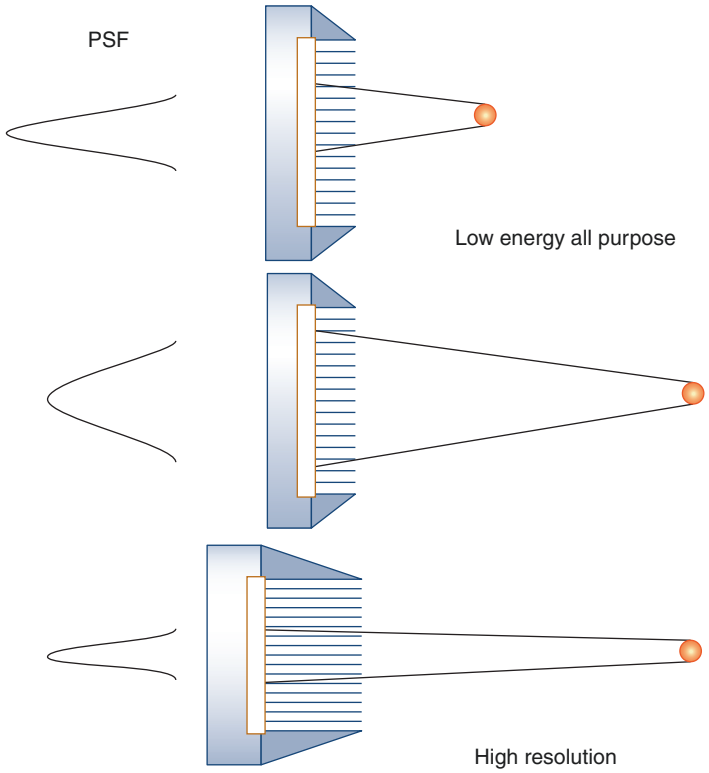

Fig. 2.16 Principle of collimation. Because γ-rays are emitted from a source uniformly in all directions, a photon from any area of the body can theoretically strike any area of the detector. Instrumentation is needed to determine the directions of the photon's emissions in order to be able to localize the source. This process is called *collimation*. For nuclear cardiology, collimators generally consist of an array of long, narrow (usually) parallel holes that exclude all photons except those that travel parallel to the direction of the hole. Collimators are rated by their sensitivity and resolution. *Resolution* is defined in Fig. 2.15; *sensitivity* is the number of photons that travels through the collimator in a certain amount of time (as a fraction of photons emitted from the source)—that is, counts per second or counts per minute. In this instance, image resolution is affected by collimation because some photons not traveling in exactly a parallel path get through the collimator holes. Thus, a single point source will appear fuzzy on the detector. How much the point "spreads out"—the width of its point spread function (PSF)—is related to the spatial resolution and depends on the length and width of the holes. More specifically, spatial resolution is given by the full width of the PSF as half its maximum. Low-energy all-purpose (LEAP) and general-purpose collimators have relatively short, wide holes that accept more photons than do high-resolution collimators with long, narrow, and/or smaller holes. Increasing the length of the hole increases resolution by decreasing the angle subtended by the hole and thus eliminates more γ-rays traveling at angles not parallel to the hole. Thus, a higher resolution is achieved at the cost of sensitivity. In general, the sensitivity and resolution of a collimator are inversely related. A very high-sensitivity collimator will have low resolution, and a very high-resolution collimator will have low sensitivity. Here, the PSFs for differently shaped collimators are shown at the *left* of the figure. Note that the width of the PSF curve is broader for LEAP collimators, indicating a lower resolution, but the total area underneath this PSF curve is higher than that of the high-resolution collimator, indicating higher sensitivity. This figure also demonstrates that the resolution of the image, as seen by the PSF curves on the *left*, depends on the distance between the source and the collimator. This is discussed in more detail in Fig. 2.17

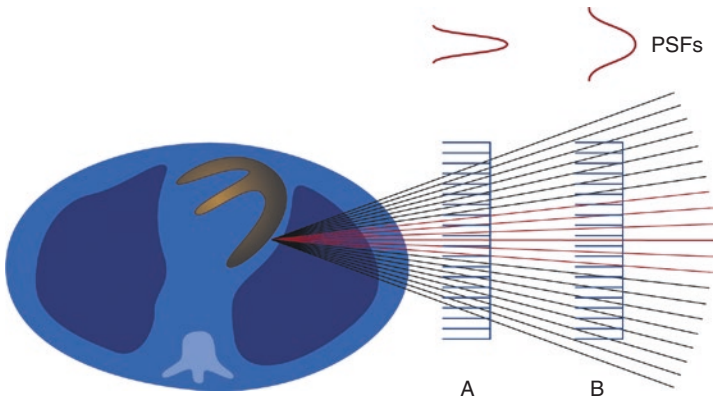

Fig. 2.17 Resolution versus sensitivity. In air, recall that the amount of radiation from a point source falling on a plane decreases as $1/r^2$. However, if a collimator is placed between the source and the detector, this relationship no longer holds. The same number of γ-rays will travel through the collimator, no matter how far the source is from the detector, because γ-rays that travel too obliquely from the line of the collimator holes will not pass through any collimator, no matter how close it is to the source. However, a ray that is near enough to being parallel to a collimator hole will be able to pass through a collimator, no matter how distant it is from the source. The primary difference between a collimator placed near the source and one placed far away from the source is which collimator hole a γ-ray will pass through

A γ-ray traveling exactly parallel to the collimator will pass through the hole that is directly "aimed" at the source. If the γ-ray is slightly oblique to the collimator, it may pass through a hole not exactly in line with the source. How far away that hole is from the "correct" hole depends on how far the source is from the collimator. In this figure, notice that when the collimator is close to the source (*A*), most of the γ-rays travel through the collimator holes that are nearly in line with that source, even when those γ-rays are slightly oblique to the holes. However, if the detector is far away from the source (*B*), the same number of γ-rays travels through the collimator but more of the oblique rays travel through holes farther away from the one directly in line with the source. This causes a blurring or loss of resolution, which is seen in the PSFs shown for each of the collimator positions at the *top* of the figure. Note that the farther away the detector is from the source, the lower and more spread out the PSF. However, the area underneath these curves does not change. Therefore, the number of photons detected stays the same with collimator-source distance, but the image resolution decreases as the distance increases. This resolution decrease with source-to-detector distance is termed the *detector response* or *geometric response*

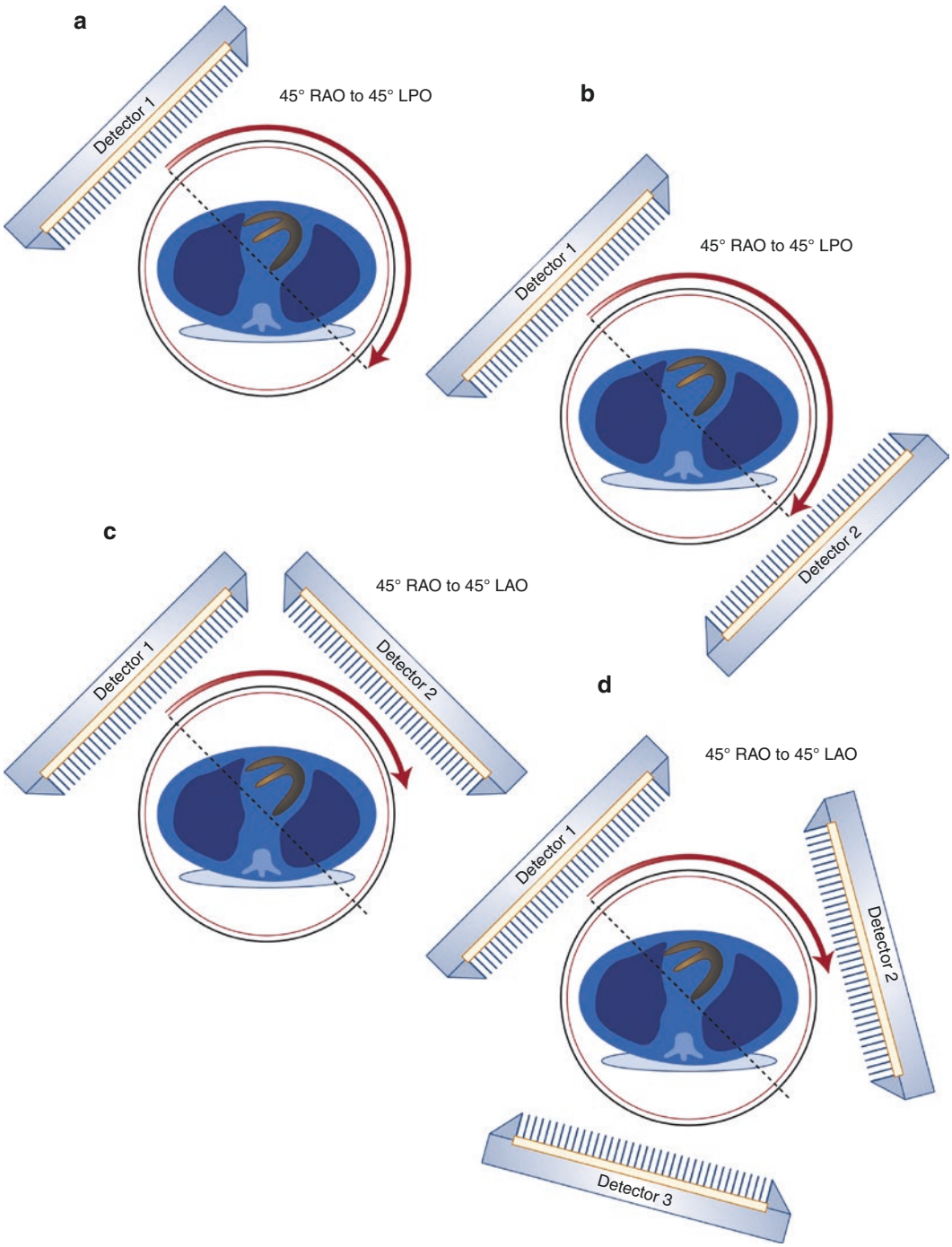

Fig. 2.18 SPECT cameras: multiheaded cameras. Multidetector SPECT systems have more than one scintillation camera attached to the gantry. (**a**) The most obvious benefit of adding more detectors to a scintillation camera system is the increase in sensitivity. Doubling the number of heads doubles the number of photons that may be acquired in the same amount of time. The user may take advantage of the increase in sensitivity by acquiring more counts, adding higher-resolution collimation, or increasing throughput. (**b**) This figure shows two large field-of-view rectangular cameras mounted opposite each other, 180° apart. This configuration may speed 360° SPECT imaging by halving the imaging time while collecting the same number of counts, because a full 360° of projections can be acquired by rotating the gantry 180°. (**c**) For cardiac SPECT, in which a 180° orbit is recommended, SPECT systems with two detectors mounted next to each other (at 90°) on the gantry allow a full 180° orbit to be acquired while only rotating the gantry through 90°. (**d**) Triple detector cameras are usually dedicated to SPECT imaging. The three heads, as discussed for double-headed systems, will result in increased sensitivity that may be used to increase throughput, counts, or resolution. If the three detectors are mounted rigidly 120° from one another, however, the system must rotate through 120° to obtain 180° of data. Thus, these systems also do not have a great impact on cardiac imaging with 180° orbits

For any multiheaded system, the primary advantage is increase in throughput, because the acquisition will take less time. However, the gain in sensitivity may be traded to give more precise images by allowing the use of higher-resolution collimators

Drawbacks of multiple-headed cameras include an increase in quality control required by the addition of the additional heads and some loss of flexibility. Double-detector systems do not allow the same flexibility of movement that is enjoyed with many single-headed systems. They may not be easily used for some types of planar imaging (e.g., gated blood pool), in which it is often difficult to position the camera correctly. One unique SPECT system acquires planar projections by rotating the patient in an upright position while the camera(s) remain(s) fixed. LAO left anterior oblique, LPO left posterior oblique, RAO right anterior oblique

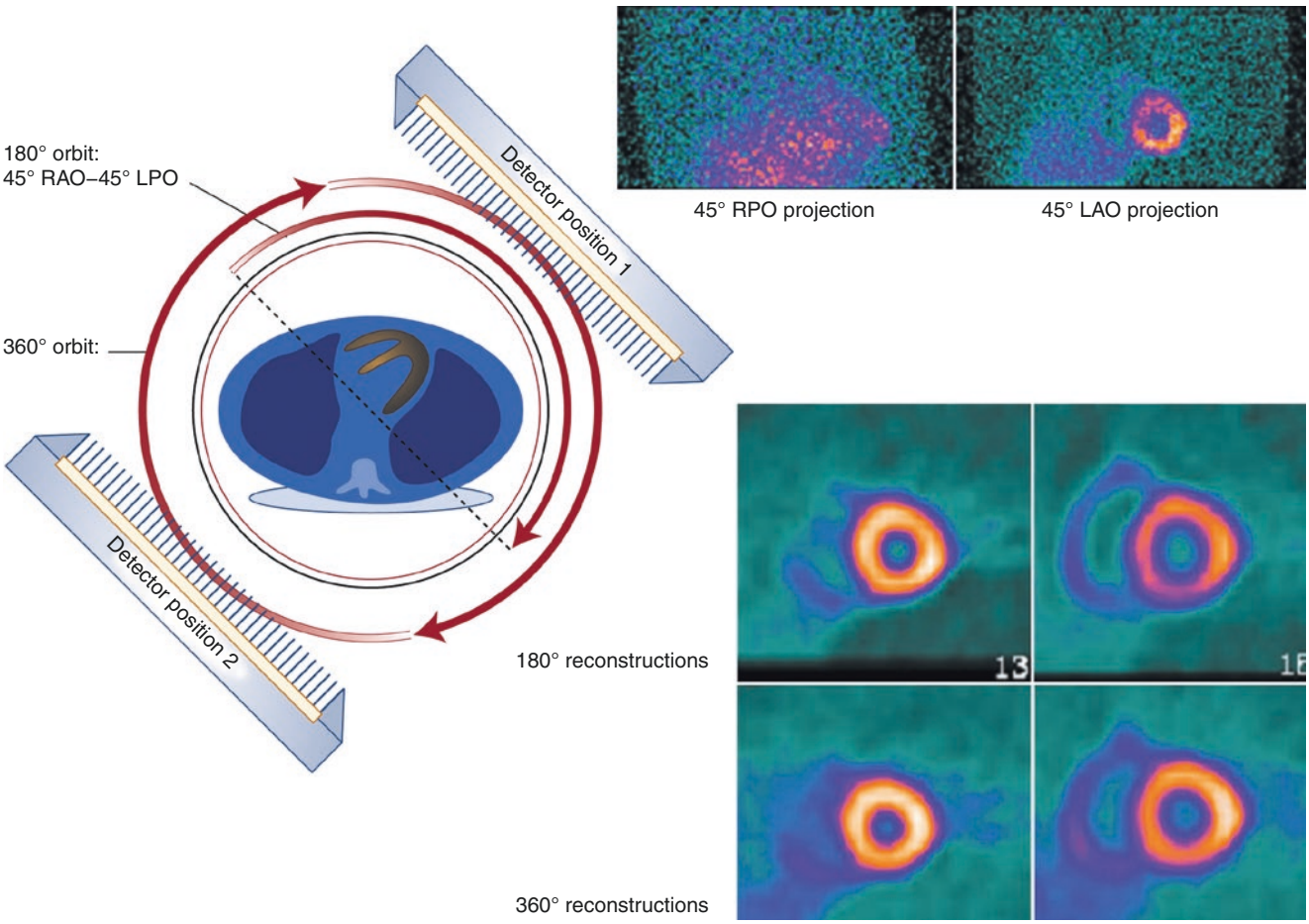

Fig. 2.19 SPECT cameras: 180° versus 360° data acquisition. Although 360° orbits are generally preferred for body SPECT, 180° orbits may be better for cardiac SPECT. The heart is located forward and to one side of the center of the thorax, resulting in a great deal of attenuation when the camera is behind the patient. The angles chosen for the 180° orbit are those closest to the heart, from the 45° right anterior oblique (*RAO*) to the 45° left posterior oblique (*LPO*). These projections are those that suffer least from attenuation, scatter, and detector response because they are the ones that get the camera head as close as possible to the heart. Projections taken from the posterior aspect of the body are generally noisier and of lower resolution than those taken from the anterior angles. This is easily seen by comparing the 45° left anterior oblique (*LAO*) projection shown here to the 45° right posterior oblique (*RPO*) projection. Reconstructions from 180° acquisitions have higher resolution and contrast than those from 360° acquisitions; this is particularly true for thallium-201 images [9–11]. However, because 180° reconstructions are not truly complete (i.e., new information is available from the other 180° of projections), occasional artifacts seen with 180° reconstructions can be avoided with 360° reconstructions. In particular, 360° reconstructions are generally more uniform than 180° reconstructions. Both of these effects can be seen on the reconstructions on the *bottom right* of this figure

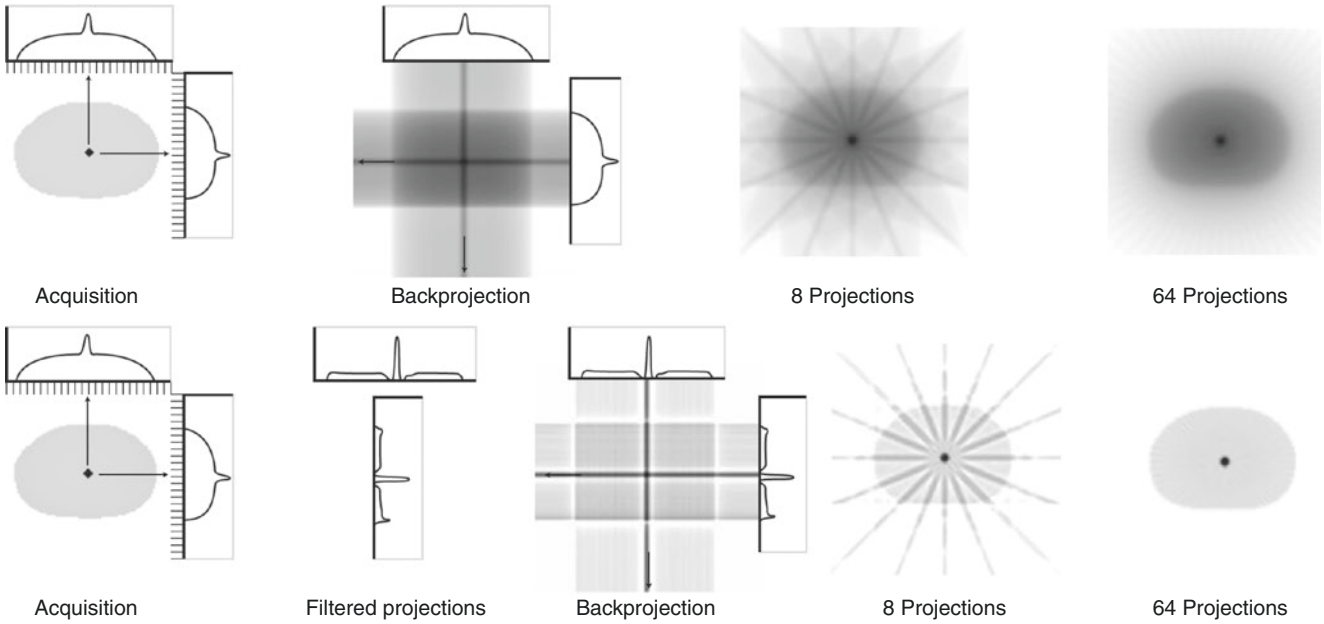

Fig. 2.20 Principle of filtered backprojection reconstruction. Filtered backprojection is an analytic method of image reconstruction. Filtered backprojection, as its name implies, is a combination of filtering and backprojection. The principle of backprojection is shown in the *top row*. When a projection image is acquired, each row of the projection contains counts that emanate from the entire transverse plane. When projection images are obtained from many angles about the body, enough information is available in each row of the set of angular projections to reconstruct the original corresponding transverse slice. Backprojection assigns the values in the projection to all points along the line of acquisition through the image plane from which they were acquired. This operation is repeated for all pixels and all angles, adding the new values with the previous, in what is termed a *superposition operation*. As the number of angles increases, the backprojection improves

Although simple backprojection is useful for illustrative purposes, it is never used in practice without the step of filtering. Note that the backprojection from the top row is quite blurred compared with the original distribution from which it was created. Also, the reconstructions created from eight projections show instances of the "star artifact," which consists of radial lines near the edges of the object. This artifact is a natural result of backprojection applied without filtering. In clinical practice, the projections are filtered prior to backprojection; filtered backprojection is shown in the *bottom row*. After the projections are acquired, a ramp filter is applied to each of them prior to backprojection. Ramp filters are discussed in more detail in Fig. 2.21. The ramp-filtered projections are characterized by enhancement of edge information and the introduction of negative values (or lobes) into the filtered projections. During the backprojection process, these negative values cancel portions of the other angular contributions and, in effect, help to eliminate the star artifact and the blurring seen in the unfiltered backprojection. However, enough projections must be acquired to ensure that proper cancellation is obtained. Radial blurring or streaking toward the periphery of the image often indicates that too few projections were acquired. Finally, a noise-reducing filter such as a Butterworth or Hanning filter is usually applied before, during, or after the backprojection operation. Such filters are discussed in more detail in Fig. 2.21

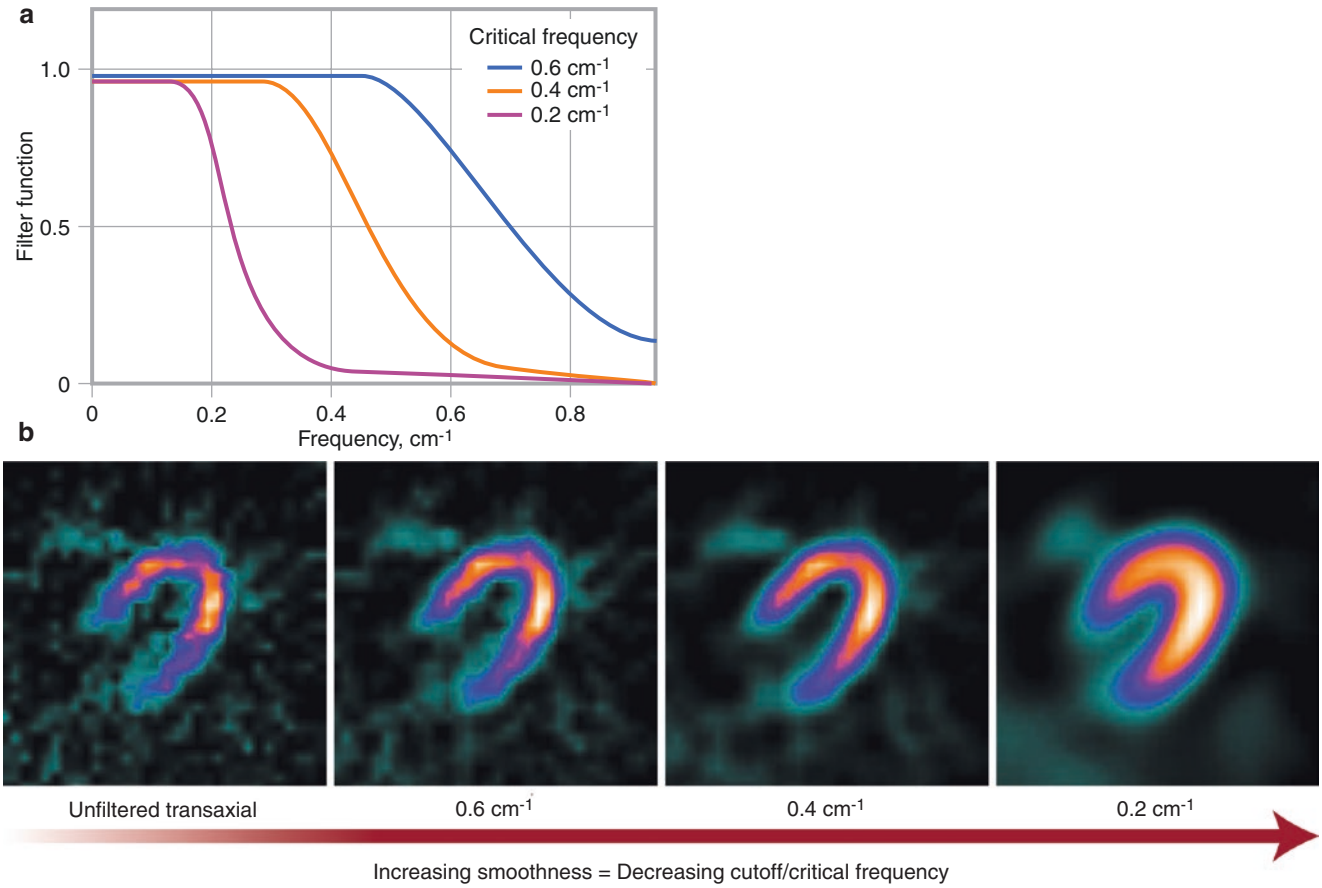

Fig. 2.21 Image filtering. Filtering is the process by which images are smoothed, sharpened, reduced in noise, or used in reconstruction, such as the ramp filter in filtered backprojection. Filtering digital images is accomplished by transforming the images from the spatial domains that are used to frequency space [12, 13]. This transformation is usually performed using a mathematical process called a *Fourier transform*. This transform represents images in terms of cycles per centimeter or variations of counts over distance. In this representation, smaller objects, edges of objects that abruptly change in counts, and image noise are all associated with high frequencies. Larger, smooth organs are associated with lower frequencies. A filter works by defining a curve that specifies how much of each frequency should be modified. If the filter value is 1 at a specific frequency, then it is not modified; if it is less than 1, it is reduced by that amount; and if it is more than 1, it is enhanced by that amount

Because the filtered backprojection reconstruction process uses a ramp filter that enhances image noise, smoothing must be applied to the reconstructed images to reduce the image noise. The most common filters used for smoothing cardiac perfusion images are the Hanning and Butterworth filters. Both these filters are known as *low-pass filters* because they tend to leave the lower frequencies alone while reducing the higher frequencies. The Butterworth filter is defined by two parameters: the critical frequency and the order of the filter. The critical frequency is used to define when the filter begins to drop to zero (known as the *cutoff frequency* for a Hanning filter). The order of the filter determines the steepness of the function's downward slope

(**a**) The *color curves* are three examples of critical frequencies for the Butterworth filter. (**b**) The four transaxial cardiac images are examples of that same transaxial image with the various critical frequencies of the Butterworth filter applied. The leftmost transaxial image has had the gray filter applied. Note that the gray filter is 1 for every frequency; thus, no smoothing is performed. This is the original noisy image that results from the filtered backprojection process. The next image has had the purple filter applied, with a critical frequency of 0.6 cycles/cm. This image appears slightly smoother than the one with no smoothing. As the other two filters are applied with increasingly lower critical frequencies, the image becomes smoother

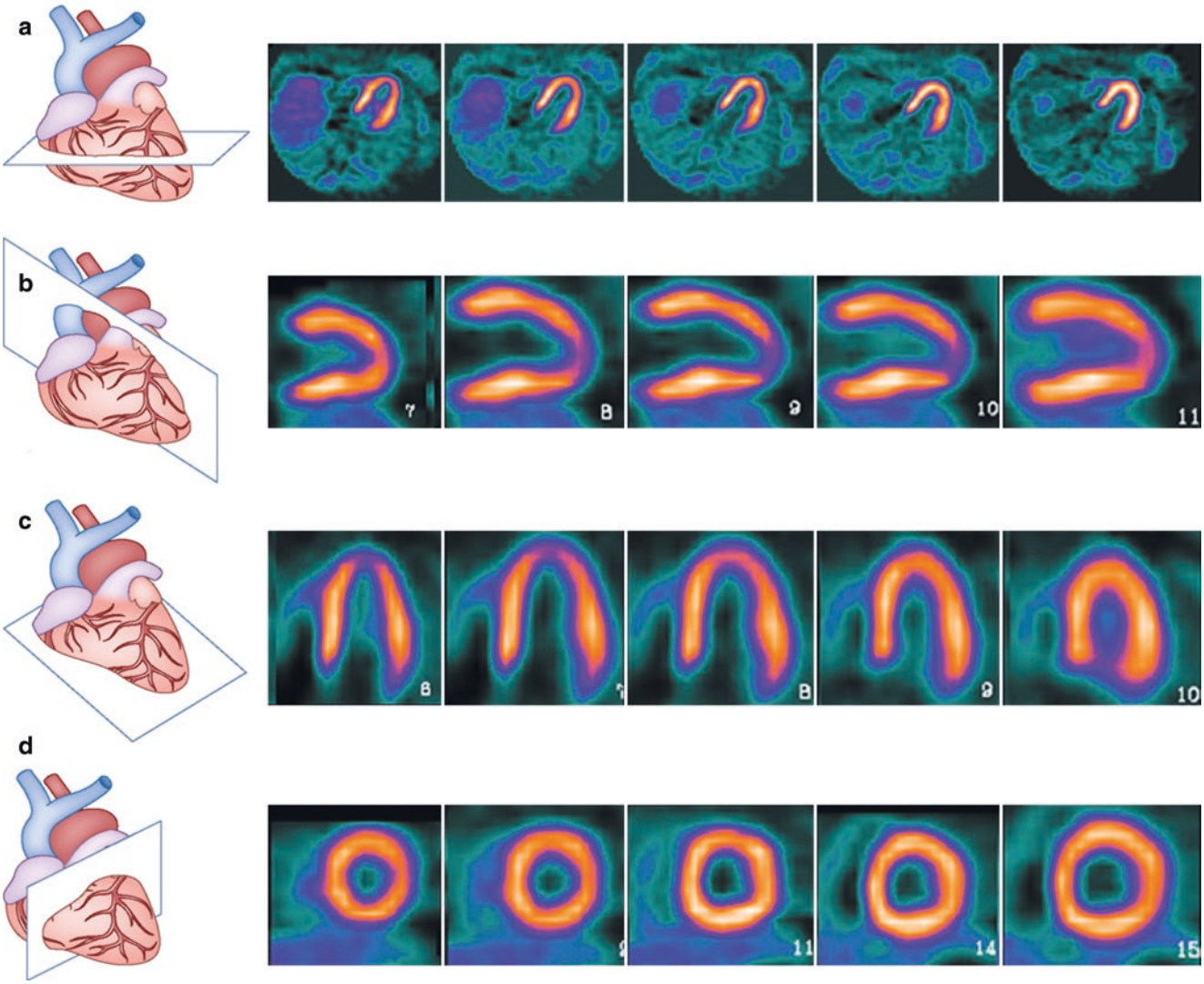

Fig. 2.22 Oblique angle reorientation. *Transaxial images*: The natural products of rotational tomography are images that represent cross-sectional slices of the body, perpendicular to the imaging table (or the long axis of the body). These images are called *transverse* or *transaxial* slices. (**a**) An example of transaxial slices is shown

Oblique images: We are not restricted to the natural *x*, *y*, and *z* directions, however, for the display of images. The computer may be used to extract images at any orientation, and these images are called *oblique images*. Because of the variation in the heart orientation of different patients, it is important that oblique slices are adjusted to try to match the same anatomy from patient to patient. The important oblique sections used for viewing cardiac images are defined as follows:

Vertical long-axis slices: The three-dimensional set of transaxial sections, some of which are shown in (**a**), is resliced parallel to the long axis and perpendicular through the transaxial slices. Each of the resulting oblique images is called a *vertical long-axis slice* (**b**). They are displayed with the base of the left ventricle toward the left side of the image and the apex toward the right. Serial slices are displayed from medial (septal) to lateral, *left to right*

Horizontal long-axis slices: The three-dimensional block of vertical long-axis slices is recut parallel to the denoted long axis and perpendicular to the stack. The resulting oblique cuts are called *horizontal long-axis slices* (**c**). They contain the left ventricle with its base toward the bottom of the image and its apex toward the top. The right ventricle appears on the left side of the image. Serial horizontal long-axis slices are displayed from inferior to anterior, from *left to right*

Short-axis slices: Slices perpendicular to the denoted long axis and perpendicular to the vertical long-axis slices are also cut from the stack. These are termed *short-axis slices*; they contain the left ventricle with its anterior wall toward the top, its inferior wall toward the bottom, and its septal wall toward the left. (**d**) Serial short-axis slices are displayed from apex to base, from *left to right*

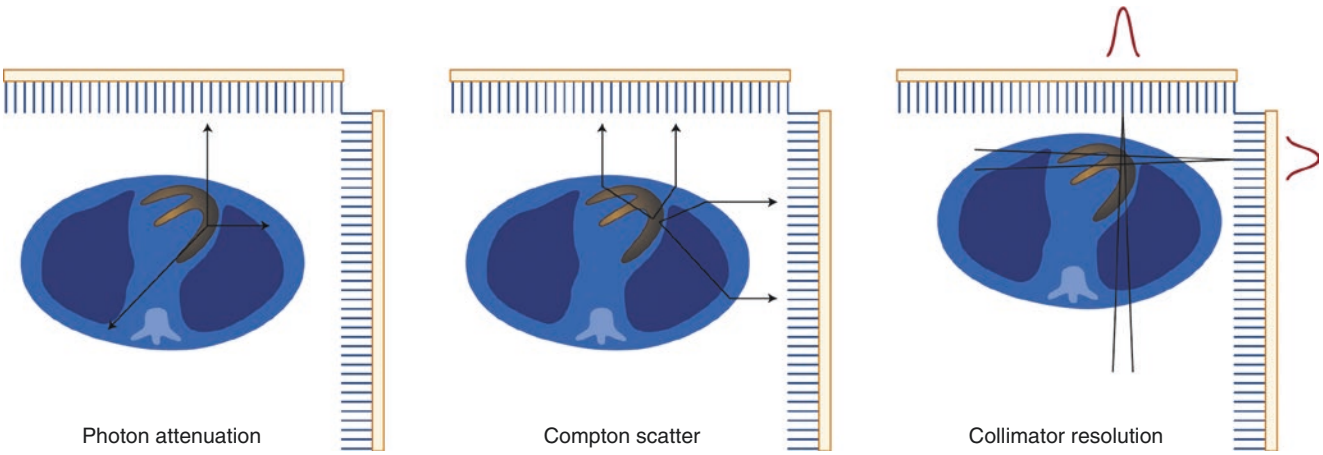

Fig. 2.23 Physical factors that may affect SPECT image formation. Accurate reconstructions of the radionuclide distribution in the body depend on accurate detection of the emitted γ-rays. However, not all of the γ-rays emitted by a radionuclide emerge from the body, and those that do are not all detected in the right place. These complicating factors degrade the resulting image. The three factors that cause degradations in SPECT are attenuation, scatter, and distance-dependent resolution or blur of collimation. Attenuation is the absorption of γ-rays by other materials and includes photons lost due to both the photoelectric effect and Compton scattering. The probability that a γ-ray is absorbed increases with the density of the material through which it must pass but decreases with increasing energy of the photon

Other γ-rays may interact with electrons in the material through which they are passing, causing them to change direction and lose energy. These γ-rays may still emerge from the body but from a direction other than their original path. If these γ-rays are detected by the gamma camera, they appear to be originating from the wrong place. Finally, γ-rays traveling in paths other than parallel to a collimator hole may still travel through that hole and be detected by the camera. This becomes more likely as the source gets farther and farther away from the collimator. The result is a blurring in the final image that depends on the distance between the source and collimator, called the *detector response*, which was discussed in Fig. 2.17

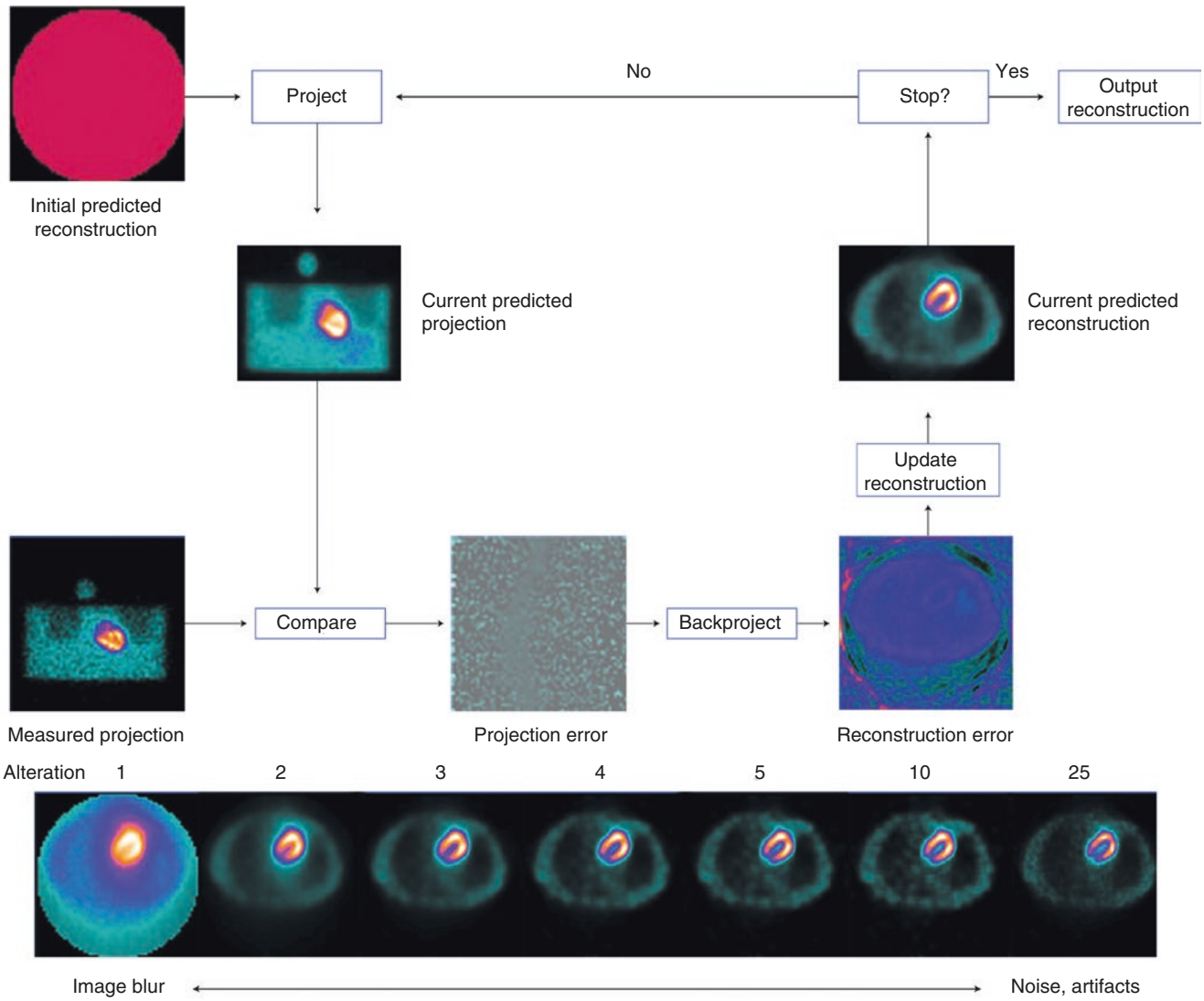

Fig. 2.24 Principle of iterative reconstruction. Iterative reconstruction techniques require many more calculations and, thus, much more computer time to create a transaxial image than does filtered backprojection. However, their great advantage is their ability to incorporate into the reconstruction process corrections for the factors that degrade SPECT images. Iterative techniques use the original projections and models of the acquisition process to predict a reconstruction. The predicted reconstruction is then used again with the models to recreate new predicted projections. If the predicted projections are different from the actual projections, these differences are used to modify the reconstruction. This process is continued until the reconstruction is such that the predicted projections match the actual projections. The primary differences between various iterative methods are how the predicted reconstructions and projections are created and how they are modified at each step. Practically speaking, the more theoretically accurate the iterative technique, the more time-consuming the process. Maximum-likelihood methods allow the noise to be modeled, whereas least squares techniques such as the conjugate gradient method generally ignore noise

The most widely used iterative reconstruction method is maximum-likelihood expectation maximization (MLEM) [14]. The MLEM algorithm attempts to determine the tracer distribution that would "most likely" yield the measured projections given the imaging model and a map of attenuation coefficients, if one is available. An example of the reconstruction of the myocardium with the MLEM algorithm is shown at the *bottom*. The point of convergence of this algorithm and the related number of iterations for clinical use are a source of debate. To date, there is no common rule for stopping the algorithms after an optimal number of iterations on clinical data, and protocols describing the optimal number of iterations are largely empirically based. As can be seen in the reconstructions at the bottom, as the iteration number increases, the images generally get less blurry but more noisy

Another approach to the MLEM algorithm for iterative reconstruction is the ordered-subsets expectation maximization (OSEM) approach [15]. This approach performs an ordering of the projection data into subsets. The subsets are used in the iterative steps of the reconstruction to greatly speed up the reconstruction. The advantage of OSEM is that an order-of-magnitude increase in computational speed can be obtained

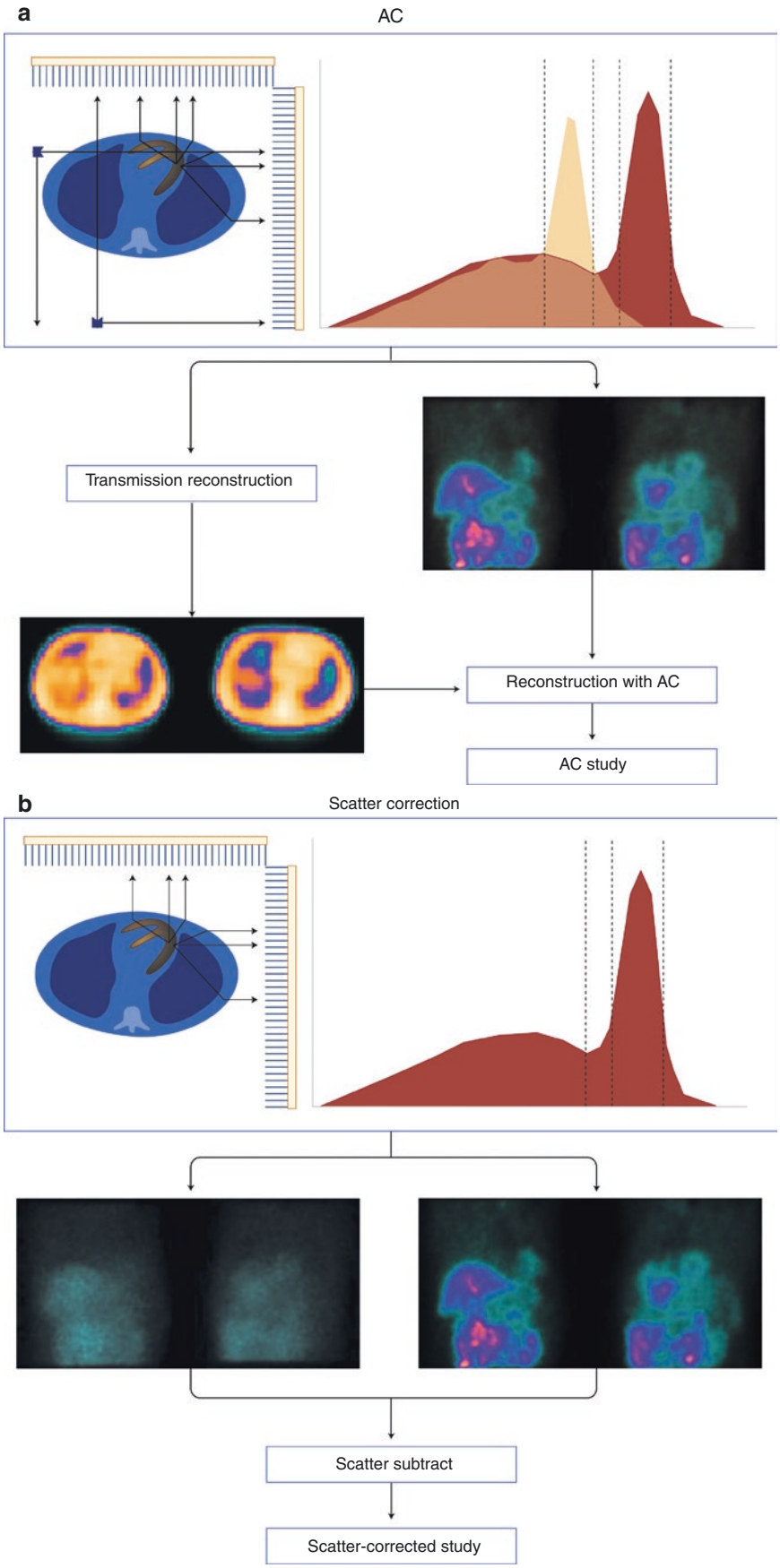

Fig. 2.25 SPECT attenuation correction (AC) and scatter correction. (**a**) SPECT myocardial perfusion imaging uses transmission scan–based AC. Transmission scanning measures the distribution of attenuation coefficients (attenuation map) of the patient, which is used in iterative reconstruction to correct for the decrease in counts resulting from photon attenuation. (**b**) SPECT scatter correction uses the Compton window subtraction method [16]. In this method, an image that consists of scattered photons is acquired by a second energy window placed below the photopeak window. This image is multiplied with a scaling factor and then subtracted from the acquired photopeak window image to produce a scatter-corrected image. Another energy window–based approach uses two energy windows, one above and one below the photopeak window, to estimate the portion of scattered photons in the photopeak window [17]

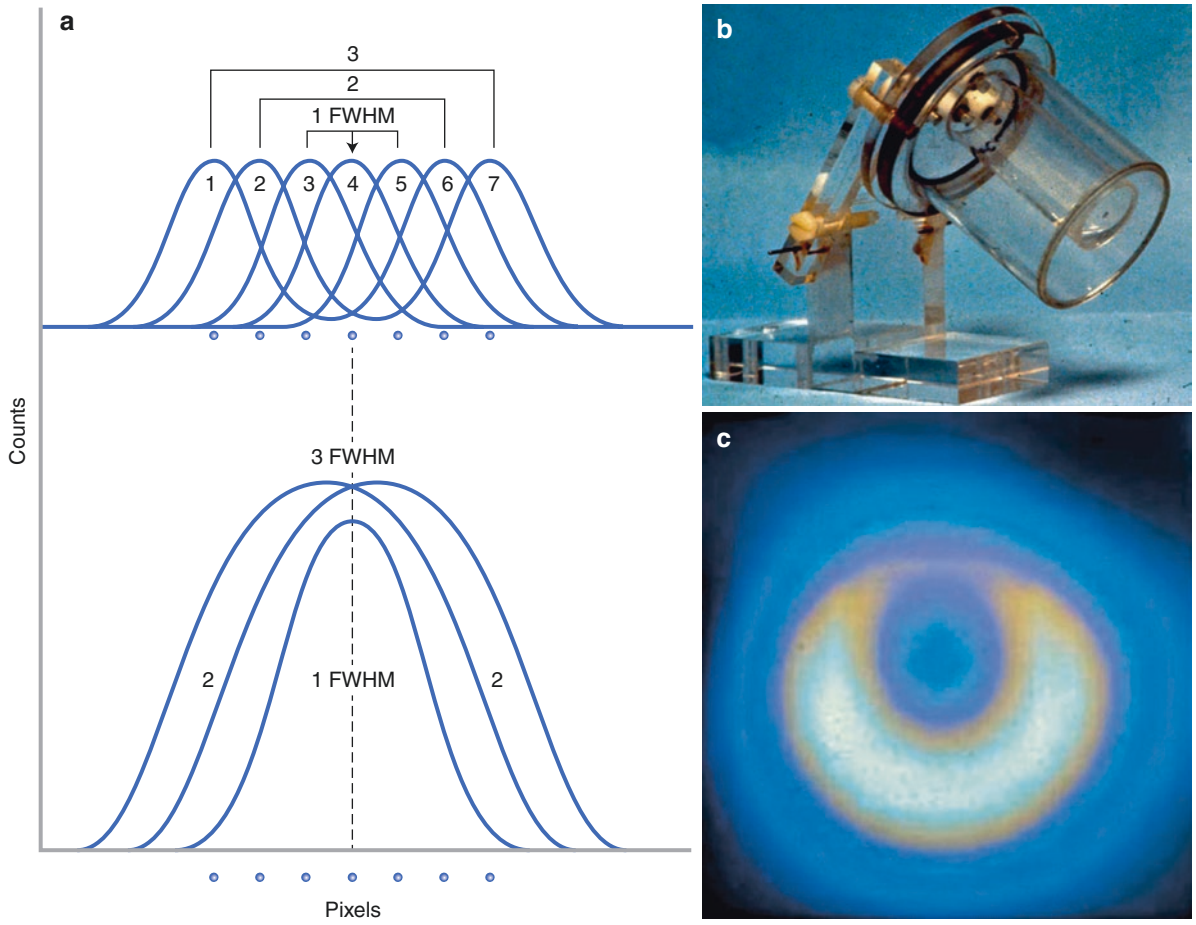

Fig. 2.26 (**a**) Partial volume effect. The inherent limitation of the resolution of nuclear imaging systems makes the image of a point source appear as a Gaussian curve. Therefore, the image of an object made up of multiple points appears as overlapping Gaussian curves, which have a higher value for the center point than for the peripheral points, even when the object has a uniform distribution of the radiotracer. As a result of this phenomenon, myocardial brightness increases when myocardial thickness increases [13] up to twice the resolution of the system (full width at half maximum, FWHM), as shown here. If the object is thicker than two times FWHM, the resulting count profile will reach a plateau representative of the true expected counts. (**b** and **c**) The partial volume effect is used quite successfully to assess left ventricular regional myocardial thickness and thickening, but care must be taken when interpreting gated SPECT images because the myocardium appears brighter in areas where it is thicker and dimmer in areas where it is thinner. These figures show a study in which a phantom representing an eccentric myocardial chamber is filled with a constant concentration of thallium-201. Note that the thinner anterior wall appears to be hypoperfused, in comparison to the inferior wall. This can be a cause of misinterpretation when, for example, the patient has a hypertrophic, thickened septum, making the left ventricular lateral wall with normal thickness and perfusion appear to be hypoperfused

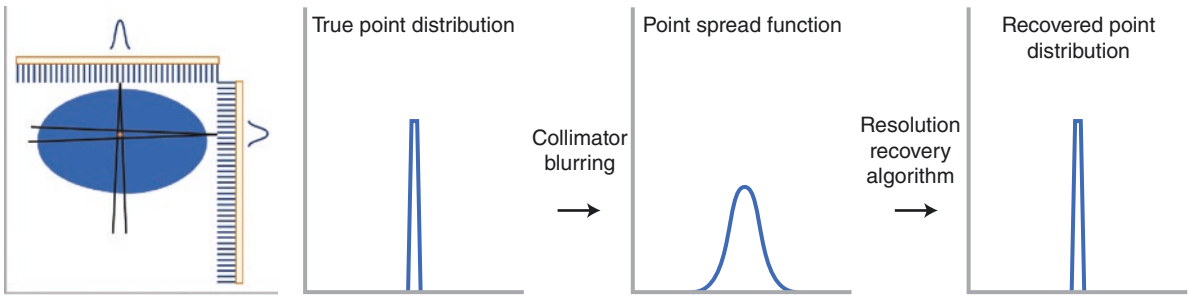

Fig. 2.27 Principle of resolution recovery. The limited resolution of nuclear imaging systems makes the image of a point source appear as a Gaussian curve (point spread function, PSF). The PSF of a nuclear imaging system increases in width with distance away from the surface of the collimator. Measurement of the PSF of the system at various distances allows the development of a resolution recovery algorithm, which deblurs the image and improves the defect contrast. Two types of resolution recovery algorithms are now commercially available: inverse filtering based on the frequency–distance principle [18], and three-dimensional modeling of the distance-dependent collimator response in iterative reconstruction [19]. As shown in this figure, the main idea of resolution recovery is to apply a mathematical algorithm to transform the blurred image response into a sharp response

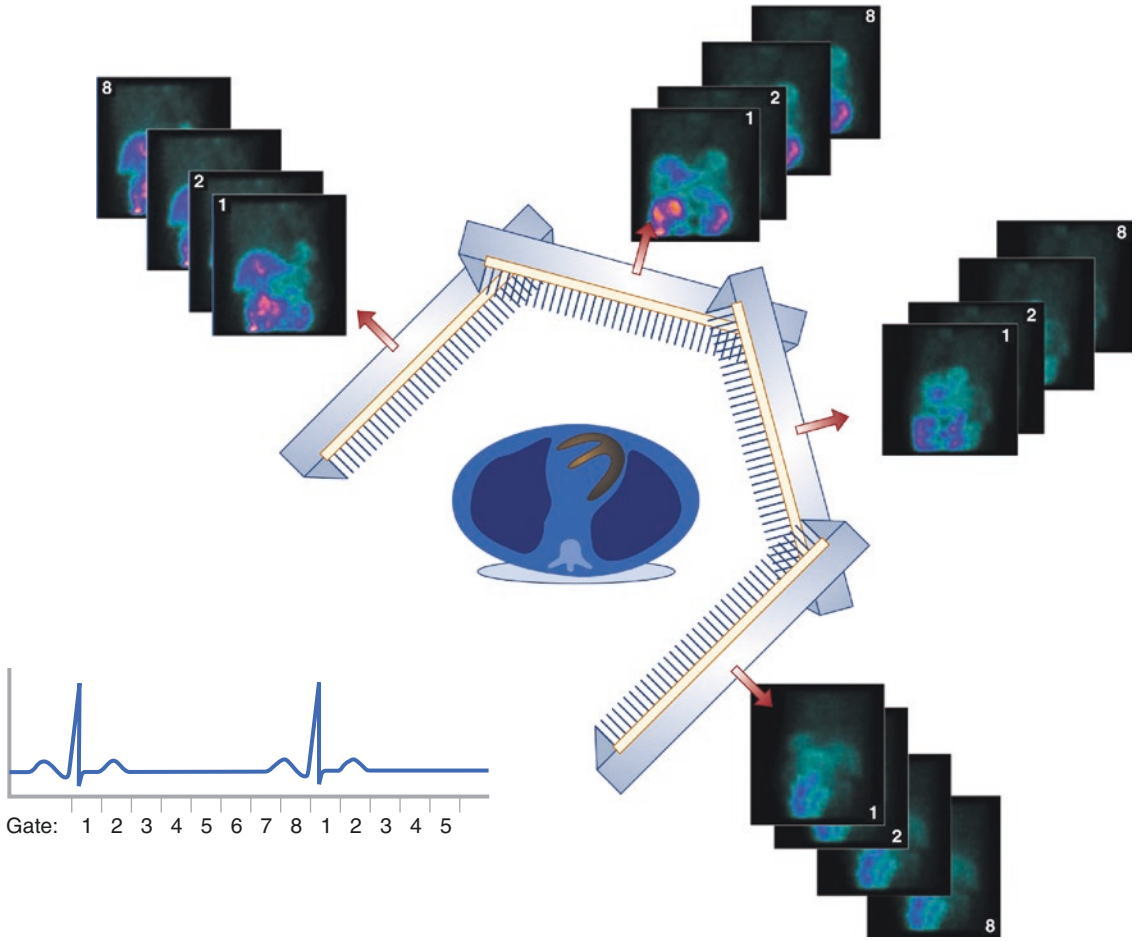

Fig. 2.28 Electrocardiogram (ECG)-gated SPECT myocardial perfusion imaging (MPI) acquisition. Similar to ungated SPECT MPI acquisition, ECG-gated SPECT MPI acquisition collects projection images at equally spaced angles along a 180° or 360° arc during the camera rotation. At each angle, instead of acquiring only one projection in the ungated acquisition mode, the camera acquires several (8, 16, or 32) projection images, each of which corresponds to a specific phase of the cardiac cycle. This is done by synchronizing the computer acquisition to the R wave from the patient's ECG. Here, the cardiac cycle is divided into eight separate frames. If the heart rate is, for example, one beat per second, the computer algorithm assigns a one eighth of a second time interval to each frame. Once the first R wave is detected, all counts are acquired into the first frame; as one eighth of a second elapses, the counts are now acquired into the second frame, and so on until the first second has elapsed or a new R wave is detected, starting the same procedure over again. This technique produces four-dimensional image volumes (three dimensions in space plus time) and allows clinicians to assess not only myocardial perfusion but also myocardial function

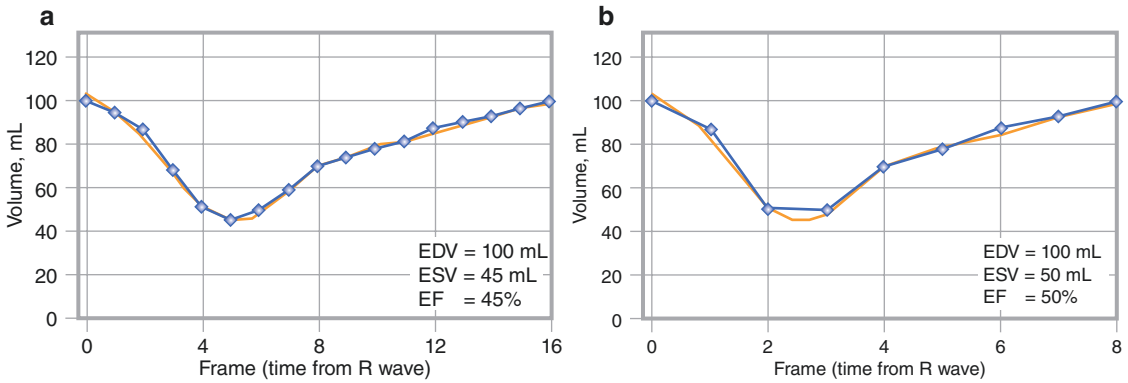

Fig. 2.29 Principle of temporal resolution. (**a** and **b**) The volume-time curve plots the value of the left ventricular cavity volume as a function of the gated SPECT time interval. The smaller the time interval (the larger the number of frames acquired during a cardiac cycle), the higher the temporal resolution and the closer the volume-time curve is to the "truth" and, thus, the more accurate the volume and ejection fraction measurements. It is generally agreed that some commonly used eight-frame-gated SPECT approaches produce errors in the measurement of diastolic function, and it has been suggested that 16-frame imaging is quite effective [20]. There are techniques that use a mathematical algorithm (the Fourier transform) to replace the discrete eight samples with a continuous curve on a segment-by-segment basis and, thus, are less dependent on higher temporal resolution to obtain accurate parameters. EDV end-diastolic volume, EF ejection fraction, ESV end-systolic volume

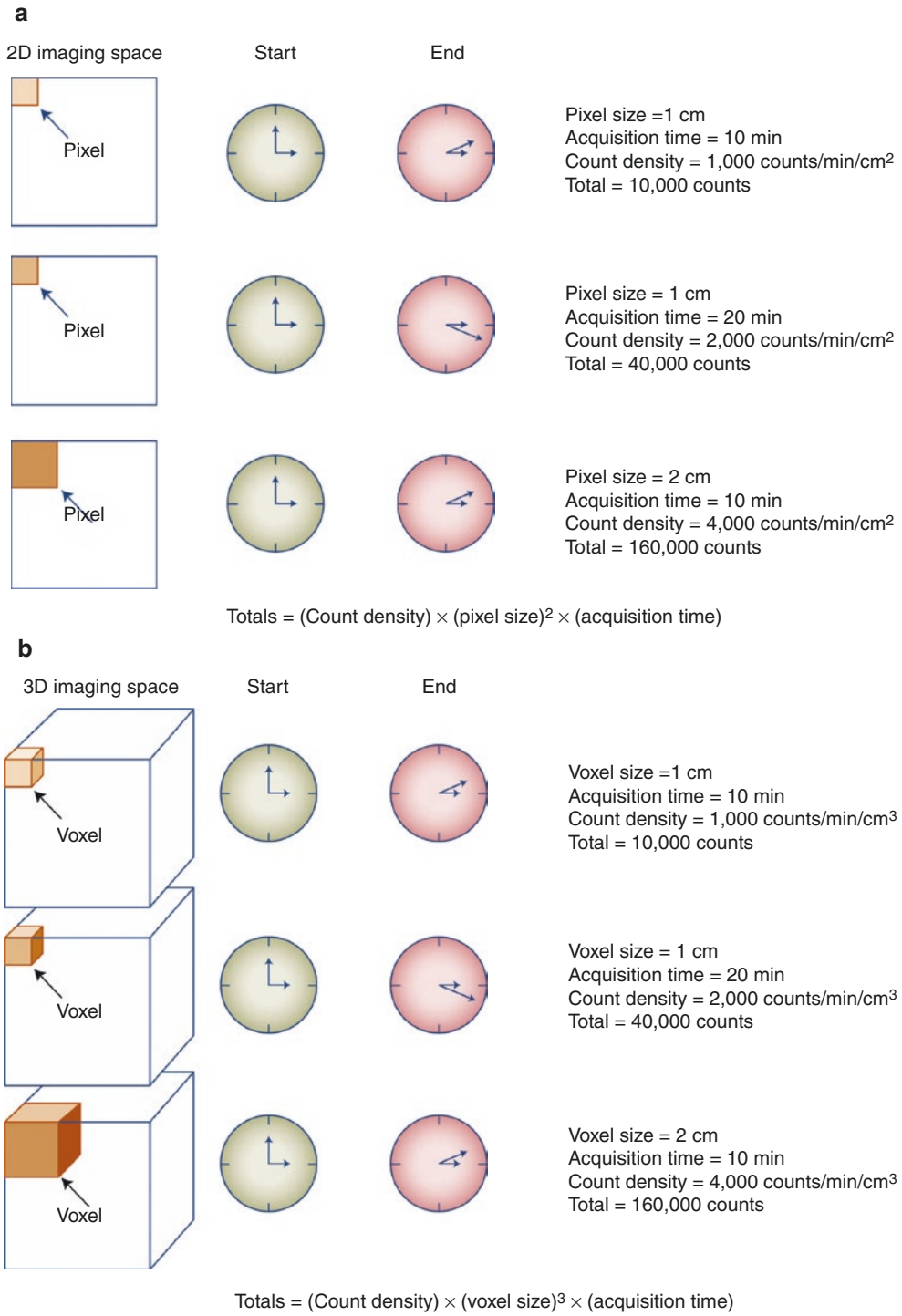

Fig. 2.30 Total counts versus count density, preset time of acquisition, and pixel/voxel size. Nuclear imaging acquires photons emitted from the patient and digitizes the data into a matrix (*image*). Each matrix position corresponds to a pixel, and the pixel value (total counts) corresponds to the number of accepted photons at that position. (**a**) The pixel value is proportional to the radiotracer concentration, the length of the acquisition, and the square of the pixel size. (**b**) If the image is three-dimensional (e.g., reconstructed tomographic image), each element of the image is cubic instead of a square and is called a "voxel." The voxel value (total counts) is proportional to the radiotracer concentration, the length of the acquisition, and the cubic (not square) voxel size. 3D three-dimensional, 2D two-dimensional

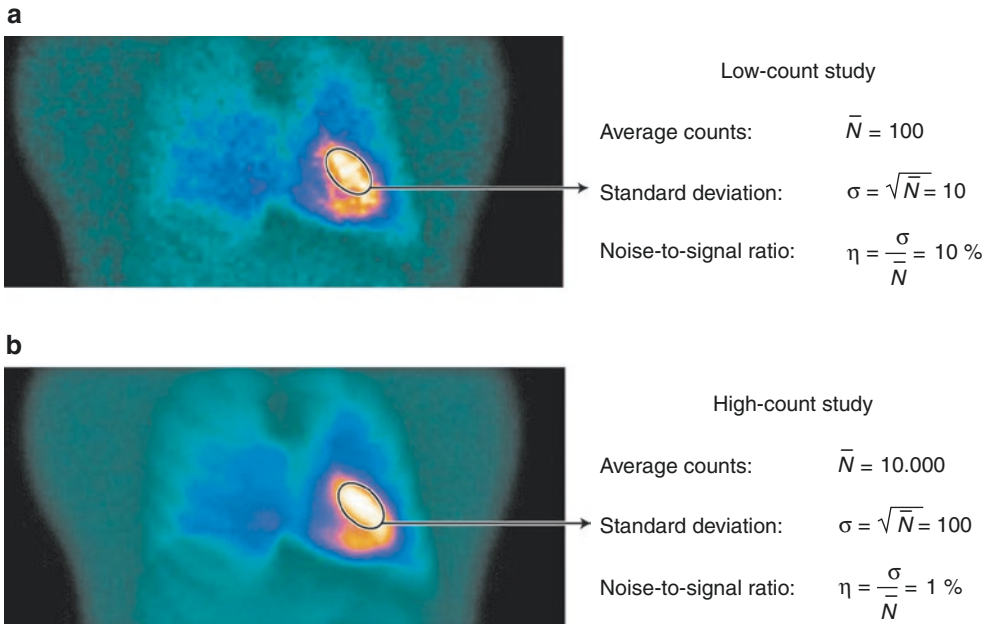

Fig. 2.31 Statistics: noise level versus total counts. Nuclear imaging measures radioactive decay, which is a random process and follows the Poisson distribution. The standard deviation of a measured pixel value (counts) from a planar image projection is the square root of the pixel value. A low-count study (**a**) has a bigger standard deviation and a higher noise-to-signal ratio such that the image appears to be noisier than that of a high-count study (**b**). This example shows that if a pixel contains 100 counts, it corresponds to a 10% error and if another pixel contains 10,000 counts, it corresponds to a 1% error

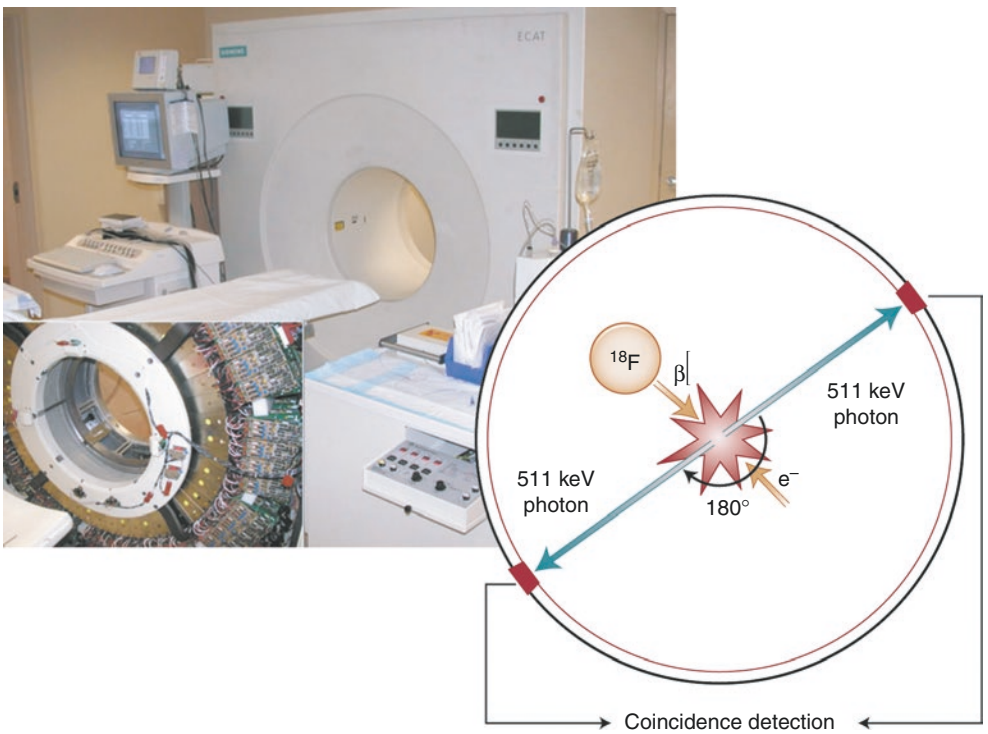

Fig. 2.32 PET scanners; electronic collimation. PET cameras detect paired photons (511 keV of energy each) produced by the positron annihilation effect. The paired 511-keV photons travel in opposite directions at a 180° angle from each other. Thus, positron decay can be localized without collimation with the use of the principle of coincidence detection, because if two detectors acquire a count within a short time window, it is assumed that they came from the same pair annihilation, so the event is positioned by drawing a straight line between the two detectors. Because PET cameras do not require collimators, these systems have a much higher sensitivity than SPECT systems. ^{18}F fluorine-18

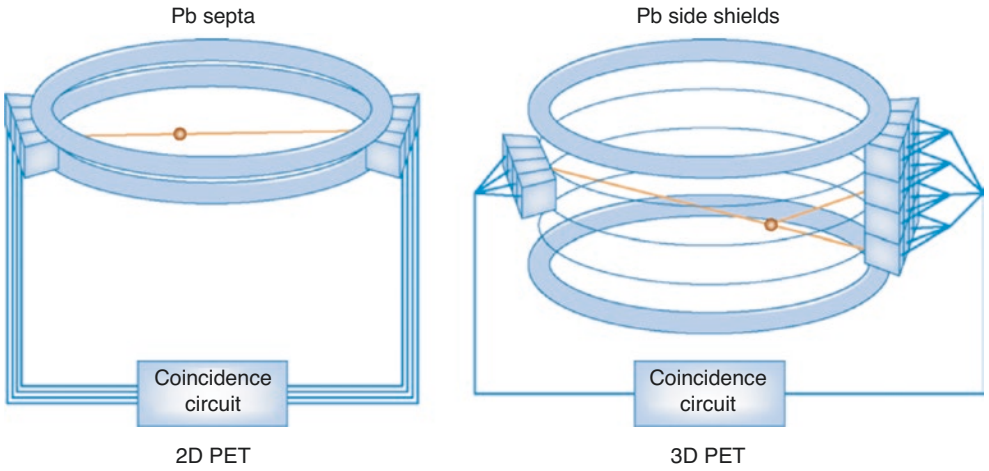

Fig. 2.33 Two-dimensional (2D) versus three-dimensional (3D) PET systems. 2D PET systems, equipped with lead (Pb) septa, accept coincidences only from crystals in the same ring of detectors. 3D PET systems, by removing the septa, accept coincidences in any ring and greatly increase the count rate and sensitivity. However, the difficulties associated with removing the septa are that it greatly increases scatter, it greatly increases random events, and it greatly increases the count rate, so it greatly increases dead time [21]. These problems must be effectively compensated for when using 3D PET in cardiac imaging

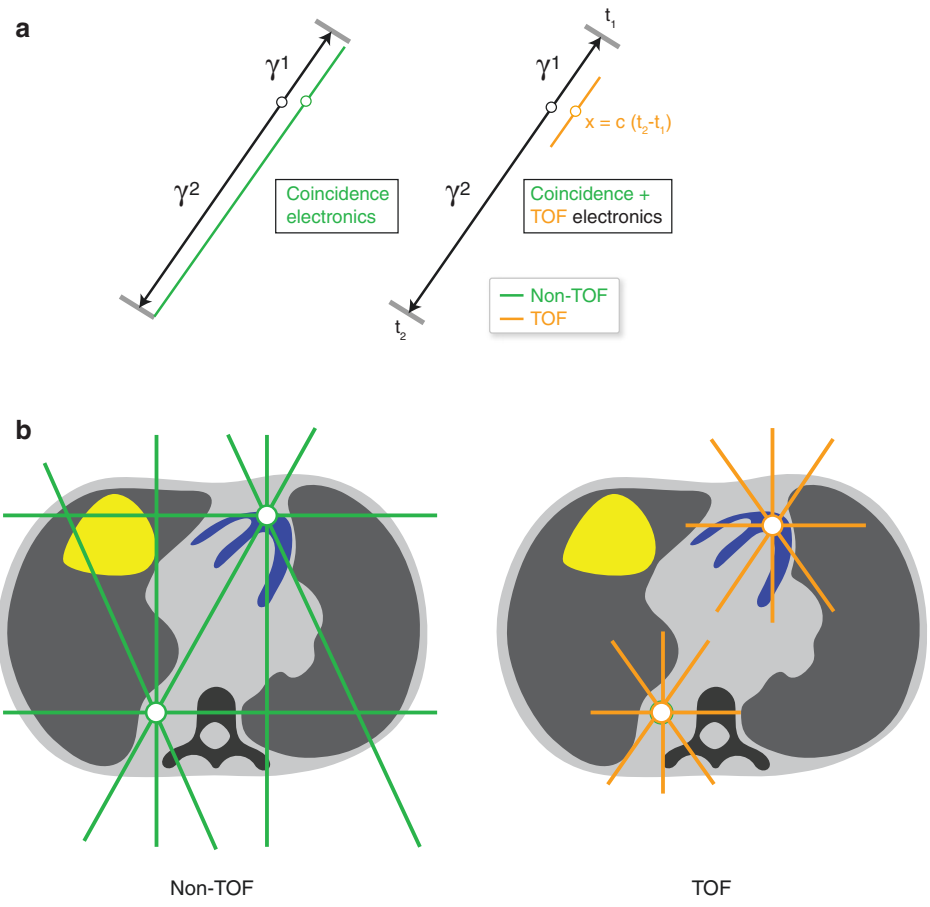

Fig. 2.34 Time of Flight (TOF) imaging vs. Non-TOF imaging. (**a**) On the left, **c**onventional PET coincidence electronics (*see* Fig. 2.32). The right panel shows that the coincidence electronics in advanced PET scanners with TOF electronics are capable of measuring the time interval between one photon (γ_1) hitting one detector and the second photon (γ_2) from the same annihilation event hitting an opposing detector. That difference in time (t_2 - t_1) multiplied by the speed of light (c) estimates the location of the annihilation event along the coincidence ray between the two detectors. (**b**) In TOF, instead of backprojecting an entire line (*left panel*), only the line segment corresponding to the time window of the event is projected. The result is increased lesion contrast and increased spatial resolution [22]

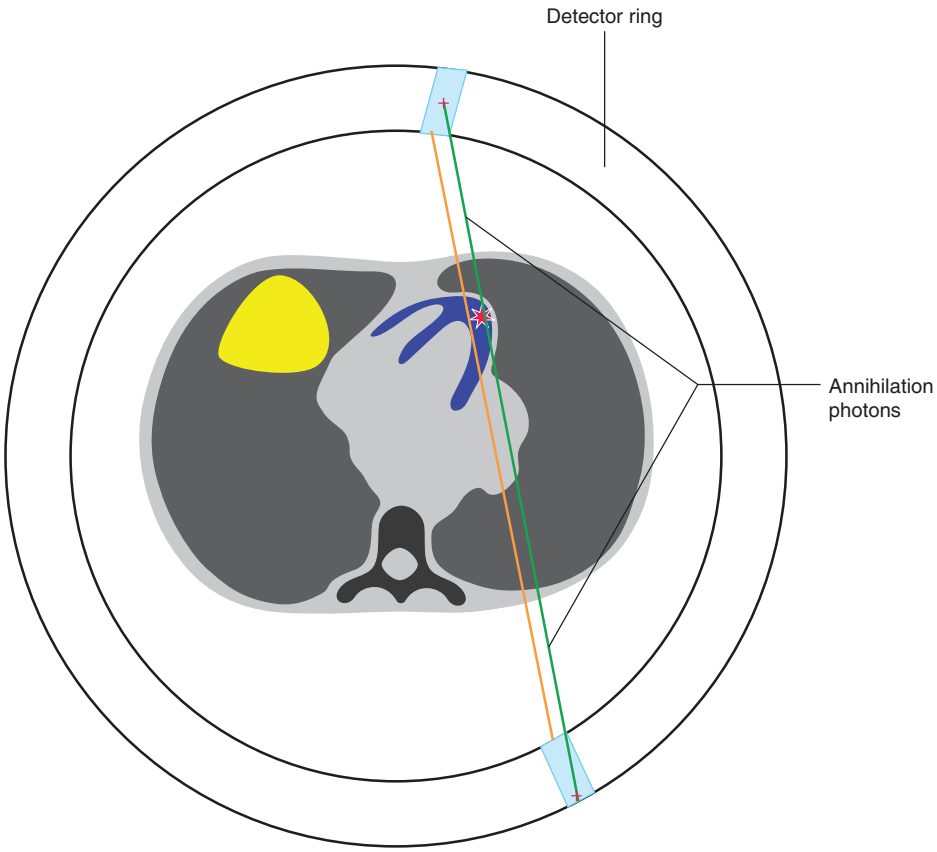

Fig. 2.35 Depth of interaction (DOI) digital PET detectors vs. conventional PET detectors. DOI detectors record both the event that the photon was absorbed by the specific detector (*blue rectangle*) and the depth within the detector (*red plus sign*) where it was absorbed. As the positron annihilation takes place further from the center of the field of view, the reconstructed line of response (*red*) is increasingly further away from the true line of response (*green*) in systems that locate the annihilation photons in the middle of the detector rather than at the true depth of the interaction, as with DOI detectors. This increased accuracy in positioning the backprojected line of response results in increased lesion contrast and increased spatial resolution [23]

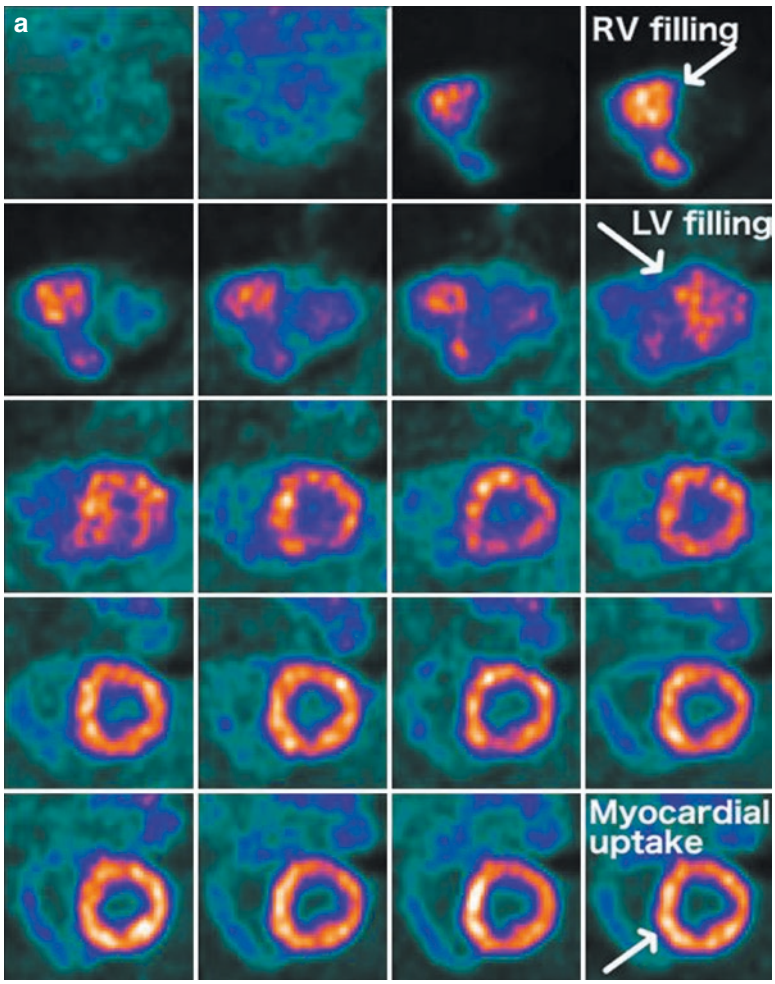

Fig. 2.36 PET-derived myocardial absolute blood flow (MBF) quantification. (**a**) Dynamic sequence of PET images. Once injected, the radiotracer rapidly travels to the right ventricle (RV), then to the left ventricle (LV), and is progressively captured by the myocardial tissue in the second half of the acquisition interval; posterior direction on top of images. (**b**) Procedure for MBF quantification. *B1*, A summed image is created from frames of the second half of the acquisition interval and used to identify regions of interest (ROIs) on the image sequence, namely the myocardium (*black lines*), and the location for the extraction of the input function (IF) (*red*); the IF represents the tracer's arterial blood concentration and is measured by sampling a small region of the LV cavity. *B2*, The segmented myocardium is subdivided into vascular territories according to standard anatomical classification. *B3*, Time activity curves (TACs) are derived by sampling the dynamic sequence of PET images in the segmented ROIs: the input function (IF) is characterized by a rapid increase of radiotracer concentration in the initial frames, followed by a rapid decrease in the second half of the acquisition time. Conversely, radiotracer concentration progressively increases in the myocardial tissue, reaching a plateau towards the end of the acquisition. The exchange of activity between blood and tissue is commonly described by means of compartmental models that allow MBF estimation. *B4*, MBF values in mL/min/g can be displayed by means of conventional polar maps; myocardial flow reserve (MFR) is computed as the MBF hyperemic values divided by the resting MBF. (**c**) Common errors and artifacts in dynamic PET acquisition and processing. Differently from myocardial relative perfusion imaging (MPI), clinical estimation of MBF can be technically more demanding, as a number of factors greatly affect MBF final values. A careful analysis of TACs can facilitate the identification of errors and/or artifacts, as in the two examples here: *C1*, Image acquisition should start at the same time as tracer infusion. In case of delayed acquisition, the initial phase of the TACs, particularly important for the IF definition, may be missing, causing the final MBF values to be completely unreliable. *C2*, Because the ROIs are commonly defined on a single summed image, patient motion and/or breathing motion can result in the misplacement of the ROIs on a number of time frames and, consequently, in inconsistent TACs. In the given example, the shifting of the heart in the posterior direction during frames 24, 25 and 26 clearly results in unsteady activity values for the IF and all myocardial tissues; during frame 27, the heart has returned to its initial position. These inconsistencies should be corrected prior to MBF calculation

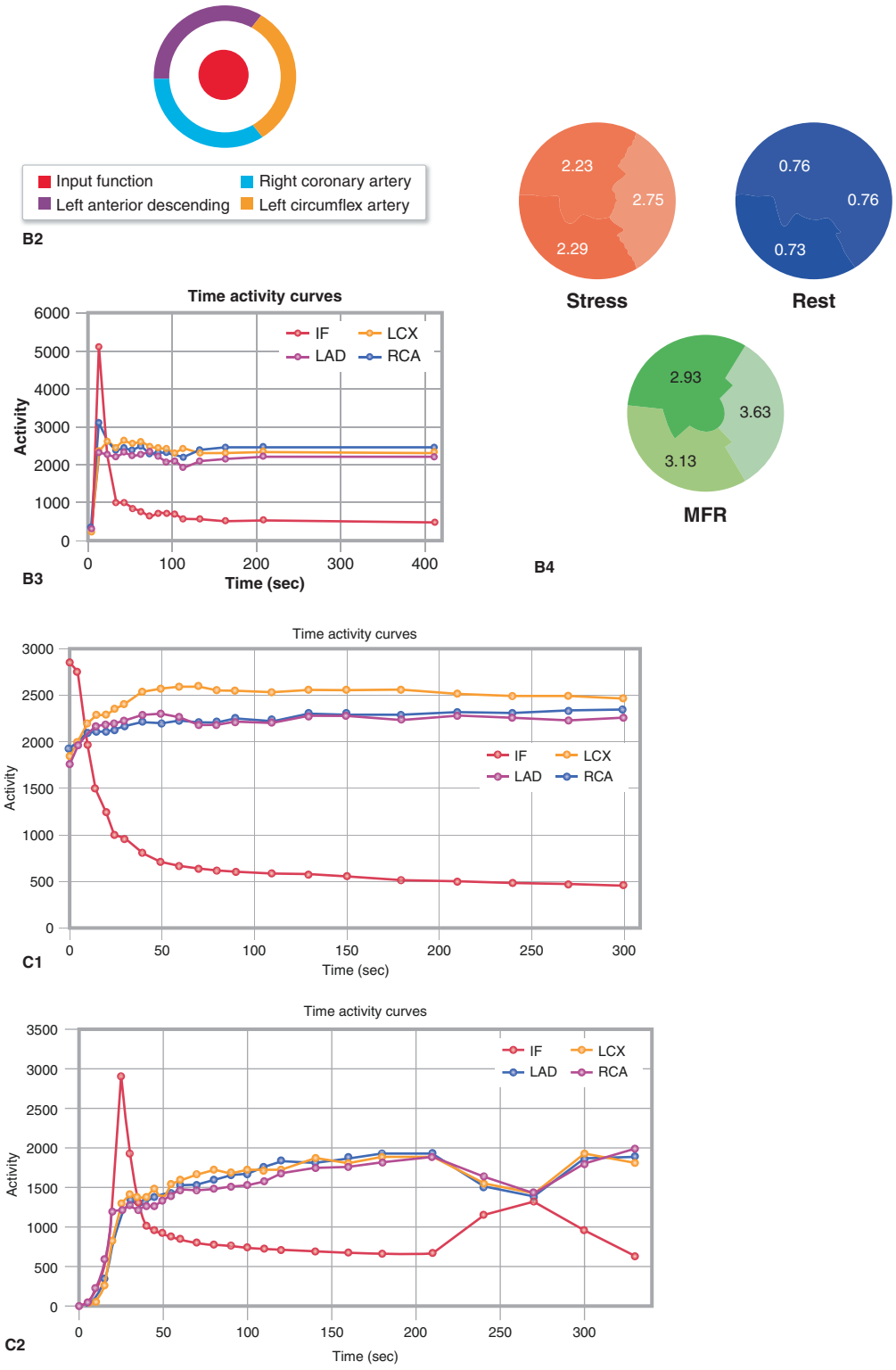

Fig. 2.36 (continued)

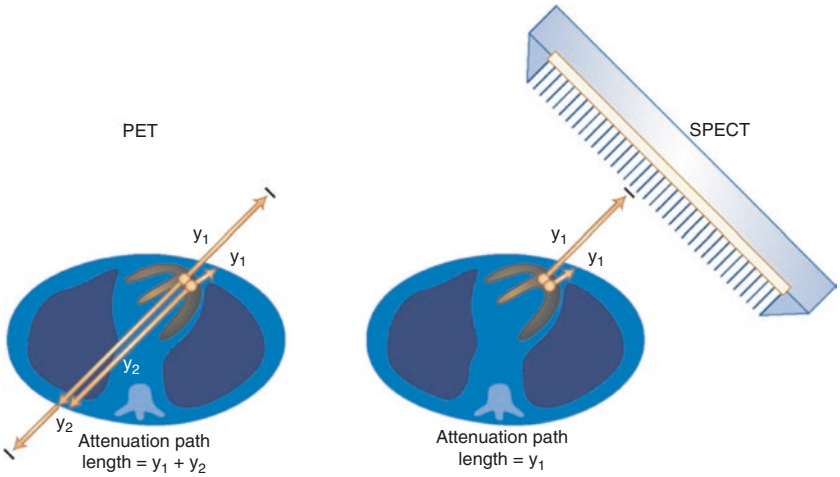

Fig. 2.37 PET *versus* SPECT attenuation correction (AC). PET imaging measures 511-keV photons. Because the two photons must be detected to record the event, the entire path length influences the attenuation. In SPECT imaging, even though the energy of the photon is lower, its path length to the detector is much shorter, so it is less affected by attenuation. Thus, the two PET photons undergo higher attenuation when they travel through the body than do the single photons measured in SPECT imaging. Therefore, there is more attenuation in PET studies than in SPECT, making PET more susceptible to attenuation artifacts. Only attenuation-corrected cardiac images should be used in clinical interpretation [24]. Unlike SPECT, PET data can be accurately corrected for attenuation by simply multiplying each projection line by the appropriate AC factor. For both PET and SPECT, a measurement of the patient-specific attenuation map is required for accurate AC and can be done either by radionuclide imaging or by radiographic CT

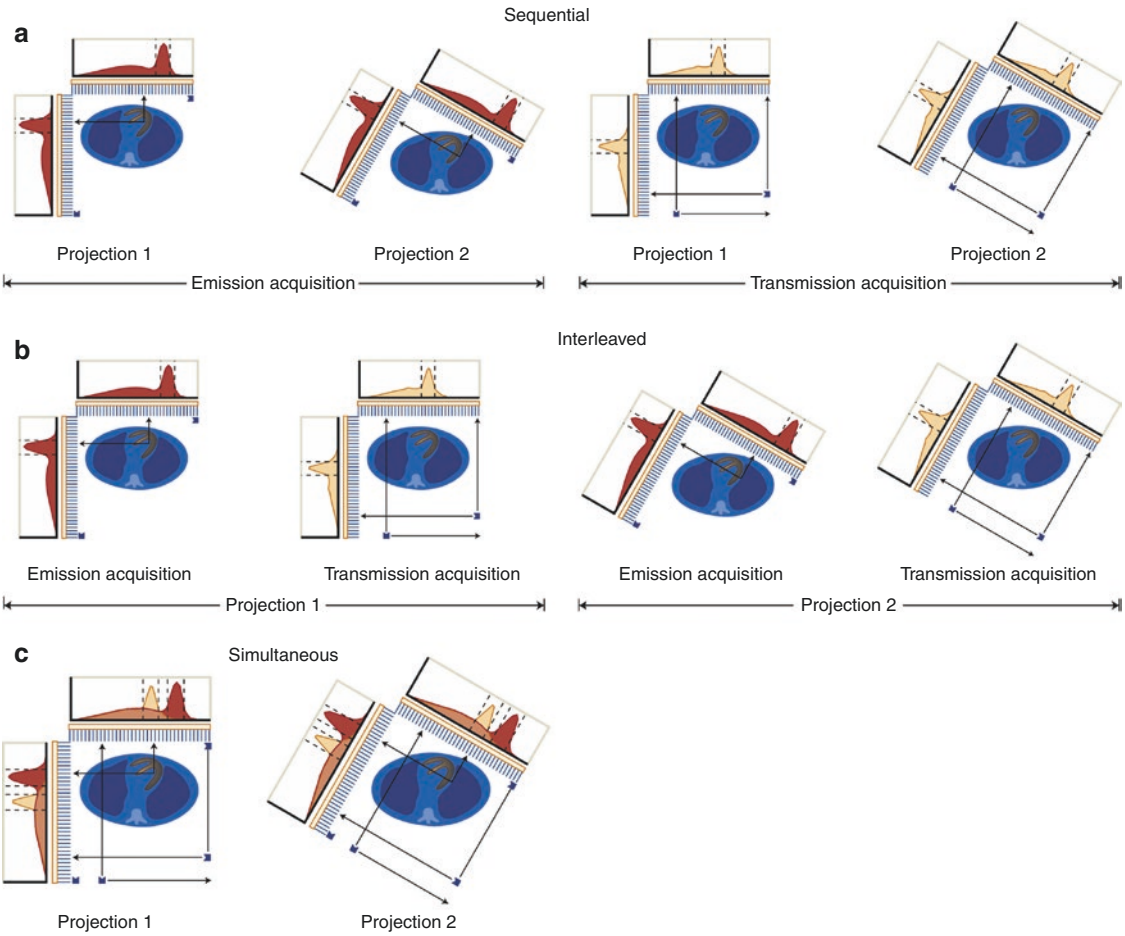

Fig. 2.38 Types of attenuation correction (AC): sequential, interleaved, and simultaneous. Accurate AC requires two acquisitions from a single study: emission and transmission. (**a**) The two acquisitions can be done sequentially, one following the other, but registration between the two acquisitions challenges the quality control of this approach in practice. (**b**) To reduce the risk of emission/transmission misalignment, the two acquisitions can be done in an interleaved mode, in which the camera acquires emission and transmission projection images sequentially at each stop and rotates around the patient only once in one study. (**c**) Simultaneous mode completely solves the problem and reduces the length of the acquisition; however, cross talk between the emission and transmission photons degrades at least one of the two acquisitions and should be properly compensated for with accurate AC

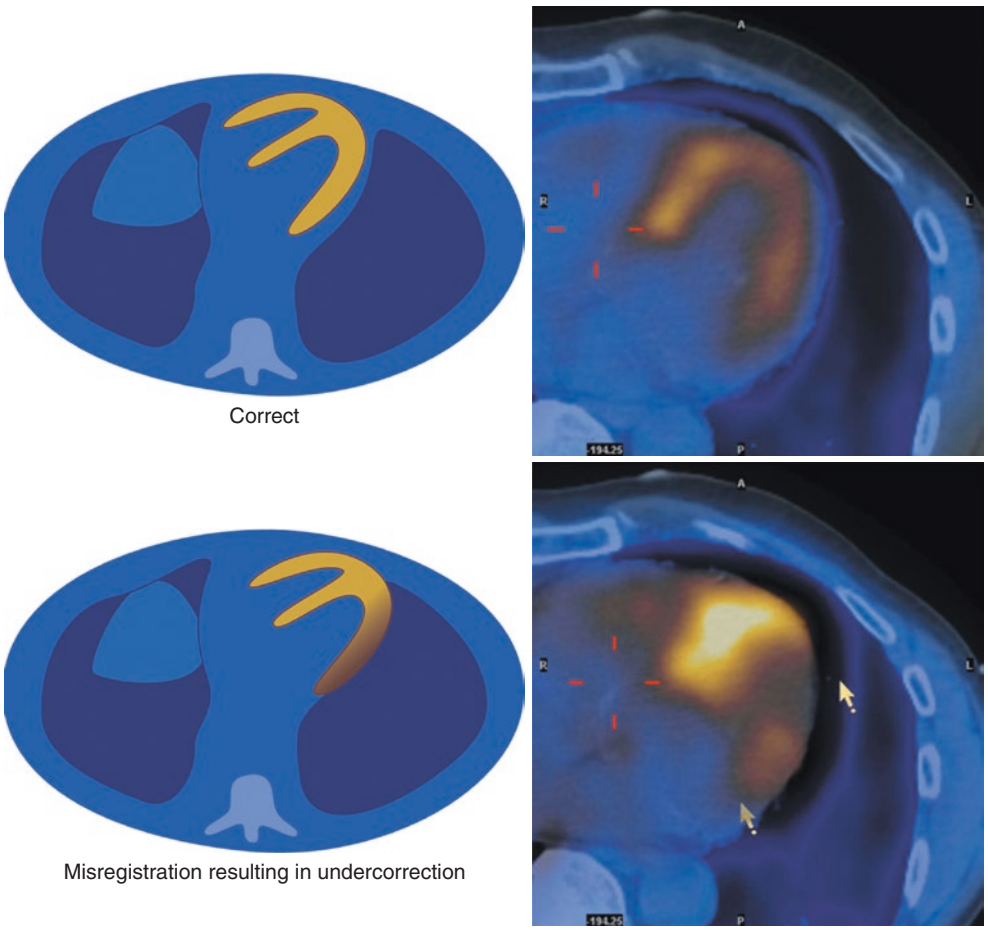

Fig. 2.39 Attenuation correction (AC) artifact due to misregistration. This figure explains the artifact caused by misregistration between the emission and transmission scans due to patient motion. AC requires that the emission scan and the transmission scan that is used to correct for photon attenuation be perfectly registered with each other. Simultaneous acquisitions of both emission and transmission scans ensure that these two are registered. When these two acquisitions are performed sequentially and the patient moves between the two acquisitions, artifacts are created. The *top left panel* shows a diagram of a transaxial emission cardiac image superimposed on the corresponding transaxial transmission image. Note that the entire cardiac silhouette lies in the pericardium, not touching the lung area, represented in *dark blue*. The *top right image* shows an actual AC emission cardiac image when correctly registered with the transmission image. The *bottom left panel* shows a diagram of a transaxial emission cardiac image superimposed on the corresponding transaxial transmission image. Note that the two images are misregistered; the free left ventricular lateral myocardial wall overlaps a portion of the lung. The *bottom right image* shows an actual attenuation-corrected emission cardiac image that is similarly misregistered in relation to the transmission image. Note that the left ventricular free wall overlaps a portion of the lung. This misregistration causes the lateral wall to be undercorrected, so it appears as though it is hypoperfused

Quality Control Procedures

Quality control (QC) procedures are necessary to ensure images of diagnostic quality. These procedures are pertinent to guarantee both the quality of studies when performing planar imaging and the quality of the planar projections used in SPECT imaging. Table 2.5 lists quality control procedures required for planar imaging.

Test	Frequency
Energy peaking	Daily
Uniformity test	Daily
Sensitivity	Manufacturer's recommendation
Resolution and linearity	Manufacturer's recommendation

Table 2.5 Quality control procedures for planar imaging

Energy peaking consists of either manually or automatically placing the correct pulse height analyzer's energy window over the photopeak energy of the radionuclide to be used. This process is usually performed with a radioactive point source imaged a distance away by an uncollimated camera or an extended sheet source on the collimated camera. Either way, the entire field of view should be illuminated by the radioactive source. This process should be performed daily, even in camera systems that perform this function automatically and track the shift of the window. A screen capture of the spectrum with the window superimposed can be used to record these results [25].

The uniformity flood field is another QC procedure that should be performed daily to document the camera uniformity. This procedure is also done using a radioactive point source and without a collimator. An intrinsic uniformity test can be performed using a source of low radioactivity (~100 μCi) in a small volume (~0.5 mL) to mimic a point source positioned at least five diameters from the camera's crystal, directly over the center of the detector. If this process proves difficult or time-consuming, it can be replaced with an extrinsic uniformity flood measurement. Extrinsic uniformity is measured with an extended radioactive sheet source that covers the entire collimated camera face [26].

Sensitivity QC tests that the device is consistently counting the same radioactive source should be performed weekly. These tests can be done at the same time the intrinsic (or extrinsic) uniformity tests are done by recording the number of counts acquired for a given time period, adjusted to the magnitude of radiation used to create the image.

The resolution and linearity test is performed to document spatial resolution and its change over time, as well as how the camera reproduces straight lines. This test consists of imaging an extended radioactive sheet flood source through a spatial resolution test phantom known as a "bar phantom." Images of the phantom should be archived to record the camera's performance and the QC procedure. These images are assessed for how straight the bar lines are imaged and for intrinsic spatial resolution. Changes in resolution are assessed by documenting the smallest bars that are discerned [25].

Table 2.6 summarizes the QC procedures necessary to ensure images of diagnostic quality when performing SPECT imaging, which are described in this chapter. Of course, all the QC procedures required for planar imaging are also required for SPECT imaging. Several excellent reviews on how to detect and account for SPECT imaging artifacts have been published [27, 28].

Test	Requirement
Center-of-rotation and multidector registration	Mandatory/Manufacturer's recommendation
Uniformity calibration	Mandatory/Manufacturer's recommendation
Motion correction	Optional

Table 2.6 Quality control procedures for SPECT imaging

Figures 2.40, 2.41, 2.42, and 2.43 illustrate areas of quality control for SPECT imaging.

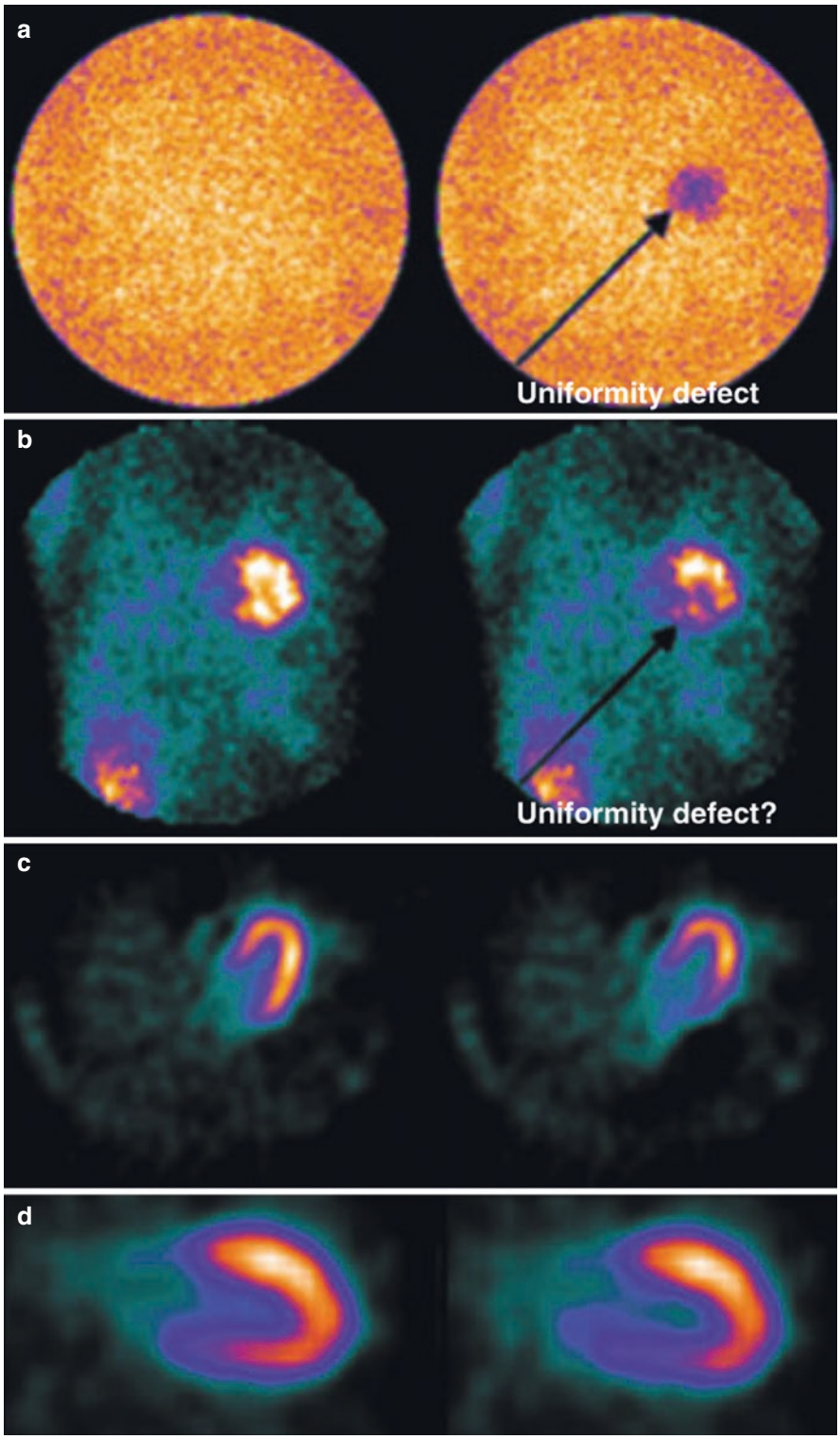

Fig. 2.40 Camera uniformity. The Joint Commission on the Accreditation of Healthcare Organizations (JCAHO) requires that a uniformity flood be acquired on each scintillation camera before clinical studies are done for any given day. These three-million-count floods can be used to detect uniformity defects. (**a**) Two examples of floods, one using a camera without a uniformity defect (*left*) and one with a uniformity defect that might be caused by a poor photomultiplier tube (*right*). (**b**) In the same patient, corresponding thallium planar projections were acquired with these cameras. Note that the planar image on the *right* shows decreased counts compared with the one on the *left*. The problem is that even if cine displays of the planar images are viewed, it will be very difficult to detect that the decreased counts in the inferior myocardial wall were caused by a camera uniformity problem rather than a true physiologic perfusion abnormality. (**c**) Correspondingly, when the transaxial slices are reconstructed, the basolateral wall is decreased in counts. Although a ring artifact is caused by this uniformity problem and can be seen in the transaxial images when imaging a uniform source, in this patient they are difficult to detect just by looking at the images if the quality control step is not performed. (**d**) The vertical long-axis images make it even harder to detect when a decrease in counts might be the result of a uniformity defect. It is very important that floods be performed every day to detect uniformity problems before they affect clinical images. Differences in positioning of the patient between rest and stress scans may cause uniformity artifacts to appear in different locations in the two images, possibly mimicking ischemia [12]

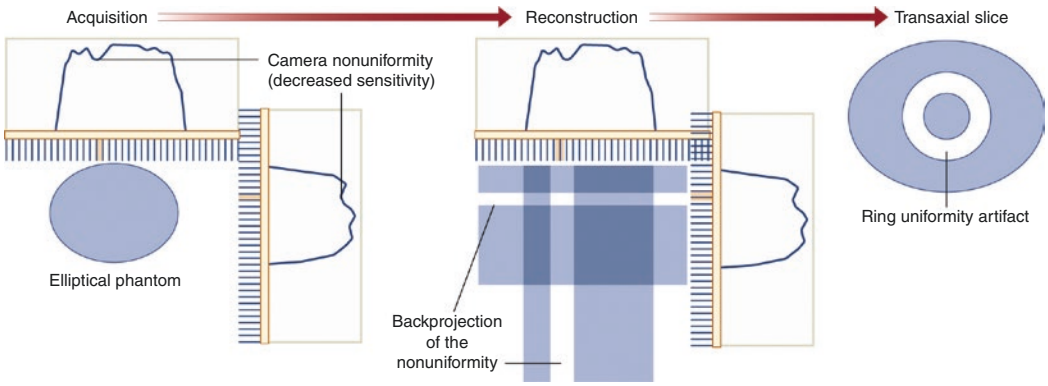

Fig. 2.41 Uniformity artifacts. Uniformity artifacts occur when one area of the camera face has decreased sensitivity compared with the other areas. This can occur when a photomultiplier tube begins to work improperly, as in Fig. 2.38, or if the collimator is damaged. For example, if an acquisition is performed of an elliptical quality control phantom that was filled with a uniform distribution of technetium, it can generate the two count profiles on the *left side* of the figure. These count profiles should be steep on the sides and fairly flat across the top, depending on the shape of the phantom. In the case of uniformity problems, regions of decreased sensitivity are seen in each of these curves, represented by a small dip at one point. The small dip will correspond to the same location on the camera in all of the projection views. When the images are reconstructed, this small dip is backprojected, as shown in the *middle image*, and with more and more projections, it will scribe out a circle in the transaxial image, as shown on the *right*. This kind of artifact may occur when the collimator is damaged and one or a few of the holes in the lead septa have been closed. To correct for small variations across the face of a collimator, 30-million-count floods are used. These high-count floods should be acquired at least once a month and are applied to images acquired with the same collimator being used by the same camera [12]

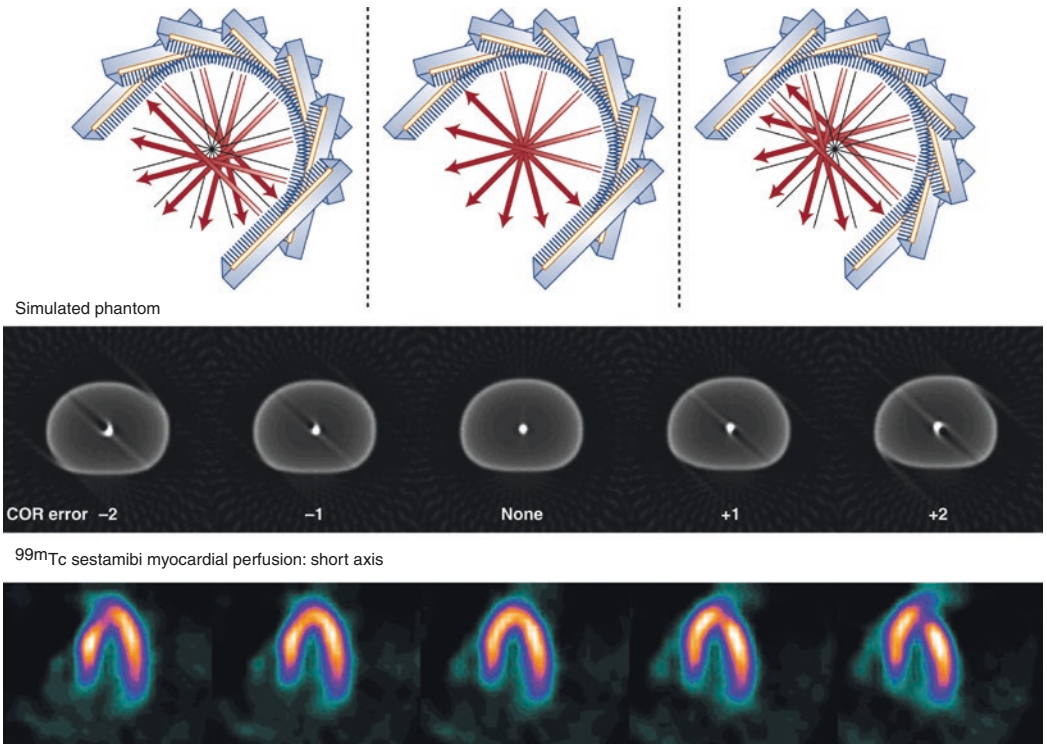

Fig. 2.42 Center of rotation (COR). COR is a calibration performed frequently to ensure that the frame of reference used by the computer in reconstructing images is aligned with the mechanical axis of rotation of the SPECT camera system. If the center of rotation is properly calibrated, a radioactive point source placed in the center of the camera orbit should project to the center of the computer matrix. These results are seen in the *middle panels*

For most cardiac SPECT, a 180° orbit is used. When a radioactive point source is used with this orbit, a point source should also be reconstructed as a point in the image. With a COR error, however, the reconstruction no longer yields a point. Instead, the point is smeared and resembles a tuning fork, with two lines in one direction and something that looks like a stem in the opposite direction ("tuning fork artifact"). If the COR calibration errs by a negative amount, the images in the *left panels* are seen. In the *middle left panels*, the smeared radioactive point sources reconstructed with this error are seen. If the error is in the positive direction, the images shown in the *top right* are seen. The camera processes that generated these errors are seen in the *top diagrams*

COR errors are easy to detect with radioactive point sources, but they may be very difficult to detect with a clinical distribution of activity. In the *bottom panels*, COR errors can be seen that correspond to the images of point sources directly above them. The COR error manifests itself in the myocardial perfusion horizontal long-axis images as an area of reduced counts on either side of the myocardium (often surrounding an area of higher counts). It is sometimes difficult to distinguish between the COR errors demonstrated here and true clinical defects, so it is extremely important that the technologists who perform the QC procedures properly calibrate the COR for the camera [12]

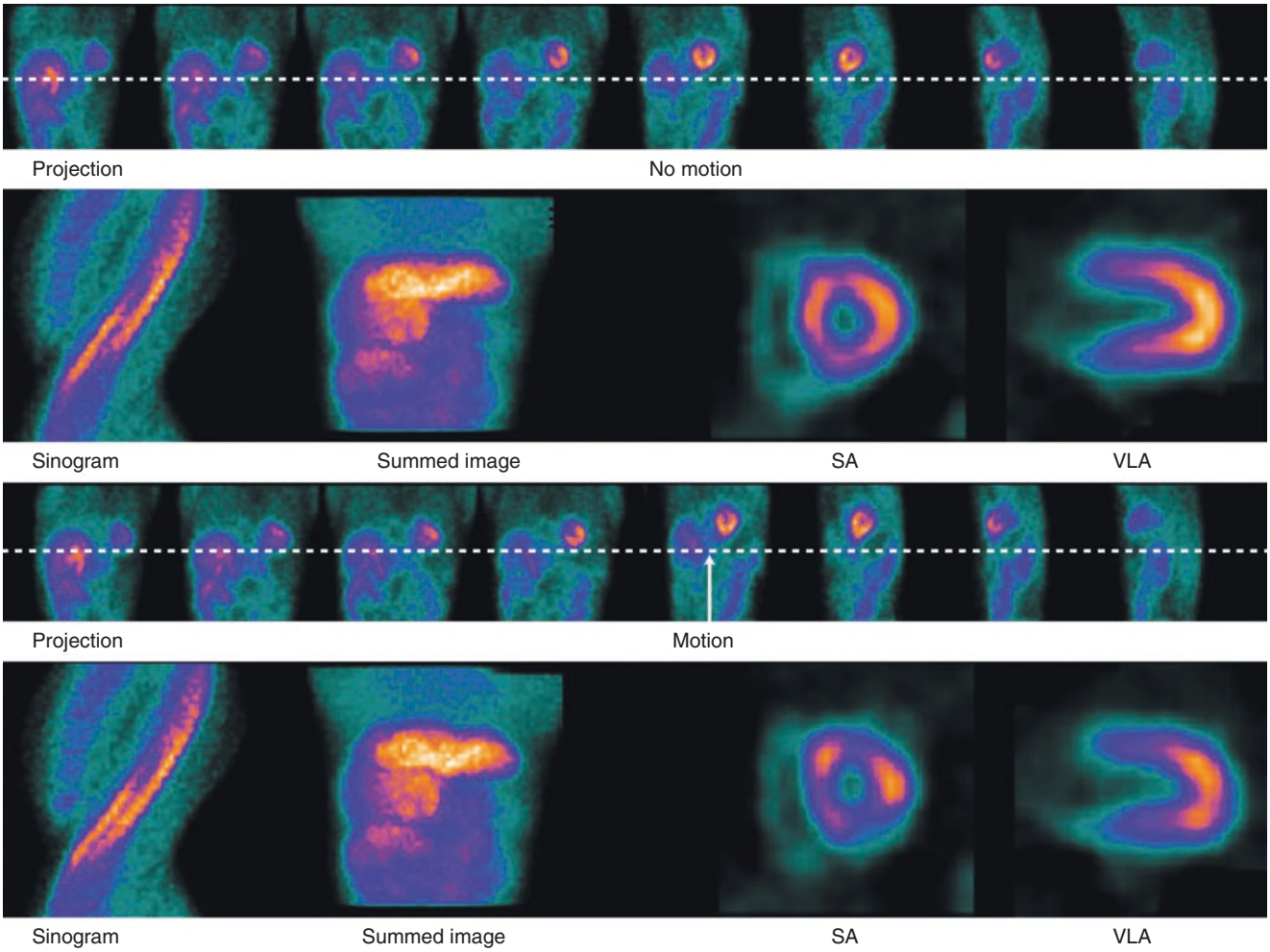

Fig. 2.43 Detecting patient motion. Patient motion can be detected by cine displays, sinograms, and summed planar images. Cine displays of the planar projections are perhaps the simplest and best way to detect patient motion. Watching the heart as it moves from right to left in the planar projections can be used to detect all types of motions. The clinician should watch the movie of the planar projections at a fairly rapid cine rate and observe any up-and-down motion of the heart, particularly in relation to a fixed horizontal line just below the heart. The best way to detect and correct motion is for the technologist to observe the patient and repeat the scan if sufficient motion occurs, to prevent the patient from having to return for a repeated scan if the original acquisition is technically impossible to interpret. The projections at the top of each of the two panels illustrate how patient motion might be detected using a cine display. If the distance between the heart and the horizontal line is compared in each of these planar projections, the *top images* show no variation in the distance between the inferior wall of the left ventricle and the line, whereas in the *bottom panel*, the heart is seen to move vertically away from the line starting with the projection to which the *arrow* points. Note that the short-axis (SA) and vertical long-axis (VLA) images in the *bottom panel* show regions of decreased counts as compared with those in the *upper panel* of the same patient with no motion. Even a slight amount of motion (3 mm) may result in an artifact in the SPECT images. If this motion is not detected by the clinician before interpreting the images, a false-positive report may result

A sinogram is another way to detect patient motion. A sinogram is an image composed of one line of pixels through the planar projections plotted vertically for each of the angular projection views. Thus, the *x-axis* of the sinogram represents pixels across the camera face, and the *y-axis* represents different planar projections, with the first planar projection at the *top*. The heart can be seen as a bright stripe from the top right to the lower left of the sinogram. The clinician looks for a break in this stripe, which would represent the patient moving to the left or right. Thus, sinograms are best for detecting horizontal motion across the table. Sinograms may also show vertical motion, but not quite as well as horizontal motion

Patient motion can also be detected by using summed projections. The summed projection is formed by adding all of the planar projections for the SPECT acquisition. The heart can be traced as a blurry horizontal line across the center of the image. To evaluate patient motion, the clinician should look for a change in the height of the heart that would indicate movement during the acquisition. This method is best used for detecting vertical motion—that is, motion of the patient along the table

There are a number of software algorithms, both manual and automatic, for correcting patient motion [29]. These algorithms work best when the motion is vertical along the table and no twisting motion has occurred. As with any algorithm, they may sometimes fail, although in general they correct for motion quite well. Sometimes, when these algorithms are applied to patients who have not moved during acquisition, the software gets confused and corrects for a nonexistent motion. It is advisable to always visually confirm that the motion correction software has performed appropriately

Advances in Cardiology Imaging

Figures 2.44, 2.45, 2.46, 2.47, 2.48, 2.49, 2.50, 2.51, 2.52, 2.53, 2.54, 2.55, and 2.56 illustrate some recent advances in imaging systems for cardiology.

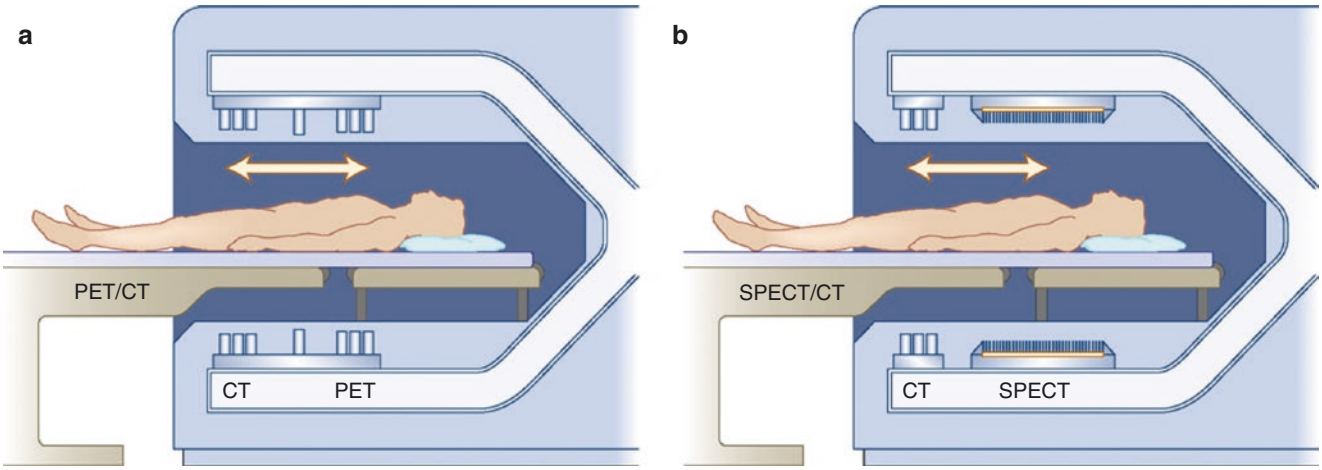

Fig. 2.44 Hybrid PET/CT and SPECT/CT imaging systems. Hybrid systems, which physically couple a CT scanner with a PET (**a**) or a SPECT (**b**) scanner, are now in routine clinical use. The coupled CT scanner, ranging from 1 to 64 slices, is commonly used for attenuation correction and, if supported by the CT scanner, can be used to evaluate coronary calcium and/or perform CT angiographic studies. An advantage of these systems is that they can provide comprehensive cardiac evaluation of anatomic information from the CT scan and physiologic information from the PET or SPECT scans in a single imaging study [30]

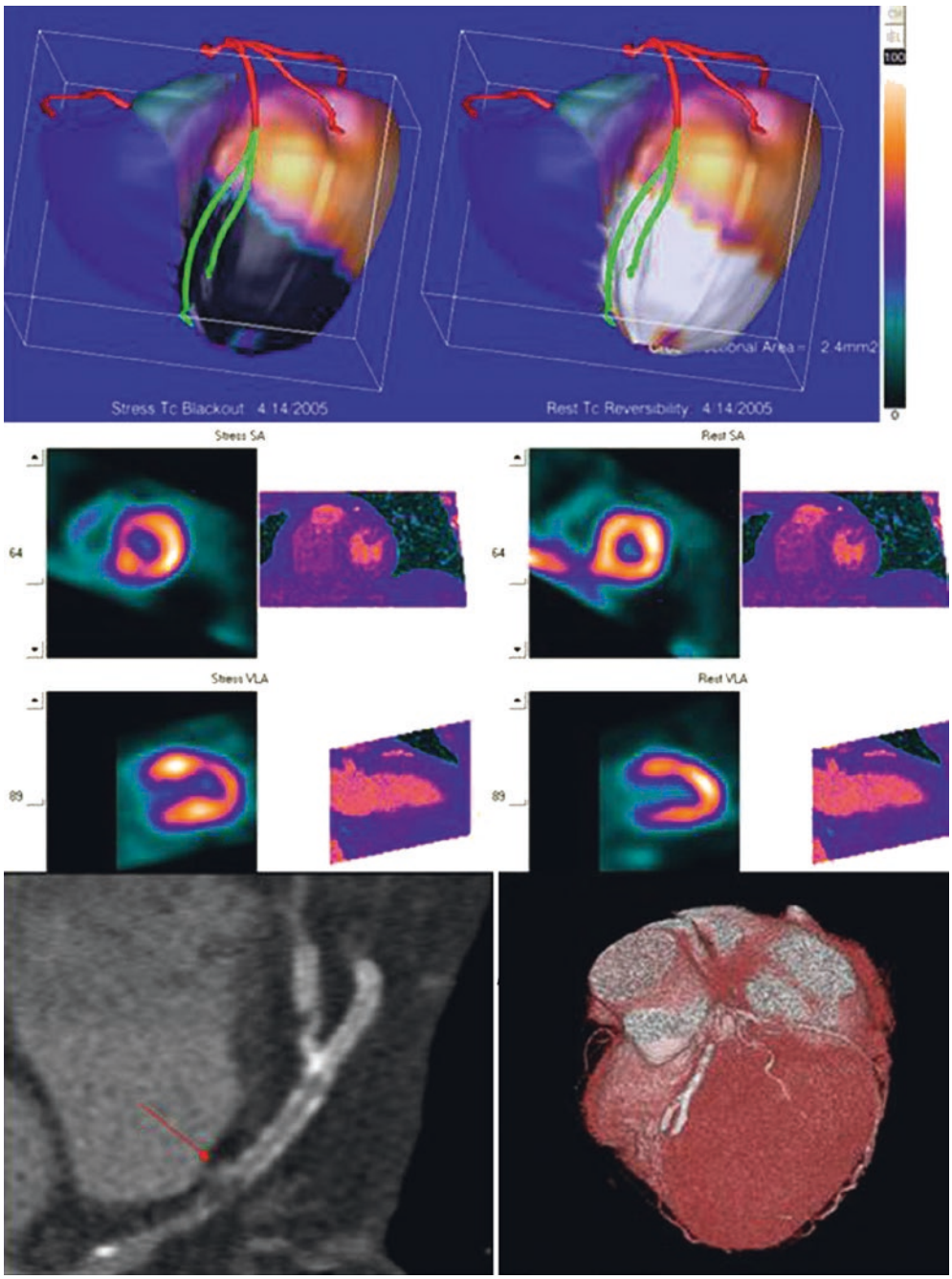

Fig. 2.45 PET/CT and SPECT/CT image fusion. Software methods are required to fuse the anatomic information from the CT angiographic (CTA) study and the physiologic information from a nuclear myocardial perfusion PET or SPECT study in three dimensions (3D). Because the emission and transmission studies are not acquired simultaneously, software fusion is needed regardless of whether a hybrid system or two stand-alone systems are used to acquire the information. Two types of fusion are used today: quantitative and qualitative fusion. In *quantitative* fusion, the 3D coronary tree is extracted from the CTA study and superimposed onto the 3D myocardial perfusion distribution using landmarks and shape operators [31]. In this approach, the quantitatively determined hypoperfused regions are highlighted in *black*, and the vessels distal to a coronary stenosis are highlighted in *green*. Compared with the accuracy of CTA, this fused information has been shown to provide significantly higher specificity and positive predictive value at no loss of sensitivity or negative predictive value [32]. This quantitative fusion approach has also been clinically validated to demonstrate increased diagnostic quality for detecting and localizing coronary artery disease compared with side-by-side displays of the nonfused perfusion and CT information [33]. In the *qualitative* approach, the 3D surface-rendered CTA study (*top right*) is painted with the 3D myocardial perfusion distribution angled in the same orientation as the CTA study. This fused qualitative information has also been reported to improve diagnostic accuracy over CTA [34]. More recently, a second-generation quantitative fusion approach has been developed, which combines the attributes of both the quantitative and qualitative approaches and uses the right ventricular epicardium for improved fusion of the arteries [35]. Shown here is the second-generation fusion of a patient with >70% stenosis in the left anterior descending coronary artery (LAD), just proximal to the stent. *Top* fusion displays show the left ventricle and translucent right ventricle detected from the CTA, color-coded for quantitative perfusion after automatic alignment of the SPECT study with the CT. Stress blackout is on the *left*, and reversibility whiteout is on the *right*. Coronary arteries are color-coded as *green* distal to the stenosis. *Middle* slice displays show aligned stress SPECT and (rest) CT coronary angiography (CTCA) on the left and rest SPECT and CTCA on the right. *Bottom* displays are zoomed multiplanar format of the stenosis in the LAD (*left*) and a typical 3D display generated from the CTA only (*right*)

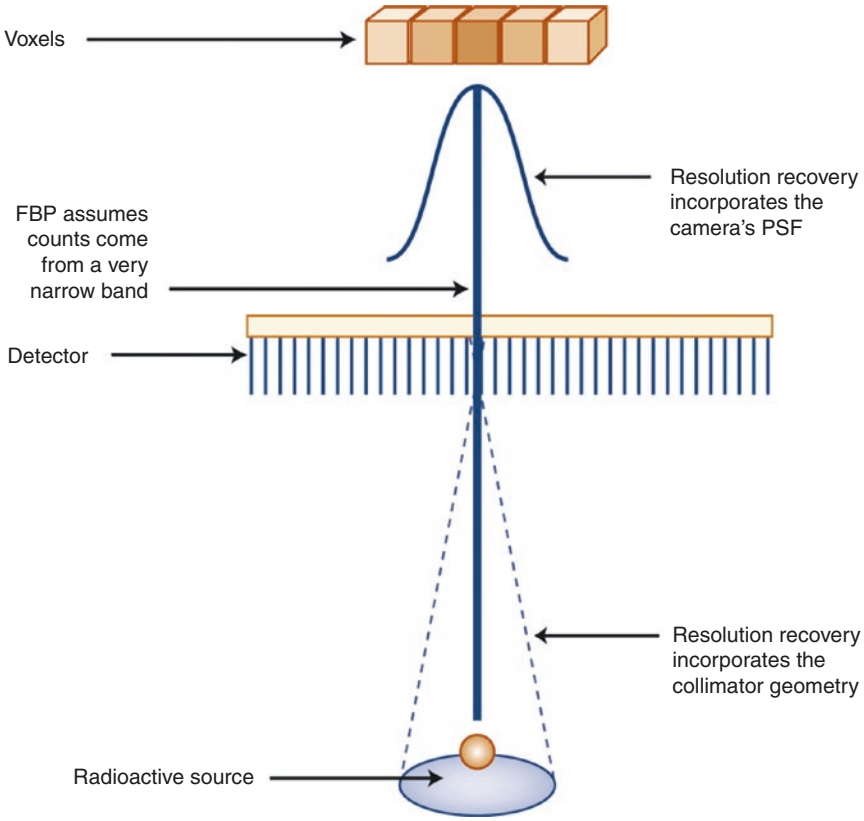

Fig. 2.46 Image reconstruction advances allow half-time acquisition. This diagram shows how conventional filtered backprojection (FBP) reconstruction assumes that the photons counted in a voxel over a collimator's parallel hole have emanated in a straight line from a radioactive source perpendicular to the detector surface and aligned with the hole. It assumes that all other photons counted from this source are either image noise or counts from other sources positioned in a very narrow line parallel to and directly in front of the hole. Recent software improvements in image reconstruction take into account the loss of resolution with distance that is inherent in parallel-hole collimators, depicted here by the cone drawn as a dashed line [36, 37]. Using this knowledge in conjunction with the properties of the entire point spread function (PSF) allows for a more accurate resolution recovery. In principle, instead of backprojecting the acquired counts from the planar projection in a straight line, the counts are backprojected (iteratively) along a cone

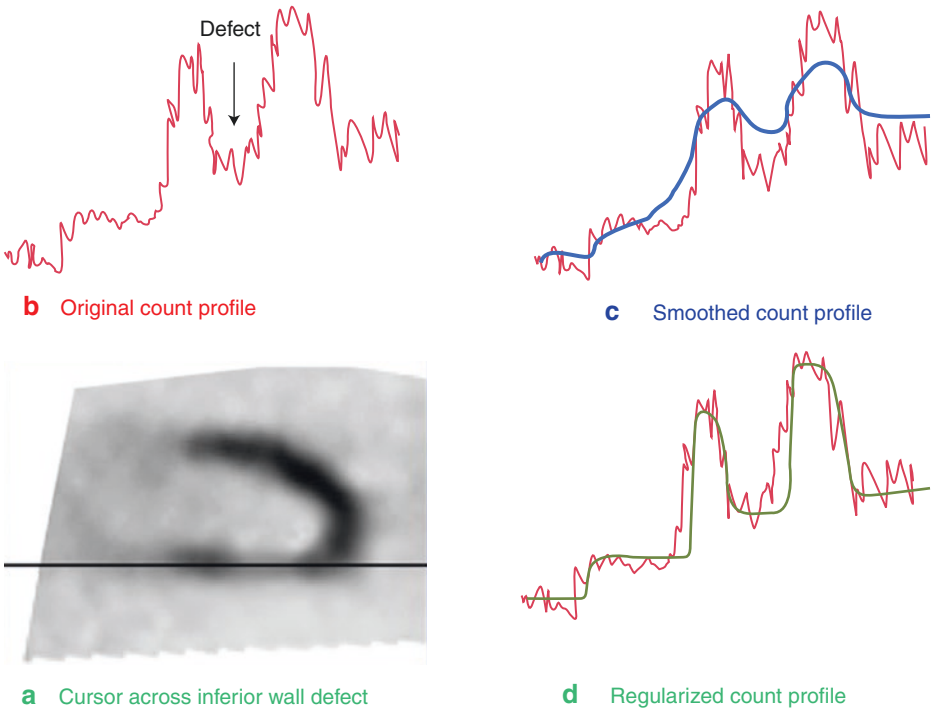

Fig. 2.47 Effect of noise regularization on defect contrast. At the same time the resolution recovery is performed, noise is suppressed or regularized because additional counts are now correctly considered (modeled) rather than treated as noise. (**a**) A vertical long-axis myocardial perfusion SPECT tomogram of a patient with a hypoperfused defect in the inferior wall. (**b**) What a noisy count profile across the inferior wall might look like if the study was not corrected for noise; the defect contrast is demonstrated as the region of reduced counts between the two normal increased count regions (albeit noisy). The larger the difference in counts between the defect and the normal region, the larger the defect contrast and the easier it is to detect it. (**c**) Superimposed on the original noisy count profile is what a conventional smooth count profile (*yellow*) might look like. The jagged high-frequency noise has disappeared, but taking with it the defect borders, reducing the difference in counts between the normal and hypoperfused regions, and thus reducing the defect contrast. (**d**) Superimposed on the original noisy count profile is a regularized count profile (*green*), which has been modeled using *a priori* physical knowledge of the imaging system. The jagged high-frequency noise has now been removed but the original defect contrast has been preserved, thus making it possible to reduce noise without compromising image contrast. It has been reported that SPECT myocardial perfusion imaging may be performed with these new resolution recovery/noise regularization algorithms using half the conventional scan time without compromising perfusion imaging results [38]. In another study, it was shown that these new algorithms, applied to half-time ECG-gated myocardial perfusion imaging SPECT acquisitions, compare favorably with the filtered backprojection (FBP) of full-time algorithms in image quality and the correlation of functional parameters. However, systematic offset in these functional parameters was reported owing to the increase in contrast of the resolution recovery–gated images over FBP images [39]

Fig. 2.48 Limitations of conventional SPECT imaging. Myocardial perfusion SPECT imaging has had widespread clinical use, owing to its well-documented diagnostic accuracy for detecting coronary artery disease. Nevertheless, the basic camera design is more than 50 years old and limited when using standard parallel-hole collimators to image the heart, as it uses only a small portion of the available, useful sodium iodide (NaI) crystal detector area

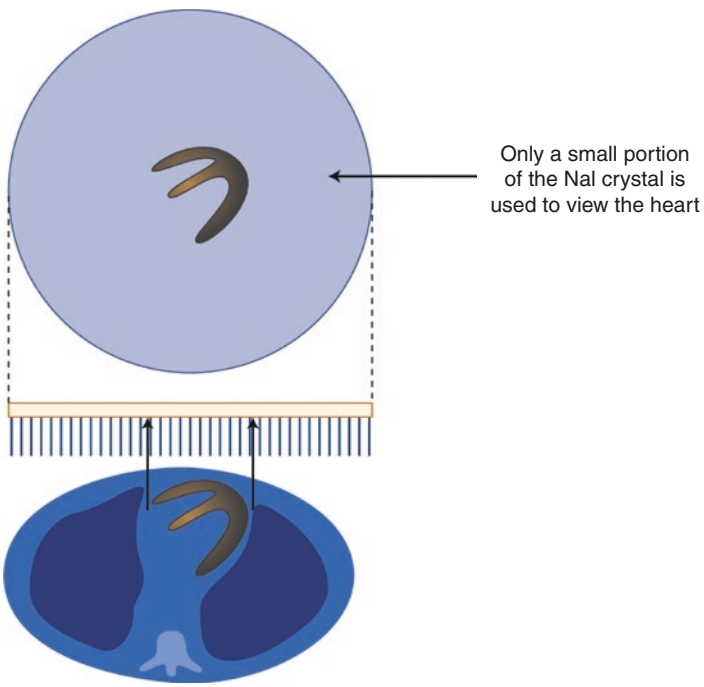

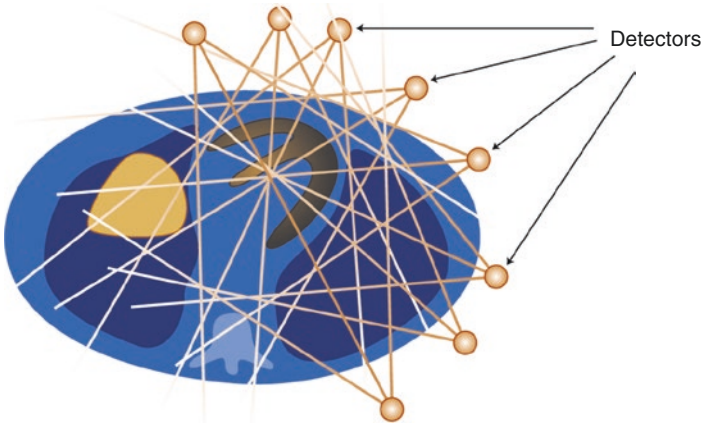

Fig. 2.49 Design of new-generation dedicated cardiac ultrafast acquisition scanners. Several manufacturers have begun to break away from the conventional SPECT imaging approach to create innovative designs of dedicated cardiac scanners. These scanners' designs have in common that all available detectors are constrained to imaging only the cardiac field of view. This diagram shows how eight detectors surrounding the patient are all simultaneously imaging the heart. These new designs vary in the number and type of scanning or stationary detectors and whether sodium iodide or cadmium zinc telluride solid-state detectors are used. They all have in common the potential for a fivefold to tenfold increase in count sensitivity at no loss (or even a gain) in resolution, resulting in the potential for acquiring a stress myocardial perfusion scan in 2 minutes or less with injection of a standard dose [36, 37, 40]

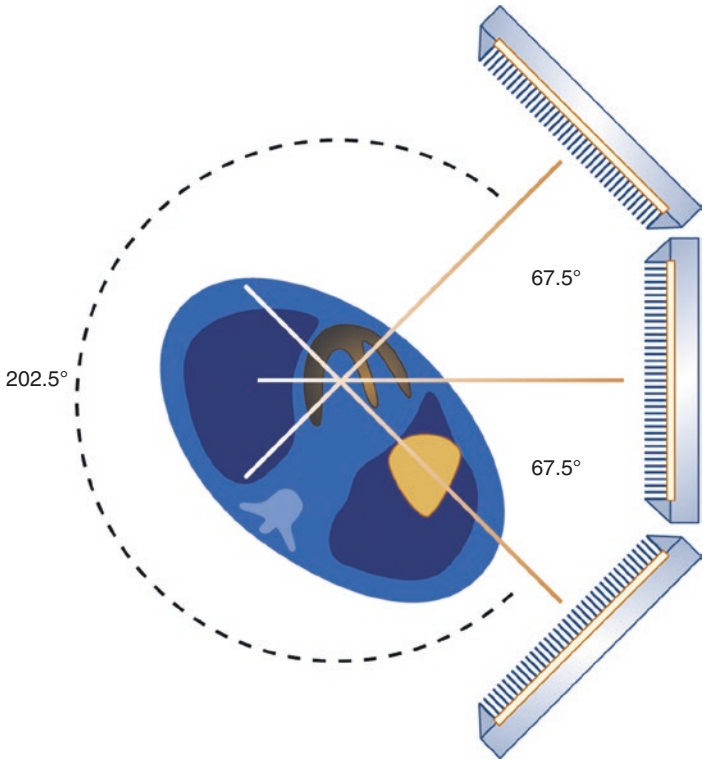

Fig. 2.50 Cardius® 3 XPO system configuration (Digirad; Suwanee, GA). This diagram shows how patient data are acquired with the Cardius® 3 XPO camera by keeping the three detectors stationary and simultaneously imaging the heart while the chair on which the patient is seated is rotated through a 202.5° arc. This commercial system is one of the first systems developed to take advantage of solid-state electronics and use more than two detectors simultaneously for imaging the heart. It uses 768 pixilated, thallium-activated cesium iodide [CsI(Tl)] crystals coupled to individual silicon photodiodes and digital Anger electronics to create the planar projection images used for reconstruction [41]. This image shows how the three detectors are fixed using a 67.5° angular separation while the patient is rotated. The typical acquisition time for a study is 7.5 minutes. In a large multicenter trial using this device and resolution recovery reconstruction, a subset of 189 patients acquired using conventional doses was compared with conventional SPECT. Using this combination, the study showed that a 5-minute rest acquisition and a 4-minute stress acquisition yielded perfusion and function information from gated SPECT myocardial perfusion imaging studies, which were diagnostically equivalent to full-time acquisition and two-dimensional ordered-subsets expectation maximization reconstructions [41]

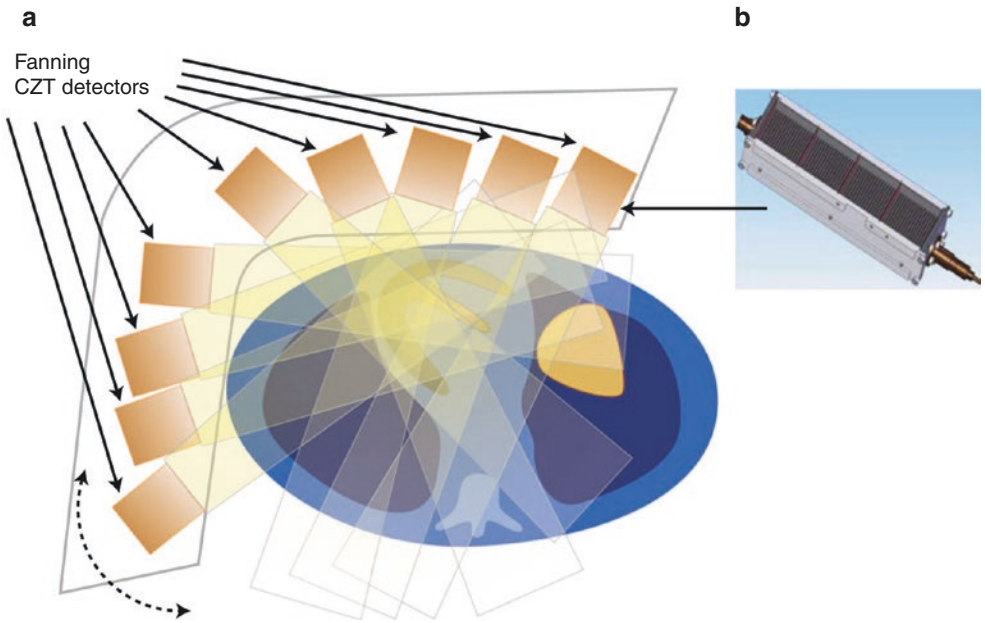

Fig. 2.51 D-SPECT® system configuration (Spectrum Dynamics Medical; Sarasota, FL). (**a**) This diagram is of the 9-cadmium-zinc-telluride (CZT) detector column configuration of the D-SPECT® system, in which each detector column uses a tungsten parallel-hole collimator that is fanned back and forth, constrained angularly to the heart's field of view. This is the first SPECT system to offer a totally different design [42–45]. This system uses solid-state detectors in the form of CZT mounted on nine vertical columns and placed in a 90° geometry, as shown in this figure. Each of the nine detector assemblies (**b**) is equipped with a tungsten, square, parallel-hole collimator. Each collimator square hole is 2.46 mm on its side, which is large in comparison to conventional collimators, which partially accounts for the increased count sensitivity. Each detector assembly is made to fan in synchrony with the other eight detector assemblies while all nine are simultaneously imaging the heart. The patient is imaged sitting in a reclining position, similar to a dentist's chair, with the patient's left arm placed on top of the detector housing

Data acquisition is performed by first obtaining a 1-minute scout scan for the nine detectors to identify the location of the heart, to set the limits of each detector's fanning motion. The actual diagnostic scan is then performed with each detector assembly fanning within the limits set from the scout scan. Reconstruction is performed using a modified iterative algorithm that compensates for the loss of spatial resolution that results from using large square holes in the collimator by mathematically modeling the acquisition, collimator, and left ventricle geometry

In a recent single-center clinical trial publication, it was concluded that using a stress/rest myocardial perfusion imaging (MPI) protocol and 4-minute and 2-minute D-SPECT® acquisitions yielded studies that highly correlated with 16-minute and 12-minute stress/rest conventional SPECT, with an equivalent level of diagnostic performance [42]. In a report of a multicenter trial using D-SPECT®, it was shown that using normal database quantitative analysis and a comparison protocol similar to the previous report correlated well with quantitative analysis of conventional SPECT MPI [43]. Another preliminary multicenter trial reported the potential for the D-SPECT® device to perform simultaneous Tl-201 (rest)/Tc-99m sestamibi (stress) 15-minute acquisitions [44]

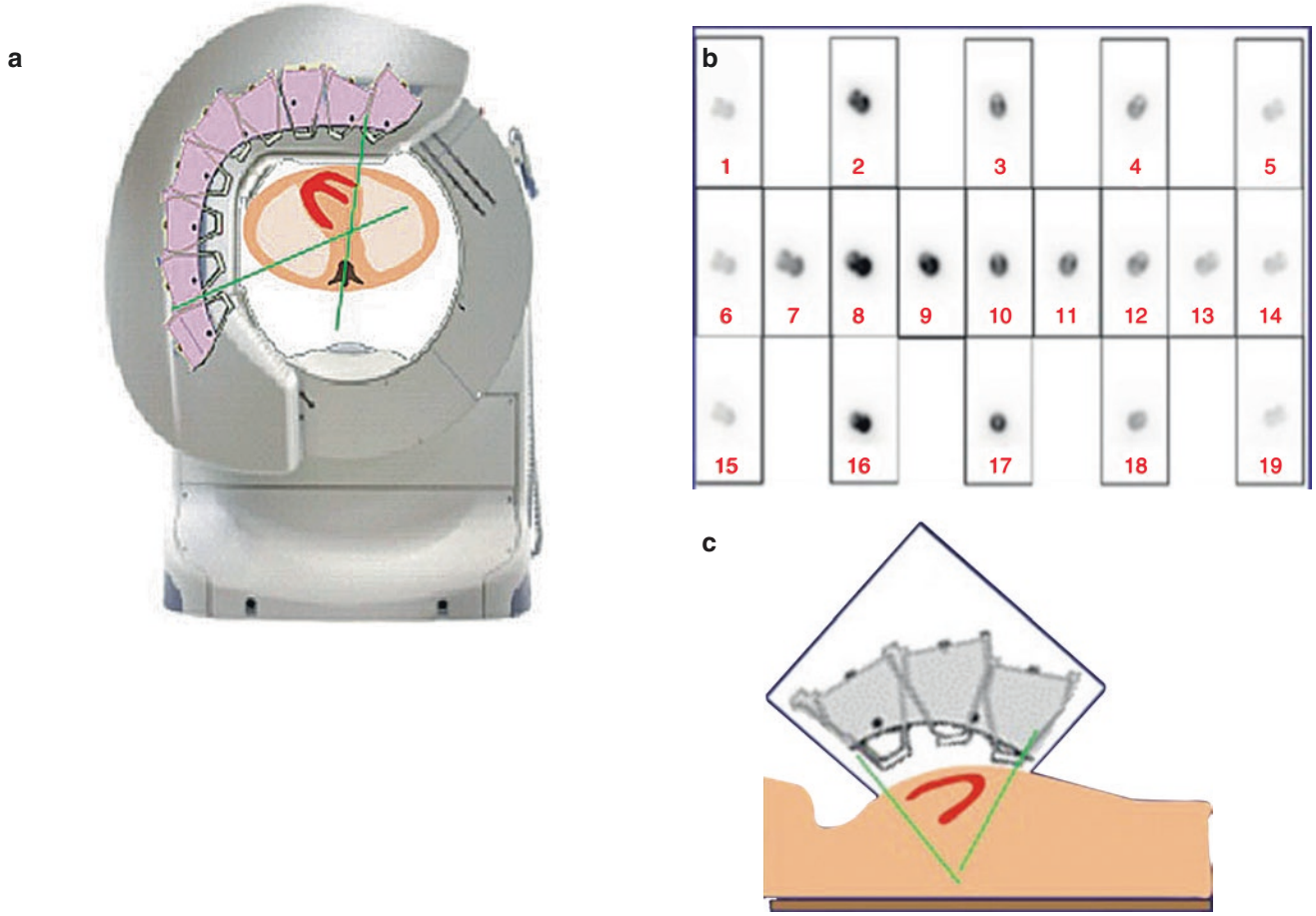

Fig. 2.52 Discovery NM 530c system configuration. The second SPECT system to offer a revolutionary new design is the system developed by GE Healthcare (Waukesha, WI) [45–48], known as the Discovery Nuclear Medicine (NM) 530c system. (**a**) The SPECT design uses Alcyone technology, consisting of an array of 19 pinhole collimators, each with four solid-state CZT pixilated detectors. (**b**) Projections from all 19 pinholes simultaneously image the heart, with no moving parts during data acquisition. Nine of the pinhole detectors are oriented perpendicular to the patient's long axis, five are angulated above the axis, and five below, for a true 3D acquisition geometry (**c**). The use of simultaneously acquired views improves the overall sensitivity and gives the complete and consistent angular data needed for both dynamic studies and for the reduction of motion artifacts. In addition, attenuation artifacts may be reduced because not all projections are viewed through the attenuator; some may view the heart from above or below. The detector assembly is mounted on a gantry that allows for patient positioning in the supine or prone positions

In the first multicenter trial, it was demonstrated that using a conventional 1-day technetium-99m (^{99m}Tc) tetrofosmin rest/stress MPI protocol and 4-minute and 2-minute Alcyone acquisitions yielded studies that diagnostically agreed 90% of the time with 14-minute and 12-minute rest/stress conventional SPECT acquisitions [46]. Importantly, this trial also showed excellent left ventricular ejection fraction correlations between the 530c and conventional SPECT for rest-gated MPI studies ($r = .93$, $P < 0.001$) and stress-gated MPI studies ($r = .91$, $P < 0.001$) [46]. A subsequent single-center trial was performed using a 1-day ^{99m}Tc tetrofosmin adenosine-stress/rest MPI protocol and a 3-minute scan for stress and 2 minutes for rest using the 530c camera compared with 15-minute conventional SPECT acquisitions for stress and rest [47]. These investigators concluded that the 530c camera allows a more than fivefold reduction in scan time and provides clinical perfusion and function information equivalent to conventional dual-head SPECT MPI

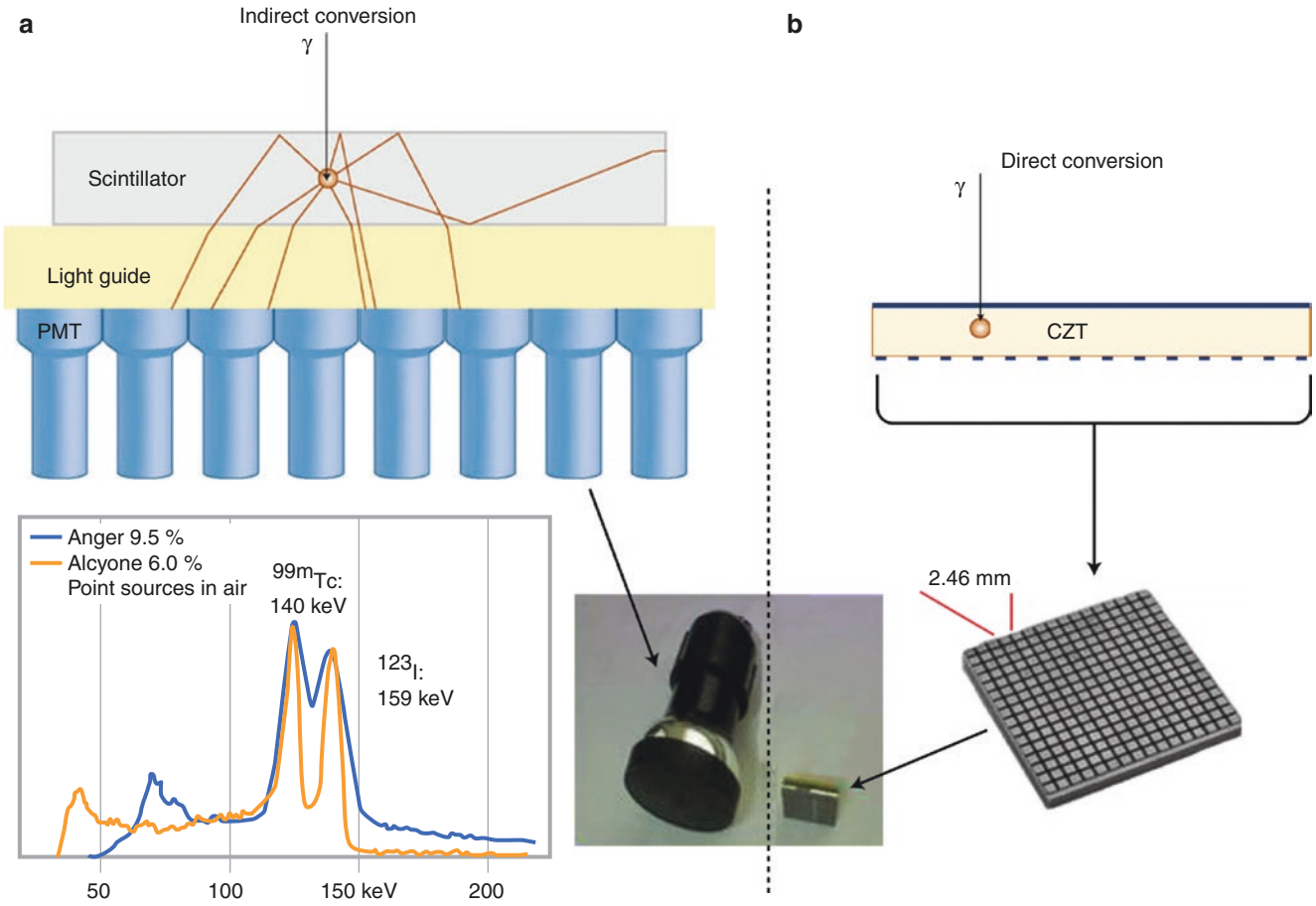

Fig. 2.53 Indirect versus direct radiation conversion. (**a**) Indirect conversion: This figure illustrates how a conventional second SPECT detector works where the NaI (Tl) crystal absorbs the γ-ray from the patient and converts its energy to visible photons, which are then converted to electrical pulses by the entire array of photomultipliers (PMT). The sum of all pulses is used as energy information, and the distribution of pulses provides the location of the event in the crystal. The large number of steps to reach these final data results is an opportunity for the information to be degraded as it is transferred from one system to another, thus reducing both the energy and spatial resolution of the system. (**b**) Direct conversion: This figure illustrates how a CZT detector works, where the detector absorbs the γ-ray from the patient, directly converting its energy to charge carriers that form an electrical pulse with the information of the energy of the event; the location is given by the location of the pixel within the CZT detector where the event took place. This more direct transfer of energy and location information results in superior energy and spatial resolution over conventional SPECT cameras. The *middle lower* insert compares the size of one photomultiplier tube (PMT) used in conventional SPECT versus the size of a CZT detector. The *lower left* panel illustrates the superior energy resolution of the CZT detector (*blue*) over conventional cameras (*purple*) by comparing a simultaneous acquisition of ^{99m}Tc and I-123 radioactive sources. (A*dapted from slides courtesy of* Aharon Peretz, Ph.D.)

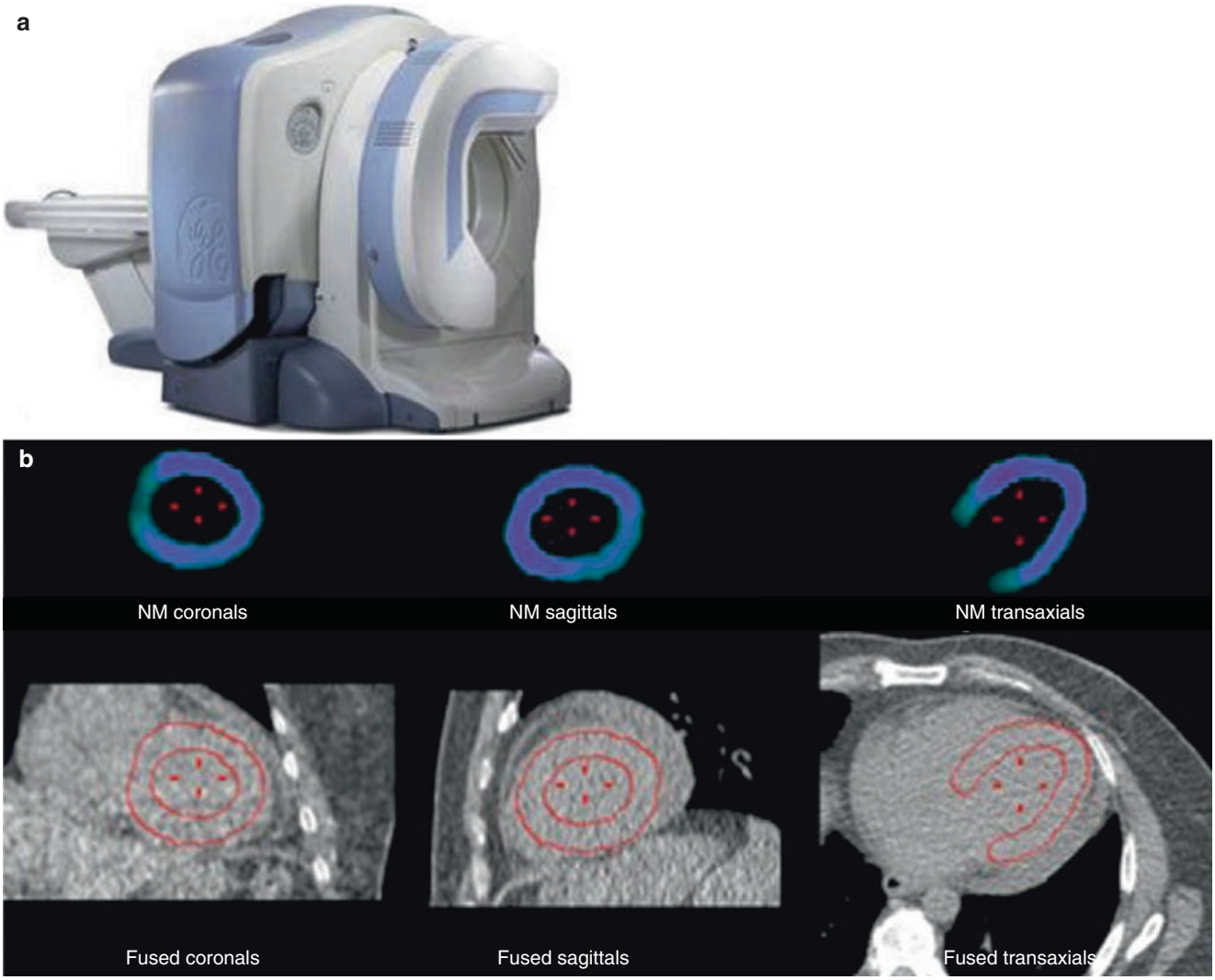

Fig. 2.54 Discovery Nuclear Medicine 570c system configuration. (**a**) The CZT detector assembly and gantry of the 530c system is physically coupled to a volumetric CT scanner for a fast SPECT/CT system configuration. (**b**) The *top row* shows the segmented SPECT images of the left ventricle (LV); the *bottom row* shows the overlay of the borders of these LV segments onto the CT transmission studies used for quality control and alignment of the emission and transmission studies. Iterative reconstruction adapted to this geometry is used to create transaxial slices of the heart and to perform attenuation correction [50, 51]

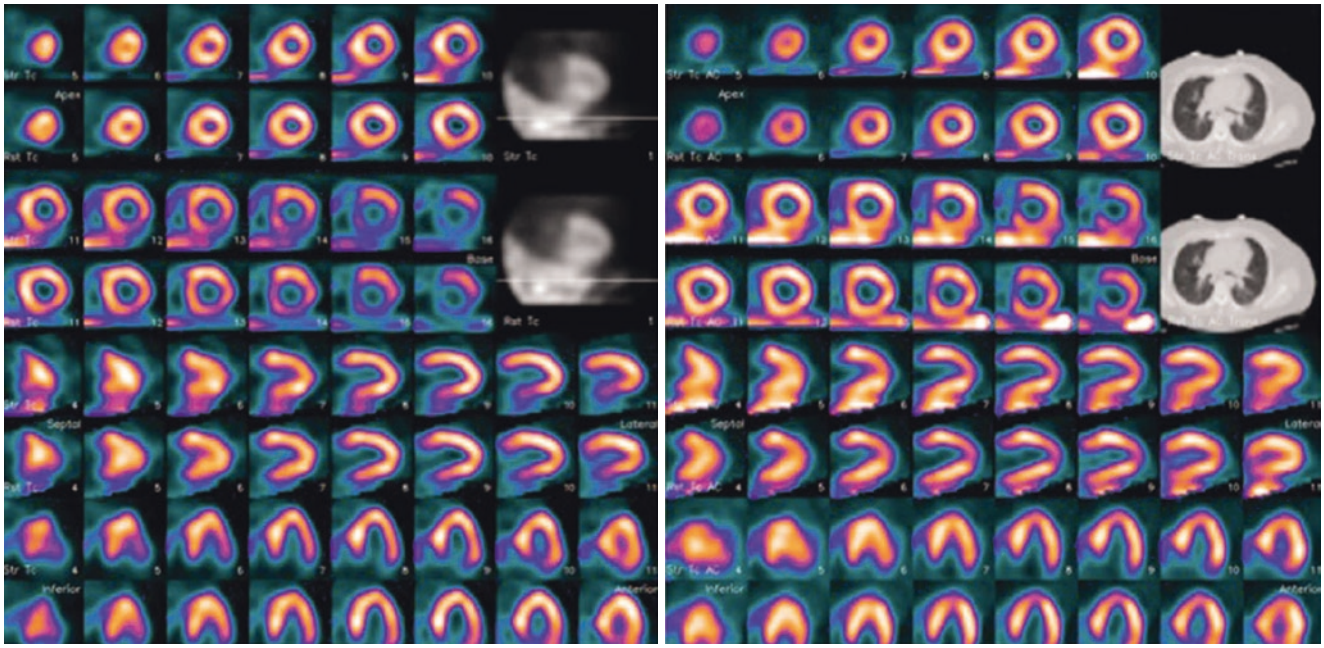

a Before AC **b** After AC

Fig. 2.55 Normal patient images with diaphragmatic attenuation used to illustrate the advantage of using attenuation correction (AC) with the Discovery NM 530c cardiac system. Results are shown from a patient who underwent rest/stress technetium-99m tetrofosmin MPI using 10 mCi for rest and 30 for stress. (**a**) 530c system images without AC are shown. Rest and stress acquisitions were 4 and 2 minutes, respectively. The figure shows short, vertical, and horizontal oblique axis slices starting with stress images in the *first row*, with the corresponding resting images immediately below. The *top right* black/white images show planar reprojections. Note the fixed defect in the inferobasal wall. (**b**) 530c system images with AC are shown. This is the same patient as in (**a**), but with the use of a CT transmission for AC, shown in the *top right* black/white panels. Note the increased tracer uniformity throughout the left ventricle and a normally perfused inferior wall

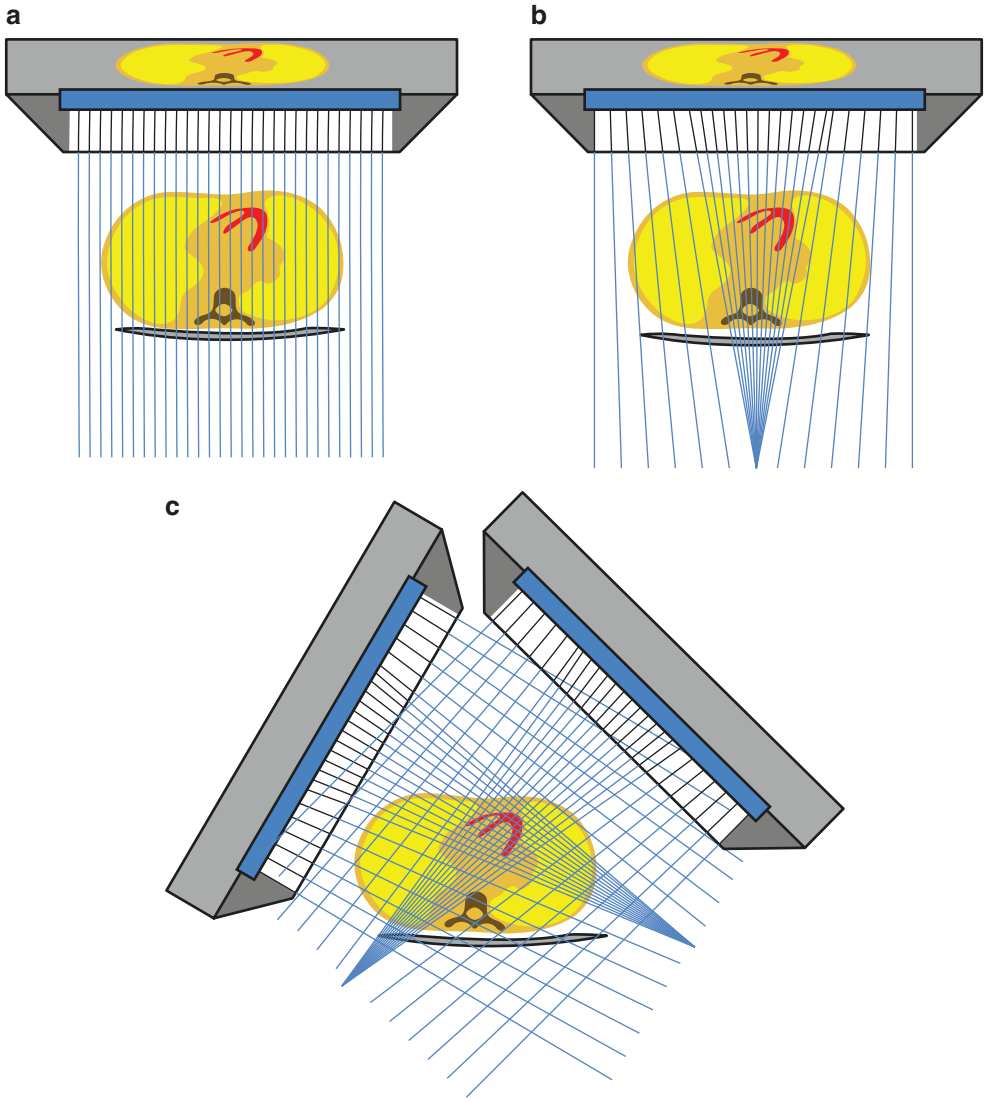

Fig. 2.56 The IQ•SPECT system (Siemens; Erlangen, Germany) achieves high sensitivity by using a unique collimator design mounted on a standard, large field-of-view, dual-detector SPECT or SPECT/CT system. The collimators used in IQ•SPECT have a central area with converging collimation designed to focus on the heart and transition to parallel-hole collimation around the periphery of the camera. This design allows increased sensitivity over the heart, where it is most needed, but avoids truncation of the body [52]. (**a**) The image of the heart formed by a parallel-hole collimator is the same size as the heart. (**b**) The IQ•SPECT collimator utilizes more of the crystal for the heart, at the expense of a smaller field of view. (**c**) The angle between the detectors is set to 76° and the heart is positioned so that it is in the region of highest magnification of both collimators throughout acquisition. Although slight mispositioning may be tolerable, poor patient set-up may be less forgiving than in standard parallel-hole collimation. Some have noted that attenuation artifacts may differ from those recognized with parallel-hole collimation and that attenuation-corrected images may be preferred [52]

The use of IQ•SPECT to reduce imaging time and/or radiopharmaceutical dose has been demonstrated. In one study, Lyon et al. [53] compared attenuation-corrected stress SPECT to IQ•SPECT using a dose of 925–1100 MBq (25–30 mCi) Tc-99m sestamibi. Several different count levels were simulated for IQ•SPECT, and were evaluated using system- and count- level–specific normal files. The study concluded that IQ•SPECT could be used to reduce both the dose and the time by half compared with conventional SPECT. Thus the standard dose could be reduced to below 550 MBq (15 mCi) and the imaging time reduced from 13 minutes (standard SPECT) to 7 minutes [53]

The high-sensitivity hardware designs discussed in Figs. 2.50, 2.51, 2.52, 2.53, 2.54, and 2.55 are dedicated-cardiac cameras, but only when the IQ•SPECT collimator is mounted is the system restricted to nuclear cardiology. When equipped with standard collimators, the system is a general-purpose SPECT or SPECT/CT, a factor that may appeal to clinics that also perform general nuclear medicine studies

Table 2.7 shows how some of the increased count sensitivity of these new systems may be traded off for a reduced injected dose and, thus, a reduced total effective dose to the patient. It is clear that these imaging systems with more efficient hardware and software also allow for high-quality images that are obtained using a lower injected radiopharmaceutical dose and, thus, a decrease in the radiation dose that is absorbed by the patient and staff. This reduction in dose comes at an increase in acquisition time, even if the total time is less than what has been traditionally used in conventional systems. Recently, the American Society of Nuclear Cardiology published an information statement [49] recommending that laboratories use imaging protocols that achieve a median dose of ≤9 mSv or less in MPI, and stress-first imaging is an important tool to meet this goal. Although many different protocols that may be implemented to accomplish this exposure goal, use of the more efficient hardware/software described would greatly facilitate this goal and allow for increases in efficiency over the imaging protocols used today.

Rest		Stress		Total	
Injected dose, *MBq*	Acquisition time, *min*	Injected dose, *MBq*	Acquisition time, *min*	Effective dose,[a] *MSv*	Acquisition time, *min*
370	4	1110	2	12	6
185	8	555	4	6	12
93	16	278	8	3	24

[a]Effective dose estimated from tissue dose coefficients using the International Commission on Radiological Protection (ICRP) Publication 60 tissue-weighting factors

Table 2.7 Reduced dose versus increased efficiency

References

1. Chandra R. Introductory physics of nuclear medicine. Philadelphia: Lea and Febiger; 1992.
2. Christensen EE, Curry TS, Dowdey JE. An introduction to the physics of diagnostic radiology. 2nd ed. Philadelphia: Lea and Febiger; 1978. p. 159.
3. Powsner RA, Powsner ER. Essentials of nuclear medicine physics. Malden: Blackwell Science; 1998.
4. Hubble JH, Seltzer SM. Tables of x-ray mass attenuation coefficients, and mass energy-absorption coefficients. Gaithersburg: National Institute of Standards and Technology; 1996. Available at: http://physics.nist.gov/PhysRefData/XrayMassCoef/tab1.html. Accessed Jul 2018.
5. Cherry SR, Sorenson JA, Phelps ME. Physics in nuclear medicine. Philadelphia: WB Saunders; 2003.
6. Beller GA, Bergmann SR. Myocardial perfusion imaging agents: SPECT and PET. J Nucl Cardiol. 2004;11:71–86.
7. Saha GB. Fundamentals of nuclear pharmacy. New York: Springer; 2003.
8. Anger HO. Scintillation camera with multichannel collimators. J Nucl Med. 1964;5:515–31.
9. Maublant JC, Peycelon P, Kwiatkowski F, Lusson JR, Standke RH, Veyre A. Comparison between 180° and 360° data collection in technetium-99m MIBI SPECT of the myocardium. J Nucl Med. 1989;30:295–300.
10. Hoffman EJ. 180° compared to 360° sampling in SPECT. J Nucl Med. 1982;23:745–6.
11. Knesaurek K, King MA, Glick SJ, Penney BC. Investigation of causes of geometric distortion in 180° and 360° angular sampling in SPECT. J Nucl Med. 1989;30:1666–75.
12. Garcia EV, Galt JR, Cullom SJ, Faber TL. Principles of myocardial perfusion SPECT imaging. North Billerica: DuPont Pharma; 1994. p. 30.
13. Galt JR, Garcia EV, Robbins WL. Effects of myocardial wall thickness on SPECT quantification. IEEE Trans Med Imaging. 1990;9:144–50.
14. Shepp LA, Vardi Y. Maximum likelihood reconstruction for emission tomography. IEEE Trans Med Imaging. 1982;1:113–22.
15. Hudson HM, Larkin RS. Accelerated image reconstruction using ordered subsets of projection data. IEEE Trans Med Imaging. 1994;13:601–9.
16. Jaszczak RJ, Greer KL, Floyd CE Jr, Harris CC, Coleman RE. Improved SPECT quantification using compensation for scattered photons. J Nucl Med. 1984;25:893–900.
17. Ogawa K, Ichihara T, Kubo A. Accurate scatter correction in single photon emission CT. Ann Nucl Med Sci. 1994;7:145–50.
18. Glick SJ, Penney BC, King MA, Byrne CL. Noniterative compensation for the distance-dependent detector response and photon attenuation in SPECT imaging. IEEE Trans Med Imaging. 1994;13:363–74.
19. Zeng GL, Gullberg GT, Tsui BM, et al. Three-dimensional iterative reconstruction algorithms with attenuation and geometric point response correction. IEEE Trans Med Imaging. 1990;22:1475–9.
20. Smith WH, Kastner RJ, Calnon DA, Segalla D, Beller GA, Watson DD. Quantitative gated single-photon emission computed tomography imaging: a counts-based method for display and measurement of regional and global ventricular systolic function. J Nucl Cardiol. 1997;4:451–63.
21. Machac J, Chen H, Almeida OD, et al. Comparison of 2D and high dose and low dose 3D gated myocardial Rb-82 PET imaging [abstract]. J Nucl Med. 2002;43:777.
22. Karp JS, Surti S, Daube-Witherspoon ME, Muehllehner G. Benefit of Time-of-Flight in PET: Experimental and clinical results. J Nucl Med. 2008;49(3):462–70.
23. Schaart DR, van Dam HT, Seifert S, Vinke R, Dendoover P, Lohner H, Beekman FJ. SiPM-Array Based PET detectors with depth-of-interaction correction. IEEE Nuc Sci Symposium Conference Record. 2008:3581–5.

24. Schelbert HR, Beanlands R, Bengel F, Knuuti J, Dicarli M, Machac J, Patterson R. PET myocardial perfusion and glucose metabolism imaging: Part 2-Guidelines for interpretation and reporting. J Nucl Cardiol. 2003;10:557–71.
25. Dorbala S, Ananthasubramaniam K, Armstrong IS, Chareonthaitawee P, DePuey EG, Einstein AJ, et al. Single photon emission computed tomography (SPECT) myocardial perfusion imaging guidelines: instrumentation, acquisition, processing, and interpretation. J Nucl Cardiol. 2018;25(5):1784–46.
26. Nichols KJ, Galt JR. Quality control for SPECT imaging. In: DePuey EG, Garcia EV, Berman DS, editors. Cardiac SPECT imaging. 2nd ed. New York: Lippincott Williams & Wilkins; 2001. p. 17–39.
27. DePuey EG. Artifacts in SPECT myocardial perfusion imaging. In: DePuey EG, Garcia EV, Berman DS, editors. Cardiac SPECT imaging. 2nd ed. New York: Lippincott Williams & Wilkins; 2001. p. 349.
28. DePuey EG, Garcia EV. Optimal specificity of thallium-201 SPECT through recognition of imaging artifacts. J Nucl Med. 1989;30:441–9.
29. Geckle WJ, Frank YL, Links JM, Becker LC. Correction for patient motion and organ movement in SPECT: application to exercise thallium-201 cardiac imaging. J Nucl Med. 1988;29:441–50.
30. Di Carli MF, Hachamovich R. New technology for noninvasive evaluation of coronary artery disease. Circulation. 2007;115:1464–80.
31. Faber TL, Santana CA, Garcia EV, Candell-Riera J, Folks RD, Peifer JW, et al. Three-dimensional fusion of coronary arteries with myocardial perfusion distributions: clinical validation. J Nucl Med. 2004;45:745–53.
32. Rispler S, Keidar Z, Ghersin E, Roguin A, Soil A, Dragu R, et al. Integrated single-photon emission computed tomography and computed tomography coronary angiography for the assessment of hemodynamically significant coronary artery lesions. J Am Coll Cardiol. 2007;49:1059–67.
33. Santana CA, Garcia EV, Faber TL, Sirineni GK, Esteves FP, Sanyal R, et al. Diagnostic performance of fusion of myocardial perfusion and computed tomography coronary angiography. J Nucl Cardiol. 2009;16:201–11.
34. Gaemperli O, Schepis T, Valenta I, Husmann L, Scheffel H, Duerst V, et al. Cardiac image fusion from stand-alone SPECT and CT: clinical experience. J Nucl Med. 2007;48:696–703.
35. Faber TL, Arepalli CD, Nye JA, et al. Second generation fusion of myocardial perfusion distributions with coronary artery data from CT angiography. J Nucl Cardiol. 2010;17(4):724–722 (abstr).
36. Garcia EV, Faber TL. New trends in camera and software technology in nuclear cardiology. Cardiol Clin. 2009;27:227–36.
37. Garcia EV, Faber TL, Esteves FP. Cardiac dedicated ultrafast SPECT cameras: new designs and clinical implications. J Nucl Med. 2011;52:210–7.
38. Borges-Neto S, Pagnanelli RA, Shaw LK, Honeycutt E, Shwartz SC, Adams GL, Coleman RE. Clinical results of a novel wide beam reconstruction method for shortening scan time of Tc-99m cardiac SPECT perfusion studies. J Nucl Cardiol. 2007;14:555–65.
39. DePuey EG, Gadiraju R, Clark J, Thompson L, Anstett F, Shwartz SC. Ordered subset expectation maximization and wide beam reconstruction "half-time" gated myocardial perfusion SPECT functional imaging: a comparison to "full-time" filtered backprojection. J Nucl Cardiol. 2008;15:547–63.
40. Sharir T, Slomka PJ, Berman DS. Solid-state SPECT technology: fast and furious. J Nucl Cardiol. 2010;17:890–6.
41. Maddahi J, Mendez R, Mahmarian J, Thomas G, Babla H, Bai C, et al. Prospective multi-center evaluation of rapid gated SPECT myocardial perfusion upright imaging. J Nucl Cardiol. 2009;16:351–7.
42. Sharir T, Ben-Haim S, Merzon K, Prochorov V, Dickman D, Ben-Haim S, Berman DS. High-speed myocardial perfusion imaging: initial clinical comparison with conventional dual detector anger camera imaging. JACC Cardiovasc Imaging. 2008;1:156–63.
43. Sharir T, Slomka PJ, Hayes SW, DiCarli MF, Ziffer JA, Martin WH, et al. Multicenter trial of high-speed versus conventional single-photon emission computed tomography imaging: quantitative results of myocardial perfusion and left ventricular function. J Am Coll Cardiol. 2010;55:1965–74.
44. Ben-Haim S, Hutton BF, Van Grantberg D. Simultaneous dual-radionuclide myocardial perfusion imaging with a solid-state dedicated cardiac camera. Eur J Nucl Med Mol Imaging. 2010;37:1710–21.
45. Garcia EV, Tsukerman L, Keidar Z. A new solid state ultra fast cardiac multi-detector SPECT system. J Nucl Cardiol. 2008;15:S3 (abstr).
46. Esteves FP, Raggi P, Folks RD, Keidar Z, Askew JW, Rispler S, et al. Novel solid-state-detector dedicated cardiac camera for fast myocardial perfusion imaging: multicenter comparison with standard dual detector cameras. J Nucl Cardiol. 2009;16:927–34.
47. Buechel RR, Herzog BA, Husmann L, Burger IA, Pazhenkottil AP, Treyer V, et al. Ultrafast nuclear myocardial perfusion imaging on a new gamma camera with semiconductor detector technique: first clinical validation. Eur J Nucl Med Mol Imaging. 2010;37:773–8.
48. Herzog BA, Buechel RR, Katz R, Brueckner M, Husmann L, Burger IA, et al. Nuclear myocardial perfusion imaging with a cadmium-zinc-telluride detector technique: optimized protocol for scan time reduction. J Nucl Med. 2010;51:46–51.
49. Cerqueira MD, Allman KC, Ficaro EP, Hansen CL, Nichols KJ, Thompson RC, et al. Recommendations for reducing radiation exposure in myocardial perfusion imaging. J Nucl Cardiol. 2010;17:709–18.
50. Herzog BA, Buechel RR, Husmann L, Pazhenkottil AP, Burger IA, Wolfrum M, et al. Validation of CT attenuation correction for high-speed myocardial perfusion imaging using a novel cadmium-zinc-telluride detector technique. J Nucl Med. 2010;51:1539–44.
51. Pazhenkottil AP, Husmann L, Kaufmann PA. Cardiac hybrid imaging with high-speed single-photon emission computed tomography/CT camera to detect ischaemia and coronary artery obstruction. Heart. 2010;96:2050. https://doi.org/10.1136/hrt.2010.201996.
52. Gremillet E, Agostini D. How to use cardiac IQ•SPECT routinely? An overview of tips and tricks from practical experience to the literature. Eur J Nucl Med Mol Imaging. 2016;43:707–10.
53. Lyon MC, Foster C, Ding X, Dorbala S, Spence D, Bhattacharya M, et al. Dose reduction in half-time myocardial perfusion SPECT-CT with multifocal collimation. J Nucl Cardiol. 2016;23:657–67.

3 Handling Radionuclides and Radiation Safety

Pat Zanzonico and H. William Strauss

Transport, preparation, administration, and imaging of radiopharmaceuticals inevitably results in low, but non-zero, radiation doses to personnel as well as patients and are thus subject to federal, state and local regulations [1–5]. Table 3.1 summarizes the relevant regulatory agencies and the scope of their regulatory oversight [6]. These agencies specify records that must be kept and procedures that must be followed to ensure the safe handling of these agents. Such regulatory oversight is not intended to extend to the actual practice of medicine; for example, there is no regulation limiting the administered activity of a radiopharmaceutical prescribed for a patient, as prescription of this activity is considered part of medical practice.

Agency (Abbreviation)	Scope of oversight	Comment
Nuclear Regulatory Commission (NRC)	Regulates civilian use of radioactive by-product materials	Regulations are found in Title 10 of the Code of Federal Regulations (10 CFR) [2]. The most important parts for medicine are Parts 19, 20, 30 and 35
Agreement States (*ie*, states to which the NRC has delegated its regulatory authority)[a]	Regulate the same radioisotopes as the NRC, as well as naturally occurring and accelerator-produced radioisotopes	Also regulate medical x-ray and other radiation-producing equipment, often through state health departments or equivalent agencies
Non-Agreement States[a]	Regulate naturally occurring and accelerator-produced radioisotopes, but regulation of radioactive by-product material is still performed by the NRC itself	Also regulate medical x-ray and other radiation-producing equipment, often through state health departments or equivalent agencies
Food and Drug Administration (FDA)	Regulates radiopharmaceutical development through the following mechanisms: Radioactive Drug Research Committee (RDRC) protocols, Investigational New Drugs (INDs), and New Drug Applications (NDAs)	Regulations are found in Title 21 of the Code of Federal Regulations (21CFR) [1]. Also regulates the performance and radiation safety requirements of medical x-ray and other radiation-producing equipment
Department of Transportation (DOT)	Regulates the transport of radioactive materials	Regulations are found in Title 49 of the Code of Federal Regulations (49 CFR) [3]
Environmental Protection Administration (EPA)	Regulates release of radioactive materials to the environment	Regulations are found in Title 40 of the Code of Federal Regulations (40 CFR) [4]

Adapted from Limacher et al. [6]; with permission from Elsevier
The following national and international *advisory* agencies provide information on radiation risks which are often used by regulatory agencies in formulating radiation-protection regulations: the National Council on Radiation Protection and Measurement (NCRP), the Biological Effects of Ionizing Radiation (BEIR) Committee of the National Research Council/National Academy of Sciences, the International Atomic Energy Agency (IAEA), the International Commission on Radiological Protection (ICRP), and the United National Scientific Committee on Effects of Atomic Radiation (UNCEAR)
[a]Over 40 states are currently Agreement States

Table 3.1 Regulatory oversight of medical uses of isotopes in the United States [6]

P. Zanzonico
Department of Medical Physics, Memorial Sloan Kettering Cancer Center, New York, NY, USA

H. W. Strauss (✉)
Molecular Imaging and Therapy Service, Memorial Sloan Kettering Cancer Center, New York, NY, USA

V. Dilsizian, J. Narula (eds.), *Atlas of Nuclear Cardiology*, https://doi.org/10.1007/978-3-030-49885-6_3

Table 3.2 summarizes the various dosimetric quantities and units relevant to nuclear cardiology [6], and Fig. 3.1 shows the regulatory dose limits for occupationally exposed individuals (such as nuclear cardiology personnel) and non–occupationally exposed individuals (such as members of the general public) [2, 5]. Importantly, as shown in Table 3.3, the average annual doses—*ie*, the total effective dose equivalents (TEDEs)—to nuclear medicine and nuclear cardiology personnel are an order of magnitude higher than the regulatory dose limit for non-occupationally exposed individuals [2, 7, 8]. The annual hand dose to radiopharmacists is a significant fraction of (but still lower than) the corresponding dose limit [2, 7, 8]. Overall, these data suggest that sound radiation safety practice is very effective in minimizing occupational doses in nuclear medicine and nuclear cardiology.

Quantity	Symbol	Definition	Conventional unit (abbreviation)	System International (SI) unit (abbreviation)	Units conversions
Exposure	X	Electric charge produced per unit mass of air by x-rays or gamma rays	roentgen (R)	Coulomb per kilogram (C/kg)	$1\ R = 2.58 \times 10^{-4}$ C/kg $1\ C/kg = 3.94 \times 10^{3}$ R
Absorbed dose	D	Energy deposited per unit mass	rad	Gray (Gy)	$1\ rad = 1 \times 10^{2}$ erg/g 1 Gy = 1 J/kg 1×10^{2} rad = 1 Gy 1 cGy = 1 rad
Kerma	K	Kinetic energy released per unit mass	rad	Gray (Gy)	$1\ rad = 1 \times 10^{2}$ erg/g 1 Gy = 1 J/kg 1×10^{2} rad = 1 Gy 1 cGy = 1 rad
Dose equivalent[a]	H	$w_R \cdot D$	rem	Sievert (Sv)	1×10^{2} rem = 1 Sv 1 cSv = 1 rem
Effective dose[b]/ Effective dose equivalent[c]	H_E	$\sum_{Tissue,T} w_T \cdot H_T$	rem	Sievert (Sv)	1×10^{2} rem = 1 Sv 1 cSv = 1 rem
Activity	A	Amount of radioactivity expressed as the nuclear transformation rate (disintegrations per second, dps)	Curie (Ci)	Becquerel (Bq)	$1\ Ci = 3.7 \times 10^{10}$ dps 1 Bq = 1 dps $1\ Ci = 3.7 \times 10^{10}$ Bq $1\ Bq = 2.7 \times 10^{-11}$ Ci

Adapted from Limacher et al. [6]; with permission from Elsevier

[a]The radiation weighting factor, w_R, reflects differences among radiations (R) in their ionization density and therefore their biological effectiveness, with more densely ionizing radiations such as alpha particles having a greater probability of producing biological damage and/or producing more severe biological damage than less densely ionizing radiations such as x-rays and gamma rays. The currently assigned values of w_R are as follows: 1 for x-rays and gamma rays and for beta particles and other electrons, 2 for protons, ≥5 for neutrons (depending on their energy), and 20 for alpha particles [11]

[b]The tissue weighting factor, w_T, reflects differences among human tissues (T) in their sensitivity to stochastic radiation damage (*ie*, cancer induction and germ cell mutagenesis and resulting heritable genetic damage). The currently assigned values of w_T range from 0.01 for brain and other "radioresistant" tissues to 0.12 for lung and other "radiosensitive" tissues. Note that $\sum_{Tissue,T} w_T = 1$. In principle, the effective dose provides a single-value metric of overall stochastic risk for any given irradiation [11]

[c]The effective dose equivalent is a quantity similar in concept to the effective dose. It is an older quantity than the effective dose but is still found in regulations (*eg*, to express the maximum permissible dose for occupationally exposed individuals) issued by the Nuclear Regulatory Commission (NRC) [2]. In addition to subtle technical differences, the effective dose equivalent differs from the effective dose in that fewer tissues are included in the summation, and the tissue weighting factors have somewhat different values

Table 3.2 Quantities and units in radiation dosimetry

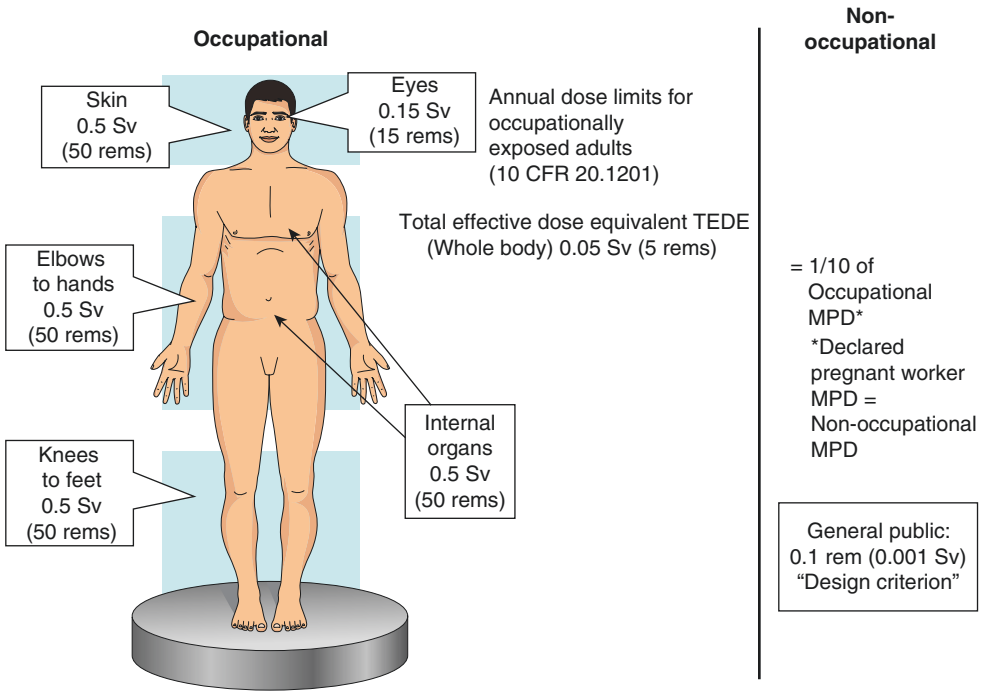

Fig. 3.1 Regulatory maximum permissible doses (MPDs) for individual occupational exposure and nonoccupational exposure, expressed as the annual limit for the effective dose equivalent. Note that the dose limits vary depending on the part of the body exposed, with the annual limit for the total (or whole-body) effective dose equivalent (TEDE) being 5 rem (0.05 Sv). The annual TEDE limit for a non-occupationally exposed individual (such as a clerk in a nuclear cardiology facility) is 0.5 rem (0.005 Sv), one tenth of that for an occupationally exposed individual. For a pregnant occupationally exposed individual who has "declared" her pregnancy (*ie*, disclosed her pregnancy to her employer), the TEDE limit is 0.5 rem (0.005 Sv) for the total duration of the pregnancy. In addition to the personnel dosimeters she would otherwise wear (typically at the collar level and possibly a ring dosimeter), a pregnant occupationally exposed individual should also wear a dosimeter in the abdominal-pelvic area to monitor the fetal radiation dose. Note that the annual TEDE for the general public is 0.1 rem (0.001 Sv); this limit actually serves as a design criterion for designing the shielding and configuration of a radiation facility to maintain the annual TEDE to individuals in adjoining public areas to less than 0.1 rem (0.001 Sv) [2])

References	Personnel	Total Effective Dose Equivalent (TEDE) (whole body),[a] *rem*	Hand dose equivalent,[b] *rem*
Bloe and Williams [7]	Nuclear medicine, General	0.18	0.99
	Nuclear medicine, PET	0.41	1.7
	Radiopharmacy	0.18	14
Owens and Hung [8]	Nuclear cardiology	0.14	0.072
	Nuclear medicine, General	0.072	0.060
	Radiopharmacy	0.29	21
	Injection	0.30	1.0

Adapted from Limacher et al. [6]; with permission from Elsevier
[a]Regulatory annual TEDE limit is 5 rem for occupationally exposed individuals [2]
[b]Regulatory hand dose-equivalent limit is 50 rem for occupationally exposed individuals [2]

Table 3.3 Average annual radiation doses to nuclear medicine and nuclear cardiology personnel

Nuclear cardiology personnel are exposed to radiation emitted by radioactive sources such as radionuclide generators, radiopharmaceutical vials and syringes, and, of course, radioactive patients. Potentially, internal exposure (or contamination) from radioactive materials that are inadvertently ingested, inhaled, or otherwise internalized may contribute to the radiation dose. Because nuclear cardiology does not utilize radioactive gases or aerosols or radiopharmaceuticals that are significantly volatile, routes of internal contamination are limited to ingestion or absorption through skin. Strict adherence to sound radiation safety practice (Table 3.4) should reduce internal exposures of personnel to insignificantly low levels, and bioassay of personnel (*eg*, whole-body surveys, counting of urine samples) is routinely not performed in nuclear cardiology.

Eating, drinking, smoking, and applying cosmetics are prohibited
Disposable waterproof gloves, a laboratory coat, and a personnel dosimeter should be worn at all times. Gloves should be changed regularly to minimize any potential spread of contamination, and a laboratory coat worn when handling radioactive materials should be stored in the area in which such materials are handled (*ie*, should not be worn outside that area)
All working surfaces should be covered with absorbent sheets having a water-impermeable plastic coating facing the benchtop
Radioactive materials should be kept in closed vials in suitably shielded containers. Syringes, vials, etc. containing radioactive materials should likewise be transported in suitably shielded containers
Shielded containers and vials containing radioactive materials should bear a label identifying the material (including the radioisotope), the activity, and the time and date of calibration of the activity
Dispensing and other manual handling of radioactive materials should be performed with suitable shielding between the user and the radioactivity
To the extent possible, dispensing and other manual handling of radioactive materials should be performed using forceps or tongs
Radioactively contaminated solid waste should be discarded in suitably shielded and labeled waste receptacles
To avoid accumulation of excessive volumes of radioactive waste, such waste should be segregated according to physical half-life for decay in storage—for example, waste with physical half-lives longer than 1 day, longer than 1 day but shorter than 1 week, and longer than 1 week but shorter than 1 month
Radioactive waste with a physical half-life longer than 1 month may be too long-lived to hold for decay in storage on-site and may therefore need to be disposed of commercially. (This is rarely, if ever, the case in nuclear cardiology, however.)
Radioactive waste can subsequently be discarded as nonradioactive waste once it is no longer *detectably* radioactive
Radioactively contaminated liquid waste should generally be discarded into the sewer system—that is, down a drain or into a toilet. The drain or toilet should then be rinsed thoroughly by running water into the drain (taking care to avoid splashing) and flushing the toiler twice
Personal items (books, clothing, etc.) should not be placed on laboratory work surfaces
When handling radioactive materials, interruptions and other distractions from the task at hand should be avoided
A suitable electronic (*ie*, real-time) radiation detector should be available and activated in the area where unsealed radioactive materials are handled
Recording of activities and other pertinent data should be performed in real time (not retroactively) and directly into the "official" laboratory record
Once the handling of radioactive materials has been completed, hands should be washed and hands, shoes, and clothing should be monitored for contamination in a low-background area

See Table 3.6 and the figures cited therein for the supplies and equipment required to implement these radiation safety measures

Table 3.4 Basic radiation safety measures for handling unsealed radioactive materials

Sound radiation safety practice is predicated on the common-sense measures of time, distance, and shielding:

- Minimize the time spent in close proximity to radioactive and other radiation sources.
- Maximize the distance from radioactive and other radiation sources. (Distance is a particularly effective way of minimizing one's radiation dose because of the "inverse-square law" [6] (Table 3.5).)
- Maximize shielding of radioactive and other radiation sources.

Distance from patient, *cm*	Imaging duration, *min*	Exposure (mR)	
		Thallium-201 3.5 mCi	Technetium-99m 30 mCi
1	40	1600	14,000
5	40	65	560
15	40	7.0	60
30	40	1.8	16
100	40	0.20	1.4

Adapted from Limacher et al. [6]; with permission from Elsevier

Table 3.5 Effect of distance from patient on exposure from radioisotopes commonly used in nuclear cardiology

Consistent with the "As-Low-as-Reasonably-Achievable (ALARA)" concept, these measures should be implemented to the extent that is practical and in a manner that does not compromise patient care. (For example, avoid rushing through the preparation and assay of a radiopharmaceutical, which potentially might result in a misadministration.) Radiopharmacies and other work areas where unsealed radioactive materials are handled should be provided with appropriate radiation safety supplies and equipment (Table 3.6 and Figs. 3.2, 3.3, 3.4, 3.5, and 3.6).

"Radiation" signage (Fig. 3.2)
Lead shields (fixed or mobile) with lead glass windows—For x-ray and gamma-ray emitters (Fig. 3.3)
Plastic shields—For beta emitters[a] (*see* Fig. 3.3)
Plastic-backed absorbent pads and/or drip trays, to contain any spills (*see* Fig. 3.3)
Syringe shields with see-through windows (*see* Fig. 3.3)
Shielded carriers—For transporting activity-containing syringes or other small sources (*see* Fig. 3.3)
Dose calibrators—To assay patient radiopharmaceutical activities and other radioactive sources (Fig. 3.4)
Personnel dosimeters (Fig. 3.5)
Tongs or forceps, to maximize the distance of the worker and the worker's hands from manually handled radioactive sources
Waste receptacles
A shielded receptacle with removable plastic lining (plastic bag) for dry waste
A shielded puncture-proof receptacle for needles and other "sharps" waste
Radiation and radioactive contamination monitoring equipment: Geiger counter for exposure-rate measurements, solid-state survey meter for assay of radioactive waste, and scintillation well counter for assay of wipes used to check for removable contamination (Fig. 3.6)
Fume hood, for working with volatile or other potentially airborne radioactive materials[a]
Personnel protective equipment (PPE)
Laboratory coat or disposable gown
Disposable waterproof gloves
Face shield—Where a risk of splatter of radioactive liquid or droplets exists[a]
Face mask—Where a risk of airborne droplets exists[a]
Shoe covers (booties)—Where radioactive contamination of the floor exists or realistically may occur[a]
Radioactive materials log/inventory (hardcopy or computerized)—To record receipt, distribution, and disposal of each radioactive material

[a]Generally not required in nuclear cardiology

Table 3.6 Basic radiation safety supplies and equipment

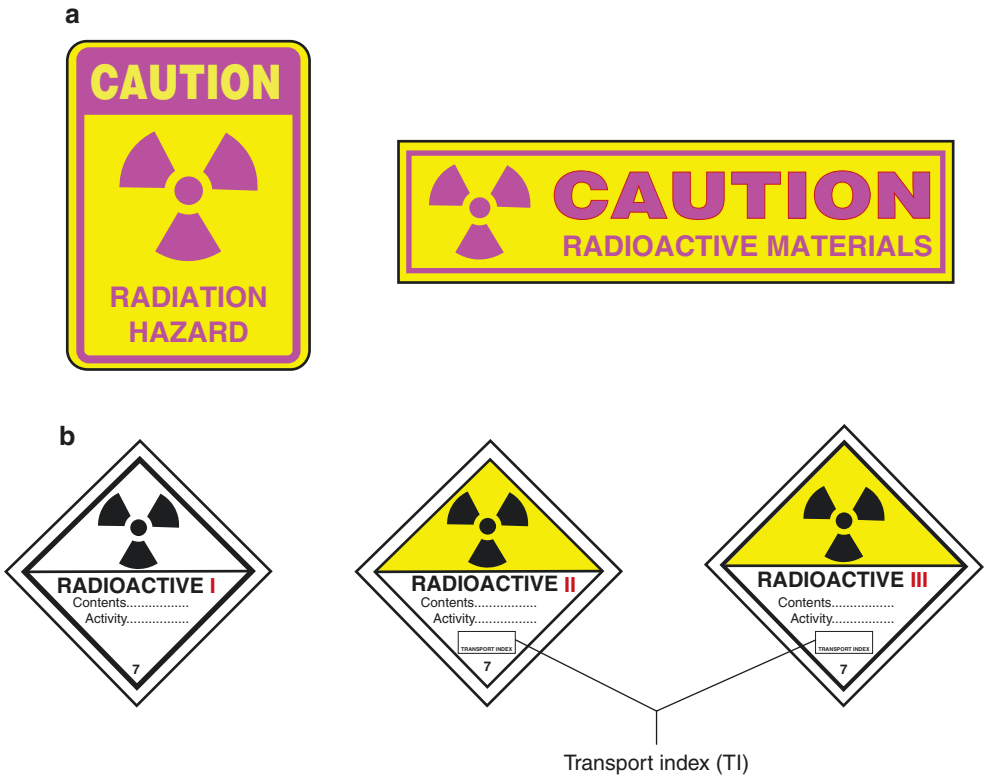

Fig. 3.2 (**a**) Radiation protection signage, including the familiar purple trefoil on yellow background. For purposes of radiation protection, nuclear cardiology and other nuclear facilities designate certain sites within the facility as "restricted" areas. A restricted area is any area to which access is controlled to protect individuals from exposure to radiation and radioactive materials. The regulatory dose limits for occupationally exposed individuals apply in a restricted area, so entry of non-occupationally exposed individuals into such an area should be controlled by a physical barrier (such as a locked door) and appropriate signage, as shown in this figure. Restricted areas include any areas where radioactive materials are used and stored; these areas require the "Caution – Radioactive Materials" signage in addition to or in place of the "Caution – Radiation Hazard" signage. In addition to restricted areas, a nuclear facility may designate sites within the facility as "controlled" areas, defined as an area outside a restricted area but within the facility boundary to which the facility can limit access for any reason. A controlled area (such an office in which sensitive information is filed) requires a physical barrier but not radiation-precaution signage. (**b**) Department of Transportation (DOT)–required signage for shipment of packages containing radioactive materials [3]. The transport index (TI) is the exposure rate (in milliroentgens per hour, mR/h) measured at a distance of 1 m from the surface of the package. Low-activity (*ie* "White 1") packages have an immeasurably low exposure rate at 1 and thus do not require a TI entry on the label

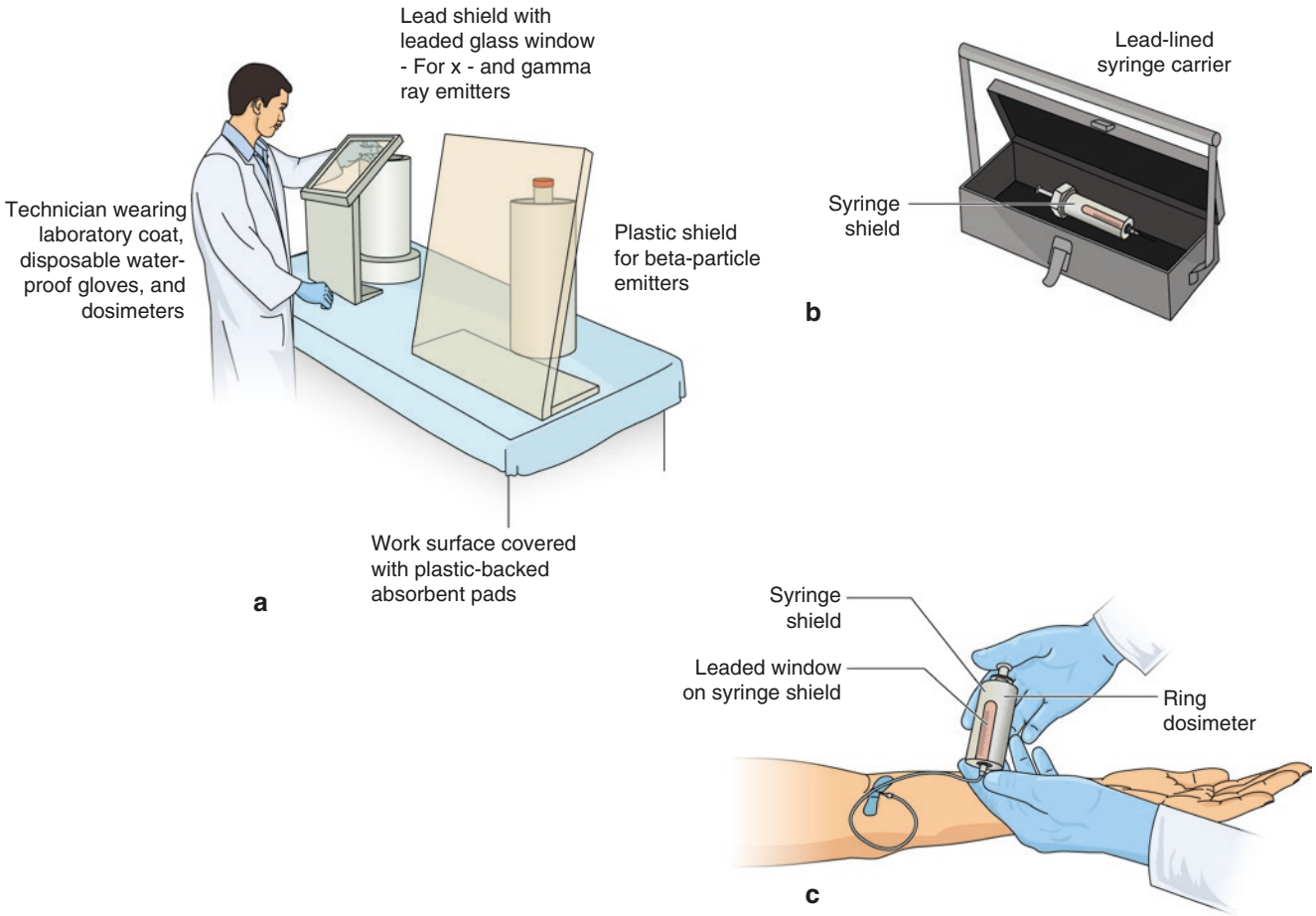

Fig. 3.3 (**a**) Set-up for working with unsealed sources of radioactivity, as detailed in Tables 3.3 and 3.4. A lead shield with a leaded glass window (sometimes called an "L shield") is required to adequately attenuate x-rays and gamma rays, as the attenuation of such highly penetrating photons increases with increasing atomic number and mass density of the stopping medium. Beta particles, on the other hand, are nonpenetrating radiations that are adequately attenuated by a thickness of plastic. The use of plastic as shielding for beta particles, rather than lead or other materials with a high atomic number, minimizes the possible production of *bremsstrahlung* ("brake radiation") x-rays, as *bremsstrahlung* production increases sharply with the increasing atomic number of the stopping medium. (**b**) Radiopharmaceutical syringe in a syringe shield in place in an opened lead-lined carrier used for transport. (**c**) Intravenous injection of a radiopharmaceutical with the syringe in place in a syringe shield. Note that a ring dosimeter is required on a finger of the individual performing the injection

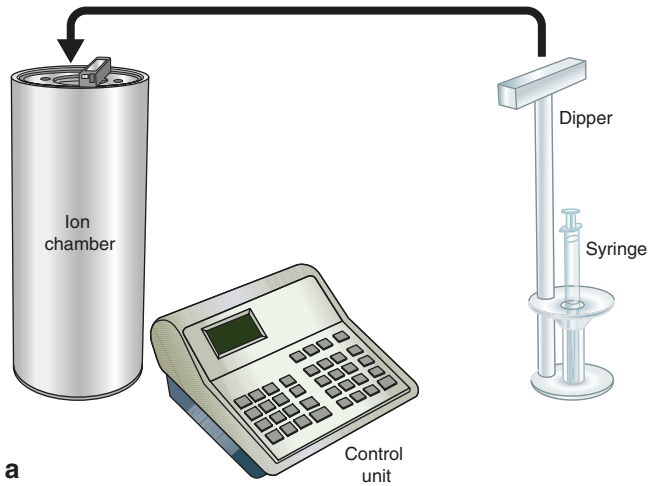

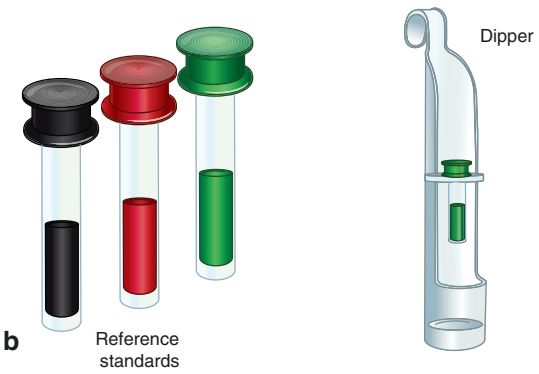

Radioisotope	Half-life	Energy of principal X- or gamma ray
Cobalt-60	272 d	122 kev
Barium-133	10.7 y	356 kev
Germanium-68	287 d	511 kev

Cobalt-57, barium-133, and germanium-68 are sometimes known as "mock" technetium-99m (gamma-ray energy: 140 keV), iodine-131 (364 keV), and fluorine-18 (511 keV), respectively.

Fig. 3.4 (**a**) The dose calibrator, an ionization chamber with a sealed-gas detector and a well-type geometry, is used to assay the activity (in units such as mCi or MBq) in a radiopharmaceutical syringe or other small radioactive source. The syringe is placed in a plastic dipper and the dipper is then used to lower the syringe into position for assay. The radioisotope is selected by pressing the corresponding button on the control panel. For some older models, the user selects "Other" and adjusts the setting of a potentiometer dial to a manufacturer-specified value for the specific radioisotope for those isotopes for which a button is not provided. For newer models, a computerized control unit with a computer screen and soft keys is provided. (**b**) Routine (daily) quality control of dose calibrators is essential to ensure that patients receive the correct activity of the prescribed radiopharmaceutical. This is generally performed using commercially available, long-lived National Institute of Standards and Technology (NIST)–traceable reference standards, that is, radioisotopes whose gamma-ray and/or x-ray energies approximate those of radioisotopes commonly used in clinical studies. Among quality control tests, constancy must be checked daily, and accuracy and linearity at least quarterly, but daily checks of accuracy are recommended. For the constancy test, an NIST-traceable reference standard, such as cobalt-57, barium-133, and/or germanium-68 is placed in the dose calibrator and the activity reading on each scale is recorded; day-to-day readings should agree within 10%. For the accuracy test (also sometimes known as the "energy linearity" test), at least two of the foregoing NIST-traceable reference sources are separately placed in the dose calibrator and the activity reading on each activity scale is recorded. For each source, the measured activity on each scale and its current actual activity should agree within 10%. Like all sealed sources, reference standards should be wipe-tested for removable contamination (*ie*, leak-tested) quarterly. The linearity test is described in Zanzonico [12]

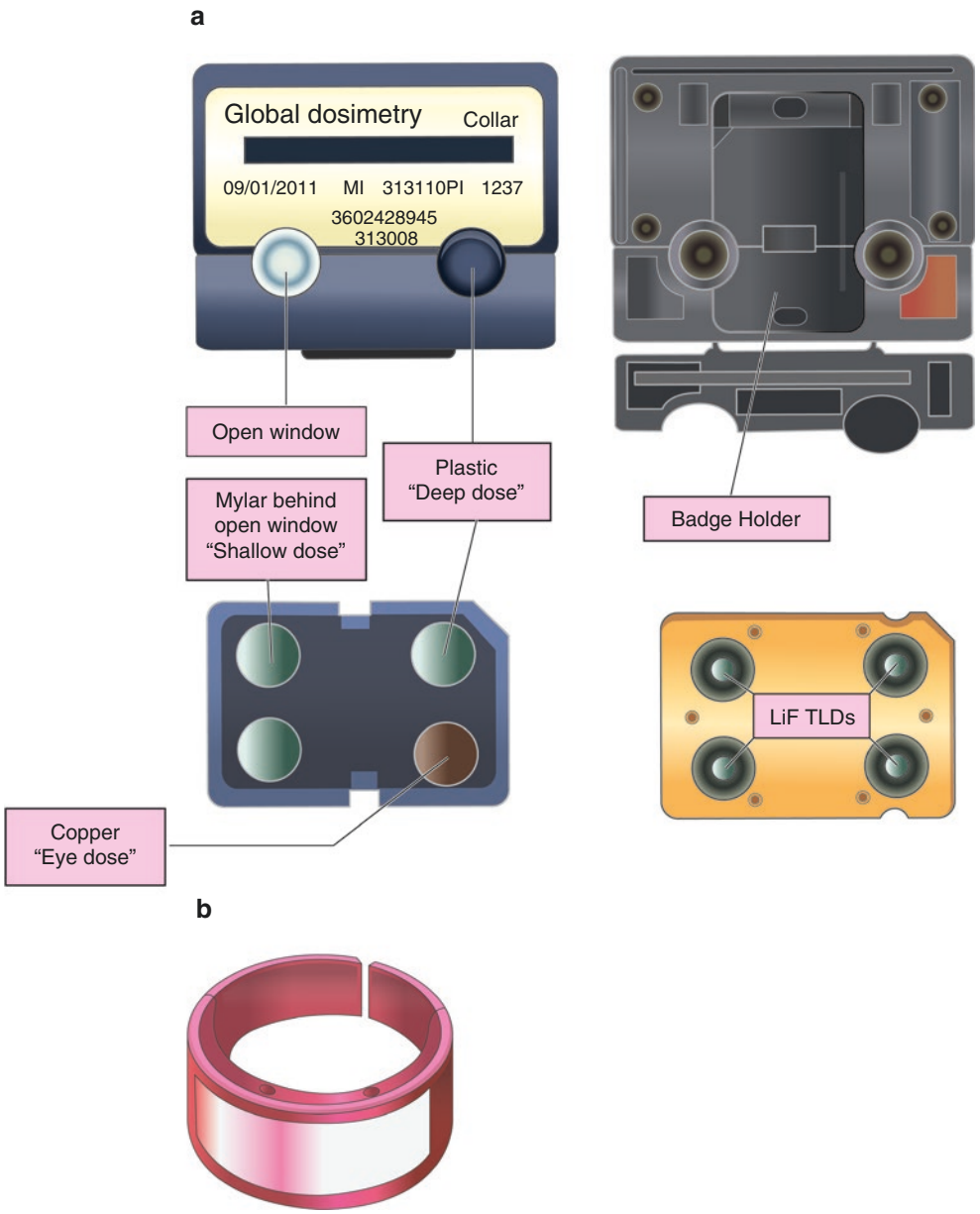

Fig. 3.5 Personnel radiation dosimeters. (**a**) The dosimeter pictured includes up to four individual lithium fluoride (LiF) thermoluminescent dosimeters (TLDs). The TLDs are each covered by a specific filter to simulate the attenuation of incident radiation by different thicknesses of tissue and thereby yield estimates of the radiation dose at specific depths: Mylar (area density: 7 mg/cm^2) to yield the skin ("shallow") dose at a depth of 0.007 cm; copper (300 mg/cm^2) to yield the lens-of-eye dose at a depth of 0.3 cm; and polypropylene plastic (1000 mg/cm^2) to yield deep ("organ") doses at a depth of 1.0 cm. TLDs are essentially storage phosphors in which electrons are raised to excited energy states by the incident radiation, a fraction of which remains trapped in these excited states. When the dosimeters are subsequently heated, these trapped electrons are released and return to their ground state, with the emission of light. The amount of light emitted is related to the number of trapped electrons and, in turn, to the radiation doses delivered to the TLD. Optically stimulated luminance (OSL) dosimeters, composed of crystalline aluminum oxide activated with carbon (AL_2O_3:C), are now used as an alternative to TLDs. OSL dosimeters work in a similar manner to TLDs except that laser light rather than heat frees the trapped electrons. In the past, personnel dosimeters used photographic film; the radiation-induced blackening (*ie*, optical density) of the film was directly related to the radiation dose. Personnel dosimeters can record doses from as low as about 10 mrem (0.1 mSv) to about 1000 rem (10 Sv). Though film-based dosimeters provide a permanent dose record, the fact that TLDs and OSL dosimeters are reusable offers significant cost savings, so most personnel dosimeters are now TLDs or OSL dosimeters. A dosimeter such as the one pictured (sometimes referred to as a "body badge" dosimeter) is typically worn at the level of the collar. (**b**) A ring dosimeter. Such a dosimeter is especially important for radiopharmacists and for personnel who inject or otherwise manually handle radiopharmaceutical syringes and other radioactive sources. As shown in Table 3.2, the hand doses to such personnel can be significant [13]

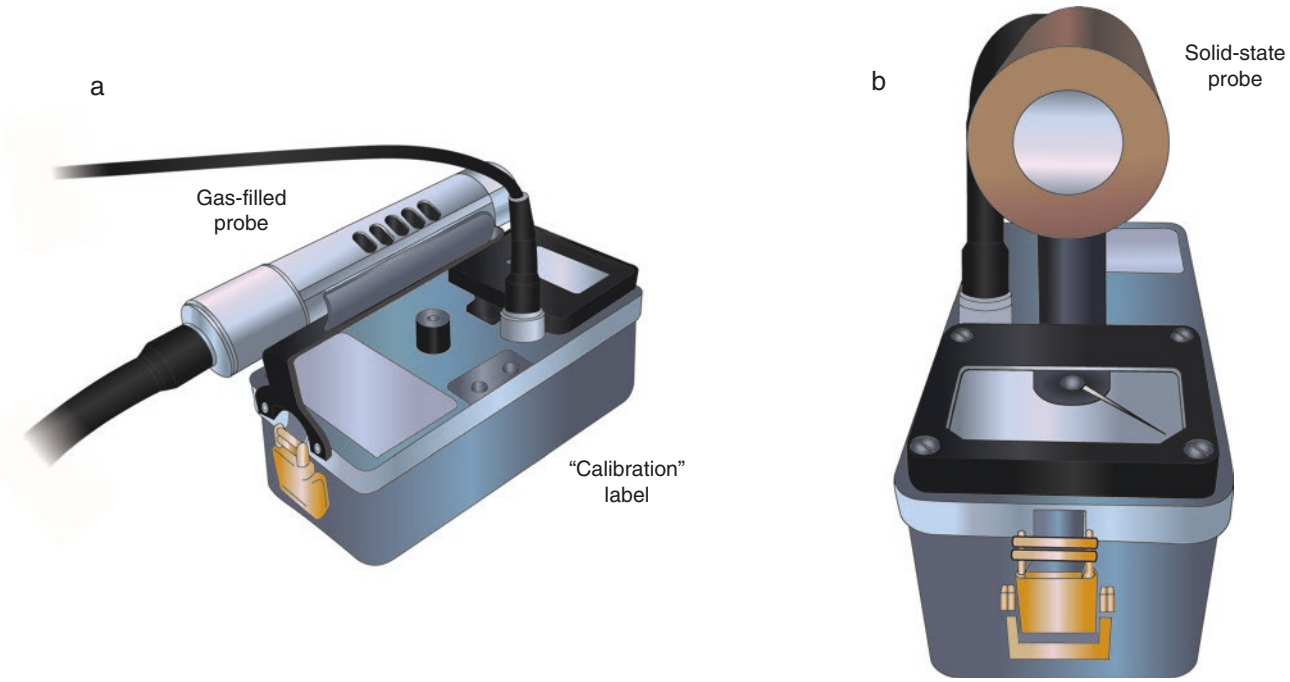

Fig. 3.6 Survey meters. (**a**) The Geiger counter (also known as a Geiger-Muller, or GM, counter) is a gas-filled ionization detector widely used to measure ambient exposure rates. It should provide a readout in terms of absolute exposure-rate units (such as mR/h) and not simply in terms of count rate (such as counts per minute, cpm). Exposure-rate measurements should be performed daily in all areas where radiopharmaceuticals are prepared, assayed, or administered; weekly in all areas where radioactive materials are otherwise used or are stored, including radioactive-waste storage areas; and quarterly in all areas where sealed radioactive sources are stored [2, 5]. Ambient exposure rates should not exceed 0.1 mR/h in unrestricted areas and 5 mR/h in restricted areas [2, 5]. If these exposure rates are exceeded, corrective action (such as the use of additional shielding) should be taken. Survey meters should be calibrated annually and a dated calibration label affixed to the meter. Surface contamination levels, checked by assaying dry wipes of potentially contaminated surfaces in a scintillation well counter, should be less than 200 disintegrations per minute (dpm)/100 cm^2 in unrestricted areas and less than 2000 to 20,000 dpm/100 cm^2 (depending on the radioisotopes in use) in restricted areas [2, 5]. If these contamination levels are exceeded, corrective action (*ie*, decontamination) should be taken. (**b**) Although grossly similar in appearance to the Geiger counter, a solid-state survey meter uses a solid detection medium and therefore provides far greater sensitivity than the gas detector–based Geiger counter. The solid-state survey meter is better suited, therefore, for assay of radioactive waste, because its higher sensitivity makes it less likely that such waste will be inadvertently routed to the general waste stream before it has decayed "completely" (*ie*, to undetectable low activities). In practice, radioactive waste being held for decay in storage should *not* be routed to the general waste stream until the count rate measured at the surface of the waste container is no greater than the background count rate. However, solid-state survey meters are not calibrated to provide readouts in terms of absolute exposure rates (*eg*, in units of mR/h) and therefore cannot be used for exposure-rate measurements

Standard lead aprons, 0.25 or 0.5 mm in thickness, are designed to provide shielding for diagnostic x-rays in general and for scattered x-rays in particular (with average energies typically well under 100 keV); they are of course required for fluoroscopy personnel. A 0.5 mm-thick lead apron is approximately equivalent to two half-value layers for the scattered radiation associated with a 100-kV x-ray beam, for example, and thereby reduces the dose by about 75% [9, 10]. Lead aprons 0.5 mm in thickness can also attenuate over 60% of thallium-201 and technetium-99m photon radiations (68–83 and 140 keV in energy, respectively) and hypothetically may reduce thallium-201 and technetium-99m personnel exposures by over 60% if worn for all such procedures [9, 10]. However, lead aprons provide no significant attenuation or dose reduction (less than 10%) for the 511-keV gamma rays encountered in positron emission tomorgraphy (PET) [9, 10]. Although the use of lead aprons in nuclear cardiology and nuclear medicine is not a widespread practice and is generally not recommended, a pregnant individual who works exclusively with thallium-201 and technetium-99m may consider wearing a lead apron during her pregnancy.

When working with radiopharmaceuticals and other unsealed sources of radioactivity, the possibility of spills exists. The emergency procedures for dealing with spills of radioactive materials differ depending upon whether the spill is a minor or a major spill [5]; the procedures are detailed in Table 3.7.

Notify all personnel in room that a spill has occurred and instruct all uninvolved individuals to exit the area
Restrict entry to room
Don two pairs of disposable waterproof gloves (so that the outer, contaminated gloves can be removed and replaced while avoiding hand contamination)
Upright the container from which the spill occurred
Cover the spill with absorbent sheets having a water-impermeable plastic coating with the absorbent side facing the spill
For a minor spill, proceed to the next steps
For a major spill or if in doubt as to the severity of a spill or how to proceed, contact the institutional Radiation Safety Office for further remediation
Spills of technetium-99m >100 mCi, indium-111 >10 mCi, and thallium-201 >100 mCi are considered major; spills of lesser activities of these radioisotopes are considered minor [2]
Decontaminate the area, discarding clean-up materials in a plastic bag for disposal as radioactive waste
Wipe the spilled liquid towards the center of the spill area with dry paper toweling, then with moist paper toweling, and then with dry paper toweling, taking care not to flood the area and spread the spill
Survey the spill area, clothes, and hands and feet
Use a survey meter for radioisotopes emitting gamma rays or x-rays
Use wipe testing for a pure beta particle–emitting radioisotope
Contaminated shoes and clothing should be removed, placed in plastic bags, appropriately labeled, and held for decay in storage
As a rule of thumb, continue decontamination until the results of the post-contamination surveys are no greater than twice the background count rate. If this level of decontamination cannot be achieved, the contaminated area may need to be shielded with lead and labeled as "contaminated" until the remaining radioactivity is eliminated by physical decay
Report the spill and remedial actions taken to the institutional Radiation Safety Office

Table 3.7 Emergency procedure for radioactive spills

In summary, the use of unsealed sources of radioactivity in nuclear cardiology results in finite radiation doses to personnel. However, with careful implementation of basic radiation safety measures, the doses to nuclear cardiology personnel are generally very low—an order of magnitude lower than the regulatory dose limit for occupationally exposed individuals and even lower than the dose limit for non–occupationally exposed individuals [2, 7, 8].

References

1. United States Code, 2012 Edition, Supplement 4, Title 21 - FOOD AND DRUGS. Office of the Federal Register, National Archives and Records Administration, Washington, DC. https://www.govinfo.gov/app/collection/uscode/2016/.
2. Title 10 - Energy, Code of Federal Regulations (10CFR), in 10. 2013, Office of the Federal Register, National Archives and Records Administration: Washington, DC. https://www.nrc.gov/materials/miau/med-use.html.
3. Title 49 - Transportation (49CFR), in 21. 2018, Office of the Federal Register, National Archives and Records Administration: Washington, DC.
4. Title 40 - Protection of Environment (40CFR), in 21. 2018, Office of the Federal Register, National Archives and Records Administration: Washington, DC.
5. NRC, Consolidated Guidance About Materials Licenses Program-Specific Guidance About Medical Use Licenses, Draft Report for Comment, NUREG-1556, Volume 9, Rev. 3, N.R. Commission, Editor. 2016: Rockville, MD. https://www.nrc.gov/reading-rm/doc-collections/nuregs/staff/sr1556/v9/r3/
6. Limacher MC, Douglas PS, Germano G, Laskey WK, Lindsay BD, McKetty MH, et al. ACC expert consensus document. Radiation safety in the practice of cardiology. American College of Cardiology. J Am Coll Cardiol. 1998;31:892–913.
7. Bloe F, Williams A. Personnel monitoring observations. J Nucl Med Technol. 1995;23:82–6.
8. Owens TP, Hung JC. The effect of job duties in contributing to radiation exposure of the nuclear medicine technologist. J Nucl Med Technol. 1995;23:87–90.
9. Huda W, Boutcher S. Should nuclear medicine technologists wear lead aprons? J Nucl Med Technol. 1989;17:6–11.
10. Murphy PH, Wu Y, Glaze SA. Attenuation properties of lead composite aprons. Radiology. 1993;186:269–72.
11. The 2007 Recommendations of the International Commission on Radiological Protection. ICRP publication 103. Ann ICRP. 2007;37:1–332.
12. Zanzonico P. Routine quality control of clinical nuclear medicine instrumentation: a brief review. J Nucl Med. 2008;49:1114–31.
13. Bushberg JT, Seibert JA, Leidholdt EM Jr, Boone JM. The essential physics of medical imaging. 3rd ed. Philadelphia: Lippincott Williams & Wilkins; 2012.

SPECT and PET Myocardial Perfusion Imaging: Tracers and Techniques

4

Vasken Dilsizian

The application of a radiotracer technique to measure physiologic parameters, such as pulmonary circulation, dates back to 1927. Despite considerable advances in the application of radiotracer technique for interrogating physiologic and pathophysiologic cardiopulmonary conditions in the early twentieth century, the spatial resolution of the scintigraphic instruments used to measure tracer concentration in the heart, lungs, and blood was limited. The advent of single-photon emission CT (SPECT) in the late 1970s and positron emission tomography (PET) in the 1980s dramatically changed the clinical utility of radiotracer technique for the assessment of myocardial perfusion, viability, and function.

Both SPECT and PET technologies use similar reconstruction processes to obtain tomographic images of the heart. However, they differ in the type of radiopharmaceuticals and kind of instrumentation used to acquire cardiac images. SPECT allows a noninvasive evaluation of myocardial blood flow by extractable tracers such as ^{201}Tl- and ^{99m}Tc-labeled perfusion tracers. PET, on the other hand, allows a noninvasive assessment of regional blood flow, function, and metabolism using physiologic substrates prepared with positron-emitting isotopes such as carbon, oxygen, nitrogen, and fluorine (Fig. 4.1, Table 4.1). Radioisotopes commonly used with SPECT emit γ-rays of varying energies and have relatively long physical half-lives. The localization of γ-rays emitted by single-photon–emitting radiotracers in the heart is conventionally accomplished by an Anger scintillation camera (gamma camera), which converts the γ-rays to light photons via sodium iodide scintillation detectors. The gamma camera limits the direction of photons entering the detector by a collimator and then positions each event electronically. More recently, new designs of high-speed SPECT cameras have been introduced, which utilize a series of small, pixilated solid-state detector columns with cadmium zinc telluride or CSI (Tl) crystals, which provide considerably more information for each detected γ-ray. In addition, the design of the solid-state detector design with wide-angle tungsten collimators combined with a novel image reconstruction algorithm provide true three-dimensional, patient-specific images localized to the heart. Compared with the conventional SPECT cameras, the high-speed SPECT systems can provide up to an eightfold increase in count rates, thereby reducing imaging times significantly from 14–15 minutes with a conventional Anger camera to 5–6 minutes with the newer solid-state cameras, while achieving a twofold increase in spatial resolution, from 9 to 12 mm for Anger cameras to 4.3–4.9 mm for cadmium zinc telluride cameras. The radioisotopes used for optimal scintigraphic registration with SPECT cameras are limited to those that emit γ-rays with an energy range that is suitable for the gamma camera and related single-photon devices, such as ^{201}Tl, ^{99m}Tc, and ^{123}I. Although clinically useful, estimates of relative myocardial blood flow by SPECT are significantly affected by attenuation artifacts that are not reliably corrected for when compared with PET attenuation-correction algorithms.

V. Dilsizian (✉)
University of Maryland School of Medicine, Baltimore, MD, USA
e-mail: vdilsizian@umm.edu

V. Dilsizian, J. Narula (eds.), *Atlas of Nuclear Cardiology*, https://doi.org/10.1007/978-3-030-49885-6_4

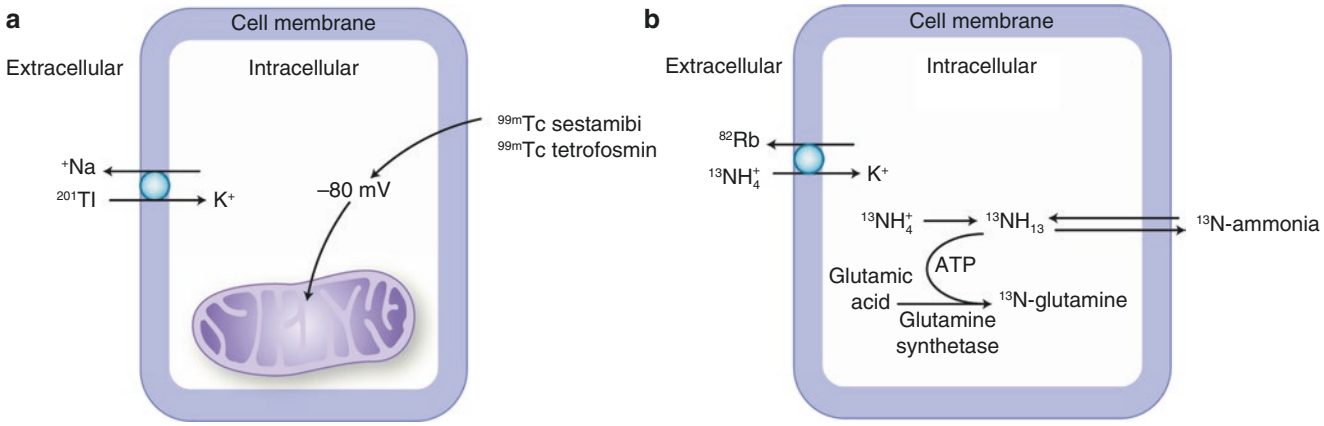

Fig. 4.1 Properties of flow tracers used for single-photon emission computed tomography (SPECT) (**a**) and positron emission tomography (PET) (**b**). To reflect regional myocardial perfusion, radiotracers commonly used with SPECT and PET must have high extraction by the heart and rapid clearance from the blood. Clinically available radiopharmaceuticals that meet these criteria for SPECT are ^{201}Tl, ^{99m}Tc-labeled sestamibi, and tetrofosmin; for PET, ^{82}Rb and ^{13}N-ammonia. If radiotracers are not highly extracted (<50%) or if the residence time in the blood is prolonged (clearance half-time of >5 minutes), they cannot be used to assess regional perfusion

Tracer	Mechanism of myocyte uptake	Usual dose, *mCi*
Properties of SPECT flow tracers		
^{201}Tl	Na–K ATPase—sarcolemma	2–3
^{99m}Tc-sestamibi	Negative transmembrane potential—mitochondria	8–40
^{99m}Tc-tetrofosmin	Negative transmembrane potential—mitochondria	8–40
Properties of PET flow tracers		
^{82}Rb	Na–K ATPase—sarcolemma	30–60
^{13}N ammonia	Trapped as ^{13}N-glutamine (mediated by ATP)—cytoplasm	10–20

Table 4.1 Properties of SPECT and PET flow tracers

Positron-emitting radioisotopes commonly used with PET emit two γ-rays, 511 keV each, and have relatively short physical half-lives. When the high-energy positron is emitted from a nucleus, it travels a short distance and collides with an electron. The result is complete annihilation of both the positron and the electron, and the conversion of the combined mass to energy in the form of electromagnetic radiation (two γ-rays, 511 keV energy each). Because the γ-rays are perfectly collinear (discharged at 180° to each other) and travel in opposite directions, the PET detectors can be programmed to register only events with a temporal coincidence of photons that strike directly at opposing detectors. This results in improved spatial (4–6 mm) and temporal resolution. Moreover, the PET system is more sensitive than a SPECT system (higher count rate) and provides a more robust soft tissue attenuation correction. The consequence of these advantages with PET is the possibility for quantitation of the tracer concentration in absolute units.

Myocardial Perfusion, Uptake, and Clearance

Regional myocardial blood flow is critically dependent on the driving pressure gradient and the resistance of the vascular bed. As illustrated in Fig. 4.2, advanced degrees of coronary artery disease may exist at rest without myocardial ischemia, owing to compensatory dilatation of the resistance vessels, and regional myocardial blood flow is preserved in both patent and stenosed coronary artery branches. Such disparity between myocardial blood flow and coronary anatomy attests to the complementary information that a physiologic study such as myocardial perfusion SPECT or PET provides, in addition to information from coronary angiography with CT or diagnostic catheterization. In a canine model, over 80% occlusion of the coronary artery was necessary before ischemia was observed under the basal state. Because the pressure drop across a stenosis varies directly with the length of the stenosis and inversely with the fourth power of the radius (Bernoulli's theorem), resistance almost triples as the severity of coronary artery stenosis increases from 80% to 90%. Consequently, during exercise or pharmacologic stress testing, when the resistance to the distal bed and the pressure distending the stenotic coronary artery declines, myocardial ischemia ensues.

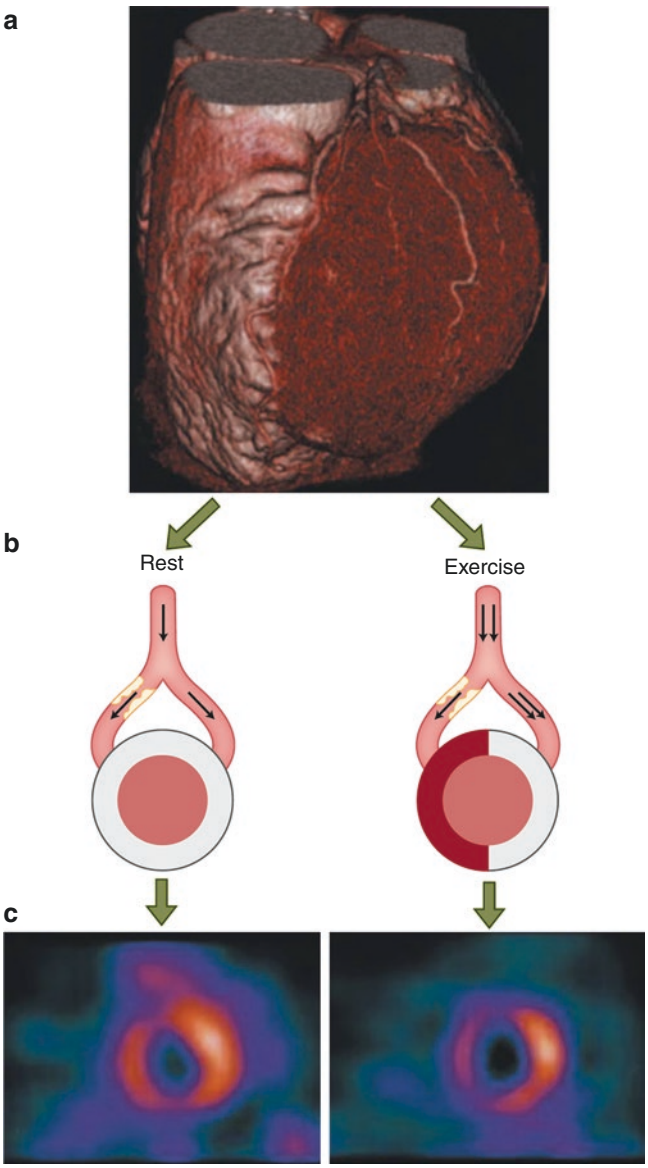

Fig. 4.2 Myocardial blood flow and coronary anatomy: disparate yet complementary information. Advanced degrees of coronary artery disease may exist at rest (**a**) without myocardial ischemia, owing to compensatory dilatation of the resistance vessels. At rest, regional myocardial blood flow is preserved in both patent and stenosed coronary artery branches (**b** and **c**), but during exercise or pharmacologic stress testing, when the resistance to the distal bed and the pressure distending the stenotic coronary artery declines, myocardial ischemia ensues

Coronary blood flow in myocardial regions without coronary artery stenosis may increase about twofold to threefold during vigorous aerobic exercise, but in the setting of moderate-to-severe coronary artery stenosis, the degree of coronary flow increase may be attenuated when compared with myocardial regions without coronary artery stenosis. The insufficient coronary blood flow increase during stress results in impaired perfusion and myocardial ischemia. In patients with coronary artery disease, an inverse relationship has been shown between the increase in myocardial blood flow and the percentage of coronary artery stenosis once the lumen is narrowed by approximately 40–50%. Thus, when a radiotracer such as thallium is injected at peak exercise, the relative differences in regional myocardial blood flow will be reflected in disproportionate concentrations of regional thallium activity on the stress images. Therefore, myocardial perfusion imaging identifies subcritical coronary artery stenosis when it is performed in conjunction with exercise or pharmacologic stress, but not at rest.

The radiotracer that most closely parallels myocardial blood flow would be expected to most accurately identify coronary artery narrowing. There are several classes of radiopharmaceuticals that meet these criteria, such as microspheres, ^{201}Tl, ^{99m}Tc-labeled perfusion tracers, ^{15}O-water, ^{13}N-ammonia, and ^{82}Rb. Differences in the first-pass extraction of these tracers ultimately determine the regional myocardial tracer uptake relative to regional blood flow (Fig. 4.3). The extraction fraction is determined experimentally in a Langendorff preparation and represents first- or single-pass extraction of the radiotracer from the blood into the myocardium. An ideal myocardial perfusion tracer would be expected to exhibit a linear relationship to myocardial blood flow over a wide range of flow rates in mL/g/minute. ^{15}O-water, a PET myocardial flow tracer, exhibits such a relationship. A linear relationship between the tracer uptake and myocardial blood flow would, therefore, differentiate between regions with normal or high blood flow (supplied by normal coronary arteries) and abnormal or low blood flow (supplied by narrowed coronary arteries). However, this is not the case for all other radiotracers commonly used in clinical practice. In an open-chest canine model of regional myocardial ischemia with dipyridamole-induced hyperemia, thallium showed a more ideal linear relationship between the tracer uptake and myocardial blood flow assessed by microspheres when compared with ^{99m}Tc-labeled myocardial perfusion agents. The extraction fraction of ^{201}Tl is high at 85%, whereas the extraction fraction of ^{99m}Tc-sestamibi is only 60% and that of ^{99m}Tc-tetrofosmin is approximately 54%. Beyond the first-pass extraction, recirculation of the radiotracer in patients allows further extraction of the radiotracers from the blood into the myocardium during that particular physiologic state (rest, exercise, pharmacologic, or mental stress).

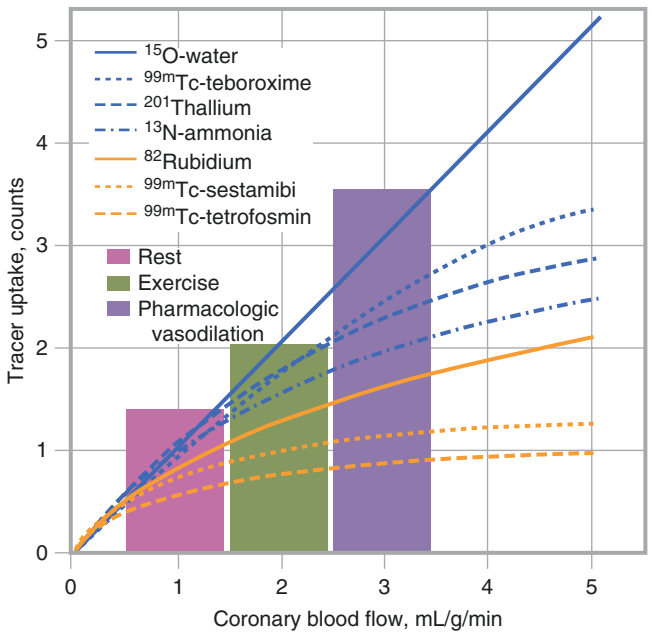

Fig. 4.3 Schematic illustration of radiotracer uptake in relation to regional myocardial blood flow

At rest, myocardial blood flow is approximately 1 mL/g/minute. During physical exercise, myocardial blood flow usually increases two- to threefold, whereas with pharmacologic vasodilation (adenosine, regadenoson, or dipyridamole), myocardial blood flow exceeds 3 mL/g/minute. All clinically available perfusion tracers for SPECT and PET demonstrate "roll-off" at high coronary blood flow levels (a deviation from the line of identity). For SPECT tracers, this "roll-off" phenomenon is particularly marked for ^{99m}Tc-sestamibi and ^{99m}Tc-tetrofosmin, and less so for ^{201}Tl. This implies that at higher flow levels, relative myocardial tracer uptake may underestimate regional myocardial blood flow and thereby also the underlying coronary artery disease. Clinical studies have shown that this underestimation of regional blood flow deficits does not affect the detection of significant (>70%) coronary artery stenosis, but it is important to point out that coronary artery stenosis between 50% and 70% may go undetected, especially with radiotracers with low extraction fraction and marked roll-off phenomenon.

Once a radiotracer is injected intravenously at peak stress, it is extracted rapidly from the blood and accumulated in the myocardium in proportion to regional blood flow. All clinically useful radiotracers have extraction fractions above 50% and are cleared rapidly from the blood in 5–7 minutes after injection (Fig. 4.4). Because ^{201}Tl has a higher first-pass extraction fraction and is cleared more rapidly from the blood than ^{99m}Tc-sestamibi and ^{99m}Tc-tetrofosmin, patients are encouraged to exercise for an additional 1 minute after an injection of ^{201}Tl at peak exercise and for 2 minutes after an injection of ^{99m}Tc-sestamibi or ^{99m}Tc-tetrofosmin at peak exercise. If exercise is stopped too early with the ^{99m}Tc perfusion tracers (that is, 1 minute rather than 2 minutes after an injection), residual radiotracer activity in the blood may be taken up at a different physiologic state (under resting condition), thereby underestimating the presence and extent of myocardial ischemia.

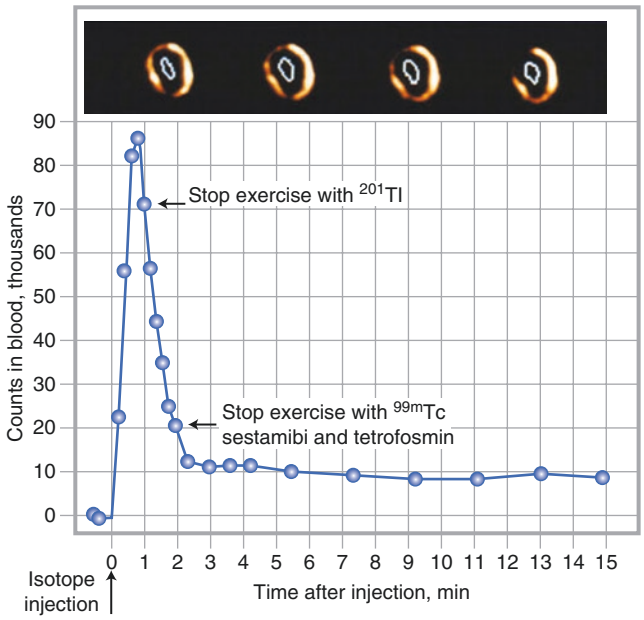

Fig. 4.4 Blood clearance of radiotracers

Image Interpretation and Quantitation

SPECT myocardial perfusion images are interpreted on the basis of the presence, location, extent, and severity of perfusion defects using a standard 17-segment model [1] and visual scoring (Fig. 4.5).

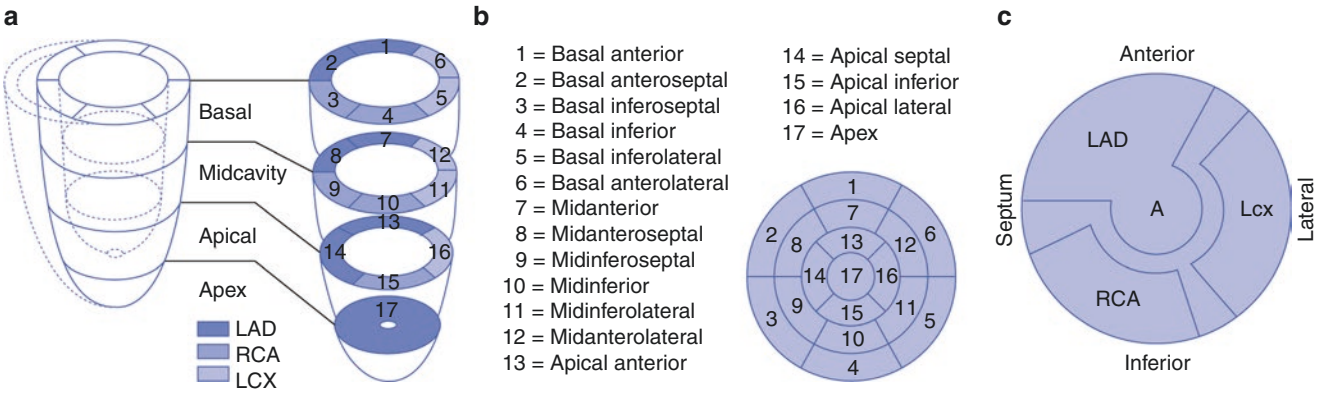

Fig. 4.5 Myocardial segmentation, standard nomenclature, and vascular territories. (**a**) A standard segmentation model divides the left ventricle into three major short-axis slices: apical, midcavity, and basal. The apical short-axis slice is divided into four segments, whereas the midcavity and basal slices are divided into six segments. The apex is analyzed separately, usually from a vertical long-axis slice. Although the anatomy of coronary arteries may vary in individual patients, the anterior, septal, and apical segments are usually ascribed to the left anterior descending (LAD) coronary artery, the inferior and basal septal segments to the right coronary artery (RCA), and the lateral segments to the left circumflex (LCX) coronary artery. The apex can also be supplied by the RCA and LCX arteries. (**b**) Data from the individual short-axis tomograms can be combined to create a bull's-eye polar plot representing a two-dimensional compilation of all the three-dimensional short-axis perfusion data. Standard nomenclature for the 17 segments is outlined. (**c**) The two-dimensional compilation of perfusion data can then easily be assigned to specific vascular territories

Because radionuclide images are intrinsically digital images, the true quantification of tracer uptake in myocardial regions is feasible [2] (Fig. 4.6).

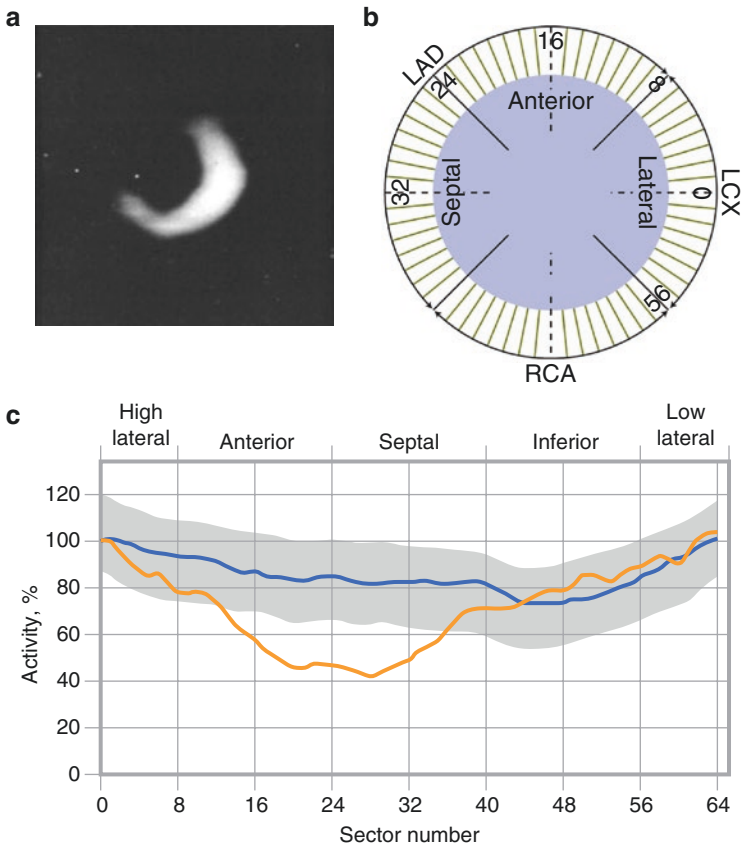

Fig. 4.6 Quantitative analysis of tracer uptake. (**a**) The methodology of semiautomatic quantitative circumferential profile analysis is applied to a short-axis ^{201}Tl tomogram obtained after exercise in a patient with coronary artery disease. (**b**) The left ventricular myocardium is divided into 64 sectors, representing four myocardial regions. (**c**) The patient's thallium uptake during stress imaging in each section (*orange line*) and the normal range (mean ± 2 SD for normal subjects; *shaded area with blue line*). The patient's count profile displays the distribution of counts in the tomogram relative to maximal counts counterclockwise, starting at 0, which represents the high lateral region, which is designated as the normal reference value of 100% (maximal count density). Whenever a region of the circumferential profile falls below the lower limit of normal, that region of the patient's myocardium is considered to have a perfusion defect. In this patient, thallium perfusion defects are apparent in the anterior and septal regions. LAD—left anterior descending; LCX—left circumflex; RCA—right coronary artery

Although normal myocardial perfusion SPECT images appear to have homogeneous radiotracer uptake, regional inhomogeneities are commonly present that are related to normal structural variation, tissue attenuation, and abdominal visceral activity, as well as technical factors associated with image acquisition. During SPECT acquisition, the camera is physically closer to the lateral wall (which is in close proximity to the lateral chest wall) than to the other myocardial regions. Consequently, the lateral region is subject to less soft tissue attenuation and is associated with a more efficient count capture. This should not be interpreted as relative hypoperfusion in all other myocardial regions (which will appear to have slightly less uptake). Thus, in normal SPECT images, the lateral region is usually the area with maximal radiotracer uptake, and it is often difficult to detect subtle perfusion defects visually within the lateral region because the activity of the radiotracer may remain greater than or similar to other myocardial regions. This would especially be the case in patients with multivessel disease, in whom an equivalent reduction in perfusion in several myocardial regions would still result in greater tracer activity in the lateral territory, termed *balanced reduction in flow*. Normal structural variations include the "drop-out" of the upper septum (transition from the muscular to membranous septum) and apical thinning (an anatomically thinner apex may appear as a perfusion defect). Figure 4.7 illustrates common variations and artifacts of myocardial perfusion SPECT.

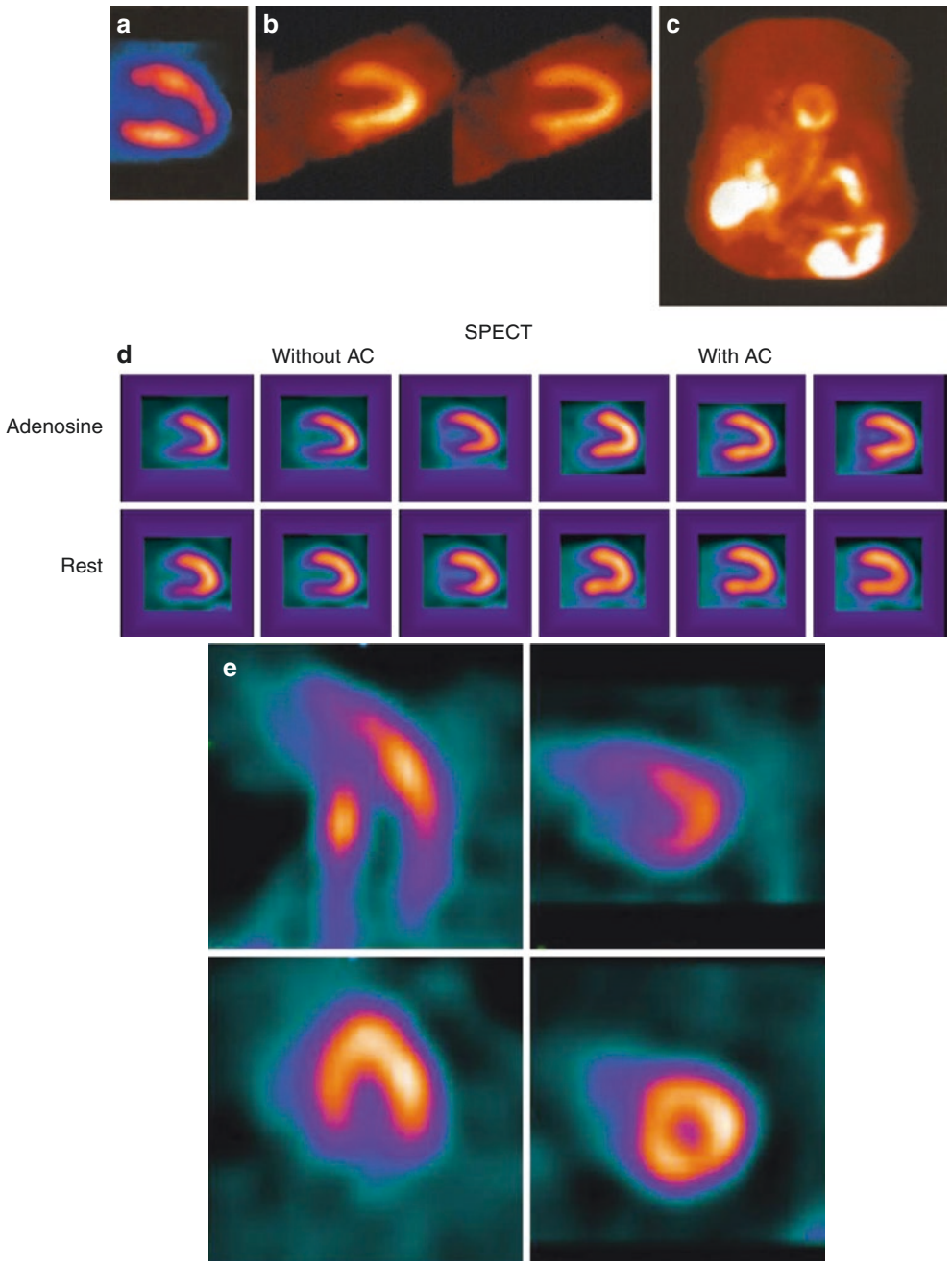

Fig. 4.7 Common variations and artifacts of myocardial perfusion SPECT. (**a**) An example of apical thinning is shown. Soft tissue attenuation can present as breast attenuation, commonly in women with large or dense breasts. (**b**) This figure is an example of a patient with breast attenuation, which shows mildly decreased uptake in the anterior region. (**c**) Breast attenuation can be recognized on the rotating planar projection images as a photopenic shadow over the heart that has the contour of a breast. The demonstration of preserved wall thickening in the anterior region by gated SPECT imaging may be helpful in differentiating an attenuation artifact from myocardial infarction. (**d**) Similarly, inferior wall attenuation can be caused by the diaphragm or by other abdominal visceral structures, such as the liver or bowel, either overlapping or near the inferior wall, or ascites and large pleural effusions. Soft tissue attenuation such as that caused by the diaphragm can be corrected with attenuation correction (AC), but attenuation due to radiotracer activity within abdominal visceral structures, such as the liver or bowel, either overlapping or near the inferior wall, cannot be resolved with an attenuation correction algorithm. Adjacent abdominal visceral activity may falsely increase the number of counts that are assigned within the heart (in which case the adjacent myocardium appears to be "hot") or may cause a "ramp filter" or "negative lobe" artifact (in which case the adjacent myocardium appears to be "cool"). (**e**) This figure is an example of a patient motion artifact exhibiting as a "hurricane sign." Images in the *top row* show the consequence of significant patient motion in creating artifactual regional perfusion defects. In the *bottom row*, when the images are reacquired in the same patient without motion artifact, the distribution of the radiotracer appears homogeneous in all myocardial regions, without regional perfusion defects

An imbalance between oxygen supply (usually due to reduced myocardial perfusion) and oxygen demand (determined primarily by the rate and force of myocardial contraction) is termed *ischemic myocardium*. A clinical presentation of such an imbalance may be symptomatic (angina pectoris) or asymptomatic (silent ischemia). If the oxygen supply–demand imbalance is transient (i.e., triggered by exertion), it represents reversible ischemia. The scintigraphic hallmark of myocardial ischemia is a reversible perfusion defect, as seen in Fig. 4.8.

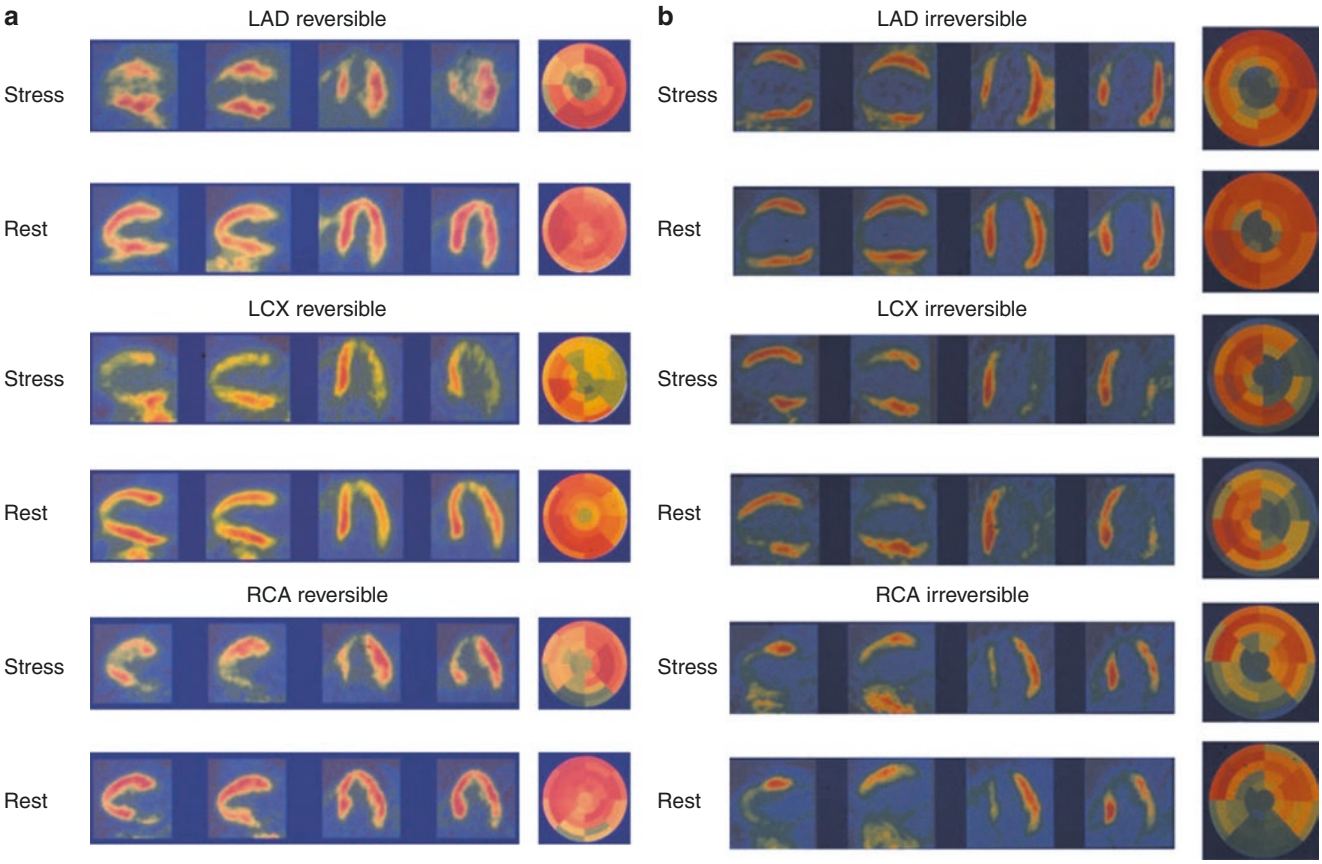

Fig. 4.8 Reversible and irreversible perfusion defects: myocardial ischemia and infarction. (**a**) Examples of reversible perfusion defects (from a transient oxygen supply–demand imbalance, as triggered by exertion) in the left anterior descending (LAD), left circumflex (LCX), and right coronary artery (RCA) territories. On the other hand, if a regional oxygen supply–demand imbalance is prolonged (i.e., during myocardial infarction), high-energy phosphates will be depleted, regional contractile function will progressively deteriorate, and cell membrane rupture with cell death will follow (myocardial infarction). The scintigraphic hallmark of myocardial infarction is a fixed or irreversible perfusion defect. (**b**) Examples of irreversible (fixed) perfusion defects in the LAD, LCX, and RCA territories

Beyond myocardial perfusion, additional important abnormal findings can be present on the rotating planar projection images, which allow the visualization of noncardiac structures such as lung, breast, and the thyroid gland. Findings such as lung uptake, parathyroid adenoma, or lung cancer, shown in Fig. 4.9, should be observed and reported.

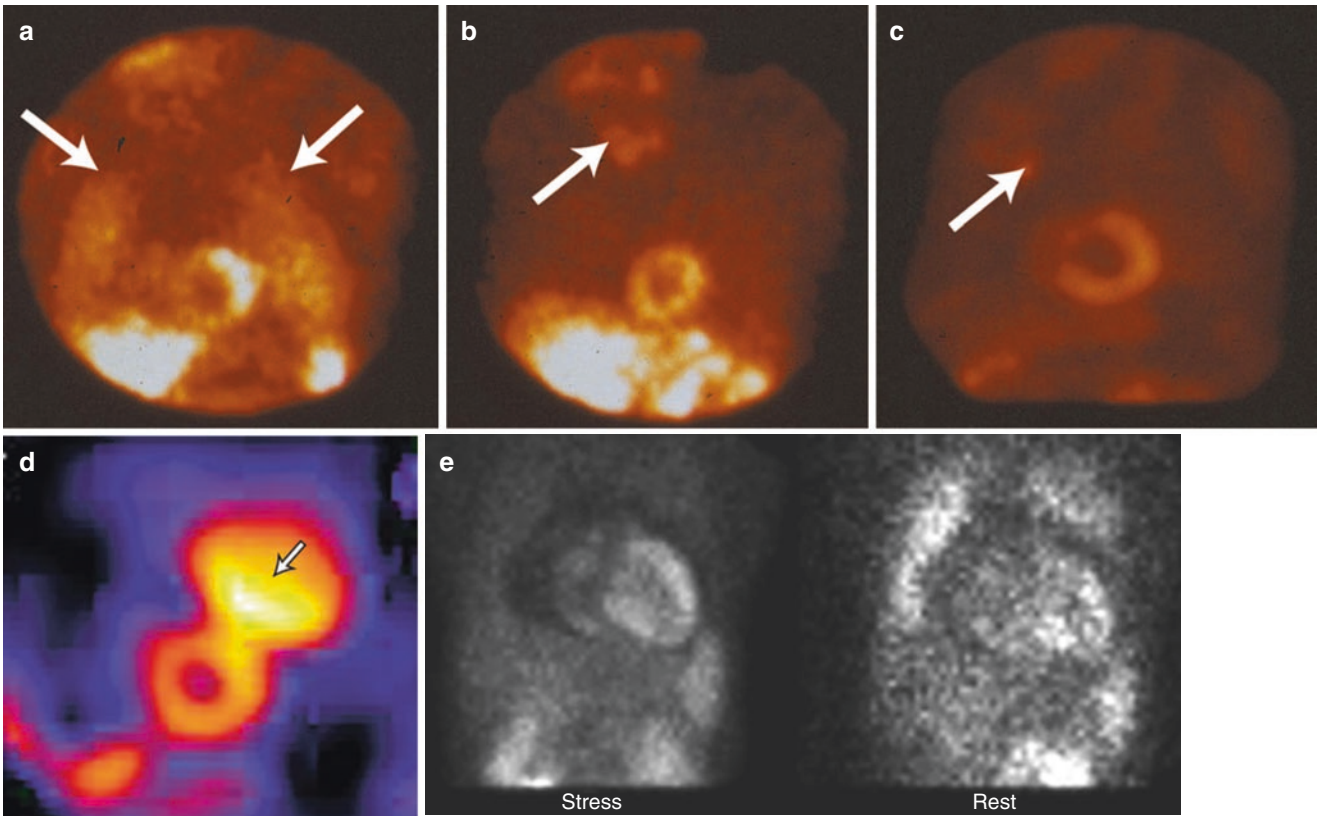

Fig. 4.9 Clinically relevant extracardiac activity. (**a**) Increased lung uptake (*arrows*) is associated with extensive coronary artery disease and an adverse prognosis. In patients with extensive myocardial ischemia and/or left ventricular dysfunction, it is likely that increases in the left atrial and pulmonary capillary wedge pressures slow the pulmonary transit of the radiotracer, thereby allowing more time for extraction or transudation of the radiotracer into the interstitial spaces of the lung. Lung uptake has been more extensively validated with ^{201}Tl than ^{99m}Tc perfusion tracers. Because of differences in the biodistribution and clearance of ^{201}Tl and ^{99m}Tc perfusion tracers, thallium images are acquired within a few minutes after exercise (minimal splanchnic and background activity), but the ^{99m}Tc-sestamibi and ^{99m}Tc-tetrofosmin are usually acquired 15–30 minutes after exercise and 30–60 minutes after pharmacologic vasodilation. (Liver uptake is more prominent than the heart if imaged too early.) Thus, lung uptake, even if it was present early after stress, may be missed with ^{99m}Tc-sestamibi and ^{99m}Tc-tetrofosmin because of the more delayed imaging after stress when compared with thallium. (**b**) An example of a patient with findings of a parathyroid adenoma (*arrow*) in stress ^{99m}Tc-sestamibi myocardial perfusion SPECT. The rotating planar projection images allow the visualization of noncardiac structures such as lung, breast, and the thyroid gland. An abnormal uptake of ^{201}Tl, ^{99m}Tc-sestamibi, and ^{99m}Tc-tetrofosmin in the neck can identify parathyroid adenoma, whereas in the chest they can identify primary lesions such as lung or breast cancer, ectopic parathyroid adenoma, or metastatic lesions. (**c**) Similarly, shown is an example of a patient with findings of a solitary lung nodule (*arrow*) on a stress ^{99m}Tc-sestamibi myocardial perfusion SPECT. (**d**) Intense ^{99m}Tc-sestamibi uptake (*arrow*), superior to the heart, represents an anterior mediastinal mass, which is compatible with thymoma. Thymomas are the most common neoplasm of the anterior mediastinum (representing 20% of all anterior mediastinal masses in the adult population), but their incidence is rather rare, only 0.15/100,000 cases. The differentiation of benign from malignant thymoma cannot be made on the basis of size or intensity of ^{99m}Tc-sestamibi uptake. Additional studies are required to further characterize the lesion. (**e**) Example of a patient with pericardial effusion. A photopenic halo of decreased activity surrounding the entire heart is consistent with pericardial effusion, which could be a consequence of myopericarditis, an infection such as tuberculous pericardial effusion, or a malignant effusion such as breast cancer, melanoma, or lung cancer. (**d** *Courtesy of* Jeffrey R. Folk; **e** *Courtesy of* Rory Hachamovitch)

Extensive literature exists on the diagnostic yield of stress SPECT myocardial perfusion imaging [3–14]. Among 1827 patients referred for the evaluation of chest discomfort (pooled data from 12 studies performed between 1989 and 1999), the overall sensitivity of myocardial perfusion SPECT for the detection of angiographic coronary artery disease was 91%, the specificity was 72%, and the normalcy rate (in subjects with low likelihood for coronary artery disease who did not undergo coronary angiography) was 91% (Fig. 4.10).

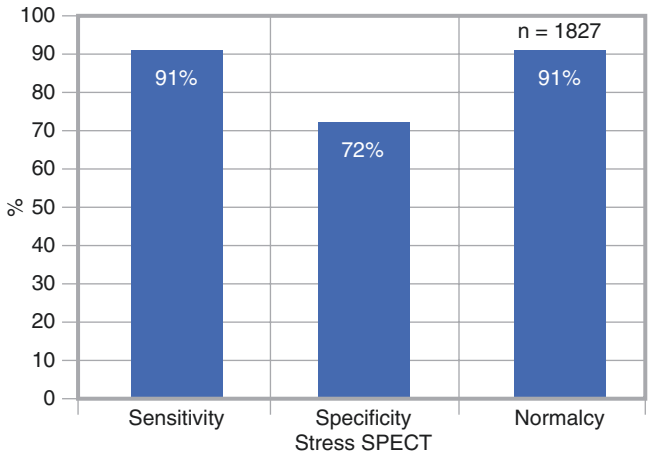

Fig. 4.10 Detection of angiographic coronary artery disease with radiotracers

The clinical indications for stress–rest myocardial perfusion SPECT imaging (Table 4.2) are well established [15]. Most patients are referred because of chest pain symptoms and suspected coronary artery disease (CAD), but patients with known CAD are referred as well. For these patients, the purpose of testing may be to evaluate the effect of therapy or to determine the cause of changes in symptom patterns. In addition, many patients are referred for risk stratification after acute myocardial infarction. Stress–rest SPECT imaging plays an important role in the preoperative evaluation of patients who are scheduled to undergo major noncardiac surgery. The most important and useful clinical application of SPECT myocardial perfusion imaging is to stratify patients into low-risk and high-risk categories and, thus, contribute to the management of patients.

Detection of coronary artery disease
Evaluation of known coronary artery disease
Risk stratification
Preoperative evaluation
Differentiation of viable from scarred myocardium
Assessment of acute chest pain in the emergency department

Table 4.2 Clinical indications for myocardial perfusion imaging

SPECT images should not be interpreted as either normal or abnormal. The prognosis of a patient is related to the degree of myocardial perfusion abnormality. Quantification or semiquantification provides that important prognostic information. Table 4.3 lists findings that characterize high-risk versus low-risk SPECT images. Among the high-risk findings are large perfusion defects in the stress images that involve multiple coronary artery territories. (If two or more coronary territories are involved, the study should be considered to be high-risk.) Large stress-induced reversible defects represent extensive myocardial ischemia, which may be associated with increased lung uptake, transient ischemic left ventricular cavity dilatation, and transient increased right ventricular myocardial visualization.

High risk
Large perfusion defect on stress imaging
Multiple coronary artery territories
Large reversible defects
Increased lung uptake
Transient left ventricular dilatation
Abnormal lung uptake
Left ventricular dysfunction (LVEF < 45%)
Low risk
Normal stress images
Small stress defect
Small regions of defect reversibility

LVEF left ventricular ejection fraction

Table 4.3 High-risk and low-risk SPECT images

One of the strongest features of stress myocardial perfusion SPECT imaging is its ability to identify low-risk patients. Patients with unequivocal normal exercise or pharmacologic stress myocardial perfusion SPECT images exhibit less than a 1% future cardiac event rate, which is the same as the general population. For patients who are in an exercise study, this presumes that the patient achieved greater than 85% of the predicted maximum heart rate for a man or woman of their age. Similarly, presuming that adequate exercise was performed, patients with small myocardial perfusion defects on stress and small regions of defect reversibility have a low risk for future cardiac events, but these patients should be treated aggressively with medical therapy owing to the presence of coronary artery disease. It is important to emphasize that stress myocardial perfusion SPECT images should always be interpreted in conjunction with clinical and electrocardiographic data. For example, a rare patient may have a markedly abnormal exercise portion of the test but normal or near-normal SPECT images. It is the responsibility of the nuclear cardiologist to determine the significance of such disparate data.

SPECT Techniques: ^{201}Tl

Figure 4.11 illustrates a stress-redistribution ^{201}Tl protocol. The initial distribution of ^{201}Tl (early after intravenous injection) is proportional to regional blood flow, but the redistribution phase, the later distribution of ^{201}Tl over a 3- to 4-hour period, is a function of regional blood volume and is unrelated to flow. During the redistribution phase, there is a continuous exchange of ^{201}Tl between the myocardium and the extracardiac compartments, driven by the concentration gradient of the tracer and myocyte viability. Thus, the extent to defect resolution, from the initial to delayed redistribution images over time (a reversible defect), reflects one index of myocardial viability. When only nonviable, scarred myocardium is present, the initial ^{201}Tl defect (an irreversible defect) persists over time without redistribution. When both viable and scarred myocardium are present, ^{201}Tl redistribution is incomplete, giving the appearance of partial reversibility. Thus, the initial phase of ^{201}Tl studies reflects reductions in flow caused by coronary artery narrowing, whereas the delayed, redistribution phase of ^{201}Tl studies reflects myocardial potassium space, differentiating viable from scarred myocardium.

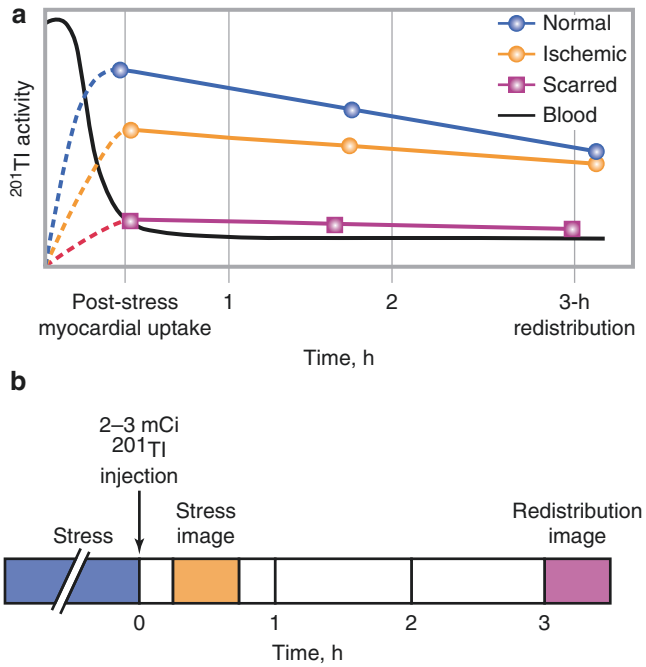

Fig. 4.11 Stress-redistribution ^{201}Tl protocol: Schematic diagrams of ^{201}Tl uptake and redistribution in normal and ischemic myocardium (**a**), and a stress-redistribution protocol (**b**)

Beyond its value as a perfusion and viability tracer, the stress-redistribution ^{201}Tl studies provide useful information regarding patient outcome and prognosis. In patients with chronic ischemic heart disease, an increased lung-to-heart ratio after stress, transient left ventricular cavity dilatation, and extensive reversible and irreversible ^{201}Tl defects have been shown to be important predictors of an adverse outcome. Similarly, the combination of reversible ^{201}Tl defects and increased lung-to-heart ratio has been shown to differentiate between low- and high-risk patients after an acute myocardial infarction. Figure 4.12 demonstrates that ^{201}Tl scintigraphy was much better than an exercise treadmill test or coronary angiography at identifying a low-risk subgroup of patients with acute myocardial infarction.

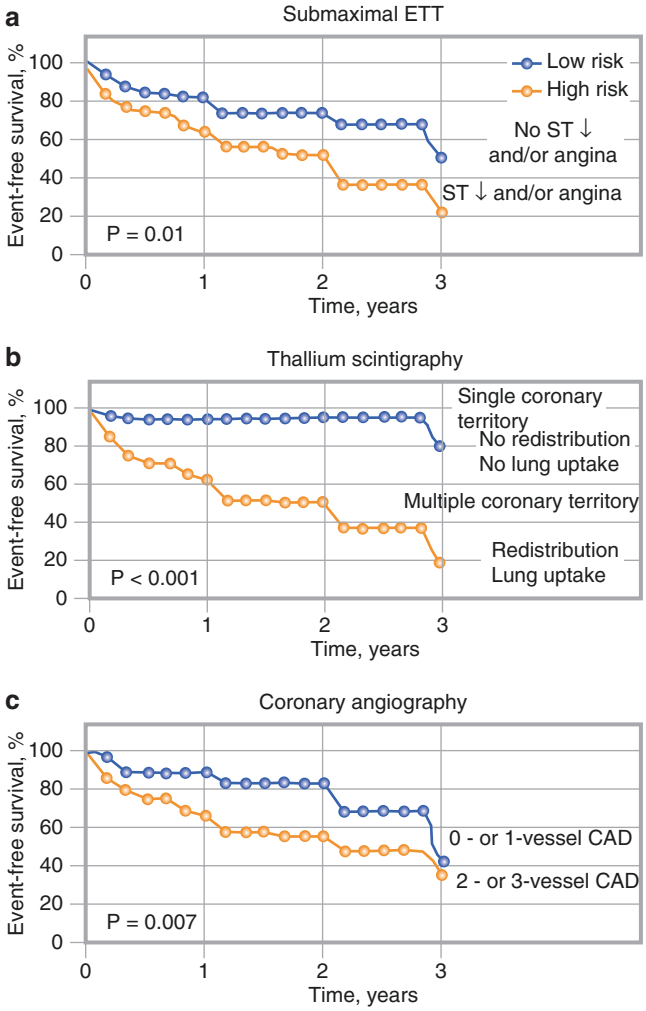

Fig. 4.12 Prognostic value of thallium scintigraphy. Among patients with acute myocardial infarction who had a predischarge submaximal exercise treadmill test (ETT), ^{201}Tl scintigraphy, and coronary angiography, ^{201}Tl identified the low-risk subgroup much better than the submaximal ETT or angiography [16]. CAD—coronary artery disease

In some patients with critically stenosed coronary arteries, the initial uptake of ^{201}Tl in the ischemic region is low and the accumulation of the tracer from the recirculating ^{201}Tl in the blood is slow. Consequently, ischemic but viable myocardium may appear to be irreversible over the 3- to 4-hour redistribution period and may mimic the appearance of scarred myocardium, but if more time is allowed for redistribution, a greater number of viable myocardial regions may be differentiated from scarred myocardium. Figure 4.13 shows a late-redistribution protocol and maps demonstrating the effect of late ^{201}Tl redistribution. However, up to 37% of segments that remained irreversible in both early and late redistribution studies showed an improvement in function after revascularization [17]. Moreover, despite implementing longer imaging time, a number of late redistribution studies had suboptimal count statistics at 24 hours. The data suggest that although late ^{201}Tl imaging improves the identification of viable myocardium when compared with early redistribution imaging, it continues to underestimate segmental improvement after revascularization.

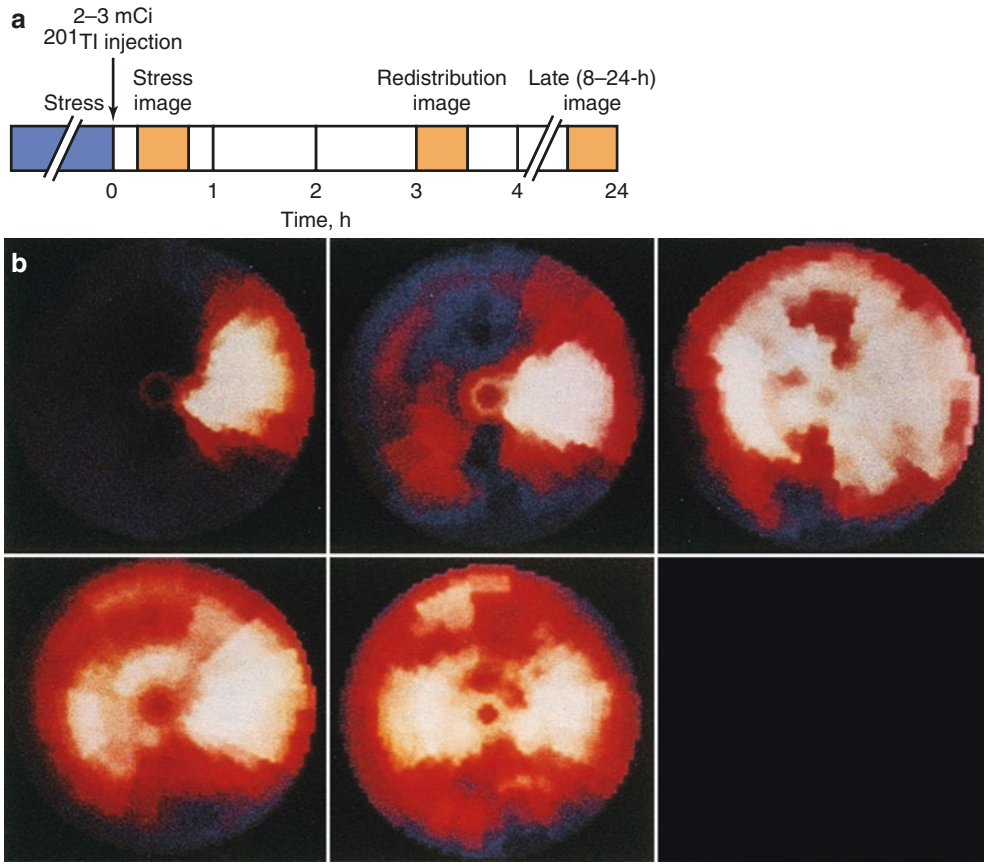

Fig. 4.13 (**a**) Late (24-hour) redistribution protocol after stress-redistribution ^{201}Tl imaging. (**b**) Polar maps demonstrating the effect of late ^{201}Tl redistribution. A bull's-eye image of ^{201}Tl immediately after exercise (*top left*) shows a marked decrease in tracer uptake throughout the anterior, septal, apical, and inferior regions, with partial redistribution in the 4-hour delayed image (*center*). However, in the late (17-hour) redistribution image (*right*), there is complete reversibility in all myocardial regions, which is suggestive of extensive myocardial ischemia rather than a scar. After successful percutaneous transluminal coronary angioplasty, the bull's-eye image of ^{201}Tl immediately after exercise (*bottom left*) shows normal distribution of the tracer throughout all myocardial regions, documenting the accuracy of late redistribution ^{201}Tl and the absence of myocardial scarring. In patients who are treated with revascularization, 95% of segments that demonstrated late redistribution showed improved ^{201}Tl uptake after revascularization. However, as with early (3–4 hour) redistribution, the absence of late redistribution underestimates the presence of viable myocardium (*right*). (**b** *From* Cloninger et al. [18], with permission from Elsevier)

The redistribution of ^{201}Tl is dependent, in part, on the blood levels of ^{201}Tl. The redistribution of ^{201}Tl in a given myocardial region depends not only on the severity of the initial defect poststress but also on the presence of viable myocytes, the concentration of the tracer in the blood, and the rate of decline of ^{201}Tl levels in the blood (Fig. 4.14). During the redistribution phase, there is continuous exchange of ^{201}Tl between the myocardium and the extracardiac compartments, which is driven by the concentration gradient of the radiotracer across the myocytes, as well as blood and myocyte viability.

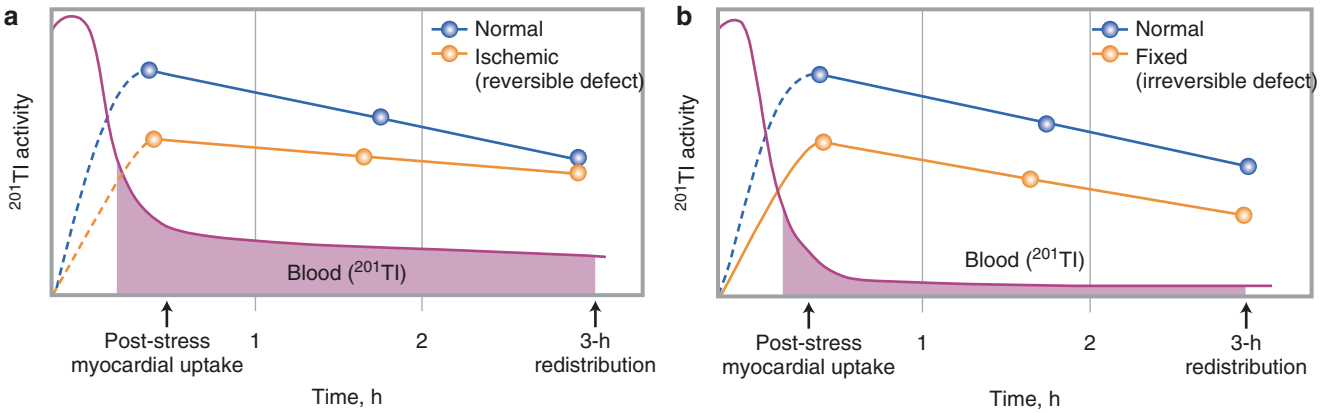

Fig. 4.14 Myocardial thallium uptake and clearance in relation to blood activity of thallium. (**a**) If the blood level of ^{201}Tl remains the same (or increases) during the period between stress and redistribution imaging, then a stress-induced defect in a region with viable myocytes that can accumulate ^{201}Tl in the redistribution phase will appear to be reversible. (**b**) If the blood level of ^{201}Tl is low (or decreases) during the imaging interval, the delivery of ^{201}Tl may be insufficient and the stress-induced ^{201}Tl defect may remain irreversible even though the underlying myocardium is viable. Thus, some ischemic but viable regions may show no redistribution on either early (3- to 4-hour) or late (24-hour) imaging, unless blood levels of ^{201}Tl are increased [19]

^{201}Tl reinjection (Fig. 4.15) differentiates ischemic but viable myocardium from scarred myocardium by augmenting the blood levels of ^{201}Tl at rest. A viable segment may be asynergic on the basis of repetitive stunning and hibernation. Thus, an asynergic but viable region may have reduced (but not absent) blood flow at rest (hibernation) or transient reduction in blood flow after a period of ischemia (stunning). Although standard stress 3- to 4-hour redistribution ^{201}Tl scintigraphy may underestimate the presence of ischemic but viable myocardium in many patients with coronary artery disease, reinjecting ^{201}Tl at rest after stress 3- to 4-hour redistribution imaging substantially improves the assessment of myocardial ischemia and viability in up to 49% of patients with apparently irreversible defects [2]. The theory that myocardial regions identified by ^{201}Tl uptake following ^{201}Tl reinjection represent viable myocardium is supported by improved regional function after revascularization and preserved metabolic activity by [^{18}F]-fluorodeoxyglucose PET. In addition, a significant inverse correlation between the magnitude of ^{201}Tl activity after reinjection and the regional volume fraction of interstitial fibrosis has been demonstrated in comparative clinicopathologic studies [20]. It is possible that the initial myocardial uptake of ^{201}Tl (postinjection) reflects regional blood flow, whereas the redistribution of ^{201}Tl in a given defect depends not only on the severity of the initial defect but also on the presence of viable myocytes, the concentration of the tracer in the blood, and the rate of decline of ^{201}Tl levels in the blood. Thus, the heterogeneity of regional blood flow observed in the initial stress-induced ^{201}Tl defects may be independent of the subsequent extent of ^{201}Tl redistribution. If the blood level of ^{201}Tl remains the same (or increases) during the period between stress and 3- to 4-hour redistribution imaging, then an apparent defect in a region with viable myocytes that can retain ^{201}Tl should improve. On the other hand, if the serum ^{201}Tl concentration decreases during the imaging interval, the delivery of ^{201}Tl may be insufficient, and the ^{201}Tl defect may remain irreversible although the underlying myocardium is viable. This suggests that some ischemic but viable regions may never redistribute, even with late (24-hour) imaging, unless serum levels of ^{201}Tl are increased. This hypothesis is supported by a study in which ^{201}Tl reinjection was performed immediately after 24-hour redistribution images were obtained [6]. Improved ^{201}Tl uptake after reinjection occurred in 40% of defects that appeared irreversible on late (24-hour) redistribution images. Thus, the reinjection of 1 mCi of ^{201}Tl at rest significantly improves the assessment of myocardial ischemia and viability.

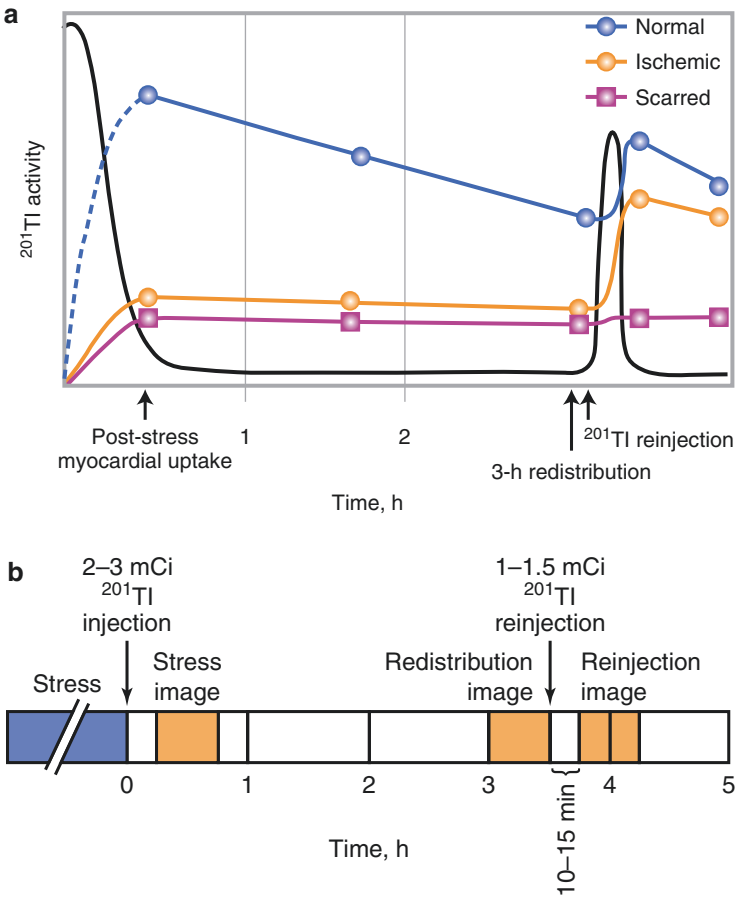

Fig. 4.15 Thallium reinjection. ^{201}Tl reinjection differentiates ischemic but viable myocardium from scarred myocardium by augmenting the blood levels of ^{201}Tl at rest. Reinjecting ^{201}Tl at rest after stress 3- to 4-hour redistribution imaging substantially improves the assessment of myocardial ischemia and viability in up to 49% of patients with apparently irreversible defects (**a**). If the blood level of ^{201}Tl remains the same (or increases) during the period between stress and 3- to 4-hour redistribution imaging, then an apparent defect in a region with viable myocytes that can retain ^{201}Tl should improve. On the other hand, if the serum ^{201}Tl concentration decreases during the imaging interval, the delivery of ^{201}Tl may be insufficient, and the ^{201}Tl defect may remain irreversible although the underlying myocardium is viable. This suggests that some ischemic but viable regions may never redistribute, even with late (24-hour) imaging, unless serum levels of ^{201}Tl are increased. Thus, the reinjection of 1 mCi of ^{201}Tl at rest immediately after either stress 3- to 4-hour redistribution (**b**) or stress 24-hour redistribution studies, followed by image acquisition 10–15 minutes later, significantly improves the assessment of myocardial ischemia and viability. (From Dilsizian [19]; with permission from Futura)

Figure 4.16 illustrates the beneficial effect of ^{201}Tl reinjection in the clinical setting. Among patients who had coronary artery revascularization, 87% of the myocardial regions identified as viable by reinjection studies had normal ^{201}Tl uptake and improved regional wall motion after revascularization. In contrast, all regions with irreversible defects in reinjection imaging before revascularization had persistent wall motion abnormality after revascularization [2]. Similar results were obtained when ^{201}Tl reinjection was performed immediately after late (24-hour) redistribution imaging. Improved ^{201}Tl uptake after reinjection occurred in 40% of regions (involving 60% of patients) that appeared to be fixed in late redistribution imaging [21].

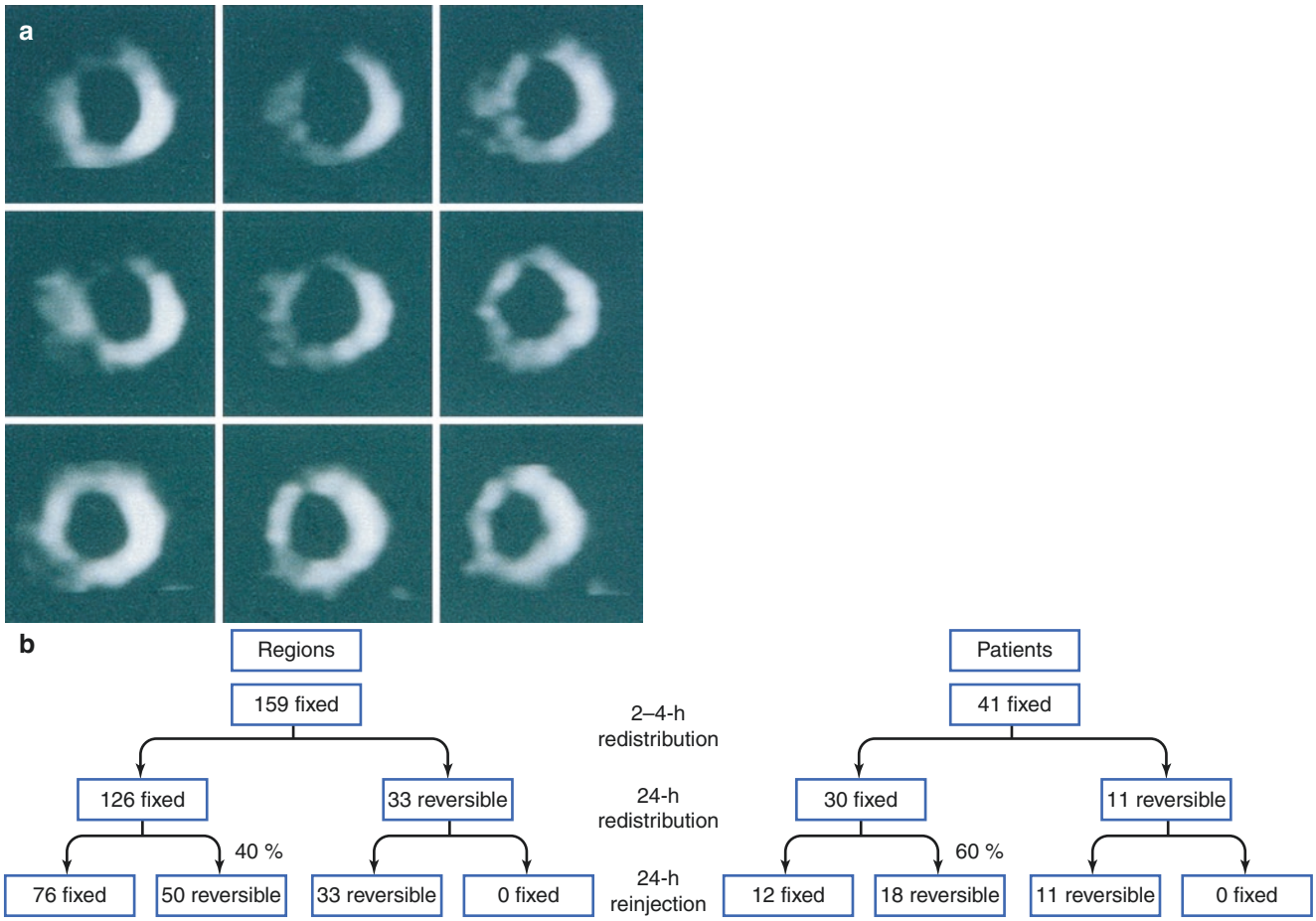

Fig. 4.16 Beneficial effect of ^{201}Tl reinjection in the clinical setting. (**a**) Short-axis tomograms demonstrate extensive ^{201}Tl defects in the anterior and septal regions in stress images (*top row*) that persist in redistribution images (*center row*) but improve markedly in reinjection images (*bottom row*) [2]. (**b**) Similar results were obtained when ^{201}Tl reinjection was performed immediately after late (24-hour) redistribution imaging. Improved ^{201}Tl uptake after reinjection occurred in 40% of regions (involving 60% of patients) that appeared to be fixed in late redistribution imaging [21]

Figure 4.17 shows the postrevascularization functional outcome of asynergic regions in relation to prerevascularization ^{201}Tl patterns of normal, reversible, partially reversible, mild-to-moderate irreversible, and severe irreversible defects using the stress-redistribution-reinjection ^{201}Tl protocol. The probabilities of functional recovery after revascularization were over 90% in normal or completely reversible defects, 63% in partially reversible defects, 30% in mild-to-moderate irreversible defects, but 0% in severe irreversible defects. Of asynergic regions with reversible defects (complete or partial) in the prerevascularization ^{201}Tl study, 79% had improved function after revascularization, but of asynergic regions with mild-to-moderate irreversible defects, only 30% had improved function ($P < 0.001$). Even at a similar mass of viable myocardial tissue (as reflected by the final ^{201}Tl content), the presence of inducible ischemia (reversible defect) was associated with an increased likelihood of functional recovery.

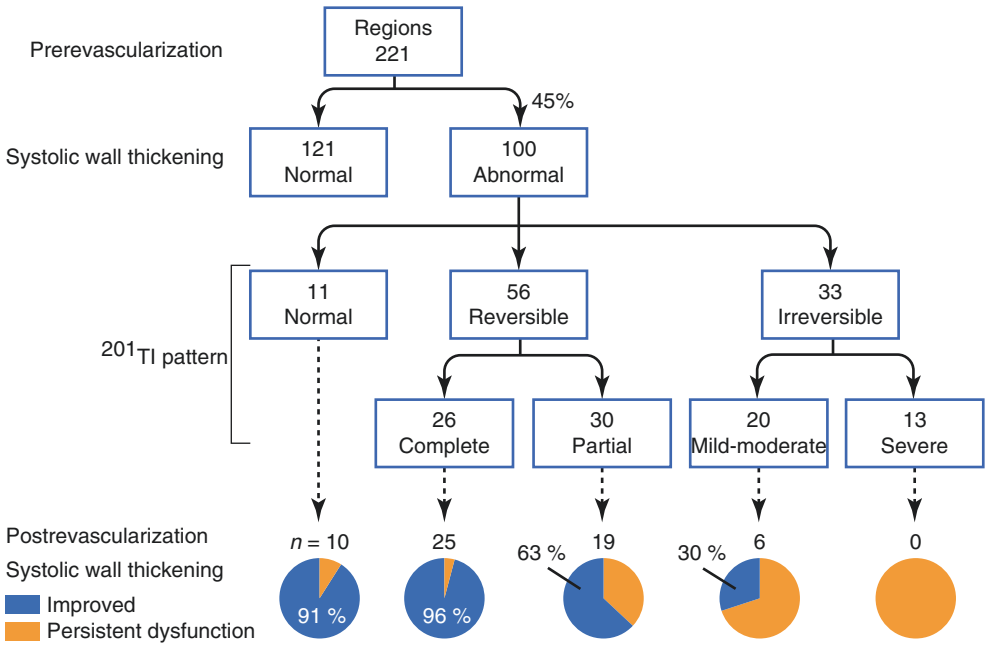

Fig. 4.17 Postrevascularization functional outcome of asynergic regions in relation to prerevascularization ^{201}Tl patterns [22]

In patients with prior myocardial infarction and left ventricular dysfunction in whom the assessment of myocardial viability is of clinical relevance, ^{201}Tl reinjection imaging provides incremental prognostic information to clinical, exercise tolerance testing, and ^{201}Tl stress-redistribution imaging (Fig. 4.18). Similarly, in patients with chronic coronary artery disease and prior myocardial infarction, the scintigraphic variable that was the strongest predictor of hard events (cardiac death or myocardial infarction) was the presence of more than three irreversible defects that remained irreversible after ^{201}Tl reinjection.

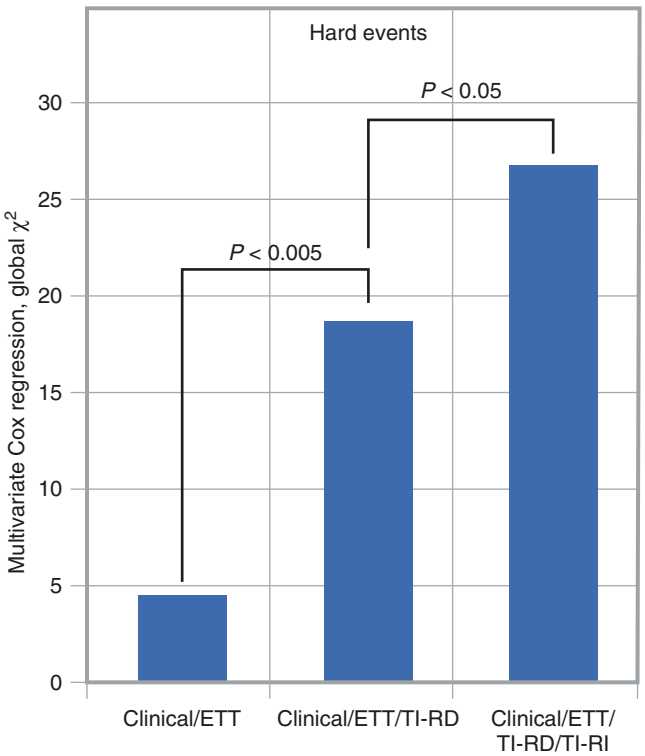

Fig. 4.18 Incremental prognostic value of ^{201}Tl reinjection (Tl-RI). Tl-RD—^{201}Tl stress-redistribution imaging [23]

The stress-redistribution-reinjection ^{201}Tl protocol provides important diagnostic information regarding both inducible ischemia and myocardial viability. In most cases, the identification of myocardial ischemia is much more important clinically in terms of patient management and risk stratification than is knowledge of myocardial viability. But if the clinical question is one of the presence and extent of viable myocardium within a dysfunctional region, not inducible ischemia, then it is reasonable to perform rest-redistribution ^{201}Tl imaging only (Fig. 4.19). Finding significant reversibility is suggestive of hibernating but viable myocardium [24].

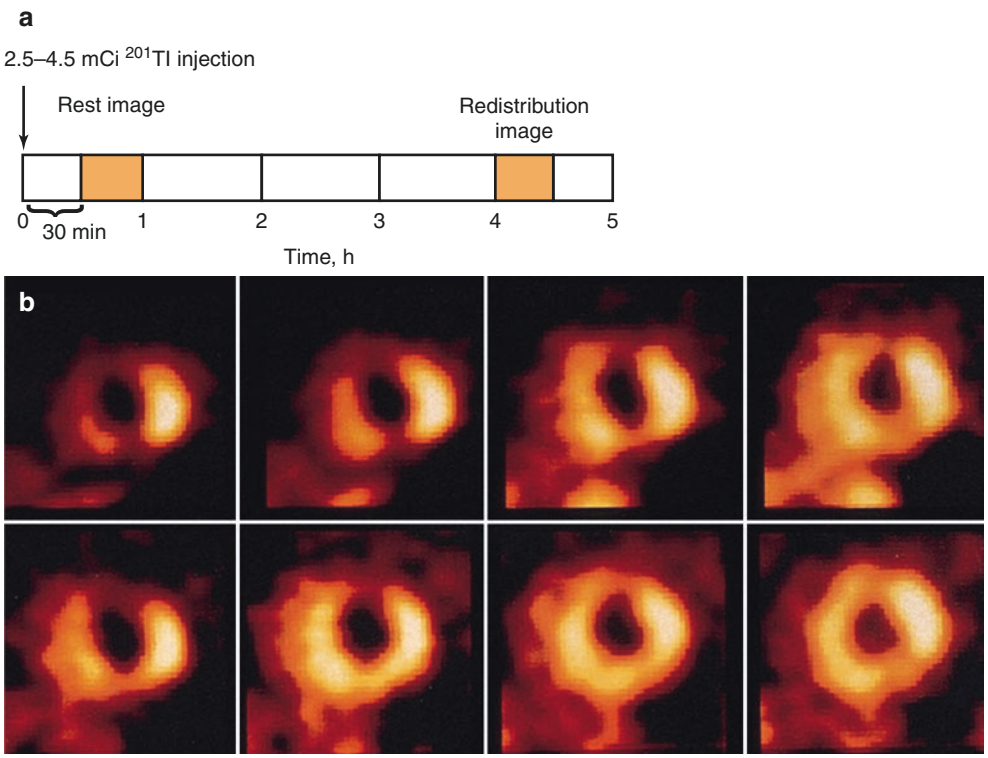

Fig. 4.19 (**a**) Rest-redistribution ^{201}Tl protocol. (**b**) Rest-redistribution short-axis ^{201}Tl tomograms are shown for a patient with chronic coronary artery disease. There are extensive ^{201}Tl perfusion defects in the anterior, distal anteroseptal, and inferior regions in the initial rest images (*top row*). In the delayed (3- to 4-hour) redistribution images (*bottom row*), the anterior region remains fixed (scarred myocardium), but the inferior and distal anteroseptal regions show significant reversibility, which is suggestive of hibernating but viable myocardium [24]

Accurate distinction between viable (hibernating or stunned) and scarred myocardium has important clinical implications. Ideally, such information may be used to guide therapeutic decisions for revascularization and risk stratification. Anatomic assessment of the coronary arteries alone does not differentiate viable from scarred myocardium, as illustrated in Fig. 4.20. The anatomic assessment of this patient's coronary arteries alone was insufficient to determine whether the myocardium subtended by the totally occluded vessels was viable or scarred. The scintigraphic finding of reduced regional blood flow (rest ^{201}Tl images) but preserved cell membrane integrity (redistribution ^{201}Tl images) in the dysfunctional myocardial regions provided the most direct evidence of myocardial hibernation. In view of the findings on the rest-redistribution ^{201}Tl study, the patient was referred for coronary artery bypass surgery with an uneventful postoperative course.

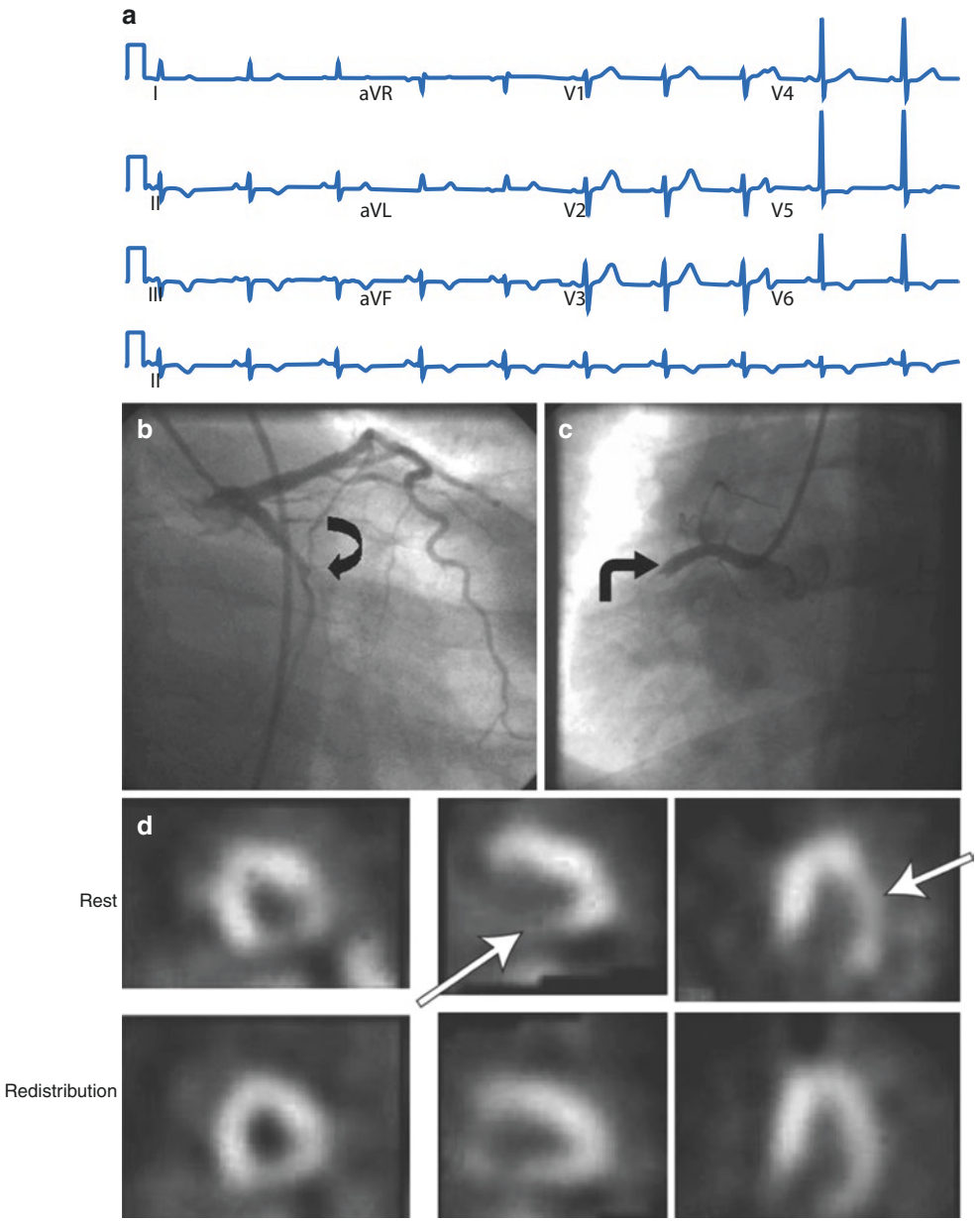

Fig. 4.20 Using a rest-redistribution ^{201}Tl study to differentiate viable from scarred myocardium. A patient with a prior history of hypertension and hyperlipidemia presents with a 2-month history of substernal chest pain. The electrocardiogram shows inverted T waves in the inferolateral leads (**a**); the coronary angiogram shows total occlusion of the left circumflex (LCX) (*arrow*) (**b**) and the proximal right coronary artery (RCA) (*arrow*) (**c**). Extensive perfusion defects in the lateral and inferior regions (**d**) in the initial rest images (*top row*; *arrows*) become reversible in the delayed (3- to 4-hour) redistribution images (*bottom row*), providing evidence for hypoperfused but viable myocardium in the LCX and RCA vascular territories. In view of the findings on the rest-redistribution ^{201}Tl study, the patient was referred for coronary artery bypass surgery with an uneventful postoperative course

Figure 4.21 demonstrates the prognostic value of rest-redistribution ^{201}Tl SPECT. In patients with chronic ischemic left ventricular dysfunction, the demonstration of redistribution on rest ^{201}Tl imaging protocols portends a higher mortality rate with medical therapy than the rate for patients with a comparable degree of left ventricular dysfunction without evidence of redistribution.

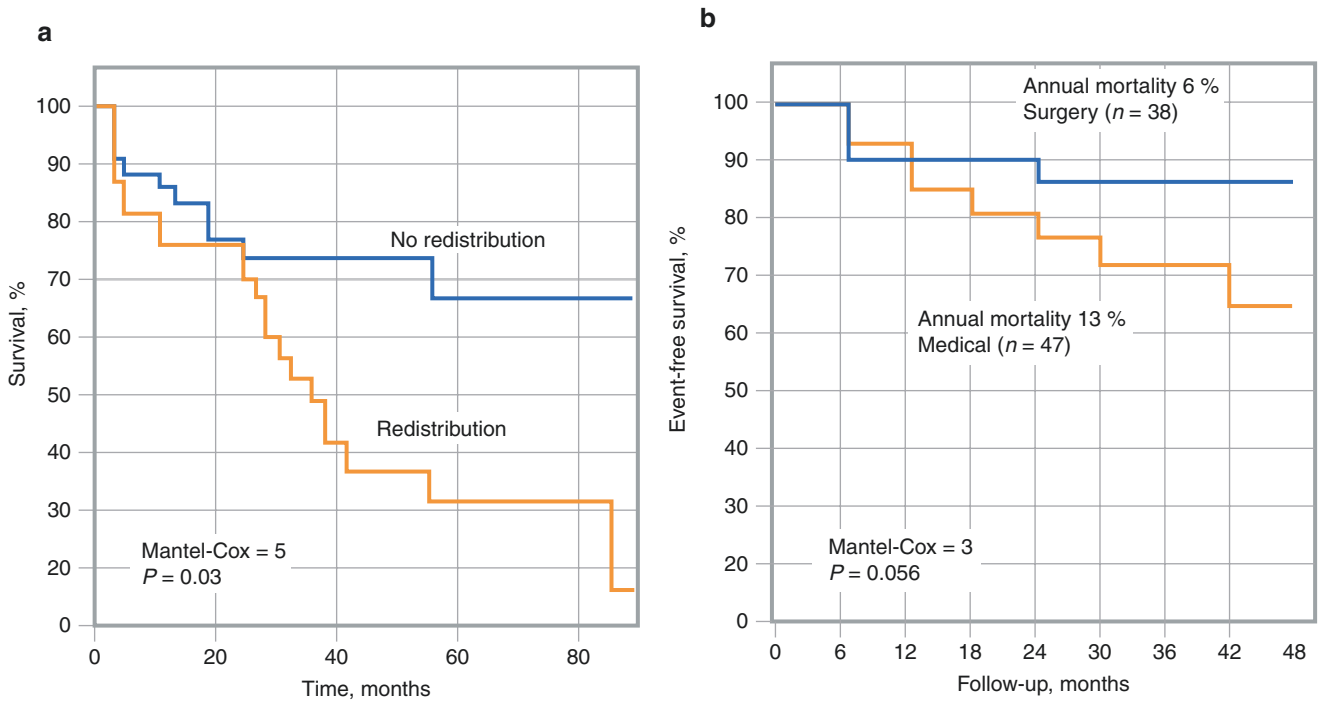

Fig. 4.21 Prognostic value of rest-redistribution ^{201}Tl SPECT. (**a**) An actuarial survival curve in 81 medically treated patients is shown; 38 patients with a mean left ventricular ejection fraction (LVEF) of 26 ± 7% showed redistribution in rest ^{201}Tl images, and 43 patients (mean LVEF, 27 ± 8%) showed no redistribution. Moreover, in a nonrandomized, retrospective study with rest-redistribution ^{201}Tl, survival and survival without myocardial infarction tended to be significantly higher in patients with chronic ischemic left ventricular dysfunction treated with coronary artery revascularization, compared with those treated with medical therapy alone. (**b**) An actuarial survival curve in 85 patients with evidence of myocardial viability by rest-redistribution ^{201}Tl is shown; 38 patients underwent coronary artery revascularization, and 47 patients were treated medically [25, 26]

Considering the survival advantage of coronary artery revascularization when compared with medical therapy in patients with chronic ischemic left ventricular dysfunction, one might question whether the preoperative assessment of myocardial viability is necessary in making revascularization decisions. Should coronary artery revascularization be considered in all patients with chronic ischemic left ventricular dysfunction, with or without evidence of myocardial viability? Figure 4.22 shows event-free survival in a retrospective study in patients with preoperative rest-redistribution ^{201}Tl testing, all of whom had coronary artery bypass surgery. Perioperative and long-term postoperative survival was significantly better in the patients with evidence of significant myocardial viability on rest-redistribution ^{201}Tl than in those with less evidence of myocardial viability.

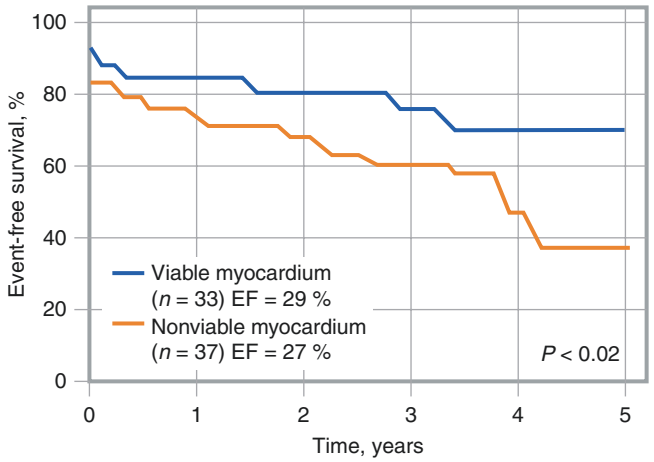

Fig. 4.22 Patient outcome (event-free survival) after coronary artery bypass surgery in patients with more or less viable myocardium as assessed by rest-redistribution ^{201}Tl and ejection fraction (EF) [27]

Table 4.4 lists the features of SPECT techniques using ^{201}Tl. The myocardial extraction of ^{201}Tl is dependent on energy utilization, membrane ATPase, and active transport. ^{201}Tl does not actively concentrate in regions of infarcted or scarred myocardium, so decreased myocardial ^{201}Tl uptake early after injection can be caused either by reduced regional blood flow or by infarction. Experimental studies with ^{201}Tl have shown that the cellular extraction of ^{201}Tl across the cell membrane is unaffected by hypoxia unless an irreversible injury is present. Similarly, pathophysiologic conditions of chronic hypoperfusion (hibernation) and postischemic dysfunction (stunning), in which regional contractile function is impaired in the presence of myocardial viability, do not adversely alter the extraction of ^{201}Tl.

Monovalent cation with biologic properties similar to potassium
60–80 keV mercury x-ray emission, 73-hour physical half-life
High first-pass extraction fraction (~85%)
Transported across myocyte sarcolemmal membrane via the Na–K ATPase transport system and by facilitative diffusion
Peak myocardial concentration within 5 minutes of intravenous injection
Rapid clearance from the intravascular compartment
Redistribution begins 10–15 minutes after injection

Table 4.4 SPECT techniques: ^{201}Tl

SPECT Techniques: ^{99m}Tc-labeled Perfusion Tracers

Alternatively, dual-isotope gated SPECT can be performed (Fig. 4.23); this technique combines rest-redistribution ^{201}Tl (for viability) with stress ^{99m}Tc-sestamibi or ^{99m}Tc-tetrofosmin (for perfusion), thereby taking advantage of the favorable properties of each of the two tracers.

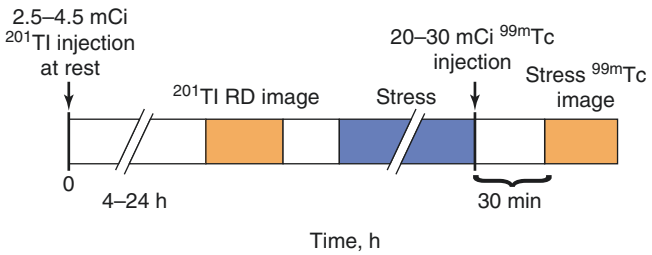

Fig. 4.23 Dual-isotope gated SPECT protocol, combining rest-redistribution ^{201}Tl (for viability) with stress ^{99m}Tc-sestamibi or ^{99m}Tc-tetrofosmin (for perfusion). RD—redistribution

Figures 4.24, 4.25, and 4.26 illustrate the differences between ^{201}Tl and ^{99m}Tc-sestamibi in various studies in animals and humans.

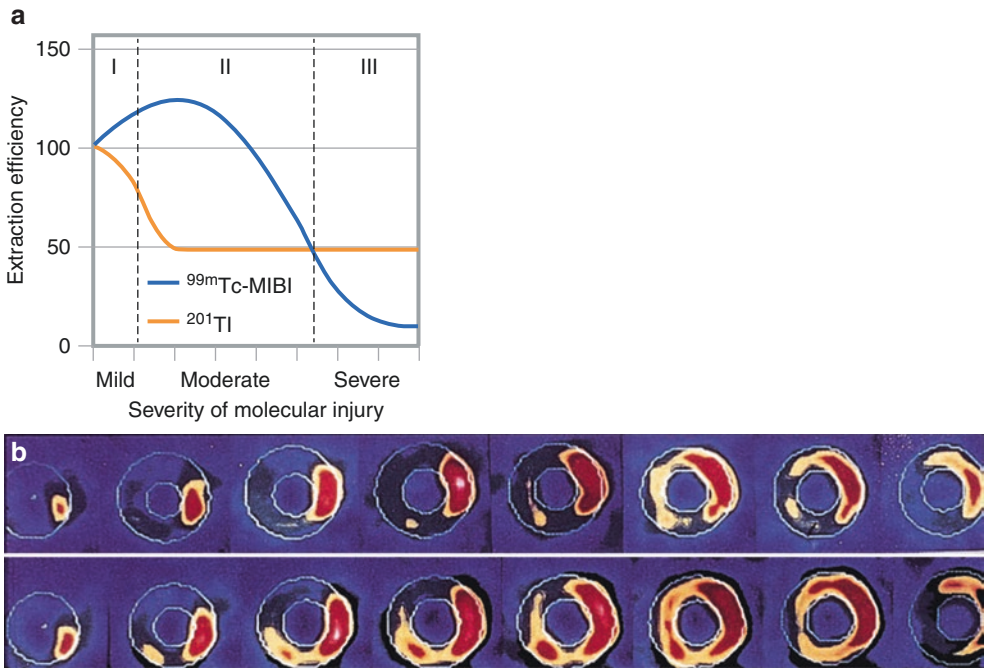

Fig. 4.24 Cellular kinetics of ^{201}Tl and ^{99m}Tc-sestamibi during metabolic inhibition in cultured chick embryo cardiac myocytes, independent of perfusion. (**a**) Oxidative phosphorylation and glycolysis were inhibited simultaneously by rotenone (10 μM) and iodoacetate (1 mmol/L), respectively, producing a decline in the myocellular ATP content. Under these conditions, the initial extraction efficiency of ^{201}Tl and ^{99m}Tc-sestamibi responded in divergent ways to ATP depletion. The extraction efficiency of ^{201}Tl declined within 20 minutes of metabolic inhibition by 50–70%, whereas the extraction efficiency of ^{99m}Tc-sestamibi (^{99m}Tc-MIBI) increased significantly within 10–20 minutes and remained elevated for the first 40–60 minutes of metabolic inhibition. The observed disparity in initial uptake rates between ^{201}Tl and ^{99m}Tc-MIBI during mild to moderate metabolic injury may explain, on a metabolic basis alone, the clinical observation that ^{99m}Tc-MIBI defects are smaller than those assessed by ^{201}Tl [28]. (**b**) Images taken with ^{201}Tl 5–10 minutes after stress (*top row*) and with ^{99m}Tc-MIBI 2 hours after stress (*bottom row*) are shown for a patient who performed the same level of exercise with both tracers. A quantitative left ventricular mass algorithm provided similar measures of total mass for ^{201}Tl (197 g) and for ^{99m}Tc-MIBI (189 g), but the stress-induced defect mass derived from ^{201}Tl imaging (41 g) is significantly larger than that detected by ^{99m}Tc-MIBI (30 g). No transmural defects are present on the ^{99m}Tc-MIBI images. (*From* Narahara et al. [29], with permission from Elsevier)

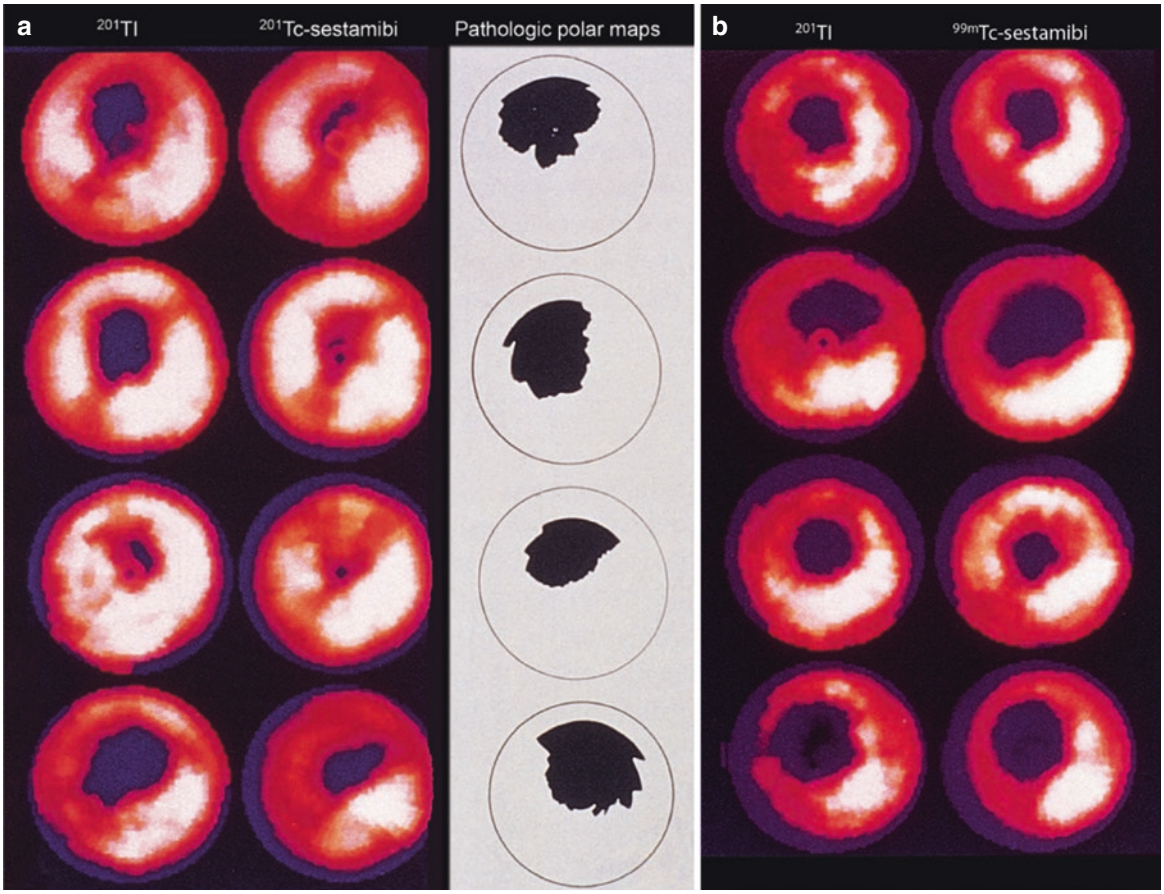

Fig. 4.25 Pharmacologic stress. In canine models of moderate (**a**) and severe (**b**) coronary artery occlusion, ^{201}Tl and ^{99m}Tc-sestamibi myocardial perfusion defect sizes are compared during pharmacologic stimulation and with postmortem staining to define the extent of the hypoperfused region. These bull's-eye displays are from four representative experiments of moderate coronary artery stenosis during pharmacologic stimulation for ^{201}Tl and ^{99m}Tc-sestamibi, and the corresponding pathologic polar displays from the same four experiments are shown. The extent of ^{201}Tl myocardial perfusion defect size (but not ^{99m}Tc-sestamibi) approaches the hypoperfused area in the corresponding pathologic display. The ^{99m}Tc-sestamibi defect size occupies only 37% of the area of the defect in the ^{201}Tl images of the same dog, and the counts within the defects are 39% higher for ^{99m}Tc-sestamibi compared with ^{201}Tl (**a**). On the other hand, when coronary artery occlusion is near total (severe), ^{201}Tl and ^{99m}Tc-sestamibi show similar defect contrast and areas (**b**). These observations in canines are similar to the experimental observations made in cultured myocytes. (*From* Leon et al. [30], with permission from Elsevier)

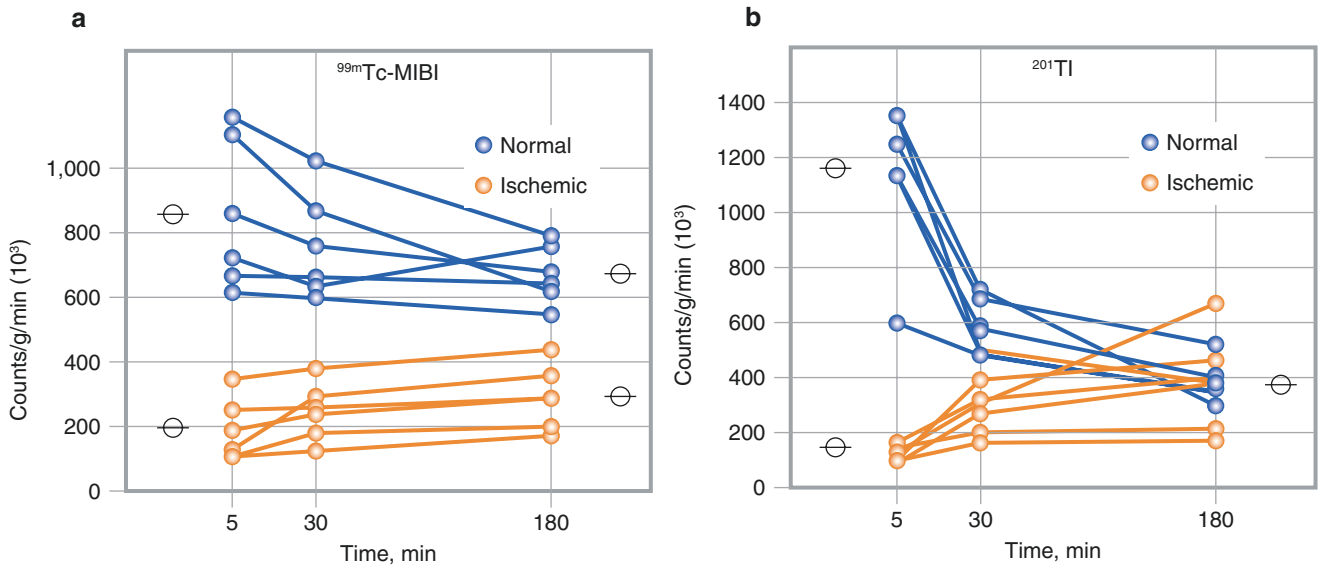

Fig. 4.26 ^{99m}Tc-sestamibi and ^{201}Tl activities in myocardial biopsies. A change in defect size of ^{99m}Tc-sestamibi (^{99m}Tc-MIBI) with time (redistribution) has been shown both in animal models and in patients with chronic coronary artery disease [31, 32]. Depending on the level of blood activity of ^{99m}Tc-MIBI after stress, continued uptake by the myocardium after the first pass may reduce the defect severity and area in the hypoperfused region. In the early comparative studies of ^{201}Tl and ^{99m}Tc-MIBI, ^{201}Tl images were acquired 5–10 minutes after injection, and the ^{99m}Tc-MIBI images were acquired 1–2 hours after injection. The 1- to 2-hour delay between ^{99m}Tc-MIBI injection and imaging was based on the best compromise between a high myocardial count rate and low background activity, and on the assumption that ^{99m}Tc-MIBI does not "redistribute" over time. Following transient ischemia and reperfusion after 5 minutes in a canine model, there was evidence for change in the defect size of ^{99m}Tc-MIBI with time (**a**), albeit more slowly and less completely than the ^{201}Tl redistribution (**b**). For both ^{99m}Tc-MIBI and ^{201}Tl, a consistent fall in the normal zone activity and rise in the ischemic zone activity are noted over the 3-hour time interval, which is consistent with redistribution. It is important to point out, however, that there is no change in the ^{99m}Tc-MIBI defect size between the 5-minute and 30-minute time intervals. In view of these and other similar reports, it is now recommended that ^{99m}Tc-MIBI images be acquired earlier, approximately 30 minutes after injection of the tracer [31]

Figure 4.27 illustrates clinically relevant change in the defect size of ^{99m}Tc-sestamibi with time (redistribution). Interpretation of ^{99m}Tc-sestamibi data should be viewed cautiously when imaging is delayed by 2 hours or more after stress (due to underestimation of the defect size and extent of myocardial ischemia), but the same concept does not apply for rest-injected ^{99m}Tc-sestamibi studies. On the contrary, delaying ^{99m}Tc-sestamibi images by 2 hours or more after rest injection may improve myocardial viability assessment.

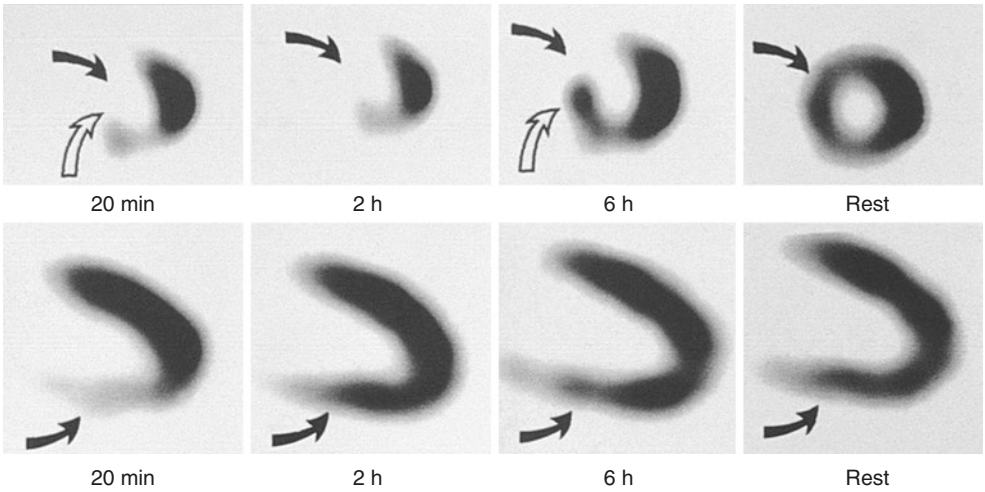

Fig. 4.27 Clinically relevant change in the defect size of ^{99m}Tc-sestamibi with time (redistribution) in two patients who experienced exercise ^{99m}Tc-sestamibi studies. Myocardial SPECT images obtained from two different patients are presented in the short-axis plane (*top row*) and in the vertical long-axis plane (*bottom row*) after exercise and at rest. In the short-axis plane, there is no change in ^{99m}Tc-sestamibi defect size from 20 minutes to 2 hours after exercise, but by 6 hours there is a significant change in the defect size in the inferoseptal region (*open arrow*) but not in the anteroseptal region (*closed arrow*). In the injected image taken at rest, complete normalization of all perfusion defects is seen, which suggests that delayed ^{99m}Tc-sestamibi images alone do not provide accurate information regarding defect reversibility. In the vertical long-axis plane, there is significant change in the ^{99m}Tc-sestamibi defect in the inferior region (*closed arrows*) from 20 minutes to 2 hours after exercise (redistribution), without further fill-in at 6 hours or in the rest-injected ^{99m}Tc-sestamibi image [33]

Considering the kinetics of ^{99m}Tc-sestamibi and ^{99m}Tc-tetrofosmin, uptake of these radiotracers in myocardial regions with reduced perfusion and partially impaired viability appears to be influenced by regional perfusion rather than myocyte viability. In view of the limitations in the clinical setting of rest-injected ^{99m}Tc-sestamibi and ^{99m}Tc-tetrofosmin for assessing myocardial viability, some investigators have proposed injecting the radiotracers during nitrate infusion. In addition to lowering the preload and afterload, nitrates may cause vasodilatation of the flow, limiting epicardial coronary arteries as well as collateral vessels. The injection of ^{99m}Tc-sestamibi during nitrate infusion (10 mg of isosorbide dinitrate in 100 mL of isotonic saline solution infused over 20 minutes) is shown to improve the accuracy of ^{99m}Tc-sestamibi for predicting the recovery of regional and global left ventricular function after revascularization. Figure 4.28 shows an example of a patient with anterior myocardial infarction and single-vessel left anterior descending (LAD) coronary artery disease [34].

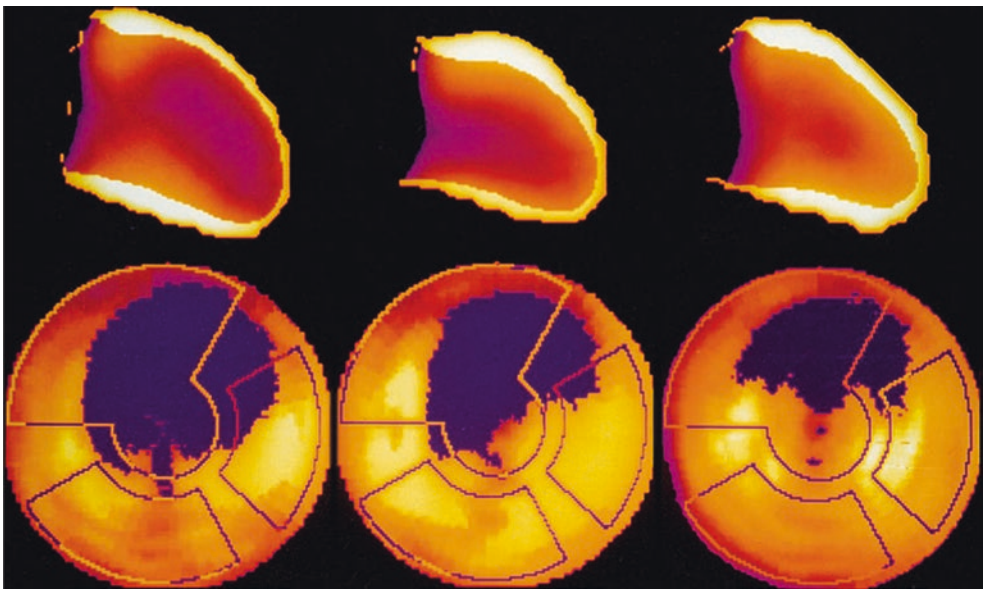

Fig. 4.28 Nitrate administration before rest ^{99m}Tc-sestamibi or ^{99m}Tc-tetrofosmin injection. In this example of a patient with anterior myocardial infarction and single-vessel left anterior descending (LAD) coronary artery disease, the prerevascularization baseline images (*left*) show anteroapical akinesis and global left ventricular ejection fraction (LVEF) of 38% in first-pass radionuclide angiography, associated with a large anterior and apical ^{99m}Tc-sestamibi perfusion defect (63% of the LAD vascular territory in the bull's-eye image at rest). The ^{99m}Tc-sestamibi images acquired after nitrate infusion (*center*) show improvement in the anteroapical wall motion associated with an increase in global LVEF to 42% and a decrease in the extent of ^{99m}Tc-sestamibi perfusion defect size to 42% of the LAD vascular territory. After revascularization of the LAD (*right*), there is improvement in the anteroapical wall motion at rest, an increase in global LVEF to 45%, and a decrease in the extent of ^{99m}Tc-sestamibi perfusion defect to 38% of the LAD vascular territory [34]. (*Courtesy of* Roberto Sciagra)

Another approach that may overcome, in part, the limitations of ^{99m}Tc-sestamibi and ^{99m}Tc-tetrofosmin in assessing myocardial viability is to quantify the severity of regional tracer activity, i.e., the severity of myocardial perfusion at rest. Figure 4.29 demonstrates a good correlation between the quantitative regional activities of ^{201}Tl (on redistribution imaging after rest injection) and ^{99m}Tc-sestamibi (at rest). In addition, dysfunctional myocardial regions that improve function after revascularization can be differentiated from dysfunctional myocardial regions that do not improve function after revascularization. In myocardial regions with decreased blood flow and partially impaired viability, the uptake of ^{99m}Tc-sestamibi appears to be influenced by regional perfusion rather than myocyte viability [35].

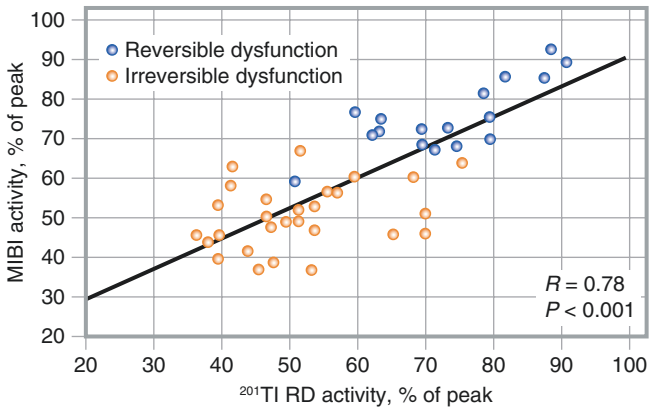

Fig. 4.29 Quantitation of severity of reduction in myocardial perfusion at rest. Among 18 patients with coronary artery disease who had revascularization, a good correlation between the quantitative regional activities of ^{201}Tl (on redistribution [RD] imaging after rest injection) and ^{99m}Tc-sestamibi (at rest) is shown. This scatterplot shows that at a 60% threshold level for both radiotracers, dysfunctional myocardial regions that improve function after revascularization (*blue circles*) can be differentiated from dysfunctional myocardial regions that do not improve function after revascularization (*orange circles*). When the severity of radiotracer defects were quantitated, the positive predictive accuracy was 80% and the negative accuracy was 96% [36]

A study comparing myocardial viability seen on rest ^{99m}Tc-sestamibi SPECT with metabolism assessed by [^{18}F]-fluorodeoxyglucose (FDG) show a mismatch, as seen in Fig. 4.30.

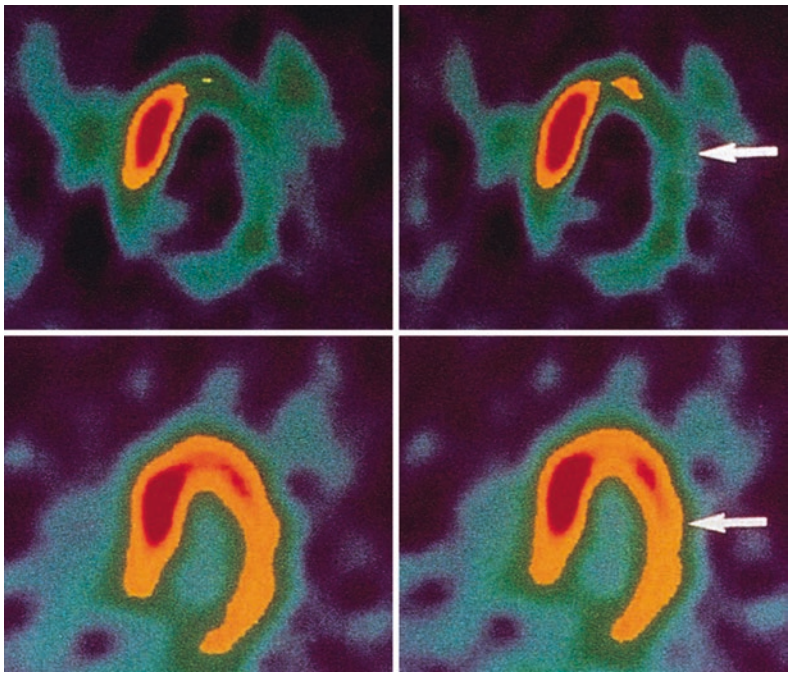

Fig. 4.30 Underestimation of myocardial viability by rest ^{99m}Tc-sestamibi SPECT. Using dual-isotope injection at rest (same physiologic state) and simultaneous acquisition using SPECT (accurate anatomical alignment), these images show mismatch between rest cardiac perfusion assessed by ^{99m}Tc-sestamibi and metabolism assessed by [^{18}F]-fluorodeoxyglucose (FDG). After oral glucose loading, the patient was injected with 10 mCi of FDG and 25 mCi of ^{99m}Tc-sestamibi at rest. Dual-isotope single acquisition SPECT was performed approximately 60 minutes later by positioning two 20% pulse-height analyzer windows symmetrically around the 140-keV photopeak of ^{99m}Tc and the 511-keV photopeak of FDG. The digital electronics of the camera permitted frame-by-frame decay correction for short-lived FDG. Thus, two separate sets of slices mapping the ^{99m}Tc-sestamibi and FDG distribution were simultaneously obtained, resulting in one-to-one correspondence in spatial registration. Rest ^{99m}Tc-sestamibi images in the horizontal long-axis plane (*top row*) show reduced perfusion in the apical and lateral regions (*arrow*). Corresponding FDG images (*bottom row*) show preserved metabolism in the apical and lateral regions, suggestive of viable myocardium (*arrow*) [37]

As listed on Table 4.5, ^{99m}Tc-sestamibi (isonitrile) and ^{99m}Tc-tetrofosmin are both lipophilic cationic complexes with similar myocardial uptake and blood clearance kinetics. However, the clearance of tetrofosmin from the lungs and the liver is faster than ^{99m}Tc-sestamibi, which may improve the resolution of cardiac images and reduce the overall radiation burden. Both ^{99m}Tc-sestamibi and ^{99m}Tc-tetrofosmin are taken up across the sarcolemmal and mitochondrial membranes of myocytes by passive distribution and are retained within the mitochondria at equilibrium, owing to a large negative transmembrane potential. Experimental studies with ^{99m}Tc-sestamibi have shown that myocardial uptake and clearance are related to the mitochondrial transmembrane potential and do not differ from ischemic to nonischemic regions. In addition, experimental studies of myocardial infarction, with and without reperfusion, have fueled optimism in the clinical use of ^{99m}Tc-sestamibi for myocardial viability assessment. In the clinical setting, however (with the exception of a few studies), both ^{99m}Tc-sestamibi and ^{99m}Tc-tetrofosmin appear to underestimate myocardial viability. Compared with ^{201}Tl and PET tracers, factors that may contribute to the impaired accumulation of ^{99m}Tc-sestamibi or ^{99m}Tc-tetrofosmin in viable regions at rest include differences in the extraction fraction, blood clearance, redistribution, and response to altered metabolic states. Perhaps a likely improvement in viability assessment could be achieved through nitrate administration before rest ^{99m}Tc-sestamibi injection and the quantitation of regional radiotracer uptake.

Lipid-soluble cationic compounds
140-keV photopeak energy, 6-hour physical half-life
First-pass extraction fraction ~60%
Uptake is passive across mitochondrial membranes
At equilibrium, retention within the mitochondria is due to a large negative transmembrane potential
Clearance from the intravascular compartment via hepatobiliary excretion
Minimal redistribution when compared with ^{201}Tl

Table 4.5 SPECT techniques: ^{99m}Tc-labeled Sestamibi and ^{99m}Tc-labeled Tetrofosmin

Table 4.6 lists the characteristics of another agent used in SPECT, ^{99m}Tc-teboroxime. ^{99m}Tc-teboroxime is a neutral, lipophilic BATO (boronic acid adducts of technetium dioxime) compound with a reported first-pass extraction of 88% at rest and 91% under hyperemic conditions. Unlike ^{99m}Tc-sestamibi and ^{99m}Tc-tetrofosmin, clearance of teboroxime from the myocardium is rapid and the washout rate is proportional to blood flow. In experimental studies, approximately two thirds of the teboroxime activity has been shown to clear from the heart, with a half-life of 3.6 minutes. Thus, both uptake and clearance of teboroxime from the myocardium are proportional to regional blood flow and are not confounded by tissue metabolism or other binding characteristics within the myocardium.

Neutral, lipophilic compound
140-keV photopeak energy, 6-hour physical half-life
High first-pass extraction fraction under hyperemic conditions (~91%)
Extraction by the myocardium remains linear even at high-flow conditions
Rapid clearance from the myocardium at a rate proportional to regional blood flow
Uptake and washout are independent of the metabolic status of the myocardial cells

Table 4.6 SPECT techniques: ^{99m}Tc-Teboroxime

PET Tracers and Techniques

Figure 4.31 shows examples of positron emission tomography (PET) myocardial perfusion images using rubidium-82 (^{82}Rb), which offer the potential for overlaying coronary anatomic information from hybrid PET/CT angiography. Gated ^{82}Rb PET images provide an indirect evaluation of abnormal myocardial perfusion as reflected in regional wall motion abnormalities during stress, as opposed to poststress with SPECT.

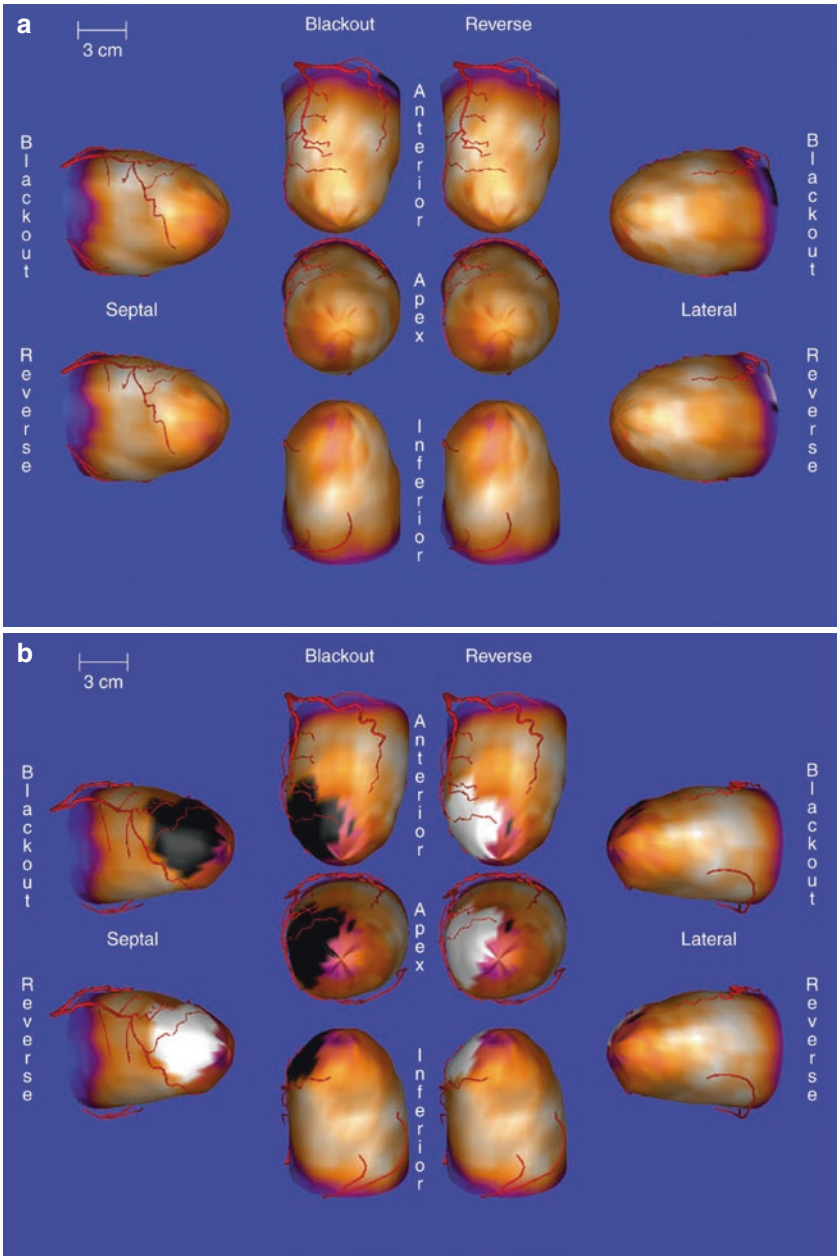

Fig. 4.31 Positron emission tomography (PET) techniques: rubidium-82 (^{82}Rb). Examples of three-dimensional (3D) surface-rendered models of normal (**a**) and abnormal (**b**) ^{82}Rb PET myocardial perfusion images are shown, with the potential for overlaying coronary anatomic information from hybrid PET/CT angiography. Although the first few minutes after the infusion of ^{82}Rb are not usually included in clinical acquisition protocols, it is precisely this period that is of interest if myocardial perfusion is to be quantified (**c**).

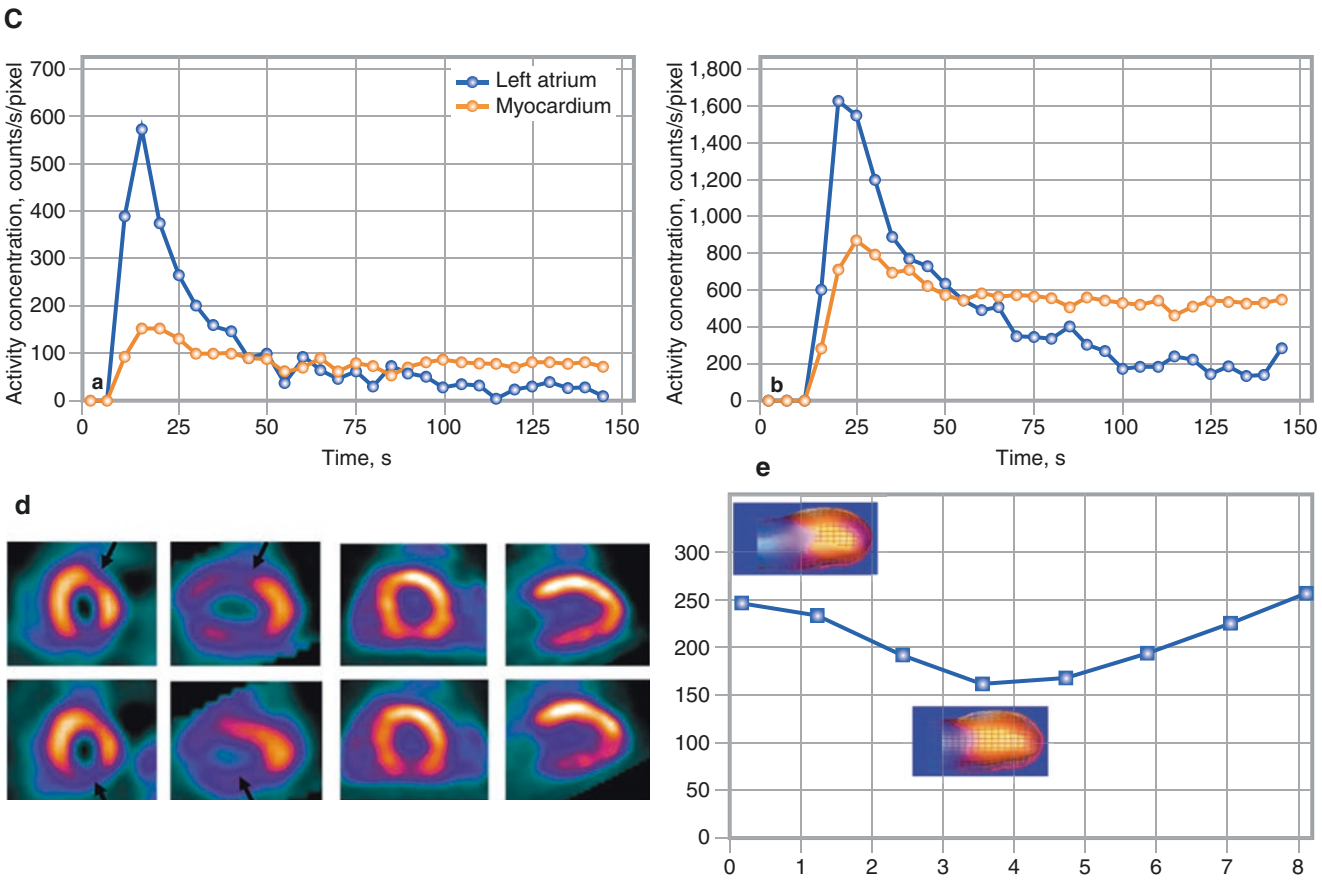

Fig. 4.31 (continued) Dynamic imaging of the heart during this time allows analysis of the ^{82}Rb concentration in both arterial blood and myocardial tissue as a function of time. ^{82}Rb time–activity curves are shown at rest (*left*) and after adenosine stress (*right*). The circles represent the activity concentration in the left atrium and in the myocardial tissue. The myocardial perfusion SPECT and ^{82}Rb PET studies show a disparity (**d**). Clinically indicated adenosine dual-isotope gated SPECT images (*left panel*) without attenuation correction show a regional ^{99m}Tc-sestamibi perfusion defect in the anterior and inferior regions (*arrows*). In the rest ^{201}Tl images, the anterior defect became reversible, but the inferior defect persisted. Corresponding ^{82}Rb PET myocardial perfusion tomograms performed in the same patient are shown in the *right panel*. PET images were acquired from a PET/CT scanner after an infusion of adenosine and 30 mCi of ^{82}Rb (*top*) and at rest following another 30-mCi infusion of ^{82}Rb (*bottom*). The ^{82}Rb PET images show normal distribution of the radiotracer in all myocardial regions, without evidence for a reversible or fixed defect to suggest myocardial ischemia or infarction. Although the high-energy positrons of ^{82}Rb degrade spatial resolution and the short half-life increases statistical noise, high-quality images free from attenuation artifacts can be produced with ^{82}Rb PET with only a 30-mCi injected dose. Finally, a three-dimensional display of gated ^{82}Rb PET images acquired during pharmacologic stress with adenosine is shown (**e**). Though gated myocardial perfusion SPECT images are acquired poststress, reflecting regional and global left ventricular function in the resting state, gated ^{82}Rb PET images are acquired during pharmacologic stress as well as at rest. As such, gated ^{82}Rb PET images provide an indirect evaluation of abnormal myocardial perfusion as reflected in regional wall motion abnormalities during stress, as opposed to poststress with SPECT. In this patient example, a surface rendering of end-diastolic and end-systolic images from gated adenosine ^{82}Rb PET is shown along with the time–activity curve. The left ventricular ejection fraction is calculated to be 36% during adenosine ^{82}Rb PET and 28% at rest. A postexercise gated SPECT left ventricular ejection fraction acquired in the same patient was calculated to be 32% [41]

Figure 4.32 presents experimental validation of ^{82}Rb for measuring myocardial blood flow. The kinetic model of ^{82}Rb is relatively "simple" because cellular trapping of ^{82}Rb is nonlinearly proportional to blood flow.

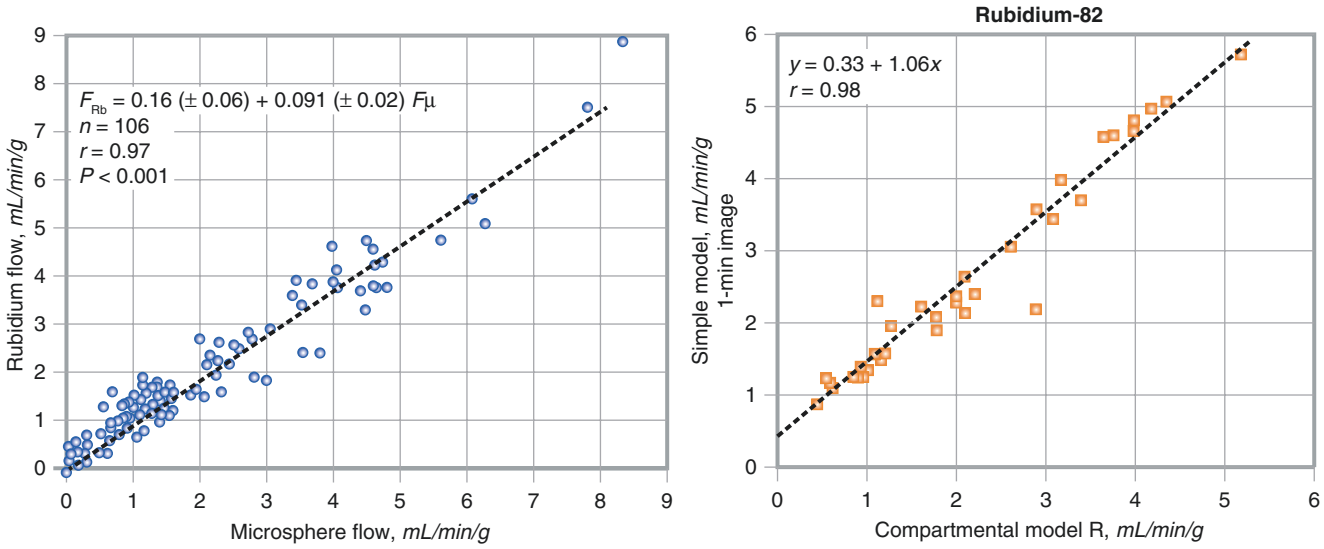

Fig. 4.32 Experimental validation of ^{82}Rb for measuring myocardial blood flow. The cellular trapping of ^{82}Rb is nonlinearly proportional to blood flow, making the kinetic model relatively "simple." (**a**) The initial verification of absolute myocardial perfusion with ^{82}Rb compared with microspheres is shown, measured by epicardial radiation detectors [42]. (**b**) Coronary flow reserve (CFR) measured by ^{82}Rb PET is validated using a "simple" flow model for flow-dependent ^{82}Rb extraction, compared with the more complex complete compartmental modeling, both having a comparable correlation with CFR measured by flowmeter [43]

PET myocardial perfusion images can reveal the severity and progression of coronary artery stenosis and coronary function, as shown in Fig. 4.33. Similarly, serial changes in PET perfusion images (Fig. 4.34) can be used to assess the response to treatment, predict outcomes, and provide insight into the progression or regression of coronary artery lesions and myocardial ischemia.

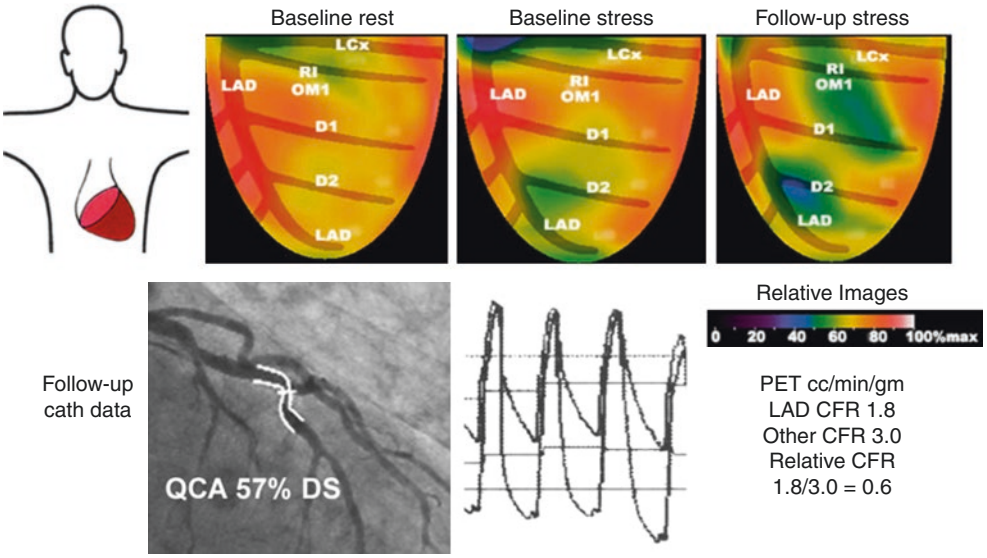

Fig. 4.33 Severity of anatomic coronary artery stenosis and coronary function. Relative uptake PET myocardial perfusion images are shown for a patient with known coronary artery disease and multiple risk factors; results at baseline (rest and stress) and 6 years later (follow-up stress) are shown. The follow-up PET study shows the progression of the stress-induced perfusion defect in the mid-left anterior descending (LAD) distribution (which was only 65% of the activity in the adjacent proximal areas of the heart) along with a new perfusion defect in the ramus intermedius or first obtuse marginal branch distribution. PET shows that the CFR in the distal LAD is reduced to 1.8, compared with an average of 3.0 in the rest of the heart proximally and 4.0 in healthy young volunteers. A coronary arteriogram shows concentric 57% mid-LAD stenosis by automated quantitative coronary arteriographic analysis (QCA); the fractional flow reserve (FFR) assessed by pressure wire measurements in the aorta and distal to the stenosis is 0.65. In view of concordant low CFR and FFR, a LAD stent was placed, with improvement in FFR to 0.92, indicating residual pressure gradient due to diffuse disease proximal to the stent. (From Gould [44]; with permission from Elsevier)

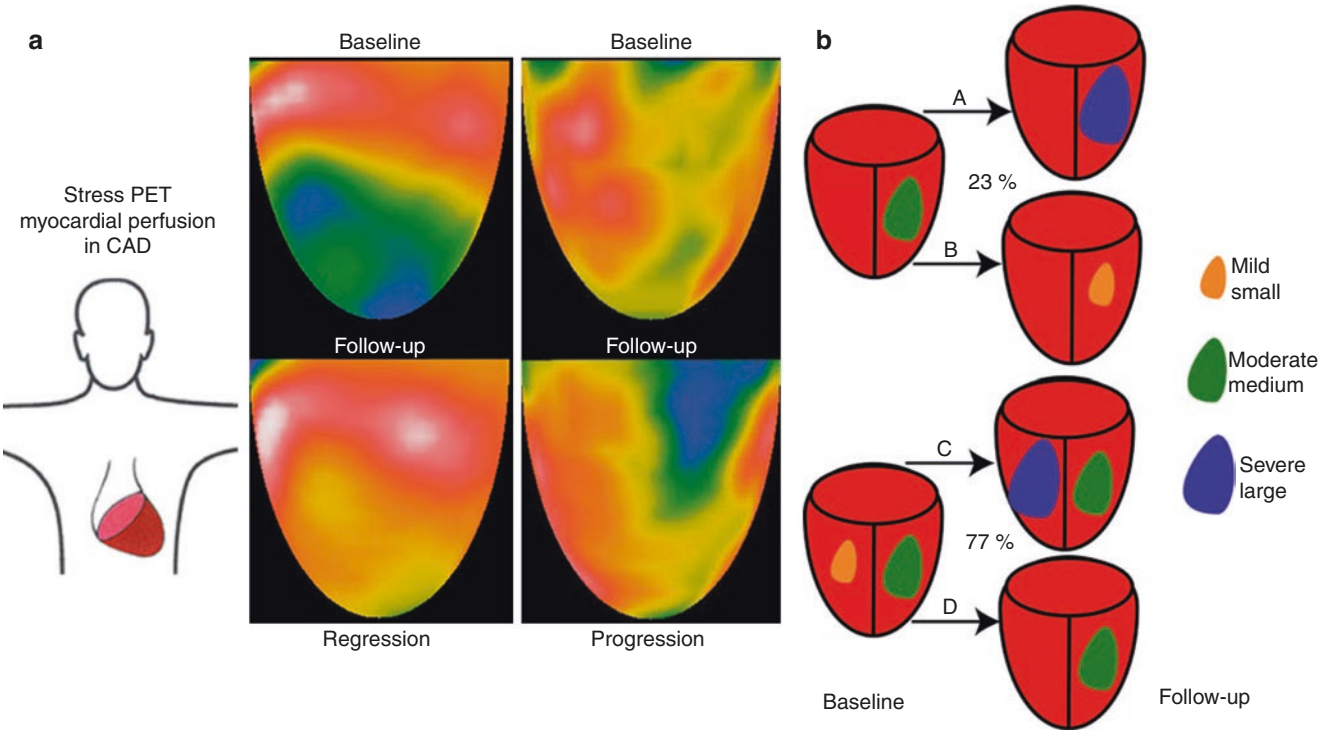

Fig. 4.34 Clinical impact of quantitative myocardial PET perfusion imaging. (**a**) Single views of stress PET relative perfusion images are shown for two different patients at baseline (*top row*) and follow-up (*bottom row*), one demonstrating regression and the other progression of coronary artery disease. (**b**) This schematic of stress PET images at baseline is compared with follow-up PET in various quadrant pairings. (From Gould [44]; with permission from Elsevier)

Figure 4.35 demonstrates the independent prognostic value of myocardial blood flow reserve (MFR) measurement by stress ^{82}Rb-PET in patients with myocardial ischemia. Patients shown to have impaired MFR had a higher incidence of major adverse cardiac events (MACE) at approximately 1 year of follow-up [45].

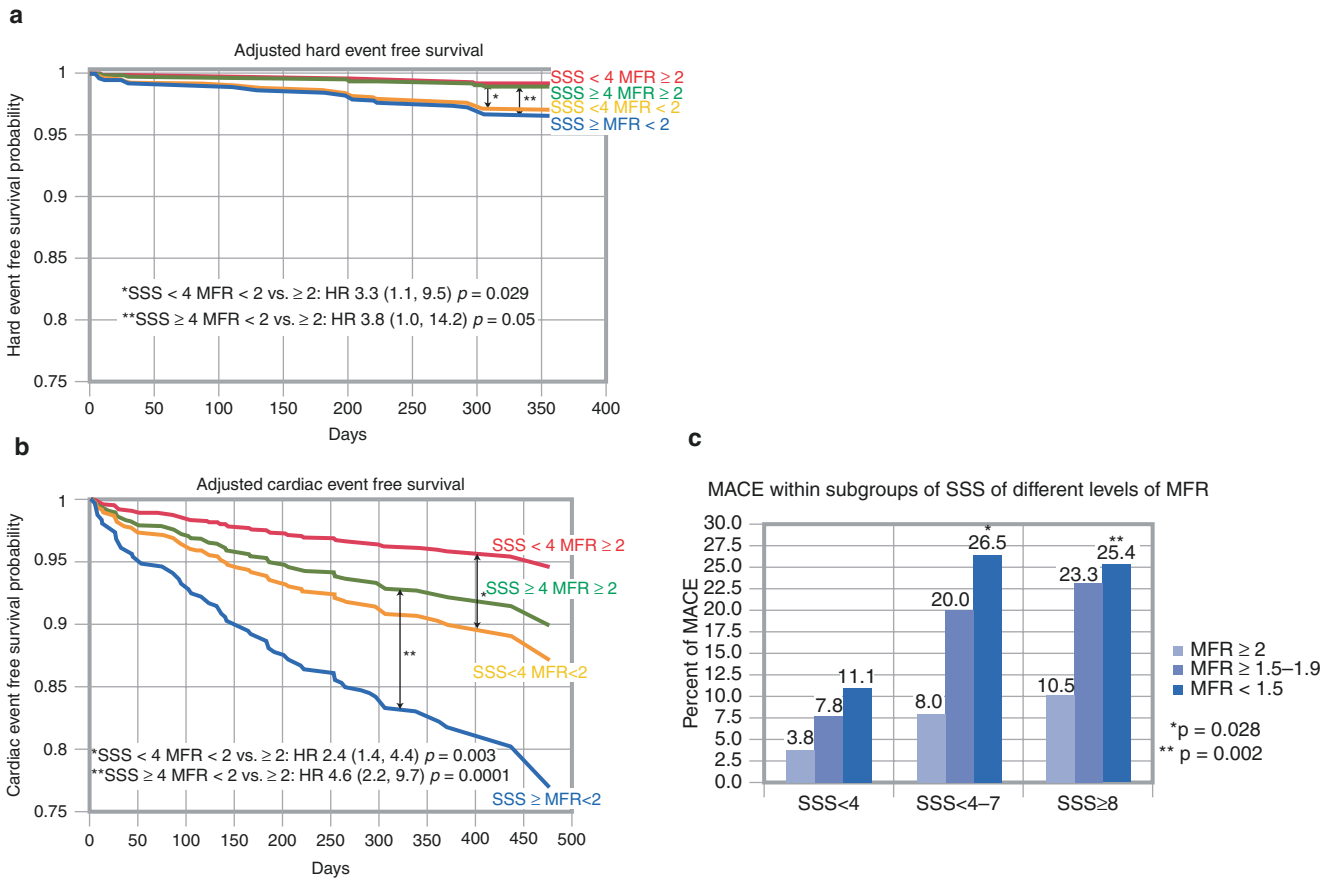

Fig. 4.35 Prognostic value of measurement by stress ^{82}Rb-PET. In a large cohort of patients referred for assessment of myocardial ischemia with ^{82}Rb-PET, the added and independent prognostic value of MFR was determined beyond the conventional relative myocardium radiotracer uptake on attenuation-corrected PET images. Patients with impaired ^{82}Rb MFR had a higher incidence of hard and major adverse cardiac events (MACE) (cardiac death, nonfatal myocardial infarction, late revascularization, or hospitalization for cardiac reasons) at approximately 1 year of follow-up. In the multivariable model analysis, ^{82}Rb MFR was an independent predictor of hard events (**a**) and MACE (**b**) over the summed stress score (SSS). MACE within subgroups of SSS for different levels of MFR is shown in (**c**). At any level of SSS, the prevalence of MACE is higher in patients with the lowest MFR (<1.5); among patients with overt ischemia, the difference from those with MFR ≥2 is statistically significant [45]

Another PET technique uses ^{15}O-water (Fig. 4.36), which is a freely diffusible tracer that correlates closely with perfusion as assessed by microspheres; its first-pass extraction fraction approaches unity. Because water can freely exchange across all normal tissue cells, the perfusable tissue fraction (PTF)—defined as the fractional volume of a given region of interest occupied by myocardium that is capable of exchanging water rapidly—should approach unity in normal myocardium and will be reduced in scarred myocardium.

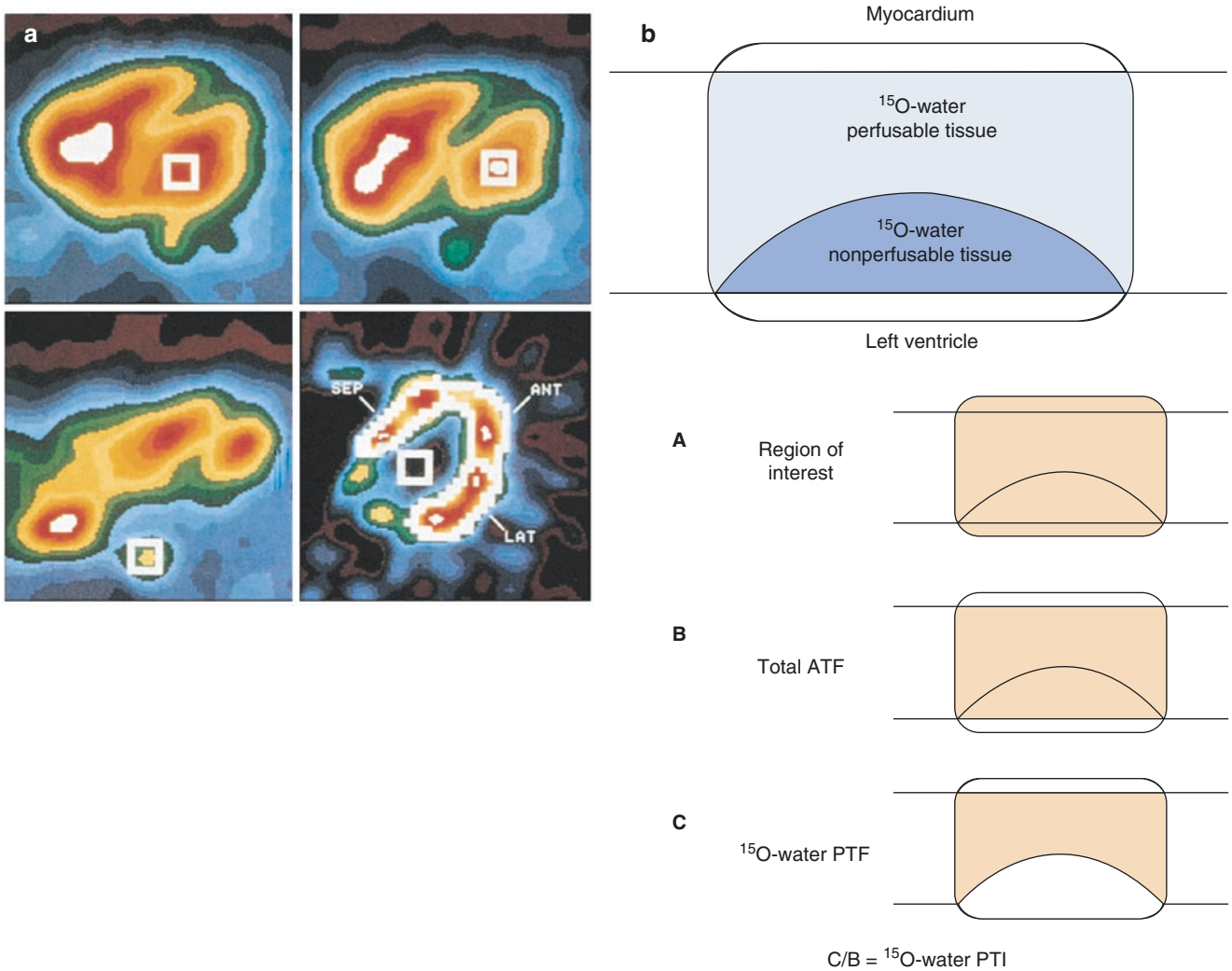

Fig. 4.36 PET techniques: ^{15}O-water. ^{15}O-water is a freely diffusible tracer that correlates closely with perfusion as assessed by microspheres, with a first-pass extraction fraction approaching unity. Because ^{15}O-water is in both the vascular space and myocardium, visualization of myocardial activity requires correction for activity in the vascular compartment. (**a**) Corrections for activity in the left atrium (*top left*), left ventricle (*top right*), and thoracic aorta (*bottom left*) are shown in a healthy patient after inhalation of 30–40 mCi of ^{15}O-carbon monoxide, which labels erythrocytes in vivo. The distribution of ^{15}O-water is shown in the left ventricular myocardium (*bottom right*) after correcting for vascular space. (**b**) The ability of ^{15}O-water to assess myocardial viability through modification of the blood flow information is shown. This method, termed *water perfusable tissue index* (PTI), is based on a measurement of perfusable tissue fraction (PTF) as a method to correct for the partial volume effects in ^{15}O-water studies [46]. PTF is defined as the fractional volume of a given region of interest occupied by myocardium that is capable of exchanging water rapidly. Using transmission and ^{15}O-blood pool images, the anatomic tissue fraction (ATF), a quantitative estimate of extravascular tissue density, is derived. The ratio of PTF to ATF thus represents the proportion of the extravascular tissue that is perfusable by ^{15}O-water. Because water can freely exchange across all normal tissue cells, the PTF should approach unity in normal myocardium and be reduced in scarred myocardium. A myocardial region of interest containing a mixture of ^{15}O-water perfusable and nonperfusable tissue is diagrammed. The volume of the region of interest is shown (*A*). ATF for the region of interest is produced by subtracting the blood pool (^{15}O-carbon monoxide) from the transmission images after normalizing the latter to tissue density (1.04 g/mL). The total ATF (*B*) represents the total extravascular tissue and contains both perfusable and nonperfusable tissue components. The ^{15}O-water PTF for the region of interest calculated from the ^{15}O-water data set identifies the mass of tissue within the region of interest that is capable of rapid trans-sarcolemmal exchange of water. Note that the nonperfusable or necrotic region is excluded from this parameter. The ^{15}O-water PTI is calculated by dividing ^{15}O-water PTF (*C*) by the total ATF (*B*) and represents the fraction of the total anatomic tissue that is perfusable by water. ANT—anterior; LAT—lateral; SEP—septal. (**a** *From* Bergmann et al. [47], with permission from Elsevier; **b** *From* Yamamoto et al. [48]; with permission from Wolters Kluwer)

The extractable perfusion tracer most commonly used with PET is ^{13}N-ammonia. At physiologic pH, ammonia is in its cationic form, with a physical half-life of 10 minutes. Myocardial distribution of ammonia is related inversely and nonlinearly to blood flow. Although the exact mechanism of ^{13}N-ammonia transport across the myocardial membrane has not been conclusively established, it has been suggested that ^{13}N-ammonia may cross cell membranes by passive diffusion or as ammonium ion ($^{13}NH+_4$) by the active sodium–potassium transport mechanism influenced by the concentration gradient across the cell membrane (Fig. 4.37). Once in the myocyte, myocardial retention of ^{13}N-ammonia involves predominantly the conversion of ^{13}N-ammonia and glutamic acid to ^{13}N-labeled glutamine mediated by ATP and glutamine synthetase. Hence, absolute quantification requires two- and three-compartment kinetic models that incorporate both extraction and retention rate constants. Quantification of ammonia is further complicated by the rapid degradation of ammonia, which occurs within 5 minutes after administration, producing metabolic intermediates, such as urea and glutamine, which are also extracted by the heart. Experimental studies suggest that the myocardial uptake of ammonia reflects absolute blood flows up to 2–2.5 mL/g/minute and plateaus at flows in the hyperemic range. In the clinical setting, 10–20 mCi of ^{13}N-ammonia is administered intravenously. Figure 4.38 shows an example of ^{13}N-ammonia PET and coronary angiography in a patient with coronary artery disease.

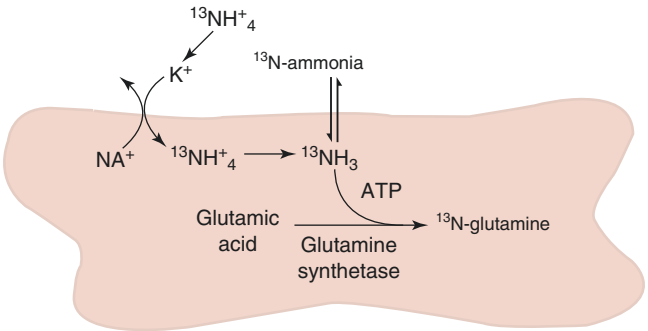

Fig. 4.37 PET techniques: ^{13}N-ammonia. It has been suggested that ^{13}N-ammonia may cross cell membranes by passive diffusion or as ammonium ion ($^{13}NH+_4$) by the active sodium–potassium transport mechanism influenced by the concentration gradient across the cell membrane. Once in the myocyte, myocardial retention of ^{13}N-ammonia involves predominantly the conversion of ^{13}N-ammonia and glutamic acid to ^{13}N-labeled glutamine mediated by ATP and glutamine synthetase

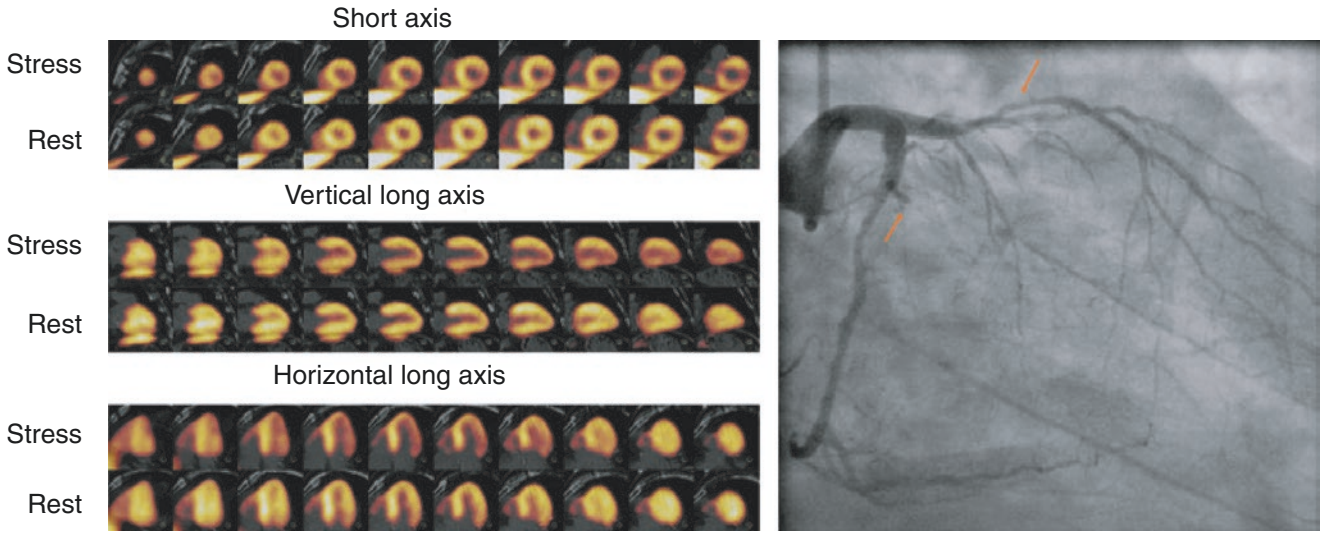

Fig. 4.38 ^{13}N-ammonia PET and coronary angiography in a patient with coronary artery disease [39]. These stress and rest ^{13}N-ammonia PET images of the heart in short-axis, vertical long-axis, and horizontal long-axis slices are shown from a 62-year-old patient who has type 2 diabetes. The stress images demonstrate a moderately decreased perfusion defect involving the lateral region of the left ventricle, extending to the inferolateral region—a defect that is completely reversible in rest images. The corresponding coronary angiography shows an occluded marginal branch of the left circumflex artery (*left arrow*), with diffuse 50% stenosis of the proximal LAD (*right arrow*) and a 50% stenosis in the mid-RCA (*not shown*). (*From* Schindler et al. [40]; with permission from Wiley)

The interplay between blood flow and metabolism in the extraction and retention of ^{13}N-ammonia is complex, as seen in Fig. 4.39. The early extraction phase of freely diffusible ^{13}N-ammonia reflects blood flow, whereas the later, slow-turnover phase reflects the metabolic trapping of ^{13}N-ammonia. Because the extent of ^{13}N-ammonia metabolism may depend on the ATP state of the myocyte, intracellular levels of ^{13}N-ammonia may reflect cellular viability, and late ammonia uptake (metabolic trapping) is a significantly better predictor of functional improvement after revascularization than is absolute blood flow. Thus, beyond ammonia's value as a perfusion tracer, late ammonia images provide important insight regarding cell membrane integrity and myocardial viability [49].

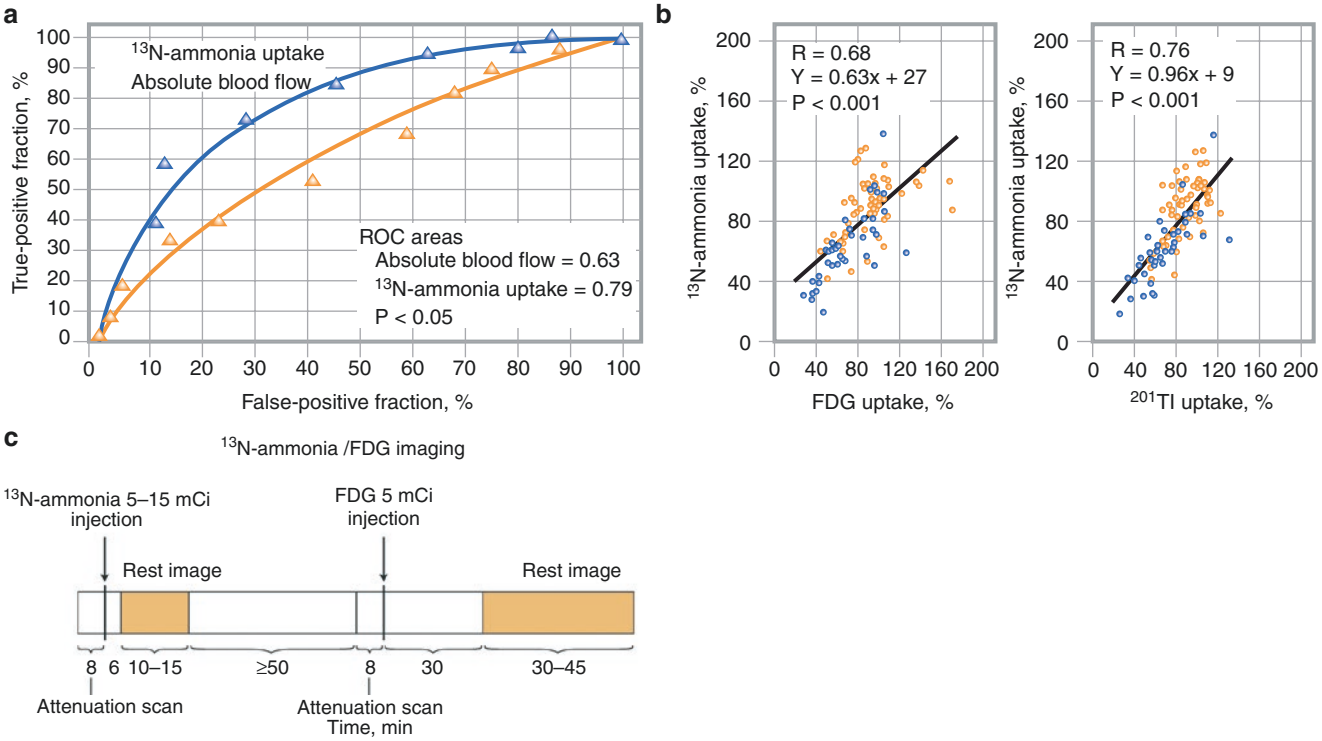

Fig. 4.39 Mechanism of ^{13}N-ammonia uptake. The interplay between blood flow and metabolism in the extraction and retention of ^{13}N-ammonia is complex. The early extraction phase of freely diffusible ^{13}N-ammonia reflects blood flow, whereas the later, slow-turnover phase reflects the metabolic trapping of ^{13}N-ammonia. In experimental animals, several investigators have shown that the myocardial extraction and retention of ^{13}N-ammonia are related not only to regional blood flow but also to myocardial oxygenation and metabolism. Under hypoxic or ischemic conditions, the reduction of intracellular ATP to concentrations in the range of the K_m for the enzyme–ATP complex could reduce intracellular ^{13}N-ammonia metabolism by glutamine synthetase. Because the extent of ^{13}N-ammonia metabolism may depend on the ATP state of the myocyte, intracellular levels of ^{13}N-ammonia may reflect cellular viability. (**a**) In patients with chronic coronary artery disease and left ventricular dysfunction, receiver-operating characteristic (ROC) curves were used to compare the abilities of late ammonia uptake (final 10–15 minutes of image acquisition) and absolute blood flow (early extraction phase, approximately 3 minutes after injection) to predict the functional improvement of asynergic regions after revascularization. The results show that late ammonia uptake (metabolic trapping) is significantly better than absolute blood flow as a predictor of functional improvement after revascularization. (**b**) There is a linear relationship between percent late ammonia uptake and [^{18}F]-fluorodeoxyglucose (FDG) uptake (*left*) and between ^{201}Tl uptake on redistribution imaging (*right*) in reversible (*orange circles*) and irreversible (*blue circles*) asynergic regions after revascularization. (**c**) Sequence and timing of ^{13}N-ammonia and FDG PET imaging for the assessment of myocardial viability. Beyond ammonia's value as a perfusion tracer, late ammonia images provide important insight regarding cell membrane integrity and myocardial viability [49]

PET approaches for the assessment of regional myocardial blood flow in mL/g/minute entail the intravenous injection of a positron-emitting perfusion tracer, such as rubidium-82, ^{13}N-ammonia, or ^{15}O-water, and the dynamic acquisition of images of the radiotracer passing through the central circulatory system to its extraction and retention in the left ventricular myocardium. Tracer kinetic models (one to three compartments) and operational equations are then applied to correct for the physical decay of the radioisotope, partial volume–related underestimation of the true myocardial tissue concentrations by assuming a uniform myocardial wall thickness of 1 cm, and spillover of radioactivity between the left ventricular blood pool and myocardium, to yield regional myocardial blood flows in absolute terms, mL/g/minute. The relative distribution of the radiotracer in the myocardium can also be assessed visually or semiquantitatively (as percent uptake relative to a reference region) from the final static image of the myocardium, obtained from the last (e.g., 900 s) frame of the PET image series, which can be displayed as a polar map. Table 4.7 summarizes the characteristics of the common PET myocardial perfusion tracers [38].

Characteristics	Rubidium-82	^{13}N-ammonia	^{15}O-Water
Half-life	78 s	9.8 minutes	2.4 minutes
Extraction	≈60%	≈80%	≈95%
Cyclotron onsite	No	Yes	Yes
Data acquisition	Dynamic, static, gated	Dynamic, static, gated	Dynamic
Scan duration	6 minutes	20 minutes	5 minutes
Dose-2D	40–60 mCi	15–25 mCi	40 mCi
Dose-3D	15–20 mCi	15 mCi	10 mCi
	30–40 mCi 3D		
	LSO		
Interval between doses	10 minutes	45 minutes	7 minutes
Image interpretation	Yes	Yes	No
Image quality	Good	Excellent	N/A

2D two-dimensional, *3D* three-dimensional, *LSO* Lutetium oxyorthosilicate

Table 4.7 PET myocardial perfusion tracers and image acquisition

Table 4.8 reviews a number of studies of the identification of flow-limiting coronary artery lesions by PET. Similar to SPECT, the identification of stress-induced scintigraphic perfusion defects by PET imaging provides important diagnostic and prognostic information. Unlike SPECT imaging, however, soft tissue attenuation correction with PET imaging is reliable and accurate. This accurate attenuation correction, in concert with the higher spatial resolution, may explain the 10% higher diagnostic accuracy of PET when compared with conventional SPECT imaging for the detection of flow-limiting coronary artery lesions. The advantages of PET imaging, however, pertain not only to the high spatial and depth-independent resolution but also to the ability to quantify the radiotracer uptake in the myocardial tissue and to assess rapid alterations of radiotracer activity concentrations in the arterial blood and myocardium, owing to a high temporal resolution in seconds. The latter advantages of PET imaging, combined with tracer kinetic compartment models, afford the noninvasive assessment of myocardial blood flow in absolute terms.

Year	Author	Radiotracer	Prior MI, %	Sensitivity, %	Specificity, %
2008	Esteves et al.	^{82}Rubidium	0	90 (36/40)	83 (10/12)
2007	Sampson et al.	^{82}Rubidium	0	93 (41/44)	83 (48/58)
1992	Marwick et al.	^{82}Rubidium	49	90 (63/70)	100 (4/4)
1992	Grover-McKay et al.	^{82}Rubidium	13	100 (16/16)	73 (11/15)
1991	Stewart et al.	^{82}Rubidium	42	83 (50/60)	86 (18/21)
1990	Go et al.	^{82}Rubidium	47	93 (142/152)	78 (39/50)
1989	Demer et al.	^{82}Rubidium, ^{13}N-ammonia	34	83 (126/152)	95 (39/41)
1988	Tamaki et al.	^{13}N-ammonia	75	98 (47/48)	100 (3/3)
1986	Gould et al.	^{82}Rubidium, ^{13}N-ammonia	Unknown	95 (21/22)	100 (9/9)
1982	Schelbert et al.	^{13}N-ammonia	0	97 (31/32)	100 (11/11)
Total				92 (573/636)	90 (192/224)

Table 4.8 Identification of flow-limiting coronary artery lesions by PET myocardial perfusion tracers

^{82}Rb (Table 4.9) is a generator-produced, short-lived, positron-emitting cation with biologic properties that are similar to potassium and ^{201}Tl. As with potassium and ^{201}Tl, the intracellular uptake of ^{82}Rb across the sarcolemmal membrane reflects active cation transport via the Na–K ATPase transport system. In patients with chronic coronary artery disease, myocardial uptake of ^{82}Rb is preserved in viable regions and is severely reduced in scarred regions. In the setting of acute myocardial injury and reperfusion, the initial uptake of ^{82}Rb reflects blood flow.

Positron-emitting cation with biologic properties similar to potassium
Emits two γ-rays, 511 keV each, with a short physical half-life of 75 s
Transported across the sarcolemmal membrane via the Na–K ATPase system
Initial uptake reflects myocardial blood flow
Kinetics of washout phase may be used as an index of viability

Table 4.9 PET techniques: ^{82}Rb

The improved diagnostic accuracy of PET over SPECT for detecting coronary artery disease (CAD) can be attributed to the higher photon energy of PET radiotracers, as well as to the improved resolution and intrinsic attenuation correction of PET cameras. The latter has enabled PET to assess absolute myocardial blood flow, from which coronary flow reserve (CFR) can be quantified noninvasively. However, outcome data with PET in patients with CAD are scarce. Figure 4.40 illustrates such outcome data In a group of patients with suspected myocardial ischemia who underwent ^{13}N-ammonia PET [50]. Beyond detection of CAD, ^{13}N-ammonia PET perfusion and CFR data are strong predictors of adverse outcome. CFR is an independent predictor of adverse outcome. It provides a 3-year "warranty" period of event-free survival for patients with normal CFR and normal PET perfusion. Conversely, in patients with abnormal perfusion, an impaired CFR has added value for predicting adverse outcomes.

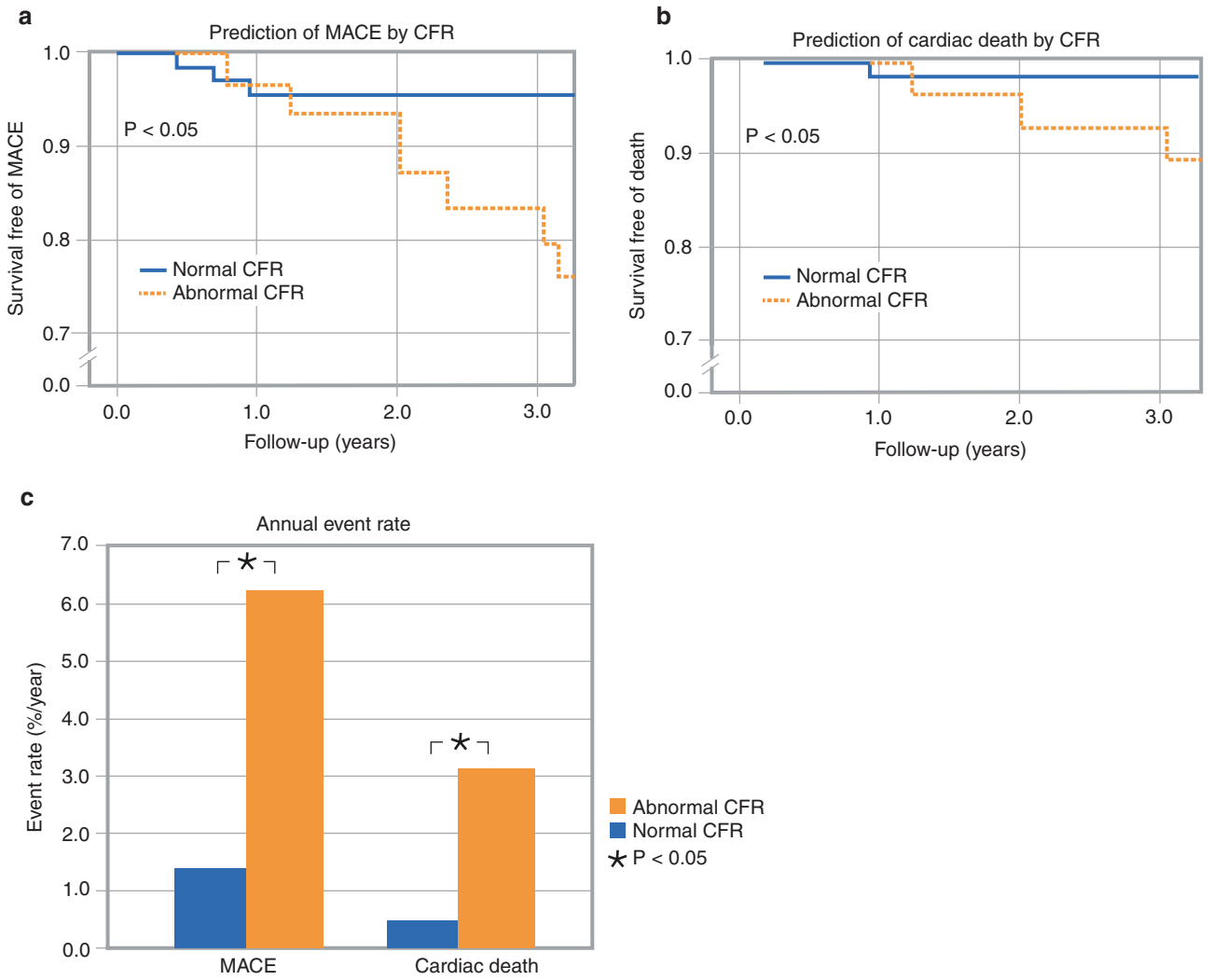

Fig. 4.40 Predictive value of major adverse cardiac events, including cardiac death, by stress ^{13}N-ammonia PET. Herzog et al. [50] assessed the long-term prognostic value of CFR over a mean of 5.4 years in patients with suspected myocardial ischemia who underwent ^{13}N-ammonia PET. Major adverse cardiac events (MACE) (cardiac death, nonfatal myocardial infarction, late revascularization, or hospitalization for cardiac reasons) occurred in 34% of the patients. Abnormal PET perfusion was associated with a higher incidence of MACE ($P < 0.001$) and cardiac death ($P < 0.05$). In patients with normal perfusion, abnormal CFR was independently associated with a higher annual event rate over 3 years compared with normal CFR for MACE (1.4% vs. 6.3%; $P < 0.05$) (**a**) and cardiac death (0.5% vs. 3.1%; $P < 0.05$) (**b**). This is reflected by the higher annual event rate (%/year) in abnormal CFR (**c**). In patients exhibiting abnormal perfusion, CFR remained predictive throughout the 10-year follow-up ($P < 0.001$). Beyond detection of CAD, ^{13}N-ammonia PET perfusion and CFR data are strong predictors of adverse outcome [50]

References

1. Cerqueira MD, Weissman NJ, Dilsizian V, Jacobs AK, Kaul S, Laskey WK, et al. American Heart Association Writing Group on Myocardial Segmentation and Registration for Cardiac Imaging. Standardized myocardial segmentation and nomenclature for tomographic imaging of the heart. A statement for healthcare professionals from the Cardiac Imaging Committee of the Council on Clinical Cardiology of the American Heart Association. Circulation. 2002;105:539–42.
2. Dilsizian V, Rocco TP, Freedman NM, Leon MB, Bonow RO. Enhanced detection of ischemic but viable myocardium by the reinjection of thallium after stress-redistribution imaging. N Engl J Med. 1990;323:141–6.
3. Maddahi J, Van Train K, Prigent F, Garcia EV, Friedman J, Ostrzega E, Berman D. Quantitative single photon emission computed thallium-201 tomography for detection and localization of coronary artery disease: optimization and prospective validation of a new technique. J Am Coll Cardiol. 1989;14:1689–99.
4. Fintel DJ, Links JM, Brinker JA, Frank TL, Parker M, Becker LC. Improved diagnostic performance of exercise thallium-201 single photon emission computed tomography over planar imaging in the diagnosis of coronary artery disease: a receiver operating characteristic analysis. J Am Coll Cardiol. 1989;13:600–12.
5. Iskandrian AS, Heo J, Kong B, Lyons E. Effect of exercise level on the ability of thallium-201 tomographic imaging in detecting coronary artery disease: analysis of 461 patients. J Am Coll Cardiol. 1989;14:1477–86.
6. Go RT, Marwick TH, MacIntyre WJ, Saha GB, Neumann DR, Underwood DA, Simpfendorfer CC. A prospective comparison of rubidium-82 PET and thallium-201 SPECT myocardial perfusion imaging utilizing a single dipyridamole stress in the diagnosis of coronary artery disease. J Nucl Med. 1990;31:1899–905.
7. Mahmarian JJ, Boyce TM, Goldberg RK, Cocanougher MK, Roberts R, Verani MS. Quantitative exercise thallium-201 single photo emission computed tomography for the enhanced diagnosis of ischemic heart disease. J Am Coll Cardiol. 1990;15:318–29.
8. Van Train KF, Maddahi J, Berman DS, Kiat H, Areeda J, Prigent F, Friedman J. Quantitative analysis of tomographic stress thallium-201 myocardial scintigrams: a multicenter trial. J Nucl Med. 1990;31:1168–79.
9. Kiat H, Maddahi J, Roy LT, Van Train K, Friedman J, Resser K, Berman DS. Comparison of technetium 99m methoxy isobutyl isonitrile and thallium 201 for evaluation of coronary artery disease by planar and tomographic methods. Am Heart J. 1989;117:1–11.
10. Iskandrian AS, Heo J, Kong B, Lyons E, Marsch S. Use of technetium-99m isonitrile (RP-30A) in assessing left ventricular perfusion and function at rest and during exercise in coronary artery disease, and comparison with coronary arteriography and exercise thallium-201 SPECT imaging. Am J Cardiol. 1989;64:270–5.
11. Kahn JK, McGhie I, Akers MS, Sills MN, Faber TL, Kulkarni PV, et al. Quantitative rotational tomography with 201Tl and 99mTc 2-methoxy-isobutyl-isonitrile. A direct comparison in normal individuals and patients with coronary artery disease. Circulation. 1989;79:1282–93.
12. Solot G, Hermans J, Merlo P, Chaudron JM, Luwaert R, Cheron P, et al. Correlation of 99Tcm-sestamibi SPECT with coronary angiography in general hospital practice. Nucl Med Commun. 1993;14:23–9.
13. Van Train KF, Garcia EV, Maddahi J, Areeda J, Cooke CD, Kiat H, et al. Multicenter trial validation for quantitative analysis of same-day rest-stress technetium-99m-sestamibi myocardial tomograms. J Nucl Med. 1994;35:609–18.
14. Azzarelli S, Galassi AR, Foti R, Mammana C, Musumeci S, Giuffrida G, Tamburino C. Accuracy of 99m-tetrofosmin myocardial tomography in the evaluation of coronary artery disease. J Nucl Cardiol. 1999;6:183–9.
15. Ritchie JL, Bateman TM, Bonow RO, Crawford MH, Gibbons RJ, Hall RJ, et al. Guidelines for clinical use of cardiac radionuclide imaging. Report of the American College of Cardiology/American Heart Association Task Force on Assessment of Diagnostic and Therapeutic Cardiovascular Procedures (Committee on Radionuclide Imaging), developed in collaboration with the American Society of Nuclear Cardiology. J Am Coll Cardiol. 1995;25:521–47.
16. Gibson RS, Watson DD, Craddock GB, Crampton RS, Kaiser DL, Denny MJ, Beller GA. Predication of cardiac events after uncomplicated myocardial infarction: a prospective study comparing predischarge exercise thallium-201 scintigraphy and coronary angiography. Circulation. 1983;68:321–36.
17. Kiat H, Berman DS, Maddahi J, De Yang L, Van Train K, Rozanski A, Friedman J. Late reversibility of tomographic myocardial thallium-201 defects: an accurate marker of myocardial viability. J Am Coll Cardiol. 1988;12:1456–63.
18. Cloninger KG, DePuey EG, Garcia EV, Roubin GS, Robbins WL, Nody A, et al. Incomplete redistribution in delayed thallium-201 single photon emission computed tomographic (SPECT) images: an overestimation of myocardial scarring. J Am Coll Cardiol. 1988;12:955–63.
19. Dilsizian V. Thallium-201 scintigraphy: experience of two decades. In: Dilsizian V, editor. Myocardial viability: a clinical and scientific treatise. Armonk: Futura; 2000. p. 265–313.
20. Zimmermann R, Mall G, Rauch B, Zimmer G, Gabel M, Zehelein J, et al. Residual 201Tl activity in irreversible defects as a marker of myocardial viability. Clinicopathological study. Circulation. 1995;91:1016–21.
21. Kayden DS, Sigal S, Soufer R, Mattera J, Zaret BL, Wackers FJ. Thallium-201 for assessment of myocardial viability: quantitative comparison of 24-hour redistribution imaging with imaging after reinjection at rest. J Am Coll Cardiol. 1991;18:1480–6.
22. Kitsiou AN, Srinivasan G, Quyyumi AA, Summers RM, Bacharach SL, Dilsizian V. Stress-induced reversible and mild-to-moderate irreversible thallium defects: are they equally accurate for predicting recovery of regional left ventricular function after revascularization? Circulation. 1998;98:501–8.
23. Petretta M, Cuocolo A, Bonaduce D, Nicolai E, Cardei S, Berardino S, et al. Prognostic value of thallium reinjection after stress-redistribution imaging in patients with previous myocardial infarction and left ventricular dysfunction. J Nucl Med. 1997;38:195–200.
24. Arrighi JA, Dilsizian V. Identification of viable, nonfunctioning myocardium. In: Brown DL, editor. Cardiac intensive care. Philadelphia: WB Saunders; 1998. p. 307–27.
25. Gioia G, Milan E, Giubbini R, DePace N, Heo J, Iskandrian AS. Prognostic value of tomographic rest-redistribution thallium-201 imaging in medically treated patients with coronary artery disease and left ventricular dysfunction. J Nucl Cardiol. 1996;3:150–6.
26. Gioia G, Powers J, Heo J, Iskandrian AS. Prognostic value of rest-redistribution tomographic thallium-201 imaging in ischemic cardiomyopathy. Am J Cardiol. 1995;75:759–62.
27. Pagley PR, Beller GA, Watson DD, Gimple LW, Ragosta M. Improved outcome after coronary bypass surgery in patients with ischemic cardiomyopathy and residual myocardial viability. Circulation. 1997;96:793–800.
28. Piwnica-Worms D, Chiu ML, Kronauge JF. Divergent kinetics of 201Tl and 99mTc-SESTAMIBI in cultured chick ventricular myocytes during ATP depletion. Circulation. 1992;85:1531–41.
29. Narahara KA, Villanueva-Meyer J, Thompson CJ, Brizendine M, Mena I. Comparison of thallium-201 and technetium-99m hexakis 2-methoxyisobutyl isonitrile single-photon emission computed tomography for estimating the extent of myocardial

ischemia and infarction in coronary artery disease. Am J Cardiol. 1990;66:1438–44.
30. Leon AR, Eisner RL, Martin SE, Schmarkey LS, Aaron AM, Boyers AS, et al. Comparison of single-photon emission computed tomographic (SPECT) myocardial perfusion imaging with thallium-201 and technetium-99m sestamibi in dogs. J Am Coll Cardiol. 1992;20:1612–25.
31. Li QS, Solot G, Frank TL, Wagner HN Jr, Becker LC. Myocardial redistribution of technetium-99m-methoxyisobutyl isonitrile (SESTAMIBI). J Nucl Med. 1990;31:1069–76.
32. Dilsizian V, Arrighi JA, Diodati JG, Quyyumi AA, Alavi K, Bacharach SL, et al. Myocardial viability in patients with chronic coronary artery disease: comparison of 99mTc-sestamibi with thallium reinjection and [18F]fluorodeoxyglucose. Circulation. 1994;89:578–87.
33. Franceschi M, Guimond J, Zimmerman RE, Picard MV, English RJ, Carvalho PA, et al. Myocardial clearance of Tc-99m hexakis-2-methoxy-2-methylpropyl isonitrile (MIBI) in patients with coronary artery disease. Clin Nucl Med. 1990;15:307–12.
34. Bisi G, Sciagrà R, Santoro GM, Rossi V, Fazzini PF. Technetium-99m-sestamibi imaging with nitrate infusion to detect viable hibernating myocardium and predict postrevascularization recovery. J Nucl Med. 1995;36:1994–2000.
35. Mehry Y, Latour JG, Arsenault A, Rousseau G. Effect of coronary reperfusion on technetium-99m methoxyisobutylisonitrile uptake by viable and necrotic myocardium in the dog. Eur J Nucl Med. 1992;19:503–10.
36. Udelson JE, Coleman PS, Metherall J, Pandian NG, Gomez AR, Griffith JL, et al. Predicting recovery of severe regional ventricular dysfunction: comparison of resting scintigraphy with 201Tl and 99mTc-sestamibi. Circulation. 1994;89:2552–61.
37. Delbeke D, Videlefsky S, Patton JA, Campbell MG, Martin WH, Ohana I, Sandler MP. Rest myocardial perfusion/metabolism imaging using simultaneous dual-isotope acquisition SPECT with technetium-99m-MIBI/fluorine-18-FDG. J Nucl Med. 1995;36:2110–9.
38. Dilsizian V, Bacharach SL, Beanlands SR, Bergmann SR, Delbeke D, Dorbala S, Gropler RJ, Knuuti J, Schelbert H, Travin M. ASNC Imaging Guidelines/SNMMI Procedure Standard for Positron Emission Tomography (PET) Nuclear Cardiology Procedures. J Nucl Cardiol 2016;23(5):1187–226.
39. Schindler TH, Dilsizian V. Coronary Microvascular Dysfunction: Clinical Considerations and Noninvasive Diagnosis. J Am Coll Cardiol Img 2020;13:140–55.
40. Schindler TH, Valenta I, Dilsizian V. PET assessment of myocardial perfusion. In: Dilsizian V, Pohost GM, editors. Cardiac CT, PET, and MR. 2nd ed. Chichester: Wiley-Blackwell; 2009. p. 95–117.
41. Lodge MA, Braess H, Mahmoud F, Suh J, Englar N, Geyser-Stoops S, et al. Developments in nuclear cardiology: transition from SPECT to PET/CT. J Invasive Cardiol. 2005;17:491–6.
42. Goldstein RA, Mullami NA, Fisher D, Marani S, Gould K, O'Brien HA. Myocardial perfusion with rubidium-82. II. The effects of metabolic and pharmacologic interventions. J Nucl Med. 1983;24:907–15.
43. Yoshida K, Mullami NA, Gould KL. Coronary flow and flow reserve by PET simplified for clinical applications using rubidium-82 or nitrogen-13-ammonia. J Nucl Med. 1996;37:1701–12.
44. Gould K. Does coronary flow trump coronary anatomy? JACC Cardiovasc Imaging. 2009;2:1009–23.
45. Ziadi MC, DeKemp RA, Williams KA, Guo A, Chow BJ, Renaud JM, et al. Impaired myocardial flow reserve on rubidium-82 positron emission tomography imaging predicts adverse outcomes in patients assessed for myocardial ischemia. J Am Coll Cardiol. 2011;58:740–8.
46. Iida H, Rhodes CG, de Silva R, Yamamoto Y, Araujo LI, Maseri A, Jones T. Myocardial tissue fraction: correction for partial volume effects and measure of tissue viability. J Nucl Med. 1991;32:2169–75.
47. Bergmann SR, Herrero P, Markham J, Weinheimer CJ, Walsh MN. Noninvasive quantitation of myocardial blood flow in human subjects with oxygen-15-labeled water and positron emission tomography. J Am Coll Cardiol. 1989;14:639–52.
48. Yamamoto Y, de Silva R, Rhodes CG, Araujo LI, Iida H, Rechavia E, et al. A new strategy for the assessment of viable myocardium and regional myocardial blood flow using 15O-water and dynamic positron emission tomography. Circulation. 1992;86:167–78.
49. Kitsiou AN, Bacharach SL, Bartlett ML, Srinivasan G, Summers RM, Quyyumi AA, Dilsizian V. 13N-ammonia myocardial blood flow and uptake: relation to functional outcome of asynergic regions after revascularization. J Am Coll Cardiol. 1999;33:678–86.
50. Herzog BA, Husmann L, Valenta I, Gaemperli O, Siegrist PT, Tay FM, et al. Long-term prognostic value of 13N-ammonia myocardial perfusion positron emission tomography. J Am Coll Cardiol. 2009;54:150–6.

Physiologic and Pharmacologic Stressors

5

D. Douglas Miller

Introduction

The global phenomena of population aging and obesity have fundamentally changed the current pattern of stress imaging, with pharmacologic stress imaging growing steadily in importance. Though clinicians prefer maximal exercise stress imaging for suitable patients, the demand for pharmacologic imaging has driven significant evolution in pharmacologic stress protocols, stimulated new drug development, and expanded indications for testing. Published evidence, expert guidelines, and clinical practice all reflect, to varying degrees, this growth and evolution. The results of exercise and pharmacologic stress imaging studies continue to influence patient management decisions in the diverse population of patients with known or suspected coronary artery disease (CAD).

The target populations benefitting most from the proven incremental diagnostic and prognostic value of drug stress imaging are those at a intermediate risk of severe CAD and related serious cardiac events due to their comorbid conditions (*i.e.*, generalized vascular disease) and/or poor functional capacity, which renders them unable to perform the preferred stress modality, maximal dynamic exercise stress.

Triaging patients for further cardiac evaluation based on clinical risk predictors and the type of surgical procedure is now recommended and widely practiced. Pharmacologic stress myocardial perfusion imaging is an excellent adjunctive method for identifying high-risk and low-risk patients from within an intermediate clinical risk pool. Stress imaging results obtained with each of the available pharmacologic stress agents are qualitatively similar for discriminating between low-risk and high-risk groups for perioperative cardiac events. The combined use of electrocardiograph-gated single-photon emission CT (SPECT) perfusion imaging and the left ventricular ejection fraction add further prognostic value. Patients with more extensive stress-induced myocardial hypoperfusion or ischemia are at highest risk of future cardiac events, and should undergo coronary angiography with the goal of prolonging survival via preoperative coronary revascularization, where appropriate. The 2016 American Society of Nuclear Cardiology imaging guidelines reflect a broad-based medical consensus in support of these expert, evidence-based recommendations for pharmacologic and physiologic stress [1].

D. D. Miller (✉)
Department of Cardiology, Augusta University Medical Center,
Augusta, GA, USA
e-mail: DDMILLER@augusta.edu

V. Dilsizian, J. Narula (eds.), *Atlas of Nuclear Cardiology*, https://doi.org/10.1007/978-3-030-49885-6_5

Physiologic Stress

The goal of exercise testing is to evaluate the physiologic response of the organs and systems involved (especially the skeletal muscle, lungs, and heart) to an increase in physical stress [2]. Figures 5.1, 5.2, 5.3, and 5.4 illustrate exercise testing and the effects of exercise on the physiology of the skeletal muscles and the respiratory and cardiovascular systems.

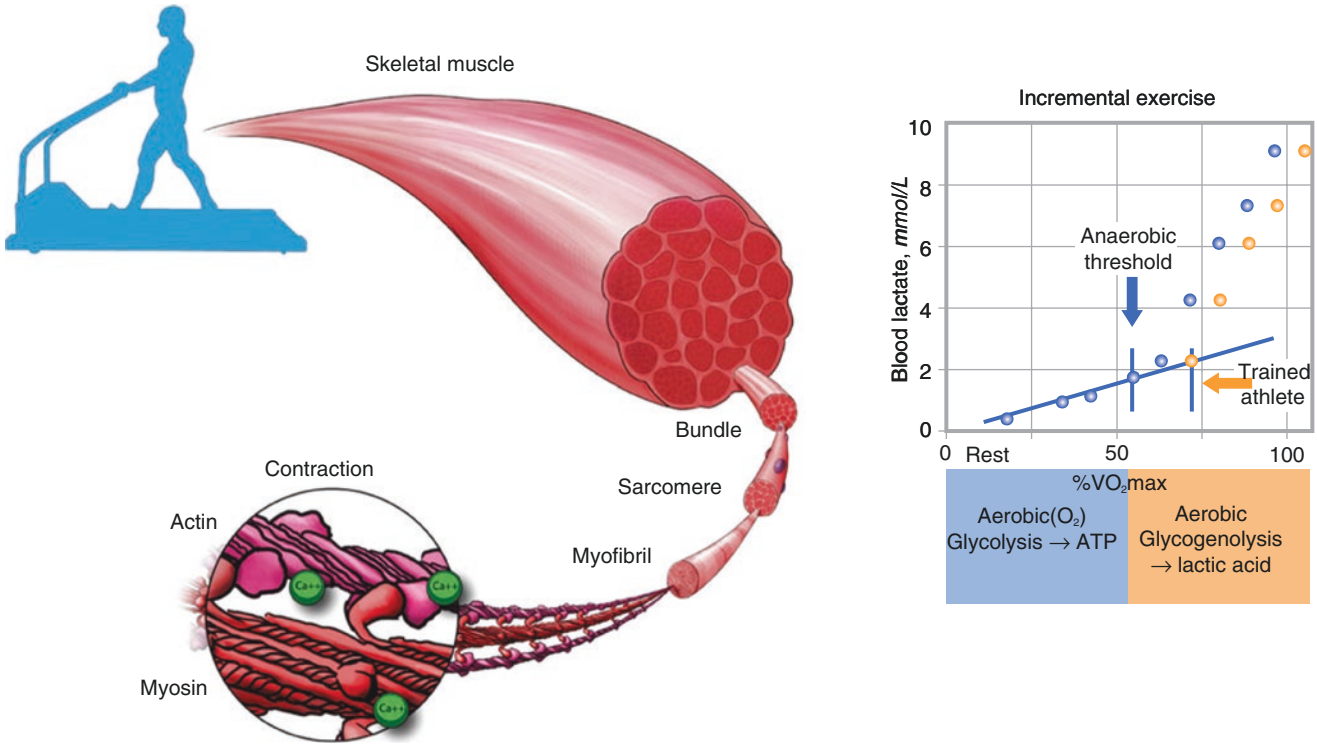

Fig. 5.1 Exercise testing. Dynamic exercise stress testing combined with noninvasive imaging remains the preferred method for the detection of obstructive coronary artery disease among candidates who can be expected to achieve greater than 85% of their age-predicted peak maximal heart rate and five metabolic equivalents (METs) [3]. One MET equals the oxygen uptake at rest (i.e., 1 MET = resting oxygen uptake = 3.5 mL of oxygen per kg/min). Functional classes III and IV are associated with less than 3 METs of exercise capacity; class I and normal individuals usually can exceed 6 METs. Postobstructive myocardial ischemia can cause regional electrocardiographic ST segment depression, myocardial blood flow tracer perfusion defects, and/or ventricular wall motion abnormalities. ATP adenosine triphosphate

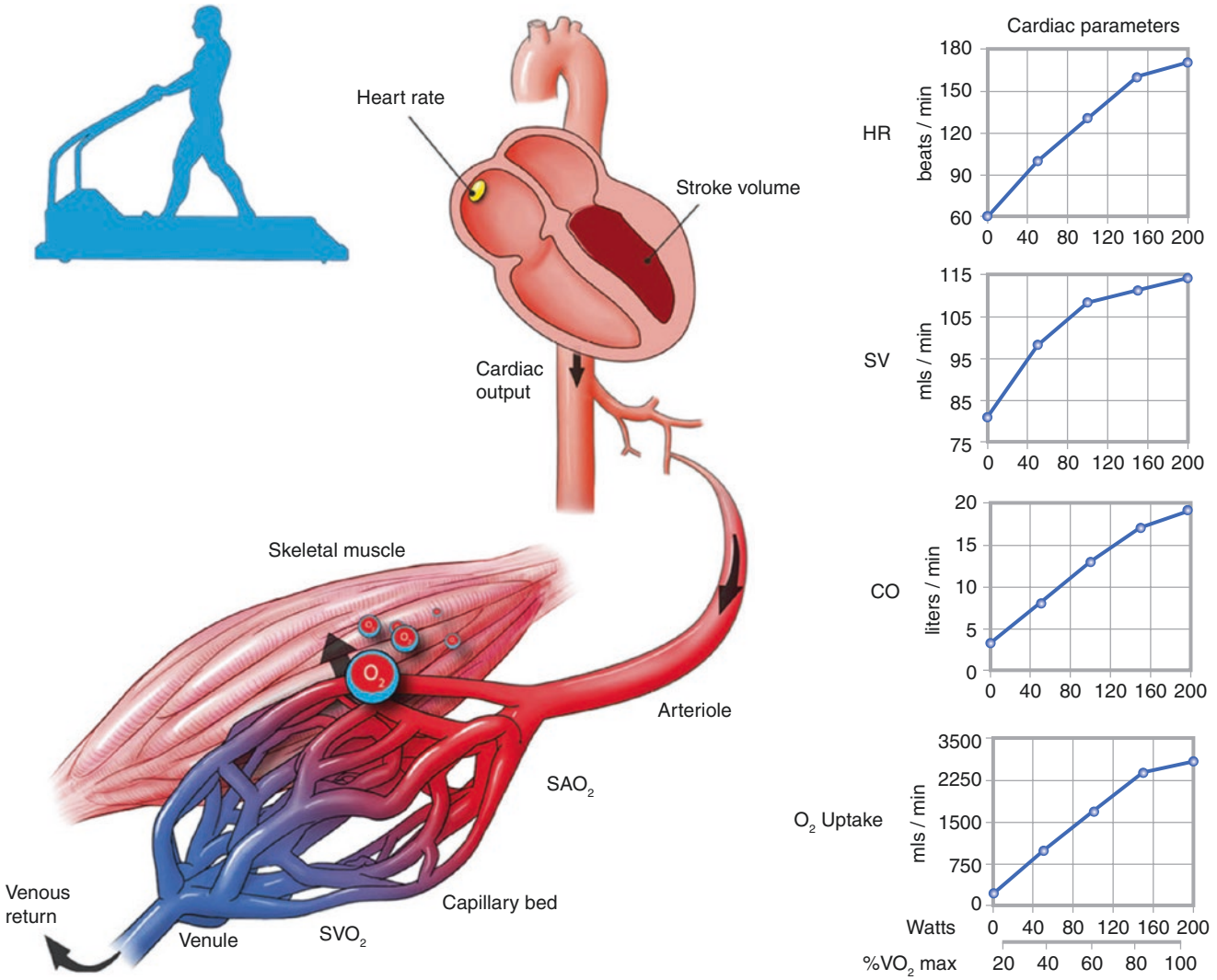

Fig. 5.2 Skeletal muscle physiology. Aerobic respiration (in the presence of oxygen, O_2) is activated during physical exercise requiring metabolic energy (adenosine triphosphate, ATP) expenditure by large skeletal muscle groups [4]. The ATP energy used during moderate exercise (such as treadmill exercise stress testing) is derived from a combination of muscle fatty acid and glucose oxidation. Skeletal muscle contraction occurs following the binding of acetylcholine to peripheral nerves, which causes transmembrane sodium and potassium transients that generate action potentials. Myofibril-level contraction occurs when the action potential triggers calcium (Ca^{++}) transients and where local ATPase activity results in actin-myosin cross-bridging. Ca^{++} is then resequestered in the presence of ATP, causing cross-bridge separation and myofibril relaxation. During exercise, muscle blood vessels dilate and blood flow increases to provide adequate oxygenation for the aerobic breakdown of pyruvic acid into ATP; ATP and creatine phosphate recycles adenosine diphosphate into ATP. If muscular exertion (i.e., metabolic demand) exceeds the available oxygen (i.e., O_2 supply), ATP generation from pyruvic acid falls short, and additional ATP must be generated by anaerobic glycogenolysis. The maximum oxygen uptake (MVO_2)—the maximum rate of oxygen consumption during the aerobic catabolism of pyruvic acid—is determined by age, gender, and body size. The anaerobic threshold (AT) occurs at 50–60% of MVO_2, the point at which excess blood lactic acid is generated. Beyond the AT, pyruvic acid is converted to lactic acid, which accumulates in the muscle, causing muscle pain and fatigue. In recovery from exercise, lactic acid diffuses from muscle, the O_2 "debt" is paid back with extra oxygenation from other sources, and excess lactic acid is catabolized by the liver into carbon dioxide and water. Trained elite athletes (especially those with good genes) have a 40–45% higher MVO_2 than untrained individuals, in association with lower lactic acid buildup and O_2 debts during exercise. Training can increase MVO_2 by approximately 10%. (The "training effect" increases the exercise heart rate and stroke volume [SV].) Athletes also exhibit a greater alveolar O_2-diffusing capacity and are able to reach 75–80% of MVO_2 aerobically without significant lactate production (i.e., exhibiting a higher AT). SV plateaus at an oxygen uptake (VO_2) of 40–60% of MVO_2 in athletes (150–170 mL/beat/min) and untrained individuals (100–120 mL/beat/min). Training effects on SV result in an increased circulating blood volume and cardiac output and reduced resting heart rate (HR) and blood pressure. Muscle training also affects VO_2 by causing longer-term changes in cellular metabolism and cardiac myocyte morphology (i.e., hypertrophy). MVO_2 declines with age, as the maximal HR declines by 7% with each decade after 30 years of age

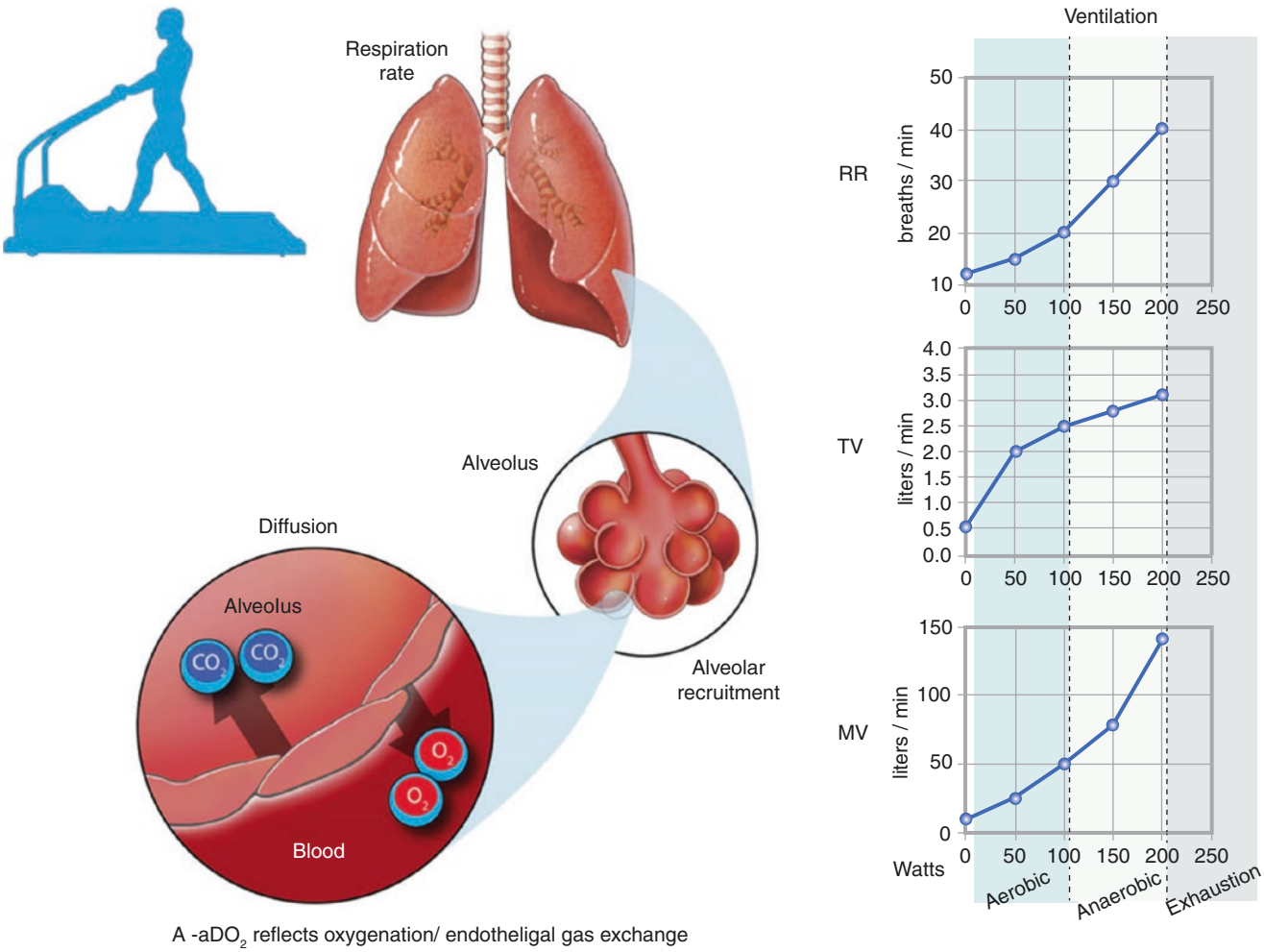

Fig. 5.3 Respiratory physiology. Respiration provides oxygen (O_2) to tissues and removes carbon dioxide (CO_2). This process requires a combination of: (1) pulmonary ventilation, (2) alveolar recruitment and O_2/CO_2 gas exchange, (3) O_2/CO_2 transport to and from cells, and (4) neural regulation of ventilation. The alveolar–arteriolar O_2 difference (A-aDO_2) reflects oxygenation and pulmonary endothelial cell gas-exchange efficiency. Pulmonary ventilation increases as the respiratory rate (RR), tidal volume (TV), and minute ventilation (MV) all increase. Resting oxygen uptake increases up to 20-fold at a near-maximum exercise level via the first three respiratory components listed above, in an effort to maintain homeostasis, a linear balance between increasing respiratory O_2 consumption and pulmonary ventilation. At maximal exercise levels, pulmonary ventilation is greater than 100 L/min, and maximal breathing capacity is greater than 150 L/min; this approximately 50% excess of pulmonary ventilation capacity means that the respiratory system is not typically rate-limiting to aerobic muscular exercise. Of note, the O_2 saturation in the arterial blood does not decrease during maximal exercise, and the arterial CO_2 levels do not rise. Central nervous system signals, as well as peripheral joint and muscular reflexes, stimulate the brain's respiratory and vasomotor centers to increase pulmonary ventilation, maintaining the normal O_2 content in the arterial blood

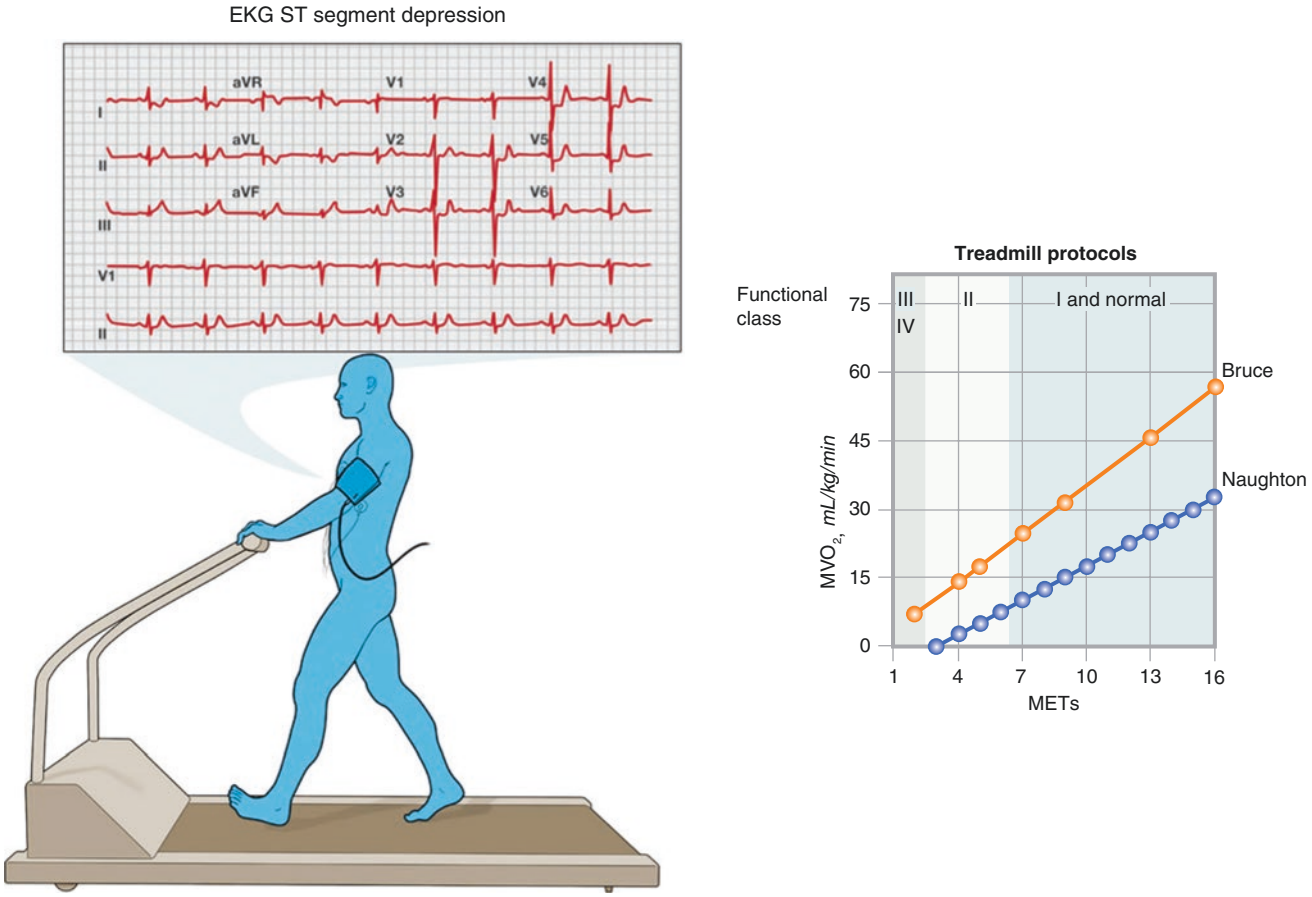

Fig. 5.4 Cardiovascular physiology. The cardiovascular system pumps oxygenated blood and nutrients to exercising muscles. Resting muscle metabolism demands approximately 20% of total blood flow, increasing to more than 80% during strenuous exercise. The cardiac output (CO), consisting of the heart rate × stroke volume, is a major determinant of oxygen (O_2) uptake (VO_2). The Fick equation is used to determine VO_2 in relation to O_2 supply to exercising muscles. The resting arterial–venous O_2 saturation difference (a-vDO_2) reflects the capillary bed O_2 extraction. A resting a-vDO_2 is 4 mL of O_2/dL of blood and is affected by arterial O_2 content, shunting of blood to muscles, and muscle extraction of O_2. Resting a-vDO_2 is greater than 5.5 mL/dL in low cardiac output states. The a-vDO_2 rises during intensive exercise to 18 mL/dL at peak effort

Exercise increases the activity of several components of the cardiovascular system:

- Heart rate (HR) (as the result of epinephrine and lactic acid release into the blood)
- Stroke volume
- Cardiac output
- Systolic blood pressure (BP)
- Mean arterial pressure
- Peripheral blood flow redistribution from inactive organs to skeletal muscle

Heart rate and blood flow are centrally controlled, with the brain centers receiving peripheral inputs. Baroreceptors in the carotid arteries, aorta, and right atrium stimulated by increased BP, cause greater parasympathetic activity, except during exercise, when sympathetic activity predominates. Chemoreceptors in the aorta and carotid arteries, which are stimulated by reduced blood oxygen concentration cause increased parasympathetic and reduced sympathetic activity.

Table 5.1 lists the variables in exercise hemodynamics, the normal peak responses, and the causes of decreases. Cardiac stroke volume (SV) is determined by left ventricular (LV) end-diastolic volume (preload), mean aortic blood pressure (BP) (or afterload), and LV contractility (from norepinephrine and epinephrine effects on calcium transients in cardiac myocytes). SV increases during exercise until reaching approximately 40% of maximum oxygen uptake (MVO_2, from 80 to 120 mL/beat). Heart rate (HR) increases during exercise until MVO_2 is reached (from 70 to 200 beats/min). Cardiac output (CO) increases during exercise until MVO_2 is reached (from 5 to >25 L/min).

Variables	Normal peak response	Decreases due to
MVO_2	>84%	CHF, COPD, ILD, pulmonary vascular disease, deconditioning
AT	>50% of MVO_2	As directly above; normal in obesity
SaO_2	>95%	ILD, pulmonary vascular disease; normal in CHF, obesity, deconditioning
PaO_2	>80 torr	As directly above
HR	>90% PMHR	Chronotropic incompetence, certain drugs, sinus and/or AV nodal block
METs	>4	CHF, structural heart or lung disease, deconditioning, PVD, MS disease
a-vDO_2	>18 mL O_2/100 mL blood	Factors limiting peripheral (skeletal muscle) O_2 extraction
SV	>120 mL/beat	CHF, structural heart disease, acute myocardial ischemia, some drugs
CO	>25 L/min	As directly above
BPs	>200 torr	As directly above

AT anaerobic threshold, *AV* atrioventricular, *a-vDO₂* arterial–venous O_2 saturation difference, *CHF* congestive heart failure, *COPD* chronic obstructive pulmonary disease, *ILD* interstitial lung disease, *METs* metabolic equivalents, *MS* musculoskeletal, *O₂* oxygen, *PaO₂* arterial oxygen pressure, *PMHR* percentage of maximal heart rate, *PVD* peripheral vascular disease, *SaO₂* arterial oxygen saturation, *torr* international pressure measurement equal to millimeters of mercury (mm Hg)

Table 5.1 Exercise hemodynamics

The hemodynamic control of systemic blood flow during exercise reflects a closed-loop circulatory system. During exercise, sympathetic stimulation constricts skeletal muscle veins, increasing venous return (VR) to the heart; the enhanced respiratory cycle also increases VR. This added VR increases preload and cardiac myocyte stretching, thereby increasing cardiac SV and CO. During exercise, blood flow to tissues is dependent on the relationship between BP (the "driving pressure" differential between the LV and right atrium) and systemic blood vessel resistance (SVR). Generally, BP increases (from 100 to 200 mm Hg) and skeletal muscle arteriolar SVR decreases during exercise.

Pharmacologic Stress

Although the coronary blood flow (CBF) levels required for optimal myocardial perfusion imaging (MPI) are best achieved during dynamic exercise stress testing, a large number of CAD testing candidates have contraindications to maximal exercise stress:

- Relative contraindications
  - Large abdominal aortic aneurysm
  - Left bundle branch block (LBBB)
  - Right ventricular pacemaker
- Absolute contraindications
  - Hypotension
  - Acute coronary syndrome within 24 h
  - Critical aortic stenosis
  - Severe left main coronary stenosis
  - Severe left ventricular (LV) outflow obstruction
  - Severe LV failure
- Debilitating medical conditions
  - Advanced age
  - Orthopedic or neurologic conditions
  - Peripheral vascular disease
  - Chronic obstructive pulmonary disease (COPD)
  - Poor general fitness
  - Certain medications (e.g., β-blockers)

Some patient populations are well suited for vasodilator stress imaging, such as patients with aortic stenosis, in whom excellent diagnostic accuracy and safety have been shown. Patients with electrocardiographic LBBB have a high false-positive rate with exercise or dobutamine stress testing due to abnormal patterns of septal perfusion and contraction. The diagnostic accuracy in patients with LBBB is 86–90% with adenosine or dipyridamole, compared with 50% or less with exercise perfusion imaging. Supplemental exercise is not advised for patients with LBBB.

The transient 2.5-fold to 3-fold increase above baseline CBF produced by intravenous vasodilator drugs is a proven, clinically useful alternative to maximal exercise stress. The premise for coronary artery disease (CAD) detection during vasodilator-induced coronary hyperemia is the differential CBF enhancement between attenuated postobstructive and normal myocardial perfusion beds [5].

There are many options for nonexercise stress testing:

- Cold pressor test
- Atrial pacing
  - Transthoracic
  - Intravenous
  - Transesophageal
- Pharmacologic stress
  - Vasodilator stress
    - Dipyridamole
    - Adenosine
    - Regadenoson
  - Inotropic/chronotropic agents
    - Dobutamine

Some techniques, such as cold pressor testing and atrial pacing, are not frequently used. More commonly used are methods of pharmacologic stress with vasodilators or inotropic agents.

General contraindications for pharmacologic stress testing include hypersensitivity to the particular stress agent or its antidote, testing within 24 h of an acute coronary syndrome, and uncompensated congestive heart failure. Dipyridamole, adenosine, and regadenoson are contraindicated for patients with hypotension, bronchospasm, and advanced atrioven-

tricular block; dobutamine is contraindicated for patients with hypertension, high-grade ventricular ectopy, uncontrolled atrial fibrillation/flutter, left ventricular outflow tract obstruction, and expanding aortic aneurysm. One study supports the safety of adenosine or dipyridamole in patients with lung disease in the absence of wheezing and if peak flow rates on spirometry are normal before testing [6]. Regadenoson safety has been well established in randomized, double-blind, placebo-controlled trials of patients with mild to moderate asthma and COPD [7–10].

Selective Adenosine-2A Receptor Agonists

Figures 5.5, 5.6, 5.7, 5.8, 5.9, 5.10, 5.11, and 5.12 introduce the development of coronary vasodilators toward the selective adenosine-2A (A_{2A}) receptor agonists.

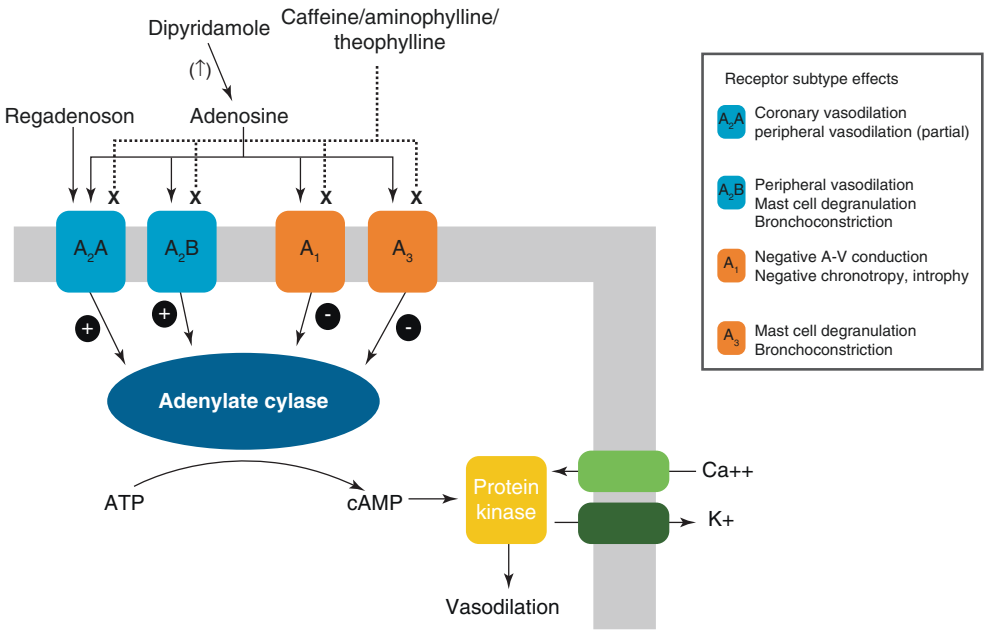

Fig. 5.5 Coronary vasodilators. The extension of first-generation (i.e., dipyridamole) and second-generation (i.e., adenosine) coronary vasodilators toward selective adenosine-2A (A_{2A}) receptor agonists has been driven by pharmacology for several reasons [11]: (1) Selectivity for the adenosine A_{2A} receptor in order to reduce side effects (i.e., A_1 and A_3 chest discomfort, A_1 atrioventricular [AV] heart block, A_{2B} and A_3 pulmonary complications, etc.). (2) Potency as a coronary vasodilator to increase coronary blood flow by more than 2.5-fold with little or no A_{2B} peripheral vasodilation effects on systemic blood pressure. (3) Rapid onset and termination of action with hyperemia for 3–4 min during radiotracer injection and uptake. (4) Standardized dose for rapid (ideally bolus) administration to increase the ease of use in the clinical setting. A number of third-generation A_{2A} receptor agonists have emerged for clinical use as coronary vasodilators in combination with myocardial perfusion imaging, each fulfilling one or more of these ideal criteria [12]. ATP adenosine triphosphate, Ca++ calcium, K+ potassium

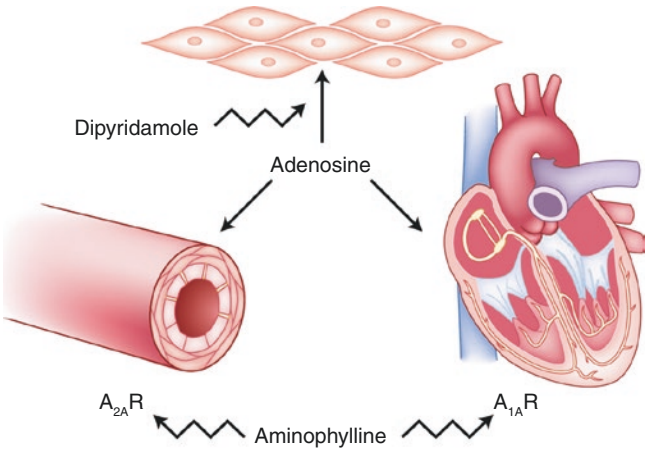

Fig. 5.6 Action of adenosine and dipyridamole on vascular smooth muscle and cardiac conduction cells. The direct and indirect action of adenosine and dipyridamole on vascular smooth muscle cells (A_2 receptors [$A_{2A}R$]) and on cardiac conduction cells (A_1 receptors [$A_{1A}R$]) is shown. Adenosine is a small, heterocyclic, endogenous compound produced by the endothelial cell. It activates $A_{2A}R$, causing vasodilatation via the production of adenyl cyclase and the subsequent local increase in cyclic AMP. Theophylline and other methylxanthines, including caffeine, are competitive antagonists of adenosine, blocking their effects at the A_2R. Adenosine enters endothelial and red blood cells by a facilitated transport mechanism. Intracellular adenosine is then deaminated or converted to other inactive metabolites. The "antidote" that reverses the effects of dipyridamole or adenosine is aminophylline. Patient preparation for pharmacologic stress testing is similar to that within 12–24 h of exercise stress, although all methylxanthines must be withheld before adenosine or dipyridamole testing [13]. β-Blockers should be withheld for 24 h before dobutamine stress testing. With vasodilator single-photon emission CT (SPECT) imaging, the increased splanchnic activity mandates a delay in image acquisition for 30–60 min following the injection of a ^{99m}Tc agent [14, 15]

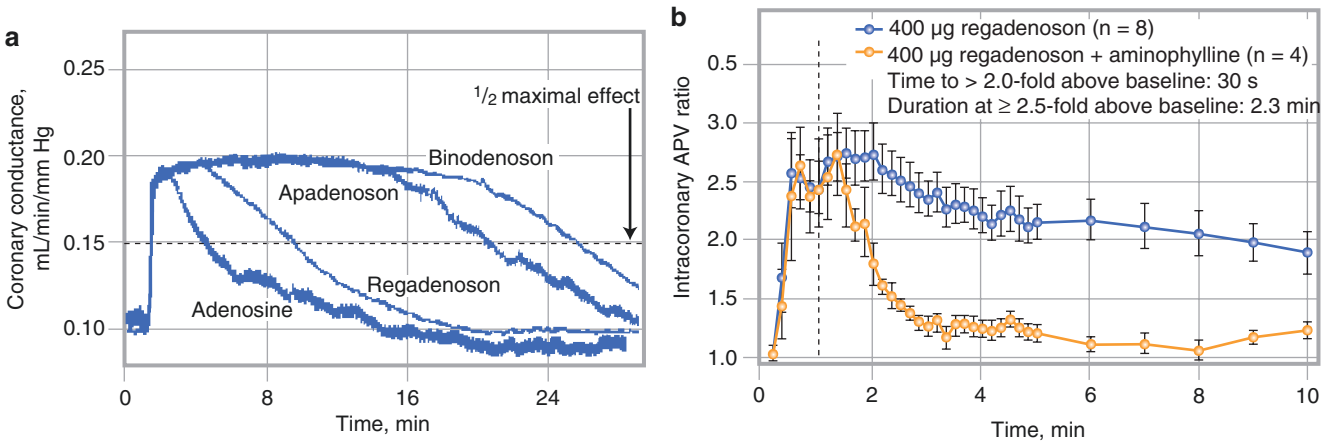

Fig. 5.7 Selective A_{2A} receptor agonists. (**a**) The time course of changes in coronary conductance caused by adenosine, regadenoson, binodenoson, and apadenoson are shown. All of the A_{2A} agonists tested achieved comparable maximal increases in coronary vasodilation to that of adenosine. However, there were differences in the duration of the coronary conductance, which is likely explained by the inverse relationship between affinity for the A_{2A} receptor and the duration of action. Low-affinity agonists, such as adenosine and regadenoson, can cause maximal coronary vasodilation that is rapid in both onset and termination. On the other hand, high-affinity agonists, such as binodenoson and apadenoson, achieve rapid maximal coronary vasodilation but exhibit a much longer termination phase, with longer duration of coronary vasodilation [16]. (**b**) The effect of regadenoson on intracoronary blood flow is shown. A rapid increase (to ≥2.5-fold over baseline) is sustained for approximately 2–3 min and decreases to less than twice the baseline level within 10 min. Flow velocity is evaluated by pulsed-wave ultrasonography in patients undergoing coronary catheterization [17]. When regadenoson is followed by aminophylline (100 mg slow intravenous bolus) 1 min later, there is a prompt and rapid decrease of coronary vasodilatation. Thus, aminophylline can be used as an "antidote" to reverse the effects of regadenoson. APV average peak velocity

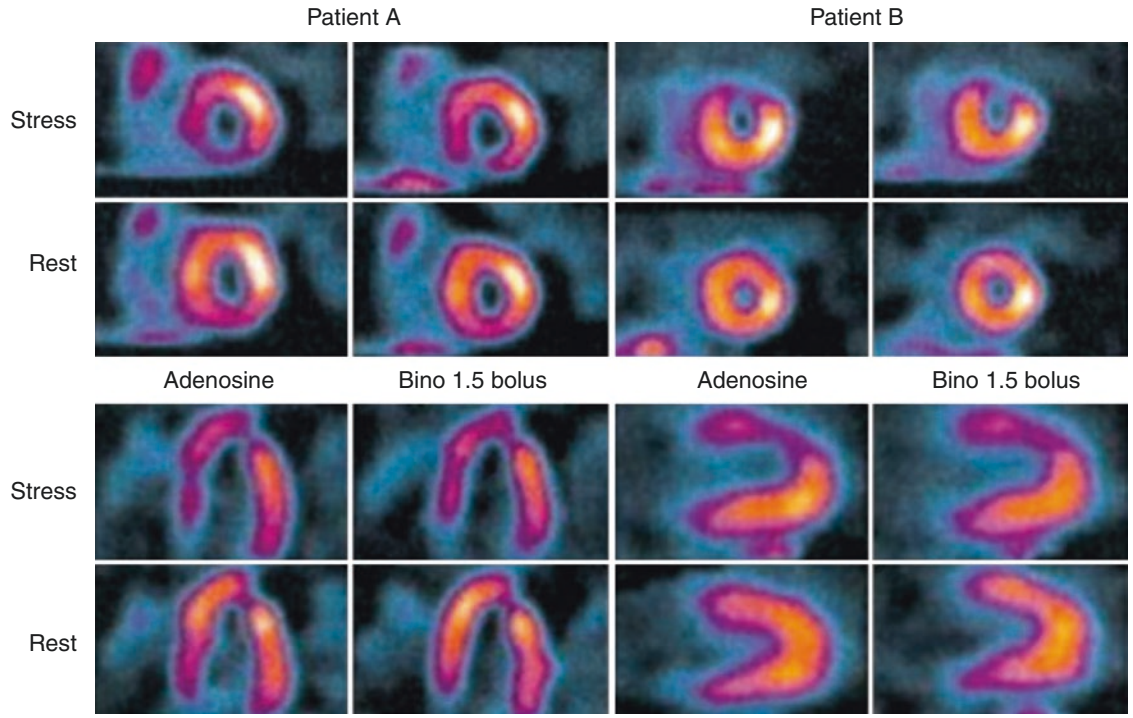

Fig. 5.8 Arteriolar vasodilator effect on the coronary adenosine A_{2A} receptor. The desirable arteriolar vasodilator effect on the coronary adenosine A_{2A} receptor is the basis for the differential effects of pharmacologic stress agents on coronary flow reserve in stenotic versus unobstructed vascular beds. The undesirable nonselective activation of the adenosine A_1, A_{2B}, and A_3 receptors contributes to the side-effect profile of these drugs, including atrioventricular heart block and bronchospasm. Selective adenosine A_{2A} receptor agonists have been tested in several clinical trials to take advantage of greater drug receptor specificity during pharmacologic stress myocardial perfusion imaging. Dose-ranging studies have identified the optimal doses to maximize coronary A_{2A} receptor-mediated vasodilatation while reducing concomitant side effects due to nonspecific stimulation of lower-affinity receptor sites. Utilizing the agent binodenoson in doses ranging from 0.5 to 1.5 μg/kg as a 30-s intravenous (IV) bolus or 1.5-μg/kg IV infusion for 3 min demonstrated good-to-excellent image concordance with adenosine SPECT [15]. This figure illustrates two examples of the concordance of SPECT image results between adenosine (Adeno) and binodenoson at a 1.5-μg/kg bolus dose (Bino 1.5 bolus). The short axis (*top left*) and horizontal long axis (*bottom left*) SPECT images in patient A demonstrate septal and apical reversible defects similar in their extent and severity after pharmacologic stress with the two agents and a fixed inferior defect. In patient *B*, the short axis (*top right*) and vertical long axis (*bottom right*) adenosine and binodenoson SPECT images show a concordantly severe reversible anterior defect

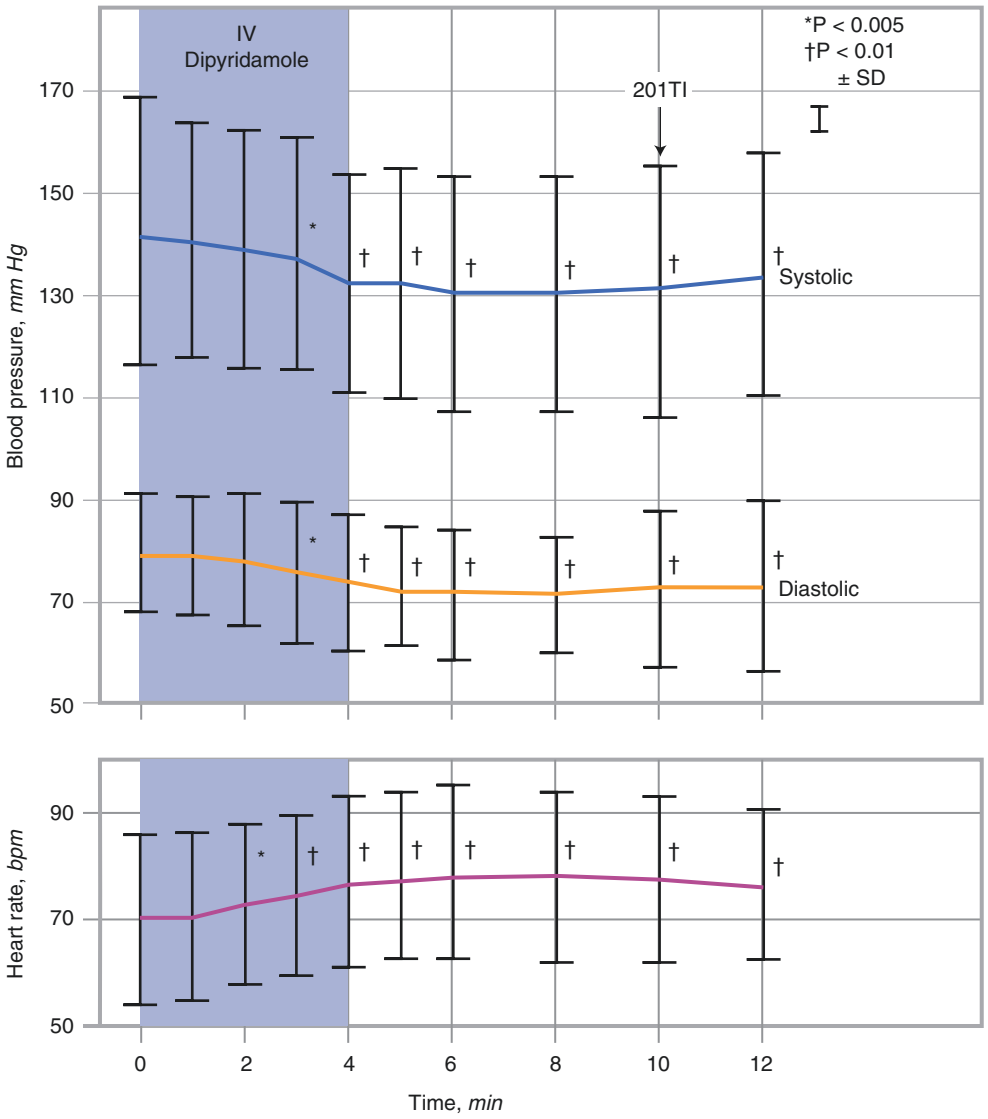

Fig. 5.9 Hemodynamic responses to intravenous (IV) dipyridamole. The response usually entails a slight (10–15%) decrease in blood pressure with compensatory (reflex) tachycardia [18]

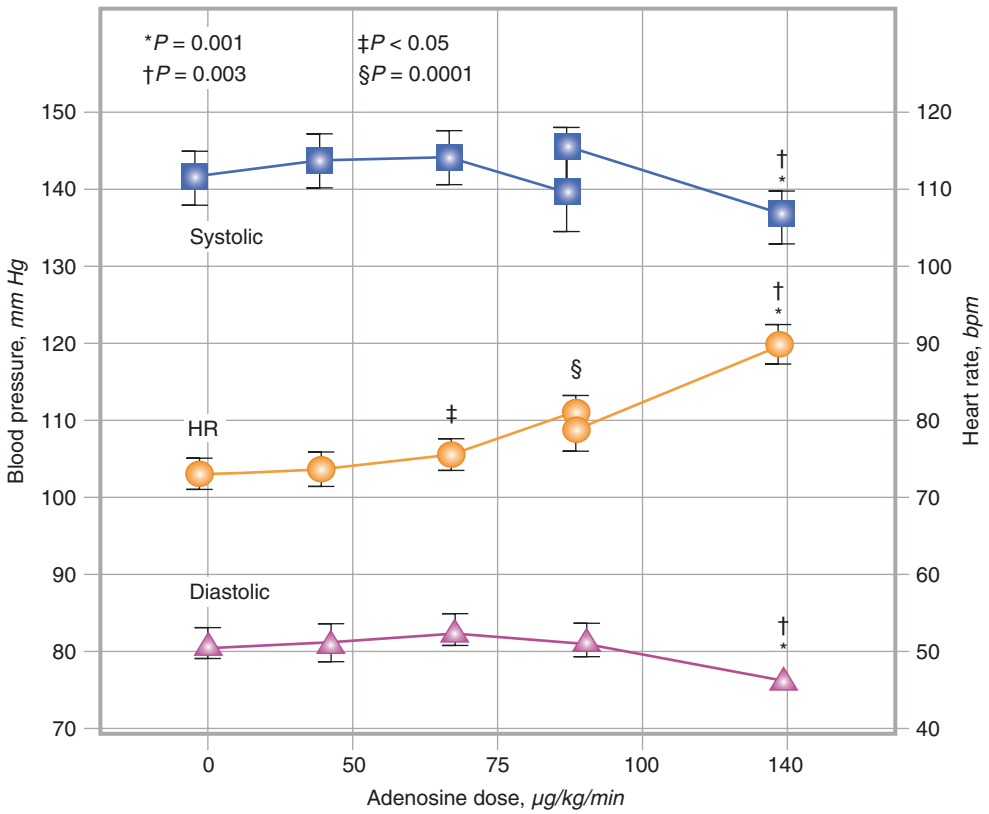

Fig. 5.10 Peripheral hemodynamic responses to adenosine. Blood pressure decreases by 10–15% in a dose-dependent fashion during infusion, with compensatory (reflex) tachycardia [17, 19]. bpm beats per minute, HR heart rate

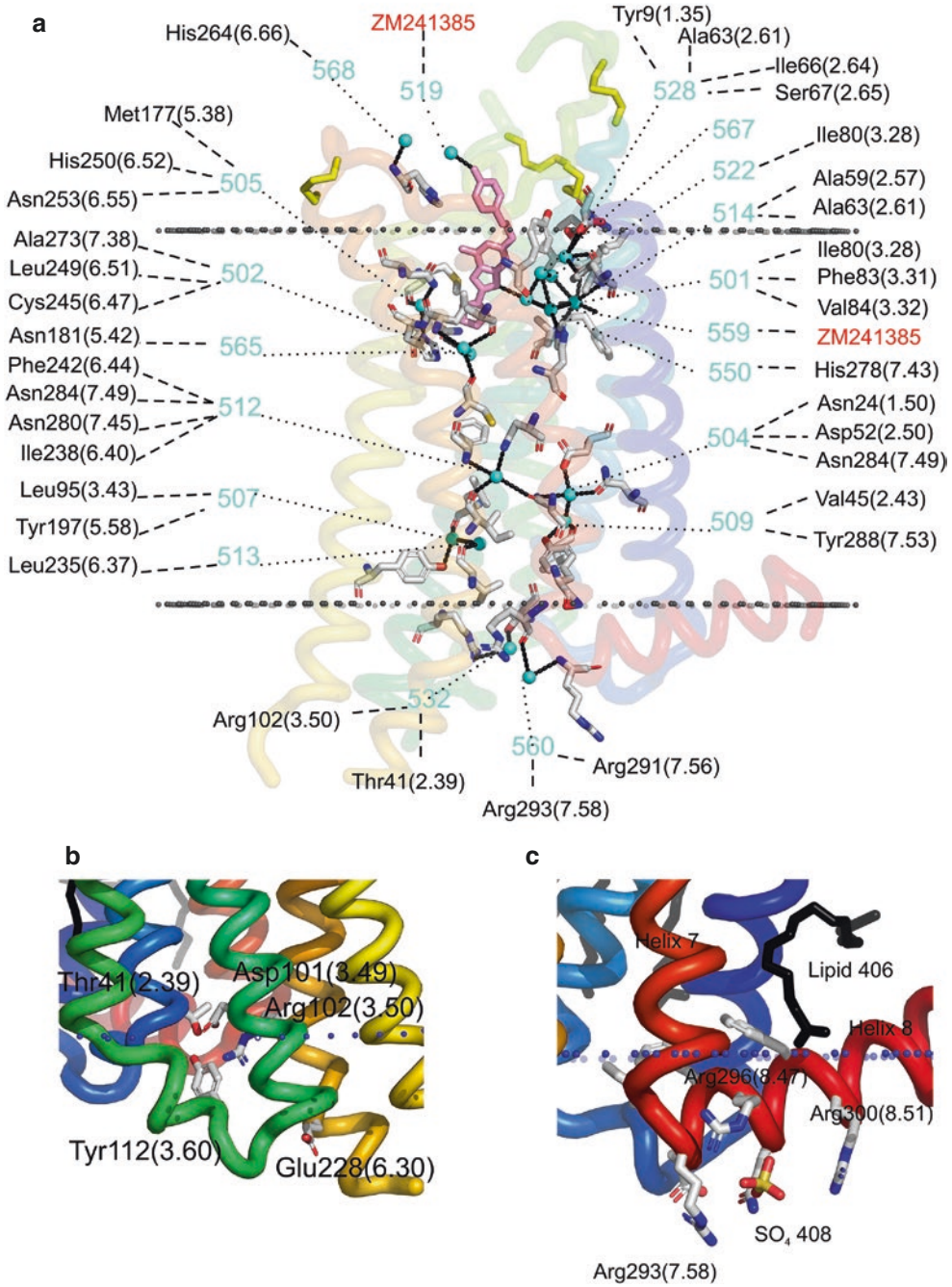

Fig. 5.11 A_{2A} receptor structure-function relationships. Extracellular adenosine plays an important role in many physiological processes. Its effects are mediated by four discrete adenosine receptors subtypes – adenosine A_1, A_{2A}, A_{2B} and A_3 – which are members of the heterotrimeric guanine nucleotide-binding protein (G protein) coupled receptor family (GPCR). These GPCR are responsive to methylxanthine antagonists, the most ubiquitous of which is caffeine. Three-dimensional (3-D) crystallography can characterize the transmembrane structural details of key regions in the human adenosine A_{2A} receptor, as it interacts with antagonists (i.e., regadenoson, ZM241385, etc.). Binding affinity and selectivity for the adenosine A_{2A} receptor by an antagonist is the result of minor sequence variations in the amino acid residues of the binding cavity. These mutations result in changes to the hydrogen bonding and aromatic interactions between the receptor and the antagonist. (*From* Piirainen et al. [20], with permission from Elsevier)

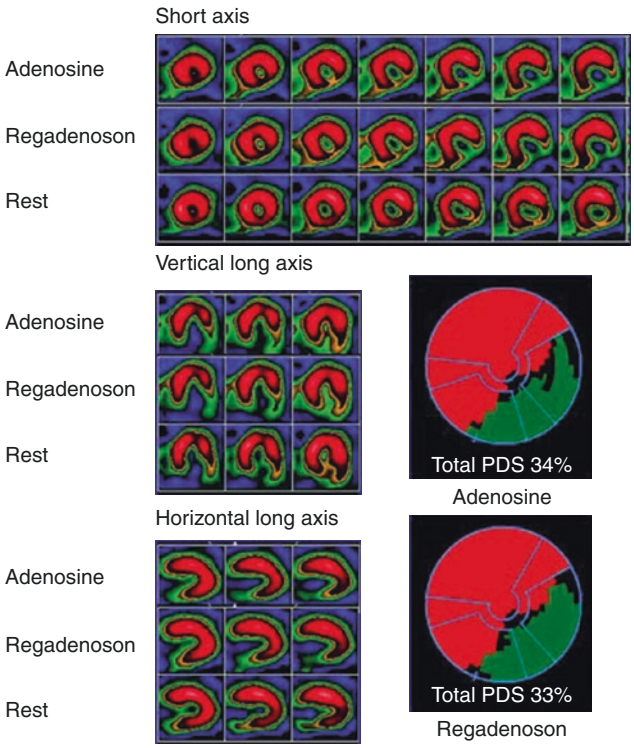

Fig. 5.12 Adenosine receptor-mediated mechanisms of action. The mechanisms of action of clinically available coronary arteriolar vasodilators are illustrated for adenosine, the adenosine analogue regadenoson, and dipyridamole. The two direct A_{2A} receptor binders (adenosine, regadenoson) activate adenylase cyclase to convert adenosine triphosphate (ATP) to cyclic adenosine monophosphate (cAMP) within endothelial cells. Dipyridamole inhibits the phosphodiesterase enzyme breakdown of cAMP and inhibits the cellular re-uptake of endogenous adenosine. Activation of A_1, A_{2B} and A_3 receptors is responsible for side effects: A_1 for atrioventricular (AV) heart block, A_{2B} for peripheral vasodilatation, and A_3 for bronchospasm. (*From* Henzlova et al. [1]; with permission from Springer Nature)

Compared with adenosine, the newer "-denoson" agents listed on Table 5.2 provide equivalent diagnostic information (i.e., "non-inferiority" to adenosine myocardial perfusion imaging), produce less hypotension (with greater heart rate rise), cause no atrioventricular (AV) node blockade and fewer general side effects, and can be used safely in patients with bronchospastic disease/chronic obstructive pulmonary disease. Both regadenoson (400–500 μg) and binodenoson (1.5 μg/kg) can be administered as an intravenous bolus. A high-grade AV block is a contraindication to Federal Drug Administration (FDA)–approved regadenoson administration; second- and third-degree AV blocks are less common with regadenoson and binodenoson than with adenosine.

Selective A_{2A} receptor agonists	Compound name	Brand name	Phase 3 trials	FDA approval
Regadenoson	CVT-3146	Lexiscan (Astellas Pharma USA; Deerfield, IL)	Advance-MPI 1, 2	Yes (04/08)
Binodenoson	MRE-0470	CorVue (King Pharmaceuticals; Bristol, TN)	Vision 302, 305	No
Apadenoson	BMS-068645, ATI146e	Stedivaze (Forest Laboratories; New York, NY)	Aspect 1, 2	No

Table 5.2 Selective A_{2A} receptor agonists

Table 5.3 compares the characteristics of stress testing with regard to responses from exercise, dobutamine, and the clinically available vasodilators dipyridamole, adenosine, and regadenoson.

Characteristics	Exercise	Dobutamine	Dipyridamole	Adenosine	Regadenoson
CBF increase	2–3 times	2 times	3–4 times	3–5 times	2–3 times
Ischemia provocation	Frequent	Common	Rare	Uncommon	Uncommon
Onset of effect	3–5 min	2–4 min	4–6 min	1–2 min	1–4 min
Duration after stopping	2–5 min	4–6 min	10–30 min	0.5–1 min	15–30 min
AV block occurrence	No	No	Rare	Common (transient)	Uncommon (transient)
Ventricular ectopy	Uncommon	Common	Rare	Rare	Rare

AV atrioventricular, *CBF* coronary blood flow

Table 5.3 Characteristics of stress testing

Pivotal Regadenoson Clinical Trials

Figures 5.11, 5.12, and 5.13 show results of some clinical trials comparing adenosine and regadenoson.

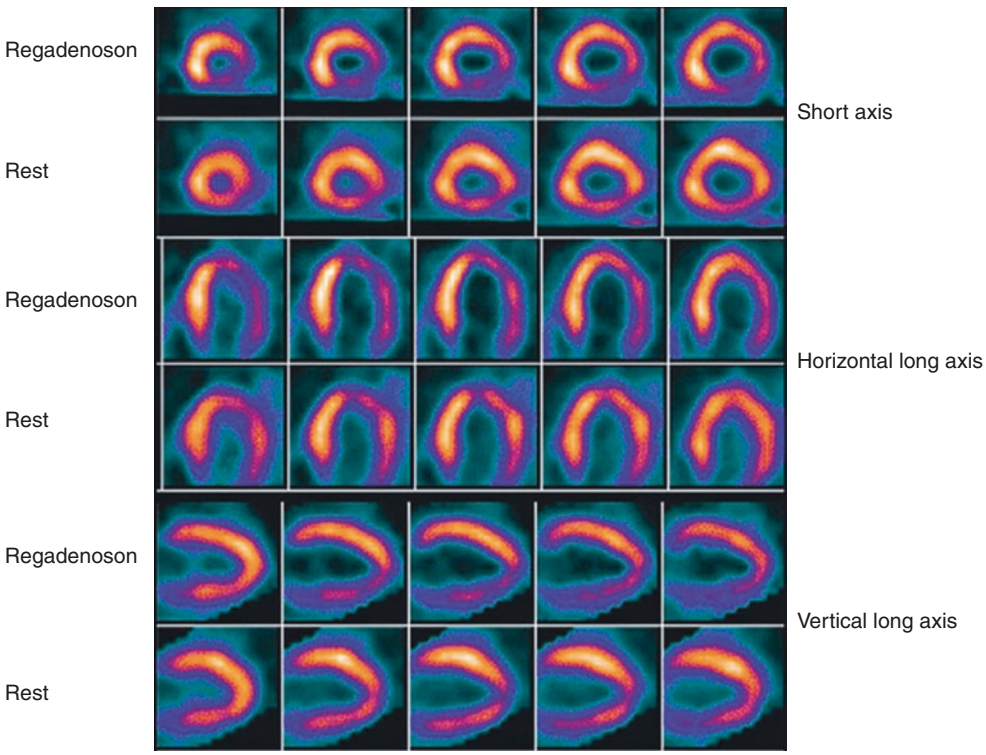

Fig. 5.13 Direct comparison of quantitative myocardial SPECT perfusion defect size following adenosine and regadenoson stress from the Adenoscan Versus Regadenoson Comparative Evaluation for Myocardial Perfusion Imaging-2 trial [21]

In addition to completed regadenoson trials [22], the National Institutes of Health [23] reported in 2010 that regadenoson myocardial perfusion imaging (MPI) has been studied in clinical trials for CAD detection to determine its safety and tolerability in patients with comorbidities:

- Moderate to severe COPD or asthma: potential bronchospasm, reduced FEV1 (forced expiratory volume in 1 s)
- End-stage renal disease (ESRD)/renal impairment [24]: renal metabolism effects (secondary)
- End-stage liver disease [25]/liver tetroxoprim (TXP) candidates: hepatic metabolism effects (primary)
- Obesity/high BMI, despite endothelin impairment of hyperemia
- Type 1 diabetes

Regadenoson is also undergoing clinical trials for CAD detection using other noninvasive imaging modalities:

- Myocardial positron emission tomography (PET)
- Myocardial MRI
- Multidetector CT (MDCT)
- Cardiac catheterization coronary fractional flow reserve (FFR)
- Echocardiography

Regadenoson has been directly compared with other existing stress modalities and agents:

- Adenosine myocardial perfusion imaging (ADVANCE MPI 1,2) [21, 22]; *see* Figs. 5.13 and 5.14
- Bruce protocol/symptom-limited exercise combined with regadenoson MPI and PET
- Dipyridamole Rubidium-82 (Rb-82) PET
- Dobutamine MRI

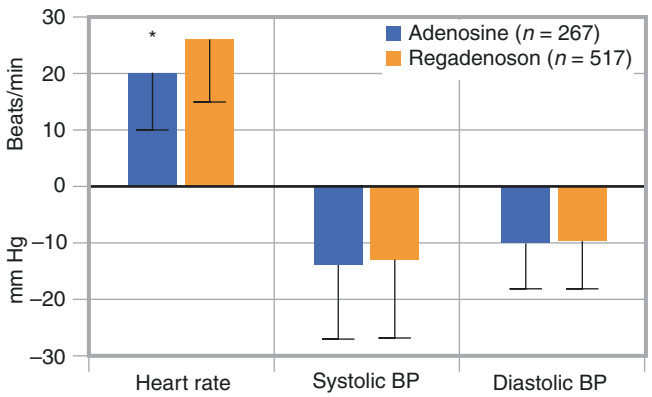

Fig. 5.14 Extensive partially reversible inferolateral myocardial SPECT perfusion defect following regadenoson stress from the Adenoscan Versus Regadenoson Comparative Evaluation for Myocardial Perfusion Imaging-1 trial [22]

Quantitative MPI analysis demonstrates comparable left ventricle perfusion defect size and severity of ischemia with regadenoson and adenosine stress [21]. *See* Fig. 5.15.

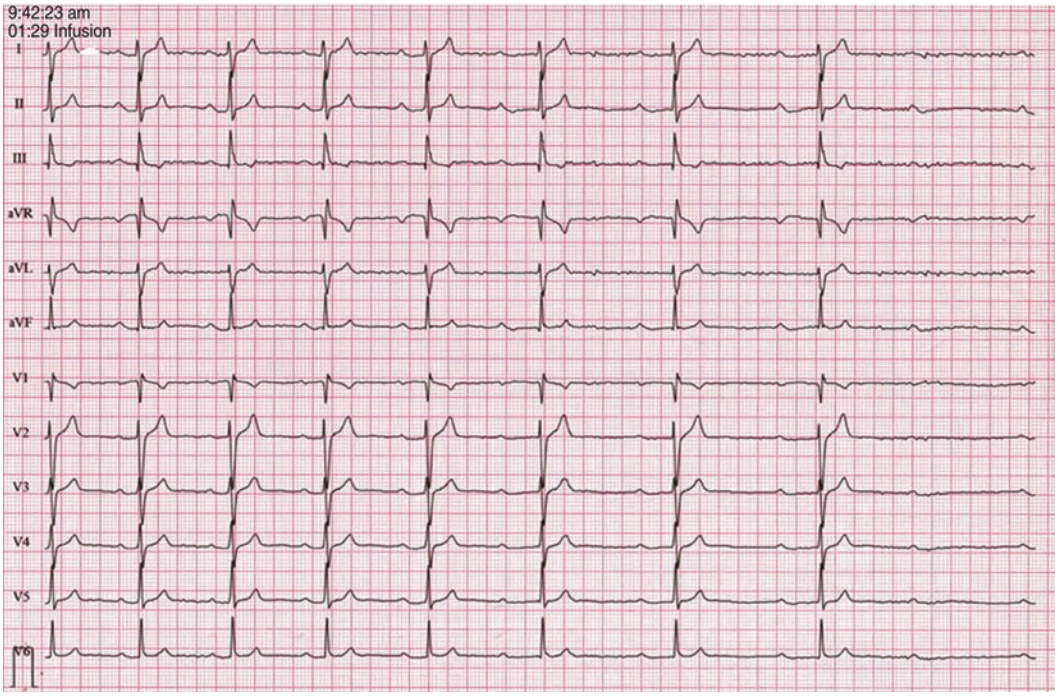

Fig. 5.15 Despite a significantly greater (*asterisk*) heart rate change following regadenoson, comparable systolic and diastolic BP changes occurred in Adenoscan Versus Regadenoson Comparative Evaluation for Myocardial Perfusion Imaging (MPI)-2 subjects undergoing adenosine (n = 267) and regadenoson (n = 517) stress in association with stress MPI [21]

Selective A_{2A} Receptor Agonist Side Effect Profiles

Figures 5.16, 5.17, and 5.18 illustrate side effects during imaging with these agents.

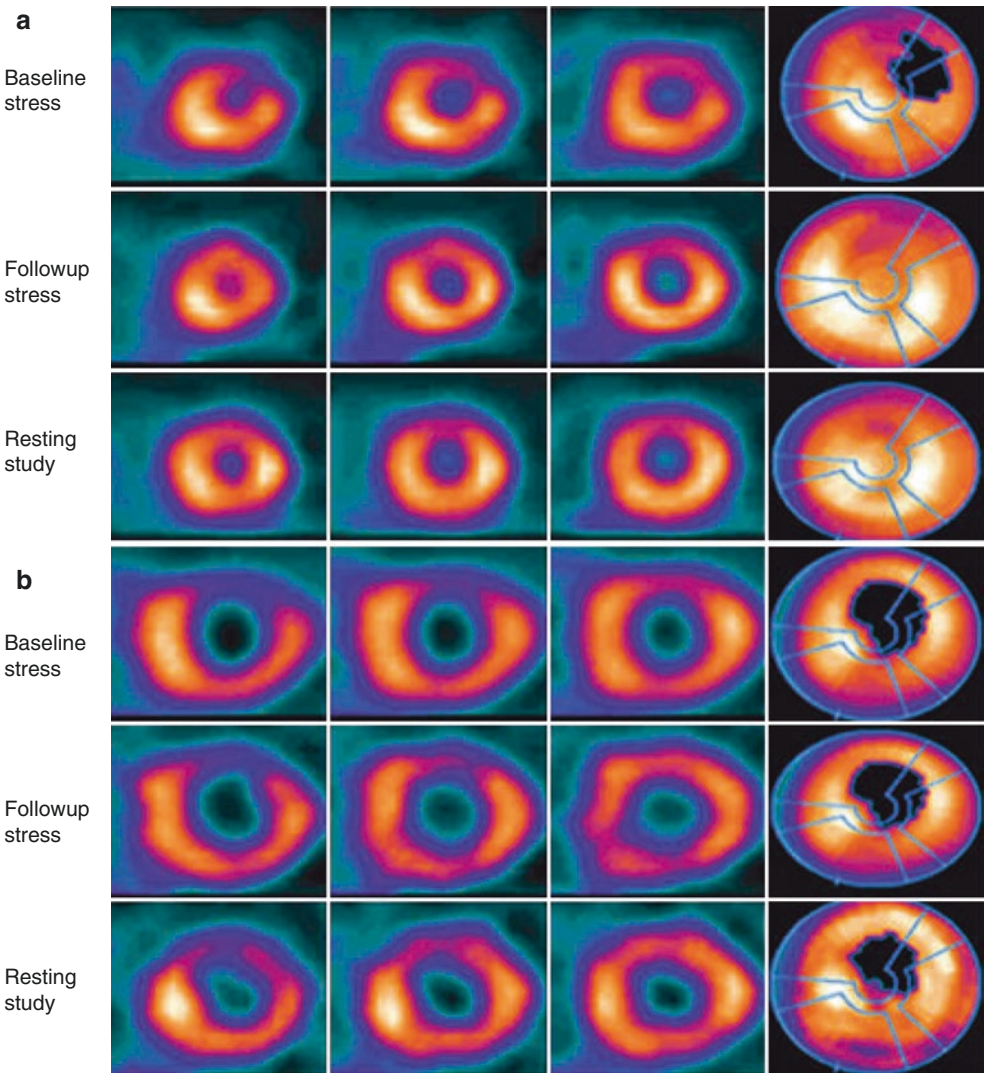

Fig. 5.16 Normal sinus rhythm progressing to transient asystole during regadenoson infusion in a pulmonary fibrosis patient being treated with n-acetylcysteine [26]

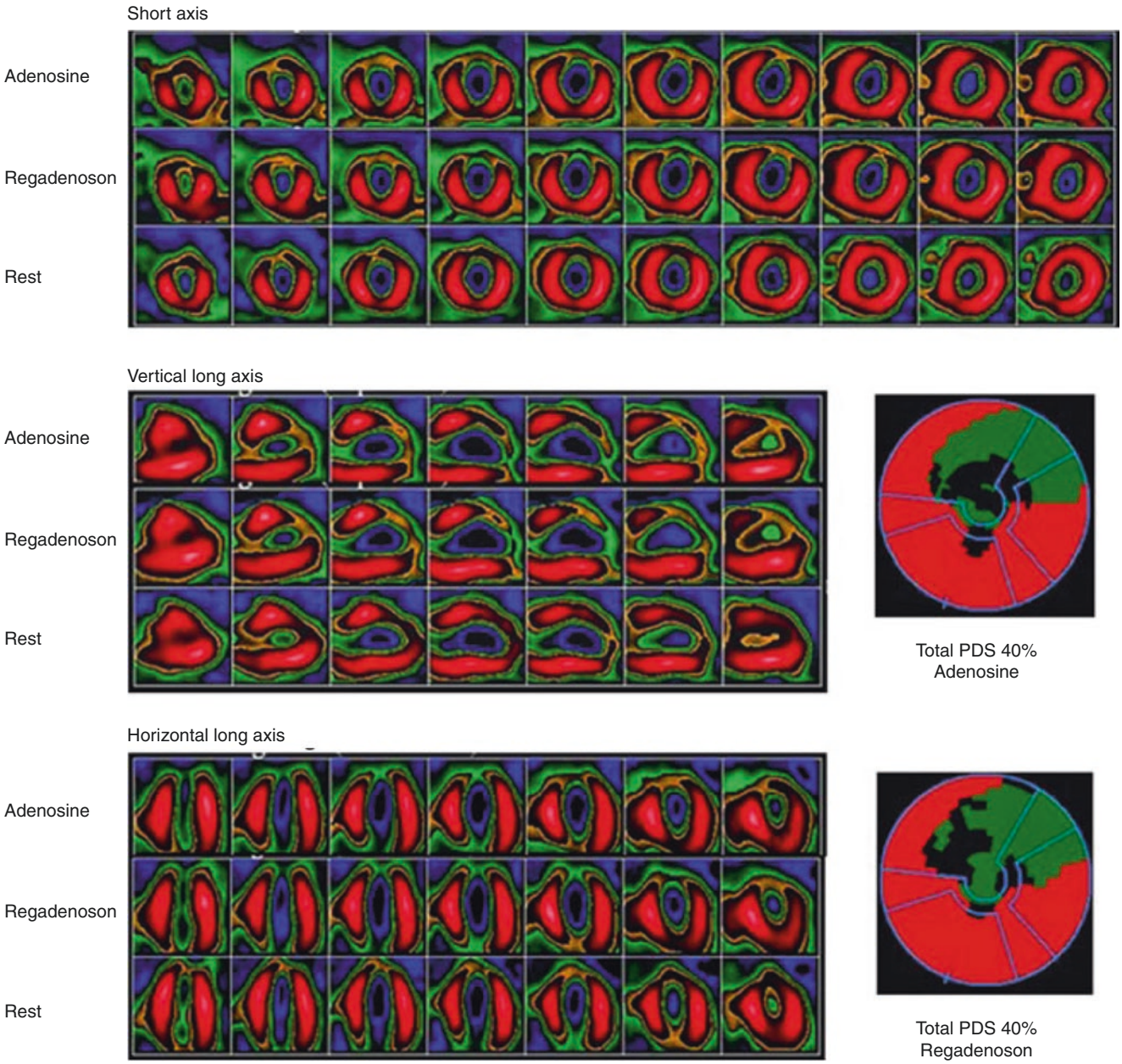

Fig. 5.17 Effects of anti-ischemic late sodium (I_{Na}) channel inhibitor drugs. Anti-ischemic I_{Na} channel inhibitor drugs such as ranolazine reduce the myocardial stiffness and microcirculatory compression occurring with ischemic activation of the late sodium channels. Recently, ranolazine has been shown to improve myocardial ischemia during exercise myocardial perfusion imaging, without any improvement in baseline reversible MPI defects induced by regadenoson or adenosine in the absence of an ischemic coronary steal phenomenon [27]. (**a**) and (**b**) show two different cases in which ranolazine reduced the ischemia on a "Followup Stress" drug stress imaging study, as compared with "Baseline Stress" (without ranolazine) [27]

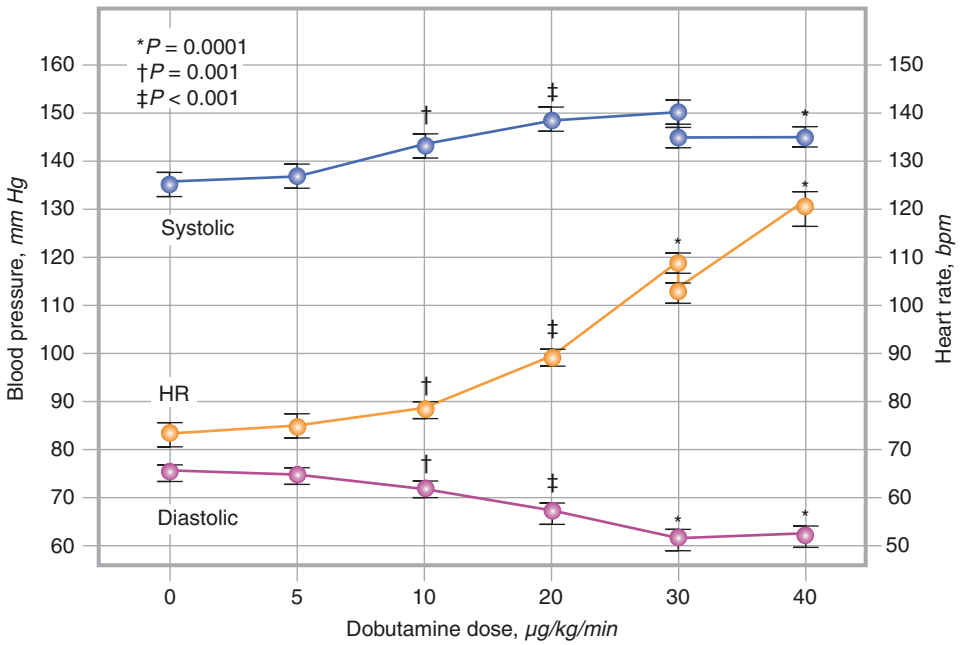

Fig. 5.18 Adenosine and regadenoson stress SPECT images. Representative adenosine and regadenoson stress SPECT images from the ADVANCE MPI-2 study, which sought to compare left ventricle (LV) myocardial perfusion defect size and severity using two drug stress agents. In this example, the adenosine and regadenoson quantitative SPECT defects are identical, with perfusion defect size (PDS) equal to 40% of the LV [21]

The three most widely tested selective A_{2A} receptor agonists—regadenoson, binodenoson, and apadenoson—have exhibited dose-dependent side effect profiles that are generally better than those experienced with adenosine stress in the same trials. Table 5.4 summarizes the side effect profiles of these agents. The major regadenoson clinical trials excluded subjects with high-grade AV blocks [22]. A single case report of normal sinus rhythm progressing to transient asystole during regadenoson infusion in a pulmonary fibrosis patient also being treated with n-acetylcysteine has been published (*see* Fig. 5.17) [26]. Post-marketing surveillance continues to assess the risk of transient high-grade heart blocks with regadenoson in a clinical referral population [11].

	Regadenoson [22]	Binodenoson [28]	Apadenoson [29]
Clinical trial	Advance MPI	Vision 305	Phase 2
Dose	400-μg slow bolus and flush	1.5-μg/kg infusion × 3 min	1–2-μg/kg slow bolus and flush
Chest pain	29%	38%	14%
Dyspnea	28%	45%	16%
Flushing	22%	38%	8%
GI discomfort	23%	34%	0%
Headache	26%	47%	8%
Dizziness	8%	19%	11%
Second- to third-degree AV block	TBD	0%	0%

AV atrioventricular, *GI* gastrointestinal, *TBD* to be determined

Table 5.4 A_{2A} receptor agonist side effect Profiles

Recent Clinical Applications

Both physiologic and pharmacologic stress myocardial perfusion imaging (MPI) studies have proven useful in the evaluation of anti-ischemic therapies [30]. The Clinical Outcomes Utilizing Revascularization and Aggressive Drug Evaluation (COURAGE) nuclear substudy utilized either quantitative electrocardiogram-gated exercise ($n = 84$) or adenosine ($n = 230$) stress MPI to detect the reduction in myocardial ischemia after percutaneous coronary intervention (PCI) with optimal medical therapy (OMT) or with OMT alone [31]. Subjects with moderate to severe pretreatment myocardial ischemia exhibited a greater benefit from PCI plus OMT.

Figures 5.19, 5.20, 5.21, and 5.22 show results of pharmacologic stress imaging.

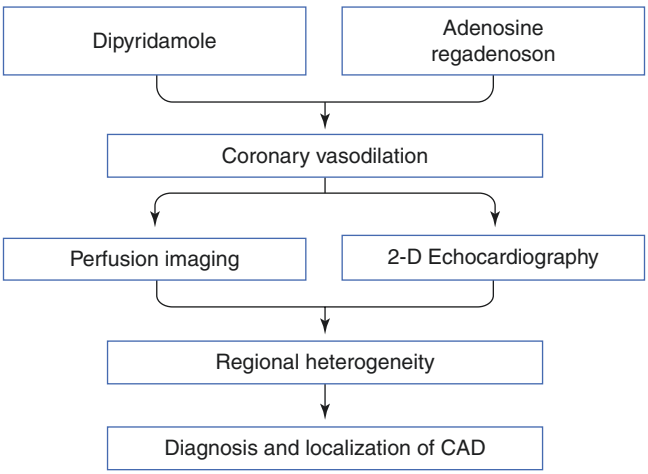

Fig. 5.19 Peripheral hemodynamic responses to dobutamine. The responses entail a predictable increase in systolic blood pressure, widening of the pulse pressure, and a chronotropic impact on heart rate, which may be augmented by atropine (0.4–0.6 mg IV bolus). ST segment alterations are predictive of significant coronary disease with exercise, but there is controversy regarding the diagnostic value of ST depression with pharmacologic stress testing [32]. ST depression is predictive of both scintigraphic evidence of myocardial ischemia and more severe coronary artery disease. Electrocardiographic changes are more common with dobutamine than with vasodilators, perhaps due to the increased cardiac workload (demand) [13]. With adenosine and dipyridamole, ST depression reflects a coronary "steal," as collateral vessels are usually associated with ST depression induced by adenosine or dipyridamole [33]

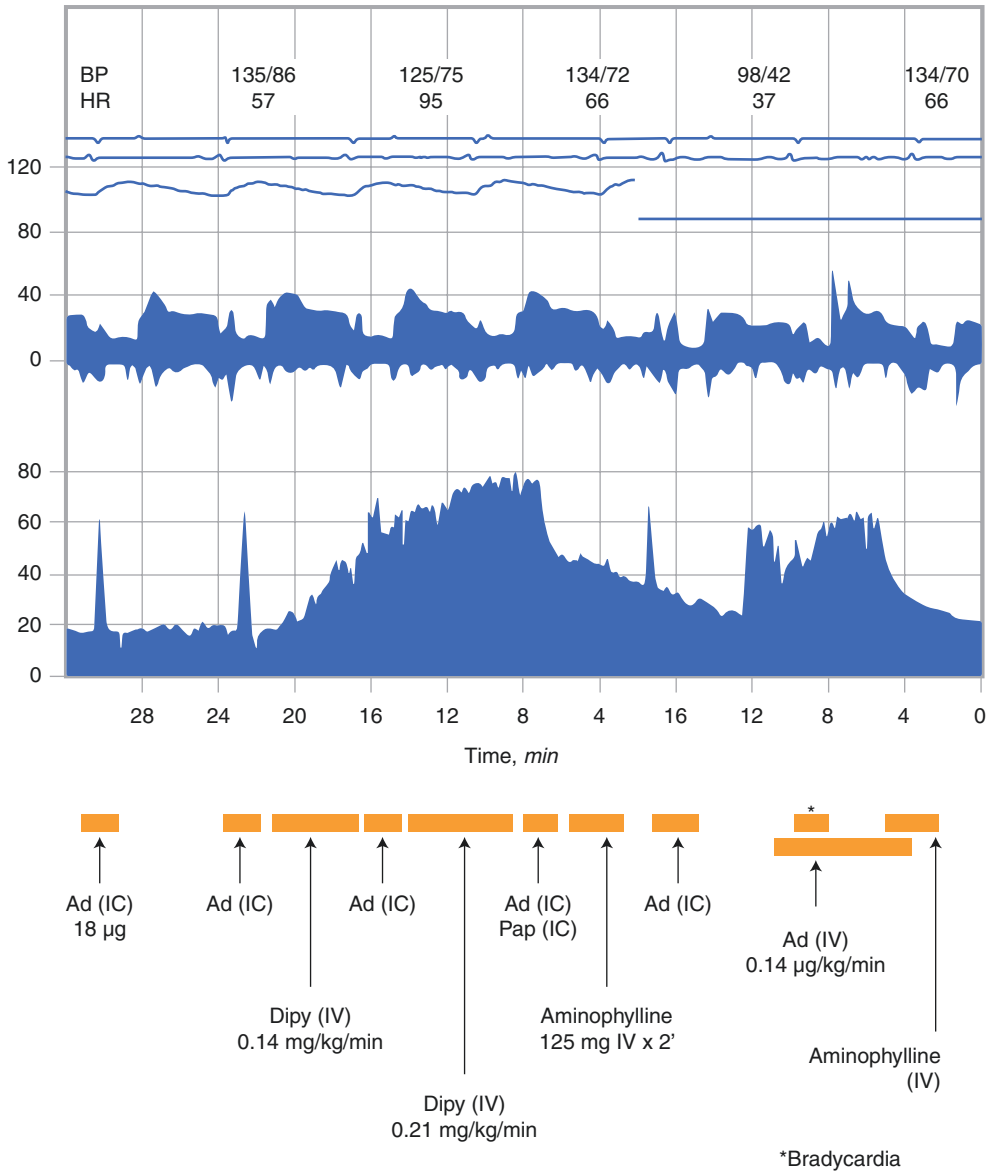

Fig. 5.20 Effects of hyperemic stress with dipyridamole, adenosine, or regadenoson on coronary vasodilation, establishing flow heterogeneity (usually in the absence of ischemia), leading to the diagnosis and localization of coronary artery disease (CAD). Adenosine, regadenoson, and dipyridamole reduce coronary vascular resistance and increase blood flow twofold to fivefold, to near maximal levels. Myocardial ischemia is not a prerequisite for the detection of obstructive CAD, because poststenotic flow disparities may be imaged in the setting of critical stenoses. In a direct comparison, dipyridamole and adenosine had similar diagnostic accuracy, with a myocardial segmental concordance of 87% [34]. 2-D two-dimensional

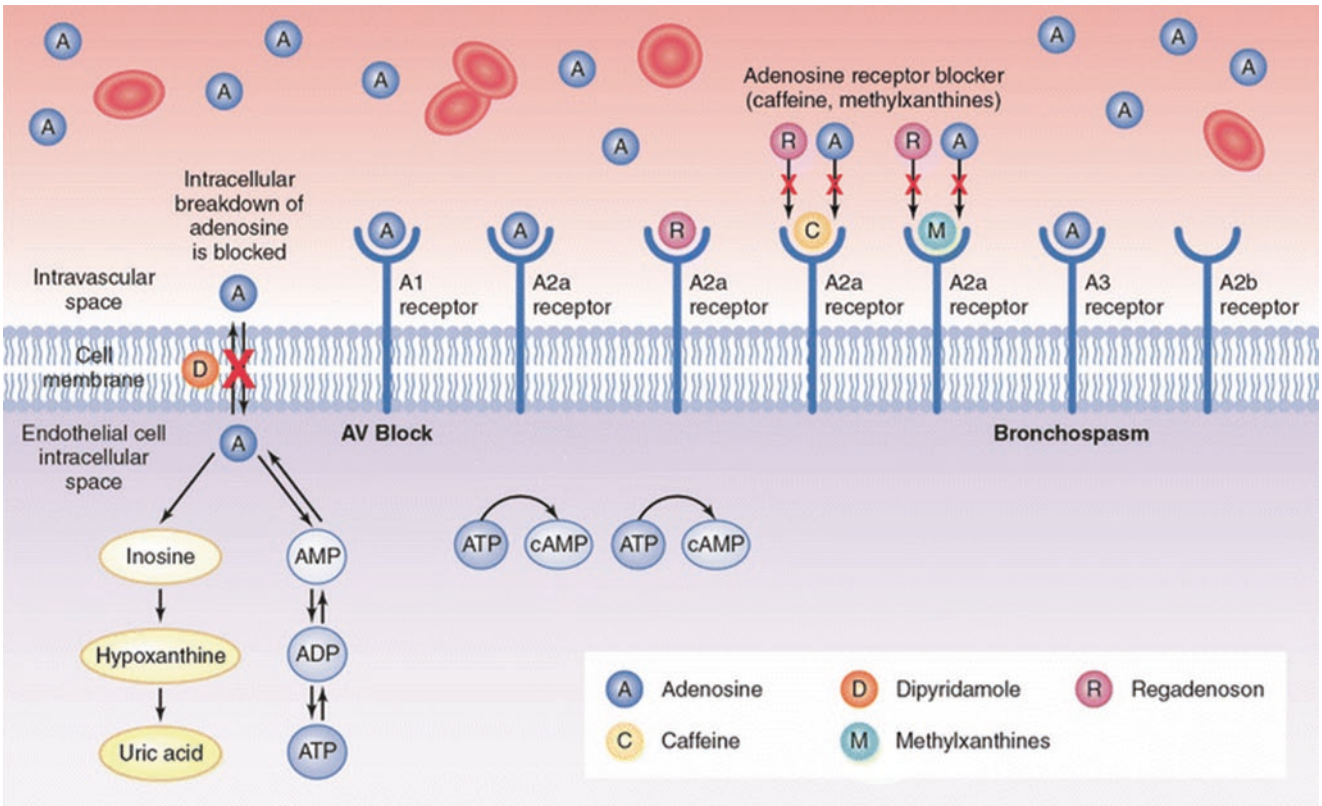

Fig. 5.21 Typical continuous coronary Doppler flow wire tracing. Typical continuous coronary Doppler flow wire tracing in a patient receiving a series of hyperemic agents, including intracoronary (IC) adenosine (Ad), IV dipyridamole (Dipy), IV Ad, and IC papaverine (Pap) [35]. Intracoronary drug boluses create a flow spike of immediate coronary hyperemia. IV Dipy creates a gradual increase in coronary flow velocity, which can gradually and serially be reversed by boluses of aminophylline. Peripheral blood pressure (BP) and heart rate (HR) are also recorded. Because the half-life of exogenous IV Ad is less than 2 s, hemodynamic changes and side effects usually resolve in less than 1 min. Therefore, drug reversal treatment is rarely indicated, as effects subside with termination of the infusion. Aminophylline, a competitive antagonist (50–250 mg by IV push), reverses the effects of IV dipyridamole. Patients with lung disease are at increased risk for bronchoconstriction, so vasodilator stress testing is contraindicated if active wheezing or respiratory failure is present. In patients with chronic obstructive pulmonary disease (COPD), routine reversal with IV aminophylline (50–250 mg IV push) may be appropriate

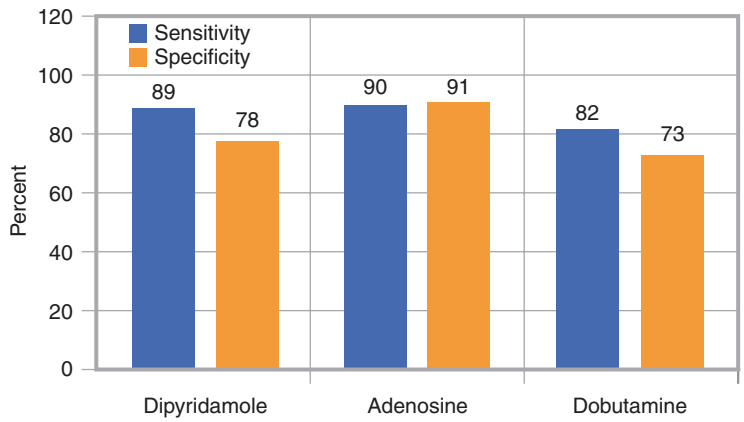

Fig. 5.22 Cumulative test accuracy data from multiple studies of pharmacologic stress imaging using dipyridamole, adenosine, or dobutamine in combination with myocardial perfusion SPECT. Average sensitivity ranges from 82% to 90%, and specificity ranges from 73% to 91%. Drug stress provides diagnostic value comparable to exercise for the detection of coronary artery disease, as well as accuracy superior to submaximal exercise testing. The diagnostic accuracy of drug stress imaging is high, regardless of age or gender. Transient left ventricular cavity dilatation or increased lung ^{201}Tl activity are markers of more severe or extensive coronary disease; these markers of disease burden also portend an increased risk for cardiac events. Adenosine, dipyridamole, and dobutamine have each been successfully employed in conjunction with all available myocardial perfusion tracers (^{201}Tl, ^{99m}Tc-sestamibi, ^{99m}Tc-tetrofosmin) [12–14]

Table 5.5 lists results of studies of combined vasodilator plus exercise stress imaging. The feasibility of combining low-level treadmill or bicycle exercise with adenosine or dipyridamole is well established. Consistently demonstrated benefits include (1) improved target-to-background activity by virtue of reduced liver and/or gut tracer uptake; (2) reduced frequency, duration, and severity of cardiac and noncardiac adverse effects; and (3) greater provocation of electrocardiogram and scan evidence of myocardial ischemia (excluding patients with LBBB) compared with vasodilator stress without combined exercise. Potential mechanisms for these benefits include (1) shunting of splanchnic blood flow to the skeletal musculature, (2) increased sympathetic nervous system activity, and (3) increased cardiac work with associated "demand-type" myocardial ischemia.

Study	Patients, *n*	Vasodilator protocol	Exercise protocol	Tracer	Vasodilator + Exercise benefits
Samady et al. [36]	41	Adenosine (6 min)	Modified Bruce (stage 2)	MIBI	ST changes improved, scan quality improved, heart:liver improved
Vitola et al. [37]	90	Dipyridamole (4 min)	Bruce (stages 1–2)	MIBI	ST changes improved, no hypotension, heart:liver improved
Thomas et al. [38]	507	Adenosine (6 min)	Treadmill (METs = 2.2)	MIBI or TI	Adverse reactions decreased (hypotension, arrhythmias); heart:liver improved
Elliott et al. [39]	19	Adenosine (4 min)	Modified Bruce (stage 0–1/2)	MIBI	Adverse reactions decreased (severity, duration); heart:liver improved
Jamil et al. [40]	32	Adenosine (6 min)	Modified Bruce (stage 0–1)	MIBI	Scan ischemia improved, sensitivity improved, NPV improved
Candell-Riera et al. [41]	72	Dipyridamole (4 min)	Bicycle (METs ≥4)	MIBI	Scan ischemia improved, sensitivity improved, NPV improved
Pennell et al. [42]	173	Adenosine (6 min)	Bicycle (25–150 W)	TI	Noncardiac side effects decreased, major arrhythmia decreased, heart:liver improved, defect reversibility improved
Thomas et al. [43]	60	Regadenoson (10 s)	Treadmill (1.7 mph, 4 min)	MIBI	Adverse reactions decreased (cardiac flushing, second-degree AV block); liver:heart improved vs. adenosine

AV atrioventricular, *METs* metabolic equivalents, *MIBI* ^{99m}Tc-sestamibi, *NPV* negative predictive value, *TI* thallium 201

Table 5.5 Combined vasodilator plus exercise stress imaging

Table 5.6 compares the side effects experienced with the use of IV adenosine, dipyridamole [44, 45], and regadenoson [22, 46] imaging in multicenter studies for both noncardiac and cardiorespiratory events. Chest pain is not necessarily associated with the presence of CAD because these agents also stimulate the nociceptors. Caution is advised in patients with severe asthma or COPD because of the direct bronchoconstrictive effects of A_{2B} and A_3 receptor agonists; A_{2A} receptor agonists also have the potential to cause or worsen bronchospasms in asthmatics [7, 8] and in patients with COPD [9, 10]. A second-degree heart block occurs in up to 1% of patients, but is generally well tolerated and brief [47].

	Adenosine, %	Dipyridamole, %	Regadenoson, %
Noncardiac			
Flushing	36.5	3.4	16
Dyspnea	35.2	2.6	28
Chest pain	34.6	19.7	13
Gastrointestinal distress	14.6	5.6	5
Headache	14.2	12.2	26
Dizziness	8.5	11.8	8
Cardiorespiratory			
Second-degree AV block	1	0	0.1
ST-T wave changes	5.7	7.5	12
Arrhythmia	3.3	5.2[a]	20[b]
Hypotension	1.8	4.6	7
Bronchospasm	0.1	0.15	N/A
Myocardial infarction	0	0.05	N/A
Death	0[c]	0.05	0

AV atrioventricular, *FDA* US Food and Drug Administration, *N/A* not applicable, *PACs* premature atrial contractions, *PVCs* premature ventricular contractions

[a]Ventricular arrhythmias

[b]PACs, PVCs, atrial fibrillation, wandering atrial pacemaker, asystole

[c]One subsequent death reported

Table 5.6 Side effects of FDA-approved intravenous Vasodilator Drug stress imaging

Preoperative Cardiac Risk Stratification

Pharmacologic Stress Myocardial Perfusion Imaging Literature

Of multiple publications on stress myocardial perfusion imaging (MPI) before noncardiac surgery [48–70], some have included some prospectively recruited patients, but most have involved patients undergoing vascular surgery (*see* Table 5.5). These studies have shown that reversible perfusion defects, which reflect ischemic "jeopardized" but viable myocardium, carry the greatest risk of perioperative myocardial infarction (MI) or cardiac death. Most studies show that fixed perfusion defects do not have independent predictive value for perioperative cardiac events. Patients with fixed defects have greater risk than patients with a normal image, but the having only a fixed defect was significantly lower than in patients with reversible defects.

Preoperative assessment of preoperative peripheral vascular disease using dipyridamole–^{201}Tl imaging offers prognostic value, seen in Fig. 5.23.

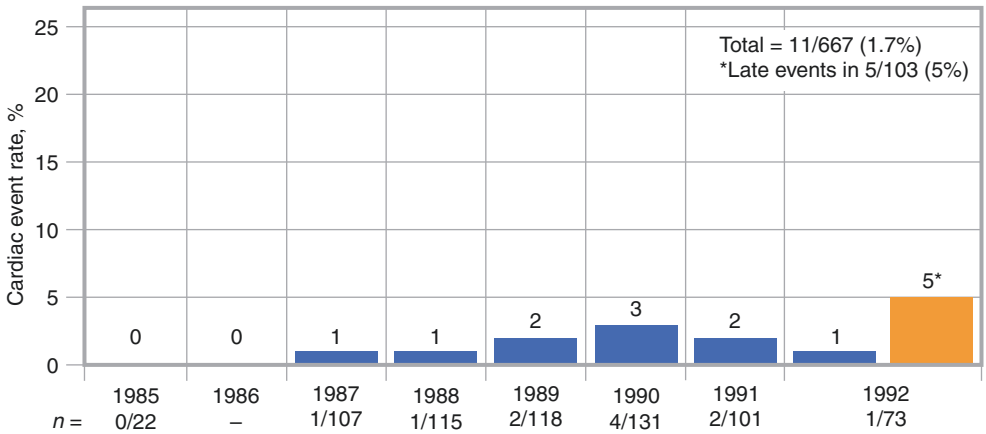

Fig. 5.23 Prognostic value of preoperative peripheral vascular disease assessment using dipyridamole–^{201}Tl imaging. In serial studies reported between 1985 and 1992 in patients with a normal scan, the rate of cardiac events (death or MI) ranged from 0% to 3% [61, 71]. The overall average hard event rate in patients with peripheral vascular disease (PVD) with a normal scan is 1.7%. Data regarding the excellent prognostic value of adenosine, dipyridamole, or dobutamine are widely reported [72]. Data have also demonstrated excellent risk stratification in patients who present with medically stabilized unstable angina [73] following an uncomplicated acute MI [74–76] and for preoperative assessment in patients before vascular surgery or organ transplantation [65, 66]

In studies of preoperative dipyridamole Tl-201 imaging between 1985 and 1994, of 2679 patients in 17 studies, 1186 (44.3%) experienced ischemia, and MI or death occurred in 178 (6.6%). In six studies involving 445 patients, 149 (33.0%) had ischemia, and MI or death occurred in 40 (9.0%).

The clinical role of cardiac imaging in evaluating patients prior to noncardiac surgery has been established [48, 72], as both the number of procedures performed each year and the age and complexity of patients referred for surgery has increased. Table 5.7 shows cardiac risk stratification for noncardiac surgical procedures. A careful history and physical examination are mandatory to assess whether preexisting medical conditions exist and to determine the likelihood of occult underlying cardiovascular disease [44, 49, 60, 77]. The decision to perform surgery and the associated cardiovascular risk must also be placed in context of the urgency and type of the procedure to be performed. This is particularly true for vascular surgery [44, 50, 58, 59, 62, 64, 67, 78–82], where there is a high (30–50%) prevalence of underlying coronary artery disease. In other procedures associated with large fluid shifts and/or blood loss that can lead to hemodynamic instability, event risk is also high. In emergency surgery for a life-threatening condition when preoperative risk stratification is not possible, perioperative medical management and careful monitoring for cardiac complications is essential [55]. In patients referred for less urgent or elective procedures, complete risk evaluation can be based on clinical variables and the results of noninvasive testing. Comparisons of stress imaging data to left ventricular function assessments, at rest or with stress, have also been performed [53, 57, 63, 69].

High (cardiac risk often >5%)
Emergency major operations, particularly in the elderly
Aortic and other major vascular surgery
Peripheral vascular surgery
Anticipated prolonged surgical procedures associated with large fluid shifts and/or blood loss
Intermediate (cardiac risk generally <5%)
Carotid endarterectomy
Head and neck surgery
Intraperitoneal and intrathoracic surgery
Orthopedic surgery
Prostate surgery
Low (cardiac risk generally < 1%)[b]
Endoscopic procedures
Superficial procedures
Cataract surgery
Breast surgery

[a]Combined incidence of cardiac death and nonfatal myocardial infarction
[b]Patients do not generally require further preoperative cardiac testing

Table 5.7 Cardiac risk stratification[a] for noncardiac surgical procedures

Current Clinical Practice Guidelines

The 2007 American College of Cardiology (ACC)/American Heart Association (AHA) Guidelines emphasize that preoperative coronary interventions are rarely indicated to reduce imminent surgical risk unless a longer term survival benefit also accrues, as shown in Fig. 5.24 [83–85].

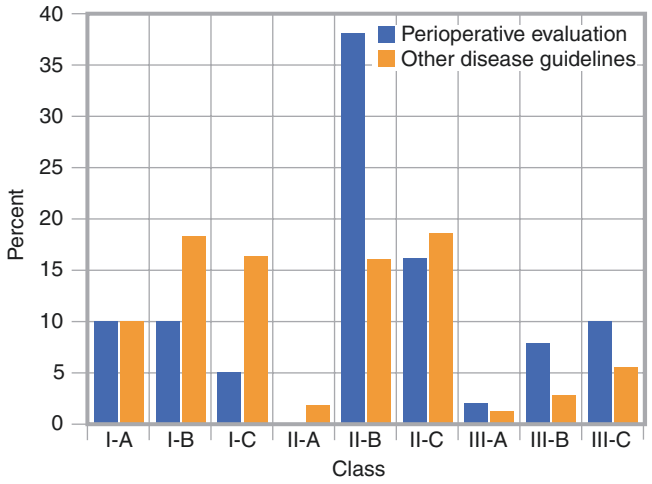

Fig. 5.24 ACC/AHA guidelines for preoperative coronary interventions

The ACC/AHA preoperative risk assessment guidelines for noninvasive stress testing before noncardiac surgery (2007) are listed in Table 5.8. The significance of preoperative risk assessment and perioperative care of patients at risk for cardiac events while undergoing noncardiac surgery is reflected by the extensive medical literature on the subject and by the intensive efforts by the ACC and the AHA to update their 2002 [83] expert practice guidelines in 2007 [84, 85]. Although both sets of ACC/AHA guidelines favored an exercise stress test (EST) in patients with a normal resting echocardiogram (EKG), exercise stress is not feasible in many vascular and high-risk surgical candidates. Also, EST lacks sensitivity and specificity compared to other approaches even in the absence of resting EKG changes.

Class I
Patients with active cardiac conditions in whom noncardiac surgery is planned should be evaluated and treated per ACC/AHA guidelines before noncardiac surgery (*Level of evidence: B*)
Class IIa
Noninvasive stress testing of patients with three or more clinical risk factors and poor functional capacity (less than 4 METs) who require vascular surgery is reasonable if it will change management (*Level of evidence: B*)
Class IIb
Noninvasive stress testing may be considered for patients with at least one or two clinical risk factors and poor functional capacity (less than 4 METs) who require intermediate-risk or vascular surgery, if it will change management (*Level of evidence: B*)
Class III
Noninvasive testing is not useful for patients with no clinical risk factors who are undergoing intermediate-risk noncardiac surgery (*Level of evidence: C*)
Noninvasive testing is not useful for patients undergoing low-risk noncardiac surgery (*Level of evidence: C*)

ACC American College of Cardiology, *AHA* American Heart Association

Table 5.8 ACC/AHA preoperative Risk Assessment guidelines for noninvasive stress testing before noncardiac surgery (2007)

There are no Class I ("should be performed") recommendations for preoperative stress imaging in the current 2007 ACC/AHA guidelines; in these guidelines, the distribution of class of recommendations and level of evidence for perioperative evaluation differs from that for other current disease guidelines [85] (Table 5.9 and Fig. 5.25). The perioperative evaluation guideline recommendations are primarily class II, reflecting conflicting evidence and/or a divergence of opinion about usefulness and/or efficacy and level of evidence (LOE) based on evidence from a single randomized clinical trial or nonrandomized studies.

Recommendation	Years	Class, %			Level of Evidence, %		
		I	II	III	A	B	C
Perioperative evaluation	2007	26	54	20	12	56	32
All disease guidelines	2002–2008	49	39	12	12	39	54

ACC American College of Cardiology, *AHA* American Heart Association

Table 5.9 Perioperative ACC/AHA guideline evaluation guideline recommendations by class

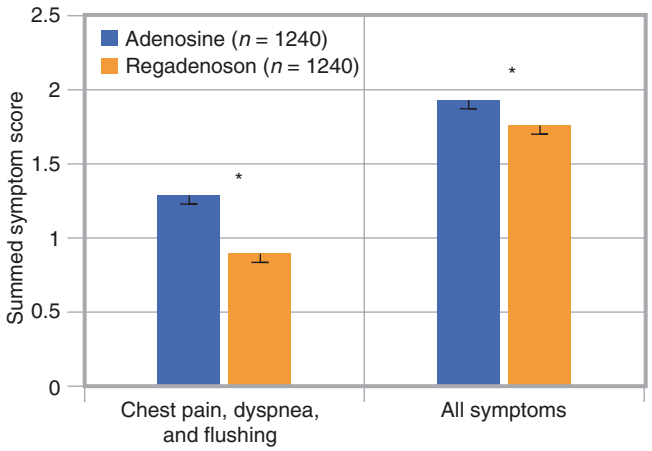

Fig. 5.25 Side effects with adenosine or regadenoson. In a direct comparison of side effects among subjects randomized in Adenoscan Versus Regadenoson Comparative Evaluation for Myocardial Perfusion Imaging-1 trial to adenosine ($n = 631$) or regadenoson ($n = 1240$), adenosine produced significantly higher (*asterisk*) subjective rates of chest pain, dyspnea, and flushing, and higher rates of all symptoms following drug stress [22]

Of note, between the publication of the 1996 ACC/AHA Guidelines and the 2007 Guidelines, a significant change was observed in the distribution of class of recommendations and LOE, which differed as compared with other updated disease guidelines (Table 5.10). A large increase in class II (+88.8%) and a large decrease in class III (−53.4%) recommendations occurred in the perioperative evaluation guidelines, reflecting positive trends in the evidence and/or expert agreement as to its clinical value. The LOE distribution across classes of recommendations in the current guidelines for perioperative evaluation (2007) and other diseases (2002–2008) also differ.

Recommendation	Years	Class, %		
		I	II	III
Perioperative evaluation	1996–2007	−9.3	88.8	−53.4
Other disease guidelines	1995–2008	−10.2	16.7	−10.6

Table 5.10 Changes in class of recommendation and level of evidence from first to current guidelines

Clinical Utility of Stress Imaging in Perioperative Risk Assessment

The goal of preoperative risk stratification is not simply to provide surgical "clearance," but to comprehensively evaluate longer-term risk and to plan care. The risk ratios for cardiac death, MI, and other complications associated with individual and/or grouped risk markers can identify patient groups that may benefit from more aggressive perioperative medical management and monitoring or from a change from surgery to less invasive treatment modalities.

The two main techniques used in the preoperative evaluation of patients undergoing noncardiac surgery who cannot exercise are to increase myocardial oxygen demand (by pacing or intravenous dobutamine) and to induce coronary hyperemia using pharmacological vasodilators. The most frequent pharmacologic stress tests in clinical use are dobutamine stress echocardiography and vasodilator stress myocardial perfusion imaging (MPI) with thallium-201 or ^{99m}technetium.

The imaging systems, radiotracers, stress protocols and agents (Fig. 5.25), image analysis, electrocardiogram gating, and quality controls of MPI have evolved technically over the past three decades. Despite the acknowledged limitations of an aging medical literature vis-a-vis modern surgical population risk profiles (i.e., pre- and post-test risks) and interventional options, preoperative stress MPI continues to exhibit major clinical utility in this common consultative setting [86]. Several major findings among published studies do remain useful:

- A greater extent of stress-induced ischemia is associated with a greater risk of perioperative cardiac events (presumably related to more severe underlying coronary artery disease).
- The absence of ischemia (i.e., a normal scan) is associated with low perioperative and near-term risk (i.e., has a high negative predictive value for cardiac events).
- Left ventricle functional impairment is an independent, incremental (with MPI findings) risk marker with the following characteristics:
  - Cardiopulmonary stress testing anaerobic threshold <11 mL/min/kg [87]
  - Resting and/or post-stress electrocardiogram-gated SPECT ejection fraction <40%
  - Poor exercise tolerance, <4 METs [84]

Recent Clinical Applications

A recently reported clinical application for preoperative pharmacologic stress imaging has been as part of a combination used for risk stratification before liver transplantation (Fig. 5.26).

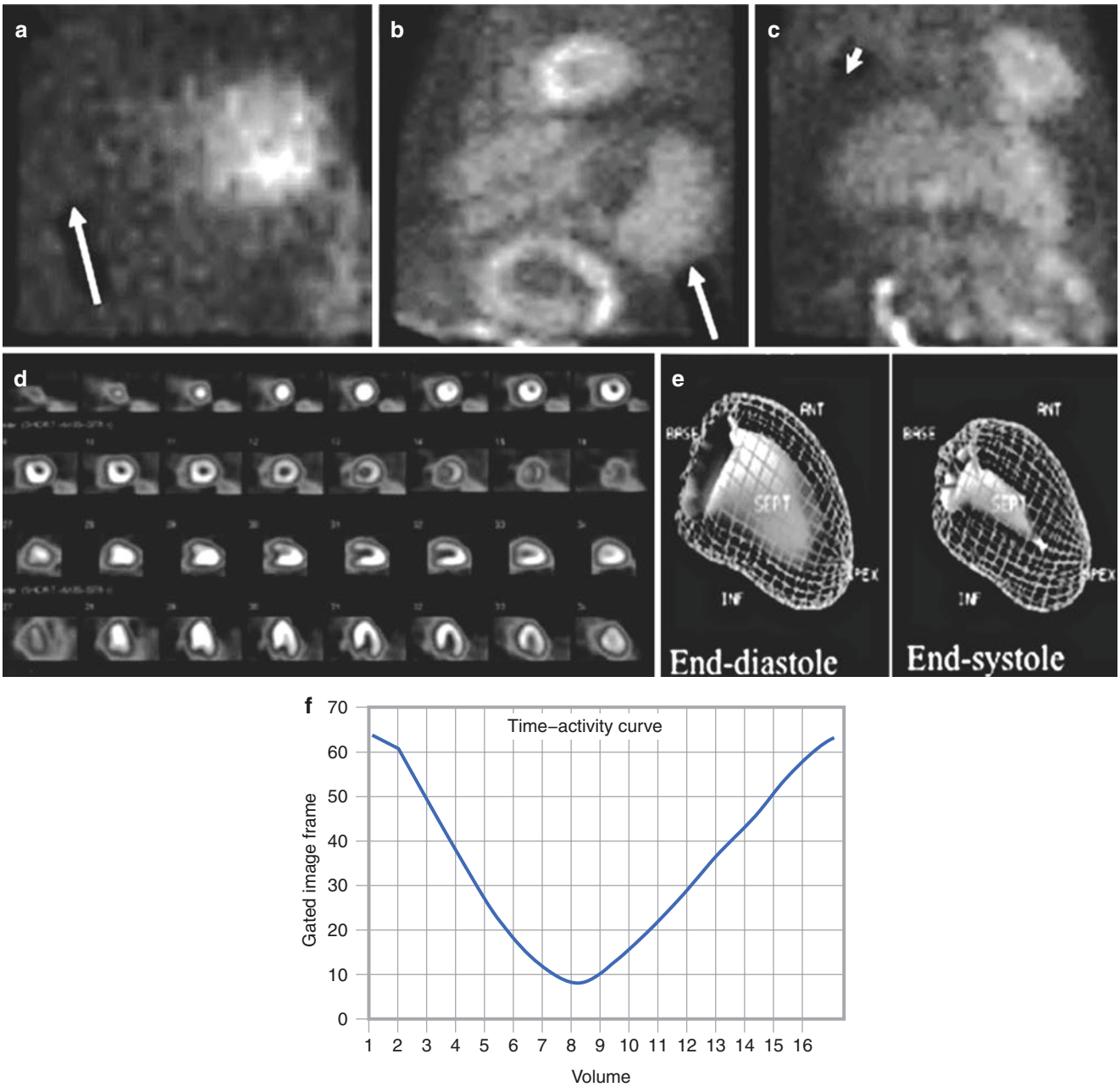

Fig. 5.26 One of the more recent reported utilities for preoperative pharmacologic stress imaging has been in combination with functional myocardial perfusion imaging [25] or cardiac MRI [88] in end-stage liver disease patients being risk stratified before liver transplantation. Regadenoson, adenosine, or dobutamine can all be safely used in this high-risk, critically ill surgical population. (**a**) Raw cine image showing a lack of tracer uptake in the cirrhotic liver (*arrow*). (**b**) Evidence of an enlarged spleen is shown (*arrow*). (**c**) Evidence of ascites is seen in another patient (*arrow*). (**d**) SPECT myocardial perfusion images in short, vertical, and horizontal long-axis projections show normal perfusion and excellent image quality. (**e**) Shown are normal left ventricle size and function on electrocardiogram-gated three-dimensional SPECT images. (**f**) The time-activity curve shows a normal left ventricle ejection [25]

Stress Imaging Modality Choice

Nonselective adenosine receptor agonists (i.e., dipyridamole, adenosine) should be avoided in patients with a risk of bronchospasm; selective A_{2A} receptor agonists may be safer [12, 22]. Randomized, double-blind, placebo-controlled trials have demonstrated the pulmonary functional tolerability of regadenoson and apadenoson in mild to moderate asthma [7, 8] and moderate to severe COPD [9, 10]. Conditions that prevent patients from being withdrawn from methylxanthine drugs (i.e., theophylline) are adenosine receptor agonist contraindications; moderate caffeine consumption does not attenuate regadenoson coronary vasodilator effects [89]. Dobutamine stress should not be used in patients with serious arrhythmias, severe hypertension, or hypotension. If echocardiographic image quality is likely to be poor, MPI or MRI is more appropriate. Concerns about heart valve dysfunction favor the use of echocardiographic stress testing. When either stress MPI, MRI, or echocardiography is appropriate, the expertise of the interpreter and/or the laboratory for identifying CAD is as important as the type of stress test utilized.

The prognostic value of pharmacologic stress myocardial perfusion imaging for major adverse cardiac events (MACE) is well established in diverse at-risk acute coronary syndrome and chronic coronary artery disease cohorts. Normal stress imaging studies confer low risk of MACE, at annual event rate ≤2% for 18–24 months (Figs. 5.27, 5.28, and 5.29).

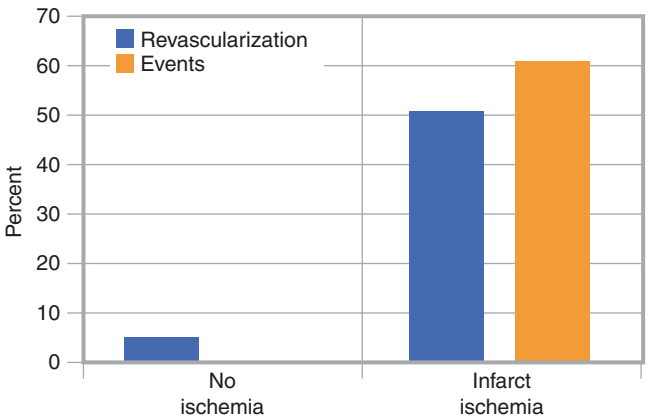

Fig. 5.27 Predictive accuracy of early post–MI imaging with dipyridamole–^{201}Tl. The presence of infarct zone ischemia is predictive of a higher rate of coronary revascularization and other cardiac events. In the absence of ischemia, revascularization and cardiac events are very low. Imaging in this multicenter study was safely performed 2–4 days after uncomplicated MI. Pharmacologic testing is useful for identifying both early and late risk for cardiac events. For example, data demonstrate that early (2–4 days) dipyridamole sestamibi perfusion imaging after an uncomplicated MI is a safe and powerful predictor of future cardiac death and recurrent MI [71] and offers incremental prognostic value to that of submaximal exercise testing [90]

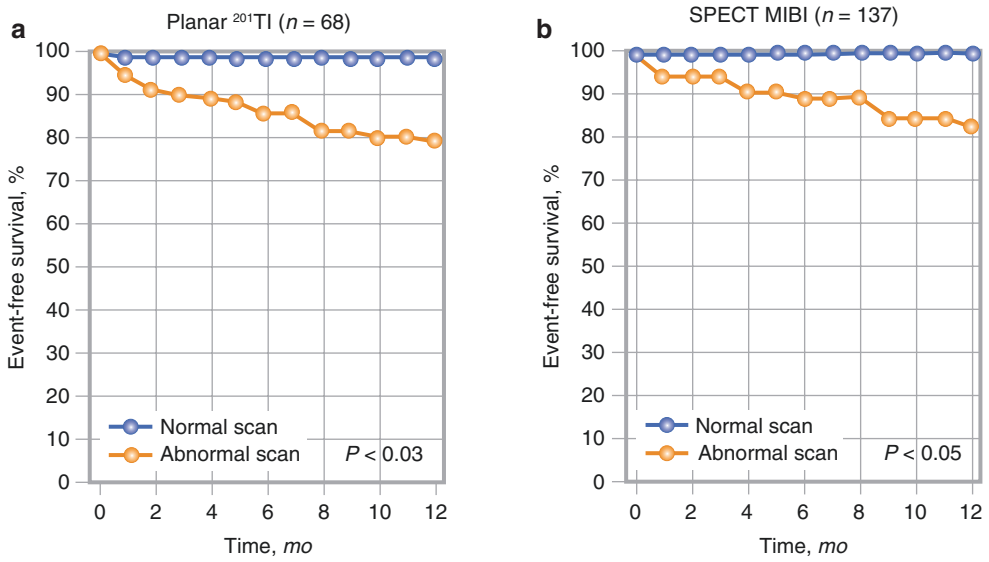

Fig. 5.28 Prognostic value of predischarge dipyridamole stress myocardial imaging for predicting cardiac death or MI in combination with planar ^{201}TI (n = 68) (**a**) or SPECT sestamibi (MIBI) (n = 137) (**b**) in patients with a medically stabilized recent ischemic event (MI or unstable angina). Both techniques identify a low-risk subset with a normal scan and few cardiac events over 1 year following the acute ischemic event. The event rate in patients with an abnormal scan is significantly higher, regardless of the imaging technique. In patients with unstable angina, the very low mortality rate associated with a normal scan supports a conservative medical management approach [53, 75]. A large prospective randomized trial, the Adenosine Sestamibi SPECT Postinfarction Evaluation (INSPIRE) trial, was designed to determine the value of sequential perfusion imaging to assess postinfarction myocardium at risk and changes following medical and revascularization therapy [76, 91, 92]

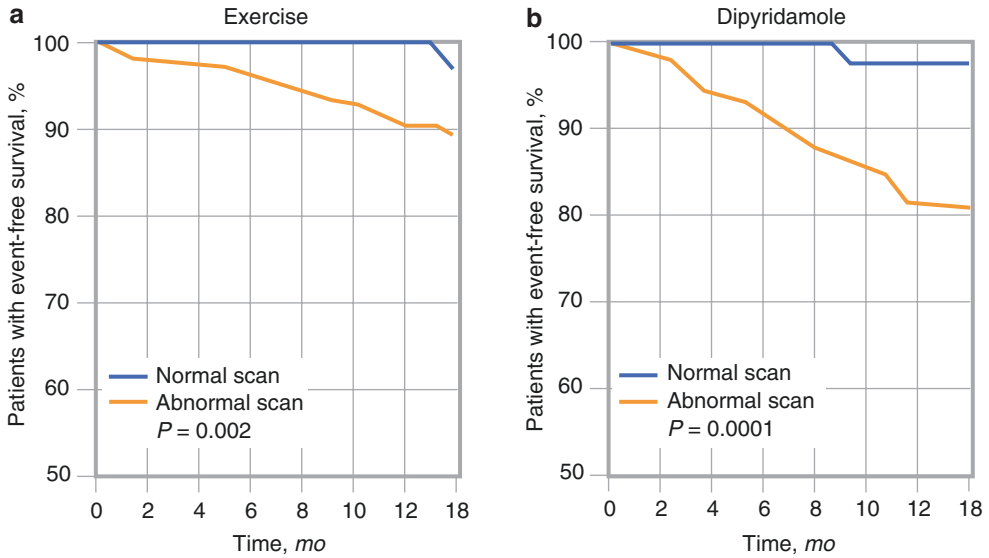

Fig. 5.29 Prognostic value of ^{99m}Tc-sestamibi imaging in patients with stable chest pain. Exercise testing (**a**) is compared with dipyridamole testing (**b**) in similar populations. A normal scan is associated with a low 18-month cardiac event rate and good cardiac event–free survival, regardless of the stress approach utilized. Significantly higher cardiac event rates and poorer cardiac event–free survival occur in the presence of an abnormal dipyridamole scan in stable patients with chest pain [70, 93, 94]. Two studies [95, 96] using adenosine stress sestamibi imaging confirmed less than 5–10% likelihood of CAD in patients with a normal scan. Other studies have demonstrated that lung uptake of ^{201}TI or ^{99m}Tc-sestamibi following pharmacologic stress is an indicator of global left ventricular dysfunction and possible multivessel disease. Transient ischemic dilatation may be seen in patients with severe and/or extensive CAD with either exercise or vasodilator stress [92, 93]

The American College of Cardiology/American Heart Association Task Force has published updated practice guidelines for perioperative cardiovascular evaluation prior to noncardiac surgery [84]. These recommendations embody expert and evidence-based considerations and identify specific clinical markers, patient functional capacity, and the type of surgery to be performed as crucial factors for deciding which patients need more intensive preoperative evaluation. The major, intermediate, and minor clinical predictors of increased perioperative cardiovascular risk are summarized (Table 5.11). A medical history and physical examination can elicit clinical risk predictors including angina, prior MI, congestive heart failure, arrhythmias, diabetes, peripheral vascular disease, and prior coronary revascularization procedures. Asymptomatic patients with known CAD who have had coronary revascularization within the past 5 years require no further evaluation. Surgery can also proceed in patients with CAD when the results of a recent cardiac catheterization or stress test reflect clinical stability.

Major
Unstable coronary syndromes
Recent MI[a] with evidence of important ischemic risks by clinical symptoms or noninvasive study
Unstable or severe[b] angina (CCS III or IV)
Decompensated congestive heart failure
Significant arrhythmias
High-grade AV block
Symptomatic ventricular arrhythmias in the presence of underlying heart disease
Supraventricular arrhythmias with uncontrolled ventricular rate
Severe valvular disease
Intermediate
Mild angina pectoris (CCS I or II)
Prior MI by history of pathologic Q waves
Compensated or prior congestive heart failure
Diabetes mellitus
Minor
Advanced age
Abnormal ECG (LV hypertrophy, LBBB, ST-T abnormalities)
Rhythm other than sinus (e.g., atrial fibrillation)
Low functional capacity (e.g., inability to climb one flight of stairs with a bag of groceries)
History of stroke
Uncontrolled systemic hypertension

CCS Canadian Cardiovascular Society
[a]*Recent* is defined as >7 days but ≤30 days
[b]May include stable angina in unusually sedentary patients

Table 5.11 Clinical predictors of perioperative events

In patients who have any of the recognized major clinical predictors of risk, a full cardiac workup is warranted prior to surgery. The appropriate assessment would include coronary angiography, echocardiography to assess LV ejection function and valvular abnormalities, or noninvasive stress imaging to detect myocardial ischemia. In the intermediate-risk category, the functional capacity of the patient and the type of surgical procedure determine whether further testing is indicated. Cardiac testing is necessary in intermediate-risk patients with a functional capacity of fewer than four metabolic equivalents and those with moderate or excellent functional capacity who are undergoing a high-risk surgical procedure.

Patients with good functional capacity who are undergoing an intermediate-risk or low-risk surgical procedure generally do not require preoperative cardiac testing. In patients with minor or no clinical risk predictors, surgery can be performed without further evaluation unless patients have poor functional capacity or the surgery is high-risk.

Although functional capacity is an important determinant of risk, exercise stress testing (with or without imaging) is not possible in many patients who require further preoperative evaluation. Patients with prior MI, congestive heart failure, or pulmonary disease; elderly or obese patients; and patients referred for peripheral vascular, orthopedic, or neurologic procedures may not be able to exercise adequately. In this setting, pharmacologic stress myocardial perfusion imaging is the preferred method of preoperative screening.

References

1. Henzlova MJ, Duvall WL, Einstein AJ, Travin MI, Verberne HJ. ASNC imaging guidelines for SPECT nuclear cardiology procedures: stress, protocols, and tracers. J Nucl Cardiol. 2016;23:606–39. Erratum in: J Nucl Cardiol. 2016;23:640–2.
2. American Thoracic Society/American College of Chest Physicians. Joint Statement of the American Thoracic Society (ATS) and the American College of Chest Physicians (ACCP) on cardio-pulmonary exercise testing. Am J Respir Crit Care Med. 2003;167:211–77.
3. Klocke FJ, Baird MG, Bateman TM, Bateman TM, Messer JV, Berman DS, et al. ACC/AHA/ASNC guidelines for clinical use of cardiac radionuclide imaging: a report of the American College of Cardiology/American Heart Association Task Force on Practice Guidelines. J Am Coll Cardiol. 2003;42(7):1318–33.
4. Suleman A, Riaz K, Heffner KD. Exercise physiology. Available at: http://emedicine.medscape.com/article/88484-overview. Accessed 17 July 2018.
5. Hendel RC. Update on myocardial perfusion imaging: role of regadenoson. Rep Med Imaging. 2009;2:13–23.
6. Shaffer J, Simbartl L, Render ML, Snow E, Chaney C, Nishiyama H, et al. Patients with stable chronic obstructive pulmonary disease can safely undergo intravenous dipyridamole thallium-201 imaging. Am Heart J. 1998;136:307–13.
7. Leaker BR, O'Connor B, Hansel TT, Barnes PJ, Meng L, Mathur VS, Lieu HD. Safety of regadenoson, an adenosine A_{2A} receptor agonist for myocardial perfusion imaging, in mild asthma and moderate asthma patients: a randomized, double-blind, placebo-controlled trial. J Nucl Cardiol. 2008;15:329–36.
8. Williams S, McArdle J, Colice G, Lankford A, Zou W, Reed C. A randomized double-blind placebo-controlled study of the safety of apadenoson in subjects with mild to moderate asthma. J Nucl Cardiol. 2010;17:724.
9. Prenner BM, Bukofzer S, Behm S, Feaheny K, McNutt BE. A randomized, double-blind, placebo-controlled study assessing the safety and tolerability of regadenoson in subjects with asthma or chronic obstructive pulmonary disease. J Nucl Cardiol. 2012;19:681–92.
10. Golzar Y, Doukky R. Regadenoson use in patients with chronic obstructive pulmonary disease: the state of current knowledge. Int J Chron Obstruct Pulmon Dis. 2014;9:129–37.
11. Gemignani AS, Abott BG. The emerging role of the selective A_{2A} agonist in pharmacologic stress testing. J Nucl Cardiol. 2010;17:494–7.
12. Hendel RC, Moreno NA, Glover DK. Pharmacologic stress using selective A_{2A} adenosine receptor agonists. Curr Cardiovasc Imaging Rep. 2011;4:217–26.
13. Pennell DJ, Ell PJ. Whole-body imaging of thallium-201 after six different stress regimens. J Nucl Med. 1994;35:425–8.
14. Wu JC, Yun JJ, Heller EN, Dione DP, DeMan P, Liu YH, et al. Limitations of dobutamine for enhancing flow heterogeneity in the presence of single coronary artery stenosis: implications for technetium-99m-sestamibi imaging. J Nucl Med. 1998;39:417–25.
15. Udelson JE, Heller GV, Wackers FJ, Chai A, Hinchman D, Coleman PS, et al. Randomized, controlled dose-ranging study of the selective adenosine A_{2a} receptor agonist binodenoson for pharmacological stress as an adjunct to myocardial perfusion imaging. Circulation. 2004;109:457–64.
16. Gao Z, Otero DH, Zablock JA, et al. Time course of changes in coronary conductance caused by regadenoson, binodenoson, CGS21680, and adenosine. Pharmacological characterization of novel A_{2A} adenosine receptor (A_{2A}AdoR) agonists. Drug Dev Res. 2000;50:93.
17. Lieu HD, Shryock JC, von Mering GO, Gordi T, Blackburn B, Olmsted AW, et al. Regadenoson, a selective A_{2A} adenosine receptor agonist, causes dose-dependent increases in coronary blood flow velocity in humans. J Nucl Cardiol. 2007;14:514–20.
18. Homma S, Gilliland Y, Guiney TE, Strauss HW, Boucher CA. Safety of intravenous dipyridamole for stress testing with thallium imaging. Am J Cardiol. 1987;59:152–4.
19. Verani MS, Mahmarian JJ, Hixson JB, Boyce TM, Staudacher RA. Diagnosis of coronary artery disease by controlled coronary vasodilation with adenosine and thallium-201 scintigraphy in patients unable to exercise. Circulation. 1990;82:80–7.
20. Piirainen H, Ashok Y, Nanekar RT, Jaakola VP. Structural features of adenosine receptors: from crystal to function. Biochim Biophys Acta. 1808;2011:1233–44.
21. Mahmarian JJ, Cerqueira MD, Iskandrian AE, Bateman TM, Thomas GS, Hendel RC, et al. Regadenoson induces comparable left ventricular perfusion defects as adenosine: a quantitative analysis from the ADVANCE MPI 2 Trial. JACC Cardiovasc Imaging. 2009;2:959–68.
22. Cerqueira MD, Nguyen P, Staehr P, Underwood SR, Iskandrian AE, ADVANCE-MPI Trial Investigators. Effects of age, gender, obesity, and diabetes on the efficacy and safety of the selective A2A agonist regadenoson versus adenosine in myocardial perfusion imaging integrated ADVANCE-MPI trial results. JACC Cardiovasc Imaging. 2008;1:307–16.
23. Gao ZG, Jacobson KA. Emerging adenosine receptor agonists: an update. Expert Opin Emerg Drugs. 2011;16(4):597–602.
24. Aljaroudi W, Hermann D, Hage F, Heo J, Iskandrian AE. Safety of regadenoson in patients with end-stage renal disease. Am J Cardiol. 2010;105:133–5.
25. Aljaroudi W, Iqbal F, Koneru J, Bhambhvani P, Heo J, Iskandrian AE. Safety of regadenoson in patients with end-stage liver disease. J Nucl Cardiol. 2011;18:90–5.
26. Grady EC, Barron JT, Wagner RH. Development of asystole requiring cardiac resuscitation after the administration of regadenoson in a patient with pulmonary fibrosis receiving n-acetylcysteine. J Nucl Cardiol. 2011;18:521–5.
27. Venkataraman R, Al Jaroudi W, Belardinelli L, Heo J, Iskandrian AE. The effect of ranolazine on the vasodilator-induced myocardial perfusion abnormality. J Nucl Cardiol. 2011;18:456–62.
28. Udelson JE, Iteld B, Weiland F, Foster J, Bonow R, Ficaro E, et al. Vasodilator induced stress in concordance with adenosine. VISION: binodenoson pivotal clinical trial program. Presented at the 57th Annual Scientific Session of the American College of Cardiology. Chicago, March 29–April 1, 2008 (Abstract 409-05).
29. Hendel R, Taillefer R, Crane P, Widner P. Preliminary experience with BMS068645, a selective A_{2A} adenosine agonist for pharmacologic stress myocardial perfusion imaging. Circulation. 2005;112:474.
30. Zoghbi GJ, Dorfman TA, Iskandrian AE. The effects of medications on myocardial perfusion. J Am Coll Cardiol. 2008;52:401–16.
31. Shaw LJ, Berman DS, Maron DJ, for the COURAGE Investigators, et al. Optimal medical therapy with or without percutaneous coronary intervention to reduce ischemic burden. Results from the Clinical Outcomes Utilizing Revascularization and Aggressive Drug Evaluation (COURAGE) Trial nuclear substudy. Circulation. 2008;117:1283–91.
32. Marshall ES, Raichlen JS, Tighe DA, Paul JJ, Breuninger KM, Chung EK. ST-segment depression during adenosine infusion as a predictor of myocardial ischemia. Am Heart J. 1994;127:305–11.
33. Nishimura S, Mahmarian JJ, Boyce TM, Verani MS. Equivalence between adenosine and exercise thallium-201 myocardial tomography: a multicenter, prospective, crossover trial. J Am Coll Cardiol. 1992;20:265–75.
34. Taillefer R, Amyot R, Turpin S, Lambert R, Pilon C, Jarry M. Comparison between dipyridamole and adenosine as pharmacologic coronary vasodilators in detection of coronary artery disease with thallium 201 imaging. J Nucl Cardiol. 1996;3:204–11.
35. Miller DD, Donohue TJ, Younis LT, Bach RG, Aguirre FV, Wittry MD, et al. Correlation of pharmacological 99mTc-sestamibi myocardial perfusion imaging with poststenotic coronary flow reserve in patients with angiographically intermediate coronary artery stenoses. Circulation. 1994;89:2150–60.
36. Samady H, Wackers FJ, Joska TM, Zaret BL, Jain D. Pharmacologic stress perfusion imaging with adenosine: role of simultaneous low-level treadmill exercise. J Nucl Cardiol. 2002;9:188–96.

37. Vitola JV, Brambatti JC, Caligaris F, Lesse CR, Nogueira PR, Joaquim AI, et al. Exercise supplementation to dipyridamole prevents hypotension, improves electrocardiogram sensitivity, and increases heart-to-liver activity ratio on Tc-^{99m} sestamibi imaging. J Nucl Cardiol. 2001;8:652–9.
38. Thomas GS, Prill NV, Majmundar H, Fabrizi RR, Thomas JJ, Hayashida C, et al. Treadmill exercise during adenosine infusion is safe, results in fewer adverse reactions, and improves myocardial perfusion image quality. J Nucl Cardiol. 2000;7:439–46.
39. Elliott MD, Holly TA, Leonard SM, Hendel RC. Impact of an abbreviated adenosine protocol incorporating adjunctive treadmill exercise on adverse effects and image quality in patients undergoing stress myocardial perfusion imaging. J Nucl Cardiol. 2000;7:584–9.
40. Jamil G, Ahlberg AW, Elliott MD, Hendel RC, Holly T, McGill CC, et al. Impact of limited treadmill exercise on adenosine Tc-99m sestamibi single-photon emission computed tomographic myocardial perfusion imaging in coronary artery disease. Am J Cardiol. 1999;84:400–3.
41. Candell-Riera J, Santana-Boado C, Castell-Conesa J, Aguadé-Bruix S, Olona M, Palet J, et al. Simultaneous dipyridamole/maximal subjective exercise with 99mTc-MIBI SPECT: improved diagnostic yield in coronary artery disease. J Am Coll Cardiol. 1997;29:531–6.
42. Pennell DJ, Mavrogeni SI, Forbat SM, Karwatowski SP, Underwood SR. Adenosine combined with dynamic exercise for myocardial perfusion imaging. J Am Coll Cardiol. 1995;25:1300–9.
43. Thomas GS, Thompson RC, Miyamoto MI, Ip TK, Rice DL, Milikien D, et al. The RegEx trial: a randomized, double-blind, placebo- and active-controlled pilot study combining regadenoson, a selective A_{2A} adenosine agonist, with low-level exercise, in patients undergoing myocardial perfusion imaging. J Nucl Cardiol. 2009;16:63–72.
44. Lette J, Waters D, Bernier H, Champagne P, Lassonde J, Picard M, et al. Preoperative and long-term cardiac risk assessment: predictive value of 23 clinical descriptors, 7 multivariate scoring systems, and quantitative dipyridamole imaging in 360 patients. Ann Surg. 1992;216:192–204.
45. Ranhosky A, Kempthorne-Rawson J. The safety of intravenous dipyridamole thallium myocardial perfusion imaging. Intravenous Dipyridamole Thallium Imaging Study Group. Circulation. 1990;81:1205–9.
46. Iskandrian AE, Bateman TM, Belardinelli L, Blackburn B, Cerqueira MD, Hendel RC, ADVANCE MPI Investigators, et al. Adenosine versus regadenoson comparative evaluation in myocardial perfusion imaging: results of the ADVANCE phase 3 multicenter international trial. J Nucl Cardiol. 2007;14:645–58.
47. Henzlova MJ, Cerqueira MD, Mahmarian JJ, Yao SS. Quality Assurance Committee of the American Society of Nuclear Cardiology. Stress protocols and tracers. J Nucl Cardiol. 2006;13:e80–90.
48. Boucher CA, Brewster DC, Darling RC, Okada RD, Strauss HW, Pohost GM. Determination of cardiac risk by dipyridamole-thallium imaging before peripheral vascular surgery. N Engl J Med. 1985;312:389–94.
49. Eagle KA, Coley CM, Newell JB, Brewster DC, Darling RC, Strauss HW, et al. Combining clinical and thallium data optimizes preoperative assessment of cardiac risk before major vascular surgery. Ann Intern Med. 1989;110:859–66.
50. Younis LT, Miller DD, Chaitman BR. Preoperative strategies to assess cardiac risk before non-cardiac surgery. Clin Cardiol. 1995;18:447–54.
51. Fletcher JP, Antico JF, Gruenewald S, Kershaw LZ. Dipyridamole-thallium scan for screening of coronary artery disease prior to vascular surgery. J Cardiovasc Surg. 1988;29:666–9.
52. Sachs RN, Tellier P, Larmignat P, Azorin J, Fischbein L, Beaudet B, et al. Assessment by dipyridamole-thallium-201 myocardial scintigraphy of coronary risk before peripheral vascular surgery. Surgery. 1988;103:584–7.
53. McEnroe CS, O'Donnell RF Jr, Yeager A, Konstam M, Mackey WC. Comparison of ejection fraction and Goldman risk factor analysis of dipyridamole-thallium-201 studies in the evaluation of cardiac morbidity after aortic aneurysm surgery. J Vasc Surg. 1990;11:497–504.
54. Younis LT, Aguirre F, Byers S, Dowell S, Barth G, Walker H, et al. Perioperative and long-term prognostic value of intravenous dipyridamole thallium scintigraphy in patients with peripheral vascular disease. Am Heart J. 1990;119:1287–92.
55. Mangano DT, London MJ, Tubau JF, Browner WS, Hollenberg M, Krupski W, et al. Dipyridamole thallium-201 scintigraphy as a preoperative screening test: a reexamination of its predictive potential. Study of Perioperative Ischemia Research Group. Circulation. 1991;84:493–502.
56. Strawn DJ, Guernsey JM. Dipyridamole thallium scanning in the evaluation of coronary artery disease in elective abdominal aortic surgery. Arch Surg. 1991;126:880–4.
57. Watters TA, Botvinick EH, Dae MW, Cahalan M, Urbanowicz J, Benefiel DJ, et al. Comparison of the findings on preoperative dipyridamole perfusion scintigraphy and intraoperative transesophageal echocardiography: implications regarding the identification of myocardium at ischemic risk. J Am Coll Cardiol. 1991;18:93–100.
58. Hendel RC, Whitfield SS, Villegas BJ, Cutler BS, Leppo JA. Prediction of late cardiac events by dipyridamole thallium imaging in patients undergoing elective vascular surgery. Am J Cardiol. 1992;70:1243–9.
59. Lette J, Walters D, Cerino M, Picard M, Champagne P, Lapointe J. Preoperative coronary artery disease risk stratification based on dipyridamole imaging and a simple three-step, three-segment model for patients undergoing noncardiac vascular surgery or major general surgery. Am J Cardiol. 1992;69:1553–8.
60. Madsen PV, Vissing M, Munck O, Kelbaek H. A comparison of dipyridamole thallium 201 scintigraphy and clinical examination in the determination of cardiac risk before arterial reconstruction. Angiology. 1992;43:306–11.
61. Brown KA, Rowen M. Extent of jeopardized viable myocardium determined by myocardial perfusion imaging best predicts perioperative cardiac events in patients undergoing noncardiac surgery. J Am Coll Cardiol. 1993;21:325–30.
62. Kresowik TF, Bower TR, Garner SA, Grover-McKay M, Slaymaker EE, Sharp WJ, et al. Dipyridamole thallium imaging in patients being considered for vascular procedures. Arch Surg. 1993;128:299–302.
63. Baron JF, Mundler O, Bertrand M, Vicaut E, Barré E, Godet G, et al. Dipyridamole-thallium scintigraphy and gated radionuclide angiography to assess cardiac risk before abdominal aortic surgery. N Engl J Med. 1994;330:663–9.
64. Bry JD, Belkin M, O'Donnell TF Jr, Mackey WC, Udelson JE, Schmid CH, Safran DG. An assessment of the positive predictive value and cost-effectiveness of dipyridamole myocardial scintigraphy in patients undergoing vascular surgery. J Vasc Surg. 1994;19:112–21.
65. Camp AD, Garvin PJ, Hoff J, Marsh J, Byers SL, Chaitman BR. Prognostic value of intravenous dipyridamole thallium imaging in patients with diabetes mellitus considered for renal transplantation. Am J Cardiol. 1990;65:1459–63.
66. Iqbal A, Gibbons RJ, McGoon MD, Steiroff S, Frohnert PT, Velosa JA. Noninvasive assessment of cardiac risk in insulin-dependent diabetic patients being evaluated for pancreatic transplantation using thallium-201 myocardial perfusion scintigraphy. Transplant Proc. 1991;23:1690–1.
67. Coley CM, Field TS, Abraham SA, Boucher CA, Eagle KA. Usefulness of dipyridamole-thallium scanning for preoperative evaluation of cardiac risk for nonvascular surgery. Am J Cardiol. 1992;69:1280–5.
68. Shaw LJ, Miller DD, Kong BA, Hilton T, Stelken A, Stocke K, Chaitman BR. Determination of perioperative cardiac risk by adenosine thallium-201 myocardial imaging. Am Heart J. 1992;124:861–9.

69. Takase B, Younis LT, Byers SL, Shaw LJ, Labovitz AJ, Chaitman BR, Miller DD. Comparative prognostic value of clinical risk indexes, resting two-dimensional echocardiography, and dipyridamole stress thallium-201 myocardial imaging for perioperative cardiac events in major nonvascular surgery patients. Am Heart J. 1993;126:1099–106.
70. Younis LT, Stratmann HG, Takase B, Byers S, Chaitman BR, Miller DD. Preoperative clinical assessment and dipyridamole thallium-201 scintigraphy for prediction and prevention of cardiac events in patients having major noncardiovascular surgery and known or suspected coronary artery disease. Am J Cardiol. 1994;74:311–7.
71. Hachamovitch R, Berman DS, Kiat H, Cohen I, Lewin H, Amanullah A, et al. Incremental prognostic value of adenosine stress myocardial perfusion single-photon emission computed tomography and impact on subsequent management in patients with or suspect of having myocardial ischemia. Am J Cardiol. 1997;80:426–33.
72. Shaw LJ, Eagle KA, Gersh BJ, Miller DD. Meta-analysis of intravenous dipyridamole-thallium-201 imaging (1985 to 1994) and dobutamine echocardiography (1991 to 1994) for risk stratification before vascular surgery. J Am Coll Cardiol. 1996;27:787–98.
73. Stratmann HG, Tamesis BR, Younis LT, Wittry MD, Amato M, Miller DD. Prognostic value of predischarge dipyridamole technetium 99m sestamibi myocardial tomography in medically treated patients with unstable angina. Am Heart J. 1995;130:734–40.
74. Brown KA, Heller GV, Landin RS, Shaw LJ, Beller GA, Pasquale MJ, Haber SB. Early dipyridamole Tc-99m sestamibi single photon emission computed tomographic imaging 2 to 4 days after acute myocardial infarction predicts in-hospital and postdischarge cardiac events: comparison with submaximal exercise. Circulation. 1999;100:2060–6.
75. Mahmarian JJ, Mahmarian AC, Marks GF, Pratt CM, Verani MS. Role of adenosine thallium-201 tomography for defining long-term risk in patients after acute myocardial infarction. J Am Coll Cardiol. 1995;25:1333–40.
76. Miller DD, Stratmann HG, Shaw LJ, Tamesis BR, Wittry MD, Younis LT, Chaitman BR. Dipyridamole technetium 99m sestamibi myocardial tomography as an independent predictor of cardiac event-free survival after acute ischemic events. J Nucl Cardiol. 1994;1:72–82.
77. Eagle KA, Singer DE, Brewster DC, Darling RC, Mulley AG, Boucher CA. Dipyridamole-thallium scanning in patients undergoing vascular surgery: optimizing preoperative evaluation of cardiac risk. JAMA. 1987;257:2185–9.
78. Koutelou MG, Asimacopoulos PJ, Mahmarian JJ, Kimball KT, Verani MS. Preoperative risk stratification by adenosine thallium-201 single-photon emission computed tomography in patients undergoing vascular surgery. J Nucl Cardiol. 1995;2:389–94.
79. Lane SE, Lewis SM, Pippin JJ, Kosinski EJ, Campbell D, Nesto RW, Hill T. Predictive value of quantitative dipyridamole-thallium scintigraphy in assessing cardiovascular risk after vascular surgery in diabetes mellitus. Am J Cardiol. 1989;64:1275–9.
80. Leppo JA, Plaja J, Gionet M, Tumolo J, Paraskos JA, Cutler BS. Noninvasive evaluation of cardiac risk before elective vascular surgery. J Am Coll Cardiol. 1987;9:269–76.
81. Levinson JR, Boucher CA, Coley CM, Guiney TE, Strauss HW, Eagle KA. Usefulness of semiquantitative analysis of dipyridamole-thallium-201 redistribution for improving risk stratification before vascular surgery. Am J Cardiol. 1990;66:406–10.
82. Cutler BS, Leppo JA. Dipyridamole thallium-201 scintigraphy to detect coronary artery disease before abdominal aortic surgery. J Vasc Surg. 1987;5:91–100.
83. Eagle KA, Berger PB, Calkins H, Chaitman BR, Ewy GA, Fleischmann KE, et al. American College of Cardiology; American Heart Association. ACC/AHA guideline update for perioperative cardiovascular evaluation for noncardiac surgery--executive summary: a report of the American College of Cardiology/American Heart Association Task Force on Practice Guidelines (Committee to Update the 1996 Guidelines on Perioperative Cardiovascular Evaluation for Noncardiac Surgery). J Am Coll Cardiol. 2002;39:542–53.
84. Fleisher LA, Beckman JA, Brown KA, Calkins H, Chaikof EL, Fleischmann KE, et al. ACC/AHA 2007 guidelines on perioperative cardiovascular evaluation and care for noncardiac surgery: a report of the American College of Cardiology/American Heart Association Task Force on Practice Guidelines (Writing Committee to Revise the 2002 Guidelines on Perioperative Cardiovascular Evaluation for Noncardiac Surgery) developed in collaboration with the American Society of Echocardiography, American Society of Nuclear Cardiology, Heart Rhythm Society, Society of Cardiovascular Anesthesiologists, Society for Cardiovascular Angiography and Interventions, Society for Vascular Medicine and Biology, and Society for Vascular Surgery. J Am Coll Cardiol. 2007;50:e159–241.
85. Tricoci P, Allen JM, Kramer JM, Califf RM, Smith SC. Scientific evidence underlying the ACC/AHA clinical practice guidelines. JAMA. 2009;301:831–41.
86. Weinstein H, Steingart R. Myocardial perfusion imaging for preoperative risk stratification. J Nucl Med. 2011;52:750–60.
87. Weinstein H, Bates AT, Spaltro BE, Thaler HT, Steingart RM. Influence of pre-operative exercise capacity on length of stay after thoracic cancer surgery. Ann Thorac Surg. 2007;84:197–202.
88. Biederman RW, Thai N, Oliva J, Dishart M, Veynovich B, Yamrozik J, et al. Exploratory use of cardiac magnetic resonance imaging in liver transplantation: a one-stop shop for preoperative cardiohepatic evaluation [Abstract]. J Am Coll Cardiol. 2011;57:e635.
89. Gaemperli O, Schepis T, Koepfli P, Siegrist PT, Fleischman S, Nguyen P, et al. Interaction of caffeine with regadenoson-induced hyperemic myocardial blood flow as measured by positron emission tomography: a randomized, double-blind, placebo-controlled crossover trial. J Am Coll Cardiol. 2008;51:328–9.
90. Brown KA, O'Meara J, Chambers CE, Plante DA. Ability of dipyridamole-thallium-201 imaging one to four days after acute myocardial infarction to predict in-hospital and late recurrent myocardial ischemic events. Am J Cardiol. 1990;65:160–7.
91. Mahmarian JJ, Shaw LJ, Olszewski GH, Pounds BK, Frias ME, Pratt CM, INSPIRE Investigators. Adenosine sestamibi SPECT post-infarction evaluation (INSPIRE) trial: a randomized, prospective multicenter trial evaluating the role of adenosine Tc-99m sestamibi SPECT for assessing risk and therapeutic outcomes in survivors of acute myocardial infarction. J Nucl Cardiol. 2004;11:458–69.
92. Younis LT, Byers S, Shaw L, Barth G, Goodgold H, Chaitman BR. Prognostic value of intravenous dipyridamole thallium scintigraphy after an acute myocardial ischemic event. Am J Cardiol. 1989;64:161–6.
93. Stratmann HG, Williams GA, Wittry MD, Chaitman BR, Miller DD. Exercise technetium-99m sestamibi tomography for cardiac risk stratification of patients with stable chest pain. Circulation. 1994;89:615–22.
94. Stratmann HG, Tamesis BR, Younis LT, Wittry MD, Miller DD. Prognostic value of dipyridamole technetium-99m sestamibi myocardial tomography in patients with stable chest pain who are unable to exercise. Am J Cardiol. 1994;73:647–52.
95. Amanullah AM, Lindvall K. Prevalence and significance of transient-predominately asymptomatic-myocardial ischemia on Holter monitoring in unstable angina pectoris, and correlation with exercise test and thallium-201 myocardial perfusion imaging. Am J Cardiol. 1993;72:144–8.
96. Nicolai E, Cuocolo A, Pace L, Nappi A, Sullo P, Cardei S, et al. Adenosine coronary vasodilation quantitative technetium 99m methoxy isobutyl isonitrile myocardial tomography in the identification and localization of coronary artery disease. J Nucl Cardiol. 1996;3:9–17.

Coronary Physiology and Quantitative Myocardial Perfusion

6

K. Lance Gould, Tung T. Nguyen, Richard Kirkeeide, and Nils P. Johnson

Why Coronary Physiology and Quantitative Perfusion?

Clinical orientation of our positron emission tomography (PET) images and quantitative data for our integrated *Cardiac Positron Imaging and Consultation Report* comprises the core of evidenced-based, optimal, highly personalized clinical care as essential to cardiology as angiograms, stents, bypass surgery, and vigorous medical management. It illustrates the power of quantitative regional myocardial perfusion as optimal gatekeeper or guidance for complex coronary artery disease (CAD) as requested by the revascularization team and referring physicians. Though our integrated technical and clinical approach may be unique, it demonstrates the principles and a standard of clinical coronary physiology for personalized patient management.

Our guiding philosophy is uncompromising, self-critical analysis of every case and every protocol, driven by hard data, which takes precedence over preconceived bias or silo thinking that may degrade our science and patient care. Continuous ongoing critical clinical and technical data review evolves our technology and protocols toward coronary physiologic truth for every patient, uncontaminated by suboptimal physiologic data, ego, financial interests, or competitive academic bias.

K. L. Gould (✉)
Weatherhead PET Center for Preventing and Reversing Atherosclerosis, University of Texas Medical School at Houston, Houston, TX, USA
e-mail: k.lance.gould@uth.tmc.edu

T. T. Nguyen · N. P. Johnson
Division of Cardiology, University of Texas Medical School at Houston, Houston, TX, USA

R. Kirkeeide
Department of Internal Medicine, McGovern Medical School, University of Texas Health Sciences Center at Houston, Houston, TX, USA

V. Dilsizian, J. Narula (eds.), *Atlas of Nuclear Cardiology*, https://doi.org/10.1007/978-3-030-49885-6_6

PET data are displayed as if looking at a patient who is transparent or as viewed by a cardiologist on fluoroscopy or a surgeon opening the chest (Fig. 6.1). The views are as if walking around the patient, seeing through to the right or septal side of the left ventricle (LV), then anterior, lateral, and inferior views, corresponding to the distributions of the three major coronary arteries. The pixel-based quantitative images define the actual perfusion size and severity of individual arteries down to tertiary branches, without assumed or standardized coronary artery distributions, which often differ from the actual regional perfusion of each coronary artery for a specific individual.

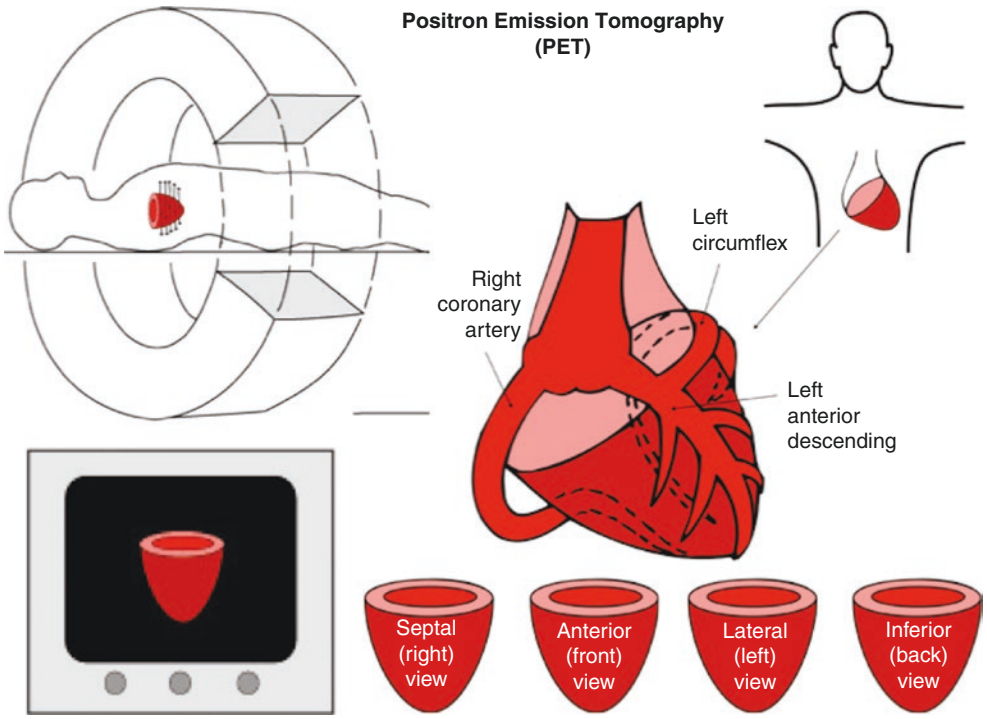

Fig. 6.1 Clinical orientation of positron emission tomography (PET) images

Our *Cardiac Positron Imaging and Consultation Report* includes a complete cardiovascular history, review of all prior tests (including angiogram, if done), physical exam, summary of conclusions, and recommendations, whether for medical treatment only, for angiography or revascularization, or for either option depending on clinical judgment, individual circumstances, and informed patient preference. Every regional and global abnormality for focal and diffuse CAD is reported, including objectively measured regional size and severity for each coronary artery (down to tertiary branches) on relative and quantitative images. The report also addresses symptoms or issues needing explanation, and includes recommendations for or against invasive procedures.

Over 40 years of our experience with quantitative coronary angiography and cardiac PET indicate that cardiologists and cardiac surgeons will not use or depend on any data or images that they cannot easily, quickly, and comprehensively understand directly related to their fluoroscopic or surgical views of the heart. These same physiologic-anatomic views, combined with comprehensive clinical integration by an experienced clinical cardiologist/physiologist consultant generates an evolving bidirectional trust within the cardiac team, in which quantitative coronary physiology drives optimal patient outcomes documented by hard outcomes in peer-reviewed publications.

The case in Fig. 6.2 illustrates the use of coronary physiology and quantitative perfusion. The *Cardiac Positron Imaging and Consultation Report* shown in Table 6.1 integrates the individual physiology, technical details, and clinical data for the same patient, as acquired routinely every day for every patient. For this case, PET shows severe stress defects (blue) in arterial distributions of the first septal perforator (basal septum) and a large first diagonal branch (anterior) with adequate only mildly reduced coronary flow capacity (CFC) (yellow) in the distribution of the left anterior descending (LAD), characteristic of LAD occlusion at their trifurcation proximal to a patent bypass graft. Myocardial steal in the septal and diagonal regions are typical for occlusion or severe stenosis with collaterals to viable myocardium.

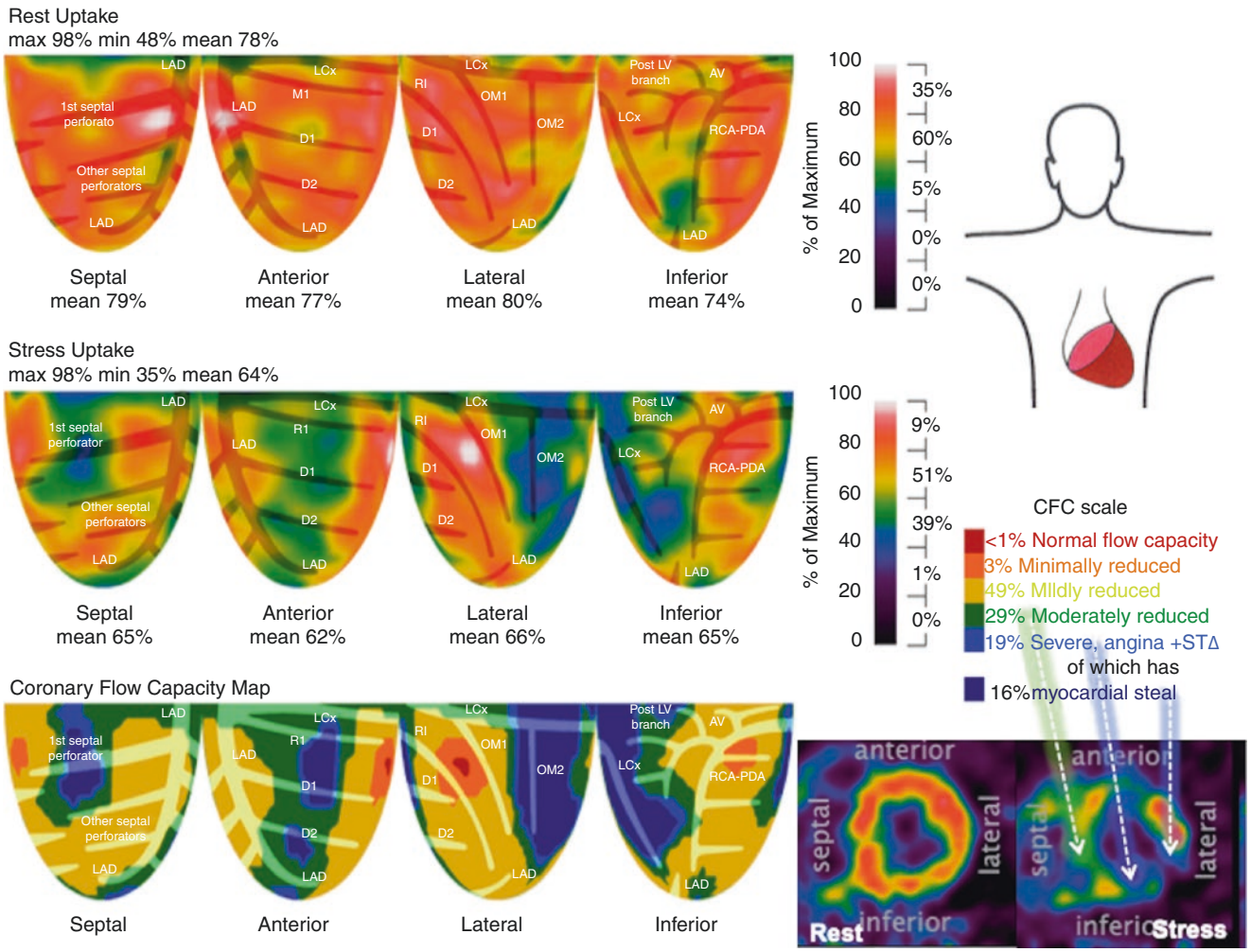

Fig. 6.2 A case study of coronary physiology and quantitative perfusion. The patient is a 66-year-old man referred for preoperative risk stratification prior to hip replacement. Cardiac history includes CAD after coronary artery bypass graft surgery (CABG) in 2009 and percutaneous coronary intervention (PCI) with a stent to the left anterior descending artery (LAD) in 2014. Residual risk factors include hypertension, hyperlipidemia, prior tobacco use, family history of CAD, atrial fibrillation, and exertion angina with dyspnea. The CFC map color codes each pixel for severity of combined stress perfusion in ml/m/g and coronary flow reserve (CFR), with the size and severity of every arterial distribution as the percentage of LV in the color-coded bar legend

1. The relative PET images show the following:
(i) A small, moderate, inferoapical, resting non-transmural scar involving 4% of the LV in the distribution of the distal LAD coronary artery, wrapping around the apex
(ii) A large, severe, lateral and inferolateral stress-induced defect involving 20% of the LV in the distribution of the mid left circumflex (LCx) coronary artery distal to the first obtuse marginal branch (OM1)
(iii) A large, moderate to severe, anterior, stress-induced defect involving 20% of the LV in the distribution of the diagonal branches off the LAD coronary artery, with a mild apical defect consistent with diffuse narrowing of a patent LAD
(iv) A small, moderate to severe, inferoseptal stress-induced defect involving 8% of the LV in the distribution of the proximal right coronary artery supplying the basal inferior septum with adequate distal perfusion suggesting adequate distal RCA perfusion due to excellent collaterals or a patent mid-RCA bypass graft
2. Coronary flow reserve (CFR) in the most severe stress-induced perfusion defect is 0.61, indicating myocardial steal in the anterior, inferoseptal, lateral, and inferolateral areas, reflecting collaterals to viable myocardium. Outside these severe defects (*blue*), absolute myocardial perfusion capacity is moderately reduced in border zones (*green*) and mildly reduced (*yellow*) diffusely throughout the heart but above thresholds for ischemia. Native arteries or bypass grafts to the LAD, RCA, and OM1 are likely patent
3. CT scan shows dense coronary calcification in all the coronary arteries
4. PET perfusion images show abnormal left ventricular contraction with anterior, lateral, and inferolateral hypokinesis and ejection fraction of 41% with stress
5. Depending on clinical judgment and circumstances, the PET findings suggest that coronary angiogram with a potential revascularization procedure may be appropriate due to the following:
(i) Angina and shortness of breath with activity and dipyridamole stress
(ii) 2.5 mm ST depression with dipyridamole stress
(iii) Large, severe, stress-induced defects involving 48% of viable myocardium
(iv) Decreased stress ejection fraction with subendocardial and transmural ischemia
(v) PET findings suggest severe stenosis or chronic Total occlusion (CTO) of a collateralized dominant LCx, whereas the pattern and distribution of the anterior defect suggest moderate stenosis of several smaller diagonals off a diffusely narrowed LAD

Excluded for simplicity, the patient identifiers, date of test, indication, brief history, the rest of the report includes 2 pages with brief history, details on the protocol, patient's blood pressure, ECG recordings, and symptomatic responses during stress, the full quantitative data and color-coded maps as shown in Fig. 6.2 for absolute flow and subendocardial perfusion, if appropriate

Table 6.1 Cardiac positron imaging and consultation report

There is a large severe defect in the mid left circumflex (LCx) distribution (blue) also with myocardial steal suggesting occlusion with collaterals. The native right coronary artery (RCA) and the first obtuse marginal (OM1) or their bypass grafts are patent (yellow to orange) with mildly reduced CFC due to diffuse CAD. The tomograms show subendocardial ischemia ranging from mild to severe to transmural ischemia.

For this high-risk case, the PET prior to angiogram focuses potential intervention on the physiologically largest, most severe and accessible target for stenting the total or subtotal occlusion of the mid LCx artery supplying a large, viable region not readily evaluable by a nonopacified artery beyond the occlusion. This pattern of severe disease proximal to patent bypass grafts is common as demonstrated later in this chapter for a different patient.

Clinical Coronary Physiology

Phasic and mean coronary blood flow measured in cc/min by an electromagnetic flow meter in experimental coronary stenosis illustrates a concept fundamental to clinical coronary physiology [1–11]. From Fig. 6.3, in the absence of stenosis (*upper tracing*), coronary flow increases to four times resting baseline flow during pharmacologic vasodilation stress. The ratio of stress to resting blood flow is called Coronary Flow Reserve (CFR), normally at least 4.0 in all mammalian species, including humans. With moderate stenosis imposed on the artery, resting perfusion remains normal but the phasic variation is damped. During vasodilation stress, however, flow increases to only two times baseline, for a reduced CFR of 2.0. The ratio of maximum stress flow with stenosis to maximum flow without stenosis is called the relative Coronary Flow Reserve (relCFR). The abnormal relCFR is expressed as a fraction of the normal CFR, seen in Fig. 6.3 as 2.0/4.0 for a relCFR of 0.5.

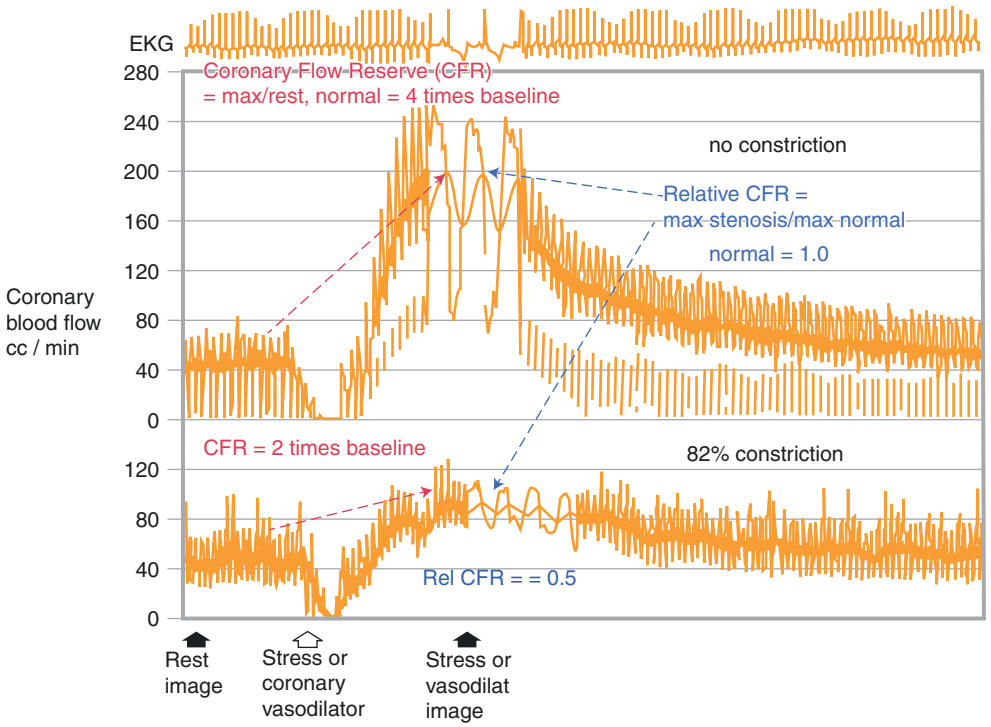

Fig. 6.3 Coronary flow reserve (CFR), rest and stress coronary blood flow. (*From* Gould et al. [1]; with permission from Elsevier)

Coronary flow in cc/min increases with the diameter of the artery and distal myocardial mass or the size of distal microvascular bed. For comparison among different-sized arteries and distal myocardial mass, the quantitative metric is cc/min/g of myocardium, called *myocardial perfusion*. Because the units of cc/min/g cancel for the ratio of stress perfusion to rest perfusion, the stress/rest perfusion ratio is still called CFR (Fig. 6.4) to reference the original concept and the terms most widely used, although some literature refers to myocardial perfusion reserve (MPR).

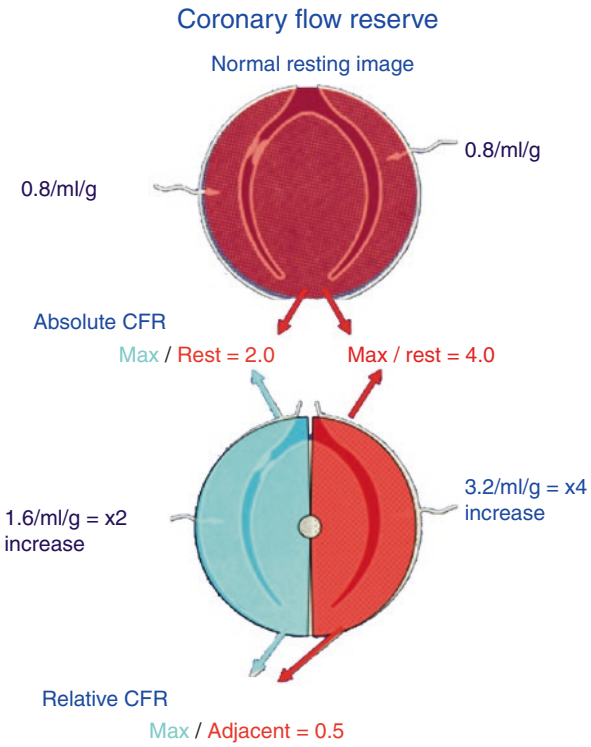

Fig. 6.4 Relative CFR and perfusion imaging

On stress perfusion images of activity alone, regional abnormalities are identified by less activity than other, higher-activity regions, or presumed normal areas, and hence are called relative defects. Therefore, non-quantitative relative stress perfusion images may have a regional defect at very high or very low absolute stress perfusion in cc/min/g. Relative stress perfusion defects are widely read out as ischemia despite having adequate or even high absolute stress flow, well above the low perfusion necessary to cause ischemia defined as angina, significant ST depression >1 mm on ECG, or regional contractile dysfunction. Most relative perfusion defects indicate differential distribution of stress perfusion without low quantitative perfusion causing ischemia defined by these criteria.

As an evolutionary survival mechanism, the mammalian coronary arterial system has the capacity to increase coronary blood flow over four times resting baseline flow in order to meet extreme conditions or activity. Because high coronary blood flow is not needed between such extraordinary demands, at resting conditions the coronary arterioles are vasoconstricted as a high-resistance microvascular bed. Therefore, coronary stenosis will not alter resting blood flow until the resistance of the stenosis is as high or higher than the resistance of the vasoconstricted coronary arterioles. Consequently, resting coronary blood flow may remain normal for severe stenosis up to 80% diameter narrowing, though mild to moderate stenosis of 50–80% diameter narrowing reduces the capacity to increase flow and CFR (Fig. 6.5).

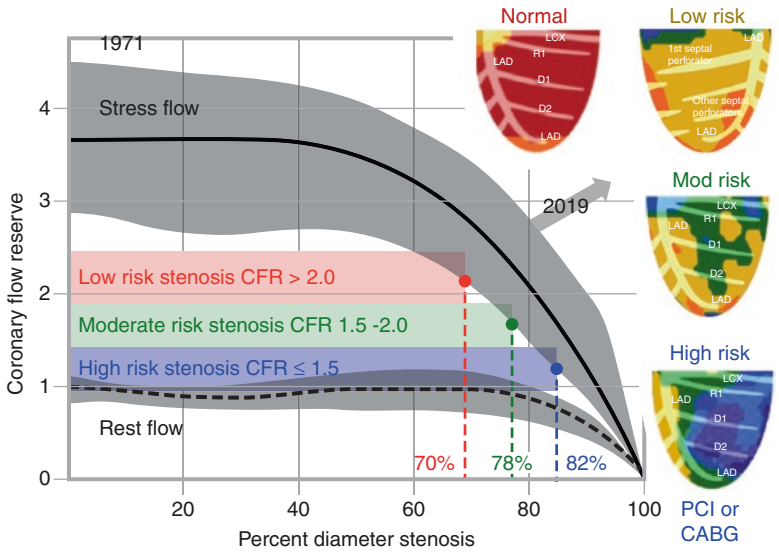

Fig. 6.5 CFR related to percent diameter narrowing of a single focal experimental stenosis. The single anterior views of PET images are color-coded for normal subjects (*red*), for mild to moderate stenosis (*yellow and green*) and for severe stenosis (*blue*), reflecting the risk of adverse coronary events superimposed on the graph of CFR versus % diameter stenosis

In patients, CAD is commonly viewed as focal stenosis but is nearly always associated with diffuse atherosclerosis or multiple stenosis causing heterogeneous, diffuse, irregular narrowing throughout the vessel [12–14] (Fig. 6.6). The pathologic anatomy and corresponding true pressure flow pathophysiology are a complex integration of multiple interactive stress flows, CFRs, and intracoronary pressures for each branching segment within each single coronary artery and its branches.

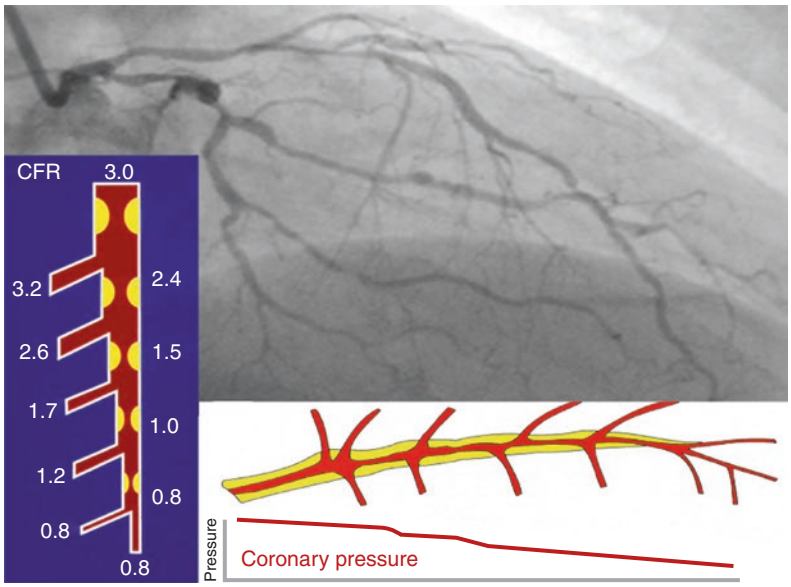

Fig. 6.6 Stenosis and diffuse CAD in patients. Each artery has a family of multiple flows, CFRs, and pressures along its length and branches

The fluid dynamic mechanisms of interspersed focal or diffuse narrowing between arterial branches is documented as "coronary branch steal." Branch steal during stress flow is caused by flow shunted away from more distal arterial segments as pressure progressively falls along the vessel length owing to cumulative viscous pressure loss from diffuse narrowing and disordered flow or vortex shedding at focal narrowing between branches [2, 12–15] (Fig. 6.7).

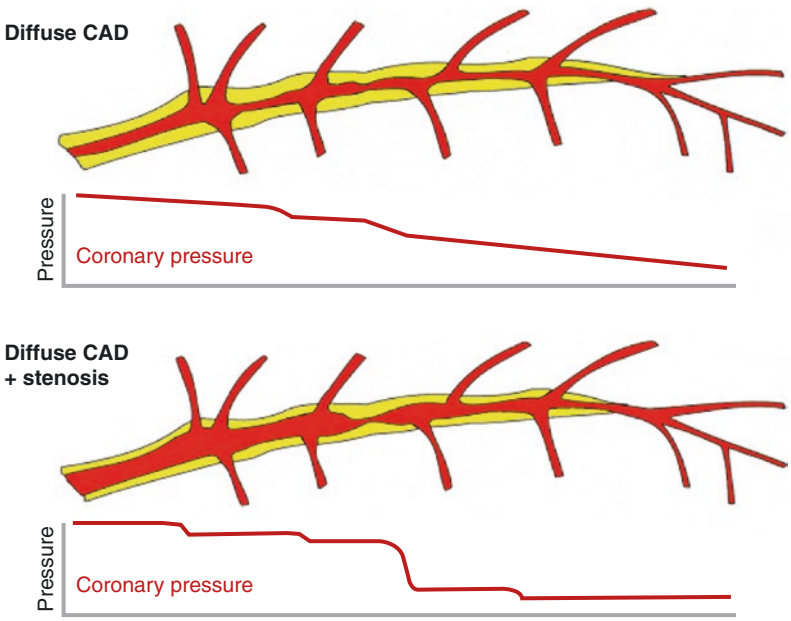

Fig. 6.7 Patterns of pressure loss along arterial length during stress flow for focal and diffuse CAD

Intracoronary pressure pull-back recordings during vasodilation stress identify sudden pressure jumps (or drops) at focal stenosis separate from or in addition to the graded gradual pressure change due to diffuse narrowing.

We developed an integrated fluid dynamic model of the entire coronary arterial tree, relating arterial diameters to summed branch lengths distal to each arterial segment and hence to myocardial mass validated experimentally. The model predicts normal arterial diameters for each vessel segment compared with the measured diameters, thereby predicting the extent of atherosclerotic narrowing in each arterial segment, shown in Fig. 6.8 as yellow thickening superimposed on the clinical angiogram [16].

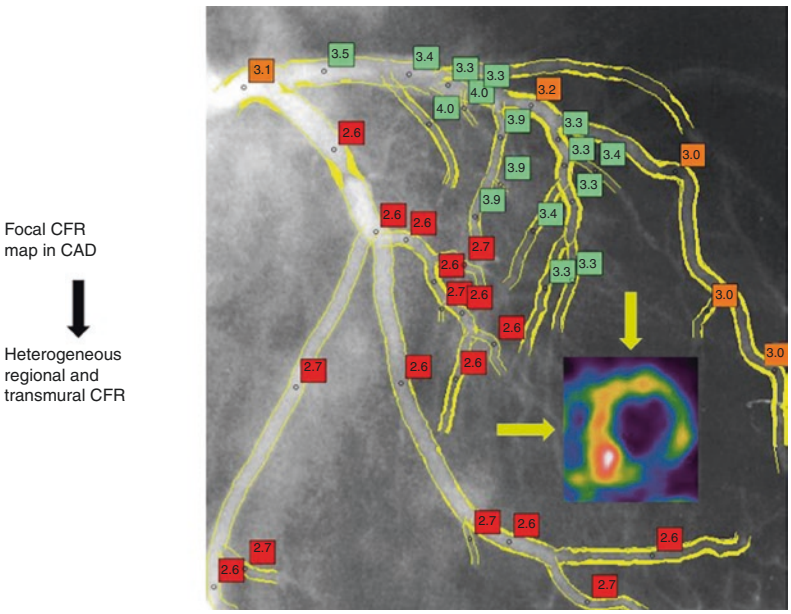

Fig. 6.8 CFR values for the entire left coronary artery tree on a clinical coronary angiogram. The extent of atherosclerotic narrowing in each arterial segment is shown as yellow thickening superimposed on the clinical angiogram. This coronary tree is then analyzed by validated fluid dynamic equations integrated for all dimensions of diameter in millimeters, relative narrowing, length of each narrowing, normal expected diameters, and branch steal for each arterial segment. The results show a wide range of CFRs for each arterial segment, labeled in *red* for the LAD, *green* for the LCx, and *orange* for a large obtuse marginal branch

This coronary tree is then analyzed by validated fluid dynamic equations integrating for all dimensions of diameter in millimeters, relative narrowing, length of each narrowing, normal expected diameters, and branch steal for each arterial segment. The results show a wide range of CFRs for each arterial segment, with no single value characterizing each artery. Therefore, there is no single CFR characterizing a single coronary artery, but rather a wide range of different CFRs along its length and among its branches.

Figure 6.9 illustrates an experimental study in which coronary blood flow was measured by electromagnetic flow meter, aortic pressure was measured by a small catheter inserted into the aorta, and intracoronary pressure was measured by a small coronary catheter implanted in the left circumflex coronary artery distal to an inflatable variable cuff stenosis [17–19]. Without a coronary stenosis, coronary blood flow increases four times during vasodilatory stress for a CFR of 4.0, with no mean aortic to coronary pressure gradient. With stenosis, CFR is reduced to 2.0 with a large pressure gradient across the stenosis. Experimentally [20] and in humans [21], myocardial ischemia does not develop until distal coronary pressure is approximately 35 mm Hg.

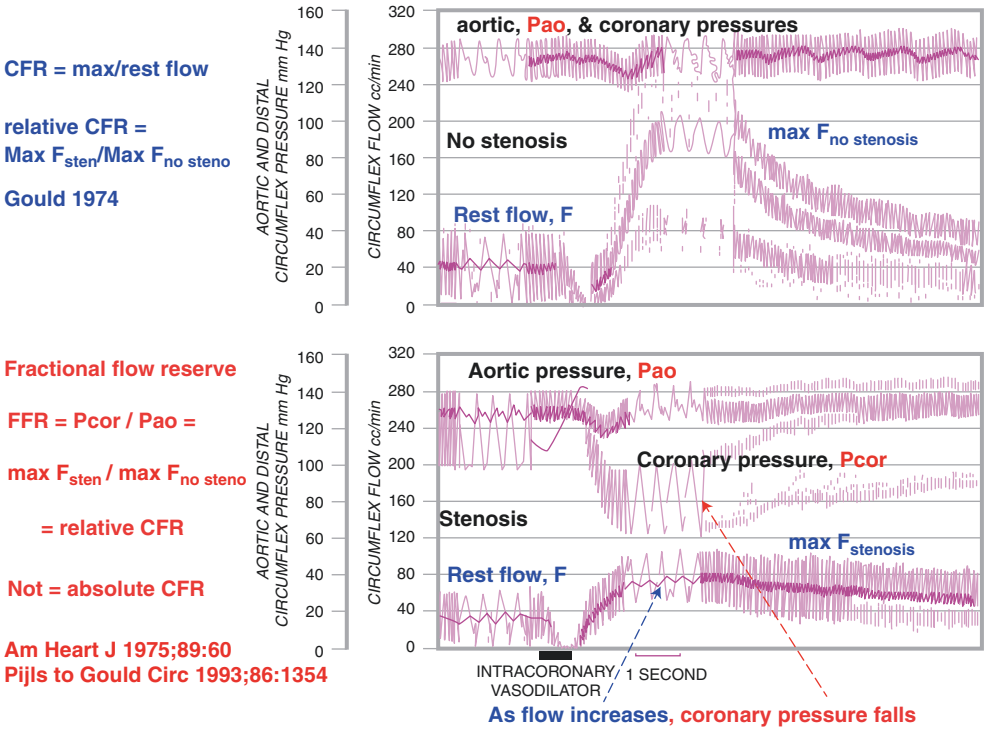

Fig. 6.9 Coronary blood flow, coronary pressure, and fractional flow reserve (FFR) in an experimental study [17–19]. In the *upper panel*, without a coronary stenosis, coronary blood flow increases four times during vasodilatory stress for a CFR of 4.0 with no mean aortic to coronary pressure gradient. In the *lower panel*, CFR is reduced to 2.0 with a peak 50 mm Hg pressure gradient across the stenosis (aorta 130 mm Hg minus coronary 80 mm Hg). (*From* Gould et al. [2]; with permission from Mosby)

For a single focal stenosis, the fractional ratio of the lowest coronary pressure during vasodilation stress to aortic pressure is called fractional flow reserve (FFR). FFR is proportional to the ratio of peak stress flow with stenosis to peak flow without stenosis (that is, relative CFR). Relative CFR and FFR therefore reflect the physiologic severity of the stenosis relative to presumed normal values.

Note that relative CFR and FFR do not indicate absolute stress flow or absolute CFR derived in cc/min/g. Relative CFR and FFR of 0.5 might be due to mild stenosis at very high values of non-ischemic absolute flow, or it might be associated with low absolute flow and CFR, causing ischemia. Relative CFR and FFR therefore do not indicate ischemia defined as angina, ST depression (STΔ), or regional contractile dysfunction; they only indicate relative regional differences in blood flow or perfusion.

Figure 6.10 shows the diastolic fluid dynamic equations for the pressure gradient–flow relation for individual heart beats during increasing flow after vasodilator stress [22, 23]. The increasingly steep pressure flow curve for each diastole indicates dynamically increasing stenosis severity due to flow-induced vasodilation around a fixed cuff stenosis that increases percent stenosis and progressive pressure loss related to flow squared. For each single heart cycle, the diastolic pressure gradient–flow curves fit a quadratic fluid dynamic equation: $\Delta P = AQ + BQ^2$ for volumetric flow; or, in terms of average cross-sectional flow velocity, $\Delta P = CV + DV^2$, where the first term quantifies pressure loss due to viscous friction and the second term quantifies pressure loss due to disordered flow or vortex shedding at the stenosis exit. The terms A, B, C, and D include constants and arterial lumen dimension raised to the fourth power.

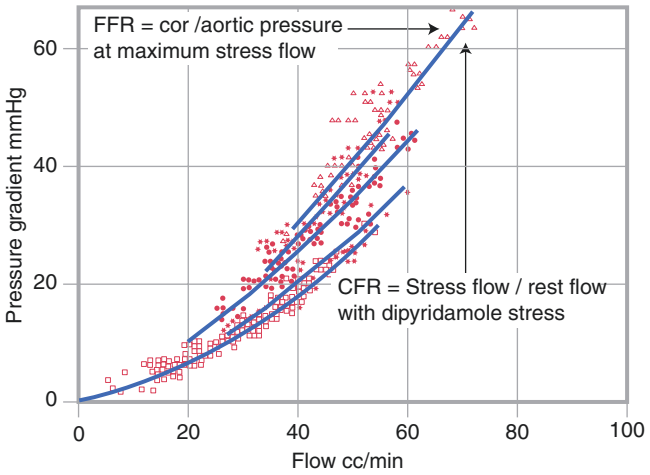

Fig. 6.10 Diastolic pressure–flow curves across a single focal stenosis related to CFR and FFR. On these composite pressure gradient–flow plots, the peak pressure gradient expressed as a ratio to aortic pressure is FFR, and the peak flow expressed as ratio to rest flow is CFR. As derived from this quadratic equation and ignoring collateral flow for simplicity (as used clinically), the relative CFR is related to FFR by the following equation:

$$FFR = P_{cor}/P_{ao} = \max Q_{sten}/\max Q_{nosten}$$

where P is aortic and coronary pressure during maximum stress flow and Q is maximum stress flow with and without stenosis. These ratios reflect relative flow reserve, not absolute perfusion of CFR based on mL/min/g, an important difference between relative and quantitative perfusion imaging abnormalities. (*From* Gould et al. [22]; with permission from Wolters Kluwer.)

The same fluid dynamic model of the coronary artery tree described for Fig. 6.8 predicts a range of coronary pressures and FFR values along each arterial branch, expressed in Fig. 6.11 as pressures relative to aortic pressure of 100 or percent rather than fractions. The coronary artery is characterized by a wide range of pressures at maximum hyperemia, with no single pressure or FFR value to summarize adequately the coronary arteries.

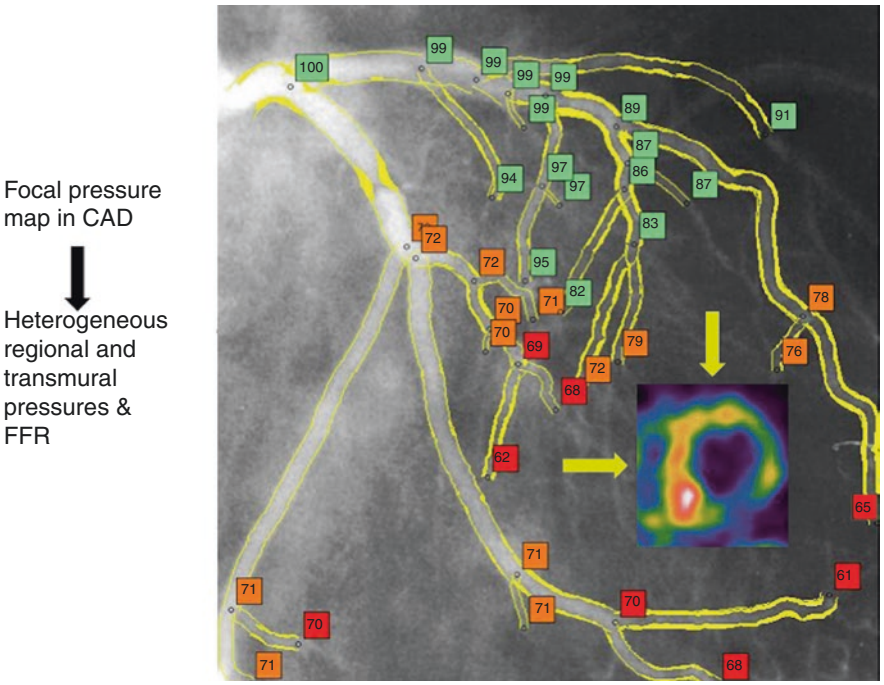

Fig. 6.11 Pressure or FFR values for the entire left coronary artery on a clinical coronary angiogram, expressed as the percentage of aortic pressure. The inset relative tomogram also shows the regional and average global subendocardial/subepicardial perfusion ratio

Though it is an essential step beyond angiographic percent diameter stenosis, a single CFR or FFR value as now determined clinically fails to capture the true pathophysiology of the coronary artery tree in CAD, as illustrated in Figs. 6.2, 6.6, 6.8, and 6.11. In contrast, as developed subsequently in this chapter, quantitative perfusion in cc/min/g on a per-pixel basis by PET maps every artery and branch of the coronary tree for rest and stress perfusion in cc/min/g, per-pixel CFR, and their combination as per-pixel CFC to account for global or regional perfusion heterogeneity.

The pixel data also provide relative stress perfusion or FFR of quantitative stress PET images (FFRpet) derived as the relative map of absolute stress perfusion in cc/min/g, as opposed to relative uptake, or the relative tomogram showing the regional and average global subendocardial/subepicardial perfusion ratio. These basic physiologic and fluid dynamic concepts are essential for understanding and using clinical coronary physiology for optimal patient management based on PET or any other technology for quantifying myocardial perfusion and physiologic severity of coronary artery disease.

Experimentally, transmural perfusion measured by radiolabeled microspheres is normally slightly lower in the subepicardium than in the subendocardium, which is subject to greater wall stress, oxygen demands, and capillary recruitment [2, 7, 20–26]. With coronary perfusion pressure falling to below 35–40 mm Hg, subendocardial perfusion falls as subepicardial perfusion is maintained (Fig. 6.12). During vasodilation stress, a low FFR due to focal or diffuse epicardial narrowing causes reduced subendocardial perfusion. Consequently, reduced subendocardial perfusion metrics are due to falling coronary pressure and FFR during vasodilator stress.

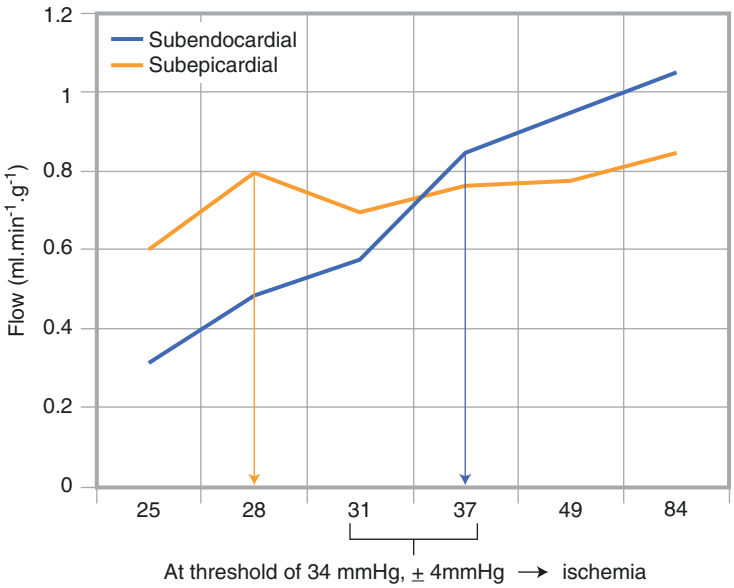

Fig. 6.12 Coronary pressure and subendocardial perfusion. (*From* Hoffman and Buckberg [24]; with permission from the Journal of the American Heart Association)

However, FFR reflects relative pressure drop as a fraction of aortic pressure that rarely reaches this low absolute distal pressure causing ischemia, thereby explaining why angina seldom occurs when clinically measuring FFR ≥0.6. Similarly, a relative subendo/epicardial perfusion ratio may indicate low absolute subendocardial perfusion but not sufficient to cause ischemia. Moreover, mild to severely reduced relative subendocardial perfusion metrics may be associated with angina and ST depression in some individuals but not in others. Like FFR, relative subendocardial perfusion metrics reflect fluid dynamic pressure-flow severity of upstream focal or diffuse narrowing, which may or may not cause ischemia, depending on reduced absolute perfusion in cc/min/g and CFR. Figure 6.13 illustrates reduced subendocardial perfusion due to mild or moderate stenosis during vasodilation stress first reported on experimental stress perfusion tomograms [7, 25].

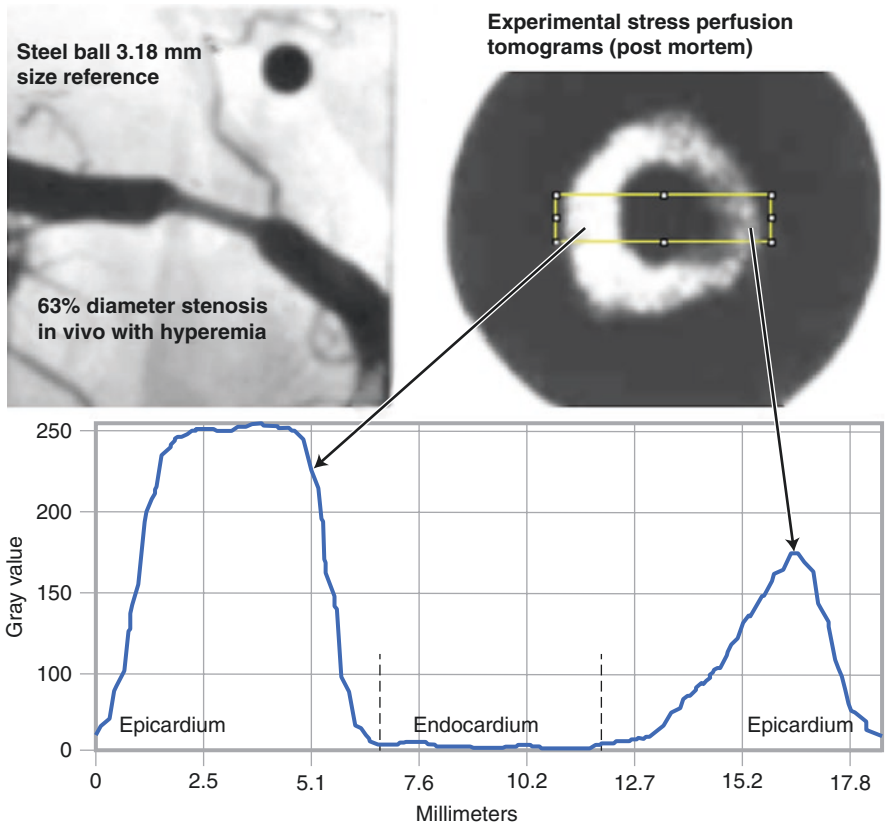

Fig. 6.13 Ex vivo cross-sectional images of in vivo relative transmural perfusion during coronary hyperemia. Intravenous thallium-201 injected in vivo during vasodilation stress and post mortem imaging of LV slices show reduced subendocardial perfusion with a mild coronary artery stenosis. The gray-scale relative activity profiles show severely reduced subendocardial perfusion extending to the subepicardium, thereby reducing transmural perfusion somewhat and hence regional relative and absolute CFR. (*From* Gould and Johnson [25]; with permission from Elsevier)

Large coronary arteries supplying greater distal myocardial mass have higher absolute flow than smaller arteries that supply smaller myocardial mass. For standardized comparison of blow flow in different arteries, flow is therefore expressed as cc/min/g, called *myocardial perfusion* as measured by quantitative PET (Fig. 6.14). The stress/rest ratio is also called *myocardial perfusion reserve*, here considered to be synonymous with coronary flow reserve (CFR), in deference to the extensive physiologic literature on the topic.

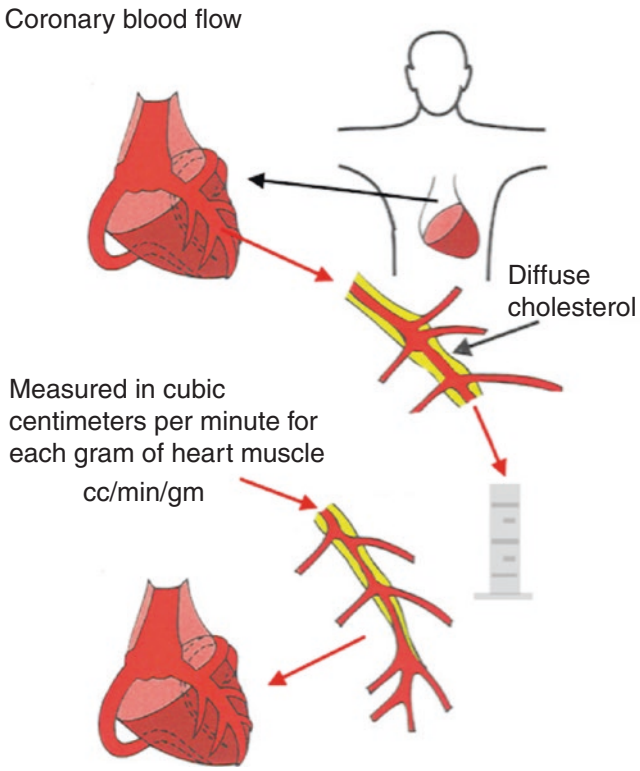

Fig. 6.14 Conceptual schematic of myocardial perfusion as blood flow per gram of myocardium distal to the point of flow measurement

The Literature: Conflicts, Explanations, Resolutions

Figure 6.15 summarizes the literature on quantitative myocardial perfusion by PET [27]. The quantitative perfusion measurements are within similar ranges on average, but several issues impede their use in individual patient management. First, variability in the literature is sufficient to generate mistrust in the values without careful testing and documentation within each PET site. Second, global perfusion measurements are not very useful for assessing the range of heterogeneous focal and diffuse narrowing to guide focal intervention. Third, most PET sites do not understand how to use the quantitative data clinically or report it visually or in text in order to generate trust or reliance by referring or invasive cardiologists for guiding management. Fourth, great variability among PET sites with different protocols and clinical relationships precludes generalized guidelines or consensus on how to make quantitative perfusion measurements, what the different metrics and values indicate, how to report them, what interventions should be done, or on systematic clinical outcomes. This chapter systematically resolves these limitations on the basis of over 8000 cases with follow-up over 10 years.

Population	N	Rest flow (cc/min/gm)	Stress flow (cc/min/gm)	CFR
Normal controls	3,484	0.82 ± 0.06	2.86 ± 1.29	3.55 ± 1.36
Risk factors only	3,592	0.85 ± 0.08	2.25 ± 1.07	2.80 ± 1.39
Established CAD	1,650	0.83 ± 0.10	1.71 ± 0.71	2.02 ± 0.70
Mixed (risk factors and/or known CAD)	4,765	0.97 ± 0.10	1.86 ± 0.58	1.93 ± 0.48
Cardiomyopathy	594	0.73 ± 0.07	1.47 ± 0.56	2.02 ± 0.67
Hypertrophic cardiomyopthy	345	0.90 ± 0.10	1.57 ± 0.33	1.84 ± 0.36
Syndrome X	348	1.06 ± 0.11	2.65 ± 1.31	2.54 ± 1.31
After cardiac transplant	184	1.14 ± 0.18	2.44 ± 1.34	2.29 ± 0.86
	N = 14,962 (from 252 unique publications)			
N-13 ammonica	5,541			
O-15 water	3,167			
Rb-82	6,175			

Fig. 6.15 Quantitative myocardial perfusion by PET in the literature [27]

The data on "ischemic" threshold of stress perfusion in cc/min/g and CFR are even more indeterminate, for several additional reasons. Only two of the reports in the table shown as Fig. 6.16 (Sambuceti and Johnson) measured perfusion during dipyridamole-induced angina or ST depression (STΔ) greater than 1 mm. In all the other reports, the criteria for "ischemia" was defined as FFR ≤0.8 or angiographic severity of ≥50% or ≥70% diameter stenosis on angiogram as a presumed indication of ischemia, rather than actual documented ischemia by angina, significant STΔ or contractile dysfunction [27]. In fact, FFR ≤0.8 during adenosine stress is rarely associated with true angina (distinct from vasodilator side effects) or significant ECG STΔ. Moreover, revascularization based on FFR is not significantly associated with reduced death or MI; hence FFR is a marker of differential relative perfusion, not ischemia. Similarly, an extensive literature documents that angiogram severity does not correlate sufficiently with individual symptoms, physiologic severity, CFR, or outcomes after revascularization to guide these procedures. Therefore, angiogram severity also does not equal ischemia defined as angina, STΔ, or stress wall motion abnormalities in individual patients.

Author	Citation	N	Isotope	Reference Standard	CFR (no units)		Stress flow (cc/min/gm)	
					Cutoff	AUC	Cutoff	AUC
Sambuceti	AJC 1993;72:990	33	N-13	Dipyridamole STΔ	1.75	0.59	1.15	0.6
Muzik	JACC 1998;31:534	51	N-13	Clinically normal group and cath data	2.74	0.91		
Nesterov	Eur J Nucl Med Mol Imaging 2009;36:1594	48	O-15	Catch %Ds>50 (plus FFR in half of cohort)			2.5	
Hajjiri	JACC Cardiovasc Imaging 2009;2:751	27	N-13	Cath %DS≥70	2.0	0.86	1.85	0.90
Kajander	Circulation 2010;122:603	107	O-15	Cath %DS≥50 or FFR≤0.8			2.5	0.95
Johnson	JACC Cardiovasc Imaging 2011;4:990	1,674	Rb-82	Dipyridamole PET Defect, angina/STΔ	1.74	0.91	0.91	0.98
Morton	JACC 2012;60:1546	41	N-13	Cath %DS≥70	1.44	0.83	1.48	0.69
Fiechter	JNM 2012;53:1230	73	N-13	Cath %DS≥50	2.0	0.92		
Danad	JNM 2013;54:55	120	O-15	Cath %DS≥50 (plus FFR in 1/3 of cohort)	2.30	0.81	1.86	0.86

Fig. 6.16 Thresholds of stress perfusion and CFR for "ischemia" [27]. AUC = area under the receiver operating characteristic curve, %DS = percent diameter stenosis, FFR = fractional flow reserve, ST = ST-segment

On the other hand, the threshold in the Johnson report in Fig. 6.16 measured stress perfusion and CFR during dipyridamole-induced angina and STΔ >1 mm. The ischemic threshold was then determined by ROC analysis for that stress perfusion and CFR that best separated patients with angina/STΔ from those without STΔ during dipyridamole stress. Interestingly, the only other report using STΔ as the definition of ischemia during dipyridamole stress reported a threshold close to that of Johnson, unlike the other, much higher perfusion thresholds for "ischemia" defined by FFR or angiographic severity as substitutes for angina, STΔ, or contractile dysfunction.

Conflicts: Which Is Best, CFR or Stress Perfusion?

Figure 6.17 is taken from a report by Gupta et al. [28] in which global stress perfusion was divided by global rest perfusion to get global CFR. Mortality risk for this calculation of global CFR ≤2.0 predicted high mortality risk over follow-up years, as expected, but it purports to claim that global stress perfusion added no predictive value to global CFR for predicting CV mortality, thereby implying no added predictive value of CFC. This conclusion conflicts with other more clinically oriented excellent cardiac PET centers measuring regional perfusion in assumed generalized arterial distributions with the opposite conclusion, namely, that stress perfusion is better than CFR for predicting significant stenosis [29, 30], as in Fig. 6.18.

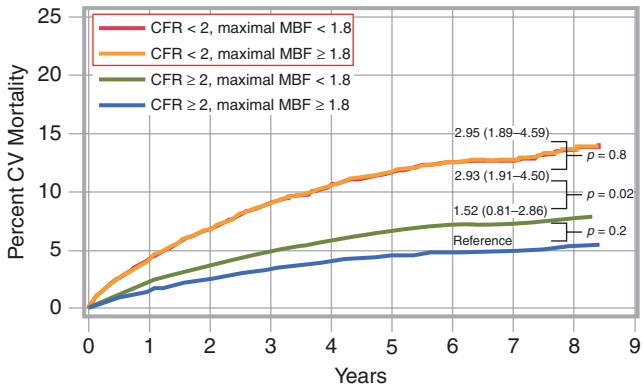

Fig. 6.17 Probability of cardiovascular mortality over time on the basis of CFR impairment and maximal myocardial blood flow (MBF). Mortality risk for this calculation of global CFR ≤2.0 predicted high mortality risk over follow-up years (*red line*) as expected. The plot purports to claim that global stress perfusion (*yellow line*) added no predictive value to global CFR for predicting CV mortality, thereby implying no added predictive value of CFC. (*From* Gupta et al. [28]; with permission from Wolters Kluwer)

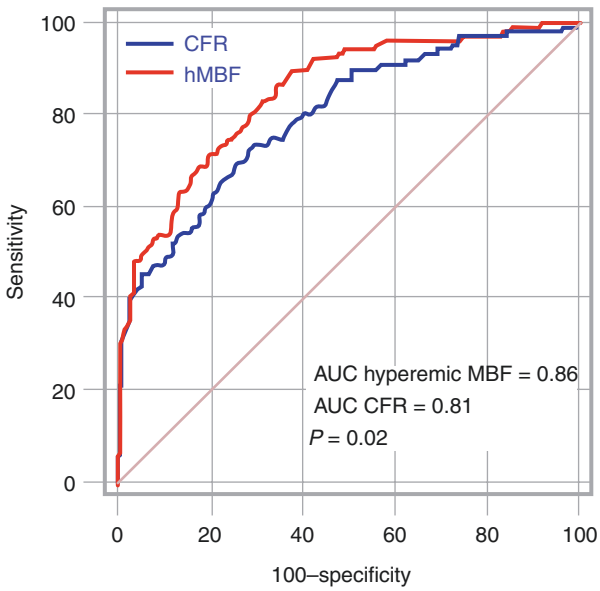

Fig. 6.18 Hyperemic MBF versus CFR for the detection of CAD. (*From* Danad et al. [29]; with permission from the Society of Nuclear Medicine and Molecular Imaging). Hyperemic MBF vs. CFR for detection of CAD. ROC curves for PET parameters tested for all coronary vessels are shown. CFR coronary flow reserve, hMBF hyperemic myocardial blood flow

The data in Fig. 6.17 are profoundly flawed by the use of global stress and CFR [2, 25]. *Global* rest-stress perfusion and *global* CFR averages out all regional rest-stress defects and all regional abnormal CFR defects, as shown in later figures. CFC is by definition the per-pixel distribution of stress perfusion and CFR specifically designed to quantify the common heterogeneous differences and concordances of these two metrics, providing essential physiologic insights for guiding management of CAD and its outcomes. Moreover, the arbitrary stress flow threshold of 1.8 cc/min/g is much higher than the stress perfusion threshold of ≤0.8 associated with documented ischemia as a regional stress PET defect, with angina and STΔ >1 mm in the largest threshold study in the literature [2, 25, 27].

In Fig. 6.18, regional stress perfusion and CFR both correlated with FFR ≤0.8 as the standard of stenosis severity, with the area under the curve (AUC) of receiver operating curves (ROC) for stress perfusion in cc/min/g slightly but significantly better than CFR. The authors concluded that regional stress perfusion provided the better diagnostic performance than regional CFR, the opposite of the prior figure [29]. Although far superior to global perfusion, the data of this figure are also flawed by failing to account for resting perfusion heterogeneity due to endothelial dysfunction that may cause sufficient corresponding heterogeneity of CFR as to falsely indicate or mimic flow-limiting stenosis, thereby decreasing its diagnostic accuracy. This flaw is corrected by mapping pixel values of both stress perfusion and CFR as CFC, accounting for this heterogeneity for the optimal quantification of physiologic severity of diffuse and focal CAD [30].

Conflicts: Which Is Best for Diagnosis of Significant Stenosis, FFR_{CT} or Quantitative PET Perfusion?

A simulated FFR predicted by CT angiography analysis (FFR_{CT}) estimates FFR, a relative CFR, based on angiographic analysis using computational fluid dynamics [31–38]. Figure 6.19 shows AUC of ROC curves for various imaging modalities showing that simulated FFR_{CT} is superior to PET for predicting invasive pressure–derived FFR (Fig. 6.19a) only after excluding the 17% of FFRct failures to produce useable data. When all cases were analyzed for intention to treat, as done for routine clinical purposes, PET is clearly superior for both per patient and per artery analysis (Fig. 6.19b) as noted by the highest AUC of the ROC highlighted in yellow.

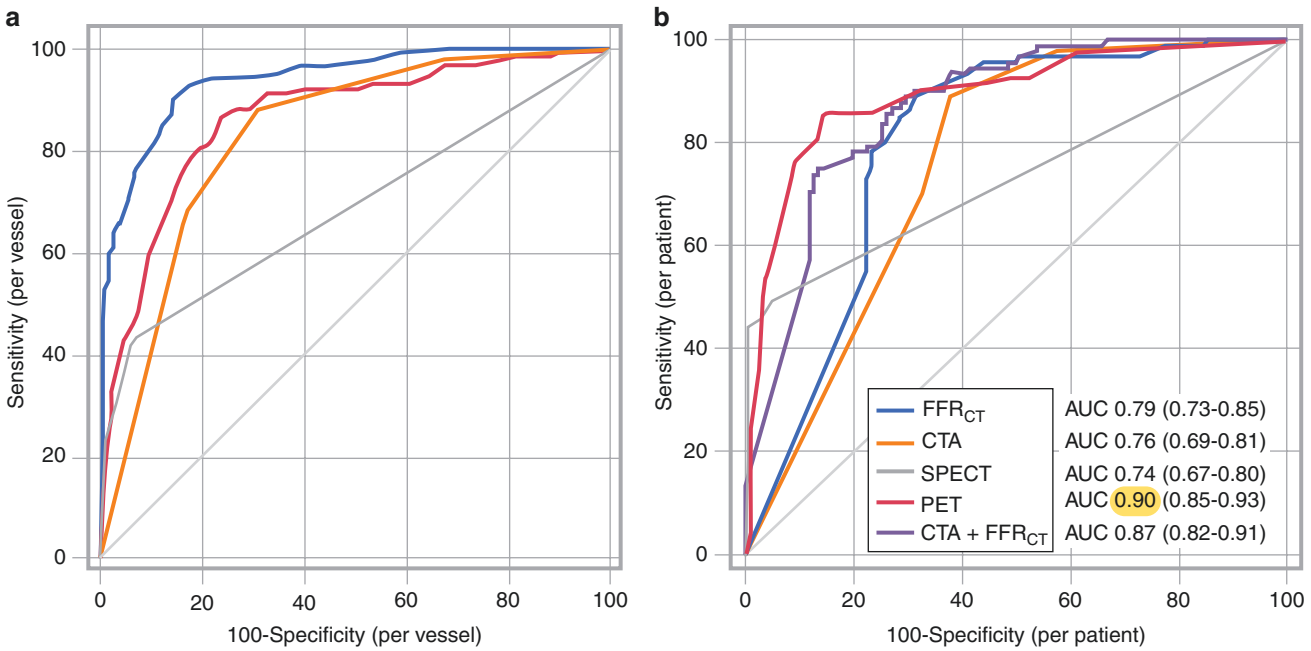

Diagnostic Performance for the Detection of CAD on an Intention-to-Diagnose Basis							
	FFR_{CT}	Coronary CTA	p Value*	SPECT	p Value*	PET	p Value*
Per vessel (n = 612)							
Sensitivity	92 (86-96)	70 (62-77)	<0.001	40 (32-48)	<0.001	80 (73-86)	0.004
Specificity	70 (65-75)	78 (74-82)	0.005	96 (94-98)	<0.001	76 (69-81)	0.013
PPV	52 (45-60)	52 (45-60)	0.727	81 (71-88)	<0.001	61 (53-68)	0.134
NPV	96 (92-98)	86 (82-90)	<0.001	80 (75-84)	<0.001	91 (87-94)	0.015
Diagnostic accuracy	77 (73-80)	76 (73-80)	1.000	81 (78-84)	0.238	80 (77-83)	0.355
AUC	0.83 (0.79-0.86)	0.80 (0.77-0.84)	0.261	0.68 (0.64-0.72)	<0.001	0.86 (0.83-0.89)	0.157

Fig. 6.19 Simulated FFR predicted by CTA analysis (FFR_{CT}) versus quantitative PET perfusion for diagnosis of significant stenosis. (**a**) ROC curves for the various imaging modalities listed. Driessen et al. [31] claim that FFR_{CT} is superior to PET for predicting invasive pressure–derived FFR, but this plot excludes the 17% of cases for which CT data were inadequate. (**b**) Analyzing all cases for intention to treat, as done for routine clinical purposes, PET is clearly superior, with the highest AUC (0.9). (*From* Driessen et al. [31]; with permission from Elsevier)

Conflicts: Which Is Best for Diagnosis of Significant Stenosis, CT Angiography (CTA) or Quantitative PET Perfusion?

In Fig. 6.20, the same PET center reported a previous paper with even stronger conclusions favoring PET. Based on the ROC curves favoring PET for predicting true pressure derived FFR ≤0.8 in this figure, Danad et al. [32] stated a strong conclusion as follows: "This controlled clinical head-to-head comparative study revealed PET to exhibit the highest accuracy for diagnosis of myocardial ischemia. Furthermore, a combined anatomical and functional assessment does not add incremental diagnostic value but guides clinical decision-making in an unsalutary fashion." Later figures explain why CTA and simulated FFR_{CT} fail to reflect the true measured physiologic severity of diffuse and focal CAD.

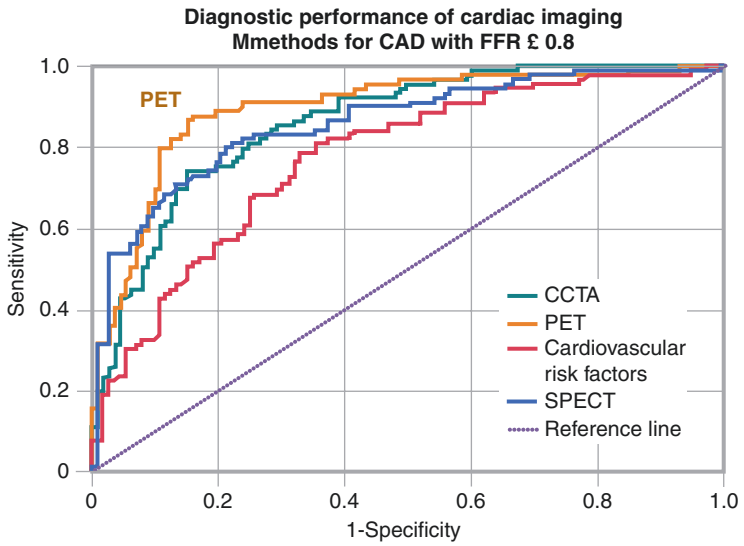

Fig. 6.20 Diagnostic performance of cardiac imaging methods for CAD defined as invasive pressure-derived FFR ≤0.8. CCTA coronary CT angiography. (*From* Danad et al. [32]; with permission from the American Medical Association)

PET superiority over CTA has been reported by other centers doing both [31–36], as summarized in the table shown in Fig. 6.21 (highlighted by the red box). The limited resolution of CTA incurs substantial uncertainty of angiographic arterial border recognition, with test-retest variability of simulated FFRct of 0.2 FFR units on the left Bland Altman scatter plot [35]. Given this variability, for the pressure-derived FFR threshold of 0.8, the simulated FFR_{CT} can be 0.6 or 1.0, an uncertainty that precludes its use for quantifying physiologic severity of CAD to guide revascularization. The right Bland Altman scatter plot is for simulated FFR based on the invasive coronary angiogram that has better resolution than CT angiogram [36]. The variability of simulated FFRangiogram called QFR is smaller than the simulated FFRct but remains unacceptably too high for reliable personalized guidance of interventions in individual patients.

The performace of different tests for anatomically and functionally significant coronary artery disease

Anatomically significant CAD					Functionally significant CAD				
Test	Sensitivity (%), (95% CI)	Specificity (%), (95% CI)	+LR (95% CI)	–LR (95% CI)	Test	Test	Sensitivity (%), (95% CI)	Specificity (%), (95% CI)	+LR (95% CI)	–LR (95% CI)
						ICA	68 (60–75)	73 (55–86)	2.49 (1.47–4.21)	0.44 (0.36–0.54)
Stress ECG	58 (46–49)	62 (54–69)	1.53 (1.21–1.94)	0.68 (0.49–0.93)						
Stress echo	85 (80–89)	82 (72–89)	4.67 (2.95–7.41)	0.18 (0.13–0.25)						
CCTA	97 (93–99)	78 (67–86)	4.44 (2.64–7.45)	0.04 (0.01–0.09)	CCTA		93 (89–96)	53 (37–68)	1.97 (1.28–3.03)	0.13 (0.06–0.25)
SPECT	87 (83–90)	70 (63–76)	2.88 (2.33–3.56)	0.19 (0.15–0.24)	SPECT		73 (62–82)	83 (71–90)	4.21 (2.62–6.76)	0.33 (0.24–0.46)
PET	90 (78–96)	85 (78–90)	5.87 (3.40–10.15)	0.12 (0.05–0.29)	PET		89 (82–93)	85 (81–88)	6.04 (4.29–8.51)	0.13 (0.08–0.21)
Stress CMR	90 (83–94)	80 (69–88)	4.54 (2.37–8.72)	0.13 (0.07–0.24)	Stress CMR		89 (85–92)	87 (83–91)	7.10 (5.07–9.95)	0.13 (0.09–018)

Note: ICA itself was used as a reference standard for the ananomically significant CAD estimates but was included as a technique when FFR was used as the reference. Not every test had enough data using FFR as reference.
CCTA coronary computed tomography angiography; CI, confidence internal; CMR stress cardiac magnetic resonance ECG electrocardiogram ICA invasive coronary angiography; LR likelihood ratio; PET, positron emission tomography; SPECT, single photon emission computed tomography (exercise stress SPECT with or without dipyridamole or adenosine); Stress echo, exercise stress echocardiography.

The performace of non-invasive test to rule-in and rule-out significant coronary artery stenosis in patients with stable angina: a meta-analysis focused on post-test disease probability

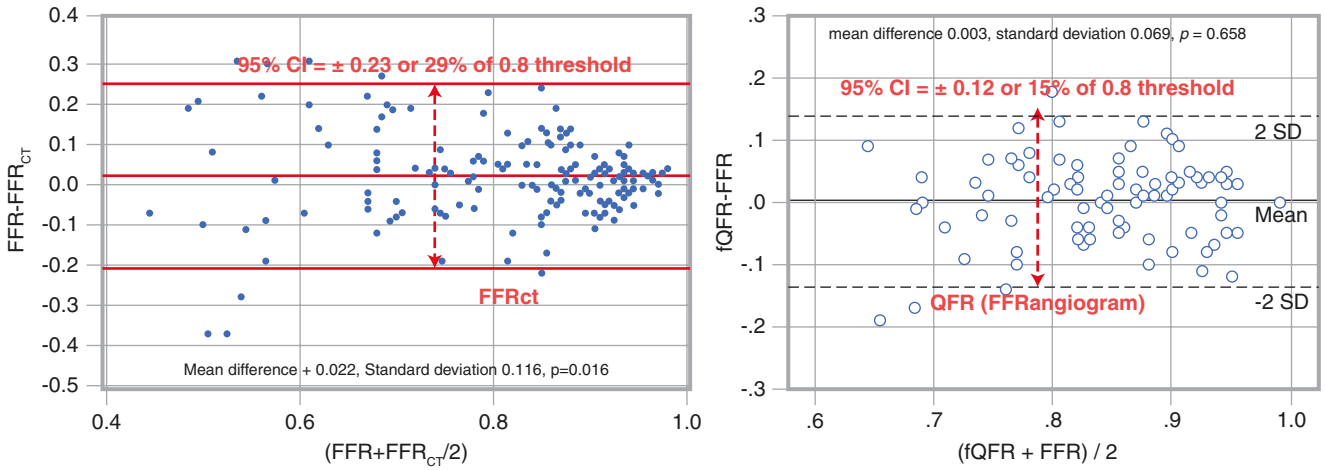

Fig. 6.21 The performance of different tests for anatomically and functionally significant CAD [34]. (*Left*, *From* Koo et al. [35], with permission from Elsevier; *Right*, Tu et al. [36], with permission from Oxford University Press)

Conflicts: What Is the Prevalence of Microvascular Disease?

Figure 6.22a reports reduced global CFR ascribed to microvascular dysfunction in 54% of cases [37], whereas Fig. 6.22b shows 1% prevalence of low CFR in the absence of regional PET perfusion abnormalities confirmed by CTA with no CAD, and 9% prevalence for non-obstructive CAD [38]. The flaw in the high reported prevalence of in Fig. 6.22a is the result of using global CFR, which fails to account for regional perfusion defects due to focal flow-limiting stenosis, which is the most common clinical manifestation of CAD, in addition to diffuse coronary atherosclerosis.

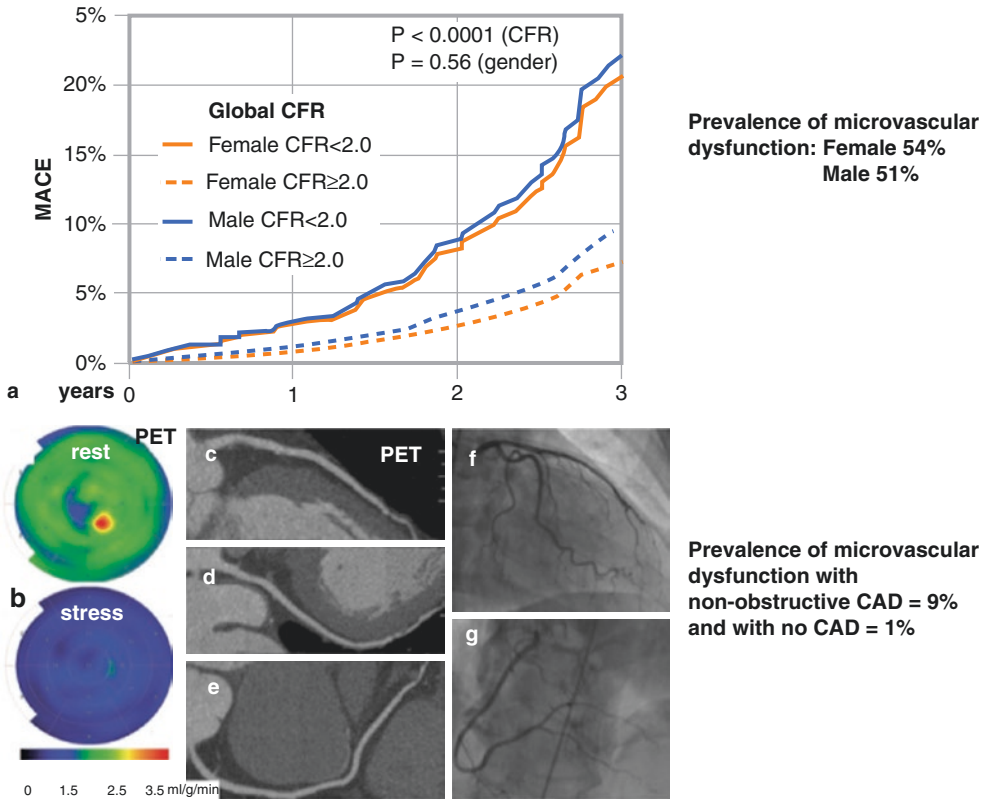

Fig. 6.22 Prevalence of microvascular dysfunction: conflicting conclusions. (**a**) Reduced global CFR is ascribed to microvascular dysfunction in 54% of cases [37]. (**b**) Prevalence of low CFR is 1% in the absence of regional PET perfusion abnormalities confirmed by CTA with no CAD, and 9% for non-obstructive CAD [38]. MACE major adverse cardiac events. (**a** *from* Murthy et al. [37], with permission from the American Heart Association; **b** *from* Stenström et al. [38]; with permission from Oxford University Press)

The table in Fig. 6.23 shows the prevalence of strictly defined microvascular angina in 5900 sequential diagnostic PETs meeting the following criteria: angina, no known CAD, global CFR ≤2.2, and no stress-induced relative defects (defined as no rest-to-stress change >5% of LV with ≤60% of maximum activity). Such strictly defined cases are uncommon, found in only 21 cases (0.4%), with females comprising 62% of the 21 cases, all with risk factors including coronary calcification and with abnormal quantitative PET perfusion images. For this analysis, the CFR threshold of 2.2 was chosen as a compromise between reported thresholds of 2.32 by Doppler wire and 2.0 by PET for microvascular impairment, compared with CFR of 4.2 ± 0.8 for 125 healthy, young volunteers [25].

Mixed Pathophysiologies of microvascular angina and function 5900 PETs

Criteria for microvas angina*	CFR ≤ 2.2*	CFR ≤ 2.2†	CFR > 2.0**	HIGH CFC°
Number of cases from 5900	21 (0.4%)	83 (1.4%)	167 (2.8%)	174 (3%)
Average maximum pixel CFR	2.27 ± 0.5	2.48 ± 0.5	3.91 ± 1.1	3.74 ± 1.2
Microvascular function	impaired	impaired	good	good
FFRpet < 0.7 for >10% LV††	9/21 (43%)	45/84 (54%)	53/167 (32%)	43/174 (25%)
Female	62%	39%	35%	48%
Risk factors or coronary Ca+	yes	yes	yes	yes
MI or death over 9 years***	2/21 (9.5%)	8/83(9.6%)	9/167 (5.4%)	6/174 (3.5%)
Approximate MI or death/yr	1%/yr	0.8%/yr	0.6%/yr	0.4%/yr

Fig. 6.23 Prevalence of strictly defined microvascular angina, subclinical coronary atherosclerosis and mortality risk in 5900 diagnostic rest stress quantitative PETs [25]. *Angina, *No known CAD*, global CFR ≤ 2.2 and no stress induced relative defects defined as rest to stress change of >5% of LV with ≤60% of maximum activity. †Angina, *Known CAD* by angiogram, procedures or events but no stress induced relative defects as defined above. ††Fractional Flow Reserve as relative absolute stress perfusion PET reflecting low subendocardial perfusion. **Angina, global CFR >2.2, no stress induced relative defects as defined above, includes *No Known CAD* and *Known CAD* by angiogram, procedures or events but no stress induced relative defects as defined above. °Angina, High Coronary Flow Capacity (>70% of the LV normal (red) or minimally reduced (orange) CFC (CFR >2.4 and stres > 1.8 cc/min/g)). +MESA risk score >7%

If the above criteria are expanded to include established CAD by angiography, procedures, or clinical events but still with no relative stress defects as defined above, prevalence of angina without obstructive CAD is somewhat greater, 83 of 5900 (1.4%), with 39% female. Approximately half had relative stress perfusion or fractional flow reserve of quantitative stress PET images <0.7 (FFRpet) for >10% of LV. This reduced FFRpet associated with reduced relative subendocardial perfusion is consistent with a fall in coronary pressure due to sufficient microvascular function to increase perfusion through mild, diffuse, epicardial coronary atherosclerosis, with a corresponding fall in coronary pressure causing low subendocardial perfusion.

During follow-up of up to 9 years, there were 8 MIs or deaths among the 83 cases of angina with diffuse but no obstructive CAD (9.6%, or approximately 1.0% per year), consistent with treated risk factors. These observations from our large cohort expand prior limited reports on strictly defined microvascular syndromes with a similar low prevalence and relatively low risk [25]. In comparison, severely reduced CFC is associated with a 30% prevalence of MI, death, or stroke during a comparable period [39].

A core relevant clinical insight is that the same strictly defined microvascular dysfunction but without angina is common (ie, global CFR ≤2.2, and no stress-induced relative defects as previously defined). Asymptomatic microvascular dysfunction as defined above was measured in 734 of 5900 patients (12.4%), with females comprising 39%; 96% had risk factors or coronary calcium. Over 9 years of follow-up, there were 20 MIs or deaths among the 734 patients (2.7%, approximately 0.3% per year), consistent with treated risk factors [25].

Thus, microvascular dysfunction defined above is common *without angina*. It is comparably prevalent in men and women and is nearly always associated with risk factors, coronary calcium, or subclinical CAD. It is associated with a relatively low risk of MI or death for treated risk factors.

In addition to the essential distinction between global and regional CFR, as shown above, global CFR may also reflect inadequate methodology that precludes reliable regional perfusion measurements. Prior literature indicating failed quantitative flow data in 12% of cardiac PETs [22] is not suitable for clinical purposes. By contrast, in our reported 5900 sequential clinical PETs with routinely quantified myocardial perfusion, only 0.7% of all studies had suboptimal flow data, due primarily to scanner failure or venous abnormalities precluding arterial input [25].

Making Physiologic Displays That Are Clinically Useful

Even though cardiologists and cardiac surgeons continuously use terms like *low coronary blood flow*, *ischemia*, and *revascularization to improve coronary blood flow*, most of them have never performed measurements or understood them quantitatively, including the threshold for ischemia or mortality risk, its relation to diffuse or multi-stenosis or to coronary pressure or FFR measurement or to subendocardial perfusion or its multiple control mechanisms. Because of the large, conflicting literature, they also may poorly understand the changes after revascularization—that is, clinical quantitative coronary physiology and the PET technology that best quantifies it.

A confusing jumble of distorted perfusion anatomy and quantitative data (as in Fig. 6.24) characterizes most displays of quantitative PET perfusion. These displays fail to inform, clarify, or improve clinical application of quantitative coronary physiology for patient management. Cardiologists will not use or depend on any data or images that they cannot easily, quickly, comprehensively, and correctly understand, interpret, and relate directly to their deeply embedded fluoroscopic, angiographic, or surgical views of the heart. Such displays also reveal a fundamental misunderstanding of the complex interdependency of coronary-specific imaging physics and dynamic coronary physiology. At the boundaries of epicardium and endocardium, activity is the lowest and most variable, thereby making the borders drawn in this figure highly uncertain. A calculated average perfusion within these boundaries is therefore also so highly variable as to preclude clinical reliability.

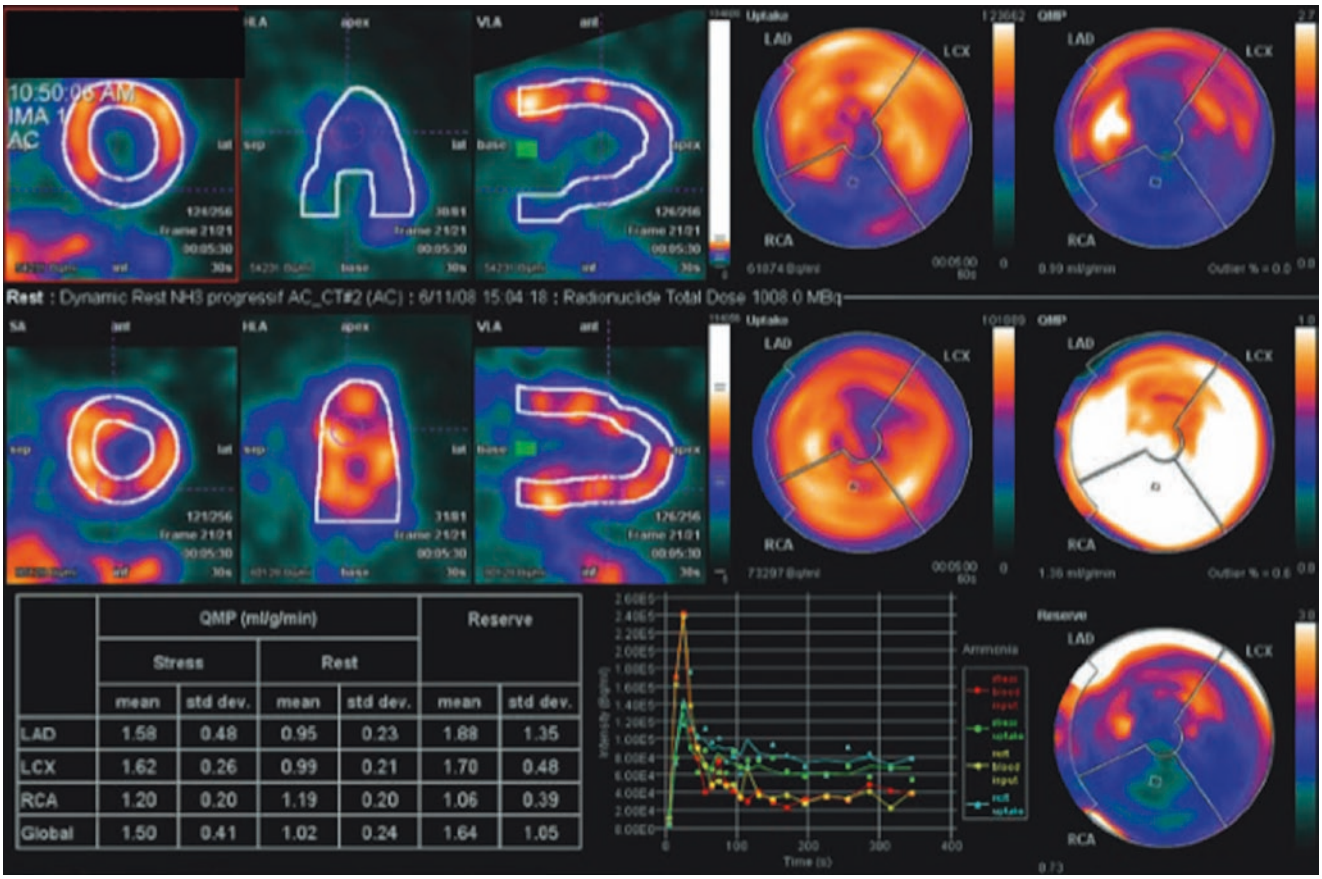

	QMP (ml/g/min)				Reserve	
	Stress		Rest			
	mean	std dev.	mean	std dev.	mean	std dev.
LAD	1.58	0.48	0.95	0.23	1.88	1.35
LCX	1.62	0.26	0.99	0.21	1.70	0.48
RCA	1.20	0.20	1.19	0.20	1.06	0.39
Global	1.50	0.41	1.02	0.24	1.64	1.05

Fig. 6.24 A confusing jumble of distorted perfusion anatomy and quantitative data, characteristic of most displays of quantitative PET perfusion that are not commonly readily understood by interventionalists

Clinically relevant and anatomically correct physiologic views (as appear later in this chapter), with comprehensive clinical integration by an experienced, self-critical, clinical cardiologist-physiologist consultant, generate an evolving bidirectional trust within the cardiac team, in which quantitative coronary physiology drives optimal patient outcomes that are documented by hard outcomes in peer-reviewed publications.

The display in Fig. 6.25 concerns a patient who had risk factors, dense coronary calcium, an equivocal or positive SPECT scan and rest stress PET at another institution. However, the referring cardiologist was not able to understand or make a clinical decision about an invasive or medical approach from this quantitative display or its report. Therefore, he sent the patient to Houston for a definitive, clinically oriented rest-stress PET recommendation, including our *Cardiac Positron Imaging and Consultation Report* with the images in Fig. 6.26.

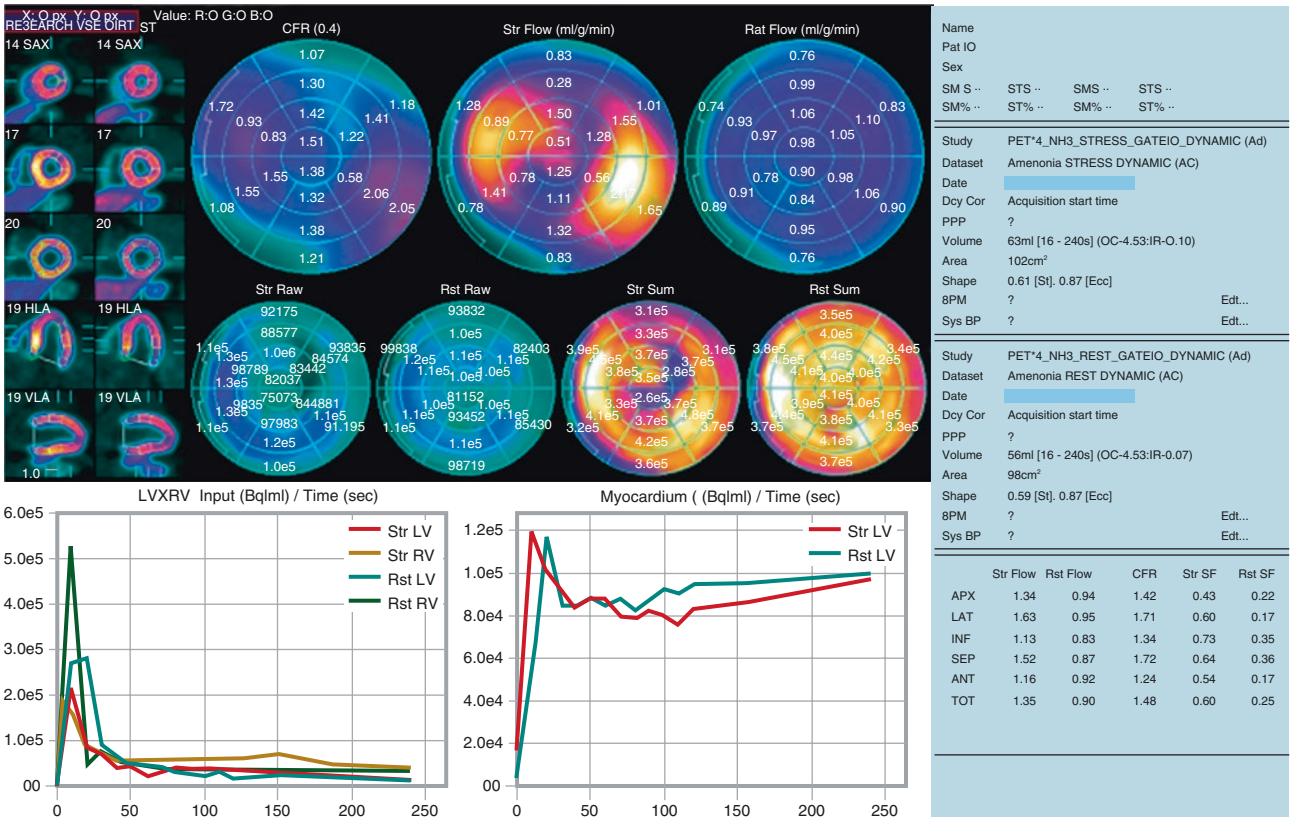

Fig. 6.25 Case example of a confusing physiologic display and report that was not readily understood by the referring cardiologist

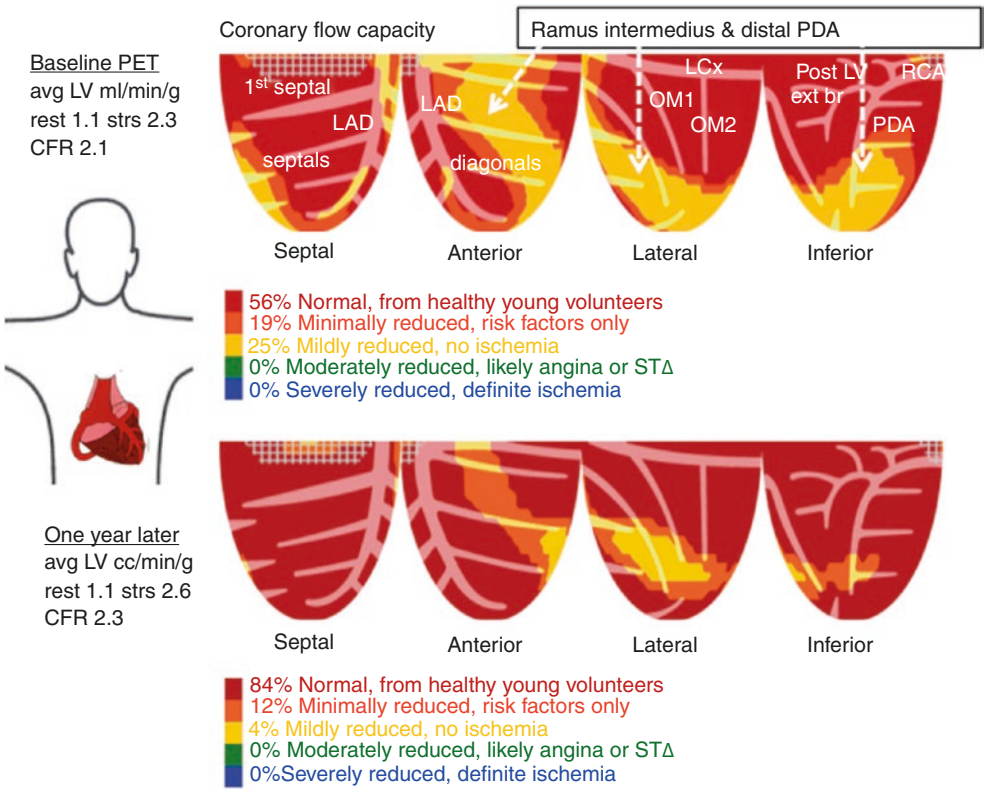

Fig. 6.26 The same case as in Fig. 6.25, definitively resolved by a CFC map. The CFC map for this patient showed mildly reduced CFC in 25% of the LV, well above ischemic levels. The distribution is characteristic of a large ramus intermedius distribution, typically extending to the lateral apex. The mildly reduced CFC in the distal and inferior apex is typical of diffuse RCA or wrap-around LAD disease. The patient had no angina or STΔ, and CFC is good to excellent throughout the remaining 75% of the LV

The referring cardiologist and patient immediately understood the images of Fig. 6.26 showing mildly reduced CFC in the distribution of Ramus Intermedius branch associated with very low risk over 10 years that would not be benefited by PCI; the risk may be increased by such a procedure since the risk of the procedure is higher than the 10-year risk of adverse events for this mildly reduced CFC [39]. The PET data and report therefore indicated intense medical management without an invasive angiogram. Both the patient and cardiologist were satisfied by the recommendation for appropriate vigorous risk factor management without an invasive procedure [2, 25, 27, 39–49].

To confirm this management decision, repeat PET 1 year later showed substantially improved CFC, which is mildly reduced in only 4% of the LV, with good to excellent CFC in the remaining 96% of LV, compared with mildly reduced CFC in 25% of the LV on the prior PET. Careful study of the prior common PET display in Fig. 6.25 indicates an abnormality corresponding to the baseline PET in Houston, but the 17-segment bulls-eye display spatially distorts the anatomic perfusion distribution and makes quantitative numbers difficult to see or interpret. The 17-segment method often mis-assigns coronary perfusion territories and cannot account for inherent morphological and regional artery-specific variability in different patients [14, 50–56].

True full-quadrant views of the LV and its coronary artery tree are visually distorted on the bulls-eye view, as illustrated by the example in Fig. 6.27, which shows a severe inferolateral and inferior apical defect. In order to fit the true full quadrant views into the pie display, basal segments must be enlarged and apical segments must be reduced in size [14]. Consequently, a stress defect comprising 19% of the LV appears visually on the bulls-eye display to comprise only 7% of the bulls-eye, primarily inferior because the lateral component is largely distorted out of the bulls-eye image. Although the calculated size of the defect as a percentage of all LV pixels is the same for both displays, the appearance is sufficiently distorted on the bullseye display to mislead visually driven decisions typical of cardiology or to breed distrust of numbers that fail to match the visual impression of size.

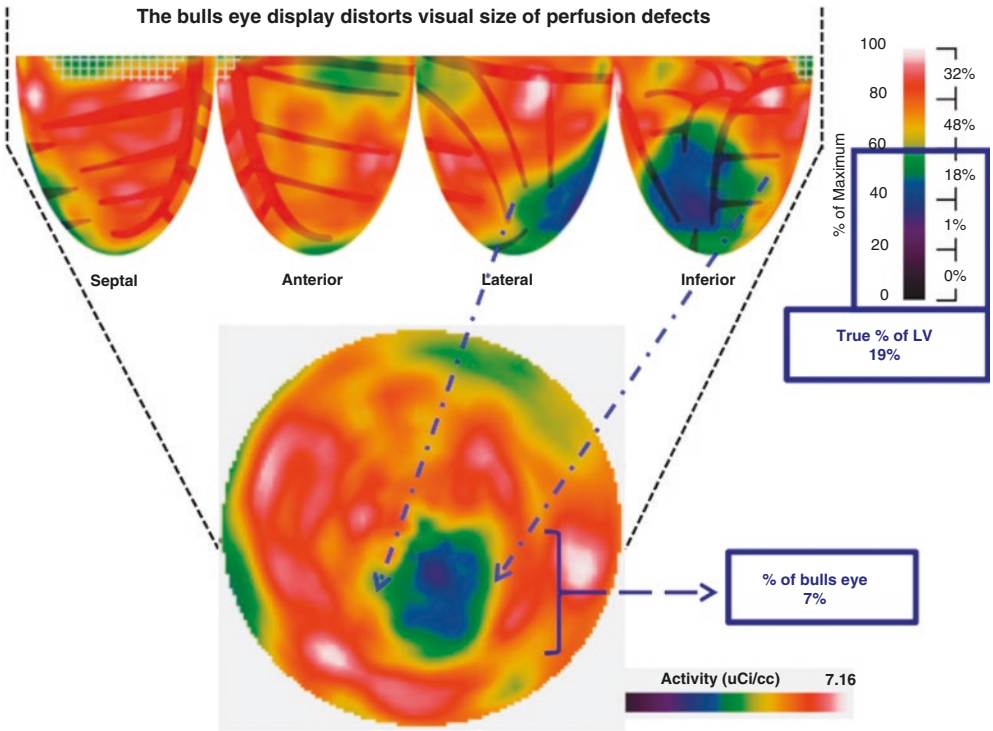

Fig. 6.27 Distortion of spatial perfusion anatomy by the bulls-eye display. To fit the full quadrant views of this example into the pie, basal segments must be enlarged and apical segments must be reduced in size. Consequently, a stress defect comprising 19% of the LV appears visually on the bulls-eye display to comprise only 7% of the bulls-eye, primarily inferior because the lateral component is largely distorted out of the bulls-eye image

Accordingly, we developed the four-quadrant topographic display to make the visual perfusion distribution match the quantitative size and severity of quantitative perfusion in coronary artery anatomic arterial distributions, as if actually looking at a transparent patient. This map of personalized perfusion anatomy for each artery and all its branches avoids the assumed generic 17-segment arterial distribution imposed on perfusion data, which forces flow values into arbitrary compartments that are commonly different from actual arterial and perfusion anatomy in any individual patient. A significant literature documents the errors and disadvantages of 17-segment bulls-eye displays [14, 50–56].

Interacting Clinical Physiology and Imaging Physics

Figure 6.28 illustrates the principles of measuring myocardial perfusion experimentally and by PET [14, 49, 57]. The interacting principles of imaging physics and quantifying myocardial perfusion derive from myocardial perfusion measured experimentally by radiolabeled microspheres. When radiolabeled microspheres are injected into the left atrium for adequate LV mixing, rapid arterial blood samples are drawn over precise time intervals to produce an arterial time-activity curve input distributed to the coronary arteries with 100% trapping of the microspheres in myocardium.

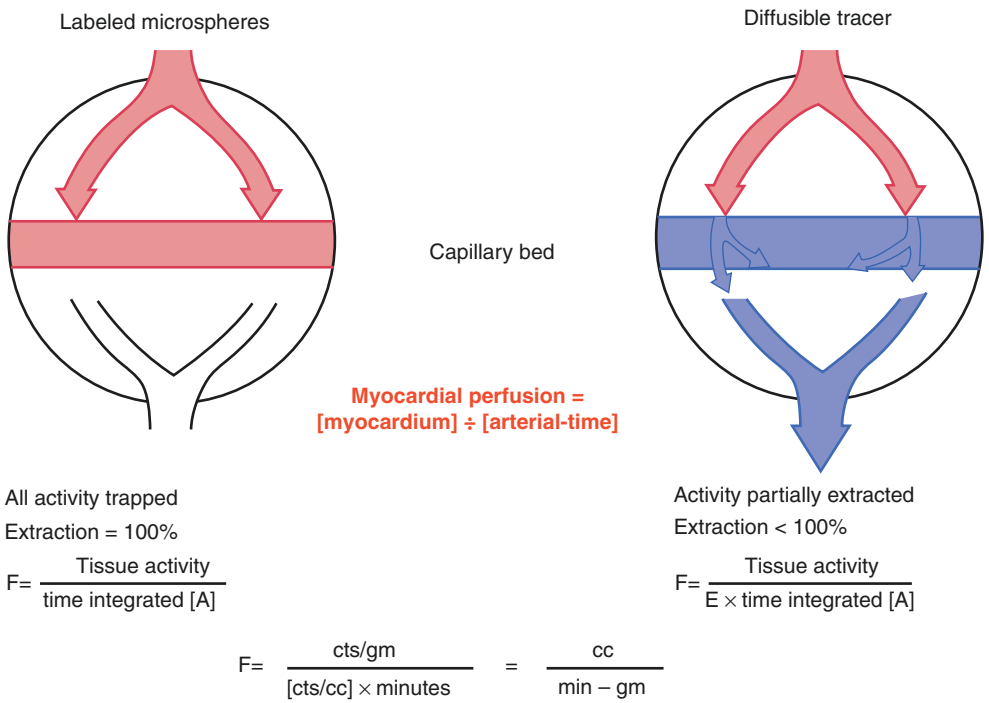

Fig. 6.28 Principles of measuring myocardial perfusion by PET [14, 49, 57]. (*From* Gould et al. [49]; with permission from McGraw-Hill Education)

Post mortem, the LV is diced into small pieces in a detailed map of each tissue sample for its location in the LV. Each myocardial sample is weighed and counted in a well counter. The measured activity in each myocardial sample divided by the arterial time-activity curve gives perfusion in cc/min/g of each small myocardial sample, which is mapped back to its position in the LV, thereby providing an LV map of perfusion in cc/min/g displayed in numbers, iso-contour lines, and gray or color scale schema.

PET perfusion imaging employs the same principle, using intravenous radionuclides that distribute as a time-activity arterial curve to the coronary arteries, best measured in the left atrium by PET imaging (for reasons shown later). Most of the radionuclides commonly used clinically are not 100% trapped by myocardium, but are only partially extracted. This extraction fraction ranges from 60% to 90%, depending on the radionuclide and on myocardial perfusion, decreasing as perfusion increases. Each pixel of quantified myocardial activity by PET divided by the arterial time-activity curve in the left atrium, corrected for partial extraction, gives cc/min/g in the LV location of that pixel.

As flow increases, myocardial trapping or extraction falls for the radionuclides most commonly used in clinical PET (Fig. 6.29). The mathematical perfusion model for each radionuclide accounts for this flow-dependent extraction to acquire the flow-independent myocardial retention for each pixel divided by the time-activity arterial input, thereby giving perfusion in cc/min/g analogous to the microsphere method. The claim that a radionuclide with high extraction measures perfusion better than a radionuclide with lower extraction is not true, as the correct perfusion model for each radionuclide has been proven experimentally to measure perfusion accurately when compared with the standard of radiolabeled microspheres.

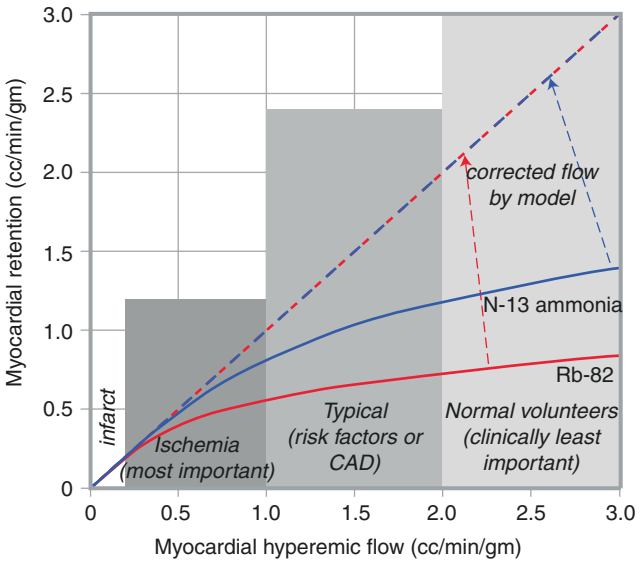

Fig. 6.29 Flow-dependent myocardial extraction of radionuclides

Figure 6.30 shows protocols for quantitative perfusion imaging using Rb-82 and dipyridamole, regadenoson, or adenosine vasodilator stress [2, 25, 27, 39–43, 49, 57–59]. Each stress has a different timing sequence to produce maximal stress perfusion, as systematically tested and reported by this clinical laboratory and now used worldwide.

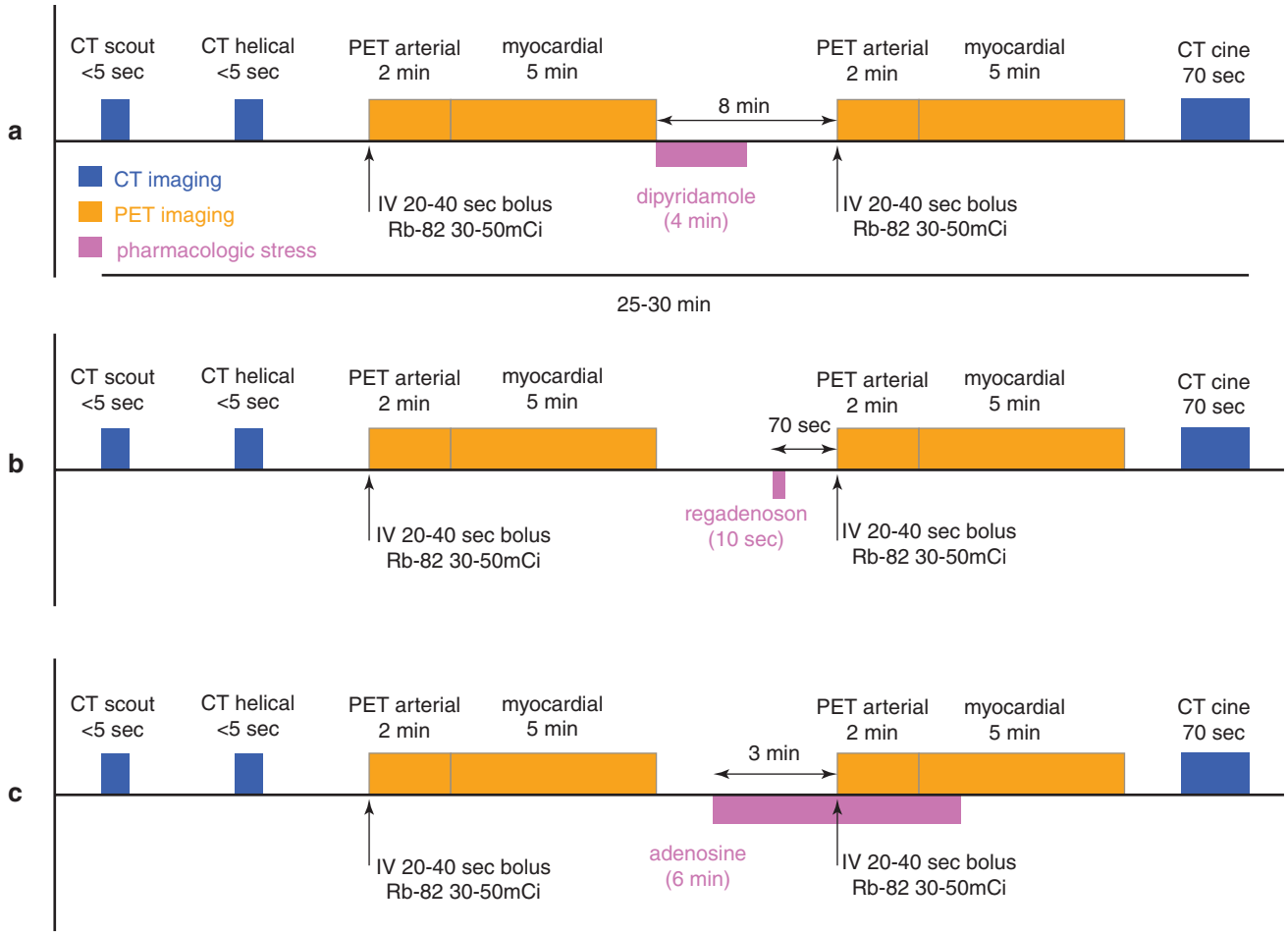

Fig. 6.30 Protocols for quantitative perfusion imaging using Rb-82 and dipyridamole (**a**), regadenoson (**b**), or adenosine (**c**) vasodilator stress. Each stress has a different timing sequence to produce maximal stress perfusion

Figure 6.31 shows normal rest and stress images of myocardial activity for one of four quadrant views, with a color bar scale of activity in μCi/cc [49]. The CT attenuation scan shows anatomy of the various vascular structures. The early arterial activity images acquired over the first 2 minutes after starting Rb-82 infusion show the left atrium and ascending aorta as sites for region of interest (ROI) placement to acquire the time-activity arterial input to the flow-model equations for each myocardial pixel. ROI placement is guided by the PET image activity, not the CT scan that is not reliable for obtaining correct arterial activity.

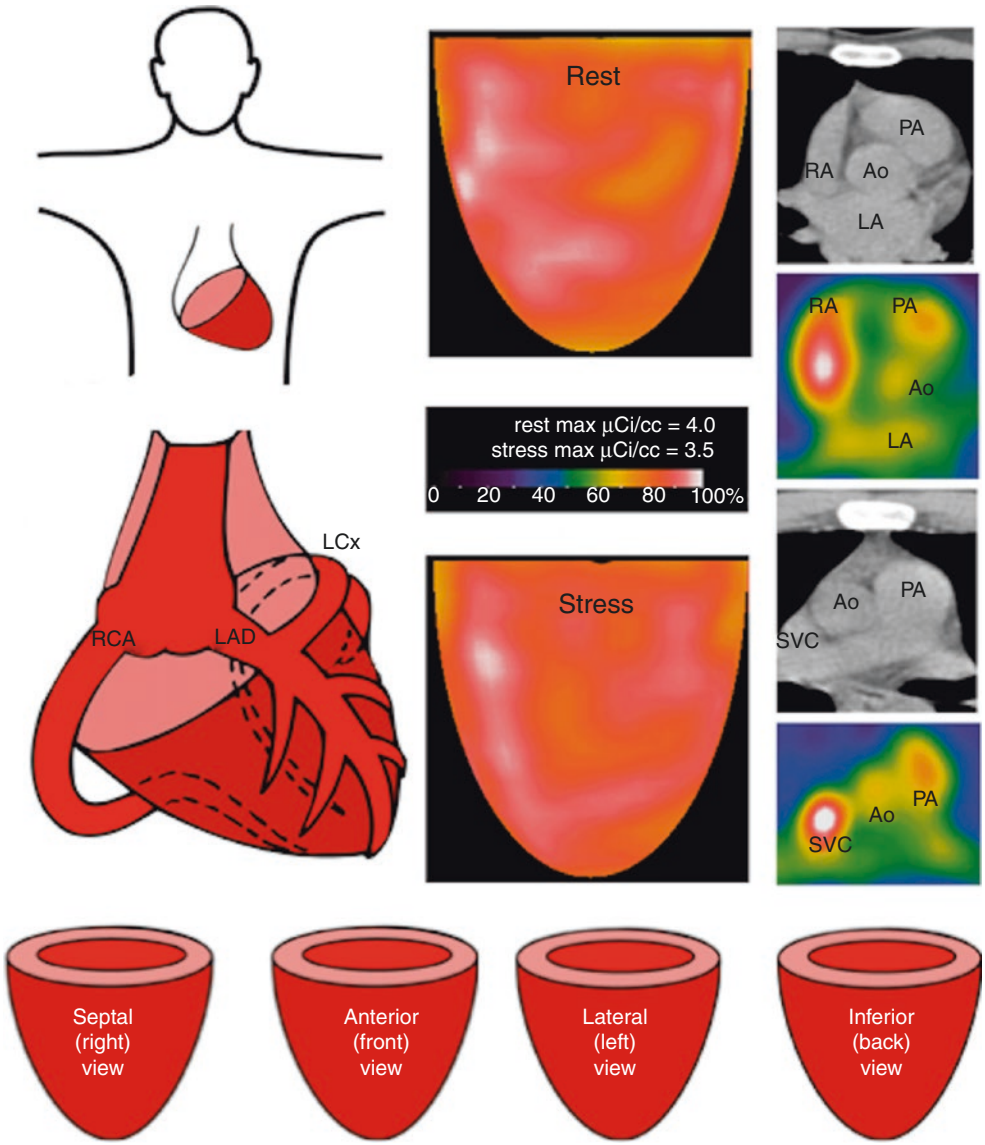

Fig. 6.31 Schematic orientation of cardiac PET images [49]. The CT anatomy is shown only to familiarize the reader with the arterial phase activity structures (LA and aorta). (*From* Gould et al. [49]; with permission from McGraw-Hill Education)

The rest and stress time-activity plots seen in Fig. 6.32 are fit to the mathematical flow model to solve for the unknowns, one of which is myocardial perfusion in cc/min/g for each pixel of the image. This method, called *compartmental modeling*, requires short serial images of 10–15 seconds each, in order to construct the time-activity curves [14, 49, 57]. However, such short images are very "noisy," with such great statistical variability of activity as to degrade calculated perfusion so much that perfusion on a pixel basis is not reliable, thereby requiring large, arbitrary segments of the LV to average out statistical uncertainty.

Compartmental modeling - four unknowns & two measured

$$M(t)=V_F C_a(t)*bte^{-at} + F[1- e^{-(0.45+0.16F)/F}] \int_0^t C_a(x)*bxe^{-ax}dx$$ Where
M(t), Ca(t) are measured. F, V_F, a, b are found by curve fitting the model.

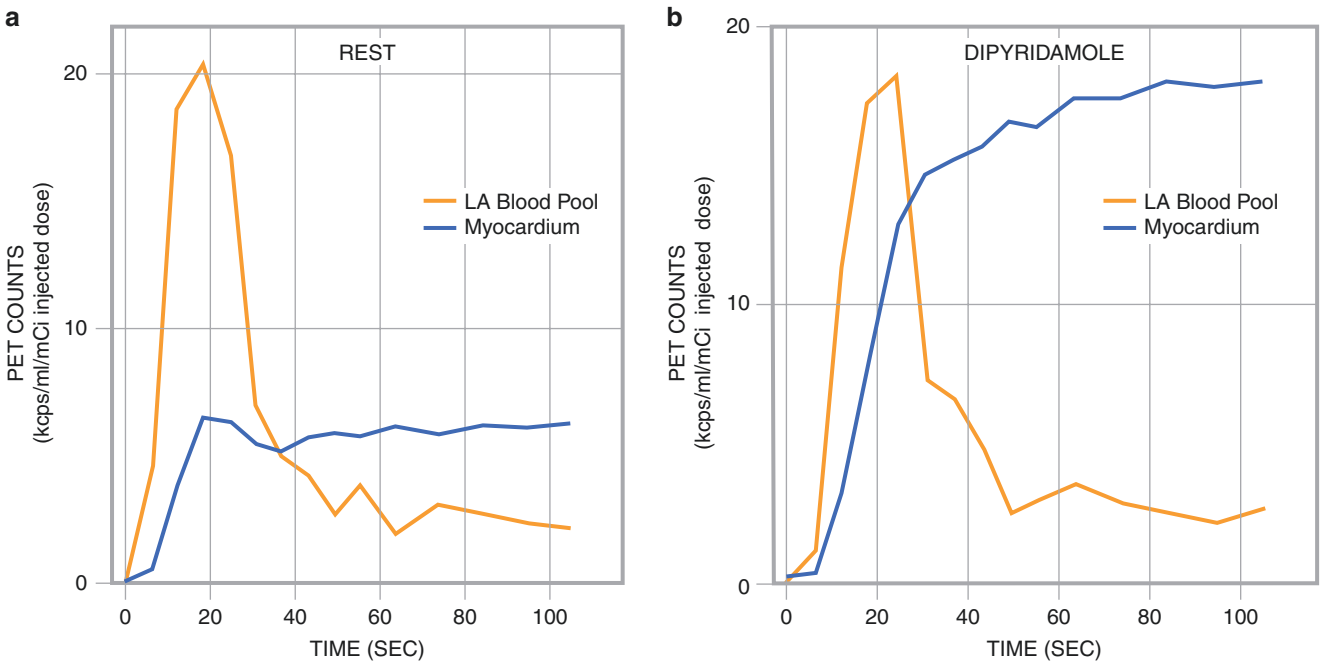

Fig. 6.32 Experimental arterial and myocardial time-activity curves. The rest and stress time-activity plots are fit to the mathematical flow model to solve for the unknowns (*red terms*), one of which is myocardial perfusion in mL/min/g for each pixel of the image. (*Reproduced with permission from* Yoshida et al. [57])

These short images are also of such poor quality as to preclude repeatable, accurate location of an ROI directly on the central left atrium or aorta for arterial activity in a dynamically moving heart. With each systole, the heart translates inferior and medially by 1–2 cm, and another 2 cm or more during the respiratory cycle [14, 49, 58]. To overcome this degradation of data, other PET sites estimate the left atrial site for ROI by back projection from later myocardial images, which may not be optimally located in the left atrium of the moving, translating heart.

To overcome such image degradation, for 2D imaging we developed a "simplified" acquisition protocol and model (Fig. 6.33), which has the least variability (±10%) reported in the literature [14, 49, 58]. Our "simple" 2D imaging model acquires a 2-minute image and a 5-minute image beginning with intravenous infusion of Rb-82 (with a half life of 75 seconds) from a commercially available Rb-82/strontium-82 generator. The single early 2-minute image provides good images for optimally placing an ROI in the central left atrium and aorta of several tomographic slices to find the optimal integrated arterial time-activity value within the range of cardiac motion, while avoiding spillover activity from venous structures, particularly the pulmonary arteries immediately adjacent to both the aorta and left atrium.

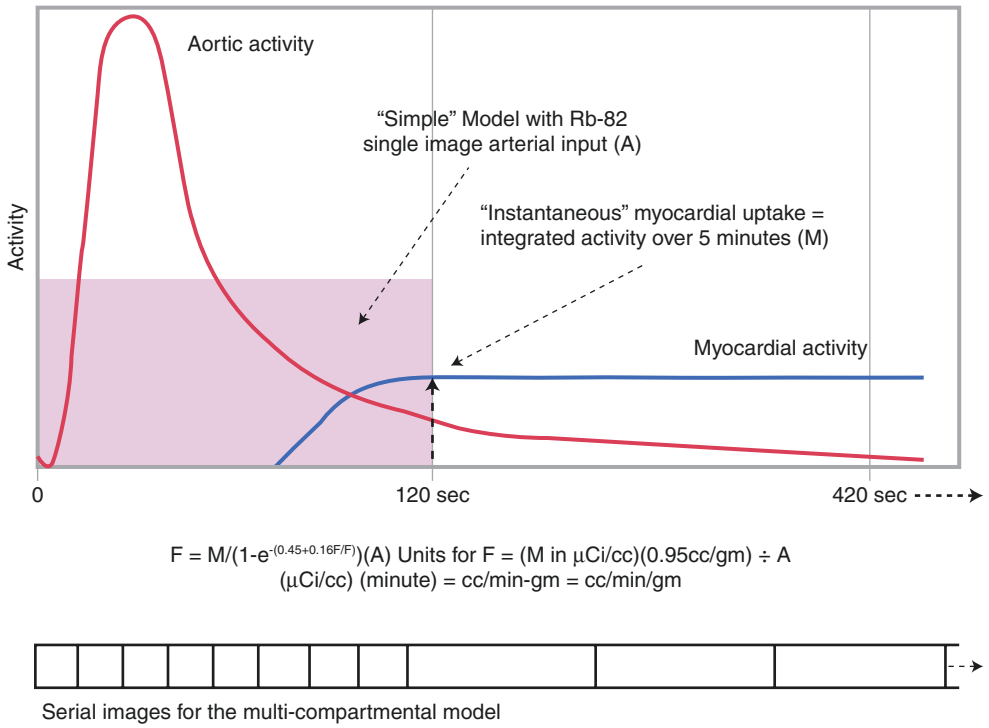

Fig. 6.33 Solution to limitations of short serial statistically poor images used in compartmental modeling. The protocols for serial short images for compartmental modeling to determine perfusion are shown schematically at the bottom of this figure. (*From* Gould et al. [49]; with permission from McGraw-Hill Education)

The good 2-minute arterial image quality also minimizes statistical noise and corresponding variability in perfusion measurements for each pixel mapped back to the LV. This approach avoids assuming arbitrary large regions for perfusion measurements needed to reduce statistical noise of short serial images in compartmental analysis. Because Rb-82 extracted into myocardium is trapped and does not "leak out" within its imaged half-life, decay-corrected myocardial activity remains constant, thereby providing high-quality myocardial images for regional per-pixel distribution of perfusion.

Figure 6.34 illustrates the proximity of venous structures, right atrium (RA), and pulmonary arteries (PA) as sources of potential activity spillover that erroneously increases arterial input and erroneously lowers perfusion values. Alternatively, heart translation and motion may move the left atrium or aorta in and out of an arbitrary, estimated left atrium (LA) or aortic (Ao) location—"smearing the activity" and thereby recording lower than true activity with consequent erroneously high perfusion values. Our high-quality 2-minute and 5-minute images avoid these issues inherent in compartmental modeling of multiple serial short, statistically poor images.

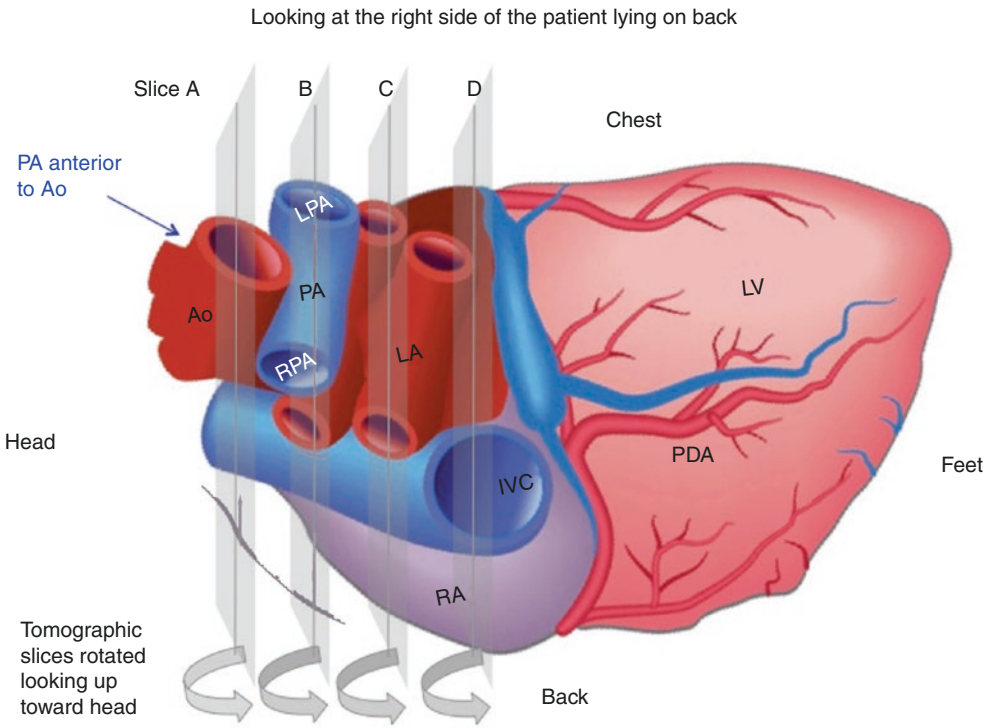

Fig. 6.34 Vascular anatomy and cross-sectional slices. IVC inferior vena cava, PDA posterior descending artery. (*From* Gould et al. [49]; with permission from McGraw-Hill Education)

Figure 6.35 presents PET and CT views of arterial activity and anatomy [49, 58–60]. The early 2-minute image during intravenous infusion of Rb-82 shows characteristic three round structures of activity that is highest in the superior vena cava (SVC), next highest in pulmonary artery (PA) and lowest in left atrium (LA) and ascending aorta because of cardiac output diluting the intravenous activity. Arterial activity is measured in the small ROIs placed optimally in the central LA and ascending aorta.

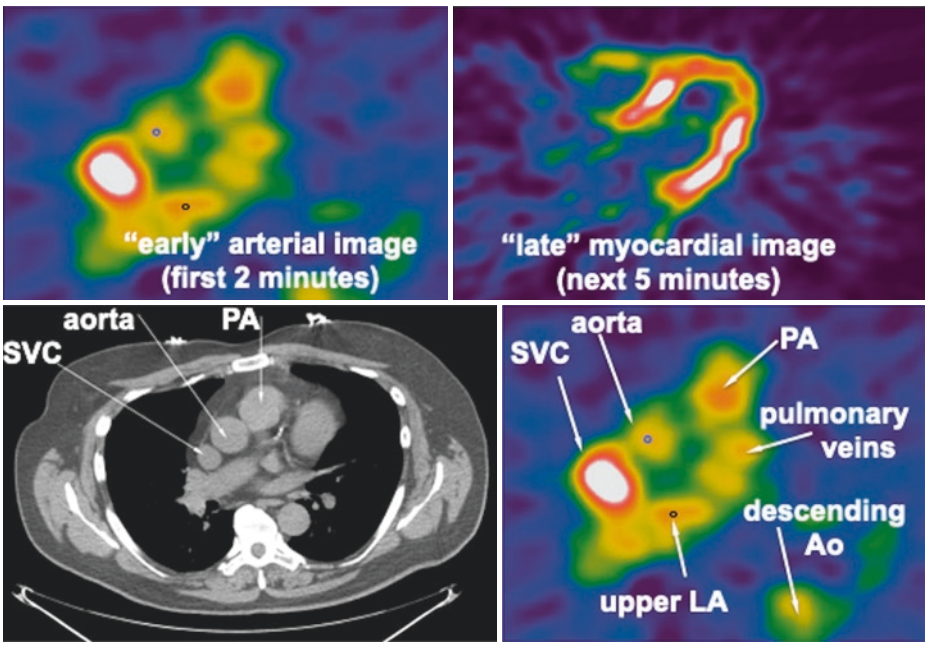

Fig. 6.35 PET and CT views of arterial activity and anatomy. Although not used for locating the arterial ROI, for teaching purposes the CT scan documents the structures as seen in slice B of Fig. 6.34 [2, 58]

Figure 6.36 illustrates experimental validation of our compartmental model and "simple" model for myocardial perfusion [14, 49, 57]. Both compartmental and simple flow models correlate with radiolabeled microspheres for Rb-82 and for N-13 ammonia.

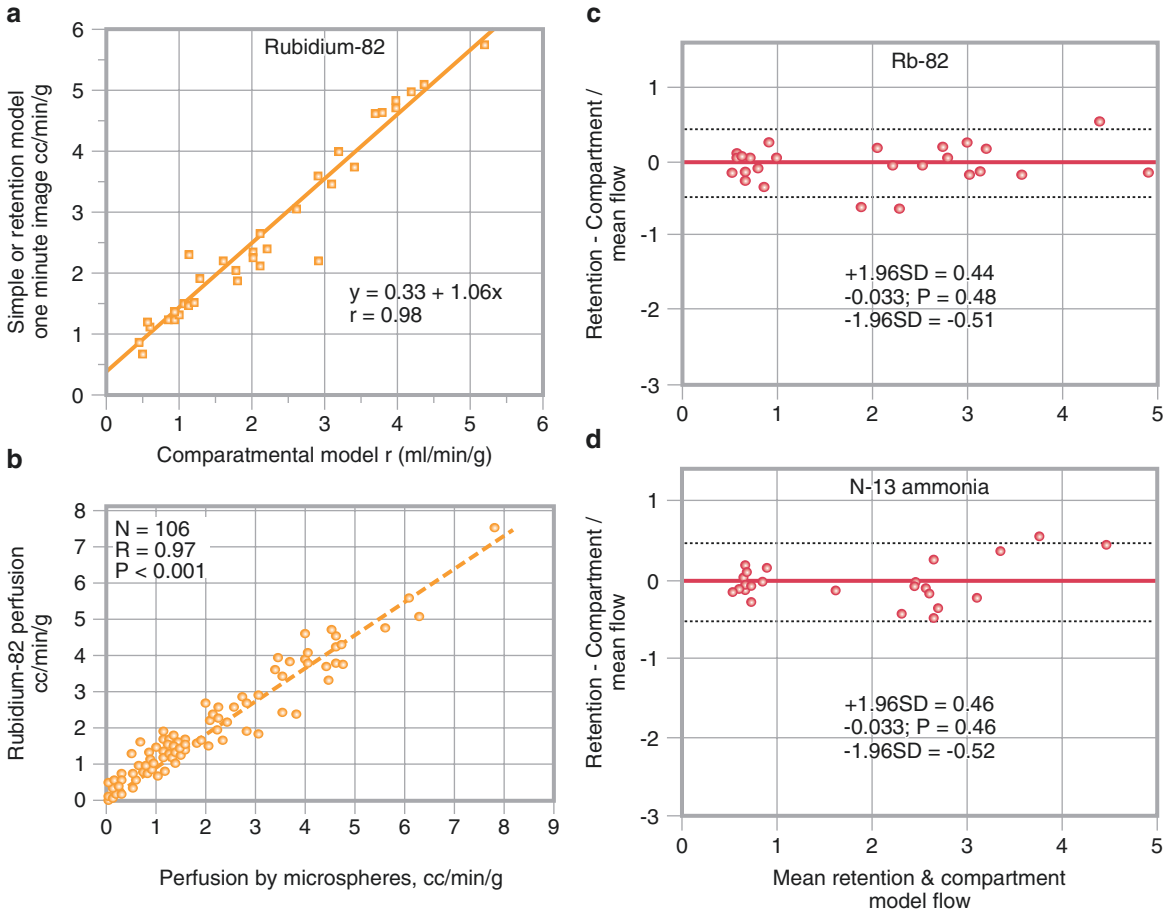

Fig. 6.36 Experimental validation of our compartmental model and "simple" model for myocardial perfusion. Both compartmental and simple flow models correlate with radiolabeled microspheres for Rb-82 (**a**) and for N-13 ammonia (**b**). The Bland Altman plots for variability between serial PET perfusion measurements for Rb-82 (**c**) and N-13 ammonia (**d**) are shown from the literature [60]. (**a** and **b**, *From* Yoshida et al. [57], with permission from the Society of Nuclear Medicine and Molecular Imaging, and from Gould et al. [49], with permission from McGraw-Hill Education. **c** and **d**, *From* Renaud et al. [60], with permission from Mosby)

Figure 6.37 shows experimental validation of perfusion using the oxygen-15 method compared with microspheres [61, 62]. Oxygen-15–labeled water from an onsite cyclotron is a freely diffusible radionuclide that requires a different model because it is not extracted or trapped by myocardium. The upper plot on this figure shows some scatter about the regression line due to variability on the PET-acquired arterial input. In the lower plot, on the other hand, the arterial input was measured by rapid serial blood samples drawn during the PET imaging. The validation of the three different radionuclides (O-15 water, N-13 ammonia, Rb-82) with their own specific acquisition protocols and models for calculating perfusion indicates that they provide equivalent perfusion measurement despite widely different behavior in the myocardium.

Image arterial and myocardial time activity curves were fitted to a single tissue compartment tracer kinetic model to estimate MBF in each myocardial region using O-15 water.

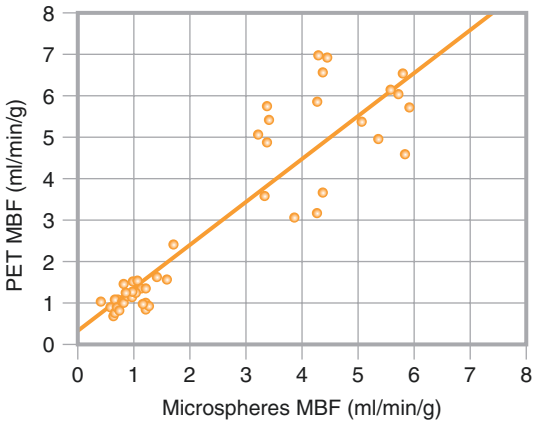

Image myocardial and blood sample time activity curves fitted to a single tissue compartment tracer kinetic model to estimate MBF in each myocardial region.

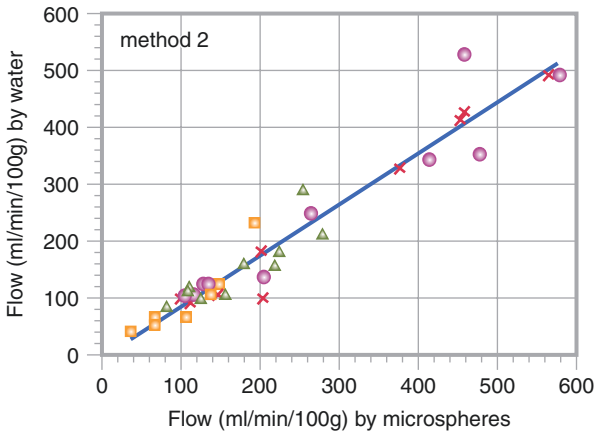

Fig. 6.37 Experimental validation of perfusion using the oxygen-15 method compared with microspheres. MBF myocardial blood flow. (*Upper panel from* Araujo et al. [61] and *lower panel from* Bol et al. [62]; with permission from the American Heart Association)

Myocardial perfusion reported in the literature was derived using two-dimensional (2D) PET scanners with a measured resolution of 1.0–1.5 cm [63]. Consequently, for constant myocardial activity corrected for time decay, activity recovery is substantially better during systole than during diastole because of the greater wall thickness during systole (Fig. 6.38). Diastolic images therefore are commonly heterogeneous owing to varying partial volume loss at different segments of the same slice, with anatomic wall thickness varying among the free wall, the papillary muscles, and the septum. The wall in systole is thicker and more anatomically uniform than in diastole. At resting heart rates, systole typically comprises one third of the cardiac cycle, but during tachycardia of stress, systole may comprise half of the heart cycle. Therefore, the partial volume loss changes dynamically with heart rate, as we have systematically demonstrated in clinical PETs with greater partial volume loss during bradycardia than tachycardia [63].

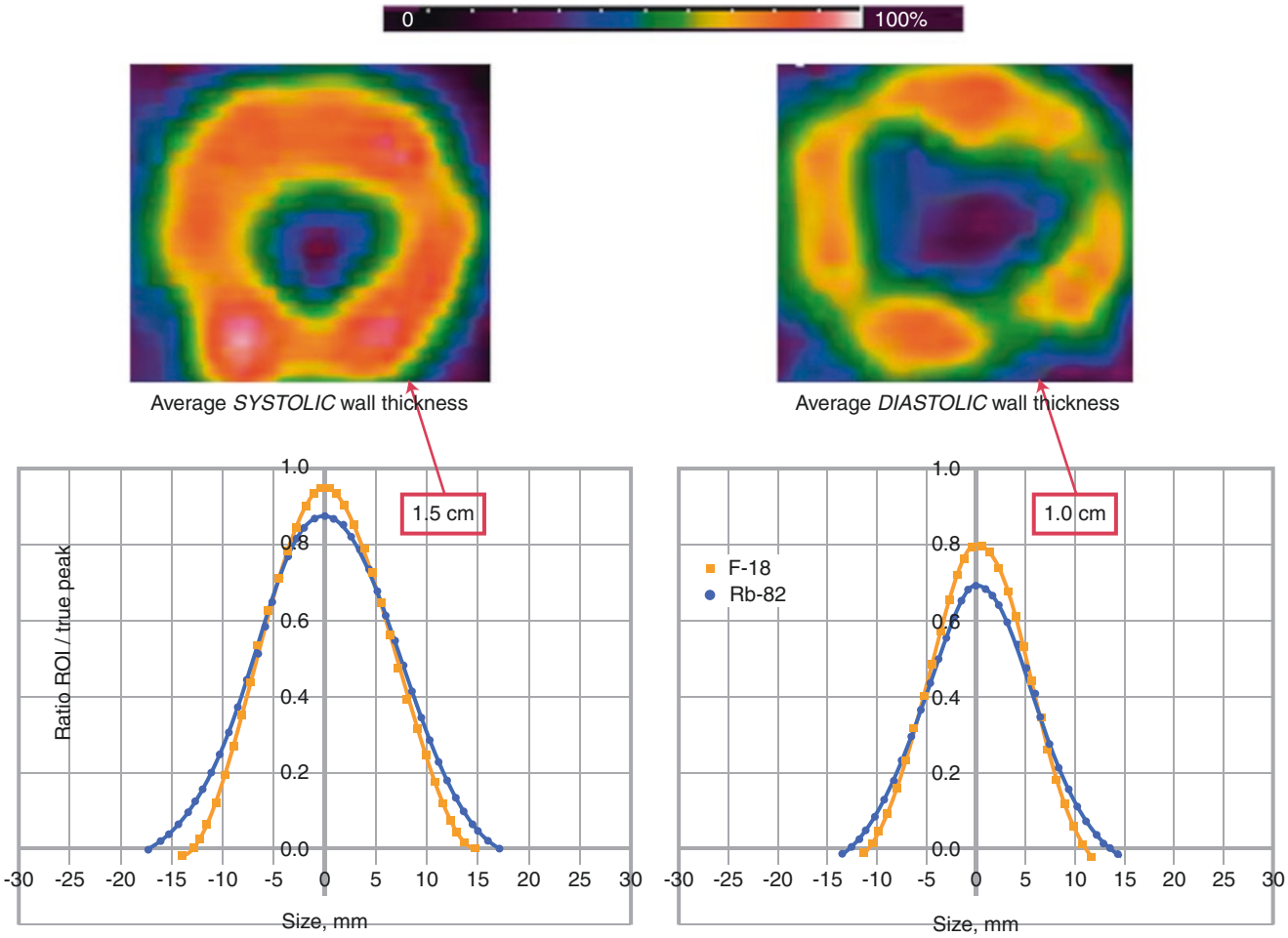

Fig. 6.38 Partial volume loss of activity recovery during systole and diastole

Activity recovery is so much greater in systole than in diastole that the average systolic activity dominates the cumulative myocardial activity over the time of acquisition [63]. Our "simple" model summarizes these complex time-varying partial volume losses by using a fixed partial volume correction based on average wall thickness derived from a branching phantom of various thickness in the one dimension of LV wall thickness for each specific scanner and radionuclide (Fig. 6.39). The correction of myocardial activity recovery in our model accounts for the longer positron ranges of Rb-82 than F-18 seen in this figure.

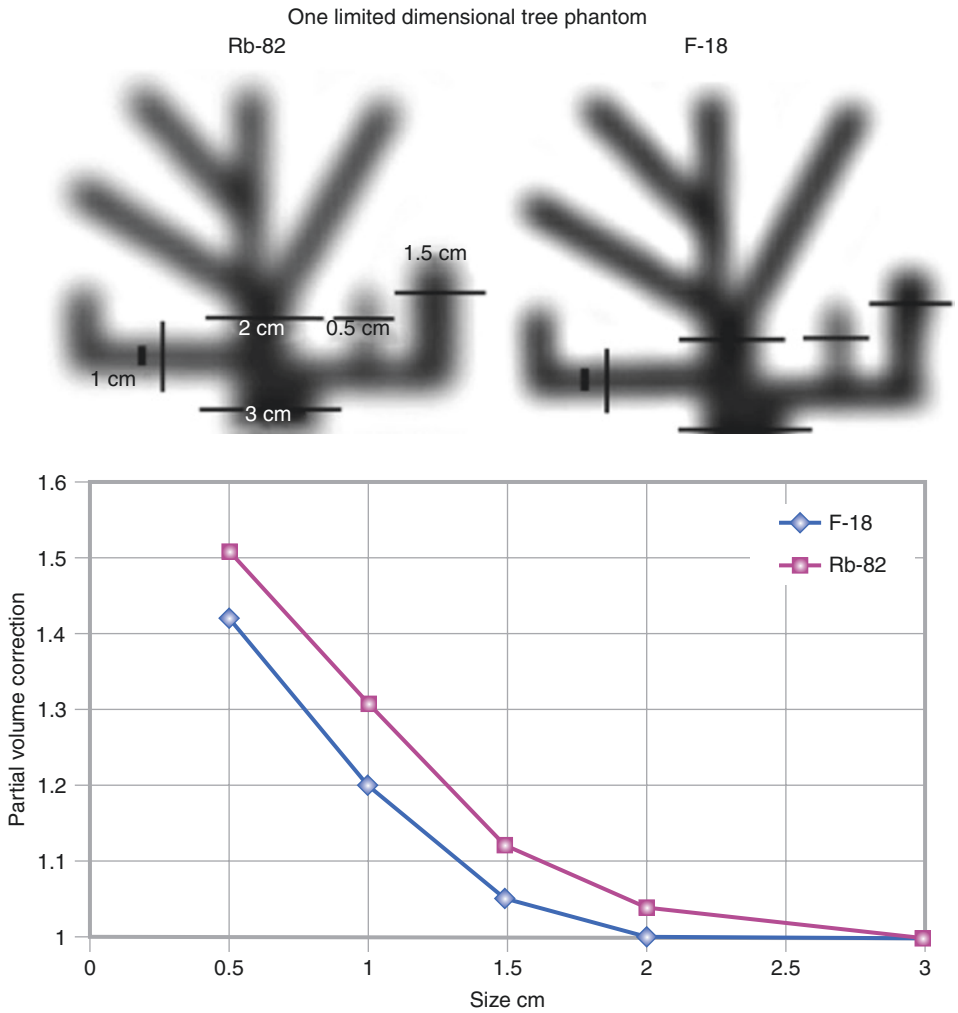

Fig. 6.39 Partial volume correction for perfusion measurements

The widely used compartmental modeling using multiple serial images calculates a partial volume correction as a term in the model equations by curve fitting time-activity curves to the model equations. However, the resulting partial volume corrections have never been extracted and published, to our knowledge. Given the low count density (statistical content) of the short serial images in a dynamically moving heart, the time-activity curves at the per-pixel level preclude the high precision and statistical pixel content required for curve-fitting the data to the model for determining the many unknowns, including partial volume correction and perfusion at the per-pixel level.

Our test-retest repeatability of PET perfusion in the same patient within minutes, ±10%, is the smallest variability reported in the literature, attesting to the validity of our simplified perfusion model and protocol [47], its good correlation to microsphere measurements experimentally [57], and its association with clinically relevant outcomes based on quantitative severity and size as a percentage of the LV [39].

Figure 6.40 shows the different positron ranges for the flow model of perfusion using Rb-82 and N-13 ammonia. On short-axis views of Rb-82, the LV wall appears thicker than for N-13 ammonia because of the longer positron range of Rb-82 [60, 63]. As shown in Fig. 6.41, this thicker appearance has no impact on our perfusion measurements based on maximal activity on radii from the LV center to the outside the myocardium. Both radionuclides provide similar validated perfusion despite differences in positron range, which is accounted for in their respective perfusion models.

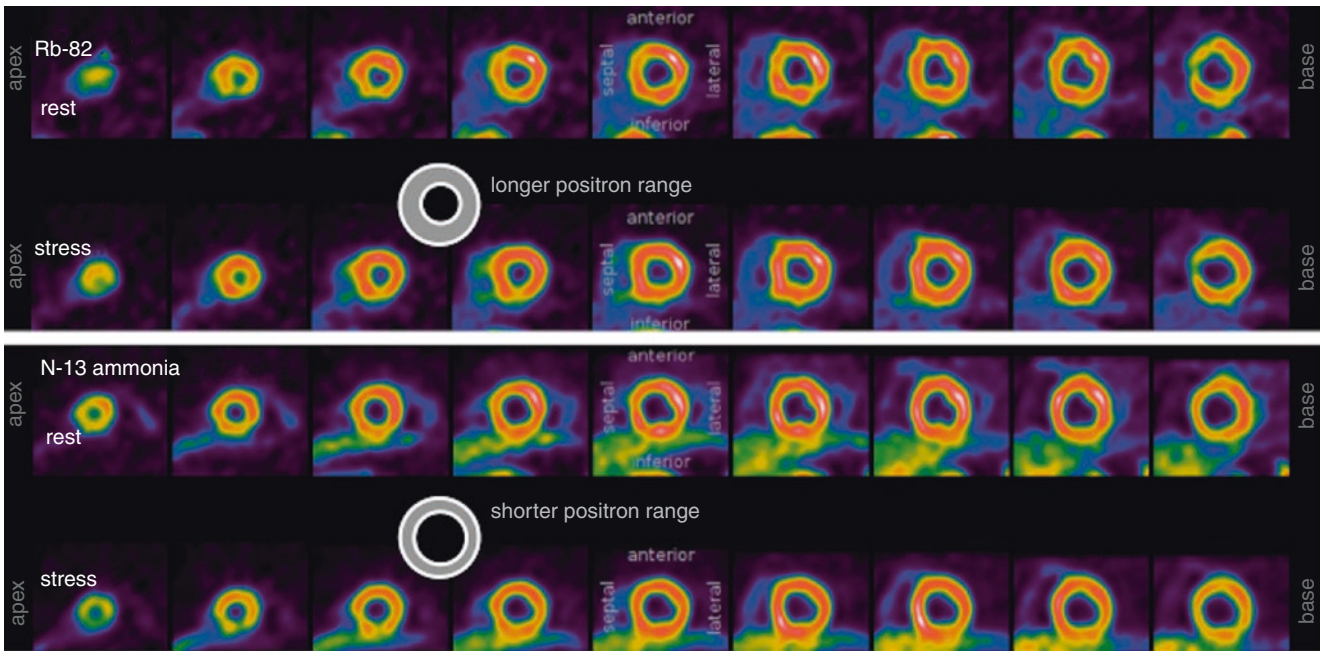

Compared to multi-compartmental analysis of sequential images (Ottawa), the simple retention model (Texas) was reported to have the following advantages:

- Values comparable to multi-compartmental analysis.
- Least variability of stress flow and coronary flow reserve.
- Most efficient simple acquisition and computation.
- Optimal ROI for arterial input.
- "Higher sensitivity for detection & localization of abnormal flow & myocardial perfusion reserve". (reference 62 Ottawa).

Fig. 6.40 Different positron ranges for the flow model of perfusion using Rb-82 and N-13 ammonia

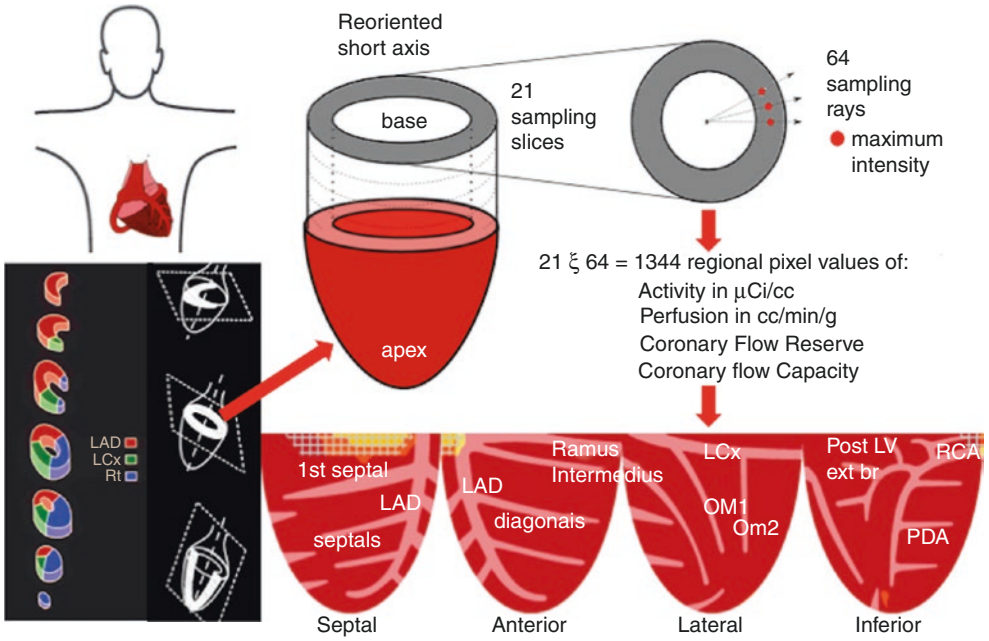

Fig. 6.41 Radial pixels—The secret for measuring pixel distribution of activity and perfusion for LV mapping in our cardiac PET processing software (FDA 510(k) 171,303)

In current literature using 2D quantitative PET, myocardial images are acquired at oblique angles to the LV long axis, are re-oriented into long- and short-axis tomographic slices in which the LV cross-section looks like a doughnut and the long axis looks like a U. In most commercial perfusion software, epicardial and endocardial borders of the long- and short-axis images are outlined automatically or manually, and average activity is calculated within these boundaries in predefined segments of the LV wall (as shown in Figs. 6.24 and 6.25, subdivided into the 17-segment model). In our view, this approach has several disadvantages (if not basic flaws) that explain some of the great variability within or among different PET sites, which undermines their clinical use.

As shown in the activity profile plots of Fig. 6.38, the smearing effect or point spread function of the scanner (due to the LV wall thickness being smaller than scanner resolution) make the location of both endocardial and epicardial borders highly uncertain at the low activity levels with variable spatial activity gradient. Every border definition method will be limited at these statistically poor, spatially changing border zones, thereby incurring comparable uncertainty of the average activity per region selected and the corresponding perfusion.

This border uncertainty contrasts with the maximal activity having the greatest statistical certainty of peak activity along each radius from LV center to outside the myocardium (*see* Fig. 6.41), which automatically by definition tracks motion and avoids uncertain border recognition. Maximal radial activity is optimally reproducible with clean partial-volume correction for every radial pixel, thereby providing maximal statistical content for efficient, robust automated spatial mapping of pixel perfusion in the LV for every artery and branch as it actually is in each individual.

The heart moves inferior and medially with the recoil of systolic ejection. It also reorients vertically, with a changing long-axis angle to the long axis of the body and scanner as the diaphragm moves vertically during respiration, which is augmented by hyperventilation during vasodilation stress. In addition, there is a slow plastic shift of the abdominal contents and diaphragm cephalad during the 15 minutes after lying supine during resting to stress imaging. These moving structures attenuate emission images over their average spatial range, in contrast to the seconds-long helical CT scan acquired unpredictably during some phase of heart and respiratory cycles during further rest and stress changes. The time-changing thoracic attenuation structures commonly cause errors in attenuation correction by either rotating rod or CT transmission scans with resulting large, severe perfusion abnormalities, for which we developed the first shift software to co-register transmission and attenuation data [64–66] (Fig. 6.42).

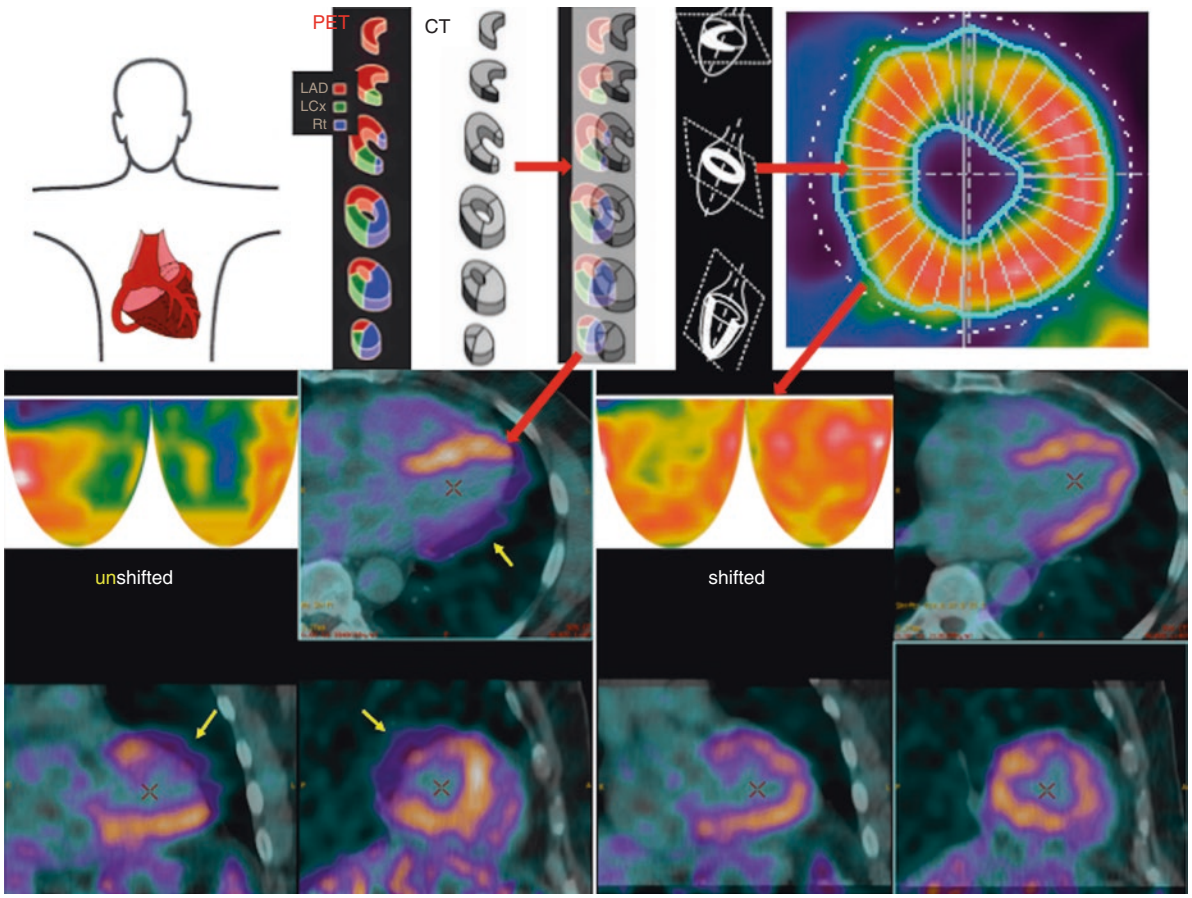

Fig. 6.42 Attenuation correction of imaged activity. This figure shows a schematic sequence (*red arrows*) of acquisition images, their rotation into short-axis and long-axis views, co-registration of schematic emission in color and CT data in black and white, and the radial maximal activity and topographic LV activity maps with a severe anterior defect (*yellow arrows*) due to erroneous attenuation correction caused by emission-transmission misregistration. After manually shifting the data to achieve co-registration, the LV activity map has only a mildly reduced activity

Figure 6.43 shows an example of fast helical CT emission-transmission mis-registration during normal inspiratory breath holding versus co-registration during normal expiratory breath holding. The double right diaphragm indicates diaphragmatic motion with a corresponding basal inferior abnormality that is mis-registration artifact propagated to the short-axis images in Fig. 6.44 and the topographic LV maps in Fig. 6.45.

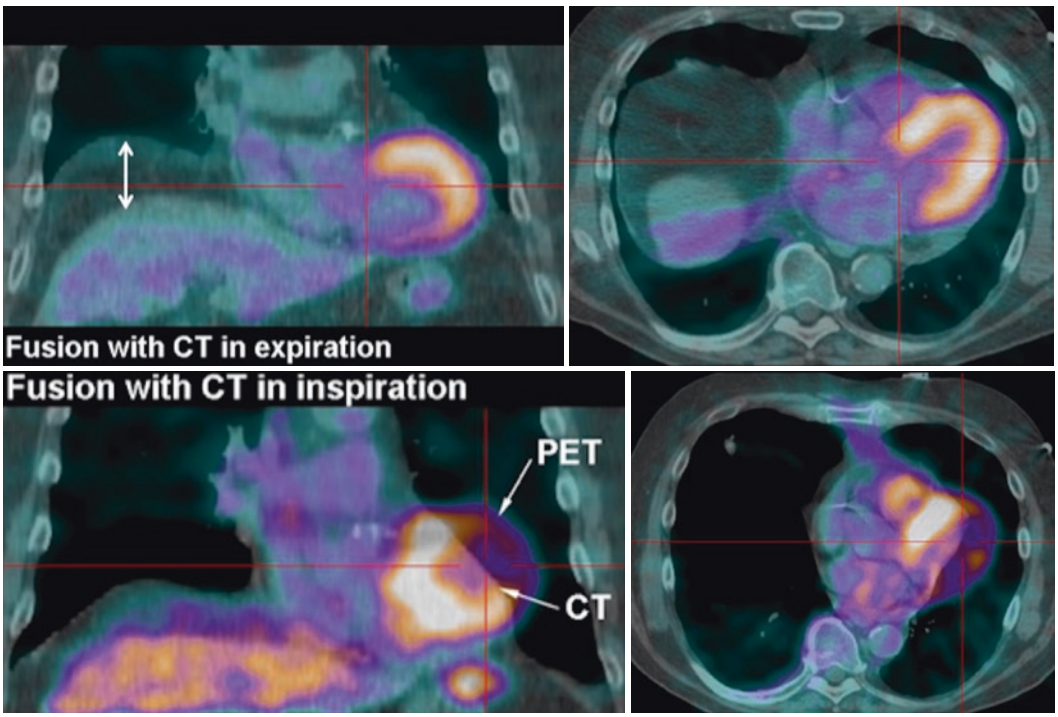

Fig. 6.43 Respiratory variation of attenuation data; an example of misregistration

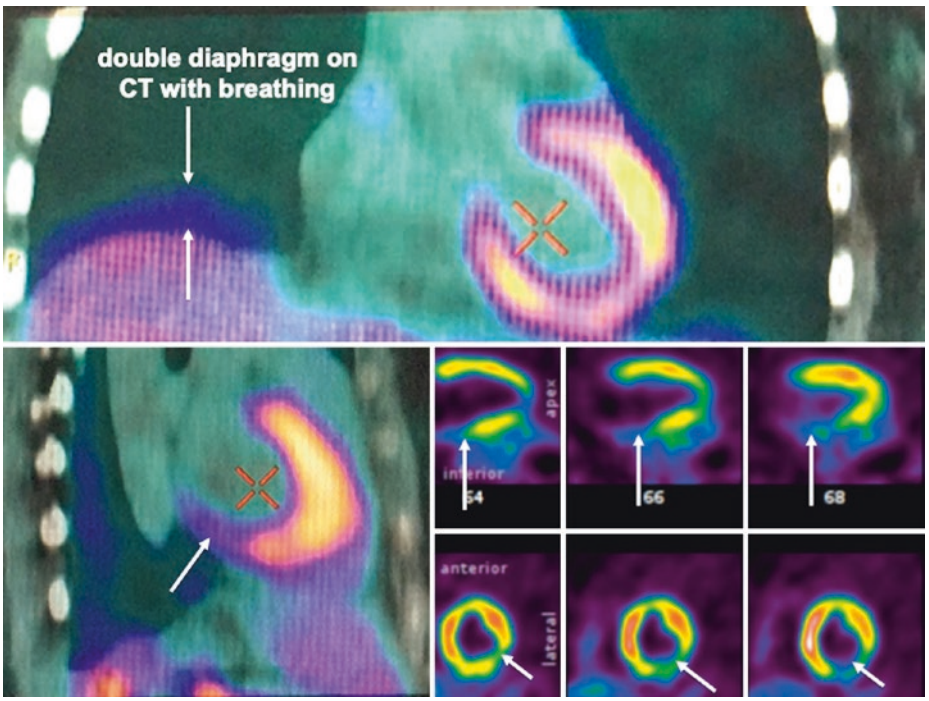

Fig. 6.44 Residual attenuation error despite cardiac emission-transmission co-registration

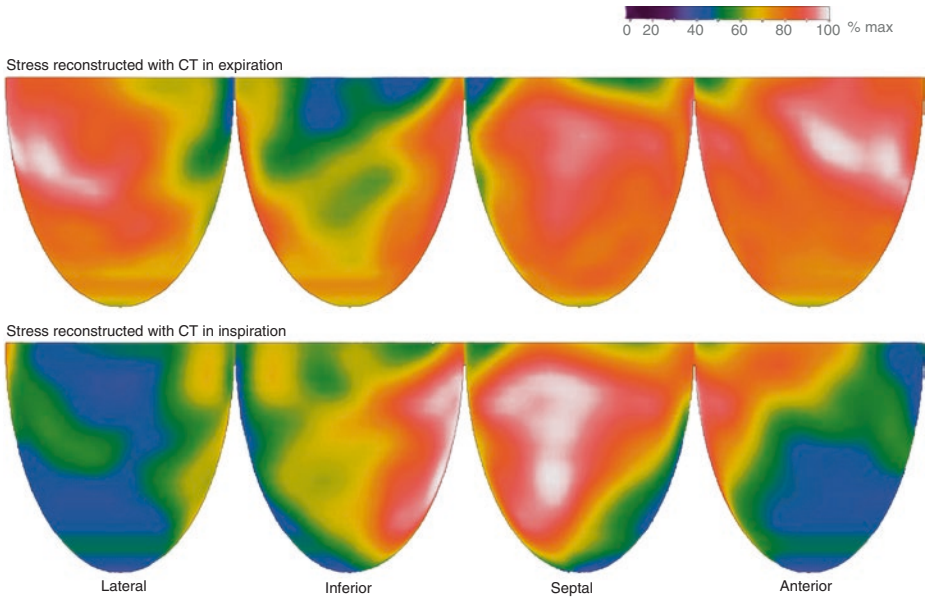

Fig. 6.45 Topographic LV maps with severe abnormalities due to erroneous attenuation correction

Figure 6.44 shows the same double diaphragm on the fast helical CT scan as in Fig. 6.43 (as well as liver activity) due to diaphragmatic motion during an intended normal expiratory breath hold. Despite correct co-registration of cardiac emission and transmission data, the double diaphragm of the fast helical CT causes a defect not correctable by shifting emission-transmission data. The defects due to emission-transmission mis-registration are least with low-dose cine CT imaging for attenuation correction acquired over 2.5 minutes and approximately two breath cycles paralleling emission acquisition during breathing.

In Fig. 6.45, the lower row shows the LV activity map before shifting rapid helical CT emission-transmission data to achieve co-registration. The upper row shows the map after manual co-registration. The residual basal inferior defect may be residual attenuation artifact due the double diaphragm or due to a small region of reduced stress perfusion. To minimize attenuation correction errors using fast helical CT scans beyond manual co-registration, we developed a protocol using a 2.5-minute cine CT scan over two normal respiratory cycles at reduced radiation dose, in order to acquire time-averaged attenuation corrections most comparable to the time-averaged acquisition of emission data without the common mis-registration on fast helical CT scans.

Figure 6.35 described placing the ROI in the left atrium or ascending aorta. Figures 6.46 and 6.47 show the consequences of erroneous arterial input on LV maps of CFC [58, 59]. In the upper row of Fig. 6.46, the ROI is outside the left atrium and a severe stenosis is not identified. With the correct ROI, the CFC maps show a severe infero-lateral defect due to severe stenosis of a dominant RCA.

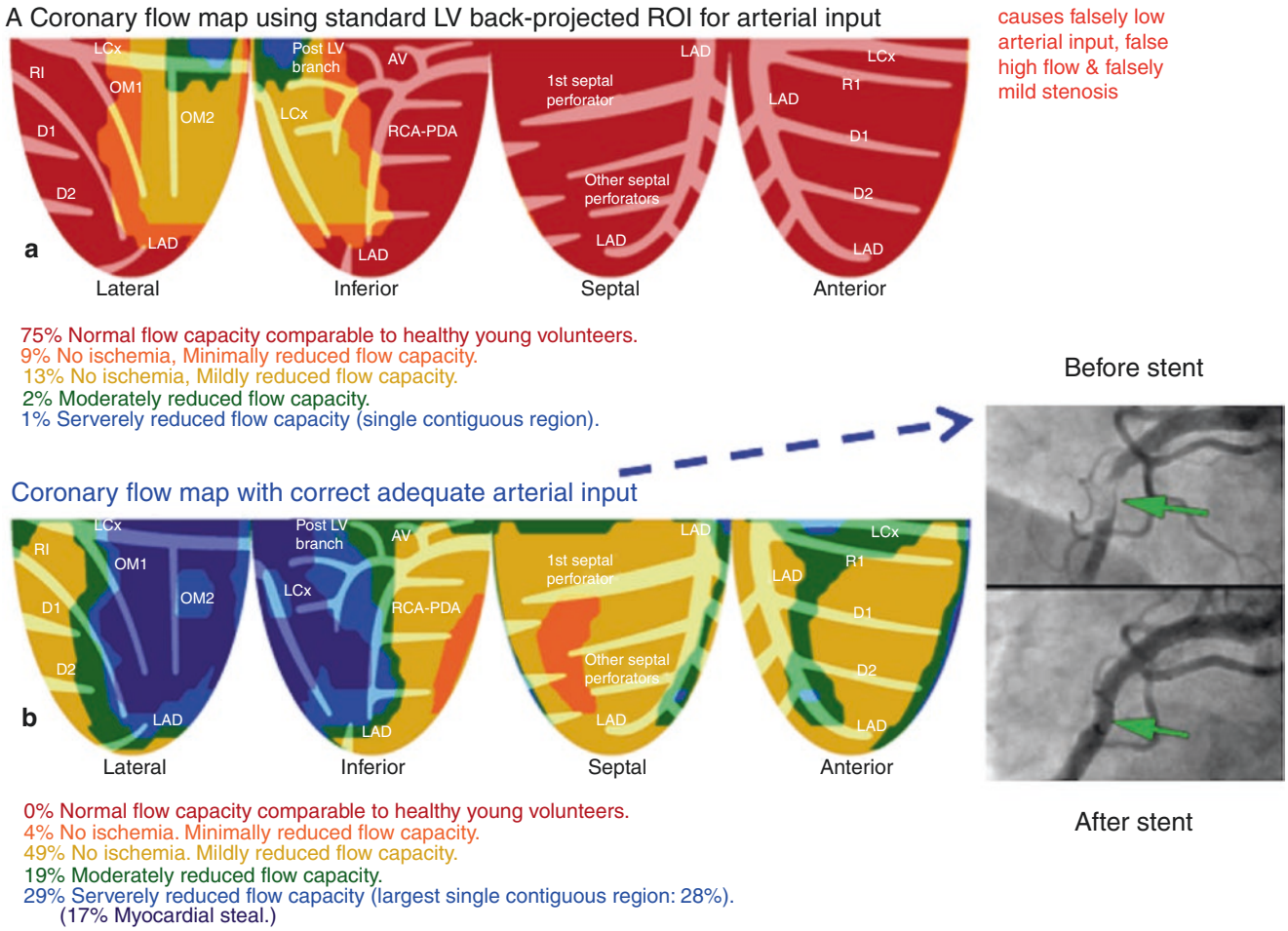

Fig. 6.46 Placement of ROI for time-activity arterial input function. For the CFC maps in the upper row, the ROI for arterial input was estimated for the left atrium just above the AV ring back, as back-projected from late LV myocardial images. This back projection from late myocardial phase images to locate the LA ROI is necessary for compartmental modeling using serial 10- to 15-second arterial phase images of such poor statistical quality that the left atrium cannot be visually located. The estimated back-projected location may not be centrally located in the left atrium, so that with heart motion, the ROI is outside the left atrium with consequent low arterial activity. In this case, the arterial activity was lower than actual arterial activity; perfusion values were increased to near-normal levels, thereby failing to identify a severe stenosis. An arterial ROI located directly on the high-quality 2-minute arterial phase images provides the correct higher arterial input, correct low perfusion, and correct CFC maps showing a severe stress abnormality, confirmed on angiography. (*From* Vasquez et al. [58]; with permission from Elsevier)

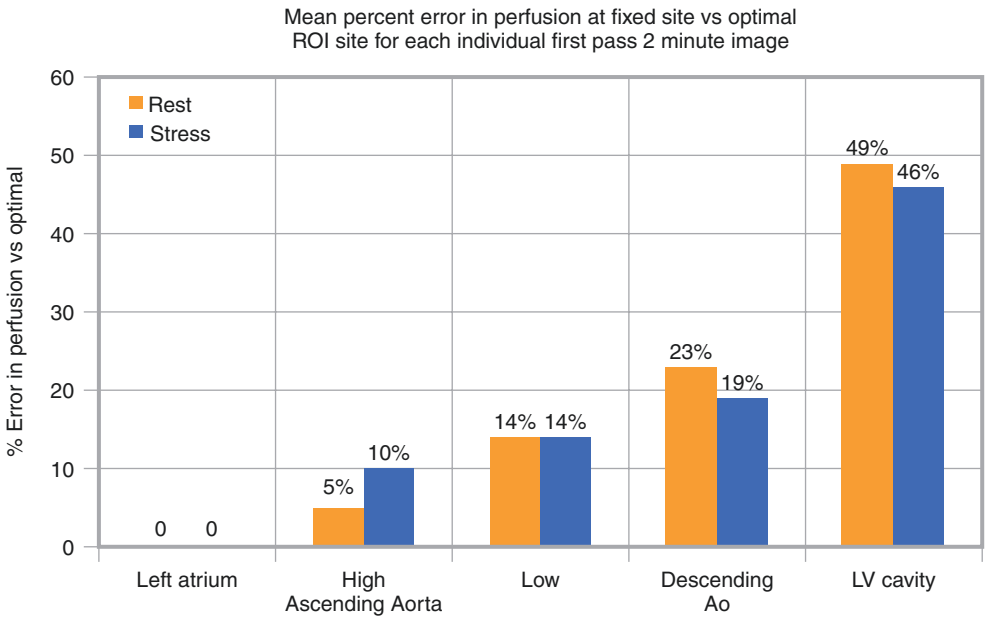

Fig. 6.47 Optimal arterial ROI site

We systematically tested for the optimal arterial ROI on multiple sites in the ascending and descending aorta, the LV cavity, and the high, mid, or low left atrium in each patient in a large series [49, 58, 59]. The optimal site was defined as the site with the highest activity without spillover from adjacent right atrium or pulmonary arteries, and the corresponding error in perfusion measurement was determined for all sites, compared with the optimal site. As shown in Fig. 6.47, the optimal site varied for individuals, but the central left atrium had the least error, with errors progressively increasing for ROIs placed in the ascending aorta, descending aorta, and LV. An ROI project to the estimated AV ring of LV is commonly used for the arterial input but causes the greatest errors in perfusion measurement because of its motion and activity spillover from the myocardium into the LV cavity. Equations purporting to correct for this spillover fail to recognize or account for cardiac motion and translation during the cardiac cycle, which may move the LV activity out of an estimated fixed LV cavity ROI.

Clinical Coronary Physiology by PET to Guide Cardiac Care

Although standard protocols call for abstinence from caffeine for at least 12 hours before vasodilator stress PET, the literature reports that 20% of subjects have caffeine in their blood (Fig. 6.48). Accordingly, we strongly emphasize 24-hour abstinence verbally, in written instructions, and with a phone call reminder 2 days before the scheduled PET. We also check serum caffeine in every patient, and have found that 6% have measurable caffeine levels despite the serial reminders about caffeine abstention. Even low caffeine levels may inhibit vasodilator stress; repeat PET without caffeine can show significant abnormalities that were missed when caffeine levels were higher.

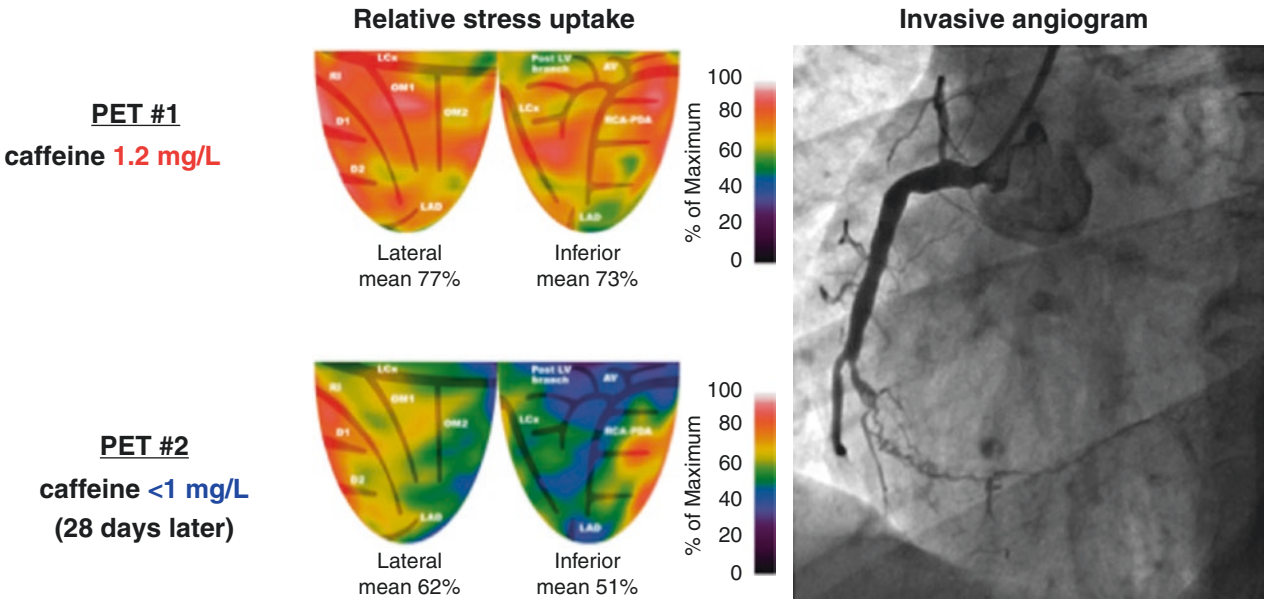

Fig. 6.48 Maximal vasodilator stress is essential. Even low caffeine levels, as in this case, may inhibit vasodilator stress. Repeat PET without caffeine can show significant abnormalities that may explain symptoms or clinical issues

Some patients have very high resting perfusion (Fig. 6.49a) with normal to high stress perfusion (Fig. 6.49b), thereby causing low, apparently abnormal CFR (Fig. 6.49c). Others may have low resting perfusion (Fig. 6.49e) with reduced stress perfusion (Fig. 6.49f) but excellent CFR (Fig. 6.49g) owing to the low resting levels. Figure 6.49 shows two topographic views of three common patterns of quantitative myocardial perfusion for which either CFR or stress perfusion alone fails to provide definitive information for clinical management that is provided by both together. These global differences in resting perfusion and CFR between individuals are called *global heterogeneity* among different subjects. *Regional heterogeneity* of resting and CFR images also is common and is largely due to endothelial dysfunction associated with risk factors. High regional rest flow (I) with uniform stress flow (J) may cause apparent regional stress defect (K). However, as illustrated in Fig. 6.49, perfusion heterogeneity is accounted for as normal (D and H) or mild diffusely reduced CFC due to non-obstructive CAD (L) that is differentiated from true segmental perfusion abnormalities on the CFC maps [2, 25, 27, 39–49], shown in Figs. 6.2, 6.5, 6.26, and 6.46, and quantitatively documented in Figs. 6.50, 6.51, and 6.52.

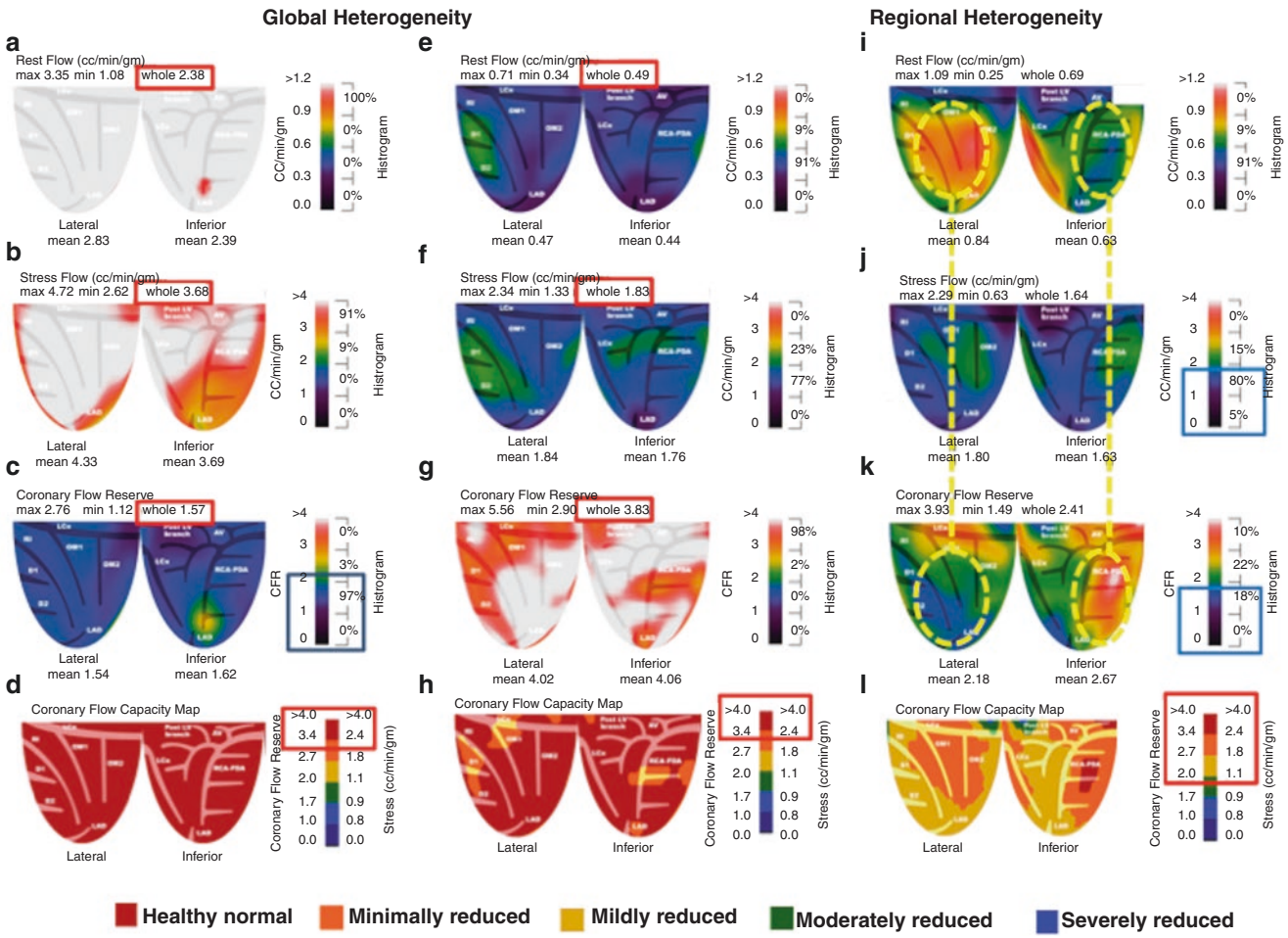

Fig. 6.49 Perfusion heterogeneity may cause misinterpretation of PET perfusion, which can be resolved by CFC maps of comprehensive clinical physiologic severity. This figure shows two topographic views of three common patterns of quantitative myocardial perfusion for which either CFR or stress perfusion alone fails to provide definitive information for clinical management that is provided by both together. For efficiency of comparisons, only two of the four topographic views are displayed, with CFR and stress perfusion scaled according to the color bars. In the first patient (**a–d**), rest perfusion is very high (**a**), stress perfusion also high (**b**), and CFR is very low (**c**) because of the high rest flow, as commonly seen with anxiety, high blood pressure, and in women. Alternatively, in another patient (**e–h**), rest perfusion may be very low owing to beta blockers (**e**), and stress flow is also low (**f**), but CFR is excellent (**g**) and well above the ischemic threshold. These global differences in resting perfusion and CFR between individuals are called *global heterogeneity* among different subjects. The integrated CFC maps (**d** and **h**) of these two subjects accounts for both CFR and stress perfusion together. For these two examples, the red regions of **d** and **h** indicate CFC comparable to that of young, healthy volunteers without risk factors. These examples show that because of the common global perfusion heterogeneity among different patients, CFR alone or stress perfusion alone may fail to characterize coronary perfusion adequately

In the third patient (**i–l**), the rest perfusion image is regionally heterogeneous (**i**) and stress perfusion images are uniformly adequate, without ischemia (**j**). As a result of the resting perfusion heterogeneity, CFR is also heterogeneous, with what appears to be a severe inferolateral stress defect due to the high inferior resting perfusion (**k**), but the CFC map (**l**), which accounts for CFR and stress perfusion, incorporates this heterogeneity and indicates only mildly reduced CFC diffusely, which is due to mild, diffuse, nonobstructive CAD with no regional stress defect or flow-limiting stenosis

Coronary Flow Capacity Color Thresholds For Clinical Groups of PETs			7-7-17			
ROC threshold between clinical groups	Normals	Norm vs no CAD	No CAD vs CAD	No isch vs prob isch	No isch vs ischemia	Steal
Stress with pet defect, angina, ECGΔ*	0 of iii	0 of iii	0 of iii	i of iii	ii of iii	CFR < 1
Clinical class (without PET data)	Normals	Risk Factors	All CAD	Probable ischemia	Stress angina/STΔ	subset steal
Number PET cases	212	2171	979	548	278	subset 218
ROC threshold between color groups	Normals	red vs orange	orange vs yellow	R,O,Y vs green	R,O,Y vs blue	steal CFR<1.0
Ordinal id number	4	3	2	1	0	Subset included
stress flow original ROC threshold cc/min/g		2.17 original	1.82 original	1.09 original	0.83 original	in the 4188
Coronary Flow Reserve original ROC threshold		2.90 original	2.38 original	1.60 original	1.27 original	CFR < 1.0
CFR AUC		0.81	0.61	0.8	0.97	
CFR Sensitivity = Specificity		74%	58%	72%	91%	
CFR 95% CI (upper - lower median)		0.84 - 0.79	0.63 - 0.59	0.83-0.78	0.98 - 0.96	
CFR - P value for AUC		< 0.001	< 0.001	< 0.001	< 0.001	
CFR standard error		0.015	0.01	0.01	0.005	
stress flow cc/min/g AUC		0.63	0.68	0.76	0.94	
stress flow Sensitivity = Specificity		60%	64%	69%	87%	
str flo 95% CI (upper - lower median)		0.66 - 0.59	0.7 - 0.66	0.78 - 0.73	0.96 - 0.93	
stress flow P value for AUC		< 0.001	< 0.001	< 0.001	< 0.001	
stress flow standard error		0.018	0.01	0.01	0.008	
Total 4188 where the subset of 218 with steal defned as CFR < 1.0 (dark blue) is already included in the 4188 PETs						

Fig. 6.50 CFC thresholds for clinical groups of PETs—an essential physiologic measurement for guiding patient care and reducing mortality. This table shows specific clinically defined groups with the number of rest-stress PET studies in each group, classified independently of and separately from any PET images or data. In order to integrate stress perfusion in mL/min/g and CFR, patients or volunteers had 4188 rest stress quantitative dipyridamole stress perfusion PET studies using Rb-82 with a DST-16 GE PET CT scanner. The wide range of stress perfusion and CFR values for each of 1344 radial pixels in 4188 studies comprises a vast number of combinations that are difficult to display and interpret. Accordingly, this huge number of possible stress perfusion and CFR pixel combinations were reduced by ROC analysis for the optimal thresholds of CFR and stress perfusion in mL/min/g that differentiated the five clinically defined groups with highest area under the curve (AUC). Stress perfusion and CFR combinations were thereby reduced to five color ranges for the clinically defined groups*, as detailed in this table and plotted in Fig. 6.51:

Red: Healthy Young Volunteers (n = 212): Healthy young volunteers under 40 years old with no vascular risk factors, normal measured lipid profile, no obesity, no measurable caffeine on blood samples for every PET, and no blood or urine cotinine levels measured for every PET

Orange: Risk Factors Only (n = 2171): Subjects with one or more vascular risk factors but no known CAD pre-PET, as defined by no history of MI, PCI, coronary artery bypass (CAB), abnormal coronary angiogram, or angina; no dipyridamole stress–induced ischemia at PET; and no myocardial scar as defined below

Yellow: Established Coronary Artery Disease (CAD) (n = 979): Subjects with CAD defined by pre-PET history of MI, PCI, CAB, or abnormal coronary angiogram. Subjects with definite or possible ischemia during dipyridamole stress, as defined below, are excluded from this group; they are classified in the next two groups. Subjects with significant myocardial scars defined as a severe fixed relative defect with rest flow ≤0.2 cc/min/g were also excluded in order to avoid the downward bias in thresholds of perfusion and CFR due to low flow of scars unrelated to stress

Green: Possible Ischemia During Dipyridamole Stress PET (n = 548): Subjects meeting any *one* of the following three criteria during dipyridamole stress PET:

A significant perfusion defect on stress images with >5% rest-to-stress change in the percentage of LV with ≤60% maximum on relative uptake stress images that is >3 SD below the mean of rest and stress relative PET images of normal young volunteers, *or*

ST depression >1 mm on ECG not present on resting ECG, *or*

Definite angina requiring reversal by aminophylline, nitroglycerin, or IV metoprolol

Blue: Definite Ischemia During Dipyridamole Stress PET (n = 278): Subjects with definite ischemia are defined as having:

A significant perfusion defect on stress images with >5% rest-to-stress change in percentage of LV with ≤60% maximum on relative uptake stress images that is >3 SD below the mean of rest and stress relative PET images of normal young volunteers, *plus* one or both of the following:

ST depression >1 mm on ECG not present on resting ECG

Definite angina requiring reversal by aminophylline, nitroglycerin, or IV metoprolol as we have previously published with AUC of 0.97 [42, 43]

Subjects with myocardial scar are excluded from this group and classified separately below so that the thresholds for stress flow and CFR would reflect the true stress perfusion and CFR changes without the downward bias due to low flow of scars unrelated to stress

* The numbers iii, ii, I, or 0 indicate the number of the following criteria of ischemia met during dipyridamole stress perfusion imaging: ECG ST depression >1 mm, definite angina requiring aminophylline reversal, relative stress defect ≤60% of maximum for >5% of LV

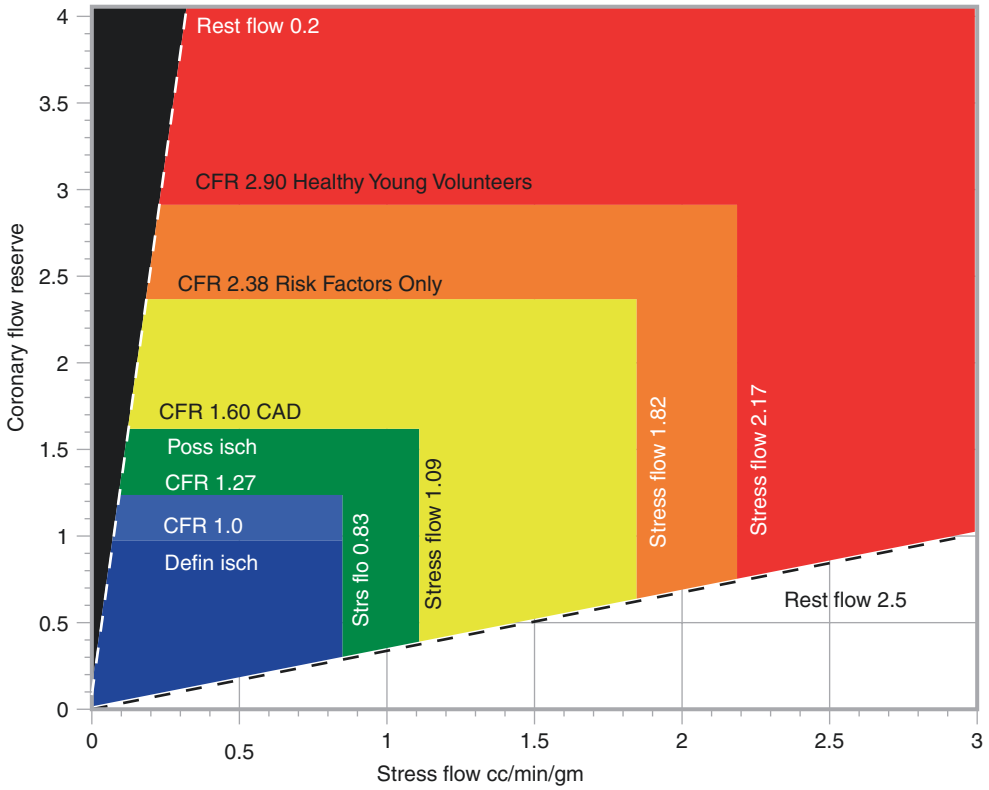

Fig. 6.51 Schema for color-coding each pixel of the CFC map. The color-coded ranges of CFR and stress perfusion for each pixel of the CFC map are based on the objective, predefined clinical groups listed in Fig. 6.50. The perfusion boundaries between the clinical groups were determined by objective ROC analysis for optimum CFR and stress-perfusion separation of the groups

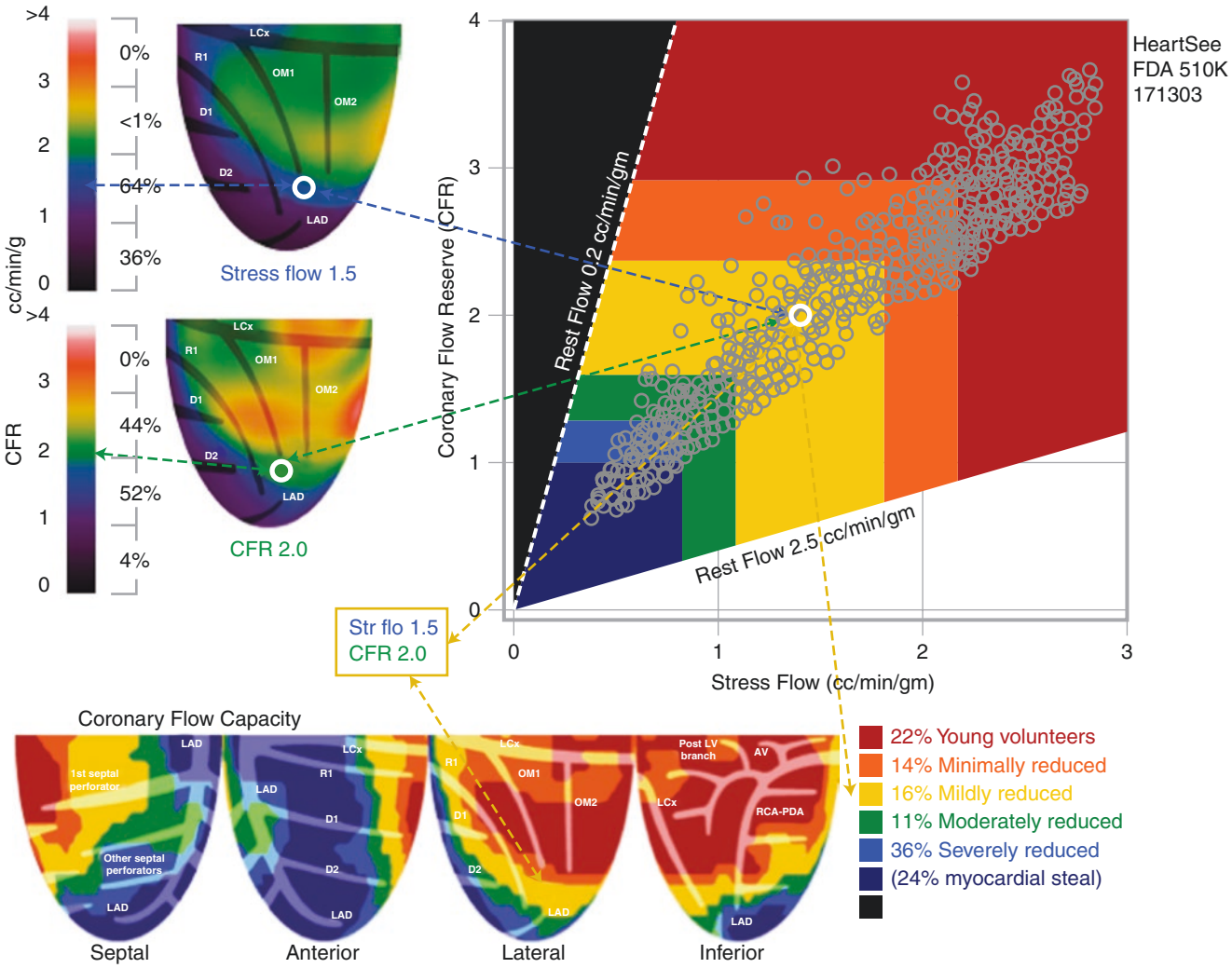

Fig. 6.52 The CFC map in this figure color-codes each pixel within five color ranges for combined CFR and stress perfusion values of each pixel, spatially maps each pixel back into its LV location with corresponding stress perfusion and CFR values, and calculates the percentage of LV for each range of combined *both* CFR *and* stress perfusion values listed in the CFC color histogram bar. The LV CFC map incorporates all perfusion metrics into a comprehensive, easily understood clinical guide derived from in-depth coronary physiology and imaging physics. (*From* Gould and Johnson [25]; with permission from Elsevier)

The table in Fig. 6.50 gives details of the CFC thresholds for clinical groups of PETs—an essential physiologic measurement for guiding patient care and reducing mortality [2, 25, 27, 39–49]. This table shows specific clinically defined groups with the number of rest-stress PET studies in each group (total 4188) classified independently of and separately from any PET images or data. The wide range of stress perfusion and CFR values for each of 1344 radial pixels in 4188 studies comprises a vast number of combinations that are difficult to display and interpret. Accordingly, this huge number of possible stress perfusion and CFR pixel combinations were reduced by ROC analysis for the optimal thresholds of CFR and stress perfusion in cc/min/g that differentiated the five clinically defined groups with highest area under the curve (AUC). Stress perfusion and CFR combinations were thereby reduced to five color ranges for the clinically defined groups, as detailed in this table and plotted in the Fig. 6.51. *CFR* is used as a synonym for *myocardial perfusion reserve* to emphasize the original physiological concepts.

Pixel values of rest-stress relative images, quantitative perfusion, and CFR comprise infinite numbers of values and combinations reflecting true perfusion heterogeneity that must be compressed into clinically relevant ranges and regional distribution for clinical utility. Figure 6.52 shows the threshold values of stress perfusion and CFR for the color-coded ranges from the above table for the CFC map incorporating all perfusion metrics into a comprehensive, easily understood clinical guide derived from in-depth coronary physiology and imaging physics to guide clinical management [2, 25, 27, 39–49].

The pixel measures of absolute and relative activity, perfusion in cc/min/g, CFR, and CFC map the distribution of perfusion metrics as they actually are in each individual with a color-scale bar (Fig. 6.53). Each map provides the following metrics for size and severity of abnormalities:

- The visual size and severity of quantitative perfusion abnormalities for each artery and its branches as they actually are, undistorted by arbitrarily selected regions or bulls-eye displays as shown in Fig. 6.27.
- The histogram for percent of LV in each severity range, located on the right edge of the color-scale bar or at the bottom of the CFC maps.
- Average values for each quadrant in the distribution of each coronary artery.
- The automated severity contour selection option, to determine the size and severity of any specifically selected defect (*see* Fig. 6.54).
- These same four metrics for abnormalities of relative myocardial activity distribution.

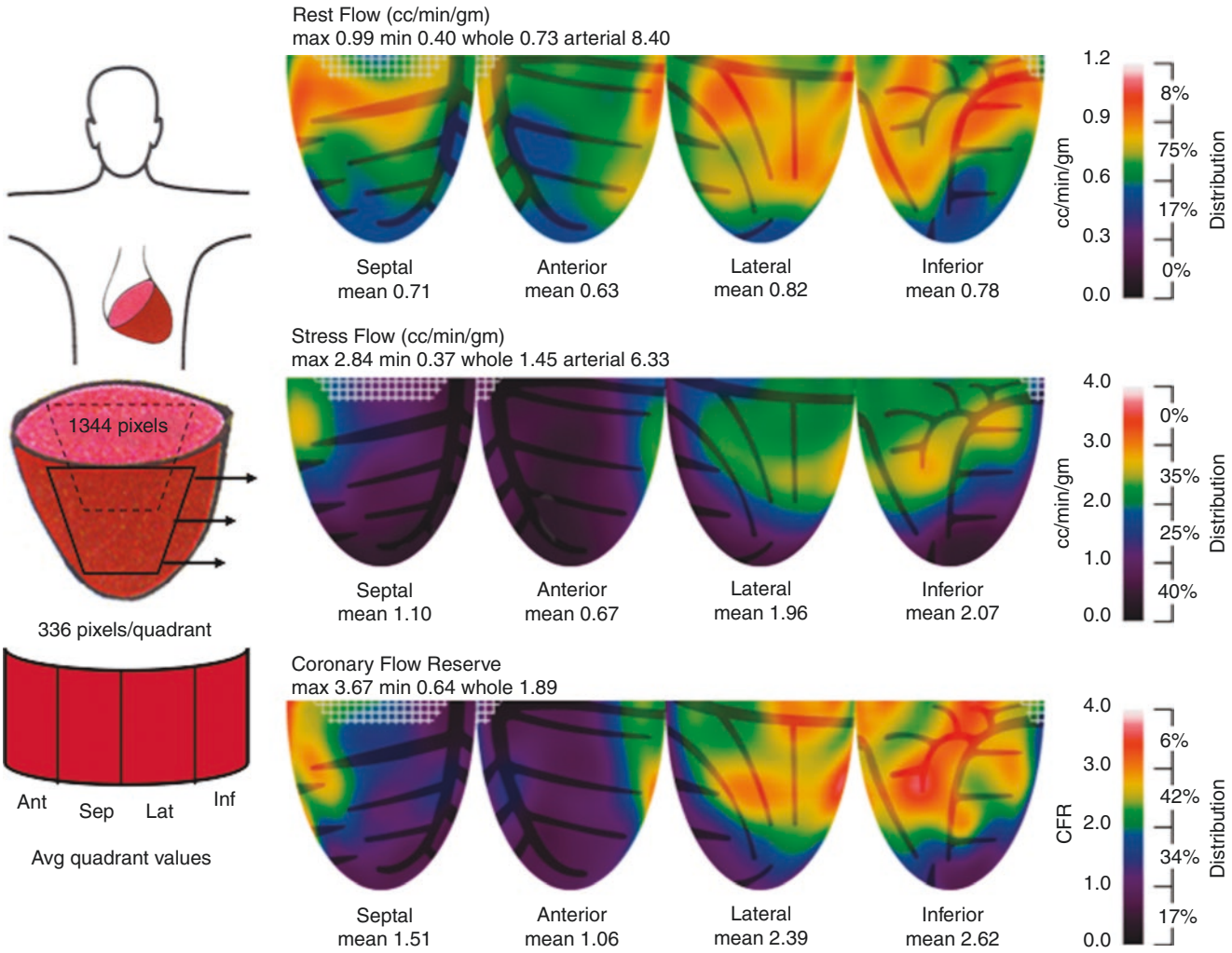

Fig. 6.53 Size and severity of perfusion abnormalities, as shown by several different metrics

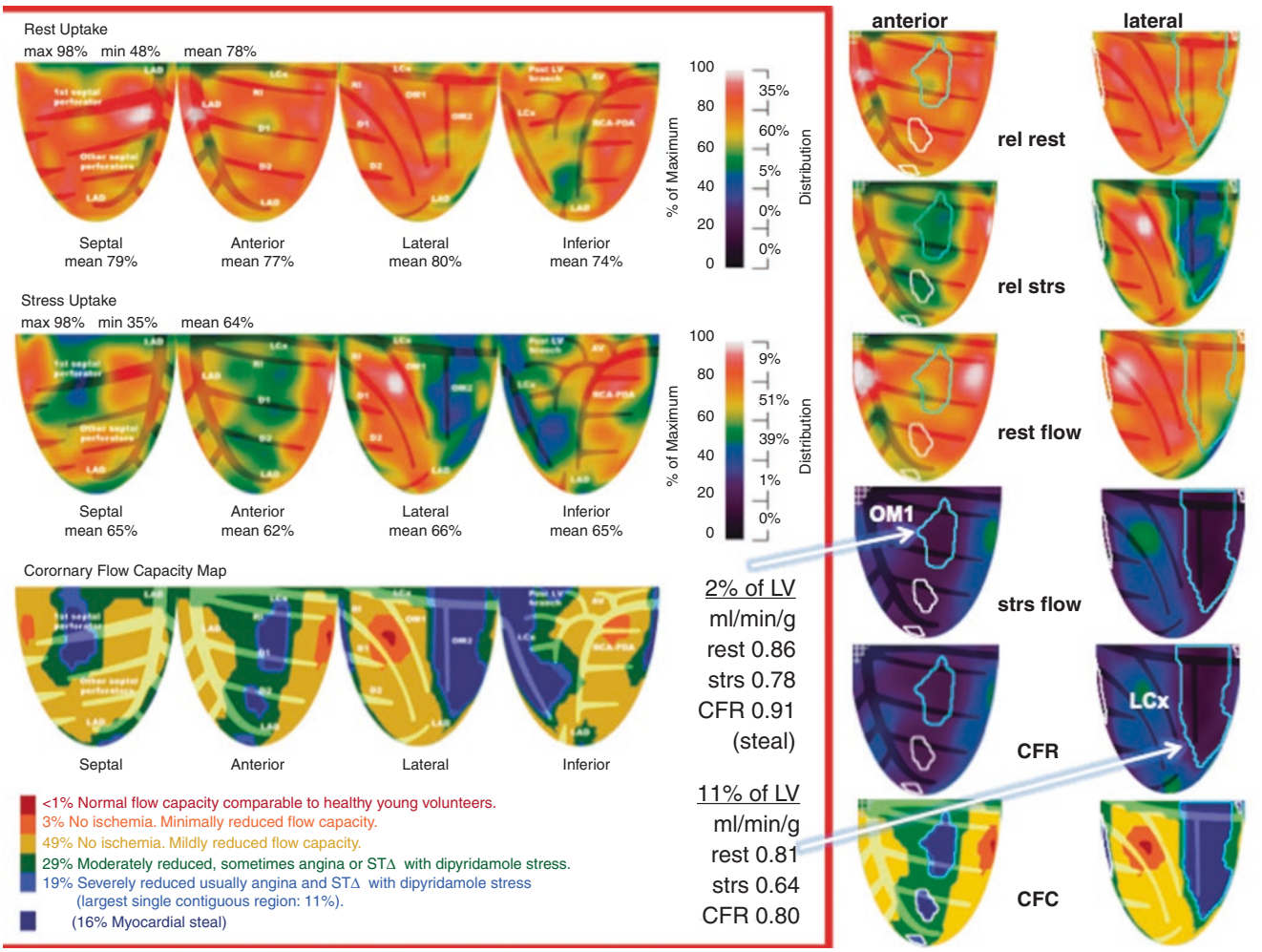

Fig. 6.54 Optional additional size-severity quantification. The three-row display at left is our routine report. The two views of all perfusion metrics for this patient (*right*) demonstrate additional size-severity quantification by iso-contour, selected by the reading physician in order to refine the visual impression

A complete set of perfusion images includes relative rest-stress tomograms, relative rest-stress LV topographic maps, rest-stress perfusion maps, and CFR and CFC maps. Because perfusion heterogeneity makes the rest-stress-CFR maps (Fig. 6.53) difficult to understand and interpret, our final report (Fig. 6.55) consists of the relative rest-stress maps as the primary data, with the CFC map as the summary of quantitative perfusion metrics; the rest-stress-CFR display (Fig. 6.53) can be added to the report as needed for each case [2, 25, 27, 39–49].

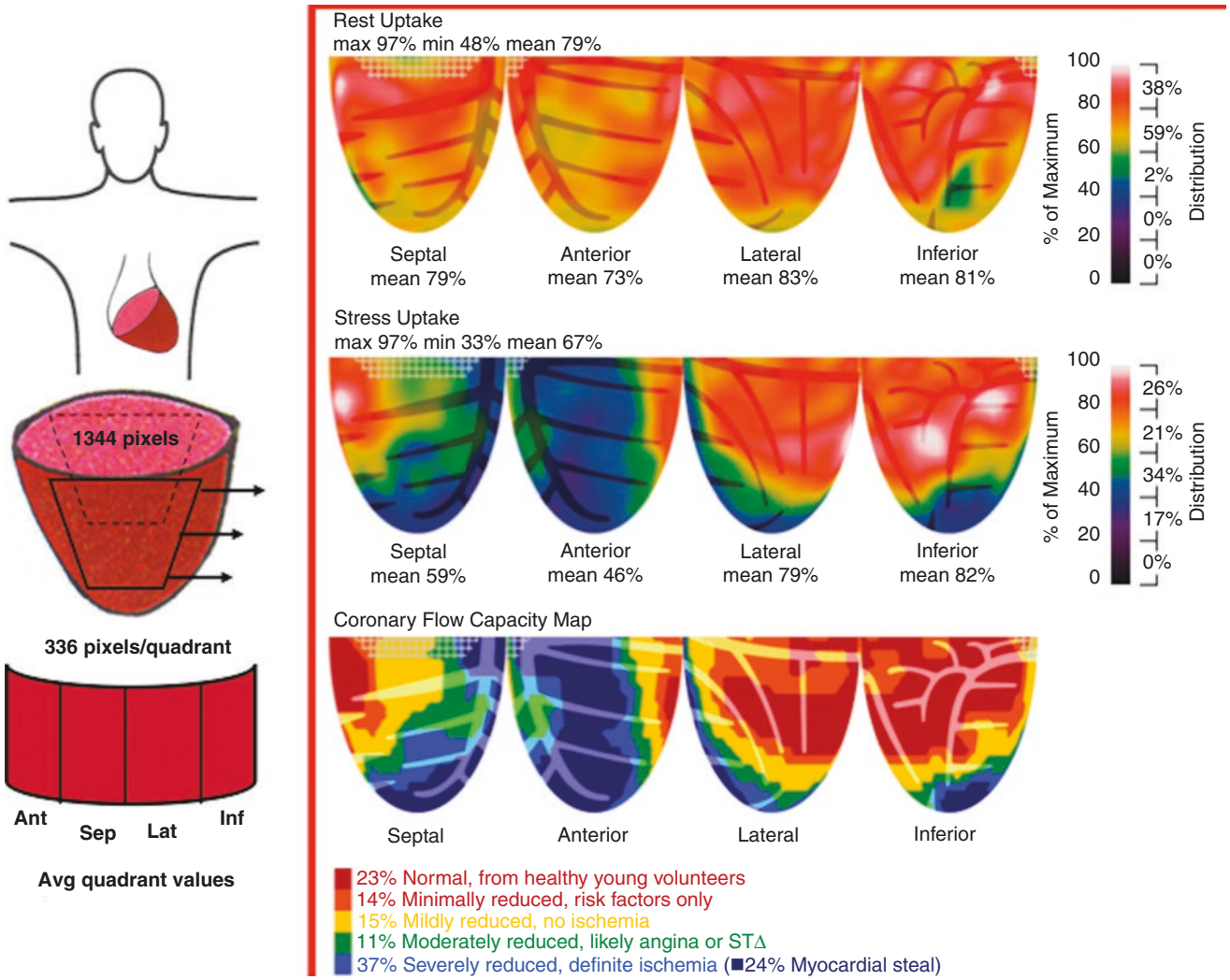

Fig. 6.55 The Primary Clinical Report summarizing coronary physiology, comprising primarily the relative rest-stress maps and CFC map

Figure 6.54 (right panel) illustrates optional, additional size-severity quantification for two of the four quadrant views for a patient to help the reading physician refine the visual impression.

In the same patient imaged serially minutes apart, the stress perfusion, CFR, and CFC maps are highly reproducible, with test-retest precision in the same patient of ±10% within minutes [47]. Indeed, even on a different day, the values remain highly reproducible, as illustrated in Fig. 6.56. Figures 6.57 and 6.58 demonstrate reproducibility by the Kolmogorov–Smirnov test comparing serial CFC histograms in the same subject [47, 48].

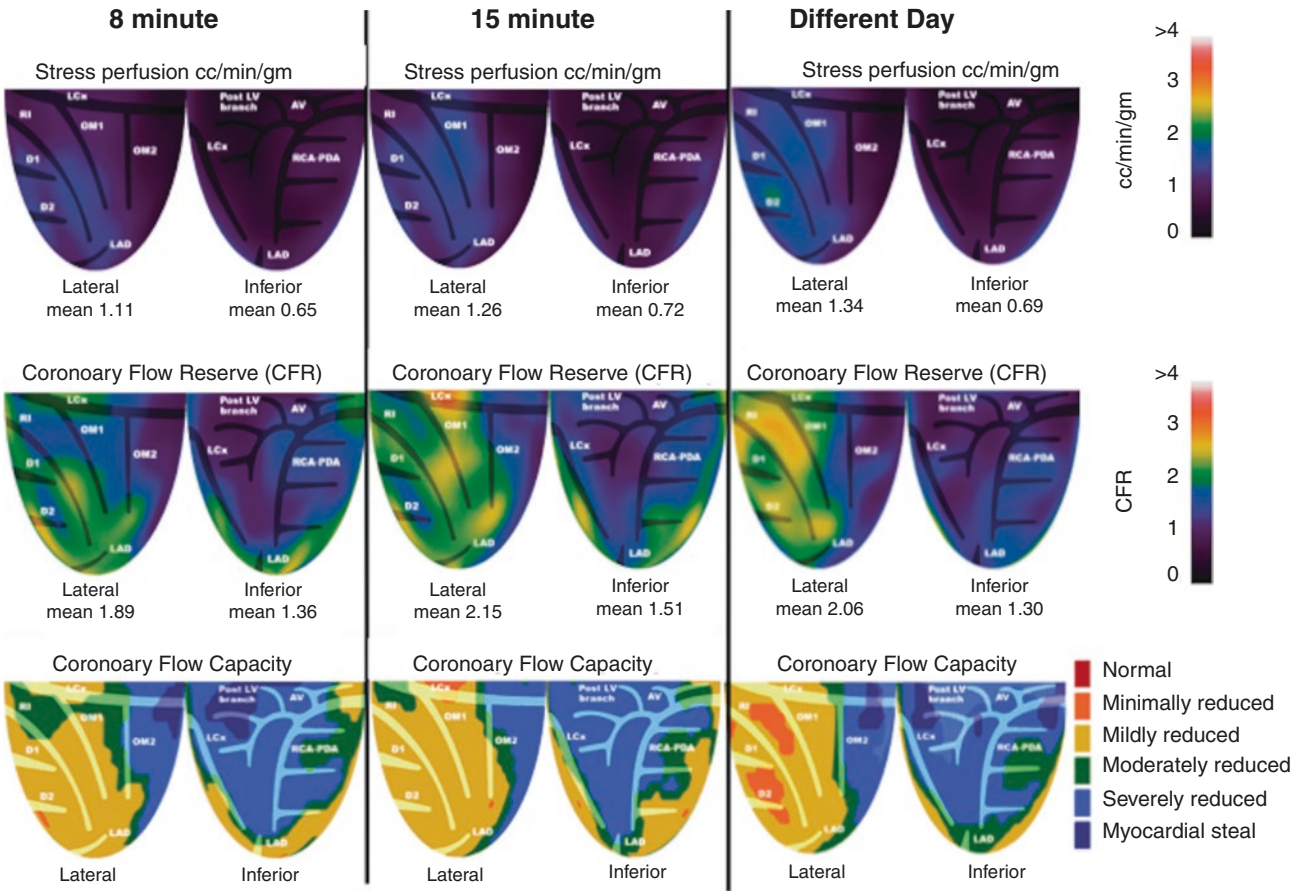

Fig. 6.56 Reproducibility of CFC maps. (*From* Kitkungvan et al. [47]; with permission from Elsevier)

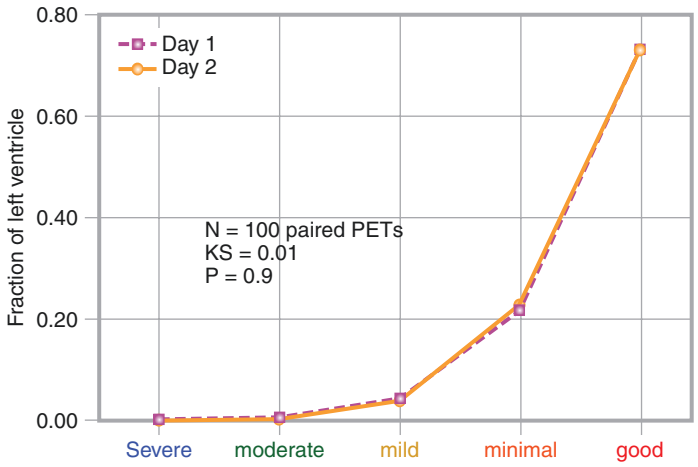

Fig. 6.57 Reproducibility by the Kolmogorov–Smirnov test for comparing two serial CFC histograms in the same subject, from 100 healthy volunteers without risk factors. (*From* Kitkungvan et al. [48]; with permission from Elsevier)

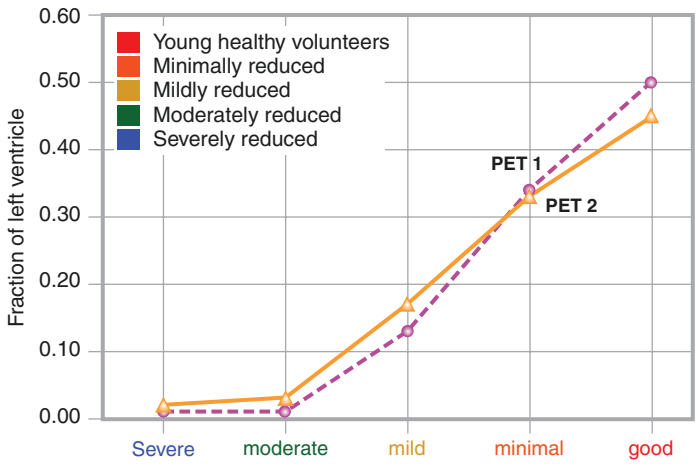

Fig. 6.58 Reproducibility by the Kolmogorov–Smirnov test for comparing two serial CFC histograms in the same subject, from 120 volunteer patients with CAD or risk factors. (*From* Kitkungvan et al. [47]; with permission from Elsevier)

The table shown in Fig. 6.59 demonstrates the reproducibility of our method of stress perfusion compared with other cardiology metrics, using the coefficient of variation (standard deviation divided by mean) [27, 44, 47].

Variability of cardiovascular measurements

Test re-test measurement	Coefficient of variation
PET flow cc/min/gm	10%
Angiogram % diameter stenosis	17%
LDL cholesterol	9.5%
ECHO ejection fraction	15%
SPECT ejection fraction	17%
SPECT sum stress scores (SSS)	29%
C reactive protein	46%

Fig. 6.59 Variability of cardiovascular measurements using the coefficient of variation (standard deviation divided by mean)

Severity of true pressure-derived FFR reduction is directly related to the risk of MI or death (Fig. 6.60). For severely reduced FFR, revascularization may be associated with reduced risk of death or MI. At high FFR, revascularization provides no improvement over medical treatment. The curve for the natural history of severity-risk may be improved by revascularization only for severely reduced FFR, below 0.65. Although the FFR threshold for PCI is commonly 0.8, this threshold is rarely associated with angina or STΔ during adenosine infusion since it reflects only relative flow reserve, not ischemia sufficient to benefit from revascularization.

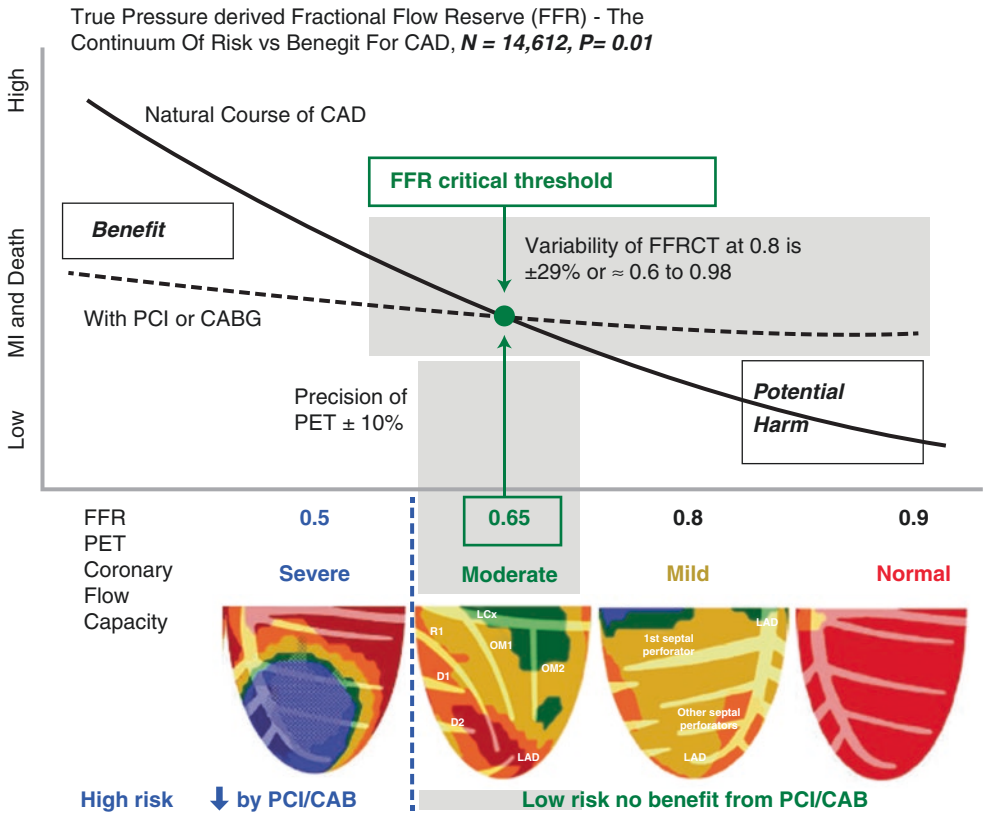

Fig. 6.60 Severity–risk continuum for FFR, PET, and FFR_{CT}

The crossover of the average statistical FFR severity-risk curves with and without PCI is FFR = 0.65. For PET, this threshold range of severity-risk for benefit of revascularization is severely reduced CFC for >0 to 3% of LV, with a precision for stress perfusion of ±10%. By comparison, at the current pressure-derived FFR threshold of 0.8, the variability for simulated FFR_{CT} ranges from 0.62 to 0.98, reflecting its Bland-Altman limits of agreement with pressure-derived FFR of 0.23 FFR units in Fig. 6.21. Simulated FFR_{CT} variability is due to the limited resolution of 0.5 mm for CT for arterial diameter of typically 3–4 mm, where blood flow is a function of radius raised to the fourth power, as well as heterogeneity among subjects regarding vasodilator capacity. This variability likely explains why PET is superior to CTA and simulated FFR_{CT} by directly assessing coronary physiologic severity, as shown in Figs. 6.19, 6.20, and 6.21.

Physiologic Severity, Revascularization, and Outcomes

Figure 6.61 demonstrates that global CFR <2.0 predicts increased major adverse cardiac events or mortality, compared with CFR >2.0 [67–69]. For global CFR <1.5, bypass surgery may be associated with improved survival in a nonrandomized cohort, but global CFR fails to account for regional or segmental quantitative perfusion or stenosis from diffuse CAD (*see* Fig. 6.62) needed to guide interventions.

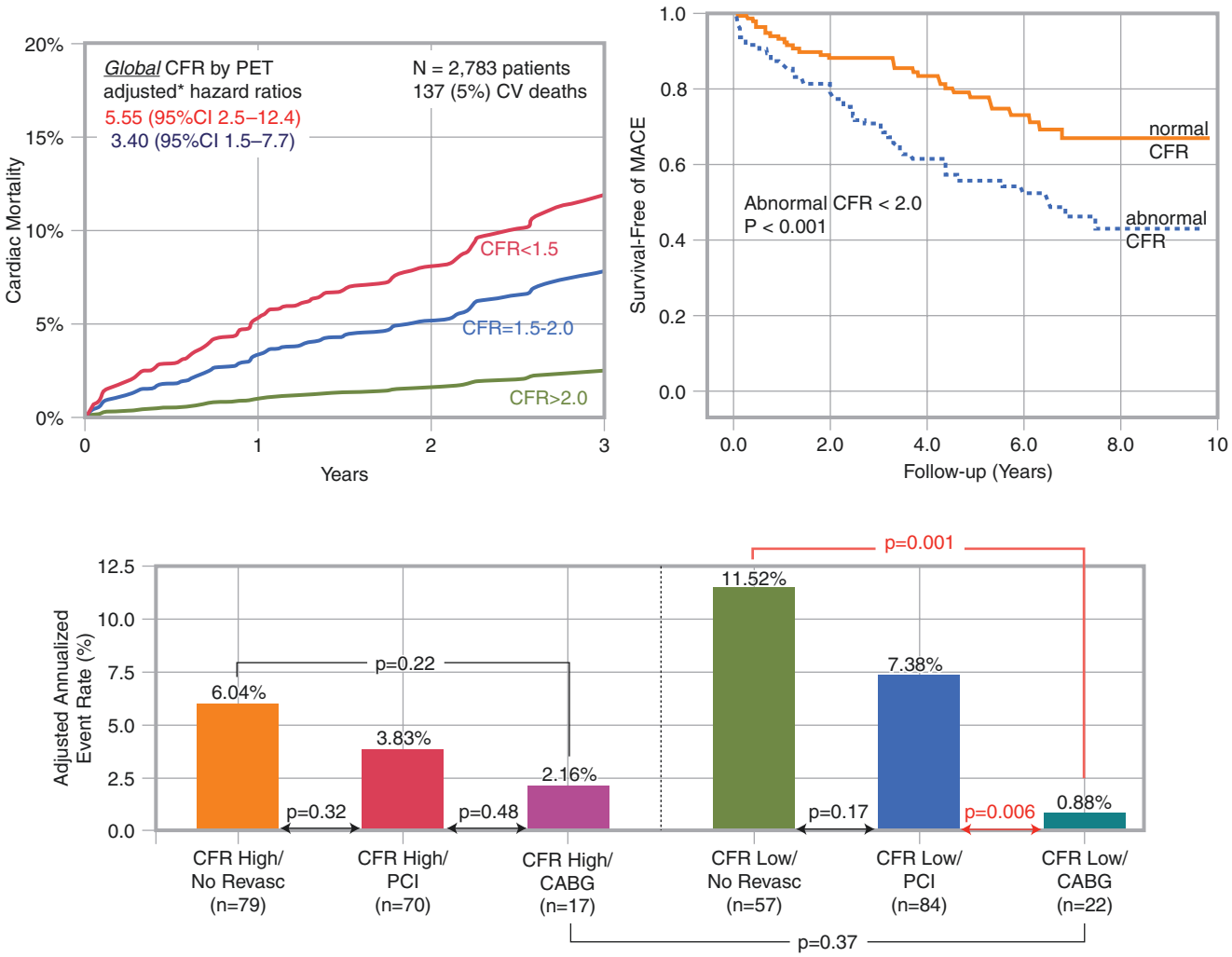

Fig. 6.61 Literature on CFR predicting major adverse cardiac events (MACE) or mortality. (*Left upper graph from* Murthy et al. [67] and *lower graph from* Taqueti et al. [69], with permission of the American Heart Association; *Right upper graph from* Herzog et al. [68], with permission of Elsevier)

Figure 6.62 shows that the failure to quantify regional physiologic severity due to stenosis as well as diffuse disease makes global CFR of little clinical value for guiding management of CAD [25]. High global CFR of 3.0 (Fig. 6.62a) fails to quantify a severe inferior stress defect. Low global CFR of 1.9 also fails to identify a severe stress defect in LAD distribution large enough to reduce global CFR (Fig. 6.62b) associated with myocardial steal indicating collaterals to viable myocardium. Thus, global CFR fails to quantify significant physiologic severity of focal stenosis needed for optimally guiding personalized clinical management in an individual patient and predicting risk or outcomes.

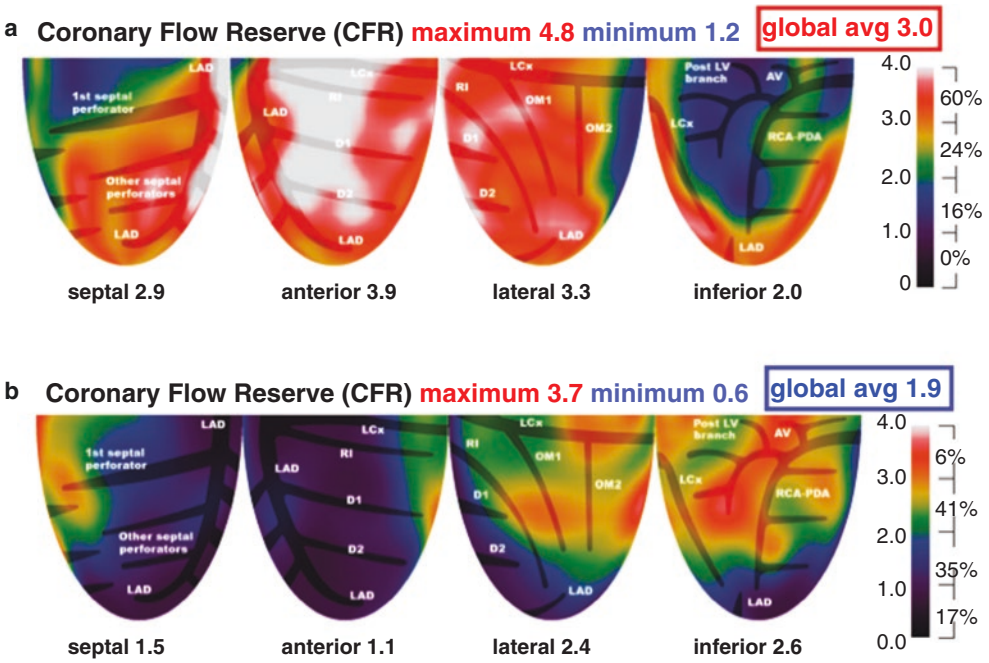

Fig. 6.62 Global CFR versus regional CFR to guide clinical management. (**a**) Global CFR is excellent at 3.0 but fails to account for a severe, high-risk inferior stress defect. (**b**) A low global CFR fails to differentiate diffuse CAD from a high-risk, severe stenosis of the LAD proximal to the first septal perforator and wrapping around the apex. Thus, both high and low global CFR fail to quantify significant focal physiologic severity needed to guide clinical management and predict risk or outcomes relevant to individual patients. (*From* Gould and Johnson [25]; with permission from Elsevier)

Figure 6.63 illustrates another case of a patient in whom global CFR is excellent at 2.97 which fails to account for the severe, high-risk, inferior abnormality because of the surrounding excellent CFR. In addition, the global CFR fails to identify inferior myocardial steal, indicating collateral perfusion beyond total or subtotal occlusion of a dominant RCA, as the CFR is excellent in the proximal LCx and OM1 distributions. The CFC map correctly quantifies this inferior abnormality in the face of excellent surrounding CFC that averages the global CFR to 2.97.

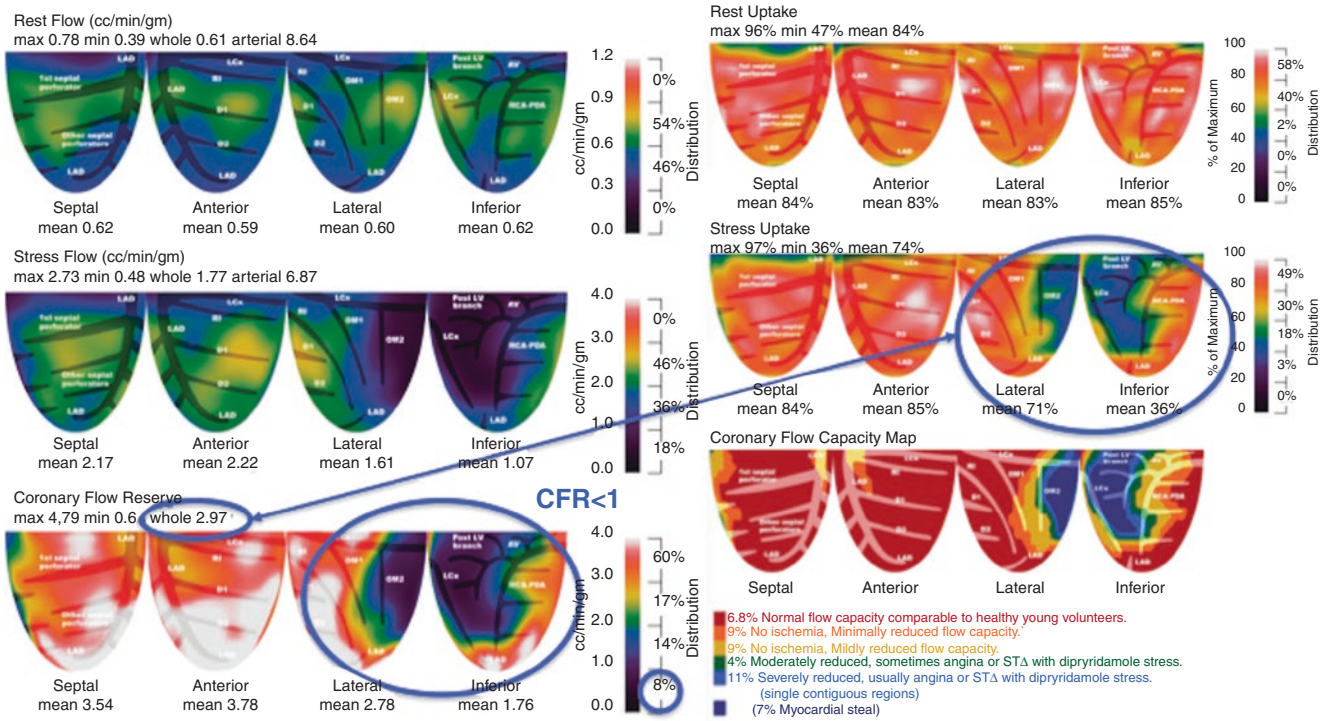

Fig. 6.63 Global CFR versus CFC to guide clinical management. The excellent global CFR in this patient fails to account for a severe, high-risk, inferior abnormality, and the global CFR also fails to identify inferior myocardial steal, indicating collateral perfusion beyond total or subtotal occlusion of a dominant RCA, as the CFR is excellent in the proximal LCx and OM1 distributions. The CFC map correctly quantifies this inferior abnormality

Figure 6.64 compares the probability of MACE-free survival over 9 years in patients with severely reduced CFC on PET versus those with no severe CFC reduction. For severe CFC abnormalities, the risk of death, MI, or stroke is 60% over the 9 years of follow-up, but the risk is low for the non-severe group. The PET scans to the right show representative severely reduced CFC (blue) or no severely reduced CFC (no blue).

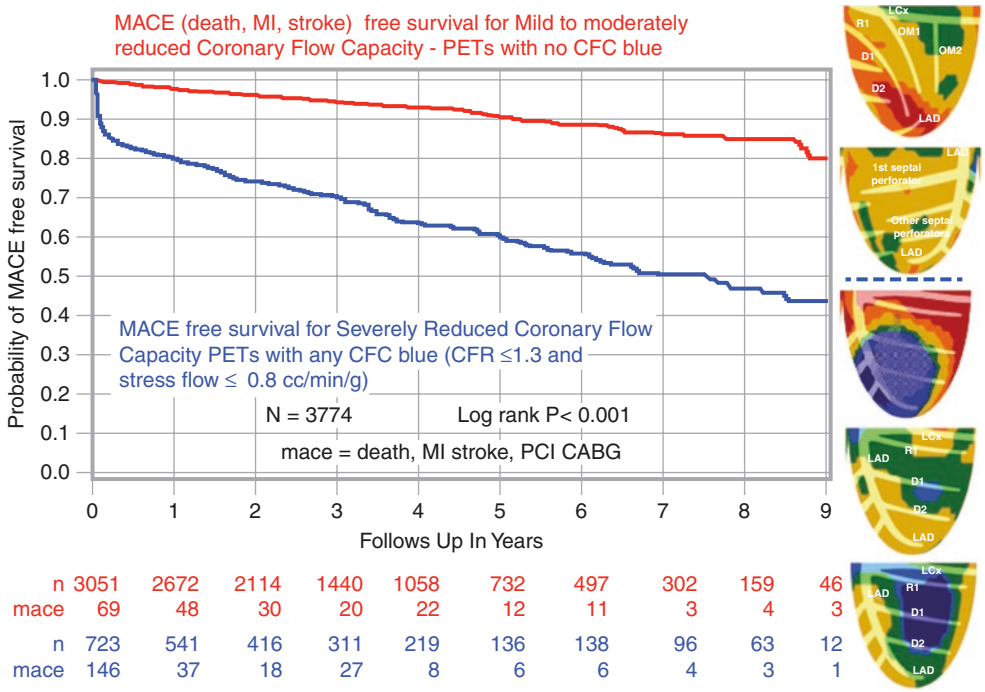

Fig. 6.64 Risk of death, MI and stroke (MACE) during 9 years of follow-up in patients with severely reduced CFC (*blue*) compared with no severe CFC abnormalities (*no blue*). The top two single CFC views (from different patients show) the range of non-severe CFC (*no blue*) associated with low risk. The lower three single views show the range of severely reduced CFC [39]

Figure 6.65 demonstrates that revascularization within 90 days after PET is associated with 54% reduced risk of death, MI, or stroke in patients with severe CFC abnormalities, compared with similar severely abnormal CFC without revascularization ($P = 0.0396$). Among patients with only mild or moderate CFC impairment, however, rates of MACE were insignificantly *higher* ($P = 0.45$) in the revascularization group. The lack of benefit with revascularization in these patients reflects their diffuse, nonobstructive CAD without severe focal stenosis by PET.

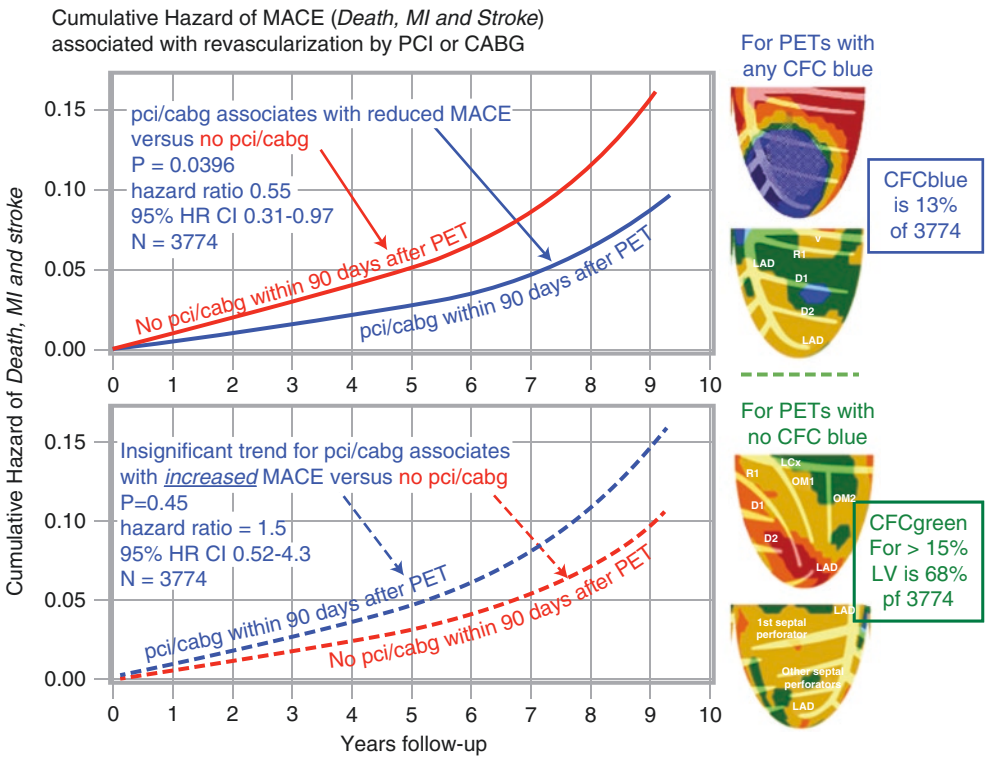

Fig. 6.65 Risk of death, MI, or stroke with and without revascularization for severely reduced CFC and for no severely reduced CFC. This figure plots cumulative hazard over 9 years showing reduced death, MI, or stroke after revascularization within 90 days after PET (*solid blue line*) versus no revascularization within 90 days after PET (*solid red line*) ($P = 0.0396$). For patients with mild or moderate CFC impairment, however, MACE was insignificantly more frequent in the revascularization group (*blue dashed line*) versus the no-revascularization group (*red dashed line*) ($P = 0.45$). The top two single CFC views (from different patients) show the range of severe CFC (*blue*) associated with high risk that is significantly reduced by revascularization. The lower two single views show CFC with no severe pixels (*no blue pixels*) associated with no benefit or increased risk with revascularization; the risk in this group reflects diffuse, nonobstructive CAD. (*From* Gould et al. [39]; with permission from the Society of Nuclear Medicine and Molecular Imaging)

In this population with high prevalence of CAD (89% with coronary calcium), PET identified 13% as severe enough to warrant coronary angiogram. Of quantitative PET-guided coronary angiograms, 80% had a revascularization procedure. Although prevalence of CAD was high in this population as confirmed by abnormal PET, the PET quantitative metrics showed mild to moderate CAD in 68% that would not benefit from angiogram or revascularization procedures but were best served by medical management alone. Thus quantitative PET was optimal and unique as the gatekeeper and guide to interventions compared to any other test reported in the literature.

As demonstration of its validity as a general concept in Fig. 6.66, invasive CFC as combined absolute coronary flow velocity reserve and CFR predicts a high risk of MACE paralleling PET CFC, from which the invasive measurements evolved [70–74].

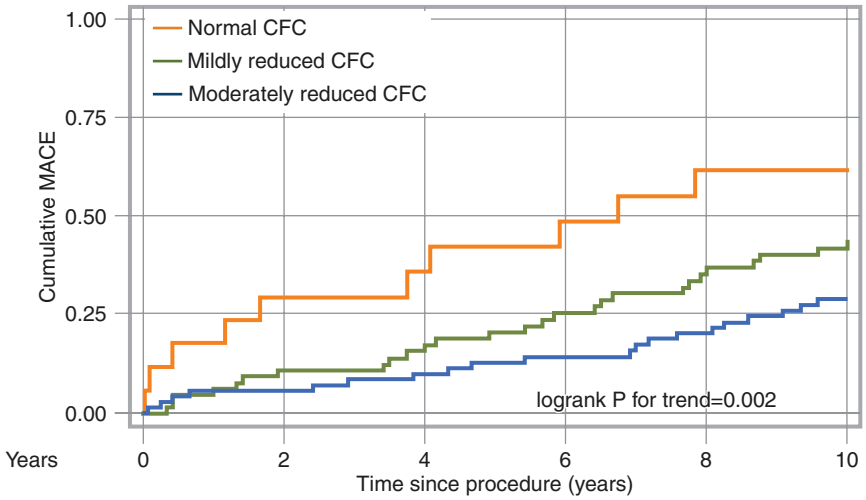

No. at. risk:

Normal CFC	70	66	63	60	55	47
Mildly reduced CFC	65	57	54	46	39	31
Moderately reduced CFC	17	11	10	8	6	5

Fig. 6.66 Invasive CFC with coronary flow velocity and MACE. (*From* van de Hoef et al. [70]; with permission from Elsevier)

As further demonstration of its validity as general concept, CFC determined as combined coronary flow by intracoronary bolus thermodilution reserve and CFR (Fig. 6.67) also a high risk of MACE paralleling PET CFC from which the invasive measurements evolved [72, 73].

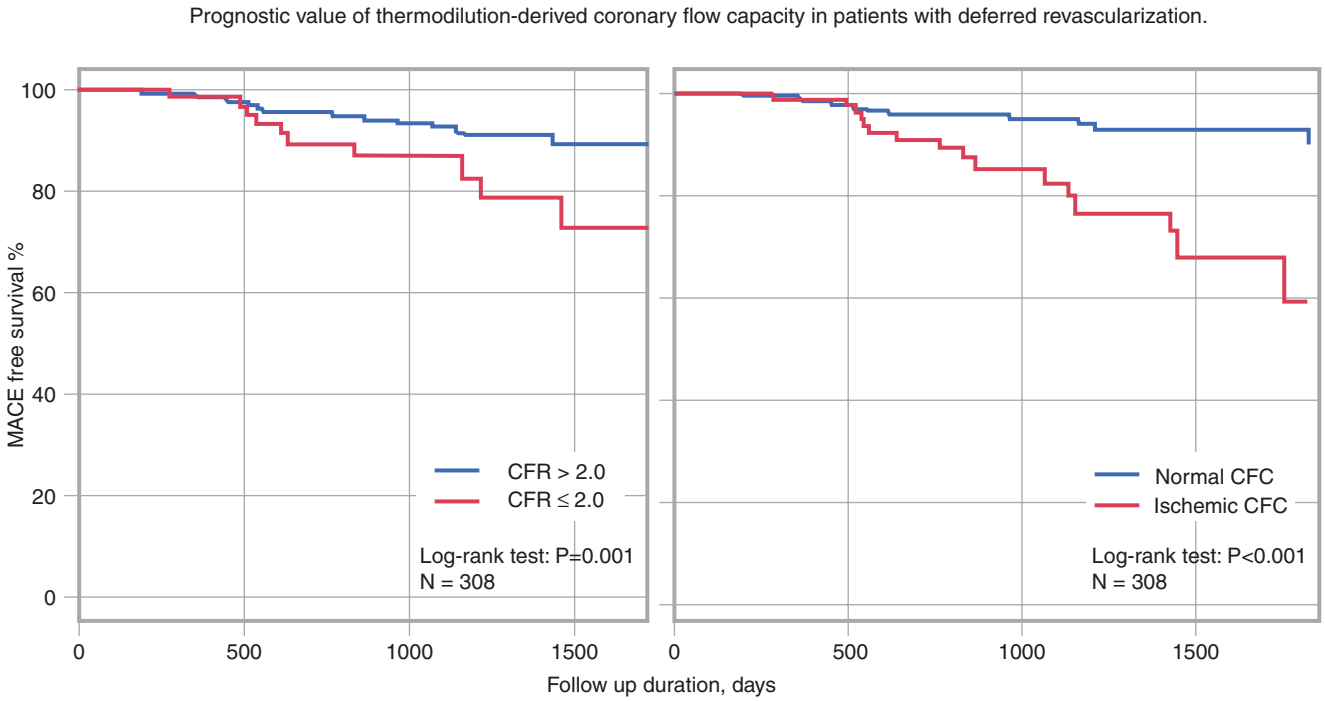

Fig. 6.67 Prognostic value of invasive CFC versus CFR with coronary thermodilution and MACE [72, 73]. (*From* Hoshino et al. [73]; with permission from from CongrHealth.com)

The pathophysiologic sequence of recurrent subclinical plaque ruptures leads to acute coronary syndromes (ACS) [75–77]. As illustrated in Fig. 6.68, 89% of acute fatal coronary events result from a series of preceding, subclinical, small plaque ruptures that heal with progressive narrowing to a severe stenosis. The last plaque rupture finally occludes the small remaining lumen, producing myocardial infarction. Most of these subclinical small plaque ruptures heal and stabilize without occluding the relatively large lumen. A large, nonstenotic lumen with an initial single occlusive plaque rupture explains only 11% of fatal infarctions at pathologic examination. This mechanism of serial plaque rupture to severe stenosis before an event explains why the most powerful or compelling indicator of high risk needing revascularization is severely reduced CFC.

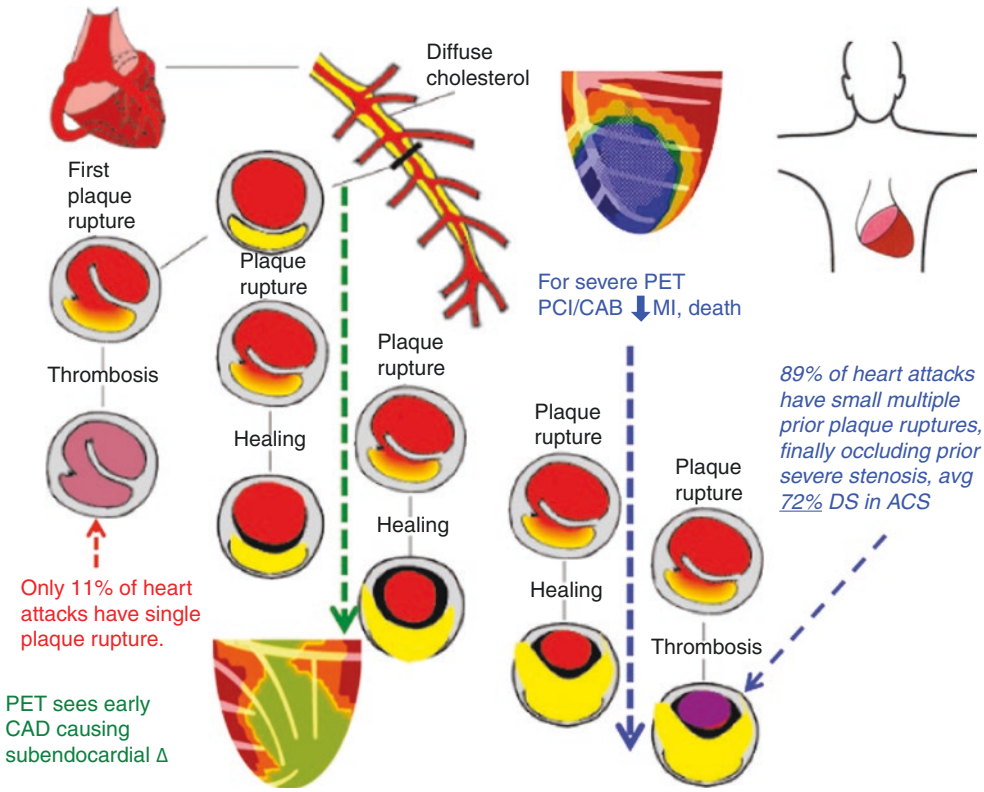

Fig. 6.68 Plaque rupture and quantitative PET perfusion [2]. DS diameter stenosis

Intracoronary optical coherence tomography–intravascular ultrasound (OCT-IVUS) in acute coronary syndromes (ACS) demonstrates severe focal lumen narrowing (averaging 72 ± 13% diameter stenosis) superimposed on varying severities of diffuse disease. This OCT-IVUS finding confirms in patients the high risk of severe stenosis superimposed on diffuse disease in ACS. This progression to severe stenosis by serial plaque ruptures may develop over days, weeks, months, or years thereby explaining the continuum of clinical manifestations from ACS to chronic "stable" CAD of varying severity.

The anatomic and physiologic severity of CAD associated with ACS defines the severity threshold at which revascularization may reduce MI and mortality in patients with chronic CAD. Quantitative PET identifies and quantifies this high-risk severity underlying ACS, thereby explaining the reduction of MACE after revascularization of severely reduced CFR (*see* Fig. 6.65).

During vasodilation stress, diffuse epicardial CAD may cause graded, base-to-apex longitudinal pressure and perfusion gradients [12–15, 78] (Fig. 6.69). In the absence of proximal stenosis, FFR measurement in the distal coronary artery correlated with PET-measured longitudinal perfusion gradients during vasodilation stress in 43% of patients in the study by Bom et al. [78]. Proximal stenosis may preclude longitudinal pressure and perfusion gradients. Longitudinal perfusion gradients do not substitute for CFC or CFR, but rather add insight on diffuse CAD that may moderate any potential benefit from stents.

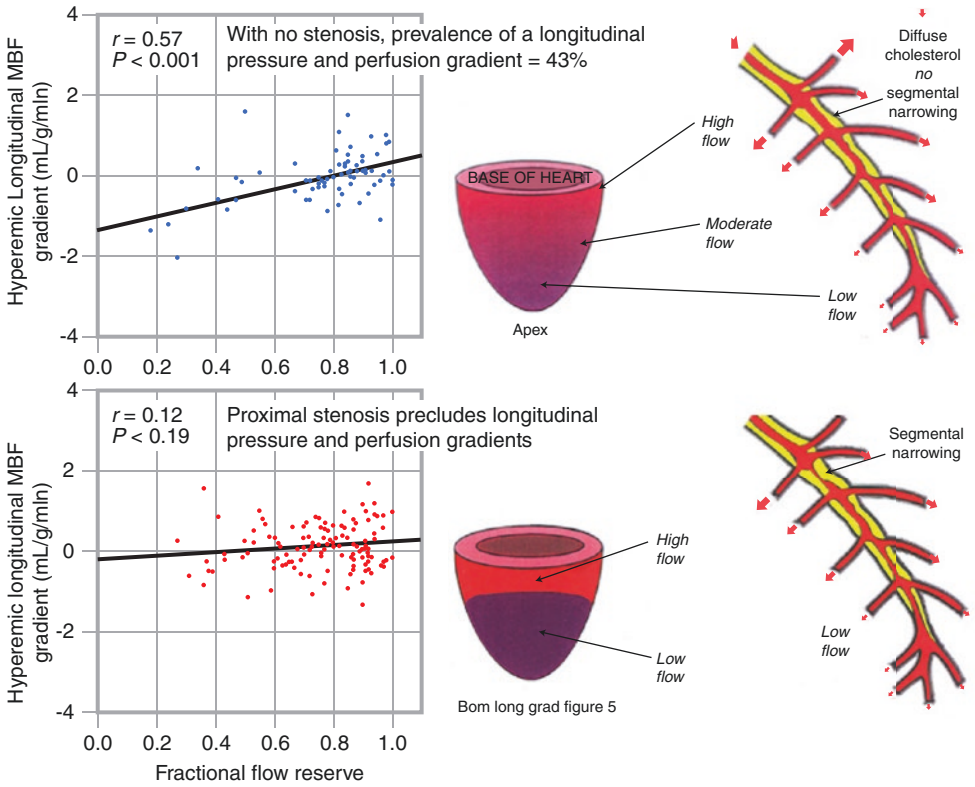

Fig. 6.69 Longitudinal perfusion gradients, another face of diffuse CAD. MBF myocardial blood flow. (From Bom et al. [78]; with permission from Oxford University Press)

Base-to-apex longitudinal pressure and perfusion gradients commonly reduce subendocardial perfusion during vasodilation stress, particularly at the apex because of cumulative pressure loss due to viscous friction along the length of the artery [2, 12, 13, 15, 25, 49, 78]. In the patient shown in Fig. 6.70, blood flow is shunted into proximal branches owing to pressure declining along the arterial length sufficient to reduce flow at the apex to values lower than resting values; this *branch steal* is documented experimentally and is clinically associated with angina.

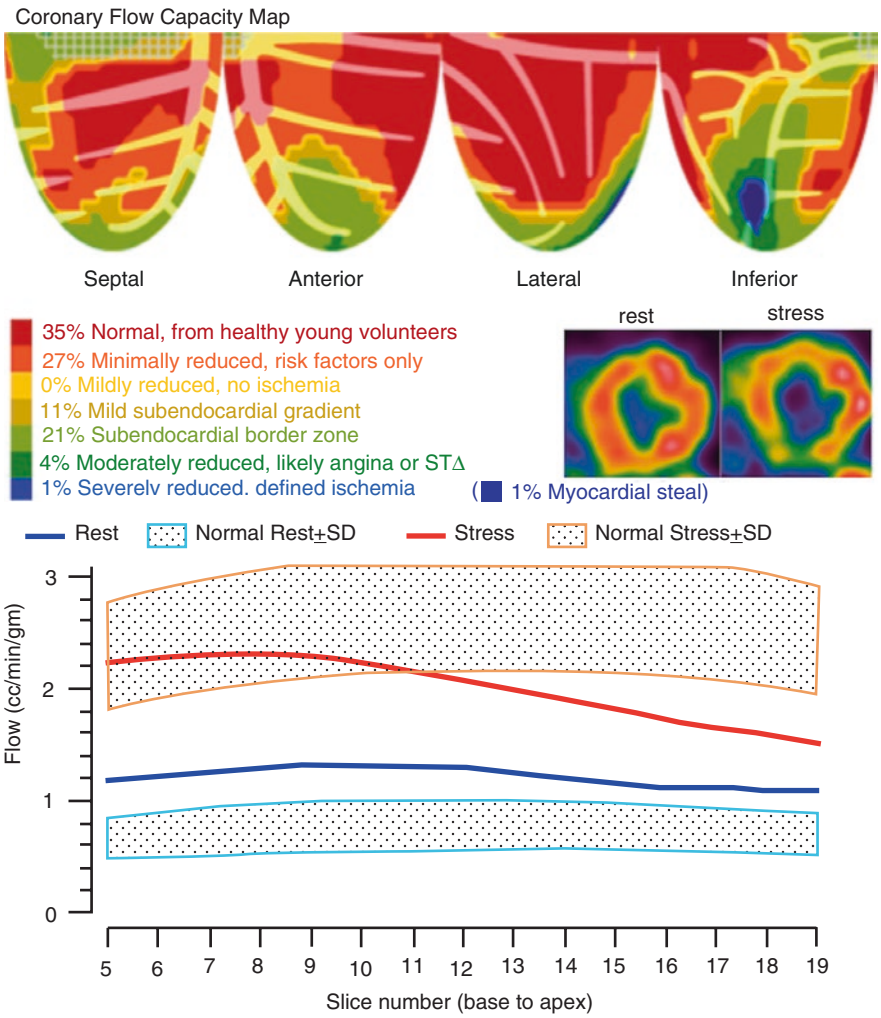

Fig. 6.70 Longitudinal perfusion gradients and subendocardial ischemia. In this patient, blood flow is shunted into proximal branches owing to pressure along the arterial length that is sufficient to reduce flow at the apex to values lower than resting values

Collaterals typically connect from a patent supply artery to an occluded artery through small distal anastomosis. Therefore, in many cases, the direction of collateral flow is from distal to proximal perfusion regions, thereby causing a reverse longitudinal gradient during vasodilation stress and myocardial steal (Fig. 6.71). In these patients, the worst perfusion defect is therefore at the base, where the occlusion is located; this area is the farthest away from the best perfusion, which is found at the source of flow through the distal collateral anastomosis.

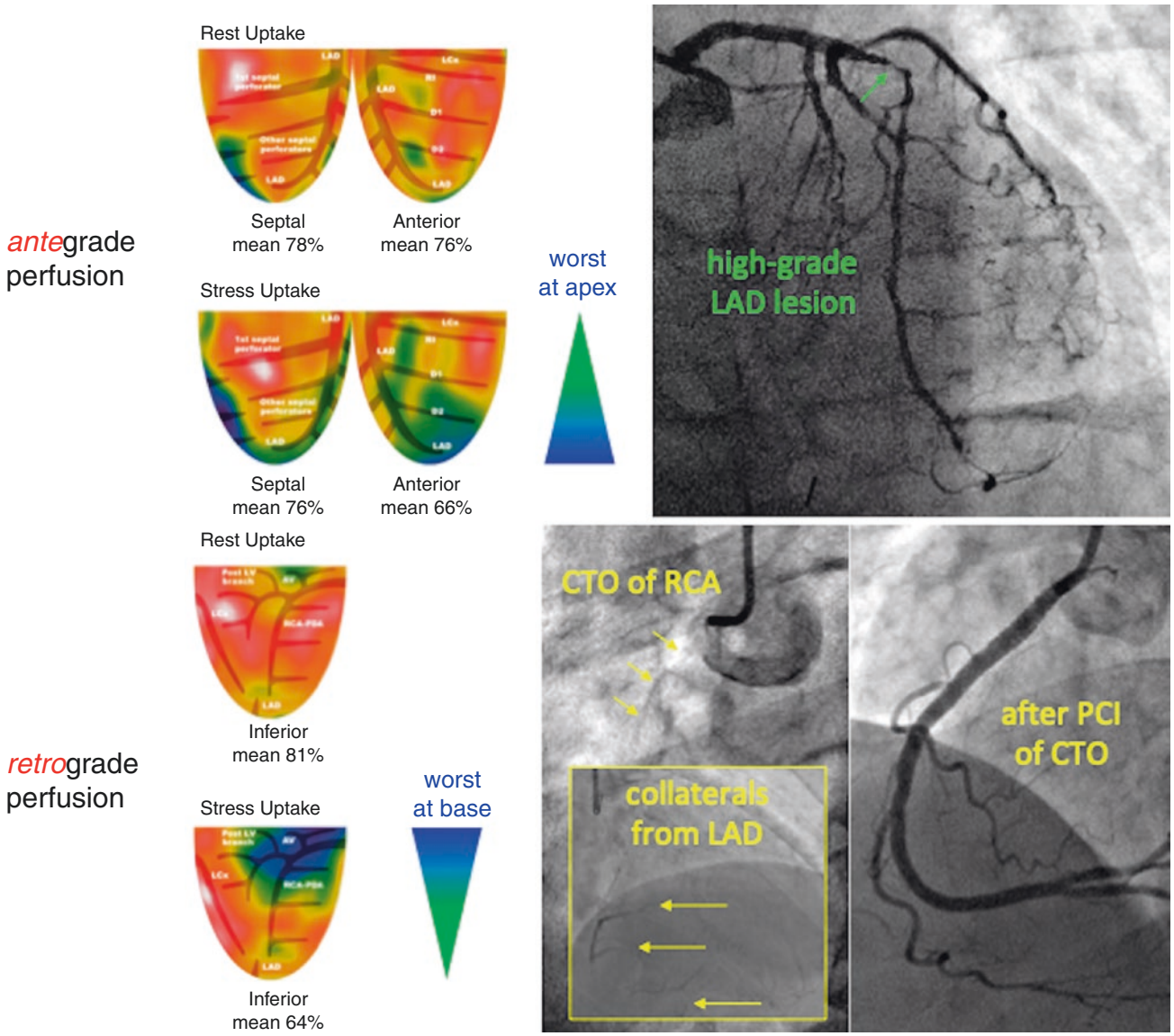

Fig. 6.71 Reverse apex-to-base longitudinal perfusion gradient: retrograde perfusion through a distal collateral anastomosis is worst at the base. CTO chronic total occlusion

Figures 6.72 and 6.73 compare phasic coronary blood flow, pressure, and transmural perfusion with normal coronary arteries versus CAD. With normal coronary arteries, systolic compression stops coronary blood flow, with post-systolic reactive hyperemia; diastolic flow is high in early diastole and falls during later diastole. This normal phasic coronary pressure and flow supply the LV with adequate transmural flow even during tachycardia and high flow demands. In patients with coronary artery narrowing or marked LV hypertrophy, however, the rapid diastolic flow cannot compensate for systolic compression, and the result is subendocardial or transmural ischemia, particularly with tachycardia of hypertension, which further impede subendocardial perfusion.

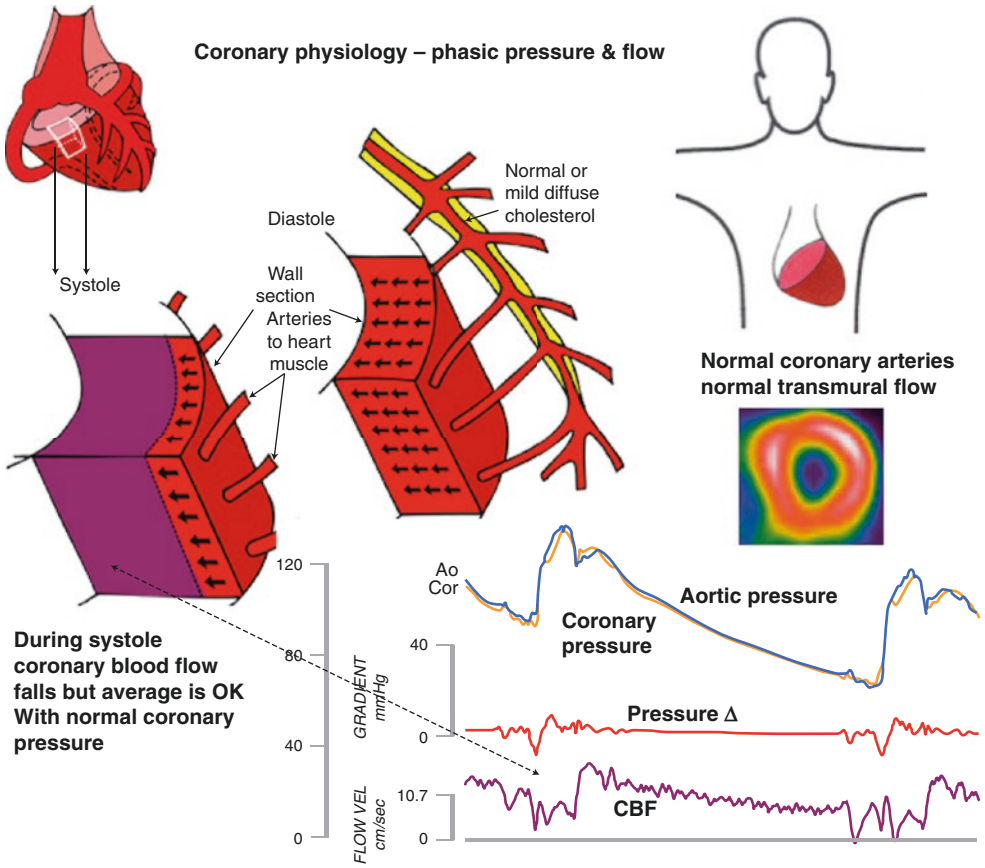

Fig. 6.72 Phasic coronary blood flow, pressure, and transmural perfusion with normal coronary arteries

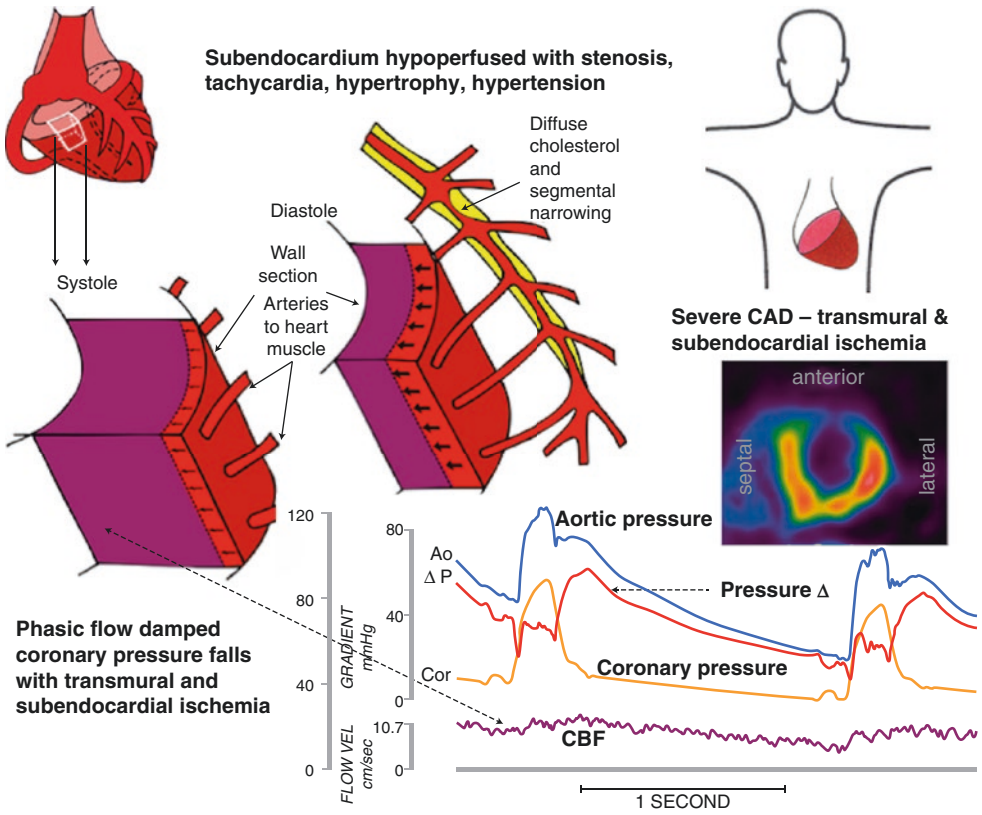

Fig. 6.73 Phasic coronary blood flow, pressure, and transmural perfusion with CAD

When patients complain of angina, we ask what size and severity of low subendocardial perfusion is causing it. In the example shown in Fig. 6.74, a large, severe LAD stress defect indicated severe stenosis or occlusion of the LAD proximal to the first septal perforator and proximal to large diagonal branches. After LAD stenting the patient still had angina, stress perfusion was much better, but a small area of mildly reduced subendocardial perfusion continued to cause moderate angina and STΔ >1 mm during dipyridamole stress, indicating subendocardial ischemia. Angina from this low-risk stress perfusion defect is explainable by the interrelated physiology of CFC (top panel of PET images), subendocardial perfusion (left tomograms and lower-right activity profiles), and FFR by PET expressed as the relative map of stress perfusion in cc/min/g (FFRpet, upper right black and brown color bar scale). The relative image of stress PET perfusion in cc/min/g is the original reference standard used to validate invasive pressure-derived FFR [79, 80], as further detailed below in Figs. 6.75, 6.76, 6.77, 6.78, 6.79, and 6.80.

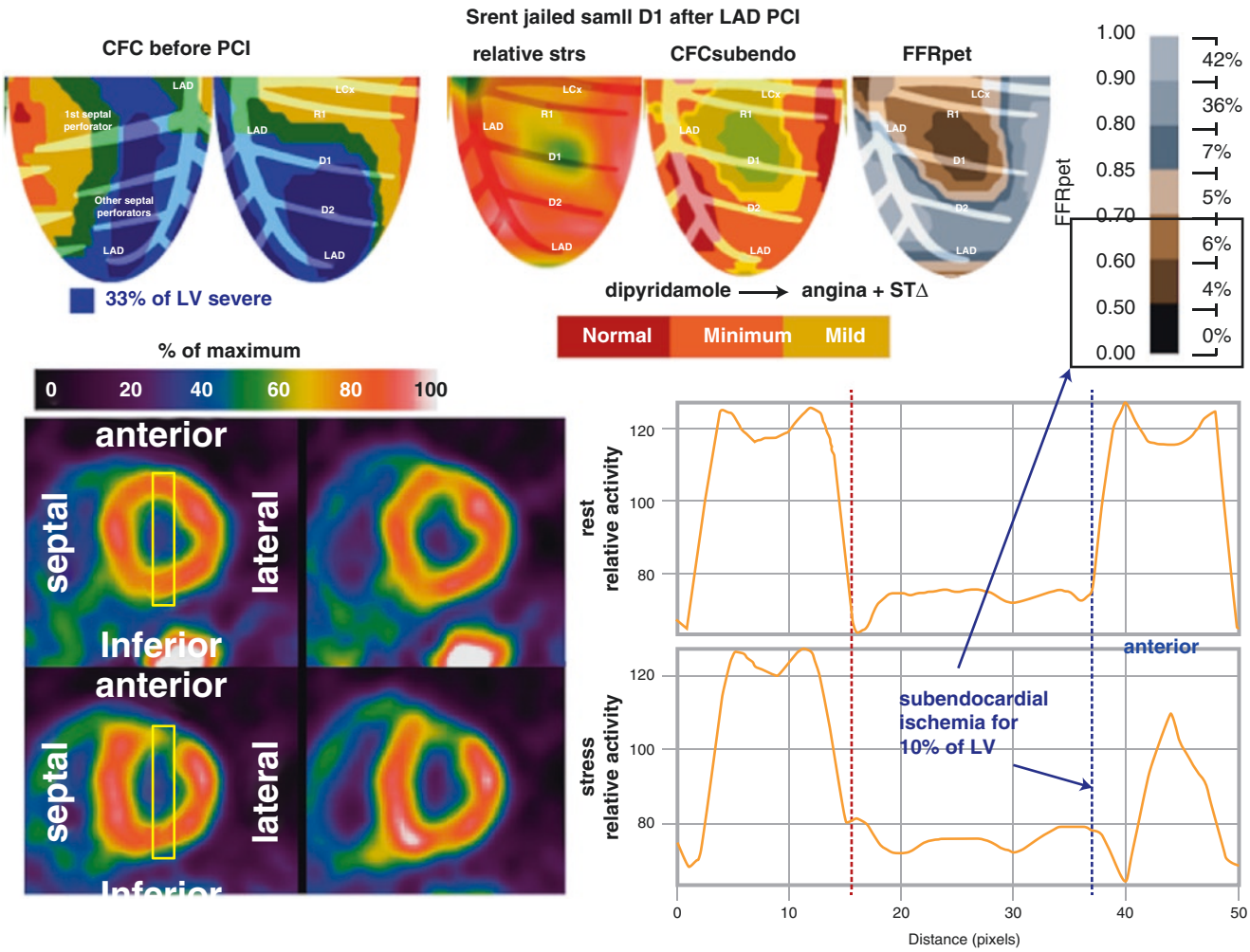

Fig. 6.74 Angina caused by reduced subendocardial perfusion. A large, severe LAD stress defect indicated severe stenosis or occlusion of the LAD proximal to the first septal perforator and proximal to large diagonal branches, but the angina continued (though it was less severe) after a stent was placed with PCI. At PET after the LAD stenting, stress perfusion is much better, with a small residual mid-anterior stress defect in a small D1 distribution caged by the LAD stent. This small area of mildly reduced subendocardial perfusion, comprising only 3% of LV (*light green* on the CFC map) caused moderate angina and STΔ >1 mm during dipyridamole stress, indicating subendocardial ischemia

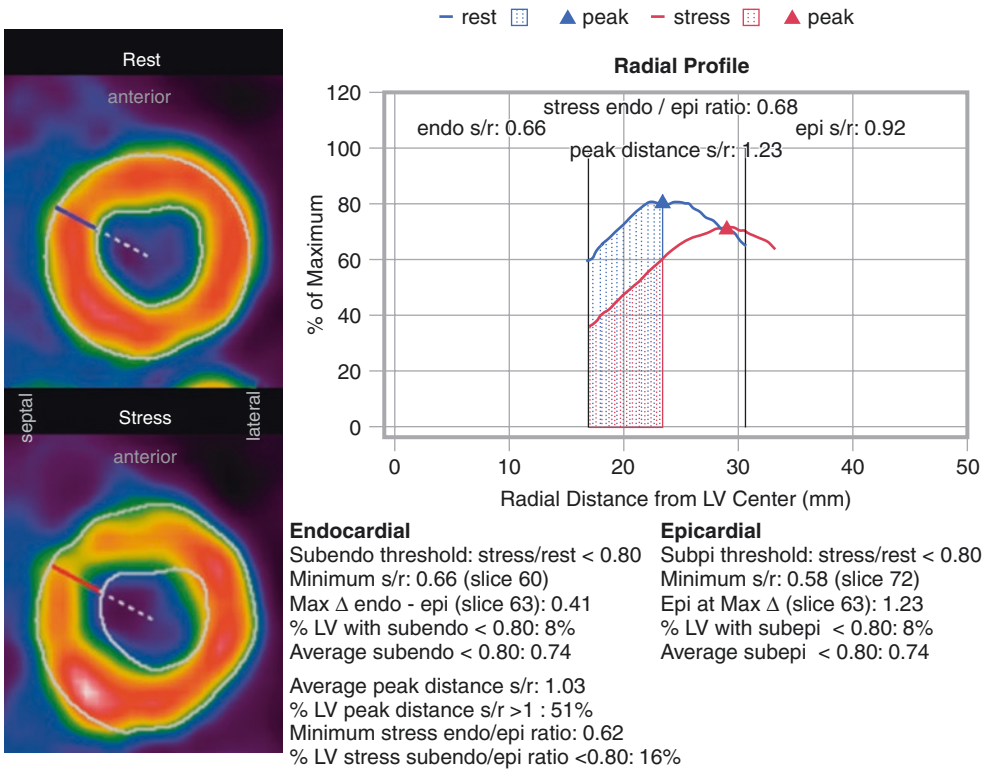

Fig. 6.75 Automated quantitative subendocardial analysis for the patient in Fig. 6.74. FFRpet below 0.7 for 10% of the LV associated with reduced subendocardial perfusion in the tomograms and activity plots is quantified as a minimum subendo/epicardial ratio of 0.62 and 16% of LV with a subendo/epicardial ratio <0.8. For each relative tomographic slice, the rest endocardial and epicardial boundaries are tracked in *white lines*. The rest endocardial boundary is projected onto the same stress slice and the stress epicardial boundary is outlined. Radial activity is tracked between these boundaries to determine the peak values at radial distance from the center of the LV (here the *blue line* for resting radial activity profile and the *red line* for stress activity profile of this tomographic slice). On each rest tomographic slice, the area from rest endocardial boundary to peak activity defines the subendocardium (*blue hatched area*) for comparison to stress activity within this same area (*red hatched area*) as the subendocardial stress/rest ratio (red area/blue area) for each of 64 radii in each of 20 tomographic slices. The subendocardial stress/rest ratio threshold of <0.8 was established from the mean ± 1.95 SD of 124 healthy volunteers under 40 years old without risk factors. This subendocardial stress/rest ratio is reported in several different ways, describing size and severity as follows: the minimum of all radii in the LV (here 0.66), the % LV with the subendocardial stress/rest ratio <0.8 (here 8%), the average subendocardial ratio <0.8 (here 0.74), and the maximum subendo-subepicardial difference of all radii (here 0.41). The final metric accounts for stress-induced LV dilatation as the radial distance from the center of the LV to the peak radial activity for each radius of each rest and stress tomographic slice, expressed for the whole LV as the average peak radial distance stress/rest (in this case, 1.03) and the % of LV with a peak radial stress/rest ratio >1.0 (here, 51%), indicating normal or minimal LV dilatation with stress

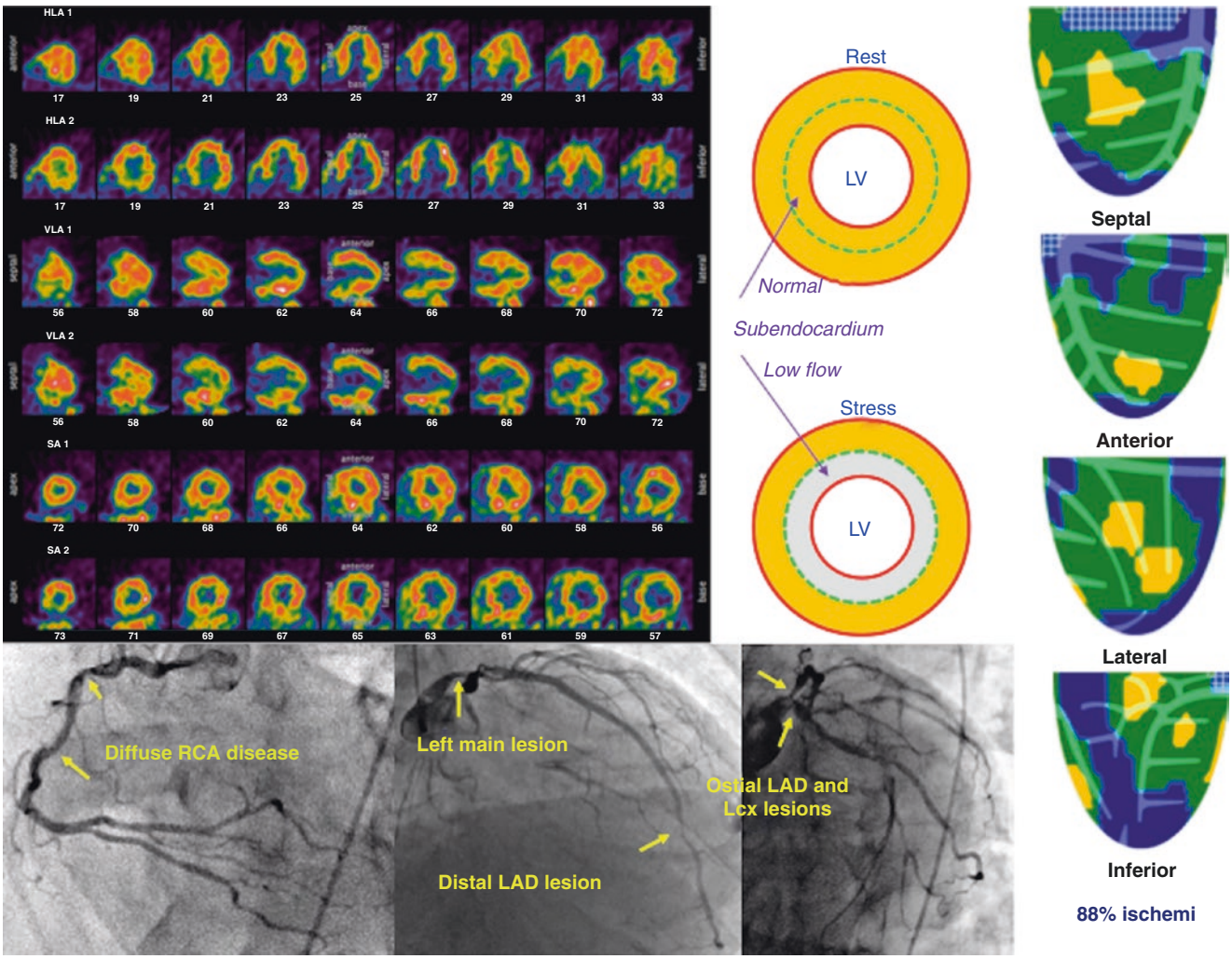

Fig. 6.76 Global subendocardial ischemia and angina

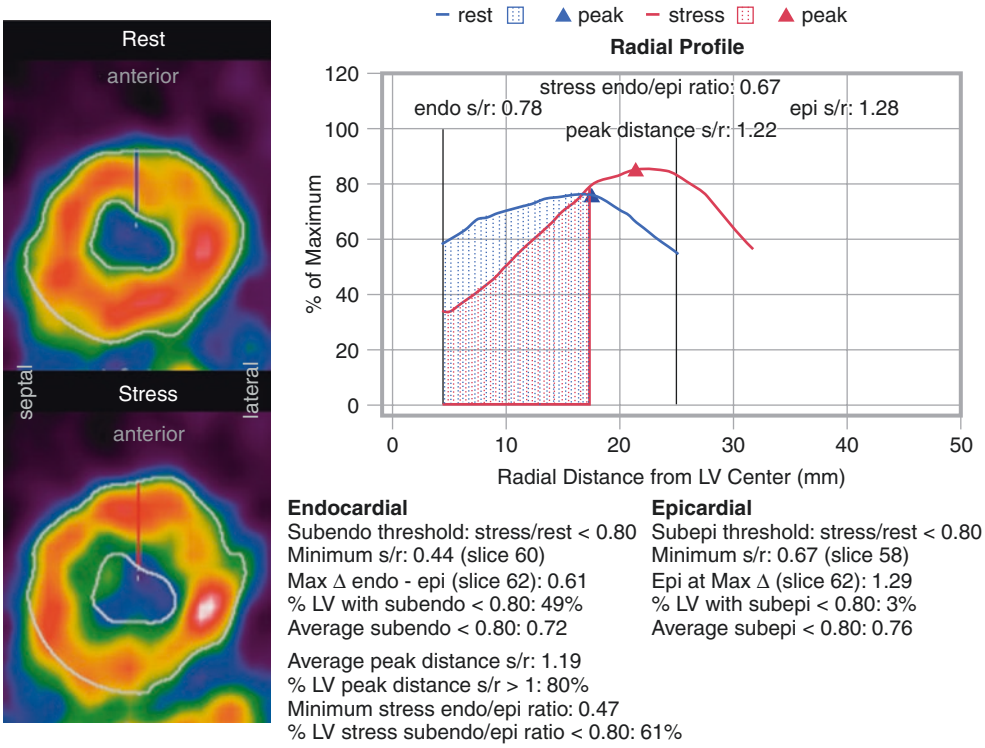

Fig. 6.77 Automated quantitative subendocardial analysis for the patient in Fig. 6.76. Using the same terms and methodology described for Fig. 6.75, the subendocardial metrics shown here include minimum subendocardial stress/rest ratio, 0.44; average subendocardial stress/rest ratio, 0.72; 80% of LV with subendocardial stress/rest ratio <0.8; minimum stress subendo/epicardial ratio, 0.47; 61% of LV with subendo/epicardial ratio <0.8; average radial peak distance stress/rest ratio, 1.19; and 80% of LV with peak distance stress/rest ratio >1.0—all results that indicate severe, diffuse subendocardial ischemia and ischemic LV dilatation

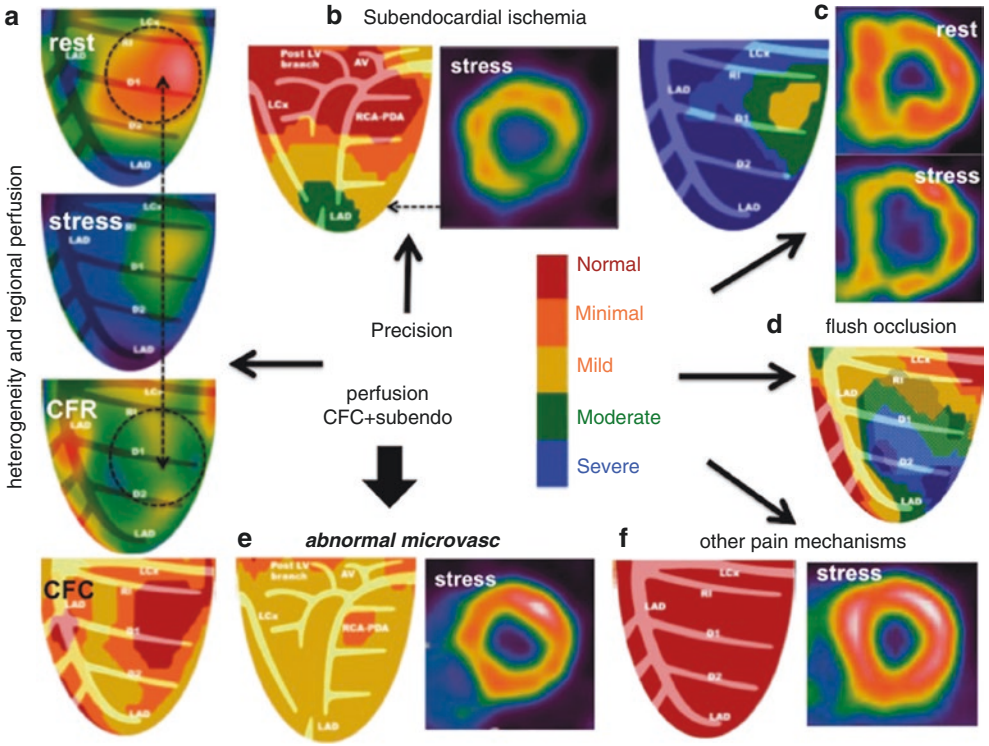

Fig. 6.78 CFC solutions for common clinical issues without angiographic stenosis, shown for efficiency in single views of CFC maps: (**a**), Abnormal CFR due to resting perfusion heterogeneity and only mildly diffusely reduced CFC; (**b**), Mild, diffuse epicardial CAD with good small-vessel function and high stress flow sufficient to cause a longitudinal perfusion gradient; (**c**), Severe, diffuse epicardial CAD with good small-vessel function (enough small-vessel function for stress flow to reduce coronary perfusion pressure, causing severe global subendocardial ischemia and LV dilatation); (**d**), Flush occlusion (chronic occlusion) of a large diagonal not seen on angiography; (**e**), Small-vessel disease with uniform regional and transmural reduction of CFC; (**f**), Angina during very high CFC with normal subendocardial perfusion, indicating altered pain mechanisms without ischemia. (*From* Gould and Johnson [25]; with permission from Elsevier)

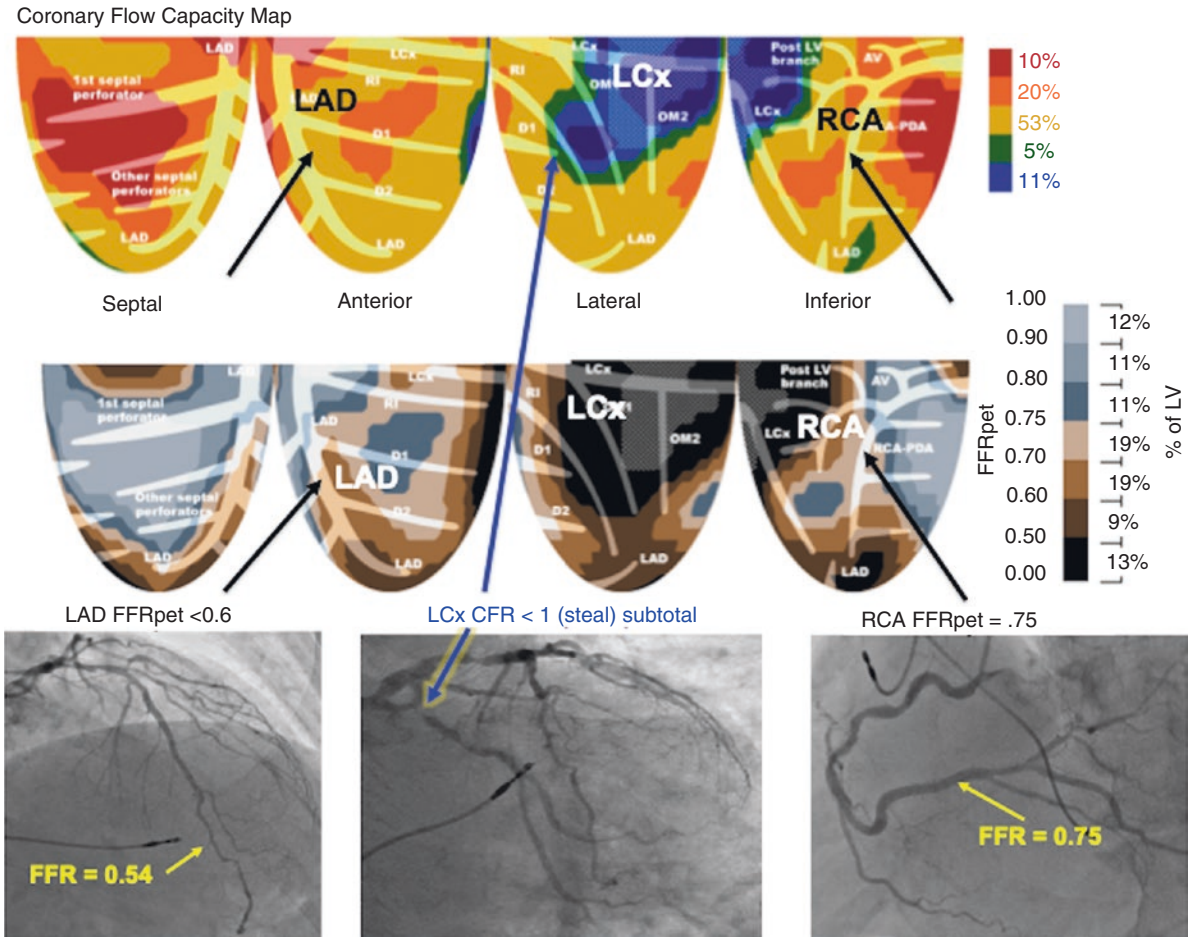

Fig. 6.79 Interrelated physiology—CFC, FFRpet, and FFR by pressure wire—in complex CAD. In this figure, CFC is mildly reduced in LAD and RCA distributions (*yellow*), indicating mild to moderate flow-limiting stenosis but severe stenosis or occlusion of the LCx (*blue*) in 11% of LV, with myocardial steal indicating collaterals. The relative map of stress FFRpet shows severe reduction to <0.6 in the LAD, to 0.7–-0.75 in the RCA (confirmed by FFRpressure) and to <0.5 in the LCx; a cumulative 41% of the LV has FFRpet <0.7

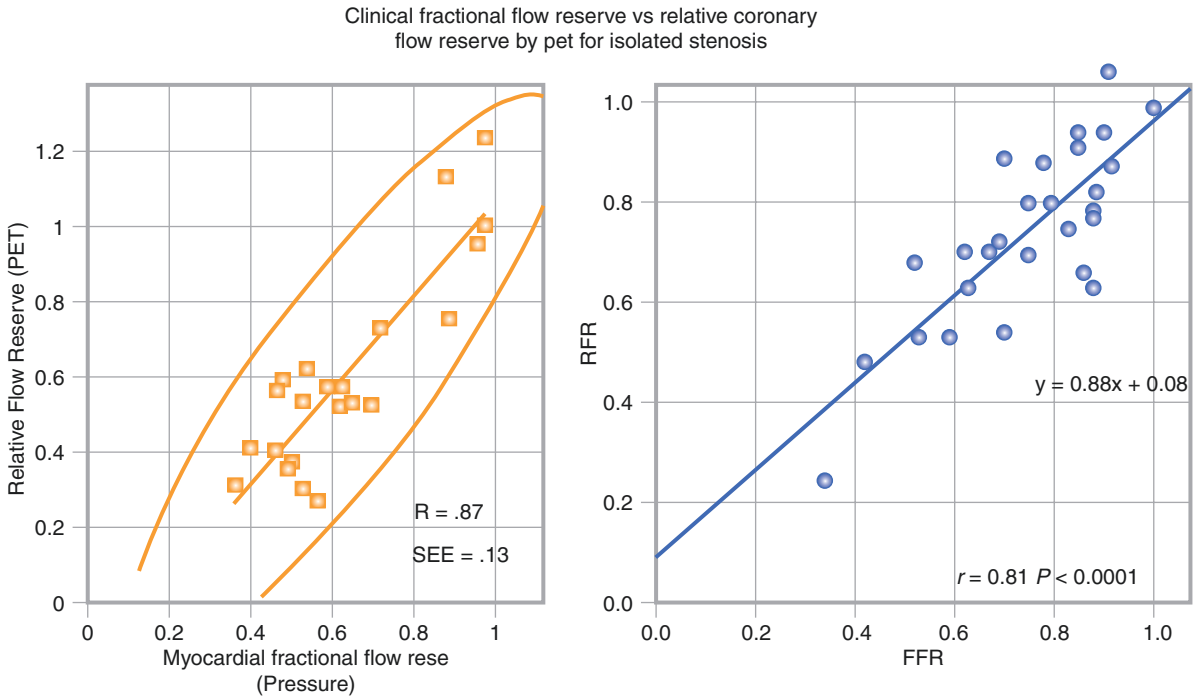

Fig. 6.80 Interrelated physiology—FFR based on intracoronary pressure. (*Left panel from* De Bruyne et al. [79] and *right panel from* Marques et al. [80]; with permission from the American Heart Association)

Typically, Invasive pressure-derived FFR is measured at one point just beyond an angiographic stenosis. However, as shown in Figs. 6.8 and 6.11, no single value of CFR or FFR characterizes a coronary artery. Instead, a range of values along the branching vessel length, as illustrated by the "FFRpet" single view on Fig. 6.74, which shows a progressively more severe gradation of values along the vessel length, with proximal iso-contour values falling from 0.75 to 0.5 most distally, owing to the diffuse CAD underlying most if not all stenosis.

This proximal-to-distal gradation parallels the range of distal-to-proximal pull-back pressures along the vessel length [15], which are not currently acquired in clinically measured FFR. Because invasive pressure-derived FFR is a single measure just distal to the stenosis, it fails to account for more distal lower values seen by PET. FFRpet values are typically worse distally than the proximal pressure measurements, which are more comparable to the higher FFRpet iso-contour just distal to the stenosis than to the lower distal values. Moreover, for an occluded artery (as for the stent-caged diagonal branch in Fig. 6.74), pressure-derived FFR cannot be measured, but the relative distribution of stress perfusion in cc/min/g or FFRpet can be mapped. In this example, the minimum FFRpet reached 0.5. Blood pressure during dipyridamole stress was 94/44 mm Hg, for a mean blood pressure of 61 mm Hg. Multiplying this by the FFRpet of 0.5 suggests a stress subendocardial perfusion pressure of 31 mm Hg, as in Fig. 6.12 [24], at which ischemia occurs experimentally [20] and in humans [21]. Figure 6.75 shows automated quantitative subendocardial analysis for the same patient. This analysis identified a small, mild defect that was associated with low risk on long-term follow-up (as in Fig. 6.65) but that nevertheless caused definite angina and significant ST depression during dipyridamole stress.

The primary subendocardial perfusion metrics are automatically determined in the software, but the operator can examine every radius on any slice by scrolling through all the slices and sweeping the radius like a clock around each slice. In addition, for each tomographic slice of the stress images, the midpoint is determined between the stress epicardial boundary and the rest endocardial boundary projected onto the stress slice. For each radius, the area within the endocardial half/epicardial half of the stress activity profile determines the stress subendo/epicardial ratio for that radius. The stress subendo/epicardial ratio for size and severity are reported as the minimum stress subendo/epicardial ratio (0.62 in Fig. 6.75) and the % of LV with a stress subendo/epicardial ratio <0.8 (16% in this example). The final metrics account for stress-induced LV dilatation of 1.03 or 3%.

For severe, balanced three-vessel stenosis, as seen in Fig. 6.76, or severe diffuse narrowing, even small increases in coronary flow may cause a severe fall in pressure along the arterial length, thereby causing diffuse subendocardial ischemia, LV dilatation, decreased ejection fraction, and TID (transient ischemic dilatation). Figure 6.77 shows the automated quantitative

subendocardial analysis for the same patient, which indicates severe, diffuse subendocardial ischemia and ischemic LV dilatation.

Figure 6.78 illustrates a number of ways in which CFC by PET can offer solutions for common clinical perfusion abnormalites with or without symptoms without apparent angiographic stenosis [23].

Figure 6.79 illustrates interrelated physiology—CFC, FFRpet, and FFR by pressure wire—in complex CAD. Low coronary pressure during vasodilatory stress parallels the corresponding abnormal map of relative stress cc/min/g (FFRpet) and absolute values of CFC (*see* Figs. 6.12, 6.13, and 6.73). FFRpet maps the entire LV with the typical graded proximal-to-distal pressure and perfusion gradient along the arterial length. The usual clinical measurement of a single intracoronary FFR based on pressure fails to reveal this essential clinical insight provided by FFRpet and the CFC maps, or an invasive pressure pullback curve.

Figure 6.80 illustrates interrelated physiology of the FFR based on intracoronary pressure. FFR was validated by comparison to relative stress perfusion in cc/min/g, thereby documenting the interrelations of CFC, FFRpet, and FFR in Figs. 6.74, 6.75, 6.76, 6.77, 6.78, 6.79, and 6.80. For these correlations, a single value of relative stress cc/min/g were an average for the predefined distribution of a major coronary artery, compared with invasive artery-specific pressure-derived FFR. This single average relative stress cc/min/g for an arterial distribution cannot therefore show the per-pixel actual arterial distributions seen in Figs. 6.74, 6.79, 6.81, and 6.95.

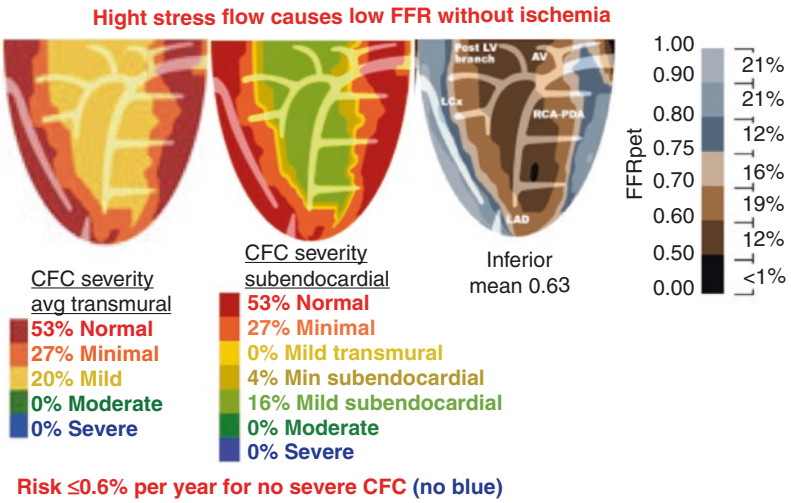

Fig. 6.81 Case example of the interrelated physiology of CFC, subendocardial ischemia, and FFRpet in an asymptomatic, active man who was able to do hard workouts without symptoms but had PET because of dense coronary calcium and hypercholesterolemia. PET showed excellent or adequate CFC (red and orange) for 80% OF LV with mildly reduced CFC (yellow) reflecting mildly reduced subendocardial to subepicardial ratio of myocardial perfusion. Relative stress flow expressed as a fraction of maximum stress ml/min/g or fractional flow reserve (FFRpet) by PET was ≤ 0.7 for 31% of LV. He had an ejection fraction of 66% by stress ECHO and no angina or STΔ during dipyridamole stress during dipyridamole stress PET. Since he is asymptomatic, should he have an invasive procedure for mild to moderately reduced subendocardial perfusion without angina? Figures 6.60, 6.64, and 6.65 indicate that the risk of MACE is very low, ≤ 0.6% per year for PET with no severely reduced CFC (no blue) suggesting that vigorous medical management is an appropriate option

Figure 6.81 shows a case example of the interrelated physiology of CFC, subendocardial ischemia, and FFRpet in an asymptomatic, active man who was able to do hard workouts without symptoms but who had PET because of dense coronary calcium. Since his CAD is asymptomatic, should he have an invasive procedure for mild to moderately reduced subendocardial perfusion without angina? Figures 6.60, 6.64, and 6.65 indicate that the risk of MACE is very low for this mild to moderately reduced CFC or FFRpet suggesting that vigorous medical management would be appropriate.

In Fig. 6.82, the relative subendocardial metrics for this same patient illustrates important new insights into the clinical coronary physiology. Low relative subendocardial perfusion does not mean ischemia or high risk if stress perfusion, CFR, and CFC are adequate and well above absolute thresholds for ischemia in cc/min/g. This patient's absolute transmural perfusion and CFC are well above the low absolute threshold for ischemia without angina or ST changes during PET stress imaging or hard exercise. Figure 6.65 shows that revascularization for mild to moderately reduced CFC is not associated with reduced MACE, as the risk of the procedure may be greater than the risk with medical treatment. When offered the objective data and the options for invasive and noninvasive management, this patient chose the noninvasive vigorous lifestyle and medical treatment.

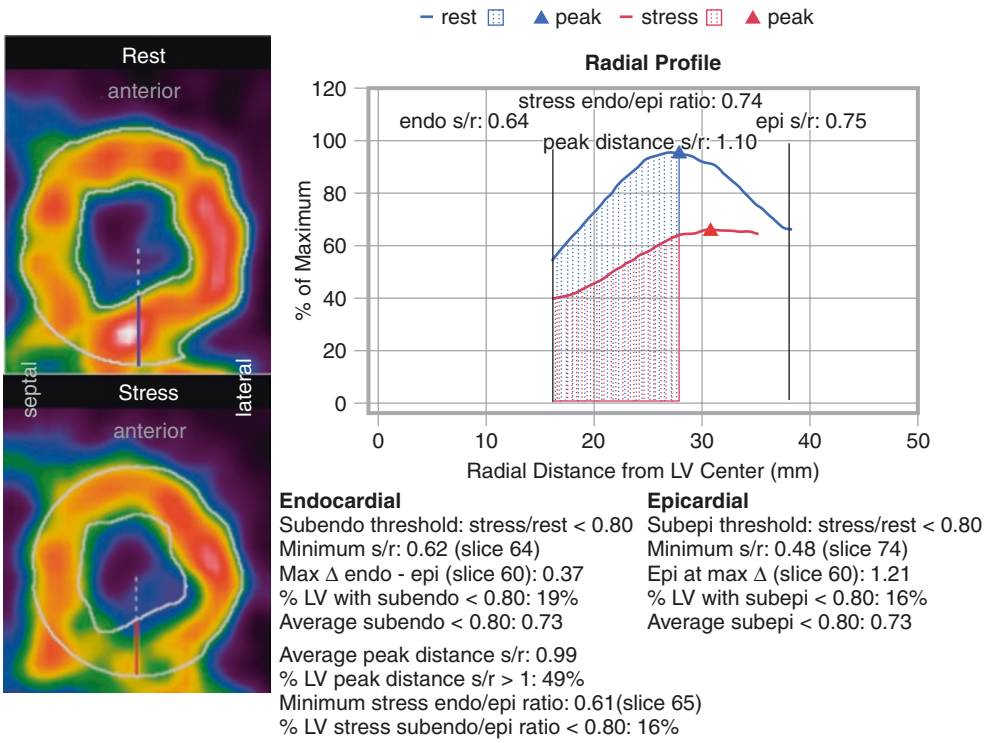

Fig. 6.82 Relative subendocardial metrics for the patient in Fig. 6.81. This case contrasts relative subendocardial metrics with absolute values of stress perfusion that are well above the threshold of low absolute perfusion for ischemia, here indicated by mildly reduced CFC (*yellow*) with no moderate (*no green*) or severely reduced pixels (*no blue*), associated with low risk. FFRpet is <0.7 (relative stress perfusion), and the diffuse and regional inferior subendocardial metrics are as follows: minimum subendocardial stress/rest ratio, 0.62; average subendocardial stress/rest ratio, 0.73; 19% of LV with subendocardial stress/rest ratio <0.8; minimum stress subendo/epicardial ratio, 0.61; 16% of LV with subendo/epicardial ratio <0.8; average radial peak distance stress/rest ratio, 0.99—all indicating CAD

Essentially all clinical outcome data in the literature and for this chapter are based on 2D PET scanners with the most widely used type of detectors, BGO (bismuth germinate oxide). 3D acquisition incurs such high activity that the standard 2D BGO system cannot make appropriate corrections for random coincidences, dead time loss, and scatter corrections. As shown in Fig. 6.83, current 3D scanners require a reduced dose of Rb-82 that limits the count density and statistical certainty required for detailed per-pixel perfusion or CFC maps to guide clinical management. Technology is being developed to make acquisition of full-dose Rb-82 and CFC pixel mapping possible using BGO as well as other non-BGO detectors, but their capacity has not yet been demonstrated clinically in the literature. The top 3D PET images on a BGO scanner show severe ring artifacts making unuseable images (upper left blue) or artifactual abnormalities (top center) compared to a normal 2D image of the same patient (right image). The graph below shows activity recovery by 3D is reduced to half of that by 2D for full dose Rb-82 using a BGO scanner.

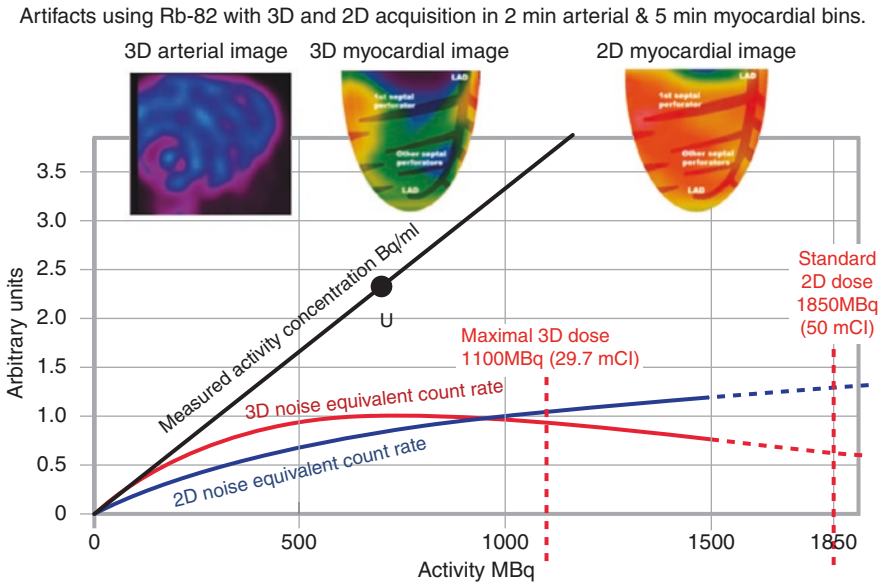

Fig. 6.83 Is all PET the same? A full 40- to 50-mCi dose of Rb-82 causes a fall in noise-free true counts for 3D acquisition (*dashed red line*) that is half of that for 2D acquisition (*dashed blue line*) [81]. Accordingly, current 3D scanners require a reduced dose of Rb-82 that limits regional and particularly per-pixel count density and statistical certainty required for detailed per-pixel perfusion or CFC maps to guide clinical management. (From Gould et al. [83]; with permissiom from Mosby)

Quantitative Myocardial Perfusion for Clinical Dilemmas

Severe CAD Missed on Angiograms

Both patients in Fig. 6.84 had known CAD with previous stents for angina. Both had ongoing angina, but coronary angiograms failed to show significant stenosis, so rest-stress PET was requested. In both cases, a severe CFC abnormality was identified and was corrected by retrograde wiring through a collateral channel.

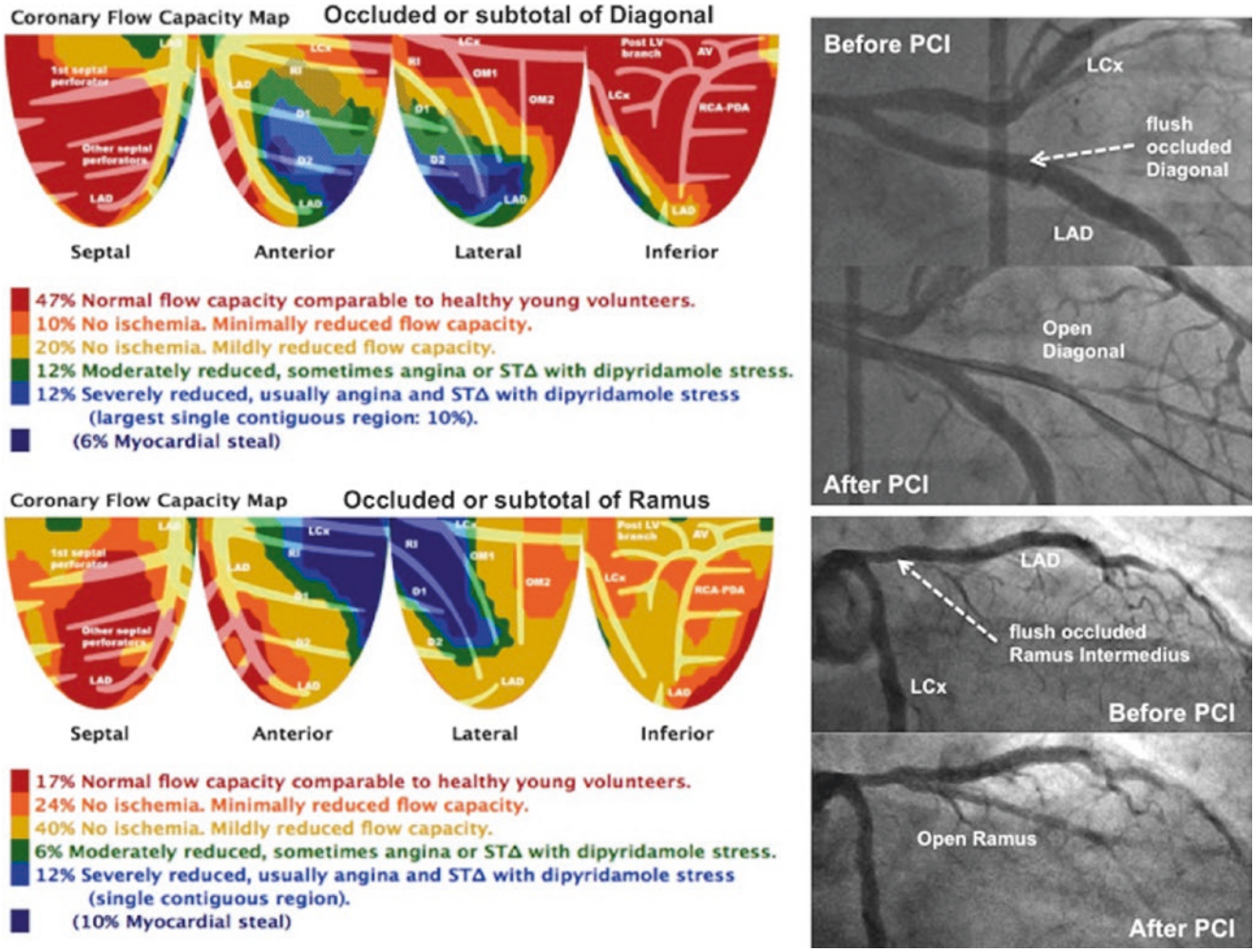

Fig. 6.84 Severe CAD missed by angiogram in two patients with previous stents for angina. Both had ongoing angina, but coronary angiograms failed to show significant stenosis, so rest-stress PET was requested. The upper case showed a large, severe CFC abnormality in the distribution of a large diagonal branch jailed by an LAD stent, with myocardial steal indicating collaterals. With this knowledge, flush occlusion was opened by retrograde wiring through a collateral channel to the origin of the diagonal, as seen on the cine inset. For the lower case, the CFC map showed a severe abnormality in the distribution of a ramus Intermedius due to flush occlusion at its origin. This insight also permitted stenting through a retrograde wire through a collateral channel

Figure 6.85 illustrates the case of a patient with angina who was told he had a normal angiogram. He requested a PET study, which showed severely abnormal CFC with 4 mm ST depression and hypotension; the ejection fraction fell from 66% to 45%, all characteristic of severe left main (LM) stenosis. Re-review and repeat of the angiogram in addition to CTA confirmed severe LM stenosis, leading to coronary bypass surgery.

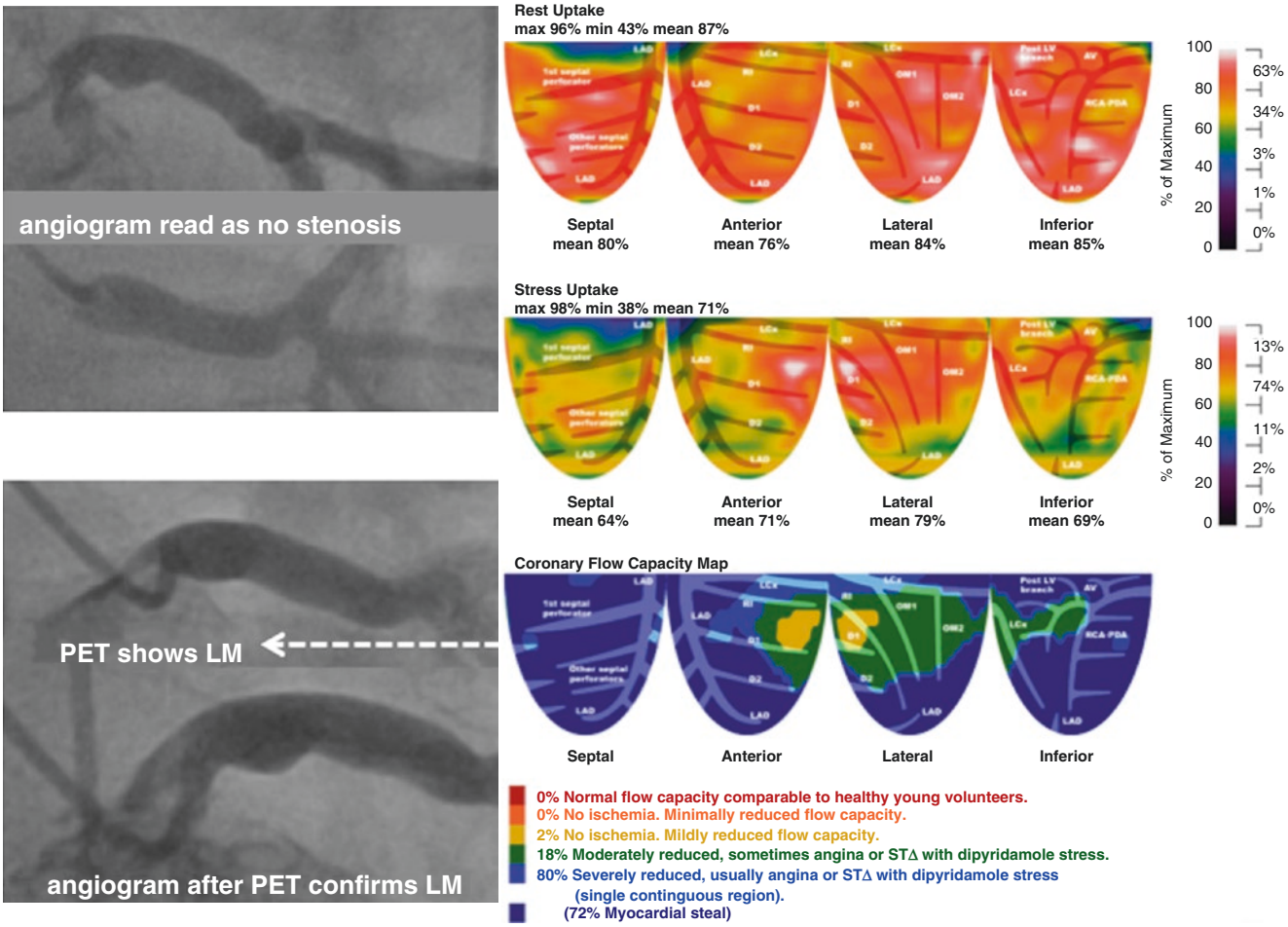

Fig. 6.85 Severe left main stenosis missed on angiogram

Recurrent Angina after Surgery

The patient in Fig. 6.86 had recurrent angina after coronary bypass surgery. Rest-stress PET showed defects indicating a patent left internal mammary artery (LIMA) to LAD graft but progressive disease proximal to the graft insertion, involving the first septal perforator and the first diagonal branch. Usually stent caged branches develop collaterals and angina resolves over weeks to months. However, if needed knowing the source, severity and size of the ischemic region, stenting through the mesh of the caging stent to open the stent blocked branch is usually an effective intervention. This pattern of stress defects in the first perforator and diagonal branches with adequate perfusion in the LAD distribution is typical of severe disease proximal to a patent bypass graft to LAD as also seen in Fig. 6.2.

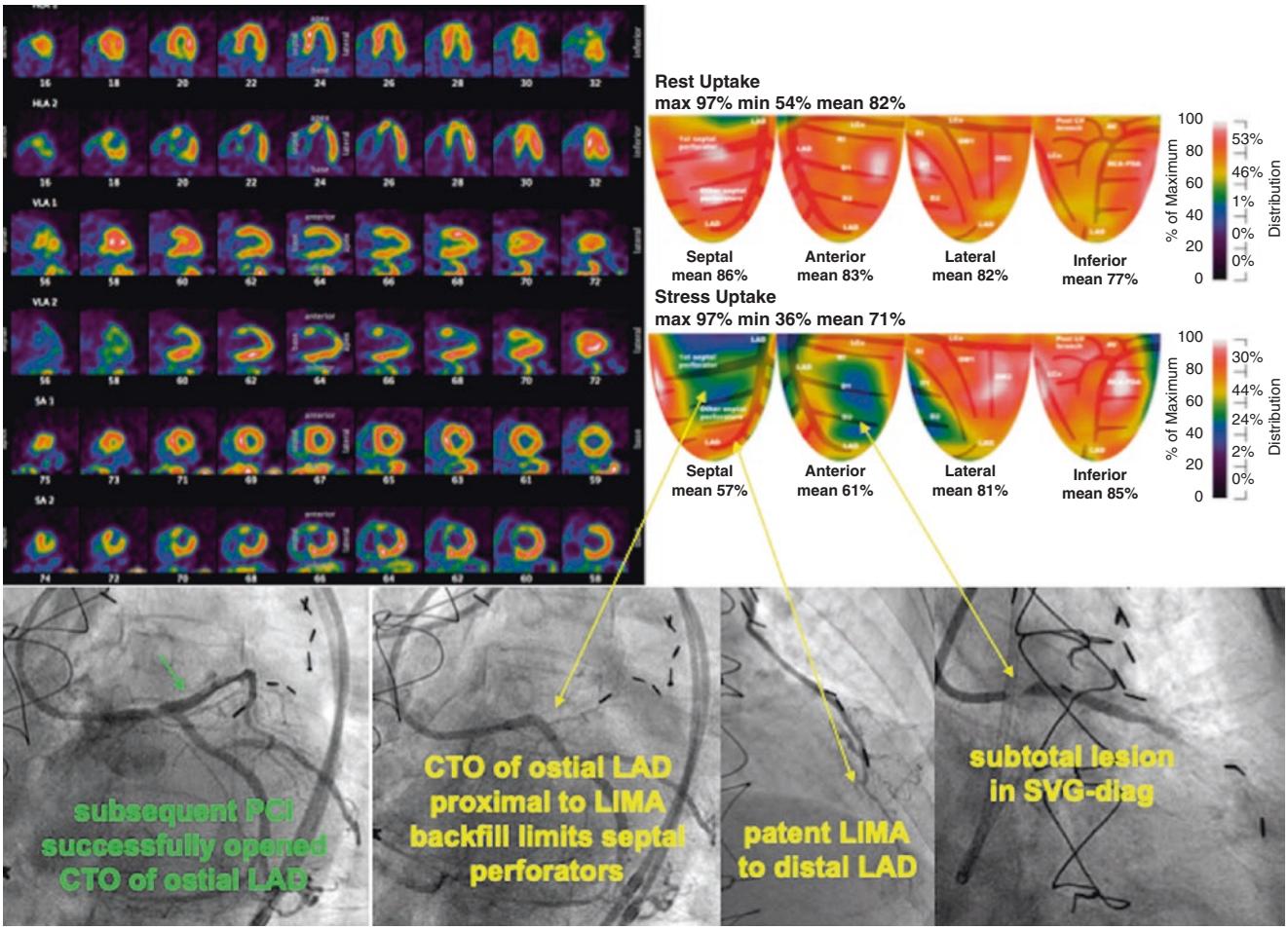

Fig. 6.86 In a patient with recurrent angina after CABG, rest-stress PET showed a large septal and moderate stress defect in a D1 distribution, indicating a patent left internal mammary artery (LIMA) to LAD graft but progressive disease proximal to the graft insertion. The proximal disease involved the first septal perforator and the first diagonal branch, producing this typical "butterfly defect" (the green areas of the septum and diagonal defects resemble wings and central yellow region in the LAD distribution with mildly reduced CFC resemble the body of a butterfly). The angiogram insets confirm the PET findings, with chronic total occlusion (CTO) of the ostial LAD and stenosis of the diagonal bypass graft. SVG saphenous vein graft

The patient in Fig. 6.87 underwent successful stenting of a severe LAD stenosis proximal to the first septal perforator, but the patient had ongoing angina for which PET was requested. The post-stent PET showed severely reduced CFC with myocardial steal; the LAD stent was occluding the first septal branch, thereby explaining continued angina, which usually resolves by progressive growth of collaterals.

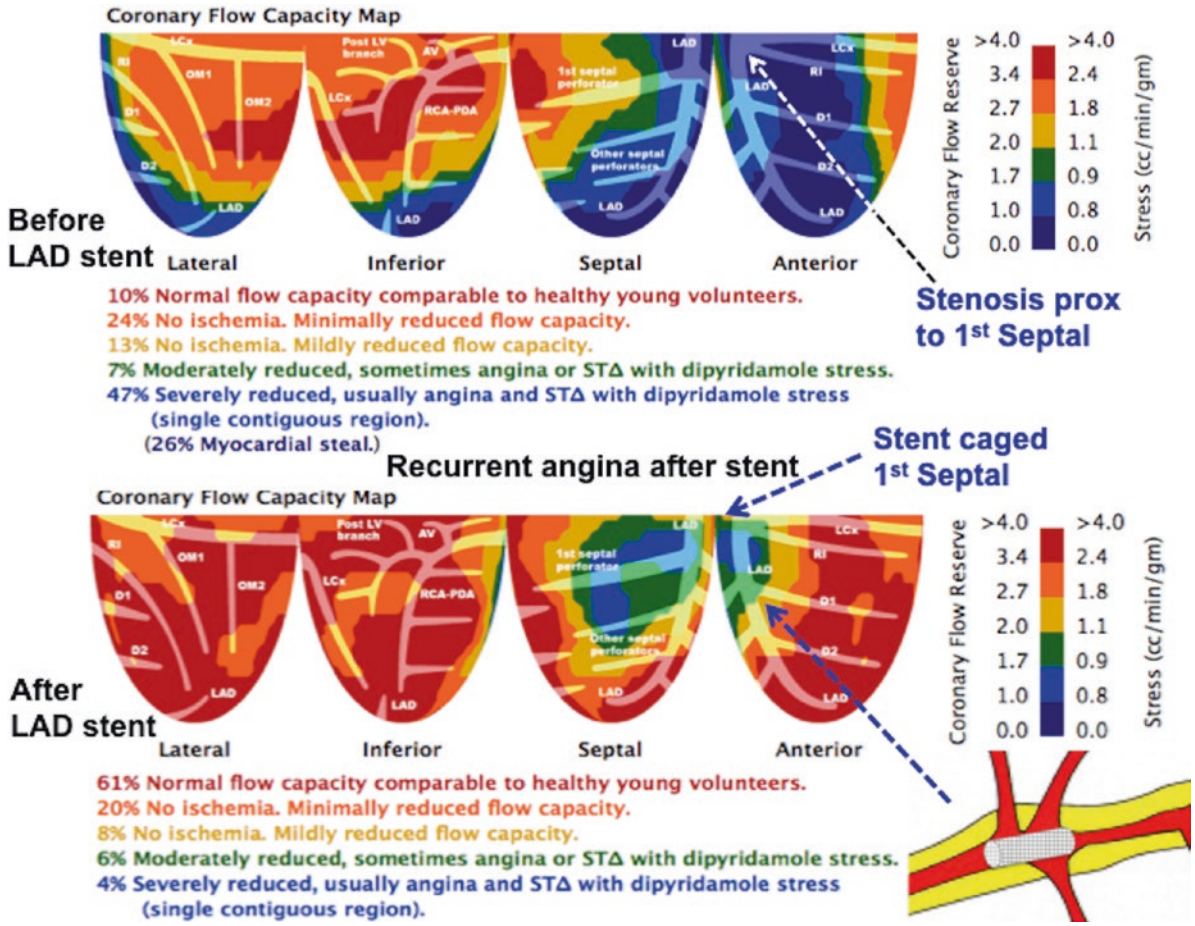

Fig. 6.87 This patient underwent successful stenting of a severe LAD stenosis proximal to the first septal perforator, which was correctly predicted by PET (*upper panel*). PET was requested because of continued angina after the LAD stent angina. The post-stent PET showed severely reduced CFC with myocardial steal indicating collaterals due to the LAD stent jailing and occluding the first septal branch, thereby explaining the continued angina. Typically, angina from septal occlusion resolves over months to a year with progressive collateral formation

Progression and Regression of CAD

Figure 6.88 shows single-quadrant views of four different patients with progression or regression on long-term follow-up of focal stenosis or diffuse CAD [82–85].

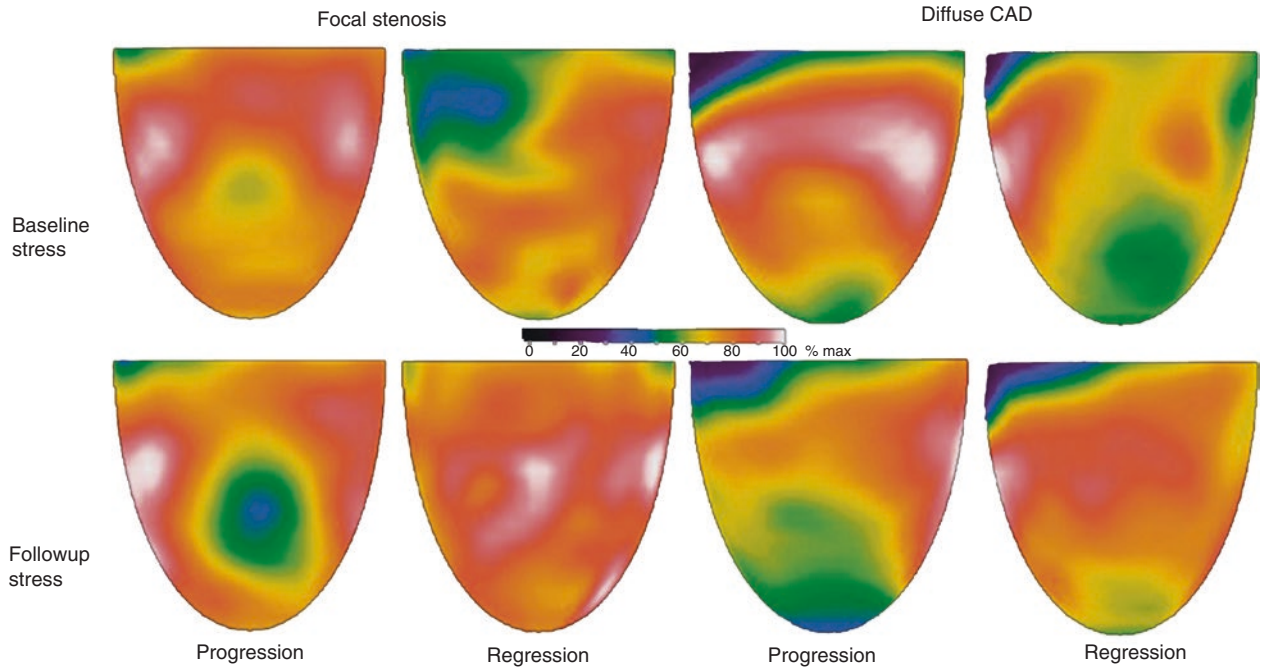

Fig. 6.88 Progression and regression of CAD four different patients, each shown at baseline (*top*) and long-term follow-up (*bottom*) with progression or regression of focal stenosis or the longitudinal base-to-apex perfusion gradient of diffuse CAD

The Unmeasured Elephants in Cardiology: Methods Thinking Versus Physiology Thinking; Subendocardial Perfusion; Low-Risk Versus High-Risk Angina

In the field of cardiac imaging, *Methods Thinking* explains many of the controversies and conflicting literature about methods and quantitative measurements, beyond differences in imaging scanners, radionuclides, and protocols. Methods Thinking means a thought silo on methodology, viewing different measurements competitively, such as CFR versus stress flow alone, or relative CFR or relative stress perfusion or relative activity images with no quantitative perfusion or longitudinal perfusion gradients, or all of these versus invasive pressure-based FFR. Methods silo thinking fails to see the essential continuum of integrated clinical physiologic quantification identifying high mortality risk that is reduced by revascularization or that incurs the lowest risk by intense lifestyle and medical treatment alone.

Figure 6.89 illustrates *Methods Thinking*. This graph shows the risk of MACE for pixel-based, size - severity abnormalities of CFC, CFR, and relative stress defect (defined as % of LV with relative activity ≤60% of maximum activity). All three PET quantitative metrics predict MACE for given size - severity. However, if CFC were not measured or plotted, narrow Methods Thinking focusing on CFR alone would conclude that CFR provides complete assessment of risk related to size-severity of abnormal quantitative perfusion. However, broader Physiologic Thinking integrating all perfusion data by also plotting size of severely reduced CFC abnormalities reveals that CFR and relative stress defects of comparable size do not provide adequate risk stratification compared to CFC.

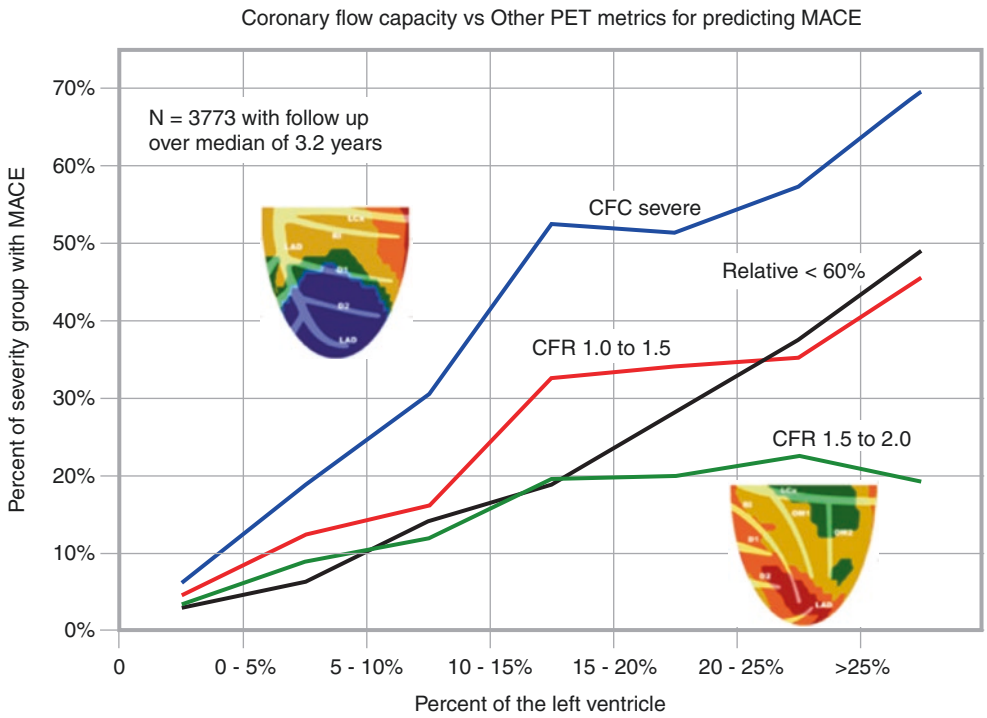

Fig. 6.89 Methods thinking

Physiology Thinking (Fig. 6.90). In addition to understanding CFC versus CFR, Physiologic Thinking explains angina and ST depression ≥1mm during dipyridamole stress with only moderately or mildly reduced CFC associated with low risk of MACE. For mildly or moderately reduced CFC, the relative tomograms show reduced subendocardial/subepicardial ratio and subendocardial ischemia. Mean transmural stress perfusion in ml/min/g is the average of high subepicardial and low subendocardial perfusion. This average may be only moderately or mildly reduced that does not reveal the transmural perfusion gradient. Physiologic thinking integrates known coronary pathophysiology with quantitative perfusion and subendocardial/subepicardial ratio on relative tomograms for clinically assessing low versus high risk angina.

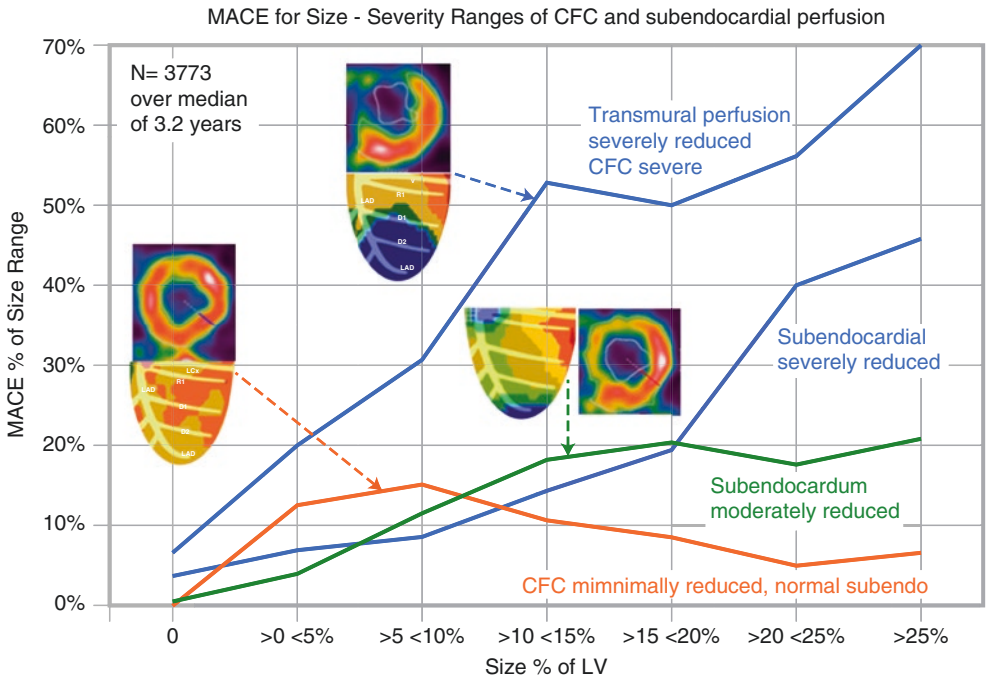

Fig. 6.90 Physiology thinking

For an asymptomatic man even during exercise, Fig. 6.91 presents an example of physiology thinking in complex CAD. All the stress perfusion abnormalities identified are in the distal distribution of the distal LAD and first obtuse marginal branch (OM1) as too small and distal for bypass surgery or stenting and well collateralized indicated by myocardial steal by PET. The large severe defect in the Left circumflex distribution (LCx) might be a revascularization target on angiogram. In view of the PET findings, repeat angiogram was recommended, to confirm the complex predominantly distal and diffuse disease and to assess the accessibility of the LCx for potential PCI. The angiogram (Fig. 6.92) confirmed the PET in each detail. Collaterals are not visible on the angiogram, but fine collaterals are commonly not visible despite physiologic evidence of their benefit by the absence of angina in daily activities, viable myocardium, and normal ejection fraction other than during dipyridamole stress with myocardial steal that does not occur during normal activities. Thus, the angiogram confirmed the PET findings of predominantly diffuse or distal disease. Because the patient had good resting LV function and no symptoms with daily activities, and the diffuse CAD was inappropriate for revascularization, the cardiologist and patient concluded that medical treatment remained the best option.

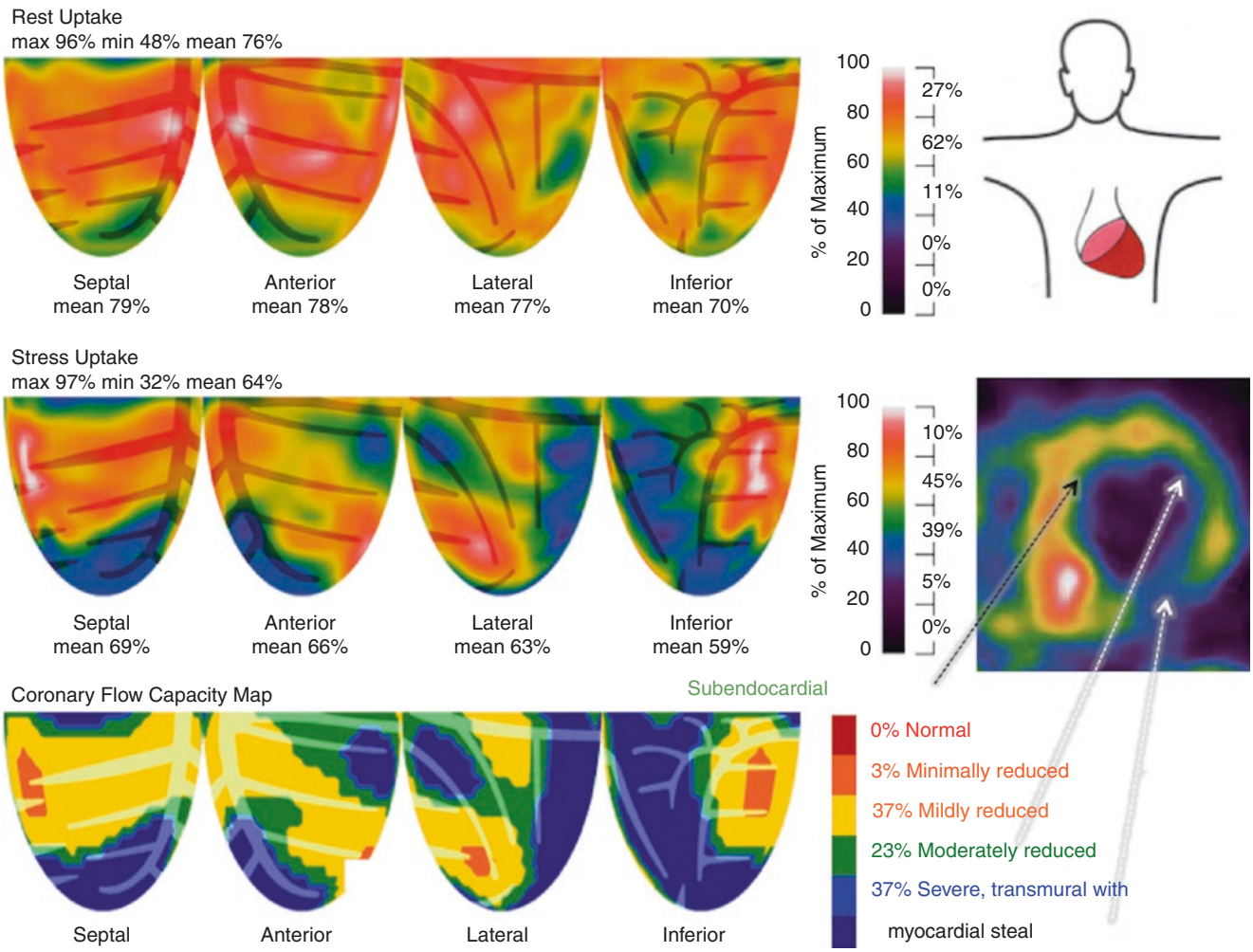

Fig. 6.91 An example of physiology thinking in complex CAD. This asymptomatic patient with stents to the LAD and RCA 2 years previously was referred for routine follow-up PET. The relative activity images show a small mid inferolateral non-transmural scar comprising 4% of LV in the typical distribution of the distal LCx (or OM3). In addition, there is a small, apical non-transmural scar comprising 3% of LV in the distal LAD distribution. With stress, the relative defects are large and severe, with CFC severely reduced to myocardial steal (*dark blue*), indicating viable myocardium with severe stenosis or occlusion and collateral perfusion in several areas: (1) the mid to distal LAD, wrapping around the apex with distal to large patent diagonals supplying the anterior wall; (2) the OM1 branch; (3) the mid LCx distal to a patent OM2; and (4) the mid RCA. CFC was mildly reduced diffusely in the remainder of the LV (*yellow*). With dipyridamole stress, the patient developed angina and 3 mm of ST depression. The ejection fraction fell from 60% to 52%, with abnormal TID of 1.28, all reflecting severe global subendocardial ischemia (as shown in the tomogram inset) in addition to regional transmural ischemia that was relieved by intravenous aminophylline, metoprolol, and sublingual nitroglycerin

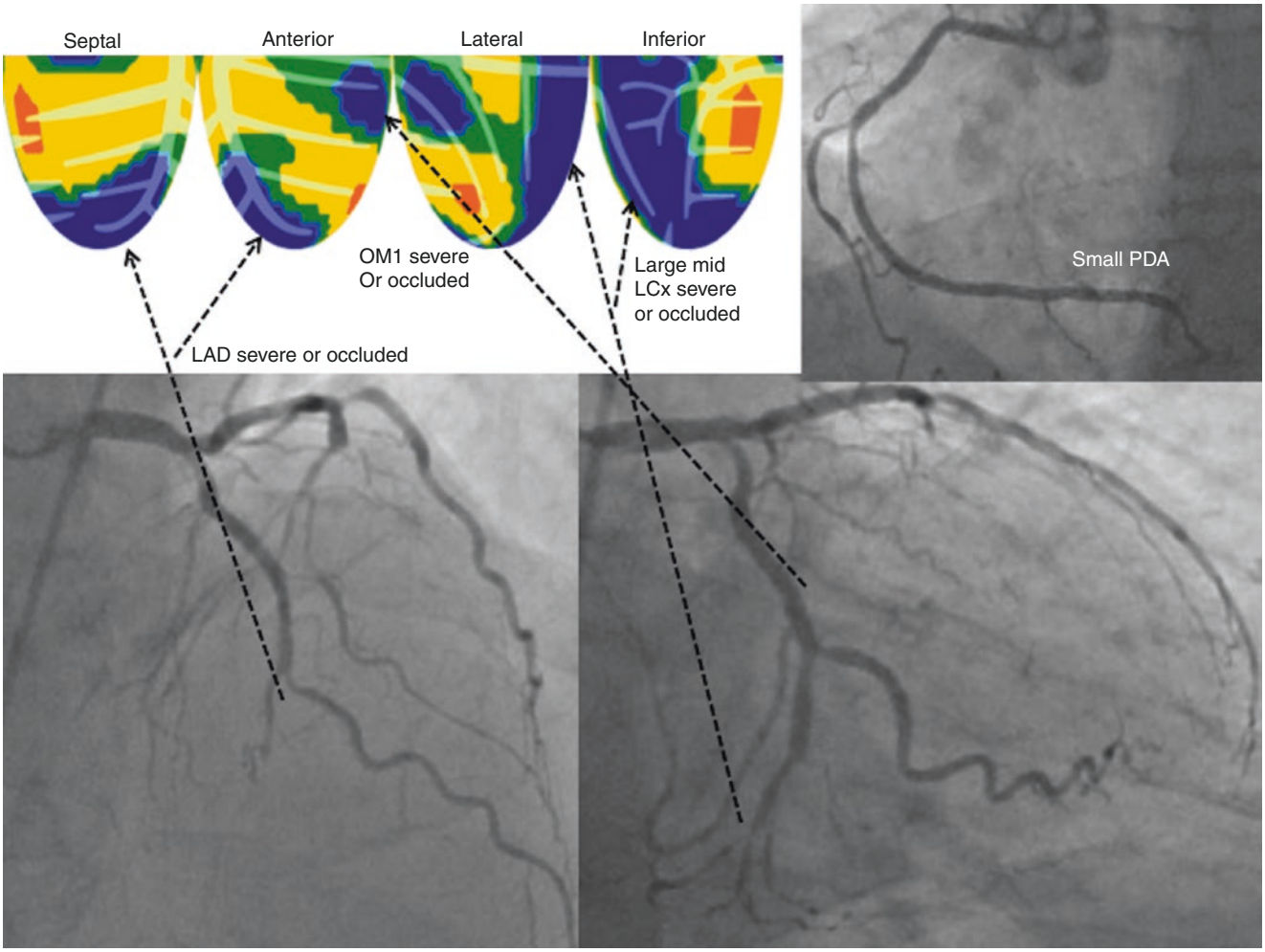

Fig. 6.92 Angiography confirming the PET findings for the patient in Fig. 6.91, showing severe diffuse distal disease of the LAD, LCx, and RCA [86]

Figure 6.93 presents an example of Methods thinking versus Physiology thinking for atypical chest pain without stenosis. The patient is a 61-year-old man with angina at rest and dyspnea on exertion without angina, poorly controlled hypertension and hyperlipidemia, dense coronary calcium, and prior stents to the LAD and LCx. Recent angiograms showed 20% diameter stenosis of LAD and RCA with patent stents. Dipyridamole stress caused definite angina and 1.2 mm ST depression, relieved by intravenous aminophylline and sublingual nitroglycerin despite very high uniform, homogeneous stress flow of 2.9 cc/min/g. These results indicate excellent small vessel function with no flow-limiting stenosis. An observer using Methods thinking would conclude that the quantitative measurements—stress perfusion, CFR, and CFC—are wrong or useless because they are not associated with definite angina and significant ST depression during stress. However, open-minded Physiology thinking about the data provides an important physiologic insight. With diffuse epicardial CAD and preserved small vessel function, the high coronary blood flow during dipyridamole stress generates falling coronary pressure owing to

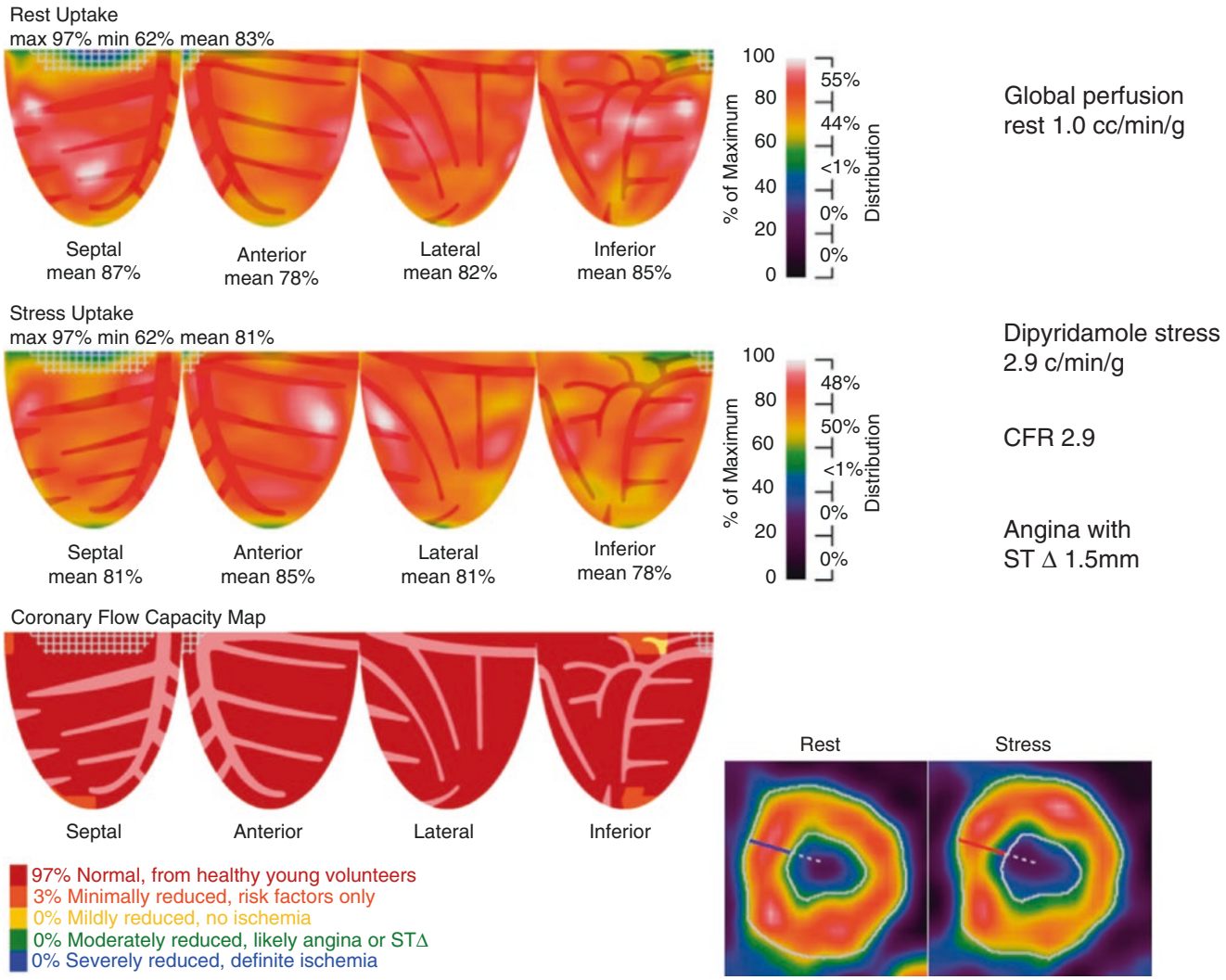

Fig. 6.93 Methods thinking versus physiology thinking for atypical chest pain without stenosis

viscous energy loss, with resulting subendocardial ischemia shown in the tomographic view. The *white dashed lines* outline the endocardial borders of the resting relative images projected onto the stress image, revealing global reduction of subendocardial perfusion, causing angina and ST depression, quantitatively analyzed in Fig. 6.94. All the results shown there are consistent with global subendocardial ischemia manifest as angina and significant ST depression during dipyridamole stress. In this case, the high stress perfusion at peak mid-wall activity is high enough to preclude a longitudinal base-to-apex gradient, as may be seen with more severe diffuse narrowing or combined stenosis plus diffuse CAD. The comprehensive physiologic data in this case explain ischemia during dipyridamole stress and, with the clinical history, suggest an element of coronary spasm associated with endothelial dysfunction of diffuse CAD needing intense management of angina and risk factors. In our database of 8000 cases with 10-year follow-up, a normal CFC is associated with a low risk of adverse events if medical treatment is adequate, as in the plots in Fig. 6.64.

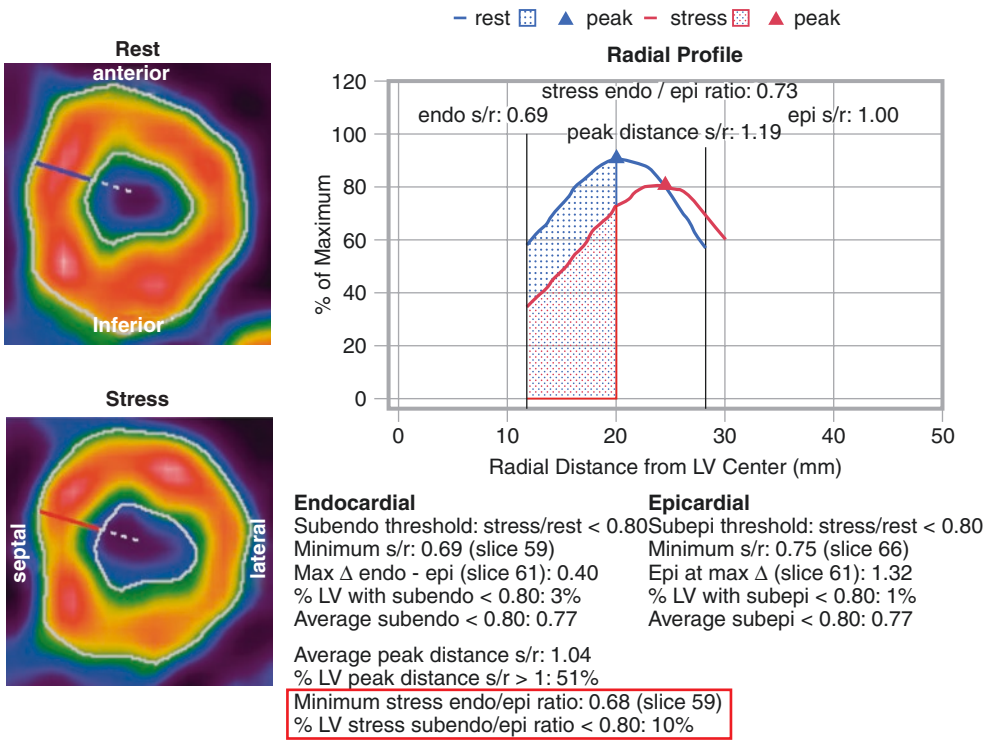

Fig. 6.94 Quantitative subendocardial analysis of the patient in Fig. 6.93. The *blue line* plots the radial relative activity profile of the rest tomogram slice, and the *red line* plots the stress radial relative activity profile of the stress tomogram slice. The distance from peak activity of the rest profile to the rest endocardial boundary defines the subendocardium. The subendocardial stress/rest ratio is the area under the red profile divided by the area under the blue profile for each of 64 radii of 20 tomographic slices for the whole LV. The stress subendo/epicardial ratio is the ratio of the subendocardial half of each radius divided by the subepicardial half of each radius across the LV wall. As outlined by the *red box*, the minimum stress subendo/epicardial ratio is 0.68, and 10% of the LV has a subendo/epicardial ratio <0.8

Figure 6.95 illustrates a case example of Physiology thinking for atypical chest pain without stenosis in a 77-year-old woman who had hypertension, hyperlipidemia, insulin-dependent diabetes, a strong family history of CAD, and dense coronary calcium by CT. More than 7 years after PCI and 4 years after a normal PET, she developed non-exertional chest pain radiating down her left arm, which she associated with spikes in blood sugar and systolic blood pressure. Because of her atypical symptoms, rest-stress PET was done. Both CFC and FFRpet at the apex were worse than on PET 4 years previously, indicating mild progression of diffuse CAD, primarily of the LAD wrapping around the apex. The short-axis relative tomo-

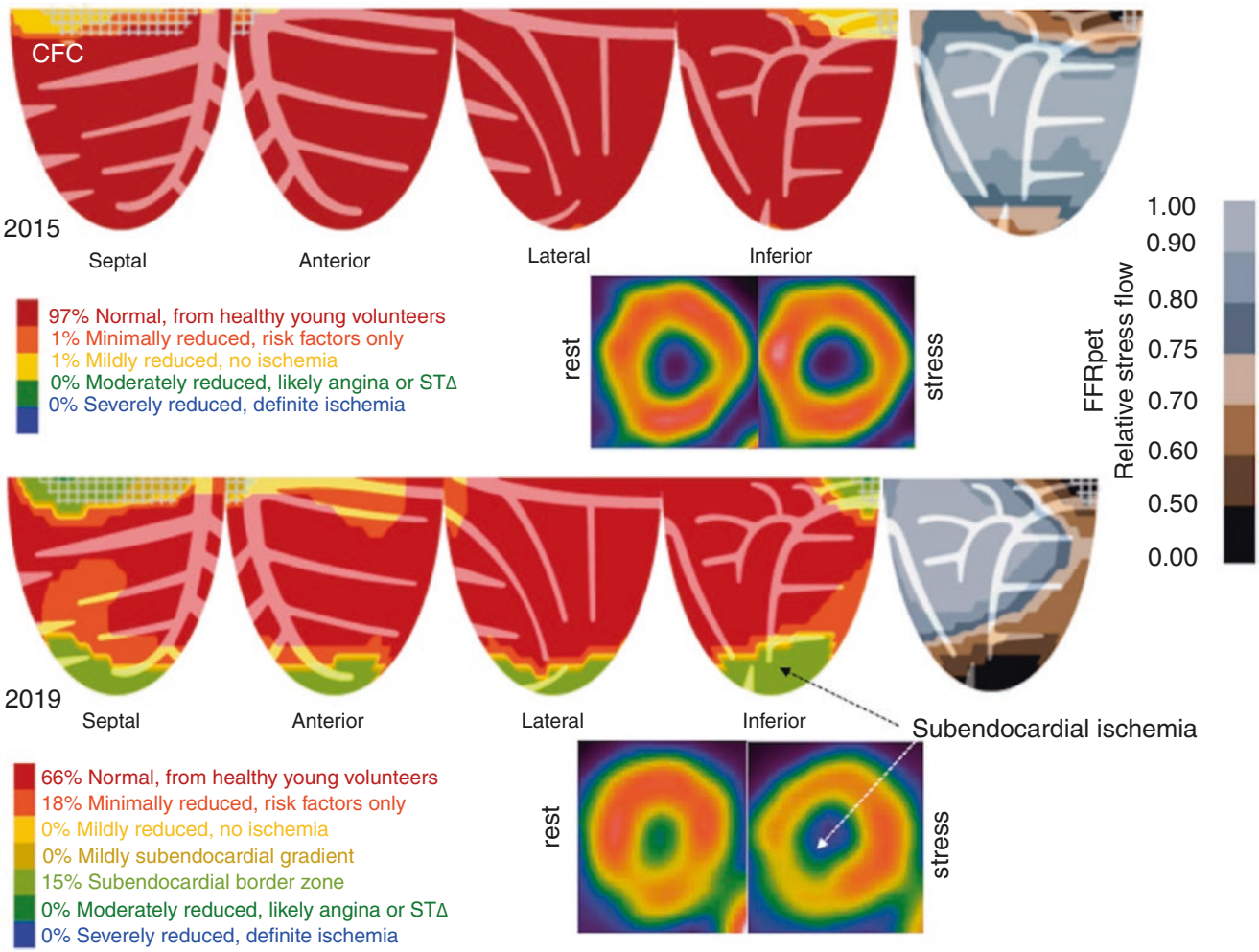

Fig. 6.95 Physiology thinking for atypical chest pain without stenosis in a 77-year-old woman who had hypertension, hyperlipidemia, insulin-dependent diabetes, a strong family history of CAD, and dense coronary calcium by CT. She underwent PCI of the RCA for angina 8 years previously. A PET 4 years previously (top) was normal, with no angina and no STΔ during dipyridamole stress. She was subsequently asymptomatic until the last 6 months, when she developed non-exertional chest pain radiating down her left arm. She definitely associated it with her blood sugar spiking to 300 mg/dL and systolic blood pressure spikes to over 180 mm Hg. Because of her atypical symptoms, rest-stress PET was done. Initial baseline blood pressure was 180/98, falling to 132/88 before stress imaging. With dipyridamole stress, she developed definite typical, moderately severe angina radiating down her left arm with 1.5 mm ST depression relieved by aminophylline (150 mg) and metoprolol (5 mg). Her PET showed high average global resting perfusion at 1.7 cc/min/g, consistent with hypertension, and high average global stress perfusion of 2.5 mL/min/g with no regional abnormalities. Ejection fraction was 77% at rest and 75% with stress, both excellent, within the range of method repeatability. Her CFC (bottom), shown in four quadrant views with the relative map of stress cc/min/g, and FFRpet (in a single inferior view) was excellent and well above ischemic levels for average transmural perfusion except at the apex. At the apex, the relative map of stress cc/min/g (FFRpet) was 0.5. Both CFC and FFRpet at the apex were worse than on PET 4 years previously, indicating mild progression of diffuse CAD, primarily of the LAD wrapping around the apex. The short-axis relative tomograms showed low subendocardial perfusion at the apex, objectively quantified in Fig. 6.96, thereby explaining her dipyridamole-induced angina and ST depression

grams showed low subendocardial perfusion at the apex, objectively quantified in Fig. 6.96, thereby explaining her dipyridamole-induced angina and ST depression. The occurrence of her angina with blood glucose spikes is consistent with its documented impairment of endothelial-mediated vasodilatation, thereby causing spiking blood pressure, increased coronary blood flow demands, diffuse coronary constriction, and thence subendocardial ischemia exacerbated by her left ventricular hypertrophy, which further compromises subendocardial perfusion. Again, "Physiology thinking" and comprehensive integrated quantification explained heratypical symptoms, which needed more intense risk factor management for low-risk angina.

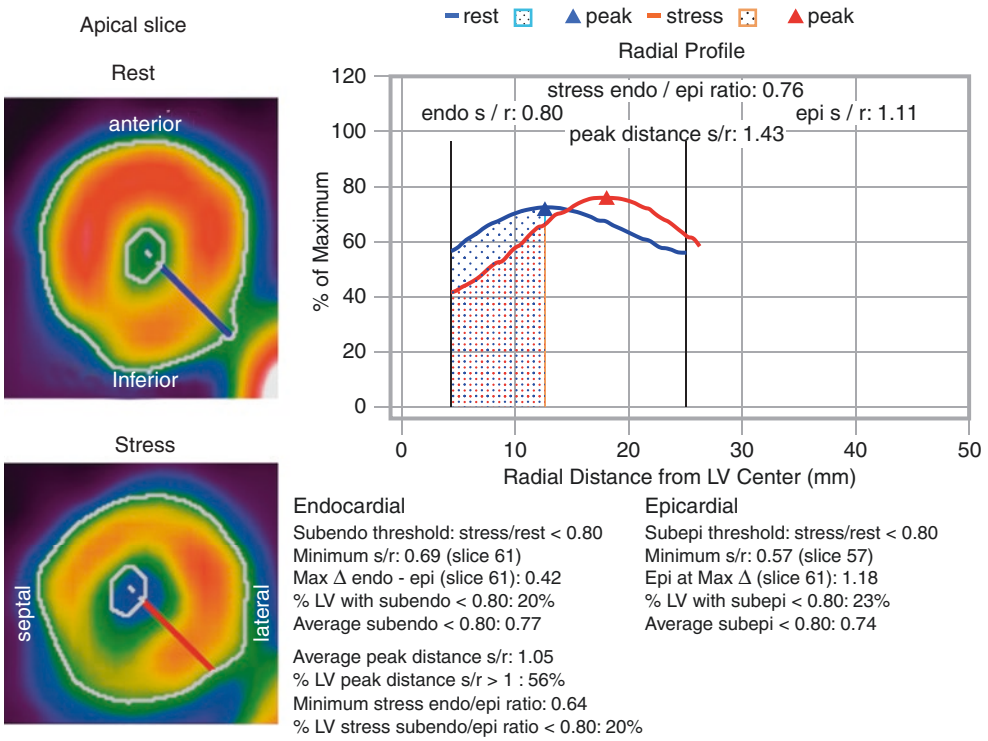

Fig. 6.96 Subendocardial analysis for the woman in Fig. 6.95, whose angina and ST change during dipyridamole PET stress are explained by mild apical subendocardial ischemia, as objectively quantified: minimum subendocardial stress/rest ratio, 0.69; average subendocardial stress/rest ratio, 0.77; 20% of LV with subendocardial stress/rest ratio <0.8; minimum stress subendo/epicardial ratio, 0.64; and 22% of LV with subendo/epicardial ratio <0.8—all results that indicate mild apical subendocardial ischemia manifest as angina and significant ST depression during dipyridamole stress. These objective findings indicate mild diffuse epicardial narrowing with excellent small vessel function sufficient to maximize coronary flow (2.5 cc/min/g) that generates a pressure gradient along the LAD, and therefore the low FFRpet and low subendocardial perfusion causing angina and ST changes

In randomized trials of revascularization guided by angiography or FFR, angina relief fails to reduce the rate of subsequent MI or death. The data and case examples in this chapter suggest a potential explanation for this apparent paradox. The case examples of severely reduced CFC (*blue*), indicating severely reduced transmural perfusion with angina (as in Figs. 6.2, 6.46, 6.54, 6.55, 6.62, 6.63, 6.74, 6.76, 6.79, 6.84, 6.85, 6.87, and 6.91) are associated with high risk of death, MI, or stroke—as shown in Fig. 6.64; the risk is reduced by revascularization in Fig. 6.65. However—as in Figs. 6.26 and 6.74 (after PCI), 6.78a, b, and e, 6.81, 6.87 (after PCI), 6.93, and 6.95—mild to moderately reduced CFC (*yellow* or *green*) is associated with low risk of death, MI, or stroke, as seen in the Kaplan Meier plots of Fig. 6.64; the risk in these cases may actually be increased by revascularization (as in Fig. 6.65) because the risk of the procedure is greater than the risk from medical treatment alone. In these cases of mild to moderately reduced CFC, angina is due to reduced subendocardial perfusion that does not reach transmural severity associated with high risk.

Moreover, abnormal subendocardial perfusion not reaching the high-risk transmural severity threshold for ischemia reveals the unpredictability of angina for mild to moderately reduced stress perfusion CFR or CFC. For example, stress perfusion CFC and subendocardial metrics for cases with dipyridamole-induced angina and significant STΔ in Figs. 6.93–6.94

and 6.95–6.96 are comparable or less severe than the case example in Figs. 6.81 and 6.82, which had no angina or ECG changes during dipyridamole or exercise stress.

The patient in Figs. 6.95 and 6.96 had initial blood pressure of 180 mm Hg with corresponding high resting perfusion of 1.7 cc/min/g, indicating high flow demands that may cause ischemia despite high stress perfusion of 2.8 cc/min/g. Her FFRpet dropped to <0.5 at the apex, suggesting a severe gradient along the LAD length, which, with LV hypertrophy and high flow demand of hypertension and dipyridamole tachycardia, explained her angina.

Finally, patients in Figs. 6.74, 6.75, 6.81, 6.82, 6.91, 6.92, 6.93, 6.94, 6.95, and 6.96 had angina and significant ECG ST depression during dipyridamole stress. However, the patients in Figs. 6.81 and 6.91 had no angina and the patient in Figs. 6.95 and 6.96 had angina only when blood sugar exceeded 300 mg/dL with no exertional angina. Of all cases with severely reduced CFC only 48% had angina or significant ST depression with dipyridamole stress. Of patients with no severely reduced CFC but reduced subendocardial perfusion, only 23% had angina or significant ST depression with dipyridamole stress.

Clinical "subendocardial ischemia" (angina with STΔ >1 mm) and FFR <0.8, are commonly invoked to justify revascularization. However, we observe reduced relative subendocardial perfusion or FFRpet <0.8 commonly with no angina or STΔ associated with exercise or dipyridamole stress. With no severely reduced CFC, such patients have a low risk of MACE that is not reduced (and may be increased) by revascularization. These examples illustrate that quantifying physiologic severity of CAD underlying angina and "Physiology Thinking" are essential for understanding each patient's symptoms and coronary physiology, for their fully informed consent, and for individualized optimal management of low-risk angina versus high-risk angina.

Figure 6.97 summarizes CFC, low-risk angina, high-risk angina, and subendocardial perfusion.

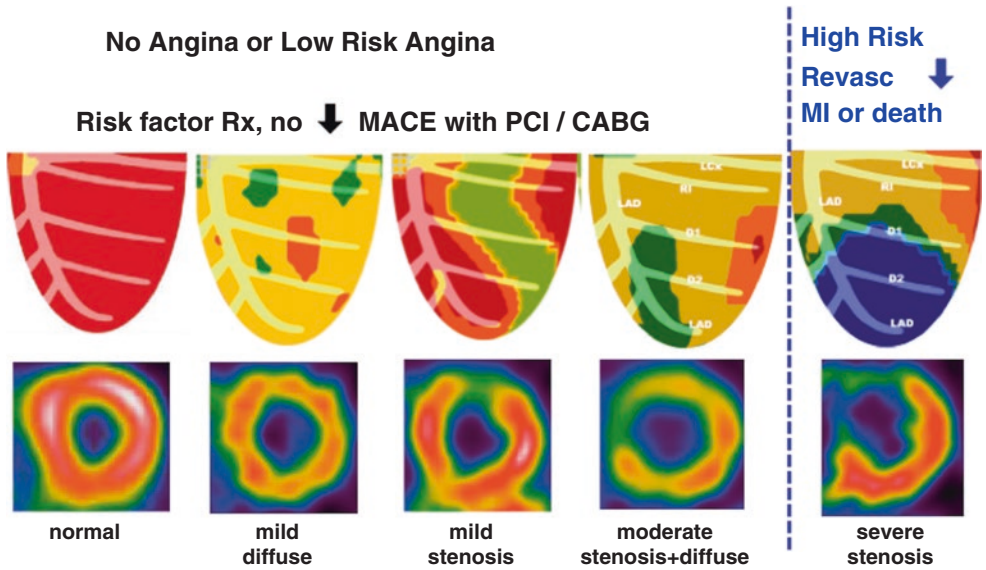

Fig. 6.97 Summary of CFC, low-risk angina, high-risk angina, and subendocardial perfusion

Subendocardial perfusion is the unmeasured elephant in cardiology, here related to mild or moderately reduced CFC (*yellow* or *green*), where the reduced relative subendocardial perfusion does not extend to severely reduced transmural perfusion. High-risk angina corresponds to severely reduced transmural CFC (*blue* CFR ≤1.3 and stress cc/min/g ≤0.8; see Figs. 6.51 and 6.52), for which revascularization reduces risk of death or MI (*see* Fig. 6.65).

Financial Support and Relationships with Industry Research supported by internal funds of the Weatherhead PET Center.

NPJ received institutional licensing and consulting agreement with Boston Scientific for the smart minimum FFR algorithm; received significant institutional research support from St. Jude Medical (CONTRAST, NCT02184117) and Philips Volcano Corporation (DEFINE-FLOW, NCT02328820) for studies using intracoronary pressure and flow sensors; and has a patent pending on diagnostic methods for quantifying aortic stenosis and TAVI physiology.

KLG receives internal funding from the Weatherhead PET Center for Preventing and Reversing Atherosclerosis and is the 510(k) applicant for FDA approved HeartSee K171303 PET software. To avoid any conflict of interest, KLG has assigned any royalties to the University of Texas for research or student scholarships; has no consulting, speakers, or board agreements; and receives no funding from PET-related or other corporate entities.

References

1. Gould KL, Lipscomb K, Hamilton GW. Physiologic basis for assessing critical coronary stenosis. Instantaneous flow response and regional distribution during coronary hyperemia as measures of coronary flow reserve. Am J Cardiol. 1974;33:87–94.
2. Gould KL, Gewirtz H, Narula J. Coronary blood flow and myocardial ischemia. In: Fuster V, Harrington RA, Narula J, Eapen ZJ, editors. Hurst's the heart. 14th ed. New York: McGraw Hill; 2017. p. 893–922.
3. Gould KL, Hamilton GW, Lipscomb K, Kennedy JW. A method for assessing stress induced regional malperfusion during coronary arteriography: experimental validation and clinical application. Am J Cardiol. 1974;34:557–64.
4. Gould KL. Noninvasive assessment of coronary stenoses by myocardial perfusion imaging during pharmacologic coronary vasodilatation. I. Physiologic basis and experimental validation. Am J Cardiol. 1978;41:267–78.
5. Gould KL, Westcott JR, Albro PC, Hamilton GW. Noninvasive assessment of coronary stenoses by myocardial imaging during coronary vasodilatation. II. Clinical methodology and feasibility. Am J Cardiol. 1978;41:279–87.
6. Albro PC, Gould KL, Westcott RJ, Hamilton GW, Ritchie JL, Williams DL. Noninvasive assessment of coronary stenoses by myocardial imaging during pharmacologic coronary vasodilatation. III. Clinical trial. Am J Cardiol. 1978;42:751–60.
7. Gould KL. Assessment of coronary stenoses by myocardial perfusion imaging during pharmacologic coronary vasodilatation. IV. Limits of stenosis detection by idealized, experimental, cross-sectional myocardial imaging. Am J Cardiol. 1978;42:761–8.
8. Gould KL, Schelbert HR, Phelps ME, Hoffman EJ. Noninvasive assessment of coronary stenoses with myocardial perfusion imaging during pharmacologic coronary vasodilatation. V. Detection of 47 percent diameter coronary stenosis with intravenous nitrogen-13 ammonia and emission-computed tomography in intact dogs. Am J Cardiol. 1979;43:200–8. *Awarded the George von Hevesy Prize for Research in Nuclear Medicine, at the World Federation of Nuclear Medicine, September 17, 1978, Washington, DC*.
9. Schelbert HR, Wisenberg G, Phelps ME, Gould KL, Eberhard H, Hoffman EJ, et al. Noninvasive assessment of coronary stenosis by myocardial imaging during pharmacologic coronary vasodilation. VI. Detection of coronary artery disease in man with intravenous N-13 ammonia and positron computed tomography. Am J Cardiol. 1982;49:1197–207.
10. Kirkeeide R, Gould KL, Parsel L. Assessment of coronary stenoses by myocardial imaging during coronary vasodilation. VII. Validation of coronary flow reserve as a single integrated measure of stenosis severity accounting for all its geometric dimensions. J Am Coll Cardiol. 1986;7:103–13.
11. Gould KL, Goldstein RA, Mullani N, Kirkeeide R, Wong G, Smalling R, et al. Noninvasive assessment of coronary stenoses by myocardial imaging during pharmacologic coronary vasodilation. VIII. Feasibility of 3D cardiac positron imaging without a cyclotron using generator produced Rb-82. J Am Coll Cardiol. 1986;7:775–92.
12. Gould KL, Kirkeeide R, Johnson NP. Coronary branch steal – experimental validation and clinical implications of interacting stenosis in branching coronary arteries. Circ Cardiovasc Imaging. 2010;3:701–9.
13. Gould KL, Nakagawa Y, Nakagawa N, Sdringola S, Hess MJ, Haynie M, et al. Frequency and clinical implications of fluid dynamically significant diffuse coronary artery disease manifest as graded, longitudinal, base to apex, myocardial perfusion abnormalities by non-invasive positron emission tomography. Circulation. 2000;101:1931–9.
14. Gould KL. Coronary artery stenosis and reversing atherosclerosis. 2nd ed. London: Arnold Publishers; 1999. *A textbook of coronary pathophysiology, quantitative coronary arteriography, and cardiac PET.*
15. De Bruyne B, Hersbach F, Pijls NH, Bartunek J, Bech JW, Heyndrickx GR, et al. Abnormal epicardial coronary resistance in patients with diffuse atherosclerosis but "Normal" coronary angiography. Circulation. 2001;104:2401–6.
16. Johnson NP, Kirkeeide RL, Gould KL. Is discordance of coronary flow reserve and fractional flow reserve due to methodology or clinically relevant coronary pathophysiology? Supplement JACC Cardiovasc Imaging. 2012;5:193–202.
17. Lipscomb K, Gould KL. Mechanism of the effect of coronary artery stenosis on coronary flow in the dog. Am Heart J. 1975;89:60–7.
18. Gould KL, Kirkeeide RL, Buchi M. Coronary flow reserve as a physiologic measure of stenosis severity. Part I. Relative and absolute coronary flow reserve during changing aortic pressure and cardiac workload. Part II. Determination from arteriographic stenosis dimensions under standardized conditions. J Am Coll Cardiol. 1990;15:459–74.
19. Pijls NHJ, van Son JAM, Kirkeeide RL, Bruyne BD, Gould KL. Experimental basis of determining maximal coronary myocardial and collateral blood flow by pressure measurements for assessing functional stenosis severity before and after PTCA. Circulation. 1993;86:1354–67.
20. Smalling RW, Kelley K, Kirkeeide RL, Fisher DJ. Regional myocardial function is not affected by severe coronary depressurization provided coronary blood flow is maintained. J Am Coll Cardiol. 1985;5:948–55.
21. Seiler C. Collateral circulation of the heart. Dordrecht: Springer; 2009.
22. Gould KL, Kelley KO, Bolson EL. Experimental validation of quantitative coronary arteriography for determining pressure-flow characteristics of coronary stenoses. Circulation. 1982;66:930–7.
23. Gould KL, Kelley KO. Physiological significance of coronary flow velocity and changing stenosis geometry during coronary vasodilation in awake dogs. Circ Res. 1982;50:695–704.
24. Hoffman JIE, Buckberg GD. The myocardial oxygen supply:demand index revisited. J Am Heart Assoc. 2014;3:e000285. https://doi.org/10.1161/JAHA.113.000285.
25. Gould KL, Johnson NP. Coronary physiology: beyond CFR in microvascular angina. J Am Coll Cardiol. 2018;72:2642–62.
26. Danad I, Raijmakers PG, Harms HJ, Heymans MW, van Royen N, Lubberink M, et al. Impact of anatomical and functional severity of coronary atherosclerotic plaques on the transmural perfusion gradient: a [^{15}O]H_2O PET study. Eur Heart J. 2014;35:2094–105.
27. Gould KL, Johnson NP, Bateman TM, Beanlands RS, Bengel FM, Bober R, et al. Anatomic versus physiologic assessment of coronary artery disease: role of CFR, FFR, and PET imaging in revascularization decision-making. J Am Coll Cardiol. 2013;62:1639–53.
28. Gupta A, Taqueti VR, van de Hoef TP, Bajaj NS, Bravo PE, Murthy VL, et al. Integrated noninvasive physiological assessment of coronary circulatory function and impact on cardiovascular mortality in patients with stable coronary artery disease. Circulation. 2017;136:2325–36.
29. Danad I, Raijmakers PG, Appelman YE, Harms HJ, de Haan S, van den Oever ML, et al. Hybrid imaging using quantitative $H_2{}^{15}O$ PET and CT-based coronary angiography for the detection of coronary artery disease. J Nucl Med. 2013;54:55–63.
30. Gewirtz H, Dilsizian V. Integration of quantitative positron emission tomography absolute myocardial blood flow measurements in the clinical management of coronary artery disease. Circulation. 2016;133:2180–96.
31. Driessen RS, Danad I, Stuijfzand WJ, Raijmakers PG, Schumacher SP, van Diemen PA, et al. Comparison of coronary computed tomog-

raphy angiography, fractional flow reserve, and perfusion imaging for ischemia diagnosis. J Am Coll Cardiol. 2019;73:161–73.
32. Danad I, Raijmakers PG, Driessen RS, Leipsic J, Raju R, Naoum C, et al. Comparison of coronary CT angiography, SPECT, PET, and hybrid imaging for diagnosis of ischemic heart disease determined by fractional flow reserve. JAMA Cardiol. 2017;2:1100–7.
33. Maaniitty T, Stenström I, Bax JJ, Uusitalo V, Ukkonen H, Kajander S, et al. Prognostic value of coronary CT angiography with selective PET perfusion imaging in coronary artery disease. JACC Cardiovasc Imaging. 2017;10:1361–70.
34. Knuuti J, Ballo H, Juarez-Orozco LE, Saraste A, Kolh P, Rutjes AW, et al. The performance of non-invasive tests to rule-in and rule-out significant coronary artery stenosis in patients with stable angina: a meta-analysis focused on post-test disease probability. Eur Heart J. 2018;39:3322–30.
35. Koo BK, Erglis A, Doh JH, Daniels DV, Jegere S, Kim HS, et al. Diagnosis of ischemia-causing coronary stenoses by noninvasive fractional flow reserve computed from coronary computed tomographic angiograms. Results from the prospective multicenter DISCOVER-FLOW (Diagnosis of Ischemia-Causing Stenoses Obtained Via Noninvasive Fractional Flow Reserve) study. J Am Coll Cardiol. 2011;58:1989–97.
36. Tu S, Barbato E, Koszegi Z, Yang J, Sun Z, Holm N, et al. Fractional flow reserve calculation from 3-dimensional quantitative coronary angiography and TIMI frame count. JACC Cardiovasc Interv. 2014;7:768–77.
37. Murthy VL, Naya M, Taqueti VR, Foster CR, Gaber M, Hainer J, et al. Effects of sex on coronary microvascular dysfunction and cardiac outcomes. Circulation. 2014;129:2518–27.
38. Stenström I, Maaniitty T, Uusitalo V, Pietilä M, Ukkonen H, Kajander S, et al. Frequency and angiographic characteristics of coronary microvascular dysfunction in stable angina: a hybrid imaging study. Eur Heart J Cardiovasc Imaging. 2017;18:1206–13.
39. Gould KL, Johnson NP, Roby AE, Nguyen T, Kirkeeide R, Haynie M, et al. Regional artery specific thresholds of quantitative myocardial perfusion by PET associated with reduced MI and death after revascularization in stable coronary artery disease. J Nucl Med. 2019;60:410–7.
40. Gould KL. Does coronary flow trump coronary anatomy? JACC Cardiovasc Imaging. 2009;2:1009–23.
41. Sdringola S, Johnson NP, Kirkeeide RL, Cid E, Gould KL. Impact of unexpected factors on quantitative myocardial perfusion and coronary flow reserve in young, asymptomatic volunteers. JACC Cardiovasc Imaging. 2011;4:402–12.
42. Johnson NP, Gould KL. Physiologic basis for angina and ST change: PET-verified thresholds of quantitative stress myocardial perfusion and coronary flow reserve. JACC Cardiovasc Imaging. 2011;4:990–8. *Awarded the 2011 Young Author Achievement Award by the Journal of the American College of Cardiology Cardiovascular Imaging.*
43. Johnson NP, Gould KL. Integrating noninvasive absolute flow, coronary flow reserve, and ischemic thresholds into a comprehensive map of physiologic severity. JACC Cardiovasc Imaging. 2012;5:430–40.
44. Johnson NP, Pijls NH, De Bruyne B, Bech GJ, Kirkeeide RL, Gould KL. A black and white response to the "gray zone" for fractional flow reserve measurements. JACC Cardiovasc Interv. 2014;7:227–8.
45. Johnson NP, Gould KL. Regadenoson versus dipyridamole hyperemia for cardiac PET imaging. JACC Cardiovasc Imaging. 2015;8:438–47.
46. Johnson NP, Gould KL, Di Carli MF, Taqueti VR. Invasive FFR and noninvasive CFR in the evaluation of ischemia: what is the future? J Am Coll Cardiol. 2016;67:2772–88.
47. Kitkungvan D, Johnson NP, Roby AE, Patel MB, Kirkeeide R, Gould KL. Routine clinical quantitative rest stress myocardial perfusion for managing coronary artery disease: clinical relevance of test-retest variability. JACC Cardiovasc Imaging. 2017;10:565–77.
48. Kitkungvan D, Lai D, Zhu H, Roby AE, Johnson NP, Steptoe DD, et al. Optimal adenosine stress for maximum stress perfusion, coronary flow reserve, and pixel distribution of coronary flow capacity by Kolmogorov-Smirnov analysis. Circ Cardiovasc Imaging. 2017;10. pii:e005650. https://doi.org/10.1161/CIRCIMAGING.116.005650.
49. Gould KL, Schelbert H, Narula J. Positron emission tomography in heart disease. In: Fuster V, Harrington RA, Narula J, Eapen ZJ, editors. Hurst's the heart. 14th ed. New York: McGraw Hill; 2017. p. 553–605.
50. Javadi MS, Lautamäki R, Merrill J, Voicu C, Epley W, McBride G, Bengel FM. Definition of vascular territories on myocardial perfusion images by integration with true coronary anatomy: a hybrid PET/CT analysis. J Nucl Med. 2010;51:198–203.
51. Bom MJ, Schumacher SP, Driessen RS, Raijmakers PG, Everaars H, van Diemen PA, et al. Impact of individualized segmentation on diagnostic performance of quantitative positron emission tomography for haemodynamically significant coronary artery disease. Eur Heart J Cardiovasc Imaging. 2019;20:525–32. https://doi.org/10.1093/ehjci/jey201.
52. Ortiz-Perez JT, Rodriguez J, Meyers SN, Lee DC, Davidson C, Wu E. Correspondence between the 17-segment model and coronary arterial anatomy using contrast-enhanced cardiac magnetic resonance imaging. JACC Cardiovasc Imaging. 2008;1:282–93.
53. Pereztol-Valdés O, Candell-Riera J, Santana-Boado C, Angel J, Aguadé-Bruix S, Castell-Conesa J, et al. Correspondence between left ventricular 17 myocardial segments and coronary arteries. Eur Heart J. 2005;26:2637–43.
54. Thomassen A, Petersen H, Johansen A, Braad PE, Diederichsen AC, Mickley H, et al. Quantitative myocardial perfusion by O-15-water PET: individualized vs. standardized vascular territories. Eur Heart J Cardiovasc Imaging. 2015;16:970–6.
55. Donato P, Coelho P, Santos C, Bernardes A, Caseiro-Alves F. Correspondence between left ventricular 17 myocardial segments and coronary anatomy obtained by multi-detector computed tomography: an ex vivo contribution. Surg Radiol Anat. 2012;34:805–10.
56. Cerci RJ, Arbab-Zadeh A, George RT, Miller JM, Vavere AL, Mehra V, et al. Aligning coronary anatomy and myocardial perfusion territories: an algorithm for the CORE320 multicenter study. Circ Cardiovasc Imaging. 2012;5:587–95.
57. Yoshida K, Mullani N, Gould KL. Coronary flow and flow reserve by positron emission tomography simplified for clinical application using Rb-82 or N-13 ammonia. J Nucl Med. 1996;37:1701–12.
58. Vasquez AF, Johnson NP, Gould KL. Variation in quantitative myocardial perfusion due to arterial input selection. JACC Cardiovasc Imaging. 2013;6:559–68.
59. Bachrach SL, Carson RE. In hot blood—quantifying the arterial input. JACC Cardiovasc Imaging. 2013;6:569–73.
60. Renaud JM, DaSilva JN, Beanlands RS, DeKemp RA. Characterizing the normal range of myocardial blood flow with ^{82}rubidium and ^{13}N-ammonia PET imaging. J Nucl Cardiol. 2013;20:578–91.
61. Araujo L, Lammertsma AA, Rhodes CG, McFalls EO, Iida H, Rechavia E, et al. Noninvasive quantification of regional myocardial blood flow in coronary artery disease with oxygen-15-labeled carbon dioxide inhalation and positron emission tomography. Circulation. 1991;83:875–85.
62. Bol A, Melin JA, Vanoverschelde JL, Baudhuin T, Vogelaers D, De Pauw M, et al. Direct comparison of [13N]ammonia and [15O]water estimates of perfusion with quantification of

regional myocardial blood flow by microspheres. Circulation. 1993;87:512–25.
63. Johnson NP, Gould KL. Partial volume correction incorporating Rb-82 positron range for quantitative myocardial perfusion PET based on systolic-diastolic activity ratios and phantom measurements. J Nucl Cardiol. 2011;18:247–58.
64. Gould KL, Pan T, Loghin C, Johnson N, Guha A, Sdringola S. Frequent diagnostic errors in cardiac PET-CT due to misregistration of CT attenuation and emission PET images: a definitive analysis of causes, consequences and corrections. J Nucl Med. 2007;48:1112–21.
65. Loghin C, Sdringola S, Gould KL. Common artifacts in PET myocardial perfusion images due to attenuation-emission misregistration. J Nucl Med. 2004;45:1029–39.
66. Johnson NP, Pan T, Gould KL. Shifted helical computed tomography to optimize cardiac positron emission tomography–computed tomography coregistration: quantitative improvement and limitations. Mol Imaging. 2010;9:256–67.
67. Murthy VL, Naya M, Foster CR, Hainer J, Gaber M, Di Carli G, et al. Improved cardiac risk assessment with noninvasive measures of coronary flow reserve. Circulation. 2011;124:2215–24.
68. Herzog BA, Husmann L, Valenta I, Gaemperli O, Siegrist PT, Tay FM, et al. Long-term prognostic value of 13N-ammonia myocardial perfusion positron emission tomography added value of coronary flow reserve. J Am Coll Cardiol. 2009;54:150–6.
69. Taqueti VR, Hachamovitch R, Murthy VL, Naya M, Foster CR, Hainer J, et al. Global coronary flow reserve is associated with adverse cardiovascular events independently of luminal angiographic severity and modifies the effect of early revascularization. Circulation. 2015;131:19–27.
70. van de Hoef TP, Echavarría-Pinto M, van Lavieren MA, Meuwissen M, Serruys PW, Tijssen JG, et al. Diagnostic and prognostic implications of coronary flow capacity: a comprehensive cross-modality physiological concept in ischemic heart disease. JACC Cardiovasc Interv. 2015;8:1670–80.
71. van de Hoef TP, van Lavieren MA, Damman P, Delewi R, Piek MA, Chamuleau SA, et al. Physiological basis and long-term clinical outcome of discordance between fractional flow reserve and coronary flow velocity reserve in coronary stenoses of intermediate severity. Circ Cardiovasc Interv. 2014;7:301–11.
72. Hamaya R, Yonetsu T, Kanaji Y, Usui E, Hoshino M, Yamaguchi M, et al. Diagnostic and prognostic efficacy of coronary flow capacity obtained using pressure-temperature sensor-tipped wire–derived physiological indices. JACC Cardiovasc Interv. 2018;11:728–37.
73. Hoshino M, Kanaji Y, Hamaya R, Kanno Y, Hada M, Yamaguchi M, et al. Prognostic value of thermodilution-derived coronary flow capacity in patients with deferred revascularization. EuroIntervention. 2019. pii: EIJ-D-19-00029. https://doi.org/10.4244/EIJ-D-19-00029. [Epub ahead of print].
74. Stuijfzand WJ, Uusitalo V, Kero T, Danad I, Rijnierse MT, Saraste A, et al. Relative flow reserve derived from quantitative perfusion imaging may not outperform stress myocardial blood flow for identification of hemodynamically significant coronary artery disease. Circ Cardiovasc Imaging. 2015;8. pii: e002400. https://doi.org/10.1161/CIRCIMAGING.114.002400.
75. Virmani R. Are our tools for the identification of TCFA ready and do we know them? JACC Cardiovasc Imaging. 2011;4:656–8.
76. Tian J, Ren X, Vergallo R, Xing L, Yu H, Jia H, et al. Distinct morphological features of ruptured culprit plaque for acute coronary events compared to those with silent rupture and thin-cap fibroatheroma: a combined optical coherence tomography and intravascular ultrasound study. J Am Coll Cardiol. 2014;63:2209–16.
77. Arbab-Zadeh A, Fuster V. The myth of the "vulnerable plaque": transitioning from a focus on individual lesions to atherosclerotic disease burden for coronary artery disease risk assessment. J Am Coll Cardiol. 2015;65:846–55.
78. Bom MJ, Schumacher SP, Driessen RS, Raijmakers PG, Everaars H, van Diemen PA, et al. Impact of individualized segmentation on diagnostic performance of quantitative positron emission tomography for haemodynamically significant coronary artery disease. Eur Heart J Cardiovasc Imaging. 2019;20:21–30.
79. De Bruyne B, Baudhuin T, Melin JA, Pijls NH, Sys SU, Bol A, et al. Coronary flow reserve calculated from pressure measurements in humans. Validation with positron emission tomography. Circulation. 1994;89:1013–22.
80. Marques KM, Knaapen P, Boellaard R, Lammertsma AA, Westerhof N, Visser FC. Microvascular function in viable myocardium after chronic infarction does not influence fractional flow reserve measurements. J Nucl Med. 2007;48:1987–92.
81. deKemp RA, Yoshinaga K, Beanlands RSB. Will 3-dimensional PET-CT enable the routine quantification of myocardial blood flow? J Nucl Cardiol. 2007;14:380–97.
82. Gould KL, Martucci JP, Goldberg DI, Hess MJ, Edens RP, Latifi R, Dudrick SJ. Short-term cholesterol lowering decreases size and severity of perfusion abnormalities by positron emission tomography after dipyridamole in patients with coronary artery disease. Circulation. 1994;89:1530–8.
83. Gould KL, Ornish D, Scherwitz L, Brown S, Edens RP, Hess MJ, et al. Changes in myocardial perfusion abnormalities by positron emission tomography after long-term, intense risk factor modification. JAMA. 1995;274:894–901.
84. Sdringola S, Nakagawa K, Nakagawa Y, Yusuf W, Mullani N, Haynie M, et al. Combined intense lifestyle and pharmacologic lipid treatment further reduce coronary events and myocardial perfusion abnormalities compared to usual care cholesterol lowering drugs in coronary artery disease. J Am Coll Cardiol. 2003;41:262–72. *Chosen for Highlights of the Year in J Am Coll Cardiol. 2003 (JACC 2003;42:2164).*
85. Sdringola S, Boccalandro F, Loghin C, Gould KL. Mechanisms of progression and regression of coronary artery disease by PET related to treatment intensity and clinical events at long-term follow-up. J Nucl Med. 2006;47:59–67.
86. Gould KL. From experimental to clinical coronary physiology. Circ Res. 2018;123:1124–6.

7 Assessment of Cardiac Function: First-Pass, Equilibrium Blood Pool, and Gated Myocardial SPECT

Elias H. Botvinick, Nick G. Costouros, Stephen L. Bacharach, and J. William O'Connell

Introduction

Radionuclide-based techniques have been used to measure ventricular function for over three decades [1–8]. As shown in Fig. 7.1a, the methods for measurement of ventricular function can be divided into two basic categories. The first category employs any tracer that can directly label the blood pool itself. One then examines the deformity of the cavitary blood pool as it is moved by the thickening and systolic motion of the myocardial walls. With these methods, one can directly image the blood pool in the ventricular cavity throughout the cardiac cycle. The second category of methods for measurement of ventricular function uses tracers that label the myocardial walls (e.g., ^{99m}Tc-sestamibi, [^{18}F]-fluorodeoxyglucose). One then examines how those walls thicken and translate, move, or contract throughout the cardiac cycle. With this method, one can directly image the myocardium throughout the cardiac cycle. Active movement or contraction of the inner endocardial wall of the ventricular chamber compresses the blood pool and deforms the ventricular cavity and is the conventional marker for systolic ventricular wall motion or function. Only this method permits the evaluation of myocardial wall thickening, a marker of systolic function and viability that can help separate passive systolic wall motion from active myocardial contraction. This method for measuring ventricular mechanical function simultaneously yields a measurement of myocardial perfusion or of metabolism (depending on the tracer used to label the myocardium), but this advantage is also a source of one of the method's disadvantages: If perfusion or metabolism is reduced in a particular segment of the myocardium, then that segment is not easily visualized, hampering visualization of wall motion or thickening in that segment. Temporal and spatial resolution of the related functional image data is not as good as for the blood pool method.

E. H. Botvinick (✉)
University of California San Francisco School of Medicine, San Francisco, CA, USA

N. G. Costouros
Department of Radiology, University of California San Francisco School of Medicine, San Francisco, CA, USA

S. L. Bacharach
Department of Radiology, Center for Molecular and Functional Imaging, University of California San Francisco School of Medicine, San Francisco, CA, USA

J. W. O'Connell
University of California San Francisco School of Medicine, San Francisco, CA, USA

V. Dilsizian, J. Narula (eds.), *Atlas of Nuclear Cardiology*, https://doi.org/10.1007/978-3-030-49885-6_7

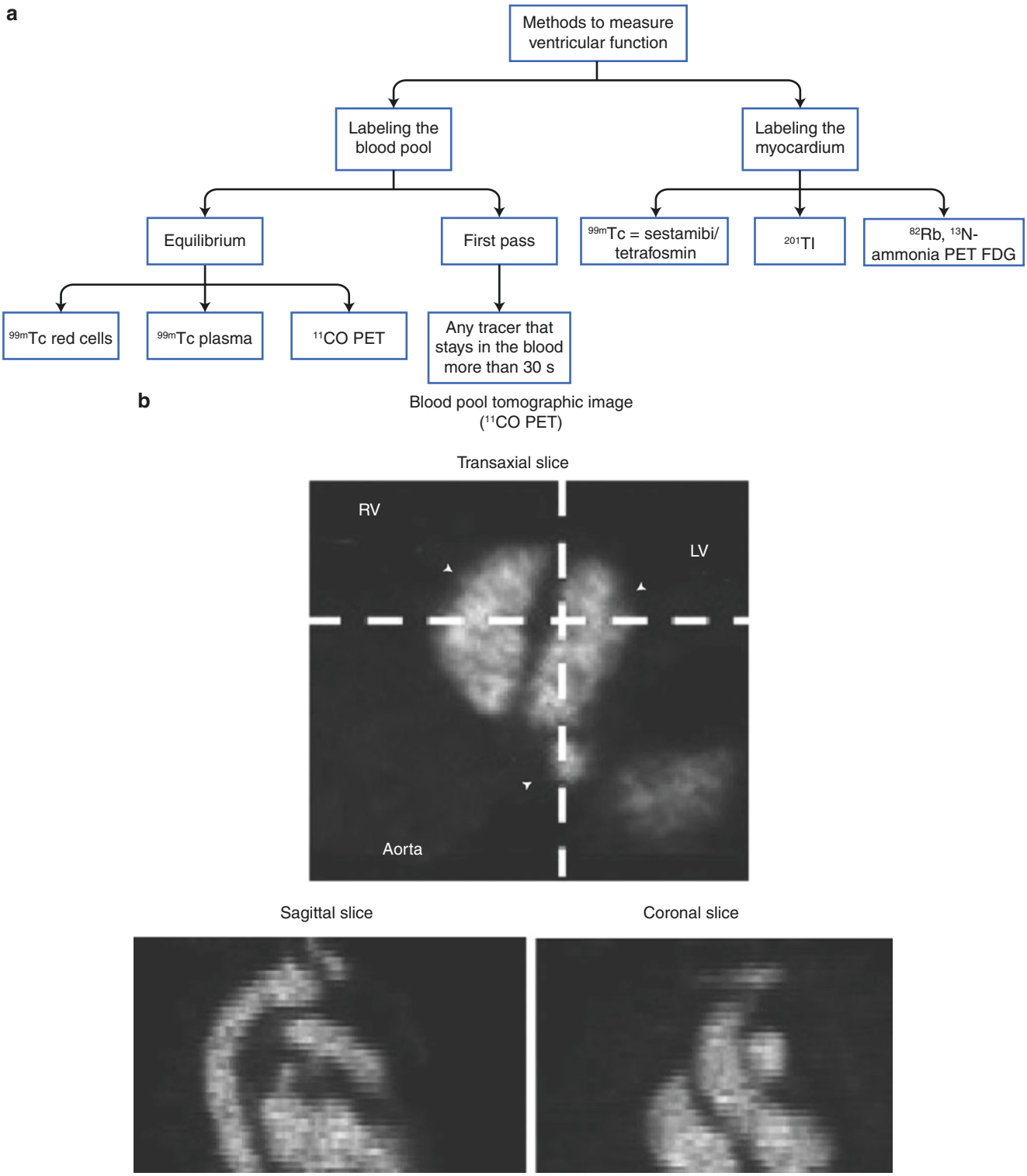

Fig. 7.1 (**a**) The methods for measurement of ventricular function can be divided into two basic categories. The first category employs any tracer that can directly label the blood pool itself. The second category uses tracers that label the myocardial walls. (**b**) Images produced from ^{11}CO PET. Transaxial slices, which display tomographic slices of the heart as it lies in the chest, are reconstructed at orthogonal angles in sagittal and coronal projections. (**c**) Diagrammatic illustration of reconstruction of the blood pool along the long axis of the left ventricle. (**d**) The resulting horizontal long-axis (HLA) and vertical long-axis (VLA) slices. ED end diastolic, ES end systolic, FDG fluorodeoxyglucose, LV left ventricle, RV right ventricle

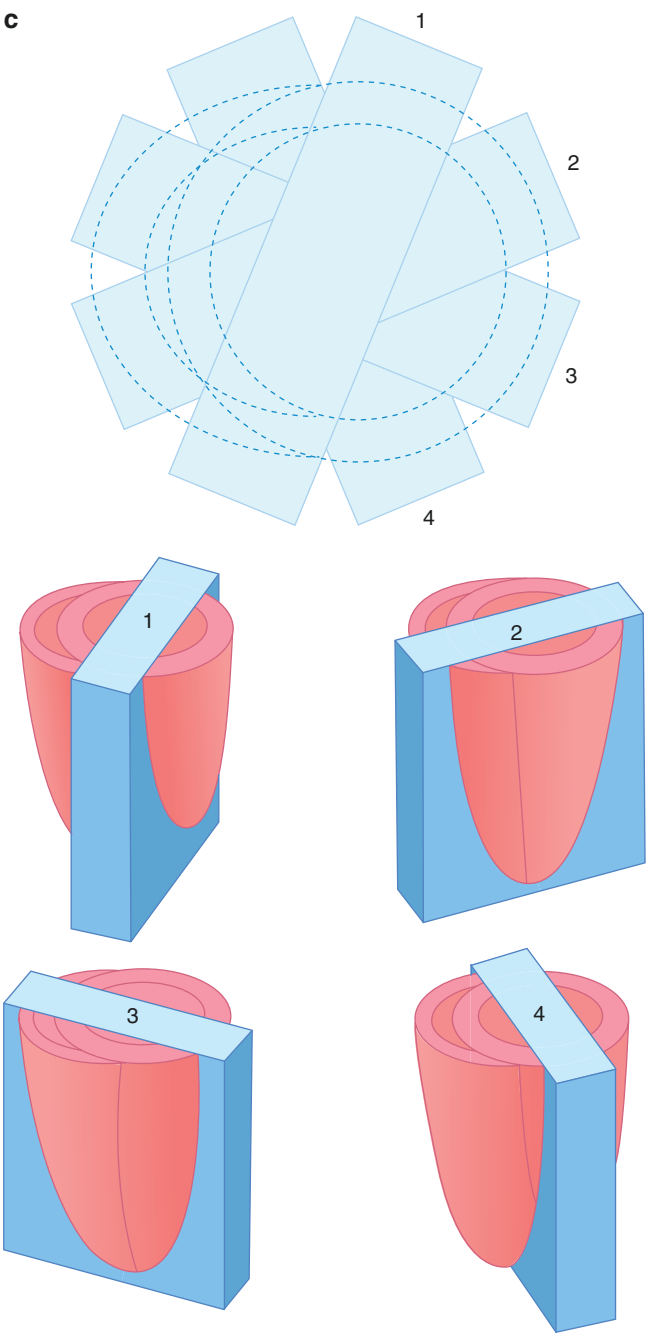

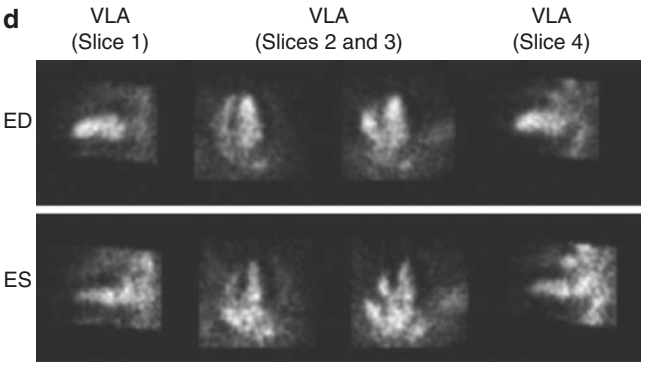

Fig. 7.1 (continued)

Both of the above methods may be gated with an electrocardiogram signal, which permits observation of either the blood pool or the myocardium throughout the cardiac cycle. The data can be displayed as a cine to either view or can be used to compute the left ventricular ejection fraction. The two methods are complementary to some extent, but give slightly different information. The blood pool method directly measures the changing volume of the blood in the cardiac chambers with time. The motion of the adjacent myocardial walls is inferred from the measured regional or global changes and motion in the blood pool contour and blood volume. The labeled myocardium methodology directly measures the motion of the walls. One must then infer changes in blood volume from that motion. Each method has its advantages and disadvantages. This chapter explores the advantages and disadvantages of both methods of measuring ventricular function, as well as how each can be applied clinically.

In recent years, there has been a rich addition of cardiac imaging methods. Each has specific advantages and disadvantages. Many are offered by imaging specialists; others are available within the cardiology practice. With this development, the cardiologist has taken an ever-increasing role in the performance of cardiac imaging studies. The American Society of Nuclear Cardiology has flourished as a vehicle of support, training, and research for all specialists seeking a role in this imaging specialty. Though some have sought a wide application, with studies performed according to the clinical setting, the specific advantage of the method, and its availability, others have simply relied on their favorite method. Studies performed and billed by the cardiologist, such as echocardiography, have found increased use. Applied mostly for its abilities and availability, this method is undeniably too often preferred, with prejudice based on non-clinical motives that are too often economic. Owing to these processes, some deserved and some not, the volume of nuclear blood pool imaging studies has diminished greatly over the years since it was the most frequently ordered nuclear cardiology study. Nonetheless, the method possesses strong advantages of accuracy, objectivity, and reproducibility. An additional major, unique advantage over echocardiography is its digital nature, with intensity/counts directly related to blood volume, permitting the formulation and derivation of parameters not available in any other way. Thus, functional imaging with the development of parametric images as "phase imaging" presents opportunities to assess characteristics of myocardial contraction that can contribute greatly to our understanding of cardiac pathology and our clinical approach to it. Soon the issue will again evolve to the question of whether the cardiology community will adapt and apply a method they do not control simply for its unique clinical advantages. The electrophysiologist may lead the way!

Blood Pool Imaging of Ventricular Function

The methods for measurement of ventricular function can be divided into two basic categories (Fig. 7.1a) The first category employs any tracer that can directly label the blood pool itself. The second category uses tracers that label the myocardial walls; one then examines how those walls thicken and translate, move, or contract throughout the cardiac cycle. For the measurement of ventricular function, labeling the blood pool has the advantage of providing a direct measure of left ventricular (LV) volumes. In the ideal circumstance, the method provides true quantitatively accurate imaging, and a measurement of absolute volume can be obtained directly from the images, since radioactivity per volume (i.e., the concentration of activity in the ventricular blood pool, or Bq/mL) can be measured within the LV chamber as well as the total Bq within the cavity. The LV volume is then calculated from the number of Bq in the entire chamber. Unfortunately, the ability to make accurate quantitative measurements of Bq/mL from image data is usually limited to positron emission tomography (PET) [9, 10]. The more common single-photon tomographic measurements can only produce quantitatively accurate results with great difficulty and actual blood counting. Inaccuracies are even greater with planar imaging. Nonetheless, single-photon emission CT (SPECT) blood pool techniques have made considerable progress in recent years [11–14]. Fortunately, for nearly all clinical applications, one is usually content to make relative measurements of ventricular function, such as ejection fraction. These relative measurements, unlike measurements of absolute volumes, depend only on relative rather than absolute accuracy of the imaging modality. For this reason, planar imaging methods can do quite well [15], although for regional measures of function using a blood pool tracer, SPECT offers some advantages [16–19].

For anatomical orientation, it is useful to first examine the higher-resolution images produced from ^{11}CO PET (Fig. 7.1b), before inspecting identical but lower resolution, SPECT gated blood pool images shown in Fig. 7.39. Transaxial slices are reconstructed at orthogonal angles in sagittal and coronal projections. Clinically, as for myocardial perfusion imaging, the blood pool is reconstructed along the long axis of the left ventricle, as illustrated diagrammatically in Fig. 7.1c, to present the horizontal and vertical long-axis slices illustrated in (**d**). Alternatively, C^{15}O has also been used, but has the disadvantage of a short (2 min) half-life. Labeling the myocardium provides direct visualization of the myocardial walls throughout the cardiac cycle. It provides only an indirect measurement of the changes in blood volume; these must be inferred from measurement of the endocardial edges, a difficult task given the resolution of nuclear techniques, but one that has proven quite feasible [20]. The method could, in principle, be used to directly measure regional myocardial thickening as well [21, 22]. The actual measurement of linear thickening has proven more difficult to accomplish with SPECT than with higher-resolution methods such as gated CT or MRI. However, intensity changes can be used to track thickening (as described below), and the gated labeled myocardial method has been widely adopted because it permits measurement of LV function simultaneously with perfusion or metabolism. Thus, one can perform two measurements with only a single injection and a single imaging session—a great logistical and financial incentive. The method has been used successfully with both SPECT and PET, but not with planar imaging.

First-Pass *Versus* Equilibrium Method

There are two methods of blood pool imaging based on the state of radiotracer mixing: the first-pass method and the equilibrium method. The first-pass method extracts data during the first passage of the radionuclide through the central circulation. The equilibrium method images the heart and calculates functional parameters when the radionuclide is fully mixed and at equilibrium, when each milliliter of blood contains the same amount of activity and blood pool counts are proportional to volume. Both methods may be gated or acquired in synchrony with the cardiac cycle to gain temporal data regarding the ventricular contraction for each beat. Tables 7.1 and 7.2 list advantages and disadvantages for each method. Aside from differences in attenuation and resolution, the two methods areidentical.

Advantages
Records and analyzes the transit of a radionuclide bolus through the central circulation
Allows imaging and the physiologic interrogation of individual chambers relatively free of adjacent chamber activity and virtually free of atrial activity
Records real-time events, which allow the characterization and quantification of individual cardiac beats
Allows short acquisition times of approximately 30 seconds at rest and 10–15 seconds at peak exercise. High-quality images can be acquired using a state-of-the-art, high-sensitivity device and, at best, a multicrystal camera. This brief acquisition time is optimal for the study of rapidly changing physiologic states.
Uses most radionuclides appropriate for a conventional gamma camera that can be safely injected intravenously in a sufficient dosage for adequate counting statistics. Macroaggregated albumin sequestered in the lungs is not appropriate, as it fails to pass the capillary network.
Can be used in combination with other imaging techniques to enhance diagnostic information
Disadvantages
Can only be used with conventional Anger cameras if they can deliver count rates of 150,000–200,000 counts per second. Many current state-of-the-art cameras are capable of this. Among other factors, the accuracy of the method varies with the statistics of the study. The greater the count density in the end-diastolic region of interest, the lower the statistical error in the calculation of ejection fraction. Much higher count density is required in patients with abnormal ventricular function than in patients with normal function to derive similar statistical reliability. The statistics applicable to the typical first-pass study result in an approximately 3% error in left ventricular ejection fraction (LVEF) calculation
Each measurement requires a separate injection, which limits the number of studies that can be acquired. Serial injections of ^{99m}Tc result in a buildup of background activity.
Study quality depends on the discreteness of the injection bolus. Up to 10% of studies will be compromised by delayed or fractionated boluses.
Patient motion or arrhythmia more easily compromises results than in an equilibrium study.
Planar methods cannot avoid structural overlap; it is difficult to separate ventricles (especially the right ventricle) from the atria (especially the right atrium).

Table 7.1 Advantages and Disadvantages of the First-Pass Method

Advantages
Presents high-resolution images
Provides excellent assessment of regional wall motion and cardiac structures, with an intraobserver variability of ±3% and an interobserver variability of ±4%
Can be fully automated to yield an objective, accurate, and reproducible left and right ventricular ejection fraction
Can be easily performed with standard, state-of-the-art, single-crystal scintillation cameras
Can be applied reproducibly for repetitive calculations with interventions
Is ideally suited for generation of functional images
Disadvantages
Must use labeled red cells
Cannot be used with any ^{99m}Tc-labeled radionuclide passing through the blood pool
Requires 2–33 minutes of acquisition time to gain adequate data with conventional, single-crystal cameras, but about 1 minute using new, high-sensitivity digital cameras
Risks loss of accuracy or "blurring" of data when applied with brief intervention
Planar methods cannot avoid structural overlap; it is difficult to separate the ventricles (especially the right ventricle) from the atria (especially the right atrium).

Table 7.2 Advantages and Disadvantages of the Equilibrium Method

The most commonly used tracer is ^{99m}Tc-labeled red blood cells. Commercially available kits are available that can easily produce this tracer [23]. Equilibrium gated blood pool imaging, as conventionally performed, is called *equilibrium radionuclide angiography*. For PET, it is possible (but not common) to also do blood pool imaging using ^{11}C-labeled carbon monoxide. This gas is breathed by the patient a few minutes before imaging begins. The quantity of ^{11}C carbon monoxide that must be inhaled is typically no greater than one might breathe in heavy traffic, so there are no deleterious physiologic effects. Both PET and SPECT blood pool imaging can give valuable three-dimensional measures, visual and quantitative, of ventricular function. SPECT blood pool imaging is of course more widely used.

First-Pass Analysis

Figure 7.2 illustrates a first-pass curve of time versus radioactivity. Such data can be generated and accurately processed with as little as 1–2 mCi of any agent that stays in the blood pool for the first circulation, but images are not available with this dose. Alternatively, volumes may be calculated from ventricular outlines using geometric considerations. A unique first-pass method of volume calculation is applied with the multicrystal camera, where image counts are sampled in a known blood volume at the attenuation distance to the mid-left ventricle and used to standardize ventricular counts during diastole and systole [24, 25].

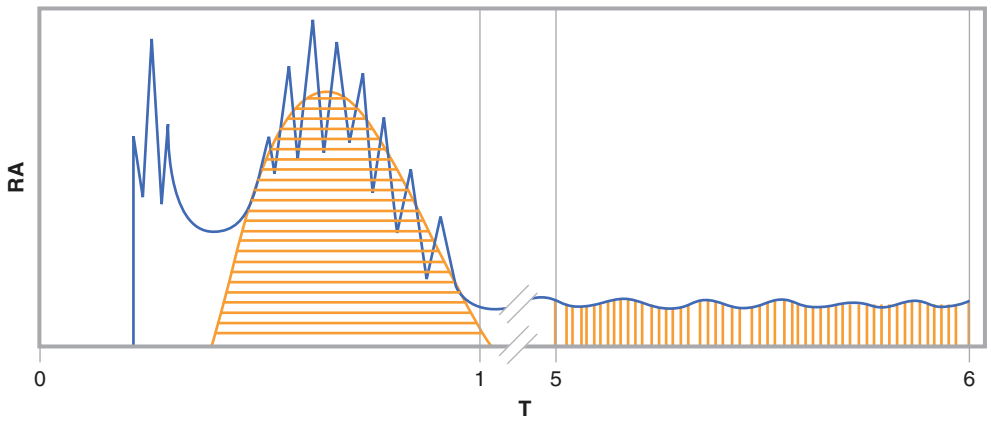

Fig. 7.2 First-pass curve analysis. Shown is a diagrammatic sketch of a first-pass time (T) in seconds versus radioactivity (RA) curve. The area under the left ventricular component (*horizontal lines*) is proportional to cardiac output and is calibrated for volume by dividing it into the integrated area under 1 minute of the equilibrium time versus the RA curve (*vertical lines*) acquired when the radiotracer is thoroughly mixed in the blood [25]

Figure 7.3 shows a first-pass analysis of the levophase, in which a region of interest is drawn on the levophase of the first-pass ventriculogram and the diastolic peaks and systolic valleys are compared to calculate the left ventricular ejection fraction (LVEF).

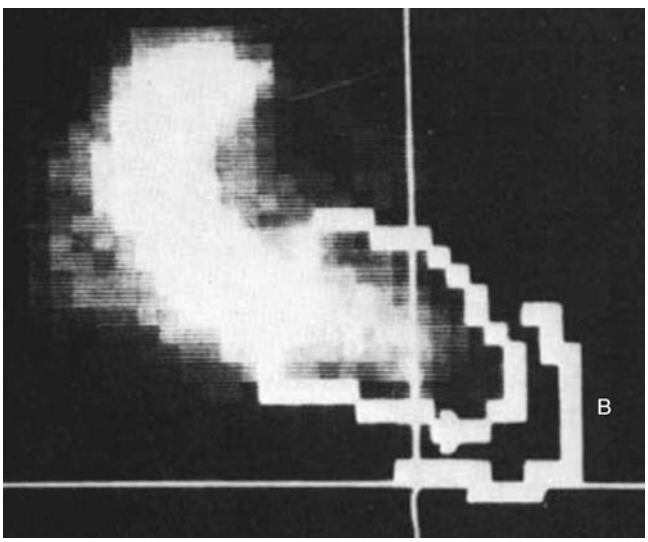

Fig. 7.3 First-pass analysis of the levophase. An irregular region of interest is drawn on the levophase of the first-pass ventriculogram. Correcting for background activity (B), the diastolic peaks and systolic valleys are compared to calculate the left ventricular ejection fraction (LVEF) [25]

First-pass imaging presents an alternative method of blood pool imaging while injecting the tracer as a bolus [6, 26–28]. Nearly all the considerations for standard gating, list mode, and phase mode can be applied to this first-pass methodology. The tracer can be a blood pool agent or almost any other imaging agent, such as Tc-MIBI (isonitrile), ^{201}Tl, Tc-tetrofosmin, or even ^{99m}Tc-pertechnetate. Regardless of the tracer's chemical form, during its first transit through the heart, most tracers stay in the arterial blood for seconds to minutes before they are taken up by the myocardium or other tissues. During that brief transit time, the tracer behaves as though it were a blood pool tracer. In an equilibrium gated study, the activity in the left ventricle (LV) is diluted by a factor of about 5000 because the tracer has been mixed with the entire volume of blood in the body, but when the tracer is injected as a bolus, the concentration of activity in the ventricular chambers is quite large during the tracer's first transit through the heart. This yields count rates that are many times higher than in equilibrium radionuclide angiography studies. Despite this much higher count rate, it is still necessary to do some form of gating in order to capture the ejection fraction. For first-pass studies, only a few beats of data need to be added together. One of the advantages of first-pass imaging is that, it can be performed with nearly any imaging agent, so one can obtain LV function data from studies done for some other purpose, such as bone scans. In addition, it is possible to position the gamma camera in a right anterior oblique view and obtain early gated images during the passage of the radioisotope through the right ventricle (RV), prior to contamination by counts from the LV. One of the disadvantages of the first transit is that one usually must obtain all the LV function information from only a small number of beats (Fig. 7.4). This means that a rapid bolus injection must be given, resulting in very high count rates during the passage of the tracer through the cardiac chambers. Such high count rates often cause unacceptable dead time in many cameras. Therefore, specialized cameras (often not using the Anger methodology) have been developed specifically for dealing with these high count rates. However, many standard cameras can perform first-pass acquisition with adequate accuracy, although the dose may need to be limited. Additionally, because the calculation of the ejection fraction is based on a few samples, it is prone to greater variability. The few samples are related to the required tight RV bolus passage.

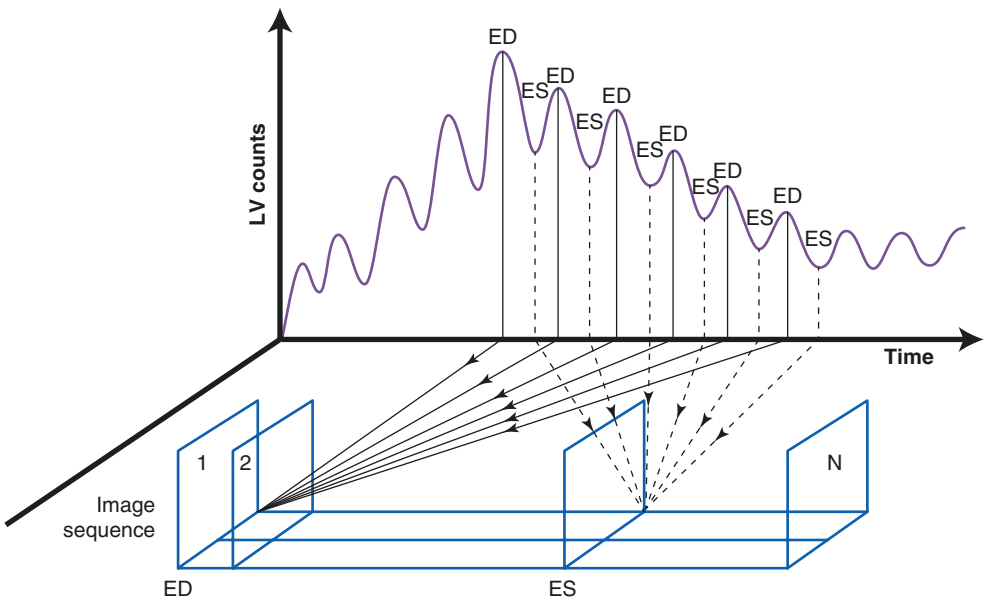

Fig. 7.4 Gated first-pass blood pool imaging. When the tracer is injected as a bolus, the concentration of activity in the ventricular chambers is quite large during the tracer's first transit through the heart. Despite this much higher count rate, it is still necessary to do some form of gating in order to capture the ejection fraction (EF). For first-pass studies, only a few beats of data need be added together. This figure illustrates the case of "gating" the first six beats of data to produce one sequence of *N* images. One of the disadvantages of the first transit is that one usually must obtain all the LV function information from only a small number of beats. Because the EF is calculated from the average values based on the magnitude of the peak counts, proportional to end-diastolic (ED) volume, and the valleys, proportional to end-systolic (ES) volume, correcting for background activity, and is based on a few samples, it is prone to greater variability [29]

Figures 7.5, 7.6, 7.7, and 7.8 present examples of the use of first-pass analysis in patients to obtain information about cardiac function.

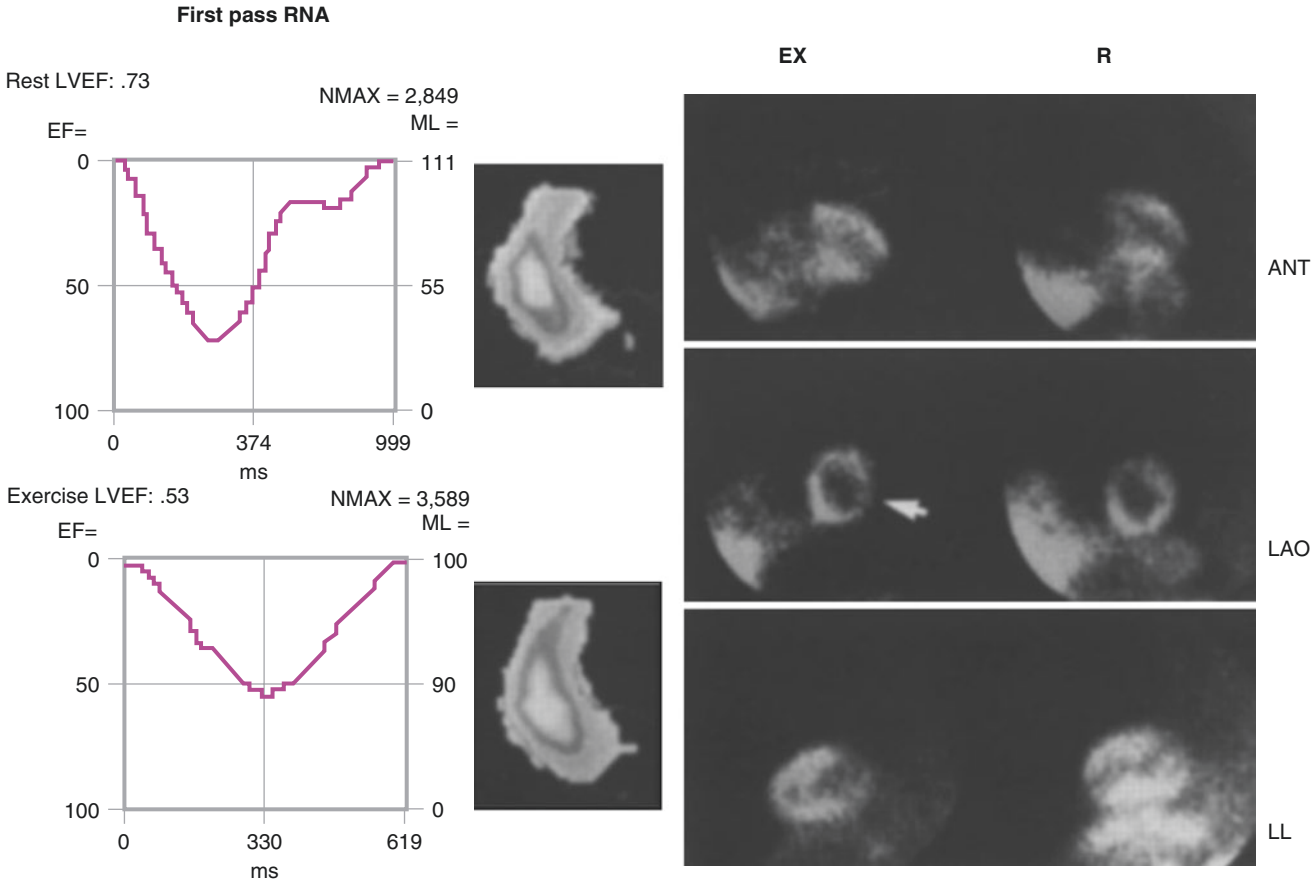

Fig. 7.5 Interaction of perfusion and function. This figure demonstrates the perfusion-function interaction [30]. Shown at the *right* are perfusion images in anterior (ANT) (*top*), left anterior oblique (LAO) 40° (*center*), and 70° (*bottom*) with exercise (EX) and at rest (R) in each image pair acquired in a 41-year-old man with a history of coronary disease, prior coronary bypass graft surgery, and atypical chest pain. On the *left* are the associated first-pass radionuclide angiography (RNA) images of the sestamibi bolus administered to evaluate LV function at rest and with exercise. Evident is a reversible inferolateral defect, cavitary dilatation, and reduced LVEF with exercise [30]

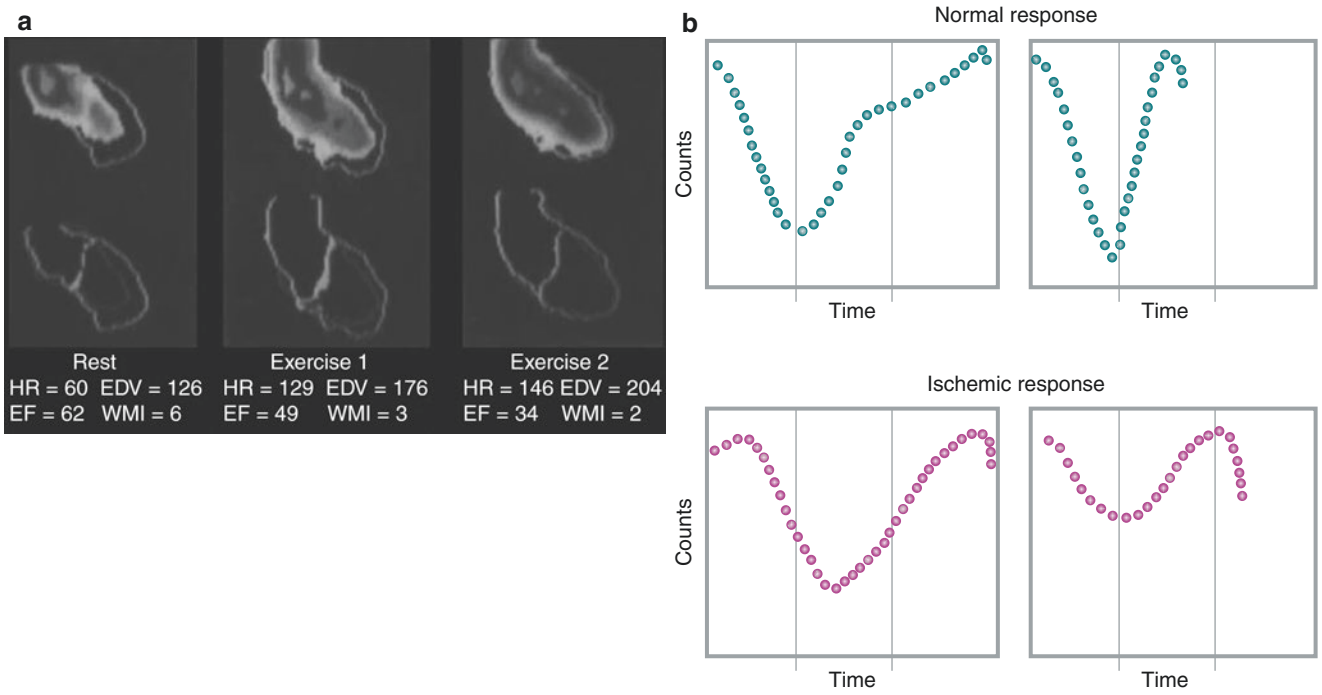

Fig. 7.6 Abnormal first-pass exercise study. (**a**) Examples of baseline (*left*), early exercise (*center*), and peak exercise (*right*) LV function in a patient with coronary disease [31]. In each panel, the end-systolic frame is related to the end-diastolic outline (*top*), while both end-diastolic and end-systolic outlines are presented below. Data presented for each period include the heart rate (HR), left ventricular ejection fraction (EF), end-diastolic volume (EDV), and wall motion index (WMI). The ischemic response is characterized (as it is with all methods that evaluate the functional response) by increased EDV and reduced WMI and EF. (From Upton et al. [31], with permission.) (**b**) Typical time versus radioactivity curves related to the normal (*top*) and ischemic (*bottom*) exercise response. In each case, the baseline curve is at the *left* and the exercise-related curve is at the *right*

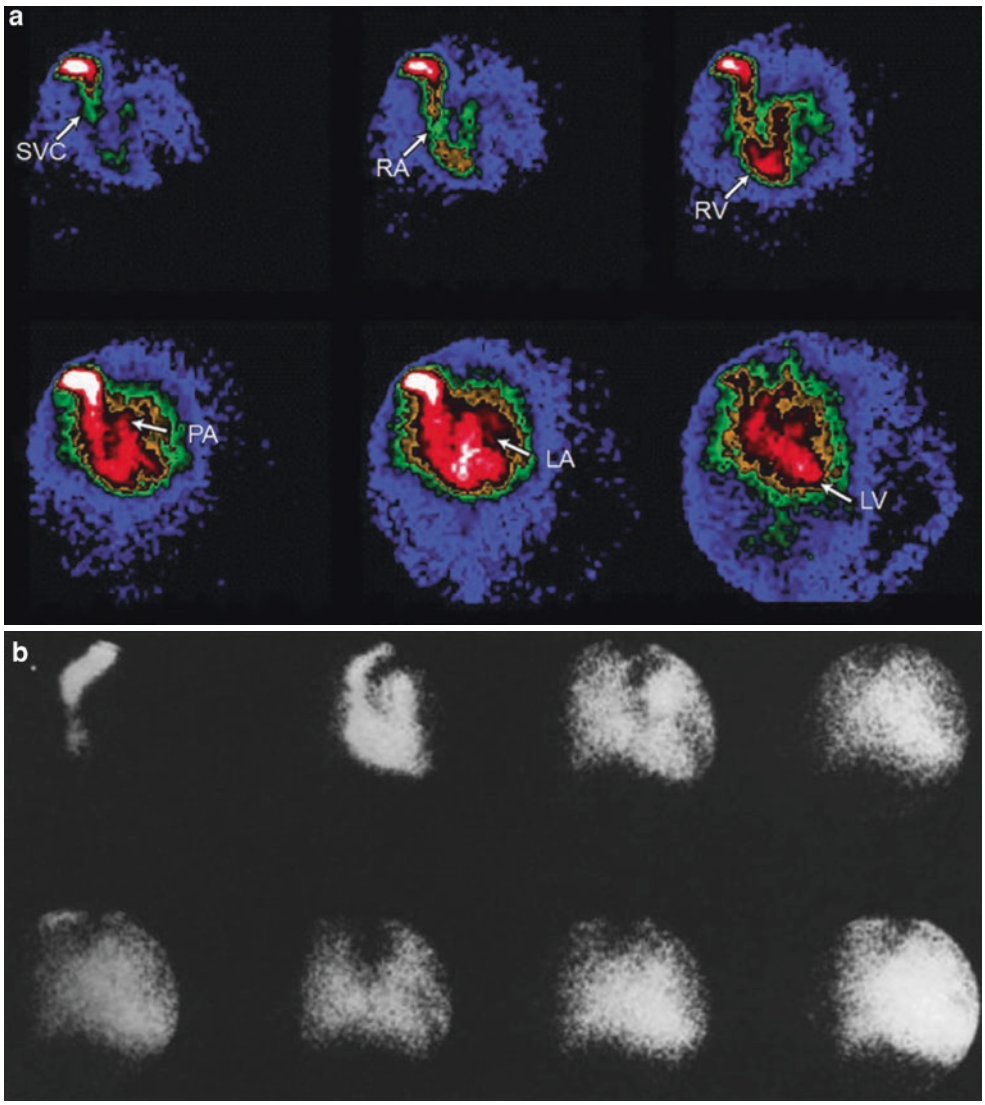

Fig. 7.7 First-pass images in a normal patient and in a patient with a left-to-right shunt. (**a**) First-pass radionuclide ventriculography. Individual frames from a first-pass acquisition illustrate the path of the bolus isotope through the superior vena cava (SVC), the right atrium (RA), the right ventricle (RV), the pulmonary outflow tract and lungs (pulmonary artery [PA]), the left atrium (LA), and the left ventricular (LV) phase, from which the isotope bolus is then distributed systemically. (From Udelson et al. [32], with permission.) (**b**) Similar images taken in a patient with a significant left-to-right shunt. The lungs were never clear, because of continued recirculation of the bolus. As a result, the LV teardrop and the levophase are not seen. This "smudge sign" generally relates to a left-to-right shunt with $Q_p/Q_s \geq 1.5$

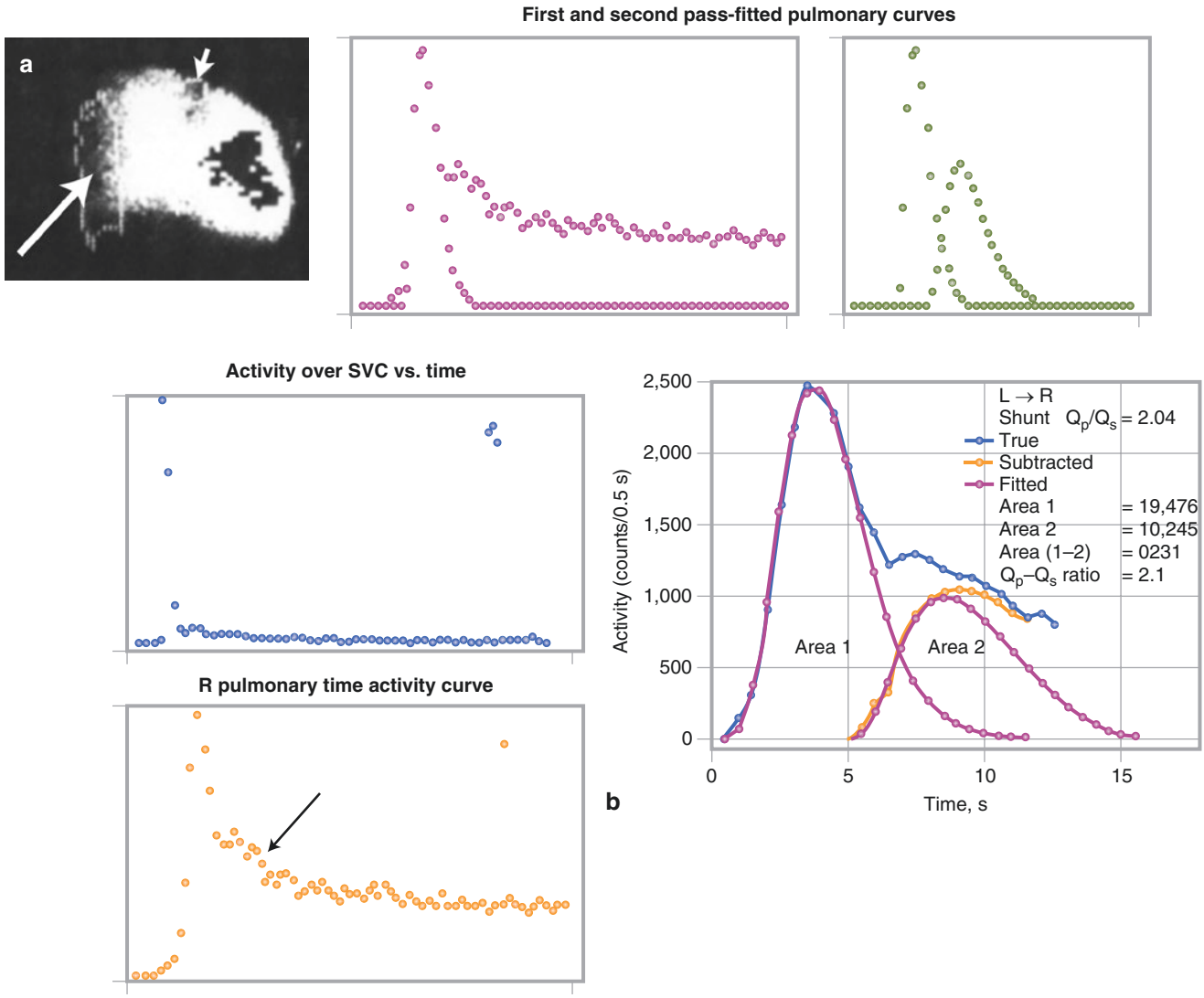

Fig. 7.8 Calculation of Q_p/Q_s. (**a**) A calculation of the left-to-right shunt magnitude in a patient with an atrial septal defect is shown according to the method of Maltz and Treves [34]. At the *upper left* is a summed view of all frames of a first-pass study performed over the central circulation. Regions of interest are taken over the superior vena cava (SVC, *short arrow*) to check on the integrity of the bolus, which must be both rapid and coherent in its delivery, and the right lung (*long arrow*), seeking recirculation via shunting. At the *upper right* are the time–activity curves generated from these regions of interest. The SVC curve confirms the rapid passage of an excellent bolus injection. The "hump" on the lung curve downslope represents the shunt recirculation through the lungs. In the *lower left*, a gamma-variate curve fits the first lung passage. At the *lower right*, the gamma-variate fitting to both the first and the second passages is shown. (**b**) The curve analysis. By principles of "dye dilution" analysis, the area under the first fitted curve, Area 1, is proportionate to systemic flow, while the area under the second passage curve, Area 2, is proportional to the shunt flow. As shown diagrammatically in this figure, Area 1 = Q_p (pulmonic) and Area 2 = Q_{sh} (shunt). Thus, Q_s (systemic) = $Q_p - Q_{sh}$ and $Q_p/Q_s = Q_p$ (Area 1)/Q_p (Area 1) − Q_{sh} (Area 2). The method is not a diagnostic tool but one meant for an accurate quantitation of such shunts between Q_p/Q_s of 1.2–3 and so is useful in prognosis and management. It is another scintigraphic method that is underutilized owing to the widespread availability and capabilities of echo Doppler examination [34]

Equilibrium Analysis

One can measure the mechanical contraction and relaxation of the heart chambers either with blood pool imaging or by labeling the walls of the myocardium. In both cases, the goal is to capture images of the blood pool (or myocardium) as the heart contracts and relaxes, that is, through systole and diastole [35]. For the measurement of myocardial function by observing the motion of the myocardial walls, any agent that remains in the walls for many minutes can be used. For blood pool imaging [20], a blood pool agent, typically labeled red blood cells, is injected and then allowed to mix with the 5–6 L of blood in a typical subject. After 3 or 4 minutes of mixing, the tracer will be uniformly distributed and the tracer is then said to be "in equilibrium." If a single heartbeat were 960 ms long (i.e., a heart rate of about 63 beats/min), we could divide up that single beat into, for example, 16 images, each 60 ms long. The first image would be acquired for 60 ms; then the second would acquire all the data in the next 60 ms, and so forth. Each image would reflect a different portion of the cardiac cycle, from end diastole through systole and back again. Unfortunately, an acquisition that was only 60 ms long would have too few counts to make an interpretable image. With the typical activities injected in a patient (10–30 mCi or 370–1110 MBq for either blood pool or myocardial imaging), one would need to acquire each image many hundreds of times longer, perhaps for 10–20 seconds or longer. To solve this problem, we use the technique of electrocardiographic (ECG) gating (Fig. 7.9). The total acquisition time of each image is not determined directly by the imaging time, but rather by the number of beats multiplied by the duration of each frame. At high heart rates, this time builds up more quickly than at low heart rates for the same image duration. Many commercial computer systems actually do a slightly more sophisticated form of data acquisition. These methods permit "beat length windowing" [5, 35, 36]. That is, data from a particular beat is added to the gated image set only if that beat is between a preselected minimum and maximum length. The user usually has to decide in advance which beat lengths to include or reject, which is sometimes problematic if the heart rate changes during the study. There are some problems with this technology. If, for example, a cardiac cycle is terminated prematurely by a premature ventricular contraction, then it could be rejected. However, the following cardiac cycle will not begin its contraction with a fully dilated left ventricular cavity; that is, it will not have filled completely, so it is the data from this subsequent cardiac cycle that should be rejected. This is problematic with some of the available beat length windowing schemes available commercially; a solution to this problem is outlined below.

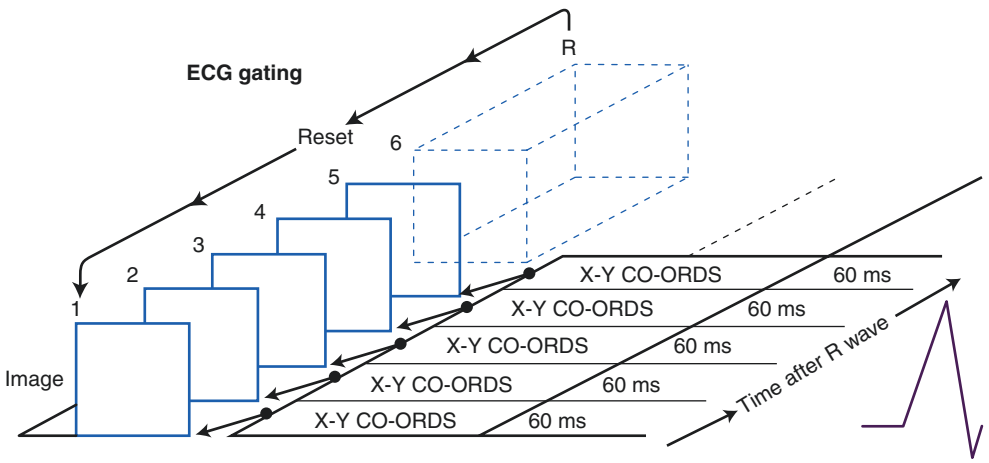

Fig. 7.9 Electrocardiographic (ECG) gating of equilibrium radionuclide angiography (ERNA). An ECG is connected to the patient and its output is put through a "trigger" device that generates a "gating" signal at each R wave peak, for example. If a single heartbeat were 960 ms long (i.e., a heart rate of about 63 beats/min), we could divide up that single beat into 16 images, each 60 ms long. Because an acquisition that was only 60 ms long would have too few counts to make an interpretable image, we use the technique of ECG gating. An ECG is connected to the patient and its output is put through a "trigger" device that generates a "gating" signal at each R wave peak, for example. For the first 60 ms after the first R wave, all the photons are sorted into the first image. After 60 ms has elapsed, all data are then sorted into the second image, and so on. Finally, at the next R wave, signifying the beginning of the next cardiac cycle, the process is repeated, and the next 60 ms of data are again added to the first image (Image 1 in the figure) and similarly for all the subsequent images. If this process continues for 300 beats, then each image is acquired for (60 ms/beat) × 300 beats = 18 seconds

Figure 7.10 illustrates the technical aspect of equilibrium radionuclide angiography (ERNA) acquisition from another viewpoint. Before acquisition, the computer monitors the R–R interval to establish the heart rate, and the mean rate is divided by the number of frames per cycle, based on the computer's memory and the software applied in frame mode acquisition. The individual frames from each beat are pooled with the same frame of subsequent beats until adequate count data are acquired, as exemplified by Fig. 7.11. Summed frames representing the total data in all image intervals are displayed as an endless loop movie and computer analyzed for the LVEF, RVEF, and ventricular size and function. Heart rate variability alters the data content of each frame and greatly distorts the data at the end of the curve [36].

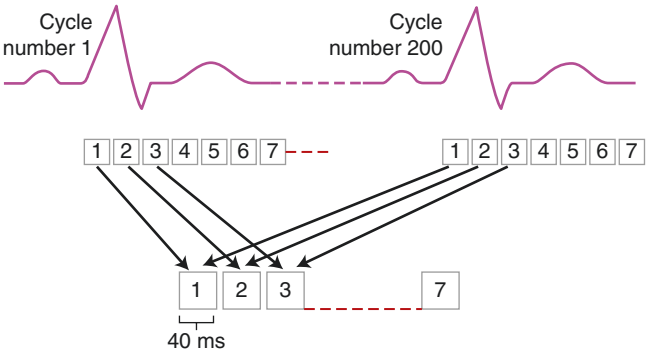

Fig. 7.10 ECG gating of equilibrium radionuclide angiography (ERNA), from another viewpoint. Before acquisition, the computer monitors the R–R interval (*top*) of multiple cardiac cycles, here 1–200. The heart rate is established and the mean rate is divided by the number of frames per cycle, based on the computer's memory and the software applied in frame mode acquisition. With a heart rate of 60 beats/min, the R–R interval is 1000 ms, and at 25 frames/cycle, the frame duration is 40 ms, a typical interval. These individual frames from each beat are pooled with the same frame of subsequent beats (*middle row*) until adequate count data are acquired in a master composite frame (*lower row*). Summed frames representing the total data in all image intervals are displayed as an endless loop movie and computer analyzed for the LVEF, RVEF, and ventricular size and function, considering that each milliliter of blood contains the same radioactivity [36]

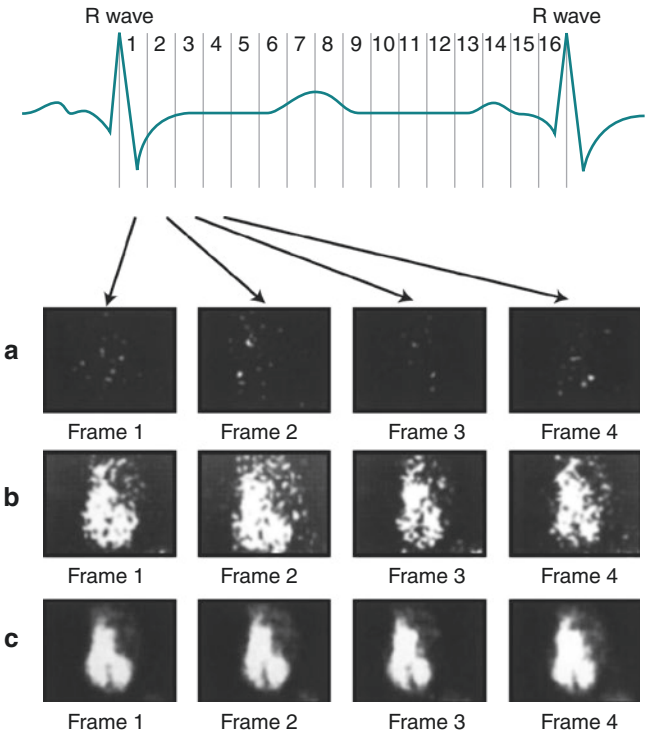

Fig. 7.11 Computer acquisition of the equilibrium study. Shown is the relationship between the cardiac cycle or R–R interval acquired over 16 separate frames or intervals and the related images in each frame over the course of the acquisition [37]. The counts acquired during frame 2 are stored in frame 2, those acquired during frame 3 are stored in frame 3, and so on. Only data accumulated over the first four frames are illustrated here. Owing to the low count rate in this study, 750 counts/frame, there is little to see after acquisition over a single cycle (**a**). However, after the accumulation and addition of the counts from 20 R–R cycles, now with 15,000 counts per frame, the cardiac chambers are taking form (**b**). With the addition of counts acquired over 400 cycles and 300,000 counts/frame, image quality is excellent and the acquisition is over (**c**) [37]

Gating Methods

Figure 7.12 illustrates a typical planar gated blood pool sequence of images that are made up of about 300 cardiac cycles "gated" together. These images can be played as a cine that will reveal the pattern of contraction. Wall motion defects can clearly be observed from such movie sequences, but because these are planar images taken from a left anterior oblique (LAO) position, the effects of motion of the anterior and posterior myocardial walls will be difficult to observe. For resting studies, two additional views are also usually acquired, an anterior view and a left lateral view. These other two views give additional visual information concerning wall motion. Only the LAO view is used to compute quantitative indices of LV function, because only this view is free from overlapping structures, albeit incompletely. The same technique can be used with gated blood pool SPECT, but in this case, there is access to all views and cross sections, so that all walls can be observed and there is no difficulty with overlapping structures [11, 12, 14, 16, 18, 38, 39].

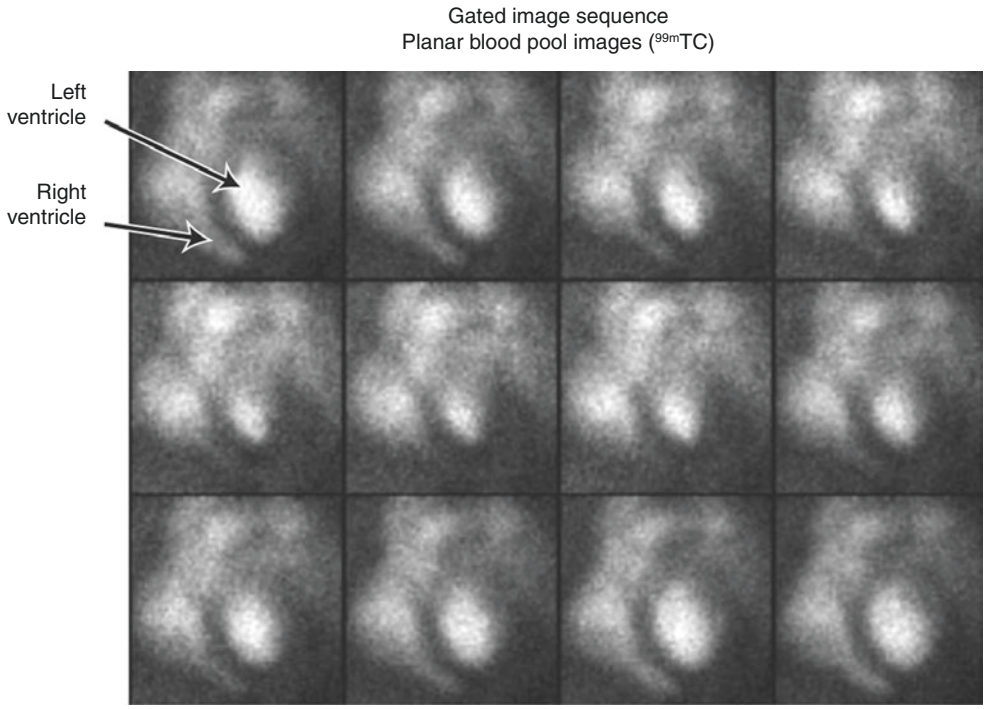

Fig. 7.12 Gated imaging sequence. This typical planar gated blood pool sequence of 12 images is made up of about 300 cardiac cycles "gated" together, as described in the previous figure. The images were taken with ^{99m}Tc-labeled red blood cells. The gamma camera was positioned in a left anterior oblique (LAO) position, approximately 45°, with a 15° caudal tilt. The caudal tilt is used to better separate the left ventricle (LV) from the left atrium. The *top left panel* shows the first image in the gated sequence triggered by the electrocardiographic R wave, at the end diastole. The LV is at the right and the right ventricle (RV) can be seen to the left (*arrow*). Each image (*left to right*, *top row to bottom*) represents an additional 60-ms elapsed time from the R wave. By about the fifth or sixth image (300–360 ms), it is clear that the LV has contracted considerably, reaching end systole. The RV is also much smaller, its apical portion almost disappearing. During the next six images, the LV begins filling in the diastolic portion of the cardiac cycle. By the 12th image, the LV is once again completely full (end diastole), and the cycle begins again. Because there are 12 images of 60 ms each, the average time between beats (the R–R time) is 60 ms × 12 = 720 ms. This corresponds to a heart rate of about 83 beats/min. These images can be played as a cine that will reveal the pattern of contraction and clearly show wall motion defects, but because these are planar images, the effects of motion of the anterior and posterior myocardial walls will be difficult to observe. In this LAO view (with caudal tilt), only the motion of the septal, apical, and lateral LV walls can be observed

Because the image intensity or counts in the gated image sequence are approximately proportional to the volume of blood (or exactly, in the case of PET), one can create an LV volume curve from the image set and draw a single region of interest (ROI) around the image. In Fig. 7.13, the planar gated image set produced an LV "volume" curve with very high temporal resolution. The word *volume* is in quotes because, in planar studies, the counts are only approximately proportional to volume as a quite linear function and because some of the counts in the planar images arise from the tissues above and below the heart, such as the soft tissue between the gamma camera and the heart. In an attempt to correct for these extraneous counts, one usually draws a second ROI adjacent to the LV cavity and takes this "background" region as a correction indicative of the extraneous counts from above and below the heart [9]. Another method uses not a single region over the LV cavity, but instead a different ROI for each image or frame. This method has the advantage of better tracking of the LV cavity and the disadvantage of introducing variability in drawing the numerous regions required. In actual practice, both methods give results that correlate quite accurately with one another, although the variable region method gives a consistently "deeper" curve and a higher ejection fraction. Practically, images for each frame are used when edges for each ROI can be applied in an automated manner. When edges must be applied manually, regions are drawn on end diastole and end systole. This procedure is semiautomated in many commercial nuclear medicine cardiac analysis packages. It has been shown that 16 frames or more are needed to provide the sampling rate required to capture the extremes of end systole and end diastole in order to gain an accurate ejection fraction and other indices of LV function [40].

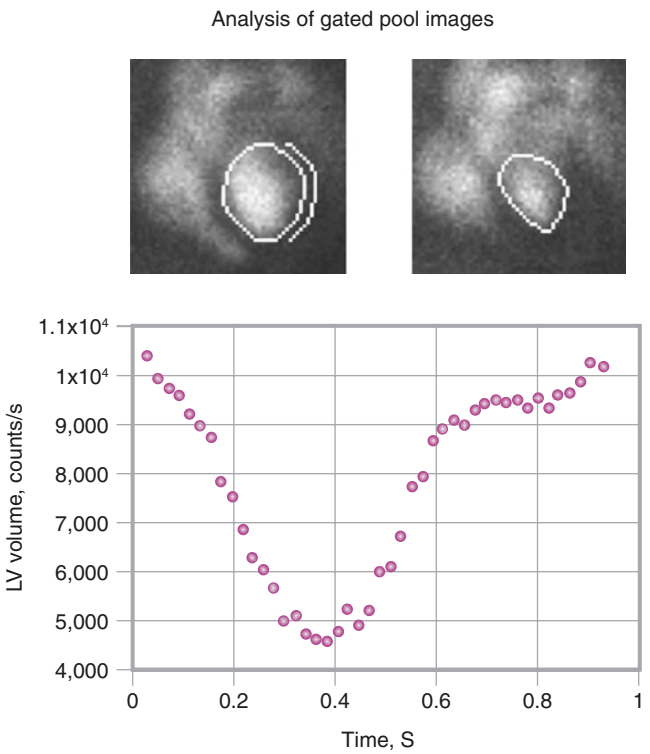

Fig. 7.13 Analysis of gated blood pool images. An LV volume curve can be drawn from the image set, and one can draw a single region of interest (ROI) around the image at the end diastole, as shown by the roughly circular ROI in the *upper left image*, and then plot the counts from within this ROI as a function of time represented by the image number against the milliseconds per image. In this figure, the planar gated image set consists of 44 images, each taken for 20 ms, thereby producing an LV "volume" curve with very high temporal resolution. The word *volume* is in quotes because, in planar studies, the counts are only approximately proportional to volume as a quite linear function and because some of the counts in the planar images arise from the tissues above and below the heart [41]

The ERNA gating method can be performed in "real time" [7, 35], with the data sorted into the images on the fly as the photons are registered by the gamma camera (often called gated "frame mode" acquisition). This method is very convenient, but sometimes it is less than ideal. For example, one may wish to retrospectively look only at beats of a certain length, which is impossible if the data are sorted into the image sequences on the fly. To enable "retrospective" analysis of the data, one can use a method called *list mode acquisition* (Fig. 7.14). In this mode of operation, the computer simply records on disk a "list" of the timing and location of every photon recorded by the camera. Typically, many millions of counts make up a gated blood pool cardiac study, so a lot of disk storage is required, which was a serious problem for older systems but is no longer an issue. Once the data have been recorded, one can read it back from the disk and perform the gating just as described previously. Why bother to write it to disk? There are several reasons. First, in frame mode, selecting the beat length window (i.e., the range of beats to accept and reject) is often problematic. One must make this decision prior to beginning the acquisition, and it is quite possible, and even common, for the heart rate to change during the course of the study if the patient becomes more comfortable on the table or even falls asleep, or, conversely, becomes uncomfortable. Thus, the heart rate may slowly shift as the study progresses. Similarly, during exercise studies it is often not possible to accurately predict the heart rate and keep it stable. In a list mode study, such difficulties are easily overcome, because one is processing the data after the fact. The computer can first display the progression of heart rates that occurred during the study, and the operator can then select whatever range of heart rates seems most suitable. This method also permits multiple levels of exercise to be studied easily. One can select any combination of heart rates and time periods desired. Finally, list mode acquisition allows the very end of the cycle, atrial contraction, to be reproduced. Again, since processing is retrospective, one can gate "backward" in time from the R wave trigger [34, 35]. If the interval from the P wave to the R wave is relatively constant from beat to beat, one can faithfully reproduce the volume increase due to atrial contraction.

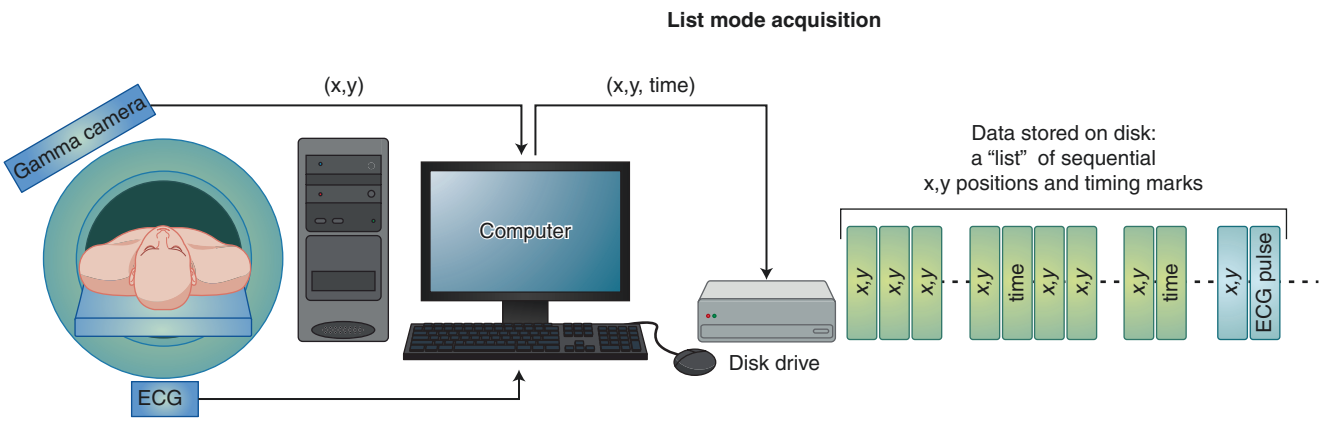

Fig. 7.14 List mode acquisition. This schematic drawing demonstrates the mechanism of list mode acquisition, which permits "retrospective" analysis of the data, which the computer has simply recorded on disk as a "list" of the timing and location of every photon recorded by the camera

The gating process assumes that the heart beats in exactly the same way, with the same contraction and relaxation pattern, from one beat to the next [41]. If the subject is in normal sinus rhythm (NSR), this approximation holds quite well, but owing to the normal sinus arrhythmia, a varying beat length requires an adjustment at the end of the cycle. The end of the cycle must be handled somewhat differently, because not all beats will be of the same length. In fact, fluctuations in the R–R interval times can be quite large, as much as 100 ms or more for a normal subject in NSR at rest. In the usual acquisitions (not list mode), this means that for beats shorter than average, the last frames, or the last few, will not accumulate for the full time, whereas for beats longer than the average, data will be thrown away. Both of these circumstances can easily be accounted for by keeping an accurate account of the actual length of each beat and, therefore, the actual acquisition time for each frame that spans the cardiac cycle. Of course, such beat length fluctuations may degrade the ability of the gated data to portray events occurring very late in the cycle as the volume increases due to atrial contraction. Not all computer systems make the compensation for this varying beat length. If such a correction is not made, the images at the end of the cycle will have an artificially reduced intensity, and quantitative data extracted from these images may be subject to error.

At first, one might think that a beat shorter than average might be a "condensed" version of an average-length beat and that a long beat is simply a uniformly stretched version of a short beat, scaled temporally with a shorter-than-average time to end systole and other characteristics. If this were true, then the assumption that all beats are identical would be violated. Fortunately, for subjects in NSR, it has been shown that at rest, fluctuations in the heart rate are caused primarily by fluctuations in the initiation of the next beat. That is, a "short" beat is shorter only because the next beat begins slightly earlier than average. Thus, at rest in normal individuals, it is only diastasis that is shorter, and the earlier parts of the cycle remain unaltered (Fig. 7.15). This is not true at higher heart rates, where there is no diastasis at all, nor is it necessarily true for subjects who are not in NSR, or for subjects in whom the filling portion of the left ventricular volume curve is so abnormal that there is no discernible diastasis at all. In these situations, the technique of "beat length windowing" is necessary, in which beats shorter or longer than some predetermined length are not included in the data. This technique may not always make physiologic sense, however, as the short beat itself in all likelihood was functioning like all other beats up until the time it was prematurely terminated. That is, it was too short simply because the next beat began too early. If the next beat began prior to complete LV filling, the beat following the short beat would *not* be identical to all the other beats. It would have a different preload and therefore a different pattern of contraction and filling. Therefore, one may wish to reject the beat following the short beat, not just the short beat itself. In fact, there may be no reason to reject the short beat. The user of the computer program for gated acquisition is usually permitted to choose not only what length beats are unsuitable but also what to do about the succeeding or preceding beats.

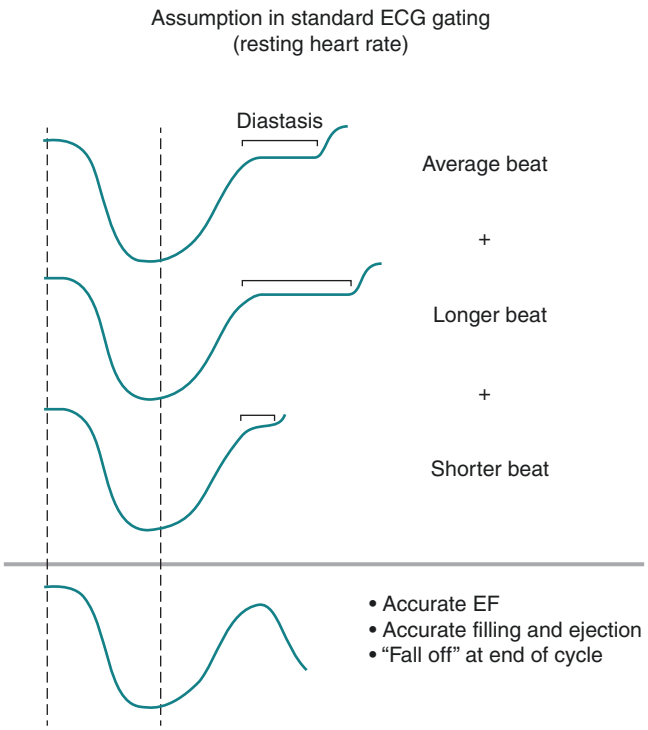

Fig. 7.15 Assumptions in standard ECG gated imaging. For subjects in normal sinus rhythm (NSR), it has been shown that at rest, fluctuations in the heart rate are caused primarily by fluctuations in the initiation of the next beat. That is, a "short" beat is shorter only because the next beat begins slightly earlier than average; it is only diastasis that is shorter, and the earlier parts of the cycle remain unaltered. EF—ejection fraction

Clinical Parameters

Figure 7.16 demonstrates the useful clinical parameters that can be extracted from the LV volume curve [35, 36]. The most useful measure is ejection fraction; others include the peak ejection rate (PER), the maximum rate at which blood is ejected by the heart; the time to end systole (TES); and the peak filling rate (PFR), the diastolic correlate of the PER. In many diseases, impending impairment of systolic function is preceded by filling that is slower and later than normal, probably due to poor ventricular compliance. Therefore, PFR, a measure of diastolic ventricular function, is often reduced even before the ejection fraction or systolic function is noticeably impaired. Figure 7.17 illustrates the application of these indices in a patient with coronary artery disease. Figure 7.18 demonstrates the effect that drugs such as verapamil can have on the filling rate.

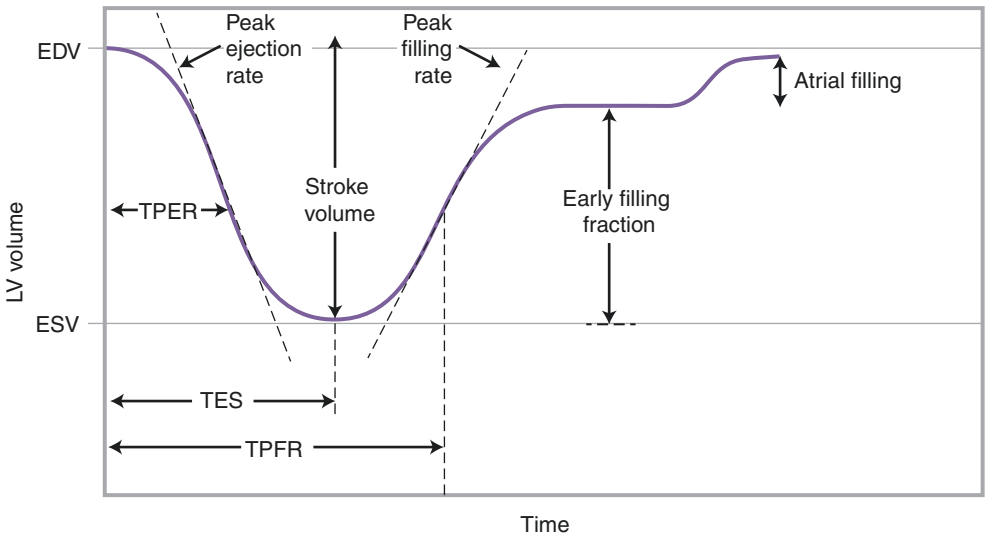

Fig. 7.16 Functional measures. The most useful measure that can be extracted from the LV volume curve is ejection fraction, which is defined as stroke volume/end-diastolic volume (EDV) = ED counts − end-systolic (ES) counts/ED counts, where the counts are assumed to have been corrected for background. Note that although the proportionality factor between "counts" and volume is in general unknown, it does not matter, because this factor will cancel out when the ratio defining ejection fraction is computed. Other parameters that can be extracted from this curve are the peak ejection rate (PER) and its time of occurrence (TPER), usually defined as the maximum negative slope of the LV curve between ED and ES. It characterizes the maximum rate at which blood is ejected by the heart. The time to end systole (TES) is, of course, defined by the minimum of the LV curve. The peak filling rate (PFR) is the diastolic correlate of the PER. ESV end-systolic volume, TPFR time to peak filling rate

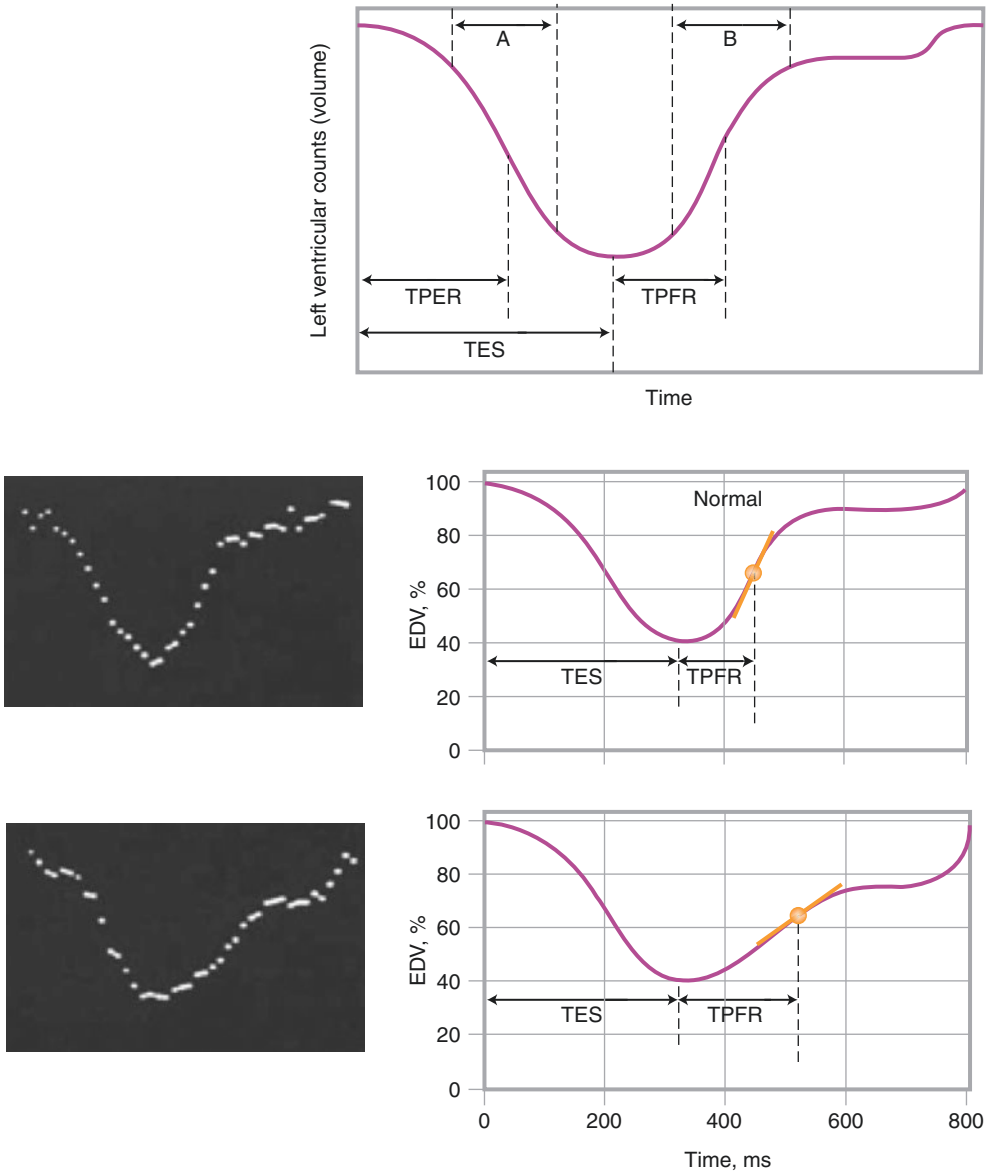

Fig. 7.17 Application of filling phase indices. Shown at the *top* is a diagrammatic left ventricular time-versus-radioactivity curve where the time to peak emptying rate (TPER), time to peak filling rate (TPFR), and time to end systole (TES) are shown in systolic (**a**) and diastolic (**b**) periods [42]. At the *bottom*, actual curves (*left*) and diagrammatic representations (*right*) are shown in a normal patient (*top*) and in a patient with coronary artery disease (CAD, *bottom*). The reduced ventricular filling rate in the latter is evident [42]. EDV end-diastolic volume

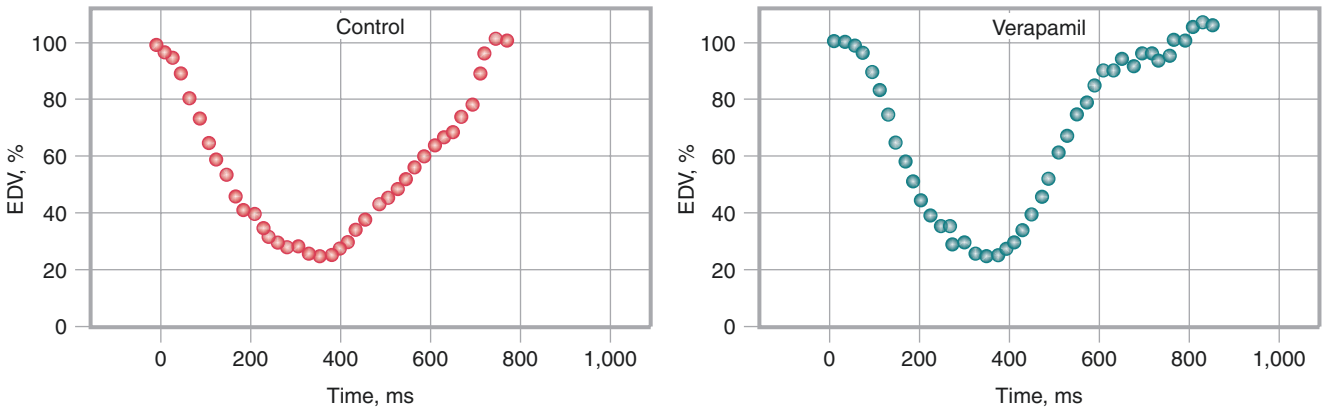

Fig. 7.18 Drug effect on filling rate. Shown is the effect of verapamil on left ventricular compliance and the filling rate in a patient with left ventricular hypertrophy. The slope and the filling rate measured in EDV per second are significantly increased with verapamil [42]

The importance of background in equilibrium blood pool studies is shown in Fig. 7.19 and Table 7.3, which lists the calculations and LVEFs derived from the varying background values shown in the figure.

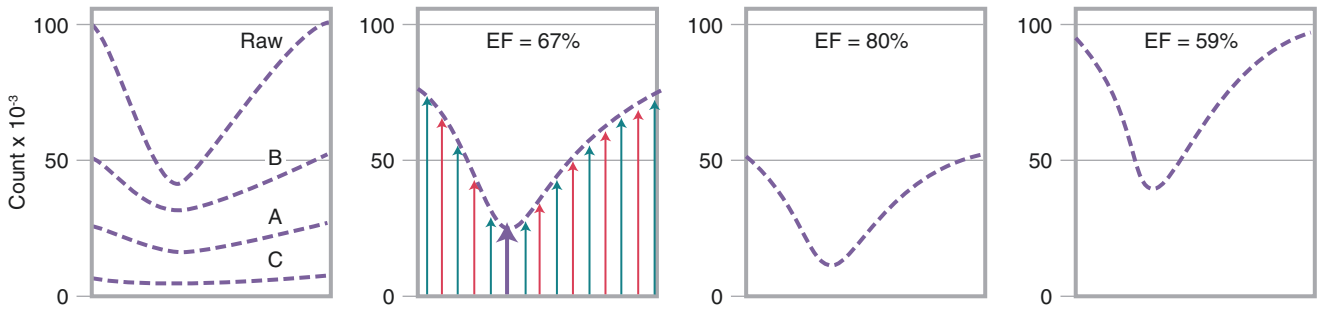

Fig. 7.19 Importance of background in equilibrium blood pool studies. Shown are three model time-versus-radioactivity curves, *A*, *B*, and *C*, which vary only in their background, the greatest in *B* and the least in *C*, as shown in the *left panel* with corresponding background-subtracted curves *A*, *B*, and *C*. The calculations and actual left ventricular ejection fractions (LVEFs) derived from these varying background values are shown in Table 7.3 [43]

Curve	LV ROI pixels	Mean count background ROI	ROI uncorrected counts	Background-corrected counts	LVEF
A	ED 500	50	100,000	75,000	67%
	ES 300		40,000	25,000	
B	ED 500	100	100,000	50,000	80%
	ES 300		40,000	10,000	
C	ED 500	10	100,000	95,000	59%
	ES 300		40,000	37,000	

ED end-diastolic, *ES* end-systolic, *LVEF* left ventricular ejection fraction, *ROI* region of interest

Table 7.3 Importance of background in equilibrium blood pool studies

The absolute LV volume can be calculated with relatively high precision from ERNAs (as well as from first-pass studies), with correction for duration of data collection (i.e., number of beats collected and frame duration), administered dose, and plasma volume. Figure 7.20 shows one method for calculating left ventricular end-diastolic volume, with the validating data comparing volumes obtained by ERNA and contrast angiography at catheterization.

Calculation method

$$\text{LVEDV} = \frac{\text{Count rate from LV in ED frame}/e^{-Ud}}{\text{Count rate/mL from blood sample}}$$

where e^{-ud} = attenuation correction

u = average linear attenuation coefficient

d = depth of the center of the LV from the chest wall

LV count rate from ED frame =

$$\frac{\text{Total LV counts in ED frame}}{\text{Time per frame x number of cycles acquired}}$$

Blood sample of known volume is withdrawn into a small test tube and counted under the same radiation detector (camera) used for radionuclide angiography. The calculated count rate is corrected for decay from the time it was withdrawn during the study to the time it was counted.

a

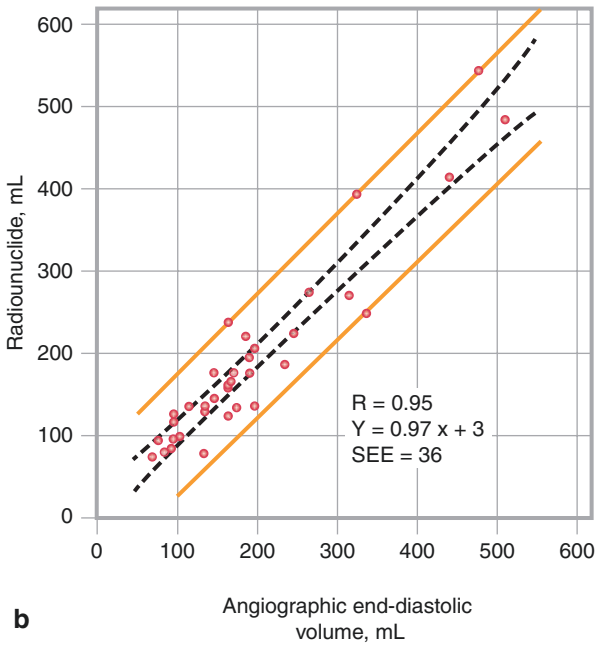

b

Fig. 7.20 Calculation of left ventricular end-diastolic volume from ERNAs, including correction for duration of data collection (i.e., number of beats collected and frame duration), administered dose, and plasma volume. (**a**) One of the many calculation methods. (**b**) The validating data comparing volumes obtained by ERNA and by contrast angiography at catheterization. ED end-diastolic, LVEDV left ventricular end-diastolic volume, SEE standard error of the estimate

Radionuclide Angiography in Clinical Cardiology

Radionuclide angiography (RNA) can be employed for diagnosis, prognostication, and evaluation of therapy in a variety of situations, but other modalities may be more appropriately applied in specific clinical settings. Table 7.4 lists the most appropriate situations for the application of RNA; for some patients it is an appropriate primary evaluation method, but for others, better alternatives clearly exist. *Italicized entities* are those for which RNA has the greatest potential applicability in clinical practice.

Useful for patients with
Chronic stable coronary artery disease (CAD)
Diagnosis
Prognostication
Assessment of efficacy of treatment
Regurgitant valvular diseases
Prognostication and timing of valvular surgery
Assessment of effects of treatment
Cardiomyopathy
Determination of functional severity, categorization for treatment selection
Assessment of effects of treatment
Useful only for highly selected applications in patients with
Acute CAD
Assessment of effects of treatment
Cardiomyopathy
Determination of functional severity, categorization for treatment selection
Assessment of effects of treatment
Diagnosis of acute right ventricular infarction
Prognostication
Stenotic valvular diseases
Mitral stenosis may be useful in prognostication

Table 7.4 Radionuclide angiography in clinical cardiology

RNA is the most widely accepted method for serial evaluation of cardiac function in patients undergoing doxorubicin therapy. LVEF is an important and universally accepted index of cardiac function, and overt congestive heart failure (CHF) due to doxorubicin cardiotoxicity is preceded by a progressive fall in LVEF. Serial studies can detect a change in cardiac function over time, and doxorubicin administration can be stopped when a predetermined fall in LVEF is observed. Both the absolute LVEF and the magnitude of fall are important strategic determinants. The guidelines for using serial RNA at rest, during the course of doxorubicin therapy, are standardized and are based upon experience with nearly 1500 patients over a 7-year period (Table 7.5) . A reduction greater than fourfold in the incidence of overt cardiac failure was observed when these guidelines were followed, and if CHF did develop, it was mild and rapidly responsive to medical therapy. A recent study has reestablished the clinical relevance and cost-effectiveness of serial LVEF monitoring with equilibrium RNA for the prevention of congestive heart failure during the course of doxorubicin therapy [15].

Baseline EF	Perform equilibrium RNA	At risk for CHF
Normal (≈50%)	At baseline	≥10% EF fall from baseline to <50%
	At ≈450 mg/m^2	
	At 250–300 mg/m^2	
≥30–<50%	At baseline	≥10% EF fall from baseline or EF <30%
	Prior to each subsequent dose	
<30%	Avoid doxorubicin	

CHF congestive heart failure, EF ejection fraction

Table 7.5 Radionuclide Angiography for the Evaluation of LVEF in Doxorubicin Therapy

Exercise RNA also has been used in patients undergoing treatment with doxorubicin, but patients with malignancies often have generalized debility, fever, anemia, or musculoskeletal problems that preclude exercise testing. Moreover, exercise testing does not appear to provide any additional information when compared with resting RNA. Some caution may be required in interpreting changes in LVEF during the course of chemotherapy, because these values also are affected by several noncardiac conditions such as anemia, fever, and sepsis. Resting RNA continues to be the most practical and effective way of monitoring doxorubicin cardiotoxicity. In some studies, diastolic dysfunction with a reduction in peak filling rate appears to precede the decrement in LVEF, as the earliest indication of chemotherapy cardiotoxicity [44]. Another study found that diastolic function adds little to LVEF [45]. The generation of measures of diastolic function is technically demanding; its reproducibility and accuracy are less than those of the calculation of LVEF [45].

Figures 7.21, 7.22, 7.23, 7.24, 7.25, 7.26, 7.27, 7.28, 7.29, 7.30, 7.31, 7.32, 7.33, 7.34, 7.35, 7.36, 7.37, and 7.38 demonstrate other appropriate applications for RNA, including the assessment of regurgitant valvular diseases, conduction abnormalities, and the application of pacing devices and cardiac resynchronization therapy.

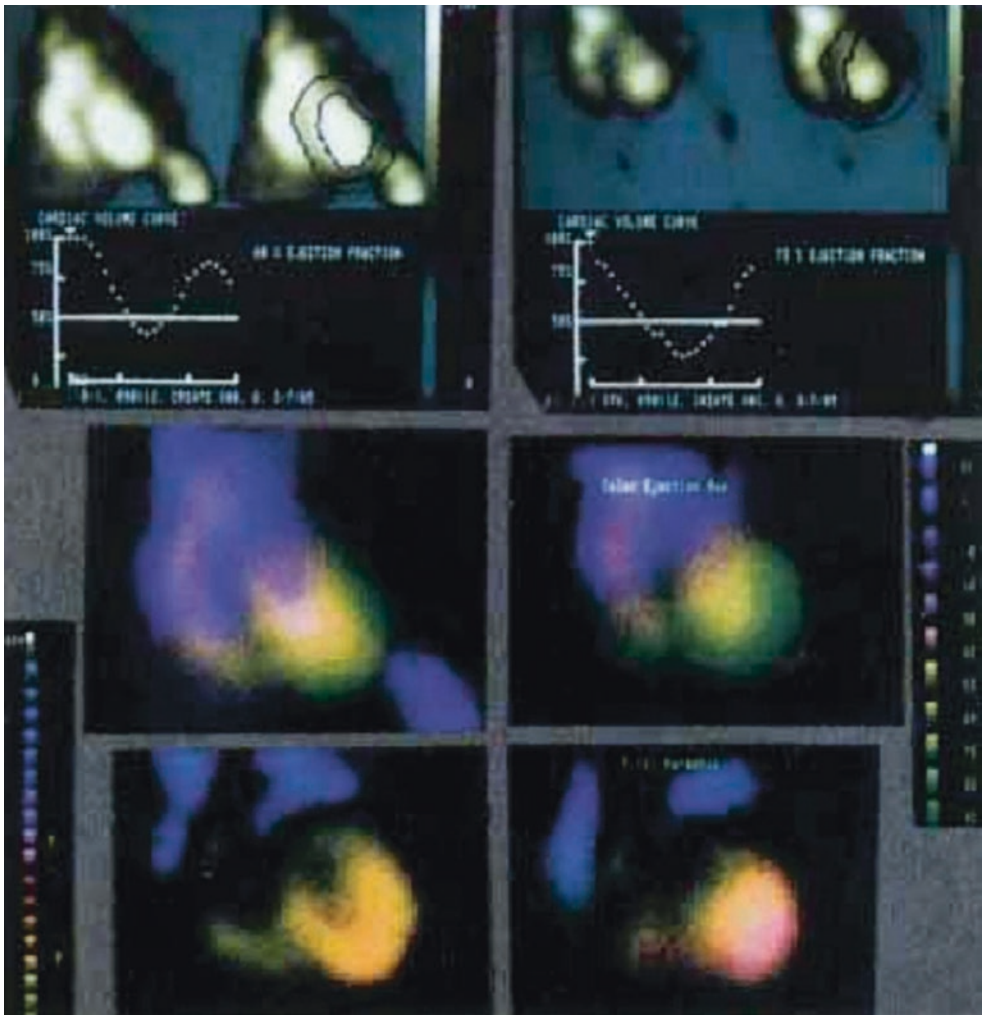

Fig. 7.21 Equilibrium blood pool assessment of aortic regurgitation. Shown are left ventricular (LV) time-versus-activity curves derived from an LV region of interest (*top panel*), ejection fraction images color-coded for regional ejection fraction (*middle panel*), and phase-amplitude images (*bottom panel*) at rest (*left*) and with maximal exercise (*right*) in a young patient with severe aortic regurgitation. Here, the LV edge is derived between the limits of the edges drawn, and the background is taken within these geometric boundaries. Dual color- and intensity-coded images, shown here, permit the integration of multiple parameters in a single image and are an example of the analytic and display potential of the scintigraphic modality. The LVEF increases with exercise. This is supported by the increased area covered by *yellow* and *green* and high ejection fraction values in the ejection fraction image. Although colors shift to later phase angles as heart rate increases, the amplitude and intensity are maintained, and apparent ventricular size decreases in all images, consistent with a normal response to exercise. The uniform phase shift, related to increased symmetry of the time-versus-radioactivity curve with increased heart rate and shortening of end diastole, represents a normal finding, as do all the image results shown here [43]

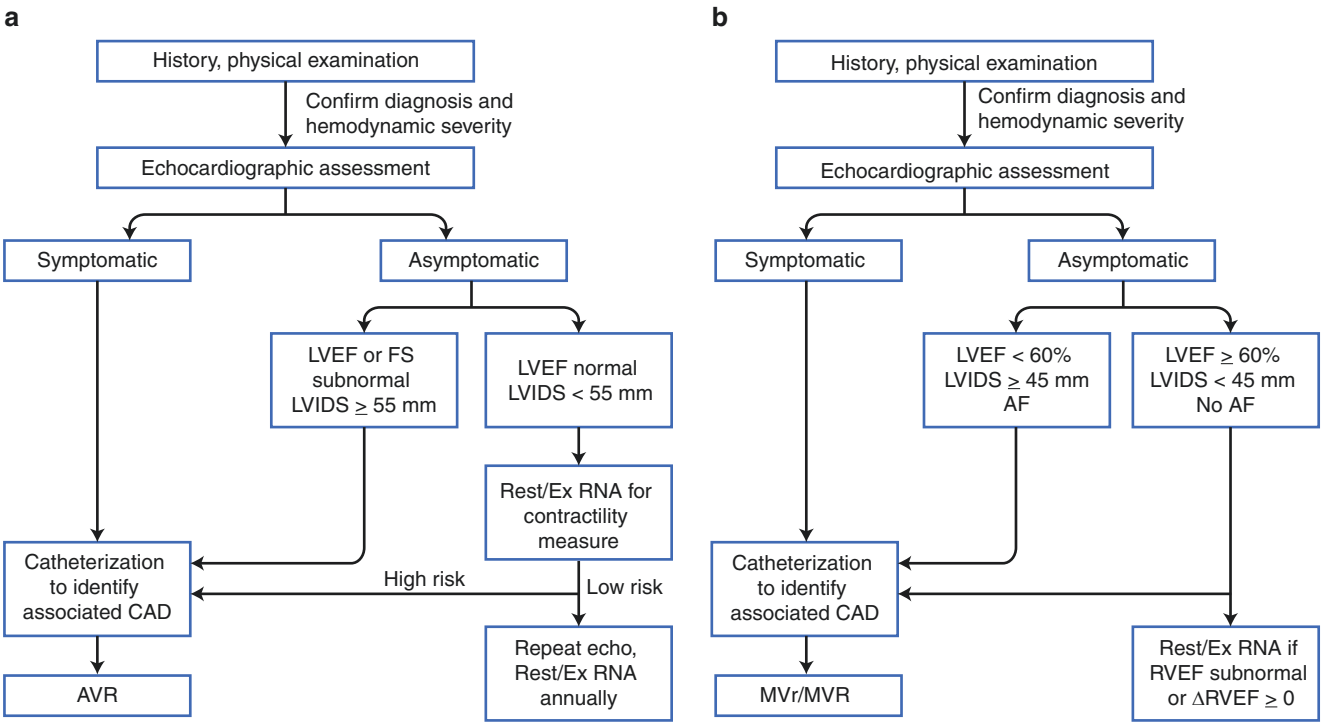

Fig. 7.22 Role of RNA in patients with aortic regurgitation (**a**) and mitral regurgitation (**b**). For asymptomatic patients with regurgitant valvular diseases, echocardiography (echo) is a primary method for diagnosis and for determination of the hemodynamic severity of disease. If echocardiography unequivocally demonstrates subnormal LVEF at rest or "high-risk" left ventricular systolic or diastolic dimension descriptors, management decisions can be made with confidence. For patients with severe aortic regurgitation (**a**) however, the geometric irregularity and regional functional variability of the large left ventricle may result in ambiguity of ejection fraction determination, obviated by non–geometry-dependent evaluation with RNA; if echocardiographic results do not indicate high risk, contractility determination by additional RNA with exercise can detect prognostically important disease. For patients with mitral regurgitation (**b**) the unique capacity of RNA to interrogate right ventricular performance adds an important prognostic dimension not available with echocardiography. In patients with mitral stenosis, a right ventricular ejection fraction (RVEF) determination by RNA carries prognostically important information, but these data have not yet reached routine use in defining management strategies in this setting. Echocardiography remains the primary evaluative modality for mitral stenosis. AF atrial fibrillation, AVR aortic valve replacement, CAD coronary artery disease, Ex exercise, FS echocardiographic fractional shortening, LVIDS left ventricular internal dimension at end systole, MVr mitral valve repair, MVR mitral valve replacement

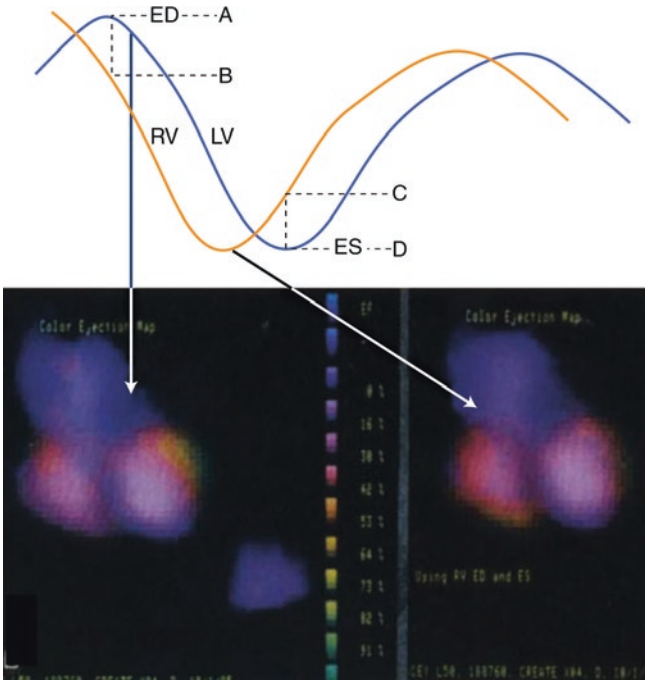

Fig. 7.23 Effect of conduction abnormality. Shown are time-versus-radioactivity curves in a patient with left bundle branch block. The LV curve lags behind the RV curve. The ejection fraction image is derived from frames chosen at LV end diastole (ED) and end systole (ES). Owing to the conduction abnormality, LVED (**a**) and LVES (*D*) correspond to points when the RV is partially filled (**b**) and incompletely emptied (**c**) giving rise to an artificially reduced RVEF. At the *bottom* are color-coded EF images in a patient with a left bundle branch block compiled using frames optimized for LVED and ES (*left*) and for RVED and ES (*right*). Note the bright *green–yellow* area at the LV base (*left*) and the augmentation of high EF colors in the RV (*right*) in these images, derived from different aspects of the same data [43]

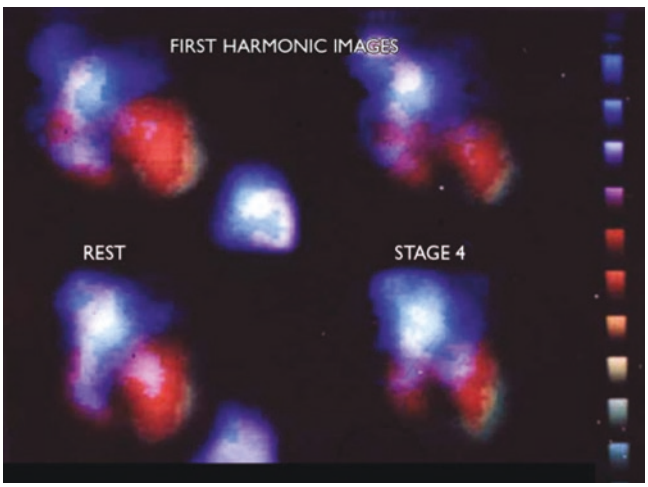

Fig. 7.24 Exercise evaluation. Shown are color ejection fraction images at rest (*left*) and with maximal exercise (*right*) in a patient with CAD (*top*) and with aortic regurgitation (*bottom*). A reduced presence of the "ejection shell," the green and yellow high ejection fraction colors at rest (*left*), demonstrates a decrement in regional function and overall LVEF at stress (*right*) in the CAD patient, whereas reduced LV size with an increased green "ejection shell" demonstrates an augmented LVEF in the patient with aortic regurgitation (*bottom*). Such functional images condense a wealth of information and provide objectivity to the assessment of the effects of intervention on ventricular size and function [43]

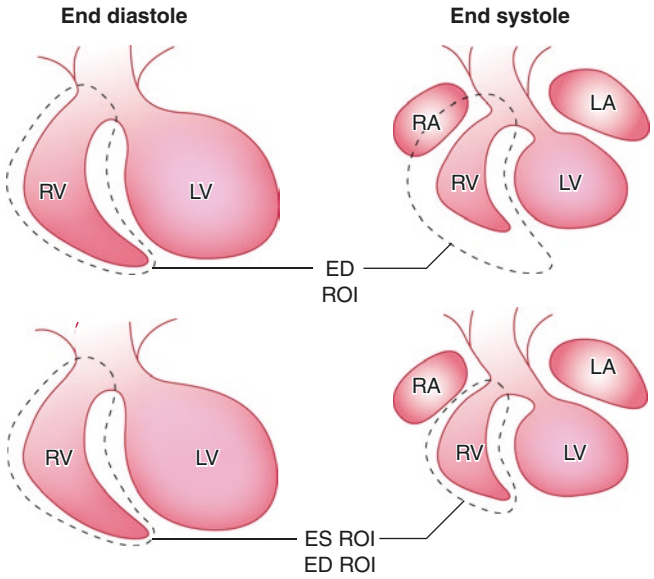

Fig. 7.25 Right ventricular (RV) ejection fraction. Shown diagrammatically is the application of an RV region of interest (ROI) to an equilibrium blood pool study in end diastole (ED) (*left*) and in end systole (ES) (*right*). At *top*, the same ED region is applied in ES with an erroneous inclusion of the right atrium (RA), which is largest in the ventricular ES below, and is ES-specific (ROI is applied with significant improvement, but without total correction for RA overlap on the RV). LA left atrium; LV left ventricle. (Adapted from Botvinick et al. [43])

Regurgitant index

$$RI = \frac{LVSVC}{RVSVC}$$

RF = Regurgitant fraction

$$RF = \frac{LVSVC - RVSVC}{LVSVC}$$

$$RF = \frac{\frac{LVSVC}{RVSVC} \quad \frac{RVSVC}{RVSVC}}{\frac{LVSVC}{RVSVC}} = \frac{RI - 1}{RI}$$

Fig. 7.26 Formulas for the regurgitant index (RI) and the regurgitant fraction (RF). These are parameters applied to determine the severity of regurgitant lesions. The RI is the ratio of the left ventricular stroke volume measured in counts (LVSVC) and the right ventricular stroke volume measured in counts (RVSVC). The amount that LVSVC exceeds RVSVC is a measure of the regurgitant volume and is expressed as the RI. The RF is that percentage of the LVSV that is regurgitating and adding to the overall LVSVC. However, scintigraphically, both measures fail to correct for right atrial overlap on the right ventricle. This error causes an underestimation of the RVSV and an exaggeration of the RI, which may be as high as 1.3 in normal subjects

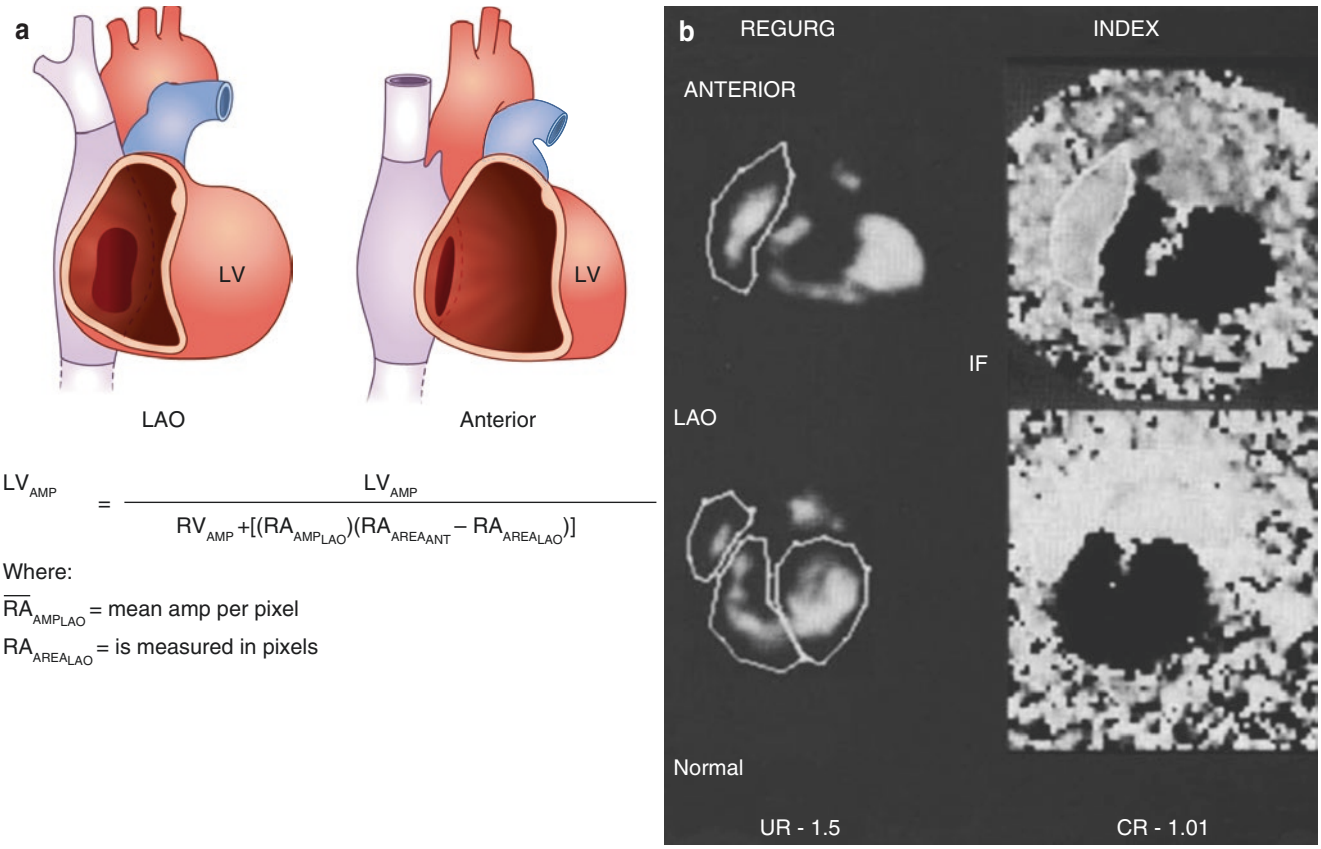

Fig. 7.27 Regurgitant index (RI) corrected for right atrial (RA) overlap. The anatomic basis (**a**) for the amplitude-based correction (AMP) of RI for RA overlap [46]. Here, right ventricular (RV) amplitude, an analogue of stroke volume, is corrected with the addition of the product of the mean per-pixel amplitude of the RA in the left anterior oblique (LAO) projection and its area, measured in pixels of the RA that are obscured by the RV, the difference in the RA area measured on anterior (ANT) and LAO projections. This correction results in the reduction of the RI to unity in normal subjects and, compared with the uncorrected value, correlates much better with other measures of valvular regurgitation, as shown in the clinical example (**b**). Given the ubiquity and capabilities of echocardiography with Doppler evaluation, it is the method of choice for evaluation of regurgitant lesions [46]

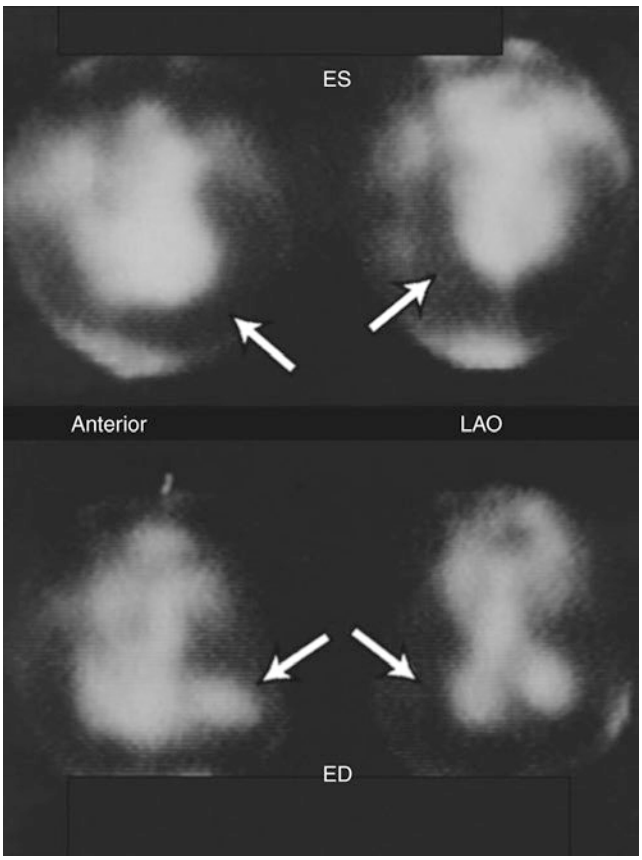

Fig. 7.28 Pericardial tamponade. Shown are left anterior oblique (LAO) and anterior views in end systole (ES) (*top*) and end diastole (ED) (*bottom*) in a man with severe fatigability and weakness several weeks after coronary bypass graft surgery. The large "photopenic" region around both ventricles indicates a large pericardial effusion (*arrows*). The small, volume-starved left ventricle is consistent with tamponade, which was the eventual diagnosis

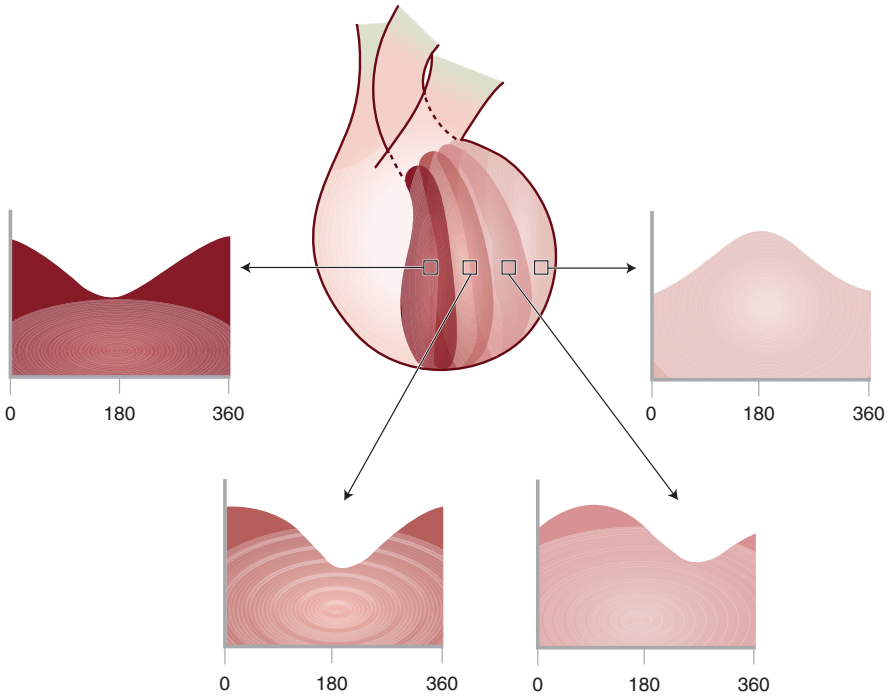

Fig. 7.29 Phase analysis. This diagram presents a ventricle that is gray-scale coded for increasing delay in contraction sequence, from the septum to the lateral wall. The resultant cosine curves, fitted to the regional time-versus-radioactivity curve, are shown below. The septum and its corresponding curve begin contraction at the R wave. The region has a phase angle of 0° and is coded as dark. The lateral wall and its related cosine curve fill when the ventricle should empty. This wall would demonstrate paradoxical motion, and the curve would have a phase angle of 180° [47]

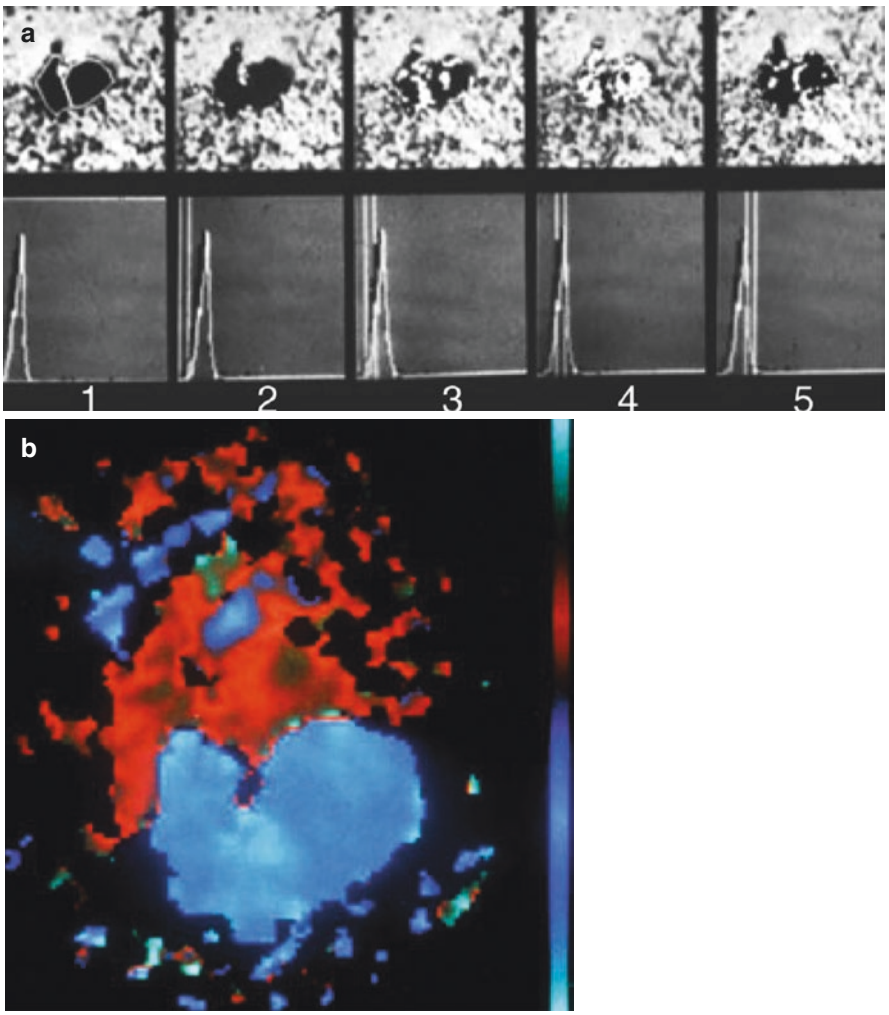

Fig. 7.30 Phase image with normal conduction. (**a**) Phase image (*top*) and left (*white*) and right (*black*) ventricular histograms (*bottom*) plotting the phase angle on the abscissa and its frequency of occurrence on the ordinate in the "best septal" LAO projection in a patient with normal conduction. The serial phase angle is sampled in the intervals of the vertical gray bars setting the histogram windows, and the corresponding spatial location is indicated by a progressive white highlight of associated pixels on the phase image, from left to right. The earliest phase angle is seen at the base of the septum. (**b**) A background subtracted color composite image of the sequential phase angle in this patient reveals symmetric phase distribution and contraction of the two ventricles

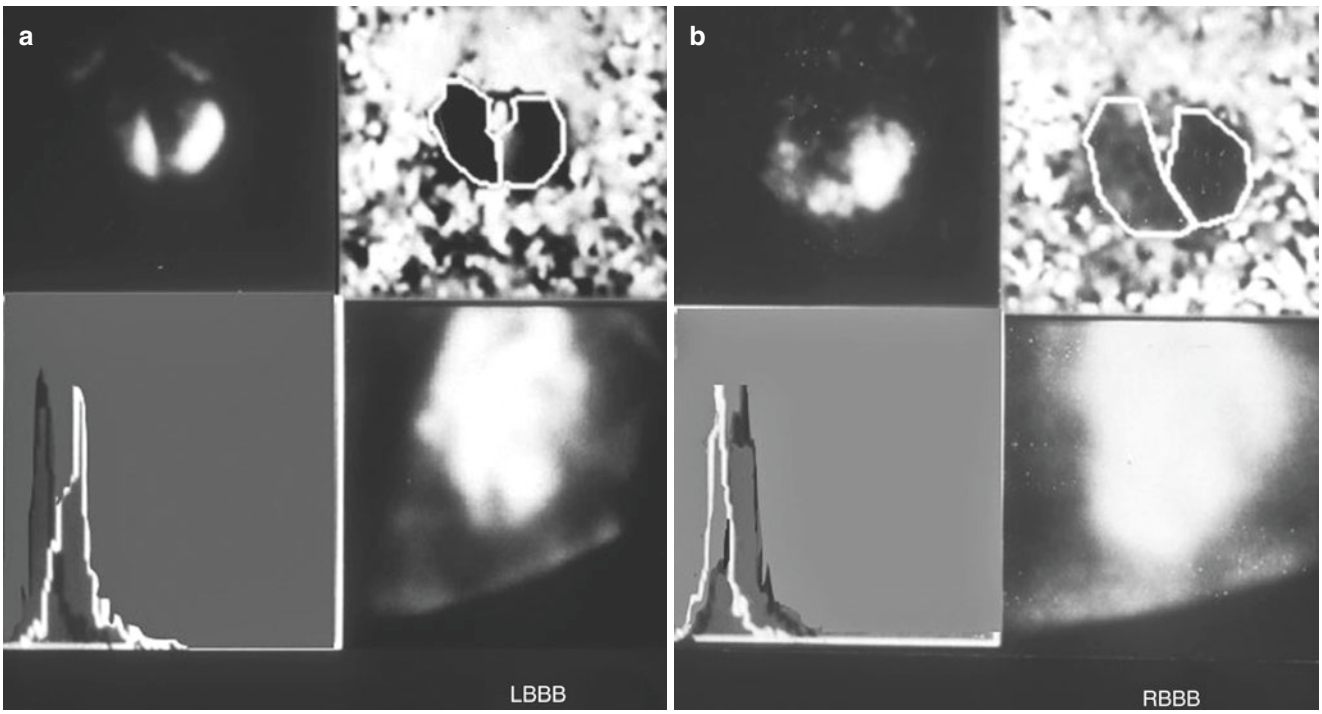

Fig. 7.31 Phase images in a bundle branch block. Shown are amplitude images (*upper left*), phase images with right and left ventricular regions of interest (*upper right*), phase histograms (*lower left*), and summed blood pool images in the "best septal" LAO projections in patients with left bundle branch block (LBBB) (**a**) and right bundle branch block (RBBB) (**b**) [45]. The phase histogram plots left (*white*) and right (*black*) ventricular histograms, with phase angle on the abscissa and its frequency on the ordinate. The right ventricular phase histogram and right ventricular activation are earliest in LBBB, whereas the left ventricular histogram and activation are earliest in RBBB [47]

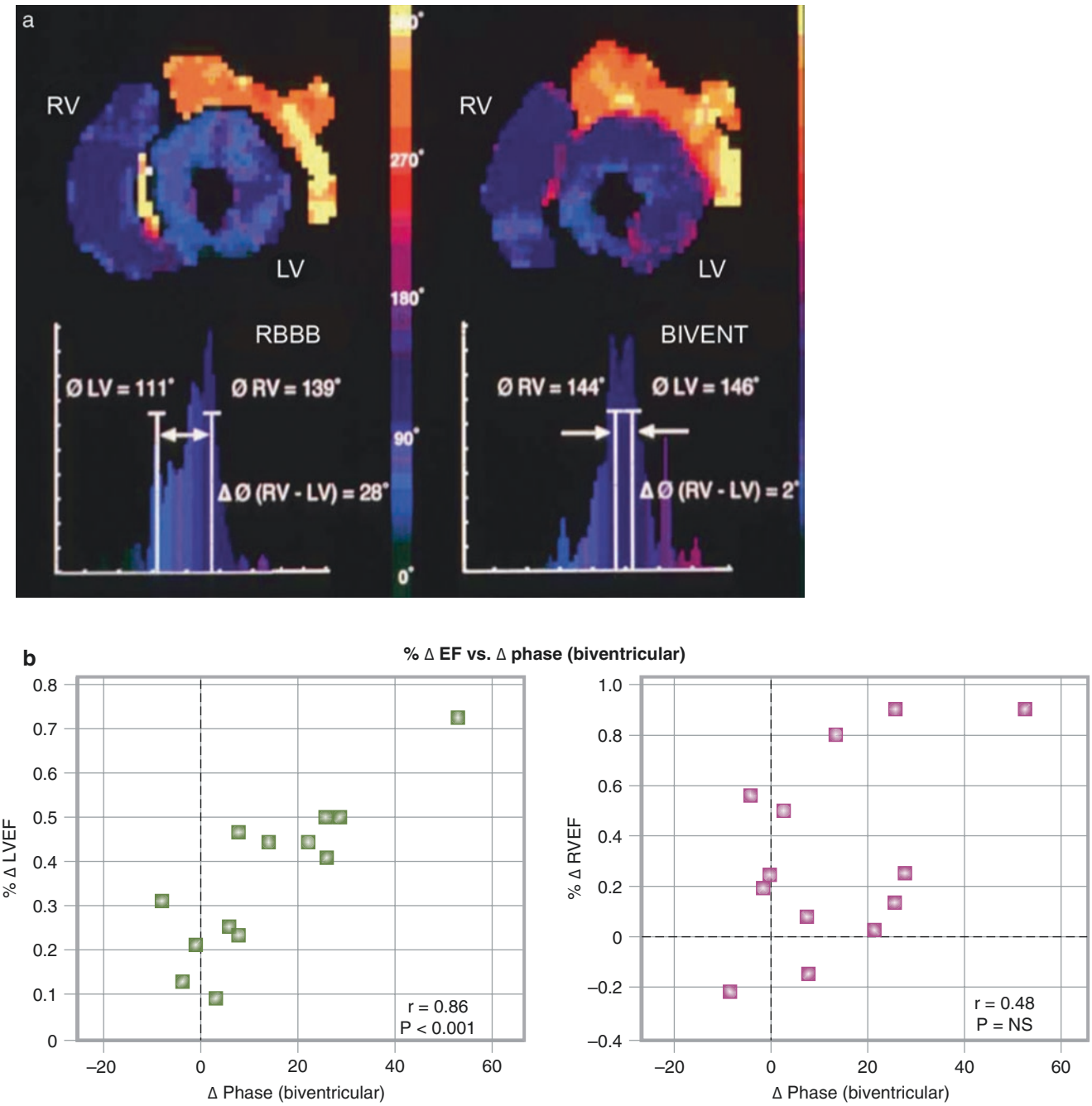

Fig. 7.32 The effects of biventricular (Bivent) pacing. (**a**) Phase images and RV and LV phase histograms from a heart failure patient with baseline RBBB are shown, before and after placement of a biventricular pacemaker [46]. The difference in the mean ventricular phase angle is reduced, with increased interventricular synchrony. (**b**) The inverse relationship between the LVEF (*left*) and the RVEF (*right*) and the interventricular phase difference. That is, the greater the reduction brought by biventricular pacing in the difference between the mean phase angles of RV and LV, the greater the subsequent improvement in LVEF. (From Kerwin et al. [48]; with permission from Elsevier)

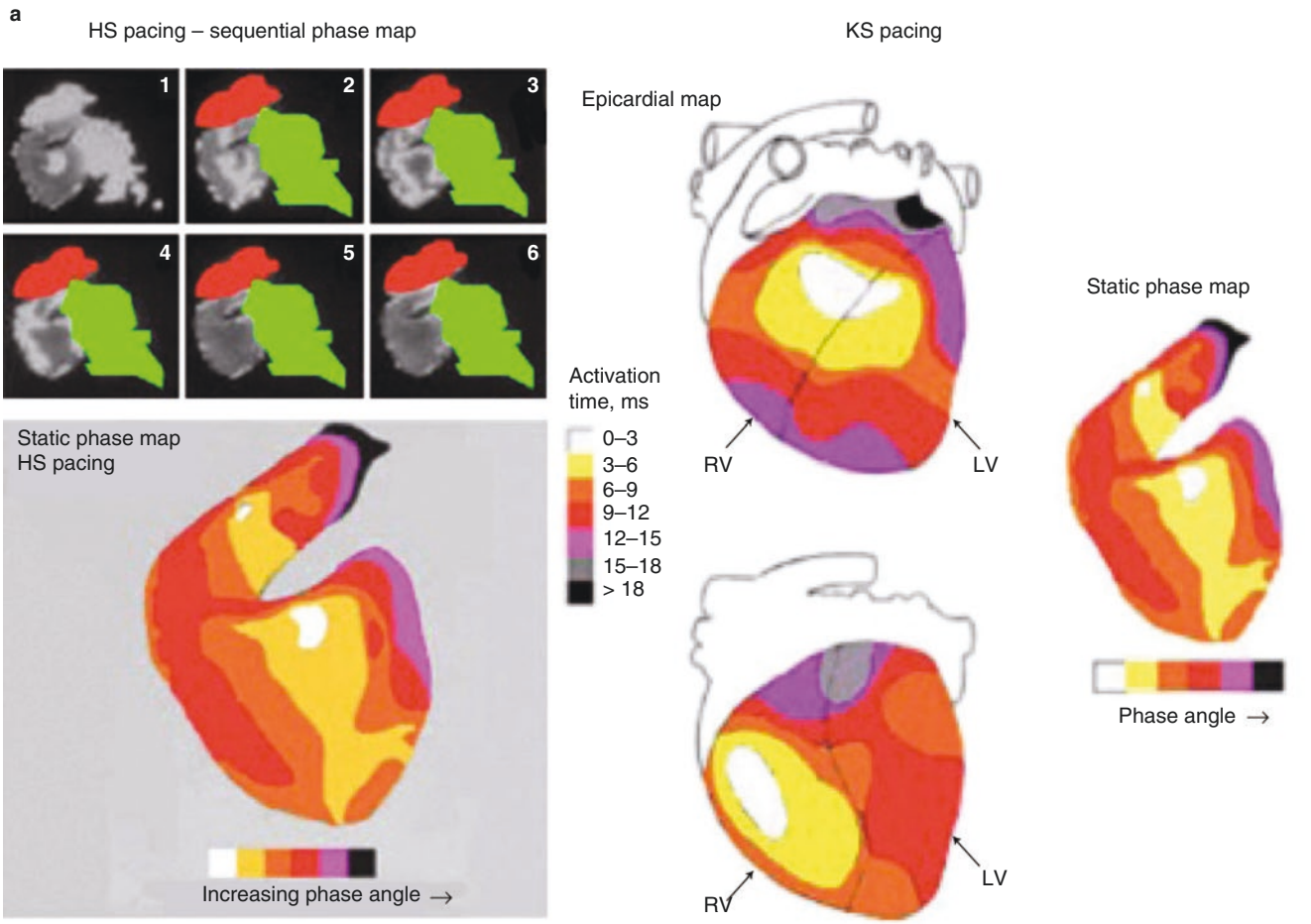

Fig. 7.33 Relationship between myocardial contraction (scintigraphic phase image analysis) and conduction (electrophysiologic mapping). This dog study was performed to validate the relationship between contraction and conduction, which is of high potential importance to patients. It could be applied with significance to answer other questions of great clinical importance, as shown in the study illustrated in Fig. 7.34. (**a**) High-septal (HS) pacing. Phase images are shown in the *top left* image. Shown in a left oblique projection are frames in a sequential phase map, from 1 through 6, demonstrating the serial progression of the phase angle and related contraction in an infarcted dog. The ventricles are in *gray* in the upper left image with progressive phase intervals shown in *white highlight*. The right atrium is masked in *red* and the left atrium in *green*. A phase map (*lower left*) is based on the images in the *top left* panel. This diagram characterizes the sequence of phase progression in six color-coded intervals to match the pattern in the *top left image*. Increasing the phase angle and contraction delay is shown in the color code (*below*). The number of phase intervals illustrated in this and subsequent figures has been chosen empirically to illustrate the sequence of progression in association with contraction patterns of varying rate and complexity. Good phase and electrophysiologic activation map (EAM) agreement is shown in the *right* panel. Shown at *right* is the same diagram of serial phase progression, the phase map. At *left* are anterior (*above*) and posterior (*below*) views of the epicardial map presented in seven color-coded intervals. The parallel of the conduction pattern on the epicardial map with the phase map sequence is evident. (**b**) Right ventricle (RV) pacing. Phase images are shown in the *top left* image. Shown in a left oblique projection (as in **a**) are frames in a sequential phase map, from 1 through 6, demonstrating the serial progression of phase angle and related contraction, with RV pacing in the same dog. The ventricles are in *gray* in the upper left image with progressive phase intervals in *white*, and the atria are again masked. Shown in the *lower left* is the phase map of the images in the *top left* panel, where the phase map is a diagram characterizing the sequence of phase progression in six color-coded intervals. Incomplete phase and EAM agreement is shown in the *right* panel. Shown at *right* is the same diagram of serial phase progression shown in the *top left* panel. At *left* are anterior (*above*) and posterior (*below*) views of the epicardial map presented in seven color-coded intervals. The parallels and inconsistencies with the phase map are evident. (**c**) Left ventricle apical (*LVa*) pacing. A phase map (*top left*) again Is a left oblique projection, with frames sequential from 1 through 6, demonstrating a serial progression of phase angle and related contraction, with LVa pacing in the same dog. The ventricles are in *gray,* with progressive phase intervals sequentially highlighted in *white*. The atria are again masked in the same way. The *bottom left* image is a phase map of the images in the *top left* panel, where the phase map is a diagram characterizing the sequence of phase progression in nine color-coded intervals to match the pattern of the *top left* panel. Good phase and EAM agreement is shown in the *right* panel. Shown at *right* is the same diagram of serial phase progression shown in the *top left* panel. At *left* are anterior (*above*) and posterior (*below*) views of the epicardial map presented in eight color intervals. The parallel with the phase map is evident. (From Munoz del Romeral et al. [49]; with permission from Springer Nature)

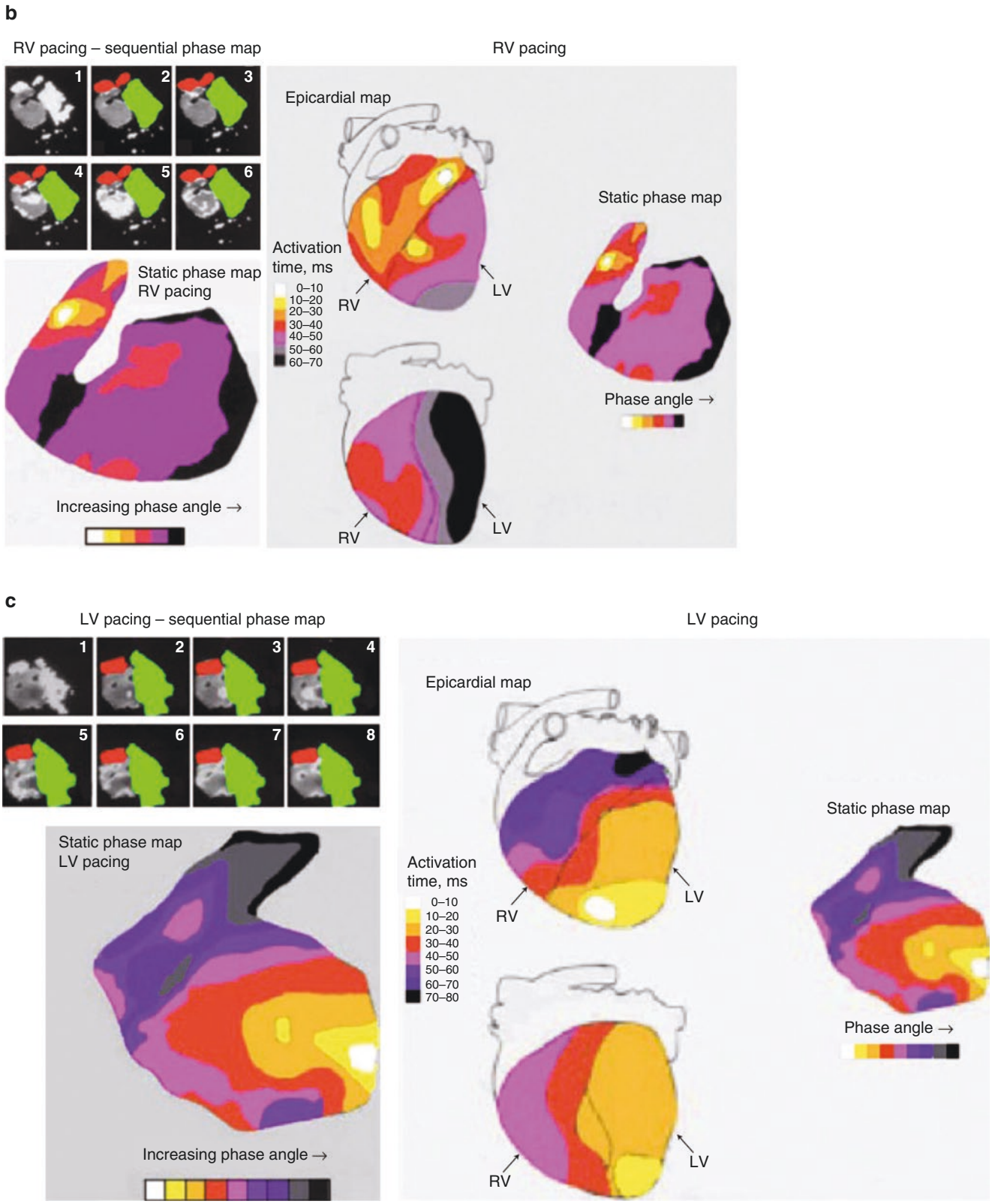

Fig. 7.33 (continued)

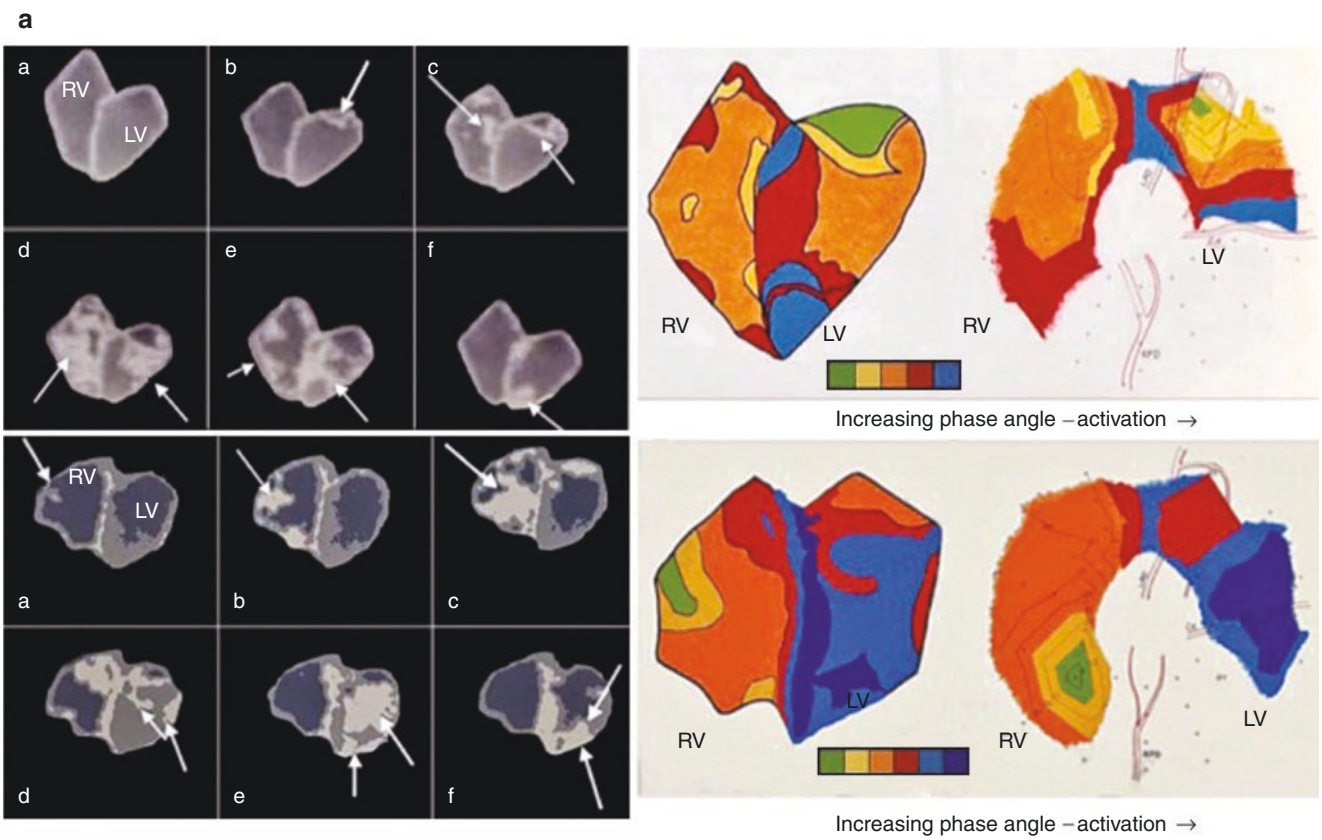

Fig. 7.34 Variable functional effects of pacing site in normal and scarred ventricles. The value of equilibrium RNA in investigative work is illustrated here in images from an animal study of cardiac resynchronization therapy that could have wide implications for the treatment of advanced heart failure patients with biventricular pacemakers. (**a**) Phase and isochronous epicardial maps. Shown are serial phase images with a masked background, in a normal animal studied with high septal (HS) pacing (*top left*) and in an infarcted animal with RV pacing (*bottom left*). Progressive whitening of the phase images in *a* to *f* delineates the course of progression of a serial phase angle and related contraction through the right and left ventricles. *Arrows* in *a* and *b* of each figure part localize the site of the earliest phase angle. Subsequent *arrows* point to areas of sequential phase angle progression. The *left* images of the *right* panels are diagrammatic color-coded phase maps that summarize the serial phase progression of the phase image in the figures they follow: *upper right*, with HS pacing, and *lower right*, with RV pacing of an infarcted ventricle. Here, the color progression, shown in the color scale at the bottom of each figure, parallels the phase progression highlighted in *white* in the preceding figures. The *right* images in the *right* panels present the related color-coded isochronous epicardial maps, which summarize the serial activation pattern, here related to their associated phase maps (*left*), drawn in the anatomically opened RV and LV, with walls exposed. The coronary distribution is roughly illustrated by the left anterior descending (LAD) coronary artery, left circumflex coronary artery, and right posterior descending coronary artery. In each case, serial phase progression related well to the epicardial activation sequence. In the normal ventricle (*upper* panels), the phase angle progressed through contiguous LV regions. Contrast phase images (*lower left*), summarized in the *left* image in the *lower right* panel in the animal with a distal LAD infarction, reveal an initially contiguous phase progression (*arrows*, *c* and *d*), until near the infarct area. Here, myocardial contraction "skips" a distal myocardial region between the *arrows* in *e*. This region demonstrates delayed phase progression (*arrow*, *f*). A similar pattern was well seen on the activation map (*lower right*, *right* image), with some variation. (**b**) Blood pool images. Shown are end-diastolic (ED) and end-systolic (ES) frames from the ERNA acquired in an animal with an LAD myocardial infarction (MI), during baseline normal sinus rhythm (NSR, *above*) and with septal pacing (*below*). Normal RV and LV wall motion (*arrows*) is evident and confirmed by the superimposition of ED (*black*) and ES (*red*) contours. (**c**) ED and ES frames from the ERNA acquired in the same animal illustrated in (**a**) now during RV pacing (*above*) and with LV apical pacing (*below*). Evident is apical hypokinesis with the RV pacing site, as well as apical dyskinesis and an apical aneurysm with LV apical pacing. Again, LV wall contours are drawn and superimposed for ED (*black*) and ES (*red*). These images clearly demonstrate variable regional LV wall motion and systolic function with a variation of the pacing site in relation to an LV infarction. This same principle could be applied to recognize the benefits of specific cardiac resynchronization therapy pacemaker locations and, potentially, to optimize them. (From Munoz Del Romeral et al. [50]; with permission from Springer Nature)

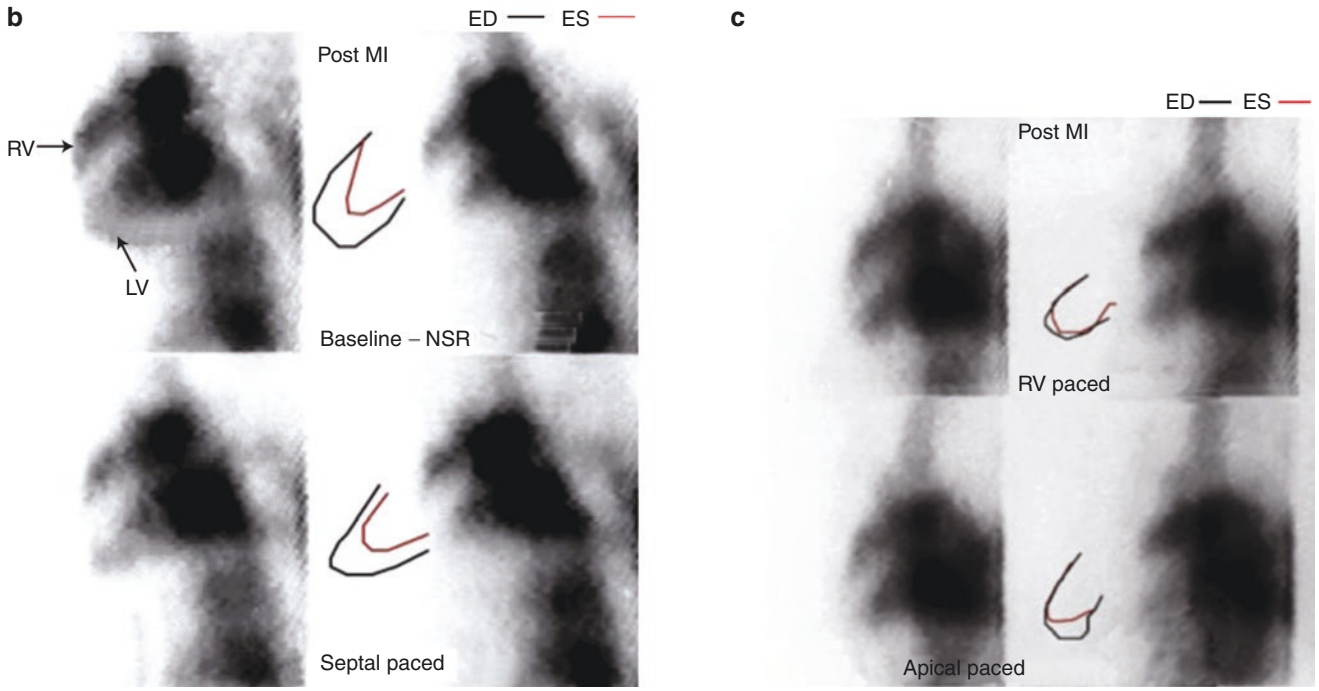

Fig. 7.34 (continued)

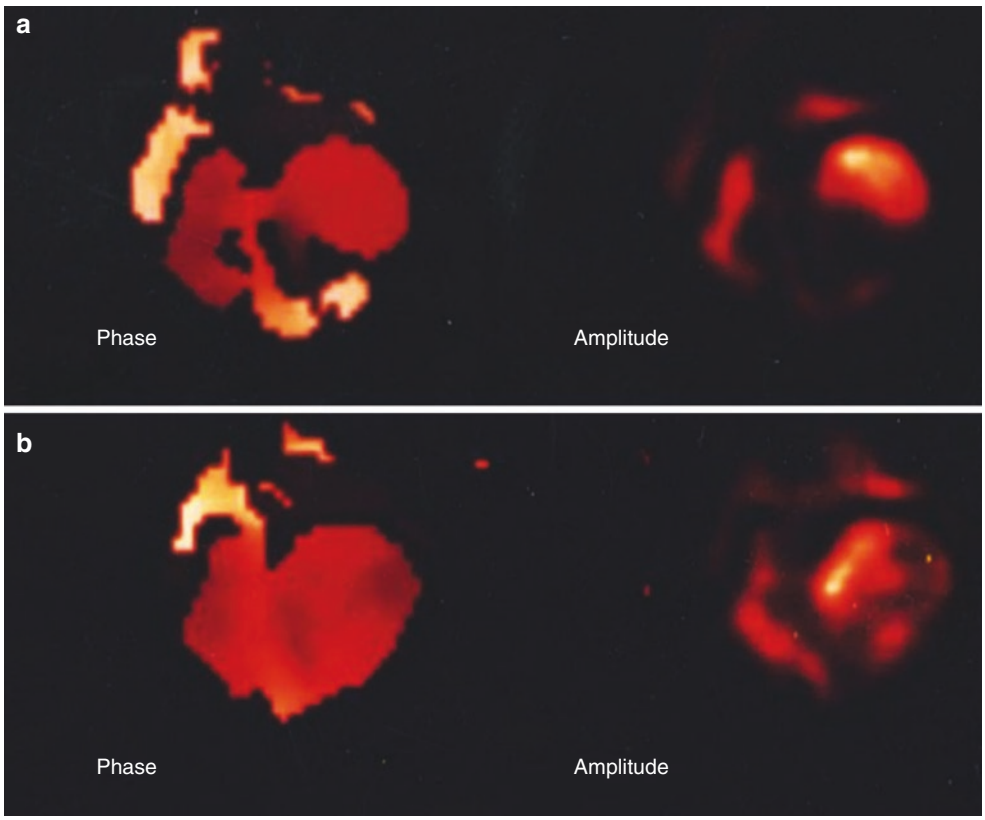

Fig. 7.35 Phase image analysis of synchrony before and after biventricular pacing. Shown are examples of phase and amplitude images derived from gated equilibrium blood pool scintigrams in a patient with advanced systolic heart failure [51]. In such patients, the placement of pacemakers in both the right ventricle and the left ventricle, as well as biventricular pacing, serves as an advanced interventional therapy, cardiac resynchronization therapy (CRT). (**a**) Images from the patient were acquired at baseline, with evidence of gross regional dyssynchrony in the phase image at *left* (white color in the septum and apex) and with reduced amplitude in most of the distal left ventricle, as shown by the low-intensity regions of the amplitude image at *right*. (**b**) The color is more homogeneous and phase is more synchronous, with much improvement in the intensity of the amplitude image following biventricular pacemaker insertion. Not surprisingly, the patient was much improved clinically following the procedure. This method has been tested and validated for accuracy and reproducibility of synchrony measurement in 48 normal subjects [51, 52]

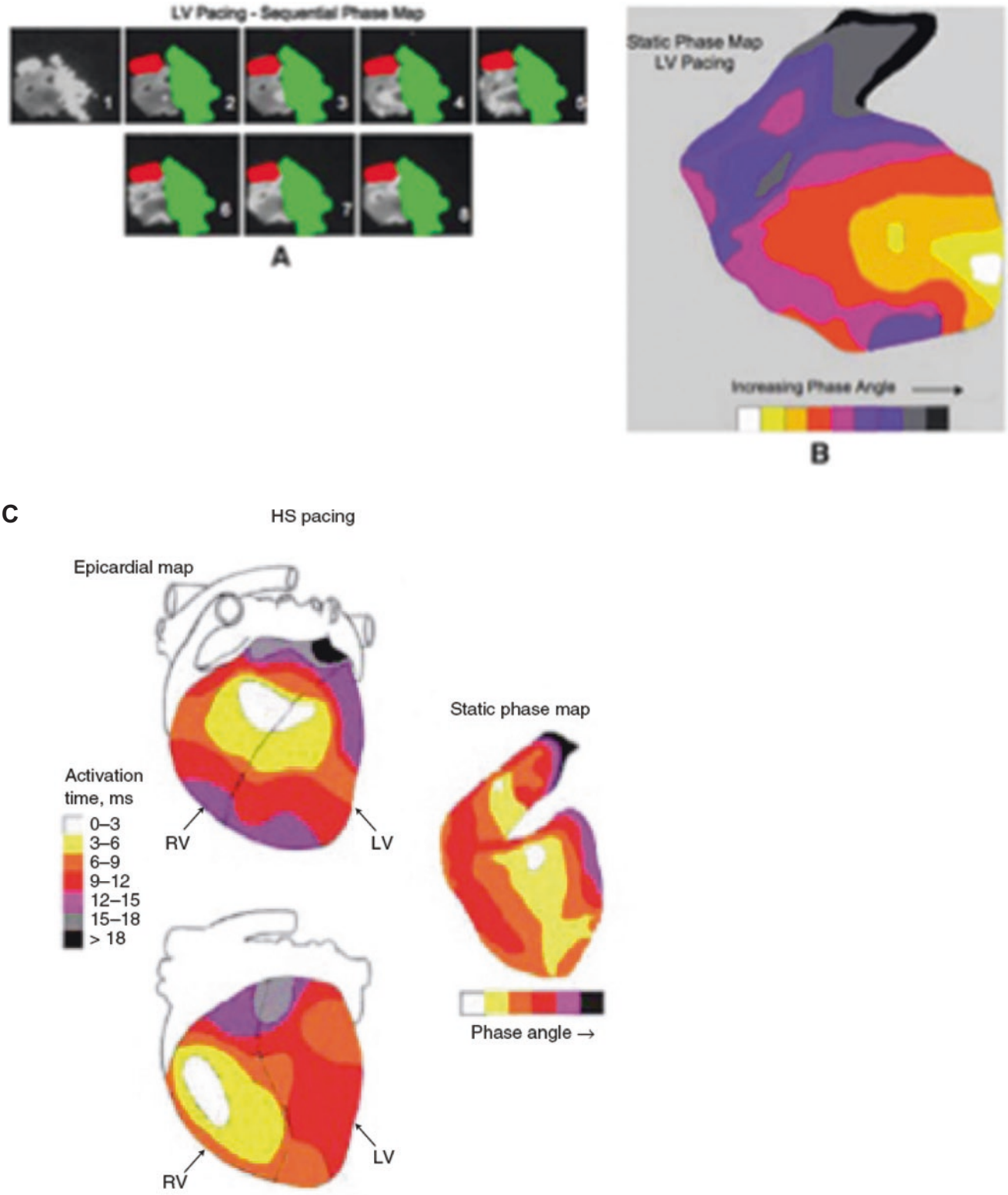

Fig. 7.36 Atrial LV pacing. (**a**) Sequential frames in phase map. Shown at *upper left*, in a left anterior oblique projection, are frames in a sequential phase map, from 1 through 6, demonstrating serial progression of phase angle and related contraction, with atrial LV pacing in a dog model. The ventricles are in gray in the *upper left* image with progressive phase intervals sequentially highlighted in white. The atria are in *green*. (**b**) Phase map. Shown is a phase map of the images in (**a**), a diagram characterizing the sequence of phase progression in nine color-coded intervals to match the pattern of (**a**). (**c**) Good phase and epicardial map agreement. Shown at *right* is the same diagram of serial phase progression shown in (**a**). At left are anterior (*above*) and posterior (*below*) views of the epicardial map presented in eight color intervals. The pattern agreement with the phase map is evident. (From Munoz del Romeral et al. [49]; with permission from Springer Nature)

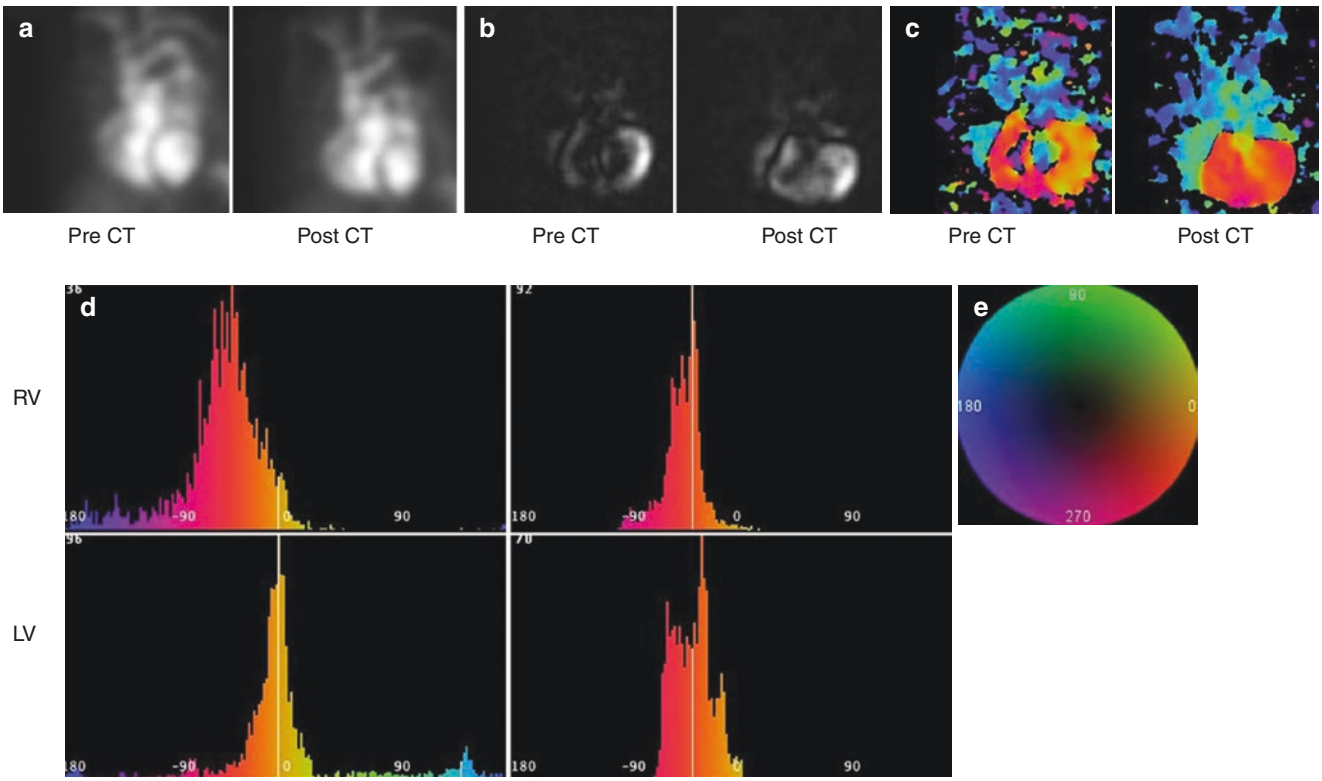

Fig. 7.37 Good outcome of cardiac resynchronization therapy (CRT). Heart failure (HF) is the most frequent cause of cardiac hospitalization in the United States, affecting 5,000,000 patients, with 250,000 deaths yearly. Both ventricular systolic function and synchrony have been shown to have significant prognostic impact in HF. CRT has been proven to reduce both the morbidity and the mortality of HF patients who become refractory to medications and present with a wide QRS. However, improvement of HF with CRT based on clinical and echocardiographic criteria is highly variable; 30–40% of patients do not improve or worsen with CRT. Scintigraphic methods that image myocardial perfusion and function have been adapted for synchrony analysis. SPECT myocardial perfusion scintigraphy combines measures of both perfusion and function, and extracted parameters have been demonstrated to measure ventricular synchrony and even to predict CRT outcomes. ERNA has advantages of higher temporal resolution, greater reproducibility, and volumetric analysis of both ventricles that can be applied for analysis of intraventricular synchrony and interventricular synchrony (IVS). Novel, objective measures of regional contraction and global mechanical synchrony based on the first harmonic fit of the ERNA ventricular time-versus-radioactivity curve, the synchrony (S) and entropy (E) parameters, have been developed and are generated by in-house software. These parameters were demonstrated to be highly reproducible, with both intraobserver and interobserver variability in the range of 2%. Applied in a simulation model, S and E were observed to discriminate better the synchrony profiles among a spectrum of patterns of wall motion than LVEF or the SD of LV phase angle (SDLVØ) measured on the phase histogram, which plots phase angle (Ø) on the abscissa versus its frequency on the ordinate within the LV region of interest (ROI). The aim was to correlate these novel parameters of S and E with clinical outcomes in patients with advanced HF undergoing CRT. (**a**) ERNA cines. Shown are best septal LAO projections of a gated ERNA acquired in a heart failure patient with excellent CRT outcome (before CRT, *left*; after CRT, *right*). NYHA class fell from III to I as ERNA LVEF increased from 22% to 35% with CRT. (**b**) Amplitude images. Shown are amplitude images with intensity proportional to amplitude, derived from cines in (**a**) (before CRT, *left*; after CRT, *right*). Note the more complete appearance of the post-CRT image. (**c**) Phase images. Shown are phase images derived from cines in (**a**) color-coded for phase angle according to the sequence on the color wheel in (**e**) (before CRT, *left*; after CRT, *right*). Note more homogeneous color distribution across both ventricles after CRT. Improved intraventricular synchrony and interventricular synchrony are evident and confirmed on related histograms (**d**)**.** (**d**) Phase histograms. Shown are RV phase histograms (*top*) and LV phase histograms (*bottom*), derived from phase images shown in (**c**) each plotting phase angle on abscissa and its frequency on the ordinate, within respective ventricular ROIs, color-coded for phase angle according to its sequence as in (**e**) (before CRT, *left*; after CRT, *right*). Reduced width and baseline scatter in both histograms after CRT supports improved LV synchrony, which increased from 0.84 to 0.97, whereas LV entropy decreased from 0.69 to 0.50, and the standard deviation of LVØ decreased from 61.7 to 19.62 with CRT, whereas improved vertical alignment of LV and RV histograms after CRT supports improved interventricular synchrony, which decreased from 41.2 to 6.92. (**e**) Color wheel. Here the color code is applied to serial phase angles in images and histograms, above and below, where the earliest ventricular phase angle is at approximately 0° [53]

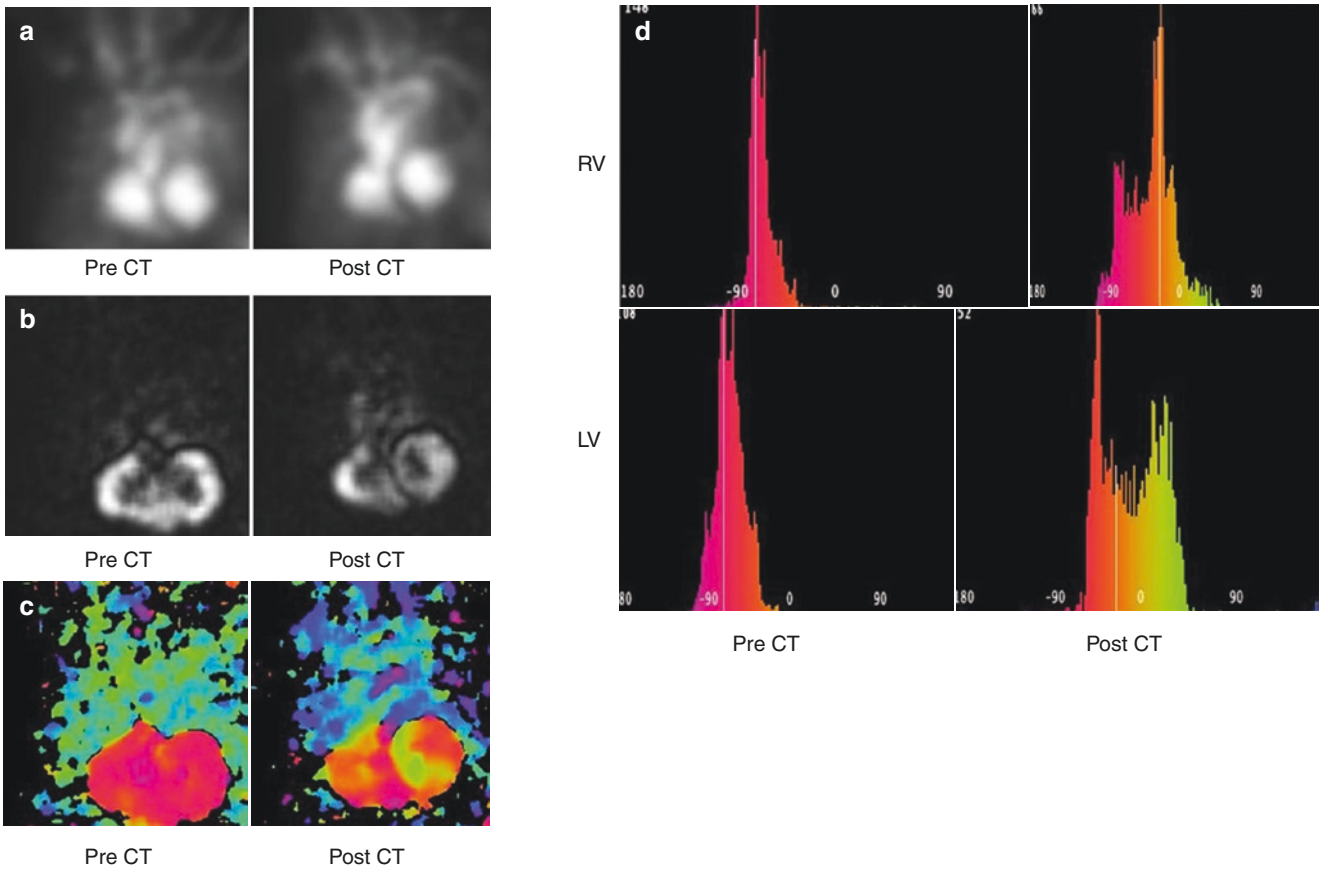

Fig. 7.38 ERNA images of a patient with poor CRT outcome. (**a**) ERNA cines. Shown are the best septal LAO projections of the gated ERNA acquired in a HF patient with a poor CRT outcome (before CRT, *left*; after CRT, *right*). NYHA class remained at III as pre-CRT LVEF of 35% fell to 30% after CRT. (**b**) Amplitude images. Shown are amplitude images derived from cines in (**a**) (before CRT, *left*; after CRT, *right*). Note the more heterogeneous appearance of the post-CRT image. (**c**) Phase images. Shown are phase images (before CRT, *left*; after CRT, *right*) derived from cines in (**a**) color-coded for phase angle according to sequence on the color wheel in Figure 7.38E. Note more heterogeneous and disparate phase distribution in each ventricle after CRT, compared with homogeneous biventricular distribution before CRT. Color and Ø changes indicate worsening of intraventricular synchrony and IVS confirmed on related histograms (**d**). (**d**) LV phase histograms. Shown are RV phase histograms, *above*, and LV phase histograms, *below* (before CRT, *left*; after CRT, *right*), derived from phase images shown in (**c**). Increased width and spectrum in both histograms after CRT indicates reduced intraventricular synchrony (LVS) as LVS fell from 0.96 to 0.87. LV entropy (LVE) increased from 0.36 to 0.66, and the standard deviation of LVØ (LVSDØ) increased from 12.29 to 28.34, whereas vertical misalignment of LV and RV histograms, apparent after CRT, supports observed increased IVS from 1.97 to 45.19 [53]

SPECT Blood Pool Imaging

With the increase in the use of echocardiographic procedures and the widespread acceptance of gated myocardial perfusion SPECT, gated planar blood pool imaging has decreased to less than 10% of all nuclear cardiac studies performed in the United States, although the percentage may be substantially higher in other countries. Conversely, the case for gated blood pool SPECT has considerably strengthened, owing to the increase in computer speed, the greater diffusion of multidetector cameras, and the general acceptance of state-of-the-art three-dimensional analysis and display techniques. We believe that gated blood pool SPECT will become the most commonly utilized nuclear cardiology method for blood pool scintigraphy, the main rationale for its use being its ability to assess both LV and RV function parameters, without a need for background subtraction. Gated blood pool SPECT images can be displayed in a parametric three-dimensional format, much like gated perfusion SPECT; because the epicardium is not visualized in blood pool imaging, a standard display will represent the LV and RV endocardium as shaded surfaces and their location at end diastole as wire grids (Fig. 7.39). The clinical circumstances in which this procedure is likely to become effective are the same as those in which resting blood pool scintigraphy is currently applied, chief among them the assessment of doxorubicin cardiotoxicity. Blood pool scintigraphy is also commonly employed in serial assessment of patients with aortic insufficiency and congestive heart failure and in patients who have undergone cardiac transplantation. Promising recent data have suggested that phase analysis from blood pool scintigraphy may be of clinical value in selecting patients who might benefit from biventricular pacing for resynchronization. Analysis of a regional and global ejection fraction on gated blood pool SPECT correlates well with independent calculations of regional wall motion based on MRI measurements and is superior to a visual analysis of wall motion [54]. Calculation of LV volumes and ejection fraction by cardiac MRI correlated well with similar measurements on gated SPECT blood pool imaging [55].

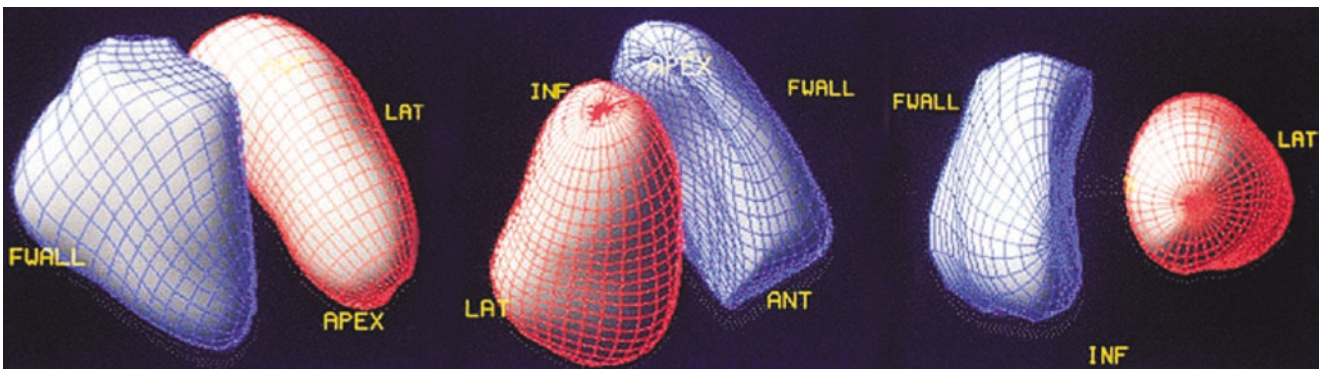

Fig. 7.39 Gated blood pool single-photon emission CT (SPECT): left and right ventricle. ANT anterior LV wall, FWALL free RV wall, INF inferior LV wall, LAT lateral LV wall

Figure 7.40 also illustrates SPECT blood pool imaging, demonstrating three-dimensional reconstructions of SPECT gated equilibrium images from multiple angles in end diastole and end systole.

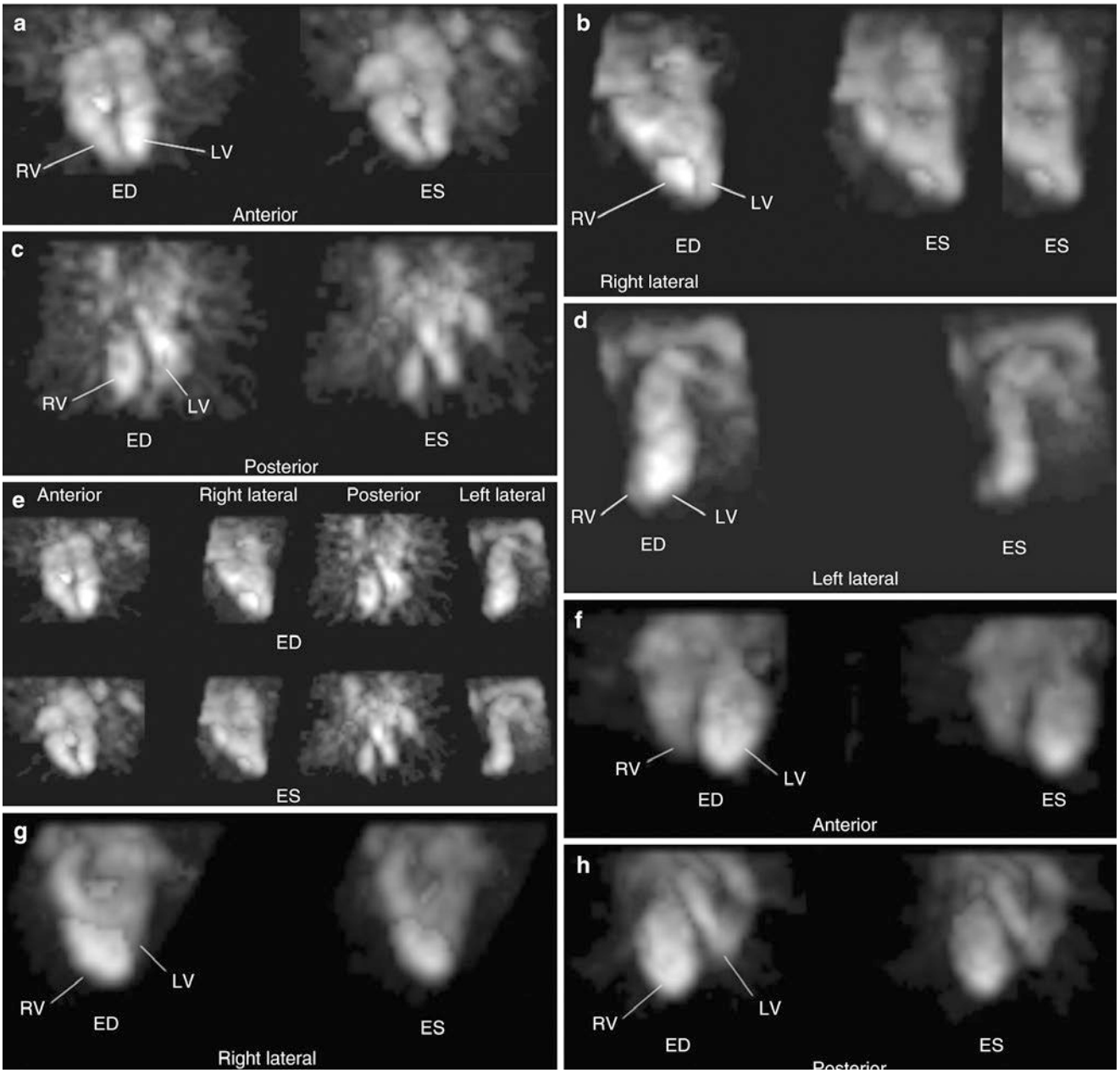

Fig. 7.40 SPECT blood pool imaging. This three-dimensional (3-D) reconstruction of SPECT gated equilibrium images of a normal ventricle in end diastole (ED) and end systole (ES) viewed from multiple angles counterclockwise around a 360° orbit, from anterior (**a**) to right lateral (**b**) to posterior (**c**) and left lateral (**d**) views. (**e**) ED and ES images in all views of this normal heart are shown in a single panel. (**f–i**) the same views as in (**a–d**) This 3-D reconstruction of ED and ES gated blood pool images (using the same views as **a–d**) shows a patient with an anterior, apical, and septal LV aneurysm. The *arrow* in (**i**) points to the dynamic base of the LV, where the distal aspects are essentially akinetic. This is not well appreciated in other views. (**j**) The ED and ES images in all views of this aneurysmal heart are shown in a single panel. (**k**) Shown is a reconstructed gated 3-D blood pool study in a patient with pre-excitation and a posterior septal bypass pathway in the LAO projection (*top*) and the posterior view (*bottom*). The sequential phase progression is sequentially highlighted in *white* from the upper left to lower right in each panel, as shown in the adjacent diagrams from *1* through *3*. In the *top panel*, the *white arrowheads* show the phase progression from the lateral left and right ventricular walls (*above*), progressing toward the middle of the image (*below*). However, in the *bottom* panel, the focus is really shown to be the posterior septum (*arrow*) [56]

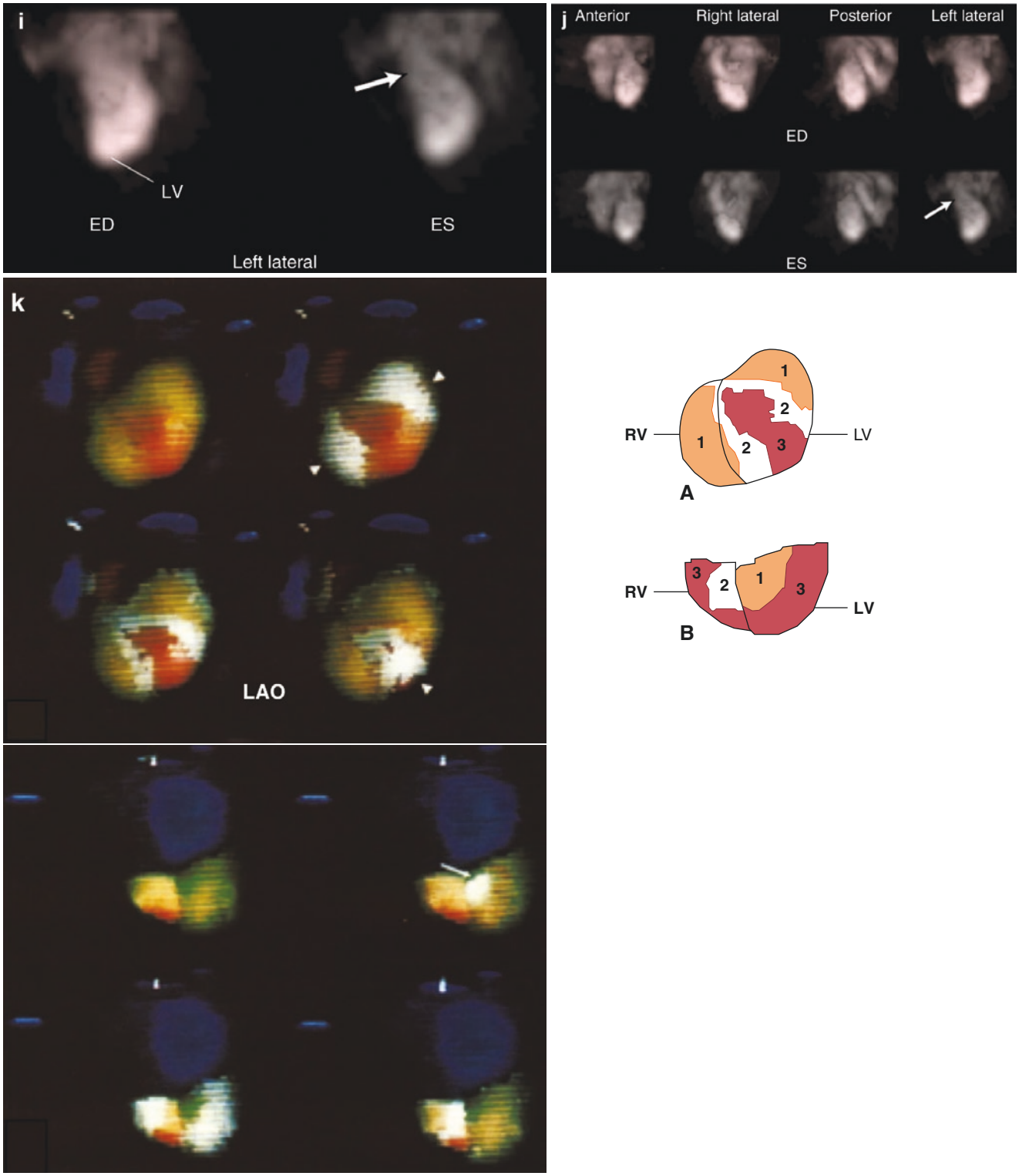

Fig. 7.40 (continued)

Gated Myocardial Perfusion SPECT

It is estimated that over 90% of myocardial perfusion SPECT studies performed in the USA in 2004 used ECG gating, which makes it possible to provide both perfusion and function information with a single radiopharmaceutical injection and a single acquisition sequence (Fig. 7.41). In our laboratory, we do not increase the injected dose or the acquisition time when gating a myocardial SPECT study: Typical parameters used are low-energy, high-resolution collimator(s), patient weight-based injection of 25–40 mCi of ^{99m}Tc-sestamibi/tetrofosmin or 3–4.5 mCi of ^{201}Tl, 3° spacing between adjacent projections, and 25-second (^{99m}Tc) or 35-second (^{201}Tl) acquisition time per projection [59]. The resulting total acquisition time can be as short as 12.5 minutes (^{99m}Tc) or 17.5 minutes (^{201}Tl) if a dual-detector camera with the detectors at a 90° angle is used.

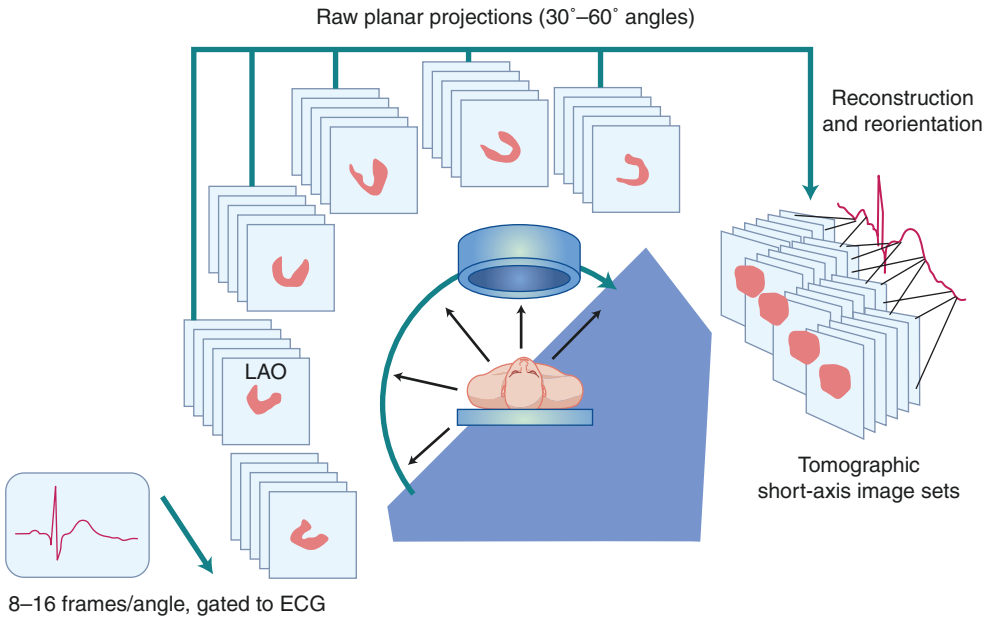

Fig. 7.41 Gated myocardial perfusion single-photon emission CT (*SPECT*): acquisition. A gated cardiac SPECT acquisition proceeds almost exactly like an ungated one: The camera detector(s) rotate around the patient, collecting projection images at equally spaced angles along a 180° or 360° arc. These projections are then filtered and reconstructed into tomographic short-axis and long-axis images [57, 58]. Gated SPECT imaging's distinguishing feature is that at each angle, several projection images (8, 16, or even 32) are acquired, each corresponding to a specific phase of the cardiac cycle. Reconstruction of all same-phase projections produces a three-dimensional "snapshot" of the patient's heart, frozen in time at that particular phase, and doing so for all phases results in four-dimensional image volumes (x, y, z, and time) from which cardiac function can be readily assessed [59]

Figures 7.42, 7.43, 7.44, 7.45, 7.46, and 7.47 demonstrate some clinical uses of phase images acquired by gated SPECT.

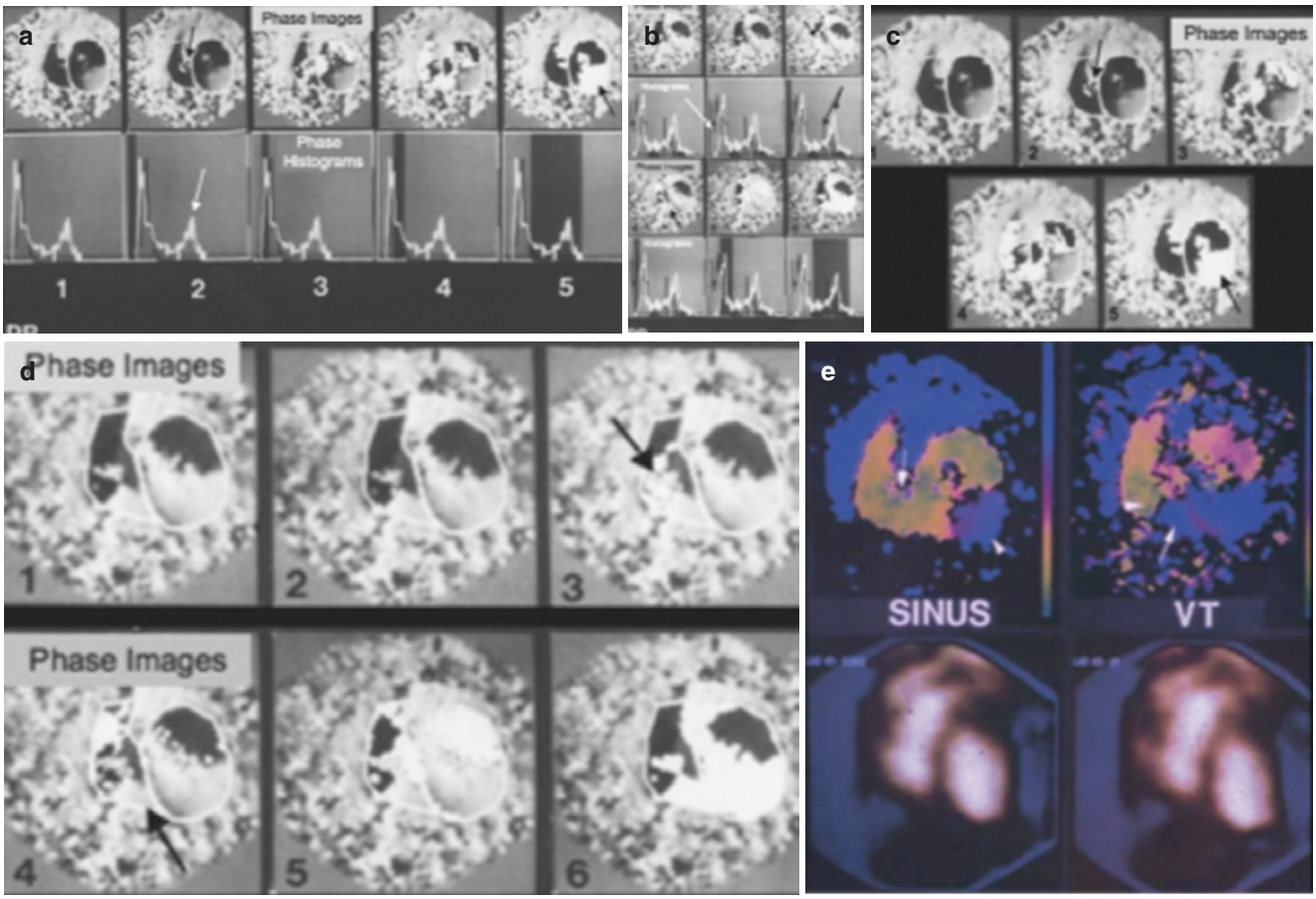

Fig. 7.42 Phase images in sinus rhythm (**a**) and ventricular tachycardia (VT) (**b**) in the "best-septal" LAO projection in a patient with VT. The phase images are displayed above their related LV (*white*) and RV (*black*) histograms, relating the phase angle, Ø, of each pixel, increasing from left to right on the abscissa, to the number of pixels with a given Ø, on the ordinate. The pixels with Ø spanned by the gray histogram sampling window are highlighted in white on the phase image, above. (**c**) and (**d**) are enlargements of the serially highlighted phase images shown in (**a**) and (**b**). In sinus rhythm (**a**), the earliest Ø is evident at the septal base (*black arrow*, panel 2) here projecting to the right, with an accompanying early LV site, a normal pattern. Initiation of both histograms is near simultaneous, but the late histogram peak of localized LVØ delay (*white arrow*, panel 2) corresponds to an apical aneurysm (*black arrow*, panel 5). In VT (**b**)**,** the RV histogram (*white arrow*, panel 2) precedes the LV. The earliest Ø is now in the distal RV, at sites highlighted in phase panels 2 and 3 (*black arrow*, phase panel 3). The late peaks on both histograms (*black arrows*, panel 3) correspond to an expanded LV aneurysm and a "new" RV apical aneurysm (*black arrow*, panel 4), distal to the VT exit site, which lies on its proximal border**.** (**e**) The lower panels present ungated blood pool images in the "best-septal" LAO projection for reference in interpreting the color phase images in sinus rhythm, sinus, and VT shown in preceding panels. These phase images present a color summary of sequential contraction, where the site of earliest Ø (in *green*) marks the septum and proximal RV (*arrow* in sinus rhythm), and the mid-RV in VT (*arrowhead*). The paradoxical motion of the apical LV aneurysm is featured in blue in sinus rhythm (*arrowhead*), and the new apical RV aneurysm is seen in blue in VT (*arrow*). Apical LV and RV scars, both supplied by an occluded left anterior descending coronary artery and a distal RV VT exit site, were confirmed at surgery. (From Botvinick et al. [60]; with permission from Springer Nature)

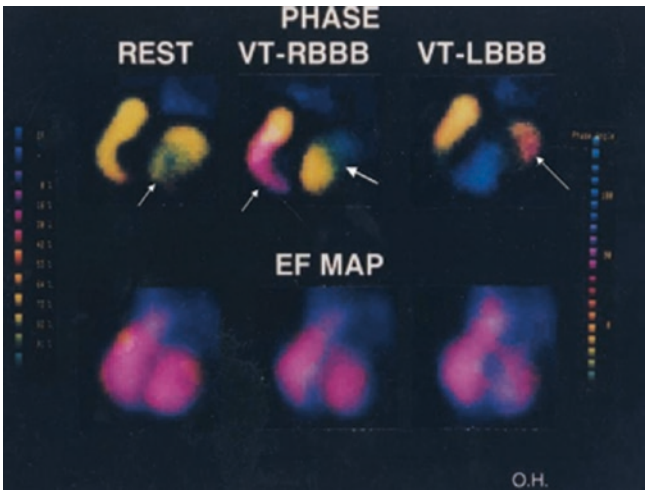

Fig. 7.43 Multiple VT exit sites: RBBB/LBBB patterns. Shown in the "best-septal" LAO projection are phase images acquired in a patient during sinus rhythm and during two different induced VT patterns, imaged at a similar rate, one with a RBBB and another with a LBBB. Below each phase image is the regional ejection fraction (EF) image, where ***green***, ***yellow***, and ***red*** indicate high values and ***blue*** **color** reflects akinetic to dyskinetic segments, as in the color scale at **right**. At rest, earliest Ø, ***green*** (***white arrow***) was confined to septal and adjacent LV regions with an RV contraction and conduction delay (***yellow***). On the related EF image, ventricular function is preserved only at the bases. The RBBB VT relates to a gross distal RV Ø delay, ***pink*** (***white arrow***), with earliest Ø at the mid- and basal LV, ***green-blue*** (***thick white arrow***), confirmed at electrophysiologic study. The function of both ventricles was modestly reduced. The LBBB VT related to a distal septal or RV apical exit site (***green***), with great delay in basal LV contraction, ***pink*** (***white arrow***). A gross Ø delay in the distal LV with aneurysm formation is evident in ***blue*** and on the EF image. (From Botvinick et al. [60]; with permission from Springer Nature)

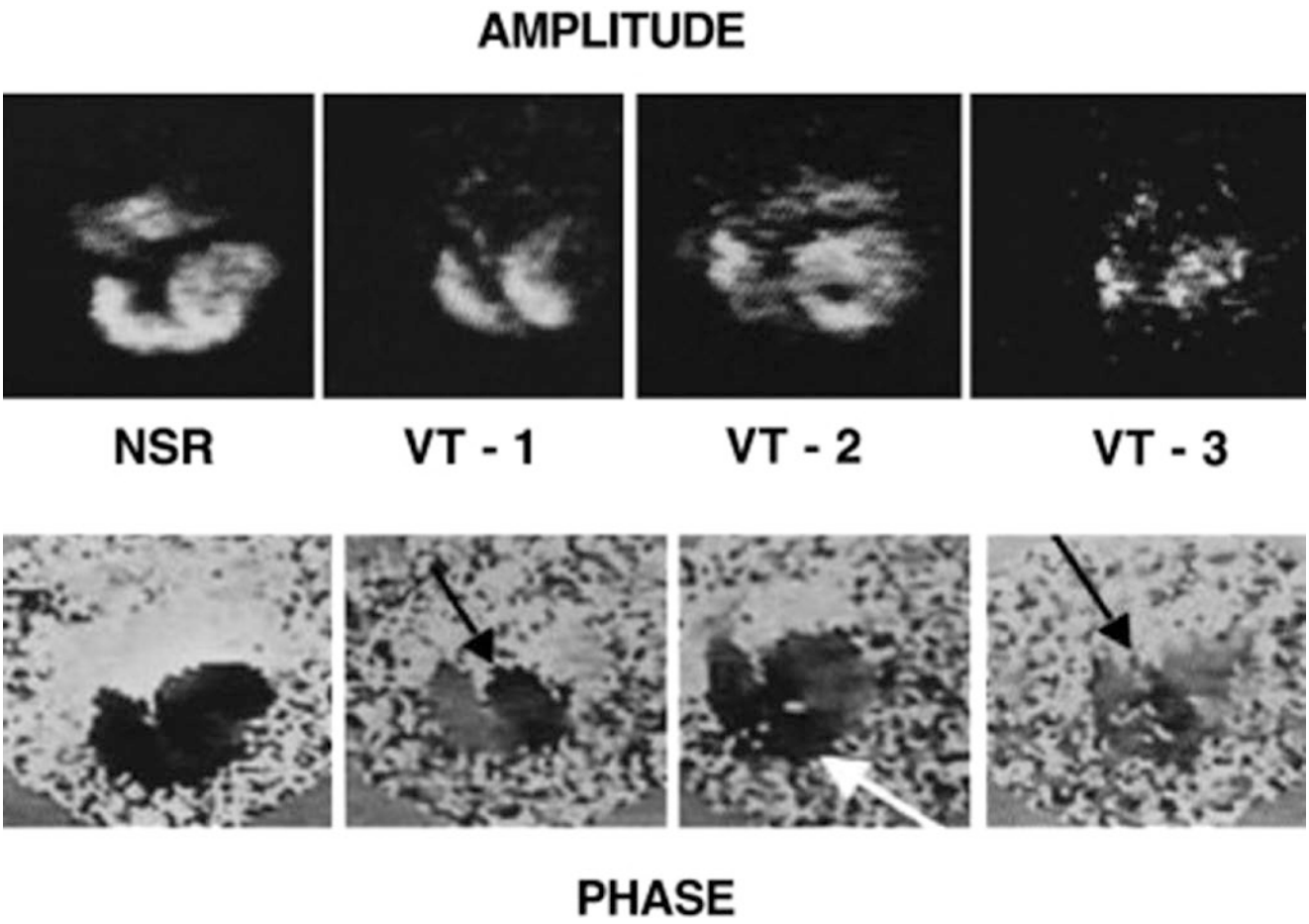

Fig. 7.44 Variable tolerance to multiple VT exit sites**.** Shown are the amplitude (*top row*), and the phase images (*bottom row*) generated from the equilibrium RNAs acquired in a patient in normal sinus rhythm (NSR) and with three VT exit sites, VT-1, VT-2, and VT-3. Intensity above is proportional to amplitude, and the phase image gray scale (*below*) parallels the contraction sequence. Regional amplitude and function were near normal in NSR; amplitude was moderately reduced with VT-1, with earliest Ø in the LV (*black arrow*), and an RBBB pattern; amplitude was well preserved with VT-2, with earliest Ø (*black*) in the RV (*white arrow*), and an LBBB pattern. The patient was intolerant to VT-3, with much-reduced amplitude and an LV septal exit site (*black arrow*), but with delayed RV and LVØ, seen in gray shades. The heart rate in each of these VT rhythms was similar. (From Botvinick et al. [60]; with permission from Springer Nature)

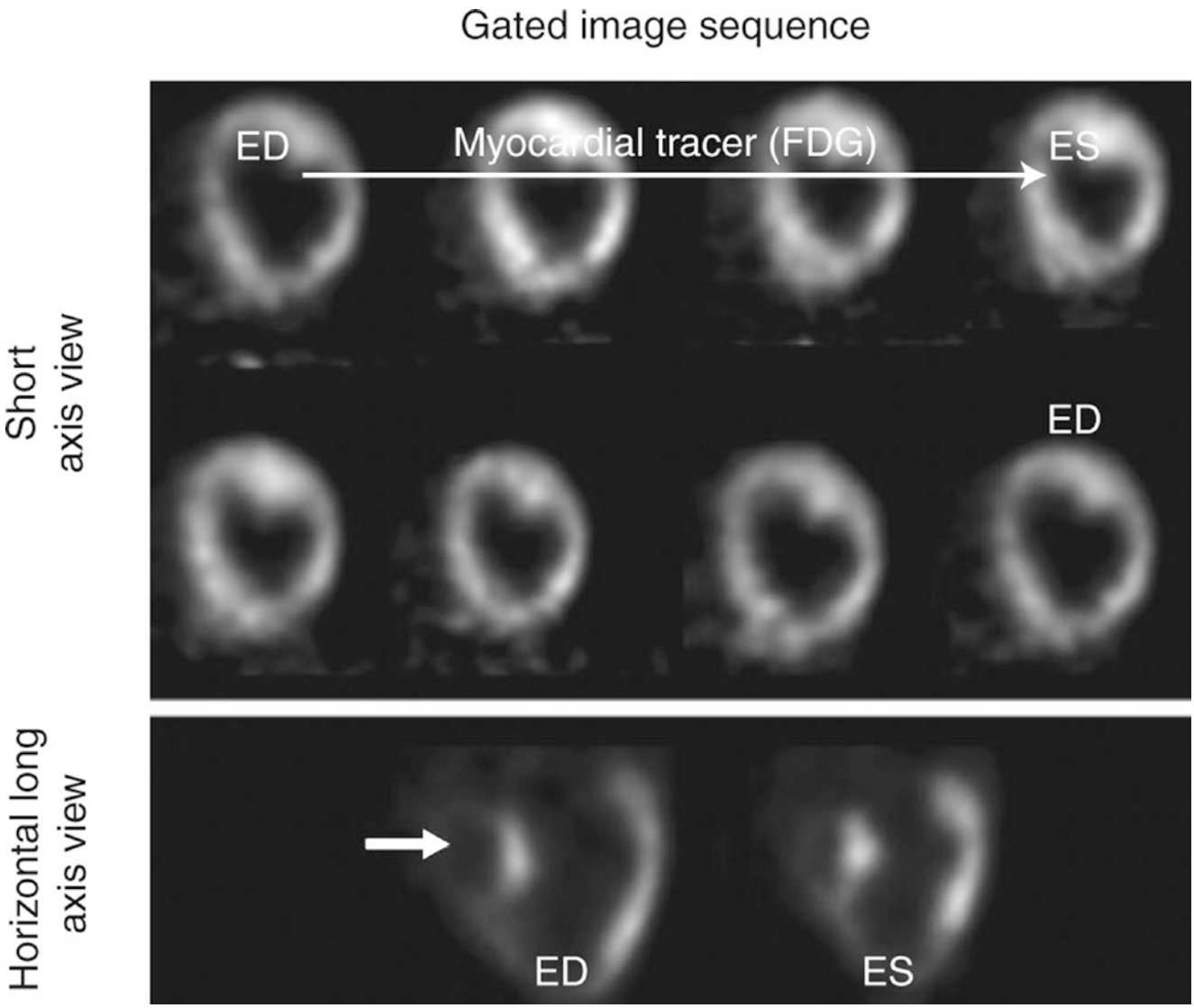

Fig. 7.45 Gated myocardial perfusion images. This sequence shows the gated set of eight images obtained from imaging a tracer that labels the myocardium, in this case ^{18}F-fluorodeoxyglucose (FDG). The small number of images and reduced sampling rate tends to slightly blur true end systolic (ES) with late systolic and early diastolic data, overestimating ES volume and underestimating ejection fraction. However, it has been shown that this effect on ejection fraction calculations is not too severe as long as the heart rate is not too low [40]. Using only eight images greatly distorts diastolic and systolic parameters such as peak ejection and filling rates, however. Note too the small right ventricle (*arrow*). ED end diastolic

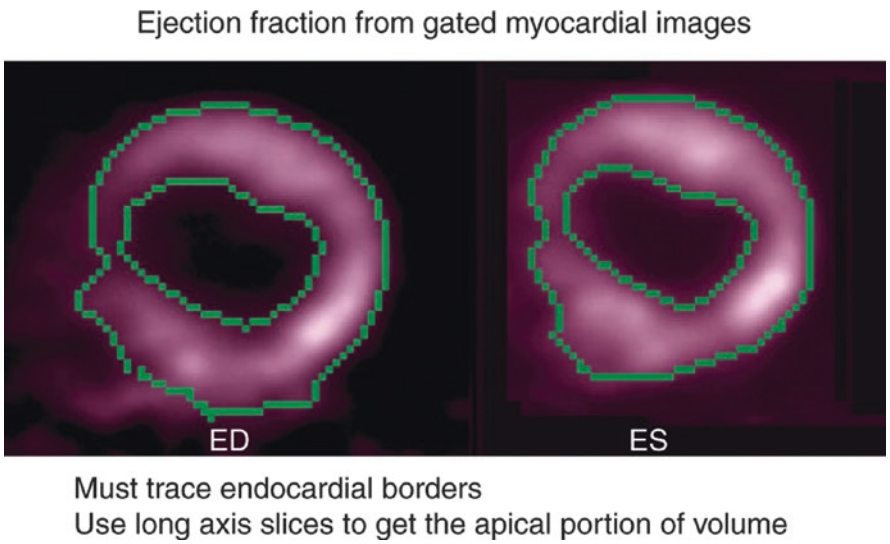

Fig. 7.46 Ejection fraction (EF) measurement. Left ventricular function can be computed from the series of gated myocardial uptake images to give a curve similar to that obtained from a gated blood pool study. Unfortunately, the resolution and noise of most SPECT perfusion studies is far worse than that shown in this gated FDG image sequence, leading to greater difficulties in accurately determining the endocardial edges and computing the EF. Unlike the gated blood pool images, counts are no longer proportional to blood volume. Instead, one must define the endocardial border from each image in the sequence for every slice, or at least end-diastolic (ED) and end-systolic (ES) frames for EF, and compute the volume from the sum of the enclosed areas of the endocardial surfaces. Short-axis slices do not give good endocardial border information near the apex, so long-axis views must also be used. This procedure has been successfully semiautomated in many commercial nuclear medicine cardiac analysis packages [16, 61]. However, the results one obtains depend to some extent on the resolution (as discussed below, regarding the partial volume effect) and noise in the images, so results can vary from one site to another and from one SPECT system to another [62]. Measurements from rest to stress should be more reliable, as the same filtering, imaging system, and other parameters are used for both. In the images shown here, the epicardial surface has also been outlined. LVEF calculated by gated myocardial perfusion SPECT was not significantly different from that of equilibrium RNA in the same 269 patients with a preserved LVEF. Myocardial perfusion SPECT lost accuracy with a small LV volume [63]

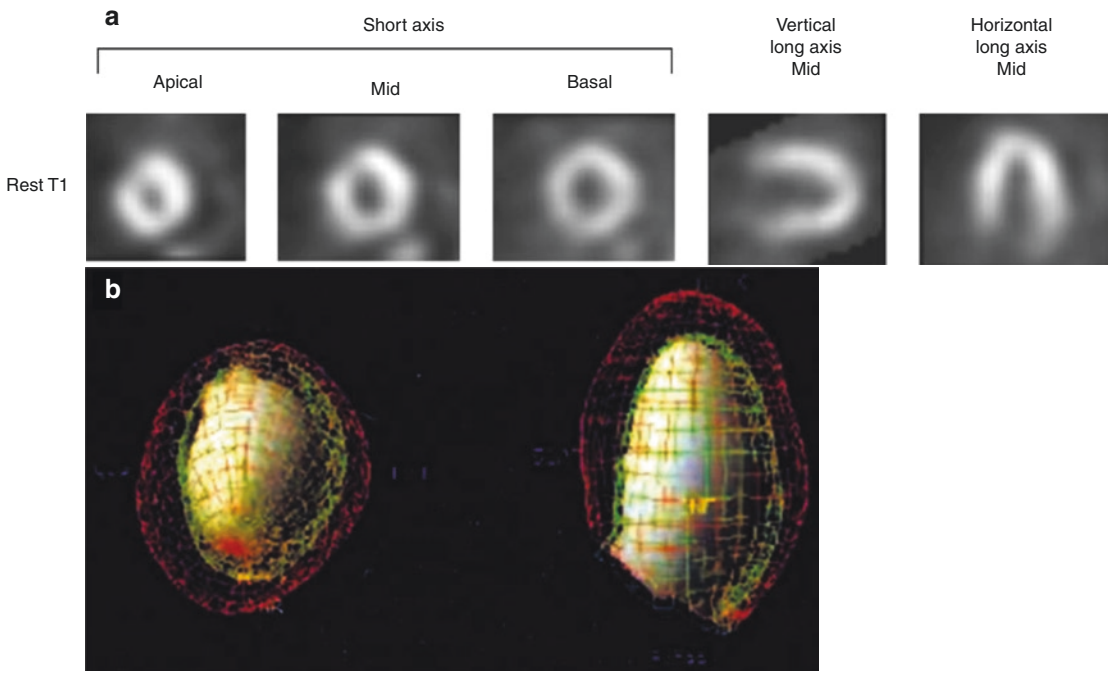

Fig. 7.47 (**a** and **b**) Display of left ventricular function. The epicardial and endocardial borders at end-diastolic (ED), end-systolic (ES), and the other points in the cardiac cycle can be put together to form the "wire cage" image as shown in this figure or even a pseudo-volumetric surface display. The epicardial and endocardial surfaces at ED are shown in *orange* and *yellow/green* in (**b**). The ES surface is shown in *gray*. Two different pseudo–3-D views are shown. These data were obtained from ^{99m}Tc-MIBI images; typical short-axis and long-axis images are shown in (**a**). Obviously, when there are severe perfusion defects, this methodology is problematic, and one must assume what the contours would have looked like had those segments of the myocardium been visible. Similarly, 3-D displays have been used to great effect in gated blood pool imaging [64–67]

Partial Volume Effect

Changes in myocardial wall thickening may be inferred from gated perfusion or metabolism images, using the so-called partial volume effect [68]. This term is somewhat misleading, in fact referring to two different phenomena that alter the relationship between image counts and intensity. The first effect is simply related to imaging an object using a scanner with less than perfect resolution. As demonstrated in Figure 7.48a, the effect becomes noticeable whenever the scanner resolution is comparable to the object being imaged. The second phenomenon related to partial volume effect is insufficient image sampling (Fig. 7.48b). Though insufficient sampling can be considered a separate phenomenon from the "partial volume effect," the consequences are quite similar. For example, systolic thickening translates into increased pixel intensity, and the contracting, thickening wall appears to brighten or move up the color scale in systole. Thickening or brightening then is gross evidence of regional myocardial viability, but cannot exclude a nontransmural infarction. The relationship between regional pixel intensity and thickening has been documented in phantoms and in correlations with echocardiography and MRI. Evidence of wall motion and thickening may be important for coronary disease diagnosis and appears to add to diagnostic specificity [69] from 84% to 92%, as motion and thickening in the presence of a "fixed" defect suggest an artifact of motion or attenuation rather than a true infarction [70].

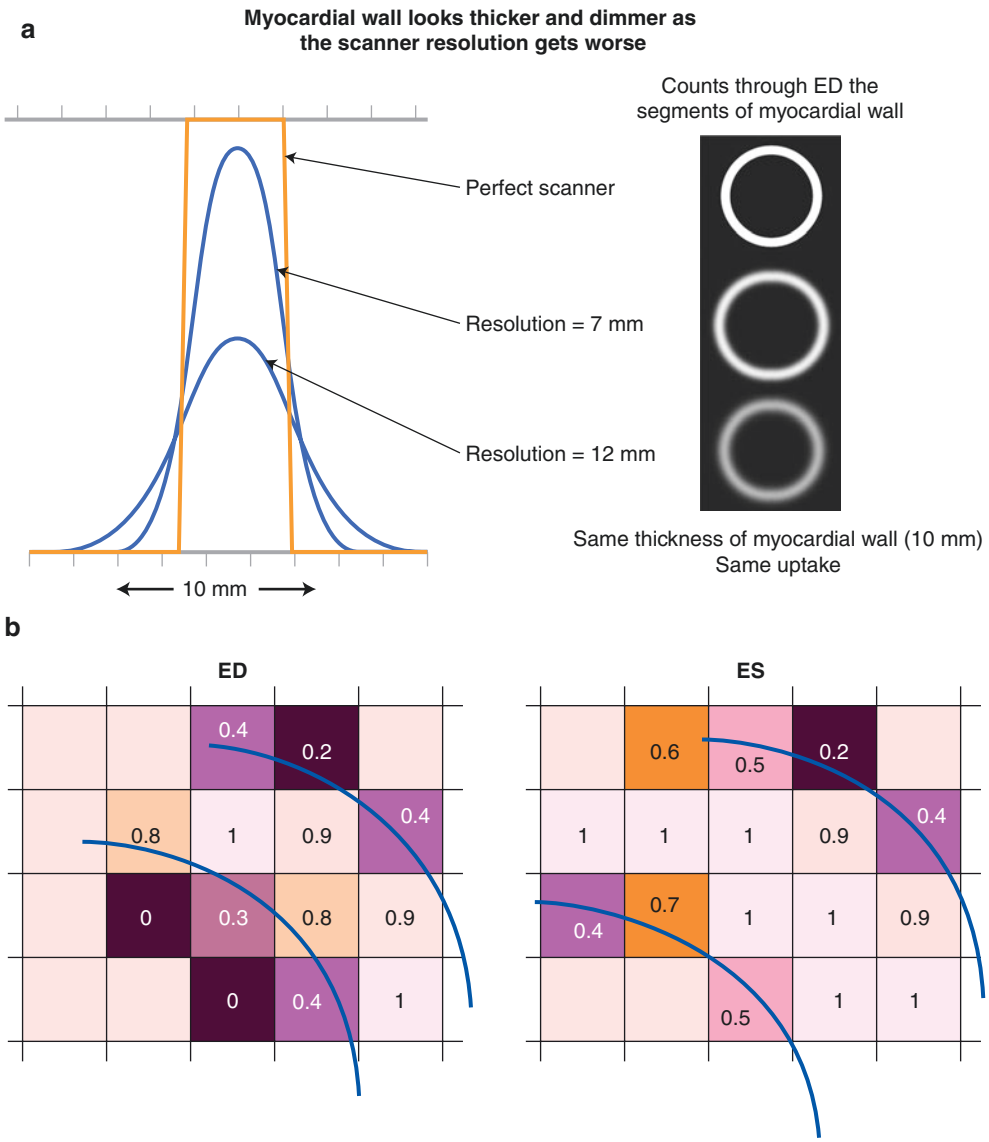

Fig. 7.48 Partial volume effect. (**a**) The *top right* image in is a simulated image of one short-axis slice of a 10-mm thick myocardial wall imaged at end diastole (ED) with a "perfect" scanner—that is, one with 0-mm resolution. The profile of counts through the line shown across the myocardial wall gives the square curve on the *left*. The width of this curve is exactly 10 mm. When the same myocardium is imaged with a scanner with a 7-mm resolution (typical of a PET scanner), the *middle right* image is obtained. It is somewhat blurrier and looks dimmer and wider, as shown on the corresponding profile on the *left*. Finally, when the 10-mm thick myocardial wall is imaged with a 12-mm full width at half-maximum scanner (typical of a very good SPECT scanner), the image at the *bottom right* results—still dimmer and apparently wider. In fact, all three images have the same total counts, the same "uptake" of tracer. As the resolution gets worse and worse, the counts get blurred more and more, giving the appearance of decreasing brightness and increasing width. If one were to add up all the counts under the three profiles, they would give exactly the same number of counts. (**b**) The second phenomenon related to partial volume effect is insufficient image sampling. Shown diagrammatically is a myocardial region in ED and end systole (ES) superimposed on a pixel grid in which only a small number of pixels span the myocardial wall (a situation typical of cardiac SPECT imaging). The *squares* represent pixels that are color-coded for and labeled with the percentage of the pixel occupied by the myocardium. Thickening brings a larger fraction of the pixels fully within the myocardial walls, producing a brighter (lighter) intensity response. Systolic thickening (for example, from 8 to 12 mm) translates into increased pixel intensity, and visually, the contracting, thickening wall appears to brighten or move up the color scale in systole [68]

Figure 7.49 illustrates a clinical application of the partial volume effect. In clinical imaging situations, the scanner has a fixed resolution, but the myocardial thickness changes with time, being thickest at end systole and thinnest at end diastole. This phenomenon suggests a method for measuring thickening [22, 23, 71]. The magnitude of the partial volume effect is determined by how poor the resolution of the scanner is compared with the thickness of the object being measured. Therefore, for a SPECT scanner with a 12-mm resolution, the partial volume effect will be less when the myocardial wall is 10 mm thick at end systole than when it is 5 mm thick at end diastole. Even though the uptake is the same, the partial volume effect will cause the thinner wall at end diastole to look dimmer, whereas the thicker wall at end systole shows minimal partial volume effect, so the uptake will appear brighter. Thus, the increase in brightness is an indication that the wall is thickening, but the degree of thickening may not be linearly related to the amount of brightening. If the myocardial wall at end systole is much thicker than the resolution, the partial volume blurring effect will be small and little brightening will occur. Therefore, although brightening always indicates thickening, a lack of brightening does not necessarily indicate that no thickening is occurring. This must be kept in mind when clinical interpretations of brightening are made.

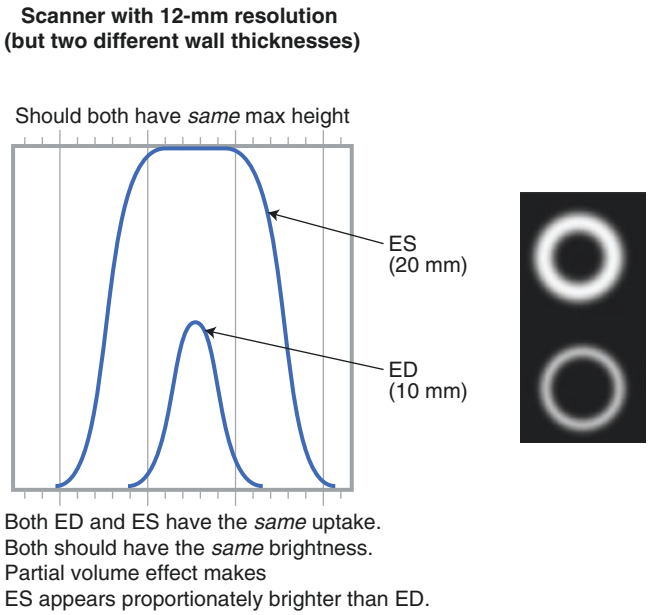

Fig. 7.49 Clinical application of the partial volume effect. The magnitude of the partial volume effect is determined by how poor the resolution of the scanner is compared with the thickness of the object being measured, so the effect will be less for a thicker myocardial wall at end systole (ES) than when the wall is thinner, at end diastole (ED). Even though the uptake is the same, the partial volume effect will cause the thinner wall at ED to look dimmer. Note that when the myocardial wall at ED is much thicker than the resolution (e.g., 20 mm or more), the partial volume blurring effect will be small and little brightening will occur between ED and ES, even though the wall does thicken

Figure 7.50 presents a clinical example of how the partial volume effect can be used to indicate whether thickening is occurring. It is important to remember that brightening always indicates thickening, but lack of brightening does not necessarily indicate that no thickening is occurring. This, as well as the related causes of thickening in the absence of brightening, must be kept in mind when clinical interpretations of brightening are made [72]. Figure 7.51 shows an example of brightening, a result of a partial volume effect, that is correlated with myocardial thickening.

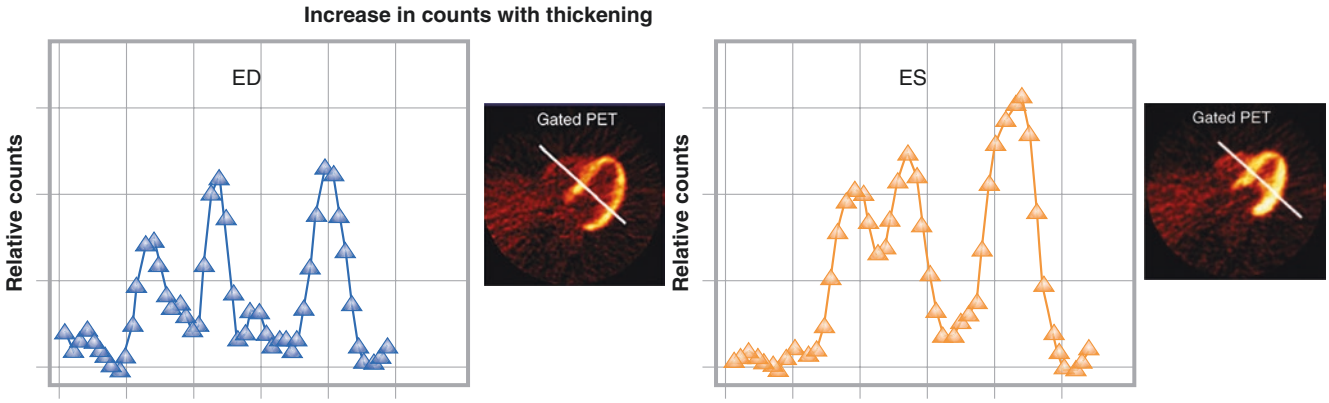

Fig. 7.50 Myocardial thickening. A clinical example of how the partial volume effect can be used to indicate whether thickening is occurring is illustrated here. The *upper left* image shows a transaxial myocardial uptake image, in this case [^{18}F]-FDG at end diastole (ED). The curve below this image is the profile of counts through the line shown in the image. The *upper right* image is the same transaxial slice, but at end systole (ES). Again, the profile through the image, as indicated, is shown below. Note that the myocardial walls in the ES image appear uniformly brighter than in the ED image, and this increase in brightness is clearly shown in the profiles. The brightness is a definitive indication that thickening has occurred. Note that the right ventricular wall also shows an increase in counts. This is clearly seen in the profile of counts, but is harder to appreciate visibly in the image

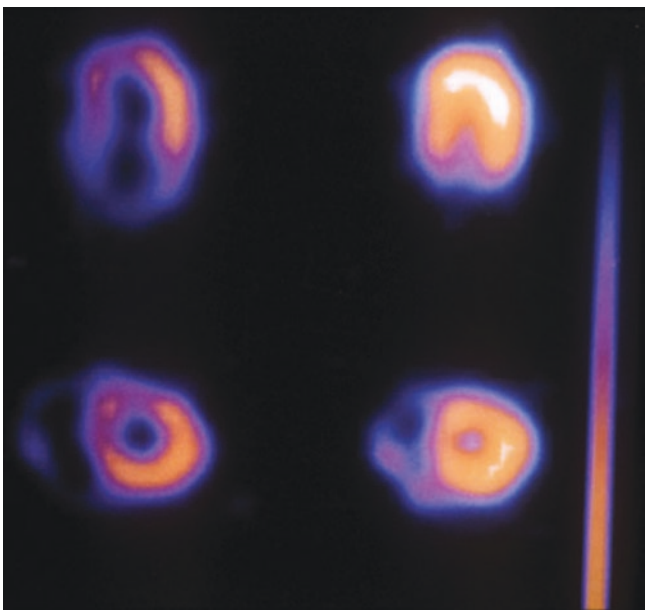

Fig. 7.51 Gated perfusion imaging. End-diastolic (*left*) and end-systolic (*right*) gated ^{99m}Tc-sestamibi perfusion images in a normal heart in selected short-axis (*top*) and horizontal long-axis (*bottom*) SPECT slices. Inward systolic motion is evident, as well as brightening, or increased intensity, during systole. The brightening, a result of a partial volume effect, is well correlated with myocardial thickening

Although the partial volume effect can be useful to determine whether thickening is occurring, it also can cause difficulties in myocardial perfusion imaging, as summarized in Table 7.6. Myocardial walls that are thin compared with the resolution of the system will appear to have less activity than they really do. The reader of an FDG scan may erroneously think that the region is nonviable, when in reality it is just thin. Similarly, if it is a perfusion scan, thin walls will erroneously appear to have reduced perfusion. If one compares two studies taken some months apart and a portion of the myocardial wall has thinned, that portion will erroneously appear to have less uptake. Of course, wall thinning is related to infarction and scar, which are also causes of reduced perfusion and uptake. Similarly, owing to their different physical properties and related associated spatial resolution, the same myocardial wall could appear broader with different intensity and erroneously appear to have relative less activity when imaged by ^{201}Tl compared with ^{99m}Tc radiotracers. All these factors must be taken into consideration when interpreting scans of myocardial uptake.

Thin myocardial walls may erroneously appear to be nonviable in FDG imaging.
Thin myocardial walls erroneously appear to have lower perfusion for ^{201}Tl and sestamibi or other perfusion agents.
Walls imaged with ^{201}Tl erroneously appear to be thicker with lower perfusion, compared with walls imaged with ^{99m}Tc perfusion agents.
Changes in myocardial thickness may make it appear that activity has changed.

Table 7.6 Partial volume effect: ambiguities and misleading effects

Gated Perfusion Imaging

Functional data may be derived from the perfusion study by either first-pass or postlocalization gated methods. As noted on Table 7.7, the first-pass method is more demanding of technique, instrumentation, and time, but it is based on a long-established method and generates a long-validated calculation of LVEF. Owing to its inconvenience and the availability of established functional data after gated imaging, first-pass acquisition is rarely performed. Equilibrium RNA is performed primarily to calculate accurate measures of ventricular function. Gated myocardial perfusion studies do provide information regarding left ventricle wall motion and LVEF, but they are performed to assess myocardial perfusion and viability. Their functional information serves as an important supplement to perfusion information, but they are never used when the primary study objective is to assess ventricular function. Their evolving application to synchrony assessment is an exception to this rule, and the gated perfusion method will gain use only as it demonstrates superiority and cost-effectiveness over other methods.

First-pass method
Needs ^{99m}Tc-based agents
Needs state-of-the-art, high-sensitivity cameras (detectors)
Performed with radionuclide administration
Can be performed with stress, but not always possible
May be performed with rest and stress
Left ventricular wall motion, volumes, and ejection fraction
Can provide right ventricular ejection fraction and wall motion
Evaluates features of background-free blood pool
Gated myocardial perfusion studies
May be performed with ^{201}Tl or ^{99m}Tc-based agents
Uses conventional cameras
Always delayed after radionuclide injection and after stress
May be performed with rest and stress
Left ventricular wall motion, volumes, and ejection fraction
Assesses left ventricular wall thickening
Accuracy dependent on endothelial border definition
Technical considerations in gated SPECT perfusion imaging
Acquisition and reconstruction of a 16-frame gated SPECT study requires 16 times as much RAM and takes 16 times as long for reconstruction.
For clinical utility, gated SPECT perfusion imaging needs a fast computer with 8 Mb of RAM and 500 Mb of hard disk space.
Requirements for vendor software:
Permit acquisition of up to 16-frame SPECT
Display time at each camera stop in seconds or in accepted beats within a user-defined R–R interval
Permit collapse of the study to an ungated study or image including only specified frames (e.g., an end-diastolic image)
Display dynamic beating short-axis slices, selected long-axis slices, and three-dimensional rendering of the beating heart
Calculate quantitative measures of regional perfusion, contraction, and wall thickening

Table 7.7 Comparison of Perfusion Methods and Technical Considerations for the Evaluation of Ventricular Function

Figures 7.52, 7.53, 7.54, 7.55, 7.56, 7.57, and 7.58 provide examples of the use of gated perfusion imaging.

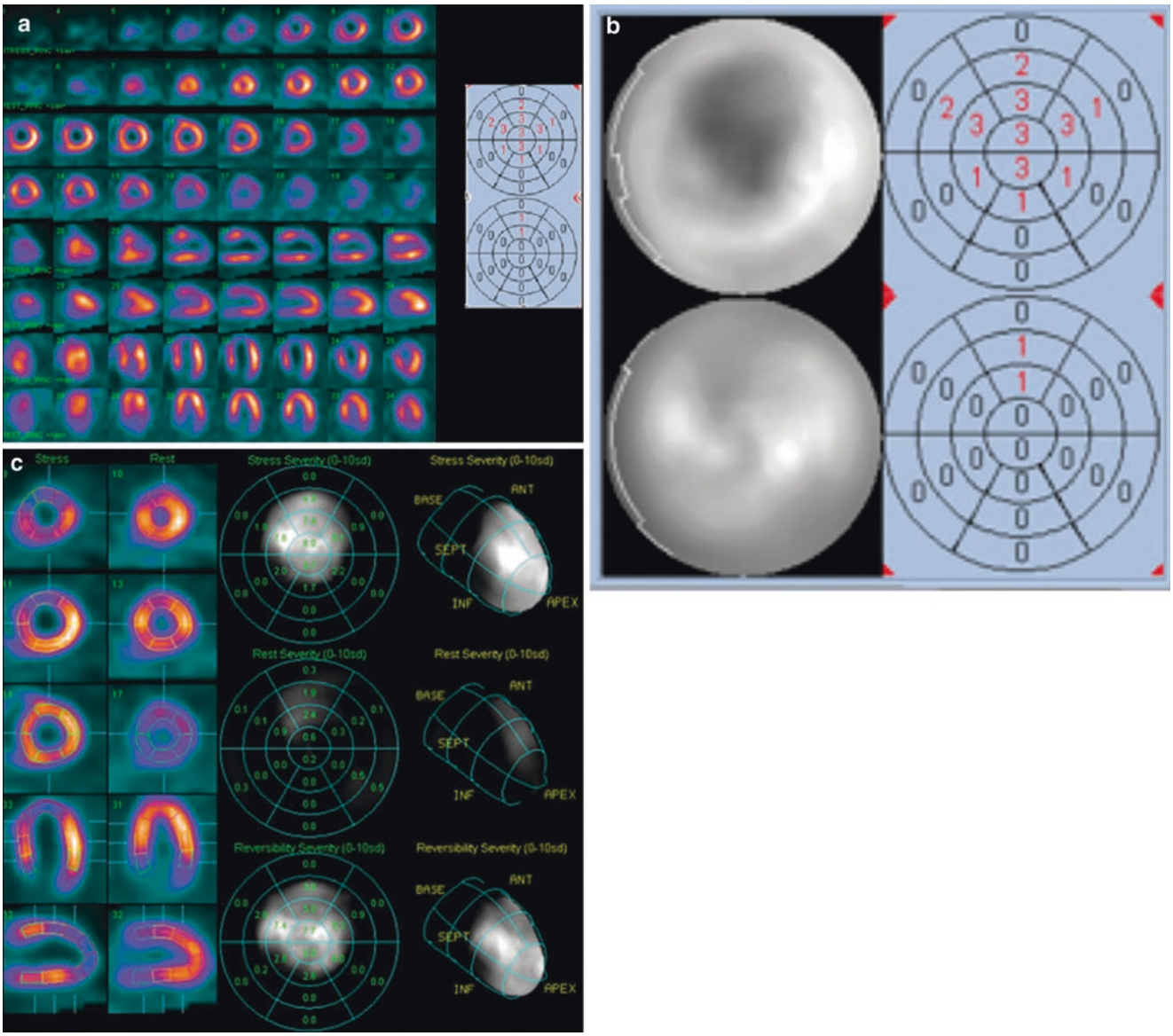

Fig. 7.52 Gated stress perfusion imaging. (**a**) Shown in the *top row* and continuing in the *third row*, from apex (*left*) to base (*right*), are color-coded SPECT stress perfusion images in a 49-year-old man with atypical chest pain and an equivocal stress test result. Images were performed with the dual-isotope ^{201}Tl rest, ^{99m}Tc stress protocol. In the *second* and *fourth rows* are the rest images in the same patient, acquired at baseline. Below these images, in alternating rows from top down, are stress and rest images in the same patient presented in vertical long axis, *left to right*, from the septum to the lateral wall, and the horizontal long axis, *left to right*, from the inferior to anterior walls. Cavitary dilatation with a gross, reversible, apical, anterior, and septal defect is evident, consistent with significant flow-limiting disease in the left anterior descending coronary artery. The summed stress score of 20 confirms the high related coronary risk. (**b**) Shown is the quantitative perfusion SPECT or quantitative perfusion AutoQuant (Cedars Sinai Hospital, Los Angeles, CA) display, with the *left panel* showing segmented stress slices, above, at the *far left*, followed by rest slices, below, and polar maps in the *right panels*, with stress above and rest below. Here the display is calibrated for the percentage of relative regional intensity. In the *right panel*, a color-coded defect is painted on a model left ventricle. (**c**) This display is similar to (**b**) but now shows, from top down, stress, rest, and difference polar maps with intensity scaled to the standard deviation derived from the normal rest–stress male activity distribution using this dual-isotope protocol. (**d**) Models of the epicardium (*orange mesh*) and endocardium at end diastole (*green mesh*) and at end systole (*solid orange*) in the anterior (*left*) and left lateral (*right*) projections taken from the gated myocardial perfusion images in this case at peak stress. Evident is anterior, apical, and septal wall motion abnormalities. Rest function was normal. Evidence of stress-induced dysfunction adds significant prognostic risk to any perfusion abnormalities induced. ANT anterior, INF inferior, SEPT septal

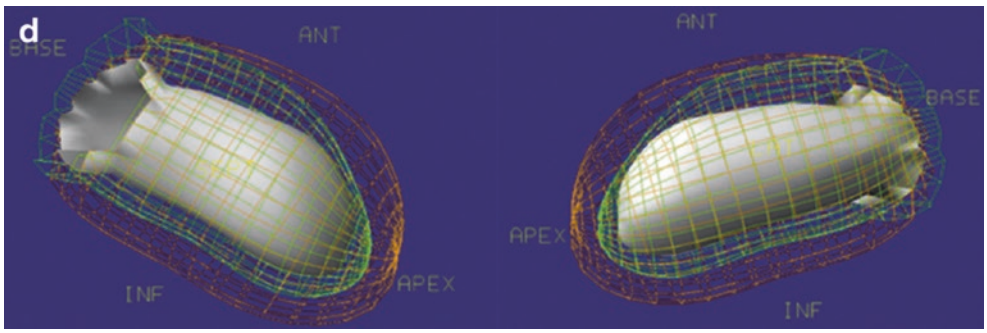

Fig. 7.52 (continued)

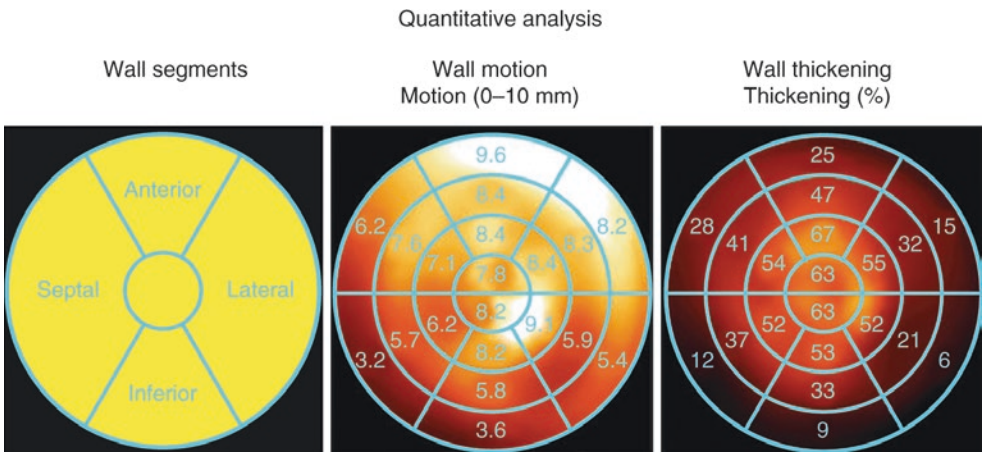

Fig. 7.53 Normal quantitative wall motion and thickening on gated perfusion imaging. Shown are AutoQuant (Cedars Sinai Hospital, Los Angeles, CA) polar maps demonstrating wall segments (*left*), normal wall motion (*center*), and normal wall thickening (*right*) [74]. Thickening is accurately measured as a percentage increase from end diastole by the linear relationship to the percentage increase in wall intensity. (From Yun et al. [74]; with permission from Wolters Kluwer)

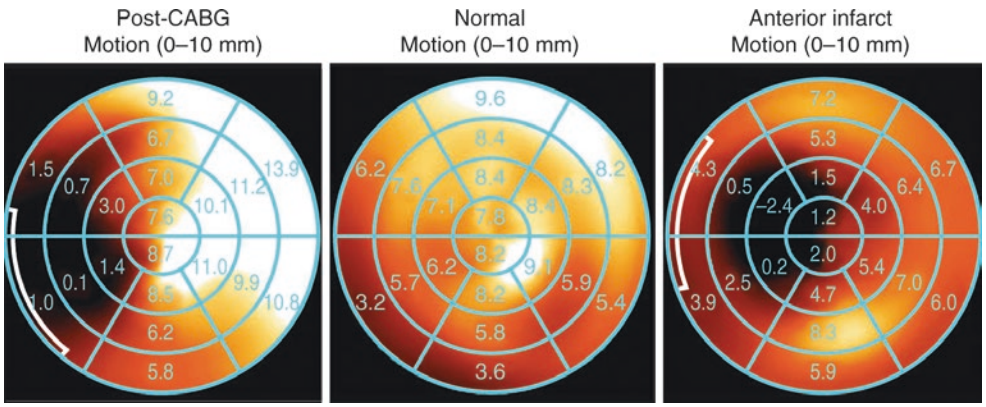

Fig. 7.54 Abnormal quantitative wall motion on gated perfusion imaging. Shown are AutoQuant (Cedars Sinai Hospital, Los Angeles, CA) polar maps demonstrating wall motion patterns in a patient after coronary artery bypass graft (CABG) surgery (*left*), in a normal patient (*center*), and in a patient with a prior anterior infarction (*right*). Abnormal septal wall motion is evident in the post-CABG and postinfarct patients. (From Yun et al. [74]; with permission from Wolters Kluwer)

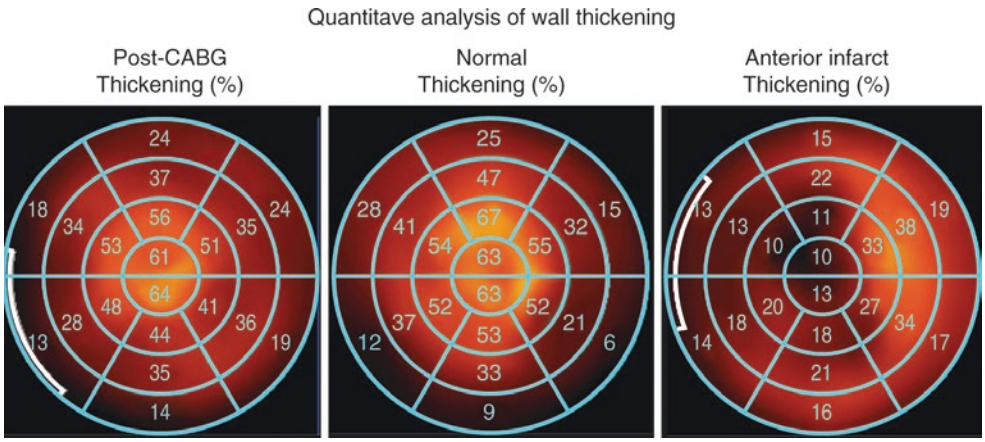

Fig. 7.55 Abnormal quantitative wall thickening on gated perfusion imaging. Shown are AutoQuant (Cedars Sinai Hospital, Los Angeles, CA) polar maps demonstrating wall thickening patterns in the same three patients as in Fig. 7.54: after coronary artery bypass graft (CABG) surgery (*left*), in a normal patient (*center*), and in a patient with a prior anterior infarction (*right*). Abnormal septal and apical wall thickening is evident only post-infarction. The abnormal wall motion after CABG is not accompanied by abnormal thickening because there is no intrinsic wall pathology. The abnormal wall motion post-CABG relates to the absence of the pericardial restraint, with a resulting anterior swing of the epicardium, seen on dynamic images, (From Yun et al. [74]; with permission from Wolters Kluwer)

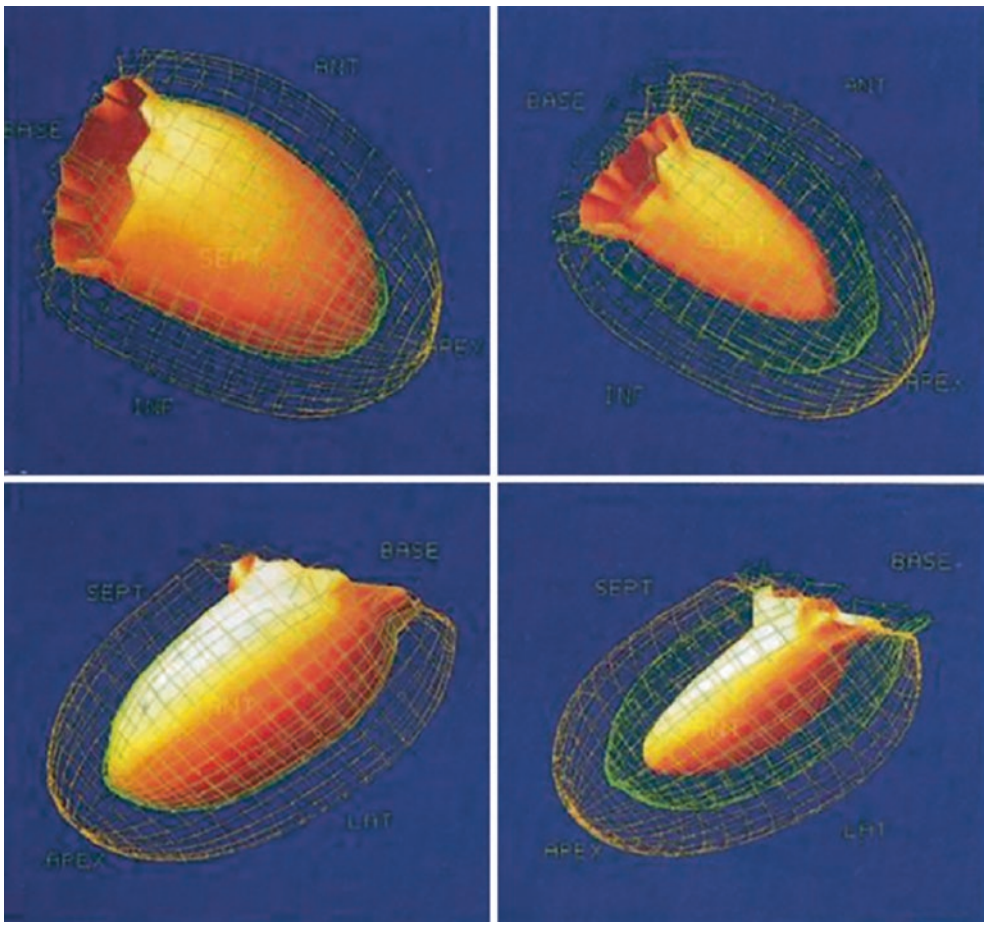

Fig. 7.56 Normal wall motion and thickening: ventricular model. Shown on the AutoQuant (Cedars Sinai Hospital, Los Angeles, CA) display of gated perfusion images is normal wall motion and thickening in anterior (*top*) and lateral (*bottom*) projections. End-diastolic frames are on the *left* and end-systolic frames are on the *right*. Here, again, the epicardium is represented by the *green mesh*, the endocardium at end diastole is the *orange mesh*, and the endocardium at end systole (*right*) is the *solid orange* surface. Note the symmetrical inward motion of the endocardium. (From Yun et al. [74]; with permission from Wolters Kluwer)

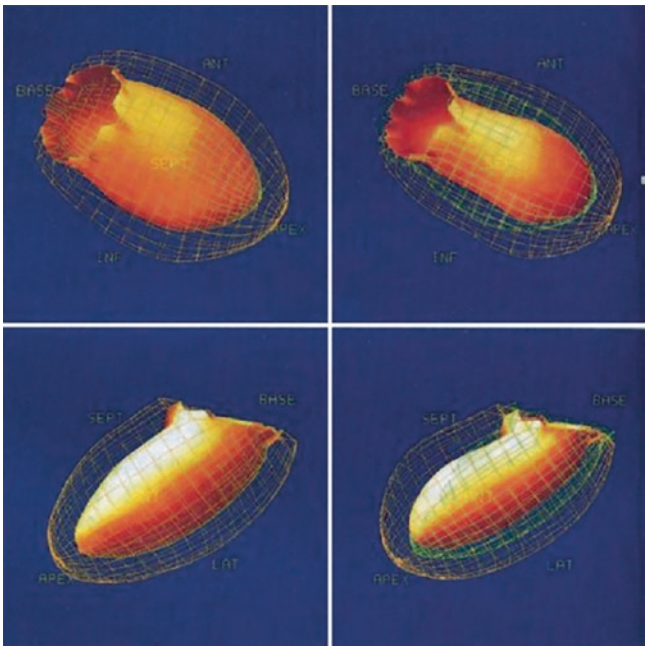

Fig. 7.57 Abnormal wall motion and thickening with anterior infarction: ventricular model. Shown on the same AutoQuant (Cedars Sinai Hospital, Los Angeles, CA) display of gated perfusion images is akinesis of the apex, septum, and distal anterior wall in anterior (*left*) and lateral (*right*) projections in a patient with a prior anterior myocardial infarction. The perfusion image showed a dense anterior, septal, and apical defect. (From Yun et al. [74]; with permission from Wolters Kluwer)

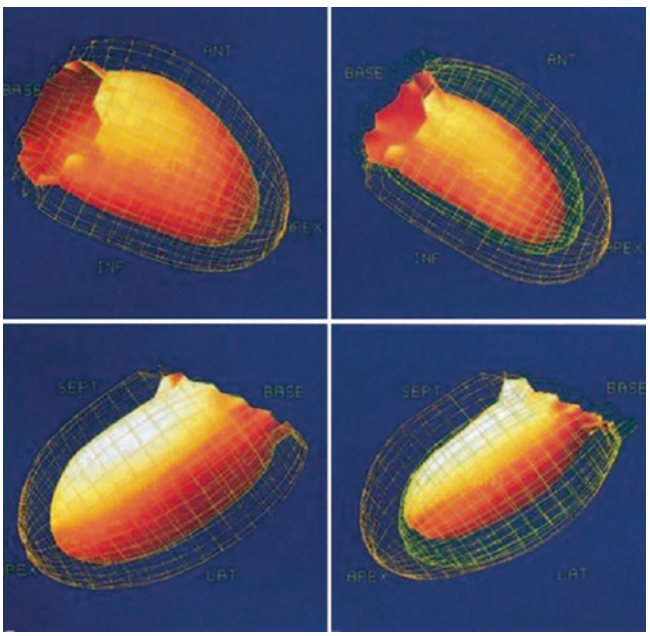

Fig. 7.58 Anterior swing after coronary artery bypass graft (CABG): ventricular model. Shown on the same AutoQuant (Meyer Instruments, Houston, TX) display of gated perfusion images as the prior figures is the pattern of abnormal wall motion seen after CABG or any cardiac surgery in the anterior (*left*) and lateral (*right*) projections. Here, the anterior swing of the epicardium is well seen in the lateral projection, where the septum appears to be akinetic but demonstrates normal wall thickening and is associated with preserved anterior wall motion, differentiating this pattern from that seen in patients after an anterior infarction. (From Yun et al. [74]; with permission from Wolters Kluwer)

References

1. Hoffmann G, Klein N. Die methode der radiokardiographischen funktions analyse. Nuklearmedizin. 1968;7:350–70.
2. Strauss HW, Zaret BL, Hurley PJ. A scintiphotographic method for measuring left ventricular ejection fraction in man without cardiac catheterization. Am J Cardiol. 1971;28:575–80.
3. Zaret BL, Strauss HW, Hurley PJ. A noninvasive scintiphotographic method for detecting regional ventricular dysfunction in man. N Engl J Med. 1971;284:1165–70.
4. Parker JA, Secker-Walker R, Hill R. A new technique for the calculation of left ventricular ejection fraction. J Nucl Med. 1972;13:649–51.
5. Green MV, Ostrow HG, Douglas MA, Myers RW, Scott RN, Bailey JJ, Johnston GS. High temporal resolution ECG-gated scintigraphic angiocardiography. J Nucl Med. 1975;16:95–8.
6. Steele P, Kirch D, LeFree M, Battock D. Measurement of right and left ventricular ejection fractions by radionuclide angiocardiography in coronary artery disease. Chest. 1976;70:51–6.
7. Bacharach SL, Green MV, Borer JS. A real-time system for multiimage gated cardiac studies. J Nucl Med. 1977;18:79–84.
8. Borer JS, Bacharach SL, Green MV. Real-time radionuclide cineangiography in the noninvasive evaluation of global and regional left ventricular function at rest and during exercise in patients with coronary-artery disease. N Engl J Med. 1977;296:839–44.
9. Freedman NMT, Bacharach SL, Cuocolo A, et al. ECG gated PET C-11 monoxide studies: an answer to the "background" question in planar Tc-99m gated blood pool imaging. J Nucl Med. 1992;33:938.
10. Boyd HL, Gunn RN, Marinho NV, Kanwatowski SP, Bailey DL, Costa DC, et al. Non-invasive measurement of left ventricular volumes and function by gated positron emission tomography. Eur J Nucl Med. 1996;23:1594–602.
11. Fischman AJ, Moore RH, Gill JB, Strauss HW. Gated blood pool tomography: a technology whose time has come. Semin Nucl Med. 1989;19:13–21.
12. Underwood SR, Walton S, Laming PJ, Jarritt PH, Ell PJ, Emanuel RW, Swanton RH. Left ventricular volume and ejection fraction determined by gated blood pool emission tomography. Br Heart J. 1985;53:216–22.
13. Ishino Y. Assessment of cardiac function and left ventricular regional wall motion by ^{99m}Tc multigated cardiac blood-pool emission computed tomography. Kaku Igaku. 1992;29:1069–81.
14. Bartlett ML, Srinivasan G, Barker WC, Kitsiou AN, Dilsizian V, Bacharach SL. Left ventricular ejection fraction: comparison of results from planar and SPECT gated blood-pool studies. J Nucl Med. 1996;37:1795–9.
15. Borer J, Supino P. Radionuclide angiography part II: equilibrium imaging. In: Iskandrian AE, Verani MS, editors. Nuclear cardiac imaging: principles and applications. New York: Oxford University Press; 2003. p. 323–67.
16. Botvinick EH, O'Connell JW, Kadkade PP, Glickman SL, Dae MW, Cohen TJ, et al. Potential added value of three-dimensional reconstruction and display of single photon emission computed tomographic gated blood pool images. J Nucl Cardiol. 1998;5:245–55.
17. Gill JB, Moore RH, Tamaki N, Miller DD, Barlai-Kovach M, Yasuda T, et al. Multigated blood-pool tomography: new method for the assessment of left ventricular function. J Nucl Med. 1986;27:1916–24.
18. Groch MW, Marshall RC, Erwin WD, Schippers DJ, Barnett CA, Leidholdt EM Jr. Quantitative gated blood pool SPECT for the assessment of coronary artery disease at rest. J Nucl Cardiol. 1998;5:567–73.
19. Groch MW, Marshall RC, Schippers D, et al. Three dimensional analysis of gated blood pool SPECT: applicability of multiple reference models. J Nucl Med. 1998;39:45P–145.
20. Germano G, Kavanagh PB, Wachter P. A new algorithm for the quantitation of myocardial perfusion SPECT. J Nucl Med. 2000;41:712–9.
21. Bartlett ML, Buvat I, Vaquero JJ, Mok D, Dilsizian V, Bacharach SL. Measurement of myocardial wall thickening from PET/SPECT images: comparison of two methods. J Comput Assist Tomogr. 1996;20:473–81.
22. Cooke CD, Garcia EV, Cullom SJ, Faber TL, Pettigrew RI. Determining the accuracy of calculating systolic wall thickening using a fast Fourier transform approximation: a simulation study based on canine and patient data. J Nucl Med. 1994;35:1185–92.
23. Garcia E, Bacharach SL, Mahmarian JJ, et al. Imaging guidelines for nuclear cardiology procedures: part 1. J Nucl Med. 1996;3:G3–46.
24. Botvinick EH. Editor. Topic 7, radionuclide angiography: equilibrium and first pass methods. Self-study program III. In: Botvinick E, editor. Nuclear medicine: cardiology. Society of Nuclear Medicine: Reston, VA; 2007.
25. Botvinick EH, Glazer H, Shosa D. What is the relationship and utility of scintigraphic methods for the assessment of ventricular function? Cardiovasc Clin. 1983;13:65–78.
26. Bodenheier MM, Banka FS, Fooshee CM. Quantitative radionuclide angiography in the right anterior oblique view: comparison with contrast ventriculography. Am J Cardiol. 1978;41:718–25.
27. Marshall RC, Berger HJ, Costin JC. Assessment of cardiac performance with quantitative radionuclide angiocardiography. Circulation. 1977;56:820–9.
28. VanDyke D, Anger HO, Sullivan RW. Cardiac evaluation from radioisotope dynamics. J Nucl Med. 1972;13:585–92.
29. Bacharach SL, Green MV, Borer SJ. Instrumentation and data processing in cardiovascular nuclear medicine: evaluation of ventricular function. Semin Nucl Med. 1979;9:257–74.
30. Wackers JF. New horizons for myocardial perfusion imaging with technetium-99m labeled isonitrile. In: Pohost GM, Higgins CB, Nanda NC, et al., editors. New concepts in cardiac imaging. Chicago: Year Book Medical Publishers; 1989. p. 93–108.
31. Upton MT, Rerych SK, Newman GE, Port S, Cobb FR, Jones RH. Detecting abnormalities in left ventricular function during exercise before angina and ST-segment depression. Circulation. 1980;62:341–9.
32. Udelson JE, Dilsizian V, Bonow RO. Nuclear cardiology. In: Libby P, Zipes DP, Mann DL, Bonow RO, editors. Braunwald's heart disease: a textbook of cardiovascular medicine. 8th ed. Philadelphia: WB Saunders; 2007. p. 287–331.
33. Garcia E, Botvinick EH, Hasagawa B, Ratzlaff N. Topic 1, physical and technical aspects of nuclear cardiology. Self-study program III. In: Botvinick E, editor. Nuclear medicine: cardiology. Society of Nuclear Medicine: Reston, VA; 2003.
34. Maltz OL, Treves S. Quantitative radionuclide angiocardiography. Determination of Qp/Qs in children Circulation. 1973;76:1049.
35. Bacharach SL, Green MV. Data processing in nuclear cardiology: measurement of ventricular function. IEEE Trans Nucl Sci. 1982;29:1343–54.
36. Strauss HW, Zaret BW, Hurley PJ. A scintigraphic method for measuring left ventricular ejection fraction in man without cardiac catheterization. Am J Cardiol. 1971;28:575–83.
37. Parker DA, Karvelis KC, Thrall JH, Froelich JW. Radionuclide ventriculography: methods. In: Gerson MC, editor. Cardiac nuclear medicine. 3rd ed. New York: McGraw Hill; 1997.
38. Links JM, Frank TL, Engdahl JC, Becker LC. Cardiac single-photon emission tomography with a 90 degrees dual-head system. Eur J Nucl Med. 1995;22:548–52.
39. Underwood SR, Walton S, Ell PJ, Jarritt PH, Emanuel RW, Swanton RH. Gated blood-pool emission tomography: a new technique for the investigation of cardiac structure and function. Eur J Nucl Med. 1985;10:332–7.
40. Bacharach SL, Green MV, Borer JS, Hyde JE, Farkas SP, Johnston GS. Left-ventricular peak ejection rate, filling rate, and ejection fraction—frame rate requirements at rest and exercise: concise communication. J Nucl Med. 1979;20:189–93.

41. Bacharach SL, et al. Assessment of ventricular function. In: Pohost GM, O'Rourke RA, Berman DS, Shah PM, editors. Imaging in cardiovascular disease. Philadelphia: Lippincott Williams & Williams; 2000.
42. Bonow R, Bacharach SL, Green MV. Impaired left ventricular diastolic filling in patients with coronary artery disease assessment with radionuclide angiography. Circulation. 1981;64:315–23.
43. Botvinick EH, Dae MW, O'Connell JW. Blood pool scintigraphy. Clin Cardiol. 1989;7:537–63.
44. Patel CD, Balakrishnan VB, Kumar L, Naswa N, Malhotra A. Does left ventricular diastolic function deteriorate earlier than left ventricular systolic function in anthracycline cardiotoxicity? Hell J Nucl Med. 2010;13:233–7.
45. Appel JM, Jensen BV, Nielsen DL, Ryberg M, Zerahn B. Systolic versus diastolic cardiac function variables during epirubicin treatment for breast cancer. Int J Cardiovasc Imaging. 2010;26:217–23.
46. Dae MW, Botvinick EH, O'Connell JW, Schiller NB, Bouchard A, Ports TA, Faulkner D. Increased accuracy of scintigraphic quantitation of valvular regurgitation using atrial-corrected Fourier amplitude ratios. Am J Noninvas Cardiol. 1987;1:155–62.
47. Frais M, Botvinick E, Shosa D, O'Connell JW. Phase image characterization of ventricular contraction in left and right bundle branch block. Am J Cardiol. 1982;50:95–103.
48. Kerwin W, Botvinick EH, O'Connell JW. Ventricular contraction abnormalities in dilated cardiomyopathy: acute effects of dual chamber simultaneous biventricular pacing to correct interventricular dyssynchrony. J Am Coll Cardiol. 2000;35:1221–7.
49. Munoz del Romeral L, Stillson C, Lesh M, Dae M, Botvinick E. The relationship of myocardial contraction and electrical excitation—the correlation between scintigraphic phase image analysis and electrophysiologic mapping. J Nucl Cardiol. 2009;16:792–800.
50. Munoz del Romeral L, Stillson C, Lesh M, Botvinick E. The variable functional effects of the pacing site in normal and scarred ventricles. J Nucl Cardiol. 2009;16:904–13.
51. O'Connell JW, Schreck C, Moles M, Badwar N, DeMarco T, Olgin J, et al. A unique method by which to quantitate synchrony with equilibrium radionuclide angiography. J Nucl Cardiol. 2005;12:441–50.
52. Lalonde M, Birnie D, Ruddy TD. deKemp RA, Wassenaar RW. SPECT blood pool phase analysis can accurately and reproducibly quantify mechanical dyssynchrony. J Nucl Cardiol. 2010;17:803–10.
53. Badhwar N, James J, Hoffmayer KS, O'Connell JW, Green D, De Marco T, Botvinick EH. Utility of equilibrium radionuclide angiogram-derived measures of dyssynchrony to predict outcomes in heart failure patients undergoing cardiac resynchronization therapy. J Nucl Med. 2016;57:1880–6.
54. Nichols KJ, Van Tosh A, Wang Y, Palestro CJ, Reichek N. Validation of gated blood-pool SPECT regional left ventricular function measurements. J Nucl Med. 2009;50:53–60.
55. Harel F, Finnerty V, Gregoire J, Thibault B, Marcotte F, Ugoloni P, Khairy P. Gated blood pool SPECT versus cardiac magnetic resonance imaging for the assessment of left ventricular volumes and ejection fraction. J Nucl Cardiol. 2010;17:427–34.
56. Oeff M, Scheinman MM, Abbott JA, Botvinick EH, Griffin JC, Herre JM, Dae MW. Phase image triangulation of accessory pathways in patients undergoing catheter ablation of posteroseptal pathways. Pacing Clin Electrophysiol. 1991;14:1072–85.
57. Germano G. Technical aspects of myocardial SPECT imaging. J Nucl Med. 2001;42:1499–507.
58. The Cardiovascular Imaging Committee, American College of Cardiology, The Committee on Advanced Cardiac Imaging and Technology, Council on Clinical Cardiology, American Heart Association, Board of Directors, Cardiovascular Council, Society of Nuclear Medicine. Standardization of cardiac tomographic imaging. J Am Coll Cardiol. 1992;20:255–6.
59. Germano G, Berman D. Acquisition and processing for gated perfusion SPECT: technical aspects. In: Germano G, Berman D, editors. Clinical gated cardiac SPECT. Armonk, NY: Futura; 1999. p. 93–113.
60. Botvinick E, Davis J, Dae M, O'Connell J, Schechtmann N, Abbott J, et al. Localization of ventricular tachycardia exit site and subsequent contraction sequence and functional effects with bedside radionuclide angiography. JACC Cardiovasc Imaging. 2008;1:605–13.
61. Nakajima K, Higuchi T, Taki J, Kawano M, Tonami N. Accuracy of ventricular volume and ejection fraction measured by gated myocardial SPECT: comparison of 4 software programs. J Nucl Med. 2001;42:1571–8.
62. Schaefer WM, Lipke CS, Standke D, Kühl HP, Nowak B, Kaiser HJ, et al. Quantification of left ventricular volumes and ejection fraction from gated 99mTc-MIBI SPECT: MRI validation and comparison of the Emory Cardiac Tool Box with QGS and 4D-MSPECT. J Nucl Med. 2005;46:1256–63.
63. Xia W, Lv Z, Wang G, Cai H, Ni J, Zhang Y, Ye B. A comparison and validation of blood-pool imaging and ECG-gated SPET myocardial perfusion imaging to assess left ventricular ejection fraction. Hell J Nucl Med. 2010;13(3):241–5.
64. Nakajima K, Nishimura T. Inter-institution preference-based variability of ejection fraction and volumes using quantitative gated SPECT with Tc-99m-tetrofosmin: a multicentre study involving 106 hospitals. Eur J Nucl Med Mol Imaging. 2006;33:127–33.
65. Honda N, Machida K, Mamiya T, Takahashi T, Takishima T, Hasegawa N, et al. Two-dimensional polar display of cardiac blood pool SPECT. Eur J Nucl Med. 1989;15:133–6.
66. Links JM, Devous MD Sr. Three-dimensional display in nuclear medicine: a more useful depiction of reality, or only a superficial rendering? J Nucl Med. 1995;36:703–4.
67. Metcalfe MJ, Cross S, Norton MY, Lomax A, Jennings K, Walton S. Polar map or novel three-dimensional display technique for the improved detection of inferior wall myocardial infarction using tomographic radionuclide ventriculography. Nucl Med Commun. 1994;15:330–40.
68. Botvinick EH, Hoffman JIE, Maddahi J, Garcia E, Rodrigues EA, Van Train K, Berman DS. Topic 5, myocardial perfusion scintigraphy-technical aspects. Self-study program III. In: Botvinick E, editor. Nuclear medicine: cardiology. Society of Nuclear Medicine: Reston, VA; 2003.
69. Indovina AG. Three-dimensional surface display in blood pool gated SPECT. Angiology. 1994;45:861–6.
70. Taillefer R, DePuey EG, Udelson JE, Beller GA, Benjamin C, Gagnon A. Comparison between the end-diastolic images and the summed images of gated Tc-99m sestamibi SPECT perfusion study in detection of coronary artery disease in women. J Nucl Cardiol. 1999;6:169–76.
71. Mok DY, Bartlett ML, Bacharach SL, et al. Can partial volume effects be used to measure myocardial thickness and thickening? IEEE Comp Cardiol. 1992;19:195–8.
72. Bacharach SL. Regional and global ventricular function. In: Dilsizian V, editor. Myocardial viability: a clinical and scientific treatise. Armonk, NY: Futura; 2000.
73. Botvinick EH, Dae MW, O'Connell JW. The scintigraphic evaluation of the cardiovascular system. In: Parmley WW, Chatterjee KC, editors. Cardiology. Philadelphia: JB Lippincott; 1983.
74. Yun J, Block M, Botvinick EH. Unique contraction pattern in patients after coronary bypass graft surgery by gated SPECT myocardial perfusion imaging. Clin Nucl Med. 2003;28:18–24.

Prognostic Performance of Myocardial Perfusion and Function

8

Lawrence M. Phillips, Robert J. H. Miller, Leslee J. Shaw, Rory Hachamovitch, Guido Germano, Jennifer H. Mieres, and Daniel S. Berman

Introduction

Since its beginnings in the early 1970s, clinical nuclear cardiology has evolved substantially, gaining both technical sophistication and enhanced imaging capabilities. In parallel to these developments, an extensive literature supporting its clinical utility and cost-effectiveness has developed. Current single-photon emission computed tomography (SPECT) myocardial perfusion imaging (MPI) allows for objective measurement of myocardial function and relative regional myocardial perfusion at rest and stress, providing accurate risk assessment in a wider variety of patient populations. The evidence for similar prognostic data derived from positron emission tomography (PET) is rapidly growing. This chapter highlights the prognostic utility of these two modalities and illustrates how this information can guide patient management decisions.

The chapter is organized as follows: First, we discuss methods for the assessment of myocardial perfusion and their associations with prognosis in patients with known or suspected coronary artery disease (CAD). (Risk stratification of patients with acute coronary syndromes is discussed in a separate chapter.) We discuss the importance of interpreting perfusion data in conjunction with pre-test assessments of risk and the cost-effectiveness of testing. Next is the largest section, which outlines the current evidence regarding clinical factors and their interactions with ischemia in the context of risk stratification. We discuss non-perfusion markers of increased risk as well as methods to improve risk stratification by combining factors. We briefly discuss the impact of changes in SPECT MPI protocols and technology on prognostication. Given the emerging role for risk stratification with coronary calcium scoring, we also discuss the interplay of evidence of atherosclerosis with perfusion imaging. Finally, we discuss the role of perfusion imaging in identifying patients who may derive survival benefit from revascularization in addition to medical therapy.

A fundamental role for nuclear cardiology is determining which patients with suspected or known CAD require invasive coronary angiography (ICA) with consideration of revascularization. In patients who have refractory anginal symptoms, perfusion imaging will not aid physicians in determining which patients should go for ICA, which will typically be pursued for symptom relief. With few exceptions, revascularization has been shown to relieve anginal symptoms in patients with CAD. SPECT MPI can be useful for identifying myocardial ischemia and determining which vessel or vessels might be most

L. M. Phillips
Department of Nuclear Cardiology, Leon H. Charney Division of Cardiology, New York University Langone Health, New York, NY, USA

R. J. H. Miller
Departments of Imaging and Medicine, Cedars-Sinai Medical Center, Los Angeles, CA, USA

L. J. Shaw
Dalio Institute of Cardiovascular Imaging, New York-Presbyterian Hospital and Weill Cornell Medicine, New York, NY, USA

R. Hachamovitch
Department of Cardiovascular Medicine, Section of Cardiovascular Imaging, Heart and Vascular Institute, Cleveland Clinic, Cleveland, OH, USA

G. Germano
David Geffen School of Medicine, University of California Los Angeles, Los Angeles, CA, USA

J. H. Mieres
Center for Equity of Care, Northwell Health, Zucker School of Medicine at Hofstra/Northwell, New Hyde Park, NY, USA

D. S. Berman (✉)
S. Mark Taper Foundation Imaging Center, Cedars-Sinai Medical Center, Los Angeles, CA, USA
e-mail: bermand@cshs.org

V. Dilsizian, J. Narula (eds.), *Atlas of Nuclear Cardiology*, https://doi.org/10.1007/978-3-030-49885-6_8

appropriate for revascularization. This information may be particularly useful for patients with known CAD or patients with multiple lesions on ICA.

Risk stratification is a mainstay in the application of SPECT MPI, as endorsed by clinical guidelines [1]. There is a strong body of evidence that the extent and severity of ischemia is closely related to cardiovascular event rates. Revascularization can effectively decrease the burden of ischemia as assessed by SPECT MPI [2]. In a single-center registry, Hachamovitch et al. showed that SPECT MPI identifies patients who may benefit from revascularization based on ischemic burden [3]. Whether selecting patients for revascularization based on the extent of ischemia improves patient outcomes was under prospective investigation in the International Study of Comparative Health Effectiveness With Medical and Invasive Approaches (ISCHEMIA) trial at the time this chapter was written [4]. In contrast, the approach focusing on anatomic findings has been shown to be less advantageous. Both the COURAGE trial and BARI 2D investigated strategies of optimal medical therapy versus revascularization, and both studies failed to show a difference in death or major adverse cardiovascular event without incorporation of the degree of myocardial ischemia in the assessment [5–7].

Pathophysiologic Basis for Risk Assessment in Myocardial Perfusion SPECT

The basis for risk stratification with SPECT MPI is the major prognostic influence of ischemia and myocardial function in patients with known or suspected CAD. These measurements include the amount of jeopardized myocardium (supplied by vessels with hemodynamically significant stenosis), the degree of this jeopardy (tightness of the individual coronary stenosis), and the amount of infarcted myocardium. An additional important factor in prognostic assessment is the stability (or instability) of the CAD process. This last consideration may help to explain what appears to be a clinical paradox: Stress perfusion tests, which in general are expected to be positive only in the presence of hemodynamically significant stenosis, are generally associated with a very low risk of either cardiac death or nonfatal myocardial infarction (MI) when normal. In contrast, it has been observed that most MI occurs in regions with coronary plaques causing less than 50% stenosis before the event [8]. It has been postulated that this paradox may be explained by the different response to stress of mild stenosis associated with stable and unstable plaques. For example, it has been shown that mild coronary narrowings associated with unstable plaque manifest a vasoconstrictive response to acetylcholine stimulation owing to abnormal endothelial function, whereas stable lesions respond with vasodilation [8]. It is possible that factors released during exercise or vasodilator stress may be similar to acetylcholine in terms of stimulation of a differential endothelial response in stable and unstable plaques. Thus, beyond the ability to define anatomic stenosis, nuclear tests (by virtue of their physiologic assessment) would be able to discern abnormalities of endothelial function associated with high risk, even in the absence of significant stenosis. The importance of coronary plaques that do not cause ischemia, which might be missed without an anatomic assessment, also needs to be recognized; this factor is discussed with respect to combined assessments of ischemia and coronary atherosclerosis.

Differentiating Outcome Type by Nuclear Test Results

Evidence in large patient cohorts has revealed that factors estimating the extent of left ventricular dysfunction (left ventricular ejection fraction, the extent of infarcted myocardium, transient ischemic dilation of the left ventricle, and increased lung uptake) are excellent predictors of cardiac mortality. In contrast, measurements of inducible ischemia are better predictors of the development of acute ischemic syndromes. These include exertional symptoms and electrocardiographic changes, as well as the extent of perfusion defect reversibility and stress-induced ventricular dyssynergy. Several reports have shown an incremental prognostic value of nuclear testing over clinical information with respect to cardiac death or the combination of cardiac death and nonfatal MI as isolated endpoints. By understanding how clinical information and nuclear test markers can be used to estimate varying outcomes, it is possible to tailor therapeutic decision-making for an individual patient based on the combination of clinical factors and SPECT MPI results. For example, a patient with severe perfusion abnormalities on stress imaging may have a five-fold to ten-fold higher likelihood of cardiac death than a patient with a normal SPECT study (Fig. 8.1). If the defects are stress-induced (reversible), therapies such as medications and revascularization may be beneficial in decreasing mortality rates [2, 3].

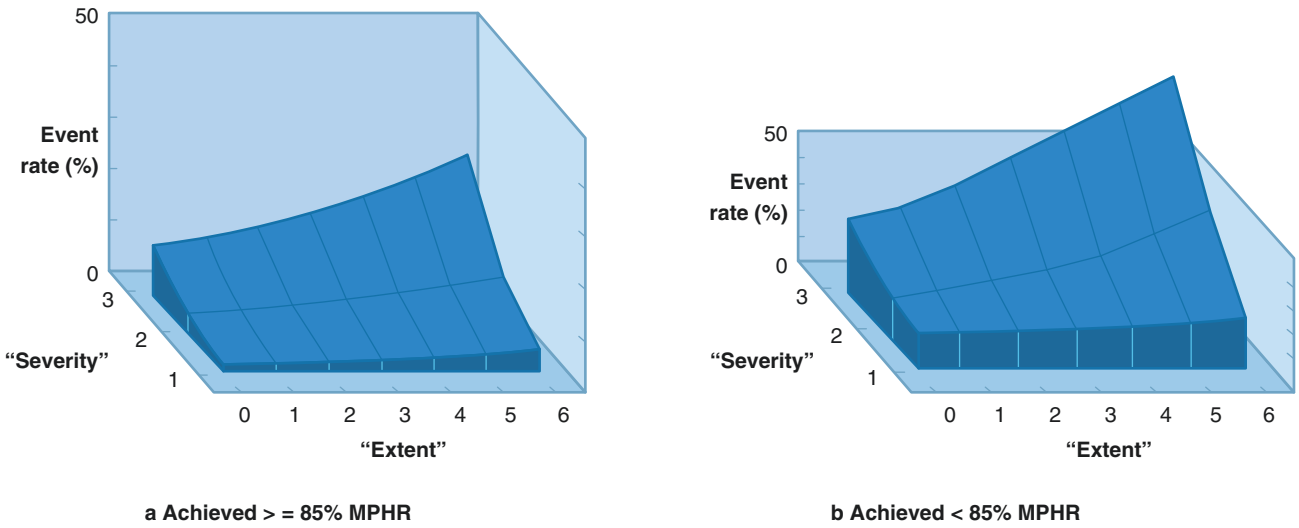

Fig. 8.1 Rates of death, myocardial infarction (MI), and late revascularization as a function of combined extent and severity of exercise-induced ischemia in patients able (**a**) and unable (**b**) to reach at least 85% of maximal predicted heart rate (MPHR), from one of the earliest reports of the prognostic use of myocardial perfusion imaging (MPI). Using planar imaging, semiquantitative interpretation employed a six-segment extent and three-level severity scoring system. Ladenheim et al. were the first to demonstrate complementary contribution of extent and severity of ischemia to prognosis, which forms the basis of all semi-quantitative and quantitative assessments of ischemia [9]. In this study of 1689 patients without known coronary artery disease, both the extent and severity of ischemia were exponentially correlated with rates of death, non-fatal MI, or late revascularization during 1 year of follow-up ($r > 0.97$, $p < 0.01$). The study was also the first to show the added value of a clinical assessment, showing a greater impact of the magnitude of ischemia in patients unable to reach adequate exercise heart rate [9]

Summing the segmental scores of the extent and severity of hypoperfusion on SPECT MPI generates a global measure of the magnitude of ischemia. To optimize the prognostic performance of stress SPECT MPI, it is crucial to maximize the information extracted from images at the time of interpretation. The extent and severity of reversible hypoperfusion are independent variables in predicting subsequent cardiac events in patients with suspected coronary artery disease. To this end, it is necessary to consider the full extent and severity of the abnormality, either semiquantitatively [10, 11], or quantitatively [12–14]. Though a 20-segment model was originally used with SPECT MPI [11], a 17-segment model is currently recommended for all forms of myocardial imaging (Figs. 8.2 and 8.3) [15]. This change resulted in more weighting given to the proximal segments of the left ventricle over the apical segments.

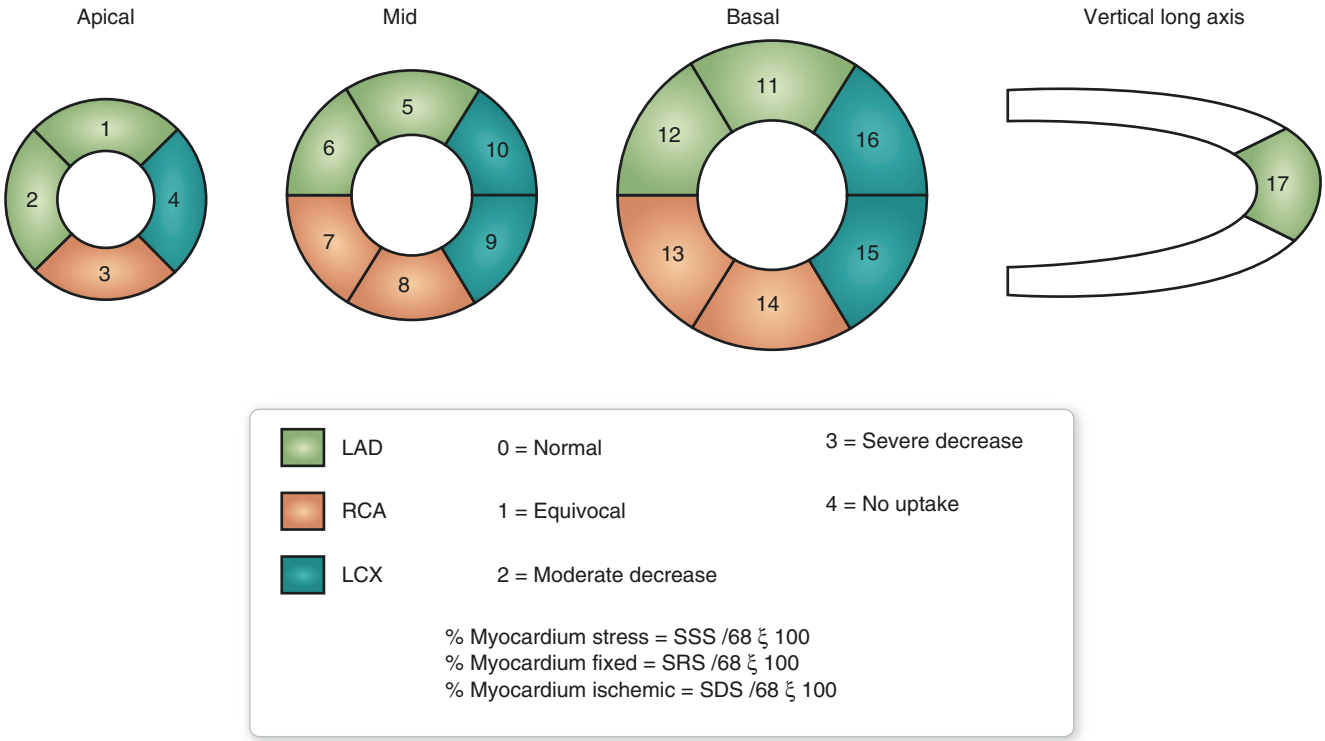

Fig. 8.2 Segmental scoring of perfusion defects. This figure outlines the segmental division of the SPECT slices and the assignment of individual segments to coronary arteries. The numbers refer to the individual segments. To account for the severity of perfusion defect, each segment is scored from 0 (normal) to 4 (absence of radioactivity). To obtain a semiquantitative view of the entire left ventricle, the totality of the perfusion defect can be calculated using summed stress scores (SSS), summed rest scores (SRS), and summed difference scores (SDS). These can be converted to a model-independent value by dividing by the maximum potential score. With the 17-segment scoring, the percentage of myocardium hypoperfused is calculated by dividing by 68 (17 × 4 = 68) and multiplying by 100 [10]. The result is the percentage of myocardium abnormal with any type of perfusion defect (SSS), fixed (nonreversible, SRS) defect, and ischemic (reversible, SDS) defect. LAD left anterior descending coronary artery, LCX left circumflex coronary artery, RCA right coronary artery

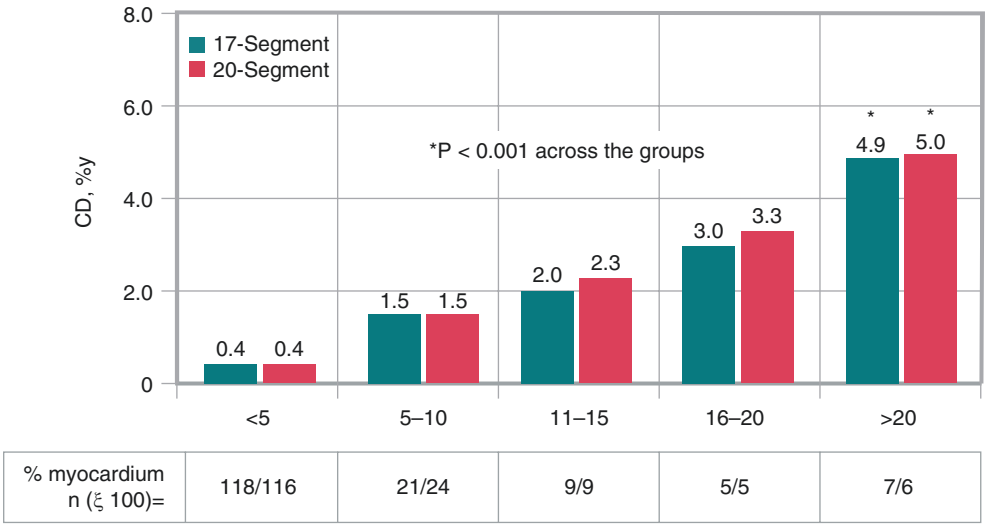

Fig. 8.3 Comparison of the relationship between global hypoperfusion and prognosis expressed using percent myocardium with abnormal perfusion at stress (% myocardium stress) derived from SPECT MPI analyzed with either 20-segment or 17-segment approaches. In a population of 16,020 patients with known or suspected coronary artery disease (CAD) followed for 2.1 years, prognostic assessment regarding cardiac death (CD) was not significantly different between models [10]

Table 8.1 lists the global perfusion parameters, which can be considered the perfusion analogues of left ventricular ejection fraction (LVEF), the most commonly employed global ventricular function parameter. The summed stress score (SSS) reflects the extent and severity of perfusion defects at stress and is affected by prior MI, hibernating myocardium, and stress-induced ischemia. The summed rest score (SRS) reflects the amount of infarcted or hibernating myocardium. The summed difference score (SDS) is a measure of the extent and severity of stress-induced ischemia. By incorporating the extent and severity of the perfusion defect, these global parameters allow an assessment of the variables shown in Fig. 8.2 to be incrementally important in assessing risk from perfusion scintigraphy. The principal problem of summed scores is that their implications depend on the particular scoring system employed; translating results to the percentage of myocardium (Table 8.1) may be more intuitive, as illustrated by Fig. 8.4, in which the extent of abnormality of the SPECT MPI provides important additional information regarding risk.

Summed scores
Summed stress score (SSS) = sum of 17 segment stress scores
Summed rest score (SRS) = sum of 17 segment rest scores
Summed difference score (SDS) = SSS minus SRS
Degree of abnormality by percentage of myocardium stress
Normal: SSS 0–3 (<5% myocardium)
Mildly abnormal: SSS 4–6 (>5% to <10% myocardium)
Moderately to severely abnormal: SSS ≥7 (>10% myocardium)

Table 8.1 Semiquantitative global indices of perfusion

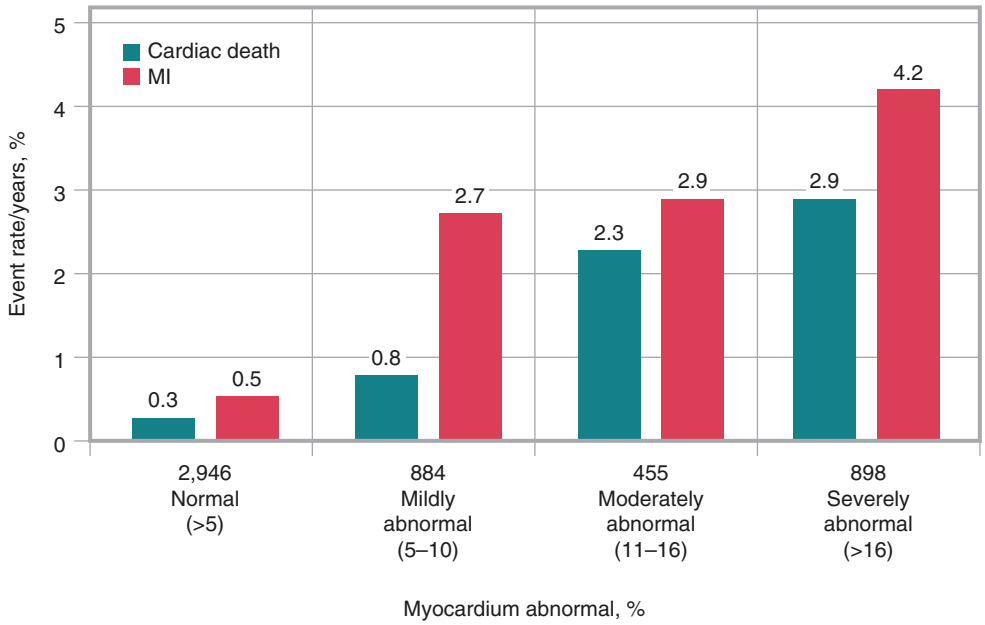

Fig. 8.4 Prediction of MI and cardiac death (CD) by SPECT MPI. The annualized cardiac death rate and non-fatal MI rate of a large group of patients undergoing stress SPECT MPI (two-thirds exercise stress, one-third adenosine stress) is shown. There was a progressive increase in the CD rate as a function of the extent and severity of perfusion defect. In contrast, the rate of nonfatal MI was low when the scans were normal, but it increased abruptly when even a mild myocardial perfusion defect was noted [16]

Figures 8.5, 8.6, 8.7, 8.8, 8.9, 8.10, 8.11, and 8.12 offer further examples of the assessment of myocardial perfusion and its prognostic value.

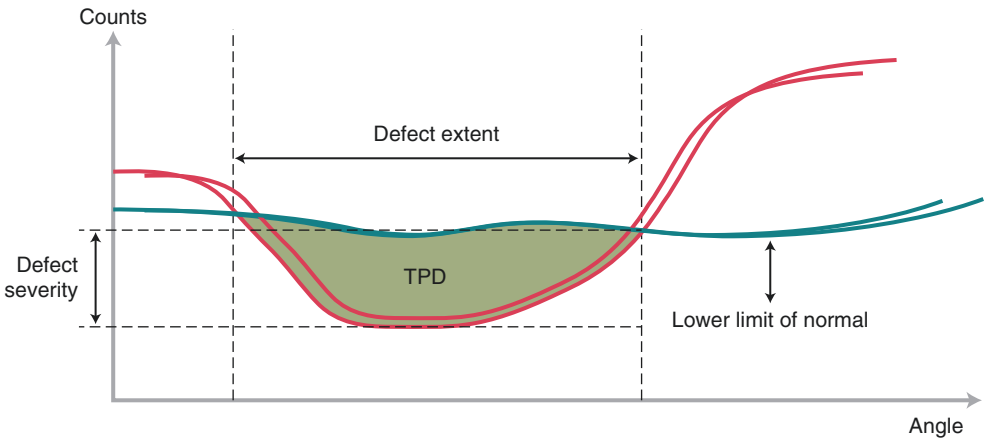

Fig. 8.5 Quantitative assessment of the combined extent and severity of perfusion defect using the total perfusion deficit (TPD). Being intrinsically three-dimensional, perfusion abnormalities with SPECT lend themselves to automated quantitative analysis. Several software packages for quantitative analysis are commercially available. This figure illustrates TPD, which is a computer-derived analogue of the visual percent myocardium that is abnormal by visual analysis, incorporating both defect extent and severity. TPD is calculated as the percentage of the total surface area of the left ventricle below the predefined uniform average deviation threshold [17, 18]. A circumferential profile for one short-axis slice is shown with corresponding normal limits [17, 19]. The area below the normal limit curve but above the circumferential profile curve for each slice defines the perfusion deficit. These areas are computed for all circumferential profiles in the myocardium and are summed, forming TPD. TPD is measured at stress and at rest, and ischemic TPD is calculated from the difference (stress TPD minus rest TPD). The reproducibility thresholds for quantitative stress, rest, and ischemic TPD have been reported to all be less than 7%, smaller than the thresholds for visual percent myocardium abnormal (10–13%) [20], suggesting that automated quantitative assessment of ischemia may be more effective than visual analysis alone. Ischemic TPD was the variable used in the Clinical Outcomes Utilizing Revascularization and Aggressive Drug Evaluation (COURAGE) nuclear substudy. Additionally, the International Study of Comparative Health Effectiveness with Medical and Invasive Approaches (ISCHEMIA) trial utilized a visually verified ischemia analysis based on TPD [2, 4, 19]

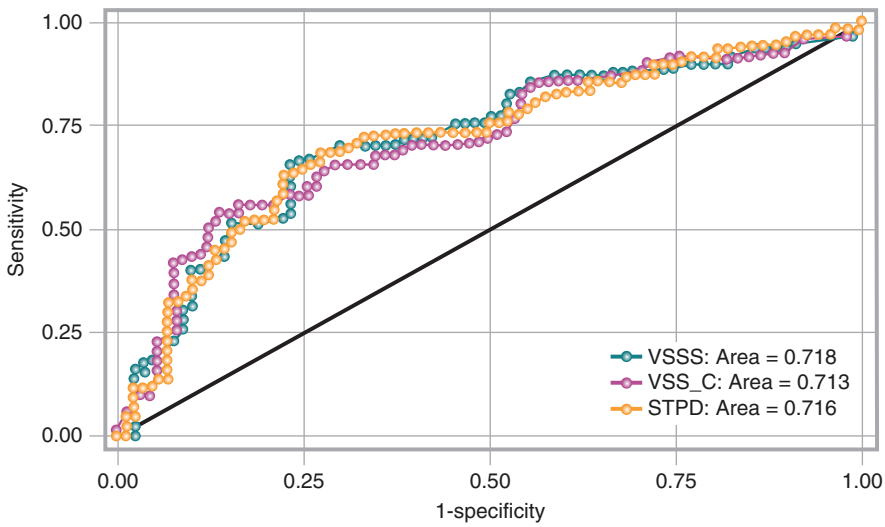

Fig. 8.6 Receiver operating characteristic (ROC) curves comparing semiquantitative visual and quantitative methods of stress perfusion assessment for prediction of cardiac death. Total perfusion deficit (TPD) is a fully automated method for determining ischemia, which incorporates extent and severity of ischemia. TPD may be more reproducible than visual scoring, particularly in the territory of the right coronary artery [20]. This study compared the prognostic ability of stress TPD (STPD) compared with visual scoring in a cohort of 81 patients who experienced cardiac death and matched controls [21]. Controls were matched by age, sex, revascularization, presence of diabetes, and presenting symptoms. Discrimination of cardiac death was similar between TPD and both the research visual summed stress score (VSSS) and clinical visual summed stress score (VSSS_C). This demonstrated that fully automated assessment of ischemia offered prognostic accuracy similar to that provided by an expert clinical reader [21]

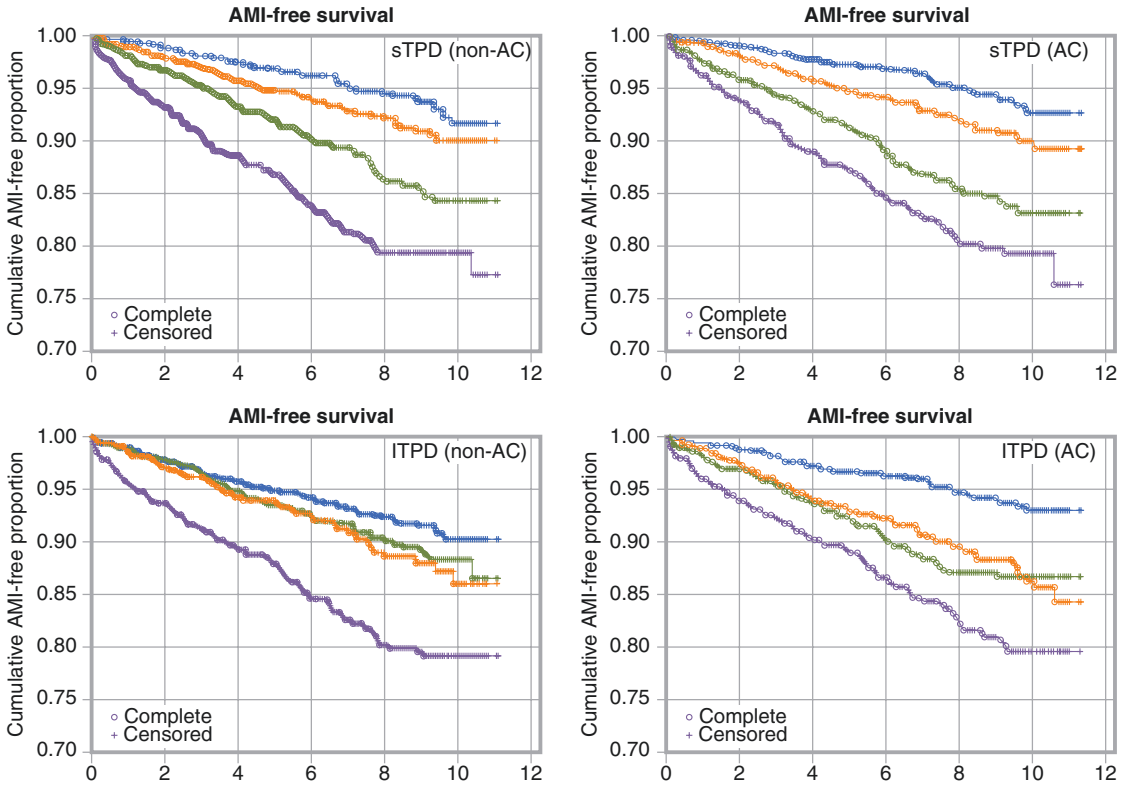

Fig. 8.7 Survival free of acute myocardial infarction (AMI) by extent of total perfusion deficit (TPD). Motwani et al. studied a cohort of 5960 patients undergoing SPECT MPI to investigate the prognostic utility of automated TPD assessment and the importance of using attenuation-corrected (AC) imaging [22]. Notably, only 10% of studies required adjustment of automated contours, suggesting that this method could be readily integrated into a clinical workflow. Figure 8.7 shows survival free of AMI stratified by quartile of stress TPD (sTPD) and ischemic TPD (stress minus rest, iTPD). The first quartile is blue, and fourth quartile is magenta. There was no significant difference in utility of TPD with or without AC ($p = 0.85$) [22]

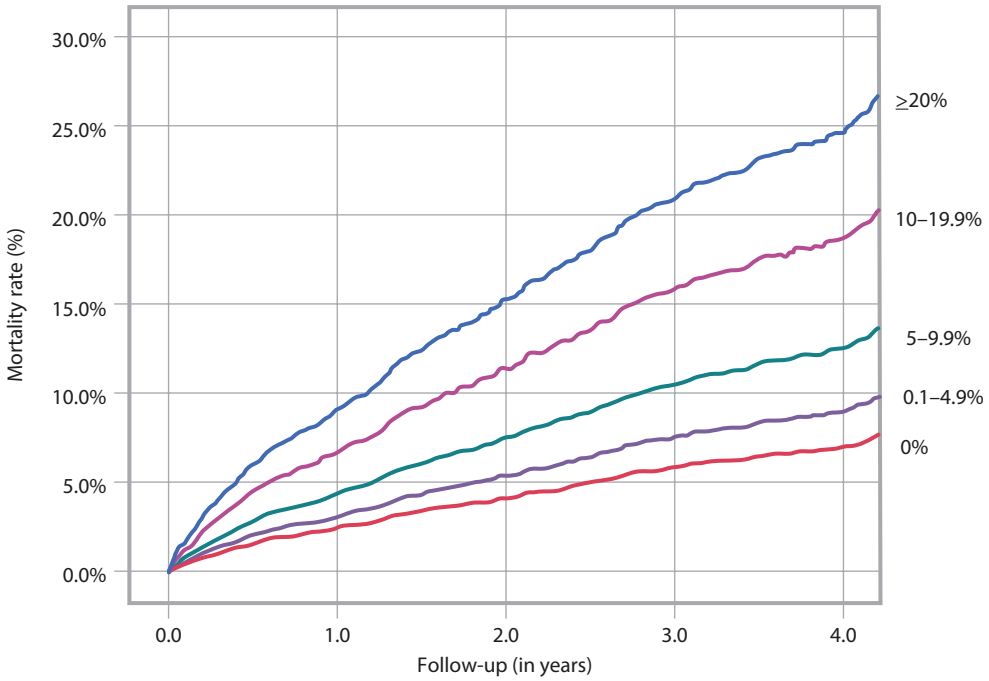

Fig. 8.8 Incidence of all-cause mortality stratified by burden of ischemia determined by positron emission tomography (PET). In this multicenter registry, patients from four centers were followed for a median of 2.2 years for incidence of all-cause mortality [23]. Increasing burden of ischemia was associated with increased all-cause mortality, with a hazard ratio (HR) of 1.4 for 0.1–9.9% ischemia and HR 3.80 for ≥20% ischemia. Similar results were shown with respect to cardiac death: HR 2.8 for 0.1–9.9% ischemia and HR 12.9 for >20% ischemia [23]

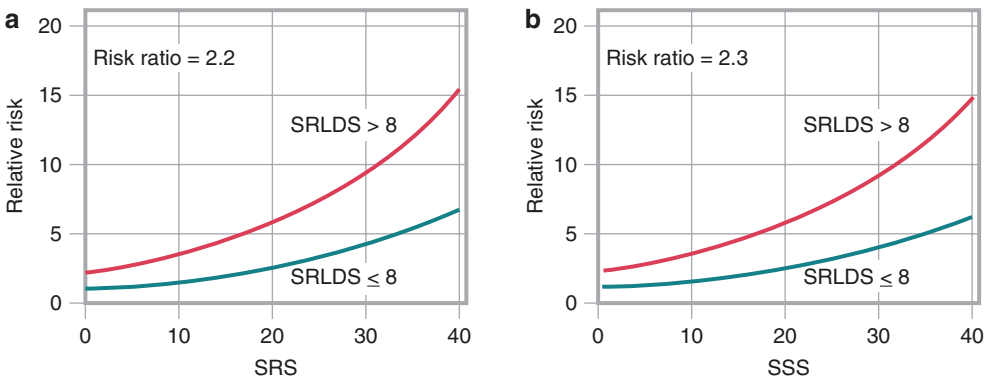

Fig. 8.9 Prognostic value of resting ^{201}Tl reversibility over summed stress score (SSS) and summed rest score (SRS). In patients with chronic CAD, the added prognostic value of resting ^{201}Tl reversibility in dual-isotope myocardial perfusion single-photon emission computed tomography (SPECT) is shown. The two curves represent differing amounts of resting reversibility as measured by the summed rest late difference score (SRLDS), which is based on the difference between the SRS of the initial rest ^{201}Tl score and the SRS on late redistribution ^{201}Tl imaging (24 hours after injection). When this score is greater than 8 (extensive resting ischemia), the relative risk with respect to subsequent cardiac events was higher than when less resting reversibility is present. The incremental prognostic value of resting reversibility persists when either the SRS (**a**) or the SSS (**b**) is considered. These data suggest that a combination of assessing both stress-induced ischemia and resting ischemia (presumably hibernating myocardium) might be more effective than stress-induced ischemia alone in evaluating the risk of patients with chronic CAD [24]

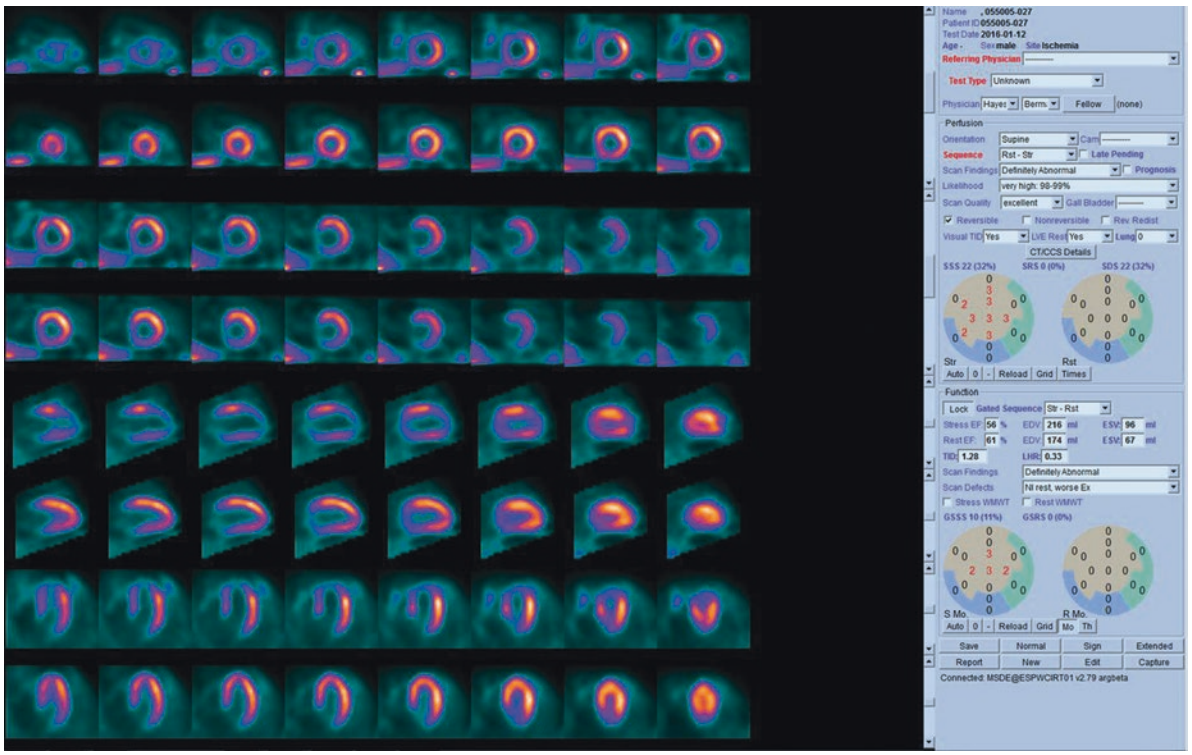

Fig. 8.10 Example of a patient from the International Study of Comparative Health Effectiveness With Medical and Invasive Approaches (ISCHEMIA) trial. The patient was imaged using a cadmium-zinc-telluride SPECT system (D-SPECT, Spectrum Dynamics, Cesaria, Israel). Exercise stress and rest ^{99m}Tc-sestamibi images are interlaced in alternate rows, which show short-axis images (*top four rows*), vertical long-axis images (*next two rows*), and horizontal long-axis images (*bottom two rows*). The SPECT MPI reveals a large, severe, reversible perfusion defect (summed difference score = 22) involving the mid to distal anterior and anteroseptal walls as well as the apex—the distribution of the left anterior descending coronary artery (LAD). Transient ischemia dilation of the left ventricle is also present, an ancillary finding associated with severe and extensive coronary artery disease (CAD) [18, 25]. Finally, there is a post-stress regional wall motion abnormality, which is also a marker of severe CAD [26]

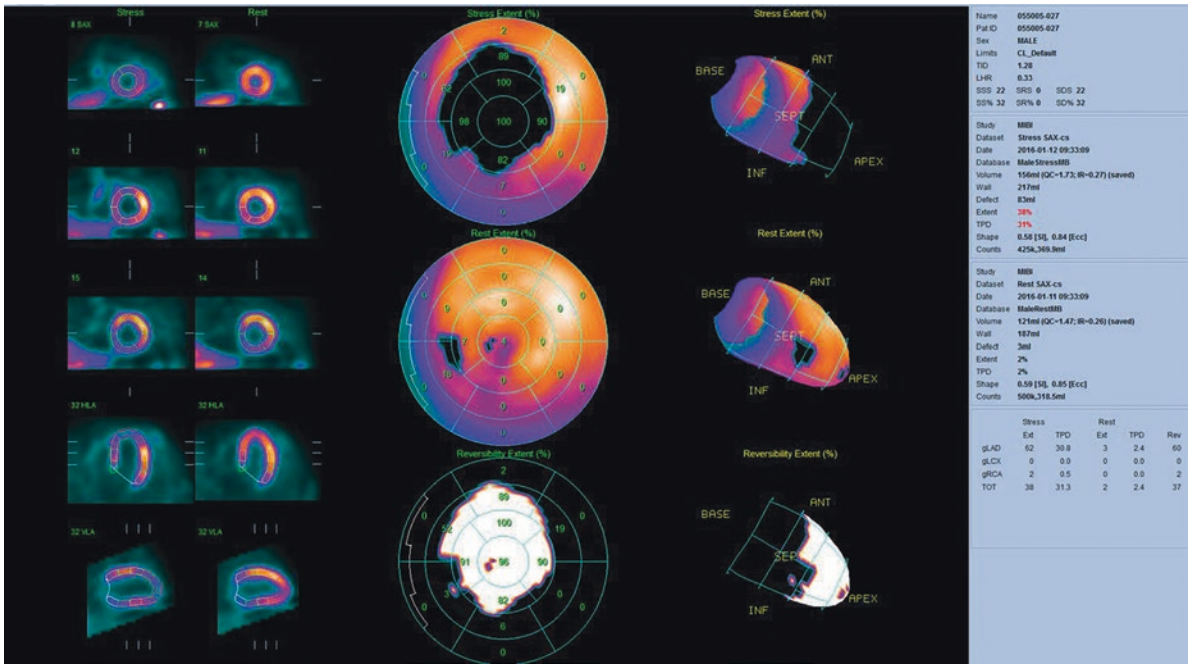

Fig. 8.11 Quantitative SPECT MPI analysis of the patient in Fig. 8.10. The total perfusion deficit (TPD) measurements revealed that 31% of the left ventricle was abnormal in the LAD territory after stress. Generally, 40% of the myocardium is considered to be supplied by the LAD. Thus, the findings are virtually indicative of a proximal stenosis of the LAD, and the severity indicates that there is a critical stenosis (>90%) [27]. The transient ischemic dilation (TID) ratio of the left ventricle was elevated at 1.28

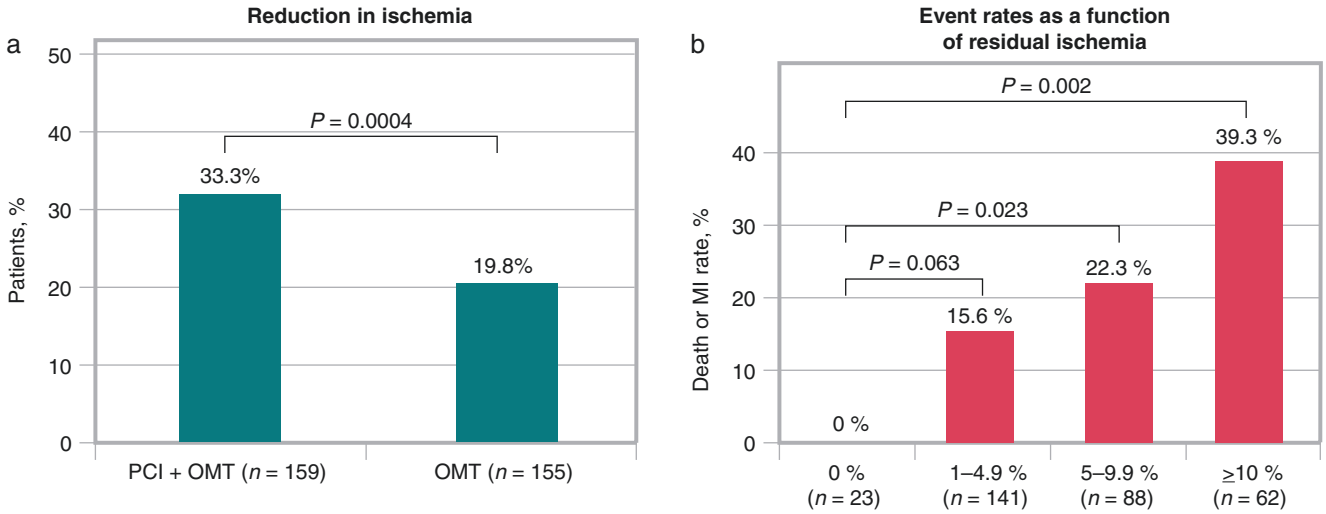

Fig. 8.12 Results from the Clinical Outcomes Utilizing Revascularization and Aggressive Drug Evaluation (COURAGE) nuclear substudy. Shaw et al. reported results of a substudy of the COURAGE trial [2]. (**a**) In this study of 314 patients in whom SPECT MPI was performed before randomization and 6–18 months after randomization, patients assigned to percutaneous coronary intervention (PCI) and optimal medical therapy (OMT) demonstrated significantly greater ischemia reduction than patients receiving OMT alone (PCI + OMT: 33% [n = 159]; OMT alone: 20% [n = 155]; $P = 0.0004$). (**b**) Importantly, the rate of death or MI was strongly related to the amount of residual ischemia on the SPECT MPI studies performed 6–18 months after randomization [2]

Interpreting Perfusion Data in Conjunction with Pre-test Assessments of Risk

Figures 8.13, 8.14, 8.15, and 8.16 illustrate the use of perfusion data in conjunction with the patient's pre-scan likelihood of CAD, clinical risk, or exercise stress results. These demonstrate the additive prognostic utility of perfusion for risk reclassification.

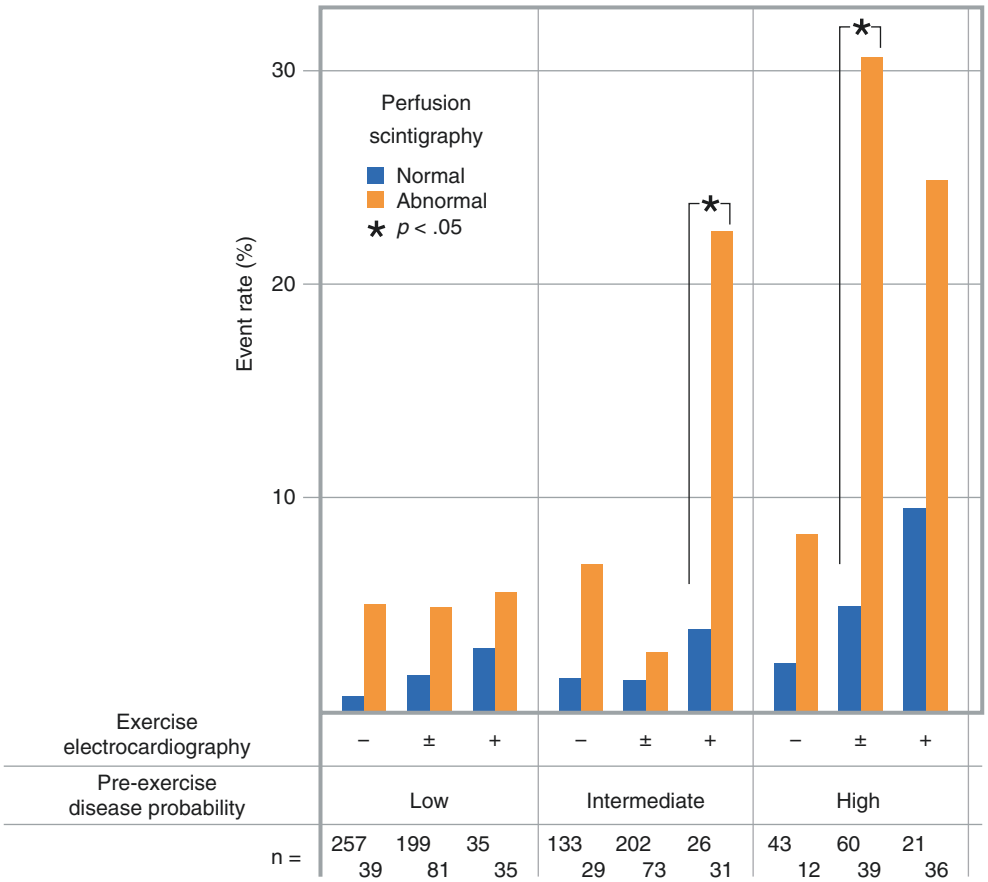

Fig. 8.13 Early data regarding the incremental prognostic utility of myocardial perfusion in addition to clinical and ECG parameters. In this study of 1659 patients who underwent MPI for known or suspected CAD, patients were followed for the development of cardiac death, non-fatal MI, or revascularization within 1 year [28]. Perfusion results were able to identify a high-risk subset of patients with intermediate pre-test probability and a positive exercise stress-test (EST) with event rates of 23% vs. 4% ($p = 0.046$). Additionally, perfusion findings were helpful in reclassifying risk in patients with high pre-test probability and equivocal EST (31% vs. 5%, $p < 0.001$) [28]

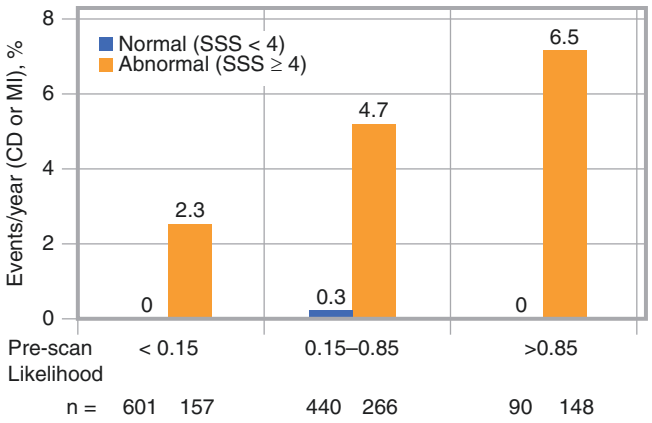

Fig. 8.14 Differential prognosis provided by stress SPECT MPI as a function of pre-scan likelihood of CAD. In a study of 1702 patients undergoing ^{99m}Tc-sestamibi imaging, a normal scan was associated with a very low (0.2%) likelihood of cardiac death (CD) or MI over a 20-month period [29]. This figure illustrates the rate of CD or nonfatal MI throughout the follow-up period as a function of SPECT results and pre-MPI likelihood of CAD (low likelihood, <0.15; intermediate likelihood, 0.15–0.85; high likelihood, >0.85). These results demonstrate that MPI could be used for prognostic purposes throughout the range of pre-test likelihood of CAD. Furthermore, the higher the pretest likelihood, the greater the differentiation in prognosis [29]. SSS summed stress score

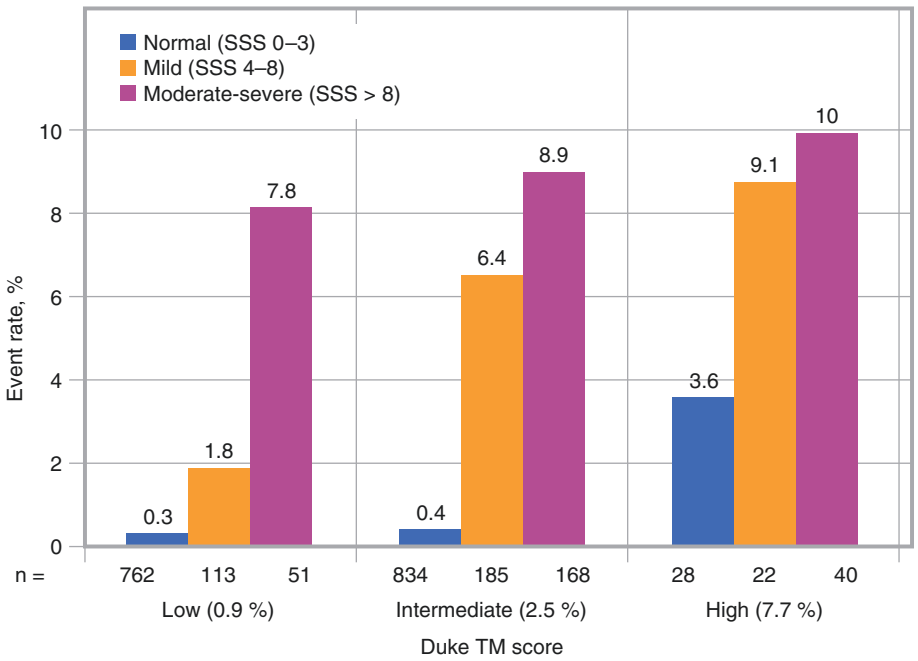

Fig. 8.15 Hard event rate (MI, cardiac death, or late revascularization) as a function of the summed stress score (SSS) and Duke treadmill (TM) score in a study of 2200 patients undergoing exercise SPECT-MPI and followed for 18.6 months. In patients with interpretable stress electrocardiograms, the Duke TM score can separate patients into low, intermediate, and high risk of cardiac events. Stress SPECT MPI studies further risk-stratify patients within each of these Duke TM score categories [30]. Patients with known CAD (prior catheterization, MI, or revascularization) were excluded. Risk stratification occurred within each category of Duke TM scores, but among the patients with high risk scores, the rate of events was not low (3.6%) despite a normal SPECT study. This demonstrates the additive prognostic utility of perfusion for risk reclassification across the spectrum of exercise testing characteristics [30]. This and other similar studies also form the basis of the "warranty period" associated with normal exercise SPECT studies [30, 31]

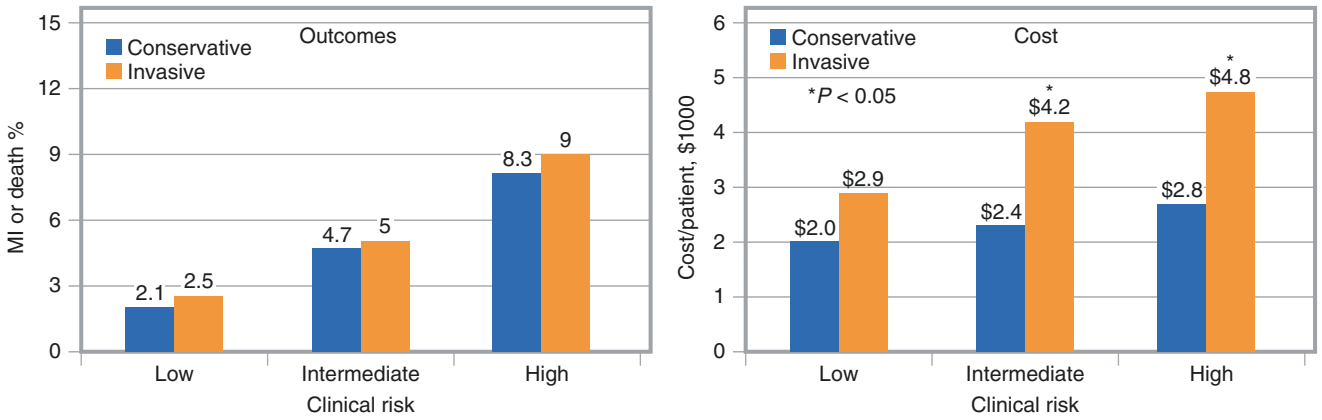

Fig. 8.16 Outcomes and rates of referral to catheterization in patients with stable chest pain, from the Economics of Noninvasive Diagnosis (END) study group [32]. In this study of 11,372 consecutive stable angina patients who were referred for stress myocardial perfusion tomography or cardiac catheterization, composite 3-year costs of care and patient outcomes were compared as a function of two strategies: invasive (direct referral for invasive coronary angiography [ICA] without stress imaging) versus conservative (initial stress myocardial perfusion tomography and selective ICA in high-risk patients). After matching patients by their pretest clinical risk of coronary disease, comparisons of invasive and conservative testing strategies revealed no difference in the rate of cardiac death or nonfatal MI, suggesting similar quality of care. Significantly, the costs of care in all risk groups were higher for the invasive strategy than for conservative care, although the difference in cost between the strategies did not reach significance in the low-risk patient subset. The cost savings identified in the intermediate-risk and high-risk patient groups were accrued predominantly by preventing ICA in patients without significant SPECT MPI abnormalities. This was also borne out by higher rates of no CAD on ICA in the invasive strategy (43% vs. 33% in patients undergoing ICA). This suggests that SPECT MPI aids in the identification of appropriate candidates for the catheterization laboratory. Hence, the use of a strategy incorporating SPECT MPI as an initial test improves cost-effectiveness without compromising patient outcomes. This finding supports the use of SPECT MPI as a reasonable alternative to ICA in patients presenting with stable angina [32]

Clinical Factors and Their Interactions with Ischemia

The largest section of this chapter, covering Figs. 8.17, 8.18, 8.19, 8.20, 8.21, 8.22, 8.23, 8.24, 8.25, 8.26, 8.27, 8.28, 8.29, 8.30, 8.31, 8.32, 8.33, 8.34, 8.35, 8.36, 8.37, 8.38, 8.39, 8.40, and 8.41, covers the role of clinical factors, including ethnicity, age, comorbidities, and stress results in combination with SPECT MPI findings for pretest risk stratification and long-term prognosis.

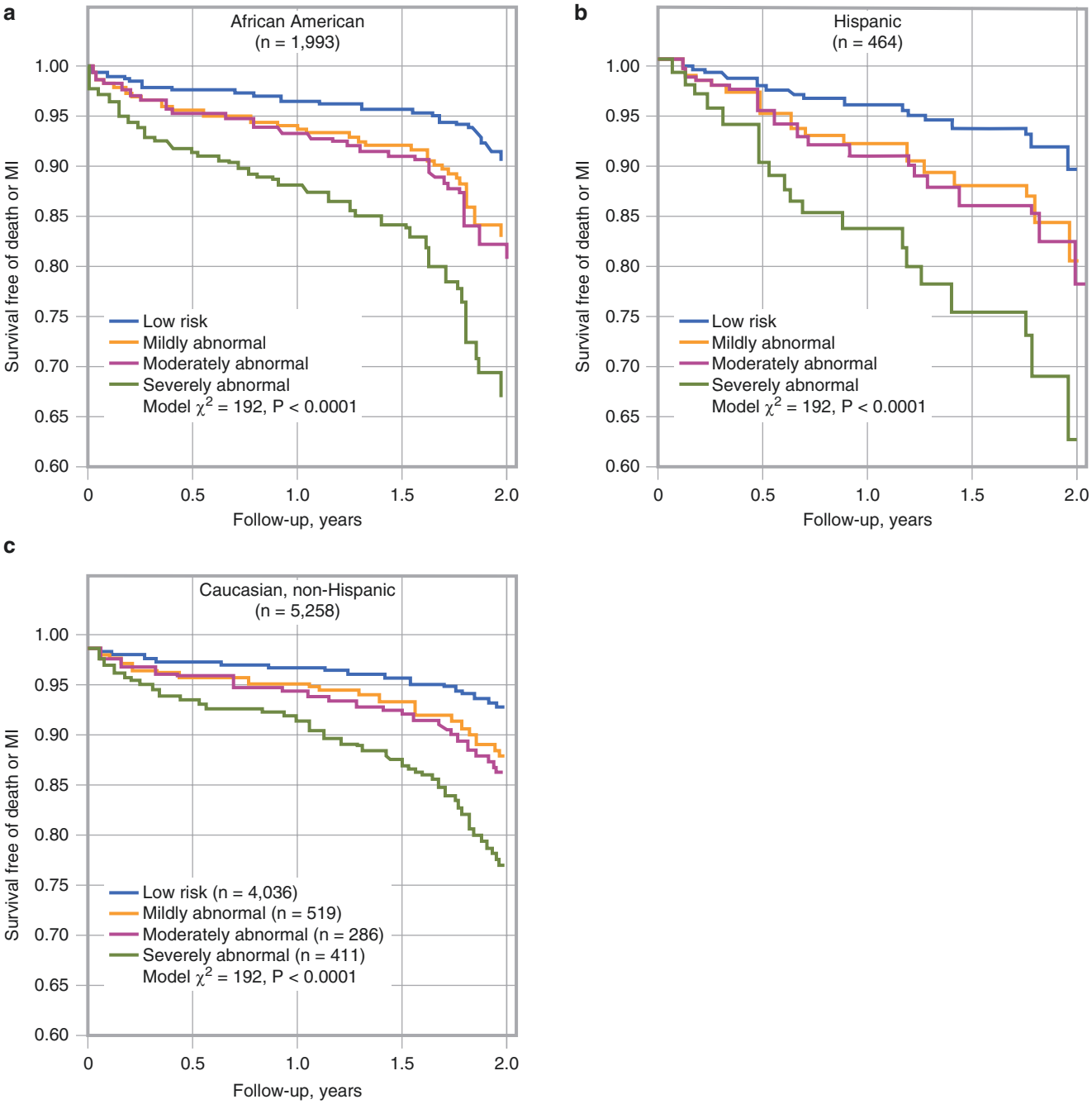

Fig. 8.17 Marked differences in event-free survival in African American and Hispanic patients versus white non-Hispanic patients undergoing stress SPECT-MPI [33]. This study was the first to find that in sufficiently large populations, effective risk stratification is possible using the 20-segment model SSS risk groupings in ethnic minorities. Predominantly because of a greater burden of comorbidities, African American patients (**a**) and Hispanic patients (**b**) have higher rates of cardiac death or nonfatal MI than white non-Hispanic patients (**c**). However, disparities may also exist in the subsequent medical therapy of ethnic minorities. Effective risk stratification is notable given that other studies have demonstrated a lower prevalence of obstructive coronary disease in African American and Hispanic patients [34]. This suggests that physiologic abnormalities may play a more important role in risk assessment for ethnic minority patients. The J-ACCESS Investigators found a low event rate in 4629 Japanese patients with normal SPECT MPI findings, with annual cardiac event rates of approximately 0.7% [33, 35]

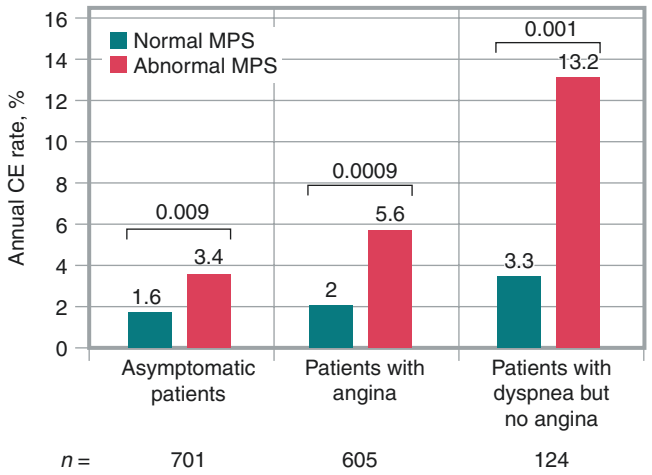

Fig. 8.18 Relationship of ischemia and symptoms for predicting long-term outcomes in diabetic patients. Zellweger et al. evaluated 1430 consecutive diabetic patients, all of whom received rest ^{201}Tl/stress ^{99m}Tc-sestamibi myocardial perfusion scans (MPS) in order to assess this relationship [36]. During the follow-up period (median of 2 years), the annual cardiac event (CE) rates (cardiac death or MI) among patients with normal MPS findings were similar for patients with angina, asymptomatic patients, and patients with shortness of breath. Among patients with abnormal MPS results, however, patients with shortness of breath had significantly higher CE rates than patients with angina ($p = 0.0008$) or asymptomatic patients ($p < 0.0001$). The outcomes for asymptomatic patients and patients with angina were similar [36]

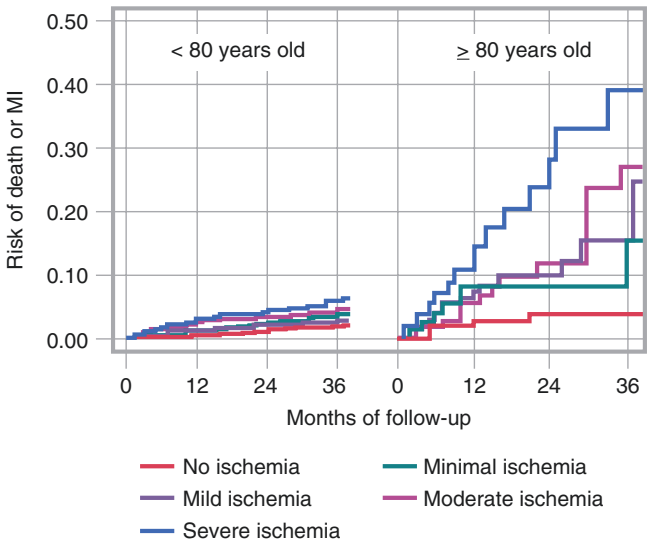

Fig. 8.19 Survival free of MI, stratified by burden of ischemia, in patients greater than 80 years old compared with younger patients. There is often concern regarding the prognostic utility of SPECT MPI in older patients, because of the high competing risk of non-cardiac death. Additionally, this group is underrepresented in most studies. Nudi et al. investigated a cohort of 13,254 patients, including 517 patients over the age of 80. There was no significant interaction between age and perfusion with respect to diagnosing significant CAD. However, there was an interaction between ischemia and age with respect to predicting the combined outcome of death or non-fatal MI, suggesting higher risk of ischemia in older patients: The hazard ratio (HR) was 4.93 in patients over 80, compared with 1.87 in younger patients [37]

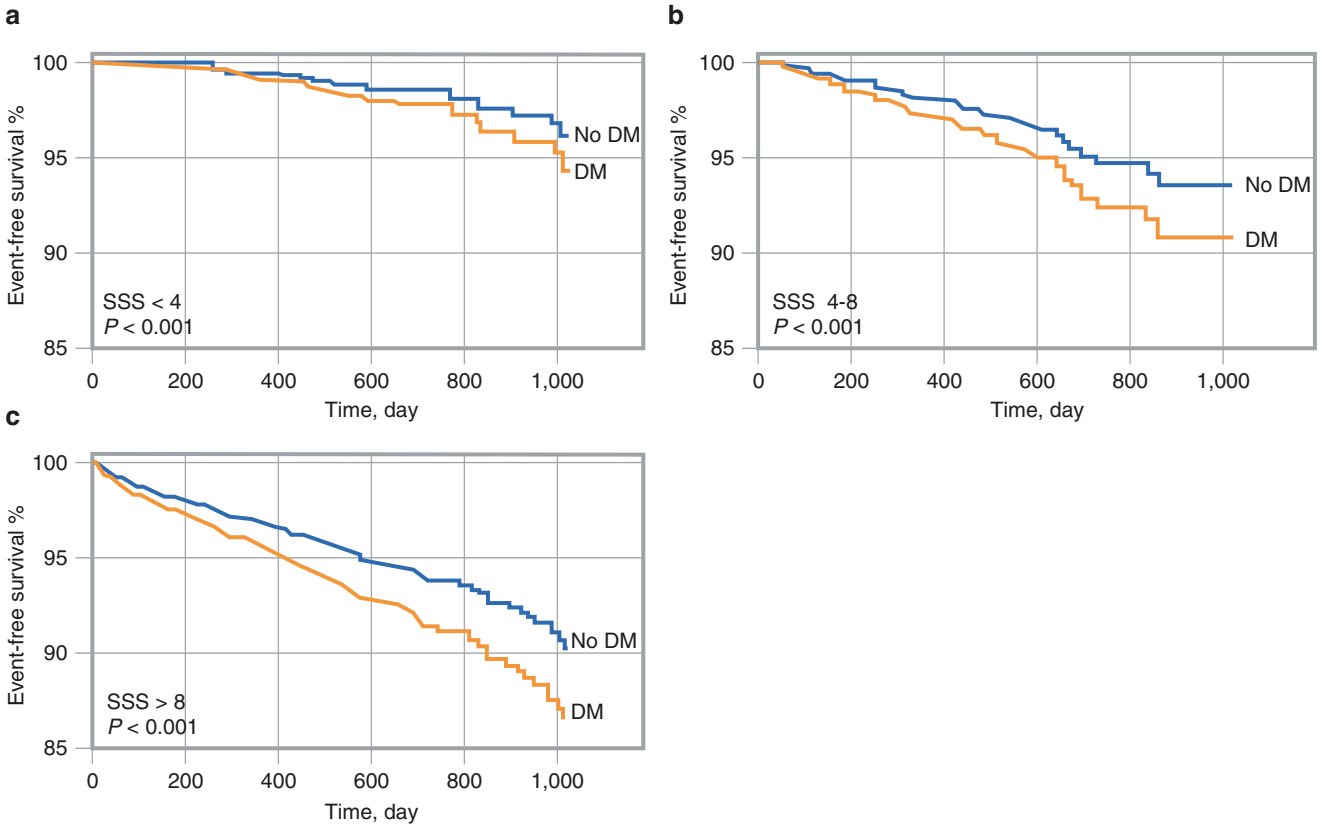

Fig. 8.20 Prognostic value of summed stress scores (SSS) from sestamibi SPECT MPI in patients with and without diabetes. Risk stratification using SPECT MPI has been proven effective in a variety of patient subgroups, most importantly among diabetic patients. This figure illustrates the hard cardiac event-free survival rate in patients with diabetes mellitus (DM) and without diabetes mellitus (no DM) categorized by the SSS as normal (SSS <4) (**a**), mildly abnormal (SSS 4–8) (**b**), and moderately to severely abnormal (SSS >8) (**c**). The study comprised 1271 patients with diabetes and 5862 patients without diabetes who underwent dual-isotope (rest ^{201}Tl/post-stress ^{99m}Tc) MPS. After adjustment for pre-scan likelihood of coronary artery disease, inability to exercise, history of coronary artery disease, and SSS, patients with diabetes had a lower event-free survival in each of the SSS categories (all $P < 0.001$). Based on these and similar results of others [38], the concept emerged that a diabetic patient with only mildly abnormal myocardial perfusion scan results might be considered for cardiac catheterization in the presence of minimal symptoms, whereas in general, patients with only mildly abnormal scans might be considered appropriate for aggressive medical management without catheterization [16, 39]. Additional data from the Detection of Ischemia in Asymptomatic Diabetics (DIAD) study [40], the Clinical Outcomes Utilizing Revascularization and Aggressive Drug Evaluation (COURAGE) trial [5] and the Bypass Angioplasty Revascularization Investigation (BARI 2D) trial [7] suggest that such a referral might not be appropriate unless there is extensive and severe ischemia [2]

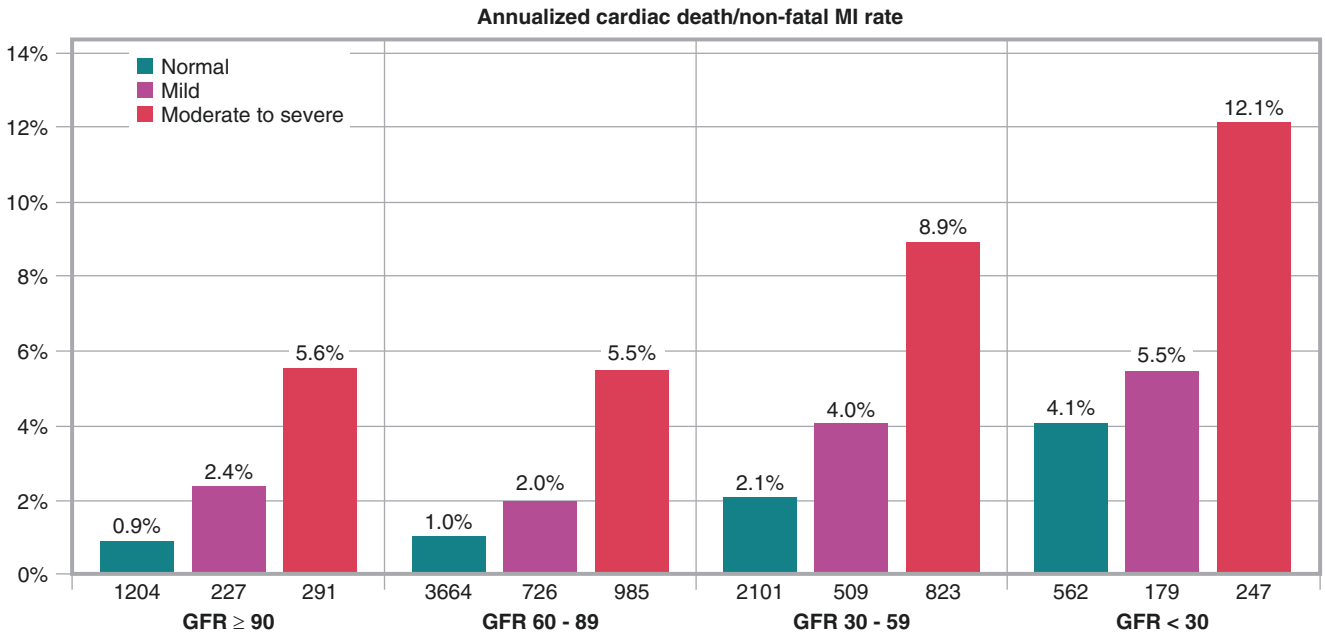

Fig. 8.21 Annualized risk of cardiac death or MI in patients with chronic kidney disease (CKD) based on degree of abnormality on SPECT-MPI. CKD is a known cardiovascular risk factor and impacts risk assessment in patients following SPECT MPI [41, 42]. In this study, 11,518 patients who underwent SPECT MPI were reassigned into categories based on their GFR and severity of perfusion defect. The rates of cardiac death and non-fatal MI notably increased as the GFR worsened, particularly in those patients with a GFR <30. Of note is the high event rate in this population, with 14.5% of the patients experiencing the combined endpoint during 5 years of follow-up. Furthermore, though SPECT MPI does provide risk stratification in the group with very low GFR, even those with normal scans did not have a low event rate [41]

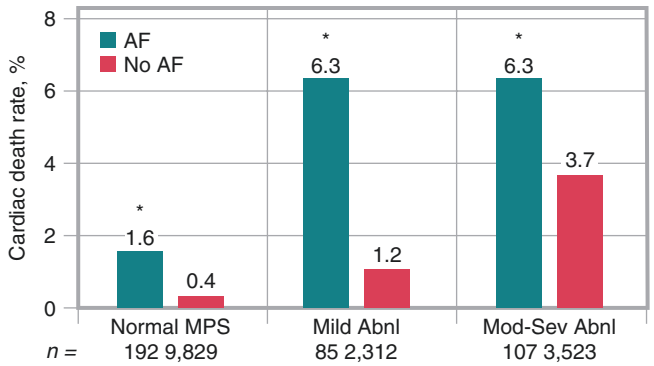

Fig. 8.22 Cardiac death rates in patients with and without atrial fibrillation (AF) as a function of SPECT MPI results. In patients with a mildly abnormal myocardial perfusion scan (MPS), those with chronic AF have been shown to have a high risk of cardiac death, whereas those without AF do not. Though patients with mildly abnormal SPECT MPI results are generally at low risk of cardiac death, this is not the case for patients with significant comorbidities [43], AF [44], or those who require pharmacologic stress [45]. In this light, the decision whether to refer a patient with a mildly abnormal perfusion scan for invasive coronary angiography becomes a function of the underlying patient condition. *$P = 0.001$; follow-up 2.2 ± 1.2 years

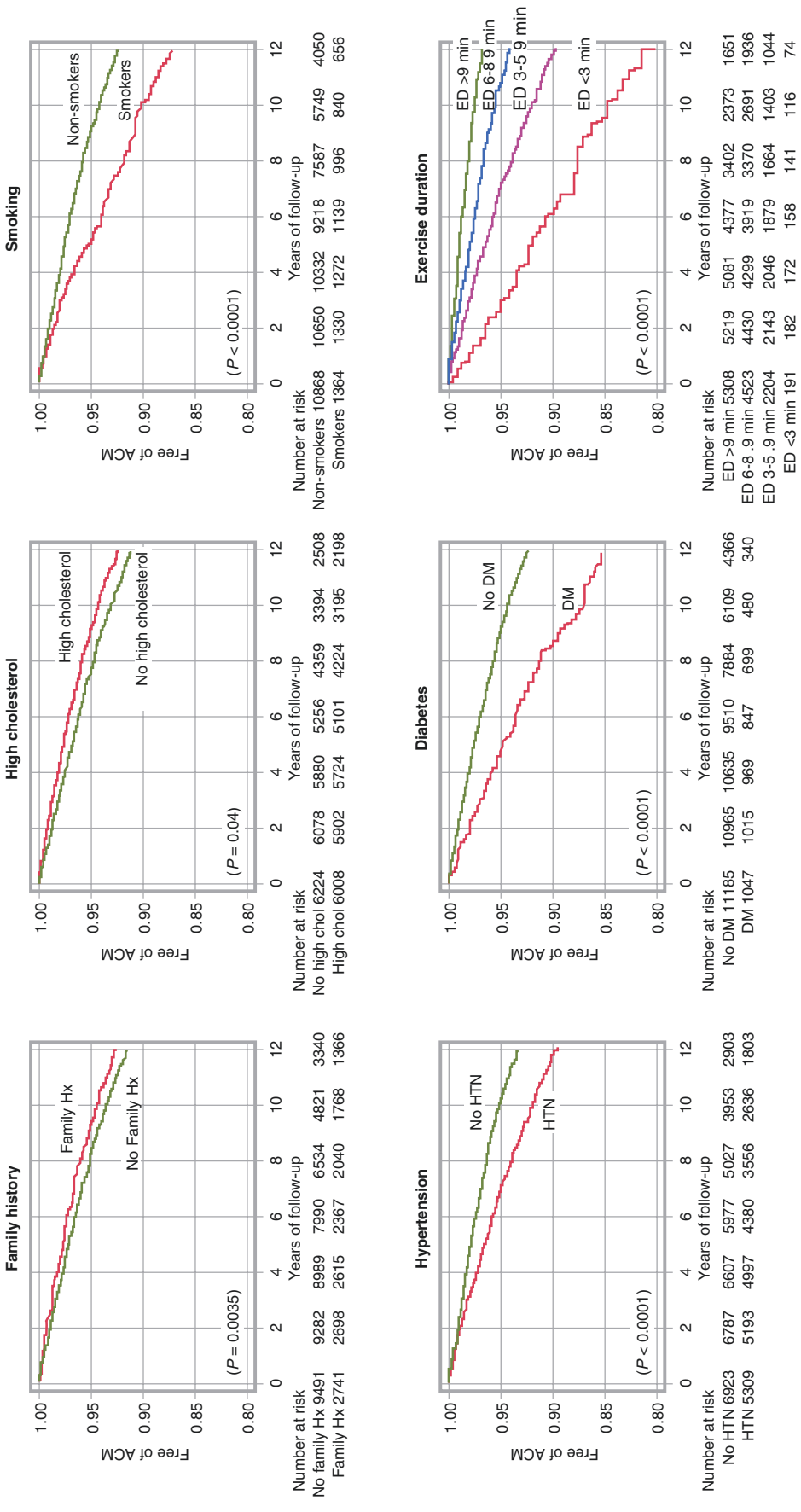

Fig. 8.23 Long-term mortality following normal exercise SPECT MPI according to coronary disease risk factors. In this study by Rozanski et al., 12,232 patients were monitored for all-cause mortality (ACM) over 11.2 years [43]. As mentioned earlier, all-cause mortality in the setting of normal myocardial perfusion is low. However, traditional cardiac risk factors and exercise duration also impact event rates, though the annualized event rate remains 1% or less in the 5 years following normal SPECT MPI, except for patients with exercise duration less than 3 minutes

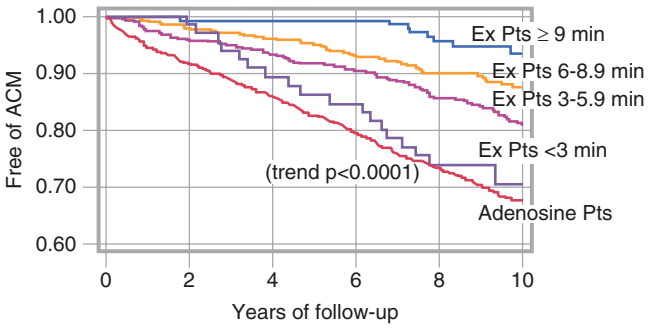

Fig. 8.24 Higher all-cause mortality (ACM) in patients requiring pharmacologic stress testing. Multiple studies have shown that patients who require pharmacologic testing have a worse prognosis than those who are able to exercise [45, 46]. Hard event rates in patients requiring pharmacologic stress remain 1.3–2.7% per year even with normal perfusion [47–50]. This rate is believed to be secondary to several factors, including concomitant chronic illnesses and physical deconditioning. In a meta-analysis by Navare et al., 24 studies were analyzed and showed the ability for both exercise and pharmacologic tests to risk-stratify patients [46]. Importantly, cardiac event rates per risk stratification categorization were higher in those patients who had pharmacologic testing. This figure shows one particular study investigating ACM rates over 10 years in 6069 patients who underwent SPECT MPI. Patients requiring pharmacologic testing had ACM rates similar to those of patients who exercised less than 3 minutes

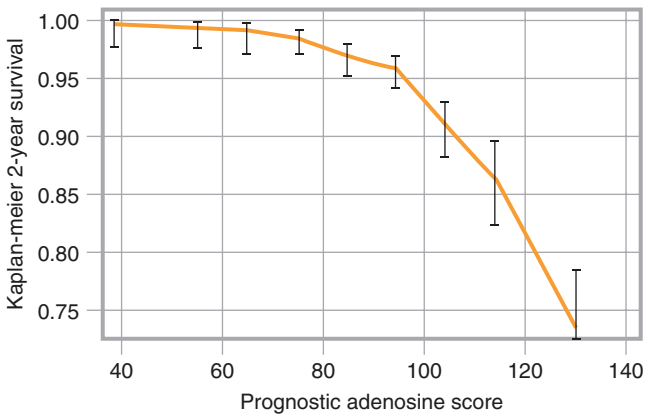

Fig. 8.25 Two-year survival stratified by prognostic adenosine score. Although the results of adenosine and exercise stress are often treated interchangeably in clinical practice, their prognostic interpretations should be handled different. Prognostication after pharmacologic stress is impacted by baseline risk of co-morbidities leading to an inability to undergo exercise stress. Optimizing the prognostic information extracted requires incorporation of multiple complementary data elements. The Cedars-Sinai group derived and validated a prognostic adenosine score in 5873 adenosine stress patients followed for 2.2 ± 1.1 years (94% complete follow-up, 387 cardiac deaths [6.6%]) [51, 52]. This figure shows risk stratification from the prognostic score, which incorporated patient age, presenting symptom, ability to walk, resting ECG, heart rate reserve, and perfusion results. Over the range of lower risk scores (approximate score < 100), the confidence intervals are relatively narrow, permitting relatively more precise estimates of risk in lower-risk patients. For values of the prognostic adenosine score greater than 100, the associated risk is sufficiently large that exact estimates are less important, even though the confidence intervals are wider

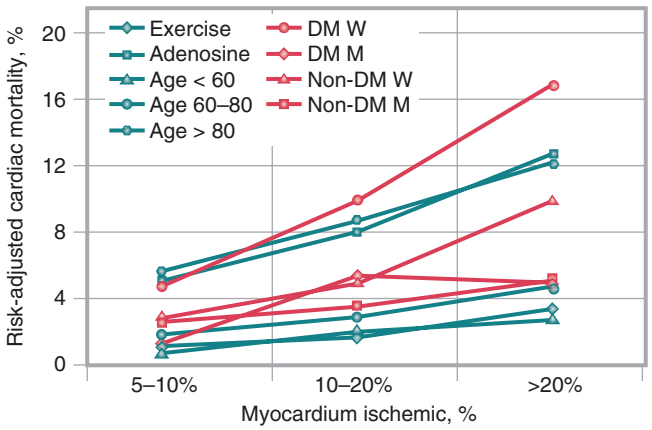

Fig. 8.26 Variability in risk-adjusted cardiac mortality as a function of ischemia detected by SPECT MPI in medically treated patients. Risk following normal SPECT MPI is dependent on the patients' underlying clinical, demographic, and historical characteristics, and this difference extends to patients with abnormal SPECT MPI results. In a large study of 10,627 patients with follow-up, there is an increase in risk-adjusted cardiac mortality rates with increasing ischemia in the subset of medically treated patients. The precise level of risk associated with the amount of ischemic myocardium (mild, 5–10%; moderate, 10–20%; large, >20%) varies widely. For example, in patients with moderate ischemia, the cardiac death risk may be as low as 2% or as high as 10%, depending on the patient subgroup. Hence, patients who cannot exercise, are older, or are diabetic will have far greater risk than those who are younger, able to exercise, or not diabetic, despite a similar extent and severity of ischemia on their stress SPECT MPI study. DM diabetes mellitus, M men, W women

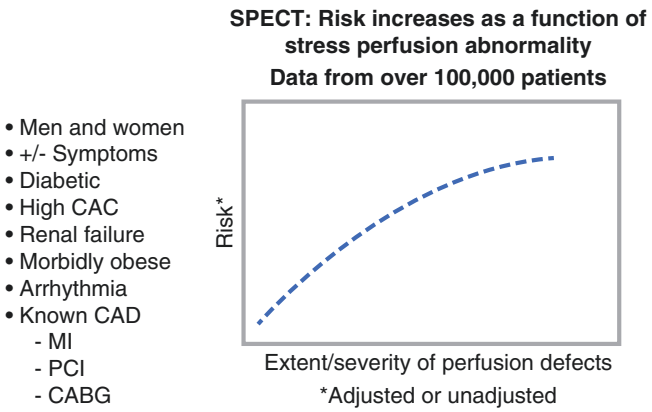

Fig. 8.27 Depiction of increasing hard event rates as a function of SPECT MPI ischemia across the spectrum of patients with suspected or known CAD. This relationship, illustrated conceptually here, has been shown to be present regardless of the type of stress test performed, the patient cohort examined (with respect to clinical characteristics or history of CAD), or the particular radiopharmaceutical employed. A decreased slope in the increase in mortality with increasing extent or severity of perfusion defect is probably primarily related to the referral of the most ischemic patients to revascularization, resulting in their being censored from the prognostic evaluation of the patients at highest risk. Existing evidence was derived in large patient populations covering each of the specific subsets listed in this figure. While the number of risk-stratification manuscripts is a strength of nuclear cardiology compared with other modalities, the current data supporting the use of this relationship for predicting benefit from revascularization has not been shown in randomized trials. CABG coronary artery bypass grafting, CAC coronary artery calcium, MI myocardial infarction, PCI percutaneous coronary intervention

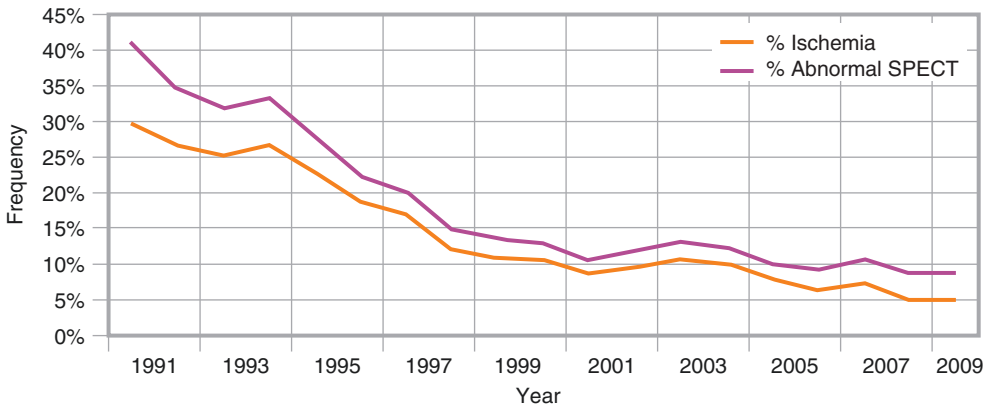

Fig. 8.28 Trends in prevalence of abnormal results (*red line*) and ischemia (*blue line*) on SPECT MPI. A trend that has been seen in clinical nuclear cardiology has been an increase in the percent of SPECT MPI studies with normal results. Many factors have been identified for this trend, including overall patient demographics and risk factors, changes and developments in pharmacotherapy, and overall patient selection. Patient selection is particularly important in the discussion of risk assessment. Pre-test likelihood of CAD remains a cornerstone of the decision tree for noninvasive testing and requires careful attention. Rozanski et al. investigated 39,515 patients without known CAD who underwent SPECT MPI [52]. Patients were assessed for abnormal SPECT or evidence of moderate to severe ischemia from 1991 to 2009. The prevalence of abnormal SPECT MPI dropped from 40.9% to 8.7% ($p < 0.001$). The prevalence of moderate to severe ischemia dropped from 20.6% to 4.6% ($p < 0.001$) [52]

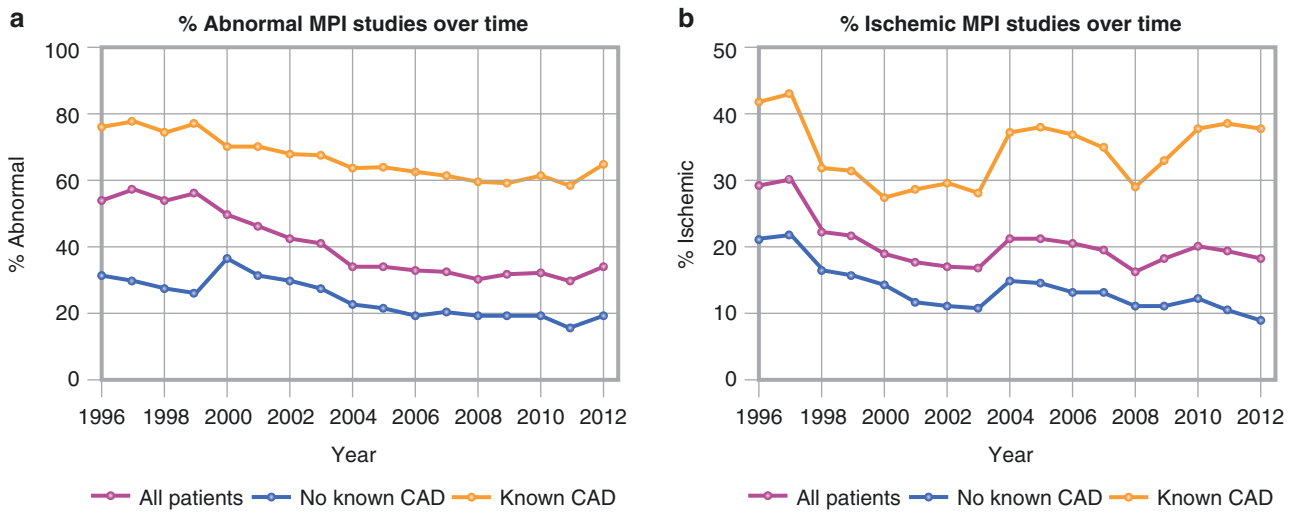

Fig. 8.29 Temporal changes in prevalence of ischemia in patients with and without known CAD. Although there have been changes in the proportion of patients without known CAD who have abnormal SPECT MPI scans, the change in patients with known CAD is less clear. Duvall et al. investigated a multicenter cohort of 108,654 SPECT MPI scans to determine the prevalence of abnormal tests and ischemia. In patients without known CAD, the prevalence of ischemia dropped from 16.9% (1996–2000) to 10.7% (2009–2012, $p < 0.001$) [53]. In patients with known CAD, however, the prevalence of ischemia increased over the same time periods (33.6% to 37.0%, $p < 0.001$)

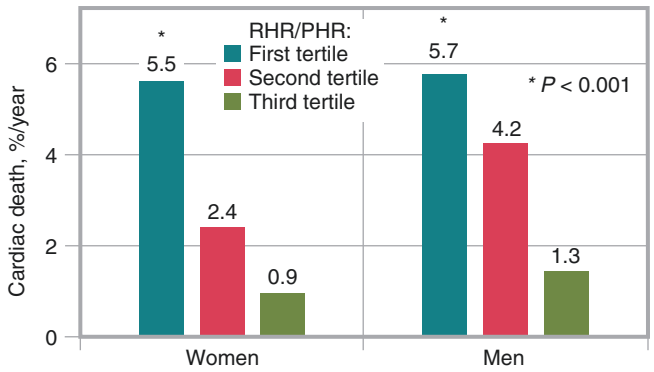

Fig. 8.30 Prognostic impact of heart rate response to adenosine on patient survival. In many respects, the results of vasodilator stress SPECT MPI studies are more difficult to understand than the results of exercise studies, since there are few non-perfusion markers. For example, although the positive predictive value of the ECG response is quite high, the negative value is not as good. Although symptoms often occur with vasodilator stress, their predictive value is poor and they are most often unrelated to coronary artery disease. Although "walking" vasodilator stress is performed, the exercise capacity is not maximal, so it is not prognostically useful. Therefore, it is potentially useful to identify additional putative markers of risk in patients who are undergoing vasodilator stress myocardial perfusion studies. To this end, Abidov et al. identified both resting heart rate (RHR) and peak heart rate (PHR) as important and powerful prognostic predictors of cardiac death in these patients [54]. These variables were both independent and incremental risk-adjusted predictors of cardiac death. Increasing values of PHR response to adenosine stress were strongly associated with improved survival, as were low RHRs. As this graph shows, an increasing ratio of RHR to PHR was associated with increasing cardiac mortality in both men and women

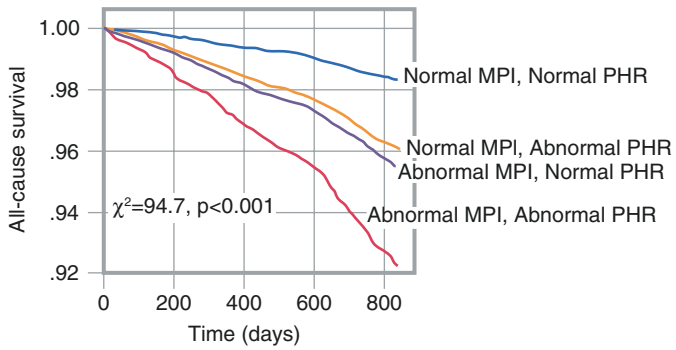

Fig. 8.31 Incremental prognostic utility of peak heart rate (PHR) in addition to perfusion results with respect to all-cause survival. Azarbal et al. [55] studied a cohort of 10,021 patients who underwent exercise SPECT MPI. Abnormal PHR was defined as an inability to achieve 85% of predicted maximal heart rate. Patients were followed for 2.0 years for cardiac death or all-cause mortality. Patients with abnormal SPECT MPI and PHR were at the highest risk of death (3.5% per year). Abnormal PHR alone was associated with a similar risk of death as patients with normal PHR and abnormal SPECT MPI

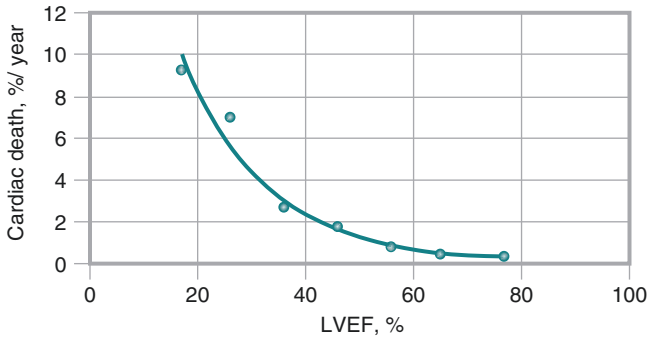

Fig. 8.32 Relationship between left ventricular ejection fraction (LVEF) measured by gated SPECT MPI and cardiac death. In 2686 consecutive patients undergoing stress ^{99m}Tc gated SPECT MPI, there was a curvilinear inverse relationship between LVEF at rest by MPS, performed after stress, and cardiac death [56]. The LVEF was the strongest predictor of mortality in this group

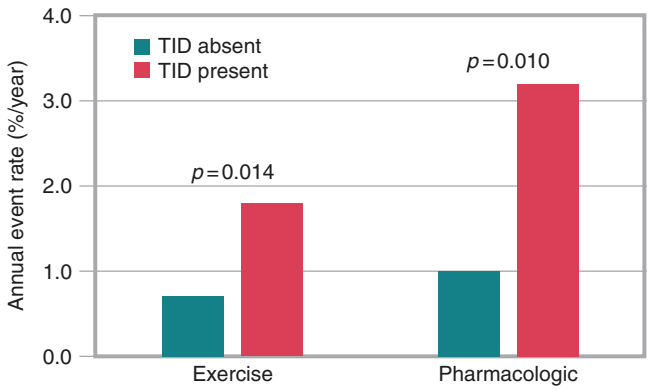

Fig. 8.33 Incremental risk associated with transient ischemic dilation (TID) of the left ventricle. There are several nonperfusion markers of high risk from SPECT MPI. TID is a measure of relative left ventricular volume with stress compared with rest (stress/rest) on ungated acquisitions. This figure demonstrates the prognostic significance of TID with SPECT MPI. This study included a primary cohort of patients with normal perfusion (summed stress score [SSS] = 0, 1560 patients) and a secondary cohort with near normal perfusion (SSS 0–3, 2037 patients) on SPECT MPI. TID was defined as the highest quartile of TID ratio. The presence of TID (*orange*) was associated with increased rates of cardiac death, nonfatal MI, or late revascularization in patients undergoing exercise or pharmacologic stress [57]. TID continued to be associated with cardiovascular events in the secondary cohort as well as in multivariable analysis (adjusted HR 2.34, p = 0.008). The prognostic significance of this finding has subsequently been questioned in patients with normal left ventricular function and in patients without diabetes or known CAD [57, 58]

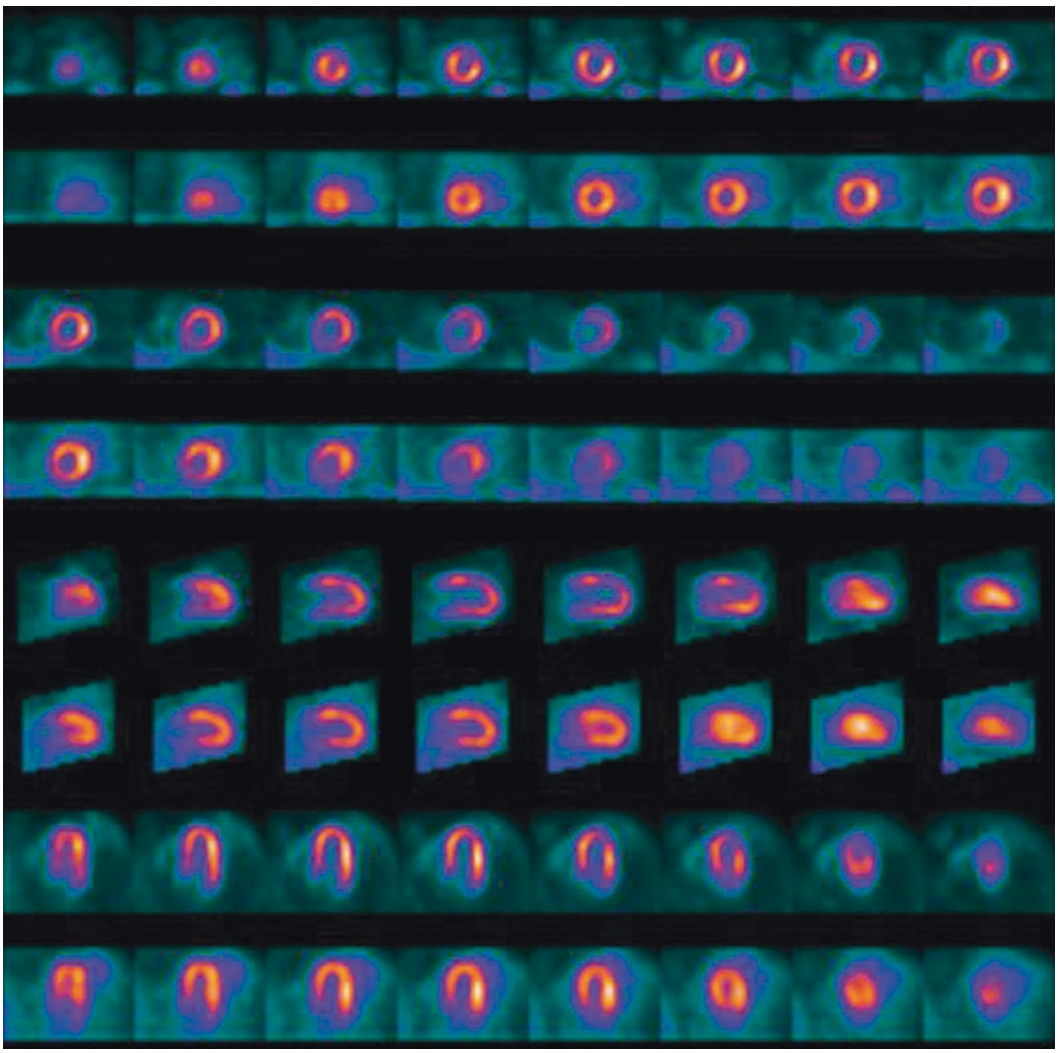

Fig. 8.34 Example of a patient with transient ischemic dilation (TID) of the left ventricle. The patient has a large volume of moderate ischemia in the mid to apical anterior and anteroseptal wall, as well as in the apical cap. This finding would be consistent with 16% ischemic myocardium using the summed difference score, and was 8% of the myocardium by total perfusion deficit. However, there is also prominent TID, with a ratio of 1.42. The patient was referred for coronary angiography and was found to have significant three-vessel disease

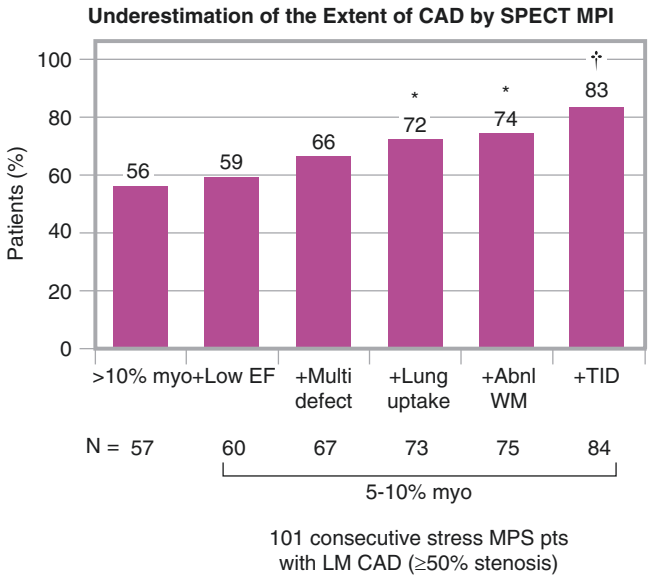

Fig. 8.35 Combining parameters to improve detection of significant left main coronary artery disease (CAD) with SPECT MPI. The ability to detect ischemia with SPECT MPI depends primarily on the presence of regional relative perfusion deficits. However, in patients with significant three-vessel disease or left main disease, there may be balanced ischemia, which may be underappreciated by regional comparison alone. This study reported SPECT MPI results in 101 patients with angiographic left main CAD (>50%) and no prior MI or revascularization. Relative perfusion alone (defined by >10% ischemia) identified 56% of patients as being at high risk [59]. The authors looked at the added diagnostic yield of combining mild perfusion deficit (5–10% ischemia) with low ejection fraction (EF, defined as <50% for women or <45% for men), multivessel disease (Multi defect), abnormal lung uptake of thallium, abnormal wall motion (Abnl WM), or transient ischemic dilation (TID) of the left ventricle. The presence of a stress defect >10% or a defect of 5–10% with any other high-risk feature increases sensitivity for left main disease from 56% to 83%

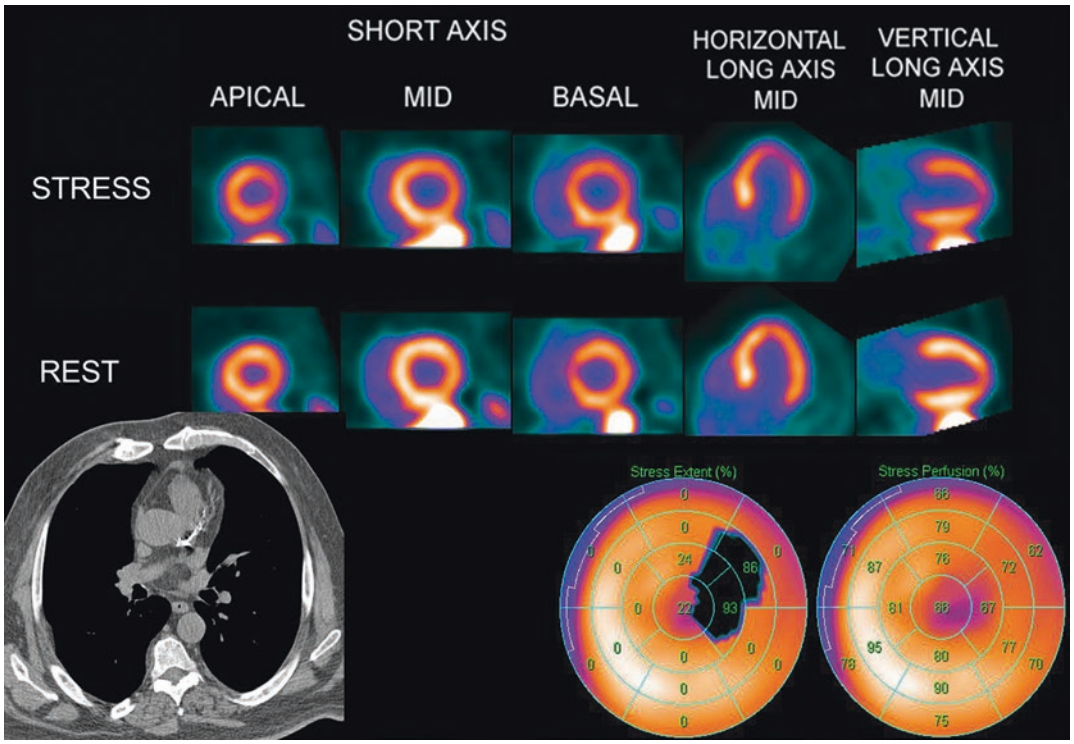

Fig. 8.36 Case example of combined SPECT MPI and coronary artery calcium (CAC) scanning. The patient was a 57-year-old man who presented with typical anginal symptoms. The SPECT MPI study revealed a mild, reversible perfusion defect in the mid and distal anterolateral segments (summed stress score [SSS} = 3). On the basis of perfusion alone, this result would be considered probably abnormal. The CAC score was significantly elevated at 1463 (97th percentile), allowing the reader increased certainty in reporting the study as abnormal. The patient underwent invasive coronary angiography, which revealed an 80% left main stenosis. This example shows the potential for combined SPECT MPI and CAC to identify significant left main disease or balanced ischemia

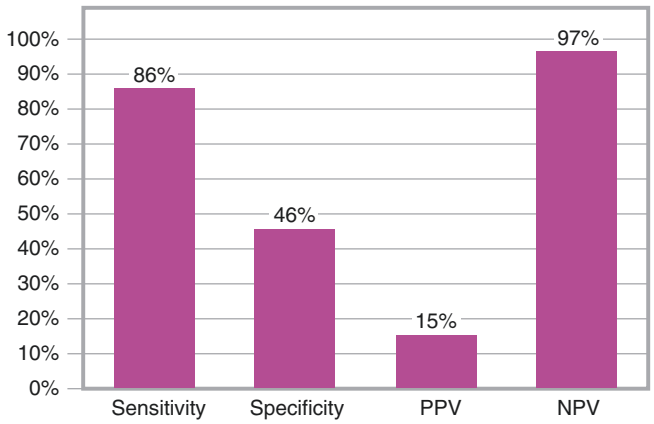

Fig. 8.37 Diagnostic accuracy of abnormal coronary flow reserve (CFR) for detecting high-risk CAD in patients with less than 10% stress perfusion deficits. PET is capable of quantifying absolute myocardial blood flow (MBF). CFR, calculated as stress MBF/rest MBF, is therefore a measure of global decreases in stress MBF which may help identify patients with balanced ischemia. Naya et al. studied a cohort of 290 patients with significant CAD angiographically (two-vessel disease including the proximal left anterior descending, three-vessel disease, or left main disease). In patients with less than 10% stress perfusion deficits, preserved CFR nearly excluded high-risk CAD with a high sensitivity (86%) and 97% negative predictive value (NPV). As compared with the SPECT findings in left main CAD in Fig. 8.34, this is a significant potential improvement in sensitivity and is a potential benefit of PET over SPECT [60]

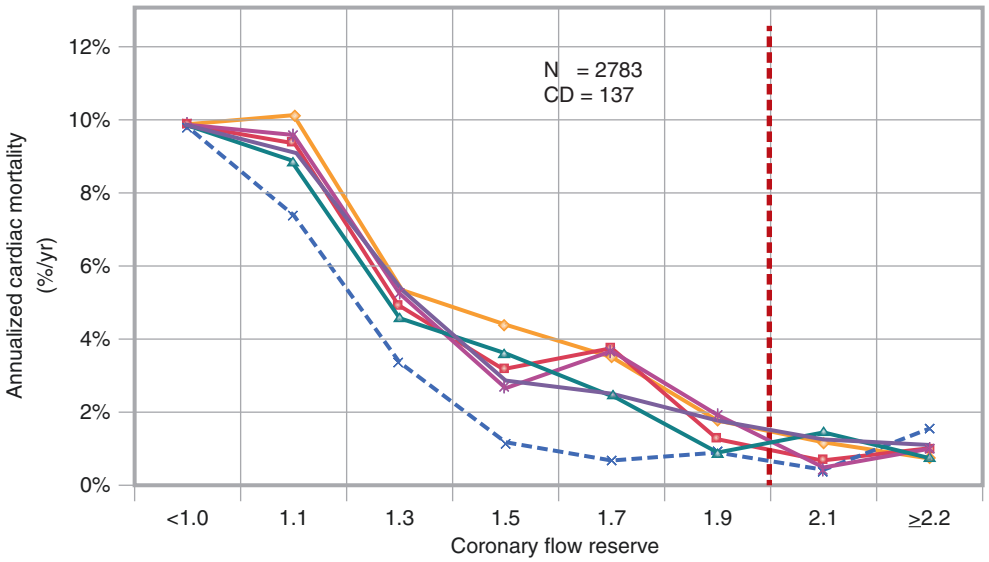

Fig. 8.38 Relationship between coronary flow reserve (CFR) and risk of cardiac death with different kinetic models. Myocardial blood flow (MBF) and CFR are additional markers of perfusion that have diagnostic and prognostic utility, but several different kinetic models yield slightly different MBF or CFR estimates. Murthy et al. compared the prognostic utility of CFR derived from several kinetic models (each represented by a different line) to determine if there were significant differences. Correlation for CFR was excellent regardless of the kinetic model used (Pearson r >0.90). However, estimates of peak MBF had only moderate correlation between models (Pearson r = 0.42–0.62). As shown on this graph, increasing risk of cardiac death was noted for CFR values <2.0 (*orange dashed line*). Given the consistency of results for CFR across kinetic models and input functions, the authors advocated for routine use of CFR for prognostication, instead of MBF estimates [61]

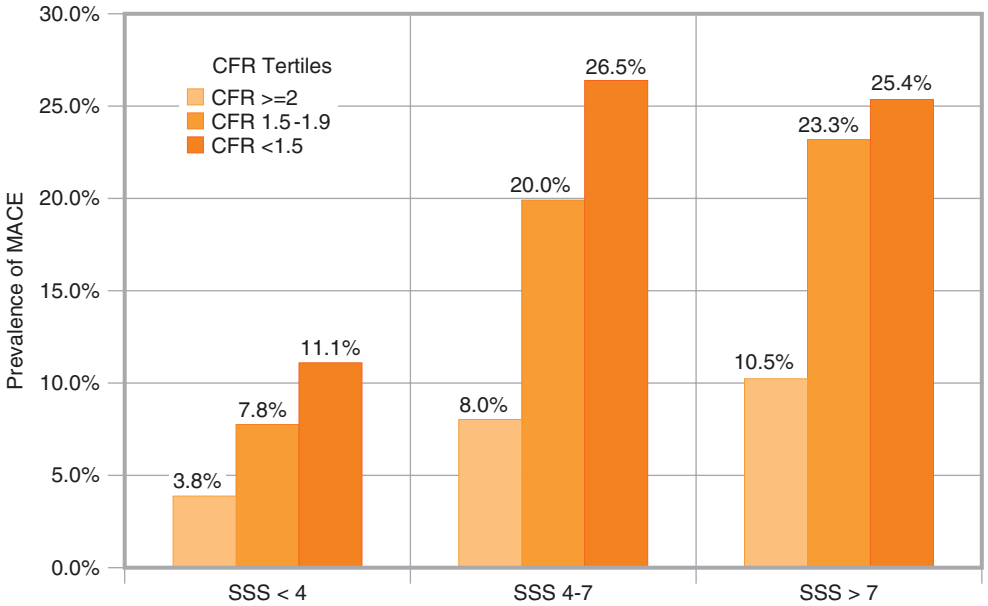

Fig. 8.39 Association between coronary flow reserve (CFR) and major adverse cardiovascular events (MACE) across the spectrum of regional perfusion abnormalities. CFR is influenced by global myocardial blood flow (MBF) as well as regional differences. The additive value of CFR over relative perfusion abnormalities was addressed in this study of 704 patients who underwent PET for assessment of known or suspected CAD [62]. Patients were followed for development of MACE (cardiac death, nonfatal MI, late revascularization, or cardiovascular hospitalization), with a median follow-up of 387 days. Perfusion abnormalities were assessed using summed stress score (SSS). Increasing magnitude of relative perfusion abnormality was associated with increased MACE events. Within each SSS category, decreasing CFR was associated with increased MACE [62]

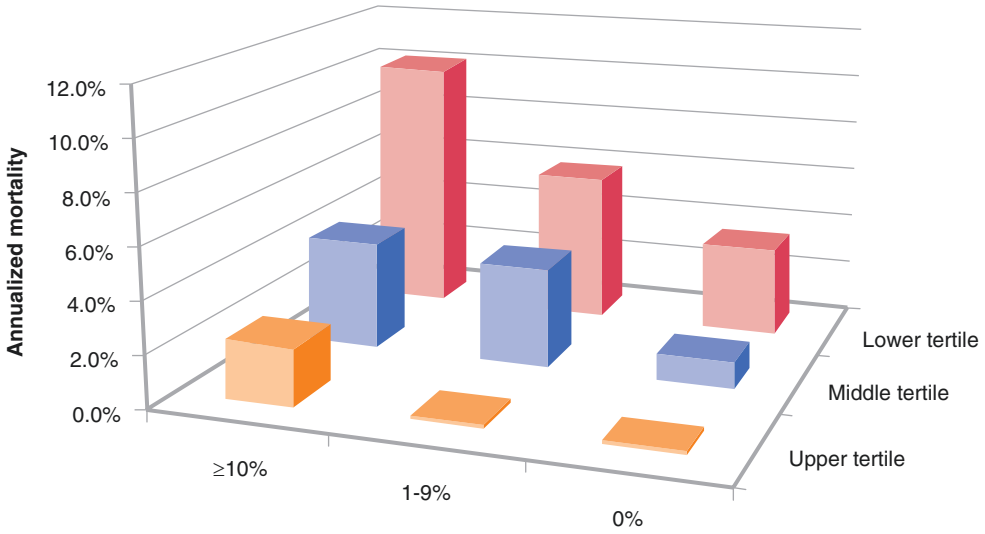

	≥10%	(n)	1-9%	(n)	0%	(n)
Lower tertile	2.4%	(119)	0.3%	(195)	0.1%	(614)
Middle tertile	4.4%	(217)	4.0%	(202)	1.1%	(509)
Upper tertile	10.2%	(416)	6.0%	(190)	3.6%	(321)

Fig. 8.40 Association of stress perfusion deficit and coronary flow reserve (CFR) with cardiac mortality. As discussed in the previous figure, CFR is influenced by global and regional perfusion abnormalities. Murthy et al. investigated the interaction between CFR and stress perfusion deficit in a cohort of 2783 patients who underwent stress and rest PET. Patients were followed for 3 years, with a primary outcome of cardiac death. Increasing stress perfusion deficit, reflecting ischemia and scar, was associated with increasing cardiac death. Within each category of perfusion deficit, cardiac death rates rose across tertiles of decreasing CFR. CFR <1.5 was associated with a 5.6-fold increase in the risk of cardiac death. Including CFR with perfusion assessment resulted in a net reclassification improvement of 0.098 [63]

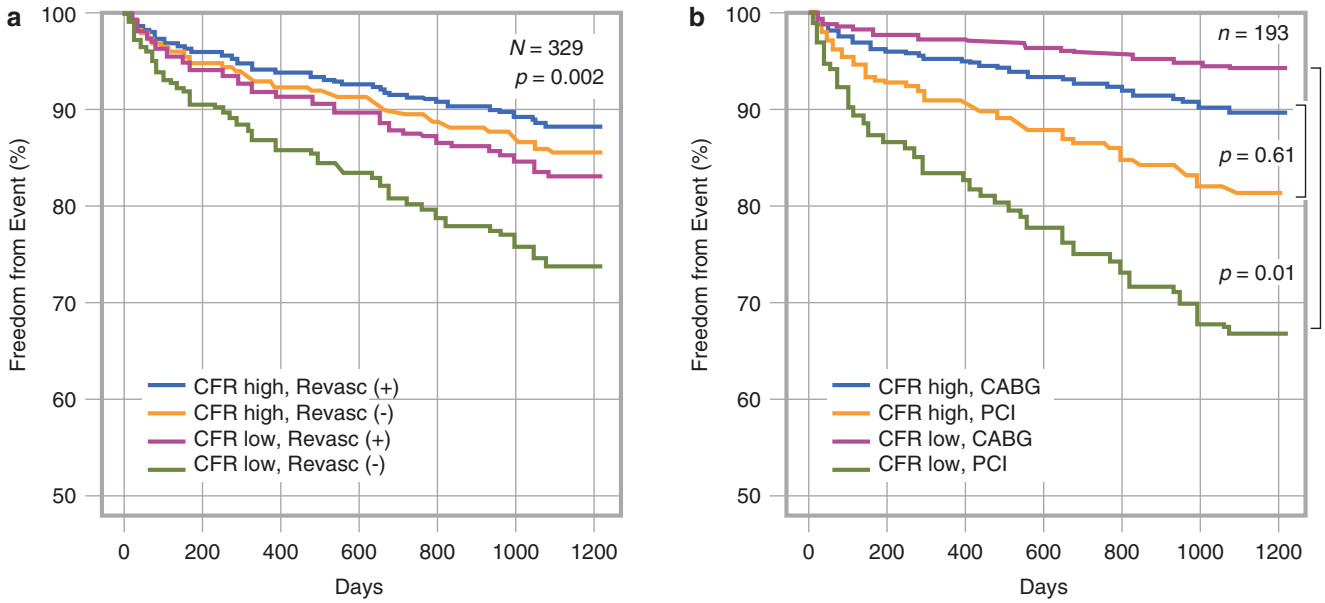

Fig. 8.41 Risk of cardiovascular death or heart failure (HF) admission according to coronary flow reserve (CFR) and revascularization. Taqueti et al. investigated the influence of CFR on outcomes in 329 patients referred for invasive coronary angiography [64]. Decreasing CFR was associated with a significant increase in cardiovascular death or HF admission (adjusted hazard ratio 2.02 per unit decrease). **Panel A** shows that outcomes were favorable in patients with high CFR (defined as ≥1.6) regardless of revascularization status. Patients with low CFR who were treated medically had the highest rates of cardiovascular death or HF admission (log rank p = 0.03). **Panel B** demonstrates outcomes in patients who received revascularization, stratified by CFR and type of revascularization—percutaneous coronary intervention (PCI) or coronary artery bypass grafting (CABG). Patients with low CFR treated with CABG had better outcomes than patients with low CFR treated with PCI (p = 0.01). These results should be interpreted carefully because several patient factors that would lead to referral for CABG are not accounted for, and the overall number of patients studied was small [64]

Over time, there has been growing support for the definition of "high risk" that now includes the cohort with established coronary heart disease as well as those whose event risk is equivalent to that of patients with obstructive coronary disease. Table 8.2 delineates the segments of the population that may be considered as risk-equivalent cohorts. The notion of defining patient cohorts who are coronary heart disease risk equivalents was initially introduced by the National Cholesterol Education Panel Adult Treatment Program III when it delineated diabetic patients as being risk-equivalent, with an ensuing event rate over 10 years of 20% or higher. In addition, the table details a number of high-risk patient subsets by categories, including those for patients with extracardiac atherosclerosis and those who have clustered risk factors. There are also subsets of patients who, by their extensive comorbidity, have an elevated risk, including the elderly, those with chronic kidney disease, and those who are functionally impaired. Functional impairment is a risk factor that is becoming more and more common with the epidemic of obesity and diabetes in the United States; it is a surrogate marker for an aggregation of risk factors. For a SPECT laboratory, it potentially encumbers up to half of the referral population and is perhaps the most overlooked risk factor in a patient's clinical history. Physicians should take care to discern a patient's physical work capacity and to decide on the use of pharmacologic stress in patients who have limited exercise abilities.

Known ischemic heart disease
Stable coronary artery disease
Post acute coronary syndrome
Prior revascularization (PCI or CABG)
Known vascular disease
Preoperative screening for noncardiac surgery
Peripheral artery disease/cardiovascular disease
Diabetic patients
High coronary calcium score
Degree of comorbidity
Elderly
Pharmacologic stress
Functionality impaired
Chronic kidney disease
Clustering risk factors
Metabolic syndrome

Cohorts whose cardiac event risk is equivalent to the population with existing ischemic heart disease (i.e., 10-year risk of cardiac death or nonfatal MI of 20% or greater)
CABG coronary artery bypass grafting, *FRS* Framingham Risk Score, *PCI* percutaneous coronary intervention

Table 8.2 Populations considered equivalent to high-risk coronary heart disease populations

The Effect of Changes in SPECT MPI Protocols and Technology

Although SPECT MPI imaging data alone can guide risk assessment, tremendous additional value is seen when adding clinical risk factors. This has been demonstrated with clinical scoring systems [51], but utilization of machine learning (Fig. 8.42) allows large multivariable datasets to be interpreted.

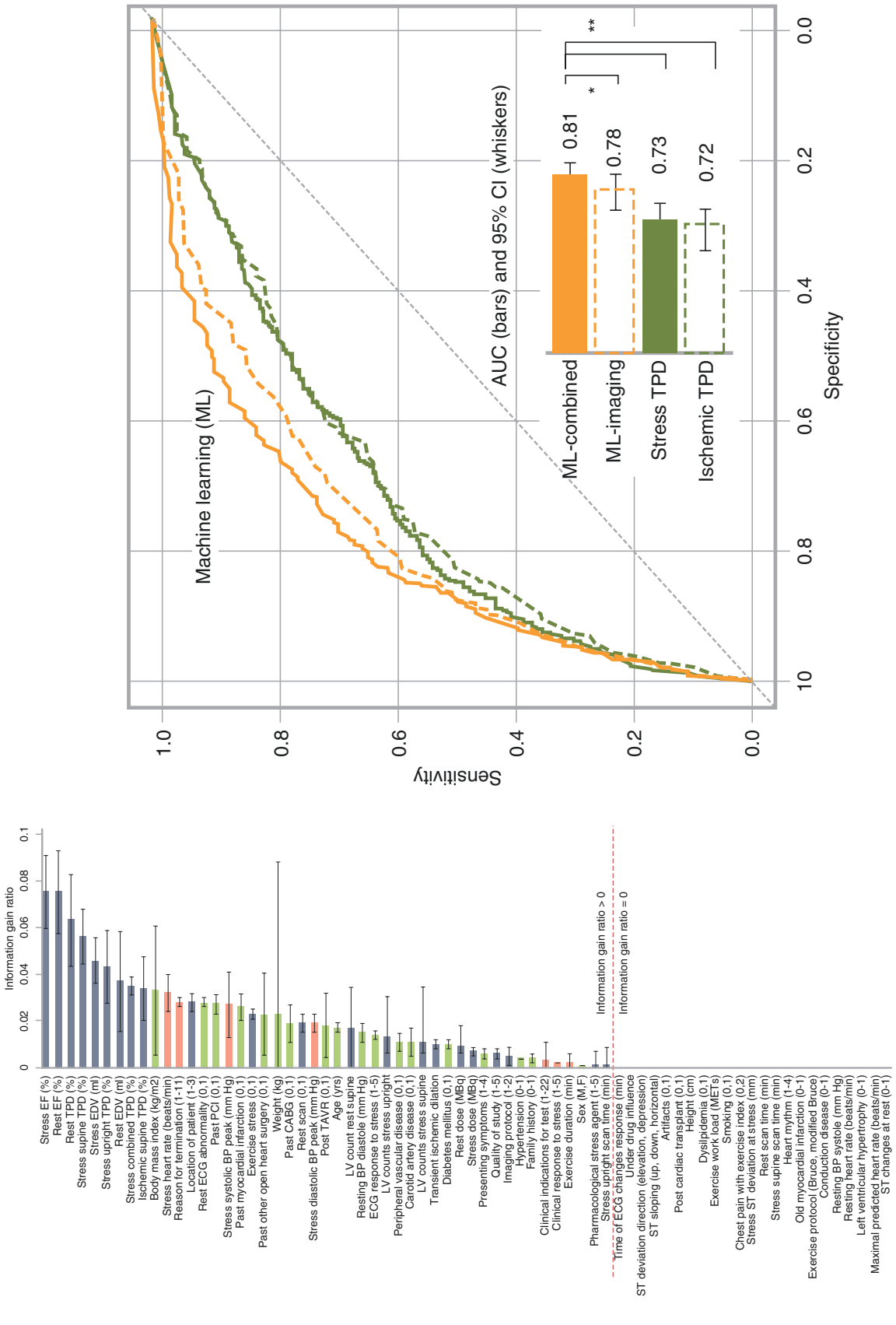

Fig. 8.42 Utilizing machine learning (ML) to improve prognostication. In a study by Betancur et al., 2619 patients who underwent SPECT MPI with assessment of 28 clinical variables, 17 stress test variables, and 25 imaging variables were monitored over 3 years for major adverse cardiovascular events (MACE). The figure outlines the process of ML to build prognostic models with the greatest differentiation. Over this period, 239 patients (9.1%) had MACE. The stress and ischemic total perfusion deficits (TPD) were predictive of MACE events (area under the curve [AUC] 0.73 and 0.72, respectively). Marked improvement in predicting MACE was achieved by utilizing an ML score derived from these 60 combined variables (clinical, stress test, and imaging: ML-combined). The ML-combined score had higher predictive accuracy than stress or ischemic TPD (AUC 0.81, $p < 0.001$) [65]

Another change reflects the increasing emphasis on reducing ionizing radiation exposure related to medical imaging. Stress-only SPECT MPI with a low-dose protocol (Fig. 8.43) is a step in this direction, along with the use of a cadmium zinc telluride (CZT) camera system (Fig. 8.44).

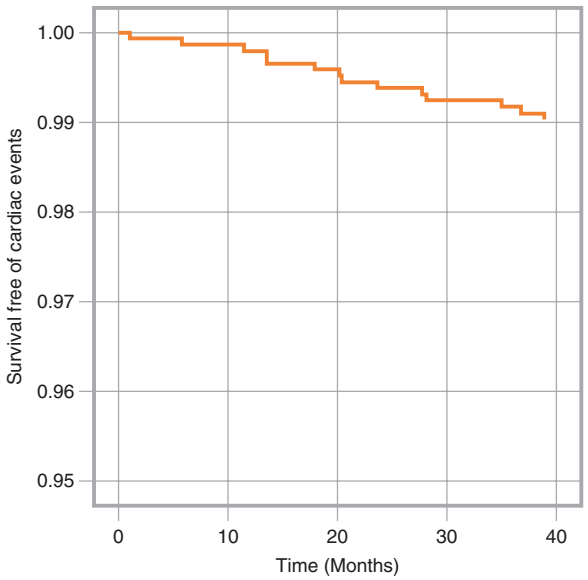

Fig. 8.43 Survival free of non-fatal MI or cardiac death in patients undergoing stress-only SPECT MPI with <1 mSv effective radiation dose. Normal stress-only SPECT MPI—reducing the radiation exposure by 75% compared with a combined rest/stress scan—has been shown to be associated with very low risk of events, comparable to the risk associated with a normal stress/rest scan [66]. Further, marked reduction in radiation dose—as low as 1 mSv—has become possible with use of cadmium zinc telluride (CZT) camera systems [67–69]. This study combined the use of stress-only imaging with a low-dose protocol utilizing a CZT camera. Stress-only exams were performed in 1400 (73.6%) of 1901 patients referred for exercise SPECT MPI, and an excellent prognosis was associated with a normal exam, even at ultra-low radiation exposure, with annualized event rates of 0.13% for cardiac death and 0.17% for non-fatal MI [70]

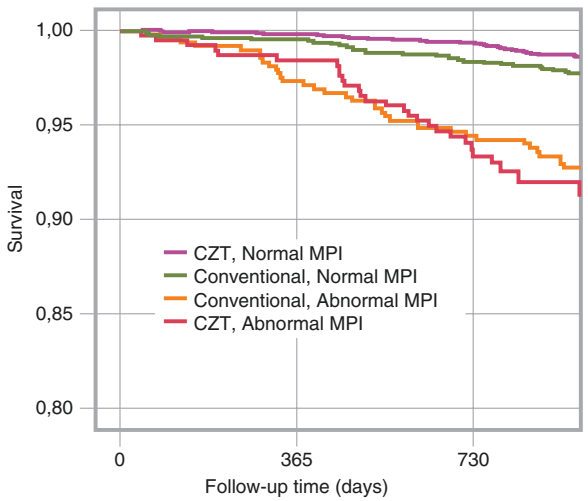

Fig. 8.44 Survival free of all-cause mortality in patients with normal or abnormal SPECT MPI assessed with a CZT system, compared with a conventional camera, in a study by Lima et al. [71]. To study the prognostic value of different camera systems, survival was compared in 3554 patients who underwent SPECT MPI with either a CZT or conventional system. The authors used propensity matching to identify a group of patients undergoing conventional imaging who were similar to patients undergoing CZT imaging. For patients imaged with a CZT system, survival was lower for those with abnormal scans (*purple*) compared with normal scans (*yellow*, $p < 0.001$). Findings were similar for patients imaged with a conventional camera (*green* and *blue*). There were no differences in all-cause mortality between camera systems ($p = 0.380$ for normal scans, $p = 0.413$ for abnormal scans)

The Role of Coronary Calcium Scoring

As illustrated in Figs. 8.45, 8.46, and 8.47 (and exemplified in Fig. 8.36), the interpretation of results of perfusion imaging can be improved by the interplay of evidence of atherosclerosis from coronary calcium scoring.

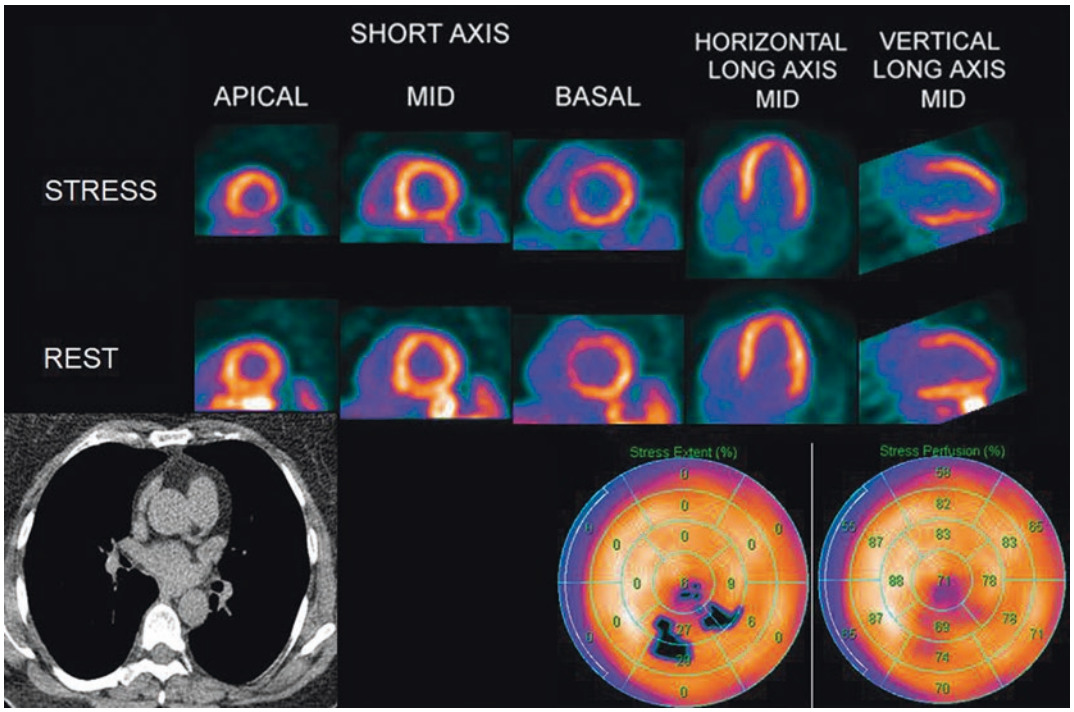

Fig. 8.45 Example of the utility of combining PET and coronary artery calcium (CAC) measurements. In this 63-year-old woman with a history of dyspnea on exertion, the PET perfusion was interpreted as a small volume of mild ischemia in the distal inferior and apical segments (summed stress score 2), interpreted as equivocal. The CAC score was 0, allowing the reader increased certainty in interpreting the scan as probably normal

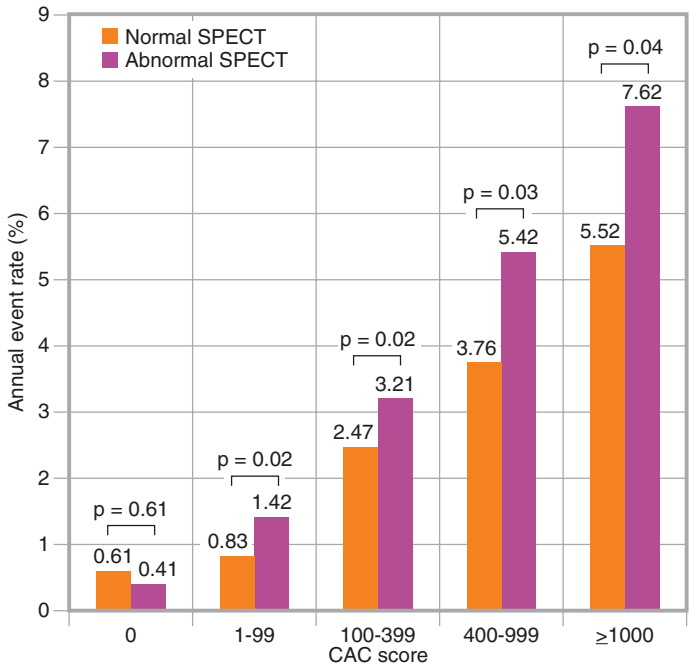

Fig. 8.46 Improved prognostication through the combination of SPECT MPI and coronary artery calcium (CAC) scores. A diagnostic approach of acquiring both SPECT MPI and non-contrast ECG-gated CAC scans routinely has gained popularity, allowing both functional assessment and evaluation for subclinical disease. This combination can be achieved with either hybrid SPECT/CT and PET/CT systems or by obtaining a separate SPECT and CAC scan. In this study by Engbers et al. utilizing a SPECT/CT system, 4897 symptomatic patients were evaluated with both SPECT MPI and coronary calcium score (CCS). Rates of major adverse cardiac events (MACE, defined in this study as late revascularization, nonfatal MI, and all-cause mortality) were monitored. Two important findings were noted: First, there was a direct relationship between patients with elevated CAC score and abnormal SPECT MPI. Second, both SPECT MPI and CAC score were independent predictors of MACE, with an incremental increase in MACE when both were abnormal, compared with either one alone [72]

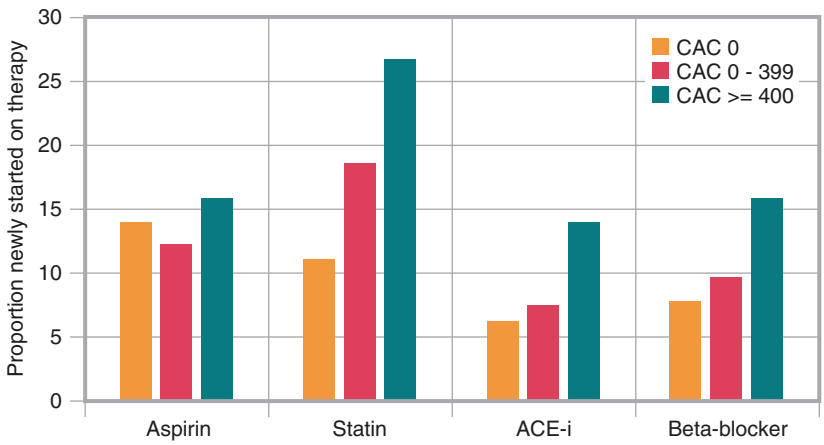

Fig. 8.47 The impact of calcium score results on medication prescription in patients with normal PET perfusion. The ability of a diagnostic test to impact patient outcomes relies on changes in patient management, including medical therapy. Bybee et al. investigated the impact of CAC scores on medical therapy initiation in 760 patients with normal PET perfusion [73]. Patients with any CAC were more likely to have a change in therapy (53.3% vs. 24.3%, $p < 0.001$). Additionally, increasing CAC was associated with a greater likelihood of medication initiation. The Scottish Computed Tomography of the Heart (SCOT-HEART) trial demonstrated a survival benefit from a strategy employing CT angiography (CTA) compared with standard care [74]. This benefit was considered to be driven to a greater degree by more intensive medical therapy in the CTA group, rather than by differences in coronary angiography or revascularization. Whether similar improvements in outcome can be derived from a strategy that includes combined SPECT or PET with CAC is not known

Using Perfusion Imaging to Assess Survival Benefit from Revascularization

Finally, Figs. 8.48, 8.49, 8.50, 8.51, and 8.52 consider the role of perfusion imaging in identifying patients who may derive survival benefit from revascularization in addition to medical therapy. Almost all studies investigating the relationship of SPECT MPI results and patient risk have included only patients who are treated medically; patients treated with early revascularization have been excluded or censored from these analyses, as the decision to refer to early revascularization is usually based on the results of the SPECT MPI study. Thus, no prognostication can be extrapolated to patients treated with revascularization. Figures 8.49, 8.50, and 8.51 show data from one large study with follow-up of patients after revascularization as well as medical therapy, comparing the benefit of each treatment.

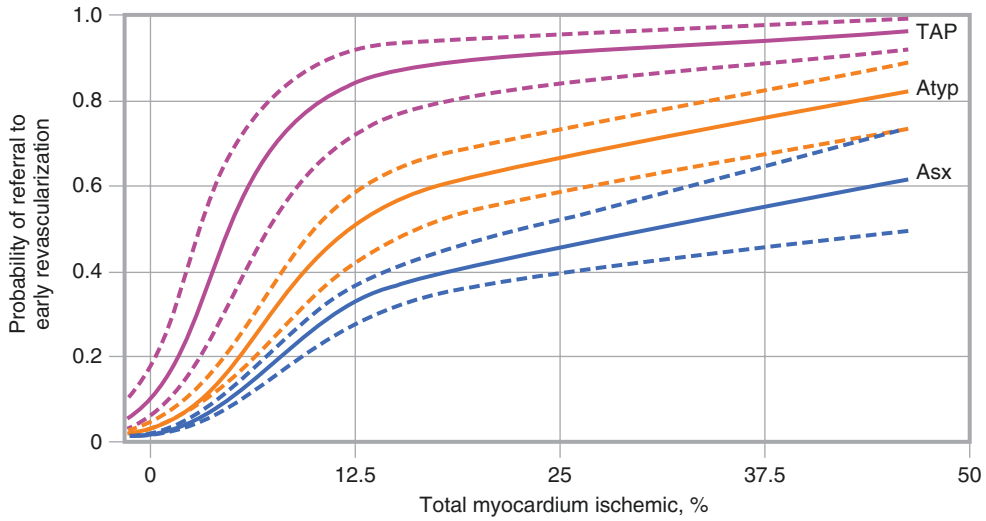

Fig. 8.48 Drivers of referral to catheterization and revascularization after SPECT MPI. It is often assumed that physicians appropriately weigh the various patient characteristics available after the stress SPECT MPI study in formulating the final management decision. In 2003, Hachamovitch et al. [75] demonstrated that the amount of ischemia was strongly related to survival benefit with revascularization. At the same time contributed 83% of the information in a multivariable model predicting revascularization, based on data in 10,627 patients without prior CAD who were referred to stress SPECT MPI. The shape of this relationship also yields insight into how physicians use SPECT MPI results. First, with increasing amounts of ischemia, there are increasing revascularization referral rates, but the relationship is nonlinear. In patients with no ischemia or mild ischemia (<12.5% myocardium ischemic), there is a steep slope between ischemia and revascularization referral; a small change in ischemia is associated with a large change in the likelihood of referral for revascularization. At approximately 10–15% of the myocardium ischemic, this relationship plateaus; increasing amounts of ischemia are associated with relatively little increase in referral rates. Referring physicians also incorporate symptoms in their referral patterns, so that for any level of ischemia, worsening presenting symptoms (asymptomatic [Asx], atypical symptoms [Atyp], or typical angina pectoris [TAP]) resulted in greater rates of referral [75]

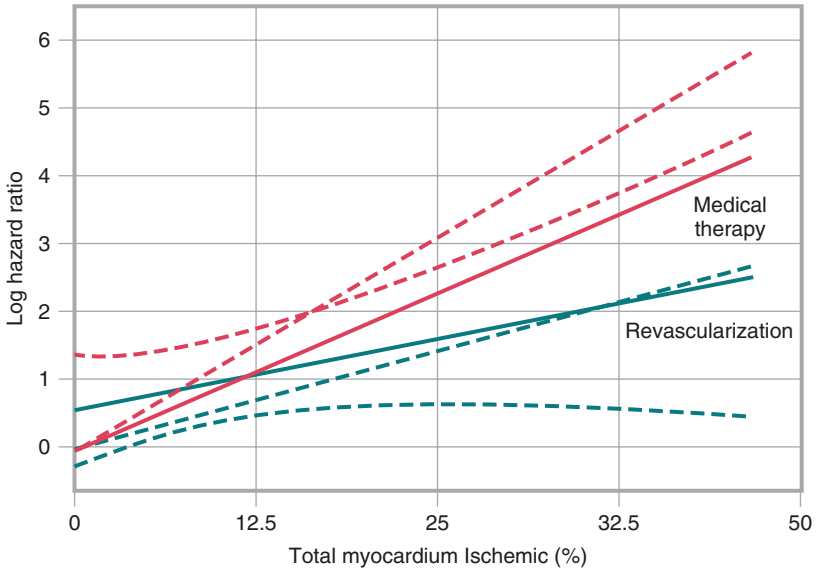

Fig. 8.49 Continuous relationship between ischemia and benefit from revascularization. Using myocardial perfusion SPECT MPI to identify patients who may benefit from revascularization. In this context, a widely cited single-center study published in 2003 examined the relationship between the extent and severity of ischemia and the survival benefit associated with subsequent revascularization [3]. In this study, 10,627 patients studied at Cedars-Sinai Medical Center without prior MI or revascularization who underwent stress SPECT MPI were followed up for a mean of 1.9 years; 3.98% were lost to follow-up. Over this period, cardiac death occurred in 146 (1.4%) patients. The authors defined patient treatment on the basis of that received within 60 days post-SPECT: 671 patients underwent revascularization and had 2.8% mortality. Medical therapy was used for 9956 patients, who had 1.3% mortality (p = 0.0004). The authors used a propensity score adjustment to compensate for patient factors leading to referral for revascularization. In the setting of no or mild ischemia, patients undergoing medical therapy as their initial treatment had a rate of survival free of cardiac death superior to that of patients referred for revascularization. On the other hand, when at least moderate ischemia (>10% of the total myocardium ischemic) was detected, patients undergoing revascularization had an increasing survival benefit over patients undergoing medical therapy [3]

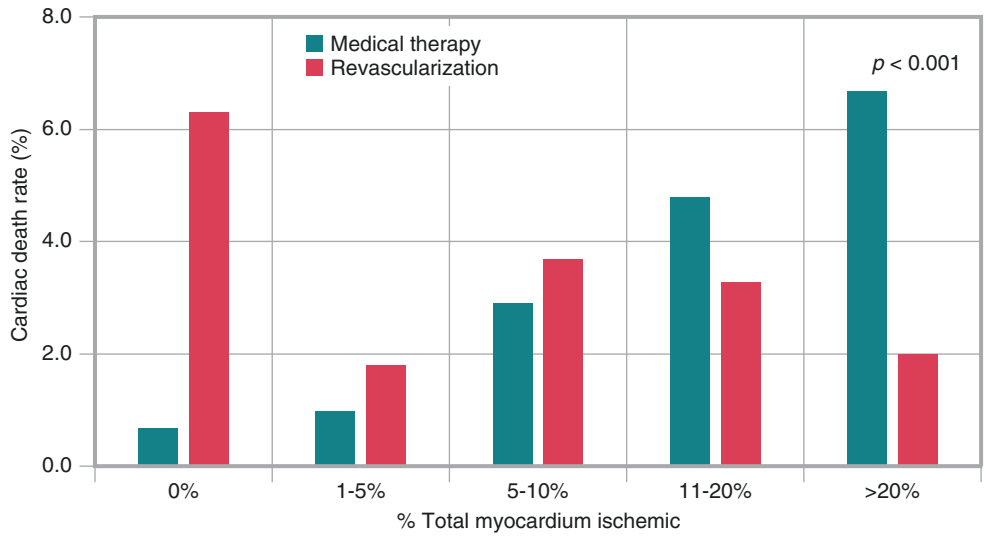

Fig. 8.50 Categorical relationship between ischemia and benefit from revascularization. Unadjusted rates of cardiac death increased with increasing burden of ischemia in patients treated with medical therapy. In patients with >20% ischemia, patients managed with revascularization experienced significantly lower rates of all-cause mortality (p < 0.001) [3]

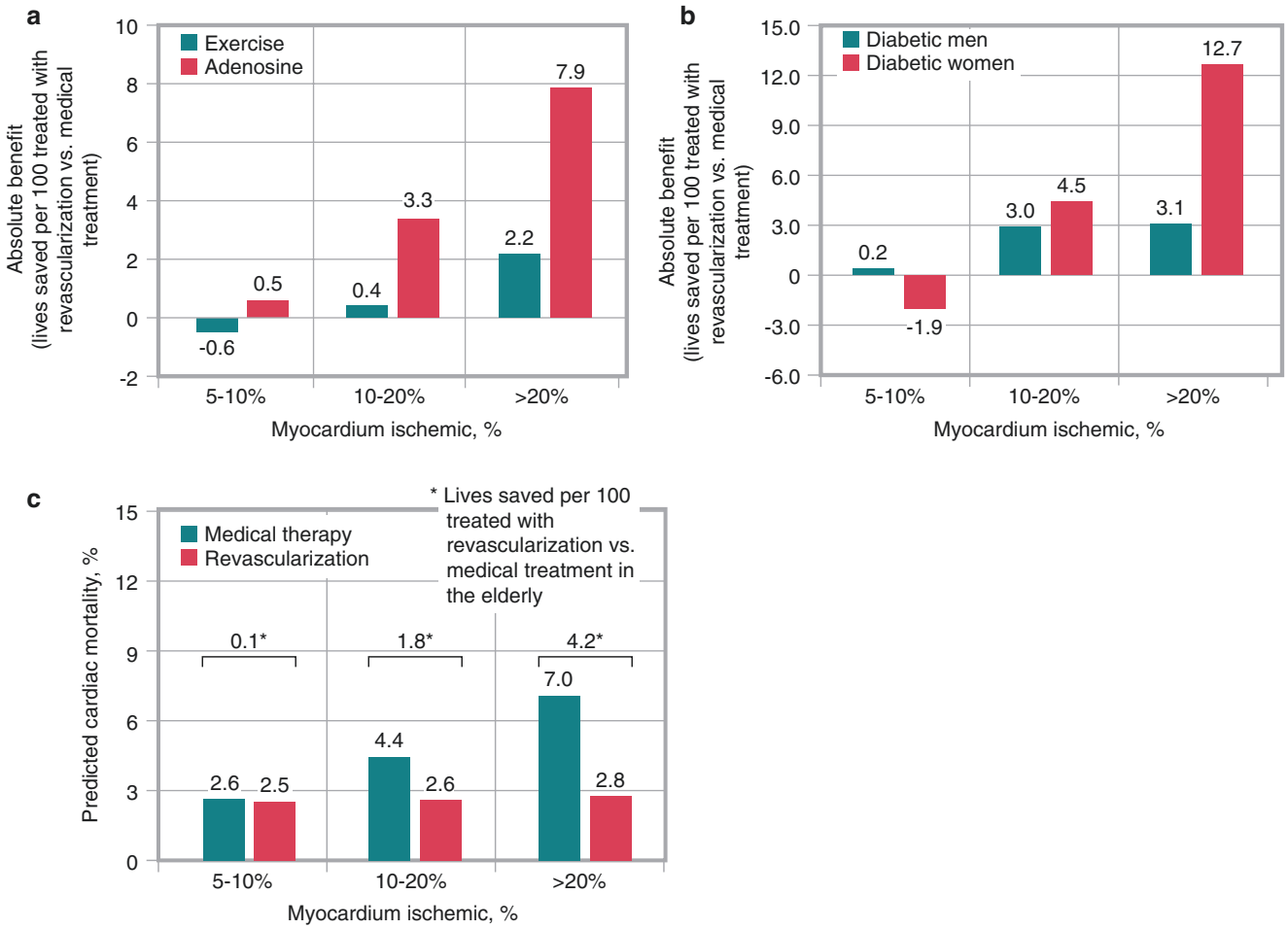

Fig. 8.51 Influence of baseline patient risk on potential benefit from revascularization. The previous figures demonstrated that the potential benefit from revascularization was driven by the extent of ischemia, but the absolute benefit (such as the number of lives saved per 100 treated with different therapies) was impacted by patient risk. Hence, the absolute benefit for revascularization over medical therapy was accentuated in the presence of greater clinical risk. This figure demonstrates the estimated absolute benefit with respect to all-cause mortality in patients undergoing pharmacologic stress (**a**), diabetic patients (**b**), and elderly patients (**c**) [3]

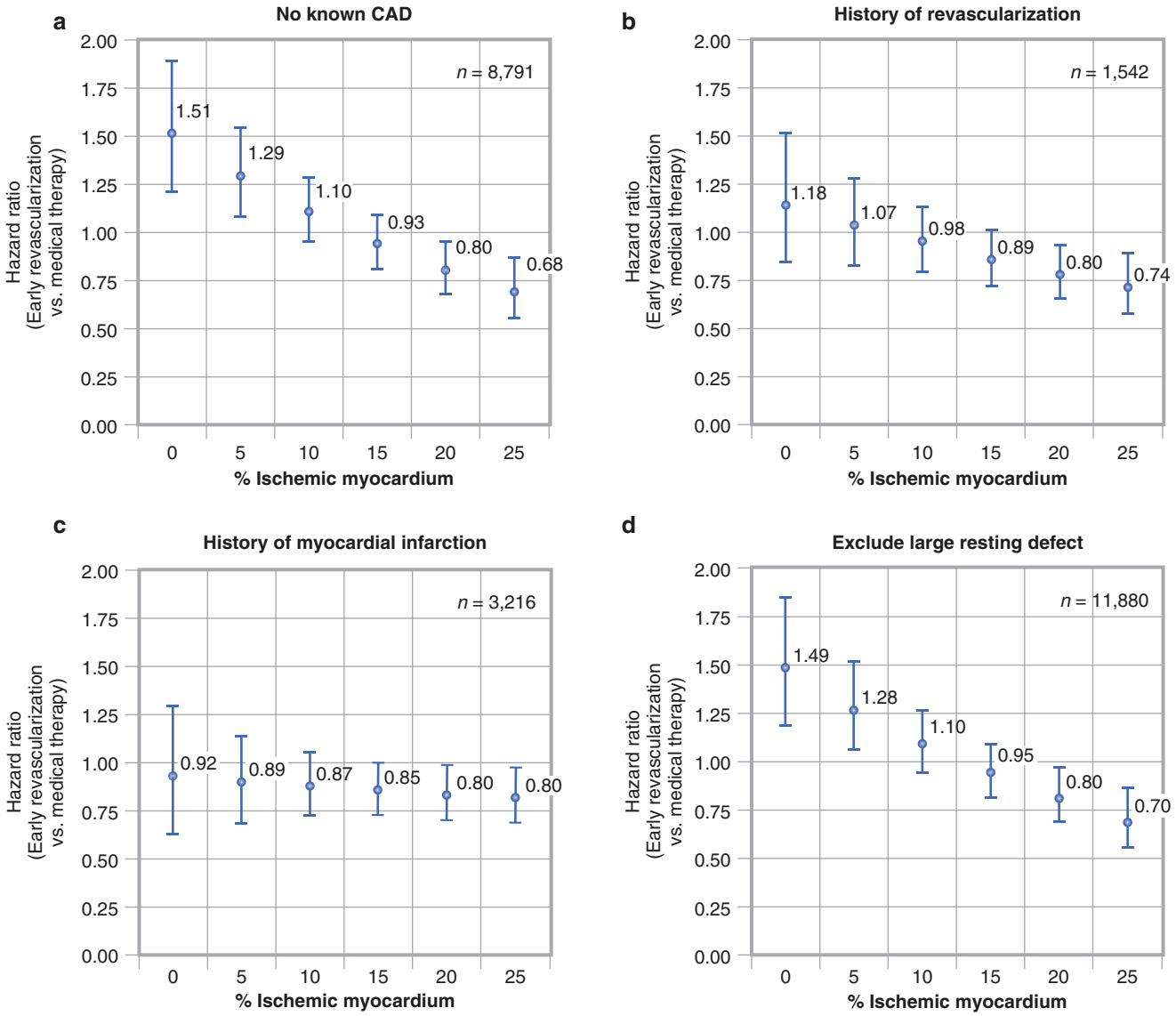

Fig. 8.52 Association between early revascularization and long-term (mean 8.7 years) all-cause mortality stratified by burden of ischemia in important patient groups. Identification of patient risk does not necessarily translate into identification of optimal patient management. The relationship between scar, ischemia, and therapeutic impact is an important one. In a single-center study (Cedars-Sinai), Hachamovitch et al. studied 13,060 patients who underwent SPECT MPI to investigate the potential impact on the potential benefit from revascularization of prior MI, revascularization, or resting perfusion deficit, using a propensity score to account for factors leading to revascularization. In patients without known CAD (**Panel A**), increasing ischemia was associated with increasing benefit from revascularization with 15% or greater ischemia. There were similar findings for the patients with a history of previous revascularization (**Panel B**), with benefit appearing to be present with 10% ischemia or more. In patients with a history of previous MI (**Panel C**), there appeared to be a survival benefit with revascularization regardless of the level of ischemia. By excluding patients with large previous MI, as shown by ≥10% resting perfusion deficits (**Panel D**), increasing ischemia was associated with increasing benefit from revascularization even in patients with previous MI, with the survival benefit appearing at 15%, similar to that observed in patients with no known CAD [76]

Acknowledgements This work was supported in part by a grant to Dr. Berman from the Miriam and Sheldon A. Adelson Medical Research Foundation and to Dr. Miller from the Arthur J E Child Fellowship grant.

References

1. Fihn SD, Gardin JM, Abrams J, Berra K, Blankenship JC, Dallas AP, et al. 2012 ACCF/AHA/ACP/AATS/PCNA/SCAI/STS Guideline for the diagnosis and management of patients with stable ischemic heart disease: a report of the American College of Cardiology Foundation/American Heart Association Task Force on Practice Guidelines, and the American College of Physicians, American Association for Thoracic Surgery, Preventive Cardiovascular Nurses Association, Society for Cardiovascular Angiography and Interventions, and Society of Thoracic Surgeons. J Am Coll Cardiol. 2012;60:e44–e164.
2. Shaw LJ, Berman DS, Maron DJ, Mancini GB, Hayes SW, Hartigan PM, et al.; COURAGE Investigators. Optimal medical therapy with or without percutaneous coronary intervention to reduce ischemic burden: results from the Clinical Outcomes Utilizing Revascularization and Aggressive Drug Evaluation (COURAGE) trial nuclear substudy. Circulation. 2008;117:1283–91.
3. Hachamovitch R, Hayes SW, Friedman JD, Cohen I, Berman DS. Comparison of the short-term survival benefit associated with revascularization compared with medical therapy in patients with no prior coronary artery disease undergoing stress myocardial perfusion single photon emission computed tomography. Circulation. 2003;107:2900–7.
4. ISCHEMIA Trial Research Group, Maron DJ, Hochman JS, O'Brien SM, Reynolds HR, Boden WE, Stone GW, et al. International Study of Comparative Health Effectiveness with Medical and Invasive Approaches (ISCHEMIA) trial: rationale and design. Am Heart J. 2018;201:124–35.
5. Boden WE, O'Rourke RA, Teo KK, Hartigan PM, Maron DJ, Kostuk WJ, et al.; COURAGE Trial Research Group. Optimal medical therapy with or without PCI for stable coronary disease. N Engl J Med. 2007;356:1503–16.
6. Phillips LM, Hachamovitch R, Berman DS, Iskandrian AE, Min JK, Picard MH, et al. Lessons learned from MPI and physiologic testing in randomized trials of stable ischemic heart disease: COURAGE, BARI 2D, FAME, and ISCHEMIA. J Nucl Cardiol. 2013;20:969–75.
7. BARI 2D Study Group, Frye RL, August P, Brooks MM, Hardison RM, Kelsey SF, MacGregor JM, et al. A randomized trial of therapies for type 2 diabetes and coronary artery disease. N Engl J Med. 2009;360:2503–15.
8. Hasdai D, Gibbons RJ, Holmes DR Jr, Higano ST, Lerman A. Coronary endothelial dysfunction in humans is associated with myocardial perfusion defects. Circulation. 1997;96:3390–5.
9. Ladenheim ML, Pollock BH, Rozanski A, Berman DS, Staniloff HM, Forrester JS, Diamond GA. Extent and severity of myocardial hypoperfusion as predictors of prognosis in patients with suspected coronary artery disease. J Am Coll Cardiol. 1986;7:464–71.
10. Berman DS, Abidov A, Kang X, Hayes SW, Friedman JD, Sciammarella MG, et al. Prognostic validation of a 17-segment score derived from a 20-segment score for myocardial perfusion SPECT interpretation. J Nucl Cardiol. 2004;11:414–23.
11. Berman DS, Kiat H, Friedman JD, Wang FP, van Train K, Matzer L, et al. Separate acquisition rest thallium-201/stress technetium-99m sestamibi dual-isotope myocardial perfusion single-photon emission computed tomography: a clinical validation study. J Am Coll Cardiol. 1993;22:1455–64.
12. Garcia EV. Quantitative myocardial perfusion single-photon emission computed tomographic imaging: quo vadis? (Where do we go from here?). J Nucl Cardiol. 1994;1:83–93.
13. Sharir T, Germano G, Waechter PB, Kavanagh PB, Areeda JS, Gerlach J, et al. A new algorithm for the quantitation of myocardial perfusion SPECT. II: validation and diagnostic yield. J Nucl Med. 2000;41:720–7.
14. Germano G, Kavanagh PB, Waechter P, Areeda J, Van Kriekinge S, Sharir T, et al. A new algorithm for the quantitation of myocardial perfusion SPECT. I: technical principles and reproducibility. J Nucl Med. 2000;41:712–9.
15. Cerqueira MD, Weissman NJ, Dilsizian V, Jacobs AK, Kaul S, Laskey WK, et al. Standardized myocardial segmentation and nomenclature for tomographic imaging of the heart. A statement for healthcare professionals from the Cardiac Imaging Committee of the Council on Clinical Cardiology of the American Heart Association. Circulation. 2002;105:539–42.
16. Hachamovitch R, Berman DS, Shaw LJ, Kiat H, Cohen I, Cabico JA, et al. Incremental prognostic value of myocardial perfusion single photon emission computed tomography for the prediction of cardiac death: differential stratification for risk of cardiac death and myocardial infarction. Circulation. 1998;97:535–43.
17. Slomka PJ, Nishina H, Berman DS, Akincioglu C, Abidov A, Friedman JD, et al. Automated quantification of myocardial perfusion SPECT using simplified normal limits. J Nucl Cardiol. 2005;12:66–77.
18. Mazzanti M, Germano G, Kiat H, Kavanagh PB, Alexanderson E, Friedman JD, et al. Identification of severe and extensive coronary artery disease by automatic measurement of transient ischemic dilation of the left ventricle in dual-isotope myocardial perfusion SPECT. J Am Coll Cardiol. 1996;27:1612–20.
19. Berman DS, Kang X, Gransar H, Gerlach J, Friedman JD, Hayes SW, et al. Quantitative assessment of myocardial perfusion abnormality on SPECT myocardial perfusion imaging is more reproducible than expert visual analysis. J Nucl Cardiol. 2009;16:45–53.
20. Xu Y, Hayes S, Ali I, Ruddy TD, Wells RG, Berman DS, et al. Automatic and visual reproducibility of perfusion and function measures for myocardial perfusion SPECT. J Nucl Cardiol. 2010;17:1050–7.
21. Xu Y, Nakazato R, Hayes S, Hachamovitch R, Cheng VY, Gransar H, et al. Prognostic value of automated vs visual analysis for adenosine stress myocardial perfusion SPECT in patients without prior coronary artery disease: a case-control study. J Nucl Cardiol. 2011;18:1003–14.
22. Motwani M, Leslie WD, Goertzen AL, Otaki Y, Germano G, Berman DS, Slomka PJ. Fully automated analysis of attenuation-corrected SPECT for the long-term prediction of acute myocardial infarction. J Nucl Cardiol. 2018;25:1353–60.
23. Dorbala S, Di Carli MF, Beanlands RS, Merhige ME, Williams BA, Veledar E, et al. Prognostic value of stress myocardial perfusion positron emission tomography: results from a multicenter observational registry. J Am Coll Cardiol. 2013;61:176–84.
24. Sharir T, Berman DS, Lewin HC, Friedman JD, Cohen I, Miranda R, et al. Incremental prognostic value of rest-redistribution (201) Tl single-photon emission computed tomography. Circulation. 1999;100:1964–70.
25. Weiss AT, Berman DS, Lew AS, Nielsen J, Potkin B, Swan HJ, et al. Transient ischemic dilation of the left ventricle on stress thallium-201 scintigraphy: a marker of severe and extensive coronary artery disease. J Am Coll Cardiol. 1987;9:752–9.
26. Sharir T, Bacher-Stier C, Dhar S, Lewin HC, Miranda R, Friedman JD, et al. Identification of severe and extensive coronary artery disease by postexercise regional wall motion abnormalities in Tc-99m sestamibi gated single-photon emission computed tomography. Am J Cardiol. 2000;86:1171–5.

27. Matzer L, Kiat H, Van Train K, Germano G, Papanicolaou M, Silagan G, et al. Quantitative severity of stress thallium-201 myocardial perfusion single-photon emission computed tomography defects in one-vessel coronary artery disease. Am J Cardiol. 1993;72:273–9.
28. Ladenheim ML, Kotler TS, Pollock BH, Berman DS, Diamond GA. Incremental prognostic power of clinical history, exercise electrocardiography and myocardial perfusion scintigraphy in suspected coronary artery disease. Am J Cardiol. 1987;59:270–7.
29. Berman DS, Hachamovitch R, Kiat H, Cohen I, Cabico JA, Wang FP, et al. Incremental value of prognostic testing in patients with known or suspected ischemic heart disease: a basis for optimal utilization of exercise technetium-99m sestamibi myocardial perfusion single-photon emission computed tomography. J Am Coll Cardiol. 1995;26:639–47.
30. Hachamovitch R, Berman DS, Kiat H, Cohen I, Cabico JA, Friedman J, Diamond GA. Exercise myocardial perfusion SPECT in patients without known coronary artery disease: incremental prognostic value and use in risk stratification. Circulation. 1996;93:905–14.
31. Gibbons RJ, Hodge DO, Berman DS, Akinboboye OO, Heo J, Hachamovitch R, et al. Long-term outcome of patients with intermediate-risk exercise electrocardiograms who do not have myocardial perfusion defects on radionuclide imaging. Circulation. 1999;100:2140–5.
32. Shaw LJ, Hachamovitch R, Berman DS, Marwick TH, Lauer MS, Heller GV, et al. The economic consequences of available diagnostic and prognostic strategies for the evaluation of stable angina patients: an observational assessment of the value of precatheterization ischemia. Economics of Noninvasive Diagnosis (END) Multicenter Study Group. J Am Coll Cardiol. 1999;33:661–9.
33. Shaw LJ, Hendel RC, Cerquiera M, Mieres JH, Alazraki N, Krawczynska E, et al. Ethnic differences in the prognostic value of stress technetium-99m tetrofosmin gated single-photon emission computed tomography myocardial perfusion imaging. J Am Coll Cardiol. 2005;45:1494–504.
34. Budoff MJ, Yang TP, Shavelle RM, Lamont DH, Brundage BH. Ethnic differences in coronary atherosclerosis. J Am Coll Cardiol. 2002;39:408–12.
35. Matsuo S, Nakajima K, Horie M, Nakae I, Nishimura T; J-ACCESS Investigators. Prognostic value of normal stress myocardial perfusion imaging in Japanese population. Circ J. 2008;72:611–7.
36. Zellweger MJ, Hachamovitch R, Kang X, Hayes SW, Friedman JD, Germano G, et al. Prognostic relevance of symptoms versus objective evidence of coronary artery disease in diabetic patients. Eur Heart J. 2004;25:543–50.
37. Nudi F, Biondi-Zoccai G, Schillaci O, di Belardino N, Versaci F, Nudi A, et al. Prognostic accuracy of myocardial perfusion imaging in octogenarians. J Nucl Cardiol. 2018;25:1342–9.
38. Berman DS, Kang X, Hayes SW, Friedman JD, Cohen I, Abidov A, et al. Adenosine myocardial perfusion single-photon emission computed tomography in women compared with men. Impact of diabetes mellitus on incremental prognostic value and effect on patient management. J Am Coll Cardiol. 2003;41:1125–33.
39. Giri S, Shaw LJ, Murthy DR, Travin MI, Miller DD, Hachamovitch R, et al. Impact of diabetes on the risk stratification using stress single-photon emission computed tomography myocardial perfusion imaging in patients with symptoms suggestive of coronary artery disease. Circulation. 2002;105:32–40.
40. Wackers FJ, Young LH, Inzucchi SE, Chyun DA, Davey JA, Barrett EJ, et al.; Detection of Ischemia in Asymptomatic Diabetics Investigators. Detection of silent myocardial ischemia in asymptomatic diabetic subjects: the DIAD study. Diabetes Care. 2004;27:1954–61.
41. Ahmed AM, Qureshi WT, O'Neal WT, Khalid F, Al-Mallah MH. Incremental prognostic value of SPECT-MPI in chronic kidney disease: a reclassification analysis. J Nucl Cardiol. 2018;25:1658–73.
42. Al-Mallah MH, Hachamovitch R, Dorbala S, Di Carli MF. Incremental prognostic value of myocardial perfusion imaging in patients referred to stress single-photon emission computed tomography with renal dysfunction. Circ Cardiovasc Imaging. 2009;2:429–36.
43. Rozanski A, Gransar H, Min JK, Hayes SW, Friedman JD, Thomson LE, Berman DS. Long-term mortality following normal exercise myocardial perfusion SPECT according to coronary disease risk factors. J Nucl Cardiol. 2014;21:341–50.
44. Abidov A, Hachamovitch R, Rozanski A, Hayes SW, Santos MM, Sciammarella MG, et al. Prognostic implications of atrial fibrillation in patients undergoing myocardial perfusion single-photon emission computed tomography. J Am Coll Cardiol. 2004;44:1062–70.
45. Rozanski A, Gransar H, Hayes SW, Friedman JD, Hachamovitch R, Berman DS. Comparison of long-term mortality risk following normal exercise vs adenosine myocardial perfusion SPECT. J Nucl Cardiol. 2010;17:999–1008.
46. Navare SM, Mather JF, Shaw LJ, Fowler MS, Heller GV. Comparison of risk stratification with pharmacologic and exercise stress myocardial perfusion imaging: a meta-analysis. J Nucl Cardiol. 2004;11:551–61.
47. Heller GV, Herman SD, Travin MI, Baron JI, Santos-Ocampo C, McClellan JR. Independent prognostic value of intravenous dipyridamole with technetium-99m sestamibi tomographic imaging in predicting cardiac events and cardiac-related hospital admissions. J Am Coll Cardiol. 1995;26:1202–8.
48. Shaw L, Chaitman BR, Hilton TC, Stocke K, Younis LT, Caralis DG, et al. Prognostic value of dipyridamole thallium-201 imaging in elderly patients. J Am Coll Cardiol. 1992;19:1390–8.
49. Calnon DA, McGrath PD, Doss AL, Harrell FE Jr, Watson DD, Beller GA. Prognostic value of dobutamine stress technetium-99m-sestamibi single-photon emission computed tomography myocardial perfusion imaging: stratification of a high-risk population. J Am Coll Cardiol. 2001;38:1511–7.
50. Amanullah AM, Kiat H, Friedman JD, Berman DS. Adenosine technetium-99m sestamibi myocardial perfusion SPECT in women: diagnostic efficacy in detection of coronary artery disease. J Am Coll Cardiol. 1996;27:803–9.
51. Hachamovitch R, Hayes SW, Friedman JD, Cohen I, Berman DS. A prognostic score for prediction of cardiac mortality risk after adenosine stress myocardial perfusion scintigraphy. J Am Coll Cardiol. 2005;45:722–9.
52. Rozanski A, Gransar H, Hayes SW, Min J, Friedman JD, Thomson LE, Berman DS. Temporal trends in the frequency of inducible myocardial ischemia during cardiac stress testing: 1991 to 2009. J Am Coll Cardiol. 2013;61:1054–65.
53. Duvall WL, Rai M, Ahlberg AW, O'Sullivan DM, Henzlova MJ. A multi-center assessment of the temporal trends in myocardial perfusion imaging. J Nucl Cardiol. 2015;22:539–51.
54. Abidov A, Hachamovitch R, Hayes SW, Ng CK, Cohen I, Friedman JD, et al. Prognostic impact of hemodynamic response to adenosine in patients older than age 55 years undergoing vasodilator stress myocardial perfusion study. Circulation. 2003;107:2894–9.
55. Azarbal B, Hayes SW, Lewin HC, Hachamovitch R, Cohen I, Berman DS. The incremental prognostic value of percentage of heart rate reserve achieved over myocardial perfusion single-photon emission computed tomography in the prediction of cardiac death and all-cause mortality: superiority over 85% of maximal age-predicted heart rate. J Am Coll Cardiol. 2004;44:423–30.
56. Sharir T, Germano G, Kang X, Lewin HC, Miranda R, Cohen I, et al. Prediction of myocardial infarction versus cardiac death by gated myocardial perfusion SPECT: risk stratification by the amount of stress-induced ischemia and the poststress ejection fraction. J Nucl Med. 2001;42:831–7.

57. Abidov A, Bax JJ, Hayes SW, Hachamovitch R, Cohen I, Gerlach J, et al. Transient ischemic dilation ratio of the left ventricle is a significant predictor of future cardiac events in patients with otherwise normal myocardial perfusion SPECT. J Am Coll Cardiol. 2003;42:1818–25.
58. Alama M, Labos C, Emery H, Iwanochko RM, Freeman M, Husain M, Lee DS. Diagnostic and prognostic significance of transient ischemic dilation (TID) in myocardial perfusion imaging: a systematic review and meta-analysis. J Nucl Cardiol. 2018;25:724–37.
59. Berman DS, Kang X, Slomka PJ, Gerlach J, de Yang L, Hayes SW, et al. Underestimation of extent of ischemia by gated SPECT myocardial perfusion imaging in patients with left main coronary artery disease. J Nucl Cardiol. 2007;14:521–8.
60. Naya M, Murthy VL, Taqueti VR, Foster CR, Klein J, Garber M, et al. Preserved coronary flow reserve effectively excludes high-risk coronary artery disease on angiography. J Nucl Med. 2014;55:248–55.
61. Murthy VL, Lee BC, Sitek A, Naya M, Moody J, Polavarapu V, et al. Comparison and prognostic validation of multiple methods of quantification of myocardial blood flow with 82Rb PET. J Nucl Med. 2014;55:1952–8.
62. Ziadi MC, Dekemp RA, Williams KA, Guo A, Chow BJ, Renaud JM, et al. Impaired myocardial flow reserve on rubidium-82 positron emission tomography imaging predicts adverse outcomes in patients assessed for myocardial ischemia. J Am Coll Cardiol. 2011;58:740–8.
63. Murthy VL, Naya M, Foster CR, Hainer J, Gaber M, Di Carli G, et al. Improved cardiac risk assessment with noninvasive measures of coronary flow reserve. Circulation. 2011;124:2215–24.
64. Taqueti VR, Hachamovitch R, Murthy VL, Naya M, Foster CR, Hainer J, et al. Global coronary flow reserve is associated with adverse cardiovascular events independently of luminal angiographic severity and modifies the effect of early revascularization. Circulation. 2015;131:19–27.
65. Betancur J, Otaki Y, Motwani M, Fish MB, Lemley M, Dey D, et al. Prognostic value of combined clinical and myocardial perfusion imaging data using machine learning. JACC Cardiovasc Imaging. 2018;11:1000–9.
66. Chang SM, Nabi F, Xu J, Raza U, Mahmarian JJ. Normal stress-only versus standard stress/rest myocardial perfusion imaging: similar patient mortality with reduced radiation exposure. J Am Coll Cardiol. 2010;55:221–30.
67. Einstein AJ, Blankstein R, Andrews H, Fish M, Padgett R, Hayes SW, et al. Comparison of image quality, myocardial perfusion, and left ventricular function between standard imaging and single-injection ultra-low-dose imaging using a high-efficiency SPECT camera: the MILLISIEVERT study. J Nucl Med. 2014;55:1430–7.
68. Nakazato R, Berman DS, Hayes SW, Fish M, Padgett R, Xu Y, et al. Myocardial perfusion imaging with a solid-state camera: simulation of a very low dose imaging protocol. J Nucl Med. 2013;54:373–9.
69. Sharir T, Ben-Haim S, Merzon K, Prochorov V, Dickman D, Ben-Haim S, Berman DS. High-speed myocardial perfusion imaging initial clinical comparison with conventional dual detector anger camera imaging. JACC Cardiovasc Imaging. 2008;1:156–63.
70. Songy B, Guernou M, Hivoux D, Attias D, Lussato D, Queneau M, et al. Prognostic value of one millisievert exercise myocardial perfusion imaging in patients without known coronary artery disease. J Nucl Cardiol. 2018;25:120–30.
71. Lima R, Peclat T, Soares T, Ferreira C, Souza AC, Camargo G. Comparison of the prognostic value of myocardial perfusion imaging using a CZT-SPECT camera with a conventional Anger camera. J Nucl Cardiol. 2017;24:245–51.
72. Engbers EM, Timmer JR, Ottervanger JP, Mouden M, Knollema S, Jager PL. Prognostic value of coronary artery calcium scoring in addition to single-photon emission computed tomographic myocardial perfusion imaging in symptomatic patients. Circ Cardiovasc Imaging. 2016;9(5). pii:e003966.
73. Bybee KA, Lee J, Markiewicz R, Longmore R, McGhie AI, O'Keefe JH, et al. Diagnostic and clinical benefit of combined coronary calcium and perfusion assessment in patients undergoing PET/CT myocardial perfusion stress imaging. J Nucl Cardiol. 2010;17:188–96.
74. SCOT-HEART Investigators, Newby DE, Adamson PD, Berry C, Boon NA, Dweck MR, et al. Coronary CT angiography and 5-year risk of myocardial infarction. N Engl J Med. 2018;379:924–33.
75. Hachamovitch R, Hayes SW, Friedman JD, Cohen I, Kang X, Germano G, Berman DS. Is there a referral bias against catheterization of patients with reduced left ventricular ejection fraction? Influence of ejection fraction and inducible ischemia on post-single-photon emission computed tomography management of patients without a history of coronary artery disease. J Am Coll Cardiol. 2003;42:1286–94.
76. Hachamovitch R, Rozanski A, Shaw LJ, Stone GW, Thomson LE, Friedman JD, et al. Impact of ischaemia and scar on the therapeutic benefit derived from myocardial revascularization vs. medical therapy among patients undergoing stress-rest myocardial perfusion scintigraphy. Eur Heart J. 2011;32:1012–24.

Imaging Cardiac Metabolism

9

Heinrich Taegtmeyer and Vasken Dilsizian

Introduction

Cardiac metabolism refers to a complex system of interconnected chemical reactions. In broad terms, metabolism provides the energy for contraction and the materials for the heart's structure and function. A defining feature of metabolism is the flux of chemical compounds that can be traced by physical methods, including radioactive decay of tracers or magnetic resonance (MR) spectroscopy. These methods are readily applied both *in vivo* and *ex vivo* for the assessment of cardiac metabolic activity [1]. Metabolic activity, in turn, is a dynamic process found only in living cells and tissues. In addition to this dynamic nature of metabolic activity, intermediary metabolites also control cell function, either as regulators of enzyme activity or as posttranslational modifiers of protein function and transcriptional activity [2, 3].

An important recent development in the field of nuclear cardiology is the concept that metabolic remodeling of the heart precedes, triggers, and sustains structural and functional remodeling, and that metabolism is inextricably linked to both physiology and molecular biology of the heart. This concept offers unprecedented opportunities for metabolic imaging [4].

The pathways of myocardial energy substrate metabolism converge on the energy-rich phosphate bonds of ATP (Fig. 9.1). ATP is largely used to maintain myocardial contraction and to regulate the membrane pumps and movements of ions in and out of the cell. For a given physiologic environment, the heart consumes the most efficient metabolic fuel for its function [6]. In the normally oxygenated heart, fatty acids account for the majority of ATP production; glucose makes only a small contribution in providing energy, unless there is an insulin surge. During an acute increase in work load (for example, inotropic stimulation), the heart immediately mobilizes its metabolic reserve contained in glycogen (transient increase in glycogen oxidation) and meets the needs for additional energy from the oxidation of carbohydrate substrates (glucose and lactate). When the oxygen supply is decreased, the heart protects itself from an oxygen-deficient state by switching its energy source to glycolysis, downregulating mitochondrial oxidative metabolism and reducing contractile function. Thus, the tight coupling between metabolism and contractile function in the heart offers a unique opportunity to assess cardiac performance in coronary flow, myocardial perfusion, oxygen delivery, metabolism, and contraction.

The advantages of imaging cardiac metabolism rest in the observer's ability to monitor and trace chemical processes in the heart by noninvasive methods. In reality, cardiac metabolism consists of a complex and highly regulated biological network of intracellular reactions that is well characterized at the biochemical level [1].

H. Taegtmeyer (✉)
The University of Texas Health Science Center at Houston,
McGovern Medical School, Houston, TX, USA
e-mail: Heinrich.Taegtmeyer@uth.tmc.edu

V. Dilsizian
University of Maryland School of Medicine, Baltimore, MD, USA

V. Dilsizian, J. Narula (eds.), *Atlas of Nuclear Cardiology*, https://doi.org/10.1007/978-3-030-49885-6_9

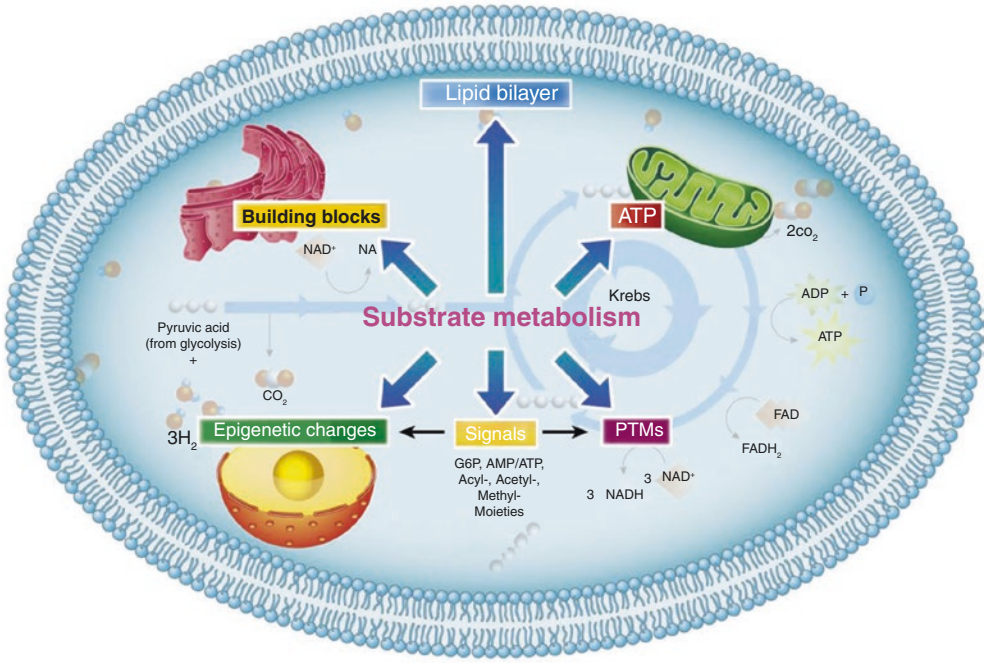

Fig. 9.1 Multiple roles of metabolism. Products of energy substrate metabolism provide ATP, building blocks of complex molecules, including proteins and ribonucleotides, as well as lipid bilayers, substrates for posttranslational modifications of proteins (PTMs), and metabolic signals such as glucose 6-phosphate (G6P), the AMP/ATP ratio, and acyl-, acetyl-, and methyl- groups serving as substrates for epigenetic changes or for PTMs. This drawing attempts to show the main features of metabolism in the heart. (*From* Davogustto and Taegtmeyer [5]; *with permission from Elsevier*)

No doubt, the interrelationship between mechanical function, myocardial perfusion, and metabolic and energy-consuming processes within the heart is complex. Existing knowledge can be reduced to a few principles: A metabolic switch from fatty acids to glucose seems pivotal in preserving myocardial viability and likely represents the earliest adaptive response to myocardial ischemia. Perhaps the most dramatic clinical application for the metabolic switch from fatty acid utilization to glycolysis is in myocardial hibernation. Hibernating myocardium represents the dysfunctional but viable myocardium, most likely the result of extensive cellular reprogramming due to repetitive episodes of chronic ischemia. This reprogramming of myocytes occurs at multiple levels. Although the true mechanism for viability remodeling in hibernation is likely to be very complex, it is thought to be related, in part, to the increased glycogen content and myocardial ATP levels in such cells, simulating the fetal heart. Because glucose transport and phosphorylation is readily traced by the uptake and retention of ^{18}F-fluoro,2-deoxy-D-glucose (FDG), hibernating myocardium is readily detected by enhanced glucose uptake in the same regions by external detectors, such as positron emission tomography (PET).

Recent clinical studies have also shown the potential utility of metabolic adaptation in the emergency department as well as for detection of coronary artery disease in the form of "ischemic memory." Ischemic memory represents prolonged but reversible metabolic recovery after transient myocardial ischemia, also known as "metabolic stunning." At the cellular level, it is the result of extensive transcriptional, translational, and post-translational metabolic changes.

Other disease entities in which metabolic imaging by nuclear techniques can play an important role include diabetic heart disease, the identification of microvascular disease and subendocardial ischemia in symptomatic patients with nonobstructive coronary artery disease, and left ventricular remodeling in hypertrophy and congestive heart failure. The understanding of this kind of left ventricular remodeling has increased dramatically in recent years. Emerging evidence suggests a role for altered metabolism in the progression of both left ventricular hypertrophy and remodeling. Some of the clinical evidence includes a variable prognosis in patients with similar left ventricular mass in hypertrophy; a loss of metabolic flexibility that may portend worse prognosis in patients with heart failure; and the development of modulators for medical treatment in heart failure, such as fatty acid oxidation inhibitors (e.g., ranolazine) and insulin sensitizers.

Metabolic adaptation serves as a mechanism of cell survival in response to an altered physiological state and represents one of the earliest responses to myocardial ischemia, left ventricular remodeling, and diabetic and uremic heart disease. Recognizing key intracellular signals that link energy substrate metabolism with gene expression may allow the discovery of more specific molecular targets for the imaging, diagnosis, and treatment of cardiovascular disease.

Evolution of Knowledge of Cardiac Metabolism

The acquisition of knowledge of cardiac metabolism is highlighted by a number of early milestones:

- *1854:* Hermann von Helmholtz discovers the first law of thermodynamics, introducing the concept that energy bound up in foodstuffs is liberated and transferred to physical work.
- *1857:* Louis Pasteur discovers that fermentation occurs in living microorganisms and can be turned off by oxygen. When the oxygen supply is diminished, the rate of glucose utilization was increased and paralleled by an increase in lactate release. This stimulation of glycolysis by hypoxia and the corollary inhibition of anaerobic glycolysis by oxidative metabolism is termed the *Pasteur effect*.
- *1895:* Oscar Langendorff demonstrates that the mammalian heart receives oxygen and nutrients through coronary circulation.
- *Early 1900s:* Ernest Starling discovers that in normally oxygenated hearts, glucose contributes only a small amount to the fuel of the heart, in the absence of insulin.
- *1904:* Ludwig Winterstein discovers the oxygen dependency of the contracting mammalian heart.
- *1904:* Franz Knoop discovers β-oxidation of fatty acids, the metabolic oxidation at the β-carbon atom of a long-chain fatty acid by successive cycles of reactions, during each of which the fatty acid is shortened by a two-carbon-atom fragment removed as acetyl-coenzyme A.
- *1924:* Otto Warburg describes the nature and function of mitochondrial respiratory enzymes. He discovers that a fundamental difference between normal and cancerous cells is the ratio of glycolysis to respiration; this observation is known as the *Warburg effect*. The concept that cancer cells switch from oxidative metabolism to glycolysis has become widely accepted and is the basis of ^{18}F-FDG positron emission tomography (PET) imaging today.
- *1930s:* C. Lovatt Evans et al. find that lactate can be readily taken up and oxidized as a fuel in the normally oxygenated heart.
- *1937:* Hans A. Krebs discovers the major metabolic cycle—known as the *Krebs cycle*, or the *citric acid cycle*—which represents the second of the three steps that convert fatty acids, glucose, and other fuels in the body into energy in the form of adenosine triphosphate (ATP).
- *1937:* Fritz A. Lipmann discovers the importance of ATP as the main energy carrier in cells; he later shared the 1953 Nobel Prize for Physiology or Medicine with Hans Krebs for his discovery of coenzyme A (CoA), a crucial link between glycolysis, the first stage in the process, and the Krebs cycle, and its importance for intermediary metabolism.
- *1950s:* Richard J. Bing, using coronary sinus cannulation and precise coronary artery flow measurements in the human heart, discovers the concept of the heart as a metabolic omnivore.
- *1960s:* Philip J. Randle discovers that fatty acids suppress glucose oxidation by inhibiting pyruvate dehydrogenase in the isolated perfused heart.
- *1960s:* Richard J. Bing introduces positron-emitting tracers for the measurement of blood flow.

Metabolic Radiotracers

By labeling various compounds of physiologic interest, valuable insights into biochemical pathways and tissue metabolism can be obtained in functional and dysfunctional myocardium (Table 9.1). Currently, the only PET myocardial metabolic radiotracer approved by the US Food and Drug Administration (FDA) and reimbursable by the Centers for Medicare & Medicaid Services is ^{18}F-fluoro,2-deoxy-D-glucose (FDG), which is the current gold standard for evaluating glucose metabolism, and myocardial viability. FDG is a glucose analogue that competes with glucose for phosphorylation by hexokinase. Once phosphorylated, it is trapped inside the cell and can be neither further metabolized nor exported back out of the cell. To assess fatty acid utilization, earlier studies used the labeled substrate ^{11}C-palmitate, which is a PET-radiolabeled straight-chain fatty acid. After its uptake into the cell and activation by binding to coenzyme A, ^{11}C-palmitate undergoes β-oxidation, ultimately leading to the release of $^{11}CO_2$. However, this technique requires a PET camera and an onsite cyclotron. As single-photon emission computed tomography (SPECT) cameras were already available to most nuclear cardiologists, the focus turned to the development of SPECT tracers for fatty acid oxidation. One of them is [^{123}I]-β-methyl-*p*-iodophenyl-pentadecanoic acid (^{123}I-BMIPP), a substrate analogue that is rapidly taken up into the cardiomyocytes and shows prolonged retention due to limited catabolism. Both ^{123}I-BMIPP and ^{11}C-palmitate interrogate myocardial fatty acid metabolism *in vivo*. The uptake and clearance of ^{11}C-palmitate from the myocyte occurs quite rapidly via β-oxidation, whereas the methyl chain in ^{123}I-BMIPP results in metabolic trapping of the radiotracer in the myocyte. A PET-radiolabeled short-chain acid that is ideal for the *in vivo* assessment of myocardial oxidative metabolism is ^{11}C-acetate.

Radiotracer	Assessment
SPECT radiotracers	
^{123}I-BMIPP	Fatty acid uptake
^{18}F-THA	Fatty acid uptake
PET radiotracers	
^{11}C-palmitate	Fatty acid metabolism
^{11}C-acetate	Oxidative metabolism
^{18}F-fluoro,2-deoxy-D-glucose	Glucose uptake
^{11}C-glucose	Glucose oxidation
^{11}C-glutamate	Amino acid metabolism
^{13}N-glutamate	Amino acid metabolism
^{11}C-methionine	Amino acid metabolism

^{18}*F-THA* F-thiaheptadecanoic acid (FTHA)

Table 9.1 Single-photon and positron-emitting metabolic radiotracers

Changes in fatty acid and glucose metabolism have been long-established parts of metabolic remodeling in various forms of heart disease, but much less is known about the alterations in amino acid metabolism and their impact on the onset and progression of cardiac disease. ^{11}C-glutamate or ^{13}N-glutamate are also useful for tracing the footprints of myocardial ischemia, and the uptake of ^{11}C-methionine in infarcted areas during the acute phase after myocardial infarction is a useful tool in monitoring the remodeling of the heart after myocardial infarction.

Figures 9.2, 9.3, and 9.4 illustrate the metabolic pathways in the heart and the ways that radiotracers and tracer analogues can assess perfusion, substrate uptake, and other evidence of metabolic activity. The flux of energy is limited to a series of moiety-conserved cycles (Fig. 9.2).

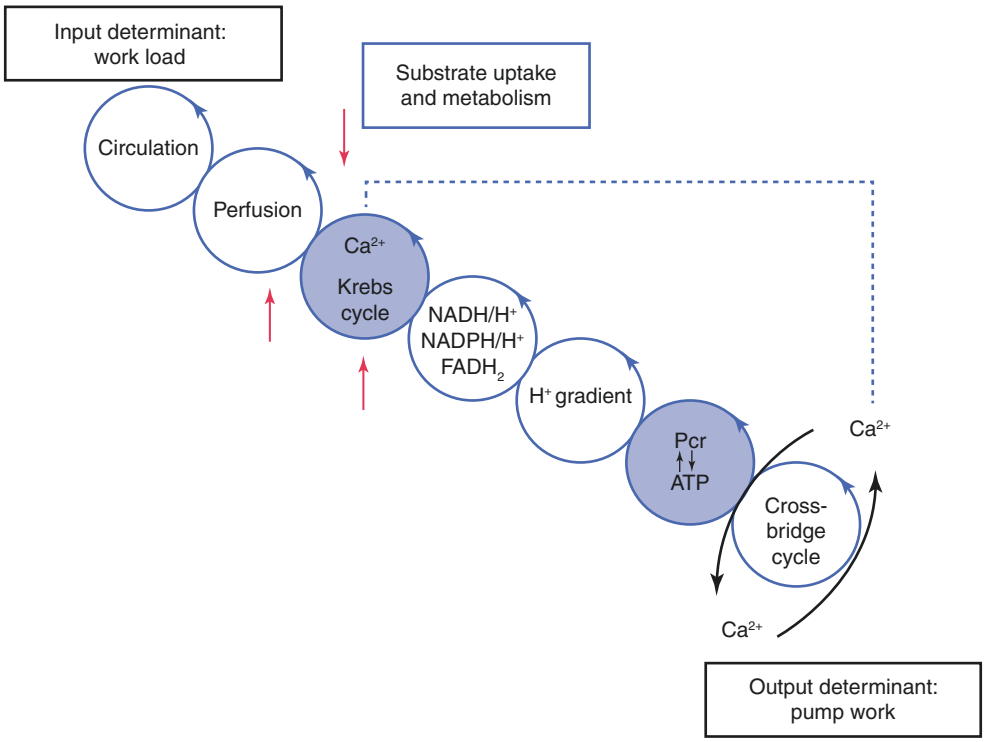

Fig. 9.2 Energy is transferred along a series of moiety-conserved cycles, starting at coronary circulation and ending at the cross-bridge formation of contractile elements [7]. Nuclear metabolic imaging uses targeted radiotracers to assess flux through specific metabolic pathways (by quantifying either the flux of energy-providing substrates or the steady-state metabolites). Radiotracer retention and/or metabolism are assessed by noninvasive techniques such as single-photon emission computed tomography (SPECT) and positron emission tomography (PET). It is convenient to follow energy transfer in the heart muscle cells from the circulation (substrate and O_2 delivery) to the cross bridges (energy utilization) through a series of moiety-conserved cycles. Specific radiotracers are available to assess perfusion and substrate uptake and delivery, as well as Krebs cycle turnover (oxygen consumption). Radiolabeled tracers in combination with SPECT or PET (*red arrows*) and nuclear magnetic resonance spectroscopy with either stable isotopes (e.g., ^{13}C) or ^{31}P (*blue cycles*) can assess various cycles noninvasively in vivo. Calcium (Ca^{2+}) is not an imaging agent, but the ion has been included because it is the signal that links contraction and mitochondrial respiration. Calcium release from the sarcoplasmic reticulum triggers calcium uptake into the mitochondria and activation of dehydrogenases in the Krebs cycle [7]. $FADH_2$ reduced flavin adenine dinucleotide, $NADPH/H^+$ reduced nicotinamide adenine dinucleotide (phosphate), PCr phosphocreatine. From Osterholt et al. with permission [7]

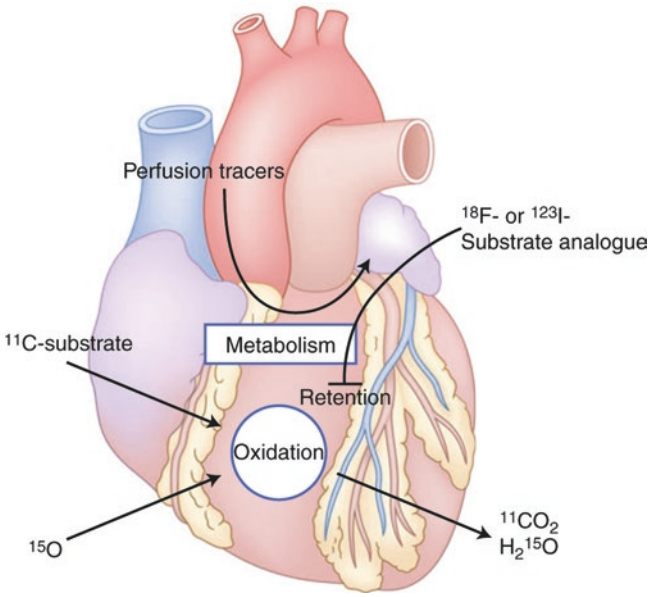

Fig. 9.3 Overview of the fate of labeled substrates and substrate analogues. Two classes of radiotracers are currently used to trace metabolic activity: labeled substrates or substrate analogues. Labeled substrates are taken up by heart muscle and either rapidly cleared or retained, whereas substrate analogues are taken up and retained only. Radiolabeled ^{11}C-substrate is taken up into the cell and undergoes complete oxidation, eventually leading to the release of $^{11}CO_2$. After their uptake into the cell, substrate analogues labeled with ^{18}F or ^{123}I are partially metabolized and then retained. The majority of perfusion tracers require preserved cellular metabolism to be taken up by the cell. Substrate oxidation rates can also be monitored using ^{15}O and measuring the release of $H_2{}^{15}O$. Adapted from Osterholt et al. [7] with permission

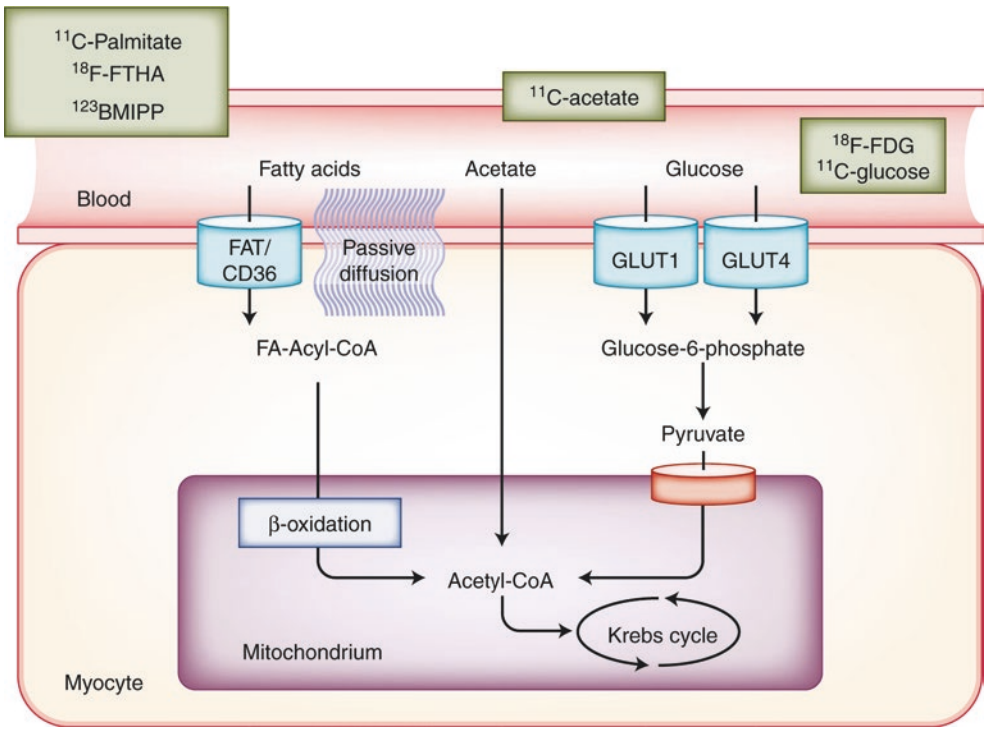

Fig. 9.4 Imaging the main pathways of cardiac metabolism. Fatty acid, glucose, and oxidative metabolism assessment with various SPECT and PET radiotracers is shown. Free fatty acids account for most ATP production when the heart is in a normal, fasting state. Following uptake of the radiotracers by active transport or diffusion, fatty acids are converted by β-oxidation into acetyl-coenzyme A (CoA). Under anaerobic or nonfasting conditions, energy production shifts to glucose metabolism. The conversion of glucose via glucose-6-phosphate and pyruvate provides the source of acetyl-CoA. Oxidative metabolism also provides an important contribution to cardiac metabolism. In mitochondria, ATP production occurs via the tricarboxylic acid (TCA) cycle. BMIPP β-methyl p-[^{123}I]-iodophenyl-pentadecanoic acid, FA fatty acid, FAT/CD36 fatty acid translocase, FDG fluorodeoxyglucose, FTHA ^{18}F-thiaheptadecanoic acid, GLUT1 and GLUT4 glucose transporters 1 and 4, THA thiaheptadecanoic acid

Metabolic Signals in Normal and Diseased Heart: Opportunities for Molecular Imaging

A refined understanding of metabolic regulation may result in the early diagnosis and treatment of subclinical myocardial ischemia and heart failure, as metabolic changes and changes in gene expression are likely to precede contractile dysfunction and other functional remodeling of the stressed heart (Figs. 9.5, 9.6, 9.7, 9.8, 9.9, 9.10, 9.11, and 9.12).

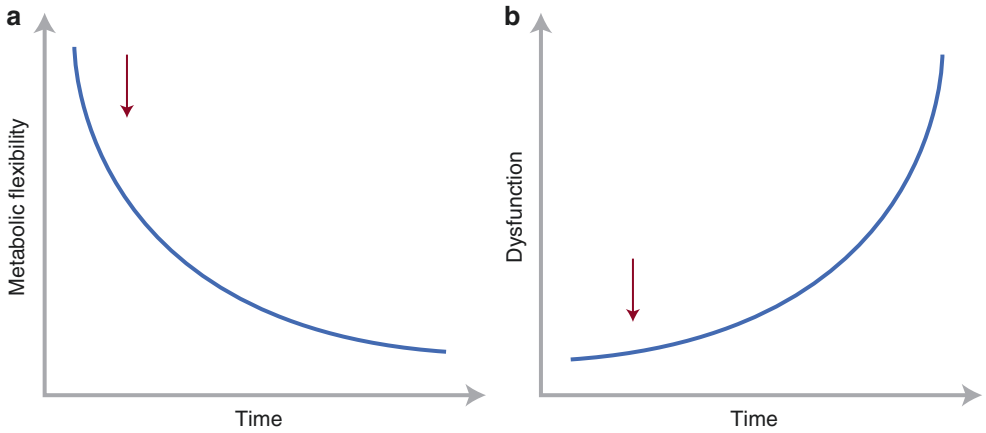

Fig. 9.5 Metabolic regulation. These hyperbolic curves illustrate a hypothetical time course of the rapid loss of metabolic flexibility antedating contractile dysfunction in the path of metabolic and functional remodeling of the stressed heart. The loss of metabolic flexibility (**a**, *arrow*) and changes in gene expression likely precede the onset of severe contractile dysfunction (**b**, *arrow*) [3]. The concept depicted in this figure is supported by the observation that transcriptional changes of enzymes and proteins of energy substrate metabolism antedate any contractile dysfunction in hearts from diabetic animals [8]

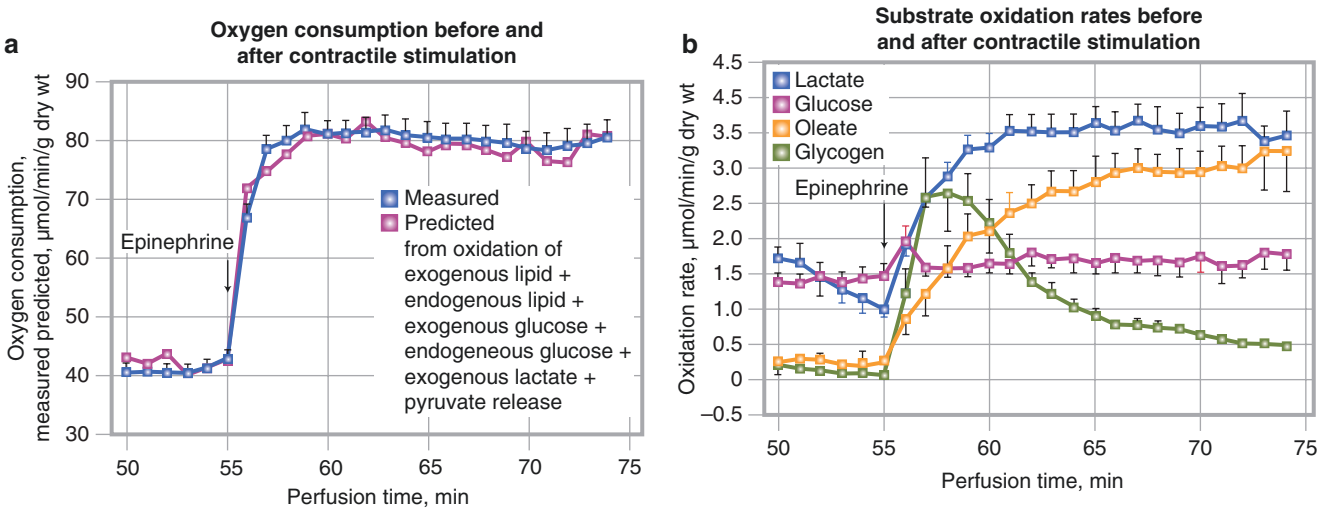

Fig. 9.6 (**a**) Measured and predicted values for oxygen consumption. Predicted rates are based on the sum of the measured rates of oxygen of every major substrate (glucose, glycogen, lactate, oleate, triglycerides, and release of pyruvate). The close agreement between measured and predicted MVO_2 validates the assumption of uniform isotopic dilution, and that every major oxidizable substrate was quantitatively accounted for in the heart. (**b**) Rates of substrate oxidation before and after inotropic stimulation. Fuel selection during acute transition from low to high workload (1 µM epinephrine and afterload increase by 40%) of isolated working rat heart is shown. When the workload is acutely increased, glycogen and, to a lesser extent, lactate become the most important energy substrates for the aerobic heart (**a**). With more prolonged adrenergic stimulation, nonesterified fatty acids and lactate are the major respiratory substrates for the heart, which is in keeping with the *in vivo* observations in the exercising state. When all relevant exogenous and endogenous substrates are examined, the increase in carbohydrate oxidation upon adrenergic stimulation is selective. Although exogenous fatty acid oxidation is not significantly changed, total β-oxidation increases by 40%, and the increase is associated with a decrease in the level of malonyl-coenzyme A (CoA). Carbohydrate oxidation is increased selectively because total β-oxidation, regulated mostly by malonyl-CoA levels in the cytosol, is independent of the activity of pyruvate dehydrogenase complex in the mitochondria. Using values of the distribution between oxidation and the release of lactate or pyruvate during adrenergic stimulation, the calculated effective value of the ATP synthesized/O_2 consumed ratio (not to be confused with the ATP/O_2 ratio calculated for complete oxidation) is 5.4 for glucose and 5.7 for glycogen, which is higher than those ratios calculated for oleate (5.0) and lactate (4.8). The higher ATP yield with glycogen during periods of high energy demand provides a potential explanation for why the heart adopts the strategy of preferential increase in carbohydrate oxidation to deal with increased energy demand. From Goodwin et al. with permission [9]

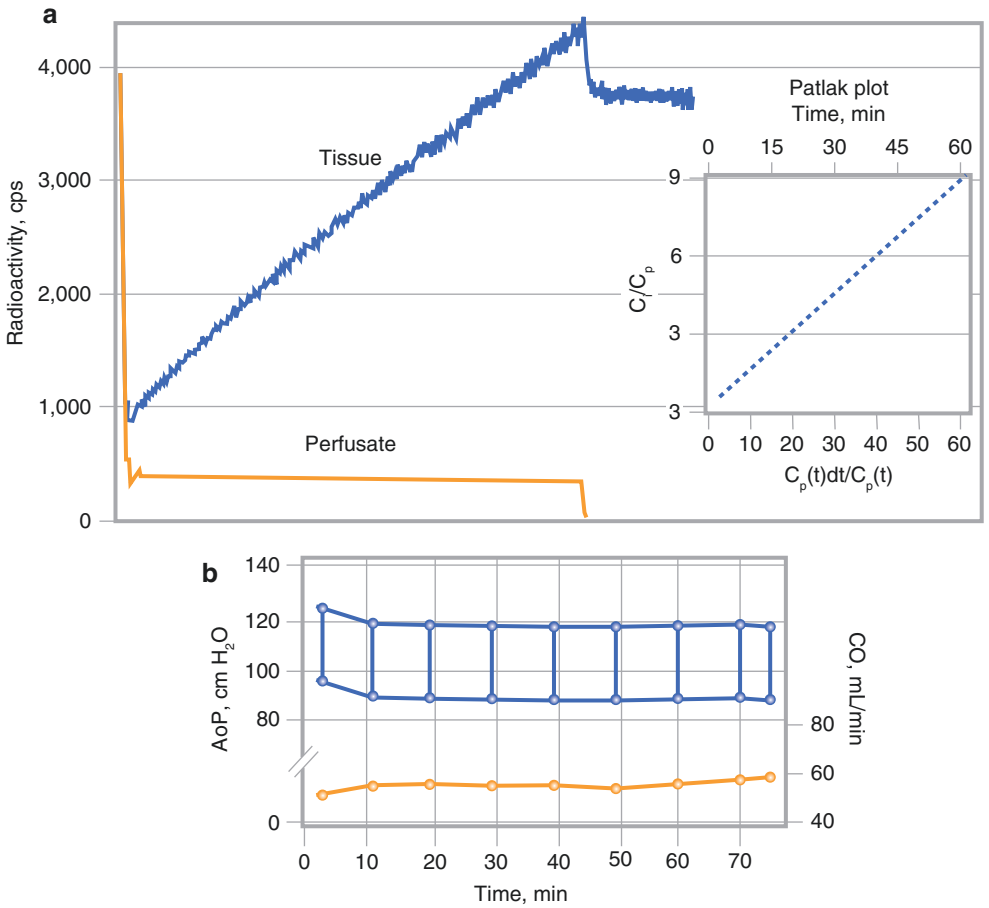

Fig. 9.7 Direct evidence that fluorodeoxyglucose (FDG) uptake traces glucose metabolism and that FDG is retained by the tissue in proportion to the rate of glucose utilization. The underlying premise of FDG PET imaging is that FDG behaves similarly to the traced substrate (glucose) with respect to facilitated transport across the sarcolemma and subsequent intracellular phosphorylation by hexokinase. The time-activity curves shown were obtained in an isolated working rat heart (afterload = 100 cm H_2O; preload = 15 cm H_2O) with Krebs–Henseleit saline containing glucose (10 mM) and FDG (350 μCi/200 mL perfusate) for the first 60 minutes. After an initial phase of tracer equilibrium (**a**), the myocardial uptake of FDG is linear (*top curve*), whereas tracer activity in the perfusate remains constant (*bottom curve*). Graphical analysis of the myocardial and perfusate FDG concentrations acquired between 5 and 60 minutes by Patlak analysis (*inset* in **a**) shows a linear plot from 20 to 60 minutes. Aortic pressures (AoP)and cardiac output (CO) are stable throughout the experiment (**b**). At 60 minutes, when the perfusion medium was changed to a buffer containing no tracer, radioactivity in the tissue fell abruptly and then remained stable for the duration of the washout period. The phenomena described above indicate clearance of the radiotracer from the heart chambers and the vascular and extracellular spaces, as well as metabolic trapping of FDG. Not shown in the figure is that tissue accumulation of FDG decreased with a reduction in work load and with the addition of competing substrates, and that insulin caused a significant increase in FDG accumulation in hearts from fasted (but not from fed) animals. These data confirm the utility of FDG to assess myocardial glucose metabolism in the clinical setting by showing that tissue uptake and retention of the tracer in the isolated working rat heart responds to physiologic interventions in the same way as glucose. Adapted from Nguyen et al. with permission [10]

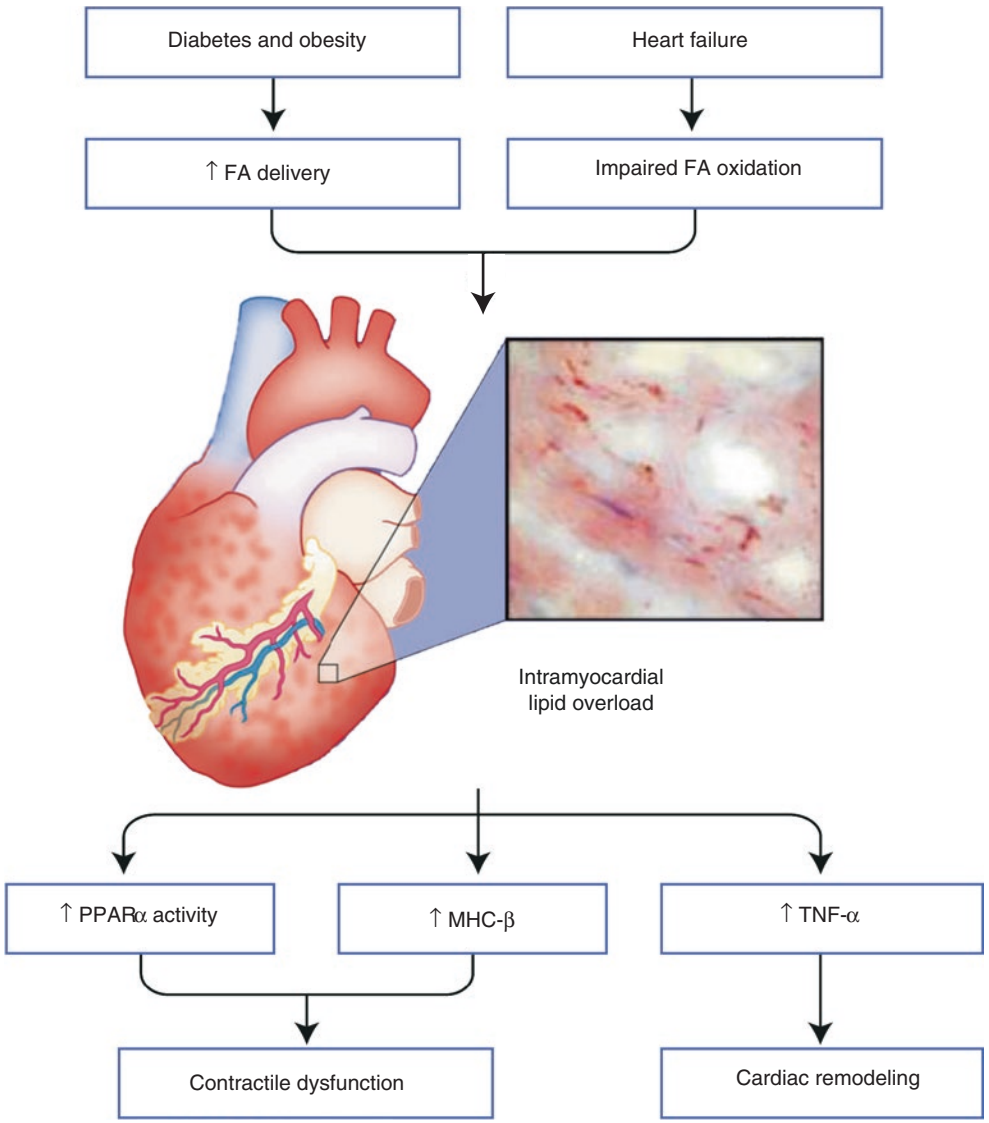

Fig. 9.8 Myocardial lipid accumulation in heart failure and diabetes. Left ventricular dysfunction in patients with diabetes and/or obesity or heart failure is associated with altered metabolism independent of the presence of underlying coronary artery disease. Although patients with a similar glycemic control (HbA1c) may have dramatically different rates of left ventricular dysfunction, both increased fatty acid (FA) delivery (e.g., diabetes, obesity) or impaired fatty acid (FA) oxidation (e.g., heart failure) result in severe intramyocardial triglyceride accumulation. Triglycerides are like a "canary in the coal mine" reflecting a host of other lipotoxic intermediates, including oxygen-derived free radicals, diacylglycerol, and ceramide. An oil-red-O stain of triglycerides is shown in failing heart muscle [11]. MHC-β myosin heavy chain-β, PPARα peroxisome proliferation-activated receptor α, TNF-β tumor necrosis factor-β

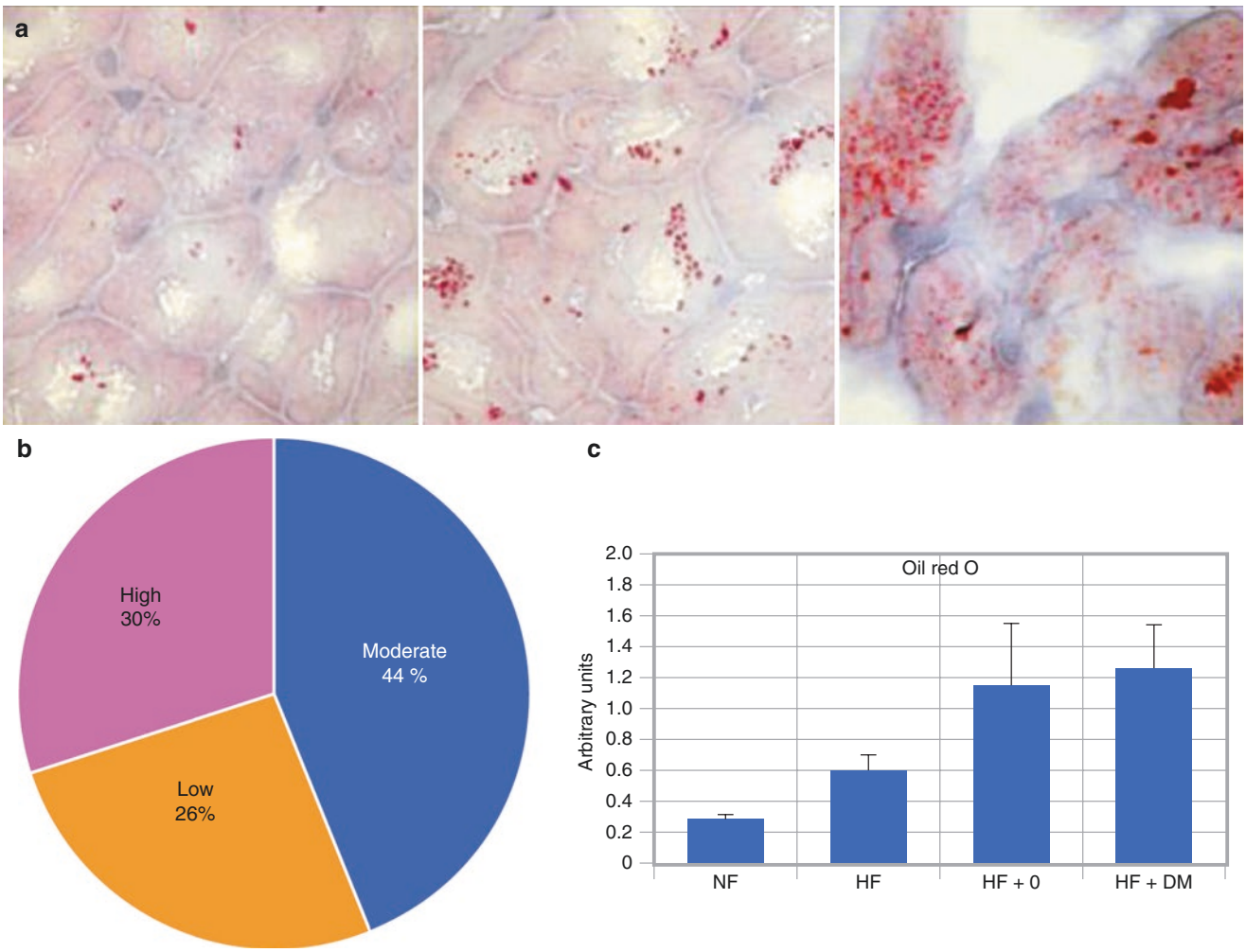

Fig. 9.9 Intramyocardial triglyceride overload. Intramyocardial triglyceride overload and changes in gene expression are associated with contractile left ventricular dysfunction in patients with nonischemic heart failure. (**a**) Low, intermediate, and high intramyocardial lipid accumulation can be appreciated histologically in heart tissue samples from these patients. (**b**) In a study of 27 nonischemic failing hearts, high amounts of intramyocardial lipid overload were present in 30% of hearts. (**c**) The highest levels of lipid staining were observed in the hearts of patients with heart failure (HF) with coexisting diabetes mellitus (DM) or obesity (O, body mass index >30). Intramyocardial lipid deposition was associated with an upregulation of peroxisome proliferation-activated receptor (PPAR) α–regulated genes, myosin heavy chain-β, and tumor necrosis factor-α. Intramyocardial lipid overload is a relatively common finding in nonischemic heart failure and is associated with a distinct gene expression profile that is similar to an animal model of lipotoxicity and cardiac dysfunction. Metabolic imaging may play an important role for detecting subclinical disease early in the process of left ventricular dysfunction and/or remodeling. Early identification may be more amenable to medical therapies such as PPAR agents, insulin, and fish oil analogues, and in prevention [11]. NF nonfailing. Adapted from Sharma et al. with permission [11]

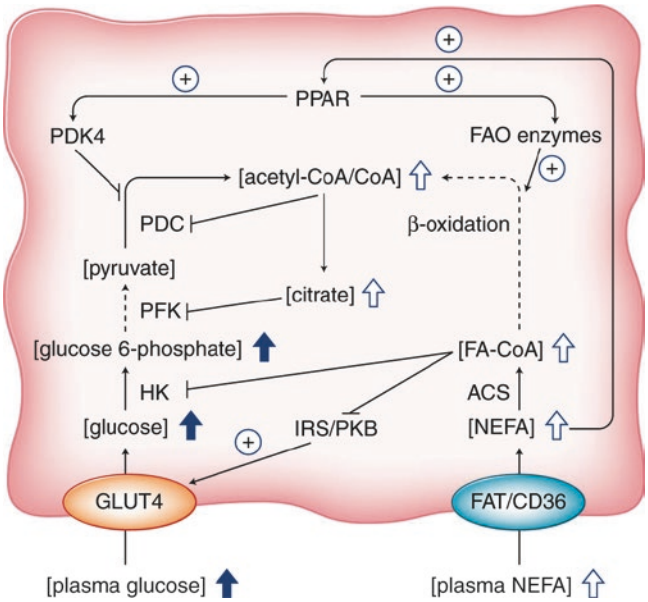

Fig. 9.10 Proposed mechanisms for fatty acid inhibition of glucose oxidation. During diabetes, levels of both plasma glucose and plasma nonesterified fatty acid (NEFA) are elevated. The latter results in increased intracellular levels of fatty acids (FAs) and their fatty acetyl-coenzyme A (FA-CoA) derivatives. FA-CoAs inhibit insulin-mediated glucose transport by inhibiting insulin receptor substrates (IRSs) and protein kinase B (PKB). FA-CoAs also can directly inhibit hexokinase (HK). Increased β-oxidation (due to increased substrate availability and increased gene expression of FA oxidation [FAO] enzymes via peroxisome proliferation-activated receptor [PPAR] activation) results in an increase in the mitochondrial acetyl-CoA/CoA ratio. The combined effects of increased PDK4 expression (induced through FA activation of PPAR) and an increased acetyl-CoA/CoA ratio severely inhibit the pyruvate dehydrogenase complex (PDC). In addition, the increased acetyl-CoA/CoA ratio promotes citrate efflux from the mitochondrion into the cytosol, where it is able to inhibit phosphofructokinase (PFK). Despite decreased insulin-mediated glucose transport, glucose uptake by the diabetic heart is comparable to uptake by the normal heart because of the hyperglycemia. Glycolytic intermediates therefore accumulate in the cardiomyocyte [12]

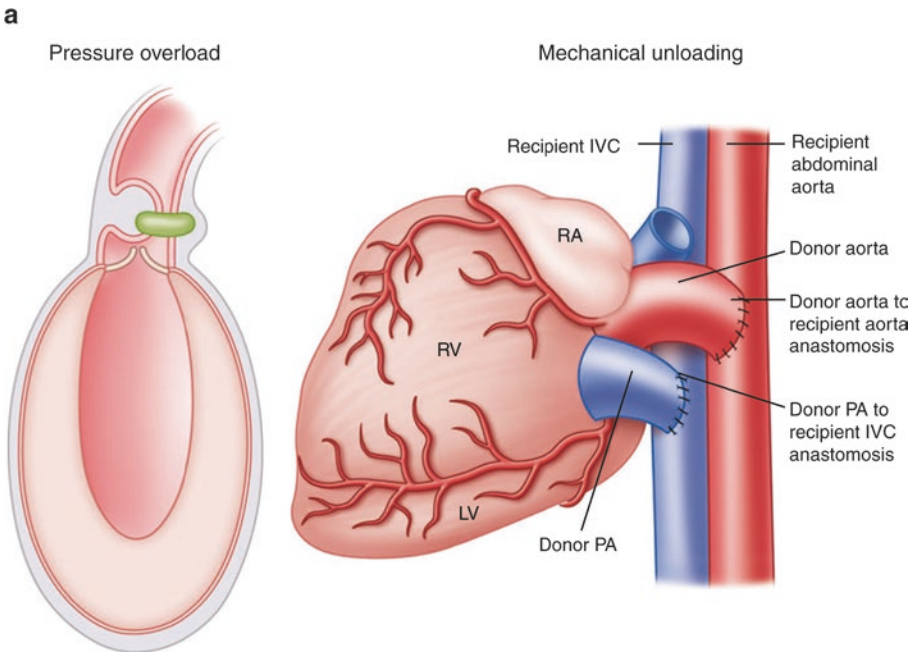

Fig. 9.11 Metabolic processes are transcriptionally regulated in response to chronic changes in the workload of the heart. (**a**) The change in cardiac mass by both pressure overload and ventricular unloading is a mechanism of adaptation accompanied by the reexpression of fetal genes. However, cardiac hypertrophy, if not treated, evolves to an uncompensated state of heart failure, whereas the process of atrophy induced by ventricular unloading rapidly stabilizes and shows no further progression thereafter. Therefore, unloading the failing heart reduces cardiac mass by a self-limited process and limits energy expenditure by preserving the expression of fetal isoforms of proteins that are regulating myocardial energetics. These mechanisms may explain the clinical improvement of patients with heart failure after treatment with a left ventricular assist device (LVAD), but the true mechanisms remain unknown. The process of unloading the heart with an LVAD is now used in clinical practice for patients with advanced heart failure awaiting heart transplantation; mechanical unloading may improve cardiac function to an extent that makes transplantation no longer necessary. Such improvement results from a better contractile performance of the myocytes after LVAD intervention, which indicates that mechanical unloading *in vivo* affects the expression of genes coding for contractile proteins and/or metabolic enzymes. These clinical results prompted investigators to assess the molecular response of the heart to unloading [13]. (**b**) The *top two panels* show the changes in left ventricular mass (lung volume/body weight [LV/BW] ratio) in response to pressure overload and unloading. The *lower panels* show the expression of α myosin heavy chain (αMHC), β MHC, SERCA 2a, and SK α-actin in (1) hypertrophied hearts compared with hearts from sham-operated rats and (2) unloaded hearts compared with control hearts up to 28 days after transplantation. Data are reported as the number of mRNA transcripts per number of 36B4 molecules (constitutive housekeeping gene product). Both conditions induced a reexpression of growth factors and proto-oncogenes, as well as a downregulation of the "adult" isoforms but not of the "fetal" isoforms, of proteins regulating myocardial energetics. Therefore, opposite changes in the cardiac workload *in vivo* induce similar patterns of gene response. Ctrl—control; SERCA 2a—sarcoplasmic/endoplasmic reticulum Ca^{2+}ATPase 2a. (*From* Depre et al. [13]; with permission from Springer Nature)

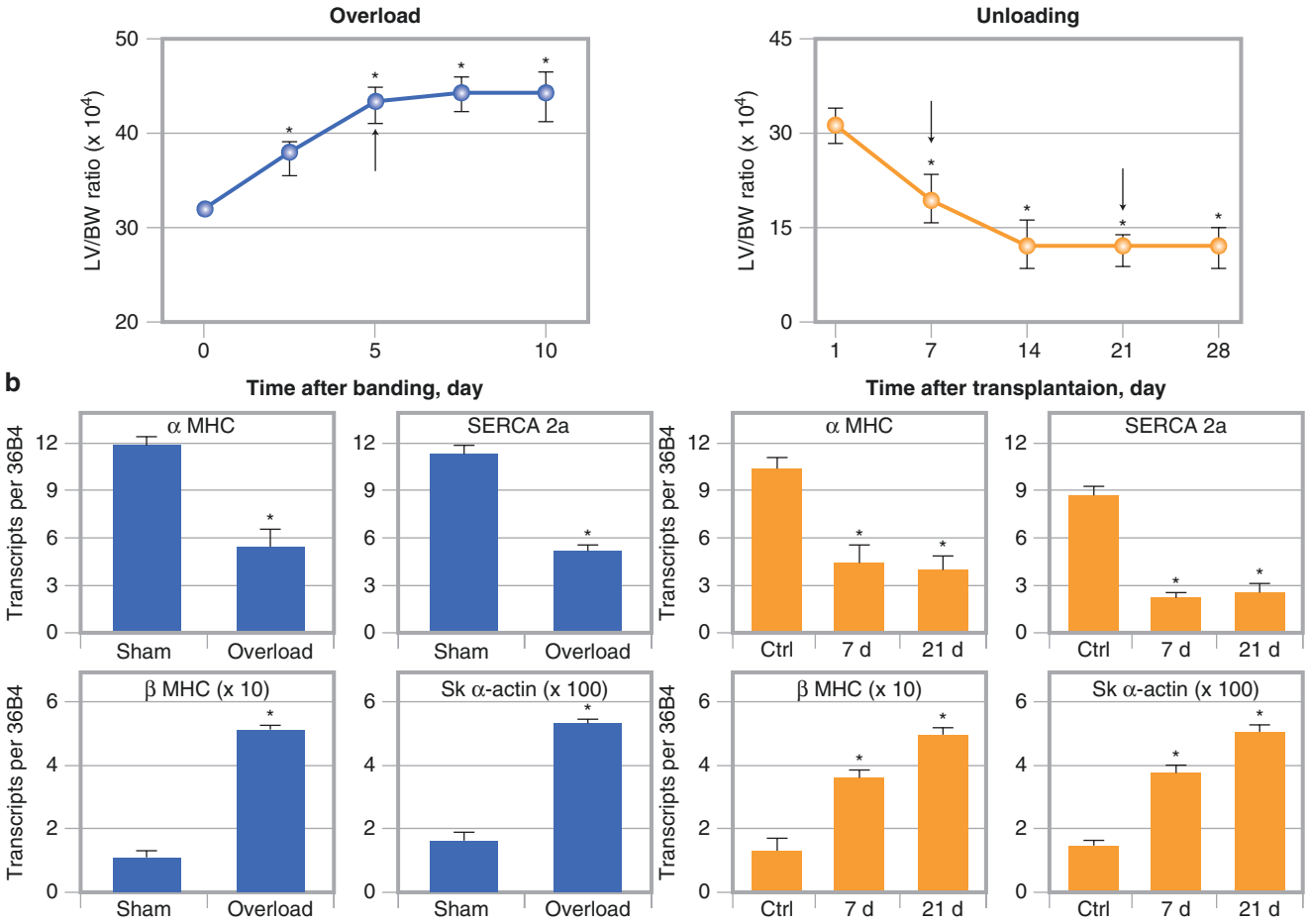

Fig. 9.11 (continued)

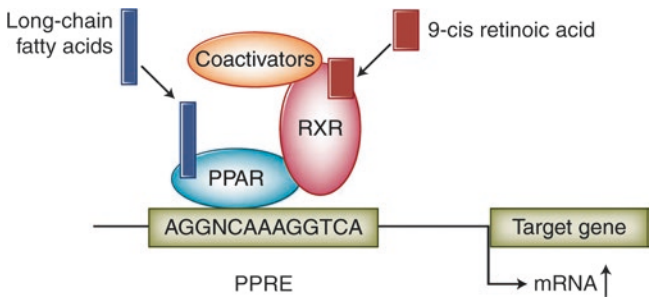

Fig. 9.12 Peroxisome proliferation-activated receptor (PPAR)-α activation of target metabolic genes as an example for the ligand activation of a nuclear receptor by long-chain fatty acids. PPARα, a transcription factor that modulates fatty acid metabolism, regulates substrate preference in the heart. In acute ischemia, there is a switch in substrate preference from fatty acids to glucose, but in response to repetitive ischemia, there is a reversible downregulation of the genes that modulate fatty acid metabolism and myosin heavy chain isoforms in the heart. When fatty acid metabolism is pharmacologically reactivated in hearts exposed to repetitive ischemia, there is worsening of contractile function, microinfarctions, and triglyceride accumulation within cardiomyocytes. These findings suggest that downregulation of fatty acid metabolic gene expression in the hibernating myocardium is an adaptive mechanism. Furthermore, modulating the myocardial metabolism may provide a pharmacologic target for cardiac protection in repetitive ischemia. Further phenotypic characterization of genetic variables such as PPAR may play an important role in the future for drug development and individualized medicine [14]. PPRE peroxisome proliferator response element, RXR retinoid X receptor. Adapted from Sharma et al. with permission [11]

Clinical Application of Myocardial Metabolism: PET and SPECT Techniques

PET Techniques: ^{11}C-Palmitate

The principle of using a metabolic tracer for myocardial imaging is based on the concept that viable myocytes in hypoperfused and dysfunctional regions are metabolically active, whereas scarred or fibrotic tissue is metabolically inactive. Under fasting and aerobic conditions, long-chain fatty acids are the preferred fuel in the heart; they supply 65–70% of the energy for the working heart, and approximately 15–20% of the total energy supply comes from glucose. Thus, early studies have focused on using PET to characterize the myocardial kinetics of the long-chain fatty acid tracer ^{11}C-palmitate. Uptake of ^{11}C-palmitate by the heart is dependent on regional perfusion, diffusion across the sarcolemmal membrane, transporter protein, and acceptance in the cytosol by binding to coenzyme A (CoA). In normally perfused myocardium, the extraction fraction of ^{11}C-palmitate is 40%. Transported across the sarcolemma by a transporter protein (CD36) of long-chain fatty acid, the myocyte fatty acids are bound to a binding protein. Metabolic activation of ^{11}C-palmitate occurs through attachment to CoA. Depending on demand, about 80% of the extracted ^{11}C-palmitate is activated for transport from the lipid pool into the mitochondria (via the carnitine shuttle) for breakdown by β-oxidation, which results in the generation of carbon dioxide that appears in the venous effluent of the coronary circulation in less than a minute after ^{11}C-acyl-CoA transfers into the mitochondria (Fig. 9.13). Following is a summary of the PET technique:

- Image acquisition starts at 15–20 mCi bolus injection of the tracer and continues 40–60 minutes.
- Initial uptake and distribution in the myocardium is determined primarily by regional blood flow.
- In the cytosol, ^{11}C-palmitate is esterified to ^{11}C-acyl-CoA, which is mediated by thiokinase, an energy-dependent reaction, resulting in trapping of the tracer in the myocardium.
- Thereafter, ^{11}C-acyl-CoA either enters the endogenous lipid pool as ^{11}C glycerides and ^{11}C phospholipids or moves via the carnitine shuttle to the mitochondria, where rapid degradation by β-oxidation results in the generation of carbon dioxide.

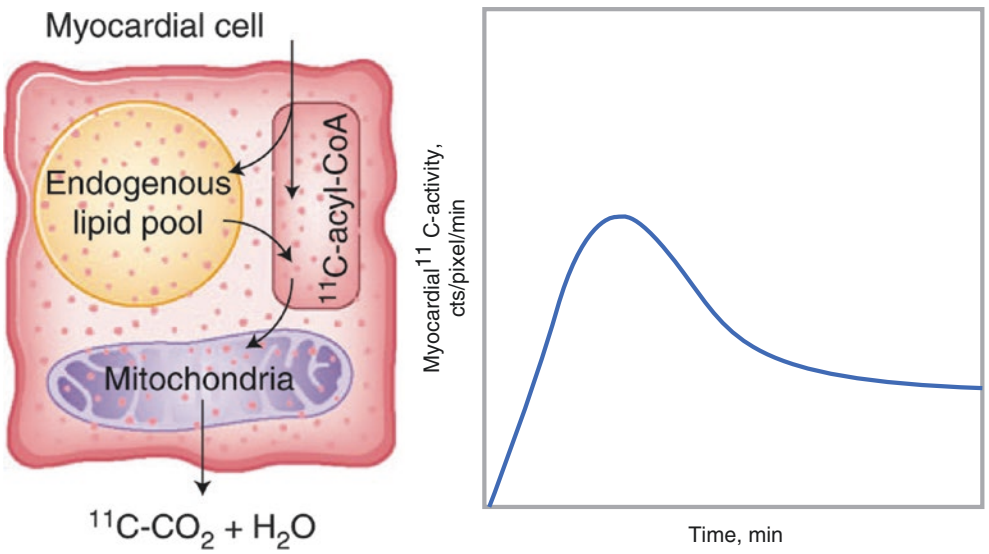

Fig. 9.13 PET of ^{11}C-palmitate. External measurement by dynamic PET imaging allows the observation of tracer inflow, peak accumulation, and release of the tracer within a particular region of interest in the myocardium. Fatty acid imaging with radioiodine-labeled fatty acid analogues such as ^{123}I-BMIPP using SPECT is also possible [15]

SPECT Technique: ^{123}I-BMIPP

Alterations in myocardial fatty acid metabolism were first evaluated noninvasively in humans using ^{11}C-palmitate, which requires an onsite cyclotron and a PET camera. Because most nuclear cardiology laboratories are equipped with SPECT cameras, investigators subsequently focused their attention on developing gamma-emitting fatty acid tracers. In contrast to palmitate, β-methyl-p-^{123}I-iodophenyl-pentadecanoic acid (^{123}I-BMIPP) is an iodine-labeled, methyl branched-chain fatty acid that is predominantly trapped in myocardial cells with limited catabolism. Uptake of BMIPP from the plasma into myocytes occurs via the CD36 transporter protein present on the sarcolemmal membrane (Fig. 9.14). Once in the cell, BMIPP will either back-diffuse to the plasma, accumulate in the lipid pool, or undergo limited α- and β-oxidation. Enzymatic conversion of BMIPP to BMIPP-CoA or triacylglycerol in the myocyte is ATP-dependent and is an irreversible step. Such conversion prevents the back-diffusion of BMIPP to the plasma and facilitates its cellular retention. The prolonged retention of BMIPP in the myocardium, combined with rapid clearance from the blood and diminished uptake in the liver and lung, results in excellent visualization and imaging of the myocardium by SPECT techniques. Thus, BMIPP provides a means of measuring myocardial fatty acid utilization *in vivo*. In the setting of myocardial ischemia, a reduction in ATP production secondary to diminished fatty acid metabolism is mirrored by decreased myocardial BMIPP uptake. BMIPP is approved for clinical use in Japan, but it has not yet received approval by the US FDA.

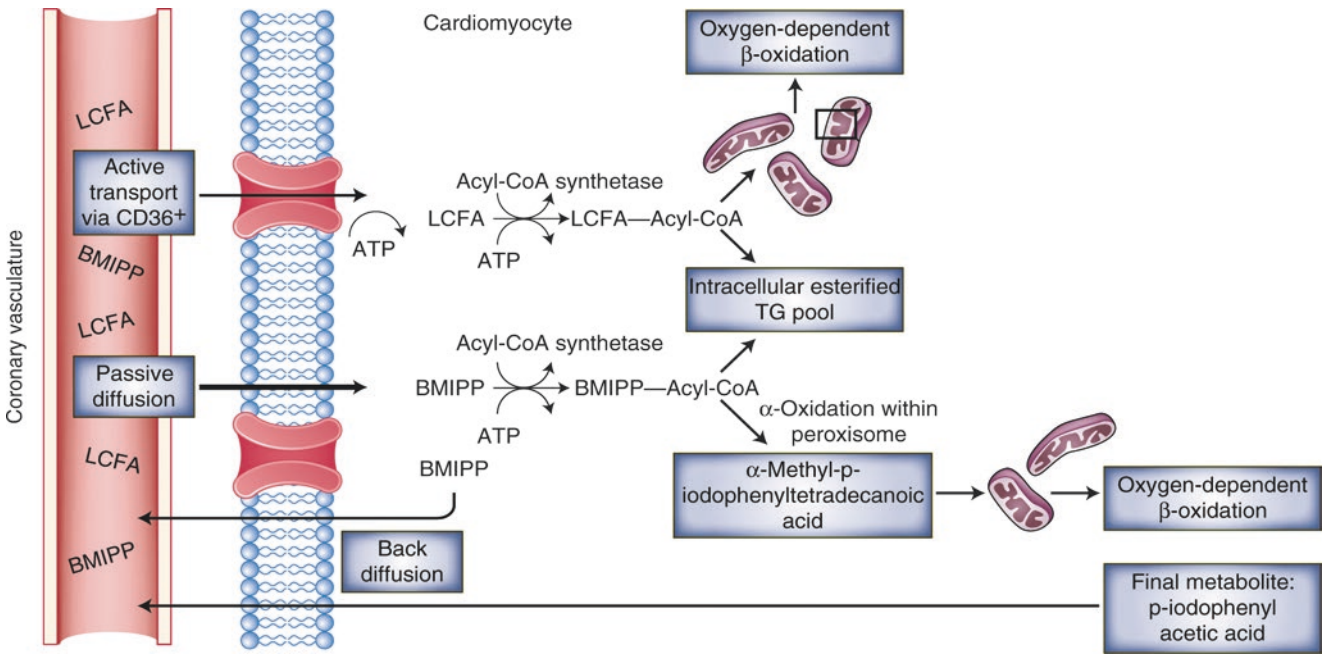

Fig. 9.14 Major metabolic pathways and regulatory steps of BMIPP in the myocyte. Under normoxic conditions, the myocardium preferentially oxidizes long-chain fatty acids (LCFAs) to generate ATP. Fatty acids enter the endothelial cell via diffusion or active transport through integral CD36+ membrane-bound proteins. The ATP-dependent activation of fatty acids by acyl-CoA synthetase involves its transformation to acyl-CoA moieties that can then undergo β-oxidation in the mitochondria. The majority of LCFA-acyl-CoA derivatives are metabolized via β-oxidation, whereas the remainder of the acyl-CoA and acyl moieties are incorporated into the intracellular esterified triglyceride (TG) pool. BMIPP, however, is not initially metabolized by β-oxidation because the methyl substitution precludes the formation of the keto-acyl-CoA intermediate. BMIPP must first undergo an obligatory initial α-oxidation conversion step in the cytosol or primarily the peroxisome, to α-methyl-p-iodopheny-tetradecanoic acid (AMIPT). AMIPT is metabolized by rounds of β-oxidation in the mitochondria to the end product, 2-(p-[^{123}I-iodophenyl) acetic acid, which does not accumulate intracellularly. BMIPP appears to be primarily activated (esterified-CoA) in the cytosol and incorporated into triglyceride storage products into the endogenous lipid pool (70%). BMIPP, if not activated, can undergo early washout back into the bloodstream [16]

PET Technique: ^{11}C-Acetate

^{11}C-acetate is a short-chain fatty acid that is avidly extracted by the myocardium, with a first-pass extraction of 63% at blood flows of 1 mL/g/min. It is metabolized predominantly by mitochondrial oxidation. Once in the cytosol, the tracer is converted to acetyl-CoA by acetyl-CoA synthetase and is oxidized by the Krebs cycle in the mitochondria to ^{11}C-carbon dioxide and water. Thus, the washout rate of ^{11}C-acetate from myocardium is directly related to the oxidative metabolism. Given the close link between the Krebs cycle and oxidative phosphorylation, the myocardial turnover and clearance of ^{11}C-acetate in the form of ^{11}C-carbon dioxide may reflect overall oxidative metabolism and provide insight into the mitochondrial function of viable myocardium (Fig. 9.15). Alternative metabolic pathways of ^{11}C-acetate include incorporation into amino acids, ketone bodies, and fatty acids by de novo synthesis or chain elongation, but these latter pathways are thought to be modest and unlikely to compromise estimation of regional myocardial oxygen consumption per minute.

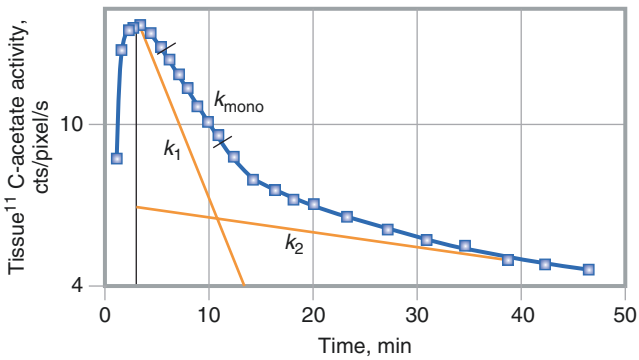

Fig. 9.15 Myocardial ^{11}C-acetate tissue time–activity curve demonstrating biexponential clearance of the tracer from myocardium. Monoexponential fitting of the early portion of the clearance phase yields the slope k_{mono}, while biexponential least-square fitting of the clearance phase yields k_1 and k_2 slopes. The rapid phase of clearance (k_1) represents oxidation of extracted ^{11}C-acetate by the mitochondria to ^{11}C-carbon dioxide, and the slower phase of clearance (k_2) represents the incorporation of ^{11}C-acetate into amino acids and other alternative metabolic pathways. In patients with recent myocardial infarction and chronic stable angina, the preservation of myocardial oxidative metabolism is shown to predict functional recovery after revascularization [17, 18]. When clearance rates of ^{11}C-acetate are within two standard deviations of the normal mean, the positive predictive accuracy for recovery of function after revascularization is 84% in patients with recent myocardial infarction and 79% in patients with chronic stable angina. Conversely, when clearance rates of ^{11}C-acetate are more than two standard deviations below the normal mean, the negative predictive values are 70% in patients with recent myocardial infarction and 83% in patients with chronic stable angina [19]

PET and SPECT Techniques: ^{18}F-FDG

^{18}F-fluorodeoxyglucose (FDG) is a glucose analogue used to image myocardial glucose utilization with PET. Following an intravenous injection of 5–10 mCi FDG, FDG rapidly exchanges across the capillary and cellular membranes and is phosphorylated by hexokinase to FDG-6-phosphate. Once phosphorylated, FDG is not metabolized further in the glycolytic pathway, fructose-pentose shunt, or glycogen synthesis. Because the dephosphorylation rate of FDG is slow, essentially it becomes trapped in the myocardium, allowing adequate time to image regional glucose uptake by PET or SPECT. In the fasting and aerobic conditions, fatty acids are the preferred source of myocardial energy production, with glucose accounting for some 15–20% of the total energy supply. In the fed state, however, plasma insulin levels increase, glucose metabolism is stimulated, and tissue lipolysis is inhibited, resulting in reduced fatty acid delivery to the myocardium. The combined effects of insulin on these processes and the increased arterial glucose concentration associated with the fed state result in preferred glucose utilization by the myocardium. Myocardial FDG uptake is influenced by metabolic and hormonal milieu, workload, and blood flow.

The diagnostic quality of FDG imaging is critically dependent on a number of factors, such as hormonal milieu, substrate availability, and regional blood flow [20]. This becomes particularly evident when studying patients with clinical or subclinical diabetes. Most clinical studies are performed after 50–75 g glucose loading with oral dextrose approximately 1–2 hours before the FDG injection. Although 90% of FDG images are of adequate to excellent diagnostic quality in nondiabetic patients, the quality of FDG images after glucose loading is less certain in patients with clinical or subclinical diabetes mellitus. Because the increase in plasma insulin levels after glucose loading may be attenuated in patients with diabetes mellitus, tissue lipolysis is not inhibited and free fatty acid levels in the plasma remain high. The quality of FDG images in diabetics may be optimized by the use of standardization schemes:

- Intravenous bolus of regular insulin
  - Most common and clinically feasible approach
  - Regular insulin is administered according to plasma glucose level and a predetermined sliding scale.
  - Plasma glucose level is assessed every 15 minutes, with the administration of additional boluses of insulin, if necessary.
  - FDG dose is injected once the plasma glucose level is below 140 mg/dL.
- Hyperinsulinemic–euglycemic clamping
  - Insulin and glucose are infused simultaneously to achieve a stable plasma insulin level of 100–120 IU/L and a normal plasma glucose level.
  - The rate of glucose infusion (20% dextrose solution with potassium chloride) is adjusted intermittently based on measured glucose levels.
  - Although it provides excellent image quality, this technique is rather tedious and impractical for routine clinical studies.
- Use of nicotinic acid derivative
  - Approximately 2 hours before the FDG dose injection, a single dose of nicotinic acid derivative is given orally, followed by glucose loading.
  - FDG image quality is comparable to that obtained after the clamping technique in the same patient population.

Metabolic Pathways and Patterns

The major metabolic pathways, as outlined in Fig. 9.16, offer opportunities to evaluate myocardial perfusion patterns with the use of PET and SPECT imaging and other techniques to find subclinical defects and determine whether myocardium remains viable after ischemia or infarction (Figs. 9.17, 9.18, 9.19, 9.20, 9.21, 9.22, 9.23, 9.24, 9.25, 9.26, and 9.27). An advantage of PET is that it can be safely performed in patients with an implanted cardiac defibrillator or renal insufficiency.

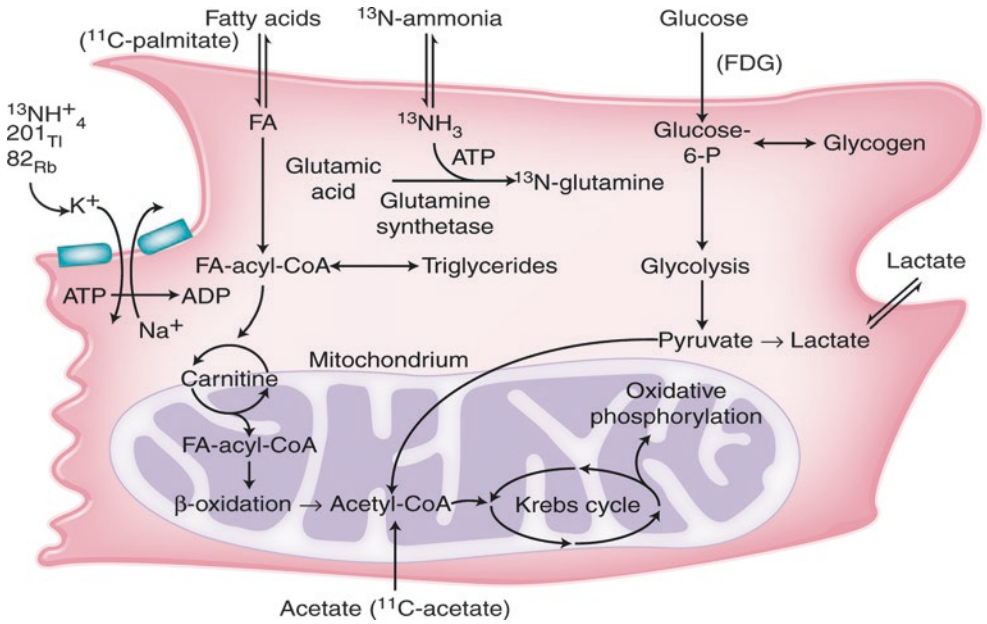

Fig. 9.16 Major metabolic pathways and regulatory steps of a myocyte. Breakdown of fatty acids in the mitochondria via β-oxidation is exquisitely sensitive to oxygen deprivation. Therefore, in the setting of reduced oxygen supply, the myocytes compensate for the loss of oxidative potential by shifting toward greater utilization of glucose to generate high-energy phosphates. Glycolysis occurs in the cytoplasm under anaerobic conditions and leads to the formation of pyruvate. For every mol of glucose metabolized through glycolysis, 2 mol of ATP are generated (anaerobic condition), and 36 mol of ATP are generated from pyruvate entering the Krebs cycle rate in the mitochondria. Protons are generated for oxidative phosphorylation. Because glycolysis can generate ATP under anaerobic conditions, glycolysis becomes an attractive alternate metabolic pathway for ATP generation in a hypoperfused myocardium with a limited supply of oxygen. Although the amount of energy produced by glycolysis may be adequate to maintain myocyte viability and preserve the electrochemical gradient across the cell membrane, it may not be sufficient to sustain contractile function. In hibernation, the adaptive response of the myocardium in the setting of prolonged resting hypoperfusion (reduced oxygen supply) is a reduction in myocardial contractile function (reduced oxygen demand), thereby preserving myocardial viability in the absence of clinically evident ischemia [21]

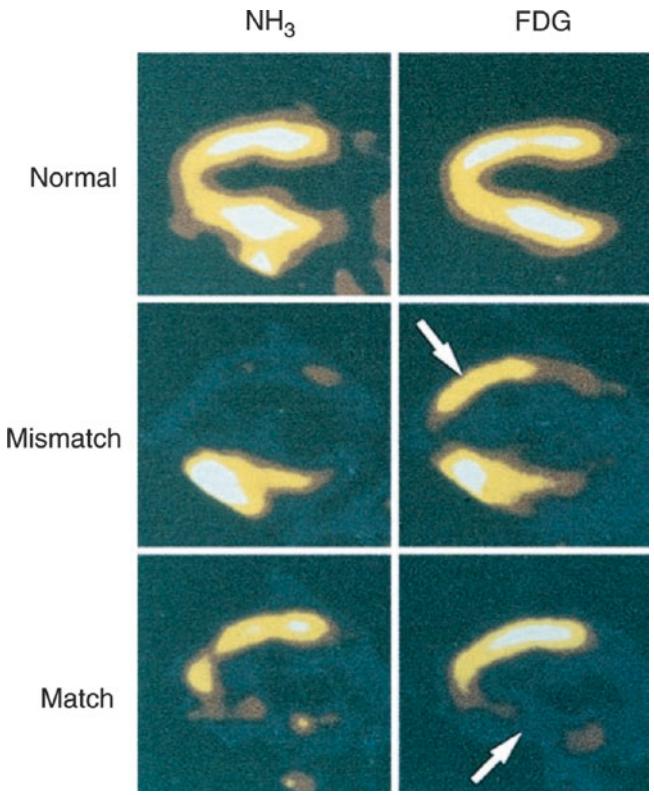

Fig. 9.17 Myocardial perfusion/metabolism PET Scans. Patterns of normal, mismatch, and match under glucose loading. Preserved or increased myocardial glucose utilization in the setting of prolonged hypoperfusion at rest is termed a *mismatch pattern*. In the NH_3 images, there is severely reduced blood flow in the anterior and lateral regions, but these have preserved metabolism in the FDG image (*arrow*), consistent with myocardial viability. Reduced or absent myocardial glucose utilization in hypoperfused myocardial regions is termed a *match pattern*. In the NH_3 images, there is severely reduced blood flow in the inferior region, which has absent myocardial metabolism in the FDG image (*arrow*), consistent with scarred myocardium. The application of such PET patterns in patients with chronic ischemic left ventricular dysfunction confers high positive and negative predictive accuracies for the recovery of regional function after revascularization, with an overall accuracy between 80% and 90% [22]. Clinically meaningful increases in global left ventricular function after revascularization are best attained if the extent of hibernating and stunned myocardium is at least 17–25% of the left ventricular mass [23]. (*Courtesy of* Dr. James Arrighi)

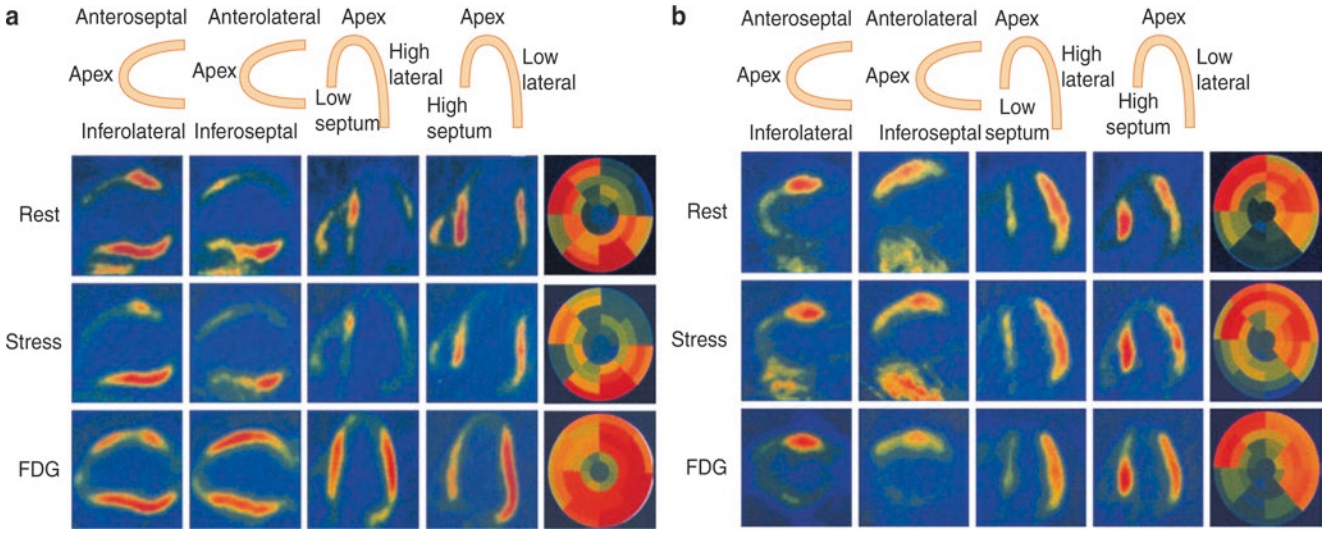

Fig. 9.18 Examples of PET mismatch and match patterns. Increased FDG uptake in asynergic myocardial regions with reduced blood flow at rest (a mismatch pattern) has become a scintigraphic marker of hibernation. (**a**) A patient with a severely dilated left ventricle, diffuse hypokinesis, and apical dyskinesis (left ventricular ejection fraction [LVEF], 12%) had severe triple vessel disease. A coronary angiogram revealed a 100% occlusion of the proximal left anterior descending (LAD) coronary artery, D1, and D2; subtotal occlusion of the proximal right coronary artery (RCA); and a 90% OM1 occlusion. In this patient, four long-axis slices (two horizontal long-axis and two vertical long-axis images) encompassing the entire left ventricle along with corresponding bull's-eye images for rest and stress ^{13}N-ammonia and FDG uptake are shown. Rest ^{13}N-ammonia images show irreversible defects in the apical and anterolateral regions, with partial reversibility in the anterior and inferoseptal regions. Stress ^{13}N-ammonia images show markedly decreased perfusion in the apical, anterior, anterolateral, and inferoseptal regions. However, FDG images acquired under glucose-loaded conditions show preserved or increased glucose utilization in all abnormally perfused myocardial regions at rest, which is the scintigraphic hallmark of hibernation. In patients with chronic ischemic left ventricular dysfunction, rest and stress myocardial perfusion images alone may significantly underestimate the presence and extent of hibernating but viable myocardium. (**b**) Decreased or absent FDG uptake in asynergic myocardial regions with reduced blood flow at rest (a match pattern) represents scarred myocardium. A patient with previous coronary bypass surgery presented with a significantly dilated left ventricle, apical dyskinesis, septal and inferior akinesis (LVEF, 36%), and congestive heart failure. A coronary angiogram revealed severe native disease of all three vessels, patent left and right internal mammary grafts to the LAD and RCA, critical stenoses of the OM1 vein graft, and a patent OM2 vein graft. In this patient, rest and stress ^{13}N-ammonia images show irreversible defects in the inferior, apical, and inferoseptal regions. FDG images acquired under glucose-loaded conditions show the absence of glucose utilization in all abnormally perfused myocardial regions at rest. Such asynergic myocardial regions, demonstrating matched reduction in perfusion and metabolism, represent scarred myocardium that is unlikely to recover function after revascularization

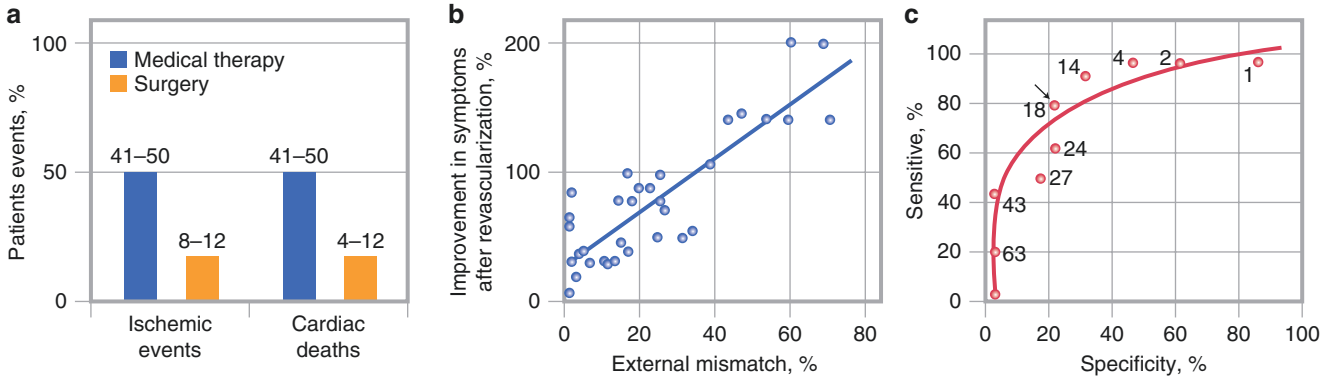

Fig. 9.19 PET mismatch and prognosis. The prognostic significance of a perfusion–metabolism mismatch pattern in ischemic cardiomyopathy has been shown in a number of nonrandomized, retrospective studies with PET [24, 25]. (**a**) Patients with a perfusion-metabolism mismatch pattern who were treated surgically had lower ischemic event rates and fewer deaths than those treated with medical therapy. In contrast, patients with a perfusion-metabolism match pattern displayed no such difference in outcomes between surgical and medical management. Moreover, the patients with myocardial viability (a mismatch pattern) who underwent revascularization manifested a significant improvement in heart failure symptoms and exercise tolerance [26, 27]. (**b**) The relation between the anatomic extent of a perfusion metabolism PET mismatch pattern (expressed as a percentage of the left ventricle) and the change in functional status after revascularization (expressed as a percent improvement from baseline) is shown. This scatterplot shows that the greatest improvement in heart failure symptoms occurs in patients with the largest mismatch defects in the quantitative analysis of PET images. (**c**) A receiver-operating characteristic curve is shown for the different anatomic extent of a perfusion-metabolism mismatch to predict a change (at least one grade) in functional status after revascularization. When the extent of PET mismatch involves 18% or more of the left ventricular mass, the sensitivity for predicting a change in the functional status after revascularization is 76%, and the specificity is 78% (the area under the fitted curve = 0.82)

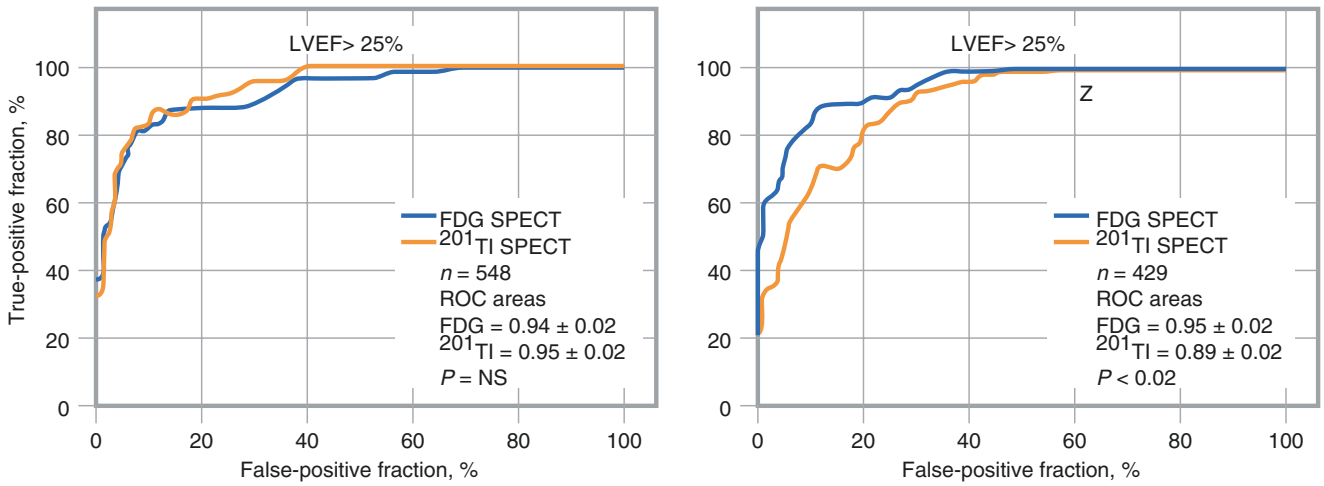

Fig. 9.20 SPECT and PET with coronary artery disease. In patients with chronic coronary artery disease, differences between high-energy collimator SPECT and PET technologies and FDG and ^{201}Tl tracers are examined for their ability to differentiate between viable and nonviable myocardium. Shown are plots of receiver-operating characteristic (ROC) curves for ^{201}Tl and FDG SPECT to predict myocardial viability as defined by a 60% FDG PET threshold value for patients with left ventricular ejection fraction (LVEF) above 25% (*left*) and for patients with LVEF 25% or less (*right*). The area under the ROC curve for FDG SPECT and ^{201}Tl SPECT are displayed for each panel. ^{201}Tl tends to underestimate the myocardial viability in patients with LVEF of 25% or less, but not in patients with LVEF above 25%. Of the severe asynergic regions, 73% of discordant regions between ^{201}Tl and FDG PET were located in the inferior segment, compared with only 27% of regions with concordance between ^{201}Tl and FDG PET (P <0.001) [28]

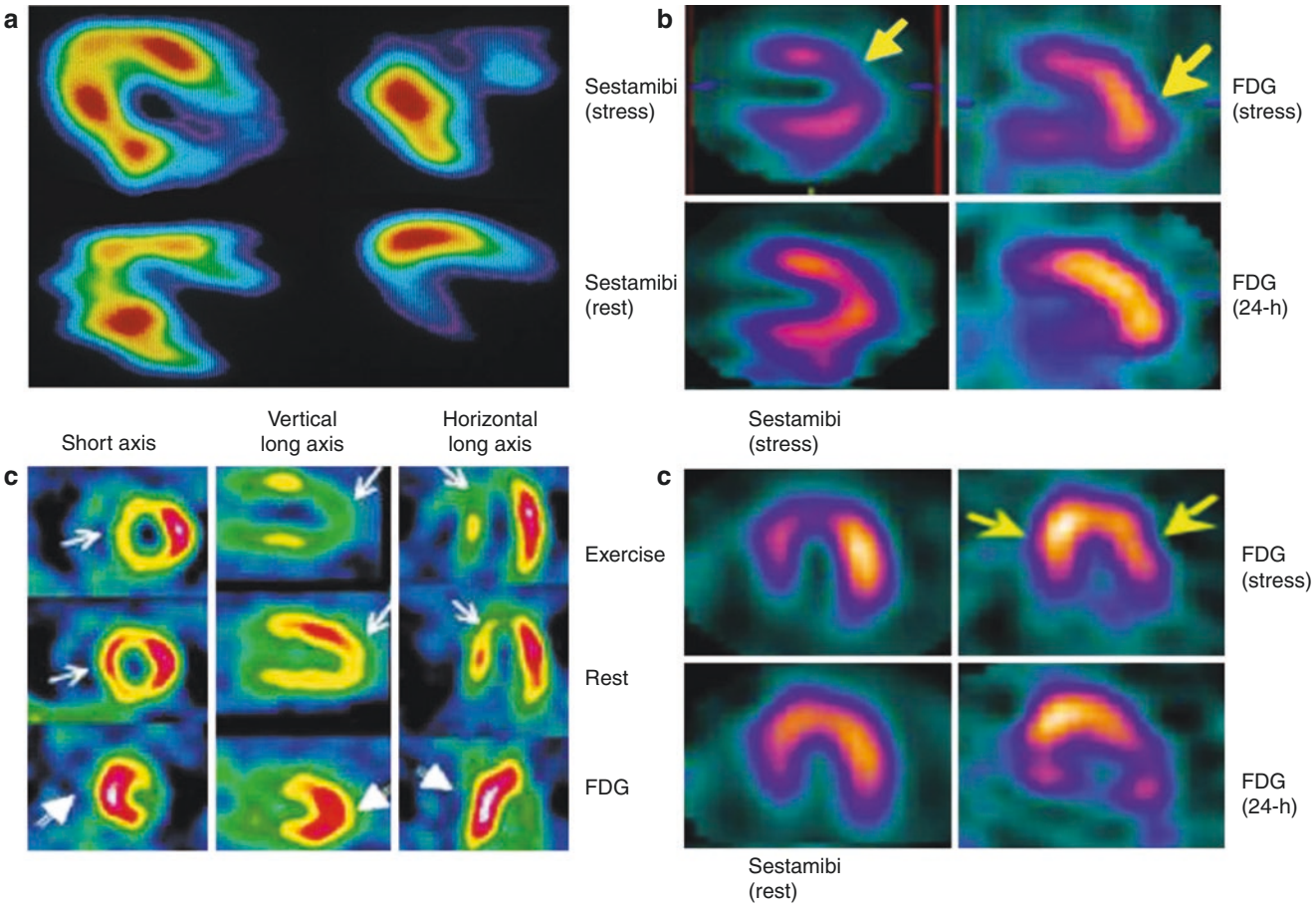

Fig. 9.21 Metabolic alterations in postischemic myocardium in patients with angina. Physical exercise is probably the most common precipitating factor responsible for myocardial ischemia in patients with coronary artery disease manifested as angina and, most importantly, left ventricular dysfunction (mismatch of supply and demand). Although the recovery of such stress-induced left ventricular dysfunction is thought to occur within minutes after the termination of exercise, persistent contractile dysfunction has been observed in some patients up to 90 minutes after the termination of exercise, which has been attributed to stunned myocardium. (**a**) Transaxial rubidium-82 (^{82}Rb) PET images reflecting myocardial blood flow at rest, during exercise, and after exercise are shown along with FDG images after exercise. At rest (*top left*), the distribution of myocardial blood flow is homogeneous in all myocardial regions. During exercise (*top right*), there are extensive blood flow abnormalities in the apical and anteroseptal regions that improve on the postexercise images (*bottom left*) and are comparable to the ^{82}Rb rest image (*top left*). FDG was injected 8 minutes after the termination of exercise. The FDG image recorded 60 minutes after tracer injection (*bottom right*) shows metabolic alterations in the previously ischemic regions. (**b**) An example of perfusion/metabolism mismatch. Shown are simultaneous myocardial perfusion and metabolism imaging after dual intravenous injection of ^{99m}Tc-sestamibi and FDG at peak exercise. Dual isotope simultaneous acquisition was carried out 40–60 minutes after the exercise study was completed. Rest ^{99m}Tc-sestamibi imaging was carried out separately. In this patient with angina and no prior myocardial infarction, there is evidence for extensive reversible perfusion defects in the anterior, septal, and apical regions (*white arrows*). The coronary angiogram showed 90% stenosis of the left anterior descending artery and 60% stenosis of the left circumflex coronary artery. The corresponding FDG image shows intense uptake in the regions with reversible sestamibi defects, reflecting the metabolic correlate of exercise-induced myocardial ischemia. (**c, d**) A persistent metabolic switch from fatty acid to glucose 24 hours after the resolution of transient myocardial ischemia on a treadmill is shown. Exercise and rest ^{99m}Tc-sestamibi perfusion (*left*) and FDG (*right*) images are shown of a 71-year-old man with exertional angina in the vertical (**c**) and horizontal long-axis (**d**) views. Reversible perfusion abnormalities involving the anterior, apical, and septal regions (*yellow arrows*) are shown on sestamibi images with intense FDG uptake in the corresponding reversible anterior and septal regions. Rest FDG PET images acquired after the reinjection of FDG, 24 hours after the treadmill study (without interim exercise), shows persistent increased metabolic activity in the regions of the exercise-induced ischemia. This patient had 90% stenosis of the left anterior descending coronary artery. Thus, metabolism plays a critical role in sustaining myocellular viability by adapting quickly to the ischemic injury response, albeit with a prolonged recovery phase, with the recovery of metabolism lagging behind perfusion for 24 hours or more [29–32]. (**a,** *From* Camici et al. [30], with permission from Wolters Kluwer)

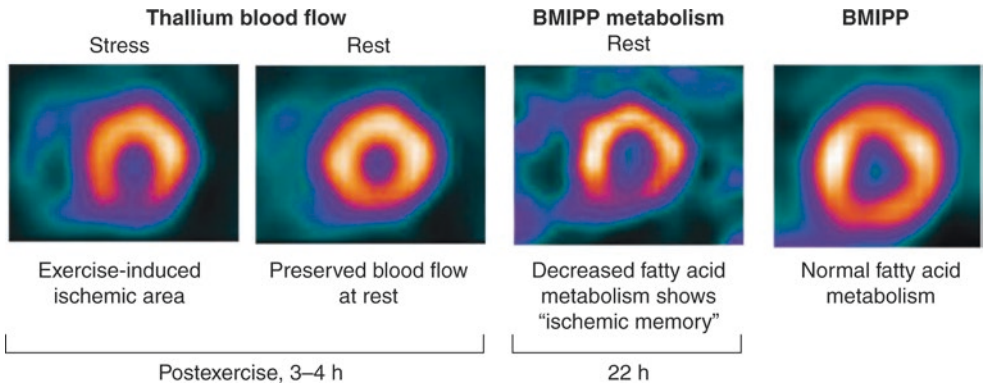

Fig. 9.22 SPECT images showing delayed recovery of regional fatty acid metabolism after transient exercise-induced ischemia, termed *ischemic memory*. Representative stress and rest reinjection short-axis thallium tomograms demonstrate a reversible inferior defect consistent with exercise-induced myocardial ischemia. A BMIPP-labeled tomogram injected and acquired at rest 22 hours after exercise-induced ischemia shows persistent metabolic abnormality in the inferior region despite complete recovery of the regional perfusion at rest, as evidenced by the thallium reinjection image. For comparison, the tomogram on the *far right* shows retention of BMIPP in the heart of a normal adult [33, 34]

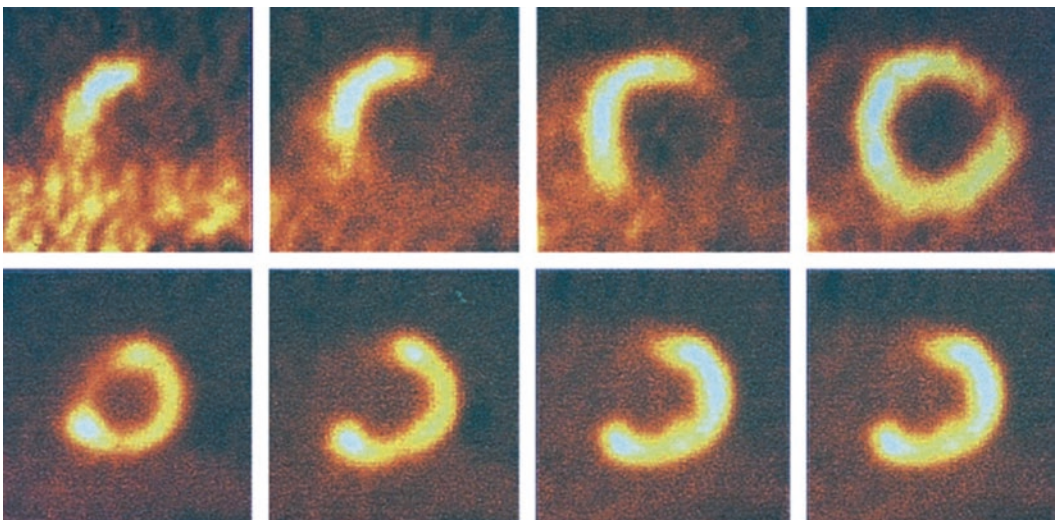

Fig. 9.23 PET scans demonstrating perfusion-metabolism mismatch (reduced blood flow with preserved or enhanced FDG uptake) in a patient with chronic ischemic left ventricular dysfunction and heart failure symptoms. The principle of using a metabolic tracer, such as FDG, is based on the concept that viable myocytes in hypoperfused and dysfunctional regions are metabolically active, whereas scarred or fibrotic tissue is metabolically inactive. Although fatty acids are the primary source of myocardial energy production in the fasting state, in the setting of reduced oxygen supply (a consequence of hypoperfusion at rest), the myocytes compensate for the loss of oxidative potential by shifting toward greater glucose utilization to generate high-energy phosphates. Thus, in chronic ischemia, aerobic metabolism is slowed while the anaerobic metabolism is accelerated, a reversal of the well-known Pasteur effect [35]. Such increased FDG uptake (anaerobic metabolism) in asynergic myocardial regions with reduced blood flow at rest has become a scintigraphic marker of hibernation. *Top row*: Short-axis [^{13}N]-ammonia scans demonstrate large lateral and inferior perfusion defects at rest. *Bottom row*: The corresponding FDG images acquired under fasting conditions demonstrate that FDG metabolic activity is preserved in the lateral and inferior regions (mismatch pattern). On the other hand, the lack of FDG metabolic activity in the anterior and septal regions reflects the utilization of fatty acid rather than glucose as the primary fuel in such normally perfused myocardial regions

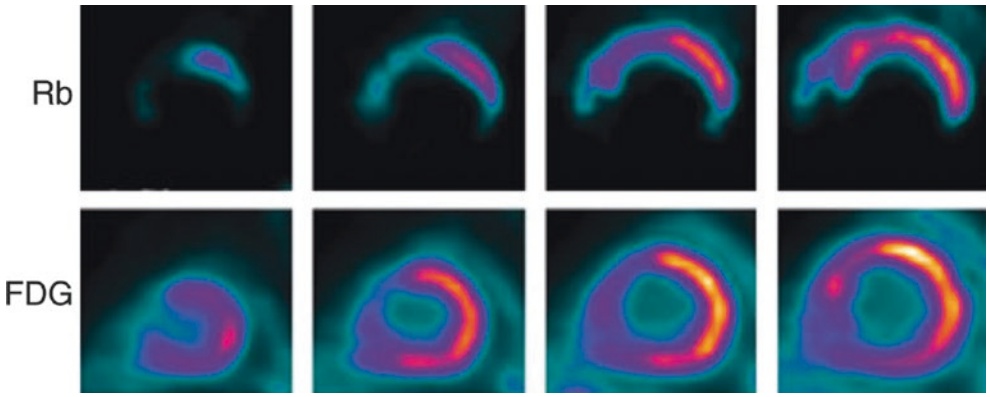

Fig. 9.24 PET scan showing a perfusion-metabolism mismatch in hibernating heart tissue as an example of preserved cardiometabolic reserve. *Top*: Rubidium (Rb)-82–labeled positron emission tomography in the short-axis view shows markedly decreased perfusion defects in the apical, inferior, inferolateral, and septal regions of the left ventricle at rest, which extends from distal to basal slices. *Bottom*: Images acquired under glucose-loaded conditions, labeled with FDG, show a perfusion-metabolism mismatch pattern (the scintigraphic hallmark of hibernation) in all abnormally perfused myocardial regions at rest. An exception is the anteroseptal region, which demonstrates a matched perfusion-metabolism pattern (compatible with scarred myocardium). Adapted from Taegtmeyer & Dilzisian with permission [33]

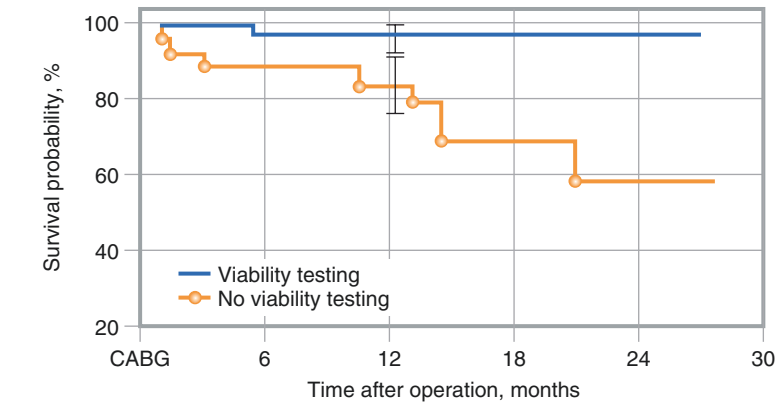

At risk, *n*					
A	35	25	18	9	5
B	34	33	22	10	1

Fig. 9.25 Myocardial viability testing prior to surgical revascularization. The determination of myocardial viability evaluation in patients with coronary artery disease and severe left ventricular dysfunction before referral to coronary artery revascularization affects the clinical outcome with respect to both in-hospital mortality and the 1-year survival rate. In this retrospective study, the perioperative and postoperative event-free survival rate was significantly lower in patients who were referred to revascularization on the basis of clinical presentation and angiographic data but without viability testing (group A) compared with those who were selected according to the extent of viable tissue determined by positron emission tomography (group B) in addition to clinical presentation and angiographic data. There were four in-hospital deaths (11.4%) in group A and none in group B ($P=0.04$). Moreover, after 12 months, the survival rate was 79% in group A and 97% in group B ($P=0.01$) [27]. CABG coronary artery bypass graft

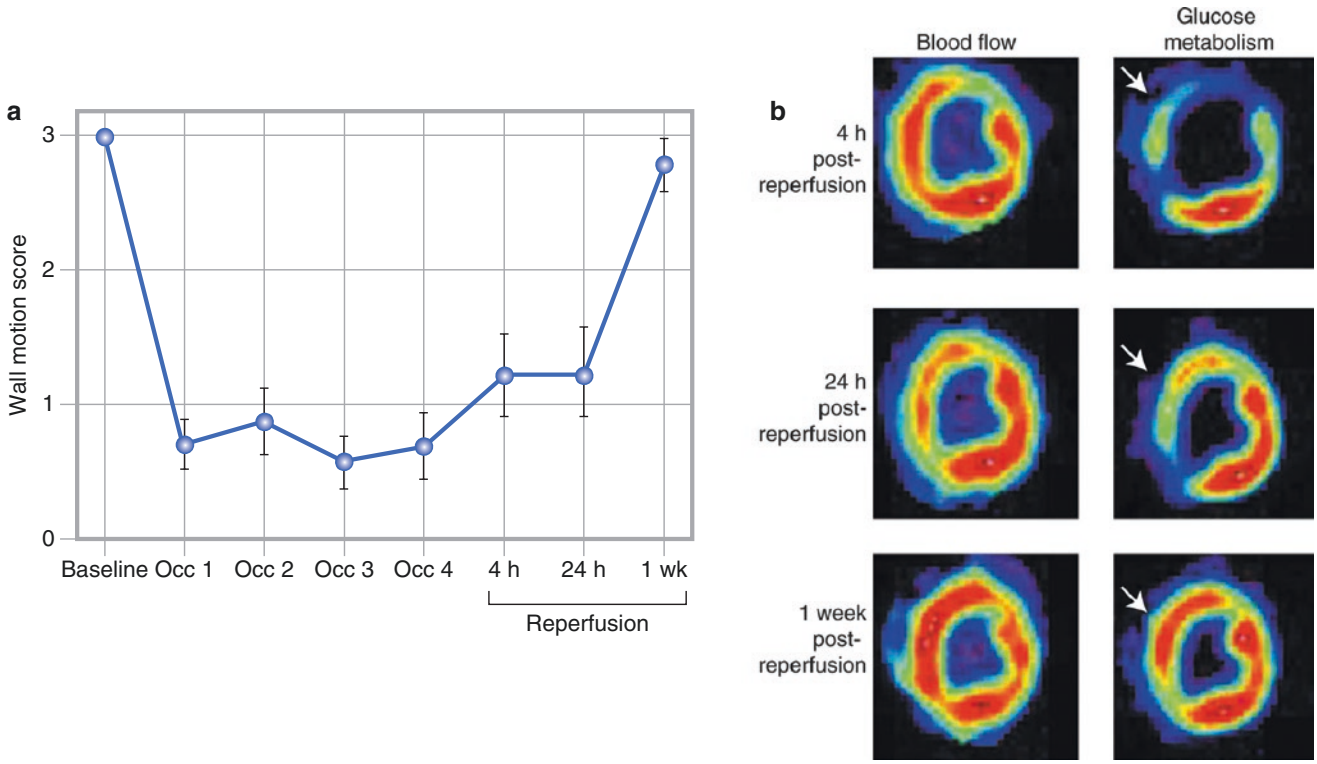

Fig. 9.26 Alterations in contractile function, regional blood flow, and glucose metabolism in myocardial stunning. (**a**) Anesthetized dogs underwent four sequential 5-minute intervals of balloon left anterior descending coronary artery occlusion (Occ), each separated by 5 minutes of reperfusion. Regional blood flow, metabolism, and function were evaluated 4 hours, 24 hours, and 1 week after reperfusion. The regional wall motion was severely depressed in the anterior and anteroseptal regions after the four cycles of ischemia, remained impaired 24 hours after reperfusion, but normalized 1 week later, which is consistent with myocardial stunning. (**b**) Representative mid-short-axis PET images of [^{13}N]-ammonia (blood flow) and FDG (glucose metabolism) were obtained 4 hours, 24 hours, and 1 week after reperfusion. In the images obtained 4 hours after reperfusion, the regional myocardial blood flow is near normal in the anterior and anteroseptal region, whereas glucose utilization is severely reduced (*arrow*). In images obtained 24 hours after reperfusion, the regional myocardial blood flow remains near normal, and there is evidence of a partial recovery in glucose utilization in the anterior and anteroseptal regions (*arrow*). In the images obtained 1 week after reperfusion, there is complete recovery of glucose utilization in the regions of stunned myocardium, which appear homogeneous with remote myocardial regions (*arrow*). These findings suggest that, in repetitive myocardial stunning, a unique metabolic adaptation occurs (abnormal glucose utilization despite the restoration of regional blood flow) that is different from the adaptation typically described in clinical and experimental models of myocardial hibernation (preserved or enhanced glucose utilization in a region with decreased regional blood flow) [36]

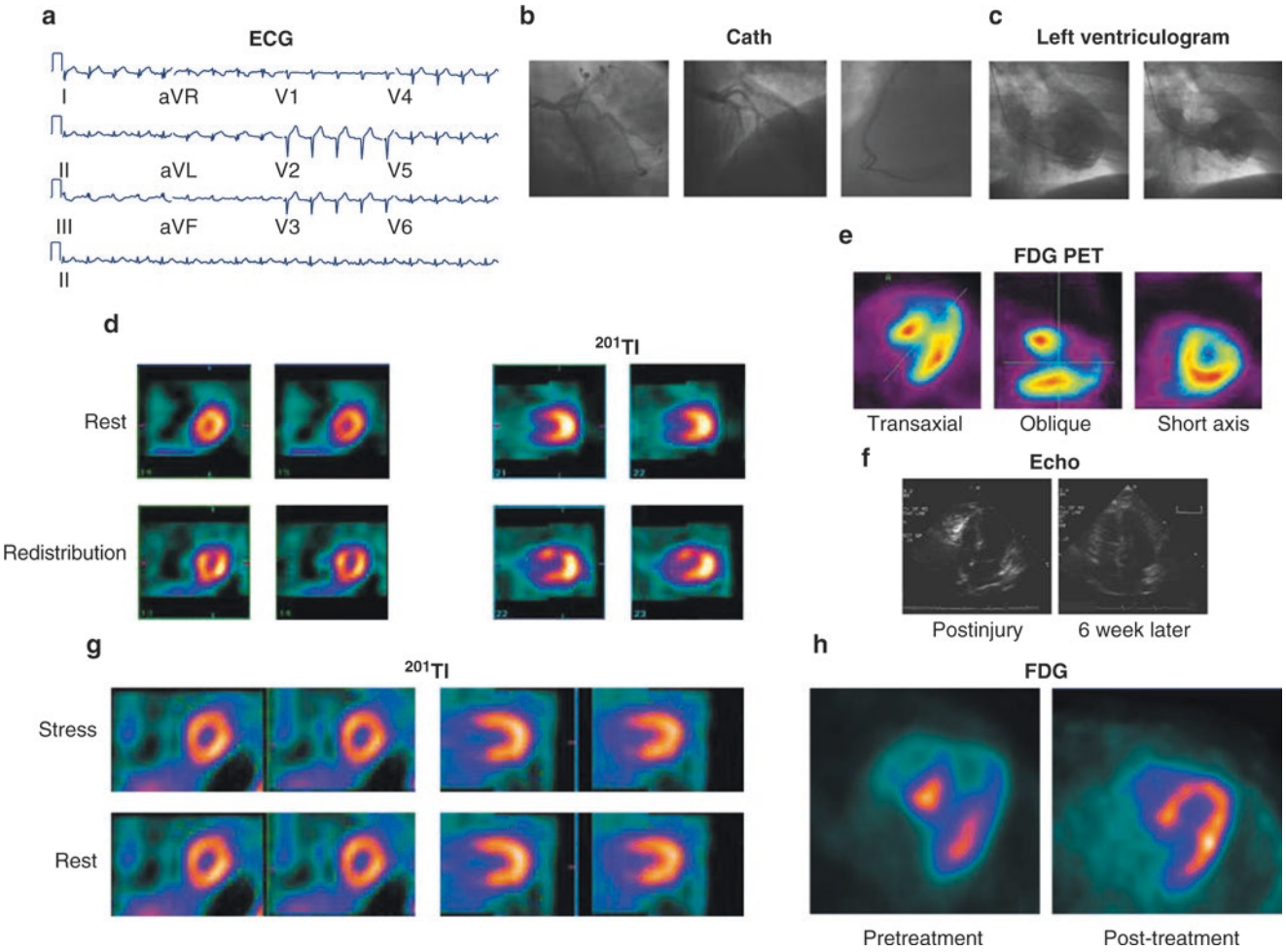

Fig. 9.27 Scintigraphic pattern of stunned myocardium. A patient with end-stage liver disease and a family history of coronary artery disease presents to the emergency department with 1 hour of new-onset chest pain. The electrocardiogram (ECG) pattern (**a**) is consistent with acute ST segment elevation myocardial infarction. The coronary angiogram (**b**) shows normal-appearing, insignificant coronary artery disease. The left ventriculogram (**c**) shows extensive left ventricular apical, anterior, and anterolateral akinesis, with a calculated ejection fraction of 30% (*left panel*, diastole; *right panel*, systole). The patient had a mild rise in cardiac enzymes (troponin, 1.5; serum creatine kinase, 76; MB, 5; %MB, 6.6), which is indicative of myocardial injury. Rest-redistribution ^{201}Tl SPECT images acquired within 1 week after the onset of chest pain (**d**) show normal perfusion at rest (*top row*), with evidence for a rapid ^{201}TI washout in the anterior region in ^{201}Tl redistribution images (*bottom row*), which is consistent with reverse redistribution. FDG PET images acquired within days after the thallium study (**e**) show severely impaired glucose utilization in the anterior and apical regions. These scintigraphic findings (abnormal glucose utilization or retention of ^{201}Tl in redistribution images despite normal regional blood flow on rest ^{201}Tl) are compatible with stunned myocardium. Repeat echocardiography (**f**), myocardial perfusion SPECT (**g**), and FDG PET studies (**h**) approximately 6 weeks after the acute ischemic injury show a complete resolution of the extensive left ventricular apical akinesis (**f**) with homogeneous and normal glucose utilization in all myocardial regions (**h**) and no evidence of myocardial ischemia (**g**). A similar presentation of transient left ventricular apical ballooning by echocardiography, termed *tako-tsubo*, has been observed in critically ill patients who are being admitted to the medical intensive care unit for noncardiac medical disorders. Elevated serum creatine kinase has been described in up to 50% of patients with ventricular apical ballooning, with a subset of these patients also exhibiting ECG evidence of Q-wave and/or ST-segment displacement. Although possible triggering factors have been suggested in the literature, the underlying pathophysiology for the left ventricular dysfunction and apical ballooning has not been elucidated. The transient nature of the apical dysfunction in a subset of patients could be attributed to transient ischemic injury and myocardial stunning. Cath catheterization, Echo echocardiogram. (*Courtesy of* Mark Kelemen and Vasken Dilsizian)

Similarly, the ability of PET to define a myocardial scar is of significant interest to electrophysiologists. A myocardial scar usually acts as the substrate for reentrant ventricular tachycardia (VT) and is present in the majority of patients with ischemic and nonischemic cardiomyopathy. During reentrant VT, an electrical wave front enters and traverses the myocardial scar via a network of electrically conducting channels. After exiting the scar, it depolarizes the rest of the ventricle and returns to the original entry site, repeating the cycle. This concept of entry sites, slowly conducting channels, and exit sites has been successfully validated in post–myocardial infarction patients during clinical electrophysiologic studies. The current "gold standard" of defining a myocardial scar is based on endocardial bipolar voltage recordings using a three-dimensional (3D) mapping system with a roving mapping catheter. Accordingly, regions with greater than 1.5 mV are classified as normal myocardium, 0.5–1.5 mV as abnormal myocardium, and less than 0.5 mV as scarred myocardium. Different from delayed–enhanced MRI and CT, which provide a morphologic substrate assessment, PET allows a metabolic characterization of the myocardial scar and its border zone. Current software developments are aimed at exporting this detailed 3D imaging information into the actual ablation procedure to provide anatomic guidance for patients with recurrent episodes of VT. In a recent study of patients undergoing VT ablation, a good correlation was found between PET-derived metabolic scar maps and endocardial voltage ($r = 0.89$, $P < 0.05$). The scar size, location, and border zone accurately predicted high-resolution voltage map findings ($r = 0.87$, $P < 0.05$). Moreover, PET/CT maps correctly predicted a nontransmural epicardial scar that was confirmed with epicardial mapping despite a normal endocardial map [37]. Figure 9.28 illustrates a fusion of CT and PET FDG images that could be used to guide VT ablation therapy.

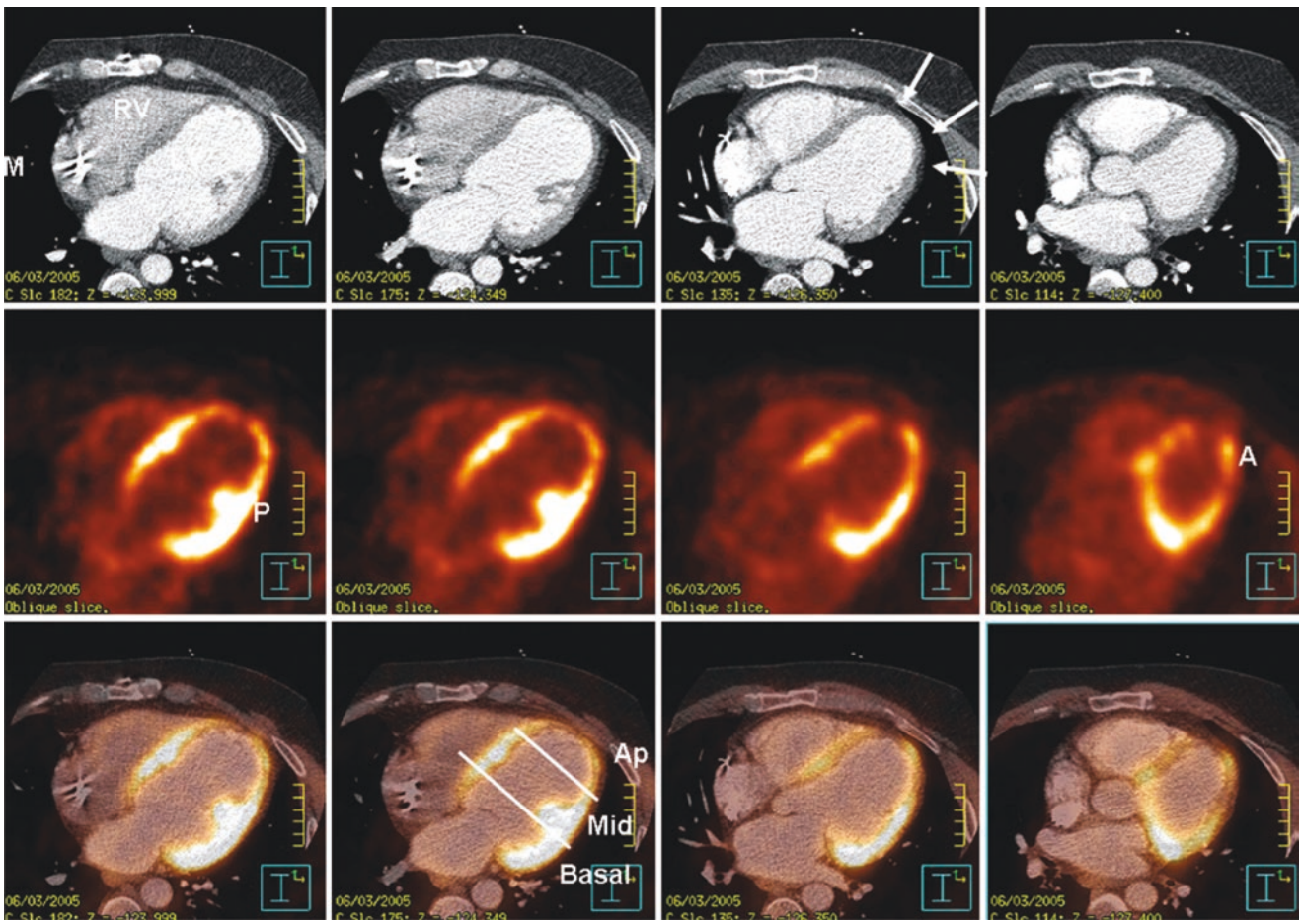

Fig. 9.28 A fusion of PET FDG and CT images for use in PET-guided ventricular tachycardia ablation therapy. *Top row:* Contrast-enhanced CT demonstrates all cardiac chambers, including the right ventricle (RV), left ventricle (LV), and a metal artifact (M) of an implantable cardioverter defibrillator lead in the right atrium. Significant wall thinning (*arrows*) is noted in the apical and lateral LV walls, which is consistent with myocardial infarction. *Middle row:* A matching decrease in signal intensity in apical and lateral wall segments is observed in PET images. A preserved metabolism of papillary muscle (P) is seen, with areas of preserved metabolic activity (A) within the lateral wall, which appears to be uniformly thinned on the CT images. *Bottom row:* PET images are fused with corresponding CT datasets to allow visualization of metabolic and anatomic datasets. The LV wall is divided into the apical (Ap), mid, and basal sections for conventional 17-segment analysis. Adapted from Dickfeld et al. with permission [37]

Figures 9.29 and 9.30 demonstrate metabolic alterations in chronic kidney disease (CKD) and renal failure. The detection of early preclinical myocardial metabolic alterations in CKD can be limited. Although the distribution of FDG uptake may visually appear homogeneous throughout the left ventricular myocardium, absolute myocardial glucose utilization may be abnormal in these patients.

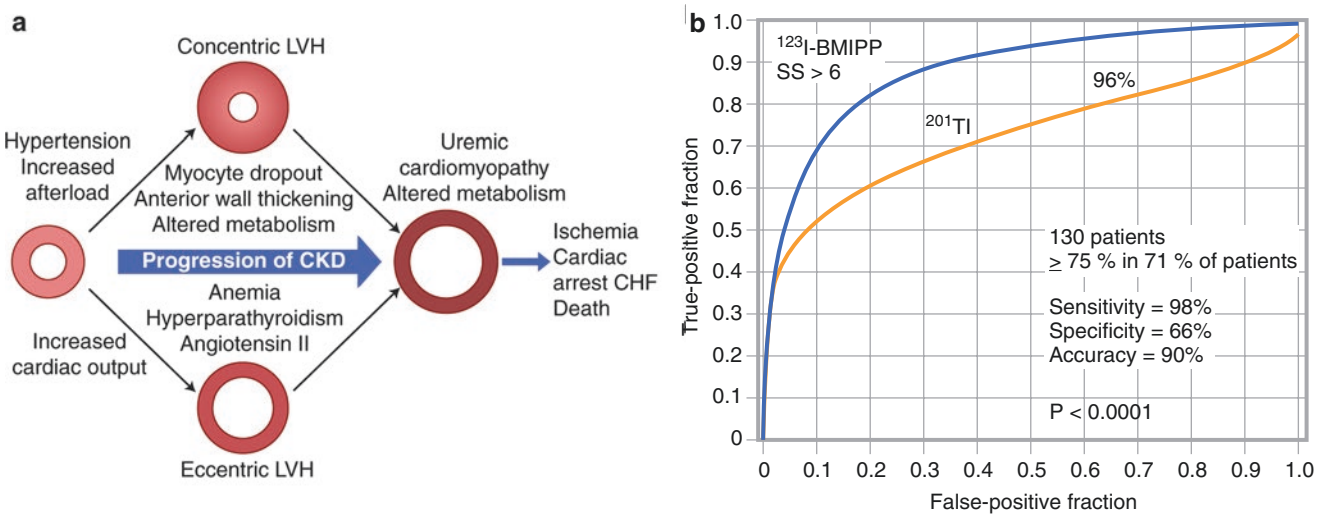

Fig. 9.29 Metabolic alterations in renal failure. (**a**) Concurrent pathogenic factors contribute to the development of uremic cardiomyopathy and an altered metabolism with declining kidney function in chronic kidney disease (CKD). Though myocardial infarction and ischemic heart disease account for a significant portion of patients with heart failure and left ventricular remodeling, several sequelae of renal failure that accrue with the loss of renal function can also contribute to left ventricular remodeling, termed *uremic cardiomyopathy*. The United States Renal Data System has reported nearly identical rates of myocardial infarction and cardiac death in dialysis patients and an approximately tenfold higher rate of heart failure in the same population [38]. The common occurrence of heart failure in the dialysis population is thought to be related to left ventricular hypertrophy (LVH), which occurs frequently in patients with CKD. Although hypertension is common among patients with kidney disease, several investigators have suggested that elevated blood pressure becomes increasingly volume-dependent, with a concomitant increase in arterial stiffening, activation of neurohormones, and endothelial dysfunction as renal function declines. Individuals with CKD, therefore, are faced with both pressure- and volume-overload states contributing to the development of left ventricular remodeling and heart failure. The cardiomyopathy typical of CKD and the associated uremia is thought to lead to a myocyte-capillary mismatch, with a diminished vascular supply relative to the number and volume of functioning myocytes [39]. The oxygen-poor milieu will lead to diffuse myocardial ischemia with an anticipated decline in aerobic myocardial fatty acid utilization and a shift to anaerobic metabolism, with increased uptake of glucose as the principal energy-providing substrate [40, 41]. The shift from a predominance of aerobic (fatty acid) to anaerobic (glucose) metabolism appears to account for a significant portion of the excessive cardiovascular morbidity and mortality observed across all stages of kidney disease. (**b**) In a prospective study of 130 asymptomatic patients with end-stage renal disease (ESRD) who were undergoing hemodialysis, the prevalence of coronary artery disease was assessed by performing dual isotope thallium and β-methyl-p-[^{123}I]-iodophenyl-pentadecanoic acid (BMIPP) SPECT imaging at rest, followed by coronary angiography [42, 43]. Significant coronary artery luminal narrowing (>75%) was present in 71.5% (93 of 130) of the ESRD patients, with an additional five patients exhibiting a coronary vasospasm. When a reduced myocardial metabolism with BMIPP (summed score of 6 or more) was used to define an abnormal scan, the BMIPP SPECT showed 98% sensitivity, 66% specificity, and 90% accuracy for detecting coronary artery disease at rest [42]. (**c**) In a subsequent publication by the same investigators, the prognostic significance of a reduced myocardial metabolism with BMIPP in conjunction with perfusion abnormalities assessed with thallium in ESRD patients was examined [40]. Among 318 prospectively enrolled asymptomatic hemodialysis patients without prior myocardial infarction, 50 (16%) died of cardiac events during a mean follow-up period of 3.6 ± 1.0 years. Kaplan-Meier survival estimates showed a 61% event-free survival at 3 years among patients with summed BMIPP score of 12 or more and a 98% score in patients with a summed BMIPP score below 12, with a graded relationship between survival and the severity of the summed BMIPP score. (**d**) When BMIPP uptake (metabolism) was assessed in relation to regional thallium uptake (perfusion), indicating myocardial ischemia, the sensitivity of the metabolism-perfusion mismatch for predicting cardiac death was 86%, and the specificity was 88%. Kaplan-Meier survival estimates showed 53% event-free survival at 3 years among patients with a BMIPP–thallium mismatch score of 7 or more, and 96% in patients with a BMIPP–thallium mismatch score below 7. These findings support the assertion that altered cardiac metabolism (indicating silent myocardial ischemia) is highly prevalent in ESRD patients and can identify the subgroup of patients who are at high risk for cardiac death. The shift from a predominance of aerobic (fatty acid) to anaerobic (glucose) metabolism appears to account for a significant portion of the excessive cardiovascular morbidity and mortality observed across all stages of kidney disease. CHF congestive heart failure

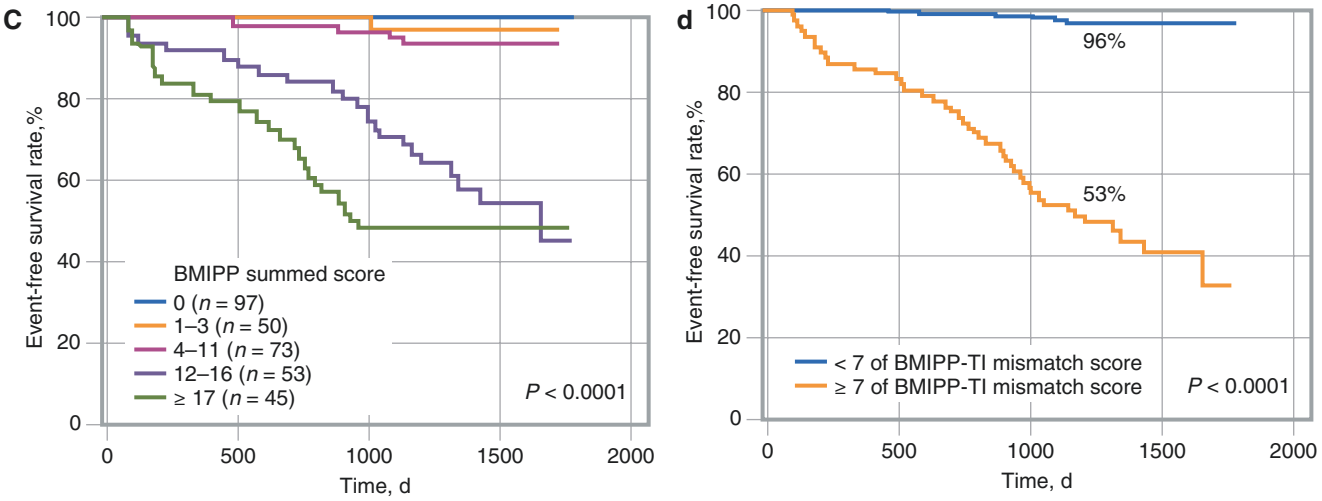

Fig. 9.29 (continued)

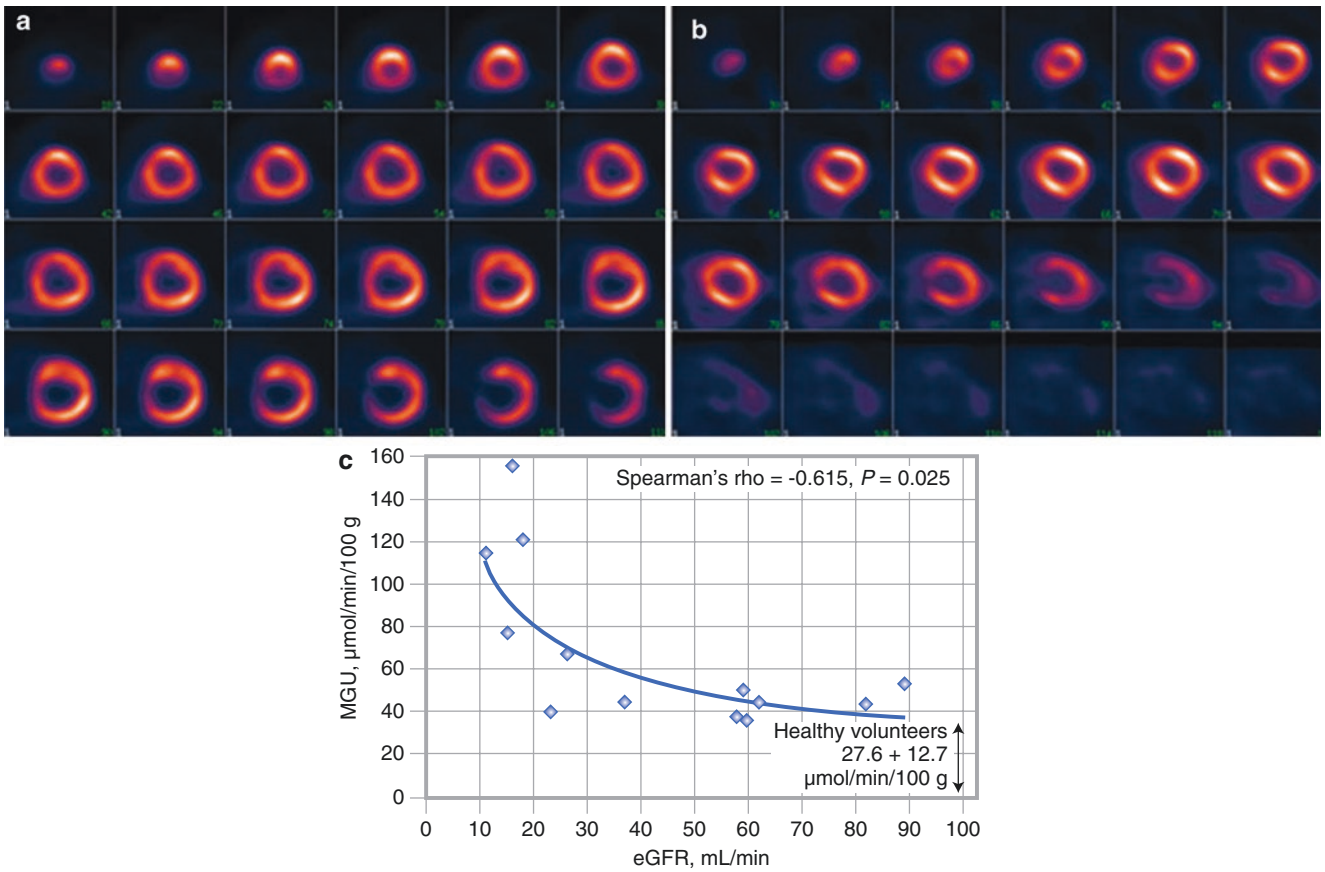

Fig. 9.30 Preclinical myocardial metabolic alterations in chronic kidney disease (CKD). Examples of myocardial FDG distribution in CKD patients exhibiting no visually discernible regional defects are shown: (**a**)**,** A CKD patient shows a dilated left ventricular cavity and concentric hypertrophy; (**b**), A CKD patient shows a normal left ventricular cavity size without hypertrophy. A quantitative assessment with PET may identify alterations in the whole myocardium glucose uptake (MGU), measured in µmol/min/100 g of myocardial tissue in the heart before clinical, functional, and prognostic consequences ensue. The feasibility of employing quantitative MGU with PET to gain additional insight into the alterations of myocardial metabolism in CKD patients was recently studied [44]. (**c**) A scatter plot of estimated glomerular filtration rate (eGFR, mL/min/1.73 m^2) versus MGU (µmol/min/100 g) is shown, as measured by an [^{18}F]-FDG PET scan in CKD. There is a significant inverse correlation between myocardial glucose uptake and renal function, assessed by eGFR. Of great interest was the degree to which myocardial glucose uptake increased with declining renal function across individuals. This increase was particularly notable among the subgroup with significant impairment in renal function, with Stage III or greater CKD. The relationship between myocardial glucose uptake and eGFR could not be ascribed to demographic factors or cardiac workload. Thus, [^{18}F]-FDG PET may be an effective tool to investigate preclinical changes in the myocardial metabolism in CKD

Finally, Fig. 9.31 demonstrates bone marrow cell homing, an example of the new fields of metabolomics and stem-cell imaging, which may offer new tools of metabolic imaging for the diagnosis and treatment of myocardial diseases.

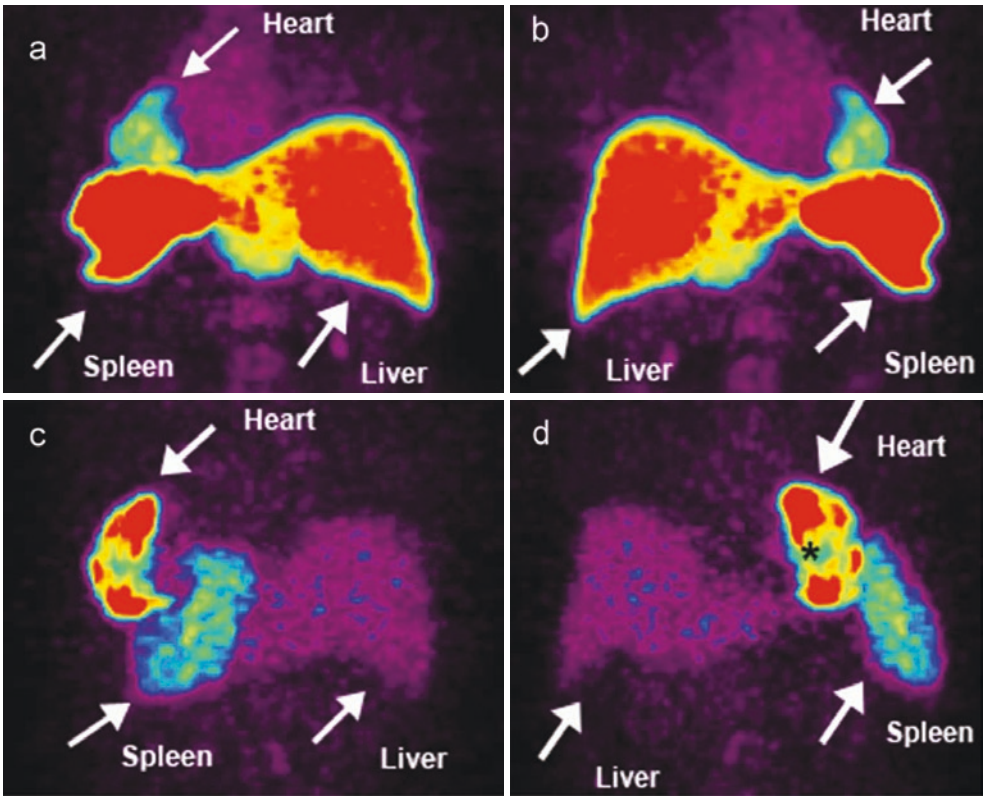

Fig. 9.31 Myocardial homing and biodistribution of FDG-labeled bone marrow cells [45]. Shown are the left posterior oblique (**a**) and left anterior oblique (**b**) views of the chest and upper abdomen of the patient taken 65 minutes after the transfer of ^{18}F-FDG–labeled, unselected bone marrow cells into the left circumflex coronary artery, and the left posterior oblique (**c**) and left anterior oblique (**d**) views of the chest and upper abdomen of another patient taken 70 minutes after the transfer of ^{18}F-FDG–labeled, CD34-enriched bone marrow cells into the left anterior descending coronary artery. In both patient examples, bone marrow cell homing is detectable in the heart (infarct center and border zone), liver, and spleen. CD34^{+} cell homing is most prominent in infarct border zone, but not infarct center (*asterisk*). Our current knowledge of the dynamics of intermediary metabolism remains fragmented and poorly integrated into the biology of the cell. The new and powerful tools of systems biology give a fresh approach to the diagnosis and treatment of different forms of heart disease. A case in point is the field of metabolomics. In analogy to the genome, transcriptome, and proteome, the metabolome has been defined as the total set of low-molecular-weight metabolites. The techniques of metabolomics allow us to analyze changes in the metabolome in a given system. A major advantage of this metabolic profiling is the comparatively small number of possible targets. The new fields of metabolomics and stem-cell imaging offer challenges to both the experimental biologist and the clinical cardiologist to refine the tools of metabolic imaging for the diagnosis and treatment of myocardial diseases. (*Courtesy of* Kai C. Wollert)

References

1. Taegtmeyer H, Young ME, Lopaschuk GD, Abel ED, Brunengraber H, Darley-Usmar V, et al. American Heart Association Council on basic cardiovascular sciences. Assessing cardiac metabolism: a scientific statement from the American Heart Association. Circ Res. 2016;118:1659–701.
2. Kundu B, Zhong M, Sen S, Davogustto G, Keller S, Taegtmeyer H. Remodeling of glucose metabolism precedes pressure overload-induced left ventricular hypertrophy: review of a hypothesis. Cardiology. 2015;130:211–20.
3. Taegtmeyer H, Golfman L, Sharma S, Razeghi P, van Arsdall M. Linking gene expression to function: metabolic flexibility in the normal and diseased heart. Ann N Y Acad Sci. 2004;1015:202–13.
4. Taegtmeyer H, Lam T, Davogustto G. Cardiac metabolism in perspective. Compr Physiol. 2016;6:1675–99.
5. Davogustto G, Taegtmeyer H. The changing landscape of cardiac metabolism. J Mol Cell Cardiol. 2015;84:129–32.
6. Taegtmeyer H, Hems R, Krebs HA. Utilization of energy-providing substrates in the isolated working rat heart. Biochem J. 1980;186:701–11.
7. Osterholt M, Sen S, Dilsizian V, Taegtmeyer H. Targeted metabolic imaging to improve the management of heart disease. JACC Cardiovasc Imaging. 2012;5:214–26.
8. Depre C, Young ME, Ying J, Ahuja HS, Han Q, Garza N, et al. Streptozotocin-induced changes in cardiac gene expression in the absence of severe contractile dysfunction. J Mol Cell Cardiol. 2000;32:985–96.
9. Goodwin GW, Taylor CS, Taegtmeyer H. Regulation of energy metabolism of the heart during acute increase in heart work. J Biol Chem. 1998;273:29530–9.
10. Nguyen VT, Mossberg KA, Tewson TJ, Wong WH, Rowe RW, Coleman GM, Taegtmeyer H. Temporal analysis of myocardial glucose metabolism by 2-[18F]fluoro-2-deoxy-D-glucose. Am J Phys. 1990;259:H1022–31.
11. Sharma S, Adrogue JV, Golfman L, Uray I, Lemm J, Youker K, et al. Intramyocardial lipid accumulation in the failing human heart resembles the lipotoxic rat heart. FASEB J. 2004;18:1692–700.
12. Taegtmeyer H, McNulty P, Young ME. Adaptation and maladaptation of the heart in diabetes: part I: general concepts. Circulation. 2002;105:1727–33.
13. Depre C, Shipley GL, Chen W, Han Q, Doenst T, Moore ML, et al. Unloaded heart in vivo replicates fetal gene expression of cardiac hypertrophy. Nat Med. 1998;4:1269–75.
14. Dewald O, Sharma S, Adrogue J, Salazar R, Duerr GD, Crapo JD, et al. Downregulation of peroxisome proliferator-activated receptor-alpha gene expression in a mouse model of ischemic cardiomyopathy is dependent on reactive oxygen species and prevents lipotoxicity. Circulation. 2005;112:407–15.
15. Feinendegen LE. Myocardial imaging of lipid metabolism with labeled fatty acids. In: Dilsizian V, editor. Myocardial viability: a clinical and scientific treatise. Armonk: Futura; 2000. p. 349–89.
16. Messina SA, Aras O, Dilsizian V. Delayed recovery of fatty acid metabolism after transient myocardial ischemia: a potential imaging target for "ischemic memory". Curr Cardiol Rep. 2007;9:159–65.
17. Gropler RJ, Siegel BA, Sampathkumaran K, Pérez JE, Sobel BE, Bergmann SR, Geltman EM. Dependence of recovery of contractile function on maintenance of oxidative metabolism after myocardial infarction. J Am Coll Cardiol. 1992;19:989–97.
18. Gropler RJ, Geltman EM, Sampathkumaran K, Pérez JE, Moerlein SM, Sobel BE, et al. Functional recovery after coronary revascularization for chronic coronary artery disease is dependent on maintenance of oxidative metabolism. J Am Coll Cardiol. 1992;20:569–77.
19. Schelbert HR. Principles of positron emission tomography. In: Skorton DJ, Schelbert HR, Wolf GL, Brundage BH, editors. Marcus cardiac imaging: a companion to Braunwald's heart disease. 2nd ed. Philadelphia: WB Saunders; 1996. p. 1063–92.
20. Dilsizian V, Bacharach SL, Beanlands SR, Bergmann SR, Delbeke D, Fischman AJ, et al. ASNC imaging guidelines for nuclear cardiology procedures: PET myocardial perfusion and metabolism clinical imaging. J Nucl Cardiol. 2009;16:651. https://doi.org/10.1007/s12350-009-9094-9.
21. Dilsizian V. Perspectives on the study of human myocardium: viability. In: Dilsizian V, editor. Myocardial viability: a clinical and scientific treatise. Armonk: Futura; 2000. p. 3–22.
22. Tillisch J, Brunken R, Marshall R, Schwaiger M, Mandelkern M, Phelps M, Schelbert H. Reversibility of cardiac wall-motion abnormalities predicted by positron tomography. N Engl J Med. 1986;314:884–8.
23. Dilsizian V, Arrighi JA. Myocardial viability in chronic coronary artery disease: perfusion, metabolism and contractile reserve. In: Gerson MC, editor. Cardiac nuclear medicine. 3rd ed. New York: McGraw-Hill; 1996. p. 143–91.
24. Eitzman D, Al-aouar Z, Kanter HL, vom Dahl J, Kirsh M, Deeb GM, Schwaiger M. Clinical outcome of patients with advanced coronary artery disease after viability studies with positron emission tomography. J Am Coll Cardiol. 1992;20:559–65.
25. Di Carli MF, Davidson M, Little R, Khanna S, Mody FV, Brunken RC, et al. Value of metabolic imaging with positron emission tomography for evaluating prognosis in patients with coronary artery disease and left ventricular dysfunction. Am J Cardiol. 1994;73:527–33.
26. Di Carli MF, Asgarzadie F, Schelbert HR, Brunken RC, Laks H, Phelps ME, Maddahi J. Quantitative relation between myocardial viability and improvement in heart failure symptoms after revascularization in patients with ischemic cardiomyopathy. Circulation. 1995;92:3436–44.
27. Haas F, Haehnel CJ, Picker W, Nekolla S, Martinoff S, Meisner H, Schwaiger M. Preoperative positron emission tomography viability assessment and perioperative and postoperative risk in patients with advanced ischemic heart disease. J Am Coll Cardiol. 1997;30:1693–700.
28. Srinivasan G, Kitsiou AN, Bacharach SL, Bartlett ML, Miller-Davis C, Dilsizian V. ^{18}F-fluorodeoxyglucose single photon emission computed tomography: can it replace PET and thallium SPECT for the assessment of myocardial viability? Circulation. 1998;97:843–50.
29. Dilsizian V. FDG uptake as a surrogate marker for antecedent ischemia. J Nucl Med. 2008;49:1909–11.
30. Camici P, Araujo LI, Spinks T, Lammertsma AA, Kaski JC, Shea MJ, et al. Increased uptake of 18F-fluorodeoxyglucose in post-ischemic myocardium of patients with exercise-induced angina. Circulation. 1986;74:81–8.
31. He ZX, Shi RF, Wu YJ, Tian YQ, Liu XJ, Wang SW, et al. Direct imaging of exercise-induced myocardial ischemia with fluorine-18-labeled deoxyglucose and Tc-99m-sestamibi in coronary artery disease. Circulation. 2003;108:1208–13.
32. Dou KF, Yang MF, Yang YJ, Jain D, He ZX. Myocardial 18F-FDG uptake after exercise-induced myocardial ischemia in patients with coronary artery disease. J Nucl Med. 2008;49:1986–91.
33. Taegtmeyer H, Dilsizian V. Imaging myocardial metabolism and ischemic memory. Nat Clin Pract Cardiovasc Med. 2008;5:S42–8.
34. Dilsizian V, Bateman TM, Bergmann SR, Des Prez R, Magram MY, Goodbody AE, et al. Metabolic imaging with beta-methyl-para-[^{123}I]-iodophenyl-pentadecanoic acid (BMIPP) identifies ischemic memory following demand ischemia. Circulation. 2005;112:2169–74.

35. Krebs H. The Pasteur effect and the relation between respiration and fermentation. Essays Biochem. 1972;8:1–34.
36. Di Carli MF, Prcevski P, Singh TP, Janisse J, Ager J, Muzik O, Vander HR. Myocardial blood flow, function, and metabolism in repetitive stunning. J Nucl Med. 2000;41:1227–34.
37. Dickfeld T, Lei P, Dilsizian V, Jeudy J, Dong J, Voudouris A, et al. Integration of three-dimensional scar maps for ventricular tachycardia ablation with positron emission tomography-computed tomography. JACC Cardiovasc Imaging. 2008;1:73–82.
38. United States Renal Data System. 2018 USRDS annual data report: Epidemiology of kidney disease in the United States. Bethesda: National Institutes of Health, National Institute of Diabetes and Digestive and Kidney Diseases; 2018.
39. Tyralla K, Amann K. Morphology of the heart and arteries in renal failure. Kidney Int. 2003;63:S80–3.
40. Nishimura M, Tsukamoto K, Hasebe N, Tamaki N, Kikuchi K, Ono T. Prediction of cardiac death in hemodialysis patients by myocardial fatty acid imaging. J Am Coll Cardiol. 2008;51:139–45.
41. Lodge MA. Evidence for inverse relationship between myocardial glucose utilization with PET and severity of renal dysfunction [abstract]. J Nucl Med. 2007;48(Suppl 2):108P.
42. Nishimura M, Hashimoto T, Kobayashi H, Fukuda T, Okino K, Yamamoto N, et al. Myocardial scintigraphy using a fatty acid analogue detects coronary artery disease in hemodialysis patients. Kidney Int. 2004;66:811–9.
43. Dilsizian V, Fink J. Deleterious effect of altered myocardial fatty acid metabolism in kidney disease. J Am Coll Cardiol. 2008;51:146–8.
44. Fink JC, Lodge MA, Smith MF, Hinduja A, Brown J, Dinits-Pensy MY, Dilsizian V. Pre-clinical myocardial metabolic alterations in chronic kidney disease. Cardiology. 2010;116:160–7.
45. Hofmann M, Wollert KC, Meyer GP, Menke A, Arseniev L, Hertenstein B, et al. Monitoring of bone marrow cell homing into the infarcted human myocardium. Circulation. 2005;111:2198–202.

Myocardial Viability

10

Vasken Dilsizian and Jagat Narula

Heart failure (HF) is evolving as an enormous cardiovascular health problem worldwide. In the United States alone, more than five million patients suffer from symptomatic disease, and more than half a million patients are newly diagnosed with HF every year. There are at least one million hospitalizations that result in 6.5 million hospital days and nearly 300,000 deaths each year. The total inpatient and outpatient costs for HF are approximately $35 billion. Two thirds of the heart failure is secondary to coronary artery disease, and not infrequently assessment of myocardial viability becomes necessary for appropriate management of these patients by non-surgical and surgical revascularization.

Although the observational data have overwhelmingly supported the need for viability assessment by various imaging strategies and have shown superior outcomes in the presence of viable myocardium, randomization data have not yet adequately addressed the need for the assessment of HF patients with significant coronary disease. The Surgical Treatment for Ischemic Heart Failure (STICH) study did not produce conclusive data, and more work may be required before this issue is settled. The objective of a myocardial viability assessment in HF is to identify prospective patients with potentially reversible left ventricular dysfunction in whom a prognosis may be favorably altered with coronary artery revascularization. The concept that impaired left ventricular function may be reversible after revascularization is now well established. Pathophysiologic paradigms have emerged, which describe the relationship between myocardial perfusion and ventricular function pertaining to myocardial stunning and hibernation. In these paradigms, myocardial function is depressed, but myocytes remain viable; therefore, left ventricular dysfunction may be completely reversible. Parallel advances in the mechanisms underlying altered myocardial states and the development of new radiotracers in nuclear cardiology have resulted in breakthroughs that contribute importantly to differentiating viable from nonviable myocardium in dysfunctional regions. This chapter discusses strategies for the identification of viable myocardium and reversibility in heart failure associated with coronary artery disease.

Requirements for Cellular Viability

To date, the most common definition of myocardial viability has been the temporal improvement in contractile function of a dysfunctional region after the restoration of blood flow. Requirements for cellular viability include sufficient myocardial blood flow, intact sarcolemmal membrane function, and preserved metabolic activity. Myocardial blood flow must be adequate to deliver substrate to the myocyte to be used in the metabolic process, as well as to remove the end products of the metabolic process. If regional blood flow is severely reduced or absent, then the metabolites and end products will accumulate, causing inhibition of the enzymes of the metabolic pathway, depletion of high-energy phosphates, cell membrane disruption, and cell death. Thus, at either extreme of the range of blood flow, myocardial perfusion tracers provide information regarding myocardial viability. In regions where the reduction in blood flow is of intermediate severity, however, perfusion information alone may be insufficient to determine viability, and additional pieces of data such as metabolic indexes would be necessary.

V. Dilsizian
University of Maryland School of Medicine, Baltimore, MD, USA

J. Narula (✉)
Icahn School of Medicine at Mount Sinai,
New York, NY, USA
e-mail: narula@mountsinai.org

V. Dilsizian, J. Narula (eds.), *Atlas of Nuclear Cardiology*, https://doi.org/10.1007/978-3-030-49885-6_10

Another requirement for myocyte viability is intact sarcolemmal membrane function to maintain electrochemical gradients across the cell membrane. Because cell membrane integrity is highly dependent on preserved intracellular metabolic activity to generate high-energy phosphates, tracers that reflect sarcolemmal cation flux as well as perfusion, such as ^{201}Tl and ^{82}Rb, or mitochondrial membrane integrity, such as ^{99m}Tc-labeled perfusion tracers, should parallel the viability information provided by markers of metabolic activity, such as [^{18}F]-fluorodeoxyglucose. Thus, in the setting of reduced regional blood flow and function, techniques that assess intact cellular membrane function or metabolic processes provide unique insight into the presence or absence of myocardial viability.

Figure 10.1 shows structural correlates of viability in normal, hibernating, and fetal myocardium. Irrespective of the inciting stimulus of decrease in regional blood flow, the myocardium undergoes metabolic, structural, and functional remodeling in response to myocardial ischemia, termed *programmed cell survival* [1]. Recent literature on programmed cell survival and apoptosis provides support of a direct link between metabolic pathways and cellular adaptation or maladaptation [2]. It has been proposed, therefore, that perhaps metabolic reprogramming of the ischemic myocardium initiates and sustains the functional and structural remodeling of hibernating myocardium.

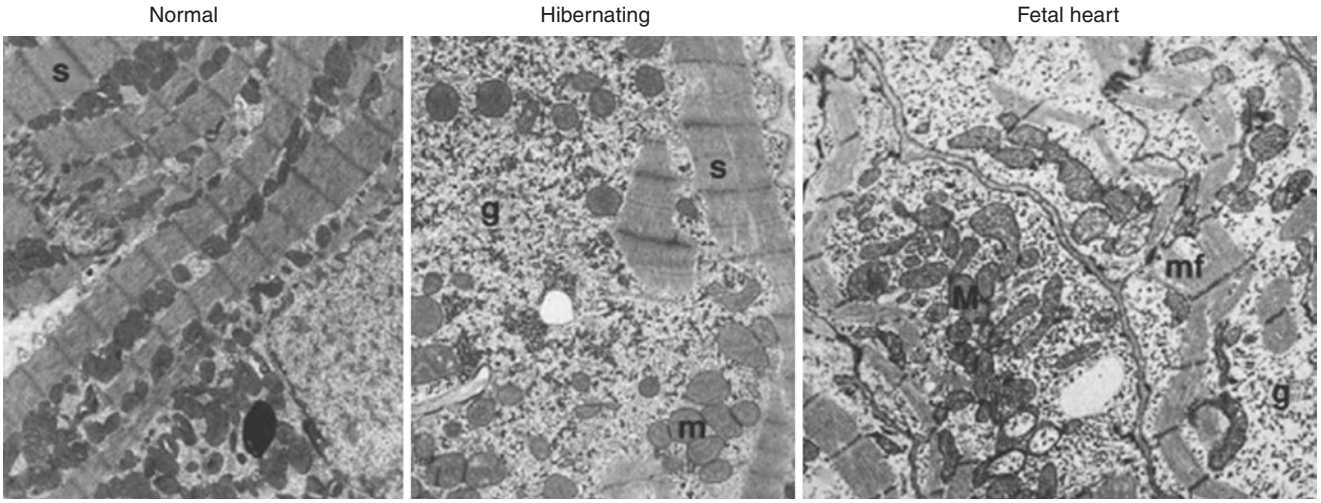

Fig. 10.1 Structural correlates of myocardial viability in normal (**a**), hibernating (**b**), and 30-gestation week fetal heart (**c**). When compared with the normal myocardium (**a**), an electron micrograph of the hibernating myocardium (**b**) shows depletion of sarcomeres (*s*) (present only at the cell periphery) and contractile filament material (*mf*), the accumulation and storage of glycogen (*g*), and the appearance of numerous small mitochondria (*m*). Because some of these structural changes of altered myocytes resemble those of embryonic cells (**c**), such changes have been attributed to a dedifferentiation process. Moreover, altered myocytes have been shown to reexpress contractile proteins that are specific to the fetal heart, such as the alpha-smooth muscle cell actin. Beyond structural similarities on electron micrography, hibernating myocardium resembles the fetal heart with its preferential metabolism of glucose and the presence of large amounts of glycogen in the cardiomyocytes [2, 3]. (Scale bar = 1.0 μm)

Pathogenetic Basis of Altered Myocardial States

Cardiac myocytes are incredibly smart cells. They duck, dive, dart, or dodge to escape annihilation. When myocardial blood flow is critically reduced, myocytes learn to restrict oxidative metabolism. Myocytes evolve (or devolve) and switch their metabolic substrates from staple to alternate sources and stall contractile activity. This could severely impair myocardial contractile function, but revascularization could help reconstitution of myocytes and restoration of myocardial function. This has been referred to as a *hibernating state*, wherein ventricular myocardium demonstrates improved contractile function when adequate blood supply is returned [4]. On the other hand, a transient loss of myocardial function after any acute ischemic insult could result in *stunning*. The ischemic insult could activate proteolytic enzymes, which may lead to degradation of contractile proteins and may result in degradation of troponin I. In severe ischemic cardiomyopathy, repetitive stunning contributes to HF. Selective loss of contractile proteins is sufficient to impair normal contractility and allow time for healing. Similarly, remodeled myocardium also invites subnormal function, but unlike hibernating myocardium, blood flow is not compromised in remodeled myocardium. Unlike stunned myocardium, remodeled cells have not suffered direct myocardial injury.

Figure 10.2 illustrates the pathogenetic basis behind cell loss and survival. Anti-apoptotic factors prevent cell loss (programmed cell survival); notably there is complete abolition of DNAses. Loss of mitochondrial CYTC1 and contractile proteins adversely influence cellular metabolism and contractile function but maintains intact cell for possible revival. Because the genetic blueprint is intact, restoration of blood supply can reconstitute contractile proteins and resolve ventricular function [9]. Ultrastructural studies (as in Fig. 10.2H) have demonstrated improved cellular architecture after implantation of a left ventricular assist device—a unique pathologic process we refer to as *apoptosis interruptus* or *programmed cell survival*.

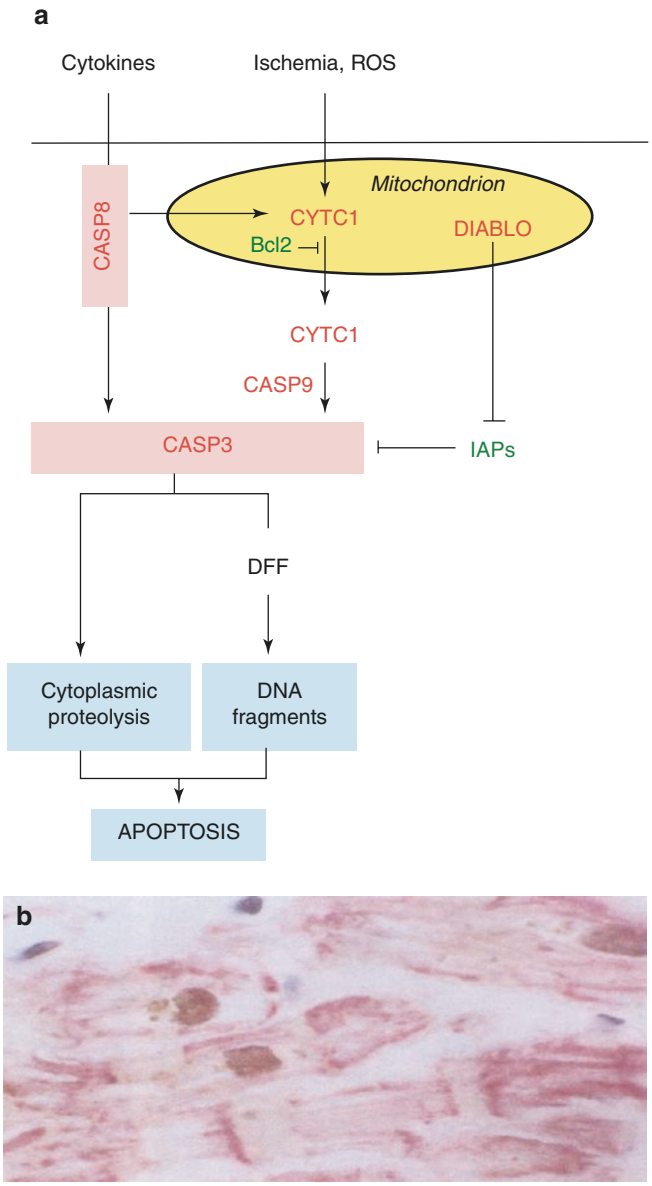

Fig. 10.2 Pathogenetic basis of altered myocardial states or programmed cell survival. (**a**) The apoptosis process, initiated by ischemic and inflammatory insults alike [5, 6]. Normally, apoptosis shows an end result of DNA fragmentation and shrinkage and removal of the cell without leaving behind a trace. (**b**) Evidence of DNA fragmentation is demonstrated by standard TUNEL staining in an explanted heart at the time of transplantation. (**c**) The upstream cascade in apoptosis shows the definitive step of release of cytochrome c (CYTC1) from the mitochondria. In the normal myocyte (left), CYTC1 is confined to mitochondria, whereas in the cardiomyopathic heart (right), the mitochondria seem to have lost CYTC1 and it is seen sprinkled in the cytoplasm. (**d**) The immunogold staining has been performed and examined ultrastructurally. Extramitochondrial cytochrome c activates caspases or proteolytic enzymes including caspase-3 (CASP3). Only minimal presence of the immunogold staining for CASP3 is noticed in the normal mitochondria (left), but large quantities are seen in cardiomyopathy (right) and can be seen concentrated in the region with proteolytic loss of contractile proteins. (**e**) Proteolytic damage in hibernation could become so extensive that the cells might demonstrate complete vacuolar degeneration (H&E stain). To protect themselves from the completion of apoptosis even in the presence of CASP3 activation (upper right), myocytes upregulate anti-apoptotic factors such as BCL2 (lower right) (Narula et al. [7]). TUNEL staining in such situations may in fact represent DNA repair (lower left) [8]. (**f**) Electron micrographs demonstrate intact nucleus (top) even with the lost CYTC1 from mitochondria (bottom). (**g**) On complete biochemical characterization, concomitant activation of pro-apoptotic factors (*red boxes*) and anti-apoptotic factors (*green boxes*) is observed. Anti-apoptotic factors prevent cell loss (programmed cell survival); notably there is complete abolition of DNAses. Loss of mitochondrial CYTC1 and contractile proteins adversely influence cellular metabolism and contractile function but maintains intact cell for possible revival. Since genetic blue print is intact restoration of blood supply could reconstitute contractile proteins and resolve ventricular function [9]. (**h**) Ultrastructural studies demonstrate improved cellular architecture after implantation of a left ventricular assist device (LVAD)

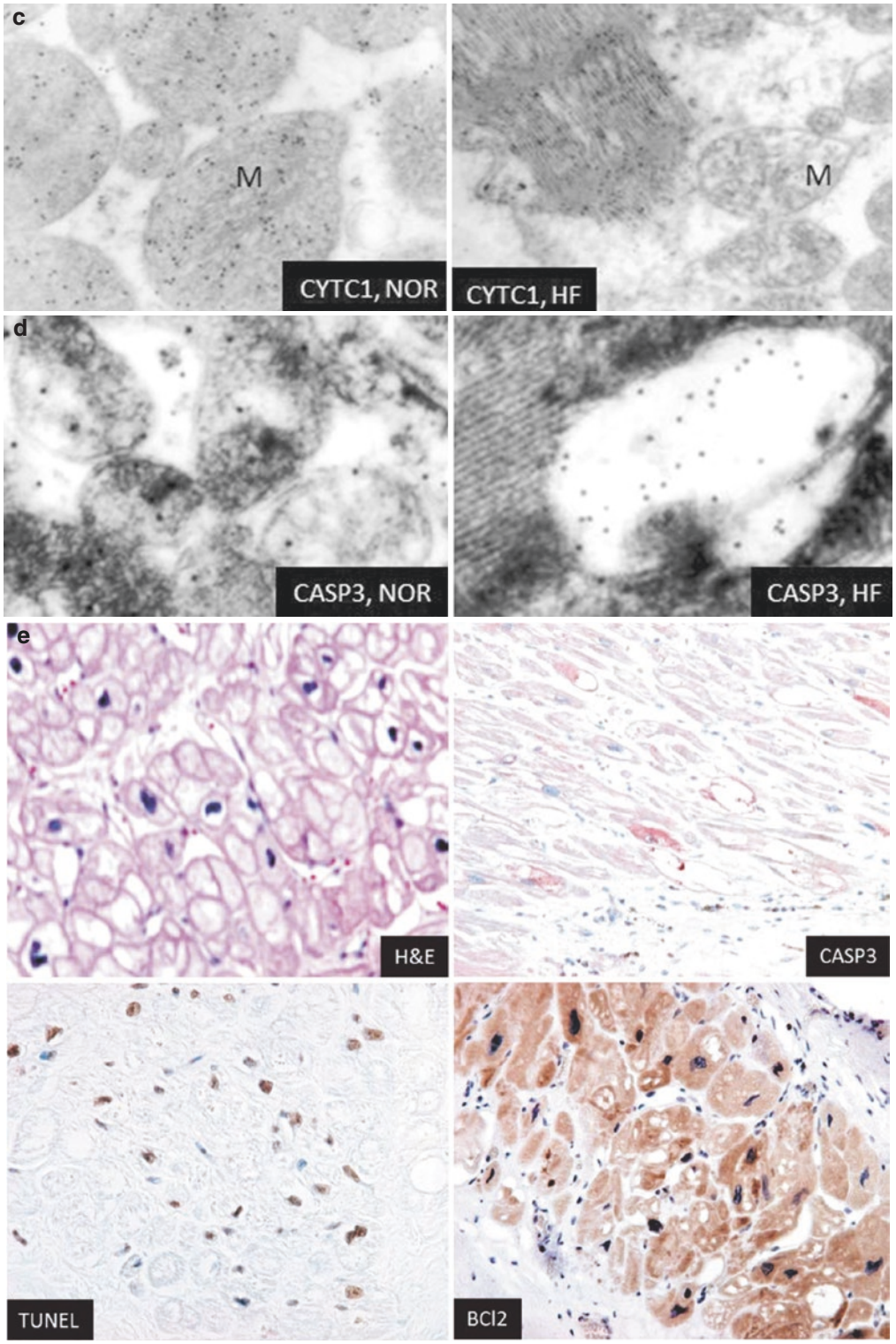

Fig. 10.2 (continued)

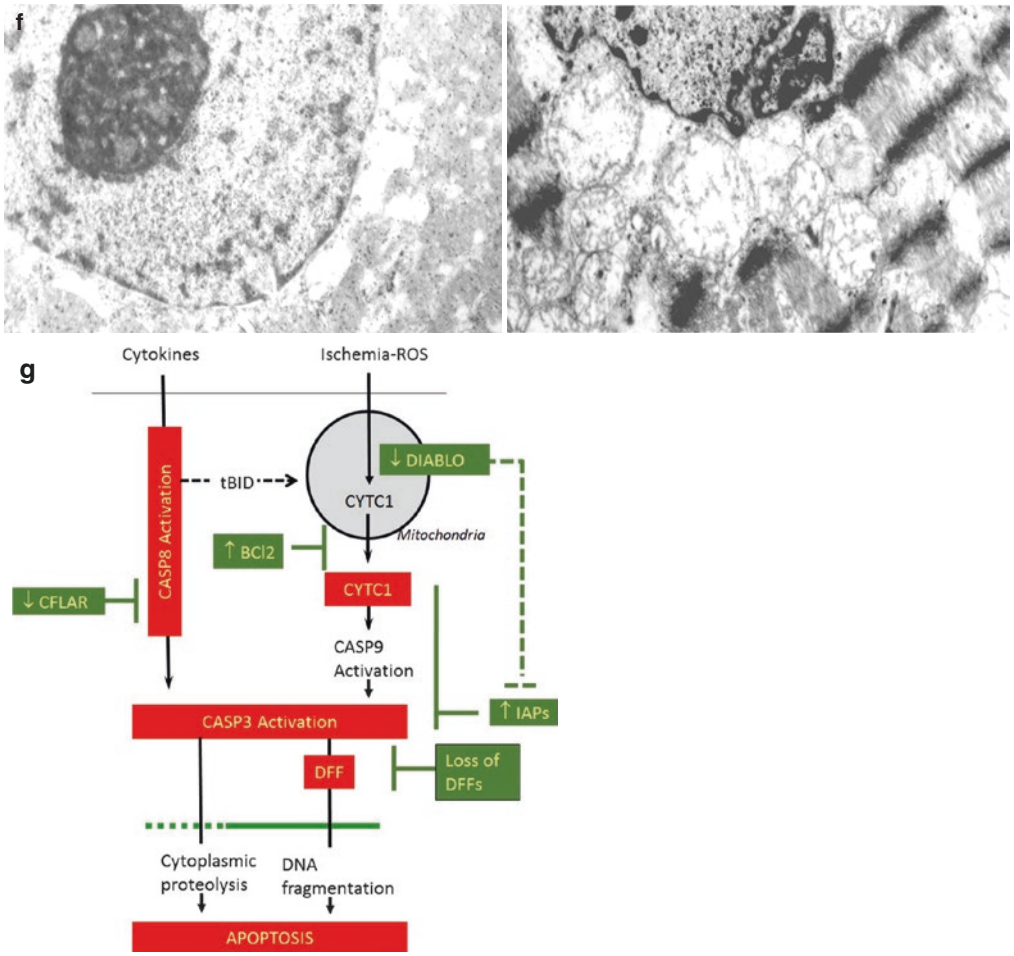

Fig. 10.2 (continued)

Figures 10.3 and 10.4 demonstrate changes in myocardium that is stunned or irreversibly damaged. Figure 10.5 outlines the various responses to myocardial ischemia, including myocardial stunning, hibernation, and ischemic preconditioning.

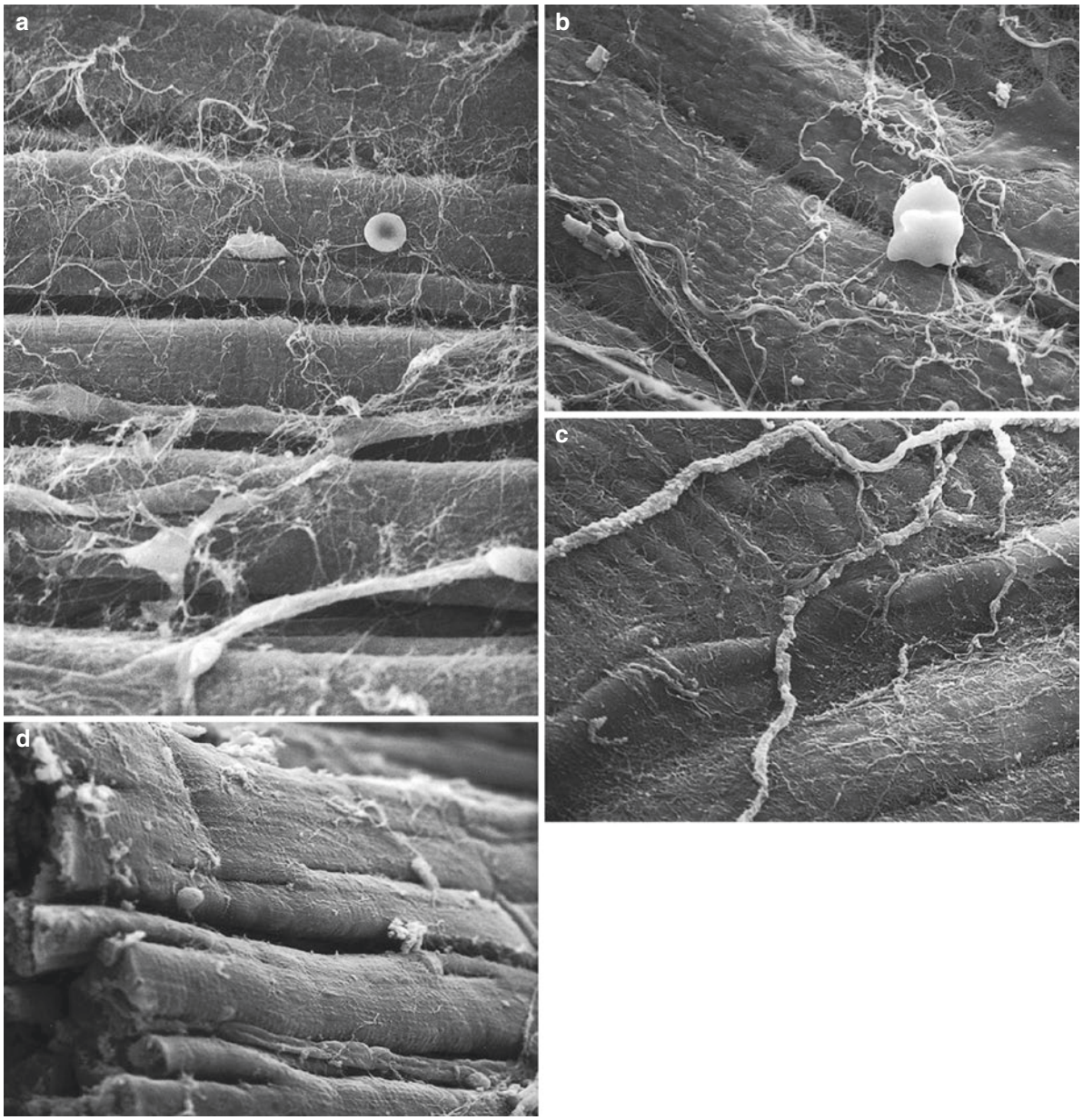

Fig. 10.3 Scanning electron micrographs from normal tissue, a nonischemic region, and stunned myocardial regions. Normal tissue (**a**) shows the usual dense and florid collagen weave enveloping the individual myocytes. There are abundant collagen struts that interconnect myocyte to myocyte and myocyte to capillary. The collagen struts are also connected to the collagen weave (×3000). In the nonischemic myocardial region (**b**), collagen cables are smooth and continuous, branch off into smaller cables, and connect with the underlying collagen weave on the surface of the myocyte (×5700). In the stunned myocardial region (**c**), the collagen cables are characterized by a rough, irregular, and notched appearance. The collagen weave is generally matted with a beaded and granular appearance, which is suggestive of degeneration (×9000). In another example of stunned myocardium (**d**), the normally ubiquitous myocyte-to-myocyte struts are minimal to absent, with nodular or nub-like structures that are likely indicative of broken collagen struts. In addition, there is almost complete absence of the perimysial weave (×2100) [10]

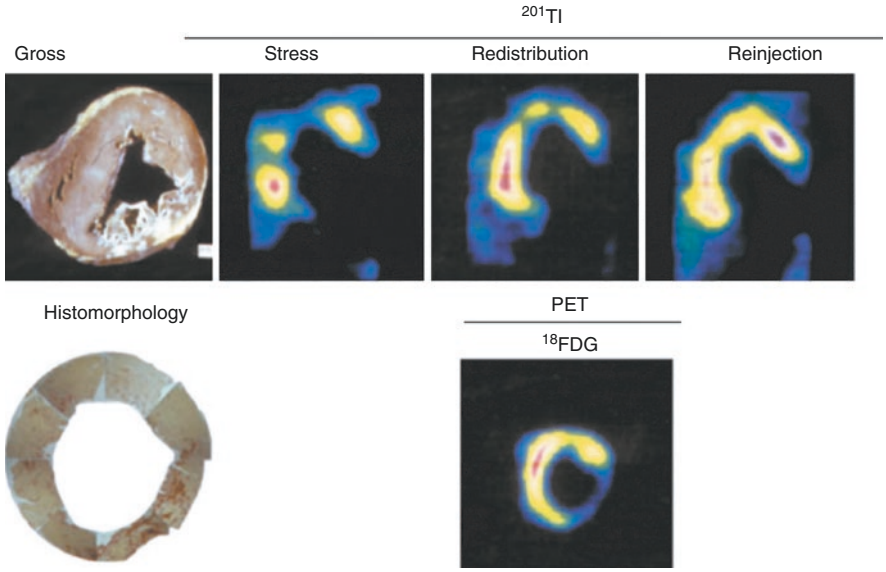

Fig. 10.4 Disparity between left ventricular contractile dysfunction and the extent of myocardial injury assessed by thallium scintigraphy. Shown here, there is a correlation between gross pathology, histomorphology, and ^{201}Tl and [^{18F}]-fluorodeoxyglucose (FDG) positron emission tomography (PET) studies from a patient with stable chronic ischemic heart disease and severe left ventricular dysfunction who underwent orthotopic cardiac transplantation. Gross pathology and histomorphology of a midventricular slice is shown (*left*) with corresponding thallium and FDG PET images (*right*). In the thallium study, there are extensive abnormalities in the anterior, septal, and inferolateral regions during stress. In the redistribution image, there is partial reversibility of the anterior region, complete reversibility of the septum, and an irreversible defect in the inferolateral region. After ^{201}Tl reinjection, there is complete reversibility of the septal and anterior regions with a persistent irreversible defect in the inferolateral region. The corresponding FDG PET image shows preserved metabolic activity and, hence, viability in all regions except for the inferolateral region. On gross pathology, there is white fibrotic myocardium in the inferolateral region, and histomorphologic analysis shows a significant amount of red-stained collagen intermixed within normal tissue. Because structural changes in the hibernating myocardium are chronic in nature and have developed over a prolonged period, some regions viable by scintigraphic or echocardiographic techniques may be irreversible despite successful revascularization [11]

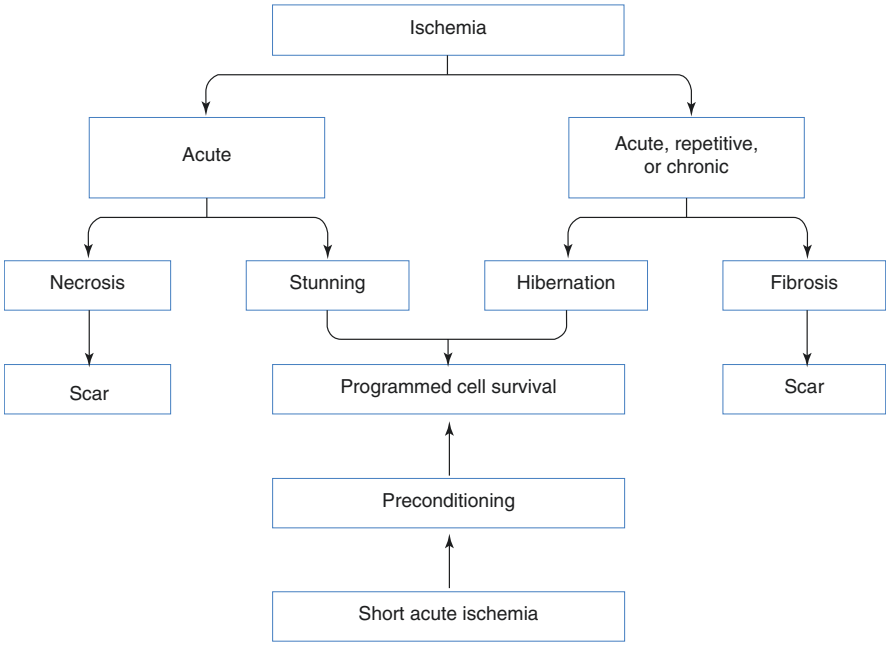

Fig. 10.5 Ischemic myocardium. An imbalance between oxygen supply, usually due to reduced myocardial perfusion, and oxygen demand, determined primarily by the rate and force of myocardial contraction, is termed *ischemic myocardium*. If the imbalance between oxygen supply and demand is transient (i.e., triggered by exertion), it represents reversible ischemia. On the other hand, if a regional oxygen supply–demand imbalance is prolonged, high-energy phosphates will be depleted, regional contractile function will progressively deteriorate, and cell membrane rupture with cell death will follow (myocardial necrosis and fibrosis). The phenomena of stunning, hibernation, and ischemic preconditioning represent different mechanisms of acute and chronic adaptation to a temporary or sustained reduction in coronary blood flow. Such modulated responses to ischemia are regulated to preserve sufficient energy to protect the structural and functional integrity of the cardiac myocyte. In contrast to programmed cell death, or apoptosis, Taegtmeyer [12] has coined the term *programmed cell survival* to describe the commonality between myocardial stunning, hibernation, and ischemic preconditioning independent of their disparate myocardial responses to acute and chronic ischemia

Left Ventricular Ejection Fraction

Left ventricular ejection fraction (LVEF) is a major determinant of survival in patients with acute and chronic coronary artery disease, as demonstrated by the Multicenter Postinfarction Trial [13], which showed a curvilinear relationship between mortality rates in the first year after myocardial infarction and predischarge LVEF (Fig. 10.6). This relationship has been demonstrated conclusively in virtually every study assessing patient outcome after myocardial infarction. It is apparent from the curve that attempts at further risk-stratification of patients with preserved left ventricular (LV) function (≥50%) will be problematic, because this cohort will have few cardiac-related deaths during the subsequent year after infarction. On the other hand, among patients with moderate-to-severe LV dysfunction, further risk stratification is both feasible and clinically relevant. LVEF is also a good indicator of the survival rate of patients with chronic stable coronary artery disease who are treated with medical therapy alone.

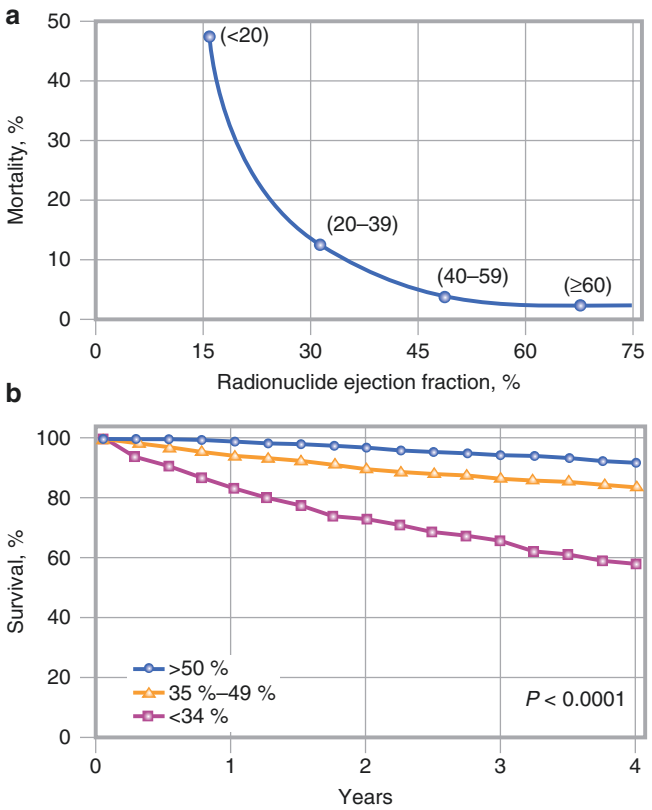

Fig. 10.6 (**a**) In patients with acute myocardial infarction, the Multicenter Postinfarction Trial showed a curvilinear relationship between mortality rates in the first year after myocardial infarction and predischarge left ventricular ejection fraction (LVEF). (**b**) In chronic stable coronary artery disease, the cumulative 4-year survival of the medically treated Coronary Artery Surgery Study registry patients based on LVEF at rest is shown. Patients with normal (>50%) or mildly reduced (35–49%) left ventricular function have an excellent 4-year survival rate on medical therapy (92% and 83%, respectively). On the other hand, patients with moderate to severely reduced (<34%) left ventricular function have a significantly lower 4-year survival rate (58%) when treated with medical therapy alone [13]

Patients with severely reduced LVEF experience greater survival benefit from surgical revascularization (Fig. 10.7), though their operative risk may be increased. More accurate prospective assessment of myocardial viability should increase the use of surgical treatment for these patients. The conventional wisdom that impaired LV function at rest is an irreversible process has been challenged by findings showing that, under certain conditions, the dysfunction may be completely reversible (Fig. 10.8). Figure 10.9 shows an example of recovery of LV function at rest in a patient following revascularization.

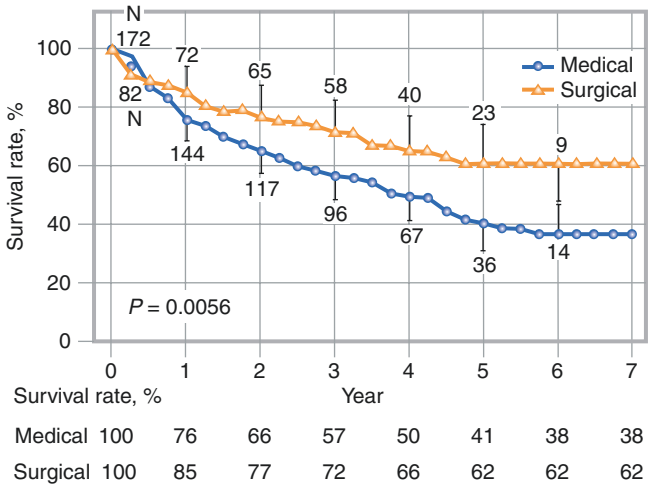

Fig. 10.7 Life-table cumulative survival for surgically and medically treated Coronary Artery Surgery Study registry patients with a severely reduced LVEF. Short-term and long-term surgical survival benefits are greatest in patients with the most severe left ventricular dysfunction. Among the patients with an LVEF of 25% or lower, the 5-year survival rate is 62% with surgical treatment and 41% with medical treatment. For surgically treated patients, the 1- and 2-year survival rates are 85% and 77% respectively, in contrast to 76% and 66% for medically treated patients. Myocardial reperfusion via revascularization ameliorates ischemic injury, recruits hibernating regions, and prevents future infarction. Because the operative risk of coronary artery bypass surgery is increased in this patient population, however, cardiac surgeons may be reluctant to operate on these patients without evidence of myocardial viability. With increased surgical expertise and improved intraoperative myocardial preservation techniques, combined with an accurate prospective assessment of myocardial viability, surgical mortality rates have decreased substantially since the 1980s [14]

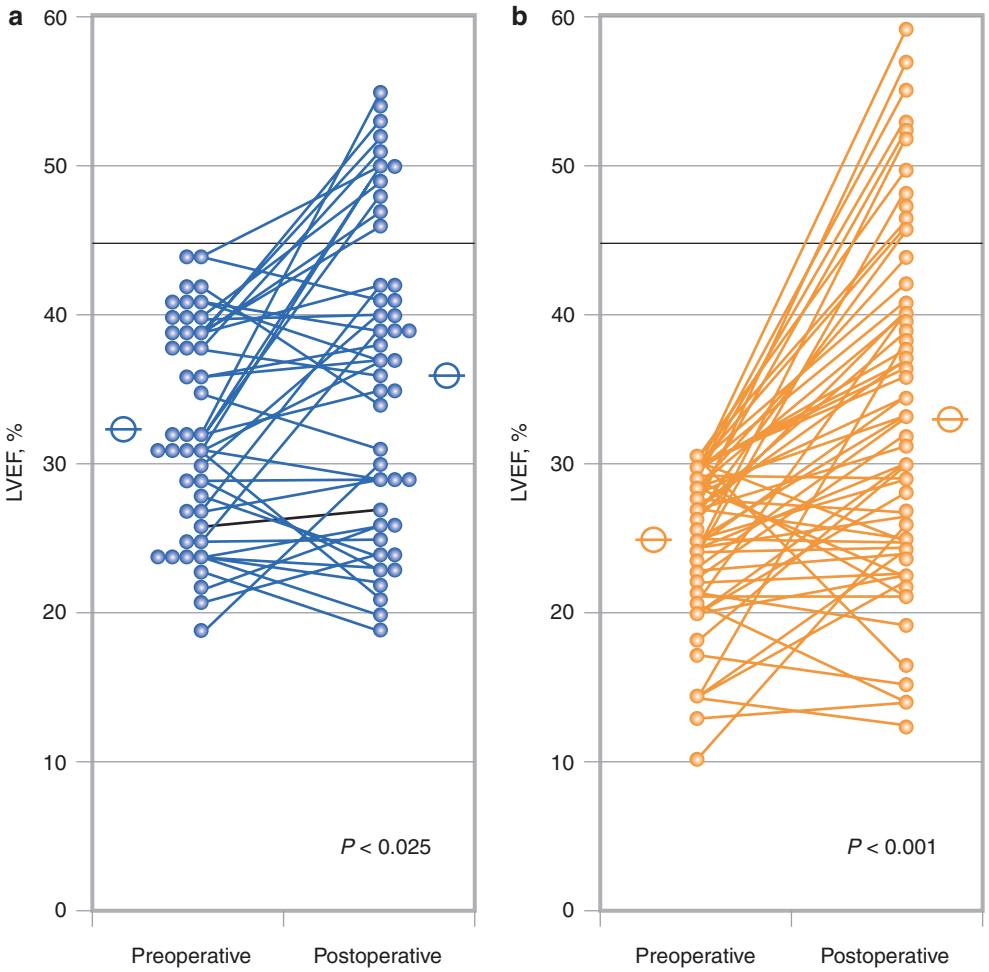

Fig. 10.8 Change in LVEF at rest before (*preoperative*) and after (*postoperative*) coronary artery bypass surgery. In patients with moderate (**a**) and severe (**b**) left ventricular dysfunction, successful coronary artery revascularization resulted in improved left ventricular function at rest in approximately one third of patients, challenging the conventional wisdom that impaired left ventricular function at rest is an irreversible process. Substantial data now exist to indicate that, under certain conditions, when viable myocytes are subjected to hypoperfusion or transient periods of ischemia, prolonged alterations in regional and global left ventricular function may occur and that this dysfunction may be completely reversible [15, 16]

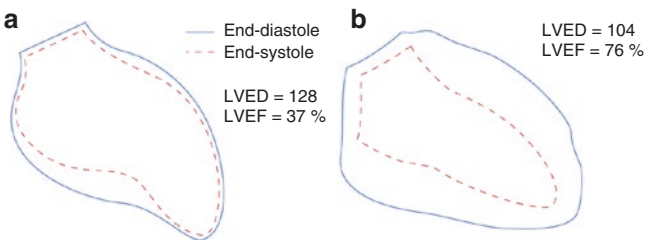

Fig. 10.9 Hibernating myocardium. Recovery of regional and global left ventricular function at rest following revascularization is shown in a patient with a totally occluded left anterior descending coronary artery and left ventricular dysfunction. Shown are end-diastolic and end-systolic silhouettes of the left ventricle from right anterior oblique contrast ventriculography before coronary artery bypass surgery (**a**) and 8 months after surgery (**b**). Preoperatively, the anteroapical region is akinetic, associated with a 37% LVEF at rest. Postoperatively, the anteroapical regional contraction is normal, and the LVEF at rest has nearly doubled to 76% [17]. LVED left ventricular end-diastolic volume

Evaluating Myocardial Viability

Figure 10.10 illustrates pathophysiologic paradigms concerning the relationship between myocardial perfusion and LV function in stunned and hibernating myocardium. The ischemic episodes that ultimately lead to myocardial stunning can be single or multiple, brief or prolonged, but never severe enough to result in myocardial necrosis. Hibernation is an adaptive response to repetitive ischemia. The contractile function of both stunned and hibernating myocardium should improve as ischemia is reduced. The myocardium of patients with chronic coronary artery disease is very likely to show both stunning and hibernation. Figures 10.11 and 10.12 show results of experiments involving stunned myocardium and short-term hibernation.

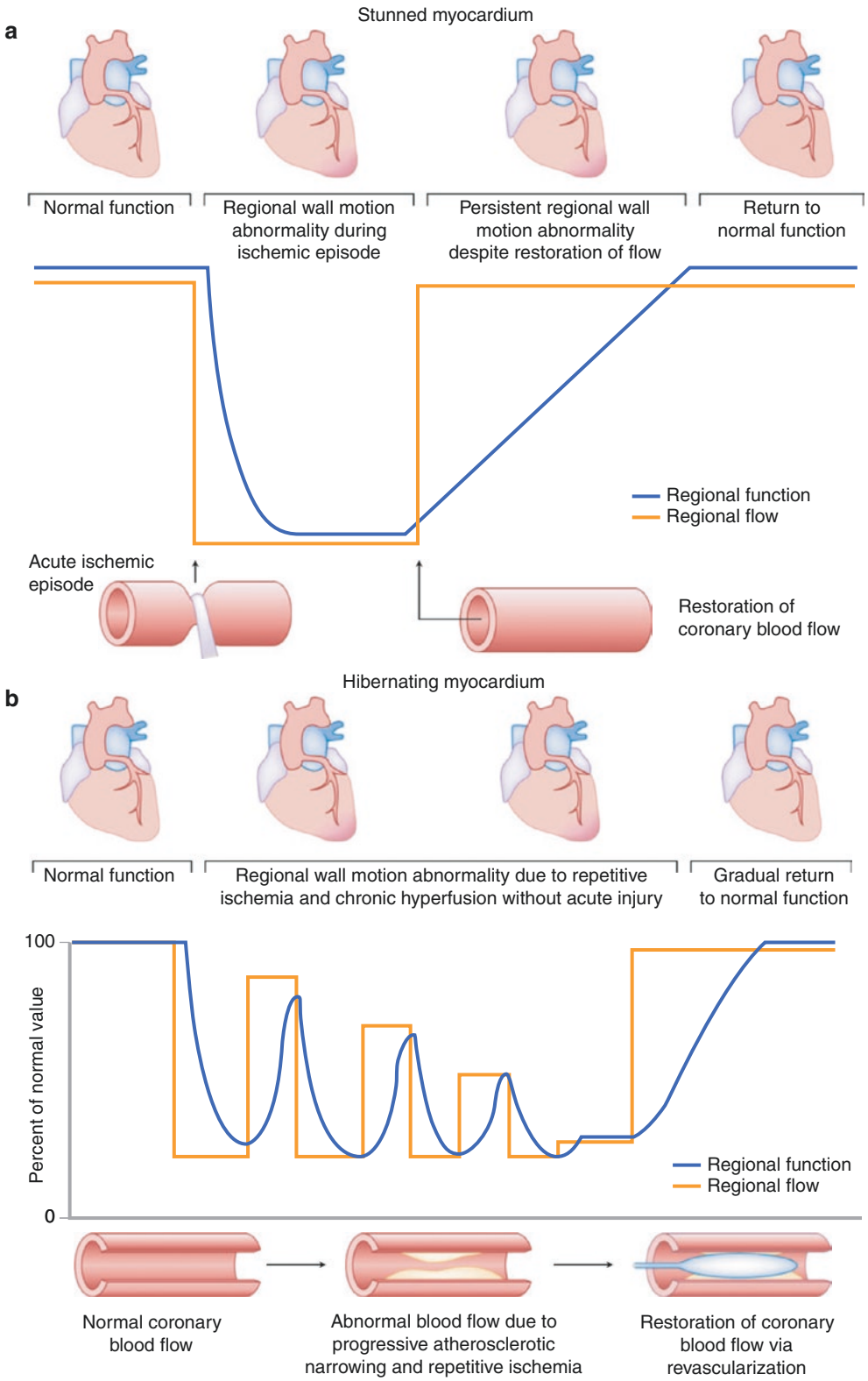

Fig. 10.10 Pathophysiologic paradigms concerning the relationship between myocardial perfusion and left ventricular function in stunned and hibernating myocardium. (**a**) "Stunned myocardium" refers to the state of delayed recovery of regional left ventricular dysfunction after a transient period of ischemia that has been followed by reperfusion [18]. The ischemic episodes that ultimately lead to myocardial stunning can be single or multiple, brief or prolonged, but never severe enough to result in myocardial necrosis. (**b**) "Hibernating myocardium" refers to an adaptive rather than injurious response of the myocardium, in which viable but dysfunctional myocardium arises from prolonged myocardial hypoperfusion at rest in the absence of clinically evident ischemia [19]. In stunning, interventions aimed at decreasing the frequency, severity, or duration of ischemic episodes would result in improved contractile function. In hibernation, interventions that favorably alter the supply/demand relationship of the myocardium, either an improvement in blood flow or reduction in demand, would be expected to improve contractile function. It is very likely, however, that in patients with chronic coronary artery disease, the adaptive responses of hibernation and injurious responses of stunning coexist

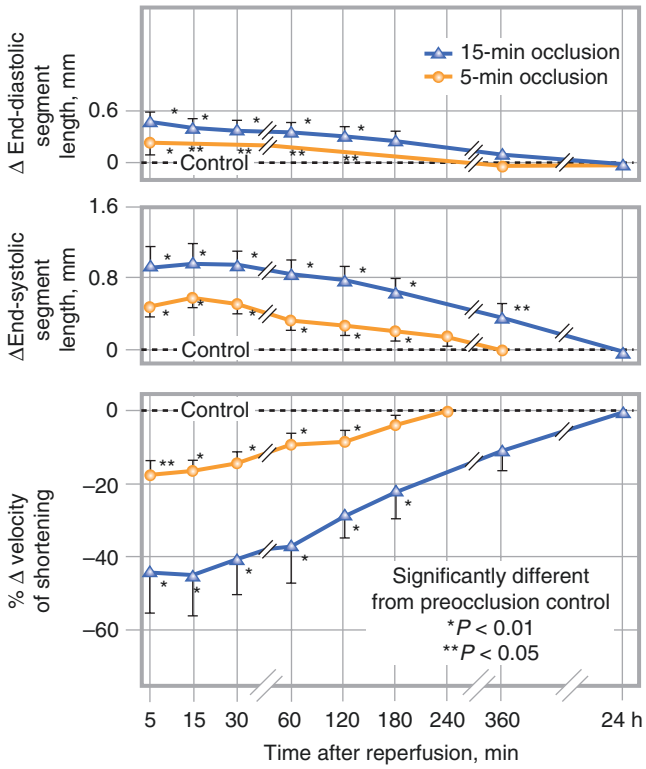

Fig. 10.11 Experimental evidence for stunned myocardium. Conscious dogs were subjected to 5 or 15 minutes of coronary artery occlusion followed by reperfusion. Recovery times for end-diastolic and end-systolic segment lengths and the velocity of shortening are shown after 5-minute (*yellow circles*) and 15-minute (*blue triangles*) occlusions. Recovery times shown range from 5 minutes to 24 hours after reperfusion. During the occlusion phase, regional systolic thickening was absent in the ischemic zone, and the electrocardiogram showed ST segment elevation. During the reperfusion phase, ST segments returned to baseline within 1 minute, and reactive hyperemia was observed within the ischemic zone, but systolic thickening remained depressed for more than 3 hours after the 5-minute coronary occlusion and for more than 6 hours after the 15-minute occlusion [20]

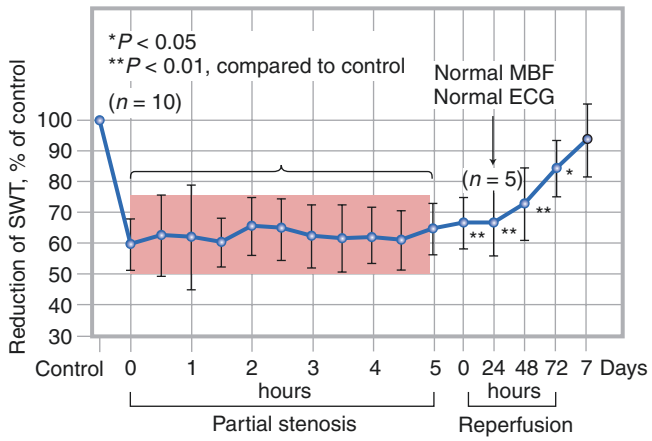

Fig. 10.12 Experimental model for short-term hibernation demonstrating a balanced reduction of myocardial function and myocardial blood flow (MBF) (contraction–perfusion match) in 10 dogs. Changes in systolic wall thickening (SWT) in the ischemic area during 5-hour partial coronary artery occlusion and after reperfusion are plotted as a percent of control at frequent intervals to indicate the sustained nature of the regional dysfunction. Data points are ±1 SD, which is within the limits of a 25–50% decrease in function (*shaded area*). After reperfusion, regional dysfunction initially remained depressed but showed a late recovery. At 24 hours after reperfusion, 5 of the 10 dogs had dysrhythmia. Thus, only the data obtained from the remaining 5 dogs were analyzed. The findings in this canine model indicate that prolonged moderate regional dysfunction caused by nontransmural ischemia during partial stenosis can be sustained for 5 hours. Furthermore, after reperfusion, there is complete recovery of regional and global contractile function within a period of 7 days. ECG electrocardiogram [21]

The earliest observation of signal-intensity changes in infarcted myocardium with contrast-enhanced cardiac magnetic resonance (CMR) dates back to 1993. While studying myocardial perfusion patterns in patients with acute and chronic myocardial infarction, increased signal intensity (greater T1 shortening after contrast) was observed in the infarcted, nonviable myocardium (approximately 10 minutes after bolus injection of the contrast) and was subsequently termed *delayed hyperenhancement*. Reversibly injured myocardium did not exhibit increased contrast concentration or enhancement. Several procedural and technologic improvements since 1993 have allowed CMR to take a more preeminent clinical role for the assessment of scarred myocardium. The current technique involves rapid infusion of a gadolinium chelate followed by a high-resolution cardiac-gated T1-weighted pulse sequence 5–30 minutes thereafter. If imaging is performed too early (<5 minutes after contrast infusion) or too late (>30 minutes after contrast infusion), it may result in underestimation or overestimation of the infarct size. A potential mechanism for the late gadolinium enhancement may relate to cellular degradation in the infarct region of the myocardium, an increase in tissue permeability in the region, and a consequent increase in the distribution volume of the extravascular space. When combined with slow washout characteristic of gadolinium chelates from infarcted myocardium, the net result is delayed contrast-enhanced T1-weighted images that appear bright in the infarcted tissue (Fig. 10.13). Because the contrast used is primarily an extracellular, interstitial agent, it has been hypothesized that it is the increased volume of distribution of the contrast molecules within the infarcted imaging voxel that is responsible for the greater shortening of the T1 relaxation time. The accuracy of this technique has been validated by comparison with histopathology [22] and nuclear techniques [23], as well as recovery of function (or lack thereof) after revascularization [24].

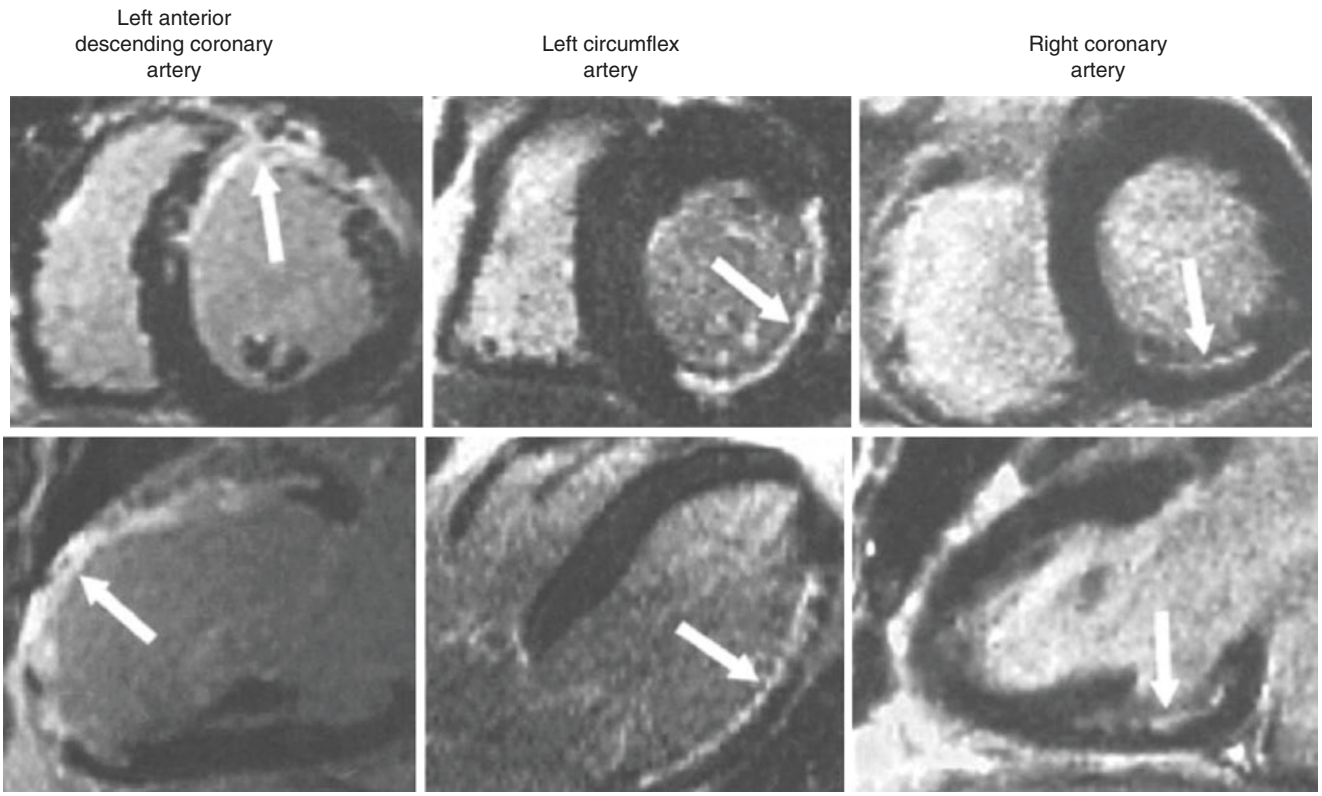

Fig. 10.13 Contrast-enhanced images obtained by cardiac MRI in chronic left ventricular dysfunction. Late gadolinium-enhanced images are shown in a short-axis view (*upper panels*) and a long-axis view (*lower panels*) in three patients. Hyperenhancement (*arrows*) is present in various coronary perfusion territories—the left anterior descending coronary artery, the left circumflex artery, and the right coronary artery—with a range of transmural involvement [24]

When taking into consideration regions with reversible defects (ischemia) and the success of revascularization (reexamining regional perfusion or vessel patency after revascularization), stress-redistribution-reinjection thallium imaging yields excellent positive and negative predictive accuracy for recovery of function after revascularization (Fig. 10.14) [26, 27]. Irrespective of the imaging modality applied, the data suggest that the recovery of function after revascularization is a continuum and is coupled to the ratio of viable to scarred myocardium within dysfunctional myocardial segments. The extent of infarct size on CMR or percent thallium defect on single-photon emission CT (SPECT) correlated with a decreasing likelihood of functional recovery after revascularization.

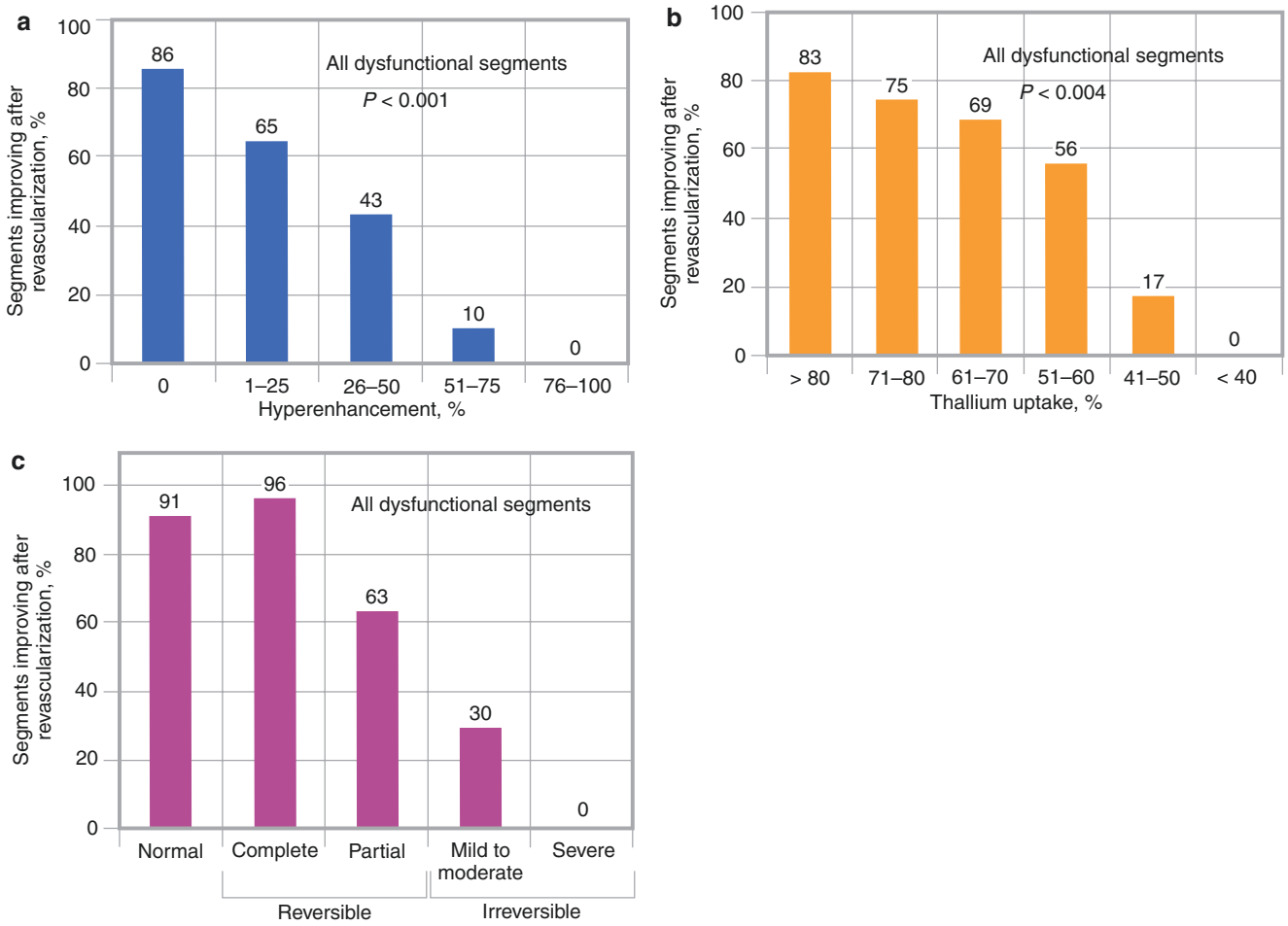

Fig. 10.14 Ratio of viable to scarred myocardium dictates recovery of function after revascularization. Shown is the relationship between the recovery of function after revascularization with contrast-enhanced CMR (**a**) [24] and two thallium protocols optimized for viability detection: rest-redistribution (**b**) [25] and stress-redistribution-reinjection (**c**) [26]. The rest-redistribution protocol assesses myocardial viability alone, while the stress-redistribution-reinjection protocol assesses myocardial ischemia and viability

Thallium SPECT protocols (Fig. 10.15) have an advantage over delayed-enhancement CMR in providing additional insight into potential mechanisms of the underlying cause of regional and global LV dysfunction. Regional LV dysfunction could be attributed to scarred, hibernating, stunned, or remodeled myocardium. Having two or three sets of images with thallium SPECT, one can tease out three scintigraphic patterns that can differentiate between the three pathophysiologic conditions of scarred, hibernating, or stunned myocardium as the underlying cause of the LV dysfunction. In the case of scarred myocardium, there will be no change in the percent LV defect size from rest to redistribution. On the other hand, if the myocardium is hibernating but viable, the percent LV defect size will get smaller from rest to redistribution images. For stunned myocardium, the pattern of "reverse redistribution" will be present, especially when the images are acquired during the acute phase of myocardial injury following either a spontaneous, pharmacologic, or mechanical intervention.

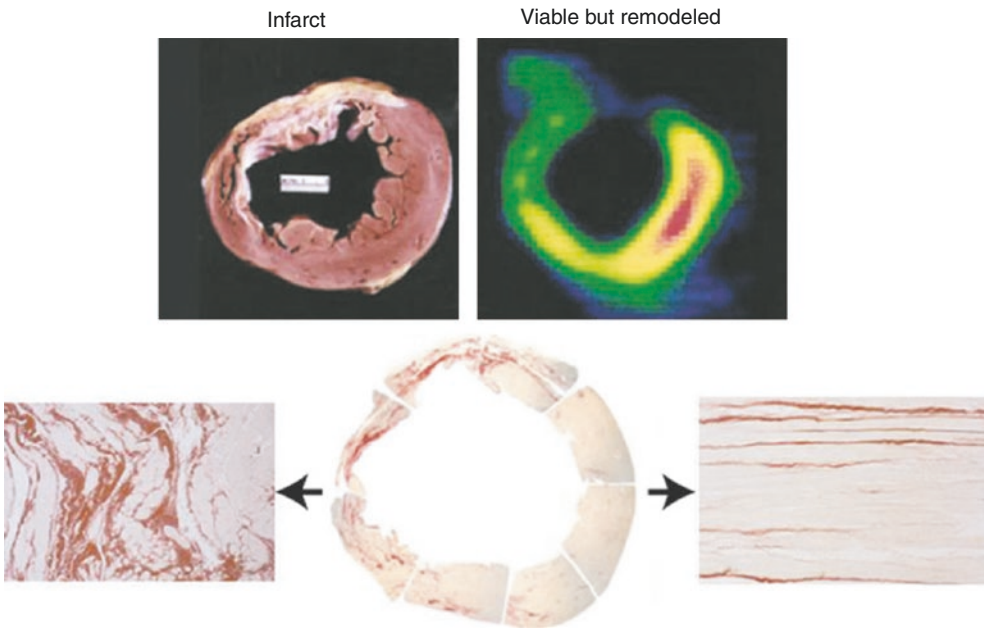

Fig. 10.15 Left ventricular (LV) remodeling. Shown is histomorphologic evidence for structural alterations in the extracellular matrix of remodeled areas of the left ventricle from a patient with stable chronic ischemic heart disease and severe LV dysfunction who underwent orthotopic cardiac transplantation. On gross pathology (*top left*), there is evidence for myocardial scarring in the anterior region, extending to the anteroseptal region, with hypertrophy of the remaining myocardial regions secondary to LV remodeling. Thallium tomogram acquired prior to cardiac transplantation (*top right*) shows severe defects in the corresponding scarred anterior and anteroseptal regions and normal uptake in the remodeled lateral region of the myocardium. Histomorphologic analysis of infarct and noninfarct myocardial segments (*bottom*), using picrosirius red stain, confirms transmural collagen replacement in the infarct region (*bottom left*), as was detected by both gross pathology and thallium SPECT. However, in the noninfarct, remodeled myocardium, layers of collagen replacement within the extracellular matrix of morphologically normal-appearing myocytes are seen that could not be detected by thallium SPECT or gross pathology [28]

Figure 10.16 demonstrates the prognostic implications of myocardial viability testing in patients with coronary artery disease and LV dysfunction. In patients with preserved myocardial viability, the annual mortality rate was significantly lower for those who were treated with revascularization, compared with those treated with medical therapy alone, but among patients without evidence of viable myocardium, there was no incremental benefit of revascularization over medical therapy. These findings support the role of myocardial viability testing in guiding therapeutic decisions.

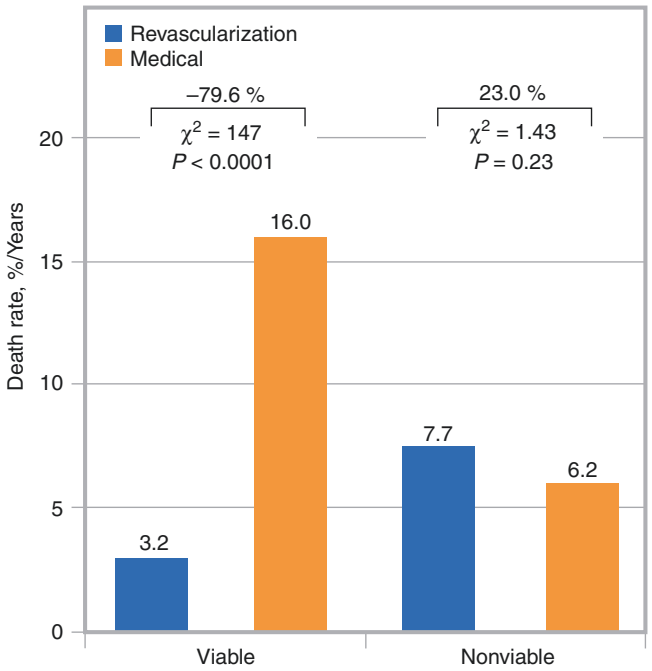

Fig. 10.16 Prognostic implications of myocardial viability testing in patients with coronary artery disease and LV dysfunction. Data from a meta-analysis of 3088 patients (mean LVEF, 32%, followed for 25 ± 10 months) demonstrates that the annual mortality rate in patients with preserved myocardial viability was significantly lower in those who were treated with revascularization (3.2%) compared with those treated with medical therapy alone (16%). This represents a 79.6% decrease in annual mortality for patients with viability treated with revascularization ($P < 0.0001$). Moreover, a direct relationship was shown between the severity of LV dysfunction and the magnitude of benefit from revascularization among patients with myocardial viability ($P < 0.001$). In contrast, among patients without evidence of viable myocardium, there was no incremental benefit of revascularization over medical therapy. These data support the role of myocardial viability testing for the management of patients with chronic LV dysfunction and in guiding therapeutic decisions for revascularization [29]

Over the past several decades, a large number of studies have demonstrated that myocardial viability may be accurately assessed using a variety of radionuclide-based techniques. These include SPECT imaging with thallium-201 or technetium-99 m labeled perfusion tracers, as well as glucose utilization with ^{18}F-2-fluoro-2-glucose PET. Using these techniques, it is possible to predict which patients are likely to have improvement in LV function after revascularization as well as improvement in heart failure symptoms and patient outcome. In patients with heart failure and active angina, the American College of Cardiology/American Heart Association guidelines suggest referring these patients directly for angiography, as they will benefit from revascularization, in terms of natural history [30]. On the other hand, in patients with known coronary artery disease and LV dysfunction without angina, the American College of Cardiology/American Heart Association/American Society of Nuclear Cardiology guidelines consider radionuclide assessment of myocardial viability as a class I indication for consideration of revascularization [31].

Regarding myocardial viability assessment and patient outcome, the PET And Recovery after Revascularization-2 (PARR-2) trial was the first to prospectively address this subject in patients with ischemic LV dysfunction [32]. The clinical strategy was to randomize patients to undergo either PET-guided viability imaging or standard non-PET-guided decision of revascularization versus medical therapy. Primary outcome events were defined as cardiac death, myocardial infarction, or repeat hospitalization at 1 year. In the PARR-2 randomized trial, there was 25% nonadherence to PET management recommendations, and the findings showed only a trend toward benefit in the PET group compared with the standard group, but when only patients who adhered to the PET-guided recommendations were considered (182 patients with ischemic cardiomyopathy and LVEF <35%), there was a statistically significant survival benefit for viability testing with PET compared with standard care ($P<0.02$) [33]. Figure 10.17 shows the differences in patient outcome with revascularization versus medical therapy depending on the PET mismatch pattern.

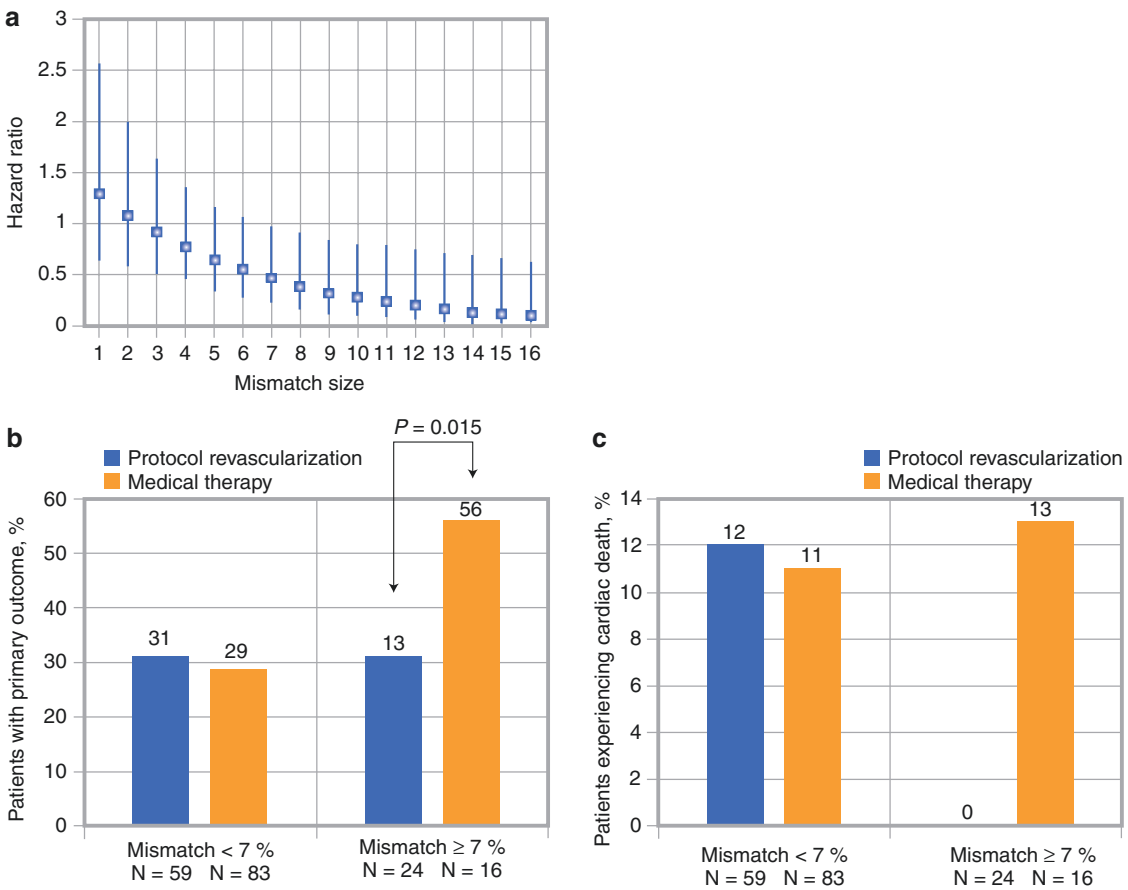

Fig. 10.17 Effects of revascularization versus medical therapy on patient outcome in patients with positron emission tomography (PET) mismatch pattern, as found in the PET And Recovery after Revascularization-2 (PARR-2) trial. (**a**) Shows the interaction hazard ratios and 95% confidence interval at various levels of PET mismatch measured as a continuous variable. As mismatch increases above 7%, there is a decreased risk of the primary outcome for those who undergo revascularization. For those with a mismatch of 7%, there is a 0.46 times lower risk for the primary outcome if revascularization is performed. (**b**) For patients with mismatch of less than 7%, there is no significant difference in the primary outcome with revascularization. In contrast, in patients with mismatch of at least 7%, a significantly lower percentage of patients had adverse events with revascularization compared with medical therapy ($P=0.015$). (**c**) No patient with mismatch of at least 7% who underwent revascularization died, compared with 13% of patients who were treated medically [33]

In the Surgical Treatment for Ischemic Heart Failure (STICH) trial, of the 1212 patients who were randomized to medical therapy alone or medical therapy plus coronary artery bypass grafting (CABG), 50% underwent a myocardial viability assessment with either SPECT or dobutamine echocardiography [34]. Figure 10.18 shows the differences in probability of death in those with an without the detection of viability. The STICH trial did have a number of limitations, however: (1) Lack of assessment for myocardial ischemia with stress SPECT or a biphasic response with dobutamine echocardiography. If patients with myocardial ischemia were excluded or not enrolled in the STICH trial (patient-referral bias) and were instead referred to CABG or multivessel percutaneous intervention, then the findings in this study are not surprising, particularly when authors classify areas with mild-to-moderate tracer content (without assessing ischemia) as viable; these are likely to represent areas of nontransmural infarction, resulting in the assigning 81% of patients to have viable myocardium. (2) Imaging selection bias during the recruitment process, with only 50% of patients undergoing viability testing (left up to the recruiting investigators). The patient population is not representative of patients undergoing viability studies with a view toward revascularization. (3) Lack of state-of-the-art myocardial viability assessment with FDG PET metabolism [35] and multiparametric CMR protocols [19].

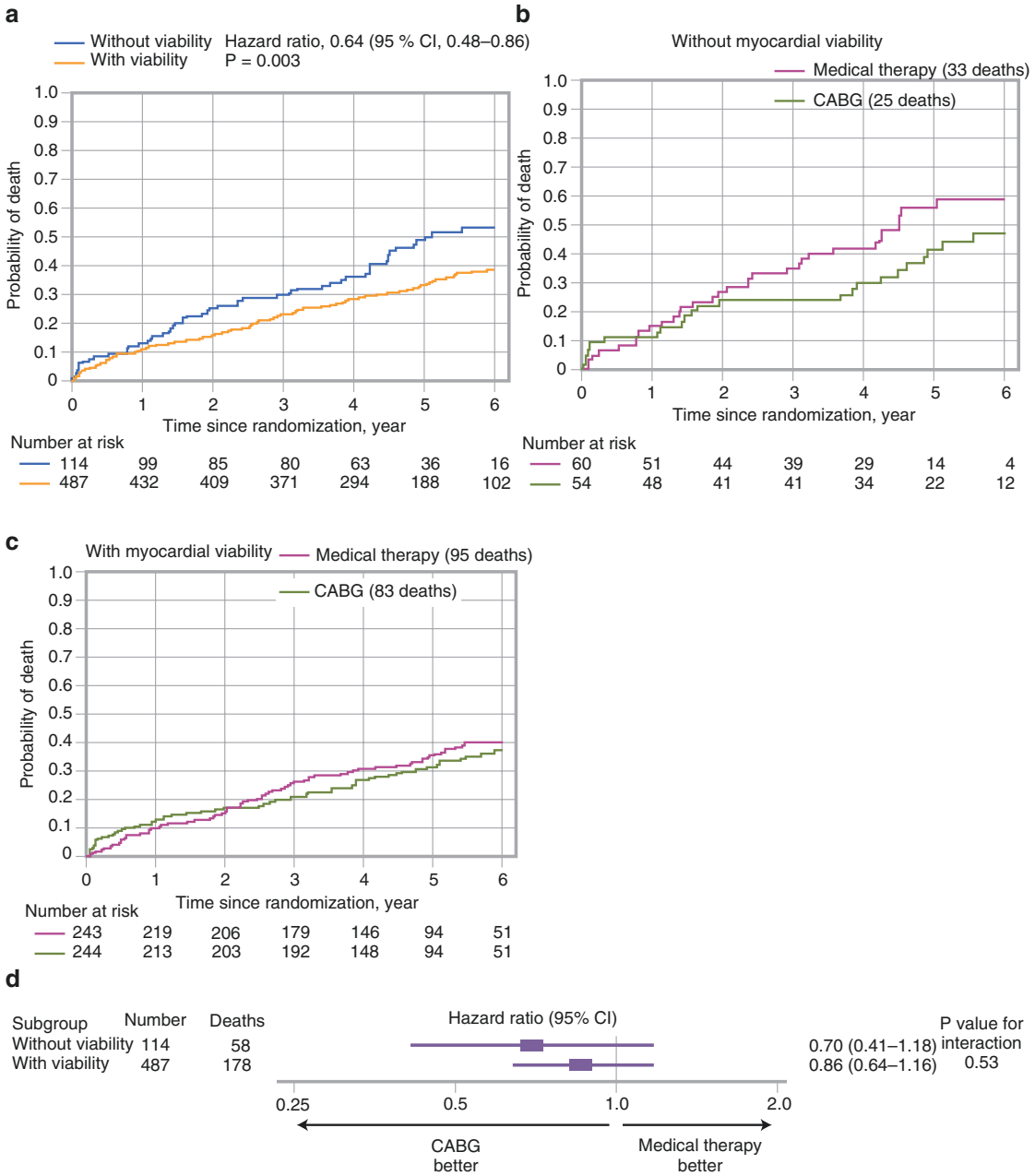

Fig. 10.18 Kaplan–Meier analysis of the probability of death according to myocardial viability status and treatment. In the Surgical Treatment for Ischemic Heart Failure (STICH) trial, of the 1212 patients who were randomized to medical therapy alone or medical therapy plus coronary artery bypass grafting (CABG), 601 (50%) underwent a myocardial viability assessment with either SPECT or dobutamine echocardiography [34]. (**a**) The number of deaths among patients with "substantial" viability using prespecified criteria was significantly lower (179, 37%) than among patients without viability (58, 51%; $P = 0.003$). After adjusting for other prognostic variables on multivariable analysis, however, the between-group difference was rendered not significant. (**b**) At 5 years in the intention-to-treat analysis, the rates of death for a patient without viability were 40.5% in the group assigned to undergo CABG and 55.8% in the group assigned to medical therapy. (**c**) Among patients with myocardial viability, the rate of death was 30.2% with CABG and 35.4% for medical therapy. (**d**) There was no significant interaction between viability imaging status and treatment assignment with respect to mortality [34]

The STICH investigators recently presented data from a longer follow-up of 601 patients with ischemic cardiomyopathy (LVEF <35%) who were amenable to CABG [36]. These patients were randomly assigned to undergo CABG with optimum medical therapy or to receive medical therapy alone. The LVEF was measured at baseline and after 4 months of follow-up in 318 patients. The primary end point was death from any cause, during the median follow-up of 10.4 years (Fig. 10.19). CABG plus medical therapy was associated with a lower incidence of death from any cause than medical therapy alone (182 deaths among 298 patients in the CABG group vs. 209 of 303 patients in the medical-therapy group; adjusted HR, 0.73; 95% CI, 0.60–0.90). No significant interaction was observed between the presence or absence of myocardial viability and the beneficial effect of CABG plus medical therapy over medical therapy alone ($P = 0.34$ for interaction). An increase in LVEF was observed only among patients with myocardial viability, regardless of treatment assignment, but there was no association between changes in LVEF and subsequent death. However, it is important to point out that the viability substudy portion of the STICH trial was not blinded or randomized. The clinicians were not blinded to the results of viability imaging, which might have excluded patients with extensive myocardial ischemia or viable, hibernating myocardium on the basis of imaging. Therefore, there is the potential for a significant ethical dilemma (clinical equipoise) by the clinician-investigators of enrolling patients with extensive ischemia or viability into a randomized trial (such as STITCH) who would otherwise benefit from revascularization (standard guideline-supported clinical practice). With these limitations in mind, the presence of viable myocardium was associated with improvement in LV systolic function, regardless of treatment, but this improvement was not related to long-term survival. These new data suggest that viability is the main driver of functional improvement but recent advances in medical therapy allow for comparable survival benefit. We believe that STICH in the long term justifies continuation of viability assessment for functional improvement and personalization of management strategy.

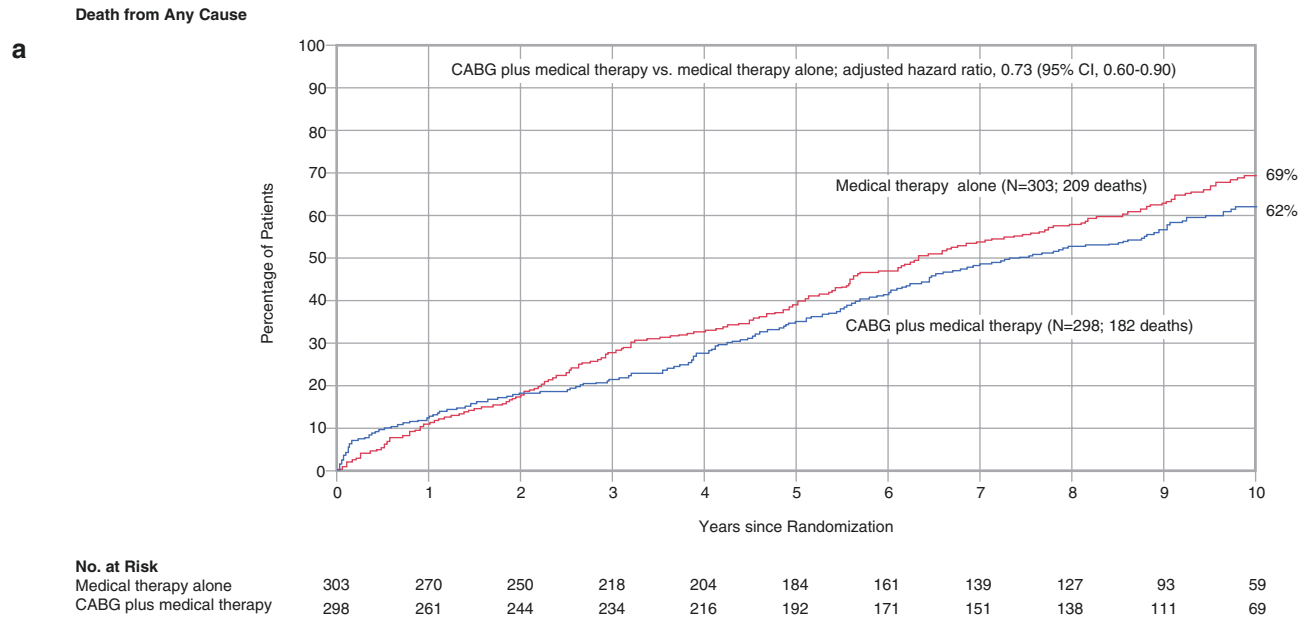

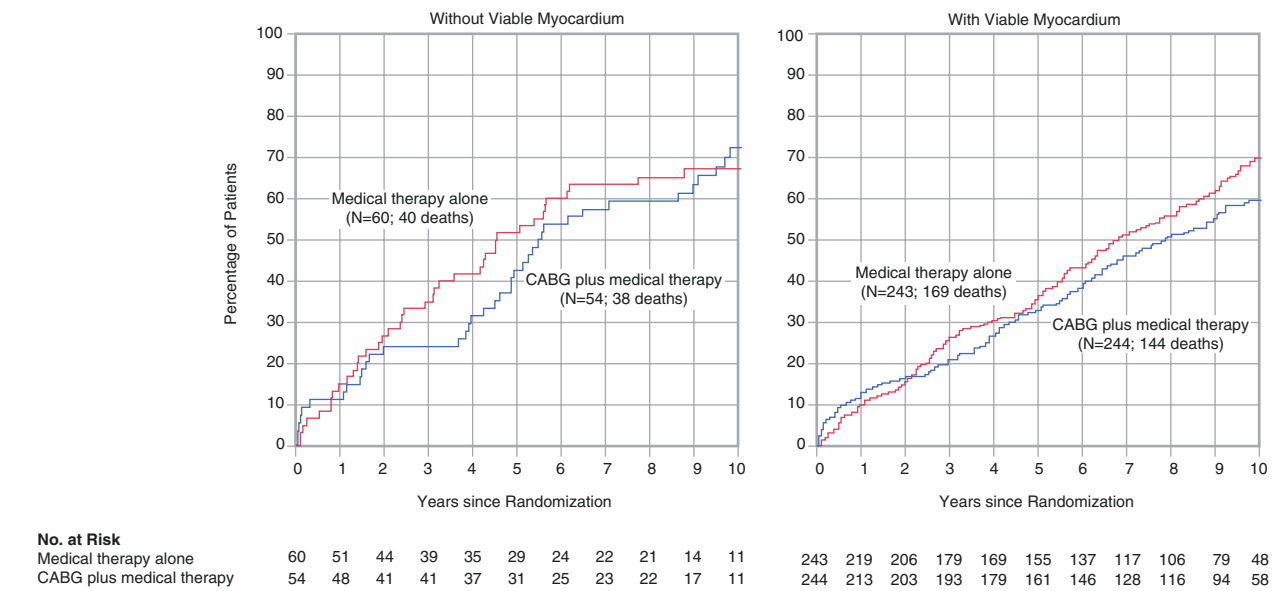

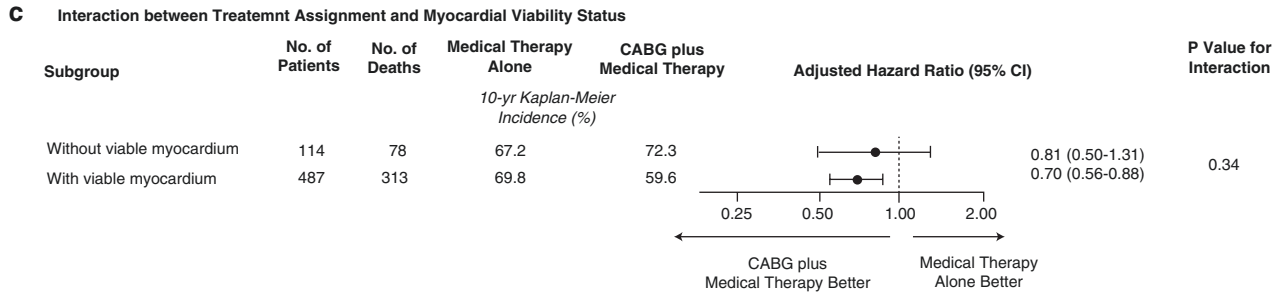

Fig. 10.19 Myocardial viability and long-term outcomes in ischemic cardiomyopathy, in longer follow-up of the STICH trial. (**a**) The incidence of death from any cause among patients who underwent a myocardial viability test, according to treatment group; results were compared with the use of a Cox proportional-hazards model with adjustment for baseline covariates. (**b**) The incidence of death from any cause among patients without viable myocardium (left panel) and among those with viable myocardium (right panel), according to treatment group. (**c**) Results of a Cox proportional-hazards model that tested for the interaction between myocardial viability and treatment, with adjustment for baseline covariates [36]. CABG coronary artery bypass grafting

Arithmetic of Altered Myocardial States

Improvements in LV function can be explained by the heterogeneity of altered myocardial substrates that may exist simultaneously in dysfunctional muscle segments. The heterogeneity can be described by simultaneous assessment of perfusion, function, and contractile reserve (CR) using gated SPECT imaging [37]. Figure 10.20 presents evidence of this heterogeneity in the results of a study of patients with ischemic cardiomyopathy using SPECT with high and low doses of dobutamine to characterize various types of myocardial dysfunction.

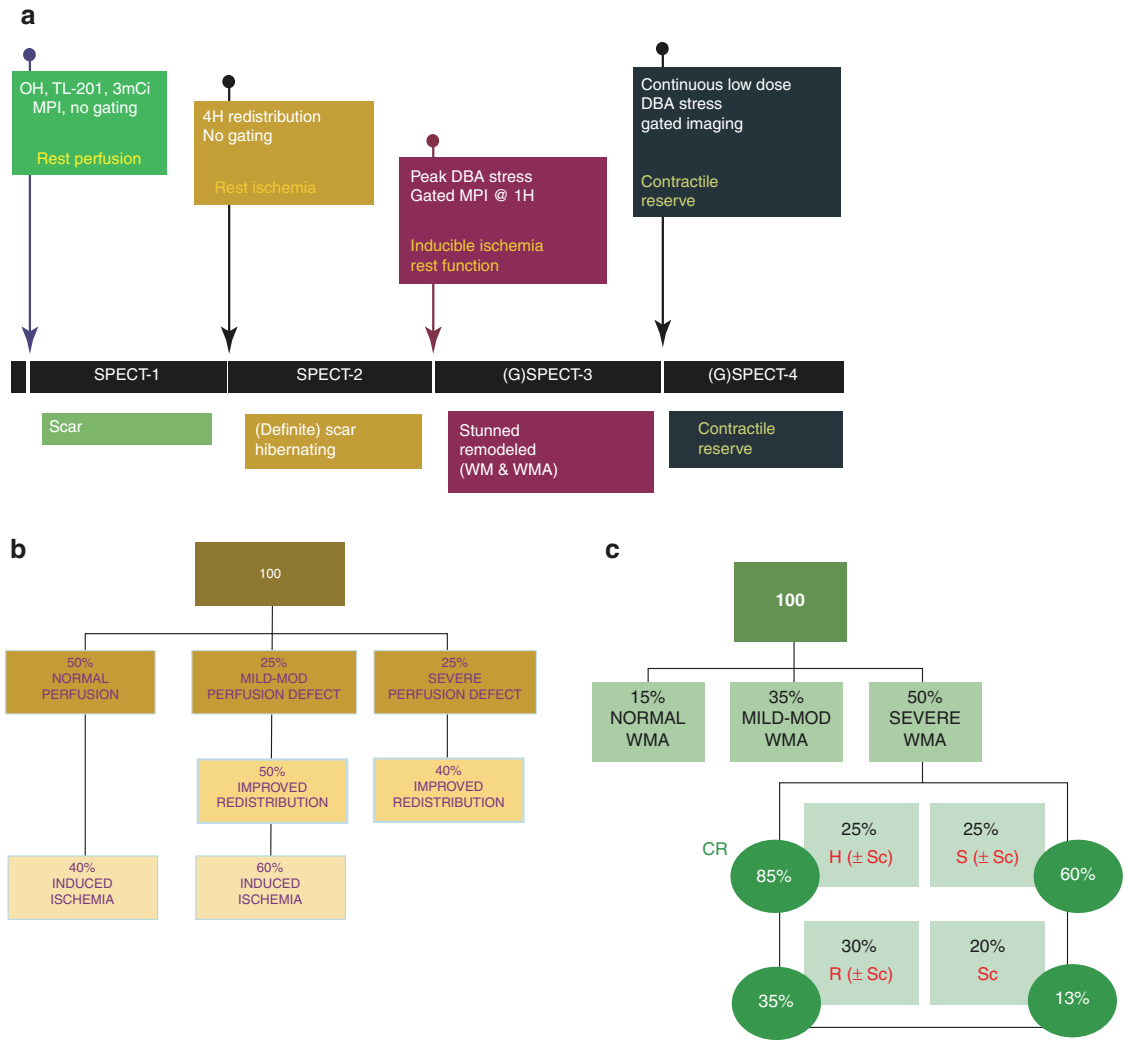

Fig. 10.20 Arithmetic of altered myocardial states. All numbers in **b** and **c** are presented as percentages and rounded to the nearest convenient number. (**a**) In a study of 54 patients with ischemic cardiomyopathy, rest and 4-hour (4H) redistribution thallium-201 (Tl-201) imaging was undertaken, followed by maximum-dose dobutamine technetium-99m sestamibi SPECT imaging. The sestamibi images were acquired 1 hour after infusion of the maximal tolerated dose of dobutamine and again during infusion of dobutamine at a low dose (10 μ/kg/min) to estimate contractile reserve. Myocardial segments were defined as hibernating, stunned, remodeled, or scarred. Based on segmental perfusion and function, several definitions of altered myocardial states were developed: *Myocardial hibernation:* Segments with severe systolic dysfunction were called hibernating if they demonstrated evidence of hypoperfusion at rest (rest ischemia). Therefore, the segments with regional dysfunction (SPECT-3 wall motion score = 0 or 1) and evidence of reversible thallium defects (SPECT-2 perfusion score > SPECT-1 perfusion score) were considered to represent hibernating myocardium. *Myocardial stunning:* The presence of function-flow mismatch (contractile abnormality with normal perfusion) has traditionally been considered as stunned myocardium. Therefore, segments with regional dysfunction (SPECT-3 wall motion score = 0 or 1) and normal thallium at rest or mild to moderate fixed thallium defects (SPECT-1 and SPECT-2 perfusion score = 2 to 4) were considered stunned if they developed ischemia with dobutamine stress (SPECT-3 perfusion score < SPECT-1 perfusion score). *Myocardial remodeling:* Segments with regional dysfunction (SPECT-3 wall motion score = 0 or 1) and normal thallium at rest or redistribution or only mild to moderate perfusion defects (SPECT-1 and SPECT-2 perfusion score = 2 to 4) and no dobutamine-inducible ischemia (SPECT-3 perfusion score = SPECT-1 perfusion score) were referred as "remodeled segments." *Myocardial scarring:* Segments with regional dysfunction (SPECT-3 wall motion score = 0 or 1) with severe fixed perfusion defects at rest, redistribution, and stress (SPECT-1, SPECT-2, and SPECT-3 perfusion score = 0 or 1) were considered as scarred or irreversibly damaged myocardium. (**b**) Of 1080 segments analyzed, the thallium perfusion pattern at rest (SPECT-1) was normal in 557 segments (52%), showed mild to moderate perfusion defects in 273 segments (25%), and showed severe defects in 250 segments (23%). Redistribution images acquired 4 hours later (SPECT-2, second row) demonstrated improvement in perfusion in 127 (47%) of the 273 segments with mild to moderate defects and in 93 (37%) of 250 segments with severe defects. The SPECT-3 images (bottom row) demonstrated ischemia in 223 (40%) of 557 segments with normal thallium perfusion and 159 (58%) of 273 segments with mild to moderate fixed thallium defects. **C,** Severe regional dysfunction was present in 584 (54%) of 1080 segments. Based on the combination of function and perfusion characteristics in these segments, 24% (n = 140) were labeled as hibernating (H); 23% (n = 136) as stunned (S); 30% (n = 177) as remodeled (R); and 22% (n = 131) as scarred (Sc). Contractile reserve (CR), represented by improvement in wall motion/thickening by low-dose dobutamine, was observed in 83% of stunned myocardial segments, 59% of hibernating segments, 35% of remodeled segments, and 13% of scarred segments ($p < 0.05$). MPI myocardial perfusion imaging, WMA wall motion abnormality

References

1. Taegtmeyer H, Sharma S, Golfman L, et al. Linking gene expression to function: metabolic flexibility in normal and diseased heart. Ann N Y Acad Sci. 2004;1015:1–12.
2. Depre C, Taegtmeyer H. Metabolic aspects of programmed cell survival and cell death in the heart. Cardiovasc Res. 2000;45:538–48.
3. Kim HD, Kim DJ, Lee IJ, et al. Human fetal heart development after mid-term: morphometry and ultrastructural study. J Mol Cell Cardiol. 1992;24:949–65.
4. Narula J, Young JB. Pathogenesis of heart failure: the penultimate survival instinct? Heart Fail Clin. 2005;1:xi–xii.
5. Narula J, Haider N, Virmani R, DiSalvo TG, Kolodgie FD, Hajjar RJ, et al. Apoptosis in myocytes in end-stage heart failure. N Engl J Med. 1996;335:1182–9.
6. Narula J, Pandey P, Arbustini E, Haider N, Narula N, Kolodgie FD, et al. Apoptosis in heart failure: release of cytochrome c from mitochondria and activation of caspase-3 in human cardiomyopathy. Proc Natl Acad Sci U S A. 1999;96:8144–9.
7. Narula N, Narula J, Zhang PJ, Haider N, Raghunath PN, Brittin R, et al. Is the myofibrillarlytic myocyte a forme fruste apoptotic myocyte? Ann Thorac Surg. 2005;79:1333–7; discussion 1337.
8. Kanoh M, Takemura G, Misao J, Hayakawa Y, Aoyama T, Nishigaki K, et al. Significance of myocytes with positive DNA in situ nick end-labeling (TUNEL) in hearts with dilated cardiomyopathy: not apoptosis but DNA repair. Circulation. 1999;99:2757–64.
9. van den Borne SW, Diez J, Blankesteijn WM, Verjans J, Hofstra L, Narula J. Myocardial remodeling after infarction: the role of myofibroblasts. Nat Rev Cardiol. 2010;7:30–7.
10. Zhao MJ, Zhang H, Robinson TF, Factor SM, Sonnenblick EH, Eng C. Profound structural alterations of the extracellular collagen matrix in postischemic dysfunction ("stunned") but viable myocardium. J Am Coll Cardiol. 1987;10:1322–34.
11. Shirani J, Lee J, Quigg RJ, Pick R, Bacharach SL, Dilsizian V. Relation of thallium uptake to morphologic features of chronic ischemic heart disease: evidence for myocardial remodeling in noninfarct myocardium. J Am Coll Cardiol. 2001;38:84–90.
12. Taegtmeyer H. Modulation of responses to myocardial ischemia: metabolic features of myocardial stunning, hibernation, and ischemic preconditioning. In: Dilsizian V, editor. Myocardial viability: a clinical and scientific treatise. Armonk: Futura; 2000. p. 25–36.
13. The Multicenter Postinfarction Research Group. Risk stratification and survival after myocardial infarction. N Engl J Med. 1983;309:331–6.
14. Alderman EL, Fisher LD, Litwin P, Kaiser GC, Myers WO, Maynard C, et al. Results of coronary artery surgery in patients with poor left ventricular function (CASS). Circulation. 1983;68:785–95.
15. Bonow RO, Dilsizian V. Thallium-201 for assessment of myocardial viability. Sem Nucl Med. 1991;21:230–41.
16. Elefteriades JA, Tolis G Jr, Levi E, Mills LK, Zaret BL. Coronary artery bypass grafting in severe left ventricular dysfunction: excellent survival with improved ejection fraction and functional state. J Am Coll Cardiol. 1993;22:1411–7.
17. Rahimtoola SH. A perspective on the three large multicenter randomized clinical trials of coronary bypass surgery for chronic stable angina. Circulation. 1985;72(Suppl V):V123–35.
18. Braunwald E, Kloner RA. The stunned myocardium: prolonged, postischemic ventricular dysfunction. Circulation. 1982;66:1146–9.
19. Greenwood JP, Maredia N, Younger JF, Brown JM, Nixon J, Everett CC, et al. Cardiovascular magnetic resonance and single-photon emission computed tomography for diagnosis of coronary heart disease (CE-MARC): a prospective trial. Lancet. 2012;379(9814):453–60.
20. Heyndrickx GR, Millard RW, McRitchie RJ, Maroko PR, Vatner SF. Regional myocardial functional and electrophysiological alterations after brief coronary artery occlusion in conscious dogs. J Clin Invest. 1975;56:978–85.
21. Matsuzaki M, Gallagher KP, Kemper S, White F, Ross J Jr. Sustained regional dysfunction produced by prolonged coronary stenosis: gradual recovery after reperfusion. Circulation. 1983;68:170–82.
22. Arnado LC, Gerber BL, Gupta SN, Rettmann DW, Szarf G, Schock R, et al. Accurate and objective infarct sizing by contrast-enhanced magnetic resonance imaging in a canine myocardial infarction model. J Am Coll Cardiol. 2004;44:2383–9.
23. Klein C, Nekolla SG, Bengel FM, Momose M, Sammer A, Haas F, et al. Assessment of myocardial viability with contrast-enhanced magnetic resonance imaging: comparison with positron emission tomography. Circulation. 2002;105:162–7.
24. Kim RJ, Wu E, Rafael A, Chen EL, Parker MA, Simonetti O, et al. The use of contrast-enhanced magnetic resonance imaging to identify reversible myocardial dysfunction. N Engl J Med. 2000;343:1445–53.
25. Perrone-Filardi P, Pace L, Prastaro M, Squame F, Betocchi S, Soricelli A, et al. Assessment of myocardial viability in patients with chronic coronary artery disease. Rest-4-hour-24-hour 201Tl tomography versus dobutamine echocardiography. Circulation. 1996;94:2712–9.
26. Kitsiou AN, Srinivasan G, Quyyumi AA, Summers RM, Bacharach SL, Dilsizian V. Stress-induced reversible and mild-to-moderate irreversible thallium defects: are they equally accurate for predicting recovery of regional left ventricular function after revascularization? Circulation. 1998;98:501–8.
27. Dilsizian V, Rocco TP, Freedman NM, Leon MB, Bonow RO. Enhanced detection of ischemic but viable myocardium by the reinjection of thallium after stress-redistribution imaging. N Engl J Med. 1990;323:141–6.
28. Dilsizian V. Cardiac magnetic resonance versus SPECT: are all non-infarct myocardial regions created equal? J Nucl Cardiol. 2007;14:9–14.
29. Allman KC, Shaw LJ, Hachamovitch R, Udelson JE. Myocardial viability testing and impact of revascularization on prognosis in patients with coronary artery disease and left ventricular dysfunction: a meta-analysis. J Am Coll Cardiol. 2002;39:1151–8.
30. Hunt SA, Baker DW, Chin MH. ACC/AHA guidelines for the evaluation and management of chronic heart failure in the adult: executive summary. J Am Coll Cardiol. 2001;38:2101–13.
31. Klocke FJ, Baird MG, Lorell BH, Bateman TM, Messer JV, Berman DS, et al.; American College of Cardiology; American Heart Association Task Force on Practice Guidelines; American Society for Nuclear Cardiology. ACC/AHA/ASNC guidelines for the clinical use of cardiac radionuclide imaging – executive summary: a report of the American College of Cardiology/American Heart Association Task Force on Practice Guidelines (ACC/AHA/ASNC Committee to Revise the 1995 Guidelines for the Clinical Use of Cardiac Radionuclide Imaging). Circulation 2003;108:1404–18.
32. Beanlands RSB, Nichol G, Huszti E, Humen D, Racine N, Freeman M, et al.; PARR-2 Investigators. F-18-fluorodeoxyglucose positron emission tomography imaging-assisted management of patients with severe left ventricular dysfunction and suspected coronary artery disease: a randomized, controlled trial (PARR-2). J Am Coll Cardiol 2007;50:2002–12.
33. D'Egidio G, Nichol G, Williams KA, Guo A, Garrard L, de Kemp R, et al.; PARR-2 Investigators. Increasing benefit from revascularization is associated with increasing amounts of myocardial hibernation: a substudy of the PARR-2 trial. JACC Cardiovasc Imaging. 2009;2:1060–8.

34. Bonow RO, Maurer G, Lee KL, Holly TA, Binkley PF, Desvigne-Nickens P, et al.; STICH Trial Investigators. Myocardial viability and survival in ischemic left ventricular dysfunction. N Engl J Med 2011;364:1617–25.
35. Dilsizian V, Bacharach SL, Beanlands SR, Bergmann SR, Delbeke D, Fischman AJ, et al. PET myocardial perfusion and metabolism clinical imaging. J Nucl Cardiol. 2009;16:651. https://doi.org/10.1007/s12350-009-9094-9.
36. Panza JA, Ellis AM, Al-Khalidi HR, Holly TA, Berman DS, Oh JK, et al. Myocardial viability and long-term outcomes in ischemic cardiomyopathy. N Engl J Med. 2019;381:739–48.
37. Narula J, Dawson MS, Singh BK, Amanullah A, Acio ER, Chaudhry FA, et al. Noninvasive characterization of stunned, hibernating, remodeled and nonviable myocardium in ischemic cardiomyopathy. J Am Coll Cardiol. 2000;36:1913–9.

Myocardial Innervation

11

Markus Schwaiger, Arnold F. Jacobson, Antti Saraste, Jagat Narula, and Frank M. Bengel

The heart is innervated by sympathetic and parasympathetic fibers of the autonomic nervous system (ANS). The ANS plays a critical role in modifying cardiac performance to respond quickly and effectively to changing demands on cardiovascular performance. The sympathetic nervous system, which has the highest density of nerve terminals in the right and left ventricles, is predominantly stimulatory, producing positive inotropic and chronotropic effects. In contrast, the parasympathetic nervous system, which exerts primarily negative chronotropic responses, has nerve fibers predominantly in the atria [1].

Two kinds of neurons, preganglionic and postganglionic, are involved in ANS signal transmission. Postganglionic neurons provide innervation to target organs and tissues via synapses between nerve terminals and receptors on the surface of end-organ cells. Signal transmission is mediated by neurotransmitters that are released into the synapse from the nerve terminal and bind with postsynaptic receptors to initiate the effector response. After the signal transmission is completed, the neurotransmitter is released back into the synapse, from where it typically diffuses into nonneuronal tissue or the circulation (unchanged or after metabolism/catabolism), or it is actively returned to the nerve terminal via transporter proteins on presynaptic cell surfaces.

The predominant sympathetic neurotransmitter is norepinephrine (NE), which is synthesized, stored, and metabolized within the sympathetic nerve terminal. Upon neurostimulation, the neurotransmitter is released by exocytosis into the synaptic cleft. A small portion of the released neurotransmitter interacts with post-synaptic α- and β-adrenergic receptors, predominantly β-1 receptors in the heart. The majority of the released neurotransmitter undergoes reuptake in the nerve terminals (uptake 1) by means of the NE transporter (a sodium/chloride-dependent transport protein), which has a high affinity for amines (catecholamines and catecholamine analogues). Inside the nerve terminal, NE is either metabolized by monoamine oxidase or sequestered in vesicles by the vesicular monoamine transporter, a proton-dependent transport protein localized in the vesicle membrane. The amine transport system (uptake 1) regulates the extraneuronal concentration of androgenic neurotransmitters and plays an important physiologic and pathophysiologic role in modifying signal transduction and extraneuronal catecholamine concentration. This regulatory role includes the reuptake of locally released norepinephrine as well as the uptake and metabolism of circulating catecholamines that enter the extracellular space. This high-affinity uptake system protects the heart from the deleterious effects of elevated levels of circulating catecholamines [2, 3].

M. Schwaiger
Department of Nuclear Medicine,
Technical University of Munich, Munich, Germany

A. F. Jacobson (✉)
Diagram Consulting, Kihei, HI, USA

A. Saraste
Turku PET Centre, Turku University Hospital and University of Turku, Turko, Finland

J. Narula
Icahn School of Medicine at Mount Sinai, New York, NY, USA

F. M. Bengel
Department of Nuclear Medicine, Hannover Medical School, Hannover, Germany

V. Dilsizian, J. Narula (eds.), *Atlas of Nuclear Cardiology*, https://doi.org/10.1007/978-3-030-49885-6_11

The predominant parasympathetic neurotransmitter is acetylcholine, which is synthesized and stored within the parasympathetic nerve terminal. Comparable to sympathetic neurons, stimulation results in neurotransmitter release by exocytosis. The predominant receptor in the heart is the M_2 muscarinic receptor, which is present in much higher density in the atria than in the ventricles. Subsequent to neurostimulation of these receptors, the action of acetylcholine is terminated by the enzyme acetylcholinesterase in the synapse, which degrades the neurotransmitter to choline and acetate. These inactive molecules are then reabsorbed into the presynaptic terminal and used to synthesize new acetylcholine.

The importance of the myocardial autonomic nervous system is magnified in patients with heart disease, as damage to one or both branches can result in imbalances that increase the risk for adverse outcomes such as heart failure progression and arrhythmic events [4, 5]. The status of the ANS also influences the effects and effectiveness of cardiac medications and interventions. These factors have led to efforts to develop imaging agents for examining this system and quantifying the deleterious effects of various heart diseases. The greatest efforts and successes have been achieved with agents specific for presynaptic and postsynaptic sympathetic neuronal targets.

The remainder of this chapter provides an overview of the tracers, both single-photon and positron emitting, and nuclear-imaging methodologies used to study sympathetic innervation of the heart, as well as their clinical applications. It is hoped that future research will provide equivalent insights and applications for imaging of the parasympathetic nervous system of the heart.

Autonomic Nervous System

Figures 11.1, 11.2, and 11.3 illustrate the structure of the ANS, its control mechanisms, and the mechanisms controlling neurotransmitter synthesis and release.

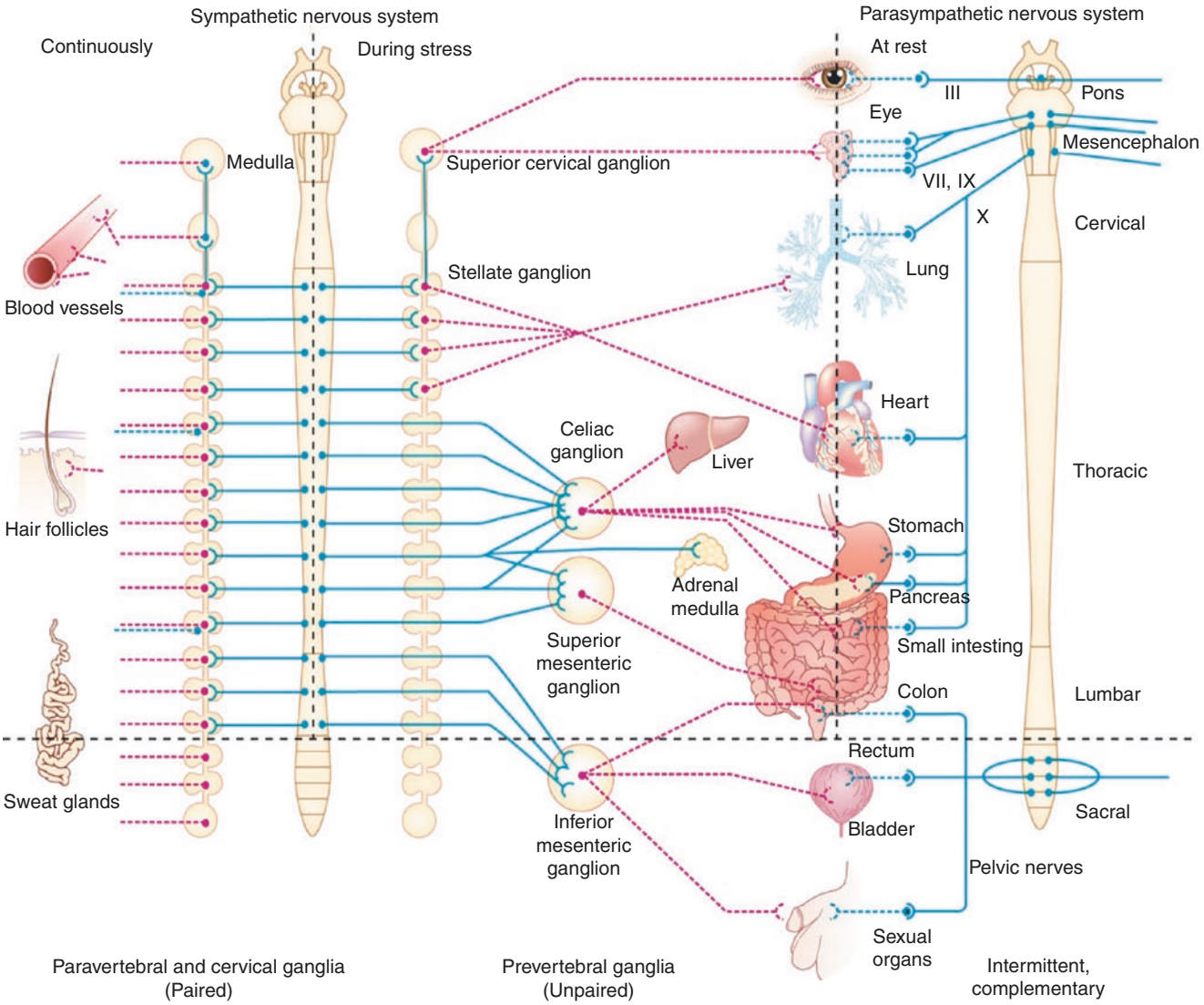

Fig. 11.1 Structure of the autonomic nervous system (ANS). The ANS is historically divided into two major efferent components, the sympathetic nervous system (cervicothoracic, SNS) and parasympathetic nervous system (craniosacral, PNS). In either case, end-organ innervation is provided by nerve fibers originating from autonomic ganglia located outside the central nervous system (CNS), which is driven by preganglionic cholinergic input from the CNS (*solid blue lines*). The main differences consist of the types of principal transmitter used by the postganglionic fibers (PNS: acetylcholine [*dotted blue lines*]; SNS: norepinephrine [*dotted red lines*]), the location of the ganglia (PNS: near or within the end organs; SNS: near the spinal cord, either paravertebral [22 pairs] or prevertebral [unpaired]), the degree of divergence and convergence of preganglionic input to postganglionic neurons (PNS: very little; SNS: considerable), and their respective functional roles. Most internal organs receive input from both the PNS and SNS (*center*). Important exceptions include skin and blood vessel (pilomotor and sudomotor) functions, which are exclusively controlled by noradrenergic and cholinergic postganglionic fibers of SNS origin only (*left*), and the adrenal gland, which functions as the equivalent of a sympathetic ganglion, causing systemic catecholamine release (80% epinephrine, 20% norepinephrine) in response to preganglionic cholinergic stimulation. In the case of most internal organs, the SNS and PNS exert opposite effects. PNS effects normally prevail at rest, whereas SNS effects predominate during stress or exercise ("flight or fight" response). In genitourinary organs, SNS and PNS functions are complementary; for example, PNS mediates erection and SNS mediates ejaculation [6]

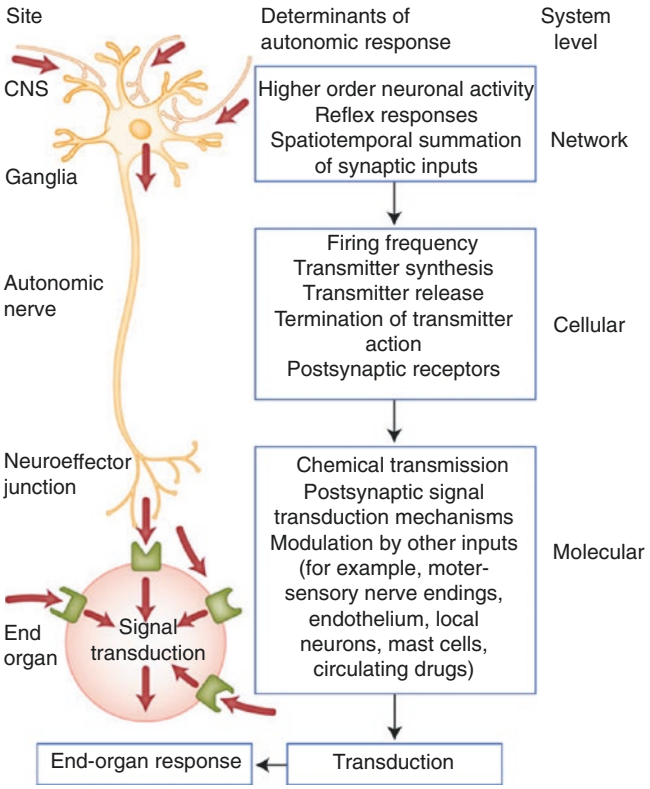

Fig. 11.2 Determinants of end-organ control by the autonomic nervous system. Control mechanisms operate concurrently at different system levels. At a neural network level, the processing and integration of patterns of neuronal activity (including reflex responses) determine the firing frequency of autonomic efferent nerve fibers. Cellular mechanisms that are operative at the level of nerve terminals determine the types, amounts, and fates of chemical transmitters released at autonomic synapses and neuroeffector junctions. At a molecular level, the membrane receptor and postsynaptic signal transduction mechanisms determine the types and magnitude of cellular effector responses. At each of these system levels, various interactions occur between distinct functional divisions of the ANS (sympathetic, parasympathetic, afferent, enteric, and local neuronal systems) involving classic (cholinergic and adrenergic) transmitters as well as a variety of nonclassic neurotransmitter systems. CNS- central nervous system [7]

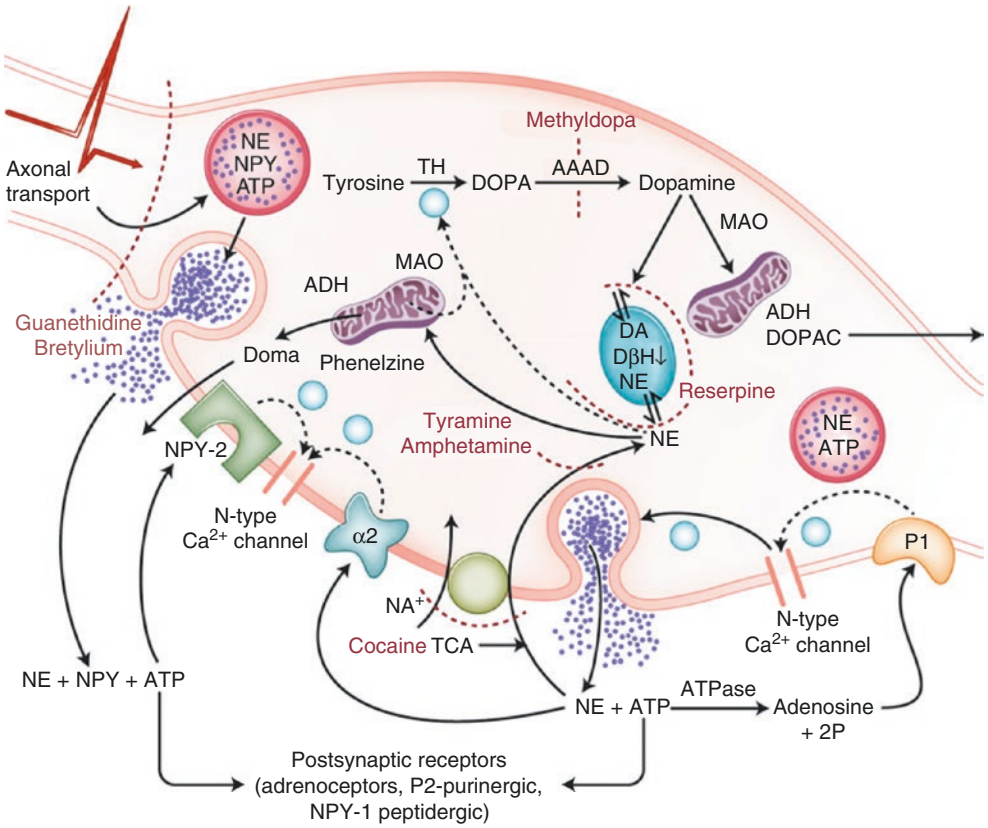

Fig. 11.3 Neurotransmitter synthesis and release at adrenergic nerve terminals. Mechanisms controlling transmitter synthesis and release at adrenergic nerve terminals are shown. Transmitters are stored in two types of synaptic vesicles: small vesicles containing only the principal transmitter norepinephrine (NE) and cotransmitter adenosine triphosphate (ATP) (each is synthesized within the nerve terminal itself) and larger, dense-core vesicles containing the polypeptide cotransmitter neuropeptide Y (NPY) and chromogranin (both of which are exclusively synthesized in the cell soma) as well as NE and ATP. The rate-limiting step for NE synthesis in the nerve terminal is tyrosine hydroxylase (TH) enzyme activity, which is negatively controlled by the cytoplasmic concentration of NE. The TH enzymatic product DOPA is decarboxylated to dopamine by (unspecific) aromatic L-amino acid decarboxylase (AAAD) in a step subject to therapeutic interference by provision of the "false" substrate methyldopa (resulting in the eventual formation of the "false transmitter" methyl-NE). Dopamine is to equal proportions either deaminated and excreted as 3,4-dihydroxyphenylacetic acid (DOPAC) or taken up into dopamine-β-hydroxylase (DβH)–containing storage vesicles via a reserpine-sensitive active uptake process and hydroxylated to NE. The cytoplasmic concentration of NE is determined by a dynamic equilibrium established between diffusion (leakage) out of storage vesicles, reserpine-sensitive (active) reuptake into storage vesicles, cytoplasmic displacement and extrusion by indirect sympathomimetics such as tyramine and amphetamine, reuptake from the extracellular space via a Na^+-dependent cotransport mechanism sensitive to inhibition by cocaine or tricyclic antidepressants (TCAs), and elimination after metabolizing to 3,4-dihydroxymandelic acid (Doma) by mitochondrial monoamine oxidase (MAO) and aldehyde dehydrogenase (ADH), a pathway sensitive to inhibition by MAO inhibitors such as phenelzine. In adrenal medullary neurons, 80% of cytoplasmic NE is methylized by *N*-methyltransferase into epinephrine before being packaged into storage vesicles. The nerve stimulation-evoked physiologic transmitter release occurs via fusion of synaptic storage vesicles with the cell membrane after the invasion of the nerve terminal by propagated action potentials (sensitive to blockade by guanethidine or bretylium) and the resulting increase in cytoplasmic Ca^{2+} through activation of voltage-sensitive (predominantly N-type) Ca^{2+} channels. Upon release, ATP, NE, and NPY produce neuroeffector responses through actions on postsynaptic membrane receptors. In addition, all three transmitters inhibit further release through action on presynaptic (P1, 2-adrenergic, NPY-2) receptors [8, 9]. Transmitter actions are terminated by hydrolysis (ATP), reuptake into nerve terminals (NE), uptake into nonneuronal tissue, and metabolism by catechol-*O*-methyltransferase (COMT) (NE), and diffusion away from the terminal and into the bloodstream (NE, NPY) [10]

Radiotracers

Several radiolabeled compounds have been synthesized to probe the sympathetic nervous system at the presynaptic and postsynaptic levels [11]. These tracers can be divided into radiolabeled catecholamines and catecholamine analogues. The most commonly employed single-photon emission CT (SPECT) tracer is metaiodobenzylguanidine (*m*IBG), which represents an analogue of the antihypertensive drug guanethidine [12]. Radiolabeled catecholamine analogues for positron emission tomography (PET) include metaminol, metahydroxyephedrine, and phenylephrine [13–15]. These "false adrenergic neurotransmitters" share the same reuptake mechanism and endogenous storage with the true neurotransmitters, but they are not metabolized and display a decreased affinity for postsynaptic receptor proteins.

As a functional analogue of NE, the uptake of *m*IBG occurs in all neuronal tissues that express the energy-dependent NE transporter (T) system (uptake-1). Although passive diffusion of [^{123}I]*m*IBG also occurs into nonneuronal cells (uptake-2), for the quantities of [^{123}I]*m*IBG used for diagnostic imaging, cellular uptake via the norepinephrine transporter (NET) system dominates.

Myocardial imaging with [^{123}I]*m*IBG has historically involved two imaging sessions, one early (15–30 minutes post-injection) and one late (3–4 hours post-injection). At both times, planar and SPECT imaging can be performed, depending on the methods that are being employed for quantitation. Quantitation of myocardial uptake is usually done in terms of the heart/mediastinum ratio (H/M or HMR) of counts/pixel values. HMR can be calculated from regions of interest drawn on anterior planar images of the thorax or from comparable volumes of interest on SPECT studies. Myocardial activity in early images reflects primarily the integrity of NET function, whereas activity in late images is affected by levels of *m*IBG storage in vesicles (mediated by vesicular monoamine transporter 2 [VMAT2]) and sympathetic neuronal stimulation controlling rates of NE and *m*IBG release [16–22]. Global and regional quantitation of [^{123}I]*m*IBG uptake, as a measure of sympathetic neuronal integrity, is most commonly based on late images. The difference between uptake in early and late images, designated "washout," is often considered an index of sympathetic nervous system activation. Quantitative assessments of both neuronal uptake and washout have been demonstrated to reflect the severity of cardiac disease and the prognosis for subsequent adverse events [23].

The most successful PET radiopharmaceutical agent for the imaging of presynaptic function is C-11 hydroxyephedrine (^{11}C-HED) [24, 25]; ^{11}C-HED is produced by the N-methylation of metaraminol using C-11 methyl iodide (Fig. 11.4). In contrast to *m*IBG, uptake of this tracer primarily reflects the transport by NET. Vesicle storage seems to occur, but binding inside the vesicle is weaker than with norepinephrine, owing to its higher lipid solubility. Based on experimental observations, myocardial retention reflects a continuing release and reuptake of ^{11}C-HED in the nerve terminal. Tracer retention is commonly quantified by calculating the retention index or retention fraction (which reflects the myocardial activity at 40 minutes), normalized to the integral of the arterial input function [18]. More recently, a tracer kinetic model for ^{11}C-HED kinetics has been developed, which allows calculation of the distribution volume within the myocardium.

As an alternative PET tracer to ^{11}C-HED, C-11 epinephrine has been proposed as a naturally occurring transmitter. Myocardial retention of this tracer represents the uptake, metabolism, and storage of catecholamines [26].

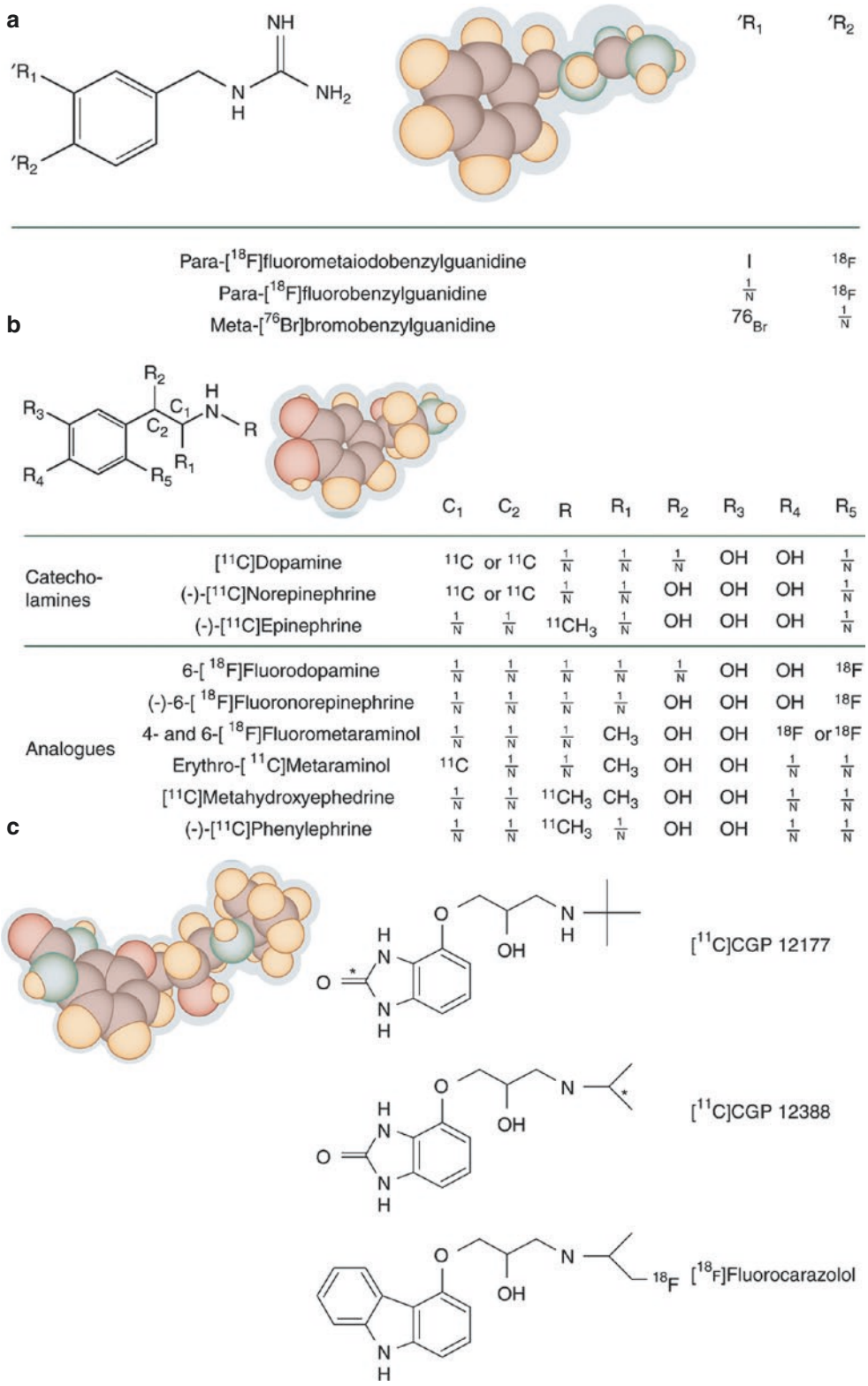

Fig. 11.4 Positron emission tomography (PET) radiotracers for mapping of cardiac sympathetic neurons. The radiotracers used for the evaluation of the sympathetic nervous system can be classified into three categories: radiolabeled analogues of benzylguanidine (**a**), radiolabeled catecholamines or catecholamine analogues (**b**), and β-adrenoceptor ligands (**c**). The common lead structure and a computed model of the prototypic compounds are provided. The ^{11}C-carbon position in panel *a* is indicated by $'R_1$ and $'R_2$ and in panel *b* by C_1 and C_2. The radiolabeled compounds are listed under the lead structures and computed models

Normal Myocardial Innervation

Figures 11.5, 11.6, 11.7, 11.8 and 11.9 demonstrate tracer activity in normal myocardium.

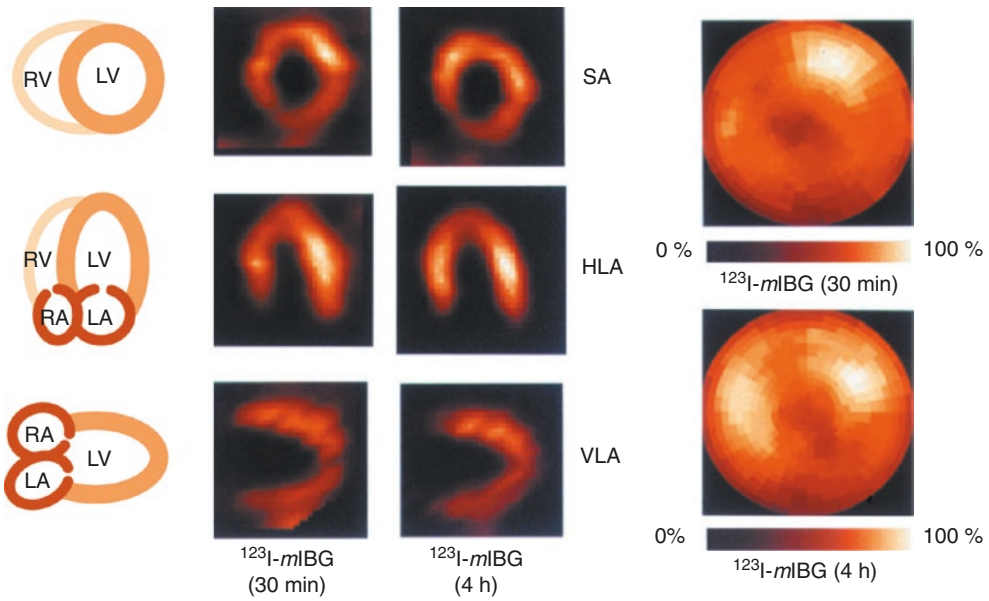

Fig. 11.5 I-123 metaiodobenzylguanidine (^{123}I-*m*IBG) distribution in normal myocardium. These single-photon emission CT (SPECT) images were obtained in a healthy volunteer 30 minutes and 4 hours after an intravenous injection of 10 mCi ^{123}I-*m*IBG. Regional myocardial tracer retention is displayed in the short-axis (SA), horizontal long-axis (HLA), and vertical long-axis (VLA) views. There is a homogeneous uptake of the tracer throughout the myocardium of the left ventricle (LV). The right ventricle (RV), right atrium (RA), and left atrium (LA) are not seen because of their thin walls. Polar maps represent the three-dimensional distribution of the tracer within the LV. The activity at the apex is displayed at the center of the map, whereas the basal parts of the LV represent the outer rings. The activity is normalized to maximal activity within the LV. The regional tracer retention was determined by the circumferential radial search for activity maxima. The individual circumferential profiles of several myocardial slices are then combined into one representative polar map. On both 30-minute and 4-hour images, there is relatively lower ^{123}I-*m*IBG activity in the inferior and inferoseptal areas, consistent with the known heterogeneity of neuronal distribution [4, 5]. The normal washout rate between early and late images is typically in the 5–20% range, whereas HF patients commonly have rates as high as 30–50% [19]. The late images are considered specific for the relative distribution of sympathetic nerve terminals, whereas washout has been used as a marker of neuronal integrity or sympathetic tone

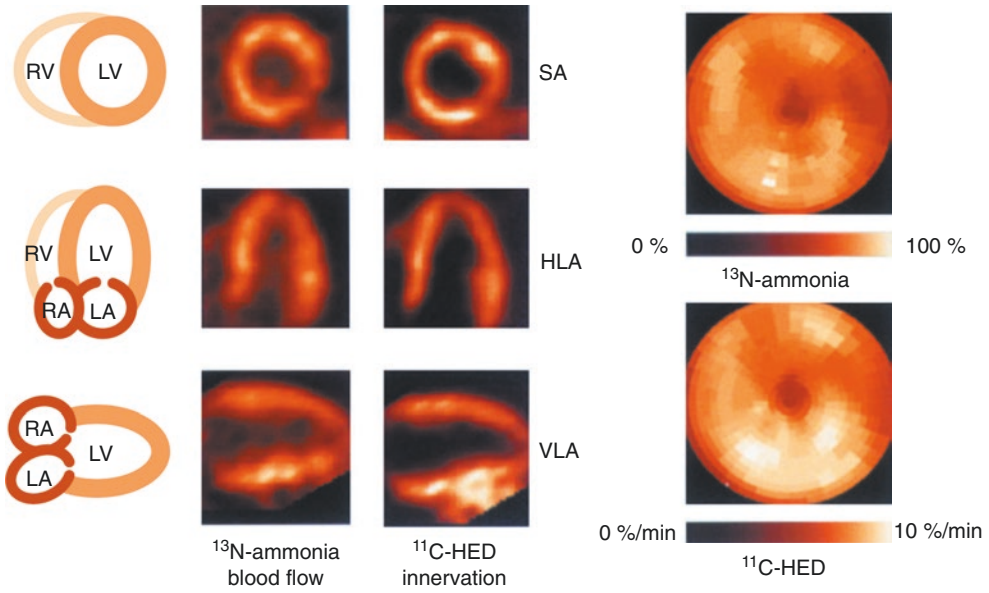

Fig. 11.6 C-11 hydroxyephedrine (^{11}C-HED) distribution in normal myocardium. These PET images in short-axis (SA), horizontal long-axis (HLA), and vertical long-axis (VLA) views were obtained following an injection of 20 mCi ^{13}N-ammonia as a blood flow marker and about 40 minutes after the intravenous injection of 20 mCi ^{11}C-HED. The myocardial blood flow is homogeneous throughout the left ventricle (LV), paralleled by the homogeneous uptake of ^{11}C-HED in all segments of the LV. Polar maps using a circumferential profile analysis display homogeneous distribution of ^{13}N-ammonia and ^{11}C-HED. The polar maps of flow are normalized to their own maxima, whereas the ^{11}C-HED data are expressed by retention index. This index represents the activity at 40 minutes normalized to arterial input function, derived from a region of interest placed over LV activity. These dynamic PET images allow for generation of myocardial and blood time–activity curves. LA left atrium, RA right atrium, RV right ventricle

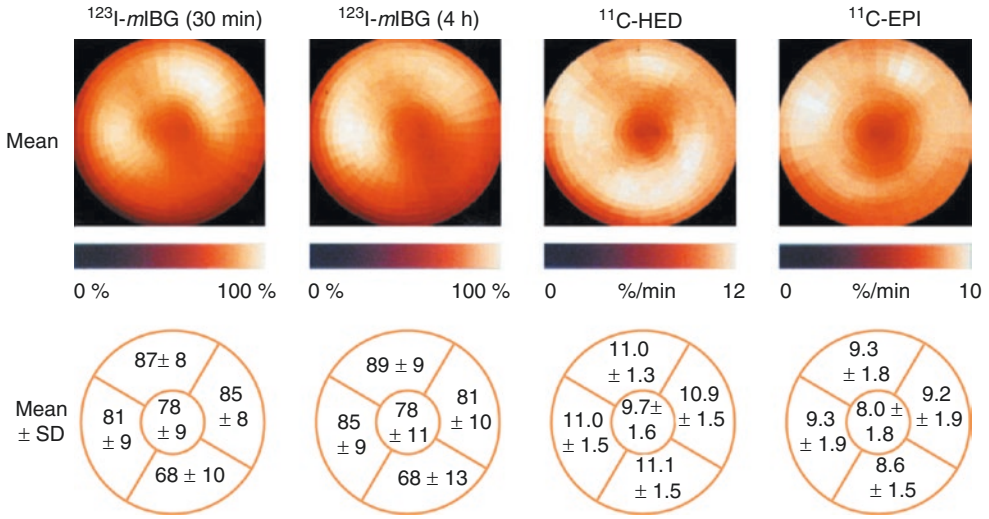

Fig. 11.7 Comparison of a normal tracer distribution of ^{123}I-*m*IBG, ^{11}C-HED, and C-11 epinephrine (^{11}C-EPI) in normal myocardium. For each tracer distribution, 10 patients were imaged following an intravenous injection of 10 mCi ^{123}I-*m*IBG, 20 mCi ^{11}C-HED, and 20 mCi ^{11}C-EPI. The relative tracer distribution normalized to the individual maximum in each patient is displayed in the *lower panel*. Note the slight heterogeneity of tracer retention at 30 minutes and 4 hours after ^{123}I-*m*IBG injection. The relative activity in the inferior segments of the left ventricle, including the apex, shows significantly lower values as compared with the anteroseptal and anterolateral segments. This may represent an attenuation artifact, but inhomogeneous density of the sympathetic nerve terminals in normal myocardium cannot be ruled out. The C-11 tracer retention is expressed as the retention index, which represents tracer activity 40 minutes after tracer injection, normalized to the arterial input function obtained after placing a region of interest over the cavity of the left ventricle [25]. The retention index is expressed as percent per minute (%/min). ^{11}C-EPI retention was obtained 30 minutes after tracer injection and was expressed as the myocardial retention index. These measurements of myocardial PET tracer uptake display greater homogeneity than *m*IBG data. The lower retention index in the apex of the left ventricle most likely represents the partial volume effect during nongated PET data acquisition. PET data are acquired with attenuation correction, but there may be biologic differences in affinity for uptake 1 between *m*IBG and HED

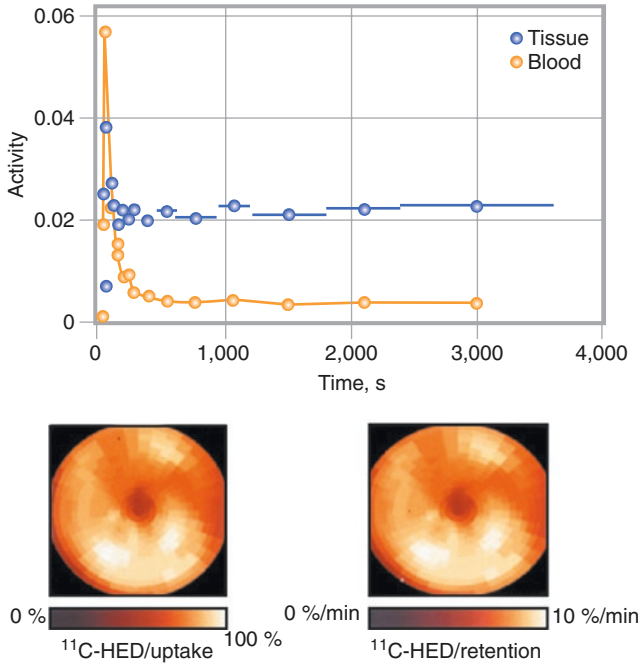

Fig. 11.8 Time–activity curve obtained after the intravenous injection of 20 mCi of ^{11}C-HED in a healthy volunteer. Dynamic PET imaging with a short framing rate allows the determination of tracer time–activity curves of the tissue and blood pool. The time–activity curves were determined using regions of interest placed over the chamber of the left ventricle for the determination of blood activity and placed over the left ventricular myocardium for the tissue activity distribution. The tracer rapidly clears from the blood, resulting in little residual blood activity minutes after the tracer injection. In contrast, the activity obtained from the myocardial region of interest shows stable retention in the myocardium over the time of observation. The initial peak of the myocardial tracer activity measured reflects contamination by blood-pool activity. Dividing this activity measured 30–40 minutes after the tracer injection by the integral of the input function, which reflects the available tracer to the myocardium during this time, yields the calculation of the myocardial retention index. This index averages over 12% in the normal heart

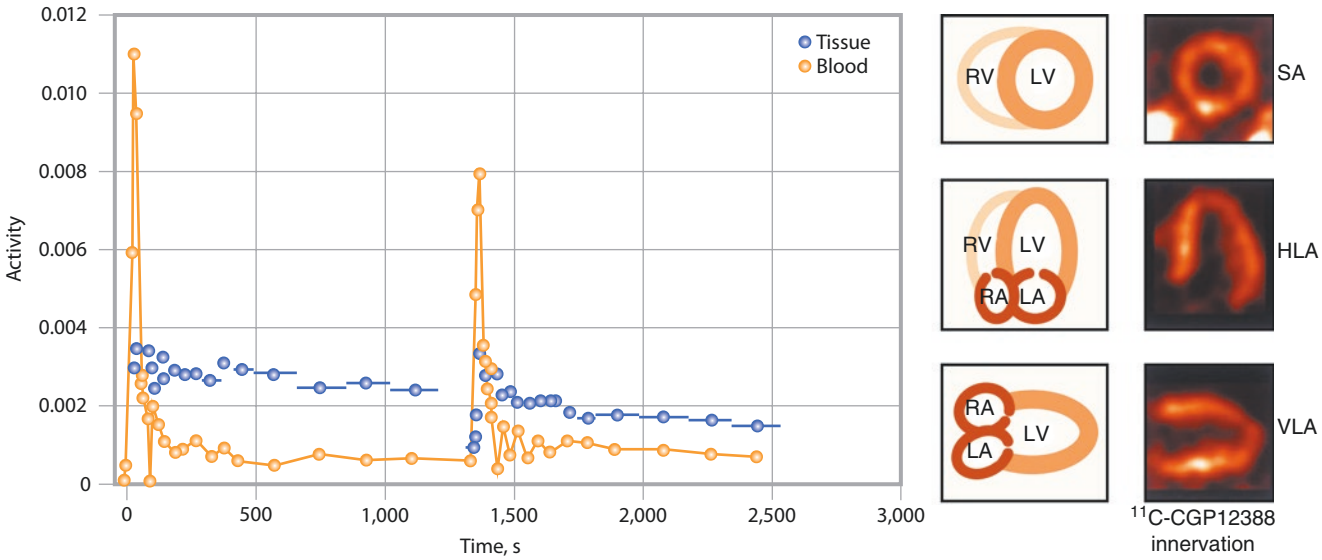

Fig. 11.9 β-Receptor distribution in normal myocardium. PET images following the intravenous injection of β-receptor antagonist ^{11}C-CGP12388 are shown in short-axis (SA), horizontal long-axis (HLA), and vertical long-axis (VLA) images. Images were obtained 40 minutes after the tracer injection and show high contrast between myocardial and nonmyocardial tissue. Pretreatment of patients with cold β-blocker β-receptor antagonists showed reduced tracer retention, suggesting high specific binding to the receptors. However, the shown retention images at 40 minutes primarily represent the delivery of tracer to the myocardium, which is determined by blood flow. To calculate the density of β-receptors in the myocardium, a tracer kinetic model has been proposed by Delforge et al. [27]. A comparison of ^{11}C-CGP measurements with β-receptor density measured in vitro resulted in a linear correlation with high correlation coefficients. Using a tracer kinetic model consisting of two tracer injections with different specific activities, the receptor density can be calculated by curve-fitting procedures of tissue and blood pool–time-activity curves [27]. LA left atrium, LV left ventricle, RA right atrium, RV right ventricle

Heart Failure

PET and SPECT innervation tracers provide valuable information about heart function (Figs. 11.10, 11.11, 11.12, 11.13, 11.14, 11.15, 11.16, 11.17, 11.18, 11.19, and 11.20). Studies have shown that the HMR on ^{123}I-*m*IBG images can distinguish between heart failure (HF) patients at low risk and high risk for mortality (Figs. 11.11, 11.12 and 11.13). PET has quantitative capabilities superior to SPECT, but many useful PET agents are labeled with isotopes that have a short half-life, such as ^{11}C (half-life 20 minutes), which are available only at facilities with on-site cyclotrons. Several ^{11}C-labeled compounds whose uptake is mediated by the NET system have been studied, including HED, epinephrine, and phenylephrine. In addition, ^{18}F-labeled compounds are being developed, including alternative halogenated benzylguanidines with structural similarities to *m*IBG. Studies on normal controls have shown similar myocardial distributions for ^{11}C-HED and epinephrine, as well as for ^{123}I-*m*IBG and the ^{11}C-labeled beta receptor agent CGP12388 [36]. Analogous to studies using ^{123}I-*m*IBG, ^{11}C-HED defects are usually larger than corresponding abnormalities on perfusion imaging. Mismatch between presynaptic neuronal function and postsynaptic beta receptor density has also been demonstrated [41]. Among clinical studies using ^{11}C-HED, PARAPET, a study of 204 patients with ischemic cardiomyopathy, is the largest. In that study, occurrence of arrhythmic death or ICD shock for VT >240 per minute or ventricular fibrillation increased in relation to the severity/extent of ^{11}C-HED defects (hazard ratio per 1% of LV 1.069 in multivariate analysis; $p = 0.003$); neither infarct volume nor hibernating myocardium were significant predictors as continuous variables [42]. Other small studies have suggested that absolute ^{11}C-HED quantification is possible using venous blood samples [43] and that dynamic PET data can be used to estimate both blood flow and neuronal uptake, thereby eliminating the need for a separate perfusion study [44].

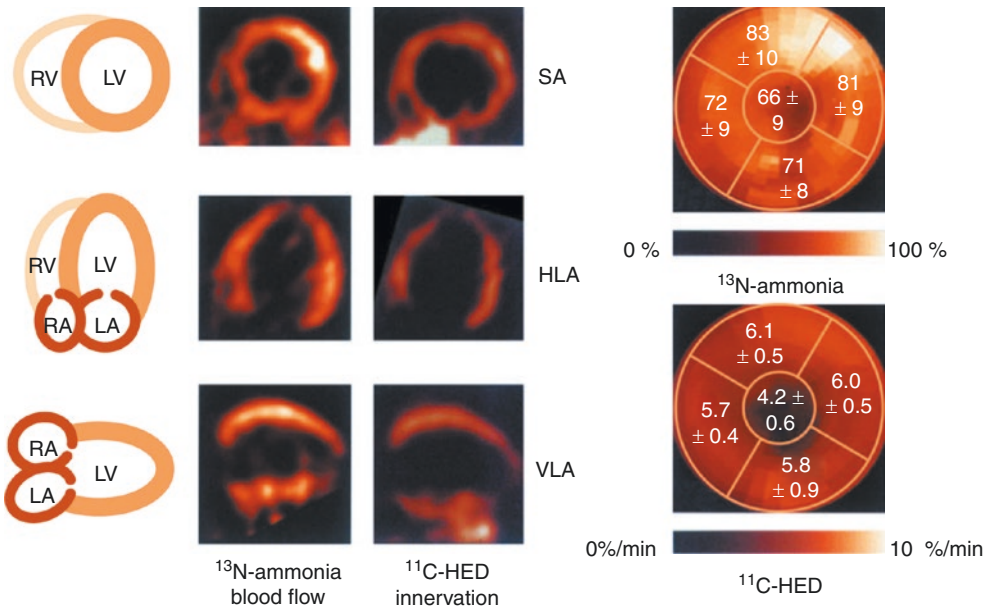

Fig. 11.10 Increased activity of the sympathetic nervous system: a hallmark of heart failure. Plasma levels of norepinephrine are elevated, myocardial norepinephrine reuptake is reduced, and myocardial β-receptors are downregulated, reflecting generalized adrenergic activation [2, 3]. Enhanced sympathetic activity increases myocardial contractility and heart rate and (via increased preload) activates the Frank–Starling mechanism. These responses are capable of maintaining ventricular performance and cardiac output for a limited time, but adrenergic activation eventually contributes to deterioration of cardiac function and the progression of heart failure. In comparison to healthy subjects, retentions of ^{11}C-HED and ^{123}I-*m*IBG are abnormally reduced in heart failure patients [20, 28, 29]. In this example, a patient with dilated cardiomyopathy and reduced left ventricular function was imaged with PET following the injection of ^{13}N-ammonia and 40 minutes after the injection of ^{11}C-HED. The tomographic slices are displayed in short-axis (SA), horizontal long-axis (HLA), and vertical long-axis (VLA) views. There is relatively homogeneous distribution of ^{13}N-ammonia, indicating the integrity of myocardial perfusion, but the retention of ^{11}C-HED is markedly reduced, indicating partial denervation of the left ventricle (LV). The quantitative retention index of ^{11}C-HED is reduced to 6% (normal >12%). The area of denervation is most evident in the distal anterior wall and apical area of the LV, which is consistent with the injury of the autonomic nervous system being a heterogeneous process in patients with congestive heart failure [28]. Furthermore, a mismatch between presynaptic and postsynaptic sympathetic function with a more pronounced reduction of ^{11}C-HED retention compared with β-adrenergic receptor density as assessed by β-receptor antagonist ^{11}C-CGP12177 is common in patients with ischemic heart failure [29]. LA left atrium, RA right atrium, RV right ventricle

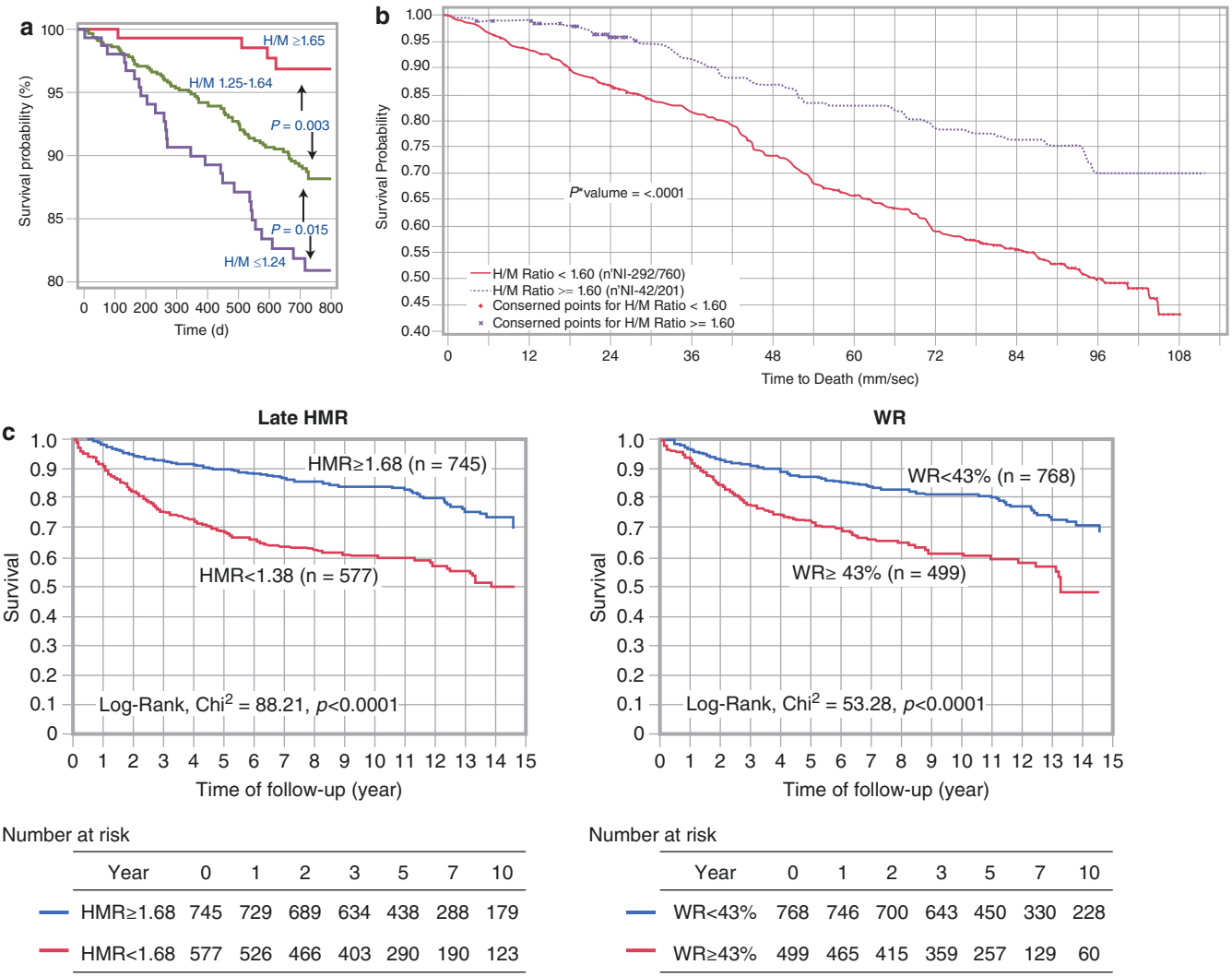

Number at risk

Year	0	1	2	3	5	7	10
HMR≥1.68	745	729	689	634	438	288	179
HMR<1.68	577	526	466	403	290	190	123

Number at risk

Year	0	1	2	3	5	7	10
WR<43%	768	746	700	643	450	330	228
WR≥43%	499	465	415	359	257	129	60

Fig. 11.11 The planar HMR has demonstrated excellent discriminative power for distinguishing between heart failure (HF) patients at low risk and high risk for cardiac and all-cause mortality. In the prospective ADMIRE-HF study of 961 NYHA class II and III HF patients, the prespecified HMR ≥1.60 identified a population with <2% annual mortality to 2 years. (**a**) Further survival analyses on the basis of the population mean HMR (1.44) ± SD (0.20) provided distinct separation of subjects into low-risk, intermediate-risk, and high-risk groups: Two-year mortality was 3.1% for HMR ≥1.65 (n = 147), 11.8% for HMR 1.25–1.64 (n = 660), and 19.1% for HMR <1.25 (n = 154) [30]. (**b**) The low-risk population (HMR ≥1.60) had persistence of the survival benefit on longer follow-up, with 5-year all-cause mortality rate of 25.8% versus 49.1% for HMR <1.60 ($p < 0.0001$) [31]. (**c**) In a prospective meta-analysis of 1322 HF patients in Japan who underwent ^{123}I-*m*IBG imaging and were followed for up to 15 years, there was significantly better survival in patients with preserved myocardial sympathetic innervation, as reflected by the threshold values of late HMR ≥1.68 and washout rate (WR) <43%. (From Nakata et al. [32]; with permission from Elsevier)

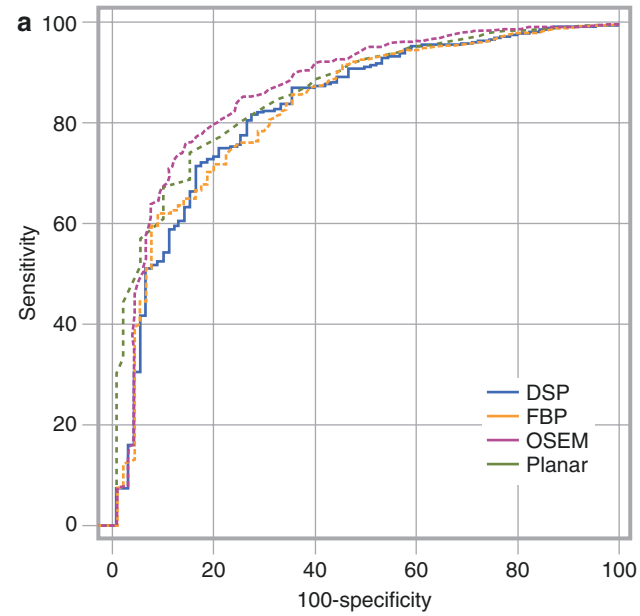

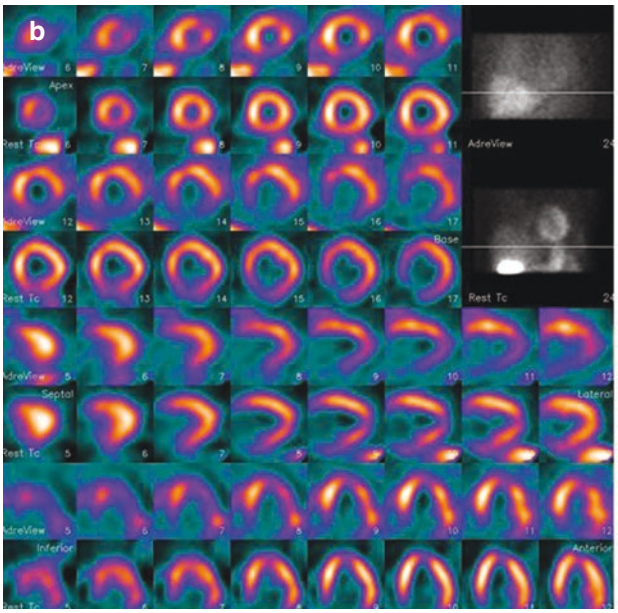

mIBG Defect Score = 14;
Innervation/perfusion mismatch

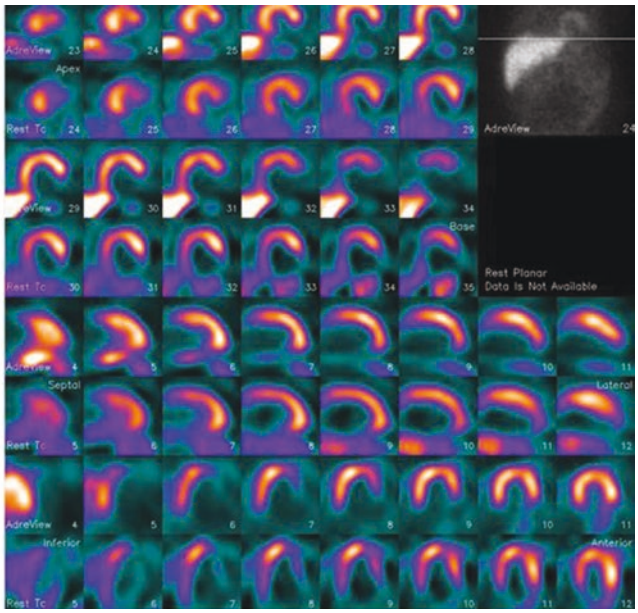

mIBG Defect Score = 22;
Innervation/perfusion match

Fig. 11.12 ^{123}I-*m*IBG SPECT can provide both global quantitation with discrimination similar to planar imaging and regional data not available on planar views. Comparisons between planar HMR determinations and measurements derived from conventional Anger camera SPECT have shown good correlation and similar capability for discriminating between normal and abnormal innervation. (**a**) ROC curve comparison of HMR discrimination between control subjects without heart disease (n = 90) and subjects with HF (n = 926). Among over 1000 patients studied with both planar and conventional ^{123}I-*m*IBG SPECT, although SPECT HMRs were consistently higher than planar, there was no difference in discrimination capability between the 90 controls and 926 HF patients using ROC curves [33]. Three SPECT reconstruction techniques were used: deconvolution of septal penetration (DSP), filtered back projection (FBP), and ordered subset expectation-maximization (OSEM). There were no significant differences among the areas under the curve (AUC) for the planar and three SPECT determinations. (From Chen et al. [33], with permission from Springer Nature.) (**b**) ^{123}I-*m*IBG and myocardial perfusion imaging (MPI) SPECT are often compared to identify perfused but denervated myocardium. Multiple studies have shown ^{123}I-*m*IBG SPECT defect severity to be predictive of adverse outcomes such as cardiac death and arrhythmic events, but innervation/perfusion mismatch severity has been less consistently predictive. SPECT studies pictured [^{123}I-*m*IBG (rows 1, 3, 5, and 7) and rest ^{99m}Tc-tetrofosmin (rows 2, 4, 6, and 8)] are from two patients with ischemic HF. MIBG defect scores are based on visual assessment using a standard 17-segment model (score 0–4, maximum 68). Patient on the left has moderate cavity dilatation on MPI, but uptake is nearly normal except for a small area at the base of the inferior septum. There is a larger abnormality in the inferior wall on the ^{123}I-*m*IBG images, representing an area of innervation/perfusion mismatch (^{123}I-*m*IBG defect score, 14). Patient on the right has a large matched defect in the inferior and inferolateral walls on both ^{123}I-*m*IBG and tetrofosmin images (^{123}I-*m*IBG defect score, 22).

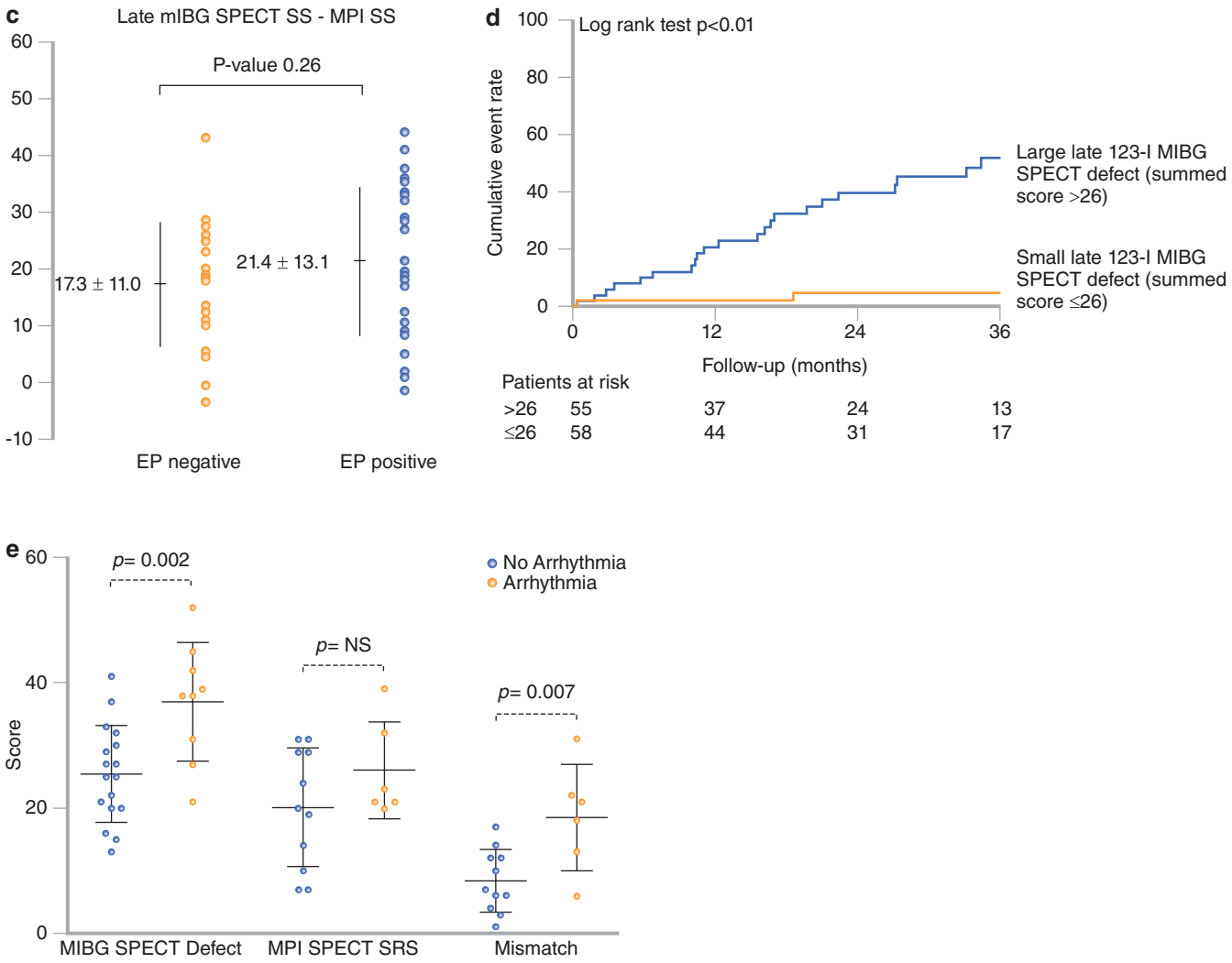

Fig. 11.12 (continued) (**c**–**e**) Discordant analyses examining the prognostic significance of mismatch between *m*IBG and MPI SPECT for the occurrence of arrhythmic events. (**c**) In a study of 50 ischemic heart disease patients referred for electrophysiology (EP) testing, the mismatch score was not predictive of inducibility of sustained VT (A) [34]. (**d**) However, a study of 116 HF patients referred for ICD implantation (B) found the ^{123}I *m*IBG/perfusion mismatch score predictive of subsequent ICD shock on univariate Cox analysis (HR = 1.06 [1.02–1.09], $p < 0.01$) but not on multivariate Cox analysis (HR = 1.01 [0.97–1.06], $p = 0.5$) [35]. (**e**) A small study of 27 HF patients referred for ICDs (C) did show significance of the mismatch score as a predictor of ICD activations during a mean follow-up of 16 months [36]. In all three studies, the *m*IBG SPECT defect score was a significant predictor of subsequent arrhythmic events. In aggregate, these and other studies have confirmed that medium to large innervation defects on *m*IBG SPECT studies (typically involving 20–50% of the myocardium) are associated with increased risk for arrhythmias

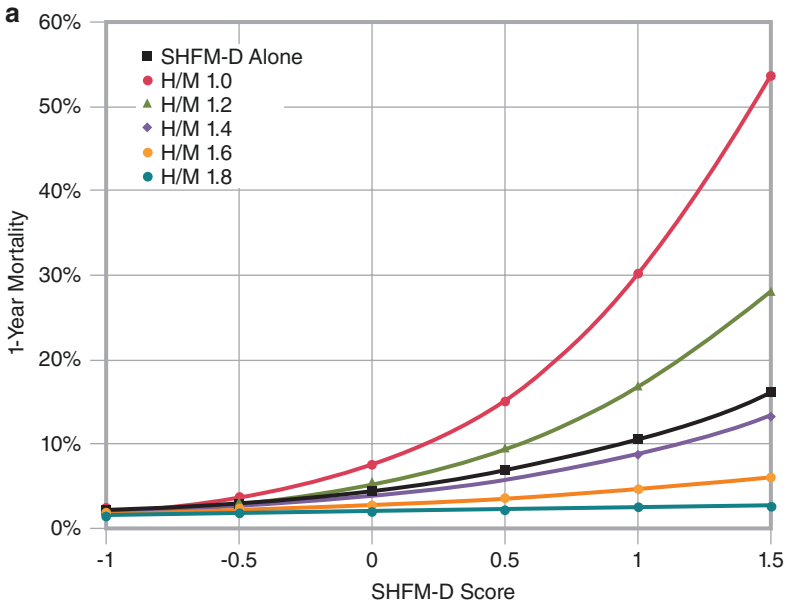

b

2y model

Age <65y	Late HMR <1.40	1.40-1.69	1.70-1.99	≥2.00
EF≤35%	9.2	5.6	3.5	1.6
35<EF<50%	7.3	4.4	2.7	1.3
EF≥50%	5.3	3.2	1.9	0.9

5y model

Age <65y	Late HMR <1.40	1.40-1.69	1.70-1.99	≥2.00
EF≤35%	23.5	14.8	9.3	4.2
35<EF<50%	19.0	11.8	7.2	3.2
EF≥50%	14.0	8.5	5.1	2.3

Age ≥65y	Late HMR <1.40	1.40-1.69	1.70-1.99	≥2.00
EF≤35%	13.2	8.2	5.2	2.4
35<EF<50%	10.6	6.5	4.1	1.9
EF≥50%	7.7	4.7	2.9	1.3

Age ≥65y	Late HMR <1.40	1.40-1.69	1.70-1.99	≥2.00
EF≤35%	32.3	21.3	13.7	6.4
35<EF<50%	26.8	17.2	10.8	5.0
EF≥50%	20.2	12.6	7.8	3.5

c

2y model

Age <65y	Late HMR <1.40	1.40-1.69	1.70-1.99	≥2.00
EF≤35%	28.3	18.8	12.3	6.0
35<EF<50%	23.5	15.3	9.9	4.7
EF≥50%	17.8	11.3	7.2	3.4

5y model

Age <65y	Late HMR <1.40	1.40-1.69	1.70-1.99	≥2.00
EF≤35%	52.5	38.5	26.8	13.6
35<EF<50%	45.8	32.4	21.9	10.8
EF≥50%	36.9	24.9	16.3	7.7

Age ≥65y	Late HMR <1.40	1.40-1.69	1.70-1.99	≥2.00
EF≤35%	37.3	25.9	17.5	8.8
35<EF<50%	31.6	21.4	14.2	7.0
EF≥50%	24.7	16.2	10.5	5.1

Age ≥65y	Late HMR <1.40	1.40-1.69	1.70-1.99	≥2.00
EF≤35%	63.1	49.3	36.3	19.7
35<EF<50%	56.7	42.6	30.3	15.8
EF≥50%	47.6	34.0	23.2	11.5

Fig. 11.13 Prediction models including *m*IBG results. There are numerous multivariate models for predicting the likelihood of adverse cardiovascular outcomes and death. *m*IBG results have been examined in conjunction with such models and have consistently proven to have independent predictive value. (**a**) The Seattle HF Model (SHFM) has been widely validated as a predictor of mortality in HF patients. The graph demonstrates the effect of adding *m*IBG imaging results to this multivariate clinical risk model for predicting 1-year all-cause mortality. Mortality estimates for the ADMIRE-HF population using SHFM version D (SHFM-D) [33] are represented by the black line with squares. Addition of the planar H/M ratio at five different levels (1.0, 1.2, 1.4, 1.6, and 1.8) is represented by the other lines in the graph [37]. Whereas an H/M ratio of 1.4 produces little change in the risk estimate, as the H/M value decreases, risk rises substantially. For an SHFM-D score of 1, equivalent to a 1-year mortality rate of about 10%, an HF patient with an H/M of 1.0 has a predicted mortality rate three times higher. Conversely, an H/M of 1.8 is associated with a greater than three times reduction in risk. Analyses of the same source data using risk models developed from four large prospective trials (EFFECT, Care-HF, MADIT-II, and PACE) produced similar results, with the addition of H/M ratio to each model providing improved HF risk assessment [38]. (From Jain et al. [38], with permission.) (**b**–**d**) Risk models were created based upon a Japanese meta-analysis population of 1322 HF patients followed for up to 15 years [39]. Practical utility dictated creation of two models, one for 2-year outcomes and one for 5-year outcomes. To provide a complete data set for 2-year analysis, 1280 patients who had definitive 2-year outcomes (death or survival) were included. Similarly, 933 patients who had complete information on 5-year outcomes were included for the 5-year analysis. The two-year logistic regression model included NYHA class, late HMR, and age as significant variables; the left ventricular ejection fraction (LVEF) was of borderline significance ($p = 0.054$). In the 5-year group, NYHA class, late HMR, age, and LVEF were significant variables. Cardiac mortality risk charts were then created using suitable aggregations of the four relevant variables. *Chart A* is for NYHA class I and II, while *Chart B* is for NYHA class III and IV. Color coding clearly shows the progressive increase in mortality risk with decreasing HMR: green <1%; blue 1.0–2.9%; red 3–9.9%; purple ≥10%. (**d**) Survival curves from a validation population of different HF patients (n = 546), in whom the 2-year cardiac death model was accurate for identifying low risk (<4%), and intermediate risk (4–12%), with actual 2-year cardiac mortality of 1.1% and 7.9% respectively. The model underestimated cardiac mortality for high-risk patients, presumably because the validation population had more severe HF than the derivation population [40]. (**a** and **b** from Nakajima et al. [39] and **c** from Nakajima et al. [40], with permission from Oxford University Press)

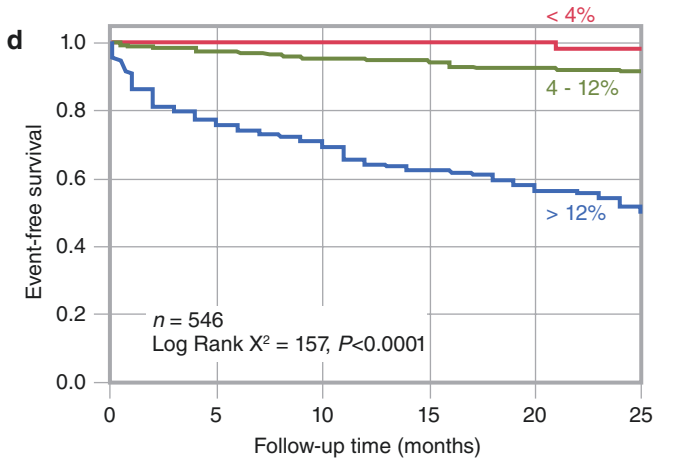

Number at risk	0 month	24 months
<4%	85	60
4-12%	291	188
>12%	170	65

Fig. 11.13 (continued)

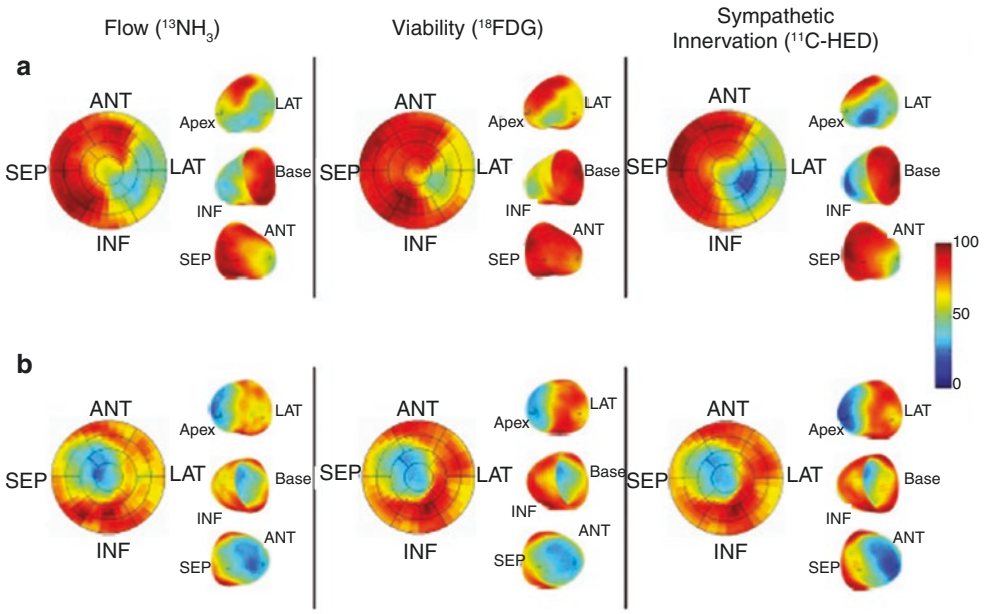

Fig. 11.14 Quantitative displays from PET imaging of myocardial blood flow ($^{13}NH_3$), viability (^{18}F-FDG), and sympathetic innervation (^{11}C-HED). Subject A, who experienced sudden cardiac arrest, had a larger innervation defect than the area of infarct shown by FDG. Subject B had a matched defect on flow, viability, and innervation imaging. (From Fallavollita et al. [42], with permission from Elsevier)

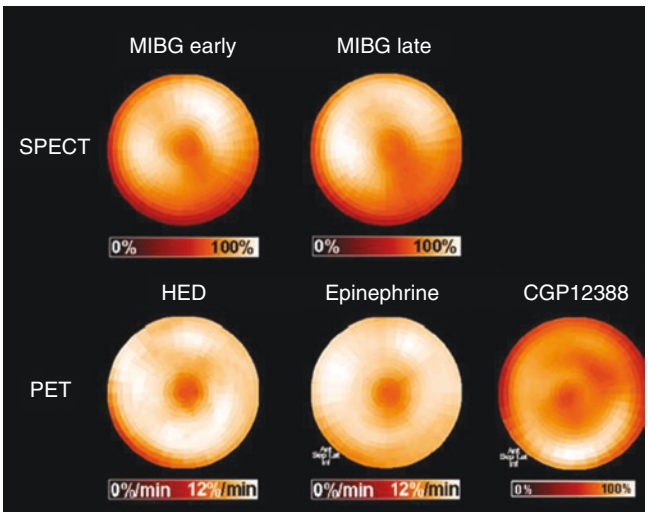

Fig. 11.15 Polar maps of myocardial distribution (center–apex to periphery–base) of *m*IBG from early (15 minutes post-injection) and late (4 hours post-injection) SPECT images of the normal heart for comparison with those of selected ^{11}C-labeled PET tracers also used in assessment of functional status of the sympathetic nervous system. The mechanism of neuronal uptake for HED and epinephrine are the same as for *m*IBG, with the norepinephrine transporter (NET) responsible for transfer of the compounds into the neuronal cytoplasm. ^{11}C-labeled CGP12388 binds to post-synaptic beta receptors, providing a means to assess the distribution and density of these adrenergic receptors. Distribution patterns for all five image sets are equivalently uniform, confirming that all tracers are interrogating attributes of the same physiological system. (From Bengel et al. [45], with permission from Springer Nature)

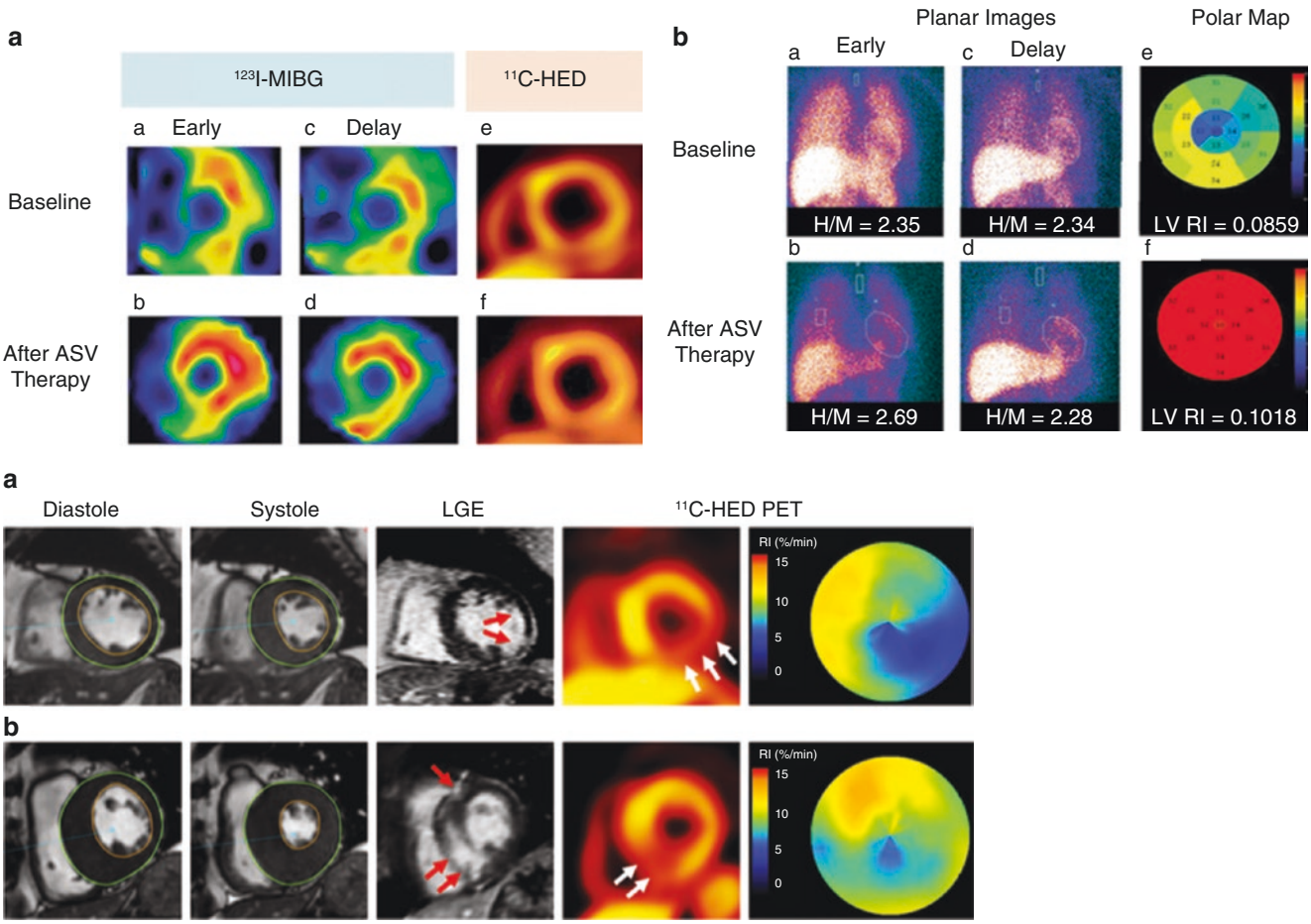

Fig. 11.16 The short half-life of ^{11}C and somewhat more rapid neuronal turnover of HED compared with *m*IBG requires use of a different quantitative technique for ^{11}C-HED. The most commonly used parameter for ^{11}C-HED is the retention index (RI), typically calculated by dividing mean global or segmental activity from a late image (between 15 and 60 minutes post-injection) by the integrated arterial activity during the entire dynamic acquisition. Comparisons can be performed with the myocardial segment with the highest RI or with data from control subjects without heart disease [46]. There is a growing body of evidence that ^{11}C-HED imaging results have diagnostic and prognostic significance comparable to those from *m*IBG imaging. In a study of early therapeutic effects of adaptive servoventilation (ASV) in HF patients studied with both *m*IBG and ^{11}C-HED, there was improvement from baseline in both early HMR and RI at 6 months after initiation of the therapy [47]. (**a**) In this example from a 27-year-old woman with HF whose LVEF increased from 38.0% to 45.0% after ASV therapy (A and B), global neuronal function improved on both *m*IBG (early HMR increasing from 2.35 to 2.69) and ^{11}C-HED (RI increasing from 0.086 to 0.102). (From Tokuda et al. [47], with permission from Springer Nature.) (**b**) Another ^{11}C-HED PET study involved 34 patients with HF with preserved ejection fraction (HFpEF) and 11 control subjects who also underwent cardiac MRI with late gadolinium enhancement (LGE) to measure left ventricular size, function, and myocardial infarct extent [48]. In the examples in Panel B1, row *a* is from a 65-year-old man with prior lateral myocardial infarction. There is lateral wall LGE consistent with subendocardial infarction (*red arrows*) and reduced ^{11}C-HED uptake (*white arrows*), which exceeds the extent of LGE. The polar map of the ^{11}C-HED RI shows a regional decrease in the inferior to lateral wall. In row *b*, from a 65-year-old man with hypertrophic cardiomyopathy, the LGE image shows hyperenhancement in the interventricular septum at the insertion points of the right ventricle (*red arrows*) and the ^{11}C-HED PET image and the polar map show regional decrease in the septal to inferior wall (*white arrows*). (**c**) Graphs shows aggregate study results. In part a, there is modest stepwise decrease in regional ^{11}C-HED RI with increasing LGE extent and decreasing wall thickening (WT). In part b, impaired regional RI (<10%/min; the lower quartile value of the control group segments) was found in 76% of all segments in 32 patients with HFpEF (excluding two patients with cardiac amyloidosis). (**d**) The majority of segments with impaired regional ^{11}C-HED RI had decreased systolic wall thickening and the presence of LGE. Numbers in parentheses are numbers of segments. (From Aikawa et al. [48]; CC-BY)

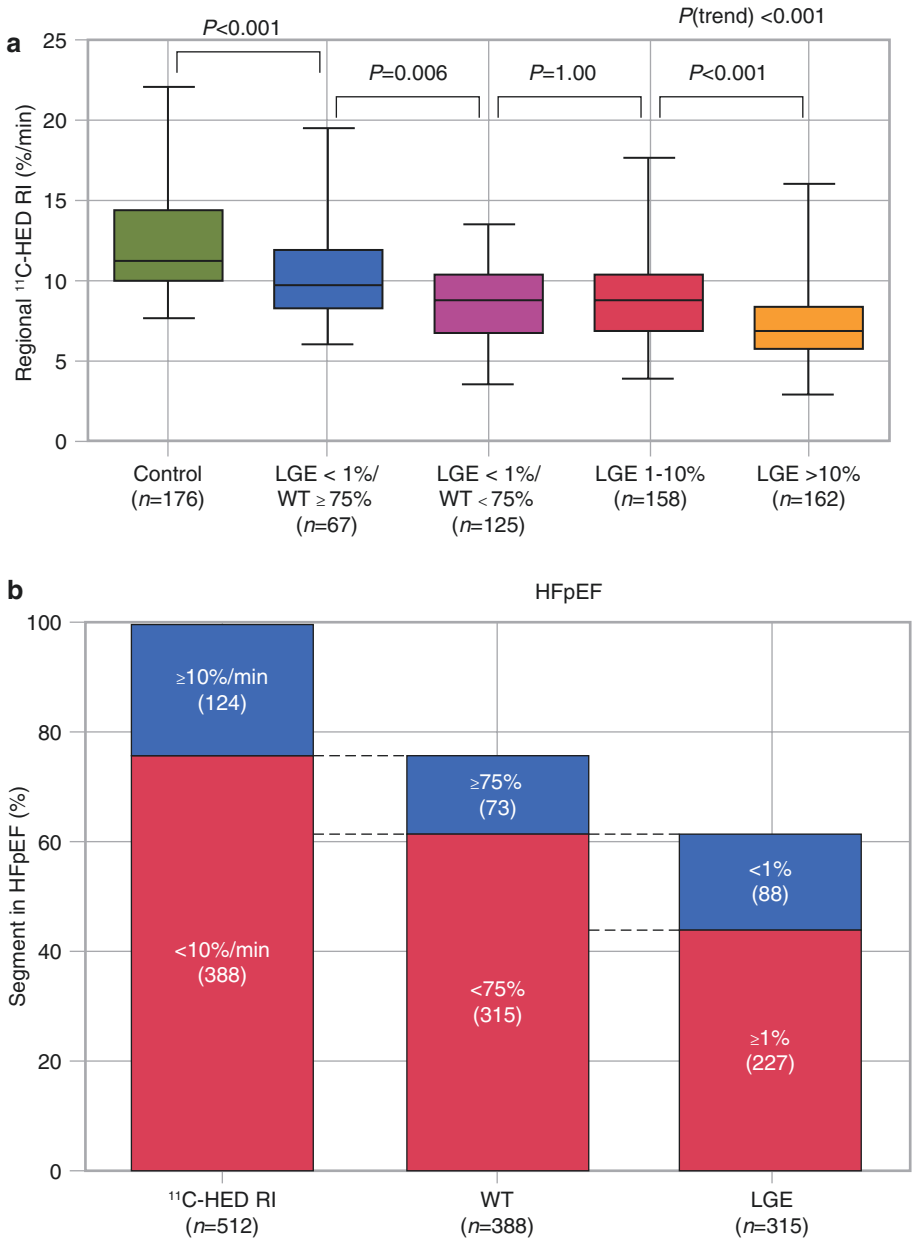

Fig. 11.16 (continued)

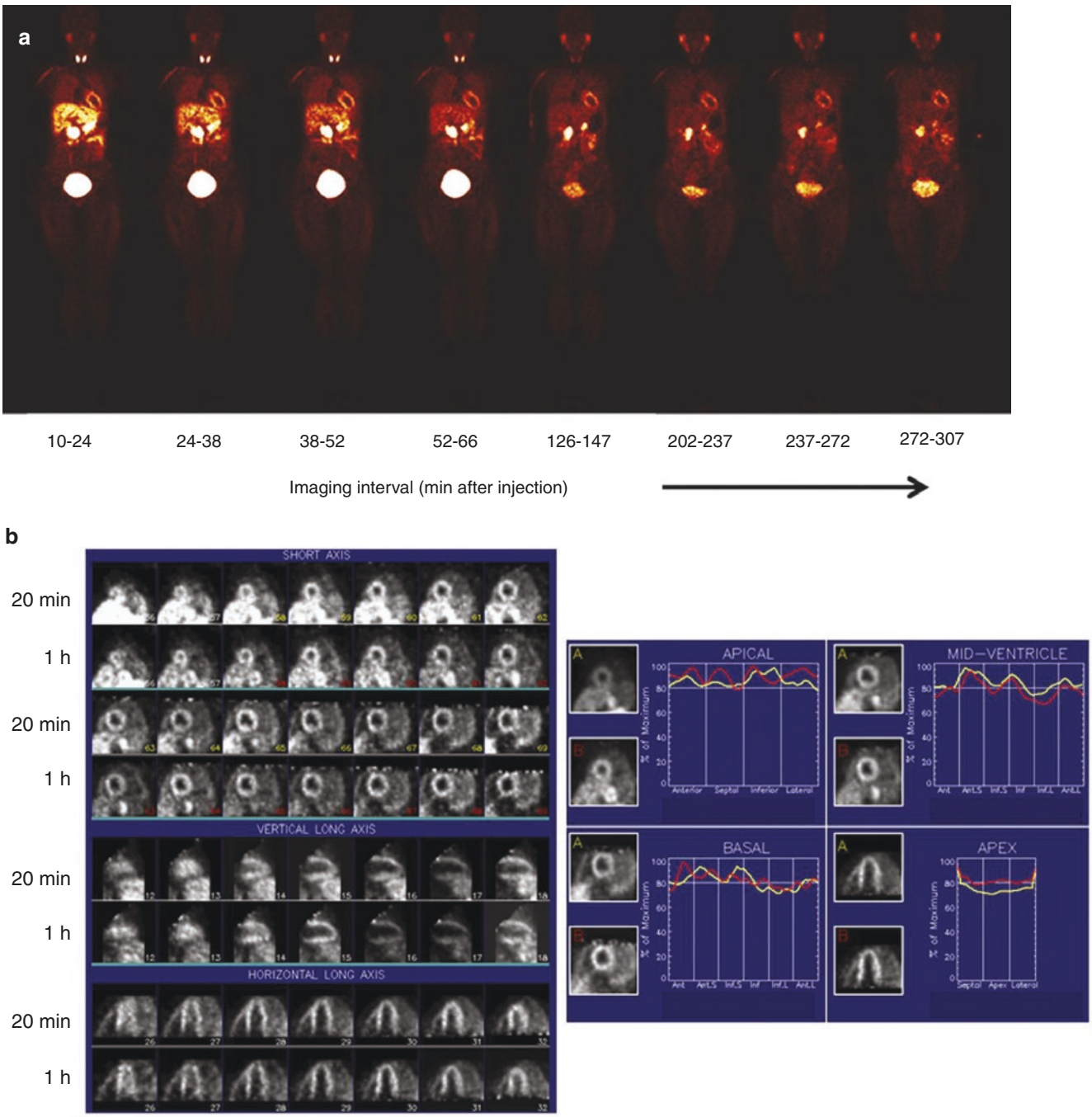

Fig. 11.17 LMI1195 is one of several ^{18}F-labeled benzylguanidines under development [49]. (**a**) Sequence of whole-body LMI1195 coronal images at mid-myocardial level in a human volunteer. Cardiac uptake is evident at 10–24 minutes after injection and remains clearly seen up to 5 hours. (**b**) Reoriented short-axis, vertical long-axis, and horizontal long-axis LMI1195 cardiac images in a healthy volunteer at 20 minutes and 1 hour after radiotracer injection (*left*) and circumferential quantitative profiles obtained in the same patient (*right*) [49]

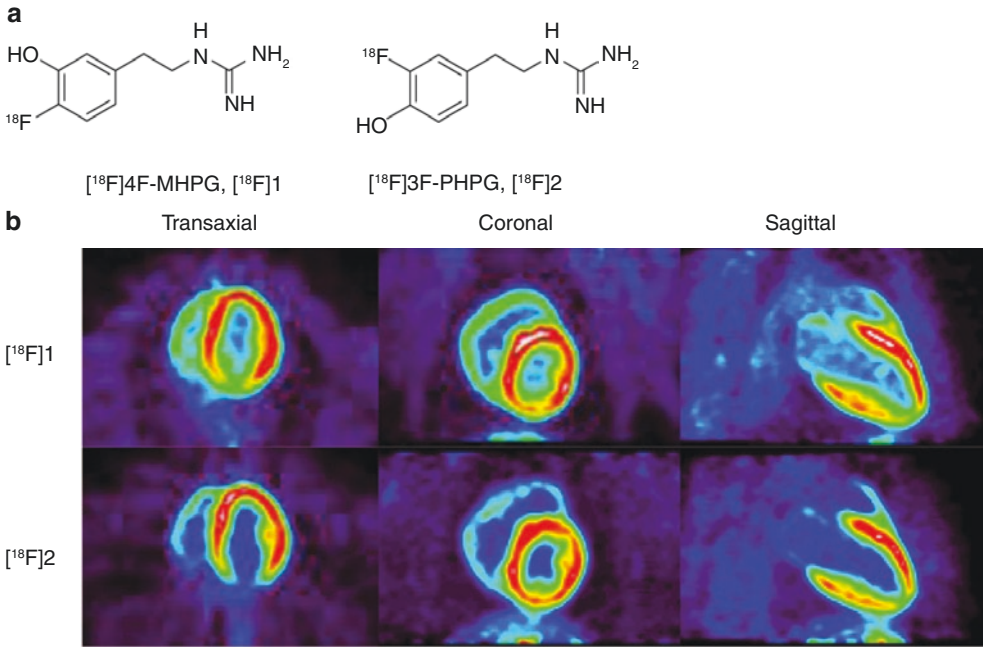

Fig. 11.18 A promising group of compounds for studying cardiac sympathetic innervation is the [^{18}F]Fluoro-Hydroxyphenethylguanidines. Preliminary animal studies have presented encouraging results, as has early human imaging [50]. (**a**) The structural formulas for two candidate molecules. (**b**) Cardiac images in rhesus macaque monkeys. (From Jung et al. [50]; with permission from the American Chemical Society)

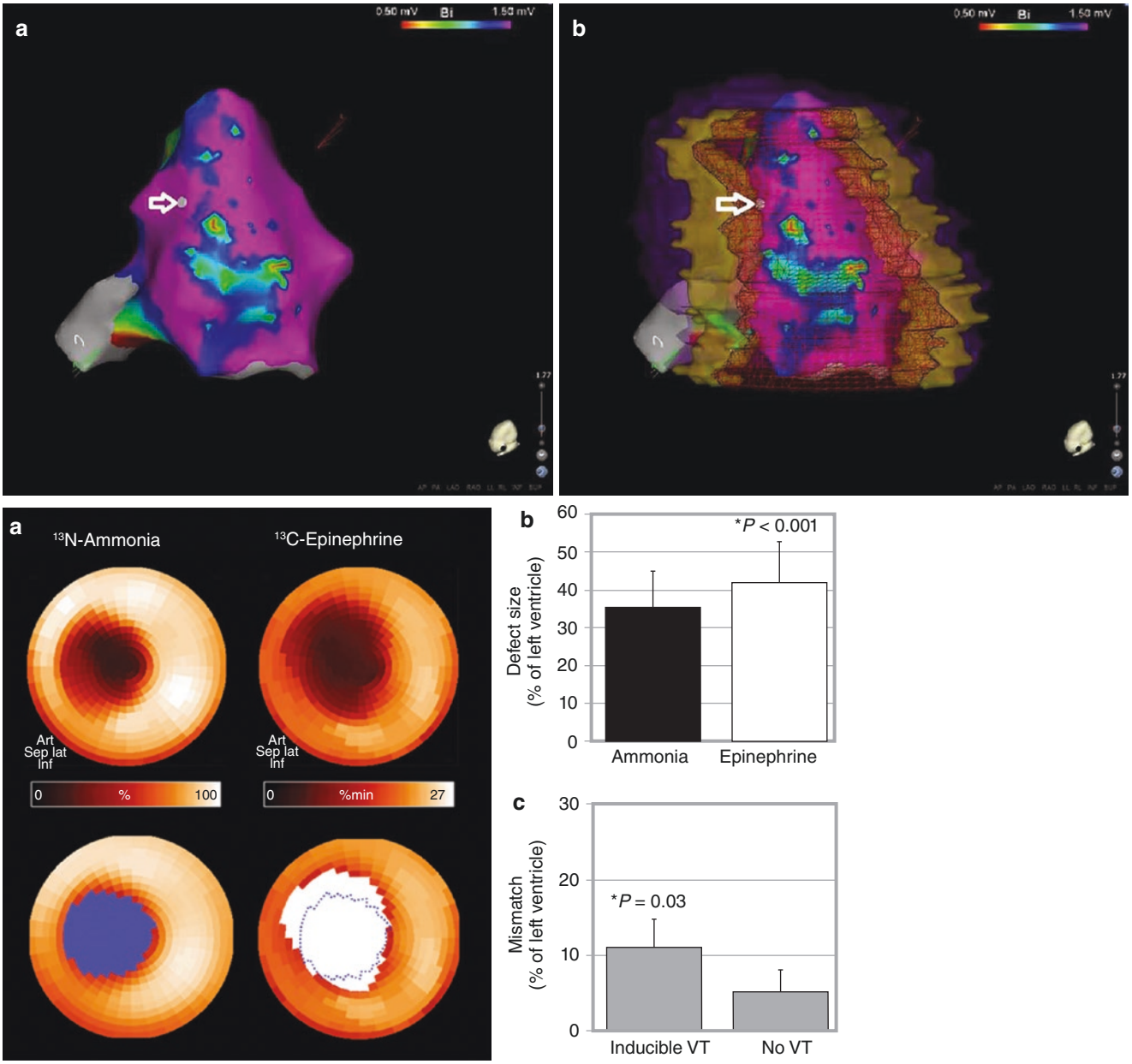

Fig. 11.19 PET and SPECT innervation tracers have been used to study the border zone surrounding myocardial infarct, a region believed to be arrhythmogenic. In a quantitative analysis of ^{123}I-*m*IBG SPECT images from coronary artery disease patients who underwent electrophysiology testing, the best predictor of VT inducibility was ^{123}I-*m*IBG uptake in the border zone (area under ROC = 0.78)—better than MPI scar extent or border zone extent [51]. In a prospective study of 15 patients referred for ischemic VT ablation and studied with ^{123}I-*m*IBG SPECT and high-density voltage mapping [52], ^{123}I-*m*IBG innervation defects were about 2.5-fold larger than bipolar voltage-defined scars, all VT ablation sites were within areas of abnormal innervation, and 36% of successful ablation sites demonstrated normal voltages (>1.5 mV). (**a**) In this example of a discordant preserved voltage-denervation location of a successful ablation site, the bipolar electroanatomic map, inferior view (A), demonstrates inferior scar with ablation site (*yellow dot*; *white arrow*) at an inferior septal location within the area of preserved bipolar voltage (>1.5 mV). Coregistration of the electroanatomic bipolar voltage map and innervation map (B) demonstrates a significantly larger area of denervation than bipolar voltage scar or border zone. The successful ablation point (*yellow dot*; *white arrow*) is located within the area of denervation close to the denervation/neuronal transition zone interface despite preserved bipolar voltage (^{123}I-metaiodobenzylguanidine transition zone in overlying transparent yellow, and normally innervated myocardium in overlying transparent purple) [52]. (**b**) Perfusion/innervation mismatch has been studied in an animal model of MI [53]. Panel A shows representative PET polar maps of myocardial perfusion (^{13}N-ammonia) and innervation (^{11}C-epinephrine). The innervation defect (*white area*) is larger than the perfusion defect (*blue area*), resulting in an area of normally perfused myocardium with impaired innervation in the infarct border zone. Panel B shows defect sizes in all animals (n = 13). Panel C compares the perfusion/innervation mismatch in subgroups with (n = 5) and without (n = 6) inducible VT. As expected, inducibility was associated with larger areas of mismatch [53]

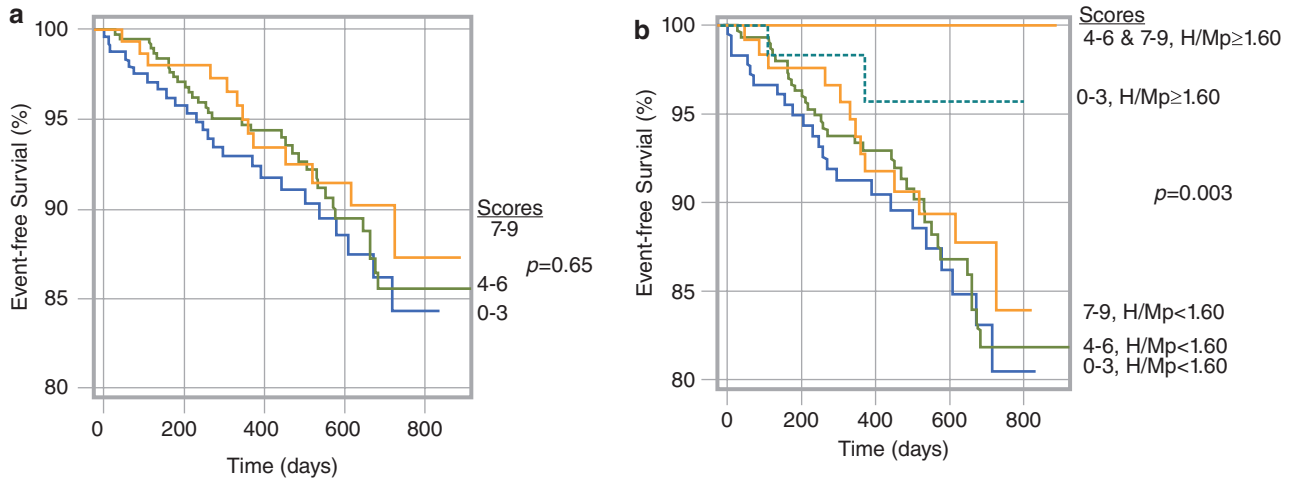

Fig. 11.20 (**a**) Survival curves from the ADMIRE-HF study categorized in terms of baseline HF medication intensity (0–9 score based on doses of beta blockers, ACE inhibitors, angiotensin receptor blockers, and aldosterone antagonists) (Panel A) and medication score and planar HMR (HMR_p) subcategorized as normal ($HMR_p \geq 1.60$) or abnormal ($HMR_p < 1.60$) (Panel B). There is no difference in 2-year survival based on the medication categories alone, but significantly better survival for patients with $HMR_p \geq 1.60$ in all medication score subgroups. This demonstrates that point-in-time assessment of cardiac sympathetic innervation status has independent prognostic value regardless of the current treatment regimen. (From Pina et al. [54], with permission.) (**b**) In an analysis of medications used by ADMIRE-HF subjects, the 71 subjects who had taken higher-potency (with respect to NET inhibition) antidepressants (tricyclic antidepressants and SNRIs) had lower HMRs than the 78 who took other neuropsychiatric medications (1.400 ± 0.189 *vs*. 1.476 ± 0.192, $p = 0.017$) [55]. Nevertheless, the predictive capability of the dichotomous HMR threshold of 1.60 was maintained, even among those taking the higher-potency inhibitors. Overall, there were no deaths to 2 years among the 13 HF patients taking the higher-potency medications who had an HMR ≥1.60, compared with 5 deaths (9%) among the higher-potency group with HMR <1.60. (From Jacobson et al. [55]; with permission from Wolters Kluwer)

Ischemic Heart Disease

Figures 11.21 and 11.22 illustrate imaging performed following myocardial infarction, suggesting that sympathetic neurons are more sensitive to ischemia than myocytes, and that denervated but viable myocardium can then form a substrate for ventricular arrhythmias.

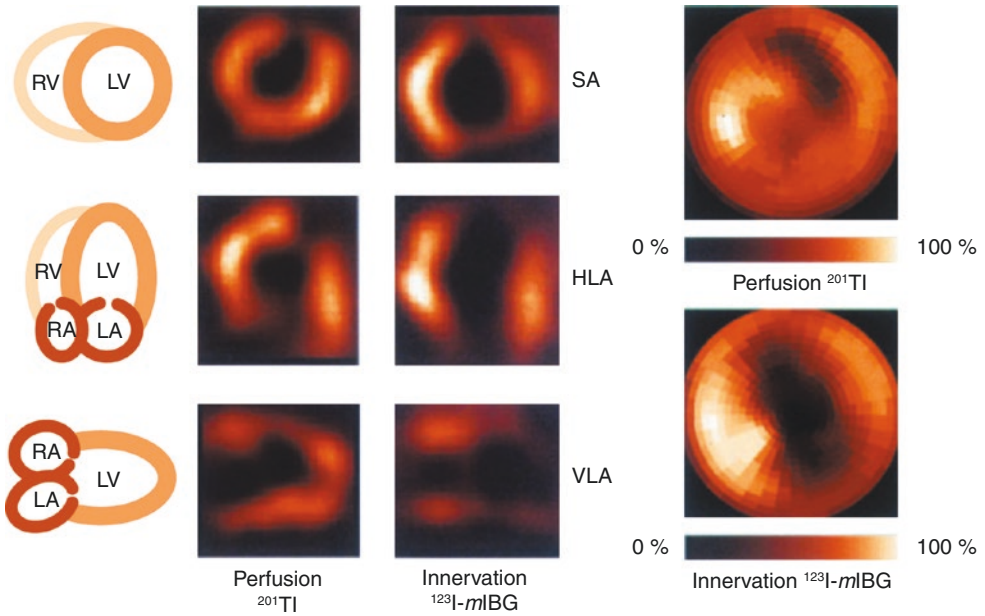

Fig. 11.21 Sympathetic nerve terminals are susceptible to ischemic damage, as illustrated in these SPECT images that were obtained in a patient within 14 days of an anterior myocardial infarction [56–58]. The tomographic slices are displayed in short-axis (*SA*), horizontal long-axis (*HLA*), and vertical long-axis (*VLA*) views. Regional retention of ^{123}I-*m*IBG 4 hours after administration of 10 mCi was compared with the myocardial perfusion as assessed from images acquired 20 minutes after an injection of 2 mCi of thallium-201 (^{201}Tl). There is a perfusion abnormality in the ^{201}Tl images involving the anterolateral wall of the left ventricle (*LV*). The images obtained after the ^{123}I-*m*IBG injection reveal a markedly larger area of reduced ^{123}I-*m*IBG retention involving the anterolateral wall as well as the distal inferior wall. Polar maps display the disparity of perfusion and neuronal abnormality, reflecting the infarct size and area of denervation. This mismatch between perfusion and ^{123}I-*m*IBG retention is present in almost 80% of patients after acute myocardial infarction and indicates that sympathetic neurons are more sensitive to ischemia than the myocytes [57]. Although reduced ^{11}C-HED retention was found in an experimental model of chronically ischemic hibernating myocardium, the dependency of the ^{11}C-HED retention on resting myocardial blood flow or flow reserve was small in patients with chronic coronary artery disease [58]. LA left atrium, RA right atrium, RV right ventricle

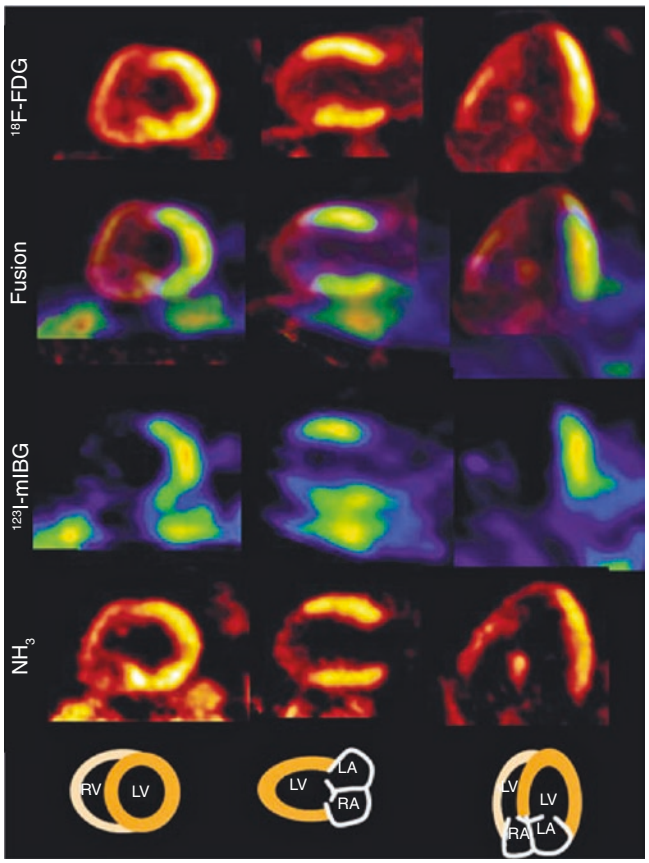

Fig. 11.22 Myocardium as a substrate for ventricular arrhythmias. It has been proposed that denervated but viable myocardium can form a substrate for ventricular arrhythmias after myocardial infarction. The mismatch pattern of innervation and viability has been shown to correlate with abnormal electrophysiologic findings [59–62]. However, its relationship to clinical arrhythmic events remains unclear [59]. The figure demonstrates a detailed assessment of viability, perfusion, and sympathetic innervation by evaluation of fluorodeoxyglucose (^{18}F-FDG) uptake with PET, ^{13}N-ammonia (NH_3) PET, and ^{123}I-*m*IBG SPECT in a patient with a previous anterior myocardial infarction and sustained ventricular tachycardia, being considered for ablation

Atrial and Ventricular Arrhythmias

Atrial fibrillation is the most common tachyarrhythmia in humans. Ablation of atrial fibrillation in the electrophysiology laboratory is becoming the preferred or definitive approach for therapy, supplanting medical therapy, surgery, and observation with or without anticoagulation. In the absence of structural heart disease, it is impossible to predict reliably whether a patient with a first self-terminated episode of atrial fibrillation will progress to permanent atrial fibrillation. ^{123}I-*m*IBG scintigraphy is emerging as a risk-stratification modality that can distinguish which individuals will progress to have permanent atrial fibrillation or permanent atrial fibrillation and congestive heart failure [63]. In 98 consecutive subjects with idiopathic paroxysmal atrial fibrillation and preserved LVEF, the role of cardiac ^{123}I-*m*IBG SPECT in the transition to permanent atrial fibrillation and the occurrence of heart failure were assessed. During a 4-year follow-up period, 35 of the subjects (36%) transitioned to permanent atrial fibrillation. A low ^{123}I-*m*IBG HMR and low LVEF were independent predictors of the transition to permanent atrial fibrillation. Further, a low ^{123}I-*m*IBG HMR, low LVEF, and a high plasma brain natriuretic peptide concentration were independent predictors of the occurrence of heart failure with permanent atrial fibrillation. Sympathetic innervation may play a key role in cardiovascular remodeling, which promotes atrial fibrillation. Figure 11.23 presents three examples of the prognostic use of ^{123}I-*m*IBG SPECT and ECG.

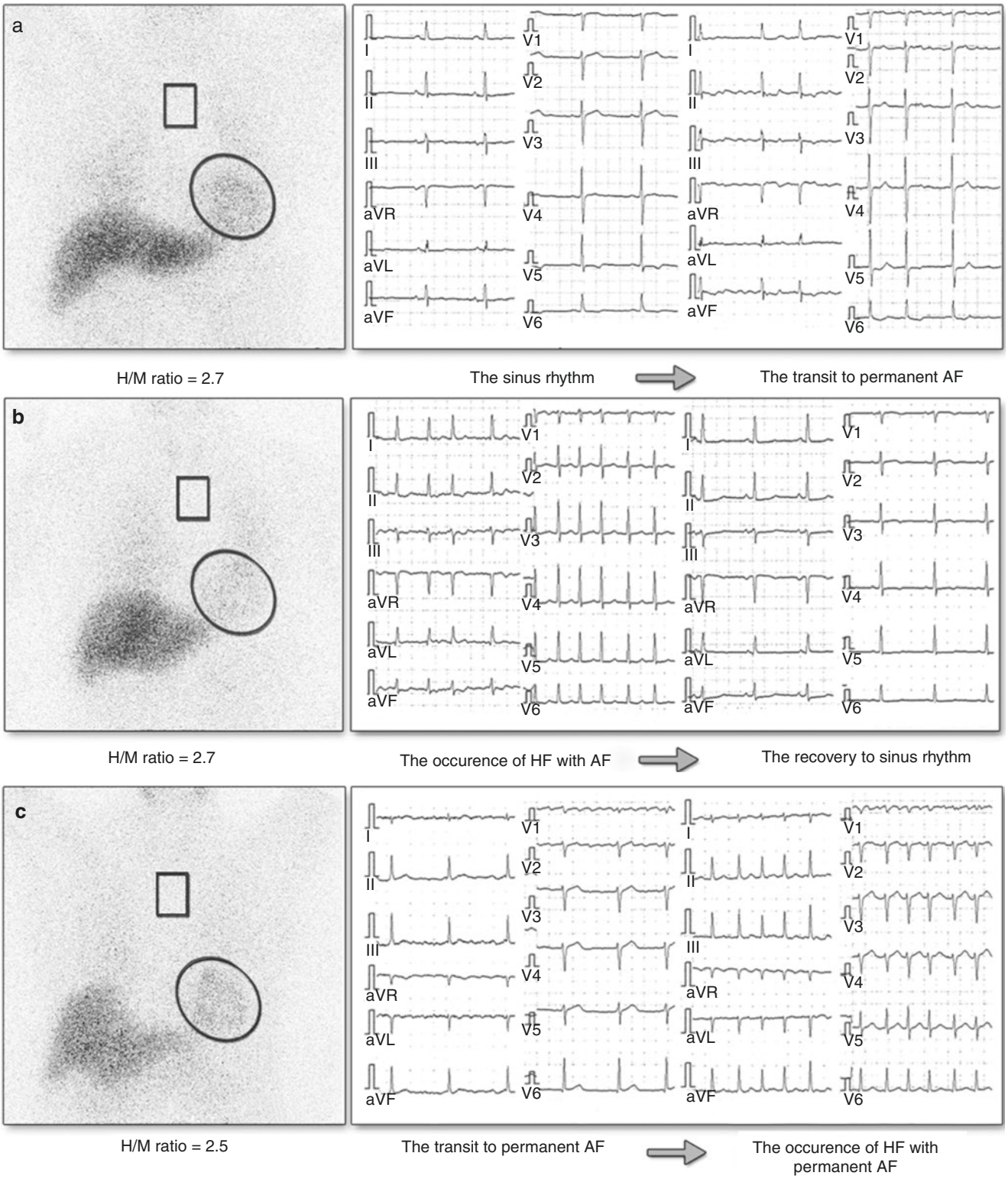

Fig. 11.23 ^{123}I-*m*IBG image examples and electrocardiography (ECG) strips for predicting atrial fibrillation (AF). In these examples of ^{123}I-*m*IBG images and ECG strips, the ovals indicate the region of interest on the heart area (H) and the rectangles indicate the region of interest on mediastinum (M). Cardiac sympathetic nervous system activity was estimated by the value of the heart/mediastinum (H/M) ratio. (**a**) A 78-year-old man with paroxysmal AF had a 2.7 H/M ratio in the ^{123}I-*m*IBG image and transited to permanent AF without the occurrence of heart failure (HF). (**b**) A 68-year-old man with paroxysmal AF had a 2.6 H/M ratio. The HF with AF occurred afterward, but the improvement of HF resulted in recovery to sinus rhythm from AF. (**c**) A 71-year-old man with paroxysmal AF had a 2.5 H/M ratio and transited to permanent AF. The HF occurred afterward, and the AF was perpetuated after the improvement of HF. These patients with paroxysmal AF had significantly lower H/M ratios than normal values (3.3 ± 0.5) (From Akutsu et al. [63]; with permission from Elsevier)

Similarly, experimental and clinical studies have linked presynaptic and postsynaptic sympathetic nervous function and the presence of ventricular arrhythmias [64–66]. Innervation imaging has demonstrated abnormalities in patients with primary arrhythmic cardiac disorders in the absence of structural heart disease, such as right ventricular outflow tract tachycardia (Fig. 11.24), Brugada syndrome, and idiopathic ventricular fibrillation [67–70].

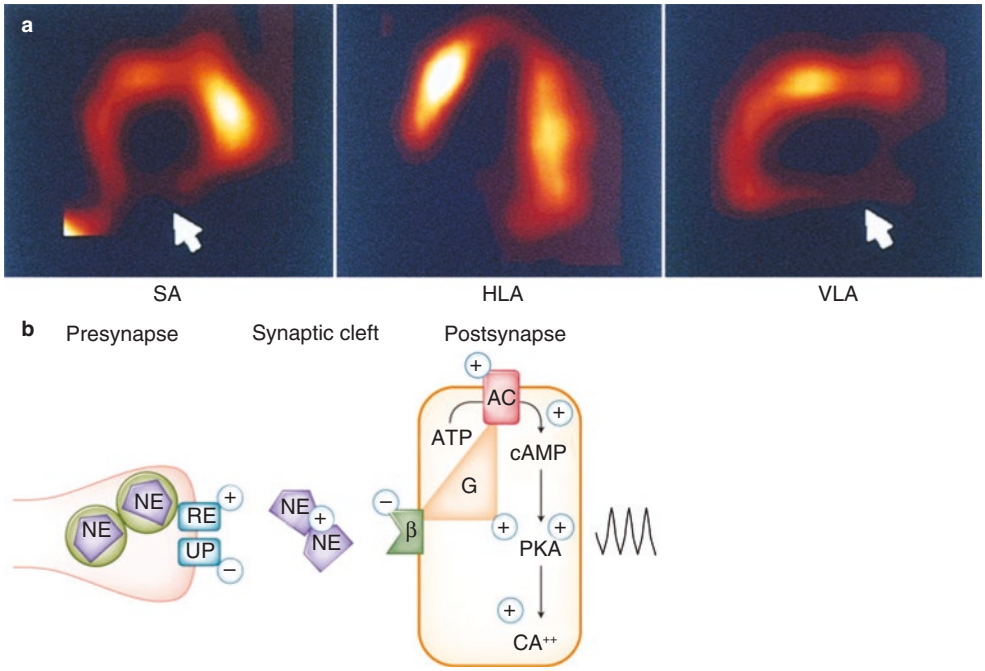

Fig. 11.24 Sympathetic denervation and ventricular arrhythmias. (**a**) ^{123}I-*m*IBG SPECT images were obtained in a 54-year-old man with idiopathic right ventricular outflow tract tachycardia. The tomographic slices are displayed in short-axis (SA), horizontal long-axis (HLA), and vertical long-axis (VLA) views. The ^{123}I-*m*IBG images acquired 4 hours following injection show a marked ^{123}I-*m*IBG retention defect in the midventricular and basal inferior walls (*arrows*), suggesting regional sympathetic denervation. Unfortunately, the right ventricle cannot be imaged by radionuclide techniques because of its thin myocardial walls. (**b**) This schematic display illustrates a proposed pathophysiologic mechanism of tachycardia in patients with idiopathic right ventricular outflow tract tachycardia. Impairment of a catecholamine clearance contributes to reduced clearance of neurotransmitter from the synaptic cleft and, thus, to myocardial catecholamine overexposure. The resulting presynaptic and postsynaptic imbalance is thought to contribute to electrical instability and arrhythmogenesis. Assuming that stimulatory G proteins (G) are upregulated in connection with downregulated β-adrenoceptors, an acute increase in synaptic norepinephrine (NE) concentration would increase cyclic adenosine 3′,5′-monophosphate (cAMP) via activation of adenylyl cyclase (AC). The increase in cAMP will produce a rise in intracellular Ca^{2+} levels by activation of protein kinase A (PKA) and will eventually trigger ventricular tachycardia. ATP adenosine triphosphate, RE release, UP uptake

Figure 11.25 shows the results of a study relating imaging findings and ventricular arrhythmias in patients treated with an implantable cardioverter defibrillator (ICD). ICDs that are capable of ECG recording at the time of arrhythmias provide an opportunity to study the association between ^{123}I-*m*IBG imaging findings and ventricular arrhythmias [70–72]. In this study, Nagahara et al. [72] prospectively followed 53 patients treated with ICD for 15 months after ^{123}I-*m*IBG imaging. Most patients ($n = 39$) had underlying structural heart disease, including nine patients with idiopathic dilated cardiomyopathy and eight patients with ischemic heart disease. The graph shows that patients who had appropriate ICD discharges due to life-threatening ventricular arrhythmias ($n = 21$) or who died of cardiac causes had significantly lower HMRs than the other patients. The value of ^{123}I-*m*IBG imaging in improving the selection of patients for treatment with ICD remains to be established in future trials involving larger numbers of patients who are representative of the common underlying etiologies of heart failure, particularly ischemic heart disease.

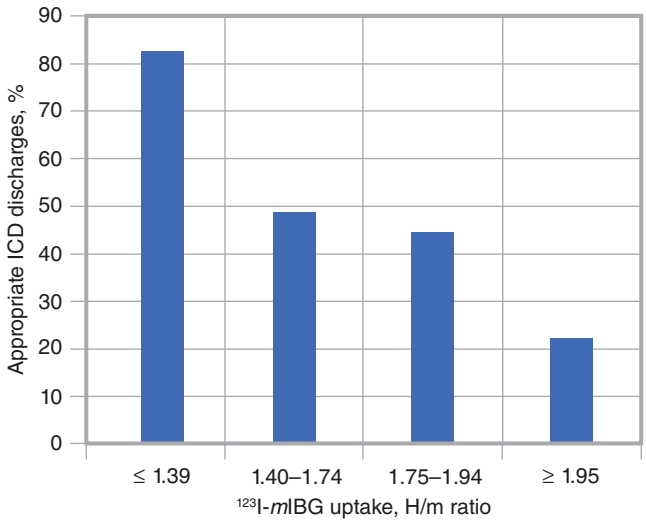

Fig. 11.25 Implantable cardioverter defibrillators (ICDs) for the study of imaging findings and ventricular arrhythmias. Patients who had appropriate ICD discharges due to life-threatening ventricular arrhythmias ($n = 21$) or died of cardiac causes had significantly lower H/M ratios than the other patients. The H/M ratio of 1.95 was the optimal cutoff value that identified arrhythmias (area under the ROC curve, 0.68) independently of many other variables, including LVEF and plasma brain natriuretic peptide (BNP) level. The event rates among quartiles of the H/M ratio are shown. When the H/M ratio was combined with either LVEF or BNP, their sensitivities were 67% and 45%, with specificities of 70% and 94%, respectively, better than those provided by LVEF alone [72]

Diabetes

Heterogeneous denervation is seen in patients with diabetic neuropathy (Fig. 11.26) and has been linked to an increased incidence of sudden cardiac death in patients with diabetic neuropathy of the heart [73]. A correlation has been established between the degree of cardiac denervation and the clinical parameters of autonomic dysfunction [74, 75]. The scintigraphic determination of presynaptic tracer uptake appears to be more sensitive than clinical parameters in detecting early involvement of the heart in diabetic neuropathy, but no prospective data are available defining the prognostic value of neuronal imaging for detection of patients with increased incidence of cardiovascular complications [73, 74, 76–78].

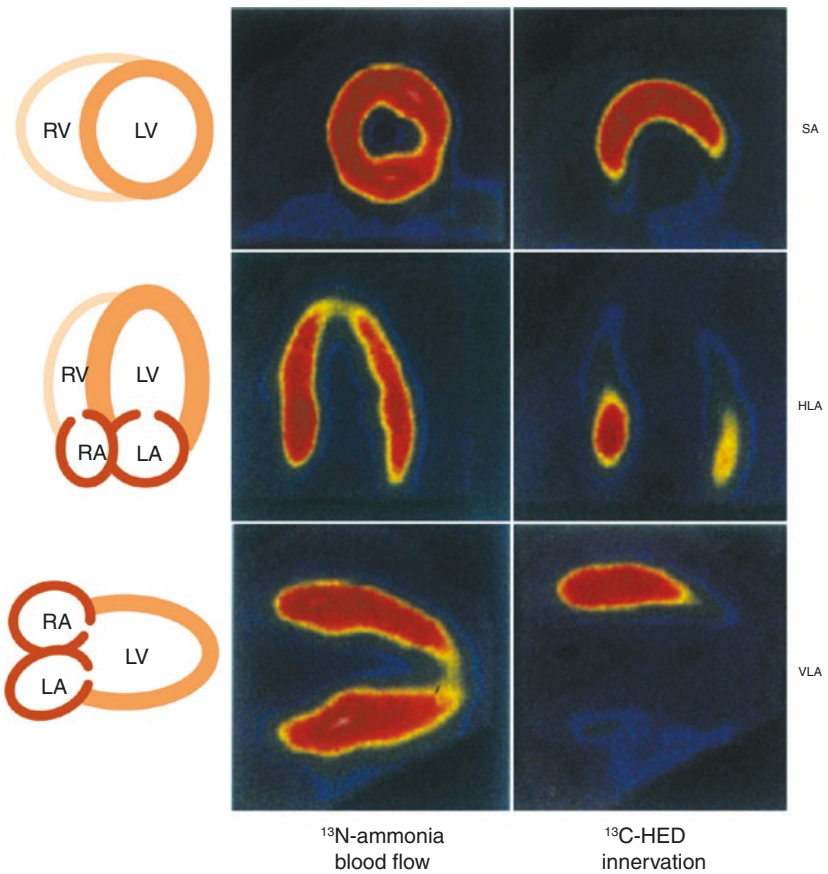

Fig. 11.26 Myocardial neuropathy in diabetes. These PET images were obtained from a patient with advanced diabetic neuropathy as defined by functional testing. Following the injection of ^{11}C-HED, short-axis (SA), horizontal long-axis (HLA), and vertical long-axis (VLA) views were obtained. The regional retention of ^{11}C-HED is compared with the regional perfusion as assessed by ^{13}N-ammonia. There is heterogeneous denervation in patients with diabetic neuropathy. The ^{11}C-HED retention is reduced most prominently in the distal aspects of the anterior wall, apex, and inferior wall of the left ventricle (LV). As the process of neuropathy proceeds, denervation starts at the apex and extends to the basal aspects of the LV. The proximal, anterior, and anterolateral wall segments are most protected from the disease process. This heterogeneity of denervation has been linked to the increased incidence of sudden cardiac death in these patients. LA left atrium, RA right atrium, RV right ventricle

Cardiac Transplantation

Cardiac transplantation represents the best model of cardiac denervation because the neuronal fibers are cut during the transplantation surgery. As time after the cardiac transplantation passes, however, there is evidence for regional reinnervation [25]. Figure 11.27 depicts the reinnervation process occurring in about 40–50% of patients. The reinnervation process does not result in complete reinnervation but shows the regional reappearance of sympathetic nerve terminals. Functional studies have shown that patients with reinnervation show greater heart rate variability, better exercise tolerance, and improved LV function with exercise [80].

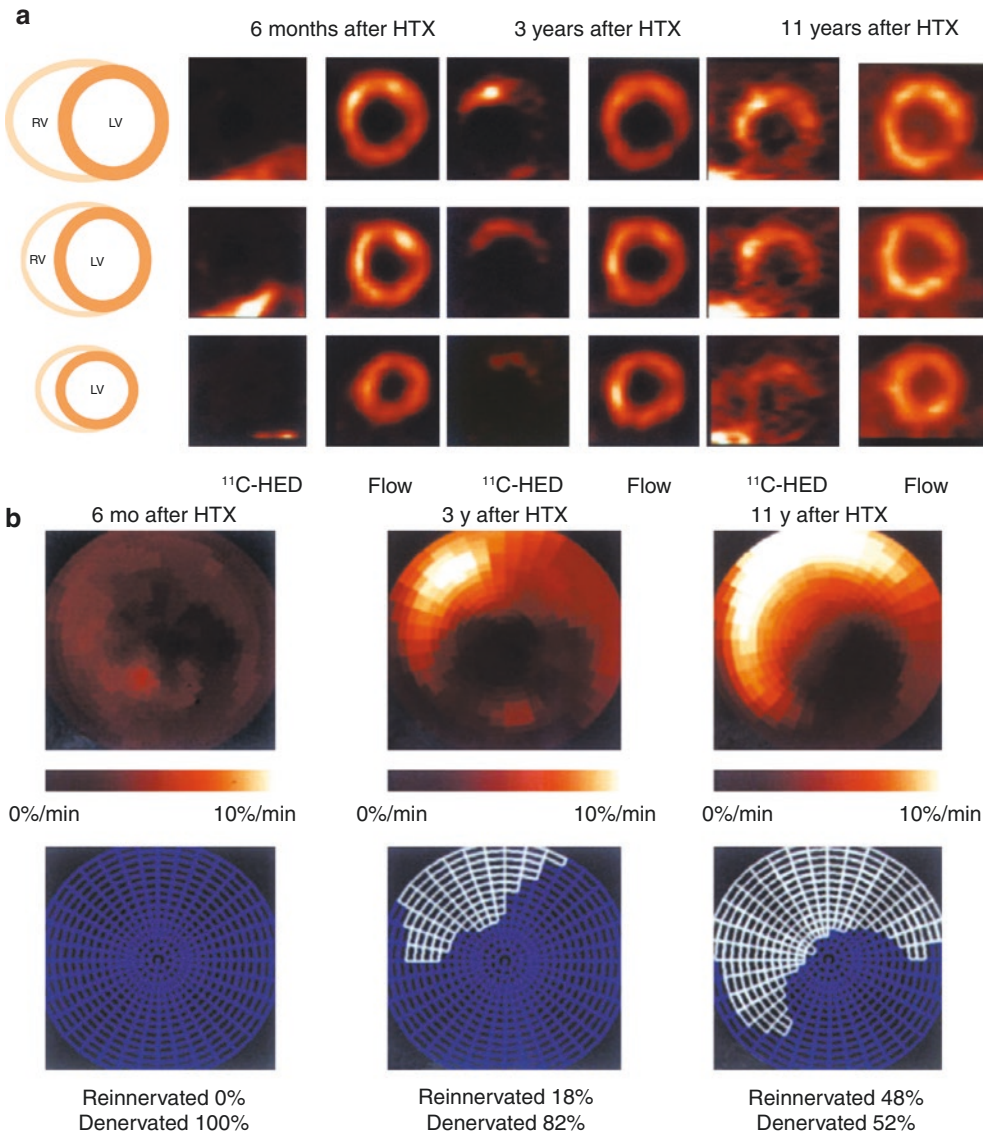

Fig. 11.27 Reinnervation of cardiac allograft. Uptake of radiolabeled catecholamines in the anterior wall, septum, and base of the left ventricle (LV) indicates the reappearance of functioning sympathetic nerve terminals. The pharmacologic integrity of these nerve terminals has been demonstrated by studies of neurotransmitter released following the intracoronary injection of tyramine [79]. A study linking regional tracer uptake with exercise capacity indicates that the reinnervation process is beneficial for the exercise performance of patients following heart transplantation [80]. (**a**) Neuronal imaging with ^{11}C-HED obtained 6 months after heart transplantation (HTX) shows little retention of the tracer in the myocardium 40 minutes after the tracer injection, in comparison to the myocardial perfusion assessed with ^{13}N-ammonia. In a patient studied 3 years after heart transplantation, myocardial perfusion is homogeneous throughout the LV, but the ^{11}C-HED images obtained 40 minutes after injection reveal the reappearance of regional ^{11}C-HED retention in the anteroseptal area of the LV. The area of reinnervation appears larger in a patient studied 11 years after transplantation, but regional denervation remains detectable in inferior aspects of the LV, which display normal perfusion. (**b**) PET–^{11}C-HED polar maps of cardiac transplantation patients at various time points after surgery. Early after transplantation, the retention index is reduced throughout the entire LV myocardium. Using a threshold of 7%/min retention index, no reinnervated area can be detected. At 3 years after transplantation, the anteroseptal areas show reinnervated territories (about 18% of the LV). The PET images obtained 11 years after transplantation show a reinnervated area of 48% of the LV, illustrating the progress of the reinnervation process in the anterior septal wall toward the apex. However, the inferior inferolateral wall remains denervated, as seen in most patients undergoing neuronal imaging late after cardiac transplantation [80–82]. RV right ventricle

References

1. Levy M. Sympathetic-parasympathetic interaction in the heart. In: Kulbertus HE, Franck G, editors. Neurocardiology. New York: Futura; 1988. p. 85–98.
2. Bristow MR, Minobe W, Rasmussen R, Larrabee P, Skerl L, Klein JW, et al. Beta-adrenergic neuroeffector abnormalities in the failing human heart are produced by local rather than systemic mechanisms. J Clin Invest. 1992;89:803–15.
3. Bristow MR, Anderson FL, Port JD, Skerl L, Hershberger RE, Larrabee P, et al. Differences in beta-adrenergic neuroeffector mechanisms in ischemic versus idiopathic dilated cardiomyopathy. Circulation. 1991;84:1024–39.
4. Somsen GA, Verberne HJ, Fleury E, Righetti A. Normal values and within-subject variability of cardiac I-123 MIBG scintigraphy in healthy individuals: implications for clinical studies. J Nucl Cardiol. 2004;11:126–33.
5. Momose M, Tyndale-Hines L, Bengel FM, Schwaiger M. How heterogeneous is the cardiac autonomic innervation? Basic Res Cardiol. 2001;96:539–46.
6. Bannister R, Mathias CJ. Introduction and classification of autonomic disorders. In: Bannister R, Mathias CJ, editors. Autonomic failure. New York: Oxford University Press; 1992. p. 1–12.
7. Milner P, Burnstock G. Neurotransmitters in the autonomic nervous system. In: Korczyn AD, editor. Handbook of autonomic nervous system dysfunction. New York: Marcel Dekker; 1995. p. 5–32.
8. Lipscombe D, Kongsamut S, Tsien RW. Alpha-adrenergic inhibition of sympathetic neurotransmitter release mediated by modulation of N-type calcium-channel gating. Nature. 1989;340:639–42.
9. Toth PT, Bindokas VP, Bleakman D, Colmers WF, Miller RJ. Mechanism of presynaptic inhibition by neuropeptide Y at sympathetic nerve terminals. Nature. 1993;364:635–9.
10. Nicholls JG, Martin AR, Wallace BG. From neuron to brain. 3rd ed. Sinauer: Sunderland; 1992.
11. Langer O, Halldin C. PET and SPECT tracers for mapping the cardiac nervous system. Eur J Nucl Med. 2002;29:416–34.
12. Kline RC, Swanson DP, Wieland DM, Thrall JH, Gross MD, Pitt B, Beierwaltes WH. Myocardial imaging in man with I-123 meta-iodobenzylguanidine. J Nucl Med. 1981;22:129–32.
13. Wieland DM, Rosenspire KC, Hutchins GD, Van Dort M, Rothley JM, Mislankar SG, et al. Neuronal mapping of the heart with 6-[18F]fluorometaraminol. J Med Chem. 1990;33:956–64.
14. Rosenspire KC, Haka MS, Van Dort ME, Jewett DM, Gildersleeve DL, Schwaiger M, Wieland DM. Synthesis and preliminary evaluation of carbon-11-meta-hydroxyephedrine: a false transmitter agent for heart neuronal imaging. J Nucl Med. 1990;31:1328–34.
15. Raffel DM, Corbett JR, del Rosario RB, Gildersleeve DL, Chiao PC, Schwaiger M, Wieland DM. Clinical evaluation of carbon-11-phenylephrine: MAO-sensitive marker of cardiac sympathetic neurons. J Nucl Med. 1996;37:1923–31.
16. Degrado TR, Zalutsky MR, Vaidyanathan G. Uptake mechanisms of meta-[123I]iodobenzylguanidine in isolated rat heart. Nucl Med Biol. 1995;22:1–12.
17. Nakajima K, Taki J, Tonami N, Hisada K. Decreased 123I-MIBG uptake and increased clearance in various cardiac diseases. Nucl Med Commun. 1994;15:317–23.
18. Bengel FM, Barthel P, Matsunari I, Schmidt G, Schwaiger M. Kinetics of 123I-MIBG after acute myocardial infarction and reperfusion therapy. J Nucl Med. 1999;40:904–10.
19. Yamada T, Shimonagata T, Fukunami M, Kumagai K, Ogita H, Hirata A, et al. Comparison of the prognostic value of cardiac iodine-123 metaiodobenzylguanidine imaging and heart rate variability in patients with chronic heart failure: a prospective study. J Am Coll Cardiol. 2003;41:231–8.
20. Patel A, Iskandrian A. MIBG imaging. J Nucl Cardiol. 2002;9:75–94.
21. Farahati J, Bier D, Scheubeck M, Lassmann M, Schelper LF, Grelle I, et al. Effect of specific activity on cardiac uptake of iodine-123-MIBG. J Nucl Med. 1997;38:447–51.
22. DeGrado TR, Zalutsky MR, Coleman RE, Vaidyanathan G. Effects of specific activity on meta-[(131)I]iodobenzylguanidine kinetics in isolated rat heart. Nucl Med Biol. 1998;25:59–64.
23. Verberne HJ, Brewster LM, Somsen GA, van Eck-Smit BL. Prognostic value of myocardial 123I-metaiodobenzylguanidine (MIBG) parameters in patients with heart failure: a systematic review. Eur Heart J. 2008;29:1147–59.
24. Schwaiger M, Kalff V, Rosenspire K, Haka MS, Molina E, Hutchins GD, et al. Noninvasive evaluation of sympathetic nervous system in human heart by positron emission tomography. Circulation. 1990;82:457–64.
25. Schwaiger M, Hutchins GD, Kalff V, Rosenspire K, Haka MS, Mallette S, et al. Evidence for regional catecholamine uptake and storage sites in the transplanted human heart by positron emission tomography. J Clin Invest. 1991;87:1681–90.
26. Münch G, Nguyen NT, Nekolla S, Ziegler S, Muzik O, Chakraborty P, et al. Evaluation of sympathetic nerve terminals with [(11)C] epinephrine and [(11)D]hydroxyephedrine and positron emission tomography. Circulation. 2000;101:516–23.
27. Delforge J, Syrota A, Lançon JP, Nakajima K, Loc'h C, Janier M, et al. Cardiac beta-adrenergic receptor density measured in vivo using PET, CGP 12177, and a new graphical method. J Nucl Med. 1991;32:739–48. [Erratum in J Nucl Med. 1994;35:921].
28. Hartmann F, Ziegler S, Nekolla S, Hadamitzky M, Seyfarth M, Richardt G, Schwaiger M. Regional patterns of myocardial sympathetic denervation in dilated cardiomyopathy: an analysis using carbon-11 hydroxyephedrine and positron emission tomography. Heart. 1999;81:262–70.
29. Caldwell JH, Link JM, Levy WC, et al. Evidence for pre- to postsynaptic mismatch of the cardiac sympathetic nervous system in ischemic congestive heart failure. J Nucl Med. 2008;49:234–41.
30. Narula J, Gerson M, Thomas GS, Cerqueira MD, Jacobson AF. I-123 *m*IBG imaging for prediction of mortality and potentially fatal events in heart failure: the ADMIRE-HFX study. J Nucl Med. 2015;56:1011–8.
31. Agostini D, Ananthasubramaniam K, Chandna H, et al. Prognostic usefulness of planar 123I-MIBG scintigraphic images of myocardial sympathetic innervation in congestive heart failure: Follow-up data from ADMIRE-HF. J Nucl Cardiol 2019. https://doi.org/10.1007/s12350-019-01859-w.
32. Nakata T, Nakajima K, Yamashina S, Yamada T, Momose M, Kasama S, et al. A pooled analysis of multicenter cohort studies of (123)I-mIBG imaging of sympathetic innervation for assessment of long-term prognosis in heart failure. JACC Cardiovasc Imaging. 2013;6:772–84.
33. Chen J, Folks RD, Verdes L, Manatunga DN, Jacobson AF, Garcia EV. Quantitative I123 mIBG SPECT in differentiating abnormal and normal mIBG myocardial uptake. J Nucl Cardiol. 2012;19:92–9.
34. Bax JJ, Kraft O, Buxton AE, Fjeld JG, Parízek P, Agostini D, et al. 123 I-mIBG scintigraphy to predict inducibility of ventricular arrhythmias on cardiac electrophysiology testing: a prospective multicenter pilot study. Circ Cardiovasc Imaging. 2008;1:131–40.
35. Boogers MJ, Borleffs CJ, Henneman MM, van Bommel RJ, van Ramshorst J, Boersma E, et al. Cardiac sympathetic denervation assessed with 123-iodine metaiodobenzylguanidine imaging predicts ventricular arrhythmias in implantable cardioverter-defibrillator patients. J Am Coll Cardiol. 2010;55:2769–77.
36. Marshall A, Cheetham A, George RS, Mason M, Kelion AD. Cardiac iodine-123 metaiodobenzylguanidine imaging pre-

dicts ventricular arrhythmia in heart failure patients receiving an implantable cardioverter-defibrillator for primary prevention. Heart. 2012;98:1359–65.
37. Ketchum ES, Jacobson AF, Caldwell JH, Senior R, Cerqueira MD, Thomas GS, et al. Selective improvement in Seattle heart failure model risk stratification using Iodine-123 meta-iodobenzylguanidine imaging. J Nucl Cardiol. 2012;19:1007–16.
38. Jain KK, Hauptman PJ, Spertus JA, Kennedy KF, Bateman TM, Jacobson AF, Stolker JM. Incremental utility of iodine-123 meta-Iodobenzylguanidine imaging beyond established heart failure risk models. J Card Fail. 2014;20:577–83.
39. Nakajima K, Nakata T, Matsuo S, Jacobson AF. Creation of mortality risk charts using 123I meta-iodobenzylguanidine heart-to-mediastinum ratio in patients with heart failure: 2- and 5-year risk models. Eur Heart J Cardiovasc Imaging. 2016;17:1138–45.
40. Nakajima K, Nakata T, Doi T, Kadokami T, Matsuo S, Konno T, et al. Validation of 2-year 123I-meta-iodobenzylguanidine-based cardiac mortality risk model in chronic heart failure. Eur Heart J Cardiovasc Imaging. 2018;19:749–56.
41. Link JM, Caldwell JH. Diagnostic and prognostic imaging of the cardiac sympathetic nervous system. Nat Clin Pract Cardiovasc Med. 2008;5(Suppl 2):S79–86.
42. Fallavollita JA, Heavey BM, Luisi AJ Jr, Michalek SM, Baldwa S, Mashtare TL, et al. Regional myocardial sympathetic denervation predicts the risk of sudden cardiac arrest in ischemic cardiomyopathy. J Am Coll Cardiol. 2014;63:141–9.
43. Harms HJ, Huisman MC, Rijnierse MT, Greuter H, Hsieh YL, de Haan S, et al. Noninvasive quantification of myocardial 11C-meta-hydroxyephedrine kinetics. J Nucl Med. 2016;57:1376–81.
44. Harms HJ, Lubberink M, de Haan S, Knaapen P, Huisman MC, Schuit RC, et al. Use of a single 11C-meta-hydroxyephedrine scan for assessing flow-innervation mismatches in patients with ischemic cardiomyopathy. J Nucl Med. 2015;56:1706–11.
45. Bengel FM, Schwaiger M. Assessment of cardiac sympathetic neuronal function using PET imaging. J Nucl Cardiol. 2004;11:603–16.
46. Thackeray JT, Bengel FM. Assessment of cardiac autonomic neuronal function using PET imaging. J Nucl Cardiol. 2013;20:150–65.
47. Tokuda Y, Sakakibara M, Yoshinaga K, Yamada S, Kamiya K, Asakawa N, et al. Early therapeutic effects of adaptive servo-ventilation on cardiac sympathetic nervous function in patients with heart failure evaluated using a combination of ^{11}C-HED PET and ^{123}I-MIBG SPECT. J Nucl Cardiol. 2019;26:1079–89.
48. Aikawa T, Naya M, Obara M, Oyama-Manabe N, Manabe O, Magota K, et al. Regional interaction between myocardial sympathetic denervation, contractile dysfunction, and fibrosis in heart failure with preserved ejection fraction: ^{11}C-hydroxyephedrine PET study. Eur J Nucl Med Mol Imaging. 2017;44:1897–905.
49. Sinusas AJ, Lazewatsky J, Brunetti J, Heller G, Srivastava A, Liu YH, et al. Biodistribution and radiation dosimetry of LMI1195: first-in-human study of a novel 18F-labeled tracer for imaging myocardial innervation. J Nucl Med. 2014;55:1445–51.
50. Jung YW, Jang KS, Gu G, Koeppe RA, Sherman PS, Quesada CA, Raffel DM. [^{18}F]Fluoro-hydroxyphenethylguanidines: efficient synthesis and comparison of two structural isomers as radiotracers of cardiac sympathetic innervation. ACS Chem Neurosci. 2017;8:1530–42.
51. Zhou Y, Zhou W, Folks RD, Manatunga DN, Jacobson AF, Bax JJ, et al. I-123 mIBG and Tc-99m myocardial SPECT imaging to predict inducibility of ventricular arrhythmia on electrophysiology testing: a retrospective analysis. J Nucl Cardiol. 2014;21:913–20.
52. Klein T, Abdulghani M, Smith M, Huang R, Asoglu R, Remo BF, et al. Three-dimensional 123I-meta-iodobenzylguanidine cardiac innervation maps to assess substrate and successful ablation sites for ventricular tachycardia: feasibility study for a novel paradigm of innervation imaging. Circ Arrhythm Electrophysiol. 2015;8:583–91.
53. Lautamaki R, Sasano T, Higuchi T, Nekolla SG, Lardo AC, Holt DP, et al. Multiparametric molecular imaging provides mechanistic insights into sympathetic innervation impairment in the viable infarct border zone. J Nucl Med. 2015;56:457–63.
54. Pina IL, Carson P, Lindenfeld J, Archambault T, Jacobson AF. Persistence of 123I-mIBG prognostic capability in relation to medical therapy in heart failure (from the ADMIRE-HF trial). Am J Cardiol. 2017;119:434–9.
55. Jacobson AF, White S, Travin MI, Tseng C. Impact of concomitant medication use on myocardial ^{123}I-*m*IBG imaging results in patients with heart failure. Nucl Med Commun. 2017;38:141–8.
56. Allman KC, Wieland DM, Muzik O, Degrado TR, Wolfe ER Jr, Schwaiger M. Carbon-11 hydroxyephedrine with positron emission tomography for serial assessment of cardiac adrenergic neuronal function after acute myocardial infarction in humans. J Am Coll Cardiol. 1993;22:368–75.
57. Matsunari I, Schricke U, Bengel FM, Haase HU, Barthel P, Schmidt G, et al. Extent of cardiac sympathetic neuronal damage is determined by the area of ischemia in patients with acute coronary syndromes. Circulation. 2000;101:2579–85.
58. Fricke E, Fricke H, Eckert S, Zijlstra S, Weise R, Lindner O, et al. Myocardial sympathetic innervation in patients with chronic coronary artery disease: is reduction in coronary flow reserve correlated with sympathetic denervation? Eur J Nucl Med Mol Imaging. 2007;34:206–11.
59. Yukinaka M, Nomura M, Ito S, Nakaya Y. Mismatch between myocardial accumulation of 123I-MIBG and 99mTc-MIBI and late ventricular potentials in patients after myocardial infarction: association with the development of ventricular arrhythmias. Am Heart J. 1998;136:859–67.
60. Simões MV, Barthel P, Matsunari I, Nekolla SG, Schömig A, Schwaiger M, et al. Presence of sympathetically denervated but viable myocardium and its electrophysiologic correlates after early revascularised, acute myocardial infarction. Eur Heart J. 2004;25:551–7.
61. Calkins H, Allman K, Bolling S, Kirsch M, Wieland D, Morady F, Schwaiger M. Correlation between scintigraphic evidence of regional sympathetic neuronal dysfunction and ventricular refractoriness in the human heart. Circulation. 1993;88:172–9.
62. Sasano T, Abraham MR, Chang KC, Ashikaga H, Mills KJ, Holt DP, et al. Abnormal sympathetic innervation of viable myocardium and the substrate of ventricular tachycardia after myocardial infarction. J Am Coll Cardiol. 2008;51:2266–75.
63. Akutsu Y, Kaneko K, Kodama Y, Li HL, Suyama J, Shinozuka A, et al. Iodine-123 imaging for predicting the development of atrial fibrillation. JACC Cardiovasc Imaging. 2011;4:78–86.
64. Schwartz PJ. The autonomic nervous system and sudden death. Eur Heart J. 1998;19:F72–80.
65. Meredith IT, Broughton A, Jennings GL, Esler MD. Evidence of a selective increase in cardiac sympathetic activity in patients with sustained ventricular arrhythmias. N Engl J Med. 1991;325:618–24.
66. Rubart M, Zipes DP. Mechanisms of sudden cardiac death. J Clin Invest. 2005;115:2305–15.
67. Wichter T, Schäfers M, Rhodes CG, Borggrefe M, Lerch H, Lammertsma AA, et al. Abnormalities of cardiac sympathetic innervation in arrhythmogenic right ventricular cardiomyopathy: quantitative assessment of presynaptic norepinephrine reuptake and postsynaptic beta-adrenergic receptor density with positron emission tomography. Circulation. 2000;101:1552–8.
68. Schäfers M, Lerch H, Wichter T, Rhodes CG, Lammertsma AA, Borggrefe M, et al. Cardiac sympathetic innervation in patients with idiopathic right ventricular outflow tract tachycardia. J Am Coll Cardiol. 1998;32:181–6.

69. Kies P, Wichter T, Schäfers M, Paul M, Schäfers KP, Eckardt L, et al. Abnormal myocardial presynaptic norepinephrine recycling in patients with Brugada syndrome. Circulation. 2004;110:3017–22.
70. Paul M, Schäfers M, Kies P, Acil T, Schäfers K, Breithardt G, et al. Impact of sympathetic innervation on recurrent life-threatening arrhythmias in the follow-up of patients with idiopathic ventricular fibrillation. Eur J Nucl Med Mol Imaging. 2006;33:866–70.
71. Arora R, Ferrick KJ, Nakata T, Kaplan RC, Rozengarten M, Latif F, et al. I-123 MIBG imaging and heart rate variability analysis to predict the need for an implantable cardioverter defibrillator. J Nucl Cardiol. 2003;10:121–31.
72. Nagahara D, Nakata T, Hashimoto A, Wakabayashi T, Kyuma M, Noda R, et al. Predicting the need for an implantable cardioverter defibrillator using cardiac metaiodobenzylguanidine activity together with plasma natriuretic peptide concentration or left ventricular function. J Nucl Med. 2008;49:225–33.
73. Langen KJ, Ziegler D, Weise F, Piolot R, Boy C, Hübinger A, et al. Evaluation of QT interval length, QT dispersion and myocardial m-iodobenzylguanidine uptake in insulin-dependent diabetic patients with and without autonomic neuropathy. Clin Sci (Lond). 1997;93:325–33.
74. Stevens MJ, Raffel DM, Allman KC, Dayanikli F, Ficaro E, Sandford T, et al. Cardiac sympathetic dysinnervation in diabetes: implications for enhanced cardiovascular risk. Circulation. 1998;98:961–8.
75. Pop-Busui R, Kirkwood I, Schmid H, Marinescu V, Schroeder J, Larkin D, et al. Sympathetic dysfunction in type 1 diabetes: association with impaired myocardial blood flow reserve and diastolic dysfunction. J Am Coll Cardiol. 2004;44:2368–74.
76. Allman KC, Stevens MJ, Wieland DM, Hutchins GD, Wolfe ER Jr, Greene DA, Schwaiger M. Noninvasive assessment of cardiac diabetic neuropathy by carbon-11 hydroxyephedrine and positron emission tomography. J Am Coll Cardiol. 1993;22:1425–32.
77. Ziegler D, Weise F, Langen KJ, Piolot R, Boy C, Hübinger A, et al. Effect of glycaemic control on myocardial sympathetic innervation assessed by [123I]metaiodobenzylguanidine scintigraphy: a 4-year prospective study in IDDM patients. Diabetologia. 1998;41:443–51.
78. Wei K, Dorian P, Newman D, Langer A. Association between QT dispersion and autonomic dysfunction in patients with diabetes mellitus. J Am Coll Cardiol. 1995;26:859–63.
79. Odaka K, von Scheidt W, Ziegler SI, Ueberfuhr P, Nekolla SG, Reichart B, et al. Reappearance of cardiac presynaptic sympathetic nerve terminals in the transplanted heart: correlation between PET using (11) C-hydroxyephedrine and invasively measured norepinephrine release. J Nucl Med. 2001;42:1011–6.
80. Bengel FM, Ueberfuhr P, Schiepel N, Nekolla SG, Reichart B, Schwaiger M. Effect of sympathetic reinnervation on cardiac performance after heart transplantation. N Engl J Med. 2001;345:731–8.
81. De Marco T, Dae M, Yuen-Green MS, Kumar S, Sudhir K, Keith F, et al. Iodine-123 metaiodobenzylguanidine scintigraphic assessment of the transplanted human heart: evidence for late reinnervation. J Am Coll Cardiol. 1995;25:927–31.
82. Estorch M, Campreciós M, Flotats A, Marí C, Bernà L, Catafau AM, et al. Sympathetic reinnervation of cardiac allografts evaluated by 123I-MIBG imaging. J Nucl Med. 1999;40:911–6.

Diagnosis and Risk Stratification in Acute Coronary Syndromes

12

James E. Udelson and Carlos D. Davila

Introduction

Since the 1970s, radionuclide myocardial perfusion imaging (MPI) has played an important role in diagnosis and in risk stratification for patients with acute coronary syndromes (ACS). Early studies using planar ^{201}Tl imaging documented the superior ability of this technique to assess both the presence and location of myocardial infarction (MI) and to predict the site of coronary disease involvement in unstable syndromes more accurately than electrocardiogram (ECG) findings alone [1]. More recently, the use of ^{99m}Tc-based agents such as sestamibi in the early hours of an infarct has provided important information on areas at risk in the setting of the coronary occlusion, while a follow-up study done several days later provided information on final infarct size and myocardial salvage when both sets of images were compared [2].

Stress MPI in the early aftermath of both unstable angina syndromes as well as acute MI carries powerful prognostic information for risk-stratifying stable post-ACS patients. Imaging for ischemia has been incorporated into numerous randomized clinical trials to better define the roles of different ACS management strategies [3, 4]. Since the 1990s, MPI has also been used to image resting perfusion in patients with chest pain syndromes and suspected ACS who do not have diagnostic ischemic ECG changes upon presentation to the emergency department, to help rule in or rule out ACS. Several published studies now consistently demonstrate very high negative predictive value (NPV) for ruling out acute ischemia or events as well as powerful risk-stratification information for those with positive tests in the emergency department setting [5–8]. Thus, single-photon emission CT (SPECT) MPI techniques can be used in the setting of ACS both for initial detection of abnormal blood flow underlying the clinical syndrome and for decision making regarding conservative vs. invasive interventional management.

Advances in hardware and software technology have allowed the combined assessment of stress and rest MPI with measures of regional and global left ventricular function using gated SPECT imaging [9]. Based on the wide availability of gated SPECT MPI of both perfusion and left ventricular function, obtaining the incremental value of adding functional information to the perfusion information in ACS is now routine.

This chapter reviews the role of radionuclide imaging techniques in the broad setting of ACS, with emphasis on decision points where the imaging data have been shown to enhance the clinician's information base in order to optimally manage patients in this setting. Also reviewed is the role of newer and emerging imaging techniques such as cardiac computed tomography (CT), cardiac magnetic resonance (CMR), and radionuclide techniques that are under development but not yet widely available, but which may have potential utility in the setting of ACS.

J. E. Udelson (✉)
Department of Medicine, CardioVascular Center, Tufts University Medical Center, Boston, MA, USA
e-mail: JUdelson@tuftsmedicalcenter.org

C. D. Davila
Division of Cardiology, Tufts University Medical Center, Boston, MA, USA

V. Dilsizian, J. Narula (eds.), *Atlas of Nuclear Cardiology*, https://doi.org/10.1007/978-3-030-49885-6_12

General Approach to Cardiovascular Imaging in ACS

Figure 12.1 illustrates the decision points in diagnosing ACS. Table 12.1 details the role of nuclear imaging and other imaging techniques with utility in the diagnosis or exclusion of ACS in the emergency department (ED), including CT, MR, and echocardiography techniques [18, 20]. Radionuclide imaging techniques involve imaging myocardial perfusion at rest (for resting ischemia or infarct) or at stress and rest (for inducible ischemia and extent of infarct).

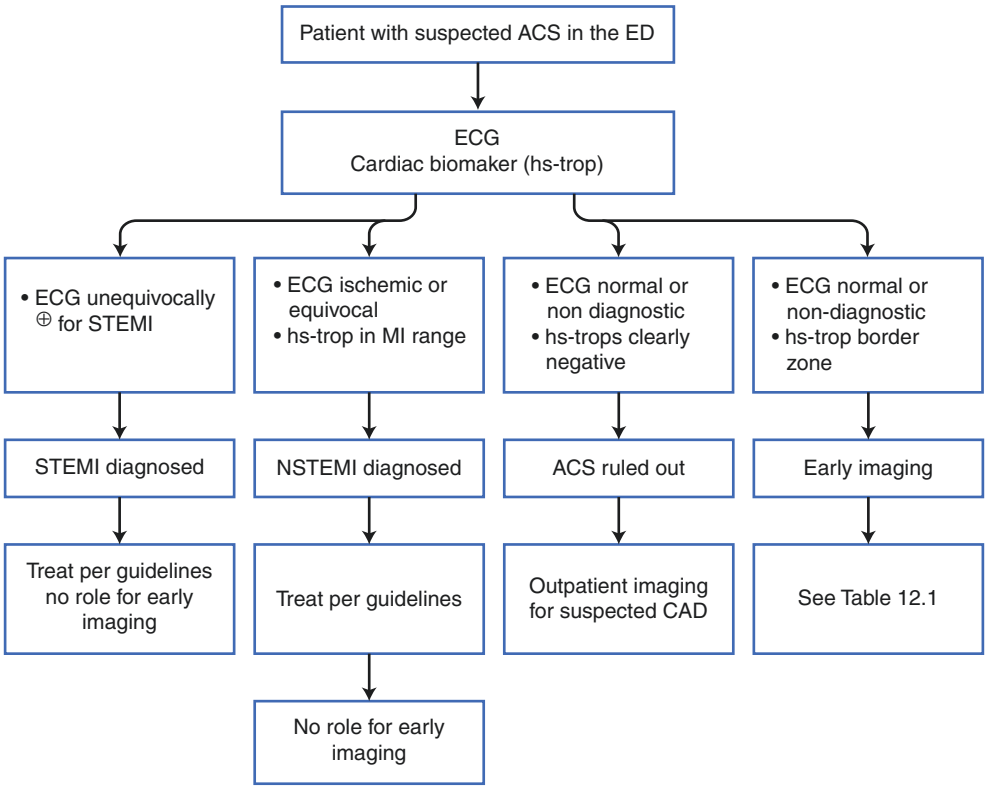

Fig. 12.1 Role of cardiac imaging in the diagnosis of acute coronary syndrome (ACS). Diagnostic decision points in the evaluation and management of ACS are given. This schematic demonstrates the role of imaging techniques in the evaluation of patients with suspected ACS. Electrocardiogram (ECG) and cardiac biomarkers (increasingly using high-sensitivity troponin [hs-trop] assays) are the first step in the evaluation of these patients and form the basis for the diagnosis of an ST-elevation myocardial infarction (STEMI) or a non–ST-elevation myocardial infarction (NSTEMI). ED emergency department

Technique	What is being imaged, and what it means
Nuclear techniques	
Acute rest perfusion imaging	Resting myocardial blood flow abnormalities suggestive of acute myocardial ischemia or prior infarct
Stress and rest perfusion imaging	Stress myocardial blood flow abnormalities suggestive of myocardial ischemia; extent of infarct
CT techniques	
Coronary CT angiography (CTA)	Abnormalities in coronary arterial lumens and walls suggestive of CAD
CT fractional flow reserve (FFR)	Fractional flow reserve of anatomic stenoses
Stress perfusion imaging	Stress myocardial blood flow abnormalities suggestive of myocardial ischemia
MR techniques	
Stress perfusion imaging	Stress myocardial blood flow abnormalities suggestive of myocardial ischemia
T2-weighted imaging	Myocardial edema suggestive of acute myocardial injury
Delayed enhancement imaging	Myocardial infarction suggestive of CAD
Resting cine imaging	Resting wall motion abnormalities suggestive of MI and CAD
Echocardiography techniques	
Stress imaging	Stress-induced wall motion abnormalities suggestive of myocardial ischemia
Resting cine imaging	Resting wall motion abnormalities suggestive of MI and CAD

CAD coronary artery disease, *MI* myocardial infarction, *MR* magnetic resonance

Table 12.1 Techniques for the diagnosis or exclusion of acute coronary syndromes (ACS)

Radionuclide Imaging Early in the Evaluation of Suspected ACS

In patients with chest pain but nondiagnostic ECG alterations, perfusion imaging may demonstrate significant abnormalities, making earlier intervention possible (Fig. 12.2). On the other hand, if no abnormality is identified (Fig. 12.3), the probability of MI and ACS is very low, and the patient may be discharged directly from the ED. Figures 12.4, 12.5, 12.6, 12.7 and 12.8 examine how perfusion imaging fits with other tests in contributing to effective clinical decision making.

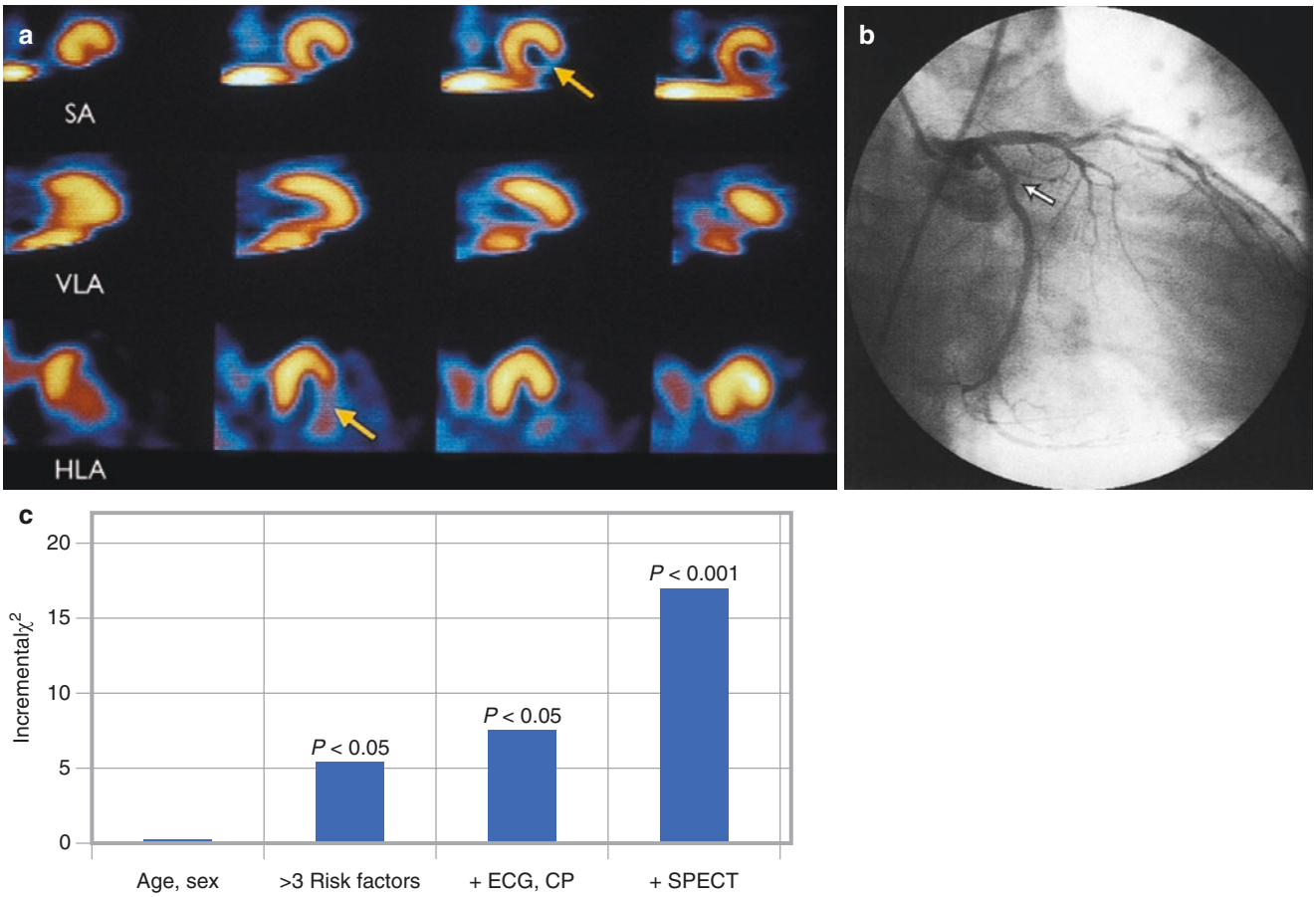

Fig. 12.2 Acute rest perfusion imaging has the ability to demonstrate significant myocardial perfusion abnormalities in patients with chest pain but nondiagnostic ECG alterations. (**a**) These short-axis (SA), vertical long-axis (VLA), and horizontal long-axis (HLA) resting single-photon emission CT (SPECT) myocardial perfusion images (MPI) are of a 39-year-old man who presented to the ED with chest pain atypical for angina and a normal initial ECG. He was injected with ^{99m}Tc-sestamibi at rest in the ED and underwent SPECT imaging soon thereafter. The images show a dense inferolateral resting perfusion defect (*arrows*), which in the setting of ongoing symptoms was most suggestive of resting ischemia and ACS. He was immediately triaged to the catheterization laboratory. (**b**) This right anterior oblique view of the left coronary artery injection shows an occluded left circumflex artery (*arrow*) in the same patient. Ischemia or infarct resulting from left circumflex occlusions is not always well seen on the standard 12-lead ECG. The patient subsequently underwent successful percutaneous coronary intervention of the left circumflex artery, with an excellent anatomic result. Had myocardial perfusion imaging (MPI) not been performed, he may have been admitted for observation, and serial biomarker analysis may have been positive for a myocardial infarction (MI). The use of MPI likely allowed for significantly earlier intervention in this case. (**c**) Analysis of the incremental value of resting MPI data to predict cardiac events in patients presenting to the ED with suspected ischemia. The incremental χ^2 value measures the strength of the association between individual factors added to a clinician's knowledge base in an incremental fashion and unfavorable cardiac events. The addition of resting SPECT MPI data (+ SPECT) in the ED setting adds a highly statistically significant value to the detection of ACS and events, even given knowledge of age, sex, multiple (>3) risk factors for coronary artery disease, and ECG changes, as well as the presence or absence of chest pain (CP) [8]

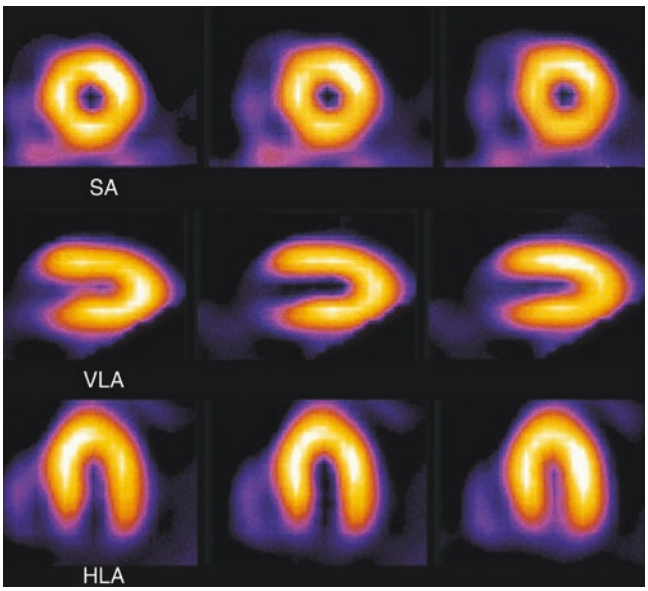

Fig. 12.3 Absence of myocardial perfusion abnormality in a patient presenting with chest pain but nondiagnostic ECG changes. These short-axis (SA), vertical long-axis (VLA), and horizontal long-axis (HLA) SPECT images are of a 52-year-old man who presented to the ED with chest pain atypical for angina and an initial ECG with nonspecific ST-segment abnormalities not diagnostic for acute ischemia. He was injected with ^{99m}Tc-sestamibi at rest in the ED and underwent SPECT imaging soon thereafter. The images show a completely normal resting perfusion pattern, and the gated SPECT imaging of resting left ventricular function (*not shown*) was also normal. This finding is associated with a very low probability of MI and ACS (*see* Figs. 12.4 and 12.6), suggesting that such a patient may be discharged directly from the ED

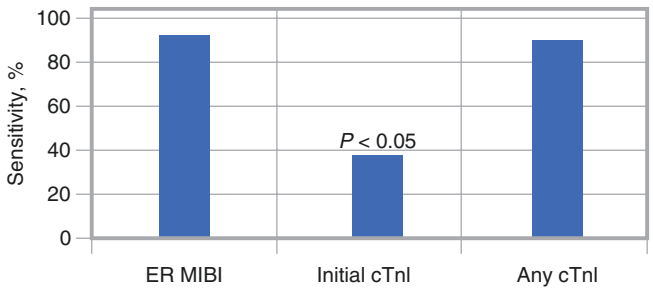

Fig. 12.4 Comparative role of myocardial perfusion imaging (MPI) and serial analysis of cardiospecific biomarkers in patients with chest pain in the emergency room (ER) setting. ^{99m}Tc-sestamibi MPI (ER MIBI) was performed, and serial analysis of cardiac troponin I (cTnI) was undertaken in patients presenting with ACS, but there were no obvious ischemic ECG changes (low to moderate risk for ACS). The sestamibi perfusion studies, performed very early during the initial evaluation, had 92% sensitivity to detect myocardial infarction, whereas the initial troponin I value, drawn at a similarly early time in the evaluation, had a sensitivity of only 39%. The sensitivity of any troponin I value on serial testing over 24 hours ultimately achieved sensitivity similar to that of the perfusion study. This study illustrated that in the presence of ACS, MPI likely will be positive earlier than serial analysis of biomarkers, allowing the opportunity for earlier intervention. It is important to note, however, that this study was performed with earlier iterations of a troponin assay with less sensitivity than contemporary high-sensitivity assays. A similar analysis has not been performed with contemporary high-sensitivity assays, which have been used for several years around the world and are beginning to be more available in the United States. Contemporary assays are likely to be positive early when ACS is present [10]

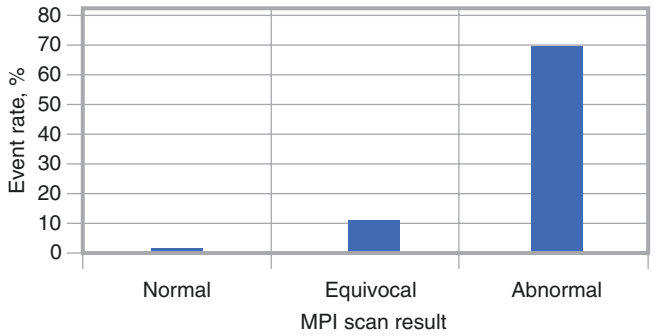

Fig. 12.5 Cardiac event rate as a function of results of resting ^{99m}Tc-sestamibi SPECT MPI in patients presenting to the ED with suspected ischemia. Patients with a normal scan demonstrate a very low event rate, and patients with an abnormal scan had a significantly higher event rate [6], which is consistent with numerous studies from the literature in this population. Patients with "equivocal" results on resting MPI—i.e., results that were neither completely normal nor definitely abnormal—likely reflect some patients whose scans were influenced by attenuation artifacts, or those who had small areas of ischemia or infarct, driving an intermediate event rate. Based on such data, equivocal scans should be considered mildly positive for purposes of clinical decision making, because the event rate is not as low as with patients who have a "normal" scan

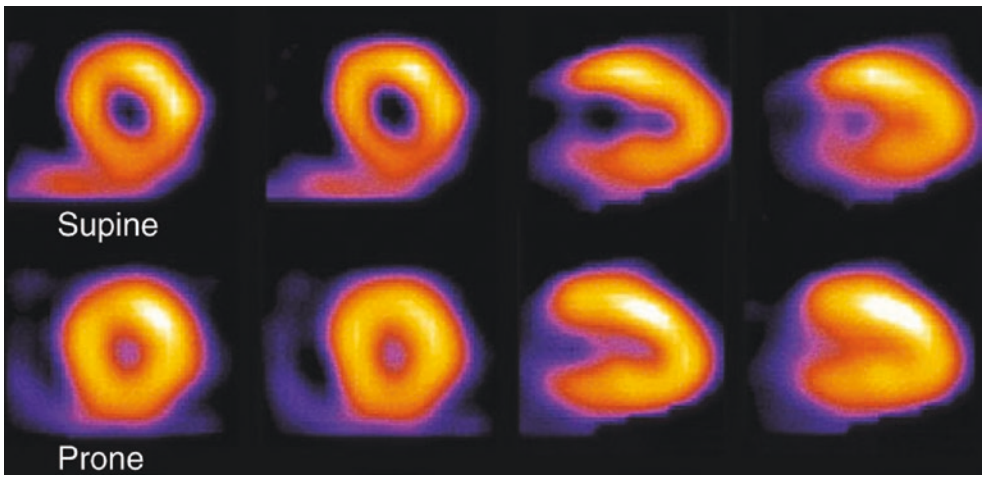

Fig. 12.6 Characterization of equivocal myocardial perfusion study results. Various strategies can be employed for clarification of equivocal studies. For instance, shown is a patient who presented to the ED with symptoms suspicious for ischemia but a nondiagnostic ECG. Initial supine resting ^{99m}Tc-sestamibi imaging (*top row*) demonstrated a possible inferobasal defect consistent with either acute ischemia in that territory or diaphragmatic attenuation artifact. Subsequently, imaging was performed in the prone position (*bottom row*). In the prone images, inferobasal myocardial perfusion appears normal, suggesting that the initial study represented diaphragmatic attenuation artifact and not ischemia. Other alternatives to clarify equivocal images include using attenuation correction algorithms in laboratories with the appropriate equipment and experience

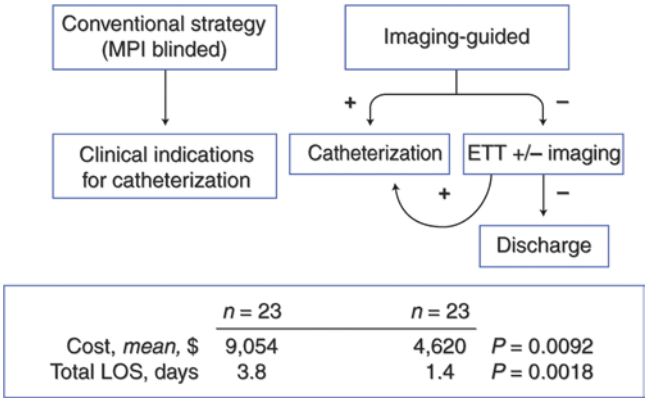

Fig. 12.7 MPI and the management of patients with nondiagnostic ECG changes. Although MPI has been shown in observational studies to have a very high negative predictive value for ruling out ACS (*see* Fig. 12.4), in none of those studies was the imaging information allowed to affect the management (i.e., the triage decision on whether to admit the patient to the hospital for observation or to discharge him or her directly home from the ED). To optimally assess the value of imaging (or any test) in this setting, a randomized trial is needed to compare the decisions made using imaging with those made with a strategy not incorporating imaging. In one such study, a small group of patients presenting to an ED with a suspected ischemic syndrome was randomized to an imaging-guided strategy or a conventional strategy (control) not incorporating imaging, with management guided by protocol. In the imaging-guided strategy, perfusion studies were reviewed and management was based on the results; in the control arm, imaging results were kept blinded. The study endpoints included length of hospital stay (LOS) and overall costs of care, with the hypothesis that both would be lower if imaging were used to guide decisions. Among patients randomized to the test arm, both LOS and costs were reduced by approximately 50% because fewer patients underwent catheterization. The results suggest that MPI could favorably affect management and lower costs in the setting of suspected ACS. This type of trial reflects "efficacy," in that decisions were driven by protocol and not solely by clinicians just being given the information [11]. ETT exercise tolerance testing

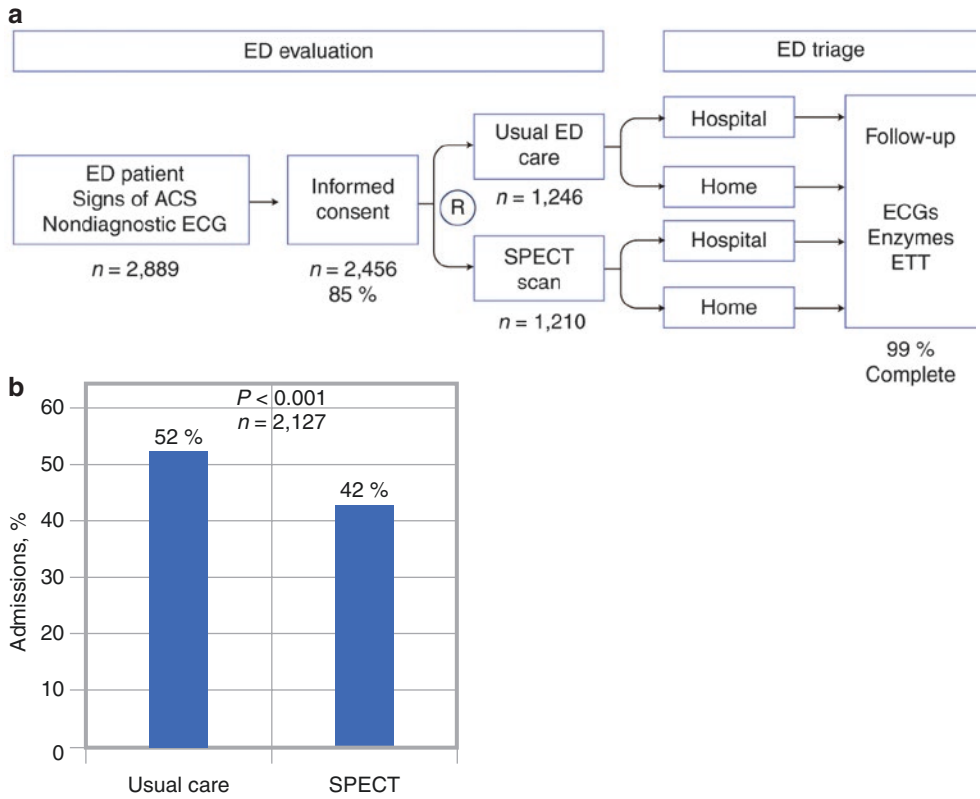

Fig. 12.8 Assessment of the role of myocardial perfusion imaging to improve clinical decision making for patients with chest pain who have nondiagnostic ECG changes. (**a**) In a large, prospective, randomized study, the ERASE (Emergency Room Assessment of Sestamibi for the Evaluation of Chest Pain) trial [12], investigators at seven sites enrolled 2456 patients with chest pain or other symptoms suggestive of acute cardiac ischemia and a normal or nondiagnostic initial ECG in the ED. Patients were randomly assigned to either the usual ED evaluation strategy or the usual strategy supplemented by results from acute resting ^{99m}Tc-sestamibi SPECT imaging. The physician incorporated the imaging information into the decision making either to admit the patient to the hospital for observation or to discharge him or her directly home from the ED; the management was not guided by protocol. The "correctness" of that decision was based on all follow-up information (available in 99% of patients at 1 month after presentation), so that the effect of incorporating the imaging information on clinical decision making could be assessed rigorously [12]. (**b**) For those patients ultimately determined not to have acute cardiac ischemia as the presenting syndrome, hospitalization was reduced from 52% with usual care to 42% with ^{99m}Tc-sestamibi imaging (odds ratio 0.68); i.e., imaging was associated with a 32% reduction in the odds of being admitted unnecessarily to the hospital for admission or observation. On 30-day follow-up, there were no differences in outcomes between the usual care group and the imaging group. This study demonstrated that the incorporation of ^{99m}Tc-sestamibi imaging into ED triage decision making provided a clear benefit in reducing unnecessary hospital admissions without inappropriately reducing admission for patients with acute ischemia [12]. In this study, clinical decisions were not mandated by protocol, so in part the trial was testing how well clinicians incorporated the imaging information to make better decisions. This type of trial is known as an "effectiveness" trial

Table 12.2 presents a summary of major clinical studies involving the relationship of myocardial perfusion imaging findings to endpoint events in patients with chest pain syndromes but nondiagnostic ECG. All published studies demonstrate a very high negative predictive value (NPV), suggesting that when such a patient has a normal resting perfusion study, the risk of myocardial infarction or ischemic event is relatively small.

Study	Number	Sensitivity, %	Specificity, %	NPV, %	Endpoint
Wackers et al. [1]	203	100	63	100	MI
Bilodeau et al. [13]	45	96	76	94	CAD (by angiography)
Varetto et al. [5]	64	100	67	100	MI
		100	92	100	CAD
Hilton et al. [6]	102	100	78	99	MI
		94	83	99	All events
Tatum et al. [7]	438	100	78	100	MI
		82	83	98	MI, revasc
Kontos et al. [14]	532	93	71	99	MI
		81	76	95	MI, revasc
Heller et al. [8]	357	90	60	99	MI
Duca et al. [15]	75	100	73	100	MI
		73	93	81	CAD
Kosnik et al. [16]	69	71	92	97	MI, revasc, or cardiac death
Kontos et al. [10]	620	92	67	99	MI
Udelson et al. [12]	1215	96	NR	99	MI
Schaeffer et al. [17]	479	77	92	99	MI

CAD coronary artery disease, *MI* myocardial infarction, *NPV* negative predictive value, *NR* not recorded, *PPV* positive predictive value, *revasc* revascularization by coronary artery bypass grafting or percutaneous transluminal coronary angioplasty

Table 12.2 Major clinical studies involving myocardial perfusion in acute chest pain and a nonischemic ECG

Multiple professional societies developed appropriate use criteria for imaging in ED patients, as listed on Table 12.3. The use of resting SPECT perfusion imaging was considered appropriate ("A") in those patients with an equivocal initial evaluation.

Indication	Appropriate use indicator
Diagnostic ECG for ST-elevation myocardial infarction (STEMI)	R
Initial history/physical examination and/or chest radiograph identifies a likely noncardiac diagnosis (pneumothorax, costochondritis, lesion of the esophagus)	R
Positive initial diagnosis of NSTEMI/ACS	
Initial ECG and/or biomarker analysis unequivocally positive for ischemia	R
Equivocal initial diagnosis of NSTEMI/ACS	
Equivocal initial troponin or single troponin elevation without additional evidence of ACS	A
Ischemic symptoms resolved hours before testing	M
Low/intermediate likelihood initial diagnosis of NSTEMI/ACS	
TIMI risk score = 0; early high-sensitivity troponin negative	R
Normal or nonischemic on initial ECG, normal initial troponin	M

A appropriate, *M* may be appropriate, *R* rarely appropriate, *TIMI* Thrombolysis in Myocardial Infarction

Table 12.3 Appropriateness criteria for cardiac radionuclide imaging in patients with acute symptoms and suspicion of ACS (urgent presentation)

Echocardiography in the Evaluation of Suspected ACS

Echocardiography is valuable for the diagnosis of ACS in ED patients with chest pain, as it can detect impaired contractility during an episode of regional ischemia (Fig. 12.9). A caveat for the use of resting echocardiography for this purpose is that wall motion abnormalities resolve rapidly with normalization of blood flow and resolution of ischemia. Thus, imaging needs to be performed during ongoing symptoms (chest pain) to optimize performance characteristics. After serial biomarkers exclude a troponin-positive ACS, stress echocardiographic imaging may be performed in the ED for diagnosis and risk stratification of possible underlying coronary artery disease (CAD) (Fig. 12.10).

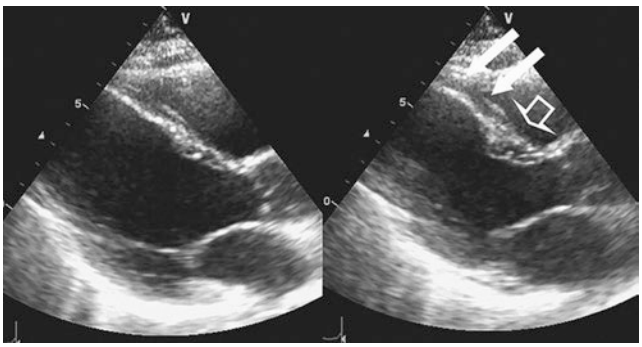

Fig. 12.9 Echocardiography shows a typical wall motion abnormality in the left anterior descending artery perfusion territory due to an anterior myocardial infarction. *Left*, diastole; *right*, systole. The *long arrows* point to the dyskinetic mid-anteroseptal wall; the *shorter arrow* points to the basal anteroseptal wall, which has preserved contractility [19]

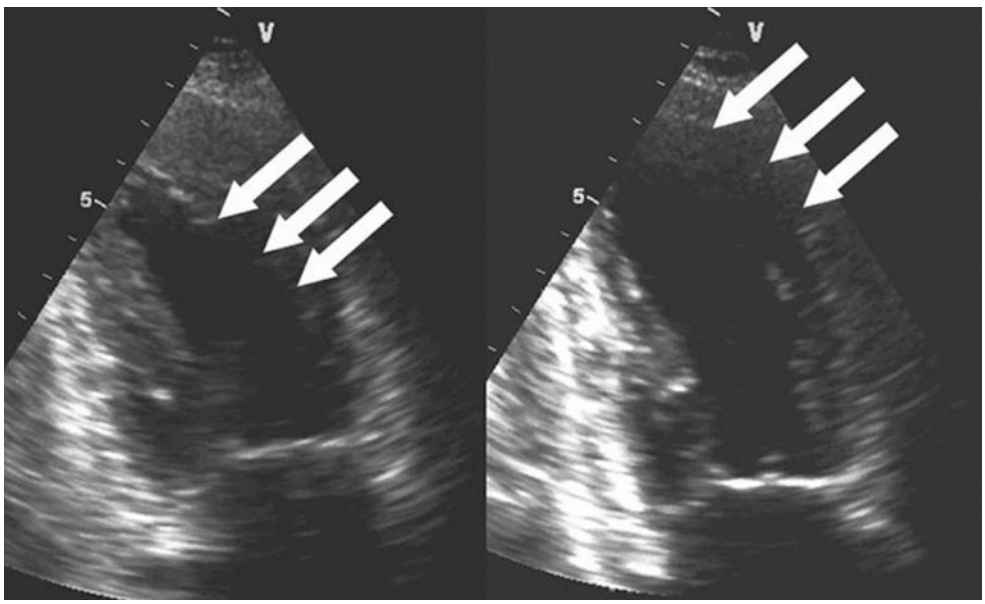

Fig. 12.10 Stress echocardiography demonstrates inducible anterior ischemia in this patient with multivessel coronary artery disease (CAD) including a severe stenosis of the left anterior descending. *Left*, baseline two-chamber view at end systole. *Right*, peak dobutamine stress two-chamber view at end systole. Note the increase in the apical left ventricular cavity due to severely reduced contraction of the anterior wall (*arrows*) [19]

Several studies (Table 12.4) have demonstrated that dobutamine stress echocardiography has a generally excellent negative predictive value for obstructive CAD in patients presenting to the ED with chest pain. Multiple professional societies have published appropriate criteria for the use of rest transthoracic echocardiography (TTE) in patients with suspected myocardial ischemia/infarction (MI) in the ED (Table 12.5) and for the use of stress echocardiography in ED patients with chest pain (Table 12.6).

Studies	Patients, *n*	Follow-up, *mo*	Positive test, *n*	ACE with positive test, *n*	PPV,%	Negative test, *n*	ACE with negative test, *n*	NPV, %
Geleijnse et al. [21]	80	6	36	0 Death	53	44	0 Death	89
				0 MI			1 MI	
				9 UA			1 UA	
Bholasingh et al. [22]	377	6	26	1 Death	30	351	1 Death	96
				2 MI			0 MI	
				2 UA			6 UA	
				3 Revasc			7 Revasc	
Nucifora et al. [23]	107	2	20	0 Death	5	87	0 Death	100
				0 MI			4 MI	
				1 Revasc			4 Revasc	
Trippi et al. [24]	137	3	7	1 MI	29	130	0 Death	98
				1 UA			0 MI	
							0 Revasc	

ACE adverse cardiac event, *MI* myocardial infarction, *NPV* negative predictive value, *PPV* positive predictive value, *Revasc* revascularizations, *UA* unstable angina

Table 12.4 Predictive accuracy of dobutamine stress echocardiography in patients presenting to the ED with chest pain

Indication	Appropriate use indicator
Diagnostic ECG for ST-elevation myocardial infarction	R
Initial history/physical examination and/or chest radiograph identifies a likely noncardiac diagnosis (pneumothorax, costochondritis, lesion of the esophagus)	R
Positive initial diagnosis of NSTEMI/ACS	
Initial ECG and/or biomarker analysis unequivocally positive for ischemia	R
Equivocal initial diagnosis of NSTEMI/ACS	
Equivocal initial troponin or single troponin elevation without additional evidence of ACS	M
Ischemic symptoms resolved hours before testing	R
Low/intermediate likelihood initial diagnosis of NSTEMI/ACS	
TIMI risk score = 0, early high-sensitivity troponin negative	R
Normal or nonischemic on initial ECG, normal initial troponin	R

A appropriate, *M* may be appropriate, *R* rarely appropriate, *TIMI* Thrombolysis in Myocardial Infarction
[a]Use of rest TTE in patients with suspected myocardial ischemia/infarction (MI) in ED patients with chest pain

Table 12.5 Appropriateness criteria for *rest* transthoracic echocardiography (TTE)[a]

Indication	Appropriate use indicator
Diagnosis unequivocally positive for NSTEMI/ACS	M
Serial ECG and troponins negative for NSTEMI/ACS	A
Serial ECG or troponins borderline for NSTEMI/ACS	A
ECG: ST elevation	R

A appropriate, *M* may be appropriate, *R* rarely appropriate

Table 12.6 Appropriateness criteria for *stress* echocardiography for evaluation of acute chest pain in ED patients

Cardiac CT Imaging in the Evaluation of Suspected ACS

Another imaging modality that can be valuable in the diagnosis of ACS in patients presenting to the ED with chest pain is coronary CT angiography (CTA) (Figs. 12.11, 12.12 and 12.13). In three recent, multicenter, randomized clinical trials of patients presenting to the ED with suspected ACS, a coronary CT angiography–based strategy for initial evaluation was tested. In the CT-STAT (Coronary Computed Tomographic Angiography for Systematic Triage of Acute Chest Pain Patients to Treatment) trial [26] of acute, low-risk chest pain, 361 patients had CTA and 338 patients had MPI as the index noninvasive test. The use of coronary CTA resulted in a 54% reduction in time to diagnosis compared with MPI (median 2.9 hours *vs*. 6.3 hours, $P < 0.0001$) and lower costs of care (median \$2137 *vs*. \$3458, $P < 0.0001$). The diagnostic strategies had no difference in major adverse cardiac events after normal index testing (0.8% in the coronary CTA arm *vs*. 0.4% in the MPI arm, $P = 0.29$), in a population in whom the prevalence of ACS was very low. In the study by Litt et al. [27], 1370 patients of low to intermediate risk presenting with possible ACS were assigned to undergo coronary CTA (908 patients) or to receive traditional care (462 patients). The primary endpoint was safety, defined as the NPV for events (myocardial infarction or cardiac death within 30 days) for patients with no obstructive CAD on CT angiography. The upper boundary of the 95% confidence interval was less than 1%, as hypothesized. Secondary endpoints involved the effect of CTA information on triage. Compared with the patients receiving traditional care, the patients in the coronary CTA group had a higher rate of discharge from the ED (49.6% *vs*. 22.7%; difference, 26.8%; 95% CI, 21.4–32.2), a shorter length of stay (median, 18.0 hours *vs*. 24.8 hours; $P < 0.001$), and a higher rate of detection of coronary disease (9.0% *vs*. 3.5%; difference, 5.6%; 95% CI, 0–11.2). In the ROMICAT-II (Multicenter Study to Rule Out Myocardial Infarction by Cardiac Computed Tomography) trial [28], 1000 patients were randomized, 501 to coronary CTA and 499 to a standard ED evaluation; the primary endpoint was the effectiveness of the CTA information to improve triage decision making. After early coronary CTA, the mean length of stay was reduced by 7.6 hours ($P < 0.001$), and more patients were discharged directly from the ED (47% *vs*. 12%; $P < 0.001$). There were no cases of missed ACS and no significant differences in 28-day major adverse cardiac events. After coronary CTA, there was more downstream testing, including left heart catheterization, and higher radiation exposure. The cumulative mean cost of care was similar (coronary CTA arm: \$4289 *vs*. standard ED evaluation: \$4060; $P = 0.65$).

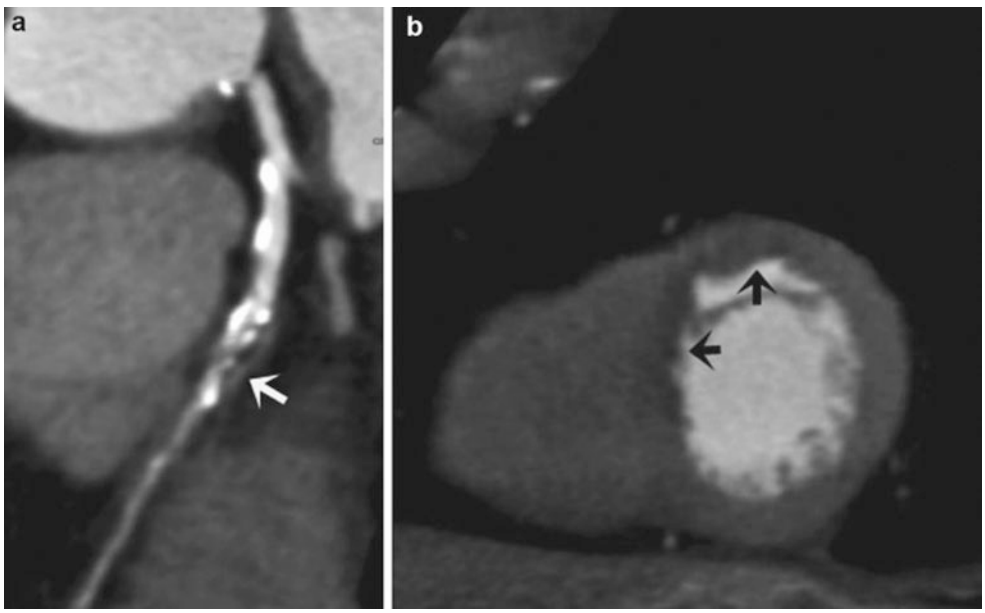

Fig. 12.11 (**a**) In 69-year-old man with chest pain, negative initial cardiac biomarkers, and a nondiagnostic echocardiogram, coronary CT angiography (CTA) demonstrated a mixed plaque with calcified and noncalcified components in a high-grade stenosis (>70%) in the mid-left anterior descending coronary artery (*arrow*). (**b**) A rest perfusion image demonstrates a perfusion defect in the anterior and anteroseptal walls (*black arrows*), which is consistent with ischemia in the distribution of the left anterior descending coronary artery. Subsequent cardiac biomarkers were elevated. (*From* Cury et al. [25], with permission from Springer Nature)

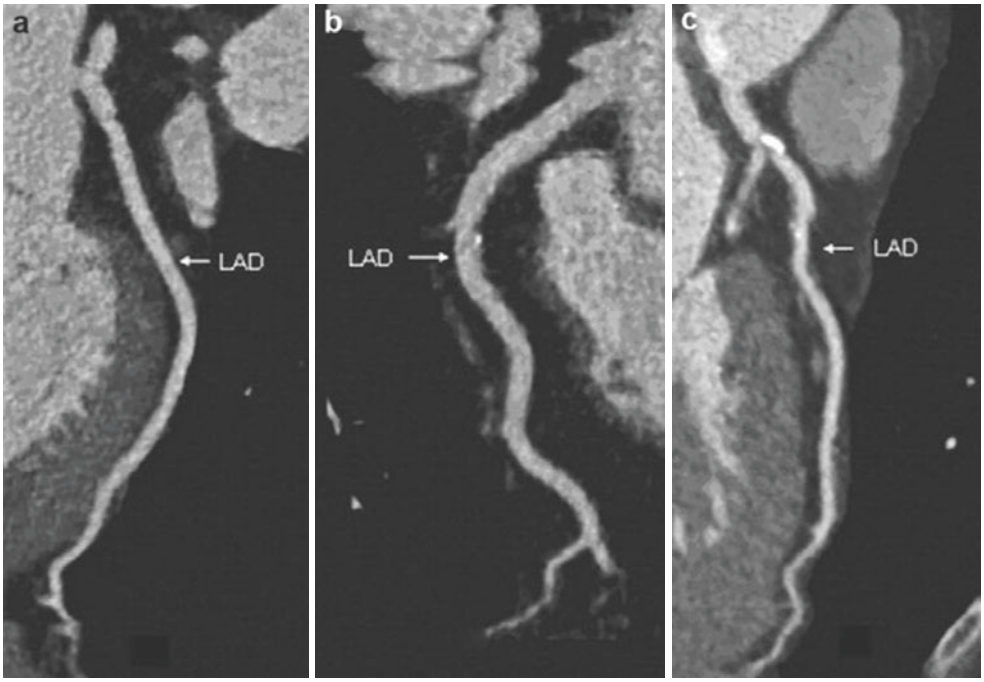

Fig. 12.12 This figure shows coronary CTA images from three patients: a 47-year-old man with substernal chest pain and dyspnea with normal coronary arteries (*arrow*) (**a**), a 58-year-old man with accelerating chest discomfort with mild coronary disease (*arrow*) (**b**), and a 60-year-old woman with progressive dyspnea and atypical chest discomfort with significant mixed plaque (*arrow*) (**c**) [26]. LAD left anterior descending artery

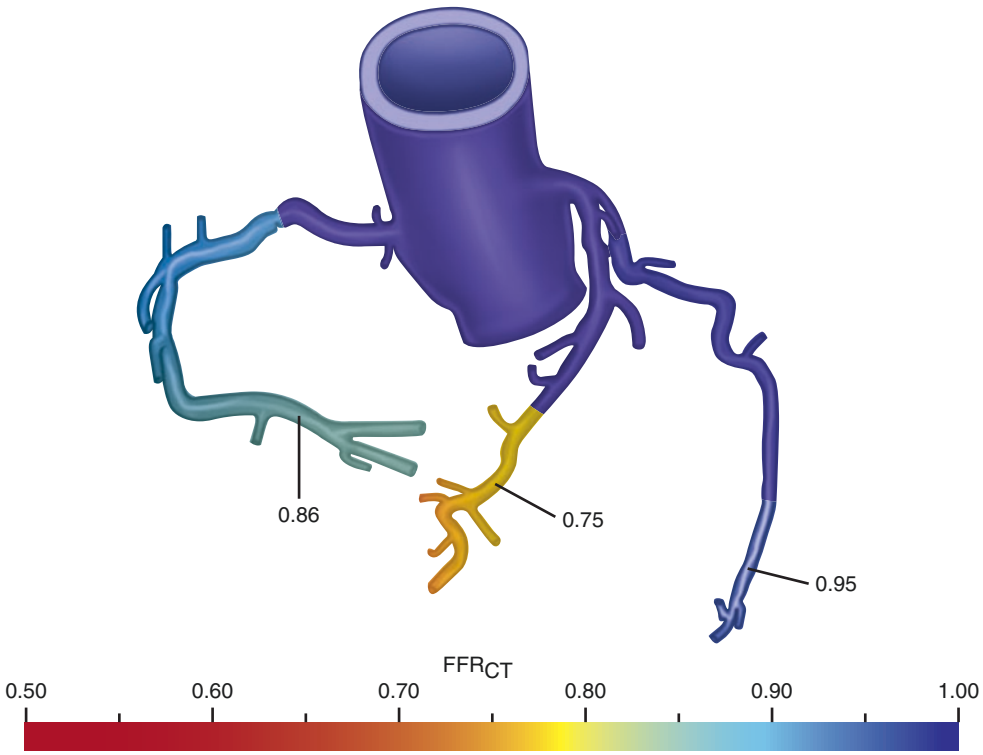

Fig. 12.13 This diagram represents the coronary circulation and specific fractional flow reserve (FFR) values derived from coronary CTA for the involved vessels [30]. An FFR value less than 0.8 is considered significant and flow-limiting

Thus, in ED patients with symptoms suggestive of ACS, a strategy based on coronary CTA improves the efficiency of clinical decision making, as compared with a standard ED evaluation, and may allow the safe, expedited discharge from the ED of many patients who would otherwise be admitted. A recent metanalysis [29] including 1869 patients from four randomized, controlled trials comparing CTA versus usual care in the ED [31] showed no significant difference in the incidence of myocardial infarction, post-discharge ED visits, or rehospitalizations. Moreover, there were no deaths. All studies reported decreased length of stay with CTA and 3 out of 4 reported significant cost savings. Importantly, 8.4% of the CTA patients underwent invasive coronary angiography versus 6.3% of those receiving usual care (OR, 1.36; 95% CI, 1.03–1.80; $p = 0.03$). Similarly, 4.6% of patients undergoing CTA, *vs.* 2.6% of those receiving usual care underwent coronary revascularization (OR, 1.81; 95% CI, 1.20–2.72; $p = 0.004$).

In conclusion, current available data show that compared with usual care, the use of CTA in the ED is associated with decreased ED cost and length of stay but increased invasive angiograms and revascularization. This latter finding is likely due to clinicians acting on the anatomic data alone.

Recently the addition of computer-derived fractional flow reserve (FFR) to CTA interpretation has allowed functional information to be incorporated with the anatomic characterization of the coronary circulation (Fig. 12.13). Briefly, FFRCT is a computational fluid dynamic modeling technique that can be applied to the resting CTA dataset to estimate lesion-specific functional characteristics of a stenotic region. FFRCT has demonstrated high diagnostic performance when compared against invasive fractional flow reserve as a reference standard. In a validation study comparing FFRCT against invasive fractional flow reserve in 251 patients with CTA stenosis 30–90%, FFRCT yielded 81% accuracy and 79% specificity. More importantly, FFRCT correctly reclassified 68% of false positive patients as true negatives, highlighting the potential role of FFRCT as a gatekeeper to invasive coronary angiography [30]. The role of FFRCT in the ED is yet to be shown. Currently several ongoing clinical trials are evaluating the efficacy, safety, and cost effectiveness of this particular modality in patients presenting to the ED with chest pain.

Table 12.7 summarizes several studies validating the use of CTA in detecting ACS, and Table 12.8 lists the professional societies' criteria for the appropriate use of cardiac CT in patients with acute symptoms who are suspected of having ACS.

Study	Scanner type	ACS prevalence	*N*	Stenosis, %	Sensitivity, %	Specificity, %	PPV, %	NPV, %
Sato et al. [31]	16-slice CT	Intermediate (71%)	31	>75	95	89	95	89
White et al. [32]	16-slice CT	Low to intermediate (21%)	69	>50	87	96	87	96
Hoffmann et al. [33]	64-slice CT	Low (14%)	103	>50	100	82	47	100
Gallagher et al. [34]	64-slice CT	Low (8%)	85	>50 or Ca >400	86	92	50	99
Rubinshtein et al. [35]	64-slice CT	Intermediate (34%)	58	>50	100	92	87	100
Goldstein et al. [36][a]	64-slice CT	Low (8%)	99	>25	100	74	25	100
Hoffmann et al. [37]	64-slice CT and DSCT	Low (8%)	368	>50	77	87	35	98
Hollander et al. [38][b]	64-slice CT and DSCT	Very low (3%)	562	>50	100	93	33	100
Total[c]			1375	25–75	92	89	48	99

DSCT dual-source CT, *NPV* negative predictive value, *PPV* positive predictive value, *SOC* standard of care

[a]In the study by Hollander et al. [38], 18 of 54 patients who had stenosis greater than 50% by coronary CTA were considered to have ACS, as they had either a positive stress test or a positive cardiac catheterization

[b]Pooled sensitivity, specificity, PPV, and NPV analyses were calculated combining the eight above studies

[c]In the study by Goldstein et al. [36], 24 patients with intermediate stenosis (25–70%) or nondiagnostic results were considered positive by multidetector CT, as they needed further workup and could not be discharged from the ED based only on the cardiac CT results

Table 12.7 Summary of studies validating coronary CTA to Detect ACS in the ED

Indication	Appropriate use indicator
Diagnostic ECG for ST elevation myocardial infarction	R
Initial history/physical examination and/or chest radiograph identifies a likely noncardiac diagnosis (pneumothorax, costochondritis, lesion of the esophagus)	R
Positive initial diagnosis of NSTEMI/ACS	
Initial ECG and/or biomarker analysis unequivocally positive for ischemia	R
Equivocal initial diagnosis of NSTEMI/ACS	
Equivocal initial troponin or single troponin elevation without additional evidence of ACS	A
Ischemic symptoms resolved hours before testing	A
Low/intermediate likelihood initial diagnosis of NSTEMI/ACS	
TIMI risk score = 0, early high-sensitivity troponin negative	A
Normal or nonischemic on initial ECG, normal initial troponin	A

A appropriate, *R* rarely appropriate, *TIMI* Thrombolysis in Myocardial Infarction

Table 12.8 Appropriateness Criteria for Cardiac CT in Patients with Acute Symptoms and Suspicion of ACS (Urgent Presentation)

Cardiac MRI in the Evaluation of Suspected ACS

Rest cardiac MRI (CMR) can evaluate regional and global ventricular function and myocardial perfusion, and can identify scar in patients presenting to the ED with chest pain if they are sufficiently stable to undergo this relatively lengthy imaging study (Figs. 12.14 and 12.15). In patients in whom ACS has been ruled out with biomarkers, a stress CMR perfusion or wall motion study can identify underlying CAD and ischemia (Figs. 12.16 and 12.17).

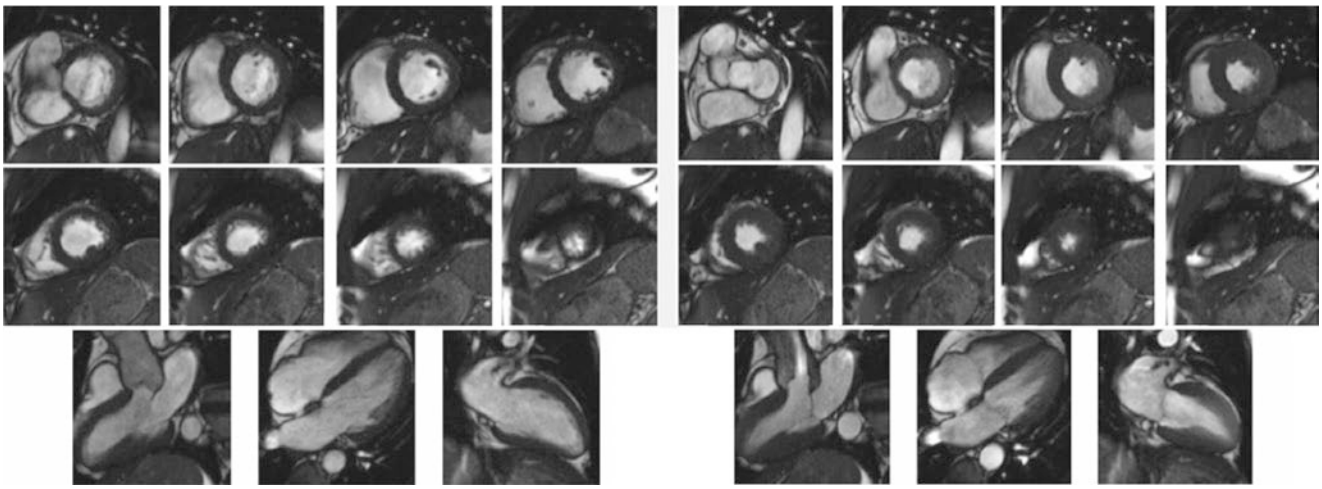

Fig. 12.14 Diastolic (*left*) and systolic (*right*) frames from cardiac MR cine images of a patient presenting to the ED with chest pain. Cine images provide an accurate and reliable assessment of wall motion. A new wall motion abnormality suggests an ACS. Conversely, a wall motion abnormality with accompanying wall thinning usually suggests an old myocardial infarction. Cine MRI may reveal nonischemic cardiac causes or noncardiac causes of chest pain. It is almost always done in conjunction with other techniques. In this case, there is no wall motion abnormality to suggest an ACS. Increased flow velocity is noted at the aortic valve, suggesting an abnormality with the valve; a bicuspid aortic valve was visualized in this patient on dedicated imaging. (*Courtesy of* Duke Cardiovascular Magnetic Resonance Center)

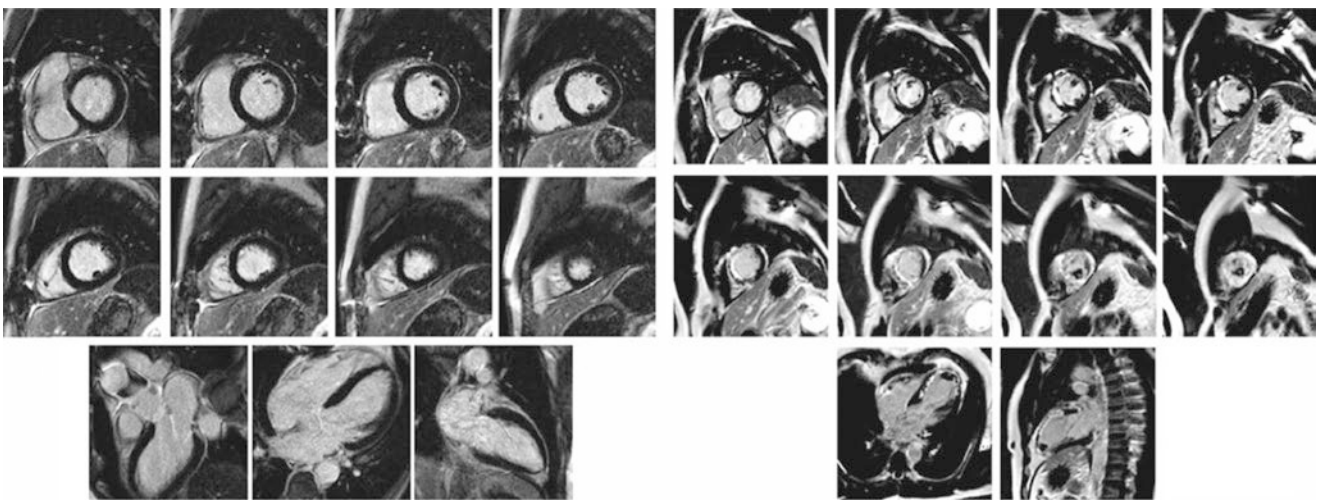

Fig. 12.15 Delayed-enhancement (DE) images from patients presenting to the ED with chest pain. DE images demonstrate viable *vs*. nonviable myocardium, with gadolinium "enhancement" in regions with expanded extracellular space, such as evolving or remote infarcts. Images are obtained approximately 10 minutes after administration of intravenous gadolinium contrast. Myocardial infarction (MI) or scarring is visualized as bright areas in the myocardium ("Bright is dead"). These examples show a patient without MI (*left*) and a patient with a large MI in the distribution of the left anterior descending coronary artery (*right*). Note the excellent visualization of the presence and extent of the MI on the *right*. Also note the presence of an apical thrombus. (*Courtesy of* Duke Cardiovascular Magnetic Resonance Center)

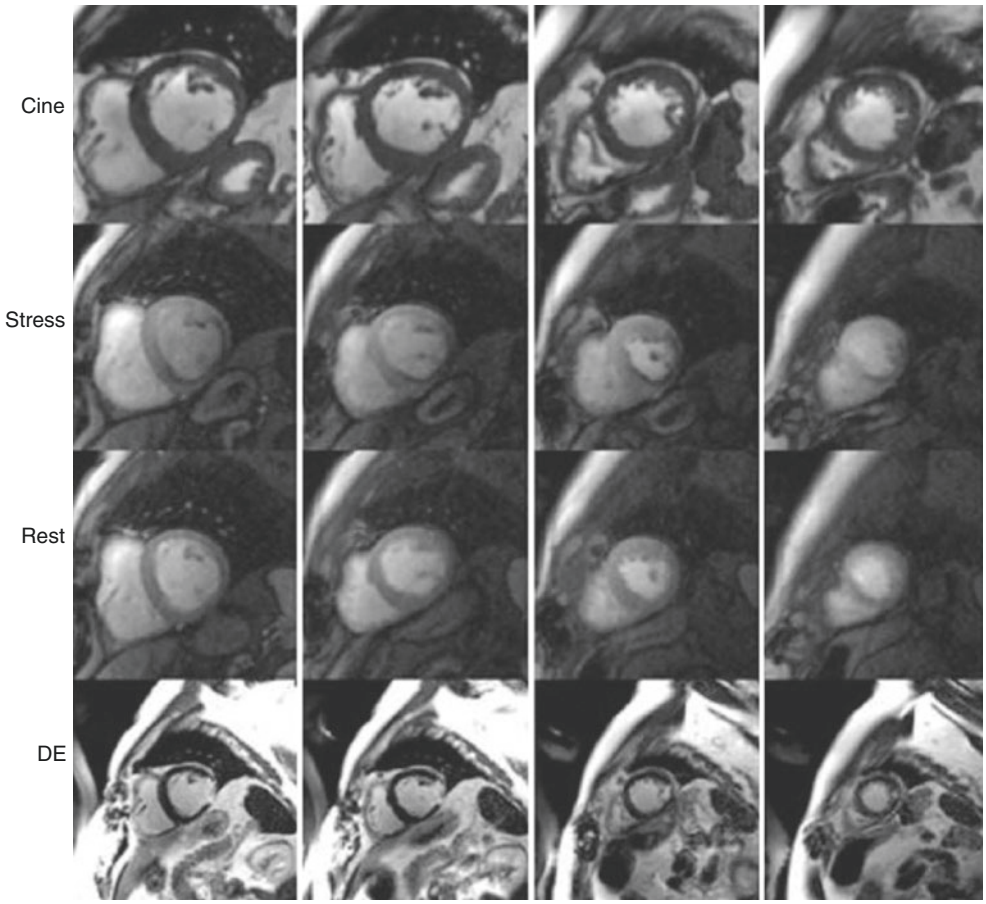

Fig. 12.16 Images from an adenosine stress cardiac magnetic resonance (CMR) study in a patient presenting to the ED with chest pain. Stress images demonstrate inferior and inferolateral perfusion defects, which are larger than the infarcted areas seen on delayed enhancement (DE)-CMR, suggesting the presence of ischemia in addition to myocardial infarction. Note the absence of perfusion defects on the rest perfusion images, which demonstrates that the perfusion defects are not artifacts and reflect ischemia. (*Courtesy of* Duke Cardiovascular Magnetic Resonance Center)

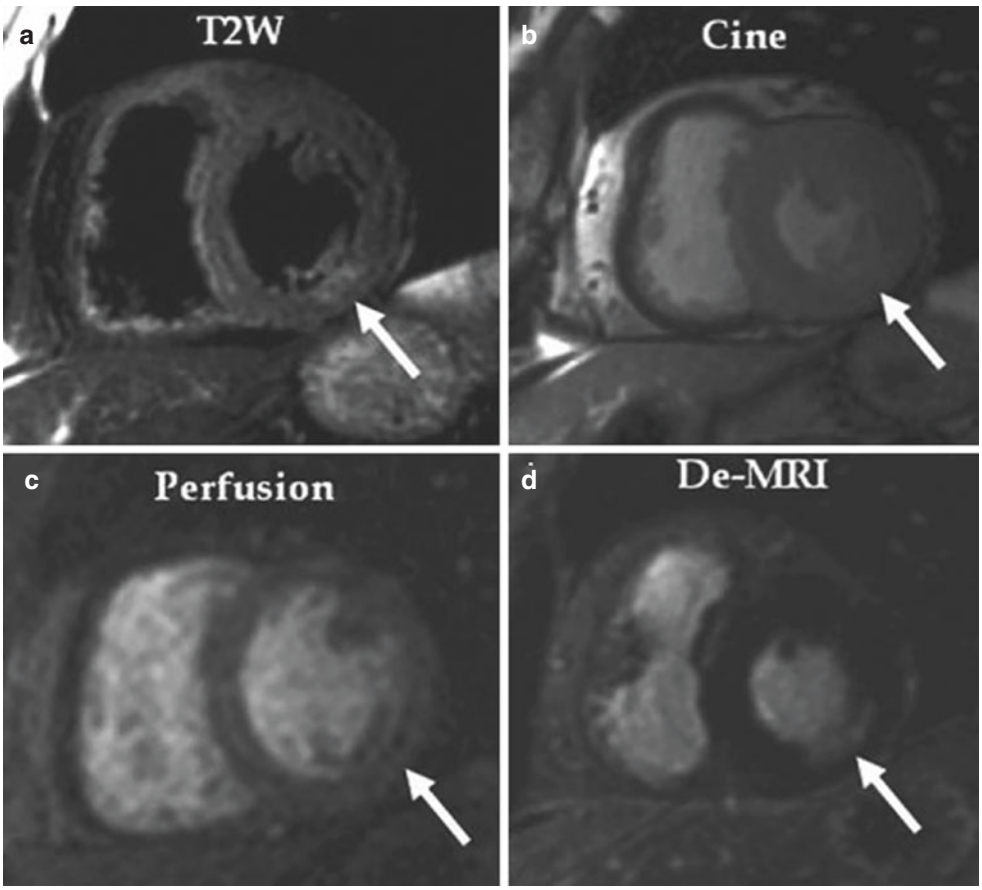

Fig. 12.17 T2-weighted MR imaging of a patient presenting to the ED with chest pain and initial normal cardiac biomarkers. T2-weighted (T2W) imaging revealed a small area of T2 hyperintensity (**a**) in the inferolateral wall (suggesting myocardial edema) with associated subtle hypokinesis (**b**), a resting perfusion defect (**c**), and delayed hyperenhancement (**d**, myocardial necrosis) in the same area (*arrows*). The troponin level was elevated 7 hours after CMR. An invasive angiogram revealed triple-vessel disease with a 95% stenosis in the posterolateral branch [41]

Studies published in 2010 [39] and 2011 [40] examined the cost-effectiveness of a strategy employing stress CMR for patients with chest pain presenting to the ED (Fig. 12.18) and concluded that costs of the treating the CMR group were reduced both during the initial hospitalization and during the year following discharge.

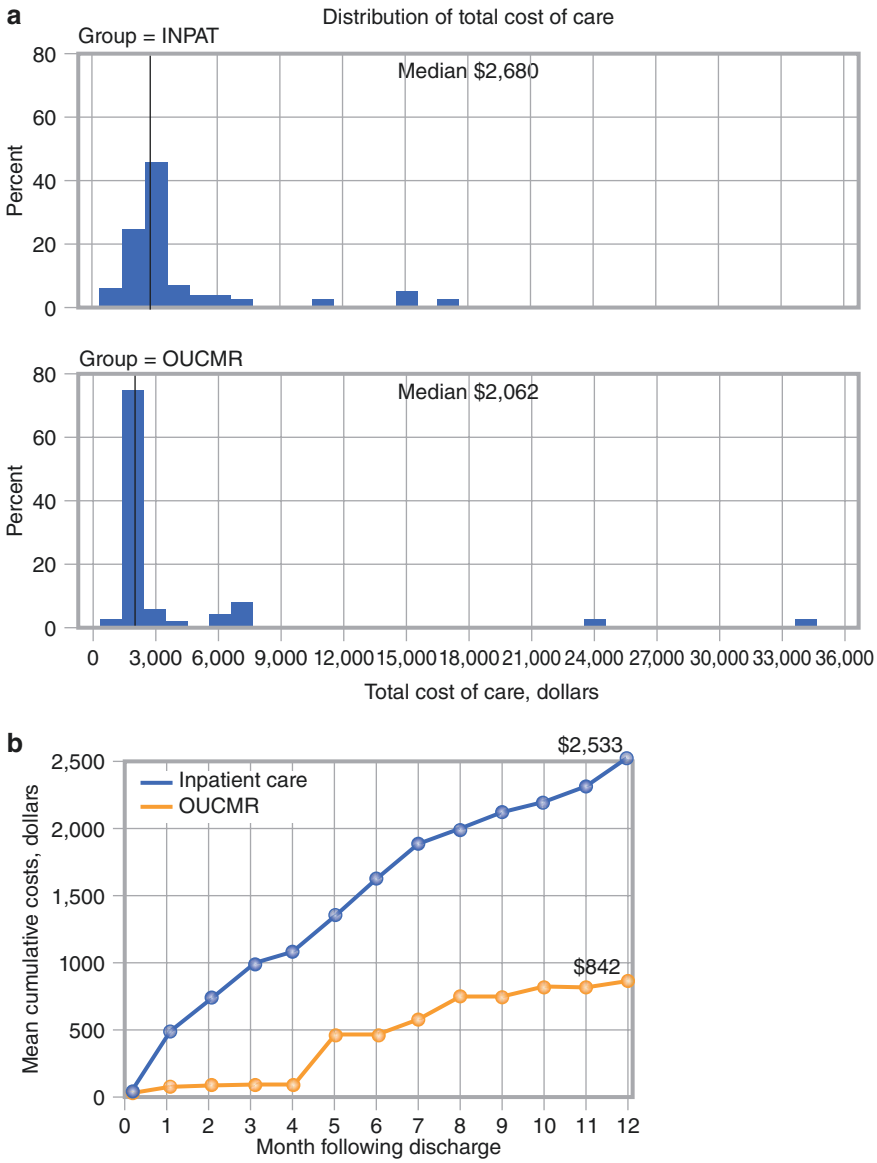

Fig. 12.18 Cost-effectiveness of a strategy employing stress CMR for patients with chest pain presenting to the ED. In a randomized trial of 109 patients with non–low-risk chest pain who would normally be managed with an inpatient care strategy, an observation-unit strategy was used, involving stress CMR; median index hospitalization cost was reduced without any cases of missed ACS. (**a**) Distributions of median index hospitalization costs for study participants in the inpatient care group (INPAT, $n = 57$) and the observation unit–stress CMR (OUCMR) group ($n = 53$) are shown [39]. (**b**) Cost accumulation by month following discharge among the study groups, excluding the index hospital visit cost, demonstrates that the OUCMR strategy reduced cardiac-related costs of medical care over the first year subsequent to discharge, without an observed increase in major cardiac events. Mean cumulative cost by study group after hospital discharge (y-axis) is displayed by month of follow-up (x-axis). Mean cumulative cost for a month is calculated as the sum of the costs across all patients up to and including that month divided by the number of patients. OUCMR participants had lower cost of care in the year after discharge from the index hospital visit ($P = 0.012$). Reduced cost was the result of fewer cardiac-related ED visits and cardiac-related hospitalizations, suggesting that an OUCMR strategy influences care utilization after discharge [40]

Table 12.9 lists the professional societies' criteria for the appropriate use of CMR in ED patients with acute symptoms who are suspected of having ACS.

Indication	Appropriate use indicator
Diagnostic ECG for ST elevation myocardial infarction	R
Initial history/physical examination and/or chest radiograph identifies a likely noncardiac diagnosis (pneumothorax, costochondritis, lesion of the esophagus)	R
Positive initial diagnosis of NSTEMI/ACS	
Initial ECG and/or biomarker analysis unequivocally positive for ischemia	R
Equivocal initial diagnosis of NSTEMI/ACS	
Equivocal initial troponin or single troponin elevation without additional evidence of ACS	M
Ischemic symptoms resolved hours before testing	M
Low/intermediate likelihood initial diagnosis of NSTEMI/ACS	
TIMI risk score = 0, early high-sensitivity troponin negative	R
Normal or nonischemic on initial ECG, normal initial troponin	R

M may be appropriate, *R* rarely appropriate, *TIMI* Thrombolysis in Myocardial Infarction

Table 12.9 Appropriateness criteria for cardiac MR in patients with acute symptoms and suspicion of ACS (urgent presentation)

Imaging of Myocardial Salvage in Patients with Acute Myocardial Infarction

Cardiovascular imaging modalities have long been used to assess infarct size, but some of the techniques also can be deployed to assess the "area at risk," the portion of the left ventricle myocardium that is at risk of infarct if reperfusion does not occur and the entirety of the "risk area" distal to the coronary occlusion becomes infarcted. The difference between the area at risk and the final infarct size after reperfusion therapy is referred to as "salvaged" myocardium (Figs. 12.19, 12.20, and 12.21).

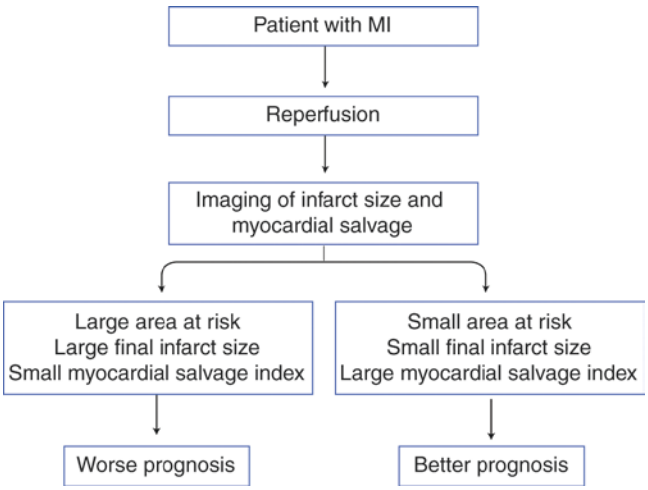

Fig. 12.19 Role of cardiovascular imaging in the assessment of the area at risk in patients with myocardial infarction (MI) and the myocardial salvage index, the proportion of area at risk that is salvaged by treatment. A small myocardial salvage index indicates a worse prognosis, and a large myocardial salvage index indicates a better prognosis

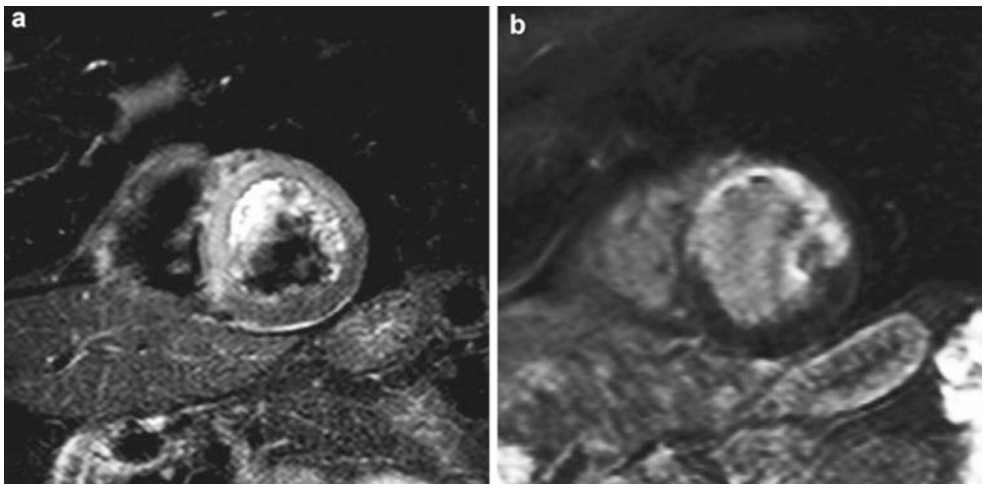

Fig. 12.20 T2-weighted CMR performed early after successful MI reperfusion is useful to retrospectively quantify the myocardium at risk and the salvaged myocardium. This example shows a T2-weighted image (**a**) and delayed enhancement (DE)-CMR image (**b**) from a 77-year-old man with an extensive anteroseptal acute MI. On short-axis T2-weighted CMR, the area at risk is visible as a hyperintense (i.e., bright gray) area and is slightly larger than the infarct area visible on DE-CMR (i.e., 29.7% *vs*. 26.2%). Thus, the degree of salvage is small. (*From* Wright et al. [42], with permission from Elsevier)

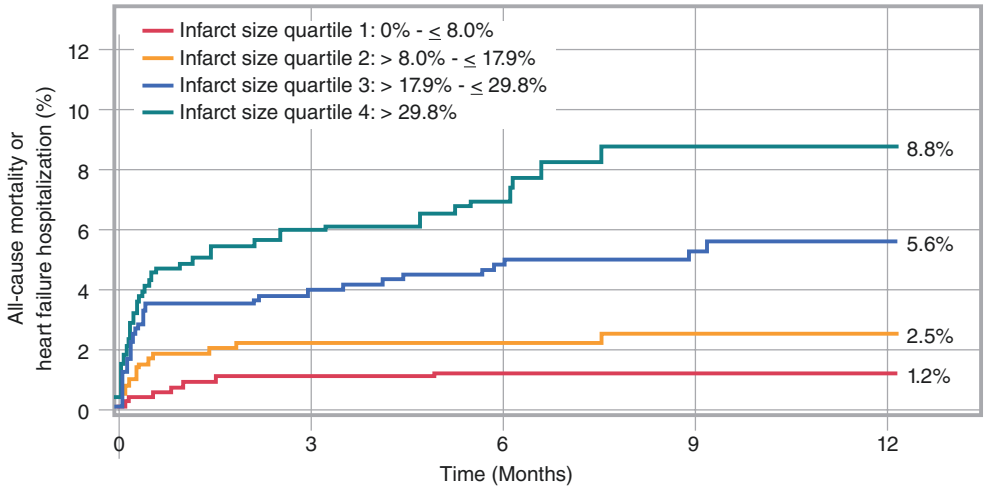

Fig. 12.21 By rapidly restoring coronary artery patency in ST-elevation MI (STEMI), reperfusion therapy reduces infarct size (IS) and mortality. The association between infarct size and subsequent all-cause mortality and/or hospitalization for heart failure (HF) was studied by patient-level pooled analysis from 10 randomized trials of primary percutaneous coronary intervention (PCI) in STEMI. Infarct size was measured by CMR or technetium-99 m sestamibi SPECT within 1 month after primary PCI. The median infarct size (% of left ventricular myocardial mass) was 17.9% (25th percentile, 8.0%; 75th percentile, 29.8%). The Kaplan-Meier estimated 1-year rates were 2.2% (54 events) for all-cause mortality, 2.5% (60 events) for reinfarction, and 2.6% (58 events) for HF hospitalization after study entry. By multivariable analysis, IS was a strong independent predictor of all-cause mortality, HF hospitalization, and the composite occurrence of all-cause mortality or HF hospitalization (as shown in this figure), but not for reinfarction. After adjustment for baseline covariates, every 5% increase in IS was independently associated with a 19% increase in 1-year all-cause mortality. Moreover, every 5% increase in IS contributed to a 20% increase in the relative hazard for all-cause mortality or hospitalization for HF within 1 year after primary PCI. (*From* Stone et al. [43]; with permission from Elsevier)

Role of Radionuclide Imaging Following an ACS

Figures 12.22, 12.23, 12.24, 12.25, 12.26, 12.27, 12.28 and 12.29 illustrate the role of imaging in decisions about treatment strategies. In clinical trials of unstable angina, up to 30% of some populations of patients have been found to have normal or near-normal coronary arteries after routine catheterization. In patients not at clinical high risk, MPI will allow more optimal selection for catheterization based on the risk-stratification information inherent in the image results.

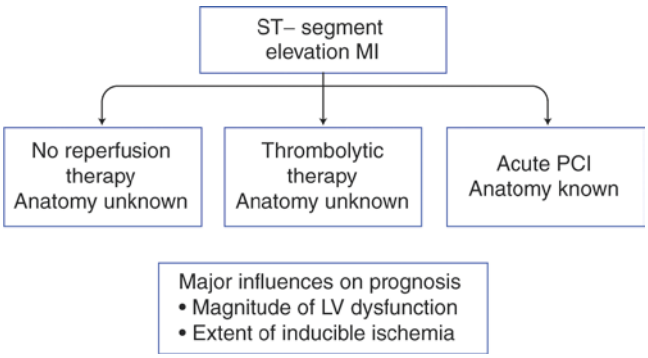

Fig. 12.22 Therapeutic pathways for patients with ST-segment elevation myocardial infarction (MI). In the contemporary therapeutic era, patients with acute ST-segment elevation MI (STEMI) may be classified by the initial treatment strategy to assess the potential application of imaging modalities to subsequent management strategy. Based on numerous factors, some patients may receive no initial reperfusion therapy and may not have initial catheterization data; therefore, their anatomy will be unknown. Others may be treated with thrombolytic therapy and not sent to the catheterization laboratory, and a third group may be managed with primary percutaneous coronary intervention (PCI) of the infarct-related vessel, and full coronary anatomic information will be at hand. For all groups, however, post-MI prognosis is predicted by the magnitude of residual left ventricular (LV) dysfunction and the presence and magnitude of inducible ischemia. An imaging study in the post-MI setting can assess these variables, which in turn may allow classification and risk stratification of patients regarding potential long-term post-MI outcomes, information that readily translates into clinical management strategies. Thus, imaging techniques can provide data that can be used specifically to direct patient management

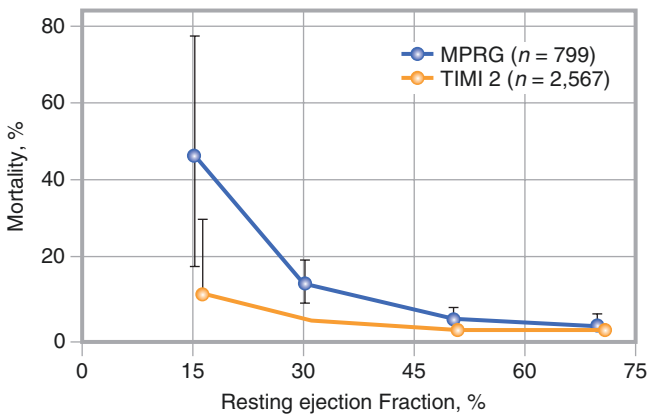

Fig. 12.23 Relation of post-MI cardiovascular mortality to the resting ejection fraction in the pre- and post-thrombolytic era. Data from the pre-thrombolytic MPRG (Multicenter Post-Infarction Research Group) and the post-thrombolytic TIMI 2 (Thrombolysis in Myocardial Infarction Phase 2) trials demonstrate that as the magnitude of left ventricular dysfunction increases, the late post-MI mortality increases. At any given ejection fraction, the mortality is lower in patients receiving thrombolytic reperfusion therapy, but a relation between ejection fraction and survival remains evident in the thrombolytic era [44]

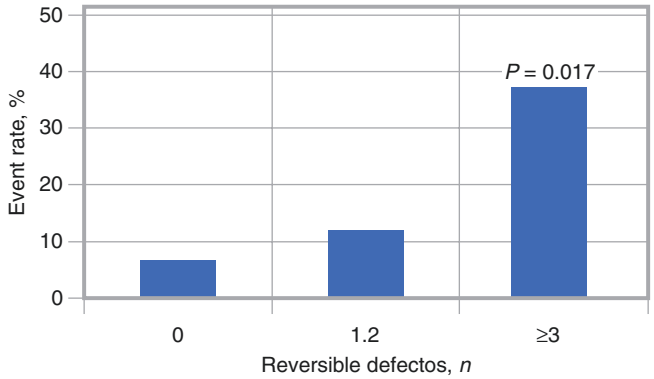

Fig. 12.24 Relation between the post-MI extent of inducible ischemia and the cardiac event rate. Patients with more extensive ischemia (documented as the number of reversible perfusion defects on ^{99m}Tc-sestamibi imaging) are at a progressively higher risk of an unfavorable outcome during late post-MI follow-up. These data, confirming the value of knowledge of the extent of ischemia in patients after MI, suggest that patients with a significant degree of inducible ischemia after MI are at risk of death or reinfarction and thus are candidates for a more aggressive, interventional post-MI treatment strategy [45]

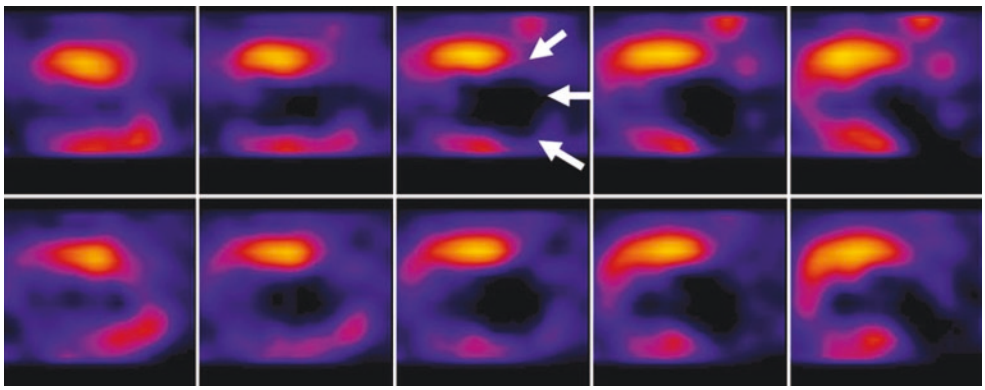

Fig. 12.25 Vertical long-axis SPECT images in a patient following acute anterior MI treated with primary PCI. The stress (*top*) and rest (*bottom*) images demonstrate a very large, severe, fixed defect in the apical, anterior, inferior, and septal walls (*arrows*). The severity of the fixed defect suggest very little myocardial viability in those walls, and the large infarct size suggests a high risk for mortality

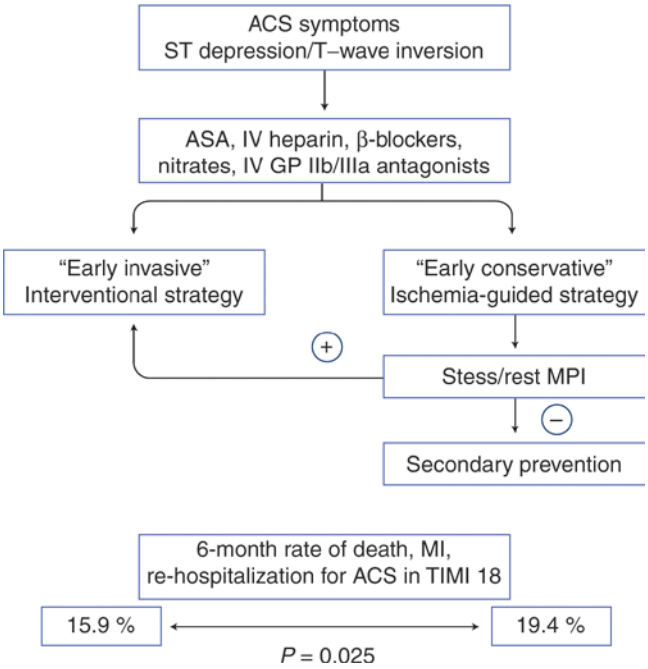

Fig. 12.26 Use of perfusion imaging in non-ST elevation in patients with ACS for the identification of patients likely to benefit from intervention. The current evidence-based paradigm suggests that such patients may derive overall benefit from an "invasive" management strategy and referral to catheterization with subsequent revascularization, particularly for the subset of patients with elevated troponin levels or other higher-risk clinical markers, such as a higher TIMI (Thrombolysis in Myocardial Infarction) risk score [46]. The role of radionuclide imaging is predominantly within the "ischemia-guided strategy," in which patients are risk stratified, with more selective referral to catheterization and revascularization based on the extent of inducible ischemia. In the TACTICS (Treat Angina with Aggrastat and Determine Cost of Therapy with an Invasive or Conservative Strategy)–TIMI 18 trial [47], patients with symptoms of ACS and ECG changes supportive of the diagnosis received the platelet inhibitor tirofiban and were randomized to an "early invasive" management strategy (referral to catheterization and revascularization based on anatomic findings at angiography) or to an "early conservative" strategy (stress testing with referral to catheterization based on the presence of significant inducible ischemia (*plus* or *minus*) or on the basis of spontaneous ischemia). In this trial, outcomes favored the invasive strategy. Because the absolute benefit of the invasive management strategy was relatively small, subgroup analysis was performed to examine whether any clinical findings could identify a subgroup in which the benefits were larger (or smaller). Subgrouping by troponin status suggested that most of the benefit of the invasive strategy was seen in the subgroup of patients identified by elevated troponins or a higher TIMI risk score, and that TACTICS-type patients without an elevation of troponin derived little benefit from the invasive strategy. These latter patients may be best managed by a more conservative approach, with risk stratification using imaging techniques followed by more selective referral to catheterization. GP glycoprotein, IV intravenous, MI myocardial infarction, MPI myocardial perfusion imaging

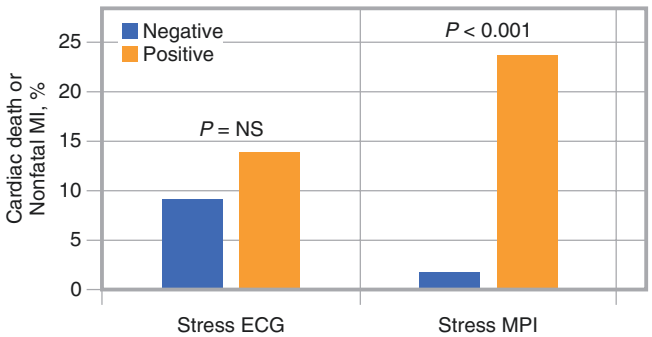

Fig. 12.27 Use of myocardial perfusion imaging (*MPI*) as the decision point in a "conservative" management strategy in non–ST segment elevation ACS. The predictive value of stress MPI and stress ECG is shown in patients who were studied after the initial stabilization of unstable angina with medical therapy. This figure summarizes the results of three studies in which the incidences of cardiac death or nonfatal MI were assessed as endpoints during follow-up after stabilization of unstable angina. The presence of reversible perfusion defects reflective of ischemia ("positive" stress MPI) was strongly predictive of cardiac events in this setting. The absence of inducible ischemia on MPI ("negative" stress MPI) identifies a low-risk group, suggesting that such patients can be managed conservatively. Data are less consistent on the use of exercise ECG in this setting [48]. NS not significant

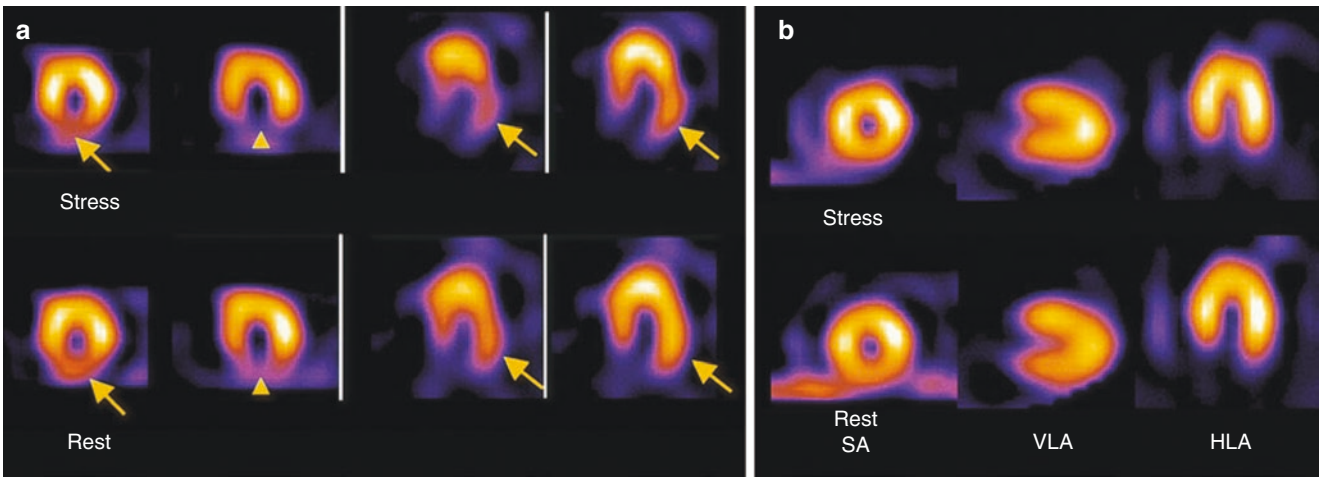

Fig. 12.28 Examples of myocardial perfusion imaging (MPI) in non–ST elevation ACS. (**a**) A positive MPI study in a patient with medically stabilized ACS/NSTEMI. After presentation, the patient's symptoms were controlled with initial medical therapy, and stress MPI was performed. There is evidence of an inferobasal infarct (*arrowheads*), but the extent of inducible ischemia involving the inferoapical and lateral walls (*arrows*) suggests that the patient is at high risk for future events, and the patient was subsequently referred to catheterization. (**b**) Stress and rest SPECT MPI appear normal in a 63-year-old woman who presented with a clinical syndrome consistent with ACS/unstable angina but nonspecific ECG changes. Symptoms abated after treatment with aspirin, heparin, β-blockers, and nitrates. The normal MPI study suggests low risk for subsequent ischemic events, and catheterization/revascularization is unlikely to improve that risk. HLA horizontal long axis, SA short axis, VLA vertical long axis

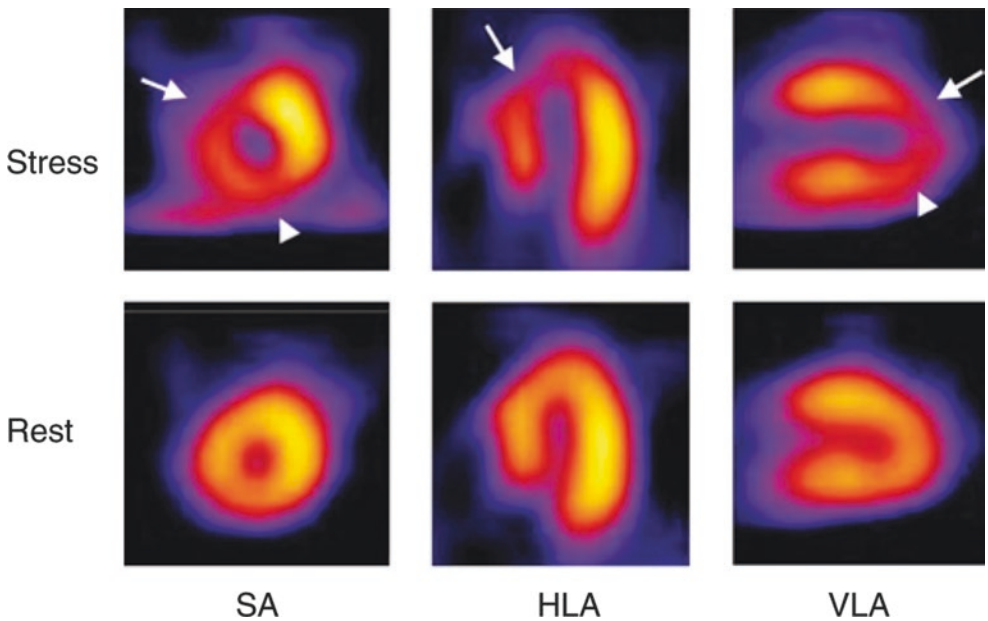

Fig. 12.29 Stress SPECT MPI can provide risk-stratification information to help guide management in complex cases, using principles derived from the published literature. In this example, an elderly woman was admitted with a non–ST elevation MI with positive troponins. On the basis of most trials and guidelines, an interventional strategy would be warranted, but the risk of catheterization would be higher than usual in this patient because of several complicating factors, including extensive peripheral vascular disease and renal insufficiency. It is not likely that such a complicated patient would have been enrolled in randomized ACS trials. In order to better define the risk–benefit ratio for moving ahead with an interventional strategy, stress MPI was performed. Extensive reversible defects on the left anterior descending territory (*arrow*) and right coronary territory (*arrowhead*), as well as transient ischemic dilatation, are seen. These findings are all consistent with very extensive and severe coronary artery disease. Thus, the potential benefit of an interventional strategy is high, putting the higher risk into context for clinical decision making. HLA horizontal long axis, SA short axis, VLA vertical long axis

References

1. Wackers FJ, Lie KI, Liem KL, Sokole EB, Samson G, van der Schoot J, Durrer D. Potential value of thallium-201 scintigraphy as a means of selecting patients for the coronary care unit. Br Heart J. 1979;41:111–7.
2. Gibbons RJ, Verani MS, Behrenbeck T, Pellikka PA, O'Connor MK, Mahmarian JJ, et al. Feasibility of tomographic ^{99m}Tc-hexakis-2-methoxy-2-methylpropyl-isonitrile imaging for the assessment of myocardial area at risk and the effect of treatment in acute myocardial infarction. Circulation. 1989;80:1277–86.
3. Boden WE, O'Rourke RA, Crawford MH, Blaustein AS, Deedwania PC, Zoble RG, et al. Outcomes in patients with acute non–Q-wave myocardial infarction randomly assigned to an invasive as compared with a conservative management strategy. N Engl J Med. 1998;338:1785–92. [Erratum in N Engl J Med. 1998;339:1091].
4. The TIMI IIIB Investigators. Effects of tissue plasminogen activator and a comparison of early invasive and conservative strategies in unstable angina and non–Q-wave myocardial infarction: results of the TIMI IIIB trial. Thrombolysis in myocardial ischemia. Circulation. 1994;89:1545–56.
5. Varetto T, Cantalupi D, Altieri A, Orlandi C. Emergency room technetium-99m sestamibi imaging to rule out acute myocardial ischemic events in patients with nondiagnostic electrocardiograms. J Am Coll Cardiol. 1993;22:1804–8.
6. Hilton TC, Thompson RC, Williams HJ, Saylors R, Fulmer H, Stowers SA. Technetium-99m sestamibi myocardial perfusion imaging in the emergency room evaluation of chest pain. J Am Coll Cardiol. 1994;23:1016–22.
7. Tatum JL, Jesse RL, Kontos MC, Nicholson CS, Schmidt KL, Roberts CS, Ornato JP. Comprehensive strategy for the evaluation and triage of the chest pain patient. Ann Emerg Med. 1997;29:116–25.
8. Heller GV, Stowers SA, Hendel RC, Herman SD, Daher E, Ahlberg AW, et al. Clinical value of acute rest technetium-99m tetrofosmin tomographic myocardial perfusion imaging in patients with acute chest pain and nondiagnostic electrocardiograms. J Am Coll Cardiol. 1998;31:1011–7.
9. Jafary F, Udelson JE. Assessment of myocardial perfusion and left ventricular function in acute coronary syndromes: implications for gated SPECT imaging. In: Germano G, Berman DS, editors. Clinical gated cardiac SPECT. Armonk: Futura; 1999.
10. Kontos MC, Jesse RL, Anderson FP, Schmidt KL, Ornato JP, Tatum JL. Comparison of myocardial perfusion imaging and cardiac troponin I in patients admitted to the emergency department with chest pain. Circulation. 1999;99:2073–8.
11. Stowers SA, Eisenstein EL, Wackers FJ, Berman DS, Blackshear JL, Jones AD Jr, et al. An economic analysis of an aggressive diagnostic strategy with single photon emission computed tomography myocardial perfusion imaging and early exercise stress testing in emergency department patients who present with chest pain but nondiagnostic electrocardiograms: results from a randomized trial. Ann Emerg Med. 2000;35:17–25.
12. Udelson JE, Beshansky JR, Ballin DS, Feldman JA, Griffith JL, Handler J, et al. Myocardial perfusion imaging for evaluation and triage of patients with suspected acute cardiac ischemia: a randomized controlled trial. JAMA. 2002;288:2693–700.
13. Bilodeau L, Théroux P, Grégoire J, Gagnon D, Arsenault A. Technetium-99m sestamibi tomography in patients with spontaneous chest pain: correlations with clinical, electrocardiographic and angiographic findings. J Am Coll Cardiol. 1991;18:1684–91.
14. Kontos MC, Jesse RL, Schmidt KL, Ornato JP, Tatum JL. Value of acute rest sestamibi perfusion imaging for evaluation of patients admitted to the emergency department with chest pain. J Am Coll Cardiol. 1997;30:976–82.
15. Duca MD, Giri S, Wu AH, Morris RS, Cyr GM, Ahlberg A, et al. Comparison of acute rest myocardial perfusion imaging and serum markers of myocardial injury in patients with chest pain syndromes. J Nucl Cardiol. 1999;6:570–6.
16. Kosnik JW, Zalenski RJ, Shamsa F, Harris R, Mittner J, Kozlowski J, et al. Resting sestamibi imaging for the prognosis of low-risk chest pain. Acad Emerg Med. 1999;6:998–1004.
17. Schaeffer MW, Brennan TD, Hughes JA, Gibler WB, Gerson MC. Resting radionuclide myocardial perfusion imaging in a chest pain center including an overnight delayed image acquisition protocol. J Nucl Med Technol. 2007;35:242–5.
18. Rybicki FJ, Udelson JE, Peacock WF, Goldhaber SZ, Isselbacher EM, Kazerooni E, et al. 2015 ACR/ACC/AHA/AATS/ACEP/ASNC/NASCI/SAEM/SCCT/SCMR/SCPC/SNMMI/STR/STS appropriate utilization of cardiovascular imaging in emergency department patients with chest pain: a joint document of the American College of Radiology Appropriateness Criteria Committee and the American College of Cardiology Appropriate Use Criteria Task Force. J Am Coll Cardiol. 2016;67:853–79.
19. Flachskampf FA, Daniel WG. Cardiac imaging in the patient with chest pain: echocardiography. Heart. 2010;96:1063–72.
20. Amsterdam EA, Kirk JD, Bluemke DA, Diercks D, Farkouh ME, Garvey JL, et al.; American Heart Association Exercise, Cardiac Rehabilitation, and Prevention Committee of the Council on Clinical Cardiology, Council on Cardiovascular Nursing, and Interdisciplinary Council on Quality of Care and Outcomes Research. Testing of low-risk patients presenting to the emergency department with chest pain: a scientific statement from the American Heart Association. Circulation. 2010;122:1756–76.
21. Geleijnse ML, Elhendy A, Kasprzak JD, Rambaldi R, van Domburg RT, Cornel JH, et al. Safety and prognostic value of early dobutamine-atropine stress echocardiography in patients with spontaneous chest pain and a non-diagnostic electrocardiogram. Eur Heart J. 2000;21:397–406.
22. Bholasingh R, Cornel JH, Kamp O, van Straalen JP, Sanders GT, Tijssen JG, et al. Prognostic value of predischarge dobutamine stress echocardiography in chest pain patients with a negative cardiac troponin T. J Am Coll Cardiol. 2003;41:596–602.
23. Nucifora G, Badano LP, Sarraf-Zadegan N, Karavidas A, Trocino G, Scaffidi G, et al. Comparison of early dobutamine stress echocardiography and exercise electrocardiographic testing for management of patients presenting to the emergency department with chest pain. Am J Cardiol. 2007;100:1068–73.
24. Trippi JA, Lee KS, Kopp G, Nelson DR, Yee KG, Cordell WH. Dobutamine stress tele-echocardiography for evaluation of emergency department patients with chest pain. J Am Coll Cardiol. 1997;30:627–32.
25. Cury RC, Feuchtner G, Mascioli C, Fialkow J, Andrulonis P, Villanueva T, et al. Cardiac CT in the emergency department: convincing evidence, but cautious implementation. J Nucl Cardiol. 2011;18:331–41.
26. Goldstein JA, Chinnaiyan KM, Abidov A, Achenbach S, Berman DS, Hayes SW, et al.; CT-STAT Investigators. The CT-STAT (Coronary Computed Tomographic Angiography for Systematic Triage of Acute Chest Pain Patients to Treatment) trial. J Am Coll Cardiol. 2011;58:1414–22.
27. Litt HI, Gatsonis C, Snyder B, Singh H, Miller CD, Entrikin DW, et al. CT angiography for safe discharge of patients with possible acute coronary syndromes. N Engl J Med. 2012;366:1393–403.
28. Hoffmann U, Truong QA, Schoenfeld DA, Chou ET, Woodard PK, Nagurney JT, et al.; ROMICAT-II Investigators. Coronary CT angiography versus standard evaluation in acute chest pain. N Engl J Med. 2012;367:299–308.
29. Hulten E, Pickett C, Bittencourt MS, Villines TC, Petrillo S, Di Carli MF, Blankstein R. Outcomes after coronary computed tomography angiography in the emergency department: a systematic review and

meta-analysis of randomized, controlled trials. J Am Coll Cardiol. 2013;61:880–92.
30. Nørgaard BL, Leipsic J, Gaur S, Seneviratne S, Ko BS, Ito H, et al.; NXT Trial Study Group. Diagnostic performance of noninvasive fractional flow reserve derived from coronary computed tomography angiography in suspected coronary artery disease: the NXT trial (analysis of coronary blood flow using CT angiography: next steps). J Am Coll Cardiol. 2014;63:1145–55.
31. Sato Y, Matsumoto N, Ichikawa M, Kunimasa T, Iida K, Yoda S, et al. Efficacy of multislice computed tomography for the detection of acute coronary syndrome in the emergency department. Circ J. 2005;69:1047–51.
32. White CS, Kuo D, Kelemen M, Jain V, Musk A, Zaidi E, et al. Chest pain evaluation in the emergency department: can MDCT provide a comprehensive evaluation? AJR Am J Roentgenol. 2005;185:533–40.
33. Hoffmann U, Nagurney JT, Moselewski F, Pena A, Ferencik M, Chae CU, et al. Coronary multidetector computed tomography in the assessment of patients with acute chest pain. Circulation. 2006;114:2251–60.
34. Gallagher MJ, Ross MA, Raff GL, Goldstein JA, O'Neill WW, O'Neil B. The diagnostic accuracy of 64-slice computed tomography coronary angiography compared with stress nuclear imaging in emergency department low-risk chest pain patients. Ann Emerg Med. 2007;49:125–36.
35. Rubinshtein R, Halon DA, Gaspar T, Jaffe R, Karkabi B, Flugelman MY, et al. Usefulness of 64-slice cardiac computed tomographic angiography for diagnosing acute coronary syndromes and predicting clinical outcome in emergency department patients with chest pain of uncertain origin. Circulation. 2007;115:1762–8.
36. Goldstein JA, Gallagher MJ, O'Neill WW, Ross MA, O'Neil BJ, Raff GL. A randomized controlled trial of multi-slice coronary computed tomography for evaluation of acute chest pain. J Am Coll Cardiol. 2007;49:863–71.
37. Hoffmann U, Bamberg F, Chae CU, Nichols JH, Rogers IS, Seneviratne SK, et al. Coronary computed tomography angiography for early triage of patients with acute chest pain: the ROMICAT (rule out myocardial infarction using computer assisted tomography) trial. J Am Coll Cardiol. 2009;53:1642–50.
38. Hollander JE, Chang AM, Shofer FS, McCusker CM, Baxt WG, Litt HI. Coronary computed tomographic angiography for rapid discharge of low-risk patients with potential acute coronary syndromes. Ann Emerg Med. 2009;53:295–304.
39. Miller CD, Hwang W, Hoekstra JW, Case D, Lefebvre C, Blumstein H, et al. Stress cardiac magnetic resonance imaging with observation unit care reduces cost for patients with emergent chest pain: a randomized trial. Ann Emerg Med. 2010;56:209–19.e2.
40. Miller CD, Hwang W, Case D, Hoekstra JW, Lefebvre C, Blumstein H, et al. Stress CMR imaging observation unit in the emergency department reduces 1-year medical care costs in patients with acute chest pain: a randomized study for comparison with inpatient care. JACC Cardiovasc Imaging. 2011;4:862–70.
41. Cury RC, Shash K, Nagurney JT, Rosito G, Shapiro MD, Nomura CH, et al. Cardiac magnetic resonance with T2-weighted imaging improves detection of patients with acute coronary syndrome in the emergency department. Circulation. 2008;118:837–44.
42. Wright J, Adriaenssens T, Dymarkowski S, Desmet W, Bogaert J. Quantification of myocardial area at risk with T2-weighted CMR: comparison with contrast-enhanced CMR and coronary angiography. JACC Cardiovasc Imaging. 2009;2:825–31.
43. Stone GW, Selker HP, Thiele H, Patel MR, Udelson JE, Ohman EM, et al. Relationship between infarct size and outcomes following primary PCI: patient-level analysis from 10 randomized trials. J Am Coll Cardiol. 2016;67:1674–83.
44. Zaret BL, Wackers FJ, Terrin ML, Forman SA, Williams DO, Knatterud GL, Braunwald E. Value of radionuclide rest and exercise left ventricular ejection fraction in assessing survival of patients after thrombolytic therapy for acute myocardial infarction: results of Thrombolysis in Myocardial Infarction (TIMI) phase II study. The TIMI Study Group. J Am Coll Cardiol. 1995;26:73–9.
45. Travin MI, Dessouki A, Cameron T, Heller GV. Use of exercise technetium-99m sestamibi SPECT imaging to detect residual ischemia and for risk stratification after acute myocardial infarction. Am J Cardiol. 1995;75:665–9.
46. Antman EM, Cohen M, Bernink PJ, McCabe CH, Horacek T, Papuchis G, et al. The TIMI risk score for unstable angina/non-ST elevation MI: a method for prognostication and therapeutic decision making. JAMA. 2000;284:835–42.
47. Cannon CP, Weintraub WS, Demopoulos LA, Vicari R, Frey MJ, Lakkis N, et al.; TACTICS (Treat Angina with Aggrastat and Determine Cost of Therapy with an Invasive or Conservative Strategy) – Thrombolysis in Myocardial Infarction 18 Investigators. Comparison of early invasive and conservative strategies in patients with unstable coronary syndromes treated with the glycoprotein IIb/IIIa inhibitor tirofiban. N Engl J Med. 2001;344:1879–87.
48. Brown KA. Management of unstable angina: the role of noninvasive risk stratification. J Nucl Cardiol. 1997;4:S164–8.

13 Imaging Cardiac Sarcoidosis, Amyloidosis, and Cardiovascular Prosthetic Infections

Sharmila Dorbala and Rodney H. Falk

Advances in cardiovascular and molecular imaging have transformed the evaluation and management of patients with infiltrative and infectious heart diseases over the past 10 years. Today, an array of tracers are available for imaging: 2-[^{18}F]fluoro-2-deoxy-g1ucose (^{18}F-FDG), a tracer of glucose metabolism to image inflammation or infection; ^{99m}technetium (^{99m}Tc)-pyrophosphate, ^{99m}Tc-3,3-diphosphono-1,2-propanodicarboxylicacid (*^{99m}Tc-DPD*), and ^{99m}Tc-hydroxy methylene diphosphonate (*^{99m}Tc*-HMDP), bone imaging tracers repurposed to image cardiac transthyretin amyloidosis (ATTR); and ^{18}F-florbetapir, ^{18}F-flutemetamol, and ^{18}F-florbetaben, targeted β-amyloid tracers to image cardiac transthyretin (ATTR) and light chain amyloidosis (AL). These advanced imaging methods are now providing substantial advantages over endomyocardial biopsy, the common reference method. Widely available, non-invasive, and immune to the challenges of sampling error, imaging improves our ability to quantify disease burden and to assess response to therapy. This chapter discusses the role of radionuclide imaging in the evaluation of cardiac sarcoidosis, cardiovascular prosthetic infection, and cardiac amyloidosis.

S. Dorbala (✉)
Division of Nuclear Medicine, Cardiovascular Imaging Section, Department of Radiology and Medicine, Brigham and Women's Hospital, Boston, MA, USA
e-mail: sdorbala@bwh.harvard.edu

R. H. Falk
Department of Medicine, Cardiovascular Medicine, Brigham and Women's Hospital, Boston, MA, USA

V. Dilsizian, J. Narula (eds.), *Atlas of Nuclear Cardiology*, https://doi.org/10.1007/978-3-030-49885-6_13

Cardiac Sarcoidosis

Cardiac sarcoidosis represents a major cause of mortality in patients with systemic sarcoidosis [1], a granulomatous disorder of unknown etiology characterized by focal noncaseating granulomas in the various organ systems [2]. Because of patchy involvement of the heart with sarcoid granulomas sampling error can limits the diagnostic yield of endomyocardial biopsy (Fig. 13.1).

Fig. 13.1 Challenges of endomyocardial biopsy in cardiac sarcoidosis. Shown is a section of an explanted heart from a patient with advanced cardiac sarcoidosis who underwent cardiac transplantation. The left ventricle shows regions of normal myocardium as well as fibrosis and inflammation. A blind endomyocardial biopsy from the right side of the interventricular septum may reveal normal myocardium, nonspecific inflammation (**a**, **b**), typical noncaseating granuloma from sarcoidosis (**c**) or myocardial fibrosis (**d**). In sarcoidosis, these pathologies may coexist in different regions of the same heart, so it is challenging to make management decisions based on random endomyocardial biopsy results. In contrast, imaging with ^{18}F-FDG PET/CT offers the ability to evaluate the whole-heart and whole-body burden of inflammation. (*From* Dorbala and Shaw [3]; with permission from Springer Nature)

As shown in Table 13.1, the current diagnostic criteria for cardiac sarcoidosis use endomyocardial biopsy or a combination of extracardiac biopsy with typical clinical and imaging features in the heart [4]. Clinical manifestations (as listed on Table 13.1 for the Heart Rhythm Society) are typically not specific to diagnose cardiac involvement. Echocardiography is not sensitive to diagnose cardiac sarcoidosis. Cardiovascular magnetic resonance (CMR), on the other hand, provides characteristic patterns of late gadolinium enhancement that are highly sensitive for the diagnosis of cardiac sarcoidosis [5]. However, neither echocardiography nor CMR can provide the necessary information on active myocardial inflammation to guide immunosuppressive therapy [5]. Moreover, CMR is contraindicated in individuals with devices not compatible with MRI. The available clinical tools to image myocardial inflammation comprise radionuclide imaging with ^{67}Gallium-citrate [6] or ^{18}F-FDG [7].

Japanese Ministry of Health and Welfare
Histological diagnosis
Cardiac sarcoidosis confirmed by endomyocardial biopsy, and histological or clinical diagnosis of extracardiac sarcoidosis
Clinical diagnosis group
Histological or clinical diagnosis of extracardiac sarcoidosis *and* two or more major criteria *or* one major criterion and two or more minor criteria:
Major criteria
Advanced atrioventricular block
Basal thinning of the interventricular septum
^{67}Gallium uptake in the heart
LVEF <50%
Minor criteria
Electrocardiography: Ventricular tachycardia, PVCs, RBBB, abnormal axis, abnormal Q wave
Echocardiography: Structural or wall motion abnormality
Radionuclide imaging: Perfusion defect on ^{201}thallium, ^{99m}technetium-sestamibi-tetrofosmin
Cardiac MRI: late gadolinium enhancement
Endomyocardial biopsy: Moderate fibrosis or monocyte infiltration
Heart Rhythm Society
Histological diagnosis from myocardial tissue
Noncaseating granuloma on endomyocardial biopsy with no alternative cause identified
Clinical diagnosis
Probable diagnosis of cardiac sarcoidosis exists if there is histological diagnosis of extracardiac sarcoidosis *and* one or more of the following are present:
Cardiomyopathy or atrioventricular block responsive to immunosuppressive therapy
Unexplained reduced LVEF (<40%)
Unexplained ventricular tachycardia
Mobitz II second- or third-degree heart block
Patchy ^{18}F-FDG uptake on cardiac PET consistent with cardiac sarcoidosis
Late gadolinium enhancement on CMR consistent with cardiac sarcoidosis
Cardiac ^{67}gallium uptake
Exclusion of other causes of cardiac manifestations

CMR cardiac magnetic resonance imaging, *LVEF* left ventricular ejection fraction, *PVCs* premature ventricular complexes, *RBBB* right bundle branch block

Table 13.1 Diagnostic criteria for cardiac sarcoidosis

Owing to its poor sensitivity, ^{67}Gallium-citrate SPECT imaging has been largely replaced in clinical practice by ^{18}F-FDG PET/CT imaging [5]. ^{18}F-FDG PET/CT imaging tracks myocardial uptake of glucose, which is increased in sarcoid granulomas because of the high glycolytic activity of the inflammatory cells. ^{18}F-FDG PET/CT thus provides high accuracy to diagnose cardiac sarcoidosis, using a reference standard of Japanese Ministry Criteria or endomyocardial biopsy, with a pooled sensitivity of 89% (95% CI, 79–96%) and a pooled specificity of 78% (95% CI, 68–86%) [8]. When compared with echocardiography, CMR, and ^{67}Gallium scintigraphy, ^{18}F-FDG PET/CT is more accurate [5]. Myocardial ^{18}F-FDG uptake, however, can be nonspecific; it cannot differentiate between normal myocardial glucose utilization, myocardial inflammation, ischemia, tumor, or infection. Hence, myocardial. ^{18}F-FDG imaging of sarcoidosis is performed with a special dietary preparation to suppress physiological glucose utilization. As myocardial uptake of ^{18}F-FDG can be physiological, interpretation of diffuse myocardial FDG uptake, as well as focal uptake in the basal lateral wall, can be challenging. For this and other reasons, although ^{18}F-FDG PET/CT can be very valuable for the initial evaluation of patients with suspected cardiac sarcoidosis, CMR is the preferred first test. Once a diagnosis of cardiac sarcoidosis is suspected on CMR or confirmed by endomyocardial biopsy, ^{18}F-FDG imaging is often performed to assess the burden of myocardial inflammation at baseline and during followup, to assess changes in response to therapy [5, 9] (Fig. 13.2).

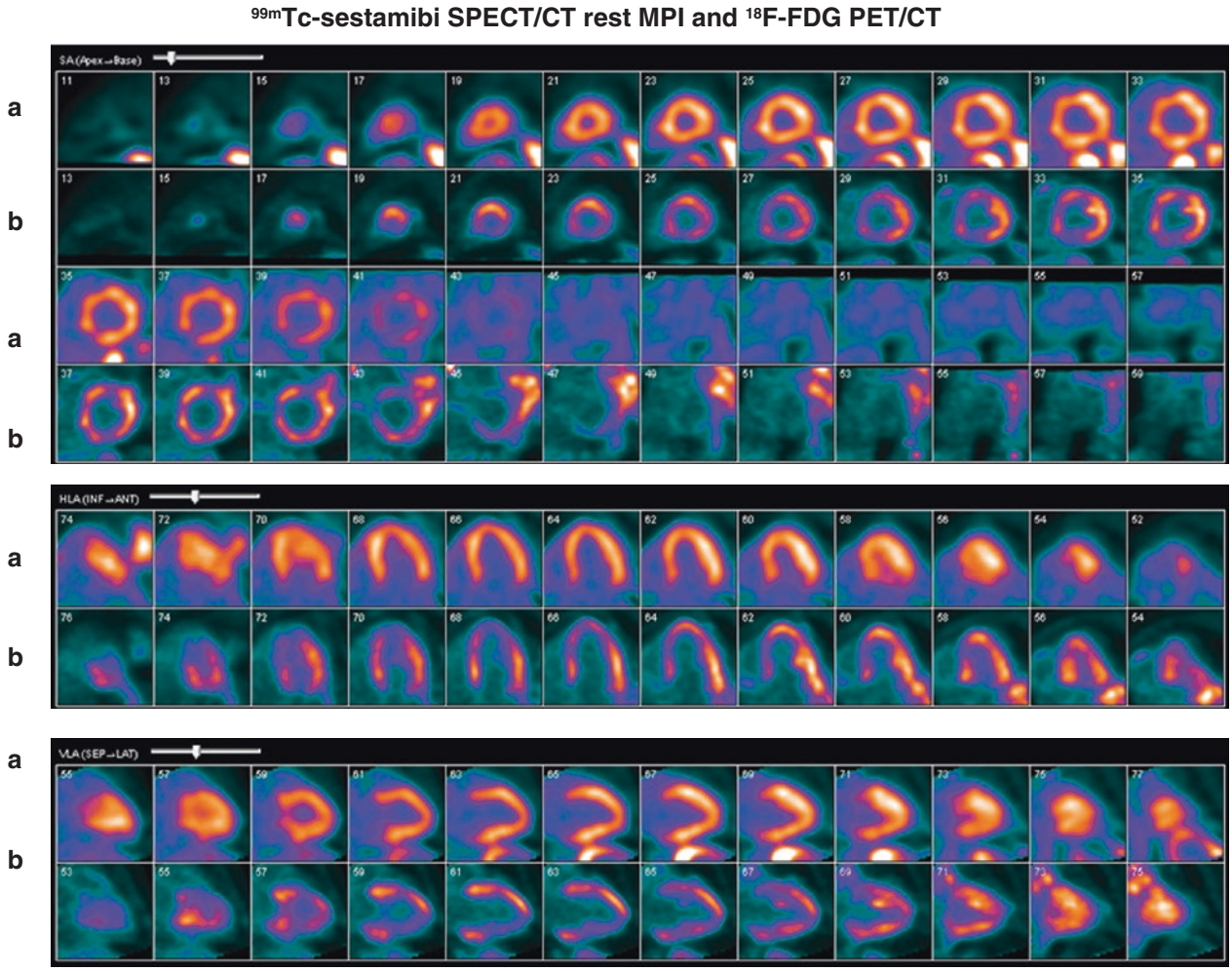

Fig. 13.2 Imaging in a patient with suspected cardiac sarcoidosis. A 44-year-old man with progressive dyspnea for 1 year underwent CT scan of the chest that revealed prominent hilar lymphadenopathy. Due to a concern for lymphoma, an ^{18}F-FDG PET scan was performed, which revealed focal cardiac FDG uptake suggestive of cardiac sarcoidosis. A CMR confirmed late gadolinium enhancement (LGE, fibrosis) and increased T2 signal (edema) of the left and right ventricles, confirming cardiac sarcoidosis. The ^{18}F-FDG scan was repeated (**a**–**d**) using the protocol for sarcoidosis. One day prior to the ^{18}F-FDG PET/CT scan, a high-fat, low-carbohydrate diet was provided for two large meals, followed by an overnight fast. On the day of the study, rest myocardial perfusion imaging (MPI) was performed with 10 mCi of ^{99m}Tc-sestamibi and gated attenuation-corrected SPECT/CT imaging (**a**). Following the perfusion scan, the patient received 8 mCi of ^{18}F-FDG intravenously and cardiac (10-minute, **b**) and whole body ^{18}F-FDG PET/CT images (3 minutes per bed position eyes to kidneys; **c** and **d**) were performed 90 minutes later in a 3D mode, using a non-gated acquisition. The images showed a pattern of focal-on-diffuse myocardial uptake of ^{18}F-FDG in the left ventricle. A pattern of diffuse myocardial uptake can represent physiological glucose utilization, so CMR images were reviewed. They showed regions of LGE corresponding to the regions of focal ^{18}F-FDG uptake in the lateral wall (**c** and **d**), confirming that ^{18}F-FDG uptake in the lateral wall was pathological. Also, extensive focal uptake was noted in the right ventricle, and in the mediastinal, hilar, and supraclavicular lymph nodes (**c** and **d**). The left ventricular ejection fraction was 64%. The patient was started on high-dose steroids (40 g PO QD, with a plan to taper) and methotrexate 15 mg orally weekly. He received an implantable cardioverter-defibrillator (ICD), which over the next 6 months revealed frequent runs of ventricular tachycardia terminated by antitachycardia pacing. CTAC–low dose CT obtained for attenuation correction

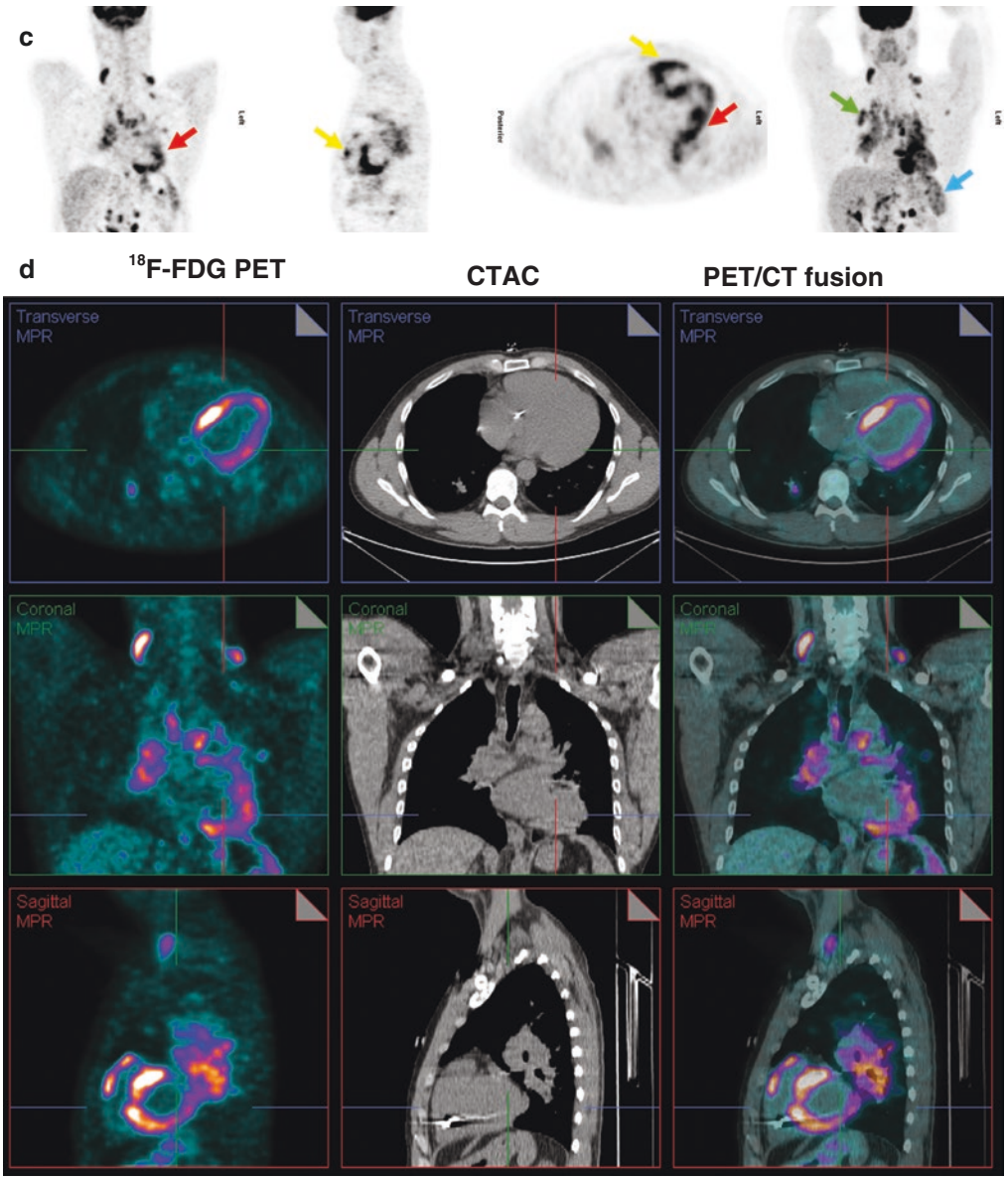

Fig. 13.2 (continued)

A pattern of normal perfusion with focally increased ^{18}F-FDG uptake, or a perfusion defect with focally increased ^{18}F-FDG uptake, is characteristic of active sarcoidosis. A perfusion metabolism mismatch pattern is also a hallmark of hibernating myocardium, hence it is imperative to exclude ischemic heart disease by stress imaging or coronary angiography before diagnosing cardiac sarcoidosis in this pattern [4, 5, 10]. In the absence of myocardial ^{18}F-FDG uptake, the presence of myocardial perfusion defects on attenuation-corrected images can signify scarred myocardium.

In one study, 118 patients with suspected sarcoidosis who underwent ^{18}F-FDG PET/CT with myocardial perfusion imaging were followed up for a median of 1.5 years. A total of 31 adverse events (27 ventricular tachyarrhythmias and 8 deaths) were observed (Fig. 13.3). A normal myocardial perfusion and no cardiac ^{18}F-FDG uptake portended the best survival free of ventricular tachyarrhythmias. If either ^{18}F-FDG PET/CT or myocardial perfusion imaging was abnormal, the rate of event-free survival was worse, and if both were abnormal, that pattern conferred the highest risk.

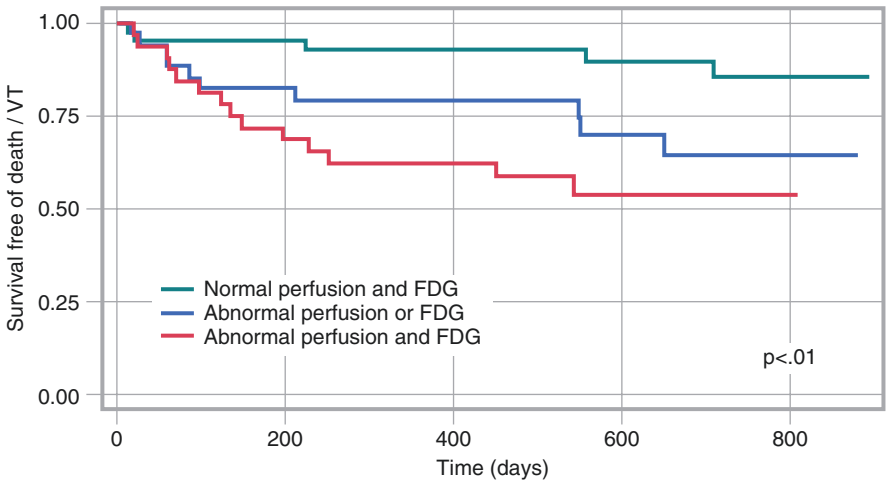

Fig. 13.3 Prognostic value of ^{18}F-FDG and myocardial perfusion imaging in cardiac sarcoidosis. (*From* Blankstein et al. [7]; with permission from Elsevier)

^{18}F-FDG PET/CT is also used to assess response to therapy (Fig. 13.4). ^{18}F-FDG imaging is performed to assess the burden of myocardial inflammation at baseline and during followup to assess changes response to therapy [5, 9]. ^{18}F-FDG PET/CT sarcoidosis imaging is a hot-spot imaging tracer. Hence, visual interpretation of the images can be limited in evaluating change. Myocardial radiotracer uptake is quantified for assessment of changes using standardized uptake value (SUV), volume of inflamed myocardium (using a threshold SUVmax value), or target-to-background ratio [9].

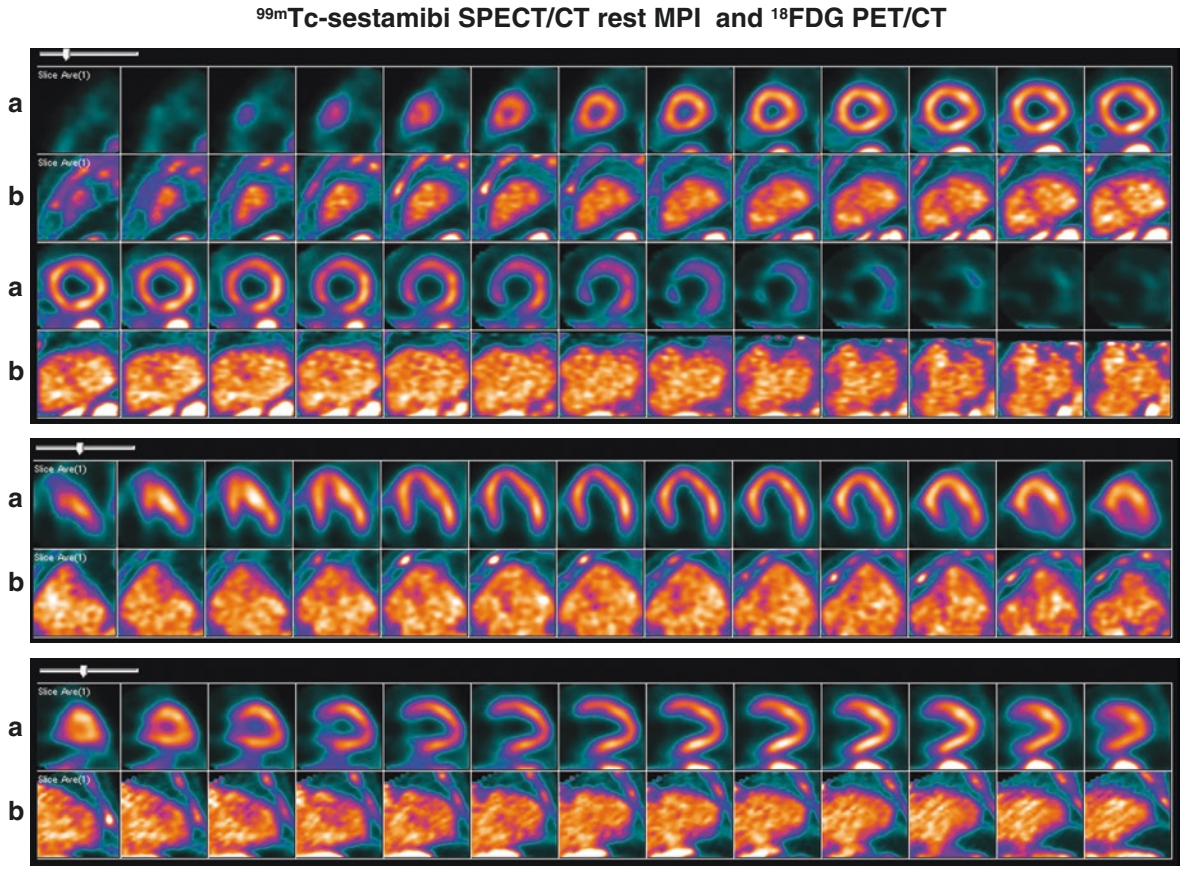

Fig. 13.4 ^{18}F-FDG PET/CT to assess response to therapy. When the patient in Fig. 13.2 returned for a follow-up ^{18}F-FDG PET/CT scan 6 months later with myocardial perfusion imaging (**a** and **b**), it revealed near-complete resolution of inflammation in the heart and in the mediastinal nodes (**c** and **d**). Myocardial perfusion was normal (**a**), except for the basal inferoseptal region, which showed a small scar (best seen on the short axis images in row 3 of **a**). His left ventricular ejection fraction was 60%

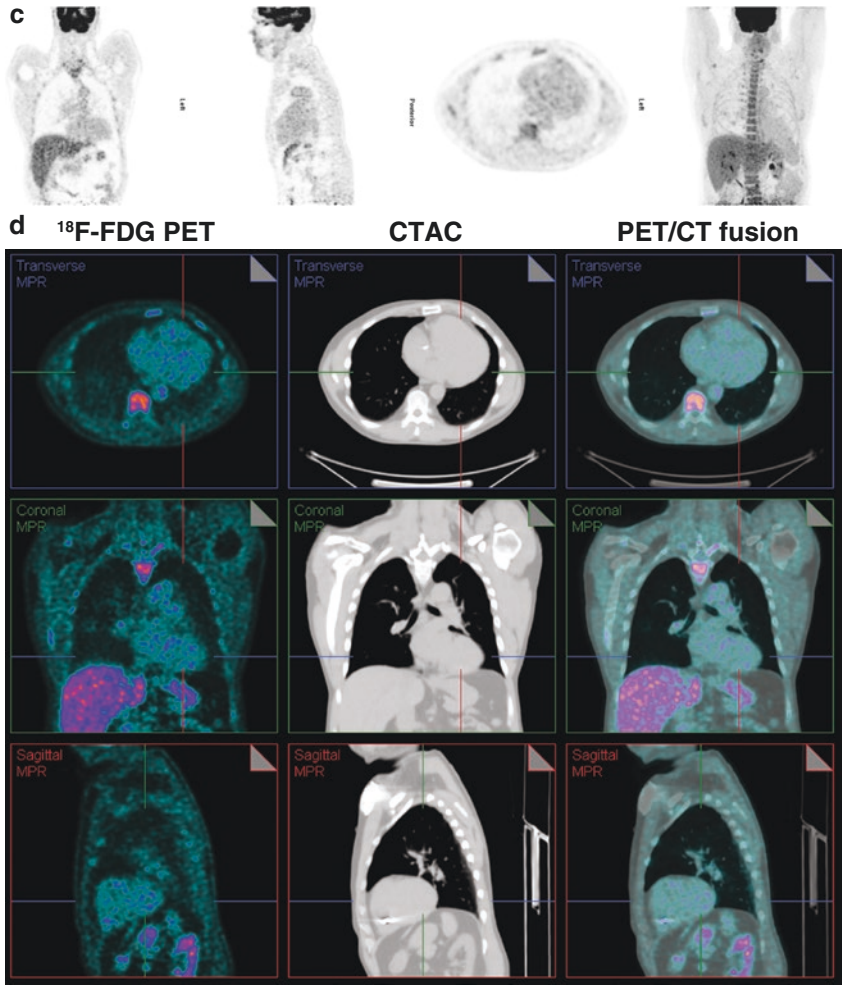

Fig. 13.4 (continued)

Figure 13.5 outlines an approach to evaluation of cardiac sarcoidosis.

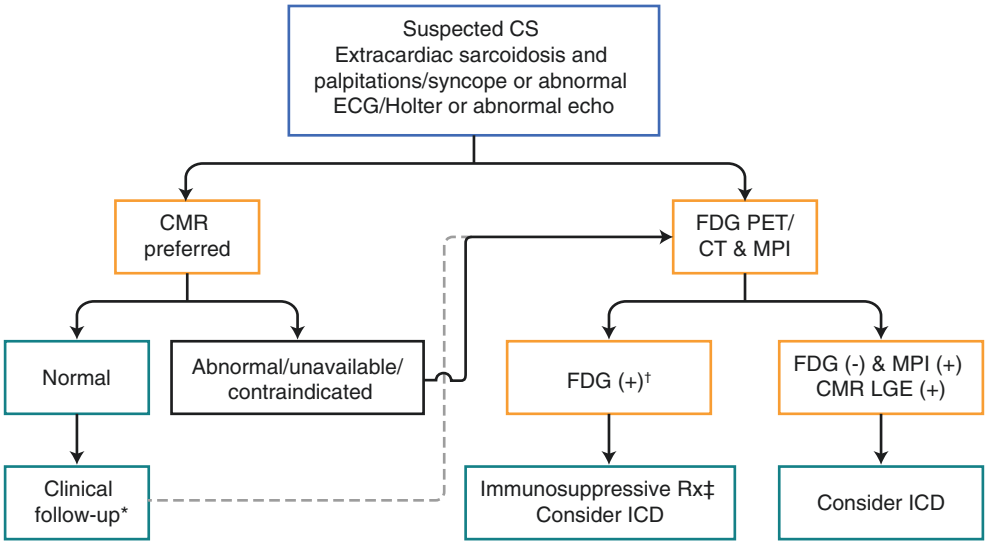

Fig. 13.5 An approach to evaluation of cardiac sarcoidosis (CS) using ^{18}F-FDG PET/CT and CMR. Patients with suspected cardiac sarcoidosis, symptoms, and imaging findings can be evaluated with either a gadolinium-enhanced CMR or ^{18}F-FDG PET/CT with myocardial perfusion imaging (MPI). Imaging findings can guide immunosuppressive therapy and ICD implantation in patients with cardiac sarcoidosis. *If clinical suspicion is high or symptoms persist, FDG-PET/CT and MPI may be considered in patients with normal CMR; †Identify coexistent inflammation; ‡Immunosuppressive therapy may be considered taking into account the amount of inflammation. (*From* Slart et al. [11] with permission from Springer Nature)

Cardiovascular Prosthetic Infection

Imaging with ^{18}F-FDG PET has transformed the evaluation and management of patients with infection involving cardiovascular prosthetics (Fig. 13.6) [13, 14] and devices [15, 16], including left ventricular assist devices [17].

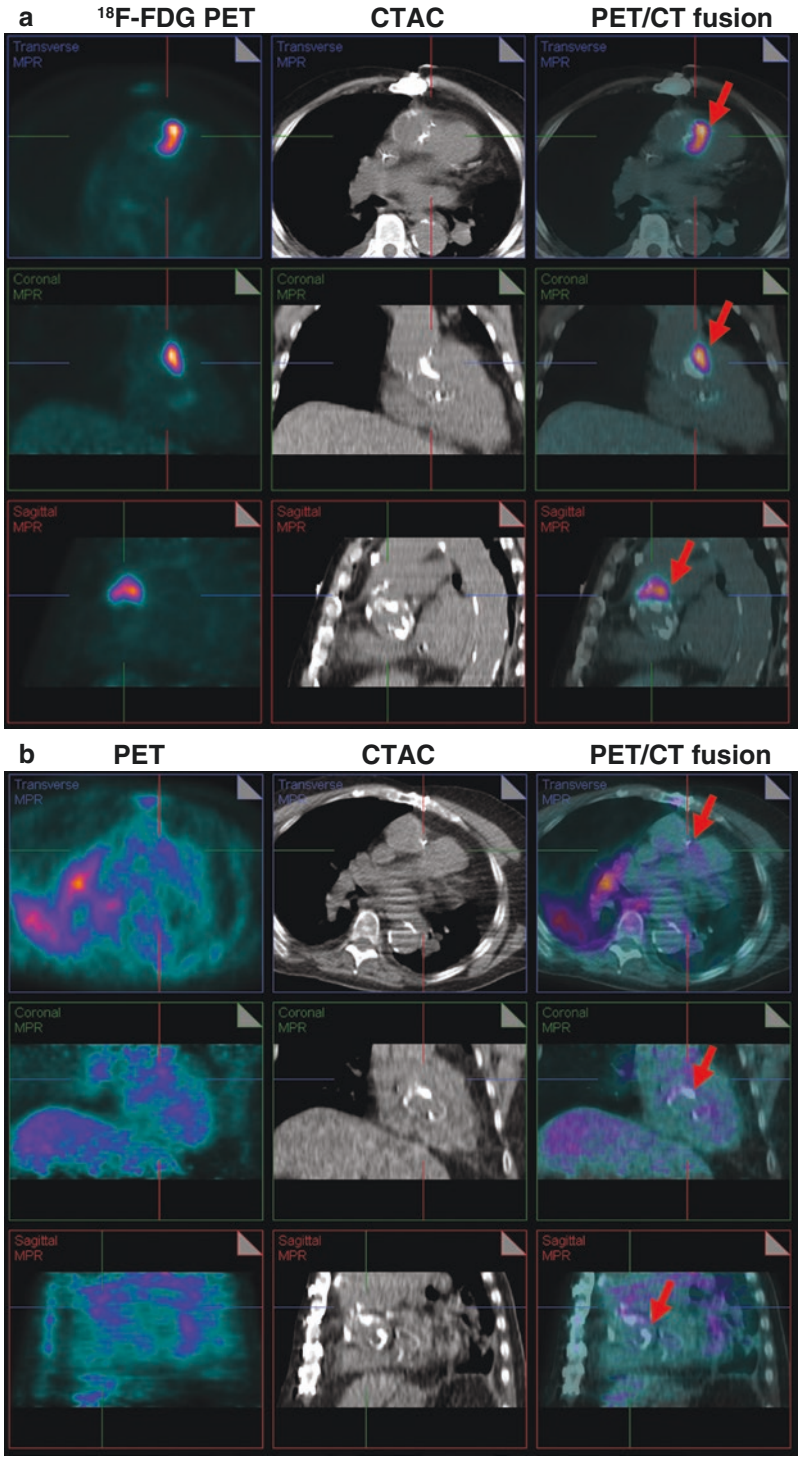

Fig. 13.6 Utility of ^{18}F-FDG PET/CT in identifying infected prosthetic material. An 88-year-old man with three prior aortic valve replacements and aortic root repair presented with fevers and blood cultures positive for *Escherichia coli*. A transesophageal echocardiogram was unrevealing. (**a**) Because of persistent fevers, an ^{18}F-FDG PET scan was performed, which showed focal intense ^{18}F-FDG uptake in the region of the ascending aorta (*red arrows*). The corresponding region on the non-contrast CT scan revealed a lucency that was suspicious for a pseudoaneurysm. Iodinated contrast could not be used, owing to renal insufficiency. The patient was deemed too high-risk for a fourth aortic surgery and was managed medically. (**b**) The same patient was rehospitalized 18 months later with altered mental status, fevers, and a pneumonia on chest x-ray. Persistent bacteremia led to concern for recurrent endocarditis. ^{18}F-FDG imaging was repeated and it revealed no uptake in the region of the aortic root

Pizzi et al. [14] showed that the addition of cardiac CT angiography with contrast to ^{18}F-FDG PET improved diagnostic accuracy for the detection of infective endocarditis (Fig. 13.7).

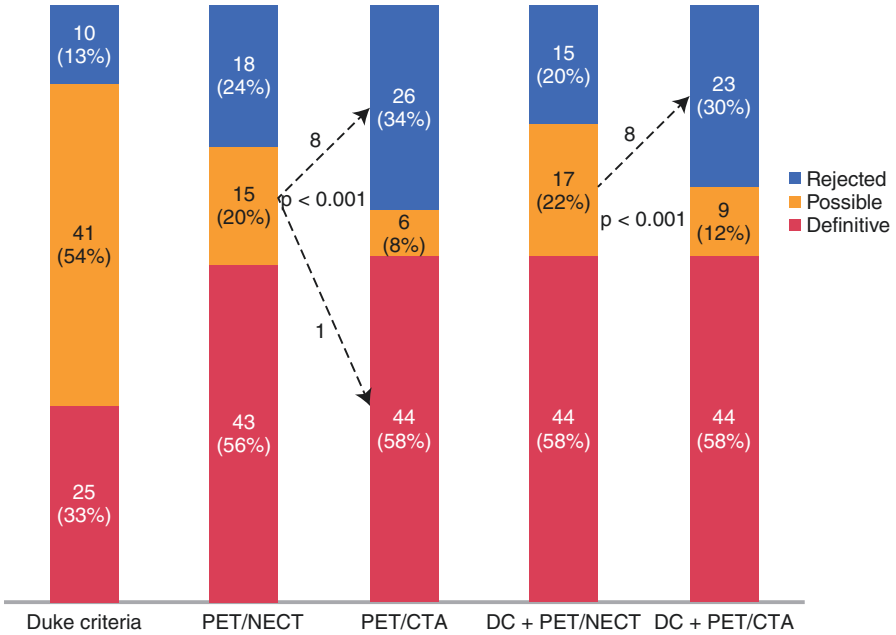

Fig. 13.7 Incremental value of ^{18}F-FDG PET/CT and contrast-enhanced cardiac CT angiography (CTA) in the diagnosis of infective endocarditis. The addition of CTA to ^{18}F-FDG PET has been shown to improve diagnostic accuracy for the detection of infective endocarditis (sensitivity, specificity, positive and negative predictive values of 91%, 90.6%, 92.8%, and 88.3% for ^{18}F-FDG PET/CT with CTA, *versus* 86.4%, 87.5%, 90.2%, and 82.9%, respectively, for ^{18}F-FDG PET/CT without contrast [NECT]), and significantly improved the detection of anatomic lesions. With the addition of CTA, the rate of infective endocarditis cases designated "possible" decreased from 20% to 8% ($p < 0.001$). Duke criteria (DC) combined with ^{18}F-FDG PET/CTA reclassified 47% of cases when compared with Duke criteria combined with non-contrast attenuation-correction CT, and a confirmed diagnosis of definite or rejected infective endocarditis was established in 88% of cases. (*From* Pizzi et al. [14]; with permission from Wolters Kluwer)

Prosthetic valve infective endocarditis is associated with high in-hospital mortality of 20–40% [18]. A multimodal imaging approach that includes echocardiography, ^{18}F-FDG PET, cardiac CT, and sometimes MRI is frequently necessary in dealing with these complex diagnostic challenges. Imaging with transesophageal echocardiography remains the first-line test in most cases of suspected endocarditis [19], but echocardiography frequently may be limited in detecting endocarditis because of shadowing from the prosthetic valves and devices. Contrast-enhanced cardiac CT plays an important role in excluding epicardial CAD prior to surgery and in diagnosing valve abscess, fistula, pseudoaneurysm, and embolic phenomenon (cerebral or abdominal CT in select cases) [19]. MRI has a limited role in prosthetic valve endocarditis. It is primarily used for brain imaging to detect cerebral lesions (found in 82%), subclinical cerebral events (found in 30–40%), and clinical or subclinical cerebral embolic events (ischemic or hemorrhagic stroke, mycotic aneurysm, or abscess) [19]. Emerging literature suggests a central role for whole-body and cardiac ^{18}F-FDG PET [13], and ^{111}Indium-labeled white blood cell scintigraphy [20, 21] is also accurate for the evaluation of prosthetic device infection, particularly when echocardiography is unrevealing or limited. Excellent systematic reviews and meta-analyses have summarized the utility and high diagnostic accuracy of ^{18}F-FDG PET/CT for infective endocarditis [22, 23] and for cardiac implantable electronic devices (pooled sensitivity 93% and pooled specificity 98%) [16]. One of the major advantages of radionuclide scintigraphy for endocarditis is the ability to perform whole-body imaging to detect septic emboli [20]. ^{18}F-FDG PET/CT imaging is useful not only to diagnose infection but also to evaluate response to therapy (*see* Fig. 13.6.B) and to predict prognosis (Fig. 13.8).

Based on the emerging literature on radionuclide imaging in infective endocarditis, The European Society of Cardiology in 2015 recommended expanding to the Duke criteria to include (1) definite vegetations on echocardiography, (2) abnormal activity detected by ^{18}F-FDG PET/CT (only if the prosthesis has been in place >3 months) or radiolabeled leukocyte SPECT/CT around the site of prosthetic valve implantation, and (3) a definite paravalvular lesion on cardiac CT [19].

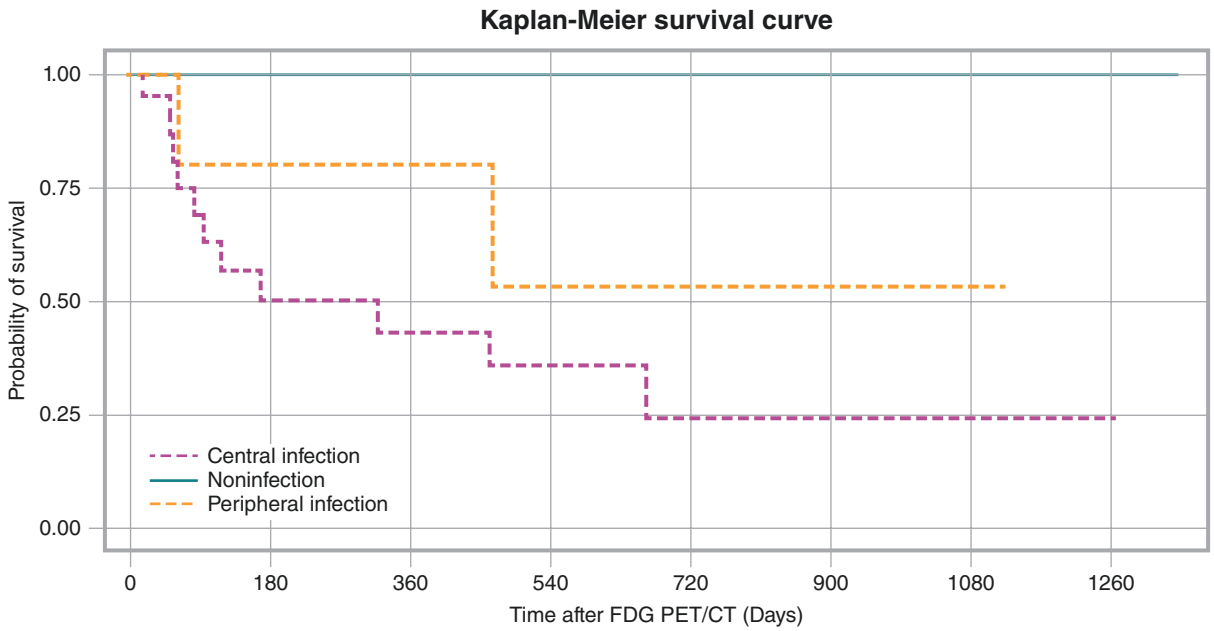

Number at risk

Noninfection	7	5	4	4	3	2	2	1
Central infection	23	8	6	5	2	1	1	1
Peripheral infection	5	4	3	2	1	1	1	0

Fig. 13.8 ^{18}F-FDG for early detection and management of infections involving a left ventricular assist device (LVAD). Kim et al. [17] evaluated 35 patients with LVAD who underwent ^{18}F-FDG PET/CT and found that 50% of the patients with infection died during a mean followup of 23 months. Patients with central infection (*red line*) had much worse survival than patients with peripheral infection (*blue line*) or no infection (*green line*). (*From* Kim et al. [17]; with permission from Elsevier)

Cardiac Amyloidosis

Cardiac amyloidosis is one of the most fatal forms of heart failure, with a median survival of less than 6 months for untreated AL amyloidosis [24] and about 4 years for ATTR amyloidosis [25, 26]. Amyloid fibrils are formed in the heart, most commonly from misfolded immunoglobulin light chains (produced by an abnormal plasma cell clone) or from wild-type or mutant transthyretin protein (produced by the liver). AL cardiac amyloidosis is treated very differently from ATTR cardiac amyloidosis, so identification of the type of amyloidosis is just as important as the diagnosis. Cardiac uptake of bone radiotracers has long been recognized to be increased in cardiac amyloidosis. In the early 2000s, investigators recognized that bone tracers are highly accurate for imaging the ATTR form of cardiac amyloidosis [27] but are unreliable in diagnosing the AL form [28]. This finding led to an explosion of clinical studies validating the utility of bone tracer cardiac scintigraphy to diagnose ATTR cardiac amyloidosis [27, 29], differentiate it from AL cardiac amyloidosis [30], and stratify risk in these patients [31, 32]. Cardiac scintigraphy with bone tracers is typically started 1 to 3 hours after injection of radiotracer (1 hour for ^{99m}Tc-PYP and 3 hours for ^{99m}Tc-DPD/HMDP); images are acquired as a planar chest study followed by a chest or cardiac SPECT study when planar imaging shows increased cardiac uptake [33]. These images are interpreted visually (positive and negative) and quantified using a visual score on the 3-hour images (Fig. 13.9) and/or a heart-to-contralateral-lung ratio on 1-hour or 3-hour planar images (Fig. 13.10) [33].

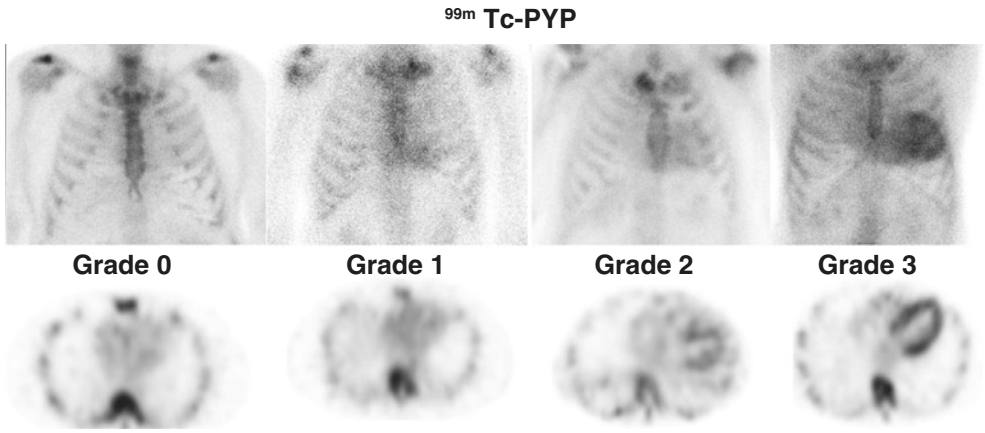

Fig. 13.9 ^{99m}Tc-pyrophosphate (^{99m}Tc-PYP) planar and SPECT chest images for the diagnosis of ATTR cardiac amyloidosis. From left to right, the images show grade 0 (no myocardial uptake), grade 1 (myocardial uptake < rib uptake), grade 2 (myocardial uptake = rib uptake) and grade 3 (myocardial uptake > rib uptake) uptake of ^{99m}Tc-PYP. Grades 2 and 3 uptake of ^{99m}Tc-PYP are highly accurate in diagnosing ATTR cardiac amyloidosis in patients without a plasma cell clonal abnormality

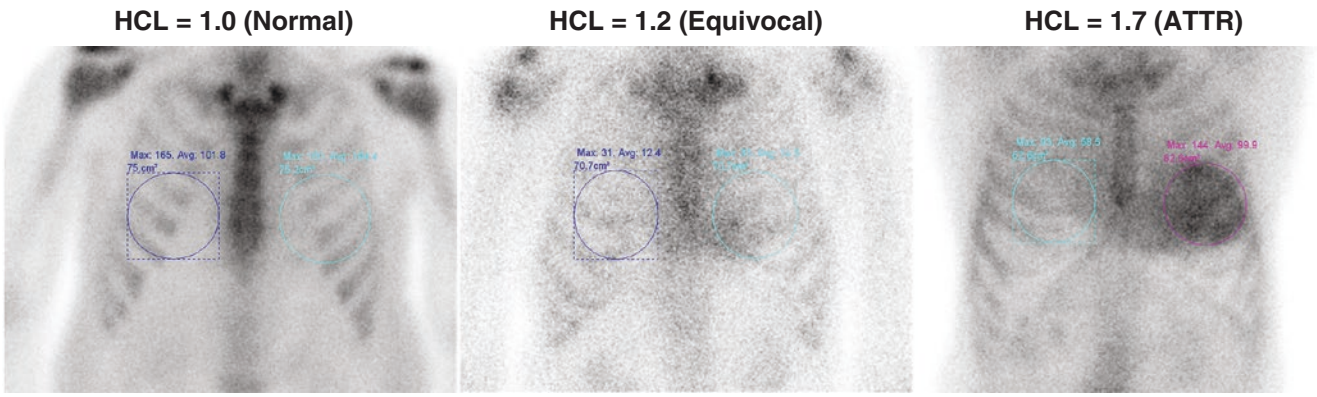

Fig. 13.10 ^{99m}Tc-PYP planar images showing the heart-to-contralateral-lung (HCL) ratio. An elliptical region of interest (ROI) is placed on the heart and mirrored on the right chest on the planar images. A ratio greater than 1.5 of the mean counts in the ROI heart compared with the contralateral chest is highly specific in distinguishing ATTR from AL cardiac amyloidosis

In a large multicenter study, grade 2 or 3 uptake of ^{99m}Tc-PYP, *^{99m}Tc-DPD*, or *^{99m}Tc*-HMDP in the context of typical symptoms and echocardiographic or CMR features demonstrated a high sensitivity (>91%) and (in the absence of a clonal abnormality) 100% specificity in diagnosing ATTR cardiac amyloidosis [34]. Heart-to-contralateral-lung ratio greater than 1.5 on 1-hour planar chest images is highly specific to distinguish AL from ATTR cardiac amyloidosis [30] and has been shown to be a marker for worse survival [31]. ^{99m}Tc-PYP imaging is typically performed when patients present with thick ventricles and heart failure, which are features of advanced amyloidosis, and bone tracer cardiac scintigraphy can diagnose ATTR cardiac amyloidosis early, particularly in gene-positive patients with hereditary TTR amyloidosis [35]. Bone tracer cardiac scintigraphy for amyloidosis has certain limitations, however. One small study showed that ^{99m}Tc-MDP, a commonly used bone scan agent, has a lower sensitivity than ^{99m}Tc-PYP to detect ATTR cardiac amyloidosis [36]. The bone tracers are also unreliable to diagnose AL cardiac amyloidosis, so if cardiac imaging shows typical features of amyloidosis and the ^{99m}Tc-PYP scan is negative, patients should be evaluated for AL cardiac amyloidosis (Fig. 13.11).

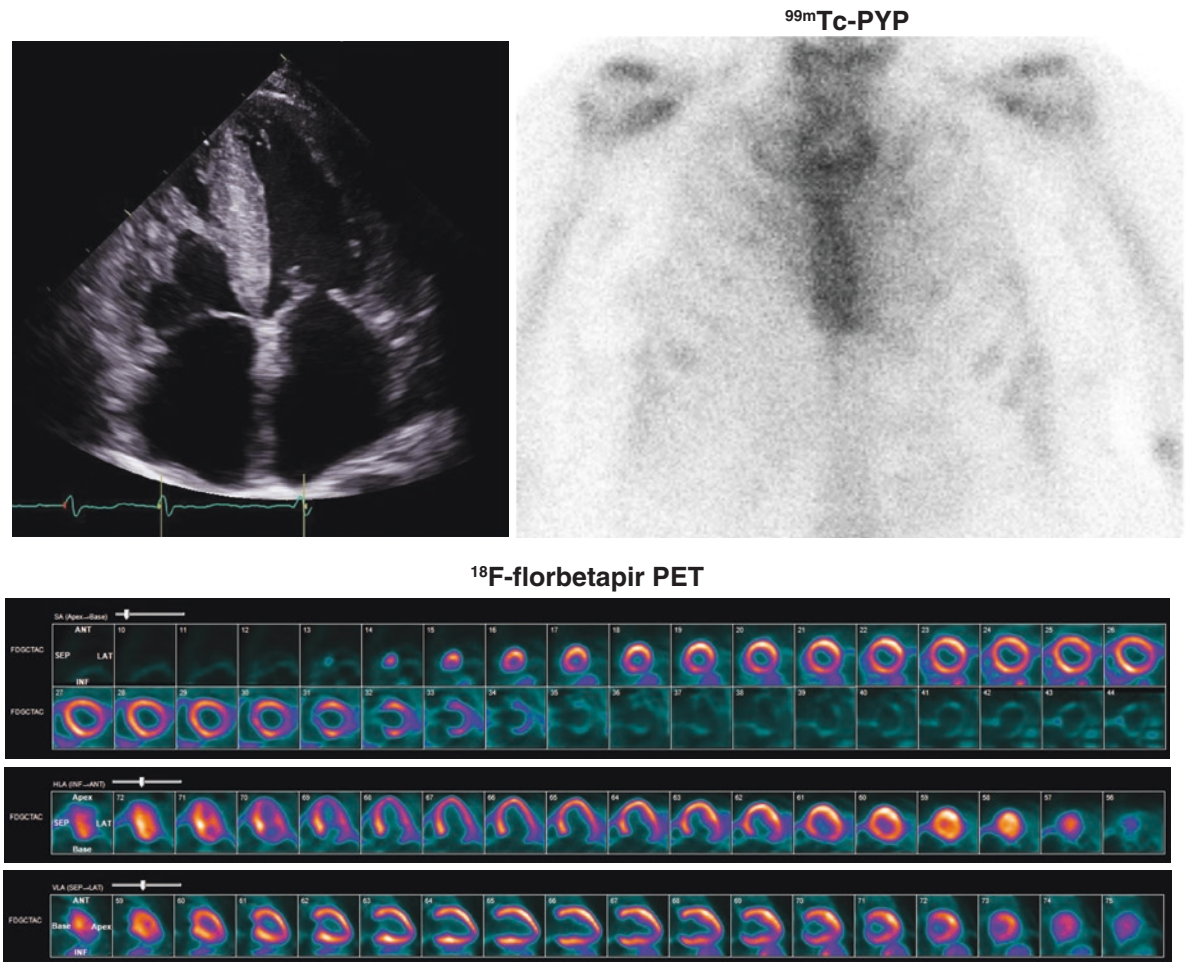

Fig. 13.11 ^{99m}Tc-PYP images in a patient with AL cardiac amyloidosis. In this 62-year-old African American man with a V122I TTR mutation, the echocardiographic *(top left panel)* and CMR imaging was consistent with cardiac amyloidosis, but the ^{99m}Tc-PYP scan *(top left panel)* was negative (grade 1), excluding ATTR cardiac amyloidosis. A complete hematological evaluation (serum free light chain levels, serum and urine immunofixation, and bone marrow biopsy) confirmed AL amyloidosis. ^{18}F-florbetapir PET/CT (*bottom*) showed diffuse myocardial uptake, confirming cardiac amyloidosis. When echocardiogram and CMR are highly suggestive of cardiac amyloidosis and the ^{99m}Tc-PYP scan is negative or shows grade 1 uptake, it is important to evaluate for AL cardiac amyloidosis

Amyloid-directed PET tracers, developed originally for imaging β-amyloid in the brain, including ^{18}F-florbetapir [12, 37], florbetaben [38], and flutemetamol, can image AL cardiac amyloidosis in the heart. These clinical PET tracers are not widely available and are expensive, but they offer the advantages of imaging both AL and ATTR amyloid deposits [12, 37] (Fig. 13.12), as well as extracardiac deposits in patients with systemic AL amyloidosis [39]; they also have been shown to detect early amyloid deposits in the heart [40].

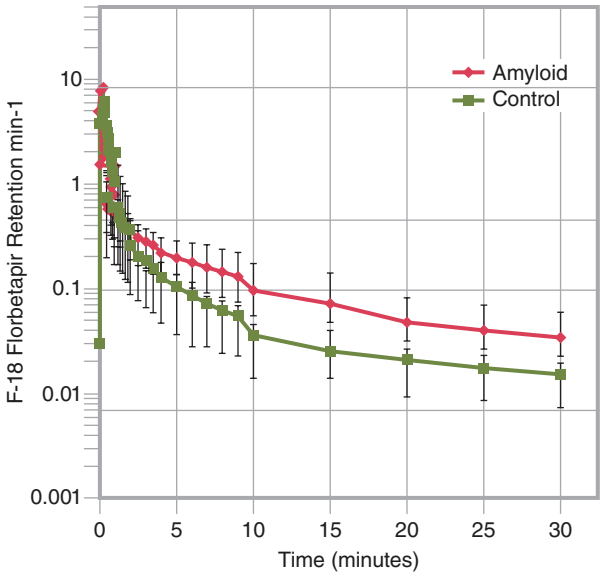

Fig. 13.12 ^{18}F-florbetapir PET/CT images and retention index in subjects with and without cardiac amyloidosis. This figure shows no myocardial ^{18}F-florbetapir uptake in the control patient (*top row*) and diffuse uptake in ATTR (*middle row*) and AL (*bottom row*) cardiac amyloidosis. The graph on the right shows that the ^{18}F-florbetapir myocardial retention index is significantly higher in the amyloid group (*red line*) than in the non-amyloid control group (*green line*)

Figure 13.13 presents a proposed approach to the evaluation of cardiac ATTR amyloidosis using bone tracer scintigraphy [34].

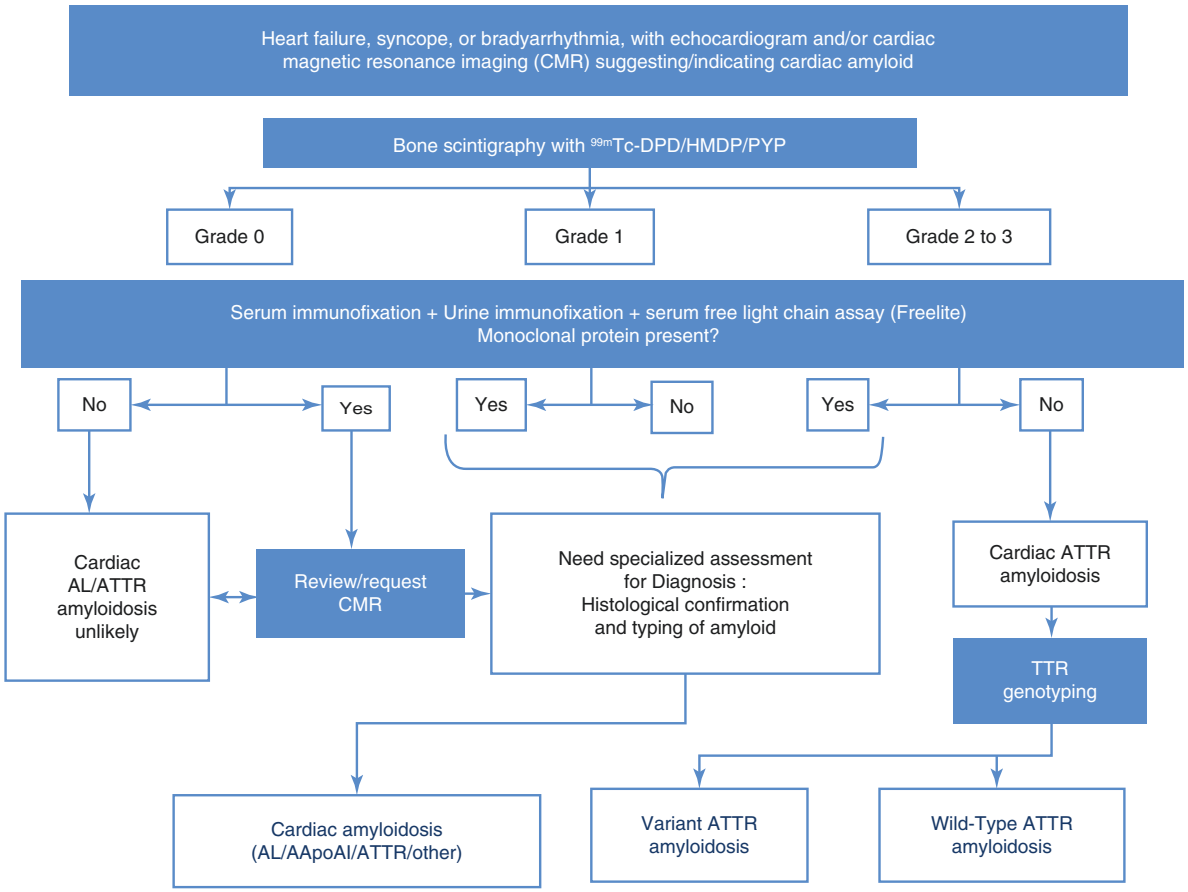

Fig. 13.13 A proposed approach to evaluation of cardiac ATTR amyloidosis using bone tracer scintigraphy. A grade 2 or 3 ^{99m}Tc-PYP myocardial uptake in the absence of evidence of plasma cell dyscrasia is nearly 100% specific for a diagnosis of ATTR cardiac amyloidosis. Endomyocardial biopsy may be considered when the ^{99m}Tc-PYP results are equivocal and the diagnosis is not clear after imaging-based evaluation. (*From* Gillmore et al. [34]; with permission from Wolters Kluwer)

Conflicts of Interest RHF has received consulting fees from Ionis Pharmaceuticals and Alnylam Pharmaceuticals and research funding from GlaxoSmithKline. SD has received consulting fees from Pfizer, AAA, and GE Healthcare.

Funding Support SD and RHF are supported by NIH RO1 grant (RO1 HL 130563 and RO1 HL 150342); SD is supported by American Heart Association Grant (AHA 16 CSA 2888 0004, and AHA19SRG34950011).

References

1. Perry A, Vuitch F. Causes of death in patients with sarcoidosis. A morphologic study of 38 autopsies with clinicopathologic correlations. Arch Pathol Lab Med. 1995;119:167–72.
2. Iannuzzi MC, Rybicki BA, Teirstein AS. Sarcoidosis. N Engl J Med. 2007;357:2153–65.
3. Dorbala S, Shaw LJ. Molecular phenotyping of infiltrative cardiomyopathies: the future. J Nucl Cardiol. 2019;26:154–7.
4. Chareonthaitawee P, Beanlands RS, Chen W, Dorbala S, Miller EJ, Murthy VL, et al. Joint SNMMI-ASNC expert consensus document on the role of (18)F-FDG PET/CT in cardiac sarcoid detection and therapy monitoring. J Nucl Cardiol. 2017;24:1741–58.
5. Slart R, Glaudemans A, Lancellotti P, Hyafil F, Blankstein R, Schwartz RG, et al. A joint procedural position statement on imaging in cardiac sarcoidosis: from the Cardiovascular and Inflammation & Infection Committees of the European Association of Nuclear Medicine, the European Association of Cardiovascular Imaging, and the American Society of Nuclear Cardiology. J Nucl Cardiol. 2018;25:298–319.
6. Okayama K, Kurata C, Tawarahara K, Wakabayashi Y, Chida K, Sato A. Diagnostic and prognostic value of myocardial scintigraphy with thallium-201 and gallium-67 in cardiac sarcoidosis. Chest. 1995;107:330–4.
7. Blankstein R, Osborne M, Naya M, Waller A, Kim CK, Murthy VL, et al. Cardiac positron emission tomography enhances prognostic assessments of patients with suspected cardiac sarcoidosis. J Am Coll Cardiol. 2014;63:329–36.
8. Youssef G, Leung E, Mylonas I, Nery P, Williams K, Wisenberg G, et al. The use of 18F-FDG PET in the diagnosis of cardiac sarcoidosis: a systematic review and metaanalysis including the Ontario experience. J Nucl Med. 2012;53:241–8.
9. Waller AH, Blankstein R. Quantifying myocardial inflammation using F18-fluorodeoxyglucose positron emission tomography in cardiac sarcoidosis. J Nucl Cardiol. 2014;21:940–3.
10. Dilsizian V, Bacharach SL, Beanlands RS, Bergmann SR, Delbeke D, Dorbala S, et al. ASNC imaging guidelines/SNMMI procedure standard for positron emission tomography (PET) nuclear cardiology procedures. J Nucl Cardiol. 2016;23:1187–226.
11. Slart R, Glaudemans A, Lancellotti P, Hyafil F, Blankstein R, Schwartz RG, Jaber WA, Russell R, Gimelli A, Rouzet F, Hacker M, Gheysens O, Plein S, Miller EJ, Dorbala S, Donal E and Document Reading G. A joint procedural position statement on imaging in cardiac sarcoidosis: from the Cardiovascular and Inflammation & Infection Committees of the European Association of Nuclear Medicine, the European Association of Cardiovascular Imaging, and the American Society of Nuclear Cardiology. Journal of nuclear cardiology : official publication of the American Society of Nuclear Cardiology. 2018;25:298–319.
12. Dorbala S, Vangala D, Semer J, Strader C, Bruyere JR, Di Carli MF, et al. Imaging cardiac amyloidosis: a pilot study using 18F-florbetapir positron emission tomography. Eur J Nucl Med Mol Imaging. 2014;41:1652–62.
13. Saby L, Laas O, Habib G, Cammilleri S, Mancini J, Tessonnier L, et al. Positron emission tomography/computed tomography for diagnosis of prosthetic valve endocarditis: increased valvular 18F-fluorodeoxyglucose uptake as a novel major criterion. J Am Coll Cardiol. 2013;61:2374–82.
14. Pizzi MN, Roque A, Fernandez-Hidalgo N, Cuellar-Calabria H, Ferreira-Gonzalez I, Gonzalez-Alujas MT, et al. Improving the diagnosis of infective endocarditis in prosthetic valves and intracardiac devices with 18F-fluordeoxyglucose positron emission tomography/computed tomography angiography: initial results at an infective endocarditis referral center. Circulation. 2015;132:1113–26.
15. Sarrazin JF, Philippon F, Tessier M, Guimond J, Molin F, Champagne J, et al. Usefulness of fluorine-18 positron emission tomography/computed tomography for identification of cardiovascular implantable electronic device infections. J Am Coll Cardiol. 2012;59:1616–25.
16. Juneau D, Golfam M, Hazra S, Zuckier LS, Garas S, Redpath C, et al. Positron emission tomography and single-photon emission computed tomography imaging in the diagnosis of cardiac implantable electronic device infection: a systematic review and meta-analysis. Circ Cardiovasc Imaging. 2017;10. pii: e005772.
17. Kim J, Feller ED, Chen W, Liang Y, Dilsizian V. FDG PET/CT for early detection and localization of left ventricular assist device infection: impact on patient management and outcome. JACC Cardiovasc Imaging. 2019;12:722–9.
18. Lalani T, Chu VH, Park LP, Cecchi E, Corey GR, Durante-Mangoni E, et al. In-hospital and 1-year mortality in patients undergoing early surgery for prosthetic valve endocarditis. JAMA Intern Med. 2013;173:1495–504.
19. Habib G, Lancellotti P, Antunes MJ, Bongiorni MG, Casalta JP, Del Zotti F, et al. 2015 ESC guidelines for the management of infective endocarditis: The Task Force for the Management of Infective Endocarditis of the European Society of Cardiology (ESC). Endorsed by: European Association for Cardio-Thoracic Surgery (EACTS), the European Association of Nuclear Medicine (EANM). Eur Heart J. 2015;36:3075–128.
20. Erba PA, Conti U, Lazzeri E, Sollini M, Doria R, De Tommasi SM, et al. Added value of 99mTc-HMPAO-labeled leukocyte SPECT/CT in the characterization and management of patients with infectious endocarditis. J Nucl Med. 2012;53:1235–43.
21. Erba PA, Sollini M, Conti U, Bandera F, Tascini C, De Tommasi SM, et al. Radiolabeled WBC scintigraphy in the diagnostic workup of patients with suspected device-related infections. JACC Cardiovasc Imaging. 2013;6:1075–86.
22. Gomes A, Glaudemans A, Touw DJ, van Melle JP, Willems TP, Maass AH, et al. Diagnostic value of imaging in infective endocarditis: a systematic review. Lancet Infect Dis. 2017;17:e1–14.
23. Mahmood M, Kendi AT, Ajmal S, Farid S, O'Horo JC, Chareonthaitawee P, et al. Meta-analysis of 18F-FDG PET/CT in the diagnosis of infective endocarditis. J Nucl Cardiol. 2019;26:922–35.
24. Kyle RA, Gertz MA. Primary systemic amyloidosis: clinical and laboratory features in 474 cases. Semin Hematol. 1995;32:45–59.
25. Connors LH, Doros G, Sam F, Badiee A, Seldin DC, Skinner M. Clinical features and survival in senile systemic amyloidosis: comparison to familial transthyretin cardiomyopathy. Amyloid. 2011;18 Suppl 1:157–9.
26. Dungu JN, Valencia O, Pinney JH, Gibbs SD, Rowczenio D, Gilbertson JA, et al. CMR-based differentiation of AL and ATTR cardiac amyloidosis. JACC Cardiovasc Imaging. 2014;7:133–42.
27. Perugini E, Guidalotti PL, Salvi F, Cooke RM, Pettinato C, Riva L, et al. Noninvasive etiologic diagnosis of cardiac amyloidosis using 99mTc-3,3-diphosphono-1,2-propanodicarboxylic acid scintigraphy. J Am Coll Cardiol. 2005;46:1076–84.

28. Gertz MA, Brown ML, Hauser MF, Kyle RA. Utility of technetium Tc 99m pyrophosphate bone scanning in cardiac amyloidosis. Arch Intern Med. 1987;147:1039–44.
29. Rapezzi C, Guidalotti P, Salvi F, Riva L, Perugini E. Usefulness of 99mTc-DPD scintigraphy in cardiac amyloidosis. J Am Coll Cardiol. 2008;51:1509–10; author reply 1510.
30. Bokhari S, Castaño A, Pozniakoff T, Deslisle S, Latif F, Maurer MS. 99mTc-pyrophosphate scintigraphy for differentiating light-chain cardiac amyloidosis from the transthyretin-related familial and senile cardiac amyloidoses. Circ Cardiovasc Imaging. 2013;6:195–201.
31. Castaño A, Haq M, Narotsky DL, Goldsmith J, Weinberg RL, Morgenstern R, et al. Multicenter study of planar technetium 99m pyrophosphate cardiac imaging: predicting survival for patients with ATTR cardiac amyloidosis. JAMA Cardiol. 2016;1:880–9.
32. Rapezzi C, Quarta CC, Guidalotti PL, Pettinato C, Fanti S, Leone O, et al. Role of 99mTc-DPD scintigraphy in diagnosis and prognosis of hereditary transthyretin-related cardiac amyloidosis. JACC Cardiovasc Imaging. 2011;4:659–70.
33. Dorbala S, Bokhari S, Miller E, Bullock-Palmer R, Soman P, Thompson R. 99mTechnetium-Pyrophosphate imaging for transthyretin cardiac amyloidosis. ASNC Practice Points. American Society of Nuclear Cardiology, Fairfax, VA. 2016. https://www.asnc.org/Files/Practice%20Resources/Practice%20Points/ASNC%20Practice%20Point-99mTechnetiumPyrophosphateImaging2016.pdf. Accessed 26 Aug 2019.
34. Gillmore JD, Maurer MS, Falk RH, Merlini G, Damy T, Dispenzieri A, et al. Nonbiopsy diagnosis of cardiac transthyretin amyloidosis. Circulation. 2016;133:2404–12.
35. Haq M, Pawar S, Berk JL, Miller EJ, Ruberg FL. Can (99m) Tc-Pyrophosphate aid in early detection of cardiac involvement in asymptomatic variant TTR amyloidosis? JACC Cardiovasc Imaging. 2017;10:713–4.
36. Lee VW, Caldarone AG, Falk RH, Rubinow A, Cohen AS. Amyloidosis of heart and liver: comparison of Tc-99m pyrophosphate and Tc-99m methylene diphosphonate for detection. Radiology. 1983;148:239–42.
37. Park MA, Padera RF, Belanger A, Dubey S, Hwang DH, Veeranna V, et al. 18F-Florbetapir binds specifically to myocardial light chain and transthyretin amyloid deposits: autoradiography study. Circ Cardiovasc Imaging. 2015;8. pii:e002954.
38. Law WP, Wang WY, Moore PT, Mollee PN, Ng AC. Cardiac amyloid imaging with 18F-florbetaben positron emission tomography: a pilot study. J Nucl Med. 2016;57:1733–9.
39. Wagner T, Page J, Burniston M, Skillen A, Ross JC, Manwani R, et al. Extracardiac (18)F-florbetapir imaging in patients with systemic amyloidosis: more than hearts and minds. Eur J Nucl Med Mol Imaging. 2018;45:1129–38.
40. Cuddy SAM, Bravo PE, Falk RH, El-Sady S, Kijewski MF, Park MA, Ruberg FL, Sanchorawala V, Landau H, Yee AJ, Bianchi G, Di Carli MF, Cheng SC, Jerosch-Herold M, Kwong RY, Liao R and Dorbala S. Improved Quantification of Cardiac Amyloid Burden in Systemic Light Chain Amyloidosis: Redefining Early Disease? JACC Cardiovascular imaging. 2020;13:1325–1336

14 Clinical Molecular Imaging of Inflammation and Calcification in Atherosclerosis

Azar Radfar, Jack P. Andrews, Marc R. Dweck, Jagat Narula, and Ahmed Tawakol

Atherosclerotic cardiovascular disease is the leading cause of mortality worldwide [1]. Once considered relatively inert gruel deposition on the vessel wall, atherosclerosis is now recognized as a highly dynamic and complex process. It involves many molecules and risk factors that trigger its development, promote its progression, and lead to complications that include atherothrombotic events in the setting of vulnerable plaque ruptures. Traditional imaging tools, such as coronary angiography, have long been used to evaluate atherosclerotic disease. Angiography provides well-validated assessments of risk through high-resolution visualization of luminal narrowing, but these luminal evaluations provide little insight into the atherosclerotic plaques that result in major cardiac events. CT angiography allows evaluation of plaque morphology and the detection of plaques at increased risk of rupture and of patients at higher risk of acute coronary events. In addition, evolving molecular imaging approaches also enable identification of high-risk plaque features and the activity of biological processes underlying the development, progression, and clinical complications of atheromatous plaques [2, 3]. Among the molecular imaging approaches, positron emission tomography–computed tomography (PET-CT) has been used and validated most extensively in human studies. This chapter focuses on PET-CT approaches to identify and characterize high-risk plaque features, and how these tools may be used to gain biological and clinical insights. Only clinically relevant imaging tools are highlighted.

A. Radfar · A. Tawakol (✉)
Cardiology Division, Massachusetts General Hospital and Harvard Medical School, Boston, MA, USA
e-mail: atawakol@mgh.harvard.edu

J. P. Andrews
University of Edinburgh, Edinburgh, UK

M. R. Dweck
Center for Cardiovascular Science, University of Edinburgh, Edinburgh, UK

J. Narula
Icahn School of Medicine at Mount Sinai, New York, NY, USA

V. Dilsizian, J. Narula (eds.), *Atlas of Nuclear Cardiology*, https://doi.org/10.1007/978-3-030-49885-6_14

Biology of At-herosclerosis

Atherosclerosis is a chronic inflammatory process. In large and medium-sized arteries, oxidized low-density lipoprotein (LDL) triggers endothelial expression of leukocyte adhesion molecules such as vascular cell adhesion molecules-1 (VCAM-1) and selectins, which then facilitate binding of circulating monocytes and T lymphocytes (Fig. 14.1). Inflammatory mediators, cytokines, and extracellular matrix molecules released by immune cells perpetuate the inflammatory cycles. Foam cells, which are oxidized, lipid-laden macrophages primarily derived from recruited monocytes, accumulate in subendothelial plaques. Released fatty debris from apoptotic lipid-filled macrophages and smooth muscle cells enhance the growing lipid-rich necrotic core. Hypoxia-induced angiogenesis produces leaky microvessels, which cause intraplaque hemorrhages, adding to plaque vulnerability. Microcalcification (which also happens in the overlying fibrous cap) may add to destabilization of the enlarging plaque [2]. Finally, metalloproteinases released by activated immune cells weaken the fibrous cap of the atheroma, thereby increasing the risk of plaque rupture and its clinical atherothrombotic complications [5].

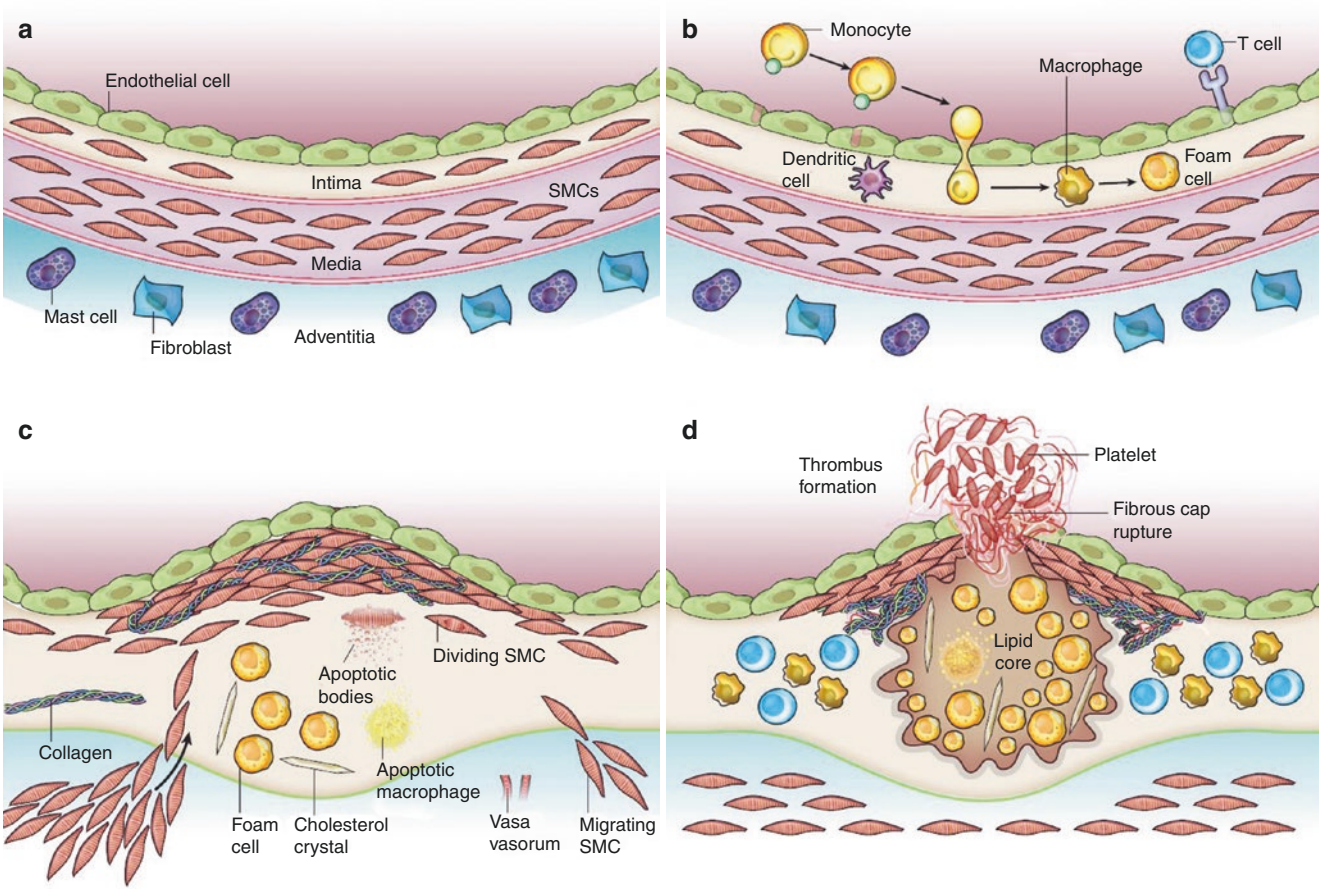

Fig. 14.1 Formation and progression of the atherosclerotic lesion. (**a**) A normal artery consists of three layers: (1) tunica intima, a monolayer of endothelial cells at the luminal side and smooth muscle cells (SMCs) at the opposite side; (2) tunica media, a muscular layer with SMCs within an extracellular matrix; and (3) adventitia, which contains mast cells, nerve terminals, and microvessels. (**b**) Early atherosclerotic plaque formation, which begins with recruitment and adhesion of migrating leukocytes to the site of intimal inflammation, and formation of foam cells through uptake of oxidized low-density lipoproteins by predominant monocyte-derived macrophages. (**c**) Plaque progression through proliferation of SMCs and augmentation of the extracellular matrix. This stage is then followed by dying of lipid-laden cells, which produces a lipid-rich necrotic core and subsequent hypoxia-induced angiogenesis, noted by microvessels. Altogether, these contribute to plaque instability. (**d**) Fibrous cap rupture, thrombus formation, and potential blood flow obstruction. (From Libby et al. [4], with permission from Springer Nature)

The critical role of inflammation in the pathobiology of cardiovascular disease (CVD) has been extensively investigated. Both experimental and clinical data now demonstrate decreased CVD through reductions in inflammation. The anti-inflammatory effect of statins was previously reported through different clinical studies. More recently, the Canakinumab Anti-inflammatory Thrombosis Outcomes Study (CANTOS) randomized controlled trial evaluated the effect of anti-inflammatory mediators on future cardiovascular events. CANTOS demonstrated a significant reduction of recurrent cardiovascular events in individuals who received interleukin-1β (IL-1β) monoclonal antibody [6], independent of lipid levels. This provided the first proof of causality between inflammation and atherothrombosis by showing that selective anti-inflammatory approaches decrease CVD events (Fig. 14.2).

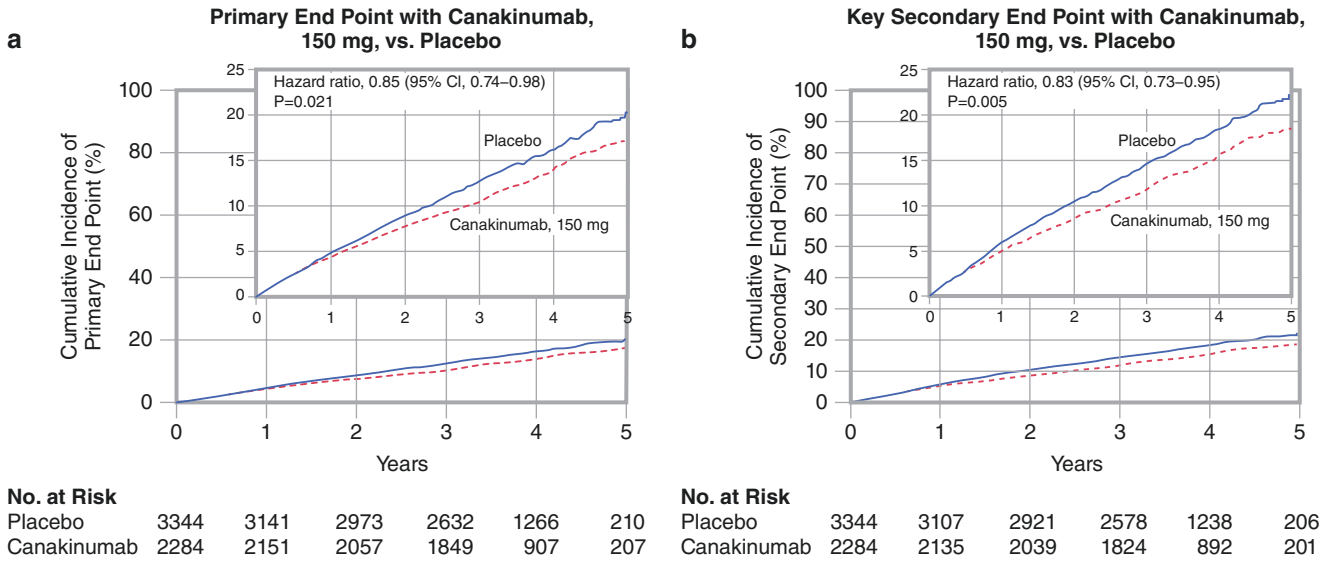

Fig. 14.2 Cumulative incidence of the primary and key secondary cardiovascular endpoints with the IL-1β antagonist canakinumab *vs.* placebo. Panel A demonstrates a reduction in the cumulative incidence of nonfatal myocardial infarction, nonfatal stroke, or cardiovascular death (primary endpoint) in the 150 mg canakinumab group versus the placebo group (p = 0.021 for the between-group difference). Panel B shows the key secondary endpoint, which also included hospitalization for unstable angina that resulted in urgent revascularization (p = 0.005 for the between-group difference). The insets show the same data with the y axis enlarged. (From Ridker et al. [6]. Copyright © 2017 Massachusetts Medical Society. Reprinted with permission from Massachusetts Medical Society)

Imaging of Cardiovascular Inflammation

Given the central role that inflammation plays in the atherosclerotic disease process, the imaging of plaque inflammation has been increasingly studied. ^{18}F-fluorodeoxyglucose (FDG) PET-CT is widely used to image metabolically active tissues including tumors, inflammatory foci, and atherosclerotic plaques [2, 7]. FDG is a radioactive analogue of glucose, which accumulates within tissues in proportion to its underlying glycolytic rate. Because inflammatory cells, as well as tumors, have high glycolytic rates, FDG PET-CT imaging is used clinically to identify malignant tissues, as well as to identify and monitor inflammatory foci, including cardiac device infection, endocarditis, and cardiac sarcoidosis (Figs. 14.3, 14.4, 14.5, and 14.6).

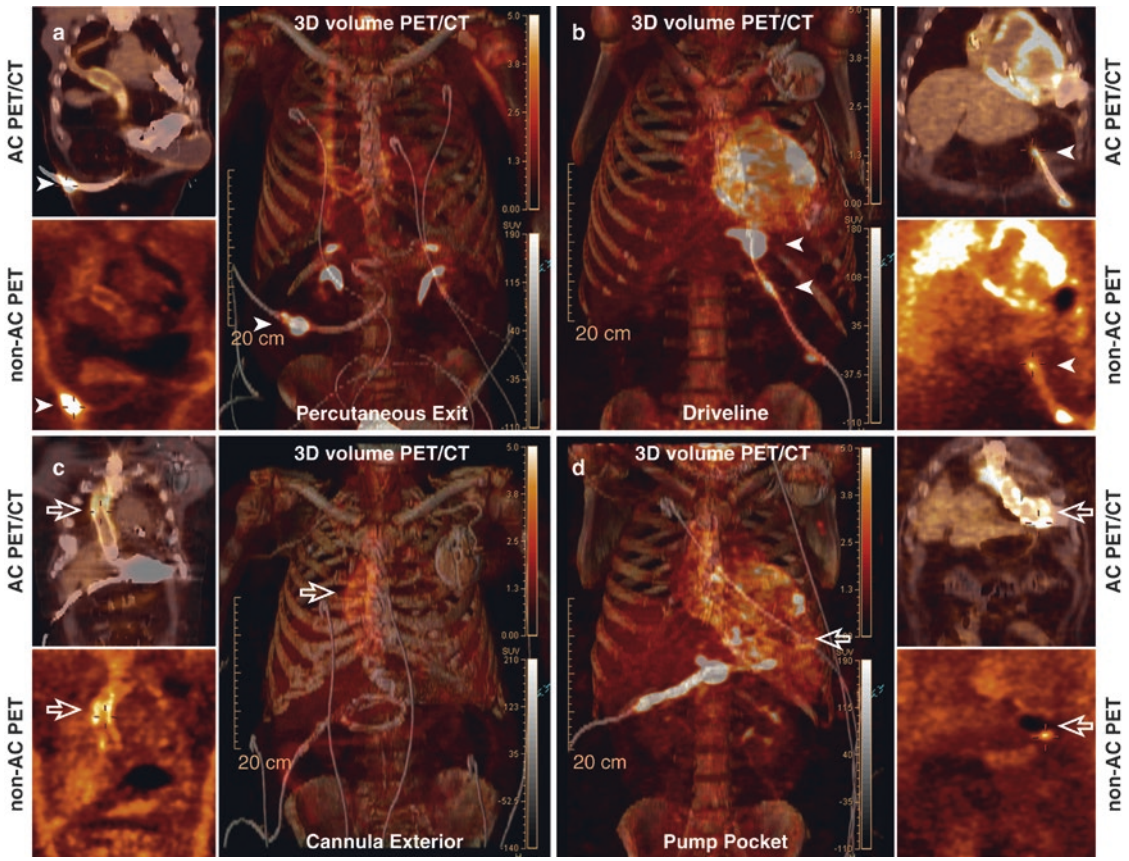

Fig. 14.3 PET-CT imaging of device infection. Representative PET images with CT attenuation correction (AC PET) and without attenuation correction (non-AC PET) are shown, adjacent to three-dimensional (3D) volume-fused PET-CT images. Increased FDG uptake, indicative of inflammation due to infection, can be seen in an individual with a left ventricular assist device (LVAD). *Arrows* highlight multiple areas of likely infection, including the percutaneous exit (**a**) driveline (**b**) cannula exterior (**c**) and pump pocket (**d**). (From Kim et al. [8]; with permission from Elsevier)

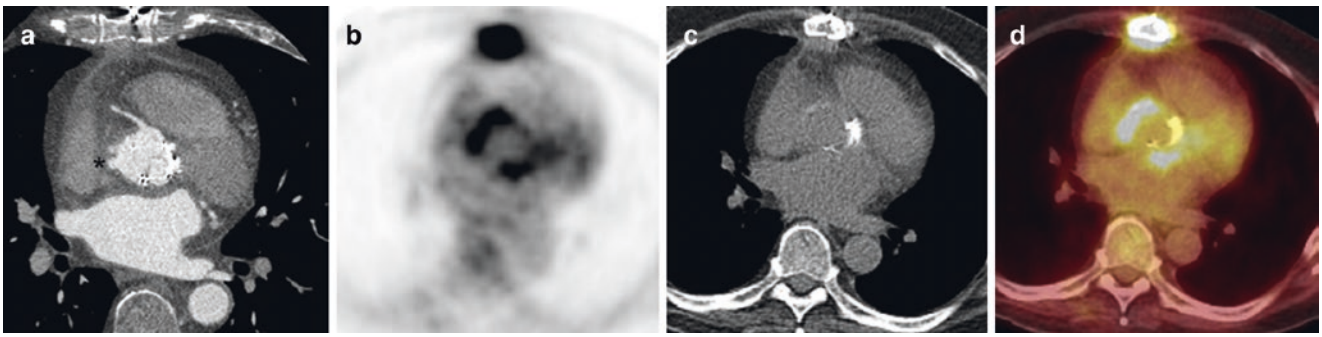

Fig. 14.4 FDG PET-CT in the evaluation of suspected prosthetic valve endocarditis. ECG-gated CT imaging demonstrates increased wall thickness of the aortic root and likely a small pseudoaneurysm (*asterisk*) (**a**). FDG-PET (**b**) CT (**c**) and FDG PET-CT (**d**) revealed high FDG uptake in the aortic wall, suggesting intense inflammatory cell activity related to infection. Surgery confirmed abscess in the same area. (From Fagman et al. [9]; with permission from Springer Nature)

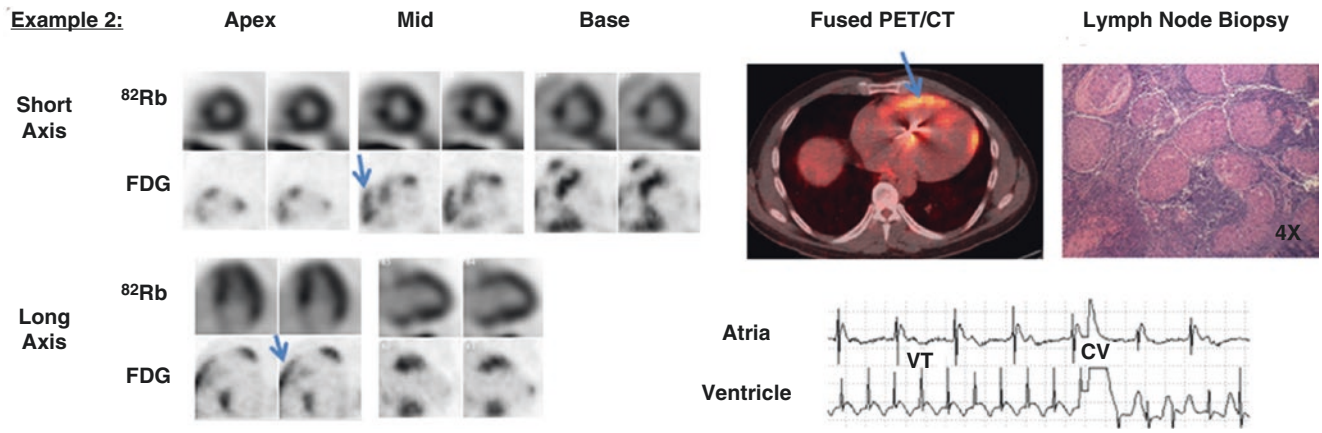

Fig. 14.5 FDG PET-CT imaging of suspected cardiac sarcoidosis. Focal myocardial FDG uptake in sarcoidosis. FDG PET-CT was performed to evaluate for possible cardiac sarcoidosis in a patient with pulmonary sarcoidosis. Hypoperfusion (^{82}Rb imaging) along with focal FDG uptake are shown, together with several focal areas of increased metabolic activity, including over the right ventricle (*arrows*). The diagnosis of sarcoidosis was confirmed by lymph node biopsy. The patient underwent ICD implantation and experienced an episode of ventricular tachycardia (VT) less than a month after implantation of the ICD (rhythm strip). (From Blankstein et al. [10]; with permission from Elsevier)

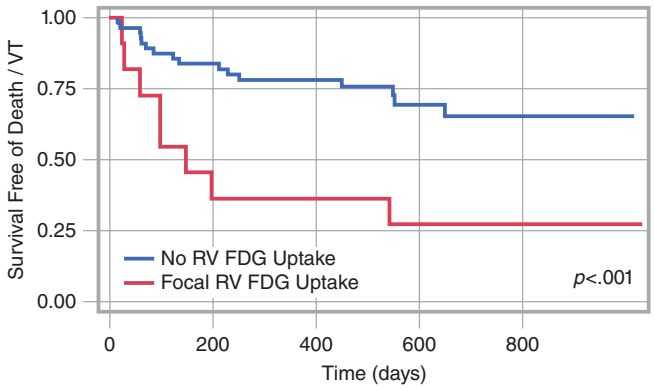

Fig. 14.6 Kaplan-Meier survival analysis for freedom from death or ventricular tachycardia (VT). Individuals were stratified by the presence or absence of inflammation identified as focal increased right ventricular FDG uptake on PET. (From Blankstein et al. [10]; with permission from Elsevier)

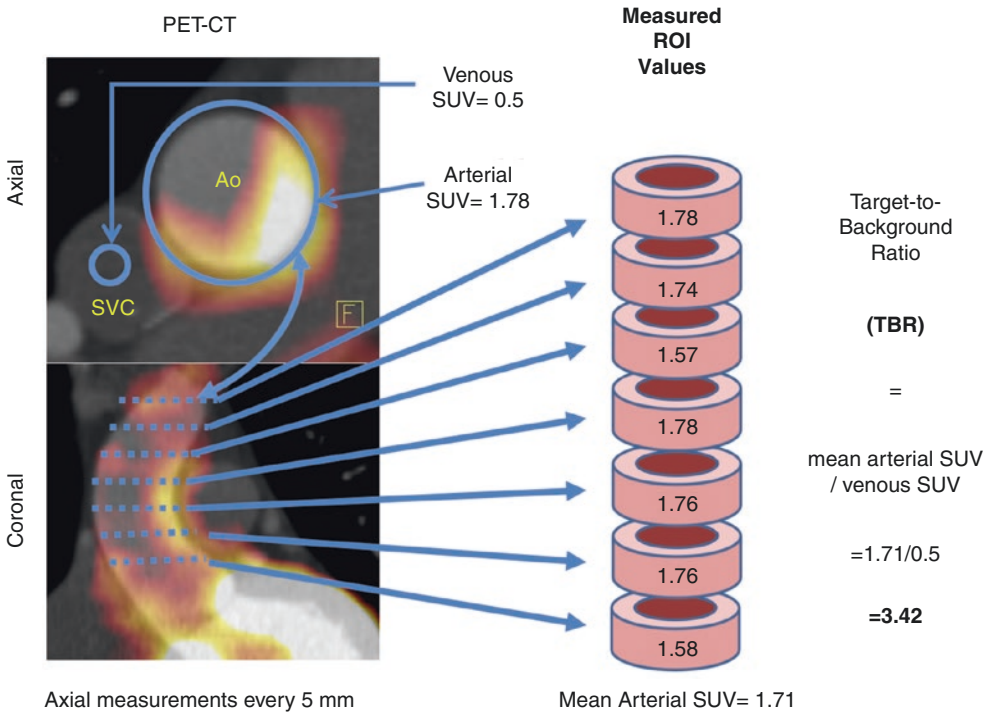

Fig. 14.7 Method for quantifying arterial FDG uptake. Aortic FDG uptake was measured in consecutive axial slices starting several millimeters above the origin of coronary arteries (to prevent interference by myocardial uptake). Regions of interest (ROI) are drawn along the long axis of the aorta and the standardized uptake values (SUV) are recorded, and then averaged to provide an average SUV (1.71 in this example). Subsequently, the arterial SUV is corrected for background blood activity (background SUV) to yield a target-to-background-ratio (TBR), which provides a reproducible approximation of arterial wall inflammation. Ao aorta, SVC superior vena cava

The propensity for FDG to accumulate in inflammatory cells additionally enables measurement of atherosclerotic plaque inflammation (Fig. 14.7). It was demonstrated that the uptake of FDG along the arterial wall correlates with the degree of macrophage staining seen histologically after endarterectomy (Fig. 14.8) [11].

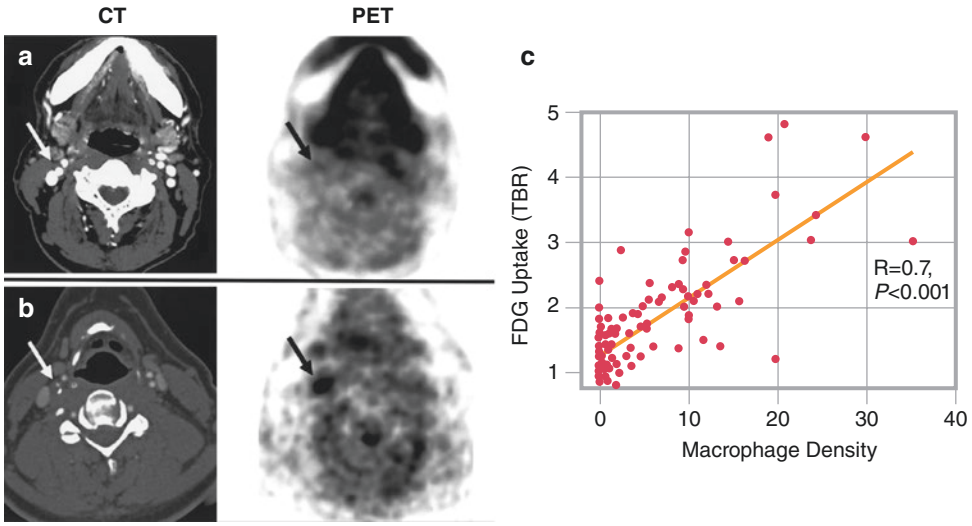

Fig. 14.8 Axial PET-CT images from two patients (**a** and **b**). Patient A showed lower FDG uptake in the carotid atherosclerotic plaque prior to endarterectomy; patient B showed higher FDG uptake. *Arrows* point at the region of the carotid plaque that was subsequently removed surgically. On histological evaluation after endarterectomy, the carotid plaque specimen from patient A contained a high amount of collagen and low inflammatory cell density. On the other hand, the carotid plaque specimen excised from patient B demonstrated a necrotic core and high macrophage staining. Across the study population (**c**) carotid FDG uptake (as TBR measured prior to endarterectomy) correlated with the histologically assessed macrophage staining of the same plaques. (From Tawakol et al. [11]; with permission from Elsevier)

In addition to FDG, several novel PET radiotracers (Table 14.1) are under investigation for molecular imaging of atherosclerotic inflammation, along with imaging other aspects of plaque biology (Fig. 14.9).

Agent	Potential mechanism of uptake
^{18}F-FLT	Structural analogue of thymidine, accumulates within areas with active DNA synthesis
^{11}C-PK11195	Affinity for translocator protein, upregulated on inflammatory cells
^{18}F-A85380	Binds arterial nicotinic acetylcholine receptors; possibly related to vascular damage
^{18}F-choline	Images increased cell wall synthesis within atheroma
^{68}Ga-DOTA-octreotate	Affinity for somatostatin receptors, which are highly expressed on macrophages
^{64}Cu-ATSM	Accumulates within hypoxic cells
^{18}F-MISO	Accumulates within hypoxic cells
^{68}Ga-NOTA-RGD	Targets integrin $a_v\beta_3$ expressed by macrophages and activated endothelial cells associated with angiogenesis
^{18}F-Galacto-RGD	Targets integrin $a_v\beta_3$expressed by macrophages and activated endothelial cells associated with angiogenesis
^{18}F-Fluciclatide	Targets integrin $a_v\beta_3$, used as a biomarker of cardiac healing and repair post myocardial infarction
^{64}Cu-DOTA-CANF	Images neo-angiogenesis via natriuretic peptide receptor affinity
^{18}F-FDG	A glucose analogue that accumulates within cells in proportion to glycolysis. Inflamed or hypoxic tissues manifest high FDG uptake.
^{18}F-FDM	An isomer of FDG. Also accumulates within inflamed tissues
^{18}F–sodium fluoride	Accumulates within areas of active microcalcification
^{68}Ga-CXCR4	Images CXCR4 receptor expressed by inflammatory cells
^{18}F-florbetapen	Imaging β-amyloid plaque

From Teague et al. [12]; with permission from Elsevier
^{11}*C-PK11195* ^{11}C-(2-chlorophenyl)-N-methyl-N-(1-methylpropyl)-3-isoquinolinecarboxamide, *A85380* 3-([2S]-azetidinylmethoxy)pyridine dihydrochloride, *ATSM* diacetyl-bis (N-methylthiosemicarbazone, *CXCR4C-X*-C chemokine receptor type 4, *DOTA-CANF* 1,4,7,10-tetraazacyclododecane-1,4,7,10-tetraacetic acid atrial natriuretic factor, *FDG* fluorodeoxyglucose, *FDM* fluorodeoxymannose, *FLT* fluorothymidine, ^{18}*F-MISO* fluoromisonidazole, *NOTA-RGD* 1,4,7-triazacyclononane-N,N′,N″-triacetic acid arginine-glycine-aspartate

Table 14.1 A partial list of current agents and their potential mechanisms of uptake used at molecular imaging of atherosclerotic plaque biology

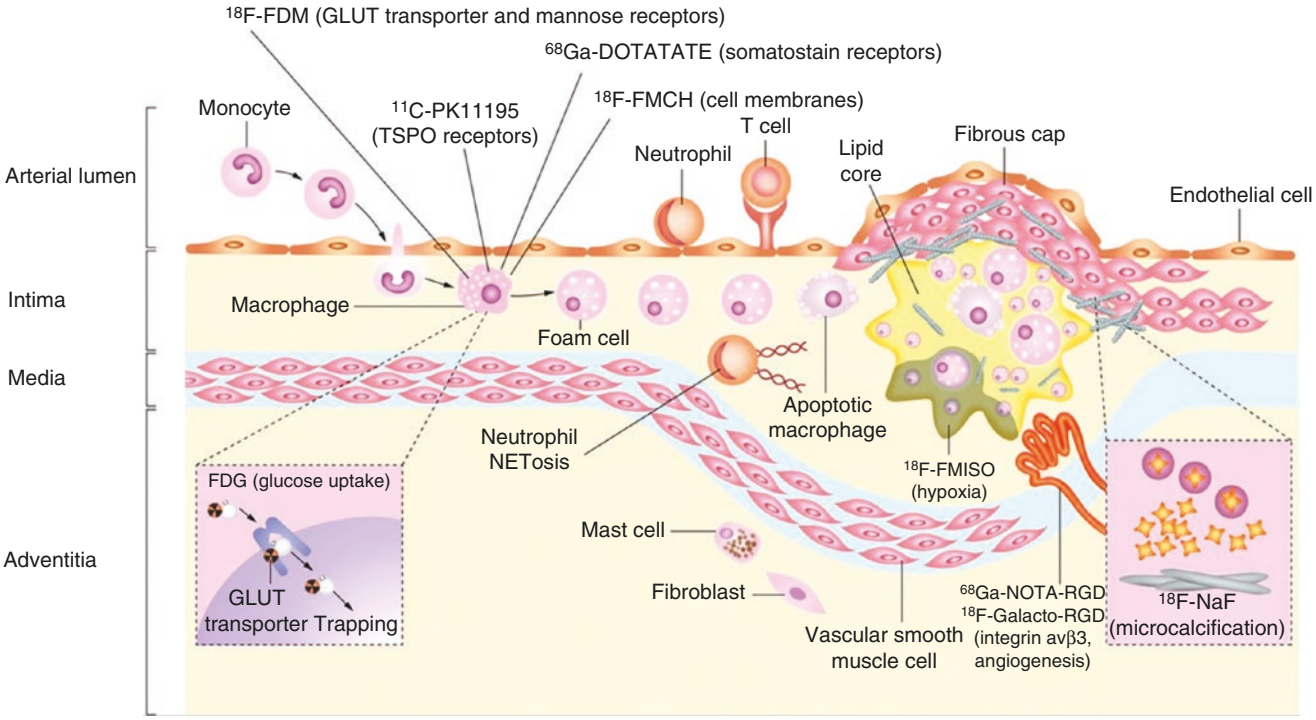

Fig. 14.9 Molecular targets for atherosclerosis imaging with PET. In developing atherosclerotic plaques, metabolically active macrophages accumulate ^{18}F-fluorodeoxyglucose glucose (FDG). ^{18}F-fluorodeoxymannose (FDM) also enters macrophages through glucose transporters and mannose receptors. ^{68}Ga-DOTATATE tracer targets somatostatin receptors expressed on activated macrophages. Macrophage infiltration can also be demonstrated by new tracers targeting translocator protein receptors (^{11}C-PK11195) and macrophage cell membranes (^{18}F-FMCH). Further radiotracers target atherosclerotic plaque features such as microcalcification (^{18}F-sodium fluoride), neoangiogenesis (^{68}Ga-NOTA-RGD, ^{18}F-Galacto-RGD), and cellular hypoxia (^{18}F-FMISO). (From Joseph and Tawakol [2]; with permission from Oxford University Press)

Insights into Clinical Risk

The arterial inflammatory signal has been repeatedly shown to provide insights into clinical risk. Animal studies have demonstrated that atherosclerotic plaques with higher FDG uptake are more likely to rupture [13]. Moreover, in humans, higher arterial FDG uptake independently associates with an increased risk of CVD events (Fig. 14.10) [14].

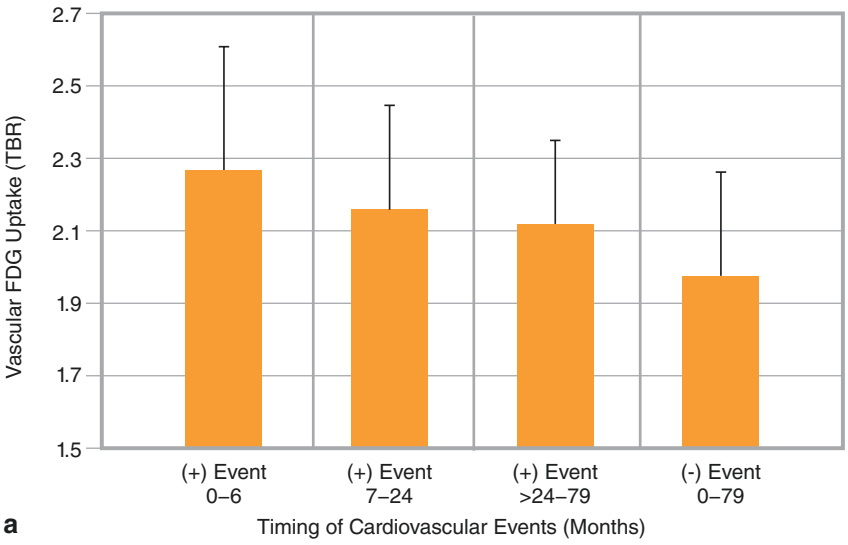

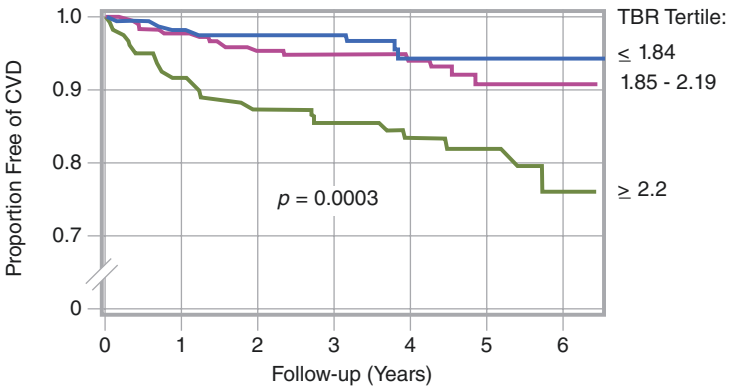

Number at Risk:							Adjusted HR:
TBR Tertile 1:167	160	149	120	75	36	10	1.0 (Referent)
TBR Tertile 2:224	216	199	170	112	58	14	1.36 (0.55, 3.35)
TBR Tertile 3:122	108	101	92	74	40	14	4.71 (1.98, 11.2)

b

Fig. 14.10 Arterial inflammation predicts subsequent incident cardiovascular disease (CVD). Clinical FDG PET-CT imaging was performed in 513 individuals without prior CAD (and without active cancer) at baseline. Subsequently, arterial inflammation was assessed on index scans, after which incident CVD events were adjudicated. Arterial inflammation (as aortic FDG uptake) was found to be substantially higher among individuals who had subsequent CVD events. Further, the FDG signal was associated with the timing of subsequent CVD: Individuals with the highest arterial inflammatory signal were prone to develop CVD sooner (**a**). The bars show the average target-to-background ratio (TBR) and standard deviation (SD) in patients who developed CVD at 0–months, 7–24 months, and > 24–79 months, or no events in 79 months. When aortic TBR values were divided into tertiles (**b**) those with the highest signals at baseline (tertile 3, TBR ≥2.2) had a > 4-fold increased risk of CVD compared with individuals with the lowest tertile TBR (p = 0.0003). (From Figueroa et al. [14]; with permission from Elsevier)

Imaging Coronary Plaque Inflammation

FDG PET-CT imaging of coronary inflammation is feasible, but myocardial uptake and coronary motion render it unreliable. Alternative approaches that more readily enable imaging of coronary plaque inflammation currently include the use of tracers that more selectively target inflammation, such as DOTATATE (Fig. 14.11), or novel technical advances that can correct for coronary motion.

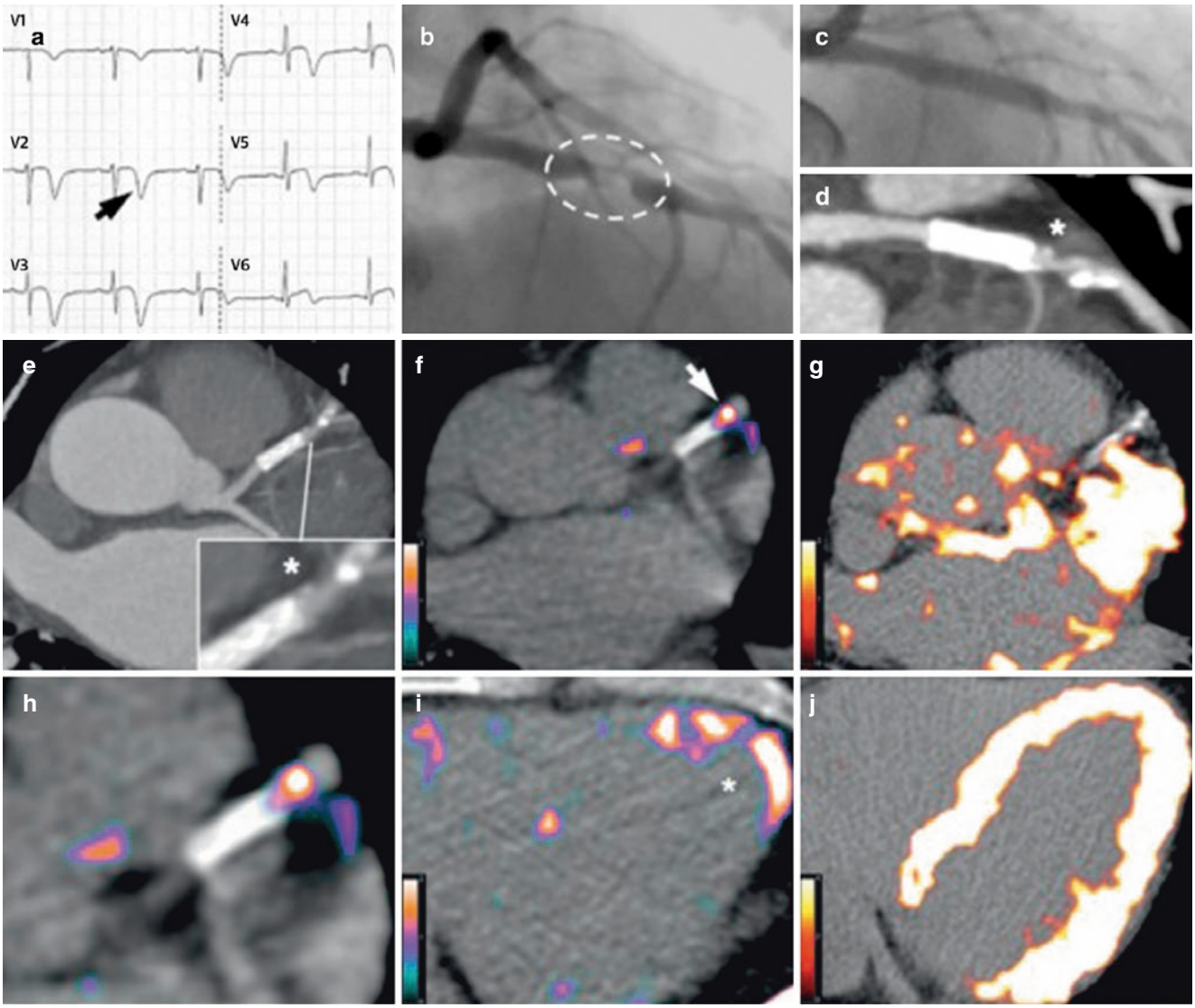

Fig. 14.11 Comparison of coronary PET imaging using gallium-68-labeled DOTATATE (^{68}Ga-DOTATATE) versus FDG, using images from a patient presenting with an acute coronary syndrome (**a**). Angiography showed a culprit left anterior descending artery lesion (*dashed oval*) (**b**). A stent was placed (**c**), but CT angiography (**d** and **e**) showed residual plaque (*asterisks*) at the distal end of the stent. ^{68}Ga-DOTATATE PET was performed (**f**, **h**, **i**), revealing focal DOTATATE uptake, indicative of intense inflammation just distal to the stent. Figure (**i**) shows infarcted myocardium (*asterisk*), which also demonstrated increased ^{68}Ga-DOTATATE PET uptake. FDG PET images (**g**, **j**) are shown for a case where myocardial FDG uptake was inadequately suppressed by the dietary preparation. This resulted in diffusely increased myocardial FDG uptake that precluded evaluation of focal coronary FDG uptake. (From Tarkin et al. [15]; CC-BY)

Imaging of Vascular Microcalcification

Atherosclerotic plaque calcification is another important hallmark of atheromatous plaques. Plaque calcification can be broadly classified into microcalcification and macrocalcification. Macrocalcification, commonly reported on CT imaging, suggests stable atherosclerotic lesions. Microcalcification, which is detectable only by molecular imaging, seems to be associated with increased susceptibility for plaque rupture, perhaps through increasing mechanical stress (Fig. 14.12). ^{18}F-sodium fluoride (NaF), a PET radiotracer long used in the diagnosis of bone metastasis, preferentially binds to microcalcification. There, hydroxyl ions in the exposed non-crystalline hydroxyapatite are substituted by ^{18}F, which enables its detection [16]. Clinical studies have demonstrated higher NaF uptake in patients with increased cardiovascular risk factors, higher calcium scores, and in symptomatic patients with high risk plaques [16] (Figs. 14.13 and 14.14). A prospective observational multicenter study, Prediction of Recurrent Events With ^{18}F-Fluoride (PREFFIR) is currently investigating NaF PET-CT to detect vulnerable coronary atherosclerotic plaques and to assesses the prognostic significance of tracer uptake [3, 18].

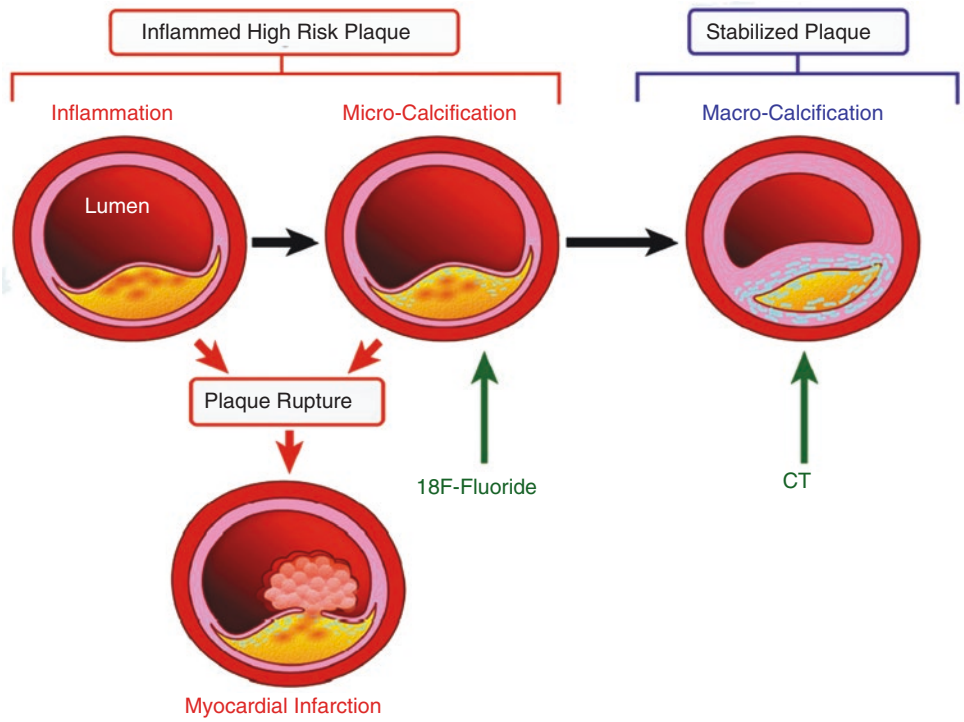

Fig. 14.12 From inflammation to calcification to myocardial infarction. Atherothrombotic events often result from the rupture of a plaque with an enlarging necrotic lipid core, worsening inflammation, and a thin, fibrous cap. Intimal calcification is considered a part of the healing process subsequent to plaque rupture or erosions. Microcalcification can be detected by ^{18}F-sodium fluoride (NaF) FDG-PET, and associates with an increased risk of rupture through ongoing inflammation that is yet to heal. On the other hand, macrocalcification occurs through progressive calcification of less-inflamed plaques; it may serve to shield the necrotic core from mechanical disturbances. Macrocalcification can be detected by conventional structural imaging techniques such as CT and represents stable plaques with lower risk of complications. (Illustration credit: Ben Smith; from Dweck et al. [3]; with permission from Wolters Kluwer)

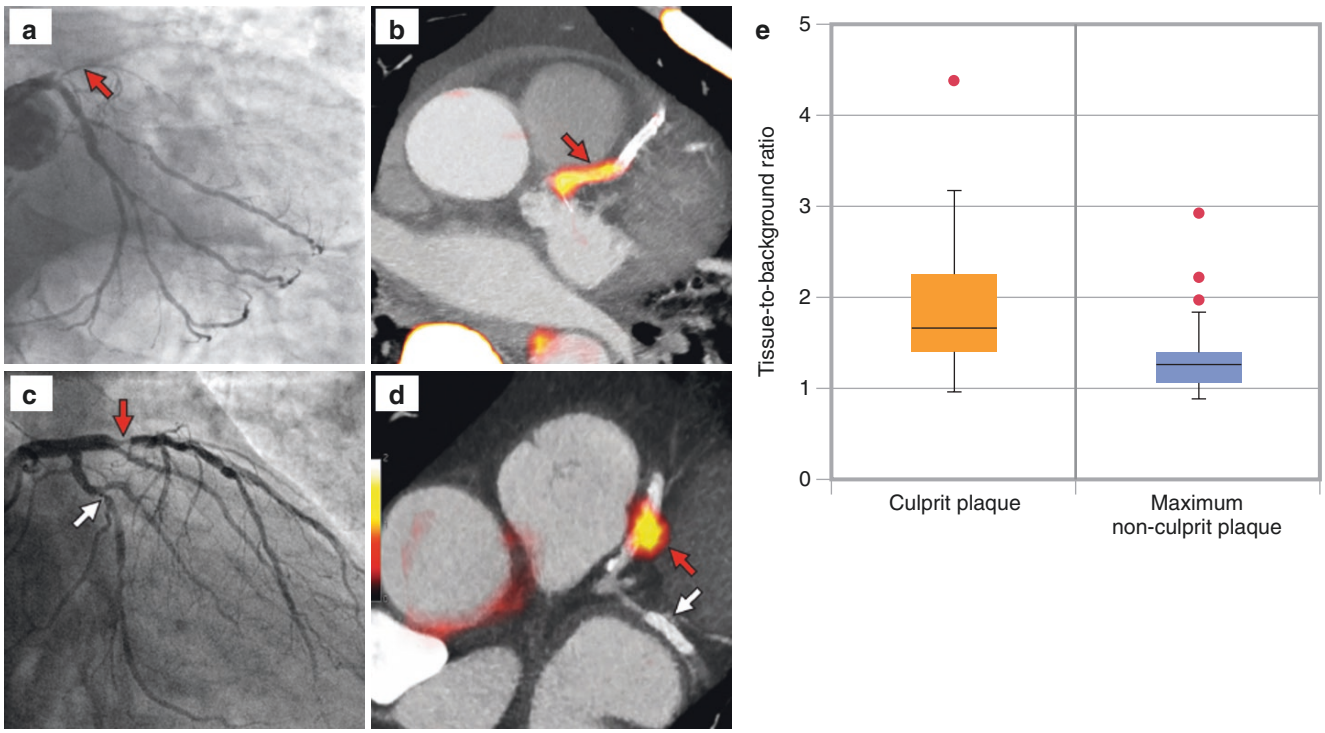

Fig. 14.13 Increased NaF uptake in coronary artery culprit lesions. PET-CT imaging, using the tracer NaF, was performed in individuals with recent myocardial infarction. *Red arrows* in coronary arteriograms of two representative patients (**a**) and (**c**) show culprit lesions in the left anterior descending artery. NaF PET-CT imaging in those same individuals (**b**) and (**d**) show intense NaF uptake in the same locations. Group mean data (**e**) reveal higher NaF activity in the culprit lesions compared with non-culprit vessels in the same patients. (From Joshi et al. [17]; CC-BY)

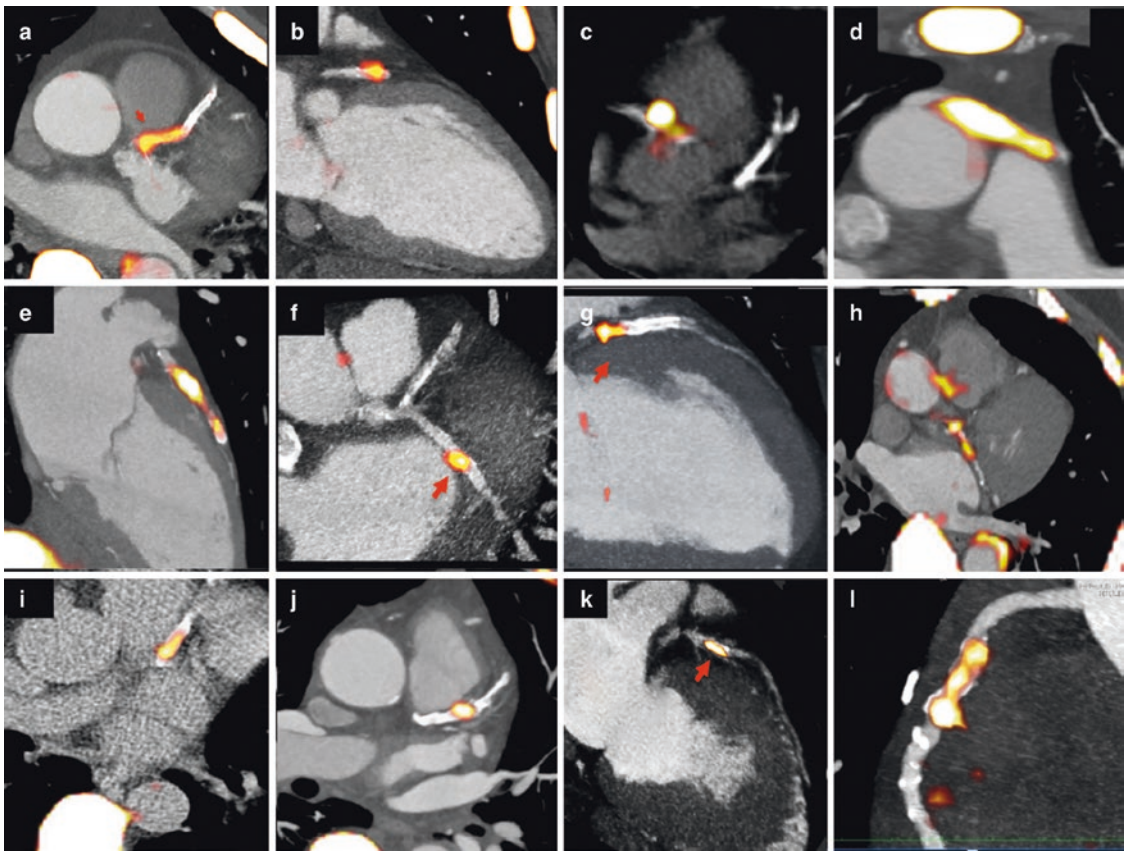

Fig. 14.14 NaF PET-CT imaging of coronary microcalcification. Images demonstrate high focal coronary NaF uptake along different vessels from several patients, including the left anterior descending artery (**a**, **b**, **e**, **g**, **i**, **j**, and **k**), circumflex artery (**f** and **h**), right coronary artery (**c** and **l**), and a saphenous vein graft (**d**). (From Dweck et al. [3]; with permission from Wolters Kluwer)

NaF PET-CT has also been used as a novel method of detecting disease activity in patients with abdominal aortic aneurysm (AAA) (Fig. 14.15), and has been reported to be a predictor of aneurysm expansion and complications in the SoFIA3 Study (NCT02229006) [19].

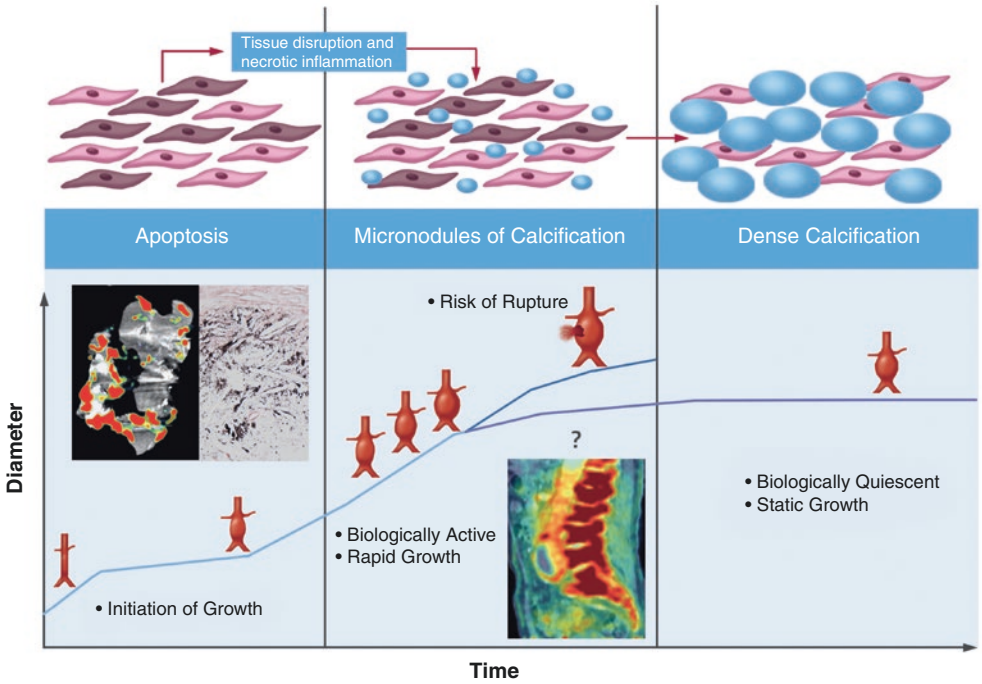

Fig. 14.15 NaF uptake in the characterization of abdominal aortic aneurysms (AAA). Higher NaF uptake within the AAA associates with an increased risk of future aneurysm expansion or clinical complications. (From Forsythe et al. [19]; CC-BY)

Gaining Insights Into Treatment Effects

It is important to review whether molecular assessments of plaque inflammation provide insight into the efficacy of therapies. FDG PET-CT imaging has been used to evaluate the impact of several drugs targeting atherosclerosis, including statins (Fig. 14.16), thiazolidinediones, cholesterol ester transfer protein modulators, lipoprotein-associated phospholipase A2 inhibitors, and P-38MAP kinase antagonists. Thus far, for each drug class tested, the changes seen on the primary FDG PET-CT imaging endpoint have been concordant with the observed clinical effect of therapy [2].

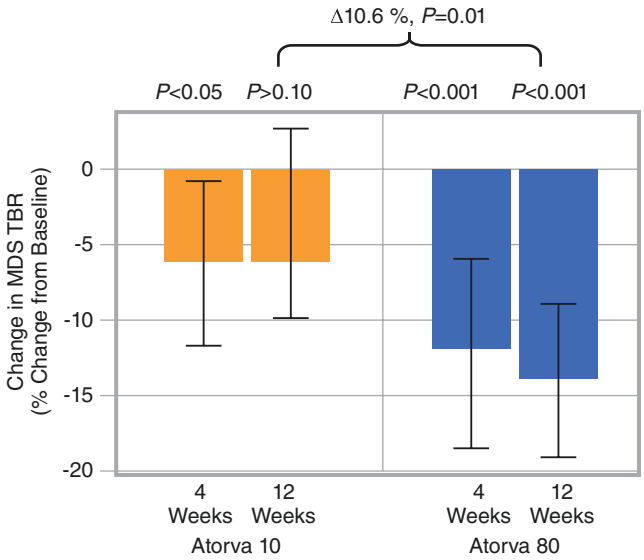

Fig. 14.16 Statin therapy and arterial inflammation in humans with or at high risk for atherosclerotic disease. Treatment with statins rapidly reduces arterial inflammation. The bars show the change (from baseline) in the most diseased segment (MDS) target-to-background ratio (TBR) in 67 individuals that were randomized to 10 mg atorvastatin versus 80 mg. Compared with baseline, atorvastatin 80 mg significantly reduced inflammation (TBR) at 4 and 12 weeks. The anti-inflammatory impact of statins was noticed as early as 4 weeks after randomization with both doses of atorvastatin. (From Tawakol et al. [20]; with permission from Elsevier)

Multitissue Imaging to Gain Unique Biological Insights in Humans

Molecular imaging of atherosclerosis with PET-CT or PET-MR provides unique opportunities for multitissue, multimodality imaging. By combining the molecular data from PET with the structural data from MR, true multimodality, multitissue imaging can be performed to study disease processes that span organs (Figs. 14.17 and 14.18).

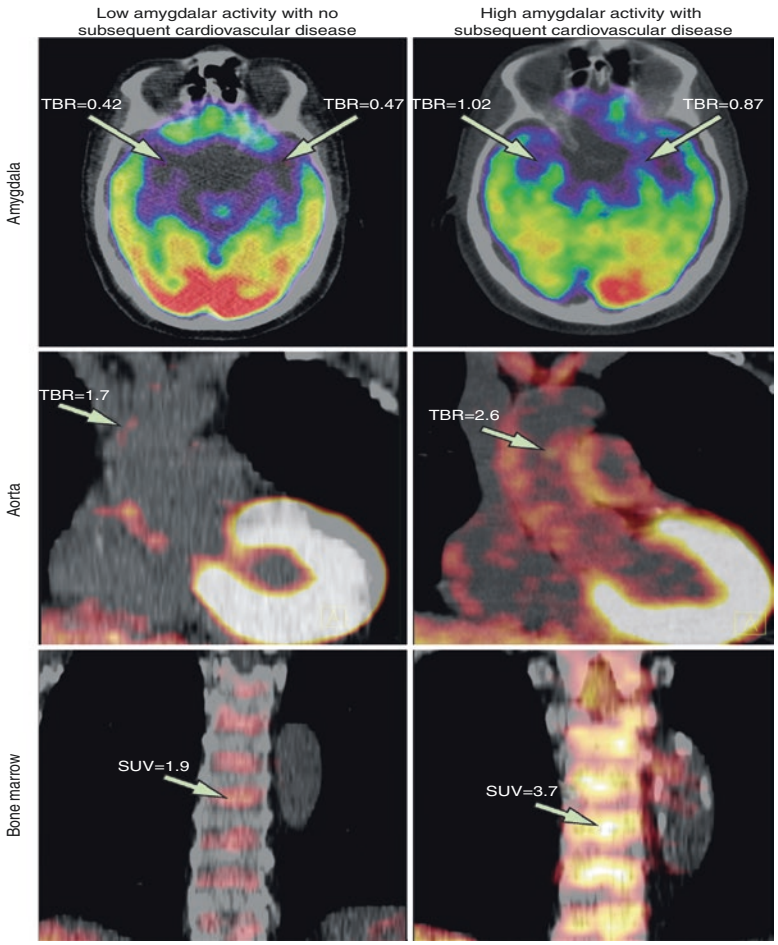

Fig. 14.17 Multimodal FDG PET-CT imaging was performed in 293 individuals who were subsequently followed for incident cardiovascular disease (CVD) events. FDG uptake was assessed in the amygdala (a neural structure that is critically involved in the stress response), the arterial wall (an index of atherosclerotic inflammation), and in the bone marrow (an index of leukopoiesis). Shown are axial views of the amygdala (top), coronal views of the aorta (middle), and coronal views of bone marrow (bottom). Higher amygdalar, arterial, and bone marrow activity are noted in a patient who developed a subsequent CVD event (right) compared with a patient who did not (left). Individuals with higher amygdalar activity had a significantly increased risk of CVD. SUV standardized uptake value, TBR target-to-background ratio. (From Tawakol et al. [21]; with permission from Elsevier)

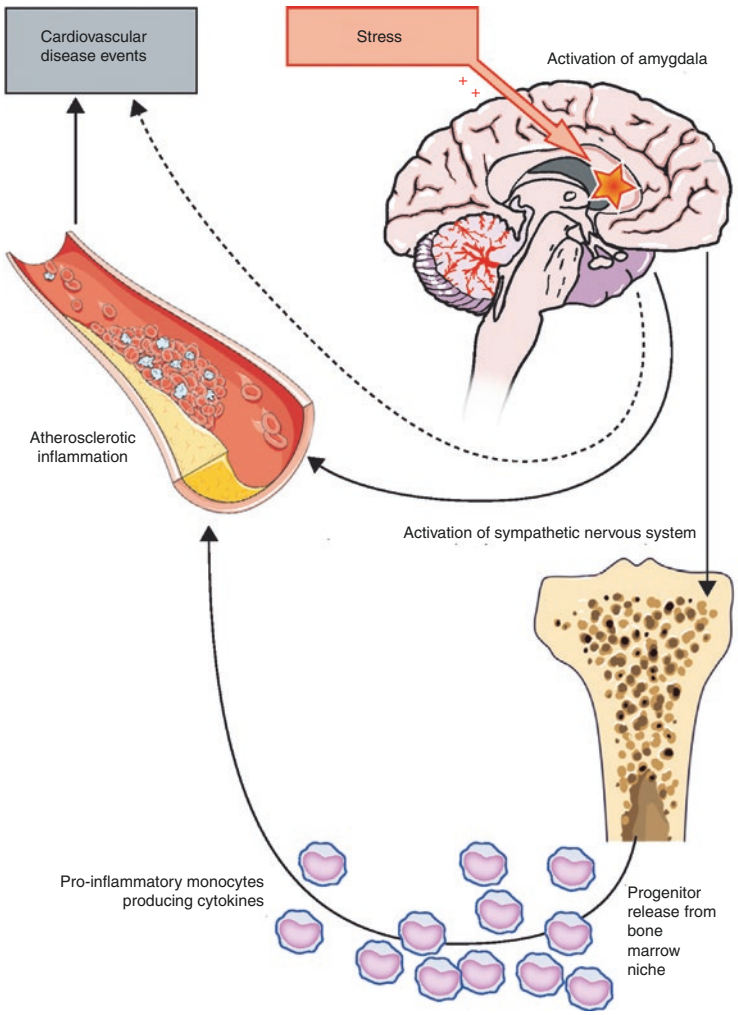

Fig. 14.18 A model linking stress to atherothrombotic events was elucidated by multimodal imaging that simultaneously evaluated the brain, bone marrow, and arterial wall. Chronic psychosocial stress results in higher stress-associated neural activity (e.g., amygdalar activity), which prompts increased activity of the sympathetic nervous system. Sympathetic efferents terminating in the bone marrow stimulate the production and release of inflammatory cells that promote worsening arterial inflammation and subsequent incident CVD events. (From Tawakol et al. [21]; with permission from Elsevier)

Potential Future Clinical Use

Evolving molecular imaging techniques, along with use of new targets and tracers, are helping to unravel the mechanisms underlying atherosclerotic plaque development and progression. Moreover, these approaches have begun to provide better insights into the risk of cardiovascular events such as acute coronary syndrome, stroke, or rupture of aortic aneurysms. In the future, molecular imaging of atherosclerosis has the potential to guide management and to assesses individual responses to therapy.

References

1. GBD 2013 Mortality and Causes of Death Collaborators. Global, regional, and national age-sex specific all-cause and cause-specific mortality for 240 causes of death, 1990-2013: a systematic analysis for the Global Burden of Disease Study 2013. Lancet. 2015;385:117–71.
2. Joseph P, Tawakol A. Imaging atherosclerosis with positron emission tomography. Eur Heart J. 2016;37:2974–80.
3. Dweck MR, Aikawa E, Newby DE, Tarkin JM, Rudd JHF, Narula J, et al. Noninvasive molecular imaging of disease activity in atherosclerosis. Circ Res. 2016;119:330–40.
4. Libby P, Ridker PM, Hansson GK. Progress and challenges in translating the biology of atherosclerosis. Nature. 2011;473:317–25.
5. Libby P. Inflammation in atherosclerosis. Arterioscler Thromb Vasc Biol. 2012;32:2045–51.
6. Ridker PM, Everett BM, Thuren T, MacFadyen JG, Chang WH, Ballantyne C, et al. Antiinflammatory therapy with canakinumab for atherosclerotic disease. N Engl J Med. 2017;377:1119–31.
7. Rudd JHF, Hyafil F, Fayad ZA. Inflammation imaging in atherosclerosis. Arterioscler Thromb Vasc Biol. 2009;29:1009–16.
8. Kim J, Feller ED, Chen W, Liang Y, Dilsizian V. FDG PET/CT for early detection and localization of left ventricular assist device infection: impact on patient management and outcome. JACC Cardiovasc Imaging. 2018; https://doi.org/10.1016/j.jcmg.2018.01.024.. [Epub ahead of print]
9. Fagman E, van Essen M, Fredén Lindqvist J, Snygg-Martin U, Bech-Hanssen O, Svensson G. 18F-FDG PET/CT in the diagnosis of prosthetic valve endocarditis. Int J Cardiovasc Imaging. 2016;32:679–86.
10. Blankstein R, Osborne M, Naya M, Waller A, Kim CK, Murthy VL, et al. Cardiac positron emission tomography enhances prognostic assessments of patients with suspected cardiac sarcoidosis. J Am Coll Cardiol. 2014;63:329–36.
11. Tawakol A, Migrino RQ, Bashian GG, Bedri S, Vermylen D, Cury RC, et al. In vivo 18F-fluorodeoxyglucose positron emission tomography imaging provides a noninvasive measure of carotid plaque inflammation in patients. J Am Coll Cardiol. 2006;48:1818–24.
12. Teague HL, Ahlman MA, Alavi A, Wagner DD, Lichtman AH, Nahrendorf M, et al. Unraveling vascular inflammation: from immunology to imaging. J Am Coll Cardiol. 2017;70:1403–12.
13. Aziz K, Berger K, Claycombe K, Huang R, Patel R, Abela GS. Noninvasive detection and localization of vulnerable plaque and arterial thrombosis with computed tomography angiography/positron emission tomography. Circulation. 2008;117:2061–70.
14. Figueroa AL, Abdelbaky A, Truong QA, Corsini E, MacNabb MH, Lavender ZR, et al. Measurement of arterial activity on routine FDG PET/CT images improves prediction of risk of future CV events. JACC Cardiovasc Imaging. 2013;6:1250–9.
15. Tarkin JM, Joshi FR, Evans NR, Chowdhury MM, Figg NL, Shah AV, et al. Detection of atherosclerotic inflammation by ^{68}Ga-DOTATATE PET compared to [^{18}F]FDG PET imaging. J Am Coll Cardiol. 2017;69:1774–91.
16. Dweck MR, Chow MWL, Joshi NV, Williams MC, Jones C, Fletcher AM, et al. Coronary arterial 18F-sodium fluoride uptake: a novel marker of plaque biology. J Am Coll Cardiol. 2012;59:1539–48.
17. Joshi NV, Vesey AT, Williams MC, Shah ASV, Calvert PA, Craighead FHM, et al. 18F-fluoride positron emission tomography for identification of ruptured and high-risk coronary atherosclerotic plaques: a prospective clinical trial. Lancet. 2014;383:705–13.
18. Prediction of Recurrent Events With 18F-Fluoride (PREFFIR). ClinicalTrials.gov [Internet]. Available from: https://clinicaltrials.gov/ct2/show/NCT02278211. Accessed 10 Jan 2019.
19. Forsythe RO, Dweck MR, McBride OMB, Vesey AT, Semple SI, Shah ASV, et al. 18 F-sodium fluoride uptake in abdominal aortic aneurysms: the SoFIA3 study. J Am Coll Cardiol. 2018;71:513–23.
20. Tawakol A, Fayad ZA, Mogg R, Alon A, Klimas MT, Dansky H, et al. Intensification of statin therapy results in a rapid reduction in atherosclerotic inflammation: results of a multicenter fluorodeoxyglucose-positron emission tomography/computed tomography feasibility study. J Am Coll Cardiol. 2013;62:909–17.
21. Tawakol A, Ishai A, Takx RA, Figueroa AL, Ali A, Kaiser Y, et al. Relation between resting amygdalar activity and cardiovascular events: a longitudinal and cohort study. Lancet. 2017;389:834–45.

Index

V. Dilsizian, J. Narula (eds.), *Atlas of Nuclear Cardiology*, https://doi.org/10.1007/978-3-030-49885-6